frontiers | Research Topics

Quantitative characterization and engineering application of pores and fractures of different scales in unconventional reservoirs

Edited by
Wenlong Ding, Shuai Yin and Hu Li

Published in
Frontiers in Earth Science

ISSN 1664-8714
ISBN 978-2-83251-485-6
DOI 10.3389/978-2-83251-485-6

About Frontiers

Frontiers is more than just an open access publisher of scholarly articles: it is a pioneering approach to the world of academia, radically improving the way scholarly research is managed. The grand vision of Frontiers is a world where all people have an equal opportunity to seek, share and generate knowledge. Frontiers provides immediate and permanent online open access to all its publications, but this alone is not enough to realize our grand goals.

Frontiers journal series

The Frontiers journal series is a multi-tier and interdisciplinary set of open-access, online journals, promising a paradigm shift from the current review, selection and dissemination processes in academic publishing. All Frontiers journals are driven by researchers for researchers; therefore, they constitute a service to the scholarly community. At the same time, the *Frontiers journal series* operates on a revolutionary invention, the tiered publishing system, initially addressing specific communities of scholars, and gradually climbing up to broader public understanding, thus serving the interests of the lay society, too.

Dedication to quality

Each Frontiers article is a landmark of the highest quality, thanks to genuinely collaborative interactions between authors and review editors, who include some of the world's best academicians. Research must be certified by peers before entering a stream of knowledge that may eventually reach the public - and shape society; therefore, Frontiers only applies the most rigorous and unbiased reviews. Frontiers revolutionizes research publishing by freely delivering the most outstanding research, evaluated with no bias from both the academic and social point of view. By applying the most advanced information technologies, Frontiers is catapulting scholarly publishing into a new generation.

What are Frontiers Research Topics?

Frontiers Research Topics are very popular trademarks of the *Frontiers journals series*: they are collections of at least ten articles, all centered on a particular subject. With their unique mix of varied contributions from Original Research to Review Articles, Frontiers Research Topics unify the most influential researchers, the latest key findings and historical advances in a hot research area.

Find out more on how to host your own Frontiers Research Topic or contribute to one as an author by contacting the Frontiers editorial office: frontiersin.org/about/contact

Quantitative characterization and engineering application of pores and fractures of different scales in unconventional reservoirs

Topic editors

Wenlong Ding — China University of Geosciences, China
Shuai Yin — Xi'an Shiyou University, China
Hu Li — Southwest Petroleum University, China

Citation

Ding, W., Yin, S., Li, H., eds. (2023). *Quantitative characterization and engineering application of pores and fractures of different scales in unconventional reservoirs*. Lausanne: Frontiers Media SA. doi: 10.3389/978-2-83251-485-6

Table of contents

frontiers | Frontiers in Earth Science

TYPE Editorial
PUBLISHED 13 January 2023
DOI 10.3389/feart.2022.1064437

OPEN ACCESS

EDITED AND REVIEWED BY
Derek Keir,
University of Southampton, United Kingdom

*CORRESPONDENCE
Hu Li,
lihu860628@126.com

SPECIALTY SECTION
This article was submitted to Structural Geology and Tectonics, a section of the journal Frontiers in Earth Science

RECEIVED 08 October 2022
ACCEPTED 25 October 2022
PUBLISHED 13 January 2023

CITATION
Li H, Ding W and Yin S (2023), Editorial: Quantitative characterization and engineering application of pores and fractures of different scales in unconventional reservoirs.
Front. Earth Sci. 10:1064437.
doi: 10.3389/feart.2022.1064437

Editorial: Quantitative characterization and engineering application of pores and fractures of different scales in unconventional reservoirs

Hu Li[1,2,3]*, Wenlong Ding[4] and Shuai Yin[5]

[1]Natural Gas Geology Key Laboratory of Sichuan Province, Chengdu, China, [2]School of Geoscience and Technology, Southwest Petroleum University, Chengdu, China, [3]Shale Gas Evaluation and Exploitation Key Laboratory of Sichuan Province, Chengdu, China, [4]School of Energy Resources, China University of Geosciences, Beijing, China, [5]School of Earth Science and Engineering, Xi'an Shiyou University, Xi'an, China

KEYWORDS

pore, fracture, unconventional reservoirs, tight reservoir, quantitative characterization

Editorial on the Research Topic
Quantitative characterization and engineering application of pores and fractures of different scales in unconventional reservoirs

In recent years, with the depletion of conventional oil and gas resources (typically represented by tight sandstone, shale, carbonate, volcanic rock, coal, gas hydrate and so on), unconventional oil and gas exploration and development has become a new hot field (Yin et al., 2019a; Yin et al., 2019b; Yin and Ding., 2019; Yin and Gao., 2019; Li et al., 2022a; Li et al., 2022b; Li et al., 2022c; Fan et al., 2022). Unconventional oil and gas reservoirs have low porosity, low permeability, strong heterogeneity, and complex diagenesis. Therefore, the quantitative characterization of pores and fractures at different scales has become the focus and challenge of high-efficiency reservoir discovery. Pores and fractures of different sizes not only affect the storage and migration capacities of unconventional oil and gas reservoirs, but also have an important impact on safe drilling and oil and gas development programs (Li et al., 2019; Yin et al., 2020a; Yin et al., 2020b; Li et al., 2020; Yin and Wu, 2020; Li et al., 2021; Li, 2022a). The set of 23 studies in this Research Topic aimed to bring together quantitative characterization and engineering application of pores and fractures of different scales in unconventional reservoirs, with the general goal of understanding multi method quantitative characterization of the tight reservoir pore and fracture systems, as well as providing a general framework for future research efforts.

The development of fine and quantitative characterization of pore structures is an effective measure to achieve efficient development of tight reservoirs (Liu et al., 2020; Xu and Gao, 2020; Xu et al., 2020). This topic covers a large number of recent advances in the

study of pores and fractures at different scales. For example, He et al. systematically studied the relationship between pyrite and nano-pores in marine shale of the Longmaxi Formation; Li et al. (2022d) analyzed the effect of water saturation on the pore structures of middle and large pores in limestone reservoirs through experiments; Lv et al. systematically studied the effects of high-temperature, overpressure, and CO_2-Charging conditions on the pore structures of sandstone; Jiao et al. studied the influencing factors and evolution law of pore development in coal measure reservoirs; Chen et al. carried out fine logging evaluation of core-scale fractures in tight oil sandstones of the Yanchang Formation, Ordos Basin; Li analyzed the coupling characteristics of fractures and faults in strike-slip fault zones. Quantitative characterization of pores and fractures at different scales can provide a basis for the prediction of sweet spots in tight reservoirs.

The combination of macro and micro research methods is an important means to realize the continuous development of pore and fracture coupling research at different scales in unconventional oil and gas reservoirs. This topic reports a large number of related studies, for example, Cheng et al. analyzed the development characteristics of different fluid components and physical properties of carbonate gas genesis; Cai et al. analyzed the coupling relationship between rock mechanical parameters and *in-situ* stress in tight sandstone. *In-situ* stress and rock mechanics parameters are the external constraints for rock deformation and rupture; He et al. systematically studied the lithofacies and microscopic pore structure characteristics of deep shales; the fault is the largest scale fracture form and Lv et al. studied the plane heterogeneity of strike-slip faults and its influence mechanism on reservoir physical properties; Tang et al. elucidated the heterogeneity of microscopic pore structures of tight sandstones using a variety of experimental methods; Wang et al. analyzed the fracture development characteristics and influencing factors of buried hill reservoirs; Xu et al. optimized the lithofacies types of continental shales; Zhang et al. analyzed the development characteristics of pores and fractures in fracture—cavity desorption in the buried hill.

The numerical simulation and engineering evaluation of pores and fractures at different scales have also made some important progress in recent years. For example, Liao et al. reported an optimized fracturing and well trajectory design model for tight oil sandstones; Luo et al. proposed a stress sensitivity evaluation model considering the starting pressure gradient; Qian et al. carried out the full inversion of complex structures concealed around a horizontal hydraulic fracturing well using perforation seismic data; Sun et al. constructed a new evaluation system of volcanic rock reservoirs based on the constraints of Energy Storage Coefficient. Yang et al. carried out numerical simulation research on the contact optimization of hydraulic and natural fractures; Yin et al. constructed the 3-D model of carbonate reef and shoal facies based on UAV oblique photogrammetry data.

We appreciate the opportunity to present this Research Topic, and hope that readers will benefit from the breadth and scope of research. This Research Topic has introduced the latest developments in the quantitative characterization and engineering application of pores and fractures of different scales in unconventional reservoirs. It is a hot Research Topic in unconventional oil and gas exploration, which has been supported by many researchers. Therefore, we applied for the Volume II of this Research Topic. We invite researchers to contribute to the new work (Volume II), which will be extended to explore as many aspects as possible in the evaluation of pores and fractures of different scales.

Author contributions

HL, SY, and WD, edited the research topic of Quantitative Characterization and Engineering Application of Pores and Fractures of Different Scales in Unconventional Reservoirs. HL and SY wrote and revised the manuscript.

Funding

This work was supported by the Open fund of Shale Gas Evaluation and Exploitation Key Laboratory of Sichuan Province (No. YSK2022002), Open fund of Natural Gas Geology Key Laboratory of Sichuan Province (No. 2021trqdz05), the key R & D projects of the Deyang science and technology plan (No. 2022SZ049) and China National Scientific and Technical Support Program (No. 2018YFC0406402).

Conflict of interest

The authors declare that the research was conducted in the absence of any commercial or financial relationships that could be construed as a potential conflict of interest.

Publisher's note

References

Fan, C. H., Xie, H. B., Li, H., Zhao, S. X., Shi, X. C., Liu, J. F., et al. (2022). Complicated fault characterization and its influence on shale gas preservation in the southern margin of the sichuan basin, China. *Lithosphere* 2022, 8035106. doi:10.2113/2022/8035106

Li, H., Tang, H. M., Qin, Q. R., Zhou, J. L., Qin, Z. J., Fan, C. H., et al. (2019). Characteristics, formation periods and genetic mechanisms of tectonic fractures in the tight gas sandstones reservoir: A case study of xujiahe formation in YB area, sichuan basin, China. *J. Pet. Sci. Eng.* 178, 723–735. doi:10.1016/j.petrol.2019.04.007

Li, H., Qin, Q. R., Zhang, B. J., Ge, X. Y., Hu, X., Fan, C. H., et al. (2020). Tectonic fracture formation and distribution in ultradeep marine carbonate gas reservoirs: A case study of the maokou formation in the jiulongshan gas field, sichuan basin, southwest China. *Energy fuels* 34 (11), 14132–14146. doi:10.1021/acs.energyfuels.0c03327

Li, H., Wang, Q., Qin, Q. R., and Ge, X. Y. (2021). Characteristics of natural fractures in an ultradeep marine carbonate gas reservoir and their impact on the reservoir: A case study of the maokou formation of the JLS structure in the sichuan basin, China. *Energy fuels* 35 (16), 13098–13108. doi:10.1021/acs.energyfuels.1c01581

Li, J., Li, H., Yang, C., Wu, Y. J., Gao, Z., and Jiang, S. L. (2022a). Geological characteristics and controlling factors of deep shale gas enrichment of the wufeng-Longmaxi Formation in the southern sichuan basin, China. *Lithosphere* 2022, 4737801. doi:10.2113/2022/4737801

Li, H., Zhou, J. L., Mou, X. Y., Guo, H. X., Wang, X. X., An, H. Y., et al. (2022b). Pore structure and fractal characteristics of the marine shale of the Longmaxi Formation in the changning area, southern sichuan basin, China. *Front. Earth Sci.* 10, 1018274. doi:10.3389/feart.2022.1018274

Li, J., Li, H., Xu, J. L., Wu, Y. J., and Gao, Z. (2022c). Effects of fracture formation stage on shale gas preservation conditions and enrichment in complex structural areas in the southern Sichuan Basin, China. *Front. Earth Sci. (Lausanne).* 9, 823855. doi:10.3389/feart.2022.921988

Li, H., Wang, J., Wang, X., Liang, W., Xu, G., and Kang, Y. (2022d). Influence of water saturation time on microstructure and mechanical properties of jointed limestone. *Front. Earth Sci.* 10, 922683. doi:10.3389/feart.2022.922683

Li, H. (2022a). Research progress on evaluation methods and factors influencing shale brittleness: a review. *Energy Rep.* 8, 4344–4358. doi:10.1016/j.egyr.2022.03.120

Liu, Y., Xian, C., Li, Z., Wang, J., and Ren, F. (2020). A new classification system of lithic-rich tight sandstone and its application to diagnosis high-quality reservoirsfication system of lithic-rich tight sandstone and its application to diagnosis high-quality reservoirs. *Adv. Geo-Energy Res.* 4 (3), 286–295. doi:10.46690/ager.2020.03.06

Xu, N. Z., and Gao, C. (2020). Study on the Special Rules of Surface Subsidence Affected by normal Faults. *J. Min Strata Control. Eng.* 2 (1), 011007. doi:10.13532/j.jmsce.cn10-1638/td.2020.01.011

Xu, G., Yin, H., Yuan, H., and Xing, C. (2020). Decline curve analysis for multiple-fractured horizontal wells in tight oil reservoirs. *Adv. Geo-Energy Res.* 4 (3), 296–304. doi:10.46690/ager.2020.03.07

Yin, S., and Ding, W. (2019). Evaluation indexes of coalbed methane accumulation in the strong deformed strike-slip fault zone considering tectonics and fractures: A 3D geomechanical simulation study. *Geol. Mag.* 156 (6), 1052–1068. doi:10.1017/s0016756818000456

Yin, S., and Gao, Z. (2019). Numerical study on the prediction of "sweet spots" in a low efficiency-tight gas sandstone reservoir based on a 3D strain energy model. *IEEE Access* 7, 117391–117402. doi:10.1109/access.2019.2933450

Yin, S., and Wu, Z. (2020). Geomechanical simulation of low-order fracture of tight sandstone. *Mar. Petroleum Geol.* 100, 104359. doi:10.1016/j.marpetgeo.2020.104359

Yin, S., Xie, R., Wu, Z., Liu, J., and Ding, W. (2019a). *In situ* stress heterogeneity in a highly developed strike-slip fault zone and its effect on the distribution of tight gases: A 3D finite element simulation study. *Mar. Petroleum Geol.* 99 (1), 75–91. doi:10.1016/j.marpetgeo.2018.10.007

Yin, S., Han, C., Wu, Z., and Li, Q. (2019b). Developmental characteristics, influencing factors and prediction of fractures for a tight gas sandstone in a gentle structural area of the Ordos Basin, China. *J. Nat. Gas Sci. Eng.* 72 (12), 103032–103114. doi:10.1016/j.jngse.2019.103032

Yin, S., Tian, T., Wu, Z., and Li, Q. (2020a). Developmental characteristics and distribution law of fractures in a tight sandstone reservoir in a low-amplitude tectonic zone, eastern Ordos Basin, China. *Geol. J.* 55, 1546–1562. doi:10.1002/gj.3521

Yin, S., Dong, Li., Yang, Xia., and Wang, R. (2020b). Experimental investigation of the petrophysical properties, minerals, elements and pore structures in tight sandstones. *J. Nat. Gas Sci. Eng.* 76 (1), 103189–103214. doi:10.1016/j.jngse.2020.103189

frontiers in Earth Science

ORIGINAL RESEARCH
published: 15 February 2022
doi: 10.3389/feart.2022.860473

Fine Logging Evaluation of Fractures in Continental Tight Oil Sandstone Reservoirs of Yanchang Formation in the Ordos Basin

Zhanjun Chen[1]*, *Anzhao Ji*[1] and *Yidong Yuan*[1,2]

[1]School of Energy Engineering, Longdong University, Qingyang, China, [2]State Key Laboratory of Continental Dynamics, Northwest University, Xi'an, China

Fractures are the main seepage channels in tight reservoirs, and they affect the distribution of high-quality reservoirs and the enrichment of hydrocarbons. Fine logging identification of fractures in the strongly heterogeneous continental tight oil reservoirs of the Upper Triassic Yanchang Formation in the Ordos Basin is a hot and difficult point in the field of petroleum geology. In this paper, taking the Yanchang Formation as an example, a fractal model was constructed to identify fractures in tight oil reservoirs using a large number of cores, conventional and micro-resistivity imaging logging data. The results show that high-angle, vertical and bedding fractures are mainly developed in the Yanchang Formation tight sandstones. There is a negative correlation between sand body thickness and fracture development degree. The fracture sensitivity parameters were used to construct a coupled fractal fracture index. The fractal model incorporates logging information from natural gamma, acoustic wave time difference, rock density, and shallow lateral resistivity. In addition, the constructed fracture fractal index realizes the functions of multi-conventional logging information fusion, which can effectively identify fracture development segments in sandstone. According to the statistics, the fracture identification rate is 83.3%. The study also found that with the increase of sandstone brittleness index, the fracture index has a "S" shape increasing trend. Therefore, the content of brittle mineral components in sandstone is an important factor affecting the development degree of natural fractures, and fractures are more likely to occur in high brittle, thin sand bodies. The highly brittle framework minerals have strong stress-supporting capacity, which can keep fractures open by resisting high overlying loads.

Keywords: ordos basin, yanchang formation, tight oil reservoirs, fractures, logging evaluation

OPEN ACCESS

Edited by:
Shuai Yin,
Xi'an Shiyou University, China

Reviewed by:
Peng Wang,
Yibin University, China
Shaoke Feng,
Chengdu University of Technology, China

****Correspondence:***
Zhanjun Chen
chenzj146@163.com

Specialty section:
This article was submitted to Structural Geology and Tectonics, a section of the journal Frontiers in Earth Science

Received: *23 January 2022*
Accepted: *31 January 2022*
Published: *15 February 2022*

Citation:
Chen Z, Ji A and Yuan Y (2022) Fine Logging Evaluation of Fractures in Continental Tight Oil Sandstone Reservoirs of Yanchang Formation in the Ordos Basin. Front. Earth Sci. 10:860473. doi: 10.3389/feart.2022.860473

INTRODUCTION

In recent years, continental tight sandstone is considered to be another new hot spot in the global unconventional oil and gas exploration and development after shale gas (Dong et al., 2018; Chen et al., 2021). Natural fractures are commonly developed in tight oil sandstone reservoirs, and the degree of fracture development is a key factor for whether low permeability reservoirs can obtain high and stable productivity (Casini et al., 2016; Bhatti et al., 2020; Bukar et al., 2021). Fractures have well geophysical responses in well logs, so well logs are often used to identify natural fractures (Hu

et al., 2020; Guo et al., 2021; Han et al., 2021; He et al., 2021). At present, the research methods of tight reservoir fractures around the world include core observation, experimental testing, conventional, imaging logging and seismic prediction (Nakaya and Nakamura., 2007; Lai et al., 2018; Li., 2021). The comprehensive evaluation of fractures involves the genesis mechanism, prediction and distribution law of fractures (Santosh and Feng., 2020; Wang and Wang., 2021; Xu and Dowd., 2010; Li, et al., 2020). Logging identifications of fracture are generally based on a single conventional log series or based on multiple log series (Dong et al., 2018; Chen et al., 2021; Han et al., 2021). Among them, fracture identification *via* multi-logging parameters has high fracture identification accuracy. Fracture identification models with multiple logging parameters are usually constructed on the basis of multiple regression method, differential equivalent model, principal component analysis, and variable-scale fractal theory (Yin and Wu., 2020; Han et al., 2021).

Large-scale tight sandstone reservoirs are developed in the Upper Triassic Yanchang Formation in the Ordos Basin. The distribution law of strong heterogeneity tight sandstone reservoirs is very complex (Cao et al., 2020; Lai et al., 2018). Previous predictions for "sweet spots" of oil reservoirs in the Ordos Basin were mainly based on studies for source rock distribution, sedimentary microfacies, petrophysical properties and diagenesis (Fan et al., 2020a; Fan et al., 2020b; Fu and Wang., 2020). However, in recent years, a large number of core-scale fractures have been found in the tight sandstones of the Yanchang Formation in the marginal areas of the Ordos Basin. Most of these fractures are vertical fractures with shearing properties, and their vertical penetration depths are mostly in the range of 1–5 m. The presence of fractures can significantly increase the permeability of tight reservoirs (Gao., 2019; Fan., 2020; Hong et al., 2020).

The strata of the Yanchang Formation in the western Ordos Basin are relatively gentle as a whole, and the horizontal fluctuation of the stratum per kilometer is usually less than 10 m. However, compared with the tectonic stability zone in the central Ordos Basin, the tectonic activity in the western Ordos Basin is relatively stronger, which is manifested by the development of small-scale faults and fractures (Lai et al., 2018; Yin, et al., 2018). However, with the in-depth exploration and development of hydrocarbons, more and more fractures have been discovered in the tight sandstones in the low-amplitude structural areas of the Ordos Basin. Although the degree of fracture development is relatively low, its influence on the migration and accumulation of oil and gas cannot be ignored (Olson et al., 2009; Peacock et al., 2018). On the one hand, these fractures can enhance the fluid migration ability and hydrocarbon accumulation, and on the other hand, they can affect the fracturing effect and well pattern deployment. Therefore, fractures are an important parameter in the evaluation of petroleum geology and engineering. For tight oil reservoirs, how to maintain long-term stable production and enhance oil recovery is the main problem faced by many oilfield companies. Therefore, it is particularly important to find an effective method for fine evaluation of fractures in tight reservoirs.

At present, there are few systematic studies on the fine logging evaluation of the tight oil reservoirs in the Yanchang Formation in the western Ordos Basin. Existing studies mainly focus on the qualitative aspects of fracture identification, fracture type classification, fracture origin and its evolution mode. In this paper, taking the Yanchang Formation as an example, a fractal model was constructed to identify fractures in tight oil reservoirs, combining a large number of cores, conventional and micro-resistivity imaging logging data. This study can provide guidance for the prediction of tight oil sweet spots in similar areas.

MATERIALS AND METHODS

Study Area and Target Layer

The study area is located in Block J (**Figure 1A**) in the west of the Yishan Slope, Ordos Basin, and the target layers are the Chang 6 and Chang 8 Members of the Upper Triassic Yanchang Formation (**Figure 1B**). The target layer has the structural form of low in the west and high in the east, but the strata in the west are buried deeper than those in the east. Nine oil groups are developed in the Upper Triassic Yanchang Formation, which are Chang 1, 2, 3, 4 + 5, 6, 7, 8, 9 and 10 Members from top to bottom. The Chang 6 and Chang 8 Members in the study area belong to delta sediments, and their provenance mainly came from the northern and NNE regions. Furthermore, the sedimentary microfacies can be further divided into distributary river channels and inter-distributary bays. In addition, the lithology of the target layer is feldspar sandstone, the porosity is mainly distributed in 5–10%, and the permeability is mainly distributed in 0.01–5 mD. The thickness of the sand bodies in Chang 6 and Chang 8 Members in the study area varies greatly, and the thickness of the strongly heterogeneous sand bodies is usually 0–25 m.

The Yanchang Formation in the study area has the characteristics of multi-layer oil-bearing, wide sand body distribution and complex hydrocarbon accumulation. The Chang 6 and Chang 8 Members are the main layers of hydrocarbon accumulation. **Figure 2** shows a well-connected section of the formation from Chang 6 to Chang 8 of the Yanchang Formation in the study area. It can be seen that the continental sediments of the Yanchang Formation are characterized by frequently interbeded sandstones and mudstones, and it is an important reason for the strong heterogeneity of hydrocarbon distribution. The areas with good lateral sand body connectivity represent distributary river channels, while in the areas on both sides of a certain main river channel, the sand bodies gradually become poorly connected (**Figure 2**). For the interdistributary bay areas, the proportion of mudstone is usually much greater than 60%. Thus, the lenticular sandstone is encased in thick mudstone (**Figure 2**).

The Chang 6 oil layer group in the study area is divided into four subgroups, Chang 6_1, Chang 6_2, Chang 6_3 and Chang 6_4

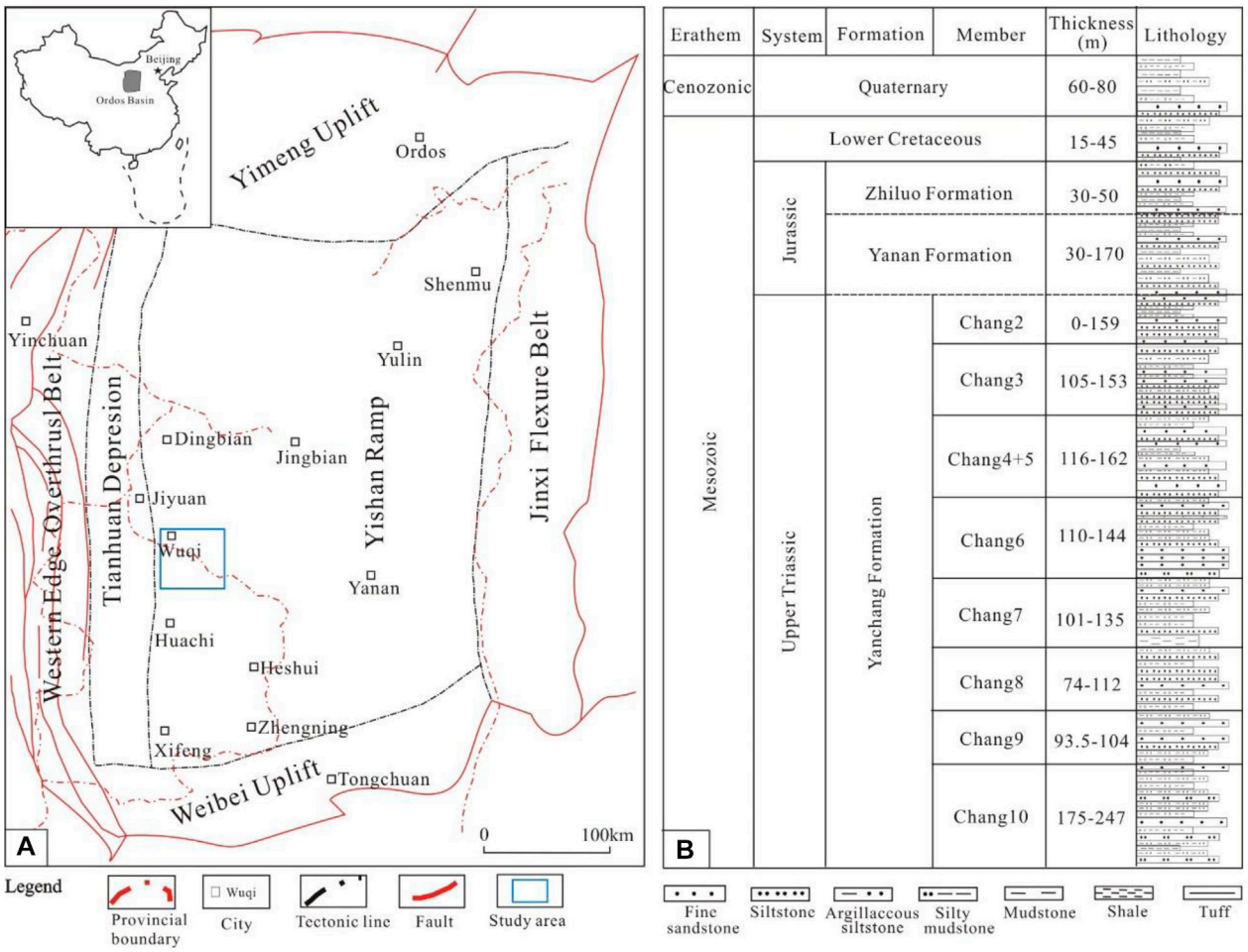

FIGURE 1 | Location of the study area and division of stratigraphic units of the Upper Triassic Yanchang Formation. **(A)** The study area is located in Block J in the west part of the Yishan Slope, Ordos Basin; **(B)** The target layer is the Chang 6 and Chang 8 Members of the Upper Triassic Yanchang Formation.

from top to bottom; while the Chang 8 oil layer group is divided into two sub-groups, Chang 8_1 and Chang 8_2, from top to bottom. The average porosity, permeability, oil saturation, and effective oil layer thickness of the target sandstone are 12%, 2.4 mD, 58%, and 6.5 m, respectively.

The target layer belongs to the delta front facies deposition, and the sand bodies have a wide distribution range and good spatial continuity. In addition, the maturity of the clastic grain composition in the sandstone is generally low, and the structural maturity is medium to good. For the interstitial component, it is mainly composed of clay minerals, carbonate minerals and matrix. The pore types of Chang 6 and Chang 8 sandstone reservoirs are mainly intergranular pores and secondary dissolved pores, which are typical low-porosity and low-permeability sandstone reservoirs.

There are a total of 150 wells in the study area, all of which have complete conventional logging. Fractures were observed in cores of 196 m target layer in 10 wells. Moreover, micro-resistivity imaging logging was conducted in 4 wells.

Construction of Fracture Index Based on Fractal Model

The essence of fracture identification based on fractal principle is to identify fractures by reducing the dimension of well logging data. The ratio (R/S) of the range (R) to the standard deviation (S) of the logging data was used to analyze the fluctuation of the data, and to determine the intervals where there may be fractures. The expressions of R and S are shown in **formula (1)** and **formula (2)** (Pang and North, 1996):

$$R(t,n) = \max_{0<u<n}\left\{\sum_{i=1}^{u} x(t+i) - \frac{u}{n}\sum_{j=1}^{n} x(t+j)\right\} - \min_{0<\mu<n}\left\{\sum_{i=1}^{u} x(t+i) - \frac{u}{n}\sum_{j=1}^{n} x(t+j)\right\} \quad (1)$$

$$S(t,n) = \sqrt{\frac{1}{n}\sum_{i=1}^{n}\left[x(t+i) - \frac{1}{n}\sum_{j=1}^{n} x(t+j)\right]} \quad (2)$$

In the formula, $R(t, n)$ is the distance of the sampling point sequence used for calculation; $S(t,n)$ is the variance of the

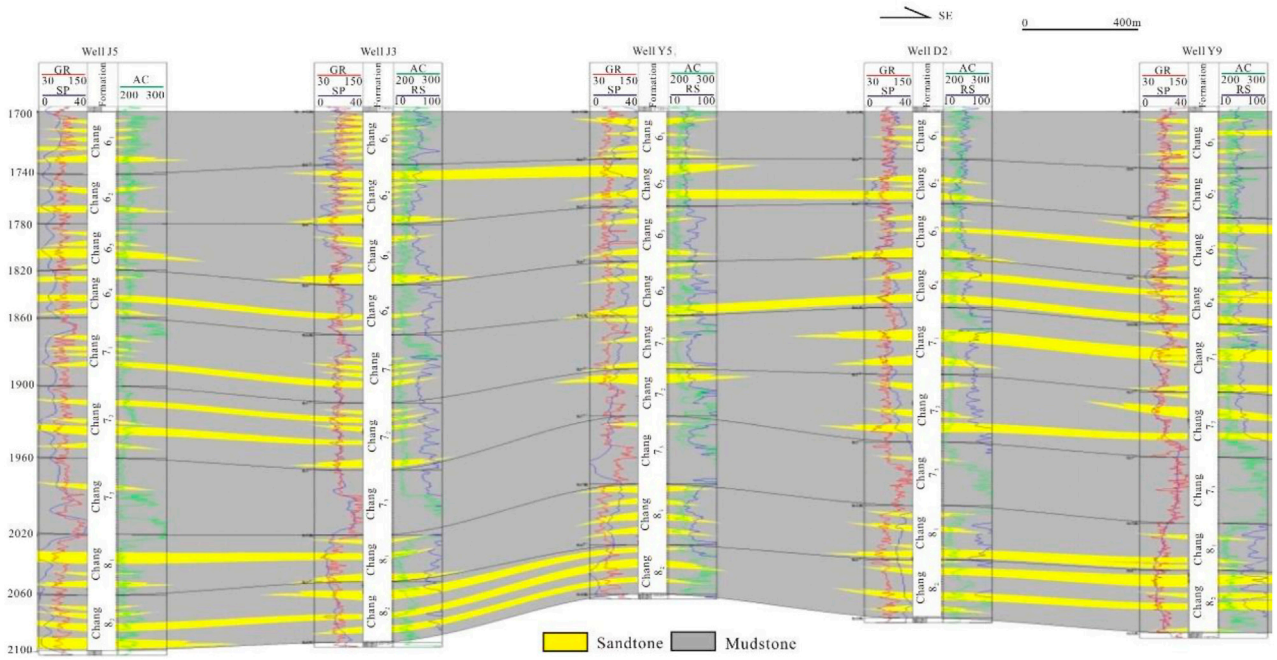

FIGURE 2 | The stratigraphic well-connected profile of the Chang 6 to Chang 8 Members of the Yanchang Formation through the J5-Y9 wells in the study area.

sampling points used for calculation; n is the number of intervals between sampling points, $n < M$; t is the serial number of the first sampling point in the sampling point; $x\ (t + i)$ is the calculated sampling point data.

In double logarithmic coordinates, $R(n)/S(n)$ has a linear relationship with n, and its slope H is called the Hurst exponent. H is related to the fractal dimension D, and has $H = 2\text{-}D$. Generally, the larger the value of fractal dimension D, the more developed the fractures (Barton et al., 2009; Camac and Hunt., 2009; Anders et al., 2014). The log curves that reflect the fractures significantly are selected to calculate the fractal dimension and weighted, and then the fractal index (FI) is obtained:

$$FI = \frac{1}{n}\left(\sum_{i=1}^{n} d_i \times D_i\right) \tag{3}$$

In the formula, FI is the indicator parameter of the rate of change of the arithmetically weighted curve; n is the number of characteristic parameters reflecting the rate of change of the curve; d_i is the weighting coefficient of the fractal dimension of the ith curve; D_i is the fractal dimension of the ith curve.

The FI is calibrated by imaging data, and the lower fracture limit is set to 1. In turn, FI was used to further screen the fractured segments. Through the construction of the fracture index (FI) based on the fractal calculation of the log curves, the fine logging identification of the fracture development segment can be realized. The input parameters of this model are all conventional logging parameters, and the fusion and gradual elimination of multi-conventional logging information is realized. The technical route of this study based on the conventional logging fracture identification model is shown in **Figure 3**.

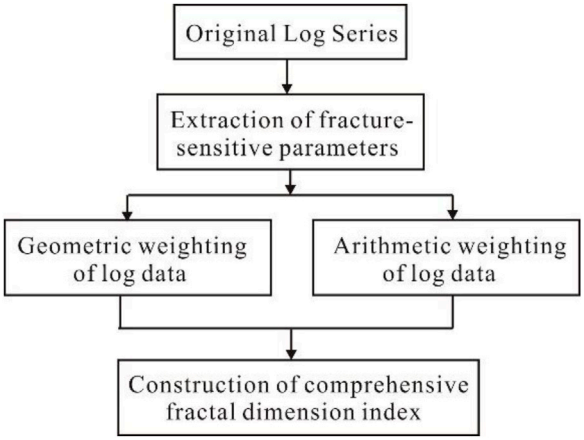

FIGURE 3 | Workflow of fracture identification model based on coupling of multiple conventional logging parameters.

Fracture Development Characteristics of Tight Sandstone Reservoirs

Outcrop and Core-scale Fractures

According to the statistical results of fracture observations in field outcrops and 196 m cores from 10 wells in the study area, high-angle, vertical and bedding fractures are mainly developed in the Chang 6 and Chang 8 tight sandstones of the Yanchang

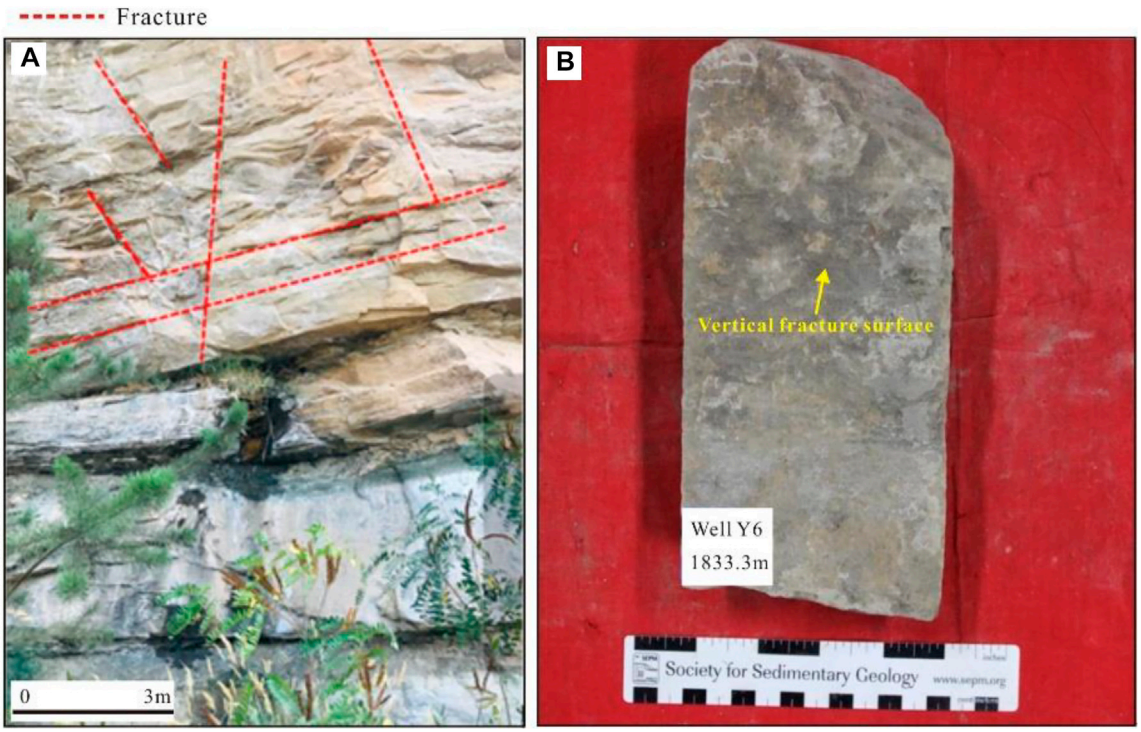

FIGURE 4 | Development characteristics of fractures in the Yanchang Formation sandstone in the study area. **(A)** Yanhe Profile, Chang 6 Member outcrop; **(B)** High angle fracture, Well Y6, Chang 6 Member, 1,833.3 m.

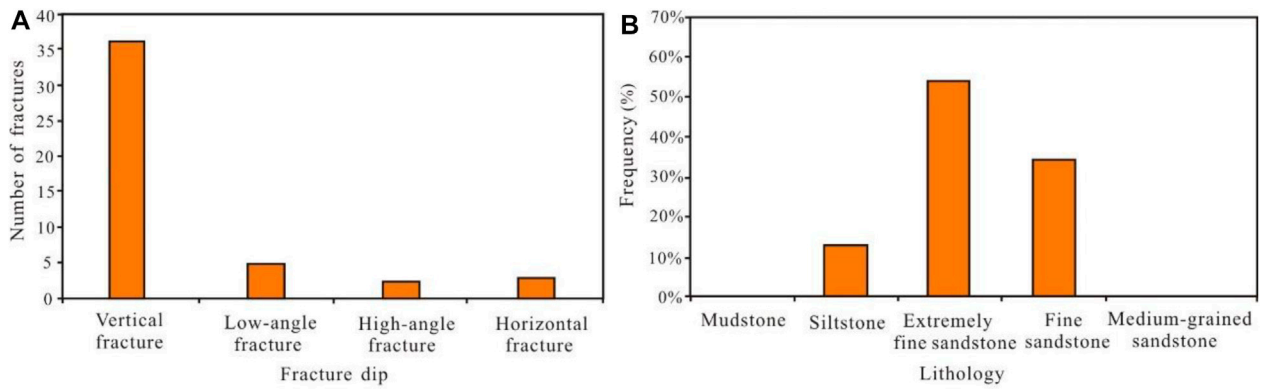

FIGURE 5 | Histogram of fracture parameter distribution. **(A)** Classification of fracture types based on fracture dip angle; **(B)** Classification of lithological types of sandstone.

Formation in the western Ordos Basin (**Figure 4**). These fractures generally have shearing properties. The shear fractures are formed by the deformation of the rock mass under the action of strong compressive stresses, so they are tectonic fractures. The fracture surfaces of the shear fractures are very straight and scratches are common, and the dead ends between the fractures can be seen as folded tails. However, bedding fractures are formed by the dislocation of bedding or weak planes in the rock mass (Xu et al., 2006; Chen., 2020; Cheng et al., 2020).

The fracture surfaces found in core observation are mostly straight and smooth, and the ends of the fractures have folded tails, rhombus knot rings and rhombus bifurcations. The fractures in **Figure 5A** have been divided into four categories: horizontal, low-angle, high-angle, and vertical fractures, and the fracture dip angles are <5°, 5°–45°, 45°–85°, and >85°, respectively. Statistics show that vertical fractures account for 81.4%, low-angle, high -angle and horizontal fractures account for 6.2, 5.4 and 7%, respectively (**Figure 5A**). Vertical and oblique fractures

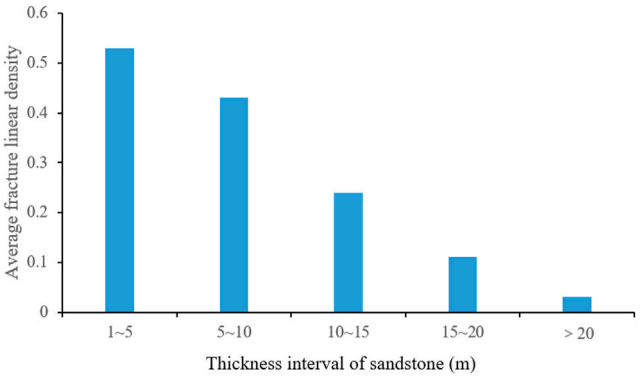

FIGURE 6 | Relationship between the thickness of fractured sand bodies and the thickness of single-layer sandstone in the Chang 6 and Chang 8 oil layer groups in the study area.

(low-angle and high-angle fractures) are mainly formed by regional tectonic shearing; bedding fractures are mainly formed by the sliding of parallel bedding with peeling lines under the combined action of sedimentary and tectonic stresses (Dcrshowitz and Einstein., 1988; Du et al., 2019). There is also a close relationship between fractures and lithology. According to the statistical results, fractures are mainly developed in fine and ultrafine sandstones in distributary river channels and mouth bars, while fractures in far sand bars, sheet sand and mudstones are relatively underdeveloped (**Figure 5B**). Fracture linear density is often used to indicate the degree of fracture development in cores. The fracture linear density in the Yanchang Formation cores in the study area is usually within 0.2/m, and is concentrated at 0.04–0.16/m.

Figure 6 is the statistical results of the relationship between fracture linear density and sandstone thickness according to imaging logging. It can be seen from **Figure 6** that with the increase of sandstone thickness, the thickness of fracture development gradually decreases. Specifically, when the thickness of the sandstone single layer is small (generally less than 5 m), the thickness of the sandstone is positively related to the thickness of the sandstone with developed fractures. When the thickness of the sandstone is large (generally greater than 20 m), the fractures in the sandstone are not developed. The stress concentration of local sand bodies is an important reason for the formation of fractures.

Fracture Identification by Micro-Resistivity Imaging Logging

Open fractures typically appear as dark sinusoids on imaging logs, while vertical fractures appear as symmetrical dark lines (**Figure 7**). When the formation fractures are half-filled or

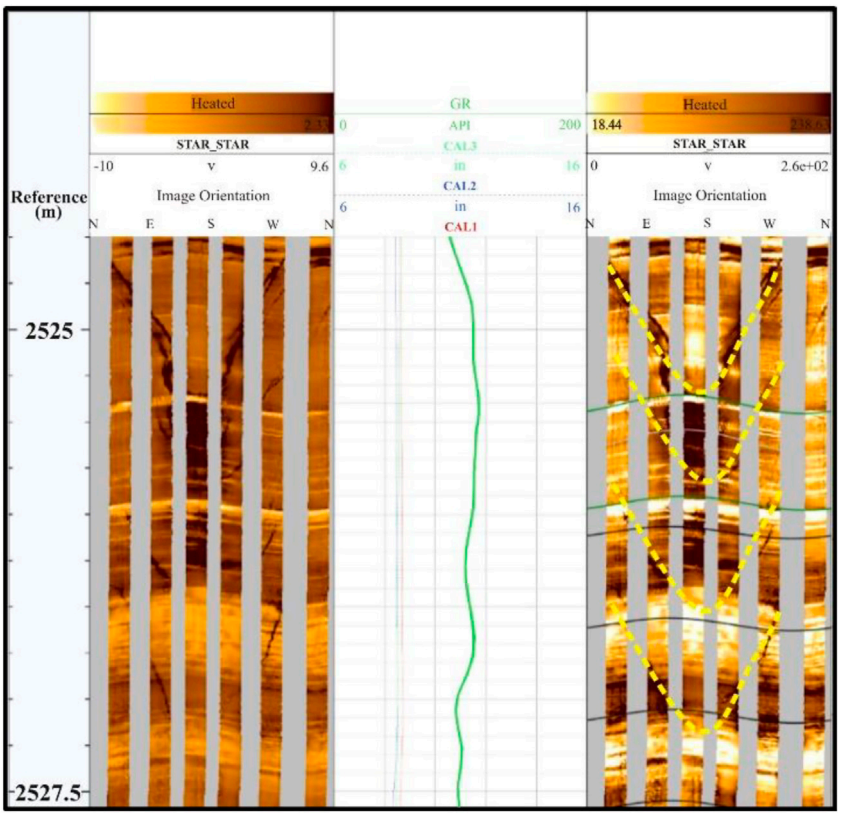

FIGURE 7 | Imaging log response of fractures in Yanchang Formation in Well D41. GR - natural gamma; CAL1~CAL3 - three well diameters measured by the six-wall dip tool.

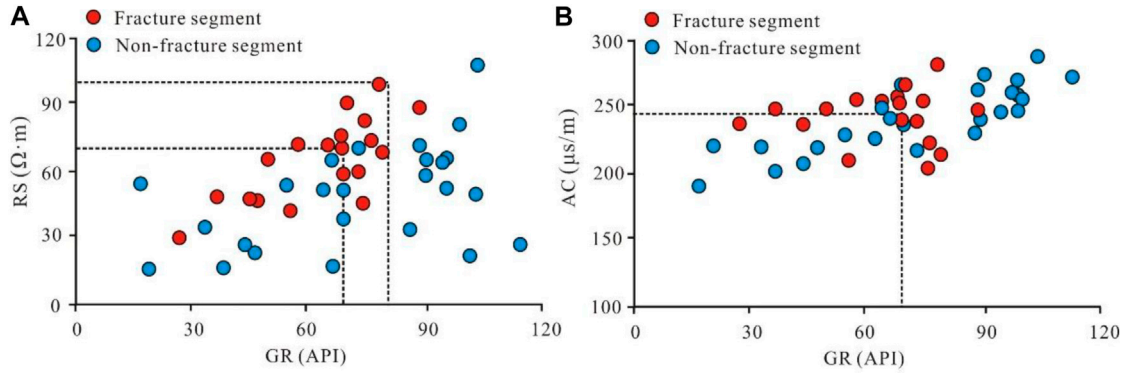

FIGURE 8 | Sensitivity analysis of fractures to conventional logging parameters of target sandstone. **(A)** Relationship between RS and GR of fractured and non-fractured sandstones; **(B)** Relationship between AC and GR of fractured and non-fractured sandstones. GR-natural gamma; RS-shallow lateral resistivity; AC-longitudinal wave time difference.

completely filled, the color of the sinusoidal curve displayed on the electro-imaging and acoustic imaging maps is different, depending on the filling degree and filling material. It is worth noting that in the identification of fractures in imaging logging, wellbore scratches, borehole collapse, and fractures induced by drilling tools due to engineering factors will interfere with the identification of normal fractures. Artificial fractures caused by these engineering factors have been excluded in this study.

Fracture Log Identification Based on Fractal Model

Fracture Sensitivity of Conventional Logging Parameters

The response of fractures on logging is mainly reflected in the series of lithology, resistivity and porosity. Lithology logging series includes natural gamma (GR), well diameter (CAL) and spontaneous potential (SP). Fractures always act as the migration channels and accumulation sites of underground fluids, and the migration and accumulation of fluids may lead to the precipitation of radioactive substances and then lead to radioactivity enhancement. However, the increase in the natural gamma value is generally weak, and it usually appears as a relative increase on a background of relatively low values of the natural gamma curves (Fan et al., 2020c; Fan et al., 2019).

In tight sandstone formations, due to the small porosity and strong brittleness of the formation, the formation is easily broken under the action of drilling torque force. This phenomenon is particularly prominent in fracture-developed areas, which can easily lead to expansion of well diameter. Therefore, the variation of well diameter can be used to predict the development intervals of fractures. Generally, when high-angle fractures are developed in the formation, the direction of well diameter expansion is consistent with the minimum horizontal principal stress of the formation, which indicates the development direction of the fractures (Laubach et al., 2009; Jiang et al., 2016; Huang et al., 2021). In fact, there are many factors that cause the change of well diameter. Lithology changes and their combined characteristics

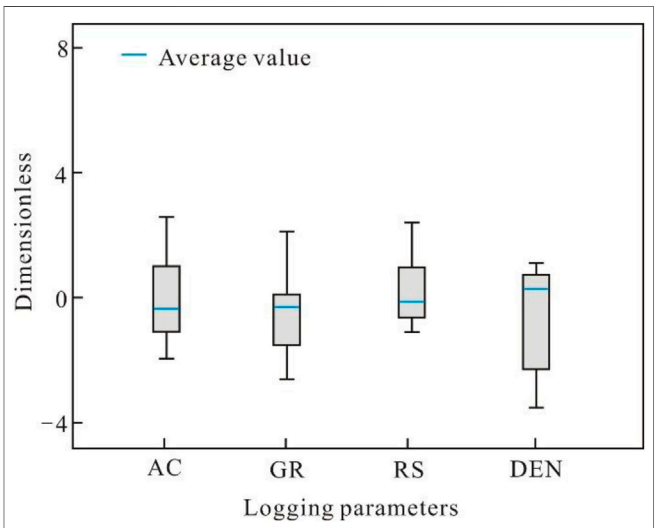

FIGURE 9 | Normalization of raw logging data. AC-longitudinal wave time difference; GR-natural gamma; RS-shallow lateral resistivity; DEN-rock density.

can cause well diameter changes. The well diameter of Chang 6 and Chang 8 reservoirs in the study area is affected by the scale of fracture development. In the low fracture development zone, the size of the wellbore drilled is basically unchanged. However, in the relatively developed area of vertical fractures, the well diameter of some wells has changed slightly (Mardia et al., 2007; Kang., 2021; Liu et al., 2021). For the natural potential, the fracture-developed intervals have better infiltration, and the natural potential curve shows a slight negative anomaly.

During the drilling process, the drilling fluid will invade the formation along the fractures in the formation, thereby changing the resistivity value of the rock. In the fracture development section, the resistivity appears abnormally low. It tends to appear as a needle-like sudden jump in low resistivity against a background of deep or shallow lateral resistivities (RD or RS).

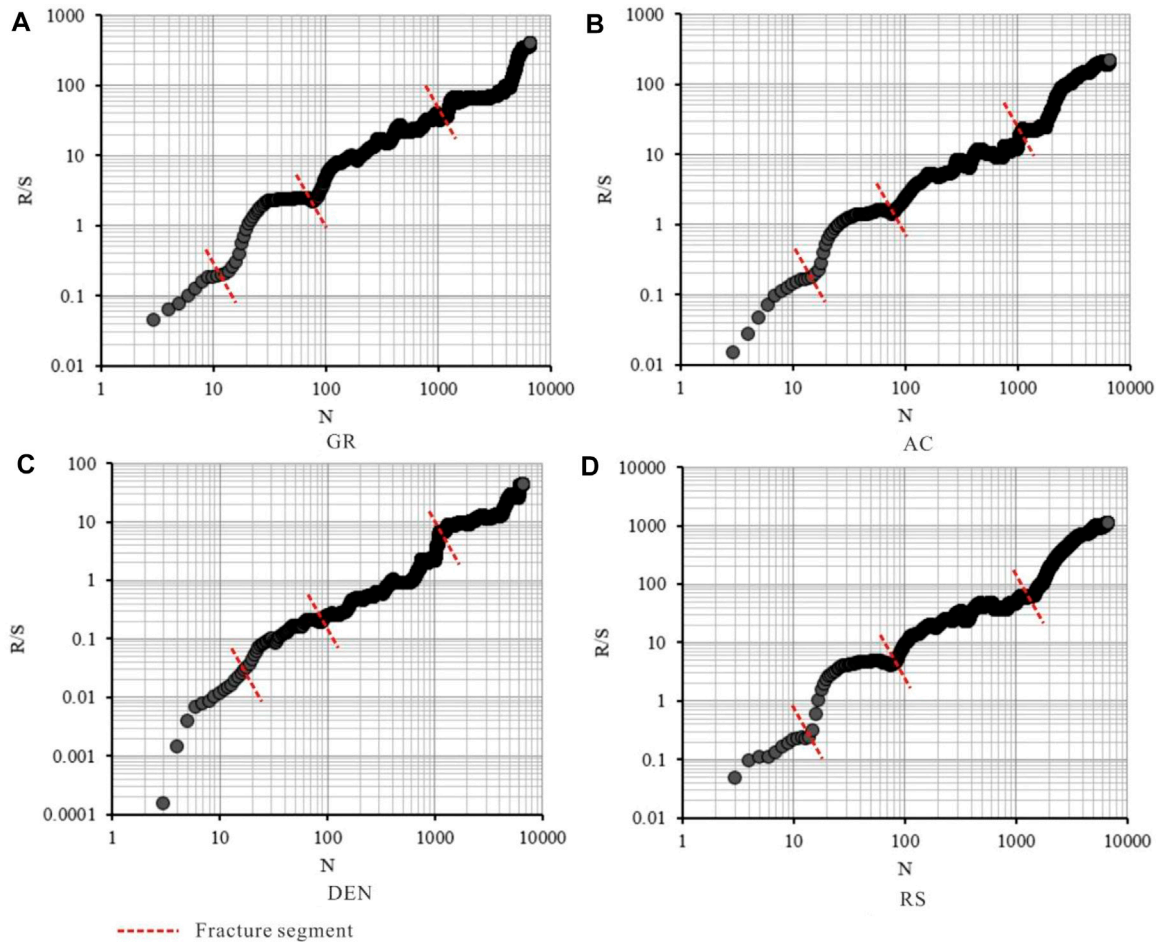

FIGURE 10 | Correlation between R/S and N of different fracture-sensitive logging parameters and their coupling relationship with fracture segment. **(A)** GR logging series; **(B)** AC logging series; **(C)** DEN logging series; **(D)** RS logging series. GR-natural gamma; AC-longitudinal wave time difference; DEN-rock density; RS-shallow lateral resistivity.

Where there are fractures, there are usually obvious abnormally low values of microlateral resistivity. For open, horizontal or low-angle fracture development sites, the octagonal resistivity (RFOC) typically exhibits low values.

Microelectrode resistivity logging has a small detection range and high vertical resolution. When the water-based drilling fluid is used to drill to the fracture-developed intervals, the micro-potential and micro-gradient curve values of the micro-electrode will decrease to a certain extent (Nelson., 1985; Ortega et al., 2006; Mizoguchi and Ueta., 2013). However, in formations with higher shale content, the relative magnitude of resistivity reduction will be attenuated due to the low resistivity background value. The Chang 6 and Chang 8 members in the study area are dominated by sandstone, mudstone and shale, with high shale content. Well sections with developed fractures generally show a small positive difference or insignificant amplitude difference between deep and shallow resistivity.

Fractures will form an obvious acoustic impedance interface in the rock, and this characteristic becomes the theoretical basis for the application of acoustic wave detection technology (Paiaman and Ghanbarian., 2021; Pang and North., 1996). When horizontal or low-angle fractures exist in the formation, the acoustic wave time difference (AC) often increases or periodically jumps. The more fractures are developed, the greater the amplitude of the increase of the acoustic wave time difference. Moreover, fractures with different occurrences have different logging responses. The smaller the fracture dip angle, the greater the increase of the acoustic wave time difference. Since the Chang 6 and Chang 8 reservoirs in the study area mainly develop high-angle and vertical fractures, the increase of acoustic wave time difference caused by fractures is not obvious.

Density logging (DEN) is the bulk density of a formation irradiated with radiation emitted by a gamma source and measured according to the Compton effect. When the density logging electrode comes into contact with the natural fractures invaded by the mud, the porosity increases accordingly, and the density value decreases accordingly (Robinson et al., 1998; Qie et al., 2021).

Conventional logging curves are comprehensive responses to the characteristics of the wellbore and surrounding formation

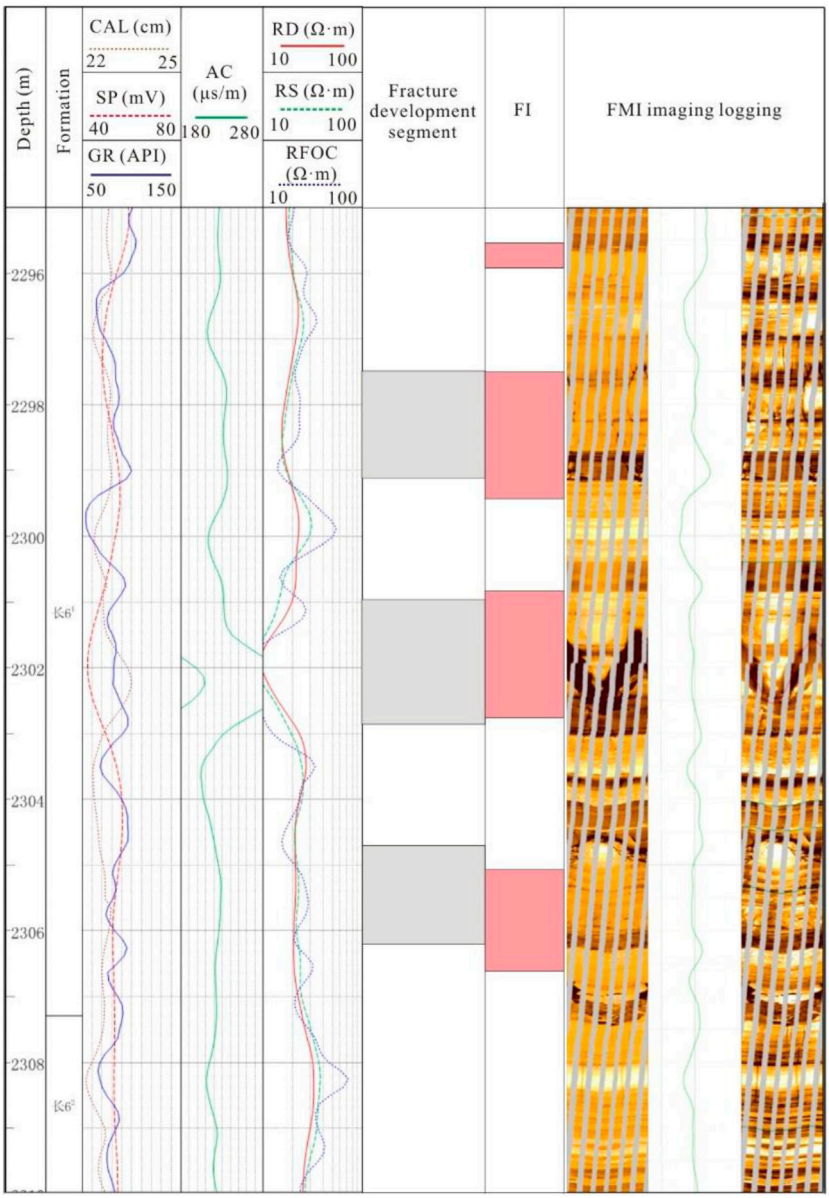

FIGURE 11 | Logging identification results of the fracture development segment in the sandstone at 2,295–2,310 m in Well D2. CAL-well diameter; SP-spontaneous potential; GR-natural gamma; AC- longitudinal wave time difference; RD-deep lateral resistivity; RS-shallow lateral resistivity; RFOC-eight lateral resistivity; FI-fracture index.

objects such as rocks, pores, fluids, fractures, and drilling fluids around the wellbore. Fractures in rock formations have special response characteristics in log data (Xue et al., 2021; Yang, et al., 2021; Zhao, et al., 2021). According to the statistical results, the porosity series logging has a better response to fractures. The response of resistivity logging to fractures is complex because of the different types of fracture fillers and the degree of filling (Sapin et al., 2012; Yin and Wu., 2020; Yin, et al., 2018). Lithologic logging has relatively poor response to fractures. According to statistics, in the fracture-developed segment of the target layer, the natural gamma value is mostly higher than 72 API, the shallow detection resistivity is generally less than 72 Ω m, the rock bulk density is less than 2.42 g/cm^3, the neutron porosity is greater than 26%, and the acoustic wave time difference is greater than 245 μs/m (**Figure 8**).

Fracture Logging Identification

In this study, the sensitivity of each single conventional logging curve to fractures is analyzed, and then the curve variation range, variation rate and fractal principle are used to predict fractures. Finally, a comprehensive fracture index is constructed by synthesizing relevant sensitive logging parameters. In order to facilitate the comprehensive analysis of the response of various parameters to fractures, the conventional logging series is first

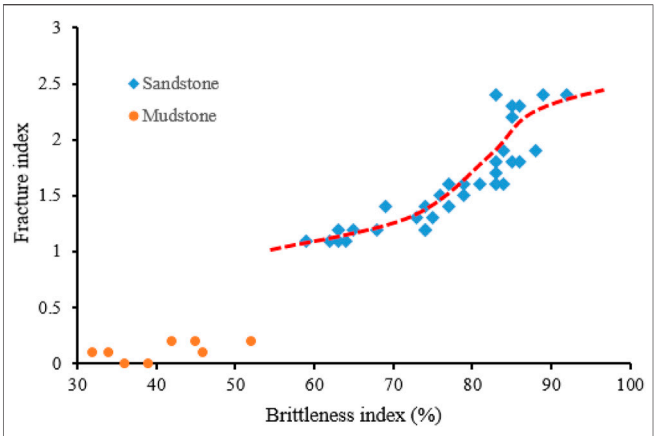

FIGURE 12 | Relationship between fracture index *FI* and rock brittleness index.

normalized. The existence of fractures will cause the increase of acoustic wave time difference and natural gamma, and cause the decrease of resistivity and rock density (Yoshida and Santosh., 2020; Zhang, et al., 2020; Zheng, et al., 2020). Therefore, **Eqs 4**, **5** are adopted to normalize the logging data respectively. The shallow lateral resistivity and rock density are normalized by **formula 5**, and the acoustic wave time difference and natural gamma are normalized by formula 6 (Pang and North, 1996).

$$X_1 = \frac{X_{max} - X}{X_{max} - X_{min}} \tag{4}$$

$$X_2 = \frac{X - X_{min}}{X_{max} - X_{min}} \tag{5}$$

In the formula, X_{max} and X_{min} are the maximum and minimum values of sandstone logging values in the target interval of a certain conventional logging curve, respectively; S is the log data reading; $X_1$and X_2 are the abnormal change indexes of the curves.

Standardized processing of raw logging data can effectively avoid the influence of different dimensions and magnitudes of data in different logging series. The distribution range of each logging parameter after processing is shown in **Figure 9**. It can be seen that all logging parameters are in the same dimension and magnitude range, and the comparability between different series of logging data is significantly enhanced.

From the correlation analysis between R/S and N of different fracture-sensitive logging parameters, it can be seen that fractures can reduce the slope of the R/S curve to a certain extent (**Figure 10**). However, not all the slope-decreasing segments of the R/S curve are fracture-developed segments (**Figure 10**). In addition, a single logging curve cannot effectively identify fractures, and only the combination of multiple fracture sensitive logging parameters can improve the accuracy of fracture identification.

In this study, a fractal-based fracture index (*FI*) was constructed, which was used to identify fractured segments in sandstone formations. **Figure 11** shows the processing results of the 2,295–2,310 m segment of Well D2. Imaging logging results show that fractures are mainly developed in the top Chang 6 oil layer group, while fractures in other oil layer groups are not developed (**Figure 11**). The thickness of sandstone with fractures is mainly distributed in 2–2.5 m. It can be seen that the fractal model in this study can well identify the fracture development segment. In this study, the number of wells interpreted by logging fractures is 8 wells, the number of segments interpreted by fractures is 96, and the number of segments consistent with the actual situation is 80. In the case of poor fracture identification, it mainly occurs in thick sand bodies, especially when the thickness of a single sand body is greater than 20 m. It is mainly due to the low degree of fracture development in thick sand bodies, so it is very difficult to extract effective fracture information. Overall, the coincidence rate of fracture logging identification using the model constructed in this paper is 83.3%. Therefore, this method can effectively identify fractures in tight oil reservoirs.

Brittleness Index of Natural Fracture Development Segments

The calculated fracture *FI* index was compared with the brittleness index of sandstone, and the results are shown in **Figure 12**. On the whole, fractures are mainly developed in the high brittle sandstone segments with brittleness index of 60–92% (**Figure 12**). The values of rock brittleness index and fracture index *FI* of mudstone are relatively low. The fracture index *FI* is lower than the threshold value of 1, indicating that the fractures are relatively underdeveloped; and the brittleness index of mudstone is usually lower than 60% (**Figure 12**).

Moreover, with the increase of the sandstone brittleness index, the fracture *FI* index has a "S" shape increasing trend. Before the brittleness index reaches 75%, the increasing trend of the fracture *FI* index is slow; when the brittleness index is in the range of 75–83%, the increasing trend of the fracture *FI* index increases slightly; when the brittleness index is greater than 83%, the increasing trend of the *FI* index gradually slowed down again (**Figure 12**). Therefore, the content of brittle mineral components in sandstone is an important factor affecting the development degree of natural fractures, and high brittle, thin sand bodies are more likely to develop fractures. In addition, highly brittle framework minerals have strong stress-supporting capacity, which can keep fractures open by resisting high overlying loads (Zhao, et al., 2020; Zhang, et al., 2006).

CONCLUSION

1) High-angle, vertical and bedding fractures are mainly developed in the Yanchang Formation tight sandstones

in the study area. There is a negative correlation between sand body thickness and fracture development degree.

2) The fracture sensitivity parameters were used to construct a coupled fractal fracture index *FI*. The fractal model incorporates logging information from natural gamma, acoustic wave time difference, rock density, and shallow lateral resistivity. Moreover, the *FI* is calibrated by imaging data, and the lower fracture limit is set to 1.
3) The constructed fracture fractal index realizes the functions of multi-conventional logging information fusion and gradual elimination, which can effectively identify fracture development segments in sandstone. The fracture identification rate is 83.3%.
4) The study also found that with the increase of sandstone brittleness index, the fracture index has a "S" shape increasing trend. Therefore, the content of brittle mineral components in sandstone is an important factor affecting the development degree of natural fractures, and fractures are more likely to occur in high brittle, thin sand bodies. The highly brittle framework minerals have strong stress-supporting capacity, which can keep fractures open by resisting high overlying loads.

DATA AVAILABILITY STATEMENT

The original contributions presented in the study are included in the article/supplementary material, further inquiries can be directed to the corresponding author.

AUTHOR CONTRIBUTIONS

ZC is responsible for the methodology and writing of this paper, AJ and YY are responsible for the logging interpretation of this paper.

FUNDING

This manuscript was supported by the National Natural Science Foundation of China Regional Science Foundation Project (42162015), Natural Science Foundation of Gansu Provincial Department of Science and Technology, China (Grant No. 20JR5RA48) and Innovation Capability Improvement Project of Gansu Provincial Department of Education, China (Grant No. 2020B-223).

REFERENCES

Anders, M. H., Laubach, S. E., and Scholz, C. H. (2014). Microfractures: a Review. *J. Struct. Geology.* 69 (B), 377–394. doi:10.1016/j.jsg.2014.05.011

Barton, C., Moos, D., and Tezuka, K. (2009). Geomechanical Wellbore Imaging: Implications for Reservoir Fracture Permeability. *Bulletin* 93 (11), 1551–1569. doi:10.1306/06180909030

Bhatti, A., Ismail, A., Raza, A., Gholami, R., Rezaee, R., Nagarajan, R., et al. (2020). Permeability Prediction Using Hydraulic Flow Units and Electrofacies Analysis. *Energ. Geosci.* 1 (1–2), 81–91. doi:10.1016/j.engeos.2020.04.003

Bukar, M., Worden, R. H., Bukar, S., and Shell, P. (2021). Diagenesis and its Controls on Reservoir Quality of the Tambar Oil Field, Norwegian North Sea. *Energ. Geosci.* 2 (1), 10–31. doi:10.1016/j.engeos.2020.07.002

Camac, B. A., and Hunt, S. P. (2009). Predicting the Regional Distribution of Fracture Networks Using the Distinct Element Numerical Method. *Bulletin* 93 (11), 1571–1583. doi:10.1306/07230909040

Cao, L., Yao, Y., Cui, C., and Sun, Q. (2020). Characteristics of *In-Situ* Stress and its Controls on Coalbed Methane Development in the southeastern Qinshui Basin, North China. *Energ. Geosci.* 1 (1–2), 69–80. doi:10.1016/j.engeos.2020.05.003

Casini, U., Hunt, D. W., Monsen, E., and Bounaim, A. (2016). Fracture Characterization and Modeling from Virtual Outcrops. *AAPG Bull.* 100 (1), 41–61. doi:10.1306/09141514228

Chen, G. B., Li, T., Yang, L., Zhang, G. H., Li, J. W., and Dong, H. J. (2021). Mechanical Properties and Failure Mechanism of Combined Bodies with Different Coal-Rock Ratios and Combinations. *J. Mining Strata Control. Eng.* 3 (2), 023522. doi:10.13532/j.jmsce.cn10-1638/td.20210108.001

Chen, J. W. (2020). Analysis of Roadheader's Rotary Table Onvibration Modal Based on Finite Element Method and Tested Data. *J. Mining Strata Control. Eng.* 2 (2), 026032. doi:10.13532/j.jmsce.cn10-1638/td.20191209.001

Cheng, J. W., Zhao, G., Sa, Z. Y., Zheng, W. C., Wang, Y. G., and Liu, J. (2020). Overlying Strata Movement and Deformation Calculationprediction Models for Underground Coal Mines. *J. Mining Strata Control. Eng.* 2 (4), 043523. doi:10.13532/j.jmsce.cn10-1638/td.20200716.001

Dcrshowitz, W. S., and Einstein, H. H. (1988). Characterizing Rock Ioint Geometry with Joint System Models. *Rock Mech. Rock Eng.* 21 (1), 21

Dong, S., Zeng, L., Dowd, P., Xu, C., and Cao, H. (2018). A Fast Method for Fracture Intersection Detection in Discrete Fracture Networks. *Comput. Geotechnics* 98, 205–216. doi:10.1016/j.compgeo.2018.02.005

Du, Q. X., Han, Z. Z., Shen, X. L., Han, C., Song, Z. G., Gao, L. H., et al. (2019). Geochronology and Geochemistry of Permo-Triassic Sandstones in Eastern Jilin Province (NE China): Implications for Final Closure of the Paleo-Asian Ocean. *Geosci. Front.* 10, 685–706. doi:10.1016/j.gsf.2018.03.014

Fan, C. H., Zhong, C., Zhang, Y., Qin, Q. R., and He, S. (2019). Geological Factors Controlling the Accumulation and High Yield of Marine-Facies Shale Gas: Case Study of the Wufeng-Longmaxi Formation in the Dingshan Area of Southeast Sichuan, China. *Acta Geol. Sin. Engl.* 93 (3), 530–560. doi:10.1111/1755-6724.13857

Fan, C., Li, H., Qin, Q., He, S., and Zhong, C. (2020a). Geological Conditions and Exploration Potential of Shale Gas Reservoir in Wufeng and Longmaxi Formation of southeastern Sichuan Basin, China. *J. Pet. Sci. Eng.* 191, 107138. doi:10.1016/j.petrol.2020.107138

Fan, C., Li, H., Qin, Q., Shang, L., Yuan, Y., and Li, Z. (2020c). Formation Mechanisms and Distribution of Weathered Volcanic Reservoirs: A Case Study of the Carboniferous Volcanic Rocks in Northwest Junggar Basin, China. *Energy Sci. Eng.* 8 (8), 2841–2858. doi:10.1002/ese3.702

Fan, C., Li, H., Zhao, S., Qin, Q., Fan, Y., Wu, J., et al. (2020b). Formation Stages and Evolution Patterns of Structural Fractures in Marine Shale: Case Study of the Lower Silurian Longmaxi Formation in the Changning Area of the Southern Sichuan Basin, China. *Energy Fuels* 34 (8), 9524–9539. doi:10.1021/acs.energyfuels.0c01748

Fan, K. (2020). Sudden Deformation Characteristic and Cuttingroofsupport Technology for Double-Used Roadways in Longtan Mine. *J. Mining Strata Control. Eng.* 2 (3), 033032. doi:10.13532/j.jmsce.cn10-1638/td.20191227.001

Fu, X., and Wang, R. F. (2020). Cooperative Self-Adaptive Control Modelof Fluid Feeding System and Hydraulic Supports in Workingface. *J. Mining Strata Control. Eng.* 2 (3), 036031. doi:10.13532/j.jmsce.cn10-1638/td.20191203.001

Gao, F. Q. (2019). Use of Numerical Modeling for Analyzing Rockmechanic Problems in Underground Coal Mine Practices. *J. Mining Strata Control. Eng.* 1 (1), 013004. doi:10.13532/j.jmsce.cn10-1638/td.2019.02.009

Guo, L. L., Zhou, D. W., Zhang, D. M., and Zhou, B. H. (2021). Deformation and Failure of Surrounding Rock of a Roadway Subjected to Mining-Induced Stresses. *J. Mining Strata Control. Eng.* 3 (2), 023038. doi:10.13532/j.jmsce.cn10-1638/td.20200727.001

Han, L., Shen, J., Qu, J., and Ji, C. (2021). Characteristics of a Multi-Scale Fracture Network and its Contributions to Flow Properties in Anthracite. *Energy Fuels* 35 (14), 11319–11332. doi:10.1021/acs.energyfuels.1c01465

He, S., Li, H., Qin, Q., and Long, S. (2021). Influence of Mineral Compositions on Shale Pore Development of Longmaxi Formation in the Dingshan Area, Southeastern Sichuan Basin, China. *Energy Fuels* 35 (13), 10551–10561. doi:10.1021/acs.energyfuels.1c01026

Hong, D., Cao, J., Wu, T., Dang, S., Hu, W., and Yao, S. (2020). Authigenic clay Minerals and Calcite Dissolution Influence Reservoir Quality in Tight Sandstones: Insights from the central Junggar Basin, NW China. *Energ. Geosci.* 1 (1–2), 8–19. doi:10.1016/j.engeos.2020.03.001

Hu, Q. F., Cui, X. M., Liu, W. K., Ma, T. J., and Geng, H. R. (2020). Law of Overburden and Surface Movement and Deformation Dueto Mining Super Thick Coal Seam. *J. Mining Strata Control. Eng.* 2 (2), 023021. doi:10.13532/j.jmsce.cn10-1638/td.20191113.001

Huang, F. R., Yan, S. X., Wang, X. L., Jiang, P. C., and Zhan, S. B. (2021). Experimental Study on Infrared Radiation Characteristics Ofgneiss under Uniaxial Compression. *J. Mining Strata Control. Eng.* 3 (1), 013011. doi:10.13532/j.jmsce.cn10-1638/td.20200730.001

Jiang, L., Qiu, Z., Wang, Q., Guo, Y., Wu, C., Wu, Z., et al. (2016). Joint Development and Tectonic Stress Field Evolution in the southeastern Mesozoic Ordos Basin, West Part of north China. *J. Asian Earth Sci.* 127, 47–62. doi:10.1016/j.jseaes.2016.06.017

Kang, H. P. (2021). Temporal Scale Analysis on Coal Mining and Strata Control Technologies. *J. Mining Strata Control. Eng.* 3 (1), 013538. doi:10.13532/j.jmsce.cn10-1638/td.20200814.001

Lai, J., Wang, G., Wang, S., Cao, J., Li, M., Pang, X., et al. (2018). Review of Diagenetic Facies in Tight Sandstones: Diagenesis, Diagenetic Minerals, and Prediction via Well Logs. *Earth-Science Rev.* 185, 234–258. doi:10.1016/j.earscirev.2018.06.009

Laubach, S. E., Olson, J. E., and Gross, M. R. (2009). Mechanical and Fracture Stratigraphy. *Bulletin* 93, 1413–1426. doi:10.1306/07270909094

Li, Y. (2021). Mechanics and Fracturing Techniques of Deep Shale from the Sichuan Basin, SW China. *Energ. Geosci.* 2 (1), 1–9. doi:10.1016/j.engeos.2020.06.002

Li, Y., Zhou, D., Wang, W., Jiang, T., and Xue, Z. (2020). Development of Unconventional Gas and Technologies Adopted in China. *Energ. Geosci.* 1 (1–2), 55–68. doi:10.1016/j.engeos.2020.04.004

Liu, B., He, S., Meng, L., Fu, X., Gong, L., and Wang, H. (2021). Sealing Mechanisms in Volcanic Faulted Reservoirs in Xujiaweizi Extension, Northern Songliao Basin, Northeastern China. *Bulletin* 105, 1721–1743. doi:10.1306/03122119048

Mardia, K. V., Nyirongo, V. B., Walder, A. N., Xu, C., Dowd, P. A., Fowell, R. J., et al. (2007). Markov Chain Monte Carlo Implementation of Rock Fracture Modelling. *Math. Geol.* 39 (4), 355–381. doi:10.1007/s11004-007-9099-3

Mirzaei-Paiaman, A., and Ghanbarian, B. (2021). A New Methodology for Grouping and Averaging Capillary Pressure Curves for Reservoir Models. *Energ. Geosci.* 2 (1), 52–62. doi:10.1016/j.engeos.2020.09.001

Mizoguchi, K., and Ueta, K. (2013). Microfractures within the Fault Damage Zone Recordthe History of Fault Activity. *Geophys. Res. Lett.* 40 (8), 2023–2027. doi:10.1002/grl.50469

Nakaya, S., and Nakamura, K. (2007). Percolation Conditions in Fractured Hard Rocks: A Numerical Approach Using Thethree Dimensional Binary Fractal Fracture Network (3D-BFFN) Model. *J. Geophys. Res.* 112 (B12), 1–15. doi:10.1029/2006jb004670

Nelson, R. A. (1985). *Geological Analysis of Naturally Fractured Reservoirs*. Texas: Gulf Publishing Company, 8–26.

Olson, J. E., laubach, S. E., and lander, R. H. (2009). Natural Fracture Characterization in Tight Gas Sandstones: Integrating Mechanics and Diagenesis. *Bulletin* 93 (11), 1535–1549. doi:10.1306/08110909100

Ortega, O. J., Marrett, R. A., and Laubach, S. E. (2006). A Scale-independent Approach to Fracture Intensity and Average Spacing Measurement. *Bulletin* 90 (2), 193–208. doi:10.1306/08250505059

Pang, J., and North, C. P. (1996). Fractals and Their Applicability in Geological Wireline Log Analysis. *J. Pet. Geol* 19 (3), 339–350. doi:10.1111/j.1747-5457.1996.tb00438.x

Peacock, D. C. P., Sanderson, D. J., and Rotevatn, A. (2018). Relationships between Fractures. *J. Struct. Geology.* 106, 41–53. doi:10.1016/j.jsg.2017.11.010

Qie, L., Shi, Y. N., and Liu, J. S. (2021). Experimental Study on Grouting Diffusion of Gangue Solid Filling Bulk Materials. *J. Mining Strata Control. Eng.* 3 (2), 023011. doi:10.13532/j.jmsce.cn10-1638/td.20201111.001

Robinson, N. I., Sharp, J. M., Jr., and Krciscl, I. (1998). Contaminant Transport in Sets of Parallel Finite Fractures with Fray Turc Skins. *J. Contaminant Hydrol.* 31 (1-2), 83–109. doi:10.1016/s0169-7722(97)00055-7

Santosh, M., and Feng, Z. Q. (2020). New Horizons in Energy Geoscience. *Energ. Geosci.* 1 (1–2), 1. doi:10.1016/j.engeos.2020.05.005

Sapin, F., Ringenbach, J.-C., Rives, T., and Pubellier, M. (2012). Counter-regional normal Faults in Shale-Dominated Deltas: Origin, Mechanism and Evolution. *Mar. Pet. Geology.* 37, 121–128. doi:10.1016/j.marpetgeo.2012.05.001

Wang, J., and Wang, X. L. (2021). Seepage Characteristic and Fracture Development of Protected Seam Caused by Mining Protecting Strata. *J. Mining Strata Control. Eng.* 3 (3), 033511. doi:10.13532/j.jmsce.cn10-1638/td.20201215.001

Xu, C., and Dowd, P. (2010). A New Computer Code for Discrete Fracture Network Modelling. *Comput. Geosciences* 36 (3), 292–301. doi:10.1016/j.cageo.2009.05.012

Xu, C., Dowd, P. A., Mardia, K. V., and Fowell, R. J. (2006). A Flexible True Plurigaussian Code for Spatial Facies Simulations. *Comput. Geosciences* 32 (10), 1629–1645. doi:10.1016/j.cageo.2006.03.002

Xue, F., Liu, X. X., and Wang, T. Z. (2021). Research on Anchoring Effect of Jointed Rock Mass Based on 3D Printing and Digital Speckle Technology. *J. Mining Strata Control. Eng.* 3 (2), 023013. doi:10.13532/j.jmsce.cn10-1638/td.20201020.001

Yang, J. X., Luo, M. K., Zhang, X. W., Huang, N., and Hou, S. J. (2021). Mechanical Properties and Fatigue Damage Evolution of Granite under Cyclic Loading and Unloading Conditions. *J. Mining Strata Control. Eng.* 3 (3), 033016. doi:10.13532/j.jmsce.cn10-1638/td.20210510.001

Yin, S., Lv, D., and Ding, W. (2018). New Method for Assessing Microfracture Stress Sensitivity in Tight sandstone Reservoirs Based on Acoustic Experiments. *Int. J. Geomechanics* 18 (4), 1–10. doi:10.1061/(asce)gm.1943-5622.0001100

Yin, S., and Wu, Z. (2020). Geomechanical Simulation of Low-Order Fracture of Tight sandstone. *Mar. Pet. Geology.* 100, 1–10. doi:10.1016/j.marpetgeo.2020.104359

Yoshida, M., and Santosh, M. (2020). Energetics of the Solid Earth: An Integrated Perspective. *Energ. Geosci.* 1 (1–2), 28–35. doi:10.1016/j.engeos.2020.04.001

Zhang, B., Shen, B., and Zhang, J. (2020). Experimental Study of Edge-Opened Cracks Propagation in Rock-like Materials. *J. Mining Strata Control. Eng.* 2 (3), 033035. doi:10.13532/j.jmsce.cn10-1638/td.20200313.001

Zhang, T., Switzer, P., and Journel, A. (2006). Filter-based Classification of Training Image Patterns for Spatial Simulation. *Math. Geol.* 38 (1), 63–80. doi:10.1007/s11004-005-9004-x

Zhao, K. K., Jiang, P. F., Feng, Y. J., Sun, X. D., Cheng, L. X., and Zheng, J. W. (2021). Investigation of the Characteristics of Hydraulic Fracture Initiation by Using Maximum Tangential Stress Criterion. *J. Mining Strata Control. Eng.* 3 (2), 023520. doi:10.13532/j.jmsce.cn10-1638/td.20201217.001

Zhao, Z., Wu, K., Fan, Y., Guo, J., Zeng, B., and Yue, W. (2020). An Optimization Model for Conductivity of Hydraulic Fracture Networks in the Longmaxi Shale, Sichuan basin, Southwest China. *Energ. Geosci.* 1 (1–2), 47–54. doi:10.1016/j.engeos.2020.05.001

Zheng, H., Zhang, J., and Qi, Y. (2020). Geology and Geomechanics of Hydraulic Fracturing in the Marcellus Shale Gas Play and Their Potential Applications to the Fuling Shale Gas Development. *Energ. Geosci.* 1 (1–2), 36–46. doi:10.1016/j.engeos.2020.05.002

Conflict of Interest: The authors declare that the research was conducted in the absence of any commercial or financial relationships that could be construed as a potential conflict of interest.

Publisher's Note: All claims expressed in this article are solely those of the authors and do not necessarily represent those of their affiliated organizations, or those of the publisher, the editors and the reviewers. Any product that may be evaluated in this article, or claim that may be made by its manufacturer, is not guaranteed or endorsed by the publisher.

frontiers in Earth Science

ORIGINAL RESEARCH
published: 03 March 2022
doi: 10.3389/feart.2022.860952

Geological Characteristics and Controlling Factors of Enrichment of Deep Shale Gas in the East Weiyuan–North Rongchang Area, Sichuan Basin, China

Yijia Wu[1,2], Hongming Tang[1]*, Jing Li[2], Zhi Gao[2], Bei Yang[2], Cheng Yang[2] and Tian Tang[2]*

[1]School of Geoscience and Technology, Southwest Petroleum University, Chengdu, China, [2]Institute of Geological Exploration and Development of CNPC Chuanqing Drilling Engineering, Chengdu, China

OPEN ACCESS

Edited by:
Shuai Yin,
Xi'an Shiyou University, China

Reviewed by:
Yue Qingyou,
Liaoning Shihua University, China
Yang Wang,
China University of Petroleum, Beijing, China

***Correspondence:**
Yijia Wu
wuyj_dyy@cnpc.com.com
Hongming Tang
swpithm@vip.163.com

Specialty section:
This article was submitted to Economic Geology, a section of the journal Frontiers in Earth Science

Received: *24 January 2022*
Accepted: *15 February 2022*
Published: *03 March 2022*

Citation:
Wu Y, Tang H, Li J, Gao Z, Yang B, Yang C and Tang T (2022) Geological Characteristics and Controlling Factors of Enrichment of Deep Shale Gas in the East Weiyuan–North Rongchang Area, Sichuan Basin, China. Front. Earth Sci. 10:860952. doi: 10.3389/feart.2022.860952

The southern Sichuan Basin is the core area of China's efficient development of deep shale gas (burial depth greater than 3,500 m). Reservoir geological characteristics determine whether shale gas can be preserved, enriched, and produced. Taking the Long 1_1 submember of the Wufeng Formation of the Upper Ordovician and the Longmaxi Formation of the Lower Silurian in the East Weiyuan–North Rongchang area as an example, we used the core, logging, production test, and other data, combining X-ray diffraction analysis, LECO Total Organic Carbon (TOC)-S analysis, optical microscopy, and argon ion polishing field-emission scanning electron microscopy, to study the shale mineral composition, geochemistry, reservoir space, pore structure characteristics, and reservoir physical properties. The following results were obtained: 1) The brittle mineral content, organic matter maturity, and TOC content are high, gradually increase from top to bottom, and reach their maxima at small layer 1 of Long 1_1. 2) Organic pores, inorganic pores, and fractures are important reservoir spaces, among which organic pores and fractures are important seepage channels for shale gas. 3) The shale pore structure revealed by electron microscopy shows that the pore structure in target layers can be divided into four types: unimodal type (mainly organic pores), bimodal type (both organic and inorganic pores), monoclinic type I (mainly organic pores), and monoclinic type II (mainly inorganic pores). The pore morphology is complex, and circular and oval shapes predominate. 4) Sedimentary facies are the main factor controlling the enrichment of shale gas, and the development of fractures is the key to obtaining high yields of shale gas. 5) The class I favorable target area is mainly distributed in wells W206, W206H1, R234H, and R233H and areas to its south, and some areas in the east of the study area.

Keywords: deep shale gas, geological characteristics, reservoir characteristics, Enrichment and high yield, controlling factors, pore structure, East-Weiyuan-north Rongchang area

INTRODUCTION

The marine shale gas resources in China are abundant. Reservoir geological characteristics have always been a hot topic in shale gas exploration and development in China and abroad since they play an important role in controlling the enrichment and production of shale gas (Fan et al., 2018; Li et al., 2019; Fan et al., 2020a; Fan et al., 2020b; He et al., 2021a). The favorable areas for marine shale gas are mainly located in Sichuan Basin, China. The main strata are the Wufeng Formation of the Upper Ordovician–Longmaxi Formation of the Lower Silurian, the main burial depth being 3,500–4,500 m. Shale gas areas have been found successively, such as Luzhou, Changning, Weiyuan, Fuling, and Dingshan, and breakthroughs in exploration and development have been made. The proven geological reserves in China are approximately $2.0 \times 1012\ m^3$. Their output is approximately $154 \times 108\ m^3$, making China the second-largest shale gas producer in the world (Nie and Jin, 2016; Nie et al., 2018; Zhang F. et al., 2020; He et al., 2021b).

The shale gas exploration technology for burial depths less than 3,500 m is well developed, forming a comprehensive geological evaluation technology of shale reservoirs that effectively guides the large-scale industrial development of medium–shallow shale gas. With the deepening of shale gas exploration and development, deep shale with burial depth greater than 3,500 m is widely distributed, with extensive resources (for example, the amount of deep shale gas in southern Sichuan is as high as $8 \times 1012\ m^3$) (Liu Y. J. et al., 2021; Li W. G. et al., 2021; Liu Y. Y. et al., 2021; Ma et al., 2021). Therefore, the development of geological theories related to the enrichment and production of deep shale gas has strategic significance for ensuring national energy security. Compared with shallow shale gas fields, there are obvious differences in geological engineering conditions of deep shale gas fields in China. For example, deep shale gas fields are mostly located in complex structural areas, with complex fold and fault relations, large *in situ* stress and stress differences, and high temperatures and pressures, so the main technologies suitable for shallow shale gas exploration and development are no longer adequate (Zhao et al., 2020; Zhang BL. et al., 2020, Zhang DD. et al., 2020; Xu F. S. et al., 2021; Xi et al., 2021a, Xi et al., 2021b). Previous studies have made great progress in understanding the geological characteristics of shale reservoirs; defined the geochemical characteristics, mineralogical characteristics, and reservoir space characteristics of the reservoirs; found that the sedimentary environment, organic matter (OM), clay minerals, brittle minerals, and fractures are the main controlling factors of shale reservoir yields; and formed a comprehensive research system for shale reservoirs (Chen et al., 2016; Li et al., 2019c; Chen S. L. et al., 2020; Li et al., 2020; Liu et al., 2020; Chen et al., 2021a; Chen et al., 2021b; Liu J. et al., 2021; Sun, 2021). However, these research results and conclusions apply mainly to shallow shale gas with a burial depth of less than 3,500 m. Due to the influence of sedimentation, diagenesis, and tectonism, deep shale gas reservoirs have higher contents of brittle minerals, more developed natural fractures, and more complex pore evolution, resulting in different shale geological characteristics and controlling factors for shale gas enrichment and yield (Yin et al., 2019; Chen F. et al., 2020; Chai et al., 2020; Xu and Gao, 2020; Yin and Wu, 2020; Zhou et al., 2020; Song et al., 2021; Tabatabaei 2021). Therefore, clarifying the geological characteristics of deep shale is needed to explore and extract deep shale gas.

The burial depth of the main shale in the East Weiyuan–North Rongchang area is 3,800–4,300 m, so the shale reservoir characteristics and the state of the shale gas and its preservation conditions are significantly different from those of medium–shallow shale gas. It is a typical area to analyze the geological characteristics and controlling factors of deep shale gas (Xiong et al., 2021; Zhao et al., 2021; Zhou et al., 2021). Therefore, we used the data from logging, core, seismic, and experimental tests to comprehensively analyze the rock and mineral characteristics, reservoir space characteristics, organic geochemical characteristics, and physical properties of high-quality deep shale reservoirs in the East Weiyuan–North Rongchang to clarify the main controlling factors of deep shale gas enrichment and high yield. We then calculated the optimal target areas, thus providing guidance for exploring and developing regional deep shale gas in this study area and similar areas.

GEOLOGICAL SETTING

The East Weiyuan–North Rongchang block is located in the Central South of Sichuan Basin. The East Weiyuan block is located in the middle-slope gentle belt of the Central Sichuan Paleo-uplift and the low-fold belt of the Southwest Sichuan Paleo-uplift. North Rongchang block is located in the middle-slope gentle belt of Central Sichuan Paleo-uplift and the low steep bend belt of the Central Sichuan Paleo-depression. The structure of the study area is relatively simple. The Northern and Western areas consist of gentle, low-amplitude, monoclinic, or nasal protrusion-like structures, with undeveloped faults, and only some small-scale faults are developed. The Zhongaoxi buried structure is in the middle, the Luoguanshan structure is in the south, and the Xishan structure is connected in the east, showing the structural characteristics of a wide syncline and a narrow anticline. Faults are developed and mostly distributed in the NE–SW direction (**Figure 1**) (Wu et al., 2021; Zhao et al., 2021). The Late Ordovician–Early Silurian is the turning period of sedimentary-tectonic evolution of the Yangtze Block. Dominated by rising sea level, the East Weiyuan–North Rongchang area forms a detention basin, which inundates the carbonate platform and provides conditions for the deposition of black shale of the Ordovician Wufeng Formation and the Longmaxi Formation at the bottom of the Lower Silurian. Overall, the Wufeng Formation–Longmaxi Formation is mainly continental shelf facies in the study area. The shelf environment consists of an inner shelf close to the shore and far away. The upper limit is near the normal wave level, and the lower water depth limit is generally approximately 200 m (Liu S. G. et al., 2021; Liu Q. Y. et al., 2021). The Wufeng Formation–Longmaxi Formation is close to the shore facies in the landward direction on the plane, and the sediments are mainly dark mud debris.

The oldest stratum exposed on the surface of the study area is the 1 Triassic Xujiahe formation, and the top is the Shaximiao Formation. The drilling data show that the stratigraphic sequence

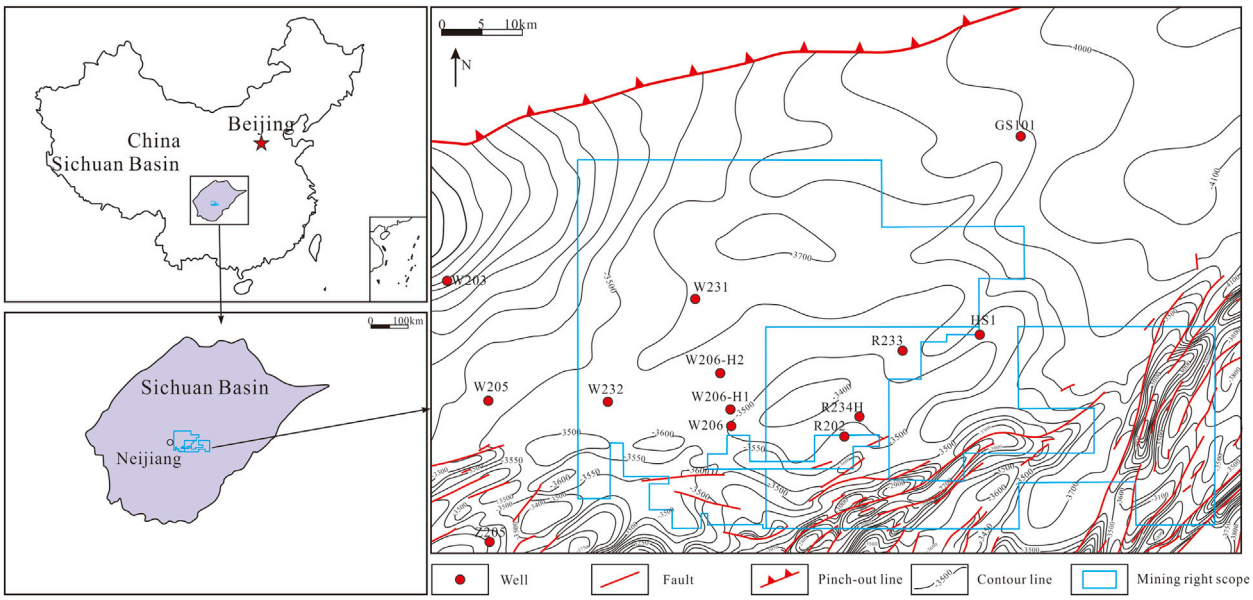

FIGURE 1 | Seismic reflection structure of the Upper Ordovician top boundary in the study area.

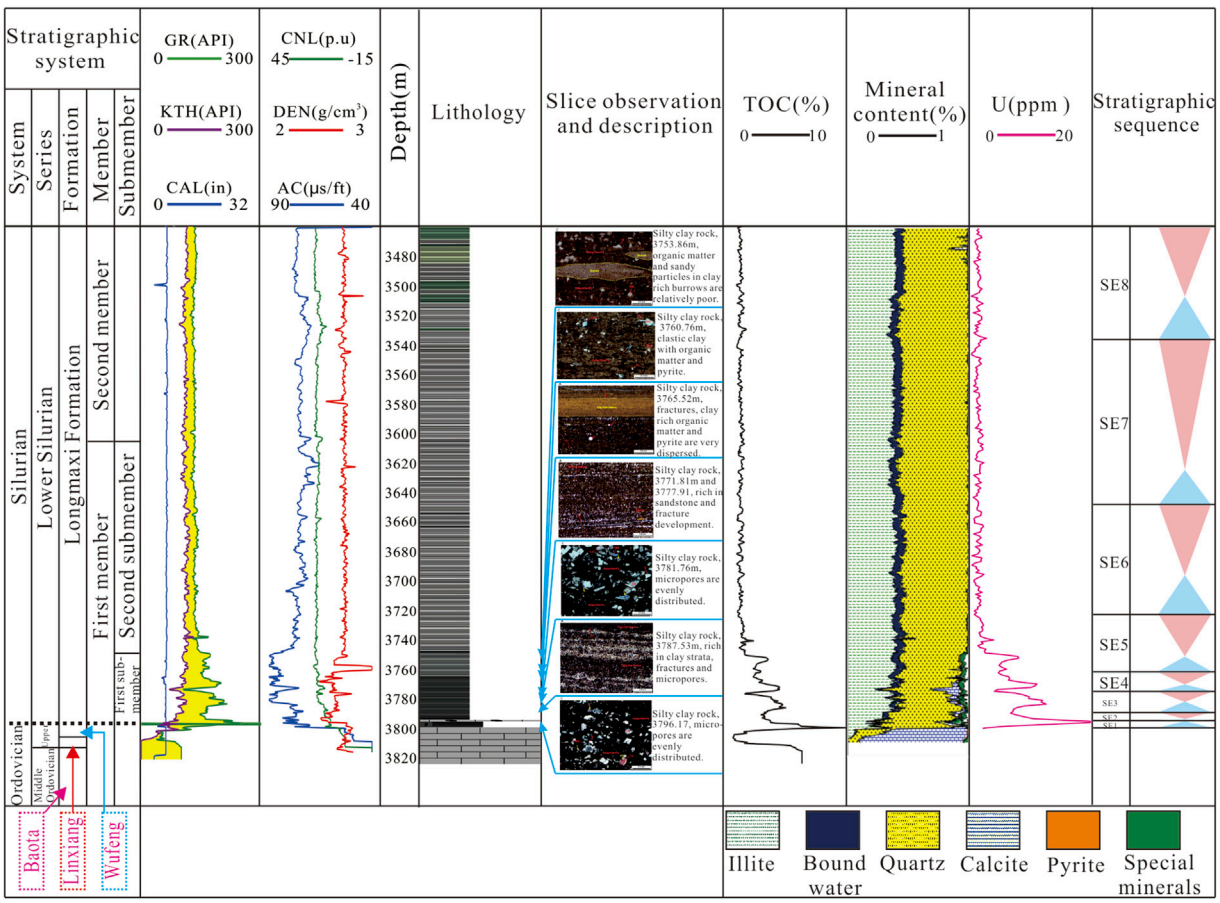

FIGURE 2 | Comprehensive histogram of the Longmaxi Formation of well W206.

from top to bottom is normal. The stratigraphic thickness of the Lower Silurian Longmaxi Formation is 283–515 m, which is in conformable contact with the overlying Shiniulan Formation. At the bottom, there is a clear boundary between the black carbonaceous shale containing carbonate rock and the grayish-brown biological limestone of the Guanyinqiao Section of the Wufeng Formation of the Lower Ordovician, forming a pseudo-conformable contact. The rock color gradually deepens from top to bottom. The upper part is grayish-green and greenish-gray shale. The middle and lower parts are grayish-black to black calcareous and carbonaceous shale, which generally is calcareous, silty, dense, and brittle, and the foliation is relatively developed (leaf bedding). The natural gamma ray is serrated, mostly with high values. The bottom is obviously uplifted compared with the upper part, with a value of 140–500 API. The Longmaxi Formation can be divided into upper and lower segments, namely, the Long 1 member and the Long 2 member. The Long 1 member can be divided into upper and lower subsegments, namely, Long 1_2 and long 1_1. Long 1_1 can be divided into four small layers, the main shale gas-producing layers (**Figure 2**).

SAMPLES AND EXPERIMENTS

Experimental Samples

The shale of the Wufeng Formation–Longmaxi Formation in the East Weiyuan–North Rongchang block was deposited in an organic-rich shelf environment (Wu et al., 2021; Zhao et al., 2021). In this study, conventional logging and imaging logging data of eight wells, including R202, R233H, W231, W232, and W206, were collected to analyze the characteristics of the reservoir lithology, reservoir space, brittle minerals, and gas-bearing. At the same time, 52 samples of five wells of Long 1_1 sub-member were collected, including 10 shales in small layer 1, 15 shales in small layer 2, eight shale in small layer 3, and 19 shales in small layer 4.

X-Ray Diffraction Analysis

The 52 samples were crushed and passed through a 200-mesh sieve. After drying, a certain number of samples were taken and analyzed by a Bruker D8 X-ray diffractometer. The working voltage was 40 kV, the current was 30 mA, and the scanning was conducted at 4°/min. Determinations were made according to the *Inorganic chemicals for industrial use-Crystal form analysis-X-ray diffraction method* (GB/T 30904-2014). The main peak area of each mineral was used to calculate the relative content (Cai et al., 2020).

Geochemical Characteristic Analysis

The OM maturity and abundance are key geochemical characteristics of shale. Since there is no vitrinite in the highly mature source rocks of the Lower Paleozoic, the maturity of the Lower Paleozoic source rocks cannot be evaluated by vitrinite reflectance (Shi et al., 2016; Yu H. et al., 2017; Rui et al., 2019; Wang et al., 2019). In this study, the maturity of the Lower Paleozoic source rocks was evaluated by studying the correlation between solid asphalt and vitrinite reflectance, fitting the conversion formula between asphalt reflectance and vitrinite reflectance, and converting the asphalt reflectance into vitrinite reflectance.

Total organic carbon (TOC) content can better characterize the OM abundance. In this study, 52 samples were crushed and passed through a 200-mesh sieve. After drying at low temperature, the carbonate minerals were removed with dilute hydrochloric acid. According to the Determination of total organic carbon in sedimentary rock (GB/T 19145-2003), the TOC content was determined with a LECO CS230 carbon/sulfur determinator (Wang et al., 2016; Zhao et al., 2017; Cai et al., 2020).

Observation by Argon Ion Polishing Field-Emission Scanning Electron Microscopy

Representative core samples from five wells were selected for SEM observation according to our core observation. First, the experimental samples were polished by argon-ion, and then small shale samples were cut into regular cuboids and put into the injection chamber of the polisher. They were bombarded with argon ions in a vacuum for 2 h, and then the SU8010 FESEM has used under the secondary electron (SE)/backscattered electron (BSE) mode. The observation was carried out to obtain images of complete shales.

RESULTS

Mineral Composition Characteristics

The XRD analysis of the first segment of the Wufeng Formation–Longmaxi Formation in the study area shows that minerals are mainly quartz, feldspar, calcite, dolomite, and clay minerals, and pyrite and marcasite contents are scarce. The brittle minerals are primarily quartz, feldspar, carbonate minerals, pyrite, and hematite, showing a gradually increasing trend from top to bottom in the vertical direction, and the content of brittle minerals peaks at small layer 1 (**Figures 3A,B**). Specifically, the content of brittle minerals in the Wufeng Formation is 62.6–89.9%, with an average of 74.9%; in small layer 1, 55.3–76.4% with an average of 64.4%; in small layer 2, 60.3–79% with an average of 67.5%; in small layer 3, 49.9–74.5% with an average of 60.2%; and in small layer 4, 45.2–72% with an average of 58.3% (**Figure 3C**). In terms of plane distribution, each well's measured brittle mineral content is generally stable, with an average greater than 60%. The brittle mineral content of the Wufeng Formation Long 1_1 sub-member reservoir increases in the east and south directions. The high-value area is distributed from well W206-H2 to well R202, the content gradually decreases toward the surrounding well area, Well W231 is a relatively low-value area, and the compressibility of shale reservoir is generally good (Zhou et al., 2016; Zhang et al., 2019; Zhu et al., 2019; Zhang et al., 2021).

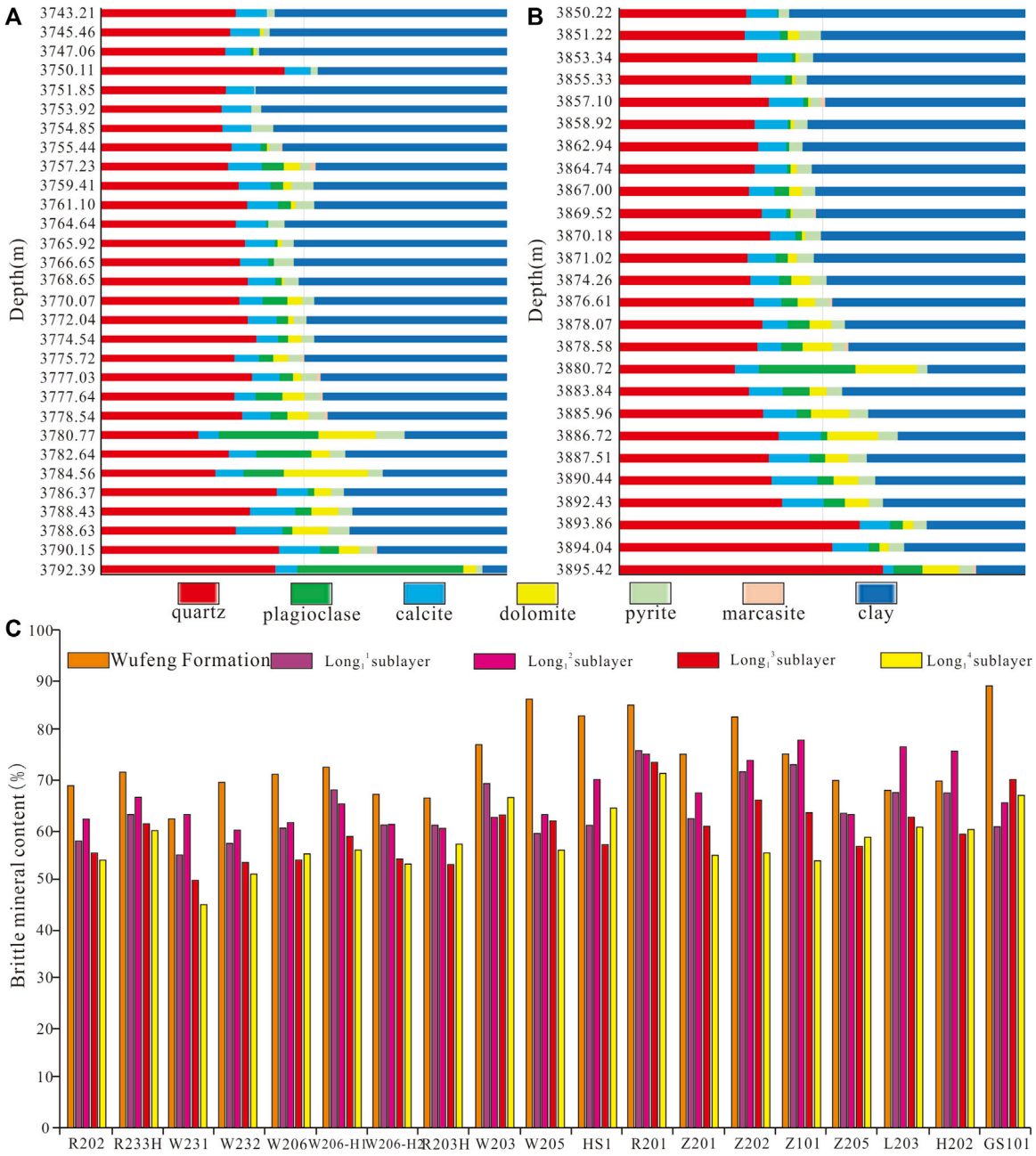

FIGURE 3 | Mineral composition in Wufeng Formation Long 1_1 sub-member in the study area. **(A)**. R233H. **(B)**. Well W206-H2. **(C)**. Brittle mineral content in the study area and adjacent areas.

TABLE 1 | OM maturity in the core analysis of sub-member Long 1_1 in the study area.

Test unit	Test method	Test data points	R_o	W231	W206-H2	R233H	W206
Collett	Conversion of asphalt reflectance	115	R_o Range (%)	2.08–2.38	2.2–2.29	2.1–2.25	-
			R_o Average (%)	2.24	2.24	2.18	-
Core lab	Graptolite reflectance measurement	303	R_o Range (%)	2.1–4	2.2–3.5	2.9–4.9	2.7–3.4
			R_o Average (%)	3	3	3.5	3

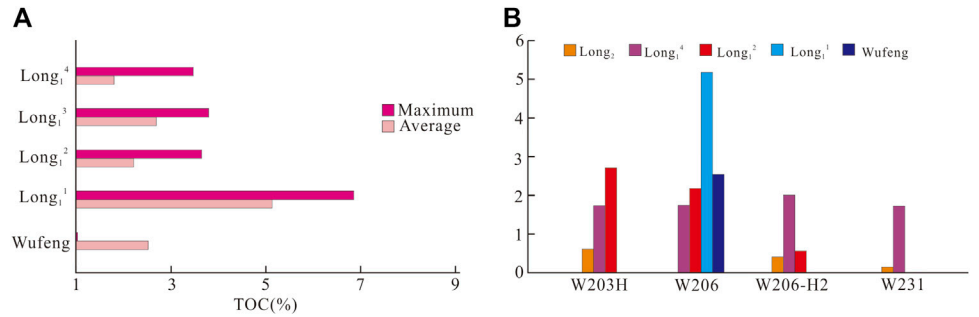

FIGURE 4 | Analysis of TOC content of each small layer by core of the Wufeng Formation Long 1_1 sub-member in the study area.

Geochemical Characteristics

The observation of cores and thin sections shows that there is no vitrinite in the highly mature source rocks of the Lower Paleozoic in the study area, only solid asphalt, which is the residue left after the gas generation of crude oil (He X. et al., 2021; He et al., 2021d; Yuan et al., 2021). Therefore, according to the correlation between solid asphalt and vitrinite reflectance, the maturity of the Lower Paleozoic source rocks can be evaluated after converting asphalt reflectance into vitrinite reflectance. Based on the empirical OM maturity measured by two core analysis methods, the average asphalt reflectance converted into R_o in Long 1_1 is 2.2%. The measured average R_o of graptolite reflectance is 3.1%, and both are over mature stages, mainly producing dry gas (**Table 1**).

To characterize shale OM abundance quantitatively, the LECO CS230 carbon/sulfur analyzer was used to determine the TOC content of gas-bearing shale from Wufeng Formation Long 1_1. The empirical analysis shows that the average TOC of each small layer of Long 1_1 and the Wufeng Formation core is 0.5–2.88%, with small layer 1 having the highest 5.18% (**Figure 4**). Consistent with shallow shale gas, small layer 1 has the highest thermal evolution and OM abundance.

Reservoir Space Characteristics

According to the observation of thin cast sections and the AIP-FESEM of typical samples from five coring wells in the study area, the main reservoir space types of the Wufeng Formation Long 1_1 are organic pores, inorganic pores, and fractures. OM forms organic pores in the later thermal evolution process. Inorganic pores can be further divided into six types (Intergranular pore, Micropore in clay minerals, Intragranular dissolved pore, Intracrystalline dissolved pores, Biological pore, OM pore), mainly including intergranular pores, intercrystalline dissolved pores, and intergranular pores. Fractures mainly include structural and nonstructural fractures, whose development degree is related to the thermal evolution degree of OM, shale brittleness, and tectonic stress. The pore types are mainly micro-nano-pores (Jarvie et al., 2007; Curtis et al., 2012; Zhang K. et al., 2020; Rashid et al., 2020; Xiao et al., 2020; Huang et al., 2021).

1) OM pores

OM pores are the main pore type of shale gas reservoirs. OM pores and their specific surface provide an adsorbent for natural gas and a space for the occurrence of free gas, which is very important for the enrichment of shale gas (Sakhaee-Pour and Bryant, 2015; Guo et al., 2018; Han et al., 2019; Ko, et al., 2017). The development of OM pores is affected by the degree of thermal evolution and the microstructure of the OM, resulting in great differences in the distribution patterns of OM pores in a single vertical well. The study area has a high degree of the thermal evolution of OM. OM pores in various forms are widely distributed. Circular and oval shapes predominate inside them, and sponge, though pore and strip shapes are observed. The pores are irregular, uneven distribution, and the pore diameter is mainly less than 50 nm (**Figures 5A–C**). Longitudinally, the TOC of small layer 1 is the highest, mainly as a sapropel formation, and the developmental degree of OM pores is significantly greater than that of other small layers.

2) Intergranular pores

Compared with conventional oil and gas reservoirs, shale reservoirs have a shallow burial depth and relatively low compaction and diagenesis, and they retain more intergranular pores. Irregular dissolved pores, including mold pores, are formed in feldspar, calcite, dolomite, and other particles. During diagenesis, compaction, and cementation, due to incomplete action, intergranular pores can develop around ductile minerals (clay flocs, microcrystalline spherulite minerals, OM, etc.) and brittle minerals (quartz, feldspar, pyrite, etc.). The pore types are linear and triangular, and the pores are generally larger than OM pores (**Figures 5D–F**).

3) Intercrystalline pores/Intercrystalline dissolved pores

Due to the irregularity of the crystals, brittle and compressive particles, such as pyrite, carbonate, and quartz, it easily form intercrystalline pores in the process of crystal packing in the study area. They are mainly includes pores developed between authigenic crystals, and the pores are clean. Most of these pores are isolated and poorly connected, so it is difficult for natural gas in the source area to flow into these pores (Zou et al., 2010; Yu et al., 2016, Yu Y. X. et al., 2017). Pyrite microspheres formed under an anoxic environment are widely distributed in the study area, present as aggregates of pyrite crystals in a

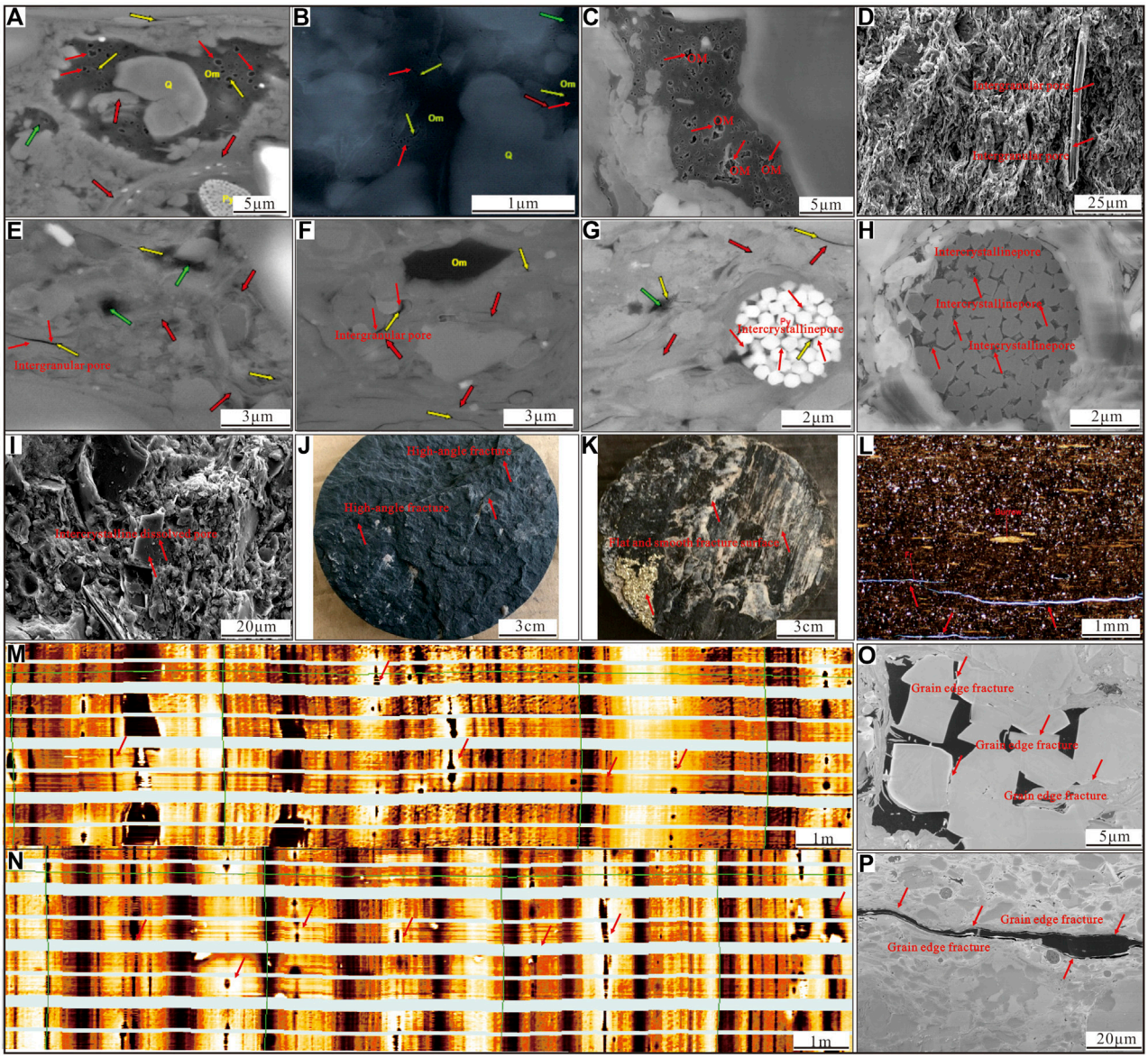

FIGURE 5 | Reservoir space types and characteristics of the Long 1_1 sub-member in the study area. **(A)**. W206, 3,787.53 m, Micropores in organic matter. **(B)**. W206, 3,765.52 m, Micropores in organic matter. **(C)**. R233H, 3,884.35 m, Organic matter pore, The pores are round-oval. **(D)**. W206H2, 3,782.52 m, The intergranular pores are lamellar. **(E)**. W206, 3,771.81 m, Flaky intergranular pores between clay particles. **(F)**. W206, 3,781.76 m, intergranular pores. **(G)**. W206, 3,787.53 m, Intercrystalline pores in pyrite particles. **(H)**. W231, 3,878.92 m, Intercrystalline pores in pyrite particles. **(I)**. R233H, 3,893.50 m, Intercrystalline dissolved pores. **(J)**. W231, 3,878.85 m, Vertical fracture, unfilled. k. R233H, 3,885.27 m, Calcite can be seen on the fracture surface, and there are scratches on the fracture surface. **(L)**. W206, 3,753.86 m, Microcracks parallel to clay bedding. **(M,N)**, characteristics of bedding fractures in the imaging logging. **(O)**. R233H, 3,879.27 m, grain edge fractures. **(P)**. W231, 3,856.62 m, grain edge fractures of organic matter.

raspberry-like shape, and mostly exist individually as regular cube shapes. Due to the non-tight packing during the crystal growth process, the intercrystalline micropores are mostly irregular (**Figures 5G,H**). OM can form many organic acids in hydrocarbon generation, and there are some acidic substances in water formation (Lyu et al., 2021; Wang et al., 2021). These substances migrate under the action of potential energy. They can selectively dissolve feldspar, calcite, and other soluble minerals so that the intercrystalline pores are dissolved in varying degrees, thus forming intercrystalline dissolved pores dominated by ellipses and triangles (**Figure 5I**).

4) Fractures

Shale reservoirs are characterized by ultralow porosity and low permeability. The development of fractures affects the physical

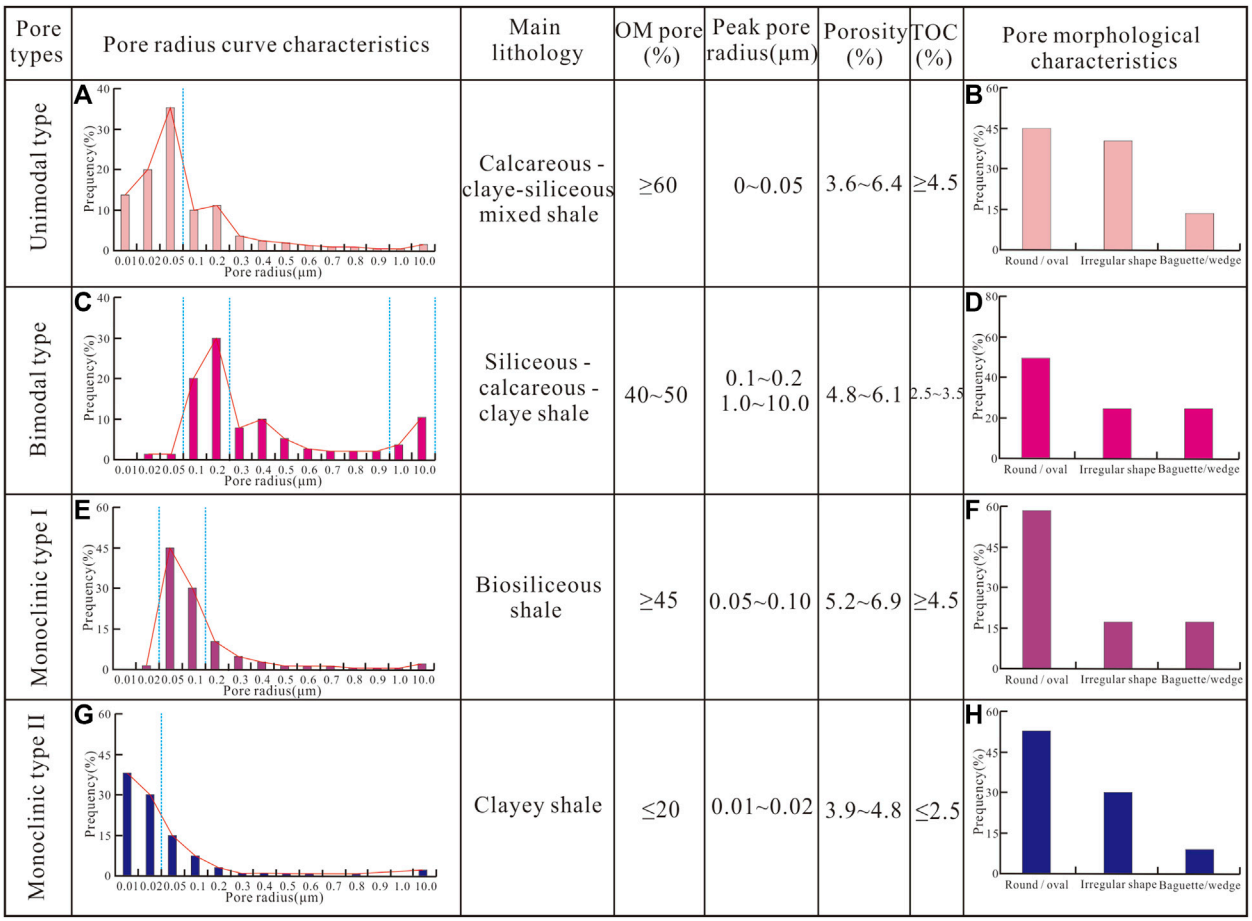

FIGURE 6 | Distribution characteristics of pore structure based on the SEM. **(A)** Pore radius curve characteristics of the unimodal type. **(B)** Pore morphological characteristics of the unimodal type. **(C)** Pore radius curve characteristics of the bimodal type. **(D)** Pore morphological characteristics of the bimodal type. **(E)** Pore radius curve characteristics of the monoclinic type I. **(F)** Pore morphological characteristics of the monoclinic type I. **(G)** Pore radius curve characteristics of the monoclinic type II. **(H)** Pore morphological characteristics of the monoclinic type II.

properties of shale reservoirs and strongly influences the formation and expansion of hydraulic pressure fractures, thus affecting shale productivity. Structural and nonstructural fractures are the main fractures developed in the study area (Zou et al., 2010; Li H. et al., 2021; Li, 2021). Structural fractures are mainly shear fractures formed by structural stress. Our core observation shows that most of them are low-angle and high-angle fractures characterized by flat and smooth fracture surfaces, a regular occurrence, far extension, and more clastic particles (**Figures 5J,K**). Similar characteristics were observed under the electron microscope. Such fractures can better connect poorly interconnected pores, thus greatly improving the seepage capacity of the reservoir (**Figure 5L**). However, if high-angle fractures develop through the layer, this may lead to the loss of shale gas, which is unfavorable to the preservation of shale gas. Foliation bedding fractures are also widely developed in the study area. These fractures show up as dark linear patterns on the map by imaging logging and are mainly the connected organic and inorganic pores in the shale. They can effectively increase the effective porosity of the reservoir, have a great influence on the horizontal seepage capacity of the reservoir (**Figures 5M, N**), and are an important weak surface for the expansion of compression fractures. In addition, microfractures in the study area are extremely well developed, with lengths usually ranging from micrometers to nanometers and widths ranging from hundreds of nanometers to several micrometers. These fractures are of structural origin and nonstructural origin. Fractures with structural origin have characteristics similar to macro-shear fractures (**Figure 5L**), and fractures with nonstructural origin are mainly developed along weak planes dominated by bedding planes and lithologic interfaces, primarily coming in three types: 1) cleavage fractures formed in flake minerals; 2) grain edge fractures formed at the interface between clay minerals and clastic particles (**Figures 5O, P**); and 3) intercrystalline fractures of clay minerals, quartz particles, and pyrite. These microfractures are intertwined into a network, and the joint

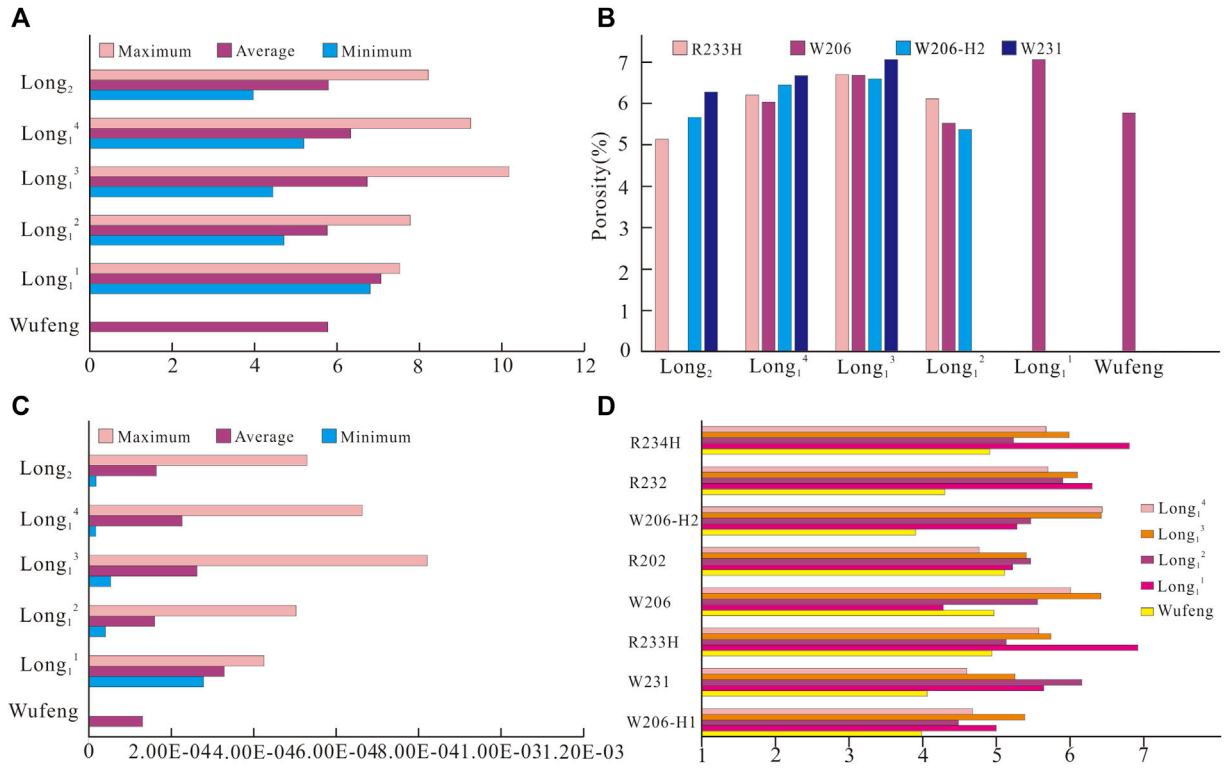

FIGURE 7 | Distribution of porosity and permeability of the Wufeng Formation Long 1_1sub-member in the study area. **(A)** Porosity of each sub-member. **(B)** Porosity of the single well. **(C)** Permeability of each sub-member. **(D)** Permeability of the single well.

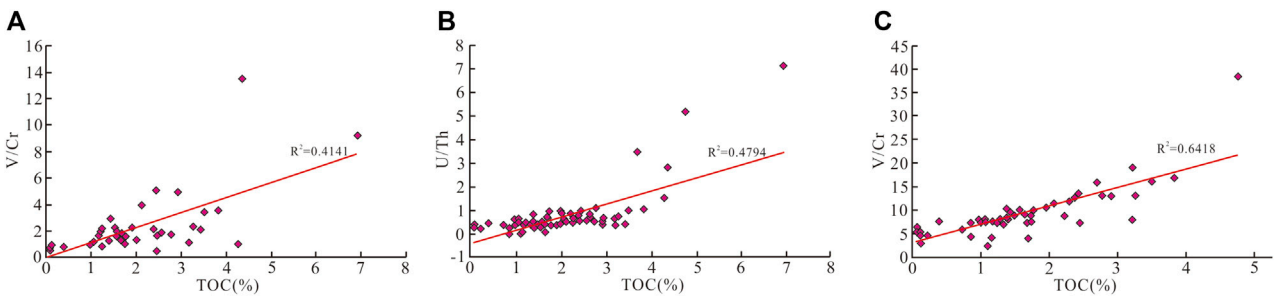

FIGURE 8 | Relationship between TOC content and V/Cr, U/TH, and Ni/CO in the study area.

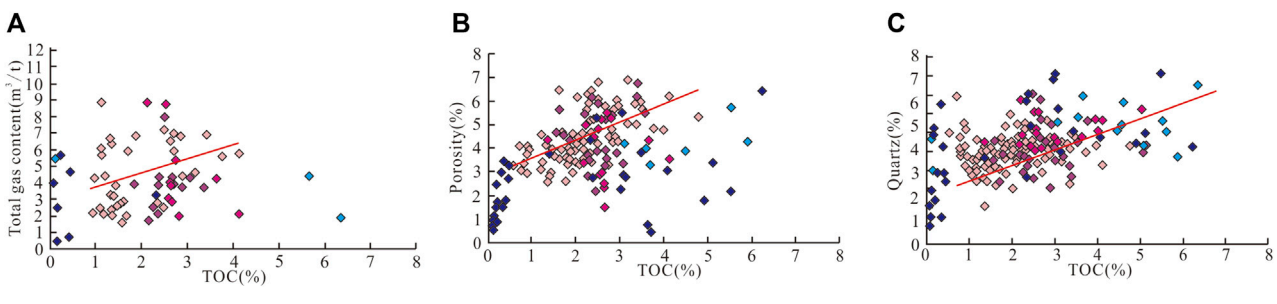

FIGURE 9 | Relationships between TOC content and porosity, gas volume, and quartz in the study area.

TABLE 2 | Sedimentary microfacies of the first member of the wufeng formation–longmaxi formation in the study area.

Subfacies	Microfacies	Horizon	Redox environment	Lithofacies	U/Th	Quartz	Carbonate	Clay	TOC	Porosity	Gas volume	Brittle minerals	Reservoir classification
Outer shelf	Deepwater silty mud shelf	Long 1_1^2, Long 1_1^4	Oxidation, weak local reduction	Ultralow-carbon, low-carbon, and medium-carbon siliceous shale facies; low-carbon and medium-carbon carbonate siliceous shale facies	0.53	41.2	8.91	32.1	2.01	5.57	3.89	56.47	Mainly II, III
	Rich organic silty mud shelf	Long 1_1^3, Wufeng Formation	Oxidation, weak local reduction	Ultralow-carbon, low-carbon, and medium-carbon siliceous shale facies; low-carbon, medium-carbon carbonate siliceous shale facies, low-carbon siliceous carbonate shale facies	0.69	39.57	14.36	27	2.67	5.5	4.33	59.87	Mainly II
	Rich organic mud shelf	Long 1_1^1	Strong reduction	Medium-carbon and high-carbon siliceous shale facies	1.55	48.67	7.69	20.3	4.98	6.27	5.86	62.68	Mainly I
	Rich organic siliceous mud shelf	Long 1_1^1	Strong reduction	High-carbon siliceous shale facies	2.21	45.31	9.86	18.9	5.21	5.68	6.22	59.96	Mainly I

action of micro-and macro fractures has an important impact on the enrichment of shale gas.

Overall, the shale reservoir space of the Longmaxi Formation in the study area is mainly composed of organic pores, inorganic pores, and fractures. Due to the multistage tectonic stress of Indosinian, Yanshan, and Himalayan orogenies, the shale of the Longmaxi Formation has the characteristics of obvious compaction and diagenesis, a high degree of thermal evolution, strong tectonic uplift, and deep burial depth, so OM well-connected pores and fractures are developed in the study area. In contrast, inorganic pores are less developed and poorly connected. Therefore, in the study area, OM pores and fractures are important seepage channels of shale gas.

Pore Structure Characteristics

The SEM analysis of shale pore structure shows that the pore structure of shale reservoirs in the Wufeng Formation Long 1 Member gradually improves from top to bottom. In contrast, the proportion of mesopores (2–50 nm) and large pores (>50 nm) increases, but small pores (<2 nm) and mesopores still predominate, accounting for 42 and 49%, respectively. According to the frequency distribution curve of pore radius, pore structure can be divided into four types (Xiong et al., 2021), i.e., unimodal (mainly organic pores), bimodal (both organic and inorganic pores), monoclinic type I (mainly organic pores), and monoclinic type II (mainly inorganic pores). Their characteristics are as follows.

Unimodal type: There is only one peak frequency of the pore radius. The pore radius has a narrow distribution range, and small pores (micropores) less than 2 nm predominate and are rich in OM (TOC≥4.5%). The lithology is mainly calcareous-clay-siliceous mixed shale. More than 60% of the pores are OM pores. Intergranular pores and intergranular pores are rare, the pores have good sortability and connectivity, and the reservoir has good physical properties (**Figure 6A**). The pore morphology is mainly circular, elliptical, or irregular, together accounting for more than 85%. The pores of other shapes, such as narrow, long, and wedge-shaped, are relatively developed, accounting for approximately 15% (**Figure 6B**).

Bimodal type: There is one peak frequency for the pore radius, the difference between primary and secondary peaks is large, the main peak is approximately 0.1–0.2 μm, and the secondary peak is about 1–10 μm. Pore size varies widely, and mesopores and large pores predominate, with relatively poor sortability and strong heterogeneity. Both organic and inorganic pores are developed, accounting for the same proportion (40–50%), the TOC content is between 2.5 and 3.5%, and the brittle mineral content is high. The organic pore distribution is uneven, the connectivity in general, and the pore structure is slightly worse than that of the unimodal type (**Figure 6C**). The pore morphology is circular and elliptical, accounting for approximately 75%. The proportion of other forms is relatively low, explained by the good compression resistance of rigid particles (**Figure 6D**).

Monoclinic type I: Organic pores predominate, inorganic pores are not developed, and the pore radii are mostly 0.05–0.1 μm. The mesopores predominate, have good sortability, and are rich in OM

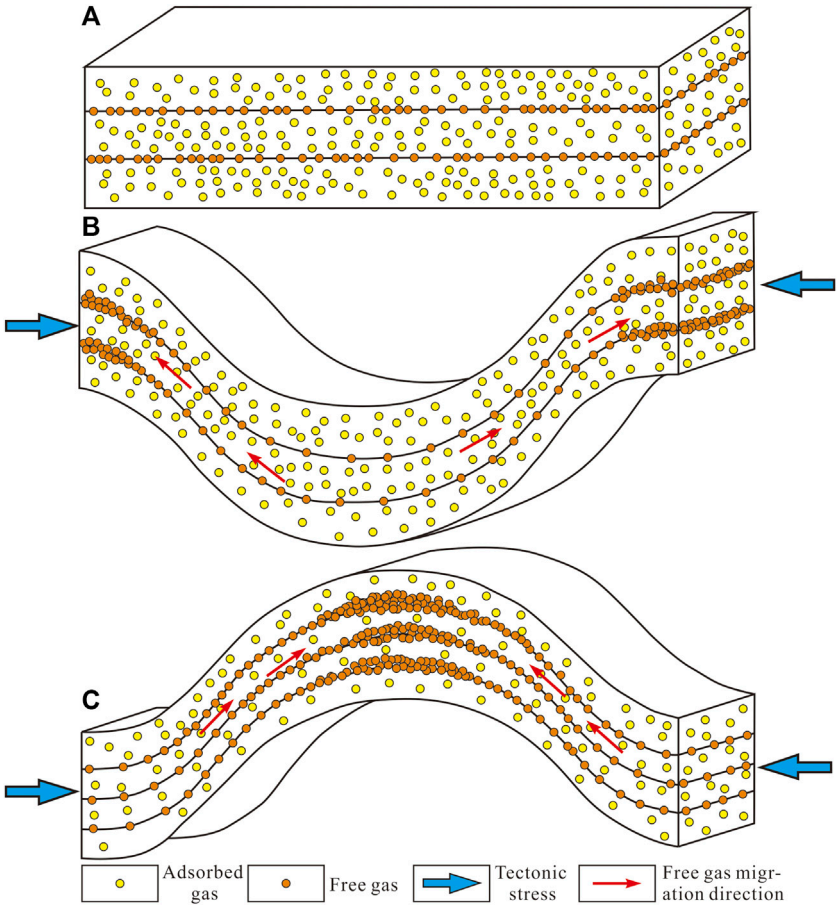

FIGURE 10 | Compound Controlling Mode of Structural Fractures in Shale Gas Reservoirs (Wang et al., 2017; Xu Z. et al., 2021). **(A)**. Model diagram of a shale gas reservoir in North America, with weak structural activity and horizontal fractures. **(B)**. Enrichment model of synclinal gas with no fractures developed at structural highs. **(C)**. Enrichment model of anticlinal gas with no fractures developed at structural highs.

(TOC≥4.5%). The lithology is mainly biological siliceous shale, and pyrite laminae are developed. The pore morphology is mainly circular or oval, accounting for approximately 60%, while irregular, narrow, and wedge-shaped pores account for more than 35%. Siliceous shale has the highest content, the pore radius of organic pores is better than that of unimodal type, and these reservoirs have the best physical properties (**Figures 6E,F**).

Monoclinic Type II: Inorganic pores predominate, organic pores are not developed, and the pore radii are mostly 0.01–0.02 μm. Small pores predominate, with good sortability but poor connectivity and low OM content (TOC<2%). The content of clayey shale is high, pyrite is rare, and round or oval pores account for approximately 55%. They have poor connectivity (**Figures 6G,H**).

Physical Characteristics

Based on the core analysis, vertically, the average core porosity of Long 1_2, each small layer of Long 1_1, and the whole Wufeng Formation is 6.24%, of which small layer 1 has the highest core porosity (7.06%) and Wufeng Formation the lowest (5.77%) (**Figures 7A,B**). Overall, core porosity gradually decreases from bottom to top. The core permeability is 1.33–3.32 × 10^{-4} MD, small layer 1 having the highest and Wufeng Formation the lowest (**Figure 7C**).

The logging results show that the porosity of the Wufeng Formation Long 1_1 sub-member of eight wells in the study area is 4.7–6.0%, with an average of 5.5%. Well W206-H1 had the lowest, Well W206 had the highest, and the distribution is mainly within 5.6–5.8%. Vertically, the porosity trend of each small layer of each well is about the same, of which small layer 3 and small layer 1 have the highest porosity, with an average of 5.84 and 5.68%, respectively, and Wufeng Formation has the lowest, with an average of 4.52% (**Figure 7D**).

The porosity decreases eastward and southward away from the denudation line in the plane distribution. The reservoir area with high porosity is distributed along with the wells W206-H2-R233H-HS1, and well W231 is a relatively low-value area; the reservoir areas with high porosity in small layer 1 are in wells W206, W205 to the northwest, and well WL203 to the south. Overall, the porosity increases with greater formation burial depth and gradually decreases to the south.

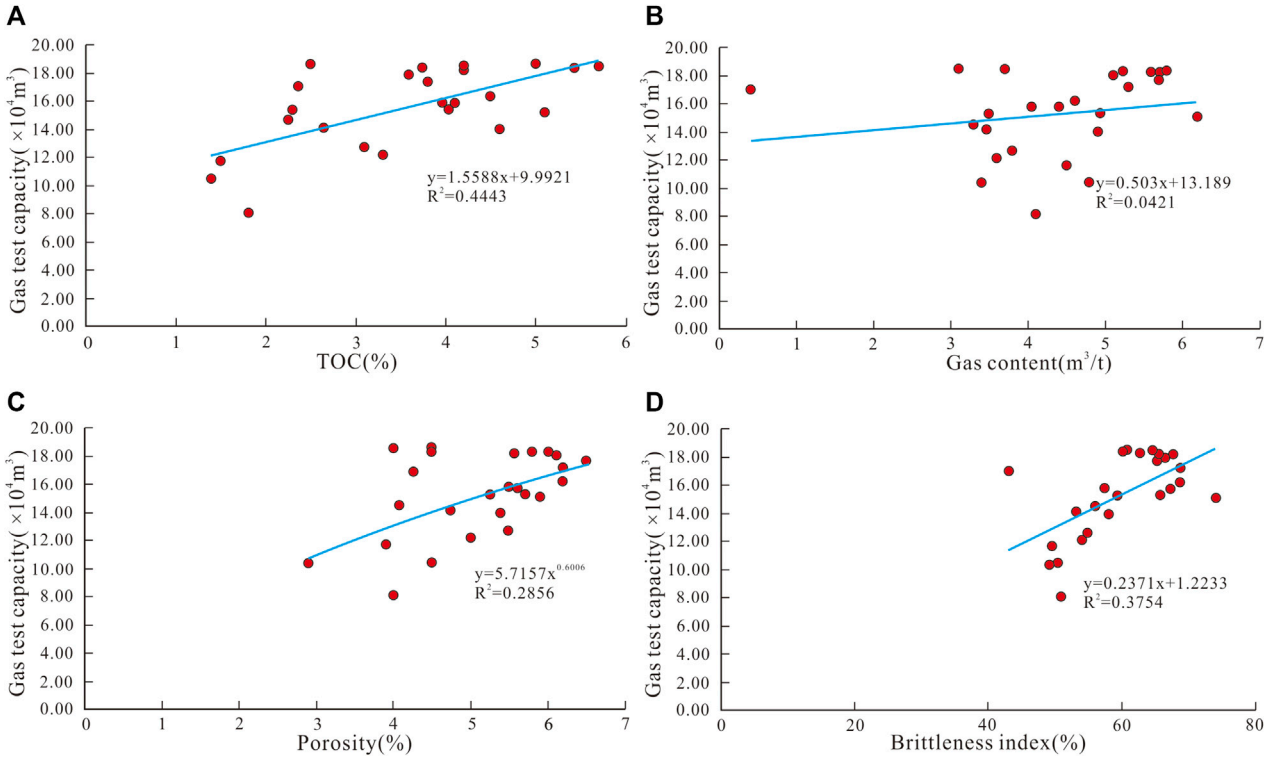

FIGURE 11 | Relationship between test production below 200,000 m^3 and reservoir physical properties in the study area.

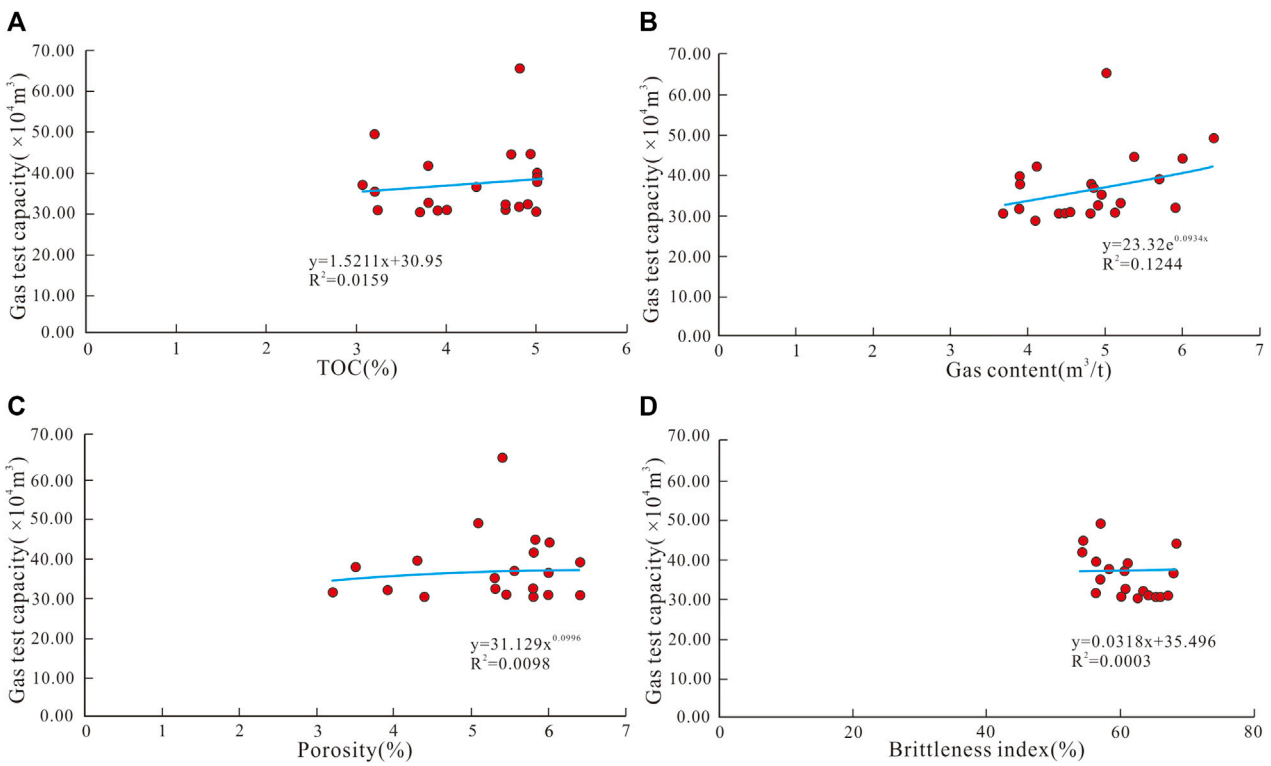

FIGURE 12 | Relationship between test production above 300,000 m^3 and reservoir physical properties in the study area.

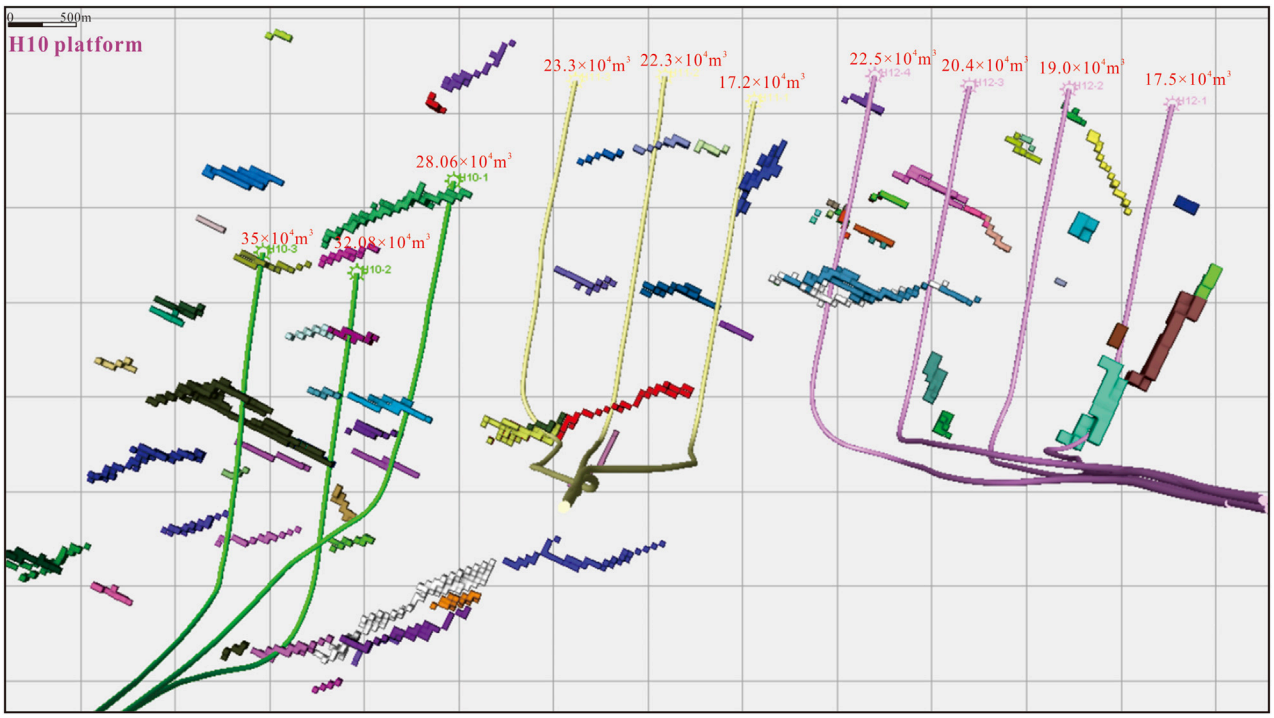

FIGURE 13 | Relationship between fracture development area and test productivity.

DISCUSSION

Controlling Factors of Deep Shale Gas Enrichment and Yield

Sedimentary Facies Are the Main Factor Controlling the Development of Shale Gas Reservoirs

1) An anoxic deep-water strongly reducing environment is a necessary condition for OM enrichment

The reducibility of sedimentary water strongly affects the preservation of OM, and an anoxic strong reduction environment is more conducive to the enrichment and preservation of OM (Loucks et al., 2009; Cheng et al., 2021). Trace element analysis showed that the U/Th ratio of the small layer 1 is > 1.25, making it a strongly reducing environment of residual hypoxia, an important and favorable feature for sweet-spot layers. The core analysis data show good positive

TABLE 3 | Comprehensive evaluation standard of selecting shale gas areas in the study area.

Evaluation parameter	Weight grade	Weight	Classification and evaluation criteria of shale gas reservoir logging		
			Class I	Class II	Class III
Total Gas Volume (m^3/t)	Level 1	0.3	>3	2–3	<2
TOC (%)	Level 2	0.3	>3	2–3	<2
Porosity (%)	Level 2	0.2	>5	3–5	<3
Brittleness Index (%)	Level 2	0.2	>55	35–55	<35

TABLE 4 | Classification standards of favorable areas in the study area.

Classification	Burial depth	The thickness of class I + II reservoirs	Reservoir evaluation index	Structural development
Class I	Below 4,000 m	>40 m	>1.4	The fault is undeveloped, and the structure is relatively simple
Class II	4000–4500 m	25–40 m	1.2–1.4	The fault is undeveloped, and the structure is relatively simple
Class III	4000–4500 m	<25 m	<1.2	Fault development

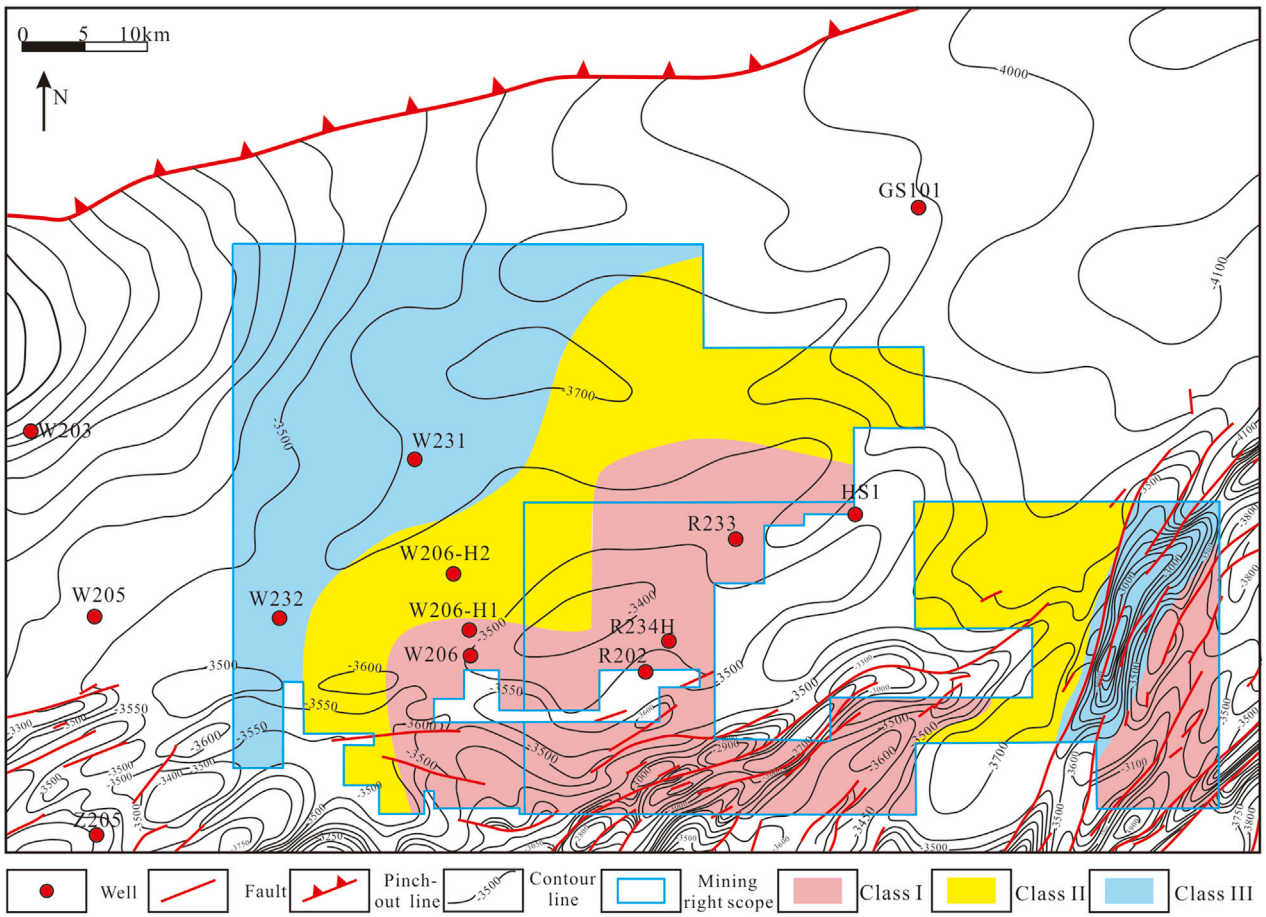

FIGURE 14 | Favorable target areas in the study area.

correlations between TOC and the V/Cr, U/Th, and Ni/Co values of trace elements, with corresponding coefficients of determination (R^2) of 0.4141, 0.4794, and 0.6418 (**Figure 8**). The higher the R^2, the more anoxic the sedimentary environment of the formation will be, and the more OM will be enriched.

2) The OM content and maturity are the key factors affecting the physical properties and gas-bearing of shale gas reservoirs

OM is the material source of shale gas. Thermal maturation makes OM generate many hydrocarbons after reaching the hydrocarbon generation threshold. After OM generates hydrocarbon, it begets high-pressure protective pores and forms organic pores in the process of hydrocarbon generation, which increases the rock's porosity. At the same time, the reduction in OM volume could produce ultrafine fractures, which is conducive to the preservation of shale gas. Many micropores and microfractures are generated in the process of hydrocarbon generation, and more free natural gas is stored in these spaces. The higher the TOC content, the larger the total volume of pores, and the larger the specific surface area available for adsorption of adsorbed gas. Thus, the total gas volume of the shale will grow. The core analysis and test data of 11 wells (including W203, W205, W206, and R233H) show that the TOC content has positive correlations with porosity, quartz, and gas content (**Figure 9**), which also confirms the positive role of OM in shale reservoir space and gas-bearing property.

3) Organic rich siliceous mud shelves and organic-rich mud shelves are the most favorable sedimentary microfacies for shale gas enrichment

The results of sedimentary microfacies analysis show that deep-water silty mud shelves, organic-rich silty mud shelves, organic-rich siliceous mud shelves, and organic-rich mud shelves in the outer shelf subfacies are the favorable microfacies for shale gas exploration and development. Among them, organic-rich siliceous mud shelves and organic-rich mud shelves are the most favorable microfacies owing to the following characteristics: high TOC content, with an average of 5%, giving them better hydrocarbon generation potential and more abundant shale gas resources; more developed pores, with an average porosity of 6%, providing enough reservoir space for shale gas enrichment; more developed shale interlayer foliation

fractures; medium-carbon and high-carbon siliceous shale facies with their high brittle mineral contents and low carbonate mineral contents (mostly less than 10%); a high biogenic silica content, greater than 45%, which is conducive to improving the hydrofracture effect of shale (**Table 2**).

Fracture Development Is the Key Factor for Achieving a High Yield of Shale Gas

Fractures are important reservoir spaces and migration channels of shale gas, playing an important role in the accumulation, preservation, exploration, and development of shale gas (Li et al., 2019c; Li et al., 2020; Li H. et al., 2021; Li 2021). Investigation of the Lower Paleozoic marine shale gas in the Sichuan Basin and its surrounding areas shows that marine shale has a good material foundation, and gas-bearing can almost be observed in each drilling. Still, the gas drilling results are very different. Therefore, the preservation conditions are key factors in determining whether shale gas can be enriched and produced. The shale gas area in North America is characterized by weak structural activity and developed horizontal fractures. Most of the shale gas is enriched in shale reservoirs uniformly (**Figure 10A**). Therefore, good single-well production can often be realized through fracturing and reconstruction of the reservoir. However, China's shale gas enrichment modes are mainly anticlinal and synclinal structural modes, and both are found in the study area (**Figures 10B,C**). Therefore, fully sealing the top and floor of the reservoir is very important for reservoir formation, and the fracture is the key to the sealing effect. If the fracture or fault is not developed at the high point of the syncline or anticline structure, the shale gas may not be lost, and the fracture could play a positive role in the accumulation of shale gas. The shale gas of the anticline structure is accumulated in the core of the anticline, while the syncline structure is concentrated in the syncline wings.

According to the correlation between the test product and the four property parameters of the reservoir in the study area, test production of less than 200,000 m^3 in a well positively correlates with the reservoir's physical properties. In contrast, the presence of a test production of more than 300,000 m^3 has a poor correlation with the reservoir's physical properties (**Figures 11**, **12**). Therefore, the development of fractures is often a direct manifestation of the poor correlation with reservoir physical properties. As the gas test production is related to geological and engineering factors, geological factors determine the shale gas enrichment, and engineering factors play an important role in improving the test production. Different fracturing and mining methods will lead to different test production in the same area. Therefore, the correlation coefficient (R^2) is small in **Figures 11**, **12**, proving that their correlation is weak. The phenomenon is normal. In addition, according to the seismic prediction results of the fracture development zone, most of the class I wells with a test production of more than 300,000 m^3 are located in areas with relatively well-developed fractures. The comparison between the test productivity data and the micro-seismic fracture monitoring data also shows that the test productivity of shale gas production wells in the fracture development area is generally larger than that in the area where fractures are not developed (**Figure 13**).

Selection of Favorable Target Areas

According to the evaluation indices for choosing shale gas areas in China and abroad, combined with the existing research results in Southern Sichuan and the actual situation of the study area, seven evaluation parameters, such as gas volume, pressure coefficient, porosity, brittle mineral content, high-quality shale thickness, burial depth, and TOC, were selected as the main evaluation indices for the selection of favorable areas. The evaluation standards for determining shale gas areas in the study area were formulated (**Table 3**). The combination of these with the location parameters, such as structure, preservation conditions, burial depth, and class I + II reservoir thickness, the classification standards of favorable areas in the study area was formulated (**Table 4**), and finally, the study area was divided into class I, II, and III favorable areas (**Figure 14**).

Class I favorable areas are a class I + II reservoirs with a thickness of more than 40 m, a reservoir index of more than 1.4, undeveloped faults, and a relatively simple structure. They lack surface nonworking areas, have a burial depth of less than 4,000 m, and are mainly distributed in the south of wells W206, W206H1, R234H, R233H, and some areas in the east of the study area.

Class II favorable areas are the areas with reservoir thickness greater than 25 m, reservoir index greater than 1.2, undeveloped faults, and a relatively simple structure. They lack nonworking ground areas, have a burial depth of less than 4,500 m, and are mainly distributed in the north of well W206H1 in the middle of the study area, a belt running through the north and south of the area where Well W206H2 is located, and the northeast of North Rongchang block.

The class III favorable areas are those with reservoir thickness less than 25 m, either with or without fracture development. They are located in the Xishan/Luoguanshan structural belt, lack ground nonworking areas, are buried within a small layer at 4,500 m, and are mainly distributed in the northwest of well W232 and well W231 in the study area.

CONCLUSION

Taking the Long 1_1 sub-member of the Wufeng Formation of the Upper Ordovician and the Longmaxi Formation of the Lower Silurian in the East Weiyuan–North Rongchang area as an example, this paper comprehensively studies the geological characteristics and controlling factors of the enrichment and high-yield of deep shale gas by XRD analysis, LECO TOC-S analysis, optical microscopy, and AIP-FESEM and identified the favorable target areas for shale gas development in the study area. The main findings and conclusions are as follows:

1) In the study area, the brittle minerals of the Long 1_1 sub-member of the Wufeng Formation–Longmaxi Formation are mainly quartz, feldspar, carbonate minerals, pyrite, and hematite. The OM is in the over mature stage, and the TOC content is high, primarily producing dry gas. Vertically, the maturity of brittle minerals and OM and TOC contents gradually increases from top to bottom, the small layer 1 having the most.

2) The reservoir space of the Long 1_1 sub-member of the Wufeng Formation–Longmaxi Formation in the study area mainly includes organic pores, inorganic pores, and fractures. The inorganic pores are mainly intercrystalline, intercrystalline dissolved pores, and intergranular pores. Organic pores and fractures are important seepage channels of shale gas, and microfractures can better connect inorganic and organic pores. According to the frequency distribution curve of pore radii, the pore structure can be divided into the unimodal type, bimodal type, monoclinic type I, and monoclinic type II. The unimodal type is the best, with small pores predominating, followed by mesopores and the developed organic pores. The unimodal type has high OM content, good sortability, and good connectivity.
3) Considering the redox environment, sedimentary facies, lithofacies, reservoir characteristics, and other factors, the sedimentary facies is the main thing controlling the development of shale gas reservoirs in the study area. The organic-rich siliceous mud shelf microfacies, organic-rich mud shelf facies, and high-carbon siliceous shale facies deposited in deep-water strongly reducing environments are the most favorable areas for developing shale gas reservoirs. Under favorable reservoir conditions, the development of fractures is the key factor in obtaining high shale gas yields.
4) Combining the reservoir evaluation index, burial depth, class I + II reservoir distribution, and structural development in the study area, we identified the favorable exploration target areas in the study area. In the class I areas, the reservoir thickness is greater than 40 m, the reservoir index is greater than 1.4, the fault is not developed, and the structure is relatively simple. The class I areas are mainly distributed in W206, W206H1, R234H, and R233H and areas to its south and some areas in the east of the study area.

DATA AVAILABILITY STATEMENT

The original contributions presented in the study are included in the article/supplementary material, further inquiries can be directed to the corresponding author.

AUTHOR CONTRIBUTIONS

YW contributed in writing, reviewing, and editing, data curation, writing-original draft preparation; JL, ZG, BY, CY and TT contributed in formal analysis, validation, and methodology, supervision, project administration; HT contributed to visualization and investigation.

REFERENCES

Cai, S. Y., Xiao, Q. L., Zhu, W. P., Wang, X. L., Yuan, H., Chen, J., et al. (2020). Characteristics and Controlling Factors of Nano Pores in Shale Reservoirs of Wufeng-Longmaxi Formations in Southern Sichuan Basin:insights from Shuanghe Outcrop in Changning Area. *Petrol. Geol. Exp.* 42 (6), 920–927. doi:10.11781/sysydz202006920

Chai, J., Ouyang, Y. B., and Zhang, D. D. (2020). Crackdetection Method in Similar Material Models Based on DIC. *J. Min. Strata Control. Eng.* 2 (2), 023015. doi:10.13532/j.jmsce.cn10-1638/td.2020.02.003

Chen, F., Zheng, Q., Ding, X., Lu, S., and Zhao, H. (2020b). Pore Size Distributions Contributed by OM, clay and Other Minerals in Over-mature marine Shale: A Case Study of the Longmaxi Shale from Southeast Chongqing, China. *Mar. Pet. Geology.* 122, 104679. doi:10.1016/j.marpetgeo.2020.104679

Chen, S., Han, Y., Fu, C., Zhang, H., Zhu, Y., and Zuo, Z. (2016). Micro and Nano-Size Pores of clay Minerals in Shale Reservoirs: Implication for the Accumulation of Shale Gas. *Sediment. Geology.* 342, 180–190. doi:10.1016/j.sedgeo.2016.06.022

Chen, S. L., Huang, B. X., Li, D., Zhao, X. L., Xu, J., and Wang, C. W. (2020a). Experiment Study on the Basic Law of High Pressure Abrasive Hydraulic Cutting for Coal-Rock Mass. *J. Min. Strata Control. Eng.* 2 (4), 047521. doi:10.13532/j.jmsce.cn10-1638/td.20200506.002

Chen, S., Liu, P., Tang, D., Tao, S., and Zhang, T. (2021a). Identification of Thin-Layer Coal Texture Using Geophysical Logging Data: Investigation by Wavelet Transform and Linear Discrimination Analysis. *Int. J. Coal Geology.* 239, 103727. doi:10.1016/j.coal.2021.103727

Chen, S., Tang, D., Tao, S., Liu, P., and Mathews, J. P. (2021b). Implications of the *In Situ* Stress Distribution for Coalbed Methane Zonation and Hydraulic Fracturing in Multiple Seams, Western Guizhou, China. *J Pet. Sci. Eng.* 204, 108755. doi:10.1016/j.petrol.2021.108755

Cheng, L., Guan, F. J., Liu, D. H., Yang, W. X., and Sun, J. (2021). Micropore Characteristics and Geological Significance of Shale Reservoirs: Case Study of Fuling Shale Gas in Sichuan Basin, China. *Geofluids*, 6636156. doi:10.1155/2021/6636156

Curtis, M. E., Cardott, B. J., Sondergeld, C. H., and Rai, C. S. (2012). Development of Organic Porosity in the Woodford Shale with Increasing thermal Maturity. *Int. J. Coal Geology.* 103, 26–31. doi:10.1016/j.coal.2012.08.004

Fan, C. H., He, S., Zhang, Y., Qin, Q. R., and Zhong, C. (2018). Development Phases and Mechanisms of Tectonic Fractures in the Longmaxi Formation Shale of the Dingshan Area in Southeast Sichuan Basin, China. *Acta Geol. Sin* 92 (6), 2351–2366. doi:10.1111/1755-6724.13732

Fan, C., Li, H., Qin, Q., He, S., and Zhong, C. (2020b). Geological Conditions and Exploration Potential of Shale Gas Reservoir in Wufeng and Longmaxi Formation of southeastern Sichuan Basin, China. *J Pet. Sci. Eng.* 191, 107138. doi:10.1016/j.petrol.2020.107138

Fan, C., Li, H., Zhao, S., Qin, Q., Fan, Y., Wu, J., et al. (2020a). Formation Stages and Evolution Patterns of Structural Fractures in Marine Shale: Case Study of the Lower Silurian Longmaxi Formation in the Changning Area of the Southern Sichuan Basin, China. *Energy Fuels* 34, 9524–9539. doi:10.1021/acs.energyfuels.0c01748

Guo, H., He, R., Jia, W., Peng, P. a., Lei, Y., Luo, X., et al. (2018). Pore Characteristics of Lacustrine Shale within the Oil Window in the Upper Triassic Yanchang Formation, southeastern Ordos Basin, China. *Mar. Pet. Geology.* 91, 279–296. doi:10.1016/j.marpetgeo.2018.01.013

Han, H., Pang, P., Li, Z.-l., Shi, P.-t., Guo, C., Liu, Y., et al. (2019). Controls of Organic and Inorganic Compositions on Pore Structure of Lacustrine Shales of Chang 7 Member from Triassic Yanchang Formation in the Ordos Basin, China. *Mar. Pet. Geology.* 100, 270–284. doi:10.1016/j.marpetgeo.2018.10.038

He, S., Li, H., Qin, Q. R., and Long, S. X. (2021b). Effects of Dissolved Organic Matter on Shale Pore Structure of Low-Mature Lacustrine Facies Organic-Rich Shale. *Energy Source A* 9. doi:10.1080/15567036.2021.1979694

He, S., Li, H., Qin, Q., and Long, S. (2021a). Influence of Mineral Compositions on Shale Pore Development of Longmaxi Formation in the Dingshan Area, Southeastern Sichuan Basin, China. *Energy Fuels* 35 (13), 10551–10561. doi:10.1021/acs.energyfuels.1c01026

He, S., Li, H., Qin, Q. R., and Long, S. X. (2021d). Influence of mineral Compositions on Shale Pore Development of Longmaxi Formation in the Dingshan Area, Southeastern Sichuan Basin, China. *Energy Fuel* 191, 107138. doi:10.1021/acs.energyfuels.1c01026

He, X., Li, W. G., Dang, L. R., Huang, S., Wang, X. D., Zhang, C. L., et al. (2021c). Key Technological Challenges and Research Directions of Deep Shale Gas

Development. *Nat. Gas Ind.* 41 (1), 118–124. doi:10.3787/j.issn.1000-0976.2021.01.010

Huang, F. R., Yan, S. X., Wang, X. L., Jiang, P. C., and Zhan, S. B. (2021). Study on Infrared Radiation Characteristics of Gneiss under Uniaxial Compression. *J. Min. Strata Control. Eng.* 3 (1), 013011. doi:10.13532/j.jmsce.cn10-1638/td.20200730.001

Jarvie, D. M., Hill, R. J., Ruble, T. E., and Pollastro, R. M. (2007). Unconventional Shale-Gas Systems: The Mississippian Barnett Shale of north-central Texas as One Model for Thermogenic Shale-Gas Assessment. *Bulletin* 91 (4), 475–499. doi:10.1306/12190606068

Ko, L. T., Loucks, R. G., and Milliken, K. L. (2017). Controls on Pore Types and Pore-Size Distribution in the Upper Triassic Yanchang Formation, Ordos Basin, China: Implications for Pore-Evolution Models of Lacustrine Mudrocks. *Interpretation* 5, SF127–SF147. doi:10.1190/int-2016-0115.1

Li, H., Qin, Q., Zhang, B., Ge, X., Hu, X., Fan, C., et al. (2020). Tectonic Fracture Formation and Distribution in Ultradeep Marine Carbonate Gas Reservoirs: A Case Study of the Maokou Formation in the Jiulongshan Gas Field, Sichuan Basin, Southwest China. *Energy Fuels* 34, 14132–14146. doi:10.1021/acs.energyfuels.0c03327

Li, H. (2021). Quantitative Prediction of Complex Tectonic Fractures in the Tight sandstone Reservoirs: a Fractal Method. *Arab. J. Geosci.* 14 (19), 1986. doi:10.1007/s12517-021-08344-0

Li, H., Tang, H. M., and Zheng, M. J. (2019). Micropore Structural Heterogeneity of Siliceous Shale Reservoir of the Longmaxi Formation in the Southern Sichuan Basin, China. *Minerals* 9, 548. doi:10.3390/min9090548

Li, H., Tang, H., Qin, Q., Zhou, J., Qin, Z., Fan, C., et al. (2019c). Characteristics, Formation Periods and Genetic Mechanisms of Tectonic Fractures in the Tight Gas Sandstones Reservoir: A Case Study of Xujiahe Formation in YB Area, Sichuan Basin, China. *J Pet. Sci. Eng.* 178, 723–735. doi:10.1016/j.petrol.2019.04.007

Li, H., Wang, Q., Qin, Q., and Ge, X. (2021c). Characteristics of Natural Fractures in an Ultradeep Marine Carbonate Gas Reservoir and Their Impact on the Reservoir: A Case Study of the Maokou Formation of the JLS Structure in the Sichuan Basin, China. *Energy Fuels* 35 (16), 13098–13108. doi:10.1021/acs.energyfuels.1c01581

Li, W. G., Yue, H., Sun, Y. P., Guo, Y., Wu, T. P., Zhang, N. Q., et al. (2021b). Development Evaluation and Optimization of Deep Shale Gas Reservoir with Horizontal Wells Based on Production Data. *Geofluids*, 4815559. doi:10.1155/2021/4815559

Liu, J. S., Yang, H. M., Wu, X. F., and Liu, Y. (2020). The *In Situ* Stress Field and Microscale Controlling Factors in the Ordos Basin, central China. *Int. J. Rock Mech. Min* 135, 104488. doi:10.1016/j.ijrmms.2020.104482

Liu, J., Yang, H., Bai, J., Wu, K., Zhang, G., Liu, Y., et al. (2021c). Numerical Simulation to Determine the Fracture Aperture in a Typical basin of China. *Fuel* 283, 118952. doi:10.1016/j.fuel.2020.118952

Liu, Q. Y., Zhu, H. Y., and Chen, P. J. (2021e). Research Progress and Direction of Geology-Engineering Integrated Drilling Technology: A Case Study on the Deep Shale Gas Reservoirs in the Sichuan Basin. *Nat. Gas Ind.* 41 (1), 178–188. doi:10.3787/j.issn.1000-0976.2021.01.016

Liu, S. G., Jiao, K., Zhang, J. C., Ye, Y. H., Xie, G. L., Deng, B., et al. (2021d). Research Progress on the Pore Characteristics of Deep Shale Gas Reservoirs: An Example from the Lower Paleozoic marine Shale in the Sichuan Basin. *Nat. Gas Ind.* 41 (1), 29–41. doi:10.3787/j.issn.1000-0976.2021.01.003

Liu, Y. J., Lai, F. Q., Zhang, H. J., Tan, Z. J., Wang, Y. F., and Tan, X. F. (2021a). A Novel mineral Composition Inversion Method of Deep Shale Gas Reservoir in Western Chongqing. *J. Petrol. Sci. Eng.* 202, 108528. doi:10.1016/j.petrol.2021.108528

Liu, Y. Y., Ma, X. H., Zhang, X. W., Wei, G., Kang, L. X., Yu, R. Z., et al. (2021b). Shale Gas Well Flowback Rate Prediction for Weiyuan Field Based on a Deep Learning Algorithm. *J. Petrol. Sci. Eng.* 203, 108637. doi:10.1016/j.petrol.2021.108637

Loucks, R. G., Reed, R. M., Ruppel, S. C., and Jarvie, D. M. (2009). Morphology, Genesis, and Distribution of Nanometer-Scale Pores in Siliceous Mudstones of the Mississippian Barnett Shale. *J. Sediment. Res.* 79 (12), 848–861. doi:10.2110/jsr.2009.092

Lyu, P. F., Ma, F., and Bao, X. Y. (2021). Experimental Study on Pore Microstructure and Methane Occurrence Characteristics of Shale of marine-continent Transition Phase. *Fresen. Environ. Bull.* 30 (1), 330–337.

Ma, X., Wang, H., Zhou, S., Shi, Z., and Zhang, L. (2021). Deep Shale Gas in China: Geological Characteristics and Development Strategies. *Energ. Rep.* 7, 1903–1914. doi:10.1016/j.egyr.2021.03.043

Nie, H. K., and Jin, Z. J. (2016). Source Rock and Cap Rock Controls on the Upper Ordovician Wufeng Formation-Lower Silurian Longmaxi Formation Shale Gas Accumulation in the Sichuan Basin and its Peripheral Areas. *Acta Geol. Sin* 90, 1059–1060. doi:10.1111/1755-6724.12752

Nie, H. K., Sun, C. X., Liu, G. X., Du, W., and He, Z. L. (2018). Dissolution Pore Types of the Wufeng Formation and the Longmaxi Formation in the Sichuan Basin, South China: Implications for Shale Gas Enrichment. *Mar. Petrol. Geol.* 101, 243–251. doi:10.1016/j.marpetgeo.2018.11.042

Rashid, F., Hussein, D., Hussein, D., Lawrence, J. A., and Khanaqa, P. (2020). Characterization and Impact on Reservoir Quality of Fractures in the Cretaceous Qamchuqa Formation, Zagros Folded belt. *Mar. Pet. Geology.* 113, 104117. doi:10.1016/j.marpetgeo.2019.104117

Rui, J., Zhang, H., Zhang, D., Han, F., and Guo, Q. (2019). Total Organic Carbon Content Prediction Based on Support-Vector-Regression Machine with Particle Swarm Optimization. *J Pet. Sci. Eng.* 180, 699–706. doi:10.1016/j.petrol.2019.06.014

Sakhaee-Pour, A., and Bryant, S. L. (2015). Pore Structure of Shale. *Fuel* 143, 467–475. doi:10.1016/j.fuel.2014.11.053

Shi, X., Wang, J., Liu, G., Yang, L., Ge, X., and Jiang, S. (2016). Application of Extreme Learning Machine and Neural Networks in Total Organic Carbon Content Prediction in Organic Shale with Wire Line Logs. *J. Nat. Gas Sci. Eng.* 33, 687–702. doi:10.1016/j.jngse.2016.05.060

Song, L., Bhattacharya, S., Webb, Z., Fowler, A., and Lee, V. (2021). Preservation of organic carbon in the Cretaceous Hue Shale on the North Slope of Alaska: Insights from pyrite morphology. *International Journal of Coal Geology* 235, 103678. doi:10.1016/j.coal.2021.103678

Sun, S.Y (2021). Study on the characteristics of continental shale reservoir and the calculation of relative permeability curve. *Fresen. Environ. Bull.* 30 (4A), 4620–4627.

Tabatabaei, H (2021). Analysis of fracture density and their effect on mud loss in Asmari reservoir via FMI/FMS log, Rag-e-Safid oil field, SW of Iran. *Himal. Geol.* 42 (1), 205–210.

Wang, C., Shi, W.Z., Zhang, X.M., Xu, Z, Yuan, Q, and Xiao, D (2017). Comprehensive evaluation of fracture system in shale reservoir and its influence on shale gas seepage and accumulation. *Petrol. Geol. Rec. Effic* 24 (1), 50–56. doi:10.13673/j.cnki.cn37-1359/te.2017.01.007

Wang, H.B., Zhou, T., and Huang, X (2021). Pore evolution and fractal dimension characteristics of shale with different maturity. *Fresen. Environ. Bull.* 30 (6B), 7596–7603.

Wang, H., Wu, W., Chen, T., Dong, X., and Wang, G. (2019). An Improved Neural Network for TOC, S1 and S2 Estimation Based on Conventional Well Logs. *J. Pet. Sci. Eng.* 176, 664–678. doi:10.1016/j.petrol.2019.01.096

Wang, P., Chen, Z., Pang, X., Hu, K., Sun, M., and Chen, X. (2016). Revised Models for Determining TOC in Shale Play: Example from Devonian Duvernay Shale, Western Canada Sedimentary basin. *Mar. Pet. Geology.* 70, 304–319. doi:10.1016/j.marpetgeo.2015.11.023

Wu, Y. J., Tang, H. M., Wang, Y., Li, J., Zeng, Y. X., Jiang, S. L., et al. (2021). Sedimentary Facies of the Longmaxi Formation Shale Gas Reservoir in the Weiyuan Area Based on Elemental Characteristics. *Geofluids*, 5021298. doi:10.1155/2021/5021298

Xi, Y., Jiang, J., Li, J., Li, H., and Gao, D. (2021b). Research on the Influence of Strike-Slip Fault Slippage on Production Casing and Control Methods and Engineering Application during Multistage Fracturing in Deep Shale Gas wells. *Energ. Rep.* 7, 2989–2998. doi:10.1016/j.egyr.2021.05.039

Xi, Y., Lian, W., Fan, L., Tao, Q., and Guo, X. (2021a). Research and Engineering Application of Pre-stressed Cementing Technology for Preventing Micro-annulus Caused by Cyclic Loading-Unloading in Deep Shale Gas Horizontal wells. *J. Pet. Sci. Eng.* 200, 108359. doi:10.1016/j.petrol.2021.108359

Xiao, D., Cao, J., Luo, B., Zhang, Y., Xie, C., Chen, S., et al. (2020). Mechanism of Ultra-deep Gas Accumulation at Thrust Fronts in the Longmenshan Mountains, Lower Permian Sichuan Basin, China. *J. Nat. Gas Sci. Eng.* 83, 103533. doi:10.1016/j.jngse.2020.103533

Xiong, L., Pang, H. Q., Zhao, Y., Wei, L. M., Zhou, H., and Cao, Q. (2021). Micro Pore Structure Characterization and Classification Evaluation of Reservoirs in Weirong Deep Shale Gas Field. *Reserv. Eval. Dev.* 11 (2), 20–29. doi:10.13809/j.cnki.cn32-1825/te.2021.02.003

Xu, F. S., Wang, F. P., Zhang, J. T., Fu, B., Zhang, Y., Yang, P. C., et al. (2021a). Strategies for Scale Benefit Development of Deep Shale Gas in China. *Nat. Gas Ind.* 41 (1), 205–213. doi:10.3787/j.issn.1000-0976.2021.01.019

Xu, N. Z., and Gao, C. (2020). Study on the Special Rules of Surface Subsidence Affected by normal Faults. *J. Min Strata Control. Eng.* 2 (1), 011007. doi:10.13532/j.jmsce.cn10-1638/td.2020.01.011

Xu, Z., Pengn, N. J., Shi, W. Z., and Shu, Z. G. (2021b). Reservoir Fracture Characteristics and Controlling Factors of Shale Gas of Wufeng-Longmaxi Formation in Fuling Area. *J. East. China Univ. Tech.* 44 (3), 267–279. doi:10.3969/j.issn.1674-3504.2021.03.008

Yin, S., Han, C., Wu, Z., and Li, Q. (2019). Developmental Characteristics, Influencing Factors and Prediction of Fractures for a Tight Gas sandstone in a Gentle Structural Area of the Ordos Basin, China. *J. Nat. Gas Sci. Eng.* 72, 103032. doi:10.1016/j.jngse.2019.103032

Yin, S., and Wu, Z. (2020). Geomechanical Simulation of Low-Order Fracture of Tight sandstone. *Mar. Pet. Geology.* 117, 104359. doi:10.1016/j.marpetgeo.2020.104359

Yu, H., Rezaee, R., Wang, Z., Han, T., Zhang, Y., Arif, M., et al. (2017a). A New Method for TOC Estimation in Tight Shale Gas Reservoirs. *Int. J. Coal Geology.* 179, 269–277. doi:10.1016/j.coal.2017.06.011

Yu, Y., Luo, X., Lei, Y., Wang, X. Z., Wang, X., Zhang, L., et al. (2016). Characterization of Lacustrine Shale Pore Structure: The Upper-Triassic Yanchang Formation, Ordos Basin, China. *J. Nat. Gas Geosci.* 1, 299–308. doi:10.1016/j.jnggs.2016.10.001

Yu, Y. X., Luo, X. R., and Cheng, M. (2017b). Study on the Distribution of Extractable Organic Matter in Pores of Lacustrine Shale: An Example of Zhangjiatan Shale from the Upper Triassic Yanchang Formation. *Ordos Basin, China. Interpretation* 5, SF109–SF126. doi:10.1190/INT-2016-0124.1

Yuan, Y. Y., Li, H., Wang, Q., and Zhong, M. Y. (2021). Influence of Different thermal Evolution Stages on Shale Pore Development. *Energy Source Part A*. doi:10.1080/15567036.2021.1942333

Zhang, B. L., Shen, B. T., Zhang, J. H., and Zhang, X. G. (2020a). Experimental Study of Edge-Opened Cracks Propagation in Rocklike Materials. *J. Min. Strata Control. Eng.* 2 (3), 033035. doi:10.13532/j.jmsce.cn10-1638/td.20200313.001

Zhang, D. D., Li, S. J., Zhang, X., Yang, Y. Y., and Chai, J. (2020b). Experimental Study on Mining Fault Activation Characteristics by a Distributed Optical Fiber System. *J. Min. Strata Control. Eng.* 2 (1), 013018. doi:10.13532/j.jmsce.cn10-1638/td.2020.01.010

Zhang, F., Jiang, Z., Sun, W., Zhang, X., Zhu, L., Li, X., et al. (2020c). Effect of Microscopic Pore-Throat Heterogeneity on Gas-phase Percolation Capacity of Tight sandstone Reservoirs. *Energy Fuels* 34 (10), 12399–12416. doi:10.1021/acs.energyfuels.0c02393

Zhang, K., Jia, C., Song, Y., Jiang, S., Jiang, Z., Wen, M., et al. (2020d). Analysis of Lower Cambrian Shale Gas Composition, Source and Accumulation Pattern in Different Tectonic Backgrounds: A Case Study of Weiyuan Block in the Upper Yangtze Region and Xiuwu Basin in the Lower Yangtze Region. *Fuel* 263, 115978. doi:10.1016/j.fuel.2019.115978

Zhang, N., Han, C., and Xie, Z. (2019). Theory of Continuous Beam Control and High Efficiency Supporting Technology in Coal Roadway. *J. Min Strat Control. Eng.* 1 (1), 013005. doi:10.13532/j.jmsce.cn10-1638/td.2019.02.004

Zhang, X. F., Qu, X. C., and Wei, Q. D. (2021). Development and Application of Multi-Dimension Multi-Parameter Monitoring and Early Warning Platform of Coal Bursts. *J. Min Strata Control. Eng.* 3 (1), 013013. doi:10.13532/j.jmsce.cn10-1638/td.20200922.002

Zhao, K. K., Jiang, P. F., Feng, Y. J., Sun, X. D., Cheng, L. X., and Zheng, J. W. (2020). Investigation of the Characteristics of Hydraulic Fracture Initiation by Using Maximum Tangential Stress Criterion. *J. Min Strata Control. Eng.* 3 (2), 023520. doi:10.13532/j.jmsce.cn10-1638/td.20201217.001

Zhao, P., Ma, H., Rasouli, V., Liu, W., Cai, J., and Huang, Z. (2017). An Improved Model for Estimating the TOC in Shale Formations. *Mar. Pet. Geology.* 83, 174–183. doi:10.1016/j.marpetgeo.2017.03.018

Zhao, Y., Li, N. Y., Yang, J., and Cheng, S. S. (2021). Optimization of Deep Shale Gas Well Spacing Based on Geology-Engineering Integration: A Case Study of Weirong Shale Gas Field. *Reserv. Eval. Dev.* 11 (3), 340–347. doi:10.13809/j.cnki.cn32-1825/te.2021.03.008

Zhou, D., Zheng, P., He, P., and Peng, J. (2016). Hydraulic Fracture Propagation Direction during Volume Fracturing in Unconventional Reservoirs. *J. Pet. Sci. Eng.* 141, 82–89. doi:10.1016/j.petrol.2016.01.028

Zhou, G., Gu, Z., Hu, Z., Chang, J., Duan, X., Liu, X., et al. (2020). Characterization and Interpretation of Organic Matter, clay Minerals, and Gas Shale Rocks with Low-Field NMR. *J. Pet. Sci. Eng.* 195, 107926. doi:10.1016/j.petrol.2020.107926

Zhou, H., Wei, L. M., Wang, T., Wang, Y., Pang, H. Q., and Zhang, T. C. (2021). Evaluation Method of Weirong Deep Shale Gas Reservoir and its Application. *Reserv. Eval. Dev.* 11 (2), 42–49. doi:10.13809/j.cnki.cn32-1825/te.2021.02.005

Zhu, W. C., Niu, L. L., Li, S. H., and Li, S. (2019). Creep-impact Test of Rock: Status-Of-The-Art and prospect. *J. Min. Strata Control. Eng.* 1 (1), 013003. doi:10.13532/j.jmsce.cn10-1638/td.2019.02.007

Zou, C., Zhang, X., Luo, P., Wang, L., Luo, Z., and Liu, L. (2010). Shallow-lacustrine Sand-Rich Deltaic Depositional Cycles and Sequence Stratigraphy of the Upper Triassic Yanchang Formation, Ordos Basin, China. *Basin Res.* 22, 108–125. doi:10.1111/j.1365-2117.2009.00450.x

Conflict of Interest: The authors declare that the research was conducted in the absence of any commercial or financial relationships that could be construed as a potential conflict of interest.

Publisher's Note: All claims expressed in this article are solely those of the authors and do not necessarily represent those of their affiliated organizations, or those of the publisher, the editors and the reviewers. Any product that may be evaluated in this article, or claim that may be made by its manufacturer, is not guaranteed or endorsed by the publisher.

frontiers in Earth Science

ORIGINAL RESEARCH
published: 10 March 2022
doi: 10.3389/feart.2022.873617

Simulation of Fracturing and Well Pattern Optimization of Fractured Tight Sandstone Reservoirs

Jianbo Liao[1], Zhongyi Zhang[2], Haizhong Tang[3], Jun Yang[3], Xiaolei Zhang[2] and Bing Wang[3]*

[1]Research Institute of Petroleum Exploration and Development Northwest Branch, Lanzhou, China, [2]Research Institute of Petroleum Exploration and Development, PetroChina Changqing Oilfield Company, Xi'an, China, [3]Research Institute of Petroleum Exploration and Development, PetroChina Yumen Oilfield Company, Jiuquan, China

The fracturing and well pattern optimization of fractured reservoirs is a hot spot in petroleum engineering. In this study, taking the tight oil reservoirs of the Yanchang Formation in the Ordos Basin as an example, an optimized plan of hydraulic fracturing and well pattern deployment of the fractured tight reservoir were systematically studied using a fluid-solid coupling model. The results show that the Chang 6 Member of Yanchang Formation mainly develop feldspar sandstone. A large number of vertical fractures are developed in Chang 6 Member, and they have significant shearing properties. The target sandstone reservoir is in the mid-diagenetic A stage. Natural fractures have a significant effect on the extension of hydraulic fractures. When the fracturing direction is parallel to the main strike of natural fractures, the extension distance of the hydraulic fractures is long and the fracturing scale is large; however, when the fracturing direction is orthogonal or oblique to the main strike of natural fractures, the extension distance of the hydraulic fractures is limited. Statistics show that the average length of hydraulic fractures when fracturing parallel to natural fractures is 1.3 times of that when fracturing perpendicular to natural fractures. In addition, after optimization of fracturing parameters, we found that the displacement should be controlled at 2–3 cubic meters/min, and the sand ratio should be controlled at 25%. The smaller the horizontal minimum principal stress difference between the fracturing layer and the shielding layer, the lower the elastic modulus, and the easier it is to control the fracture height. Microseismic monitoring results show that the half-fracture length and fracture height are mainly distributed in 80–140 m and 15–25 m, respectively. The optimized fracture half-length was 120 m and the half-fracture height was 20 m. Finally, the well pattern of the target layer is optimized considering natural fractures. Through this study, we found that the reverse five-spot well pattern is suitable for the efficient development of tight oil reservoirs of the Chang 6 Member in this area.

Keywords: tight oil sandstone, hydraulic fracturing, natural fractures, microseismic monitoring, numerical simulation

OPEN ACCESS

Edited by:
Wenlong Ding,
China University of Geosciences, China

Reviewed by:
Shaoke Feng,
Chengdu University of Technology, China
Teng Zhao,
China University of Geosciences, China

****Correspondence:***
Jianbo Liao
ljb1773@126.com

Specialty section:
This article was submitted to Structural Geology and Tectonics, a section of the journal Frontiers in Earth Science

Received: *11 February 2022*
Accepted: *18 February 2022*
Published: *10 March 2022*

Citation:
Liao J, Zhang Z, Tang H, Yang J, Zhang X and Wang B (2022) Simulation of Fracturing and Well Pattern Optimization of Fractured Tight Sandstone Reservoirs. Front. Earth Sci. 10:873617. doi: 10.3389/feart.2022.873617

INTRODUCTION

At present, the exploration and development of continental tight sandstone oil has achieved great success in China (Zou et al., 2013; Yin et al., 2018; Li et al., 2020). The development of continental tight sandstone oil is difficult, which puts forward higher requirements for the integration technology of geology and engineering of tight oil (Li et al., 2018; Hong et al., 2020; Abouzar and Ghanbarian, 2021; Ding et al., 2021). The integrated construction of tight oil geology and engineering is to maximize the stable production of crude oil. Therefore, the core issue of this technology is the dynamic optimization and timely matching of engineering and geological parameters (Chitrala et al., 2013; Wang et al., 2019; He et al., 2020; Mahmud et al., 2020; Yoshida and Santosh, 2020).

The continental tight oil reservoirs in the Yanchang Formation in the Ordos Basin are characterized by strong heterogeneity, small single sand body thickness, and low natural productivity (Zou et al., 2013; Yin and Wu, 2020). In recent years, the development of fracturing and well pattern optimization technologies have provided a huge space for the upgrading of reserves production in such oil reservoirs (Salamon, 1984; Ma et al., 2019; Dong et al., 2020; Khan et al., 2020; Xue et al., 2021). However, with different development methods, the complexity of fluid flow between different well patterns in tight oil reservoirs increases. Thus, the effect of different fracturing and well pattern mode on oil production capacity is difficult to predict (Jaeger and Cook, 1976; McBride, 1989; Du and Aydin, 1993; Zhang et al., 2017; Gao, 2021). For tight fractured reservoirs, the presence of natural fractures aggravates the anisotropy of the reservoir, which in turn has a significant impact on the development effect of reservoir (Li and Zhang, 1997; Shuai et al., 2013; Luo et al., 2018; Xi et al., 2019; Zhao et al., 2020). The existence of natural fractures will reduce the strength of the rock mass significantly, and even make the rock lose its "strength". For the fracturing of wells with natural fractures, it is generally believed that the problem of continuous expansion of fractures under the action of fracturing fluid can also generate new fracturing fractures (Zou et al., 2013; Yin and Wu, 2020). Moreover, due to the differences in the mechanical properties, occurrence, quantity, and distribution of fractures in and around the well, the problems of fracture propagation and energy loss during fracturing become very complicated. For tight oil reservoirs, the injection-production well pattern and the natural fracture system must have a reasonable configuration relationship. The previous often adopted the well pattern deployment with parallel fracture main strikes (Ma et al., 2019; Zhao et al., 2020).

In the fracturing and well pattern optimization simulation process, the construction of the fracture network is very important, and the commonly used methods are usually based on the finite element and discrete element principles (Zhao et al., 2020). In addition, the fracturing effect can be verified by comparing with the microseismic monitoring results (Shuai et al., 2013; Luo et al., 2018). The finite element and discrete element models can quantitatively characterize the coupling relationship between fluid and solid and the extension law of hydraulic fractures.

In this study, taking the Upper Triassic Yanchang Formation in the western margin of the Ordos Basin with relatively developed fractures as an example, the numerical simulation of volume fracturing and well pattern optimization of tight oil based on multiple porous media model were systematically conducted. This study can provide a reference for the integrated construction of geology and engineering of continental tight oil.

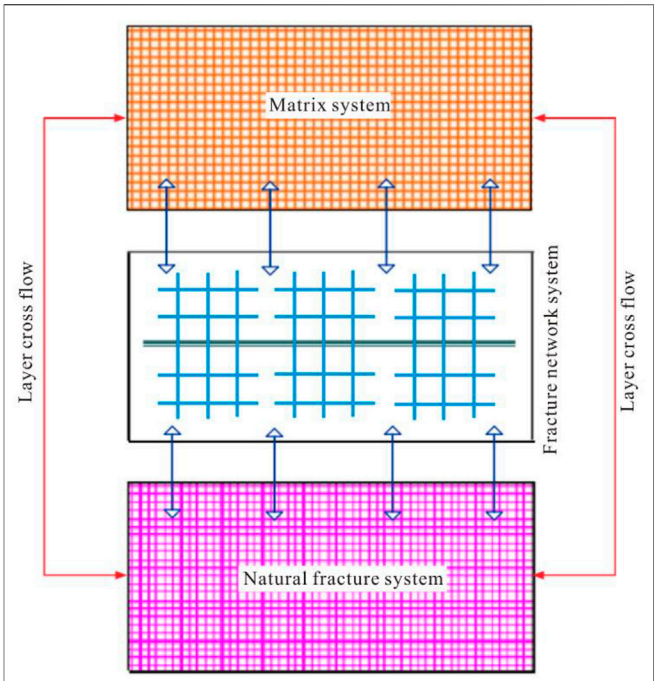

FIGURE 1 | Schematic diagram of the physical model of volume fracturing based on multi-porous media model (Modified after Ren et al., 2019).

METHODS

Hydraulic Fracturing of Tight Sandstone Reservoirs

In this study, a physical model for volume fracturing of tight oil based on multiple porous media was established (**Figure 1**). It is based on the dual continuum model and can well describe the matrix and natural fracture systems. Moreover, the DFN (discrete fracture network) model was used to describe the network fracture system. Obviously, the complex fracture network formed by volume fracturing is integrated into the matrix and the natural fracture systems at the same time (**Figure 1**). The assumptions are: 1) The multi-porous medium is fully saturated and isotropic; 2) Reservoir matrix framework, fractures and fluids are compressible; 3) The deformation of the rock skeleton is a linear elastic micro-deformation, and it follows the Terzaghi effective stress principle; 4) The seepage of the fluid in the fracture obeys Darcy's law, and there is a quasi-steady-state channeling flow between the matrix and the fracture system; 5) The initial stress field is uniformly distributed and isothermal, single-phase seepage occurs without considering the effect of gravity; 6) The porosity, permeability and compressibility of multi-porous media are all dynamically variable.

In addition, in order to more accurately and intuitively characterize the water flooding process in the well pattern and the effect of fracture seepage on the productivity of the fractured wells, the logarithmic grid refinement technology was used in the modeling. The use of this technique can not only describe the hydraulic fractures finely, but also avoid the problems of long calculation time and non-convergence of the Local Refinement Grid (LGR) method (Gurocak et al., 2012; Lommatzsch et al., 2015).

In this study, an enhancement function was introduced to describe the propagation of hydraulic fractures. This function is mainly used to describe the dynamic propagation of the fracture tip. The function representing the displacement of the fracture cover is:

$$u = \sum_{I=1}^{N} N_I(x)\left[u_I + H(x)a_I + \sum_{\alpha=1}^{4} F_\alpha(x) b_I^\alpha\right] \tag{1}$$

In the formula, $N_I(x)$ is the shape function of the set nodes; u_I is the displacement vector; $H(_x)$ is the discontinuous function related to the fracture surface activity; a_I and b_I^α are the degrees of freedom of the nodes in the model, respectively; $F_\alpha(x)$ is the asymptotic function of the propagated fracture tip.

The initiation and propagation of hydraulic fractures are directly related to the stress and pore pressure of the rock skeleton:

$$\sigma = \bar{\sigma} + \alpha p_m I \tag{2}$$

where σ and $\bar{\sigma}$ are the total stress and effective stress, respectively; α is the Biot coefficient.

Then, the equilibrium equation of the formation is:

$$\int_V (\nabla \cdot \sigma + f) \cdot \delta v dV - \int_S (\sigma \cdot n^T - t) \cdot \delta \boldsymbol{v} dS = 0 \tag{3}$$

In the formula, σ is the total stress matrix; f is the physical force matrix; t is the surface force matrix; δv is the virtual work matrix; n is the unit normal vector of the vertical fracture surface.

The continuity equation representing the fluid flow capability of the reservoir is:

$$\frac{1}{J}\frac{\partial}{\partial t}(J\rho_w\phi) + \frac{\partial}{\partial x}(\rho_w \phi v_w) = 0 \tag{4}$$

In the formula, J is the volume ratio of the reservoir rock after deformation and before deformation; ρ_w, ϕ and v_w are the fluid density, rock porosity and fluid seepage velocity, respectively.

Monitoring of Microseismic Hydraulic Fractures

During artificial fracture monitoring, the monitoring system have six microseismic observation stations around the fracturing well with the mid-deep point of the fracturing layer as the center. The shape, orientation, height and occurrence of fractures in fracturing wells can be obtained through on-site monitoring, and then the spatial distribution of the complex fracture network in the formation can be obtained.

When artificial fractures are formed by fracturing a well, microseisms will inevitably occur along the fracture surface.

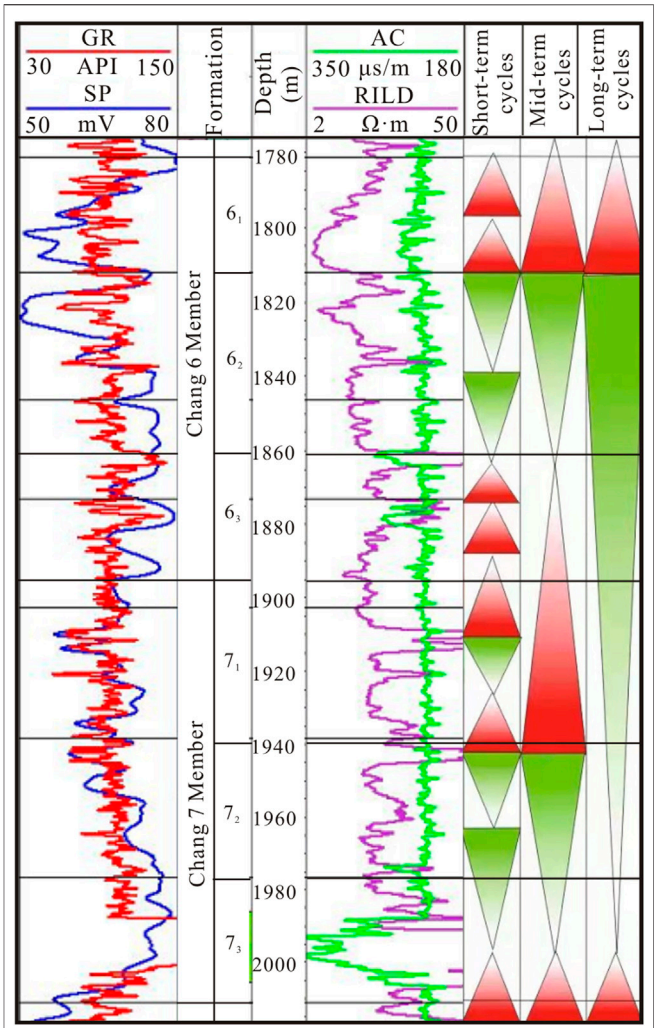

FIGURE 2 | Sedimentary characteristics of Chang 6 and Chang 7 Members of the Upper Triassic Yanchang Formation in Well Z1. GR—natural gamma; SP spontaneous potential; AC—longitudinal wave time difference; RILD—resistivity.

The distribution of the microseismic source reflects the contour of the artificial fracture, and the microseismic source location formula is:

$$\begin{cases} t_1 - t_0 = \dfrac{1}{v_p}\left(\sqrt{(x_1 - x_0)^2 + (y_1 - y_0)^2 + z^2}\right) \\ t_2 - t_0 = \dfrac{1}{v_p}\left(\sqrt{(x_2 - x_0)^2 + (y_2 - y_0)^2 + z^2}\right) \\ t_3 - t_0 = \dfrac{1}{v_p}\left(\sqrt{(x_3 - x_0)^2 + (y_3 - y_0)^2 + z^2}\right) \\ t_4 - t_0 = \dfrac{1}{v_p}\left(\sqrt{(x_4 - x_0)^2 + (y_4 - y_0)^2 + z^2}\right) \\ t_5 - t_0 = \dfrac{1}{v_p}\left(\sqrt{(x_5 - x_0)^2 + (y_5 - y_0)^2 + z^2}\right) \end{cases} \tag{5}$$

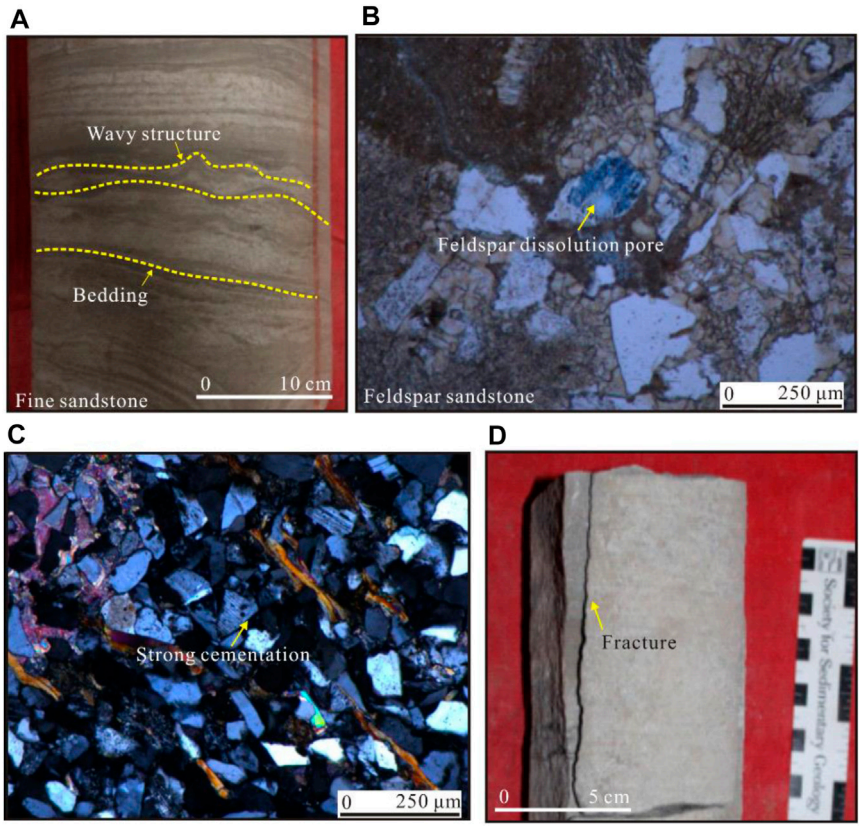

FIGURE 3 | Core and thin section observations of the target formation (Chang 6 Member) in the study area. **(A)** Well A1, 1707.87 m, wavy and lenticular bedding; **(B)** Well A2, 1840 m, feldspar dissolution pores; **(C)** Well B1, 1739 m, strongly cemented feldspar sandstone; **(D)** Well B2, 623 m, vertical fracture.

In the formula, t_1, t_2, ... t_5 are the microseismic moments recorded by the geophone; t_0 is the seismic moment; v_p is the p-wave velocity; (x_1, y_1), (x_2, y_2), (x_3, y_3), (x_4, y_4), (x_5, y_5) are the coordinates of the monitoring station; Z is the depth of the seismic source. In this study, it is stipulated that the X-axis is along the east-west direction, and the east is the positive direction; the Y-axis is along the north-south direction, and the north is the positive direction; the Z-axis is the vertical direction. t_0, x_0, y_0, z are the seek unknowns.

RESULTS

Reservoir Characteristics of Tight Oil Sandstone

The study area is located in Block X of the Western Margin Thrust Belt of the Ordos Basin, and the target layer is the Chang 6 Member of the Yanchang Formation. The Chang 6 Member in this area belongs to the delta front sediments, and distributary channel and interdistributary bay microfacies are developed. Reservoirs are mainly distributed in distributary channel sand bodies. The distributary river channel facies mainly develop coarse sandstones, while on both sides of the main river channel, siltstone and silty mudstone are mainly developed (**Figure 2**). The interdistributary bay is dominated by silty mudstone and mudstone, and the natural potential (GR) curve is low and flat.

The tight sandstone of Chang 6 Member was formed under relatively strong hydrodynamic conditions, and wavy and lenticular bedding structures are developed (**Figure 3A**). Compaction, pressure solution, cementation, dissolution and tectonic rupture are the main types of diagenesis in the Chang 6 Member. It can be observed under the microscope that the debris particles have obvious fixed distribution characteristics. Also, the particles are usually in close concavo-convex line contacts. Some of the rigid particles are crushed and broken. After bending deformation, plastic minerals (such as mudstone debris and mica) are squeezed into intergranular pores to form pseudo-matrix, which in turn leads to a large reduction in the quanty of original pores of the reservoir (**Figures 3B,C**).

The dissolution types in the Chang 6 reservoir in the study area include the dissolutions of clastic minerals (quartz, feldspar, debris and mica), matrix and authigenic minerals (such as calcium). Among them, feldspar dissolution is the most common, which can significantly improve the petrophysical properties of the reservoir (**Figure 3B**).

The cementation types in the Chang 6 Member include clay, siliceous, calcareous and feldspar cementations (**Figure 3C**). Clay cements include kaolinite, illite and chlorite, and their content is 1–9%, with an average of 2.85%. The clay cements usually grow perpendicular to the pore surface and toward the pore center. The contents of siliceous cements range from 0 to 0.5%, with an

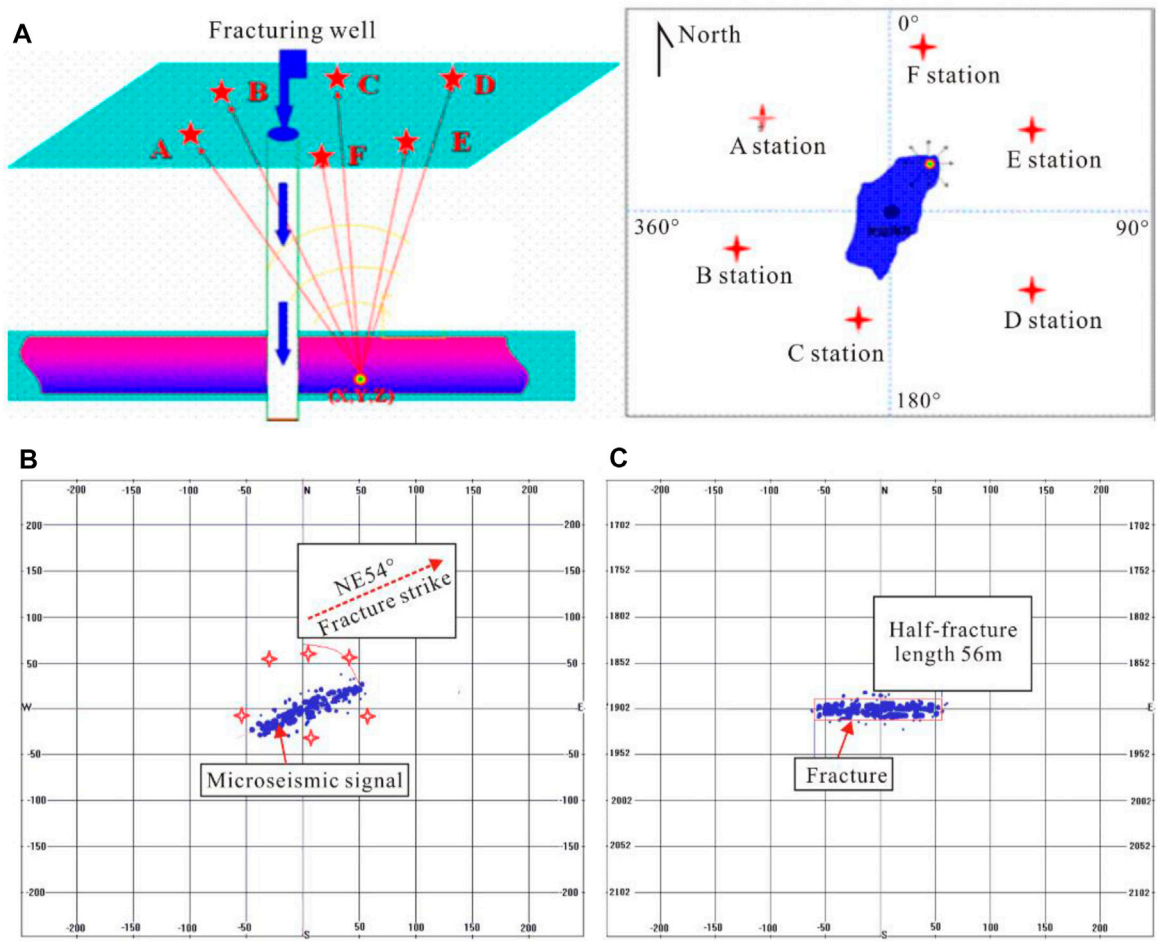

FIGURE 4 | Microseismic fracture monitoring of Well N1. **(A)** Distribution of 6 seismic monitoring stations; **(B)** Main strike of hydraulic fractures; **(C)** Half-length of hydraulic fractures.

average of 0.1%. They are mainly derived from montmorillonite, illite and pressure solution process. The contents of carbonate cements range from 0.5 to 30%, with an average of 6.05%. The carbonate cements are dominated by iron calcite components. In addition, fractures are also developed in the Chang 6 Member, and these fractures are mainly vertical fractures with shearing properties (**Figure 3D**). Fractures can significantly improve the seepage capacity of the reservoir.

Through the analysis of diagenesis of Chang 6 sandstones in the Yanchang Formation, it can be seen that the clastic particles in the Chang 6 sand bodies are mainly in line contacts. Moreover, iron carbonate minerals and authigenic quartz crystals are relatively developed, and Type I quartz overgrowth is common. Under the microscope, pores are always filled with kaolinite, and hair-like aggregates of illite and chlorite envelope can be seen as well. Moreover, the reservoir spaces of the target reservoir are mainly composed of primary intergranular and dissoltion pores, and carbonate cement dissolution pores can be seen as well. However, the dissolution effect of the target layer is not too strong. Based on the comprehensive information, the sandstone reservoir of the Chang 6 Member in the study area is in the mid-diagenetic A stage.

Comparison of Hydraulic Fracture Parameters

According to the microseismic fracture monitoring, the three-dimensional spatial distribution information of the fractures can be obtained (**Figure 4**). In this study, there are a total of six base station observation stations from A to F for microseismic fracture monitoring. In this way, the extension direction, length and height of the fractures can be observed in an all-round and intuitive manner.

The shape and spatial distribution of hydraulic fractures in the fractured segment of Well N1 are shown in **Figure 4C**. It can be seen that the fracture spreads along the NE45° direction, the half-length of the fractures is 56 m, and the height of the fractures is 20 m. Statistics show that the natural fractures in the Chang 6 Member of the study area are mainly distributed along the direction of NE40°~70°. In addition, the maximum principal stress of the Chang 6 Member is in the NE direction. Therefore, fracturing along the NE direction can achieve the best fracturing effect.

The comparison of hydraulic fracture parameters obtained based on microseismic monitoring and fracturing simulation is shown in **Figure 5**. FracPT software was used for hydraulic

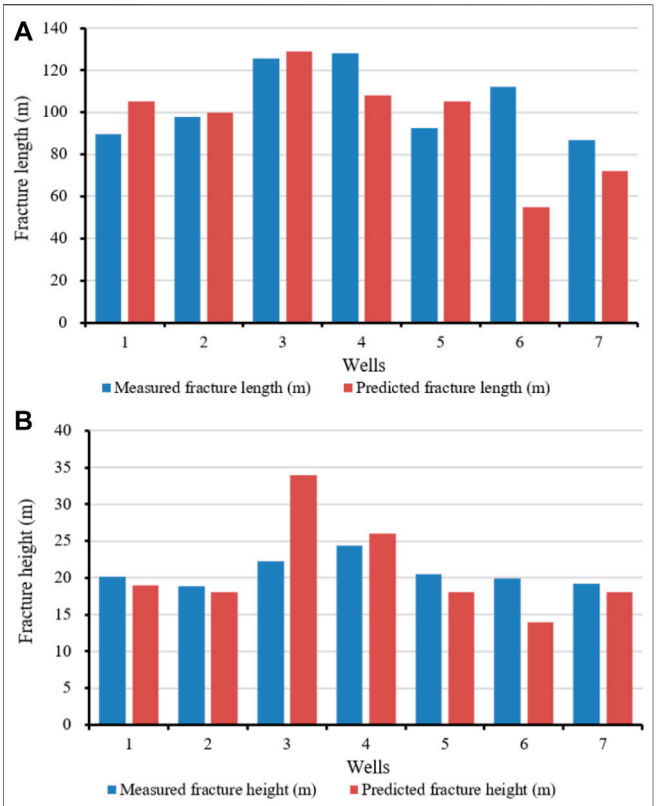

FIGURE 5 | Comparison of hydraulic fracture parameters for fracturing simulation and microseismic monitoring. **(A)** Distribution of fracture length; **(B)** Distribution of fracture height.

fracturing simulation. It can be seen that the fracture simulation results are in good agreement with the microseismic monitoring interpretation. The length and height of the hydraulic fractures obtained from the simulation are well consistent with the measured results, and the relative error of the calculated results is less than 5% (**Figure 5**). Therefore, the fracture simulation results in this study are reliable.

Engineering Factors and Fracturing Effects

The tight sandstone reservoirs of Chang 6 Member in the study area are developed by water injection (Liu et al., 2020; Hower and Groppo, 2021). The injection of water can increase the energy of the formation, thereby displacing the crude oil. The main factor that determines the quality of fracturing construction is the optimal selection of fracturing reconstruction measures, that is, the improvement of fracturing construction technology and the optimization of fracturing parameters. In this study, the effects of pre-fluid, sand-carrying fluid and displacement on the fracturing effect were analyzed.

The difference between the pre-fluid and the sand-carrying fluid is that the pre-fluid does not contain proppant, while their other conditions are exactly the same (Mahmoodi et al., 2019; Li and Li., 2021; Zhao et al., 2021). The main function of the pre-fluid is to press open the formation under the action of a large pressure, thereby providing space for the subsequent injected sand-carrying fluid. The optimum amount of pad fluid is when the pump injection is complete, the pad fluid is just completely filtered off into the formation and forms good fracture support. Furthermore, a higher conductivity can be maintained (Peng et al., 2018; Zhang et al., 2020; Qie et al., 2021; Yang et al., 2021).

The pre-fluid has a certain influence on the fracture morphology. Excessive pre-fluid will overextend the fracture length and narrow the fracture width, thus reducing the proppant laying concentration. Large amounts of fracturing fluid leaching into the formation can cause damage to the formation (Santosh and Feng, 2020; Zang et al., 2020; Wang and Wang, 2021). If the amount of pre-fluid is too small, the fracture length cannot meet the design requirements, and sand plugging may occur, resulting in economic losses.

The amount of pre-fluid affects the length and width of hydraulic fractures and the laying concentration of proppants. Generally, the volume of pre-fluid in reservoirs with poor petrophysical properties should not be too large. The pre-fluid volume of the Chang 6 Member in the study area is mainly 10–30 cubic meters. It can be seen from **Figure 6A** that the amount of pre-fluid has a certain relationship with the amount of fluid produced after fracturing. Theoretically, for reservoirs with better petrophysical properties, the larger the

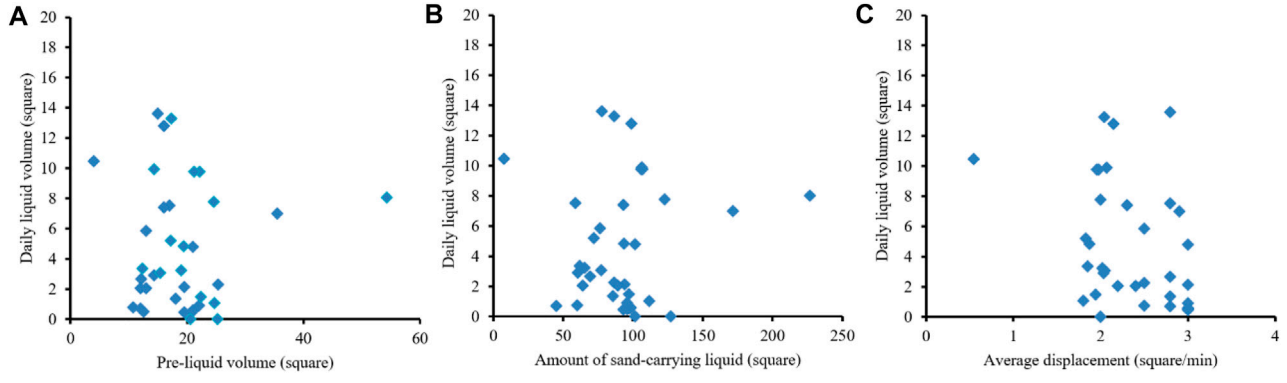

FIGURE 6 | Effects of pre-fluid volume, sand-carrying fluid and displacement on fluid production during fracturing. **(A)** Pre-liquid volume and daily liquid volume; **(B)** Amount of sand-carrying liquid and daily liquid volume; **(C)** Average displacement and daily liquid volume.

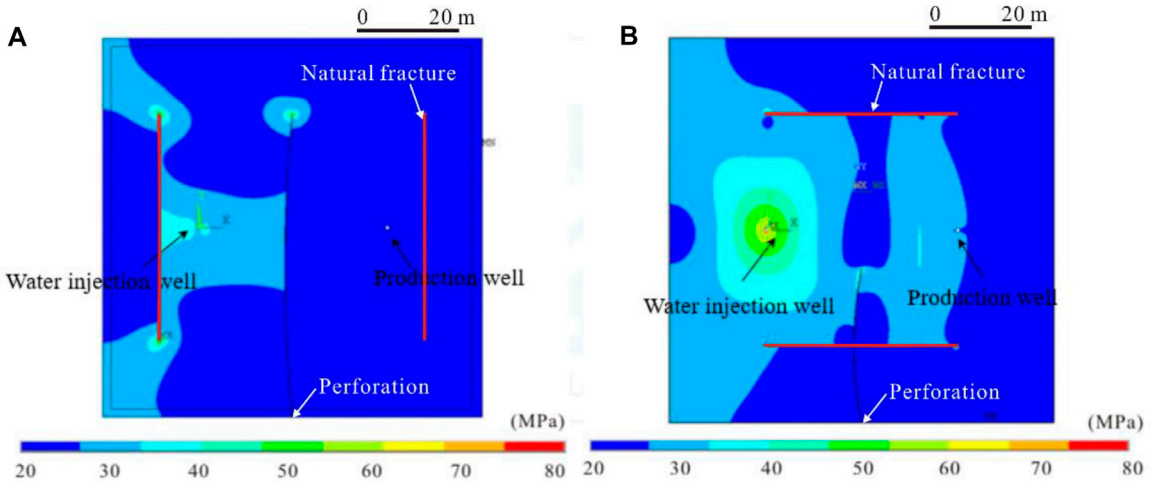

FIGURE 7 | Hydraulic fracturing effect under the condition that the fracturing direction is parallel or perpendicular to the main strike of natural fractures. **(A)** The fracturing direction is parallel to the main strike of natural fractures; **(B)** the fracturing direction is perpendicular to the main strike of natural fractures.

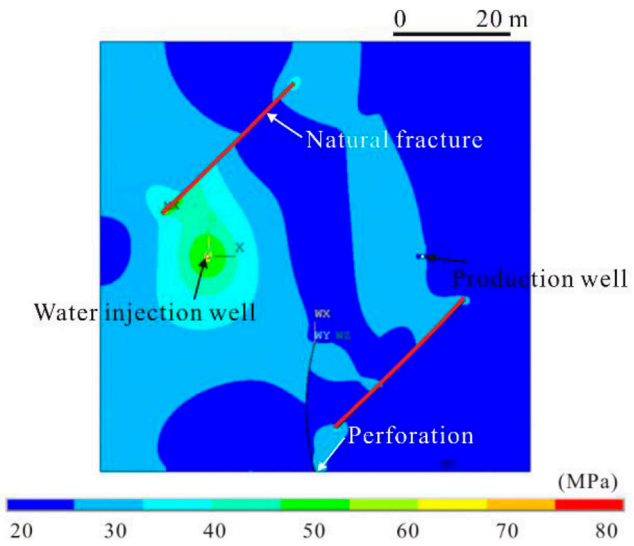

FIGURE 8 | Effect of hydraulic fracturing under the condition that the fracturing direction is oblique to the main strike of natural fractures.

amount of pre-fluid, the larger the scale of fractures, and the greater the probability of obtaining larger test oil production. However, for reservoirs with poor physical properties, the amount of pre-fluid should not be too large. If it exceeds a certain range, it will damage the reservoir, which is not conducive to improving the production of fracturing oil testing.

The sand-carrying fluid is injected into the formation after the fore-fluid has opened the formation. It carries the proppant into the fractures, thereby increasing the conductivity of oil and gas (Bhatti et al., 2020; Bello et al., 2021; Guo et al., 2021). Then, the amount of sand-carrying fluid is also crucial to the fracturing effect. The amount of sand-carrying liquid is affected by the amount of sand added and the sand ratio. The greater the amount of sand-carrying liquid, the lower the laying concentration, and the larger the amount of sand-carrying liquid, the less effective the fracturing. Statistics show that the amount of sand-carrying liquid in the Chang 6 member of the study area is mainly in the range of 50–130 cubic meters (**Figure 6B**).

In addition, displacement also has a significant effect on the size of the reservoir being reformed. Excessive displacement will make the upper and lower extension heights of hydraulic fractures too high, which is not conducive to laying of proppants. Excessive displacement affects the propping efficiency of the proppants and the conductivity of hydraulic fractures, and also increases the friction of the formation. It has a detrimental effect on fracturing equipments. Too low displacement is not conducive to the sand-carrying effect of fracturing fluid, especially in the case of high sand ratio. In addition to this, low displacement increases the fracturing construction time. The fracturing displacement of the Chang 6 Member in the study area is mainly 1.5–3.0 cubic meters per minute (**Figure 6C**).

In general, for reservoirs with good petrophysical properties, the larger the displacement, the larger the scale of hydraulic fractures and the higher the productivity. However, for reservoirs with poor petrophysical properties, if the fracturing displacement is too large, the hydraulic fracture height will be larger. In this case, the hydraulic fractures may also penetrate the formation, so the displacement should also be properly controlled.

DISCUSSION

Influence of Natural Fractures on Fracturing Effect

In this study, the effect of natural fractures on the fracturing effect was analyzed. When natural fractures exist, the fracturing morphology under the combined conditions of injection and production wells is shown in **Figure 7**. In **Figure 7A**, the fracturing direction is parallel to the main strike (NE45°) of

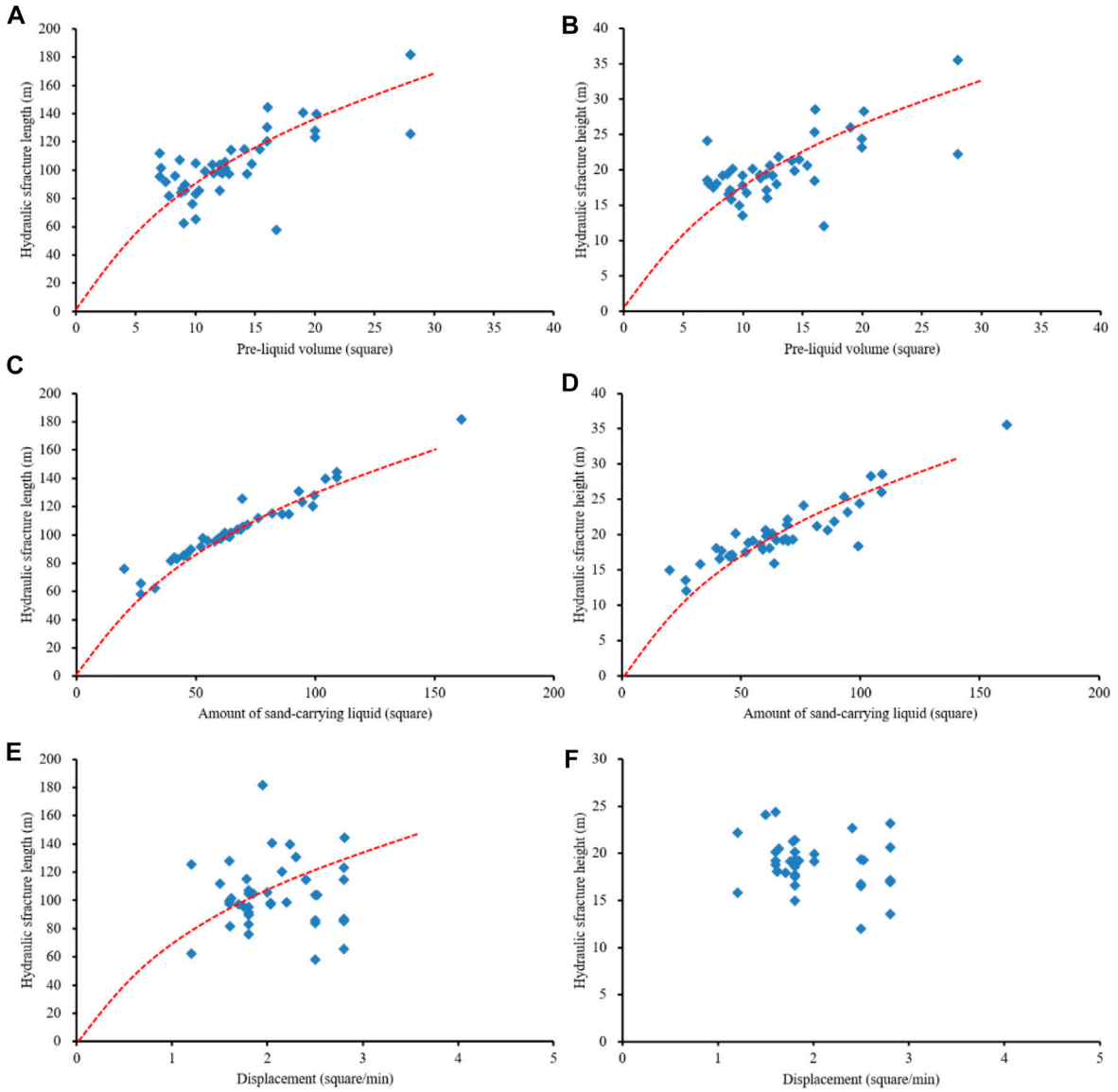

FIGURE 9 | Relationship between fracturing construction parameters and hydraulic fracture parameters. **(A)** Pre-liquid volume and hydraulic fracture length; **(B)** Pre-liquid volume and hydraulic fracture height; **(C)** Amount of sand-carrying liquid and hydraulic fracture length; **(D)** Amount of sand-carrying liquid and hydraulic fracture height; **(E)** Displacement and hydraulic fracture length; **(F)** Displacement and hydraulic fracture height.

natural fractures, and in **Figure 7B**, the fracturing direction is perpendicular to the main strike (NE45°) of natural fractures. The simulation results show that the extension distance of the hydraulic fractures parallel to the main fracture strike is long and the fracturing scale is large. In addition, when the fracture is deflected to the injection well to a certain extent, it spreads in the direction away from the injection well. During the whole fracturing process, the pore pressure changed stably and steadily expanded from the water injection area to the fracturing area of the oil well (**Figure 7**). According to the statistical results, the length of hydraulic fractures when fracturing parallel to the main strike of natural fractures is 1.3 times of that when they are perpendicular to the strike of natural fractures.

When the main strike of natural fractures is orthogonal to the fracturing direction, the results of hydraulic fracture expansion are shown in **Figure 8**. In such cases, the extension distance of the hydraulic fractures is short, the scale of fracturing expansion is small, but the opening is wide. The fractures were also deflected to some extent towards the injection well. During the whole fracturing process, the change of pore pressure is unstable, which is not conducive to the uniform advancement of the injected water to the oil well, and it is easy to form water channeling (**Figure 8**). Statistical results show that when the fracturing is oblique to the main strike of natural fractures, the length of the hydraulic fractures is half of the hydraulic fractures parallel to the main strike of natural fractures.

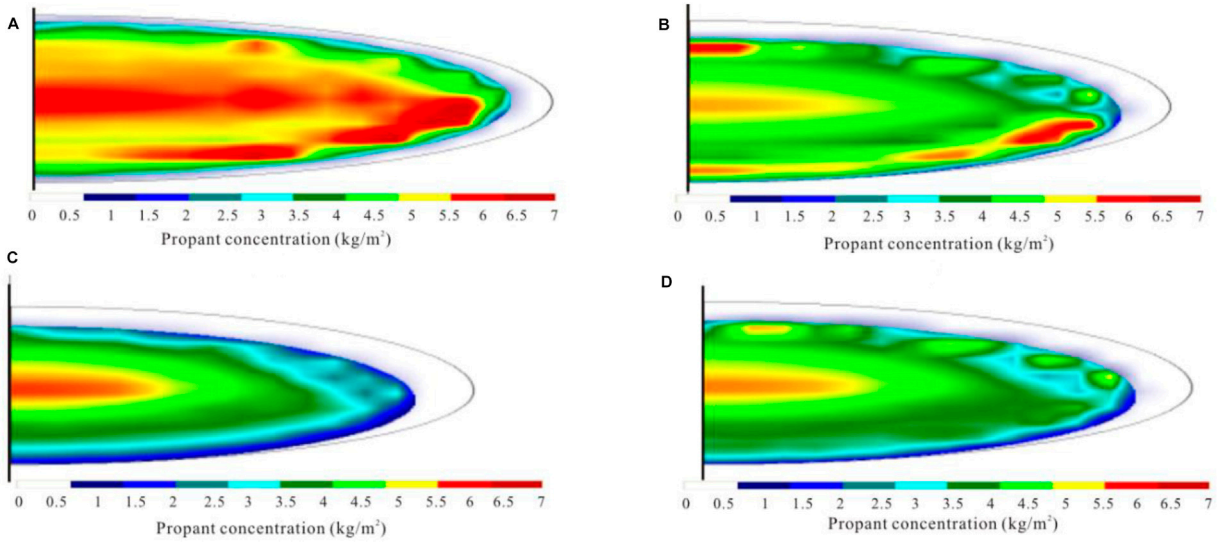

FIGURE 10 | Simulation results of hydraulic fracture morphology under different displacement conditions in Well A1. **(A)** 1.0 m^3/min; **(B)** 2.0 m^3/min; **(C)** 3.0 m^3/min; **(D)** 4.0 m^3/min.

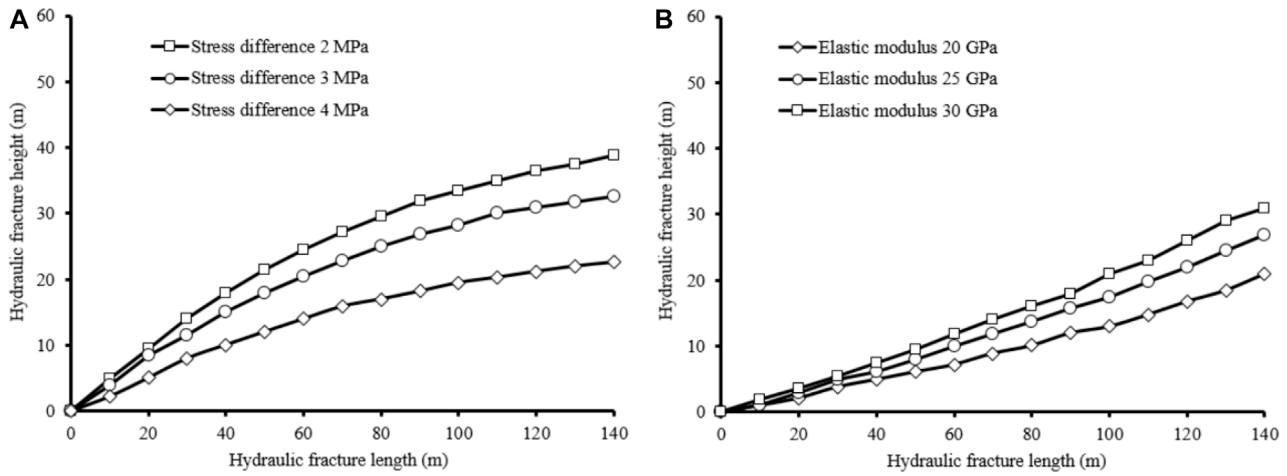

FIGURE 11 | Influence of *in-situ* stress and elastic modulus on hydraulic fracture height. **(A)** The influence of the stress difference between the fracturing layer and the shielding layer on the hydraulic fracture height; **(B)** The influence of the elastic modulus on the extension scale of the hydraulic fracture height.

Optimization of Construction and Mechanical Parameters

The correlations between fracturing construction and hydraulic fracture parameters are shown in **Figure 9**. Some fracturing construction parameters, such as pre-fluid and sand-carrying fluid, have a good positive correlation with the simulated fracture length, height and width (**Figures 9A–D**). However, the correlation between displacement and fracture length, especially fracture height, was not significant (**Figures 9E,F**). **Figure 9E** shows a weak correlation due to several high-displacement and low-fracture-length points. This shows that the excessively high displacement cannot effectively increase the volume of fracturing.

Further, we compared the simulated hydraulic fracture morphologies under different displacements (**Figure 10**). The results show that in the process of displacement changed from 0 to 2 cubic meters/min, the fracture length and height gradually increased; however, when the displacement was greater than 2 cubic meters/min, the reservoir reformed volume didn't increase significantly. Excessive displacement will also cause hydraulic fractures to penetrate the adjacent layers, so the displacement should be controlled at 2~3 cubic meters/min, and the sand ratio should be controlled at 25%. For the tight sandstone of the Chang 6 Member in the study area, the optimized fracture half-length is 120 m and the half-fracture height is 20 m.

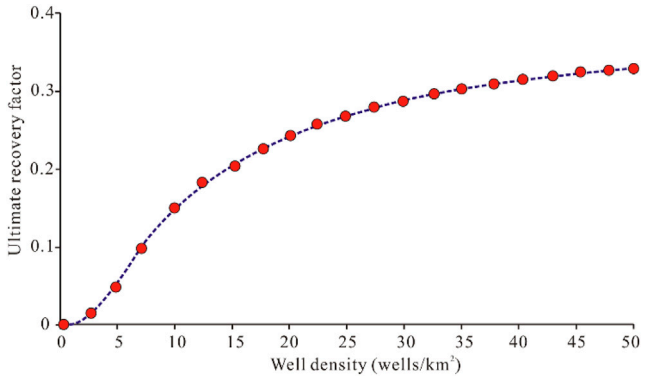

FIGURE 12 | Relationship between well pattern density and ultimate recovery factor.

The fracture height should be effectively controlled during the fracturing process of tight reservoirs. Generally, the main means of controlling fracture height include: high *in-situ* stress barrier, reducing fracturing fluid viscosity, and reducing displacement. The horizontal minimum principal stress difference between the fracturing layer and the shielding layer is the most significant factor affecting the fracture height. Artificial "floating temporary plugging agent" or "settling temporary plugging agent" is to use artificial barrier to control the fracture height. When the stress difference is greater than 2 MPa, hydraulic fractures are generally not easy to penetrate the formation. **Figure 11** shows the effect of the stress difference and elastic modulus of the fracturing layer and the shielding layer on the fracture height. It can be seen that the greater the stress difference between the fracturing layer and the shielding layer, the lower the elastic modulus, and the easier it is to control the fracture height.

Optimization of Well Spacing in Fractured Reservoirs

Well spacing optimization requires the determination of the ultimate recovery factor first. The empirical formulas for ultimate recovery of tight oil sandstone reservoirs are:

$$ER = 0.214289\left(K/\mu_0\right)0.1316 \tag{6}$$

$$ER = 0.05842 + 0.08461\log\left(k/\mu_0\right) + 0.3464\varphi + 0.003871S \tag{7}$$

$$ER = 0.1893 - 0.01264\phi + 0.0005S + 0.075\log\left(k/\mu_0\right) = 0.3355W_f \tag{8}$$

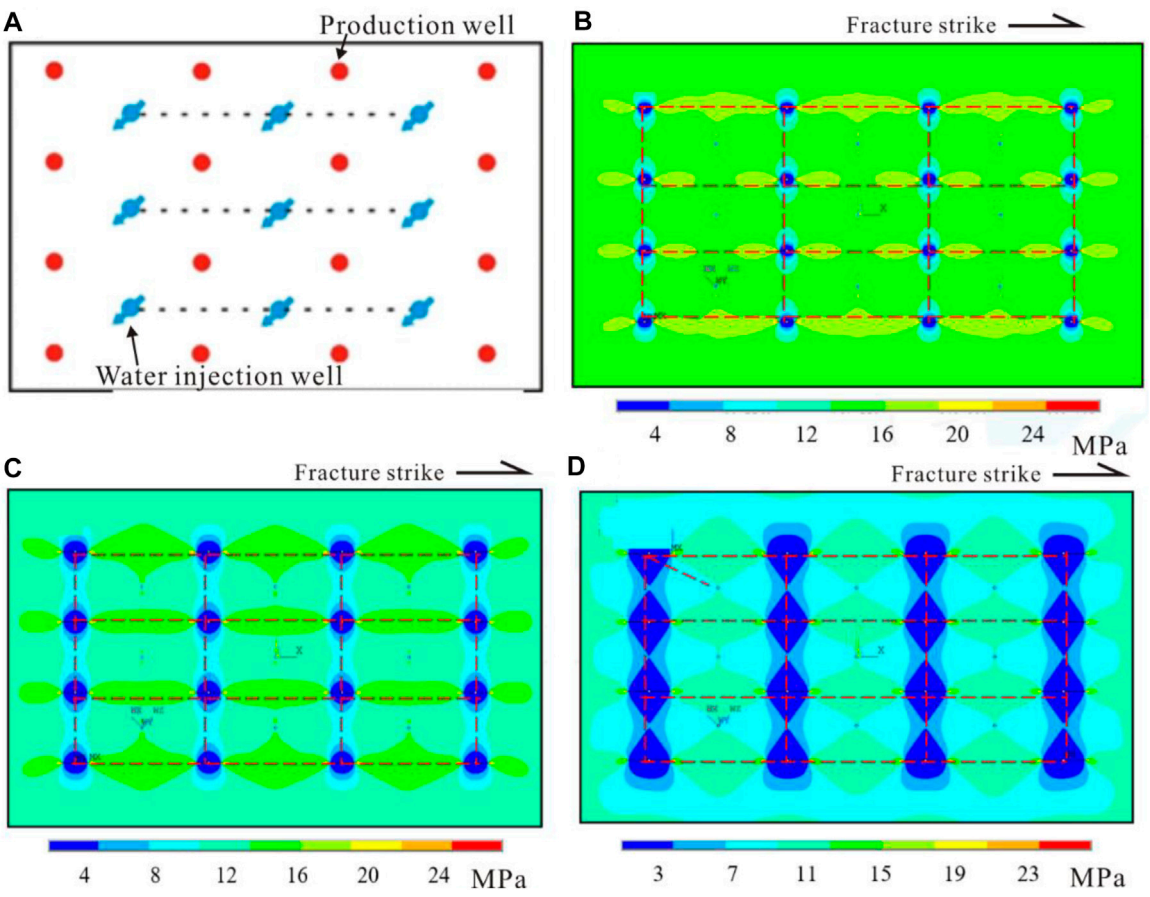

FIGURE 13 | Simulation results of pressure changes at different times based on well pattern design of reverse five -point method. **(A)** Reverse five-point well pattern design; **(B)** Pressure change after 10 years; **(C)** Pressure change after 20 years; **(D)** Pressure change after 30 years.

where ER is the recovery factor; k is the average absolute permeability; μ_o is the viscosity of crude oil in the original formation; ϕ is the effective porosity of the formation; S is the well pattern density; and W_f is the degree of water flooding control.

According to the above formulas, the water flooding recovery factors of the Chang 6 Member are 15.8, 7.3 and 37.4%, respectively, and the average value is 20.2%. Based on the actual data of 144 oil fields or development units in China, Beijing Petroleum Exploration and Development Research Institute has calculated the coupling relationship between ultimate recovery factor and well pattern density according to fluid mobility in tight reservoirs (**Figure 12**). Since fractures are relatively developed in the tight sandstone reservoirs of the Chang 6 Member, the well spacing is appropriately widened. Finally, the optimized well spacing and row spacing of Chang 6 Member are 480 and 150 m, respectively.

Well Pattern Optimization

In order to improve the development effect of tight oil reservoirs, the injection-production well pattern and fracture system need to achieve a reasonable configuration system. The direction of well rows should be parallel to the main strike of natural fractures. Deploying wells parallel to the fracture strike can realize water injection of fracture-parallel direction and oil displacement of fracture-perpendicular direction.

The well pattern deployment forms suitable for tight oil sandstone reservoirs mainly include the reverse five-point, seven-point and nine-point methods. Among them, the inverse five-point method is suitable for low-amplitude area reservoirs with weak development of natural fractures. When the matrix permeability is strong, and the water absorption capacity of the water injection well is equivalent to the liquid production capacity of the oil production well, the square inverse five-point method is suitable. When the matrix permeability is weak, and the water absorption capacity of the water injection well is not equivalent to the liquid production capacity of the oil production well, the rectangular reverse five-point method is more suitable.

The reverse seven-point injection-production well pattern is suitable for reservoirs with relatively developed natural fractures with a fixed strike. When the water absorption capacity of the water injection well is greater than twice that of the oil production well, the reverse seven-point method is most suitable.

The reverse nine-point injection-production well pattern is suitable for low-amplitude structural areas where natural fractures are generally less developed. The line connecting the water injection well and the well angle should be parallel to the fracture trend, so as to enlarge the injection-production well spacing in the fracture direction or reduce the row spacing. In this way, the fracturing scale and productivity can be increased.

Figure 13 shows the variation of formation pressure around the well under different production cycle conditions under the reverse five-point well pattern. It can be seen that a pressure drop funnel is formed around the oil well, and the hydrocarbon pressure inrushes along the fracture direction. As the development cycle increases, the formation pressure decreases gradually (**Figure 13**).

For the reverse seven-point and nine-point well patterns, the stress changes around the well in different production periods have similar characteristics. Combining the actual production capacity of different types of well patterns, it is found that the initial productivity of the anti-seven and anti-nine point well patterns is high, but its productivity declines relatively quickly for fractured reservoirs. The comparison results show that the production capacity of the reservoir with the reverse five-spot well pattern is relatively stable. Therefore, the reverse five-spot well pattern is more suitable for the efficient development of the continental tight oil reservoirs in the Chang 6 Member of the Yanchang Formation.

CONCLUSION

1) Natural fractures have a significant effect on the extension of hydraulic fractures. When the fracturing is parallel to the main strike of natural fractures, the extension distance of the fracturing fracture is long and the scale of fracturing expansion is large; while when the fracturing is orthogonal or oblique to the strike of natural fractures, the extension distance of the hydraulic fracture is significantly reduced.
2) Statistics show that the average length of hydraulic fractures when fracturing parallel to natural fractures is 1.3 times of that when fracturing perpendicular to natural fractures. In addition, the optimization results of fracturing parameters show that the displacement should be controlled at 2–3 cubic meters/min, and the sand ratio should be controlled at 25%. The smaller the horizontal minimum principal stress difference between the fracturing layer and the shielding layer, the lower the elastic modulus, and the easier it is to control the fracture height.
3) Microseismic monitoring results show that the half-fracture length and fracture height of fractures are mainly distributed in 80–140 m and 15–25 m, respectively. Finally, we optimized the fracturing construction parameters, and the optimized fracture half-length was 120 m and the half-fracture height was 20 m.
4) Finally, the well pattern of the target layer is optimized considering natural fractures. Through this study, we found that the reverse five-spot well pattern is suitable for the efficient development of tight oil reservoirs of the Chang 6 member in this area.

DATA AVAILABILITY STATEMENT

The original contributions presented in the study are included in the article/Supplementary Material, further inquiries can be directed to the corresponding author.

AUTHOR CONTRIBUTIONS

JL is responsible for the idea and writing of this paper and ZZ, HT, JY, XZ, and BW are responsible for the data interpretation.

FUNDING

This research was financially supported by the Forward Looking Basic Strategic Technology Research Projects of China National Petroleum Corporation (Study on Reservoir Forming Law and the Key Technology of Lithologic Stratigraphic Reservoirs) (No. 2021DJ0406).

REFERENCES

Abouzar, M., and Ghanbarian, B. (2021). A New Methodology for Grouping and Averaging Capillary Pressure Curves for Reservoir Models. *Energ. Geosci.* 2 (1), 52–62. doi:10.1016/j.engeos.2020.09.001

Bello, A. M., Jones, S., Gluyas, J., Acikalin, S., and Cartigny, M. (2021). Role Played by clay Content in Controlling Reservoir Quality of Submarine Fan System, Forties Sandstone Member, Central Graben, North Sea. *Mar. Pet. Geology.* 128, 105058. doi:10.1016/j.marpetgeo.2021.105058

Bhatti, A. A., Ismail, A., Raza, A., Gholami, R., Rezaee, R., Nagarajan, R., et al. (2020). Permeability Prediction Using Hydraulic Flow Units and Electrofacies Analysis. *Energ. Geosci.* 1, 81–91. doi:10.1016/j.engeos.2020.04.003

Chitrala, Y., Moreno, C., Sondergeld, C., and Rai, C. (2013). An Experimental Investigation into Hydraulic Fracture Propagation under Different Applied Stresses in Tight Sands Using Acoustic Emissions. *J. Pet. Sci. Eng.* 108, 151–161. doi:10.1016/j.petrol.2013.01.002

Ding, F., Xie, C., Zhou, X., Jiang, C., Li, K., Wan, L., et al. (2021). Defining Stratigraphic Oil and Gas Plays by Modifying Structural Plays: A Case Study from the Xihu Sag, east China Sea Shelf Basin. *Energ. Geosci.* 2 (1), 41–51. doi:10.1016/j.engeos.2020.08.002

Dong, S., Zeng, L., Lyu, W., Xia, D., Liu, G., Wu, Y., et al. (2020). Fracture Identification and Evaluation Using Conventional Logs in Tight Sandstones: A Case Study in the Ordos Basin, China. *Energ. Geosci.* 1 (3–4), 115–123. doi:10.1016/j.engeos.2020.06.003

Du, Y., and Aydin, A. (1993). The Maximum Distortional Strain Energy Density Criterion for Shear Fracture Propagation with Applications to the Growth Paths ofEn Échelonfaults. *Geophys. Res. Lett.* 20, 1091–1094. doi:10.1029/93gl01238

Gao, F. Q. (2021). Influence of Hydraulic Fracturing of strong Roof on Mining-Induced Stress Insight from Numerical Simulation. *J. Mining Strata Control. Eng.* 3 (2), 023032. doi:10.13532/j.jmsce.cn10-1638/td.20210329.001

Guo, L. L., Zhou, D. W., Zhang, D. M., and Zhou, B. H. (2021). Deformation and Failure of Surrounding Rock of a Roadway Subjected to Mining-Induced Stresses. *J. Mining Strata Control. Eng.* 3 (2), 023038. doi:10.13532/j.jmsce.cn10-1638/td.20200727.001

Gurocak, Z., Solanki, P., Alemdag, S., and Zaman, M. M. (2012). New Considerations for Empirical Estimation of Tensile Strength of Rocks. *Eng. Geology.* 145-146, 1–8. doi:10.1016/j.enggeo.2012.06.005

He, X., Zhang, P., He, G., Gao, Y., Liu, M., Zhang, Y., et al. (2020). Evaluation of Sweet Spots and Horizontal-Well-Design Technology for Shale Gas in the basin-margin Transition Zone of southeastern Chongqing, SW China. *Energ. Geosci.* 1, 134–146. doi:10.1016/j.engeos.2020.06.004

Hong, D., Cao, J., Wu, T., Dang, S., Hu, W., and Yao, S. (2020). Authigenic clay Minerals and Calcite Dissolution Influence Reservoir Quality in Tight Sandstones: Insights from the central Junggar Basin, NW China. *Energ. Geosci.* 1 (1–2), 8–19. doi:10.1016/j.engeos.2020.03.001

Hower, J. C., and Groppo, J. G. (2021). Rare Earth-Bearing Particles in Fly Ash Carbons: Examples from the Combustion of Eastern Kentucky Coals. *Energ. Geosci.* 2 (2), 90–98. doi:10.1016/j.engeos.2020.09.003

Jaeger, J. C., and Cook, N. G. W. (1976). *Fundamentals of Rock Mechanics*. London: Chapman & Hall, 128–130.

Khan, E. U., Saleem, M., Naseem, A. A., Ahmad, W., Yaseen, M., and Khan, T. U. (2020). Microfacies Analysis, Diagenetic Overprints, Geochemistry, and Reservoir Quality of the Jurassic Samanasuk Formation at the Kahi Section, Nizampur Basin, NW Himalayas, Pakistan. *Carbonates Evaporites* 35 (3), 95–96. doi:10.1007/s13146-020-00622-4

Li, L., Huang, B., Li, Y., Hu, R., and Li, X. (2018). Multi-scale Modeling of Shale Laminas and Fracture Networks in the Yanchang Formation, Southern Ordos Basin, China. *Eng. Geology.* 243, 231–240. doi:10.1016/j.enggeo.2018.07.010

Li, L., and Li, S. J. (2021). Evolution Rule of Overlying Strata Structure in Repeat Mining of Shallow Close Distance Seams Based on Schwarz Alternating Procedure. *J. Mining Strata Control. Eng.* 3 (2), 023515. doi:10.13532/j.jmsce.cn10-1638/td.20210225.001

Li, Y., Zhou, D., Wang, W., Jiang, T., and Xue, Z. (2020). Development of Unconventional Gas and Technologies Adopted in China. *Energ. Geosci.* 1 (1–2), 55–68. doi:10.1016/j.engeos.2020.04.004

Li, Z. M., and Zhang, J. C. (1997). *Crustal Stress and Hydrocarbon Exploration and Development*. Beijing: Petroleum Industry Press, 138–140.

Liu, Y., Gao, M., and Zhao, H. (2020). Detection of Overlying Rock Structure and Identification of Key Stratum by Drilling and Logging Technology. *J. Mining Strata Control. Eng.* 2 (2), 023038. doi:10.13532/j.jmsce.cn10-1638/td.2020.02.004

Lommatzsch, M., Exner, U., Gier, S., and Grasemann, B. (2015). Dilatant Shear Band Formation and Diagenesis in Calcareous, Arkosic Sandstones, Vienna Basin (Austria). *Mar. Pet. Geology.* 62, 144–160. doi:10.1016/j.marpetgeo.2015.02.002

Luo, Y., Huang, H., Yang, Y., Hao, Y., Zhang, S., and Li, Q. (2018). Integrated Prediction of deepwater Gas Reservoirs Using Bayesian Seismic Inversion and Fluid Mobility Attribute in the South China Sea. *J. Nat. Gas Sci. Eng.* 59, 56–66. doi:10.1016/j.jngse.2018.08.019

Ma, S. W., Ren, D. Z., Zhou, L. F., Dong, F. J., Shi, S., Mumuni, A., et al. (2019). Impacts of Diagenesis of Tight sandstone Gas Reservoir on Reservoir Physical Properties: A Case Study, Sulige Gas Field, Ordos Basin, China. *Interpretation* 7 (3), 1–4. doi:10.1190/int-2018-0173.1

Mahmoodi, S., Abbasi, M., and Sharifi, M. (2019). New Fluid Flow Model for Hydraulic Fractured wells with Non-uniform Fracture Geometry and Permeability. *J. Nat. Gas Sci. Eng.* 68, 1–14. doi:10.1016/j.jngse.2019.102914

Mahmud, H., Hisham, M., Mahmud, M., Leong, V., and Shafiq, M. (2020). Petrophysical Interpretations of Subsurface Stratigraphic Correlations, Baram Delta, Sarawak, Malaysia. *Energ. Geosci.* 1 (3–4), 100–114. doi:10.1016/j.engeos.2020.04.005

McBride, E. F. (1989). Quartz Cement in Sandstones: A Review. *Earth-Science Rev.* 26, 69–112. doi:10.1016/0012-8252(89)90019-6

Peng, J., Wong, L. N. Y., and Teh, C. I. (2018). A Re-examination of Slenderness Ratio Effect on Rock Strength: Insights from DEM Grain-Based Modelling. *Eng. Geology.* 246, 245–254. doi:10.1016/j.enggeo.2018.10.003

Qie, L., Shi, Y. N., and Liu, J. S. (2021). Experimental Study on Grouting Diffusion of Gangue Solid Filling Bulk Materials. *J. Mining Strata Control. Eng.* 3 (2), 023011. doi:10.13532/j.jmsce.cn10-1638/td.20201111.001

Salamon, M. D. G. (1984). Energy Considerations in Rock Mechanics: Fundamental Results. *J. South. Afr. Inst. Min. Metall.* 84, 233–246.

Santosh, M., and Feng, Z. Q. (2020). New Horizons in Energy Geoscience. *Energ. Geosci.* 1 (1–2), 1–2. doi:10.1016/j.engeos.2020.05.005

Shuai, Y., Zhang, S., Mi, J., Gong, S., Yuan, X., Yang, Z., et al. (2013). Charging Time of Tight Gas in the Upper Paleozoic of the Ordos Basin, central China. *Org. Geochem.* 64, 38–46. doi:10.1016/j.orggeochem.2013.09.001

Wang, J., and Wang, X. L. (2021). Seepage Characteristic and Fracture Development of Protected Seam Caused by Mining Protecting Strata. *J. Mining Strata Control. Eng.* 3 (3), 033511. doi:10.13532/j.jmsce.cn10-1638/td.20201215.001

Wang, M., Yang, Z., Shui, C., Yu, Z., Wang, Z. Y., and Cheng, Y. (2019). Diagenesis and its Influence on Reservoir Quality and Oil-Water Relative Permeability: A Case Study in the Yanchang Formation Chang 8 Tight sandstone Oil Reservoir, Ordos Basin, China. *Open Geosciences* 11 (1), 37–47. doi:10.1515/geo-2019-0004

Xi, K., Cao, Y., Liu, K., Wu, S., Yuan, G., Zhu, R., et al. (2019). Diagenesis of Tight sandstone Reservoirs in the Upper Triassic Yanchang Formation, Southwestern Ordos Basin, China. *Mar. Pet. Geology.* 99, 548–562. doi:10.1016/j.marpetgeo.2018.10.031

Xue, F., Liu, X. X., and Wang, T. Z. (2021). Research on Anchoring Effect of Jointed Rock Mass Based on 3D Printing and Digital Speckle Technology. *J. Mining*

Strata Control. Eng. 3 (2), 023013. doi:10.13532/j.jmsce.cn10-1638/td.20201020.001

Yang, J. X., Luo, M. K., Zhang, X. W., Huang, N., and Hou, S. J. (2021). Mechanical Properties and Fatigue Damage Evolution of Granite under Cyclic Loading and Unloading Conditions. *J. Mining Strata Control. Eng.* 3 (3), 033016. doi:10.13532/j.jmsce.cn10-1638/td.20210510.001

Yin, S., Lv, D., and Ding, W. (2018). New Method for Assessing Microfracture Stress Sensitivity in Tight sandstone Reservoirs Based on Acoustic Experiments. *Int. J. Geomechanics* 18 (4), 1–11. doi:10.1061/(asce)gm.1943-5622.0001100

Yin, S., and Wu, Z. (2020). Geomechanical Simulation of Low-Order Fracture of Tight sandstone. *Mar. Pet. Geology.* 100, 1–10. doi:10.1016/j.marpetgeo.2020.104359

Yoshida, M., and Santosh, M. (2020). Energetics of the Solid Earth: An Integrated Perspective. *Energ. Geosci.* 1, 28–35. doi:10.1016/j.engeos.2020.04.001

Zang, D., Bao, Z., Li, M., Fu, P., Li, M., Niu, B., et al. (2020). Sandbody Architecture Analysis of Braided River Reservoirs and Their Significance for Remaining Oil Distribution: A Case Study Based on a New Outcrop in the Songliao Basin, Northeast China. *Energy Exploration & Exploitation* 38 (6), 2231–2251. doi:10.1177/0144598720951280

Zhang, B., Shen, B., and Zhang, J. (2020). Experimental Study of Edge-Opened Cracks Propagation in Rock-like Materials. *J. Mining Strata Control. Eng.* 2 (3), 033035. doi:10.13532/j.jmsce.cn10-1638/td.20200313.001

Zhang, S., Huang, H., Dong, Y., Yang, X., Wang, C., and Luo, Y. (2017). Direct Estimation of the Fluid Properties and Brittleness via Elastic Impedance Inversion for Predicting Sweet Spots and the Fracturing Area in the Unconventional Reservoir. *J. Nat. Gas Sci. Eng.* 45, 415–427. doi:10.1016/j.jngse.2017.04.028

Zhao, K. K., Jiang, P. F., Feng, Y. J., Sun, X. D., Cheng, L. X., and Zheng, J. W. (2021). Investigation of the Characteristics of Hydraulic Fracture Initiation by Using Maximum Tangential Stress Criterion. *J. Mining Strata Control. Eng.* 3 (2), 023520. doi:10.13532/j.jmsce.cn10-1638/td.20201217.001

Zhao, Z., Wu, K., Fan, Y., Guo, J., Zeng, B., and Yue, W. (2020). An Optimization Model for Conductivity of Hydraulic Fracture Networks in the Longmaxi Shale, Sichuan basin, Southwest China. *Energ. Geosci.* 1, 47–54. doi:10.1016/j.engeos.2020.05.001

Zou, C. N., Yang, Z., Tao, S. Z., Yuan, X. J., Zhu, R. K., Hou, L. H., et al. (2013). Continuous Hydrocarbon Accumulation over a Large Area as a Distinguishing Characteristic of Unconventional Petroleum: The Ordos Basin, North-Central China. *Earth-Science Rev.* 126, 358–369. doi:10.1016/j.earscirev.2013.08.006

Conflict of Interest: Authors ZZ and XZ were employed by the PetroChina Changqing Oilfield Company and authors HT, JY, and BW were employed by the PetroChina Yumen Oilfield Company.

The remaining author declares that the research was conducted in the absence of any commercial or financial relationships that could be construed as a potential conflict of interest.

frontiers in Earth Science

ORIGINAL RESEARCH
published: 18 March 2022
doi: 10.3389/feart.2022.873715

Numerical Study on the Use of Alternating Injection Hydraulic Fracturing Technology to Optimize the Interaction Between Hydraulic Fracture and Natural Fracture

Yang Yang[1], *Lingzhi Xie*[1,2]*, *Bo He*[1] *and Peng Zhao*[2]

[1]Institute of New Energy and Low-Carbon Technology, Sichuan University, Chengdu, China, [2]College of Architecture and Environment, Sichuan University, Chengdu, China

Hydraulic fracturing is a key technology for shale gas production. Activating the natural fracture (NF) system in shale reservoirs and forming a complex fracture network can greatly improve the effect of fracturing. The effect of fracturing is mainly influenced by geological factors and operational parameters of a reservoir. Effectively reforming a reservoir under unfavourable geological conditions and maximizing the activation of NFs in the reservoir can substantially increase its reformed volume and the production of shale gas. Alternating fluid injection (AFI) fracturing technologies using multiple fracturing fluids with different viscosities can activate closed NFs while retaining the high conductivity of the principal fracture to achieve a larger stimulated reservoir volume (SRV). In this paper, a hydraulic-mechanical coupling finite element method (FEM) of a reservoir is established, and AFI fracturing technology is numerically simulated using the continuum method. In addition, the fracture propagation stage and path propagation for AFI technology are discussed. The results show that AFI fracturing technology can form principal fractures with high conductivity and activate NFs in a reservoir to form comparatively complex fracture propagation paths.

Keywords: hydraulic fracturing, finite element method, alternating fluid injection, shale gas, natural fracture

OPEN ACCESS

Edited by:
Shuai Yin,
Xi'an Shiyou University, China

Reviewed by:
Taotao Yan,
Taiyuan University of Technology, China
Chaojun Fan,
Liaoning Technical University, China

***Correspondence:**
Lingzhi Xie
xielingzhi@scu.edu.cn

Specialty section:
This article was submitted to Structural Geology and Tectonics, a section of the journal Frontiers in Earth Science

Received: *11 February 2022*
Accepted: *01 March 2022*
Published: *18 March 2022*

Citation:
Yang Y, Xie L, He B and Zhao P (2022) Numerical Study on the Use of Alternating Injection Hydraulic Fracturing Technology to Optimize the Interaction Between Hydraulic Fracture and Natural Fracture. Front. Earth Sci. 10:873715. doi: 10.3389/feart.2022.873715

1 INTRODUCTION

Unconventional reservoirs such as shale, sandstone, and coal are rich in natural gas resources (Yin et al., 2020; Guo et al., 2021). Enhancing the extraction of shale gas demands successful reservoir stimulation treatment due to the low permeability characteristics of shale rock (Li, 2020; Zhao P. et al., 2021). Hydraulic fracturing and horizontal well technology are currently the most widely used shale gas exploitation technologies (Weng, 2015; Yin and Ding, 2018). There are many natural fractures (NFs) in shale reservoirs (Gale et al., 2014; Wang et al., 2020) that strongly influence the effect of reservoir stimulation on hydraulic fracturing (He et al., 2020). Making full use of the NF system and forming a complex fracture network in a reservoir can achieve a larger stimulated reservoir volume (SRV) and reservoir permeability (Mayerhofer et al., 2010; Zhao et al., 2020a).

When hydraulic fractures (HFs) propagate and encounter NFs in the reservoir, the following three behaviours occur: HFs offset along NFs, HFs cross NFs, and HFs are arrested by NFs (Sarmadivaleh, 2012). The interaction of these behaviour modes is influenced by geological

factors, such as *in situ* stress differences, NF dip angles and NF tensile strengths, and operational parameters, such as the fracturing fluid viscosity and injection rate (Zhang et al., 2020b). In hydraulic fracturing tests, the *in situ* stress difference and approach angle are the most studied influencing factors. Blanton (1982) studied the influence of *in situ* stress and approach angle on the interaction between HFs and NFs and proposed an interaction criterion including these two factors. Warpinski and Teufel (1987) conducted a triaxial hydraulic fracturing test and suggested a criterion that includes the approach angle, stress difference and shear slip of NFs, which can predict the interaction behaviour mode of HFs and NFs. Renshaw and Pollard (1995) introduced an interaction criterion of frictional NFs and HFs at orthogonal angles, and Gu et al. (2012) expanded this criterion to nonorthogonal fractures. The mechanical properties of NFs also affect the interaction between HFs and NFs. Zhou et al. (2008) included the shear slippage of pre-existing fractures to investigate the interaction between HFs and pre-existing fractures based on the work of (Blanton, 1982). However, when the geological conditions of a reservoir are not suitable for activating NFs by conventional methods, special hydraulic fracture design is critical to activating NFs and forming complex fracture networks in hydraulic fracturing. Therefore, research on fracturing fluid viscosity and injection rate is gradually increasing. Chuprakov et al. (2014) proposed an analytical model, referred to as OpenT, of fluid penetration that describes the influence of fluid viscosity and injection rate on the interaction of HFs and NFs. He et al. (2015) confirmed through hydraulic fracturing tests that high-viscosity fracturing fluids and high injection rates tend to penetrate rather than activate natural fractures. Zou et al. (2016) indicated that low-viscosity fracturing fluid is more likely to enter NFs through computerized tomography (CT) scanning of shale samples after hydraulic fracturing, thereby forming a complex network of fractures. However, for reservoirs where it is difficult to achieve large SRVs, a variety of fracturing fluids with different viscosities are used for multi-stage fracturing (Duan et al., 2019; Cao et al., 2020; Chen G. B. et al., 2021; Wang and Wang, 2021), and research on multi-stage fracturing with multiple fluids has begun. Alternating Fluid Injection (AFI) technology is a fracturing technology that uses different fracturing fluids at different stages of multi-stages fracturing, aiming to transform geological conditions that are not conducive to the formation of complex fracture networks (Gao et al., 2021b; Fan et al., 2021; Fan et al., 2022). Hou et al. (2019) proposed a technology of alternating injection of fluids with different viscosities, which improved the activation of NFs under conditions that were not conducive to the formation of complex fracture networks (such as high differential stress). According to these experiments, using sequenced hydraulic fracturing and multiple fracturing fluids with different viscosities is a promising technology.

However, the experimental methods are limited by accuracy and sample size (Zhang et al., 2020a; Lan et al., 2021; Yang et al., 2021), and it is difficult to evaluate the fracturing effect of variable viscosity alternating injection technology. Large-scale simulations of hydraulic fracturing can obtain the whole fracture morphology and quantitative analysis of SRV changes. Therefore, it is appropriate to use numerical methods to study alternating injection technology. Numerical methods can be divided into continuum approaches and discontinuity approaches according to the description of fractures. In the discontinuity approaches, fractures are described as geometric discontinuities where fluid flows to simulate fracture propagation. Discrete element method (DEM) is suitable method for simulating hydraulic fracturing of rock reservoirs, which can clearly show the fracture propagation path and the final fracture network shape (Yoon et al., 2017; Gao, 2021a). Zhai et al. (2020) used the cohesive zone model to study the propagation of HFs in random natural fracture shale reservoirs under different working conditions. Zhao H. et al. (2021) applied the discrete fracture network model (DFN) to study the propagation of carbon dioxide fracturing networks in shale reservoirs and analysed the influence of different natural fracture densities on the shape of the fracture network. Rezaei et al. (2019) used the boundary element method (BEM) to study the propagation of the fracture network in a large-scale two-dimensional reservoir model with many natural fractures and focused on the influence of NF dip on the expansion of the fracture network. In the continuum method, the extended finite element method (XFEM) was adopted to simulate fracture propagation by adding discontinuous displacement degrees of freedom to describe the fracture width and other properties (Vahab et al., 2019; Zheng et al., 2020a). Although the extended finite element method provides visual descriptions of fractures in the continuum model, it is difficult for researchers to embed natural fractures using this method, and the calculation efficiency is not high. The smeared crack model based on the finite element method (FEM) offers a practical balance between calculation efficiency and accuracy and is easy for researchers to embed fracture into this model (Bazant and Oh, 1983). In the FEM, fractures are simplified as anisotropic damage elements. Therefore, the propagation of these fractures is expressed as damage zones, and this method has adequate efficiency to study the interaction between HFs and NFs (Tang et al., 2018; Zhao Z. et al., 2020).

Although there are many studies on the fracture propagation process of hydraulic fracturing, most of them consider only the injection of one type of fracturing fluid, and research on the alternate injection of multiple fracturing fluids of different viscosities is very rare. Therefore, it is of practical significance to simulate the stimulation effect of alternating fluid injection multi-stage fracturing technology through numerical methods and to observe the final fracture network morphology. In this paper, an FEM model of a shale reservoir with an embedded fracture is established to simulate the interaction between HFs and NFs and explore the effect of alternating injection of fracturing fluids with different viscosities on the SRV and the maximum capability of this technology.

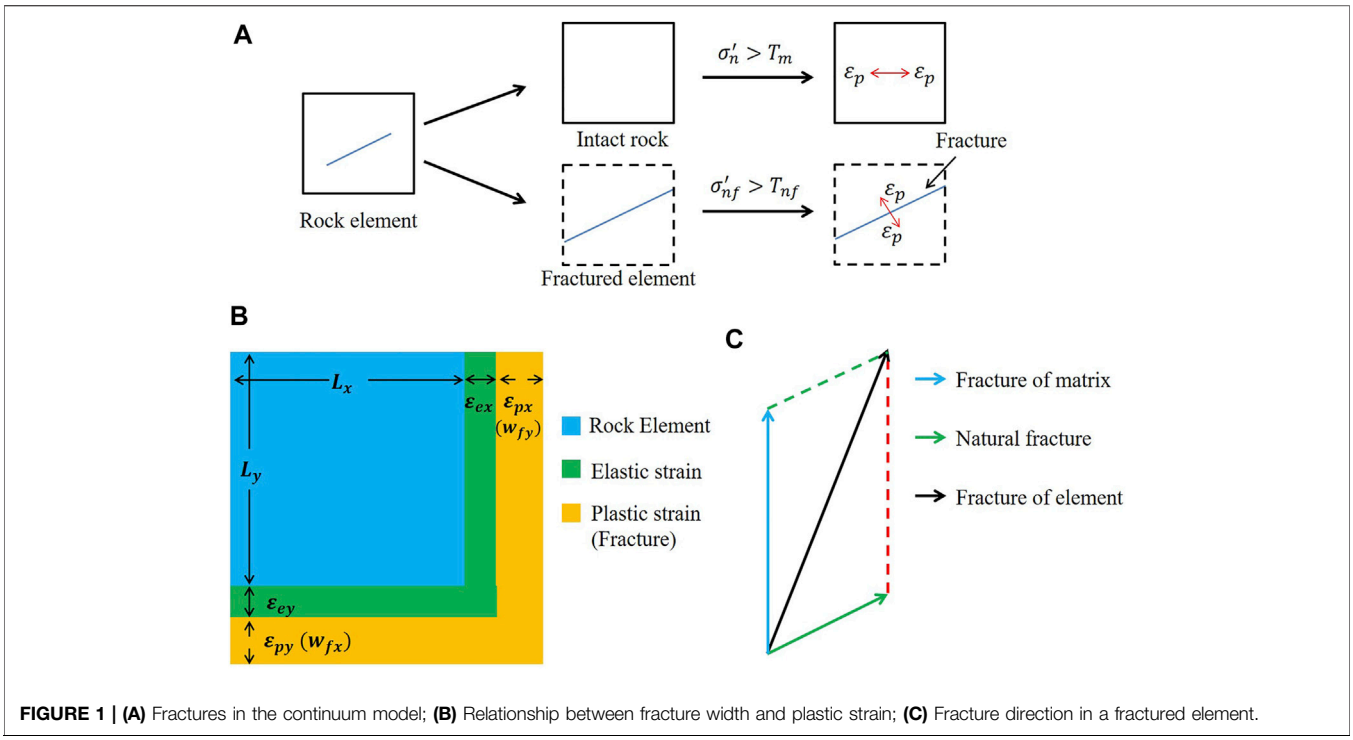

FIGURE 1 | (A) Fractures in the continuum model; **(B)** Relationship between fracture width and plastic strain; **(C)** Fracture direction in a fractured element.

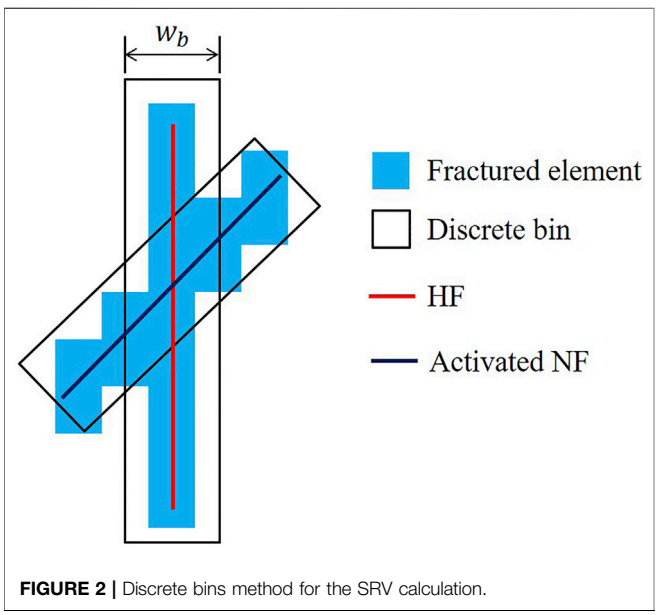

FIGURE 2 | Discrete bins method for the SRV calculation.

2 NUMERICAL MODEL

2.1 Fundamental Theory

In the FEM model of hydraulic-mechanical coupling, shale is treated as a porous material according to the extended formula of Biot's consolidation theory (Zienkiewicz and Shiomi, 1984). The fracturing fluid in the shale is treated as a single-phase flow.

2.1.1 Deformation Governing Equations of Shale

The mass balance differential equation of shale is as follows:

$$\bar{\nabla}\boldsymbol{\sigma} - \rho\frac{d^2\boldsymbol{u}}{dt^2} + \gamma_b \boldsymbol{g}_v = \boldsymbol{f} \tag{1}$$

where ρ is the density of shale; $\boldsymbol{u}$ is the displacement; $\bar{\nabla}$ is the matrix differentiation operator; $\boldsymbol{\sigma}$ is the total Cauchy stress; γ_b is the bulk weight of shale; $\boldsymbol{g}_v$ is the direction of gravity; and $\boldsymbol{f}$ is the applied force.

According to the principle of effective stress, the relationship between effective stress and total stress is as follows:

$$\boldsymbol{\sigma}' = \boldsymbol{\sigma} + \alpha p_w \boldsymbol{I} \tag{2}$$

where $\boldsymbol{\sigma}'$ is the effective stress; $\boldsymbol{\sigma}$ is the total stress; α is the Biot coefficient, which is assumed to be 0.7 in this paper; p_w is the pore pressure; and $\mathbf{I}$ is the second-order identity tensor.

The effective stress is the force applied on a rock skeleton, which determines the elastic strain of the rock, and its relationship is as follows:

$$\boldsymbol{\sigma}' = \mathrm{D}: \varepsilon^e \tag{3}$$

where D is the fourth-order elasticity tensor and ε^e is the second-order elastic strain tensor.

The geometric equation including the relationship between strain and displacement is as follows:

$$\varepsilon = \bar{\nabla}^T \boldsymbol{u} \tag{4}$$

where ε is the total strain.

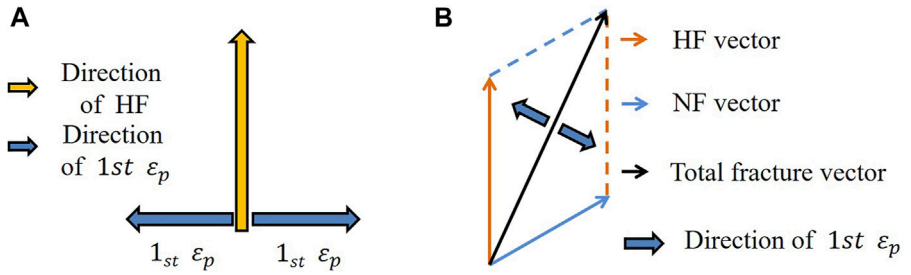

FIGURE 3 | Schematic of hydraulic fracture visualization **(A)** In elements without NFs; **(B)** In elements with NFs.

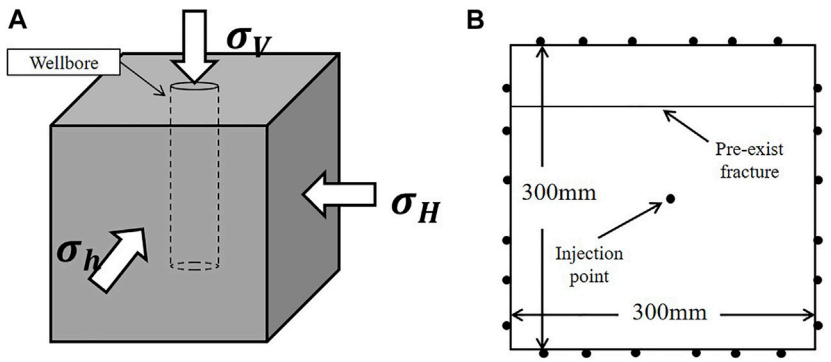

FIGURE 4 | (A) Schematic diagram of the hydraulic fracturing sample; **(B)** the FEM model used in the verification.

TABLE 1 | Parameters used in Gu's actual triaxial hydraulic fracturing experiment.

Case	β(°)	$\Delta\sigma$ (MPa)	Published results	Simulation results
Case 1	90	6.89	Crossing	Crossing
Case 2	90	0.69	No crossing	No crossing
Case 3	75	10.34	Crossing	Crossing
Case 4	75	1.37	No crossing	No crossing
Case 5	45	10.34	No crossing	No crossing
Case 6	45	1.37	No crossing	No crossing

TABLE 2 | Parameters used in the model validation.

Category	Parameter	Value
Fluid	Viscosity	1 Pa·s
	Injection rate	0.5 ml/s
Sample	Tensile strength	4.05 MPa
	Tensile strength	1 kPa
Pre-existing fracture	Shear strength	1 kPa
	Coefficient of friction	0.615

2.1.2 Fluid Flow Model

According to the mass conservation relationship of fluid flow, the following equation can be obtained:

$$\nabla^T \mathbf{q} + \alpha \frac{d\varepsilon_v}{dt} + \frac{1}{Q^*}\frac{dp_w}{dt} = s \tag{5}$$

where ∇ is the gradient operator; $\mathbf{q}$ is the flow flux vector; ε_v is the volumetric strain of the shale; Q^* is the compressibility parameter; and s is the flow source.

Fluid flow conforms to Darcy's law, and the relationship between flow flux and pore pressure is as follows:

$$\mathbf{q} = \frac{\mathbf{K}}{\gamma_f}\left(-\nabla p + \gamma_f \mathbf{g}_v\right) \tag{6}$$

where $\mathbf{K}$ is the second-order permeability tensor.

The compressibility parameter in **Eq. 5** can be calculated as follows:

$$\frac{1}{Q^*} = \frac{n}{K_f} + \frac{\alpha - n}{K_{sk}} \tag{7}$$

where K_f is the bulk modulus of the fluid and K_{sk} is the bulk modulus of the shale skeleton.

2.2 Fracture Initiation and Propagation Based on the Continuum Model

According to the model of initiation, fractures can be divided into toughness-dominated fractures and viscosity-dominated fractures. For the continuous model whose mesh size is much larger than the fracture tip, viscosity-dominated fractures are usually used to simulate the initiation of fractures, that is, when

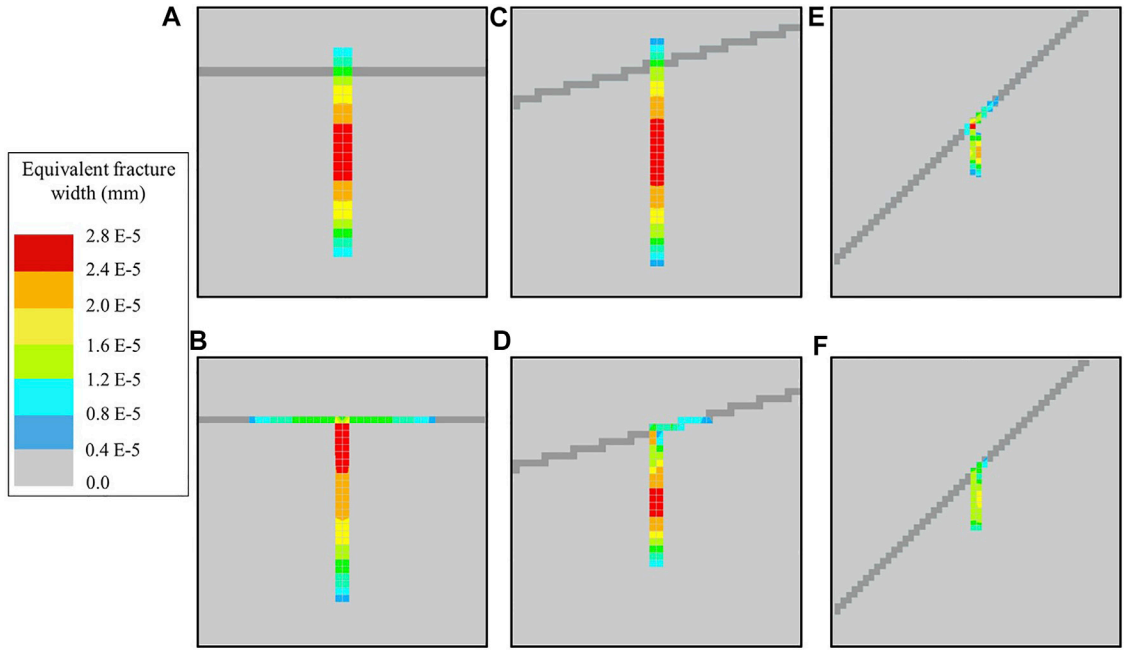

FIGURE 5 | Width of HF **(A)** Case 1, **(B)** Case 2, **(C)** Case 3, **(D)** Case 4, **(E)** Case 5 and **(F)** Case 6.

the elelemnt stress exceeds the corresponding strength, fractures are generated (Zhou, 2013; Li et al., 2016). In this case, the strength criterion is suitable for determining rock failure. In this paper, the anisotropic maximum tensile stress criterion is used to determine the initiation and propagation of fractures.

For a shale matrix, the failure planes of the material can be described as follows:

$$\sigma_n^{'} = T_m \tag{8}$$

where $\sigma_n^{'}$ is the tensile stress at the failure plane and T_m is the tensile strength at the failure plane.

The strength of natural fractures in shale is lower than that of the matrix, and the failure plane of natural fractures can be obtained by the following formula:

$$\sigma_{nf}^{'} = T_{nf} \tag{9}$$

where $\sigma_{nf}^{'}$is the tensile stress at the NF failure plane and T_{nf} is the tensile strength at the NF failure plane.

When HF propagates in a rock matrix, the propagation direction is usually perpendicular to the direction of the maximum principal stress of the shale formation. In some cases, a single rock element includes multiple failure surfaces, and the failures of these surfaces do not affect each other (**Figure 1A**). In each time step, the program checks whether the stress element meets the failure criterion. Generally, the stress element is subject to the following conditions: ① The minimal principle effective stress exceeds the critical tensile stress; and ② the normal effective stress exceeds the NF tensile strength. The cases of the resulting fractures are as follows: 1) When only condition ① is satisfied, the fracture is along the direction of maximum principal stress; 2) when only condition ② is satisfied, the fracture is along the preset NF direction; and 3) when both ① and ② are satisfied at the same time, the fracture in the element can be decomposed into two fractures in specific directions (**Figure 1C**).

2.3 The Relationship Between Permeability and Fracture Properties

In **Section 2.2**, the plastic strain and deformation after material failure can be obtained. However, it is necessary to link the material strain with the fluid parameters to achieve a complete HF propagation fluid mechanics coupling process. When the shale is still intact rock, fluid flows in the pores of the rock and can be described by Darcy's law. In the fracturing process, due to the low permeability of shale, fluid flow is blocked, resulting in an uneven distribution of rock pore pressure; that is, there is a difference in pore pressure between the injection point and the surrounding area. When the pressure difference accumulates to a certain value, i.e., the effective stress reaches the failure strength, the rock is damaged, and the permeability of the rock element is divided into two parts: the permeability of the fracture and the permeability of the porous medium.

Obviously, it is necessary to calculate the equivalent fracture width in order to calculate the permeability. Based on the equivalent continuum method, the strain of fractured rock consists of fracture strain and intact rock strain. The deformation of intact rock can be approximated as elastic strain, while plastic strain is completely caused by fracture deformation. Therefore, the fracture width corresponds to the

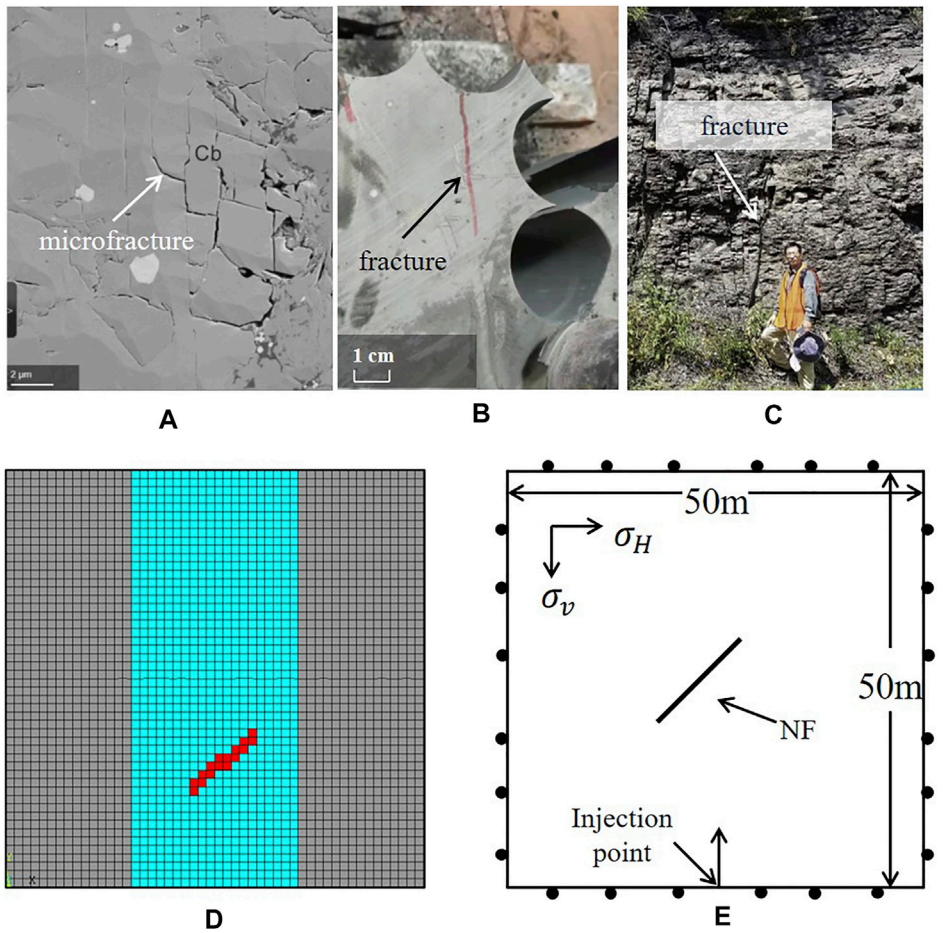

FIGURE 6 | (A) micro-fracture (Chen J. et al., 2021); **(B)** sample-scale fracture; **(C)** large-scale fracture (Zheng et al., 2020b); **(D)** FEM model of fractured reservoir; **(E)** boundary condition of reservoir model.

TABLE 3 | Parameters of the reservoir model.

Group	Parameters	Value
Matrix	Elastic modulus	15 GPa
	Poisson's ratio	0.2
	Permeability	8.62×10^{-12}
	Tensile strength	6 MPa
	Density	2,400 kg/m^3
	Biot coefficient	0.7
NF	Cement strength	0.5 MPa

result of the continuum model (**Figure 1B**) shown in the following equation:

$$\mathrm{w_f} = L_e \cdot \boldsymbol{\varepsilon_p}\left(\delta_{ij} - \mathbf{n_i n_j}\right) \tag{10}$$

where $\mathbf{w_f}$ is the equivalent fracture width vector; L_e is the element size; and $\boldsymbol{\varepsilon_p}$ is the plastic strain tensor.

To clearly distinguish the permeability of fractures and pores, several assumptions must be made. First, when rock breaks, the permeability of the pores remains unchanged. The increase in the permeability of the shale element is entirely the result of the initiation and expansion of fractures. Thus, based on the cubic law of fluid flow, the relationship between the equivalent permeability and fracture width can be established:

$$\mathbf{k} = \mathbf{k_m} + \mathbf{k_f} \tag{11}$$

$$\mathrm{k_f} = \frac{\rho g}{d_e}\frac{(\mathrm{w_f})^3}{12\mu} \tag{12}$$

where k is the permeability of a certain rock element; $\mathrm{k_m}$ is the permeability of intact rock element before the formation of fractures; $\mathbf{k_f}$ is the permeability of fractures after rock failure; N is the total number of pre-existing failure planes in the element; μ is the viscosity of the fracturing fluid; w_f is the fracture width of the rock element; and ρg is the bulk density of the fluid.

2.4 Algorithm of the Hydraulic Fracturing Program

This program is a secondary development based on the above theories and methods on the ANSYS® platform. First, the reservoir parameters are input, and a reservoir model with a

TABLE 4 | List of cases used in this paper.

Group	Case	$\Delta\sigma$ (MPa)	β (°)	μ (mPa·s)	Q (m^3/s)
Case 1	Case 1.1	3.5	60	3	0.005
	Case 1.2	3.5	60	200	0.005
	Case 1.3	2.5	45	3	0.005
	Case 1.4	2.5	45	200	0.005
	Case 1.5	3.5	30	3	0.005
	Case 1.6	3.5	30	200	0.005
Case 2	Case 2.1	3.5	45	3	0.005
	Case 2.2	3.5	45	50	0.005
	Case 2.3	3.5	45	100	0.005
	Case 2.4	3.5	45	150	0.005
	Case 2.5	3.5	45	200	0.005
	Case 2.6	3.5	45	500	0.005
	Case 2.7	3.5	45	1,000	0.005
Case 3	Case 3.1	3	45	350	0.004
	Case 3.2	3	45	350→3	0.004
	Case 3.3	3	45	3	0.004
	Case 3.4	3	45	3→350	0.004
Case 4	Case 4.1	2	30	350	0.004
	Case 4.2	2	30	350→3	0.004
	Case 4.3	2	30	3	0.004
	Case 4.4	2	30	3→350	0.004

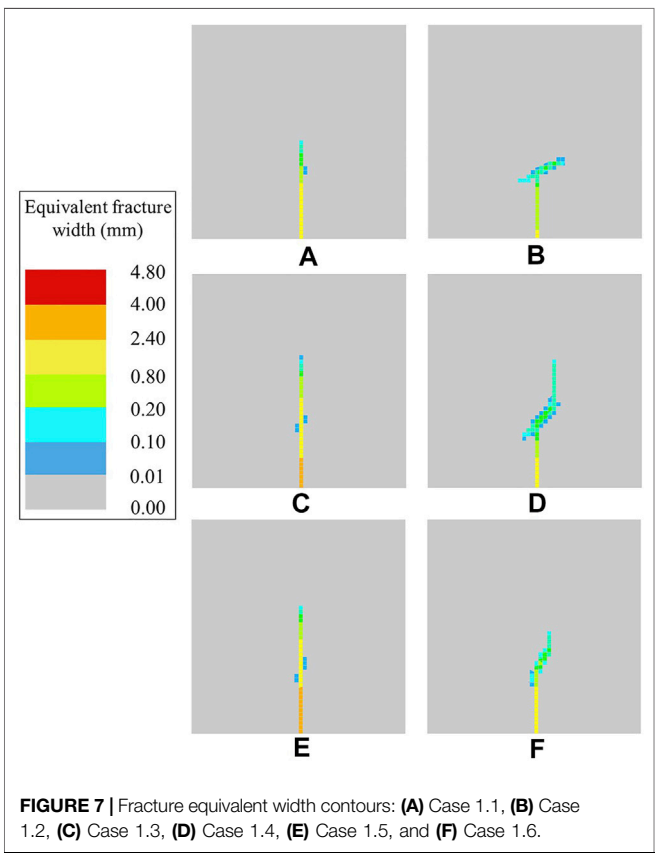

FIGURE 7 | Fracture equivalent width contours: **(A)** Case 1.1, **(B)** Case 1.2, **(C)** Case 1.3, **(D)** Case 1.4, **(E)** Case 1.5, and **(F)** Case 1.6.

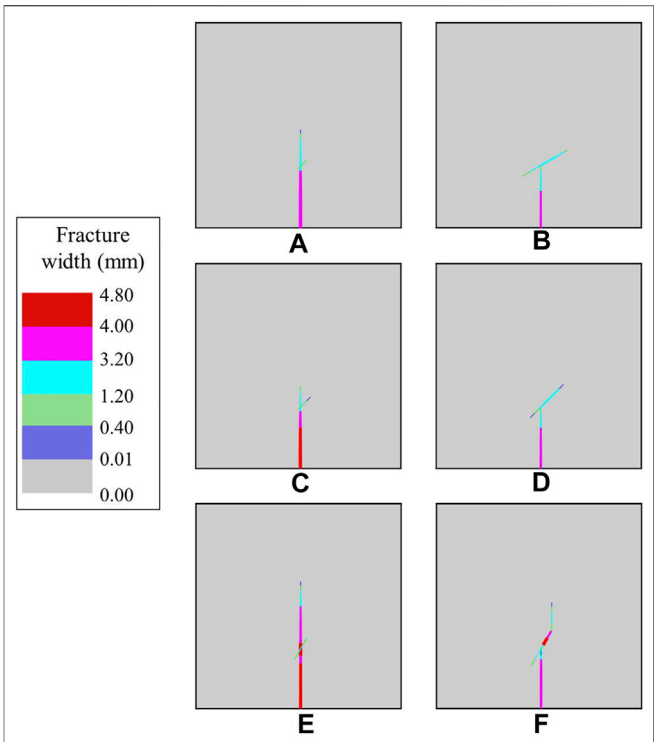

FIGURE 8 | Fracture width and propagation path in hydraulic fracturing: **(A)** Case 1.1, **(B)** Case 1.2, **(C)** Case 1.3, **(D)** Case 1.4, **(E)** Case 1.5, and **(F)** Case 1.6.

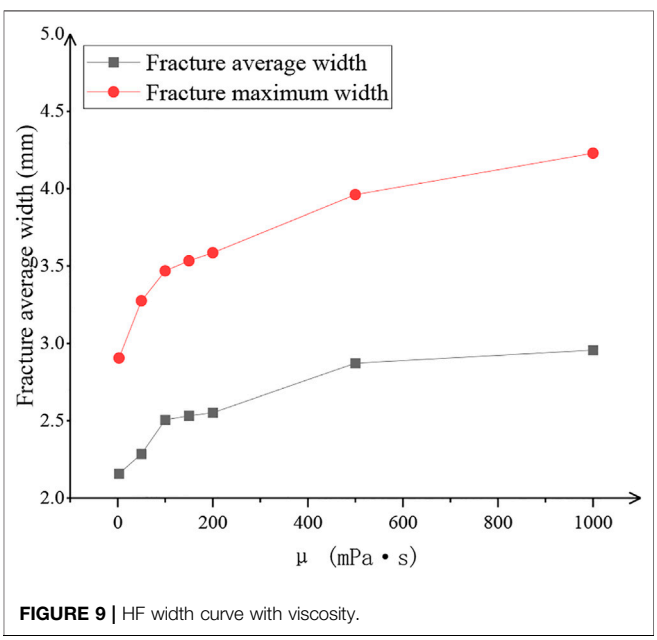

FIGURE 9 | HF width curve with viscosity.

natural fracture is built. Then, fluid is injected into the reservoir for fracturing, and whether the shale rock material breaks is determined. If a rock element of the reservoir is damaged, then the material permeability corresponding to this element is updated for the subsequent calculation. The program continues to loop through these steps until the entire fracturing process is completed.

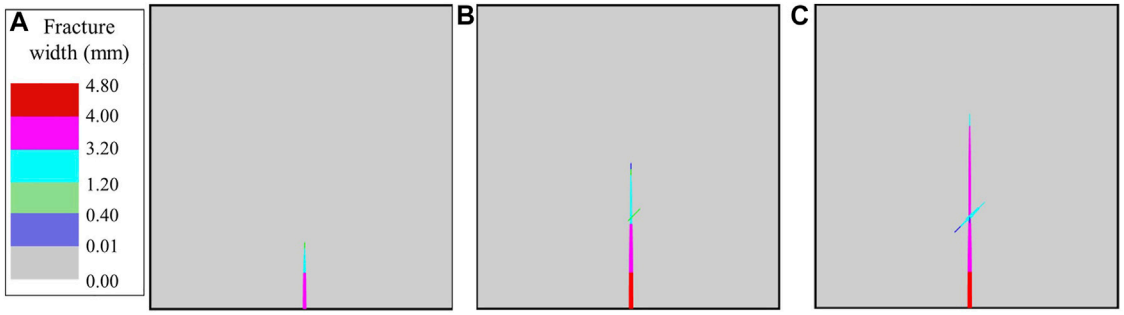

FIGURE 10 | Fracture width for AFI technology: **(A)** stage 1, **(B)** stage 2, and **(C)** stage 3.

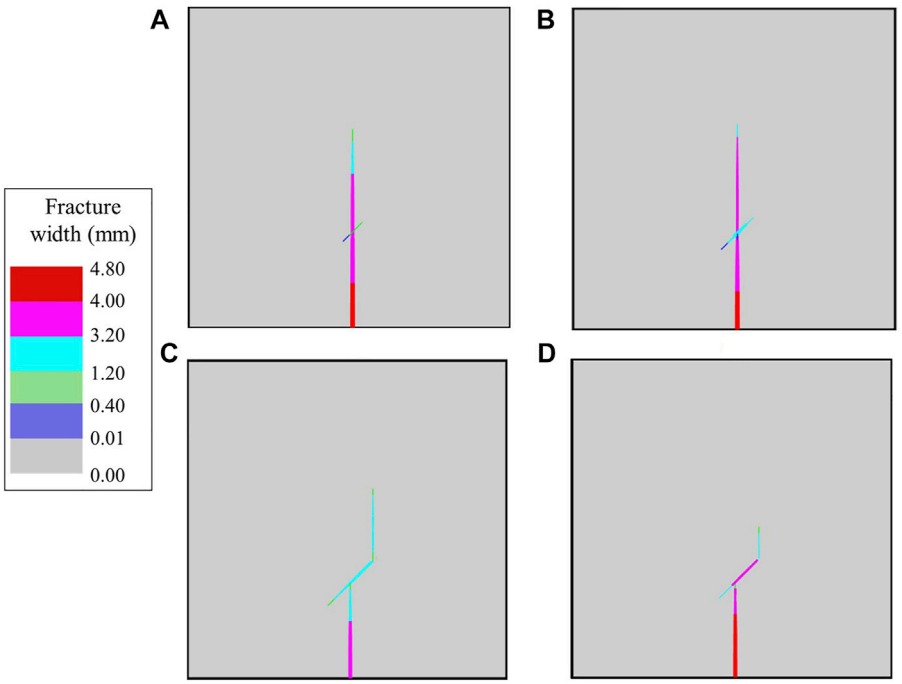

FIGURE 11 | Fracture width and path of the reservoir with a NF with dip angle of 45°: **(A)** 350 mPa·s, **(B)** 350→3 mPa·s, **(C)** 3 mPa·s, and **(D)** 3→350 mPa·s.

2.5 Evaluation of the Fracturing Effect

Fracture and reservoir properties can be easily obtained using numerical methods, allowing the fracturing effect to be quantified. The total area of the reservoir fracture network and the SRV are two indicators that are used frequently for measuring the effect of reservoir fracturing.

The SRV is commonly used as the standard for measuring the effect of stimulation in shale reservoirs. It is calculated by using the discrete bins method (Mayerhofer et al., 2010), which packs the fracture elements into several bins with a fixed width and a certain length to approximately calculate the SRV (**Figure 2**) using the equation below:

$$V_{SR} = \sum_{n} BL_f \mathrm{w_b} \tag{13}$$

where V_{SR} is the stimulated reservoir volume; n is the number of bins; B is the thickness of the plane; L_f is the fracture length; and w_b is the width of the bins.

The fracture network permeability, which corresponds to reservoir permeability and hydraulic fracture conductivity, is another method for evaluating the fracturing effect (Ofoegbu and Smart, 2019). The total fracture network permeability is computed as follows:

$$k_f = \frac{\sum_{i=1}^{m} \mathrm{w_i^3}}{12} \tag{14}$$

where k_f is the total permeability of the fracture network; w_i are the fracture widths in the ith element; and m is the number of elements that have been damaged.

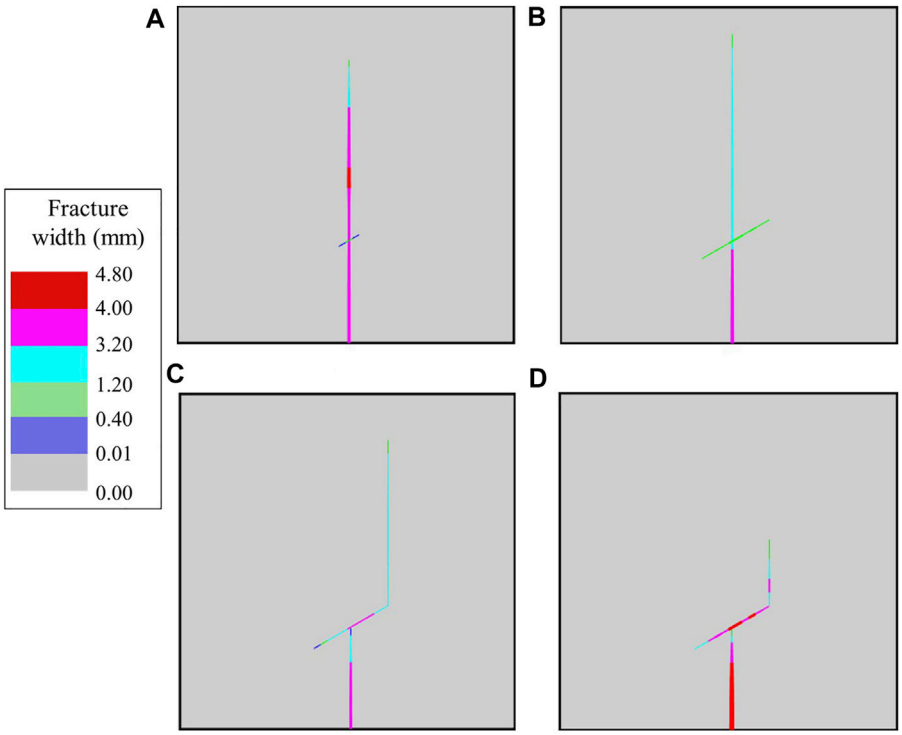

FIGURE 12 | Fracture width and path of the reservoir with a NF with dip angle of 30°: **(A)** 350 mPas, **(B)** 350→3 mPa·s, **(C)** 3 mPa·s, and **(D)** 3→350 mPa·s.

2.6 Hydraulic Fracture Visualization

In the FEM, the fractures are treated as damage elements instead of discontinuities, which prevents the propagation path and properties of the fractures in the continuous model from being clearly displayed. In this paper, to visually display the fractures in the FEM, two assumptions are made: 1) The propagation direction of HFs in the shale matrix element is perpendicular to the direction of the maximum plastic strain of the element (**Figure 3A**); and 2) in the elements with NFs, the plastic strain is decomposed into the direction of the minimum principal stress and the direction perpendicular to the NF (**Figure 3B**). In addition to the above assumptions, some fractures are corrected and merged in this process.

3 VALIDATION OF THE FINITE ELEMENT METHOD MODEL OF HYDRAULIC FRACTURING

In this section, the correspondence between the numerical model and the true triaxial hydraulic fracturing test is verified.

Experiments are commonly used to determine the reliability of numerical models before simulations are conducted. The focus of this article is the interaction between HFs and NFs. Therefore, experiments related to the interaction of fractures are selected to verify the validity of the model. Gu et al. (2012) used silicone oil as the fracturing fluid in actual triaxial hydraulic fracturing tests (**Figure 4A**) and studied the interaction between hydraulic fractures and natural fractures in a sandstone sample with a single pre-existing fracture. In order to correspond to the boundary conditions of the test, a two-dimensional FEM model of the horizontal *in-situ* stress plane was established and a pre-exist fracture was embedded (**Figure 4B**). And, the parameters used in Gu's experiment are shown in **Table 1**. In addition to the parameters in **Table 1**, other basic parameters are used in this model, which are listed in **Table 2**.

To verify the numerical model, a 300 mm × 300 mm two-dimensional hydraulic fracturing model is established. A natural fracture is embedded in the model, which is consistent with the experiment. For fracturing, a concentrated fluid is injected into the model's centre. The HFs gradually approaches the NFs, leading to one of two results: crossing or no crossing.

Where β is approaching angle, which is the angle between the propagation direction of hydraulic fracture and the direction of natural fracture; $\Delta\sigma$ is *in-situ* stress difference, which is equal to $(\sigma_1-\sigma_3)$.

In this paper, a numerical model with the same parameters as the experimental model of Gu et al. (2012) is used to simulate fracture interaction, and the equivalent fracture width results are shown in **Figure 5**. However, to ensure the convergence of the FEM simulation, a small value, 1 kPa, is used instead of 0 for the strength of the pre-existing fracture.

As shown in **Figure 5**, the interaction between HFs and NFs is divided into two situations: Crossing or no crossing. In detail,

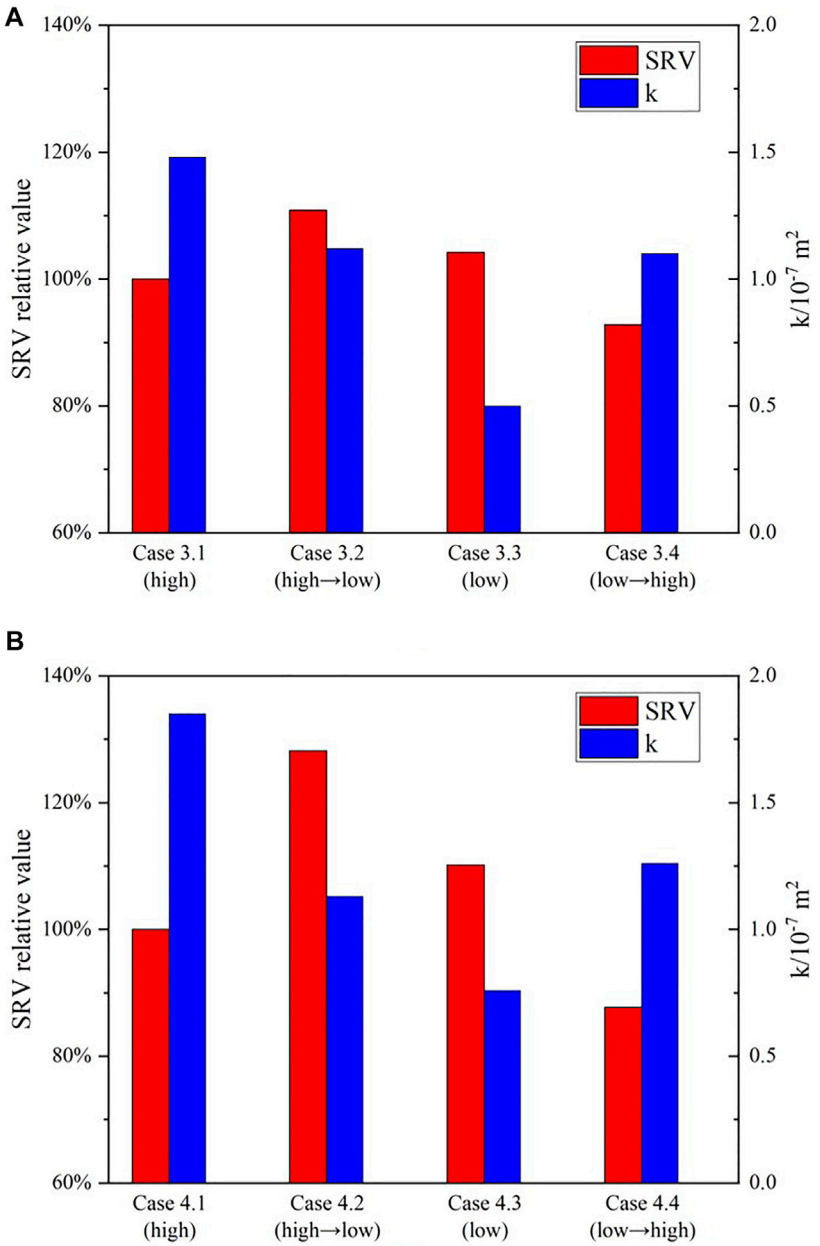

FIGURE 13 | The SRV and permeability of reservoir **(A)** NF dip angle is 45°; **(B)** NF dip angle is 30°.

Cases 1 (**Figure 5A**) and 3 (**Figure 5C**) cross, and Cases 2, 4, 5 and 6 (**Figures 5B,D–F**) do not cross. In addition, the colours of the elements in **Figure 5** indicate the widths of different fractures, which are calculated by **equation (8)**. The light grey area in **Figure 5** represents the intact part of the matrix, and the dark grey band represents the inactive pre-existing fracture.

After verification, the results of the interaction between HFs and NFs based on the continuum method are consistent with the results of the actual triaxial hydraulic fracturing experiment. Therefore, this model can effectively simulate the interaction between HFs and NFs and obtain accurate results.

4 NUMERICAL SIMULATION OF HYDRAULIC FRACTURING BASED ON THE CONTINUUM METHOD

In this section, the hydraulic fracturing simulation is conducted with the validated hydraulic fracturing numerical model to study the influence of fluid viscosity on the effects of fracturing. To fully demonstrate the role of viscosity, this section is divided into the following parts: **Section 4.1** describes the establishment of the engineering-scale hydraulic fracturing FEM model and its boundary conditions. **Section 4.2** studies the influence of different

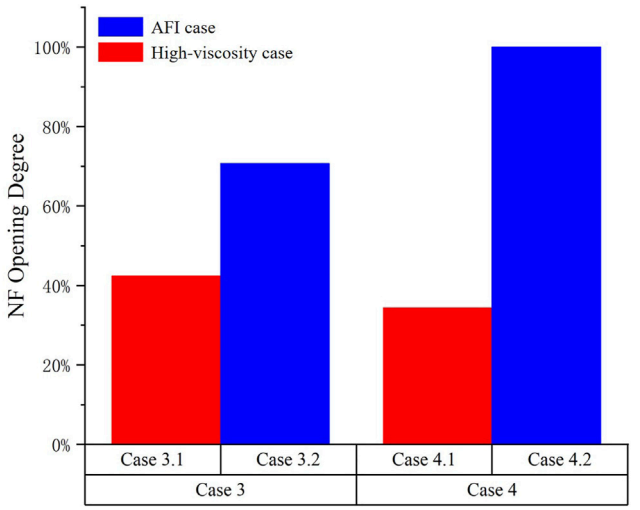

FIGURE 14 | NF opening degree of the AFI and high-viscosity cases.

viscosities on fracture interactions. **Section 4.3** introduces the alternating fluid injection (AFI) technology process and discusses how it improves the fracture interaction mode. **Section 4.4** studies the influence of AFI technology on the fracturing of the reservoir.

4.1 Reservoir Finite Element Method Model of Hydraulic Fracturing

There are natural fractures of different scales in shale reservoirs, including micro-fractures (**Figure 6A**), macro-fractures in samples (**Figure 6B**), and large-scale fractures in shale reservoirs (**Figure 6C**). Micro-fractures and sample-scale fractures affect the mechanical properties of the rock, while large-scale fractures in the reservoir affect the direction of HF propagation and the final fracture network morphology. To simulate the propagation of HF in shale reservoirs with NFs, a large-scale reservoir model is built to perform engineering-scale numerical simulations of shale hydraulic fracturing.

As shown in **Figure 6D**, the size of the FEM model of the reservoir is 50 × 50 m. The grey elements are permeable and without fractures which represents an area not affected by fracturing. The middle blue area represents the part of the reservoir affected by fracturing, and the red elements represent the embedded NF. Notably, if the angle of the NF differs, then the position of the red element also differs. **Figure 6D** shows only the case where the NF dip angle is 45°. In the model, there are 2,500 fluid mechanical coupled elements, including 984 rock matrix elements, 16 NF elements and 1,500 elements for the simulation of seepage.

As shown in **Figure 6E**, the model applies normal displacement and pore pressure constraints to the four sides of the reservoir. To simulate the real formation situation, initial *in situ* stresses in the horizontal direction and vertical direction are applied, and the *in situ* stresses are balanced. After hydraulic fracturing start, a concentrated fluid load is applied to the reservoir and acts on the element at the boundary to simulate fluid injection. The parameters used in the simulation are shown in **Table 3**.

4.2 The Role of Fluid Viscosity in Hydraulic Fracturing

The numerical simulation cases were divided into single fluid injection fracturing and AFI cases. The simulation cases and parameters are listed in **Table 4**.

In this section, the role of fracturing fluid viscosity in fracturing is discussed from the aspects of fracture morphology and evaluation of the reservoir stimulation effect.

The viscosity of the fracturing fluid is the main parameter that can be controlled. Viscosity is a physical quantity that measures frictional resistance during fluid flow. High-viscosity fluid has great resistance in the direction of flow, and it is difficult for it to enter the pores of shale. In contrast, low-viscosity fluid tends to enter the NFs in shale

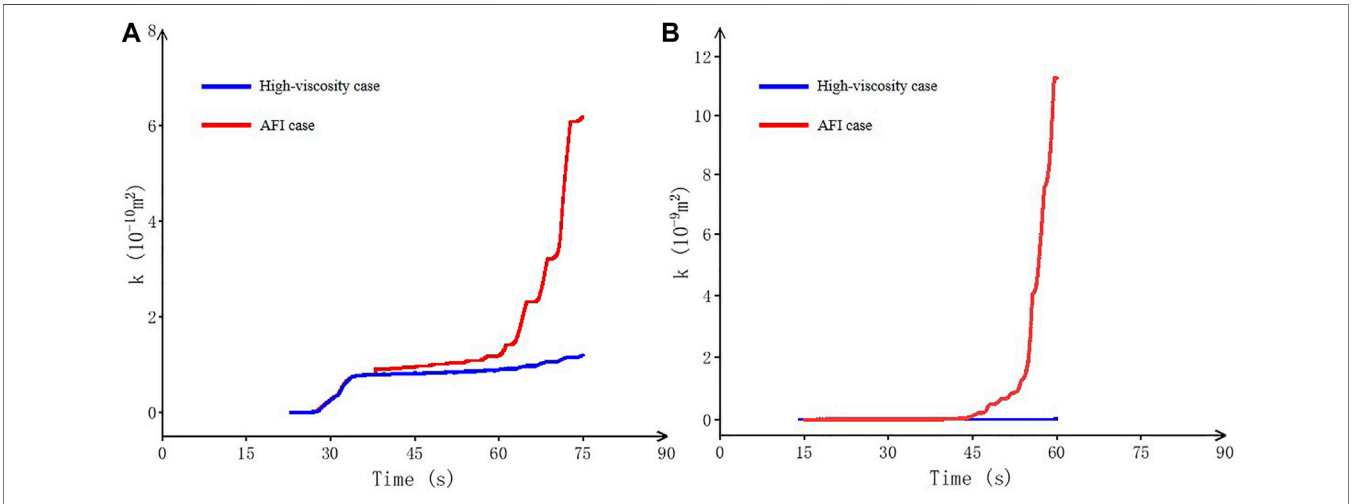

FIGURE 15 | NF permeability time history curve of the AFI and high-viscosity cases **(A)** NF dip angle is 45°; **(B)** NF dip angle is 30°.

due to its low resistance during flow, thereby accumulating pressure in the NFs and activating them.

Figure 7 shows the equivalent fracture width of HFs for different viscosities and approach angles. From top to bottom, the approach angles are 60°, 45°, and 30°. In **Figures 7A,C,E**, high-viscosity fracturing fluids are used; in **Figures 7B,D,F**, the parameters of the fracturing fluid are those of water. **Figure 7** clearly shows that when the viscosity of the fracturing fluid is relatively high, the HFs pass the NF without activating it; when the viscosity is low, the HFs propagate along the NF, offset, and increase the complexity of the fracture network.

However, the fracture manifestation in **Figure 7** does not show the fracture propagation path and fracture network shape. Therefore, according to the method in **Section 2.6**, the fracture equivalent width illustration is transformed into the fracture propagation path diagram shown in **Figure 8**.

In addition, the viscosity can affect the properties of the fracture, such as the fracture width. Although analytical models such as the Kristianovich-Geertsma-de Klerk (KGD) model give the relationship between the width of 2-D HFs and viscosity, they are suitable only for short fractures. **Figure 9** shows fracture width vs. viscosity of some commonly used fracturing fluids; the HF width increases with increasing viscosity.

4.3 Alternating Fluid Injection Technology

Alternating fluid injection technology is used in this paper to stimulate reservoirs with unfavourable formation parameters. AFI is usually divided into three stages: Stage 1, the use of high-viscosity fracturing fluid to fracture the reservoir (**Figure 10A**); stage 2, HFs pass through the NFs and expands mainly in the direction of the maximum principal stress (**Figure 10B**); and stage 3, continuous injection of replacement fluid, i.e., low-viscosity fracturing fluid, activates the NFs, and a more complex fracture network forms (**Figure 10C**). **Figure 10** shows this complete process.

As shown in **Figure 10**, the HFs formed by the high-viscosity fracturing fluid approach and pass through the NFs; then, the low-viscosity fracturing fluid is injected in the NFs. Subsequently, the expansion of the NFs resumes, and the shapes of the HFs become more complicated. As a result, fracturing through AFI technology can not only obtain fractures with stronger conductivity but also activate NFs to form a complex fracture network.

To demonstrate the effect of AFI, this article conducts a set of control experiments, namely, fracturing with high-viscosity fracturing fluid; AFI technology with a sequence from high- to low-viscosity fluid; fracturing with low-viscosity fracturing fluid; and fracturing with a sequence from low- to high-viscosity fluid. The final fracture paths are shown in **Figure 10**.

Figure 11 shows the final fracture path of the reservoir with a NF with dip angle of 45°. It can be seen that the fracture length is longest in the case of the high-viscosity fracturing fluid (**Figure 11A**), but the SRV is narrow. The two cases of low-viscosity fracturing fluid (**Figure 11C**) and the sequence from low-viscosity to high-viscosity fracturing fluid (**Figure 11D**) are similar. And for the sequence from low-viscosity to high-viscosity fracturing fluid, the main fracture does not pass through the NFs and the length of fracture is shortest. The AFI technology that switches from high-viscosity to low-viscosity fluid (**Figure 11B**) simultaneously produces the longest main fracture and the largest SRV. In addition, there are three potential expansion directions for the fracture network after AFI fracturing, which greatly increases the potential of forming a complex fracture network.

Figure 12 shows the final fracture path of the reservoir with a NF with dip angle of 30°. Similarly, fractures created by high-viscosity fracturing fluids (**Figure 12A**) have ideal length and width, but lower SRV; fractures created by low-viscosity fracturing fluids (**Figure 12C**) can activate NF, but have smaller fracture widths. A sequence from low- to high-viscosity produces fracture with shortest length (**Figure 12D**). The HF fractured by AFI technology has crossed and dilated NF (**Figure 12B**), which keeps relatively large fracture width simultaneously.

4.4 The Influence of Alternating Fluid Injection on Effect of Reservoir Stimulation

The viscosity of the fracturing fluid has a considerable impact on fracture properties, and it is an important operating parameter that can be manually controlled. When evaluating the effect of reservoir stimulation, two indicators, the SRV and reservoir permeability, are commonly used. **Figure 13** shows the SRV and reservoir permeability after fracturing in the four cases.

Figure 13A shows that compared to other fracturing technologies, AFI increases the SRV of reservoirs under the same geological conditions. Case 3.1 (high-viscosity) is set as the basis for comparison, and the SRV values of the other cases are expressed as percentages of the base value. In addition, compared with low-viscosity fracturing technology, AFI can effectively increase reservoir permeability. Compared with traditional hydraulic fracturing with high-viscosity fracturing fluid, AFI technology has the advantage of strong flow conductivity, and its permeability is almost the same as that of high-viscosity fracturing technology.

Similarly, **Figure 13B** shows that the SRV of the AFI technology case is significantly higher than the control high viscosity fracturing fluid case. SRV of low-viscosity fluid fracturing case is higher than the high-viscosity case but reservoir permeability is lower than the high-viscosity case. In addition, the fracturing case that switches viscosity from low to high has lowest SRV but relatively high permeability.

Combining **Figures 13A,B**, it can be seen that the reservoir permeability of the high-viscosity fracturing fluid case and the low-viscosity to high-viscosity fracturing fluid case are high, but the SRV are low; the low-viscosity fracturing case has comparatively high SRV but low permeability. Overall, AFI case has both the highest SRV and good reservoir permeability, and is the recommended fracturing technology.

NFs in reservoirs are potential conductivity approaches, and the effect of fracturing technology on the properties of NF is also an important indicator. To evaluate the effect of NF activation in the reservoir and the opening degree of NFs permeability are introduced. Since both the low-viscosity case and the low-to-high viscosity case fully activate NF, these two cases will be omitted from this section.

As shown in **Figure 14**, the NF opening degree of AFI technology (Case3.2 and 4.2) is higher than that of high-viscosity fracturing (Case3.1 and 4.1). Moreover, it can be directly found that as the dip angle decreases, the advantages of AFI technology become more obvious. It shows that AFI technology can help activate low-angle NFs in the reservoir and obtain a more complex fracture network.

Figure 15 indicates that before the viscosity of the fracturing fluid changes, the NF permeability curves of the two cases overlap. After changing the viscosity, the permeability curve of AFI technology (Case3.2 and 4.2) continues to rise sharply; in contrast, the curve of the high-viscosity fluid hydraulic fracturing case (Case3.1 and 4.1) rises slowly. Obviously, compared with traditional high-viscosity fracturing technology, AFI technology can effectively activate NFs and form a complex fracture network to improve the SRV and permeability of the reservoir.

5 CONCLUSION

In this paper, through the secondary development of ANSYS, an FEM model of reservoir hydraulic fracturing is established. The validity of the model is verified, and hydraulic fracturing cases are simulated with different parameters.

1) The FEM has high computational efficiency and can be used to conduct numerical simulations of long-term hydraulic fracturing of engineering-scale 3D reservoirs. The traditional FEM can play a role in the numerical simulation of large-scale hydraulic fracturing.
2) Fracturing fluid viscosity has a significant effect on the width of HF. Furthermore, at different stages of fracturing, viscosity has different effects. When the NF is not opened, reducing the viscosity can activate the NF and change the interaction mode between HF and NF; while when the NF has been dilated, changing the viscosity at this time cannot change the interaction mode.
3) Numerical simulation results show that in terms of common evaluation methods such as the SRV, reservoir permeability and NF opening degree, the AFI process has obvious advantages over pure high-viscosity fracturing, pure low-viscosity fracturing and hydraulic fracturing.
4) The comparison of fracturing simulation results with different NF dip angles shows that the reservoir geological conditions are unfavorable, that is, when the NF dip angle is low, the advantages of AFI technology are more obvious.

DATA AVAILABILITY STATEMENT

The original contributions presented in the study are included in the article/Supplementary Material, further inquiries can be directed to the corresponding author.

AUTHOR CONTRIBUTIONS

YY and LX are responsible for the idea and writing of this paper and BH and PZ are responsible for the analysis.

FUNDING

This paper was financially supported by the National Natural Science Foundation of China (Grant No. 11872258).

ACKNOWLEDGMENTS

We are also grateful for the constructive comments from the reviewers and our editor.

REFERENCES

Bažant, Z. P., and Oh, B. H. (1983). Crack Band Theory for Fracture of Concrete. *Mat. Constr.* 16, 155–177. doi:10.1007/BF02486267

Blanton, T. L. (1982). "An Experimental Study of Interaction between Hydraulically Induced and Pre-existing Fractures," in Proceedings of the SPE Unconventional Gas Recovery Symposium, Pittsburgh, Pennsylvania, May 1982, 1–13. doi:10.2118/10847-MS

Cao, X., Wang, M., Kang, J., Wang, S., and Liang, Y. (2020). Fracturing Technologies of Deep Shale Gas Horizontal wells in the Weirong Block, Southern Sichuan Basin. *Nat. Gas Industry B* 7 (1), 64–70. doi:10.1016/j.ngib.2019.07.003

Chen, G. B., Li, T., Yang, L., Zhang, G. H., Li, J. W., and Dong, H. J. (2021a). Mechanical Properties and Failure Mechanism of Combined Bodies with Different Coal-Rock Ratios and Combinations. *J. Mining Strata Control. Eng.* 3 (2), 023522. doi:10.13532/j.jmsce.cn10-1638/td.20210108.001

Chen, J., Lan, H., Macciotta, R., Martin, C. D., and Wu, Y. (2021b). Microfracture Characterization of Shale Constrained by Mineralogy and Bedding. *J. Pet. Sci. Eng.* 201, 108456. doi:10.1016/j.petrol.2021.108456

Chuprakov, D., Melchaeva, O., and Prioul, R. (2014). Injection-Sensitive Mechanics of Hydraulic Fracture Interaction with Discontinuities. *Rock Mech. Rock Eng.* 47 (5), 1625–1640. doi:10.1007/s00603-014-0596-7

Duan, H., Li, H., Dai, J., Wang, Y., and Chen, S. a. (2019). Horizontal Well Fracturing Mode of "increasing Net Pressure, Promoting Network Fracture and Keeping Conductivity" for the Stimulation of Deep Shale Gas Reservoirs: A Case Study of the Dingshan Area in SE Sichuan Basin. *Nat. Gas Industry B* 6 (5), 497–501. doi:10.1016/j.ngib.2019.02.005

Fan, C., Wen, H., Li, S., Bai, G., and Zhou, L. (2022). Coal Seam Gas Extraction by Integrated Drillings and Punchings from the Floor Roadway Considering Hydraulic-Mechanical Coupling Effect. *Geofluids* 2022, 1–10. doi:10.1155/2022/5198227

Fan, C., Yang, L., Wang, G., Huang, Q., Fu, X., and Wen, H. (2021). Investigation on Coal Skeleton Deformation in CO2 Injection Enhanced CH4 Drainage from Underground Coal Seam. *Front. Earth Sci.* 9, 766011. doi:10.3389/feart.2021.766011

Gale, J. F. W., Laubach, S. E., Olson, J. E., Eichhuble, P., and Fall, A. (2014). Natural Fractures in Shale: A Review and New Observations. *Bulletin* 98 (11), 2165–2216. doi:10.1306/08121413151

Gao, F. (2021a). Influence of Hydraulic Fracturing of strong Roof on Mining-Induced Stress Insight from Numerical Simulation. *J. Mining Strata Control. Eng.* 3 (2), 023032. doi:10.13532/j.jmsce.cn10-1638/td.20210329.001

Gao, R., Kuang, T., Zhang, Y., Zhang, W., and Quan, C. (2021b). Controlling Mine Pressure by Subjecting High-Level Hard Rock Strata to Ground Fracturing. *Int. J. Coal Sci. Technol.* 8, 1336–1350. doi:10.1007/s40789-020-00405-1

Gu, H., Weng, X., Lund, J., Mack, M., Ganguly, U., and Suarez-Rivera, R. (2012). Hydraulic Fracture Crossing Natural Fracture at Nonorthogonal Angles: A

Criterion and its Validation. *SPE Prod. Oper.* 27 (1), 20–26. doi:10.2118/139984-PA

Guo, L. L., Zhou, D. W., Zhang, D. M., and Zhou, B. H. (2021). Deformation and Failure of Surrounding Rock of a Roadway Subjected to Mining-Induced Stresses. *J. Mining Strata Control. Eng.* 3 (2), 023038. doi:10.13532/j.jmsce.cn10-1638/td.20200727.001

He, Q., Suorineni, F. T., and Oh, J. (2015). "Modeling Interaction between Natural Fractures and Hydraulic Fractures in Block Cave Mining," in Proceedings of the 49th US Rock Mechanics/Geomechanics Symposium, San Francisco, California, June 2015.

He, X., Zhang, P., He, G., Gao, Y., Liu, M., Zhang, Y., et al. (2020). Evaluation of Sweet Spots and Horizontal-Well-Design Technology for Shale Gas in the basin-margin Transition Zone of southeastern Chongqing, SW China. *Energ. Geosci.* 1 (3), 134–146. doi:10.1016/j.engeos.2020.06.004

Hou, B., Chang, Z., Fu, W., Muhadasi, Y., and Chen, M. (2019). Fracture Initiation and Propagation in a Deep Shale Gas Reservoir Subject to an Alternating-Fluid-Injection Hydraulic-Fracturing Treatment. *SPE J.* 24 (041), 1839–1855. doi:10.2118/195571-PA

Lan, S. R., Song, D. Z., Li, Z. L., and Liu, Y. (2021). Experimental Study on Acoustic Emission Characteristics of Fault Slip Process Based on Damage Factor. *J. Mining Strata Control. Eng.* 3 (3), 033024. doi:10.13532/j.jmsce.cn10-1638/td.20210510.002

Li, S., Li, X., and Zhang, D. (2016). A Fully Coupled Thermo-Hydro-Mechanical, Three-Dimensional Model for Hydraulic Stimulation Treatments. *J. Nat. Gas Sci. Eng.* 34, 64–84. doi:10.1016/j.jngse.2016.06.046

Li, Y. (2021). Mechanics and Fracturing Techniques of Deep Shale from the Sichuan Basin, SW China. *Energ. Geosci.* 2 (1), 1–9. doi:10.1016/j.engeos.2020.06.002

Mayerhofer, M. J. J., Lolon, E. P. P., Warpinski, N. R. R., Cipolla, C. L. L., Walser, D., and Rightmire, C. M. M. (2010). What Is Stimulated Reservoir Volume? *SPE Prod. Oper.* 25 (01), 89–98. doi:10.2118/119890-PA

Ofoegbu, G. I., and Smart, K. J. (2019). Modeling Discrete Fractures in Continuum Analysis and Insights for Fracture Propagation and Mechanical Behavior of Fractured Rock. *Results Eng.* 4, 100070. doi:10.1016/j.rineng.2019.100070

Renshaw, C. E., and Pollard, D. D. (1995). An Experimentally Verified Criterion for Propagation across Unbounded Frictional Interfaces in Brittle, Linear Elastic Materials. *Int. J. Rock Mech. Mining Sci. Geomechanics Abstr.* 32 (3), 237–249. doi:10.1016/0148-9062(94)00037-4

Rezaei, A., Siddiqui, F., Bornia, G., and Soliman, M. (2019). Applications of the Fast Multipole Fully Coupled Poroelastic Displacement Discontinuity Method to Hydraulic Fracturing Problems. *J. Comput. Phys.* 399, 108955. doi:10.1016/j.jcp.2019.108955

Sarmadivaleh, M. (2012). "Experimental and Numerical Study of Interaction of a Pre-existing Natural Interface and an Induced Hydraulic Fracture,". Ph.D Thesis (Perth, Australia: Curtin University).

Tang, H., Li, S., and Zhang, D. (2018). The Effect of Heterogeneity on Hydraulic Fracturing in Shale. *J. Pet. Sci. Eng.* 162, 292–308. doi:10.1016/j.petrol.2017.12.020

Vahab, M., Khoei, A. R., and Khalili, N. (2019). An X-FEM Technique in Modeling Hydro-Fracture Interaction with Naturally-Cemented Faults. *Eng. Fracture Mech.* 212, 269–290. doi:10.1016/j.engfracmech.2019.03.020

Wang, H., Shi, Z., Zhao, Q., Liu, D., Sun, S., Guo, W., et al. (2020). Stratigraphic Framework of the Wufeng-Longmaxi Shale in and Around the Sichuan Basin, China: Implications for Targeting Shale Gas. *Energ. Geosci.* 1 (3), 124–133. doi:10.1016/j.engeos.2020.05.006

Wang, J., and Wang, X. L. (2021). Seepage Characteristic and Fracture Development of Protected Seam Caused by Mining Protecting Strata. *J. Mining Strata Control. Eng.* 3 (3), 033511. doi:10.13532/j.jmsce.cn10-1638/td.20201215.001

Warpinski, N. R., and Teufel, L. W. (1987). Influence of Geologic Discontinuities on Hydraulic Fracture Propagation (Includes Associated Papers 17011 and 17074). *J. Pet. Technol.* 39 (2), 209–220. doi:10.2118/13224-PA

Weng, X. (2015). Modeling of Complex Hydraulic Fractures in Naturally Fractured Formation. *J. Unconventional Oil Gas Resour.* 9, 114–135. doi:10.1016/j.juogr.2014.07.001

Yang, J. X., Luo, M. K., Zhang, X. W., Huang, N., and Hou, S. J. (2021). Mechanical Properties and Fatigue Damage Evolution of Granite under Cyclic Loading and Unloading Conditions. *J. Mining Strata Control. Eng.* 3 (3), 033016. doi:10.13532/j.jmsce.cn10-1638/td.20210510.001

Yin, S., and Ding, W. (2018). Evaluation Indexes of Coalbed Methane Accumulation in the strong Deformed Strike-Slip Fault Zone Considering Tectonics and Fractures: a 3D Geomechanical Simulation Study. *Geol. Mag.* 156, 1052–1068. doi:10.1017/S0016756818000456

Yin, S., Dong, L., Yang, X., and Wang, R. (2020). Experimental Investigation of the Petrophysical Properties, Minerals, Elements and Pore Structures in Tight Sandstones. *J. Nat. Gas Sci. Eng.* 76, 103189. doi:10.1016/j.jngse.2020.103189

Yoon, J. S., Zang, A., Stephansson, O., Hofmann, H., and Zimmermann, G. (2017). Discrete Element Modelling of Hydraulic Fracture Propagation and Dynamic Interaction with Natural Fractures in Hard Rock. *Proced. Eng.* 191, 1023–1031. doi:10.1016/j.proeng.2017.05.275

Yushi, Z., Shicheng, Z., Tong, Z., Xiang, Z., and Tiankui, G. (2016). Experimental Investigation into Hydraulic Fracture Network Propagation in Gas Shales Using CT Scanning Technology. *Rock Mech. Rock Eng.* 49 (1), 33–45. doi:10.1007/s00603-015-0720-3

Zhai, L., Zhang, H., Pan, D., Zhu, Y., Zhu, J., Zhang, Y., et al. (2020). Optimisation of Hydraulic Fracturing Parameters Based on Cohesive Zone Method in Oil Shale Reservoir with Random Distribution of Weak Planes. *J. Nat. Gas Sci. Eng.* 75, 103130. doi:10.1016/j.jngse.2019.103130

Zhang, B., Shen, B., and Zhang, J. (2020a). Experimental Study of Edge-Opened Cracks Propagation in Rock-like Materials. *J. Mining Strata Control. Eng.* 2 (3), 033035. doi:10.13532/j.jmsce.cn10-1638/td.20200313.001

Zhang, Q., Zhang, X.-P., and Sun, W. (2021b). A Review of Laboratory Studies and Theoretical Analysis for the Interaction Mode between Induced Hydraulic Fractures and Pre-existing Fractures. *J. Nat. Gas Sci. Eng.* 86, 103719. doi:10.1016/j.jngse.2020.103719

Zhao, H., Wu, K., Huang, Z., Xu, Z., Shi, H., and Wang, H. (2021a). Numerical Model of CO2 Fracturing in Naturally Fractured Reservoirs. *Eng. Fracture Mech.* 244, 107548. doi:10.1016/j.engfracmech.2021.107548

Zhao, P., He, B., Zhang, B., and Liu, J. (2021b). Porosity of Gas Shale: Is the NMR-Based Measurement Reliable? *Pet. Sci.*doi:10.1016/j.petsci.2021.12.013

Zhao, P., Xie, L., Ge, Q., Zhang, Y., Liu, J., and He, B. (2020a). Numerical Study of the Effect of Natural Fractures on Shale Hydraulic Fracturing Based on the Continuum Approach. *J. Pet. Sci. Eng.* 189, 107038. doi:10.1016/j.petrol.2020.107038

Zhao, Z., Wu, K., Fan, Y., Guo, J., Zeng, B., and Yue, W. (2020b). An Optimization Model for Conductivity of Hydraulic Fracture Networks in the Longmaxi Shale, Sichuan basin, Southwest China. *Energ. Geosci.* 1 (1-2), 47–54. doi:10.1016/j.engeos.2020.05.001

Zheng, H., Pu, C., and Sun, C. (2020a). Study on the Interaction between Hydraulic Fracture and Natural Fracture Based on Extended Finite Element Method. *Eng. Fracture Mech.* 230, 106981. doi:10.1016/j.engfracmech.2020.106981

Zheng, H., Zhang, J., and Qi, Y. (2020b). Geology and Geomechanics of Hydraulic Fracturing in the Marcellus Shale Gas Play and Their Potential Applications to the Fuling Shale Gas Development. *Energ. Geosci.* 1, 36–46. doi:10.1016/j.engeos.2020.05.002

Zhou, J., Chen, M., Jin, Y., and Zhang, G.-q. (2008). Analysis of Fracture Propagation Behavior and Fracture Geometry Using a Tri-axial Fracturing System in Naturally Fractured Reservoirs. *Int. J. Rock Mech. Mining Sci.* 45 (7), 1143–1152. doi:10.1016/j.ijrmms.2008.01.001

Zhou, L., and Hou, M. Z. (2013). A New Numerical 3D-Model for Simulation of Hydraulic Fracturing in Consideration of Hydro-Mechanical Coupling Effects. *Int. J. Rock Mech. Mining Sci.* 60, 370–380. doi:10.1016/j.ijrmms.2013.01.006

Zienkiewicz, O. C., and Shiomi, T. (1984). Dynamic Behaviour of Saturated Porous media; the Generalized Biot Formulation and its Numerical Solution. *Int. J. Numer. Anal. Methods Geomech.* 8 (1), 71–96. doi:10.1002/nag.1610080106

Conflict of Interest: The authors declare that the research was conducted in the absence of any commercial or financial relationships that could be construed as a potential conflict of interest.

frontiers in Earth Science

ORIGINAL RESEARCH
published: 29 March 2022
doi: 10.3389/feart.2022.870547

A Numerical Experiment of Full Waveform Inversion of Complex Structures Concealed Around a Horizontal Hydraulic Fracturing Well Using Perforation Seismic Data

Guang Qian, Jiashun Yu, Jianlong Yuan and Xiaobo Fu*

College of Geophysics, Chengdu University of Technology, Chengdu, China

It is difficult to image the details of complex structures concealed around a horizontal hydraulic fracturing well using seismic data from the ground surface. In this paper, an approach is proposed to solve this problem by non-linear full waveform inversion (FWI) using perforation seismic data. The feasibility of the approach was investigated using numerical modeling based on an experimental model built from the well-known SEG/EAGE overthrust model, which contains complex geological structures with faults. First, seismic modeling was performed to produce experimental synthetic data, including three sets of perforation seismic data recorded by different acquisition systems deployed in observation wells and on the ground surface, and another set of conventional seismic reflection data with both sources and receivers deployed on the ground surface. Then, FWI was performed separately on each data set using an initial velocity model which was heavily smoothed to remove the target structures. The inversion results show that the concealed complex structures around the well were successfully recovered by FWI using perforation data, while the benchmark image from the FWI using conventional seismic data was poor. Particularly, the experiments also demonstrated that FWI using perforation seismic data can image the faults around a horizontal hydraulic fracturing well, while this is unable to achieve using conventional ground surface seismic data. This conclusion was also proved to be valid for noisy data deteriorated either by synthetic Gaussian or field noises. Further experiments demonstrated that FWI using perforation data recorded from wells outperformed that of surface data in terms of structure imaging accuracy characterized by quantitative errors.

Keywords: complex structure, horizontal well, perforation data, full waveform inversion, imaging, numerical modeling

OPEN ACCESS

Edited by:
Shuai Yin,
Xi'an Shiyou University, China

Reviewed by:
Peng Wang,
Yibin University, China
Li Ang,
Jilin University, China
Ying Tang,
Xi'an Shiyou University, China

****Correspondence:***
Jiashun Yu
j.yu@cdut.edu.cn

Specialty section:
This article was submitted to Structural Geology and Tectonics, a section of the journal Frontiers in Earth Science

Received: *07 February 2022*
Accepted: *28 February 2022*
Published: *29 March 2022*

Citation:
Qian G, Yu J, Yuan J and Fu X (2022) A Numerical Experiment of Full Waveform Inversion of Complex Structures Concealed Around a Horizontal Hydraulic Fracturing Well Using Perforation Seismic Data. Front. Earth Sci. 10:870547. doi: 10.3389/feart.2022.870547

INTRODUCTION

Concealed complex structures, such as natural faults and fractures, usually exist near injection wells for hydraulic fracturing in shale gas exploitation (Maxwell et al., 2009; Vidic et al., 2013; Clarke et al., 2014; Rutqvist et al., 2017; Ladevèze et al., 2019; Li et al., 2020; Zheng et al., 2020). If these concealed structures are not properly detected before the injection operation, it may lead to serious

consequences. For example, leakage of injection fluid can occur and contaminate groundwater during the injecting process (Mair et al., 2012; Flewelling and Sharma, 2014; Edwards et al., 2017; Edwards and Celia, 2018). It may also cause deformation or breakage of horizontal wells (De Pater and Baisch, 2011; Green et al., 2012), or induce earthquakes in natural faults around the injection area (Atkinson et al., 2016; Bao and Eaton, 2016; Ellsworth, 2013; Schultz et al., 2015; Schultz et al., 2018). On the contrary, if the detailed structures could be well detected and seismic velocity of the injection area could be obtained before the injecting process, it will provide not only important information for the injection design but also accurate velocity parameters for the location of microseismic activities induced by the hydraulic fracturing operation (Witten and Shragge, 2017).

It is difficult to obtain the detailed underground structures and accurate seismic velocity in the injection area (Li et al., 2019). Conventional surface seismic reflection exploration can image stratified structures in the injection area (Hennings et al., 2012), but it is difficult to provide details of the concealed complex structures around horizontal wells. Seismic tomography inversion using first arrival time generated by perforation shots or microseismic events can image the macrostructure in the area around horizontal wells (Warpinski et al., 2005; Pei et al., 2008; Pei et al., 2009; Zhang et al., 2009; Bardainne and Gaucher, 2010; Li et al., 2013). However, the details of the structure are difficult to characterize because the seismic phases behind the first break are neglected. These phases carry much information about the detailed features of the complex structures. Comparatively, full waveform inversion (FWI) makes full use of waveform, which contains not only the information of arrival time but also the dynamic effects of the media applied on the waves. This information of the seismic data is of great help for the recovery of the complex structures with high accuracy (Virieux and Operto, 2009; Sirgue et al., 2010; Operto et al., 2015; Virieux et al., 2017).

FWI is a non-linear inversion method. It normally requires high-quality data with a high signal-to-noise ratio (S/N) and an initial velocity model with good approximation to the actual velocity structure. In this regard, offshore seismic exploration has the advantage, and most applications of FWI are implemented to offshore seismic data (Operto et al., 2015; Sirgue et al., 2010; Virieux et al., 2017). In contrast, the shallow surface conditions of onshore seismic exploration are much more complex and would result in lower S/N ratio data. It is difficult for FWI to recover the detailed geological structures with noisy data (Zhang et al., 2016). In addition, if the hydraulic injection site is in a densely populated or rugged mountain area, it is difficult to use an ideal acquisition system for surface seismic reflection exploration. This will result in the hidden complex structures near horizontal wells being inadequately illuminated. However, if seismic sources can be placed below these hidden complex structures, the energy of the source can directly pass through these structures and be recorded by geophones on the ground surface or in observation wells. This will greatly improve the illumination of the hidden complex structures. For this reason, we propose to use an FWI scheme to invert the detailed structures around the horizontal well using perforation data as its sources are located along the horizontal well. Receiving geophones can be deployed on the ground surface, if conditions are permitted or deployed in observation wells to record seismic data. When the location and onset time of the perforation shots are generally known (Pei et al., 2009; Tan et al., 2014), this excitation and acquisition configuration is promising for FWI to invert the complex structures around the horizontal well.

EXPERIMENTS

Theory

The goal of FWI is to approach the target model by iteratively updating the initial model. In the iterative process, the difference between the synthetic and observed data is gradually reduced to an acceptable level. A classic misfit function of FWI can be defined as an L_2 norm:

$$E = \frac{1}{2}\sum_{Ns}\sum_{Nr}\|\mathbf{d}-\mathbf{u}\|^2, \tag{1}$$

where Ns and Nr are the number of sources and receivers, respectively, $\mathbf{d}$ represents the observed data, and $\mathbf{u}$ represents the synthetic data, which is a function of the medium parameter $m(\mathbf{r})$ at the current iterative FWI updating stage and can be synthesized by wave equation modeling.

The minimization problem of **Eq. 1** requires calculating the gradient direction of E with respect to the model parameter m as a variable during the iterative process of FWI, i.e., $\partial E/\partial m$. A quick and effective way to compute the gradient is using the adjoint-state method (Plessix, 2006):

$$\frac{\partial E}{\partial m} = -\sum_{Ns}\int_0^T \lambda_s \frac{\partial^2 u}{\partial t^2}dt, \tag{2}$$

where λ_s is the back-propagating residual wavefield, i.e., $\mathbf{d}$-$\mathbf{u}$. Thus, the conjugate gradient method (Hestenes and Stiefel, 1952) is used to update the model iteratively:

$$\mathbf{m}_{k+1} = \mathbf{m}_k + \alpha_k \mathbf{p}_k, \tag{3}$$

here the vector m_k denotes the parameter model at the k^{th} step during the FWI iterative process, and α and $\mathbf{p}$ are the step length and the search direction, respectively, for the updating change of the model. We can use the inexact linear search method (Nocedal and Wright, 2006) to obtain α. For $\mathbf{p}$, we can use the method of Dai and Yuan (1999):

$$\mathbf{p}_{k+1} = -q_{k+1}^{\mathrm{T}}\left(\frac{\partial E}{\partial \mathbf{m}}\right)_{k+1} + \beta_{k+1}\mathbf{p}_k, \tag{4}$$

where $\frac{\partial \bullet}{\partial \mathrm{m}} \triangleq \left(\frac{\partial \bullet}{\partial m(\mathrm{r}_1)}, \frac{\partial \bullet}{\partial m(\mathrm{r}_2)}, \cdots, \frac{\partial \bullet}{\partial m(\mathrm{r}_n)}\right)^T$ with $\mathrm{r}_i, i = 1, 2, \cdots, n$ being the spatial position vector, T is the matrix transpose, and $\mathbf{q}$ is a preconditioning operator (Plessix and Mulder, 2004; Shin et al., 2001):

$$q_k = \left\{\int_0^T |\mathbf{u}(\mathbf{m}, t)|^2 dt\right\}^{-1}. \tag{5}$$

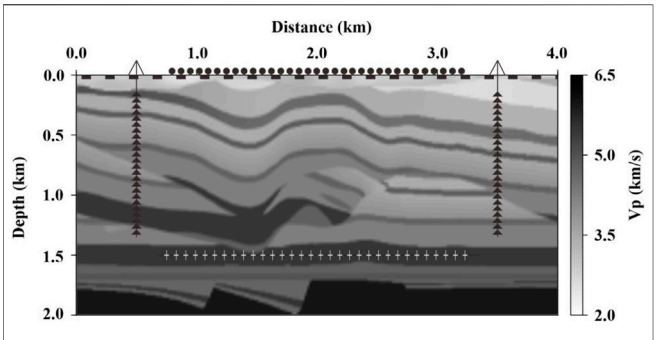

FIGURE 1 | Overthrust model with concealed structures. The black solid lines are the trajectories of the vertical observation wells and horizontal wells. The solid black circles at the top of the model represent the surface seismic sources. The black dashed line represents the receivers. The black triangles represent the receivers in the two wells located at $x = 0.5$ and 3.5 km, respectively. The white cross symbols represent the perforations in the horizontal well which is located at the depth of $z = 1.5$ km. These form an acquisition system covering the complex fold structures with faults in the model.

β in **Eq. 4** is a scalar, which can be obtained by the method of Dai and Yuan (1999):

$$\beta_k = \frac{\left(\frac{\partial E}{\partial \mathbf{m}}\right)_{k+1}^{\mathrm{T}}\left(\frac{\partial E}{\partial \mathbf{m}}\right)_{k+1}}{\mathbf{p}_k^{\mathrm{T}}\left\{\left(\frac{\partial E}{\partial \mathbf{m}}\right)_{k+1} - \left(\frac{\partial E}{\partial \mathbf{m}}\right)_{k}\right\}}, \tag{6}$$

Modeling

Geological Model

A two-dimensional velocity model (**Figure 1**) was extracted from the well-known SEG/EAGE overthrust model (Aminzadeh et al., 1994) for our experiments. The horizontal dimension of the model is 4 km, the depth dimension is 2 km, and the P-wave velocity ranges from 2.0 to 6.5 km/s. There exist complex fold structures with faults in the model. There are three wells within the model area (**Figure 1**), including a horizontal well laying at the depth of 1.5 km, and two vertical observation wells on the horizontal coordinates of 0.5 km, on the left side, and 3.5 km, on the right side, separately. The design of the horizontal well is referred to the statistics of Edwards and Celia (2018), the depths of horizontal wells are normally between 1.5 and 3.0 km, the length is 1.0–3.0 km, and the spacing of perforation shots is 20–40 m.

Acquisition Systems

To compare the inversion results of perforation and surface seismic reflection data, four acquisition systems were designed:

1) surface excitation and surface recording (SS);
2) perforation excitation and surface recording (PS);
3) perforation excitation and one well recording (PO);
4) perforation excitation and two well recording (PT).

There are 125 conventional seismic sources on the ground surface (the solid black circles at the top of the model in **Figure 1**) for the SS acquisition system, and the same number of perforation sources in the horizontal well (the white crosses in the horizontal well at the depth of 1.5 km) were used for the acquisition systems of PS, PO, and PT. All sources are distributed horizontally in the range of 0.75–3.25 km with a space interval of 20 m.

To record two-component velocity data (Vx and Vz represent the horizontal and vertical velocity components, respectively), 65 two-component receivers are deployed on the ground surface spanning 0.06–3.9 km (the black dashed line in **Figure 1**), with a spatial interval of 60 m. Similarly, 25 receivers are deployed in each observation well in the depth ranging between 0.1 and 1.3 km (the black triangles in **Figure 1**), with a spacing interval of 50 m.

Synthetic Data

The velocity model in **Figure 1** is discretized using a spacing interval of 20 m in both horizontal and vertical directions. The total number of grid points is 200*100 = 20000. For forward modeling, a free surface boundary condition is used at the top of the model. The perfectly matched boundary condition (PML) with a thickness of 10 grid points is adopted on the other three sides. A pulse function with a frequency band of 0–20 Hz is used as the source signal. The time sampling interval for forward modeling is 0.5 ms. The total time history of the modeling is 2.5 s. The wavefields are solved using the method of Köhn (2011). The synthetic seismograms of the velocity components (i.e., Vx and Vz) are recorded by the observation system of SS, PS, PO, and PT, which will be used as the names of the data sets in the following context. The wavefields recorded are shown in **Figure 2**.

RESULTS

FWI software used in this study was developed based on the open codes published by Köhn et al. (2012). The initial velocity model (**Figure 3**) used for the modeling was obtained by applying Gaussian smoothing ($\sigma = 20$, radius = 50) to the exact velocity model, as shown in **Figure 1**. After smoothing, the complex structures in **Figure 1** completely disappeared.

An inversion frequency range of 0–20 Hz is used to cover the effective frequency band of the synthetic data. It is organized into 10 groups, namely, 0–2 Hz, 0–4 Hz, and so on up to 0–20 Hz. FWI is first performed on the frequency ground of 0–2 Hz with the initial model shown in **Figure 3**. The final inversion model of 0–2 Hz was used as the initial model for the next inversion performed on 0–4 Hz. The inversion is progressively performed in such a manner from low to high frequencies until the inversion of the last frequency group (0–20 Hz) is completed. This inversion strategy was adopted from Virieux and Operto (2009) to reduce the instability of the non-linear inversion accordingly.

Using the data sets of SS, PS, PO, and PT (**Figure 2**) separately, the inversion results in four corresponding images of the hidden complex structures near the horizontal well are shown in **Figures 4–7**. Each image shows the progressive results of 0–2, 0–8, 0–14, and 0–20 Hz. It can be seen that the inversion result of the first frequency group (0–2 Hz) of SS (**Figure 4A**) is the same as the initial model, without showing the definite structure (**Figure 4A**). When the frequency reaches up to 8 Hz, the stratum where the horizontal

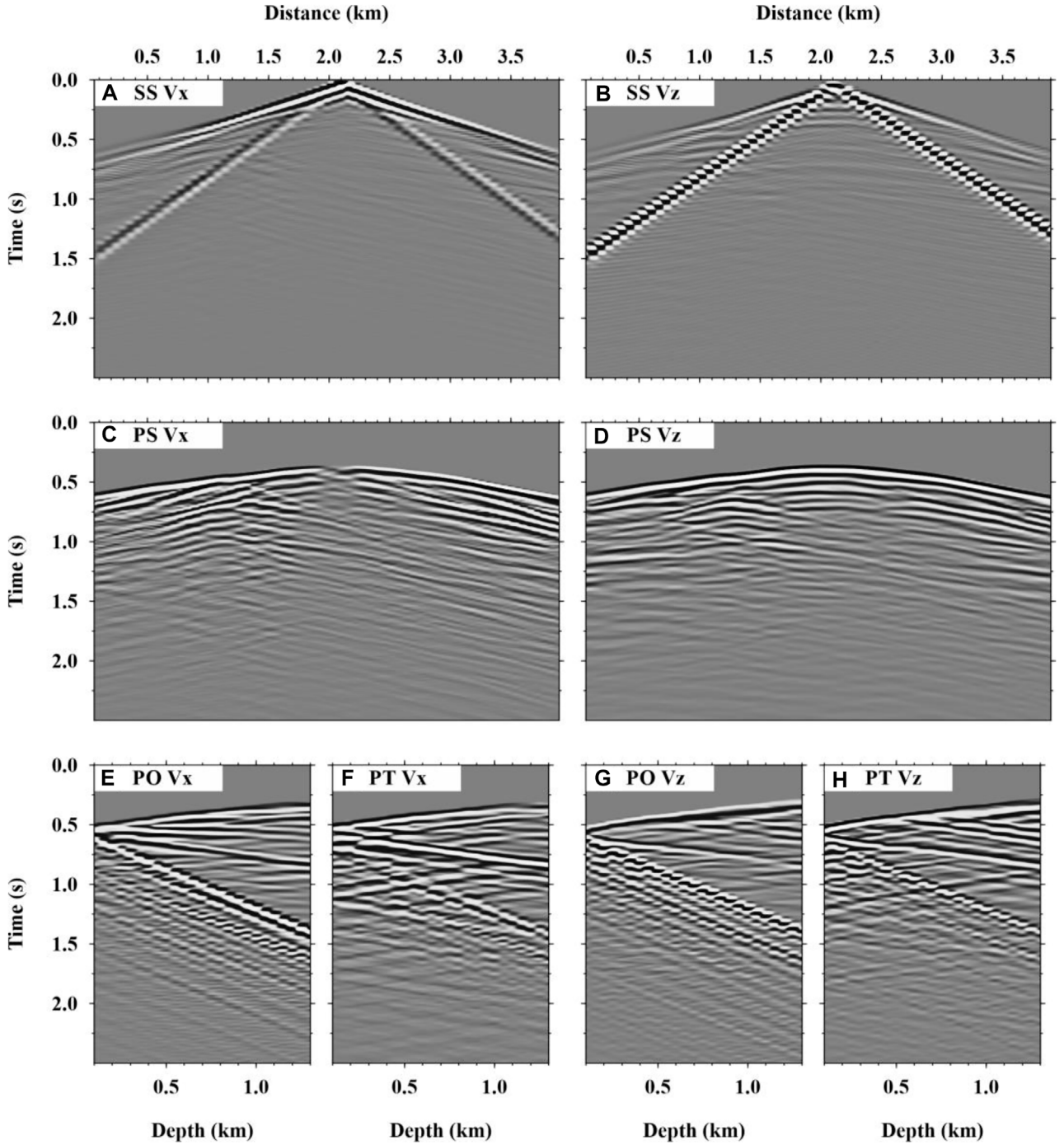

FIGURE 2 | Synthetic seismograms. **(A,B)** are the Vx and Vz components, respectively, of SS. Similarly, **(C,D)** are of PS, **(E,G)** are of PO, and **(F,H)** are of PT. The data of PT were recorded using the array on the vertical well on the right-hand side of the model.

well is located and the buried fault above the horizontal well begin to appear (arrows in **Figure 4B**). With the frequency inversion continuing up to 14 Hz, the folds and faults are well recovered (**Figure 4C**). When the frequency reaches 20 Hz, the inversion results have reached a steady state. The shape of the overburden stratum structure of the horizontal well is removed, but the spatial resolution of the overthrust fault near the horizontal wells is very low (arrows in **Figure 4D**).

Figure 5 shows the inversion results of the PS data. From the inversion results of the 0–2 Hz data (**Figure 5A**), the low-frequency components mainly recover the large-scale structures between the receiver array (black dashed line) and the perforations (black plus

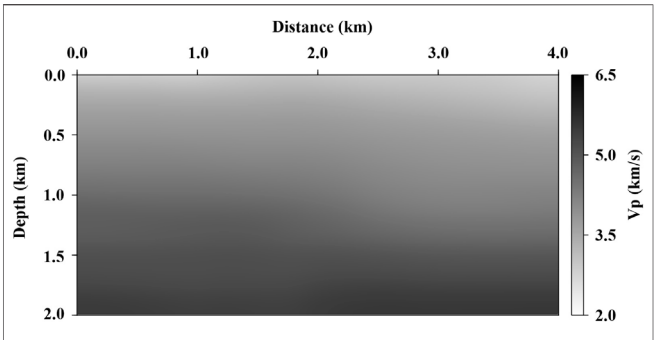

FIGURE 3 | Initial velocity model obtained by applying Gaussian smoothing to the exact model shown in **Figure 1**.

symbols). With the 8 Hz data, not only the folded strata can be imaged but also the deep faults are well recovered (arrows in **Figure 5B**). When the inversion frequency reaches 14 Hz, the overall structure becomes significantly clearer (**Figure 5C**). When the inversion reaches the last frequency group of 0–20 Hz (**Figure 5D**), the results are only slightly improved from that of 14 Hz (arrows in **Figure 5D**), indicating that the inversion reaches a stable stage in the frequency band above 14 Hz.

The inversion results of the PO data are shown in **Figure 6**. The inversion results of 0–2 Hz data (**Figure 6A**) show velocity updates in the area near the vertical observation well. When the frequency reaches 8 Hz, the shallow folded strata and deep faults have been successfully recovered (**Figure 6B**). When the inversion frequency reaches 14 Hz, the overall structure of the model on the observation side is clearer than that of 8 Hz. In addition, the velocity accuracy is also further improved (**Figure 6C**). Similar to that of PS, only a slight improvement is achieved when the inversion reaches the last frequency group of 0–20 Hz (**Figure 6D**), indicating that the inversion reaches a stable stage in the frequency band above 14 Hz.

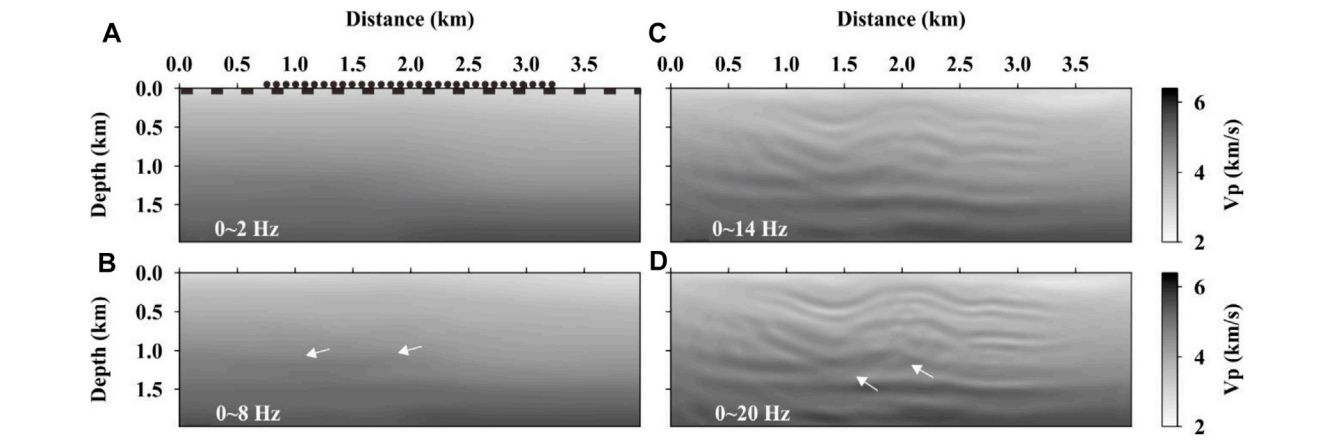

FIGURE 4 | Inversion results of SS data. The acquisition system is represented by the solid black circles (sources) and dashed line of blocks (receiver array) at the top of **(A)**. **(A–D)** Iterative inversion results as gray images of the frequency groups of 0–2, 0–8, 0–14, and 0–20 Hz, respectively.

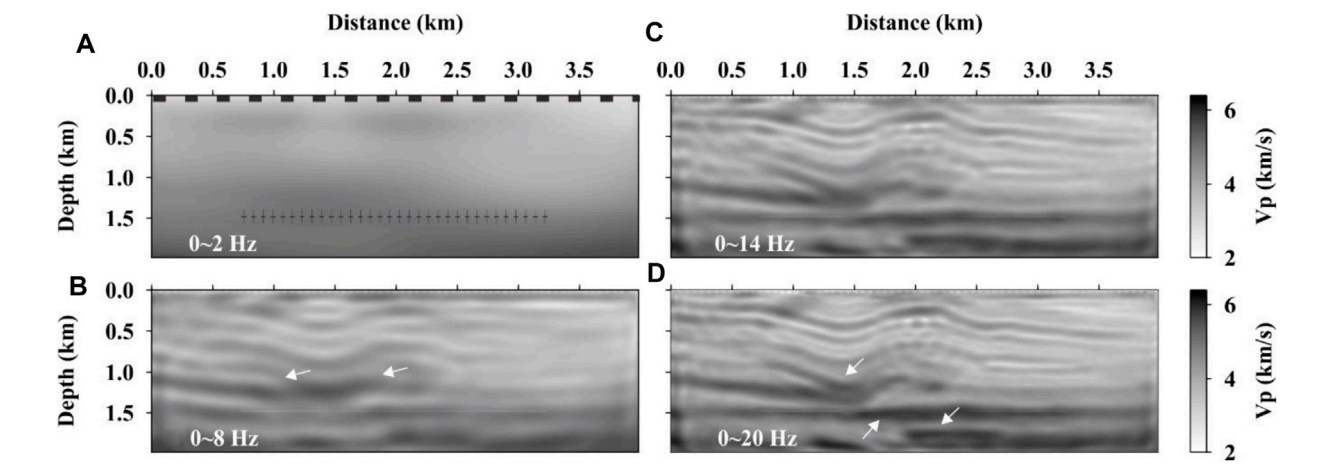

FIGURE 5 | Inversion results of the PS data. **(A)** Dashed line of black blocks at the top represents receivers, and the black cross symbols at the depth level of 1.5 km represent the perforations in the horizontal well. **(A–D)** Iterative inversion results of the frequency groups of 0–2, 0–8, 0–14, and 0–20 Hz, respectively.

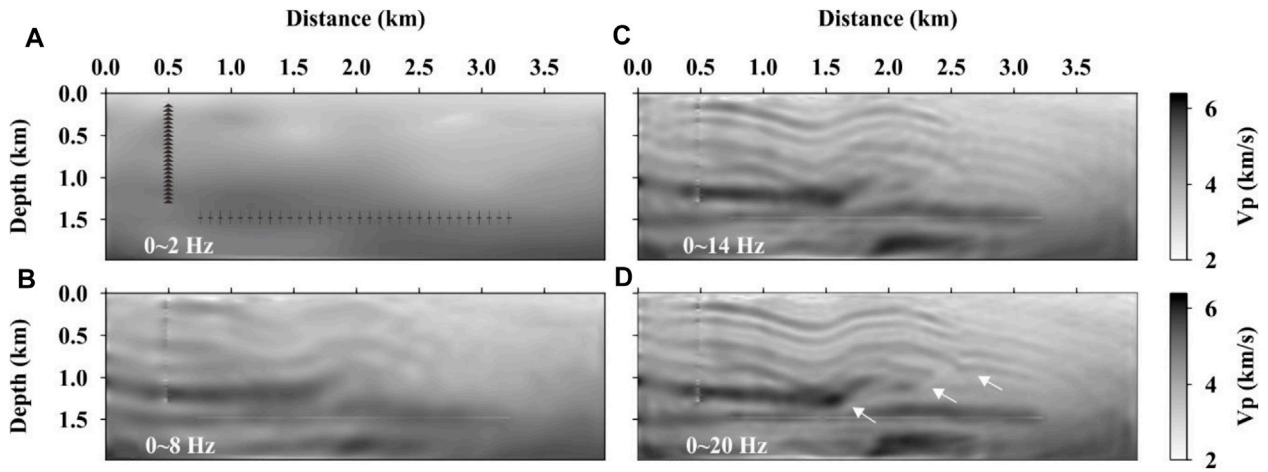

FIGURE 6 | Inversion results of the PO data. The black triangles on the left and the black cross symbols at the depth level of 1.5 km shown in **(A)** represent the receivers in the observation well and the perforations in the horizontal well, respectively. **(A–D)** Iterative inversion results of the frequency groups of 0–2, 0–8, 0–14, and 0–20 Hz, respectively.

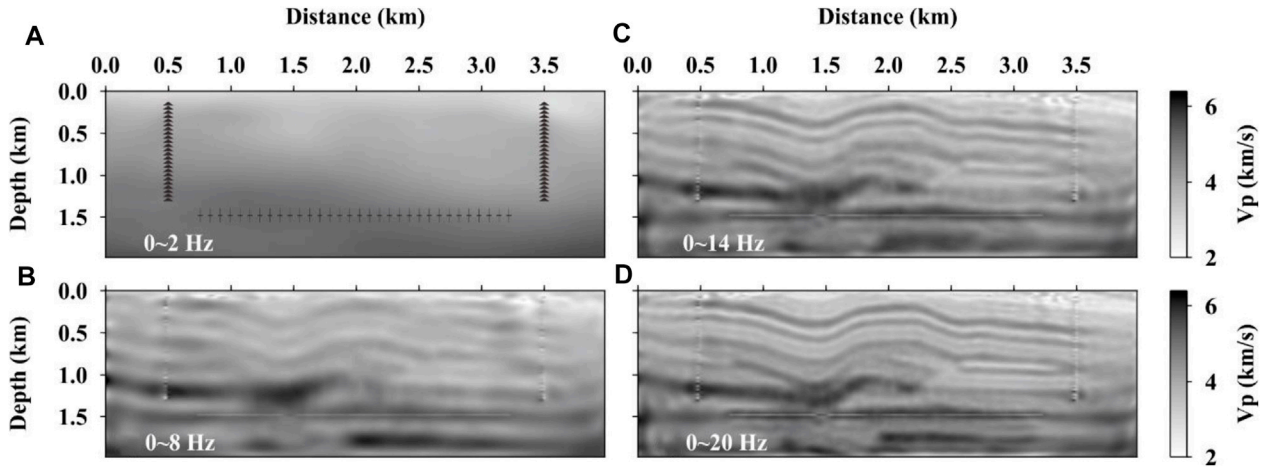

FIGURE 7 | Inversion results of the PT data. Black triangles on each side and the black cross symbols at the depth level of 1.5 km in **(A)** represent the receivers in the vertical observation well and the perforations in the horizontal well, respectively. **(A–D)** Iterative inversion results of frequency groups of 0–2, 0–8, 0–14, and 0–20 Hz, respectively.

The PT data results (**Figure 7**) show that the inversion of the 0–2 Hz data is updated over the whole model, as it would be anticipated as the receivers now deployed on both sides compared with the signal side receiving of PO. However, the outline of the structure is yet not evident (**Figure 7A**). When the inversion frequency reaches 8 Hz, the result clearly shows the shallow folded strata and deeply buried faults (**Figure 7B**). The imaging quality at this frequency band is better than that of SS (**Figure 4B**), PS (**Figure 5B**), and PO (**Figure 6B**), indicating that the inversion convergence of PT is faster than the others. With the frequency reaching 14 Hz, most of the structures have been recovered (**Figure 7C**). When the inversion reaches the final frequency group (**Figure 7D**), the spatial resolution of the whole structure is further improved and the result is very close to the real model (**Figure 1**).

ANALYSIS AND DISCUSSIONS

Error Analysis

To look into the detailed difference between the inversion results of the four data sets, the absolute error between each inverted velocity model (**Figures 4–7**) and the actual velocity model (**Figure 1**) was calculated (**Figure 8**). It shows that SS has a very large error (**Figure 8A**). The error of PS near the horizontal well is smaller than that of SS (**Figure 8B**). Although the error of PO is small in the area near the

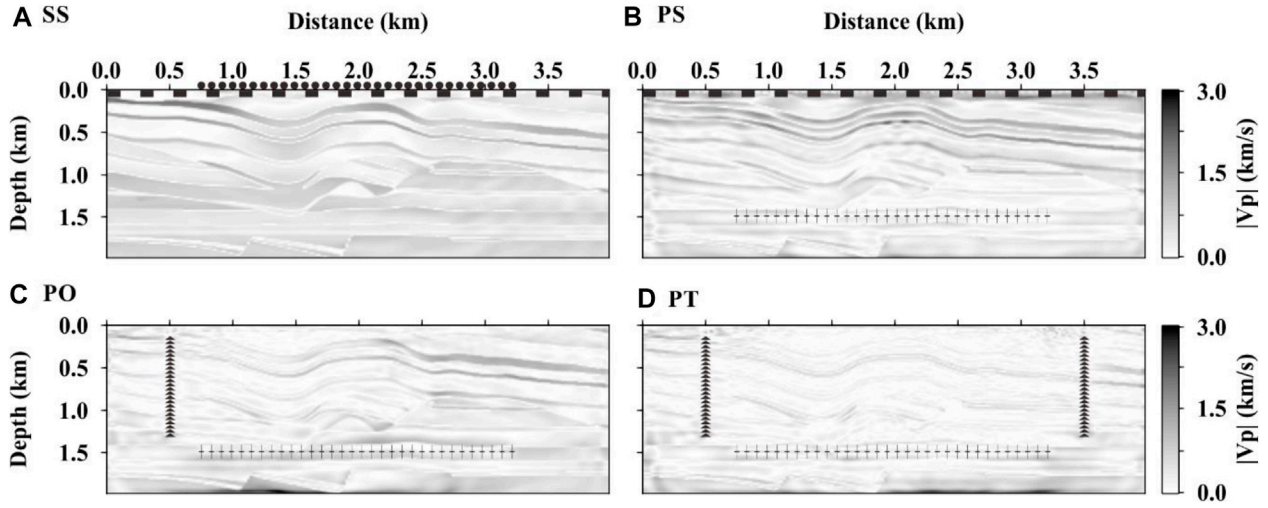

FIGURE 8 | Absolute error of the final inverted velocity models relative to the actual velocity model. As marked at the top left corner of each panel, **(A–D)** Errors of SS, PS, PO, and PT data, respectively.

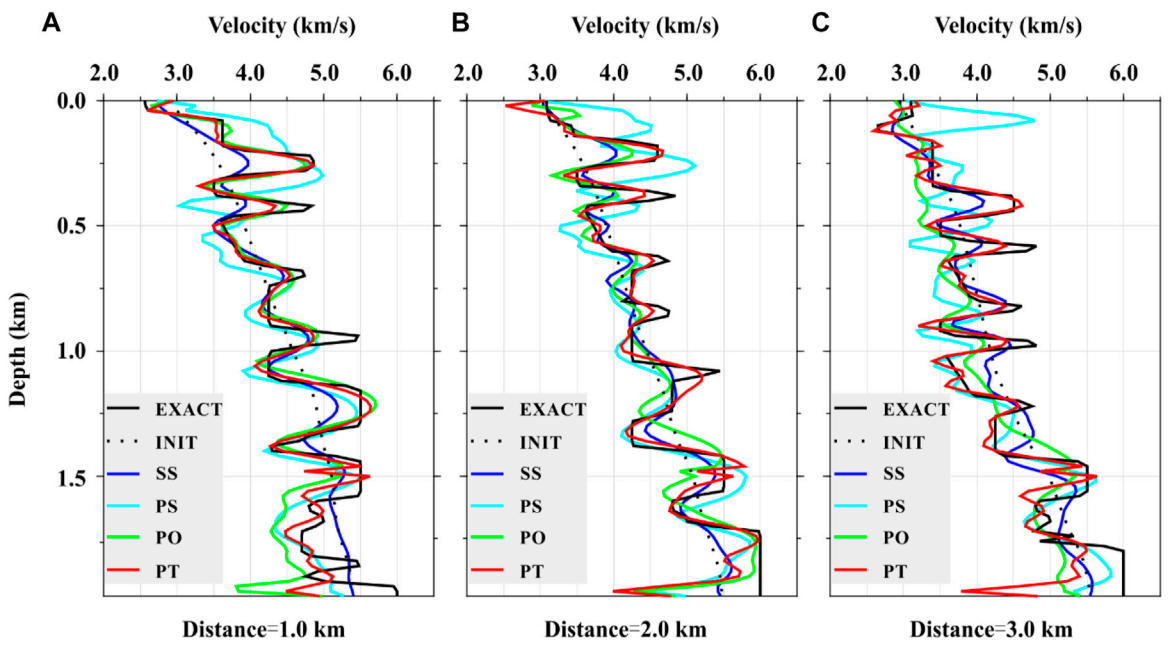

FIGURE 9 | Velocity profiles versus depth from the inversion results at distances of 1.0 km **(A)**, 2.0 km **(B)**, and 3.0 km **(C)**. Velocity profiles of the initial model and the actual model are also plotted as references.

observation well on the left (**Figure 8C**), the error of PT is the smallest over the whole model compared to other data sets, indicating that PT outperforms PO and PS (**Figure 8D**).

The velocity profiles versus depth at locations of distances 1.0, 2.0, and 3.0 km are extracted from the inverted models. Along with the initial model, the profiles are shown against the exact model in **Figure 9**, to demonstrate the difference variation versus depth. It can be seen that the inversion results of the SS data (solid blue line) are largely different from the exact model. Although the inversion from the PS data (solid cyan line) is poor in the shallow region above the depth of 0.5 km, it is in good agreement with the actual velocity structure below 0.5 km. The inversion results of PO (solid green line) in the area near the observation well on the left (**Figure 9A**) are in good agreement with the exact model, and the results far away from the observation well area are very poor (**Figure 9C**). All inversion results for PT (solid red line) are close to the exact curves, which mean PT delivers the best inversion.

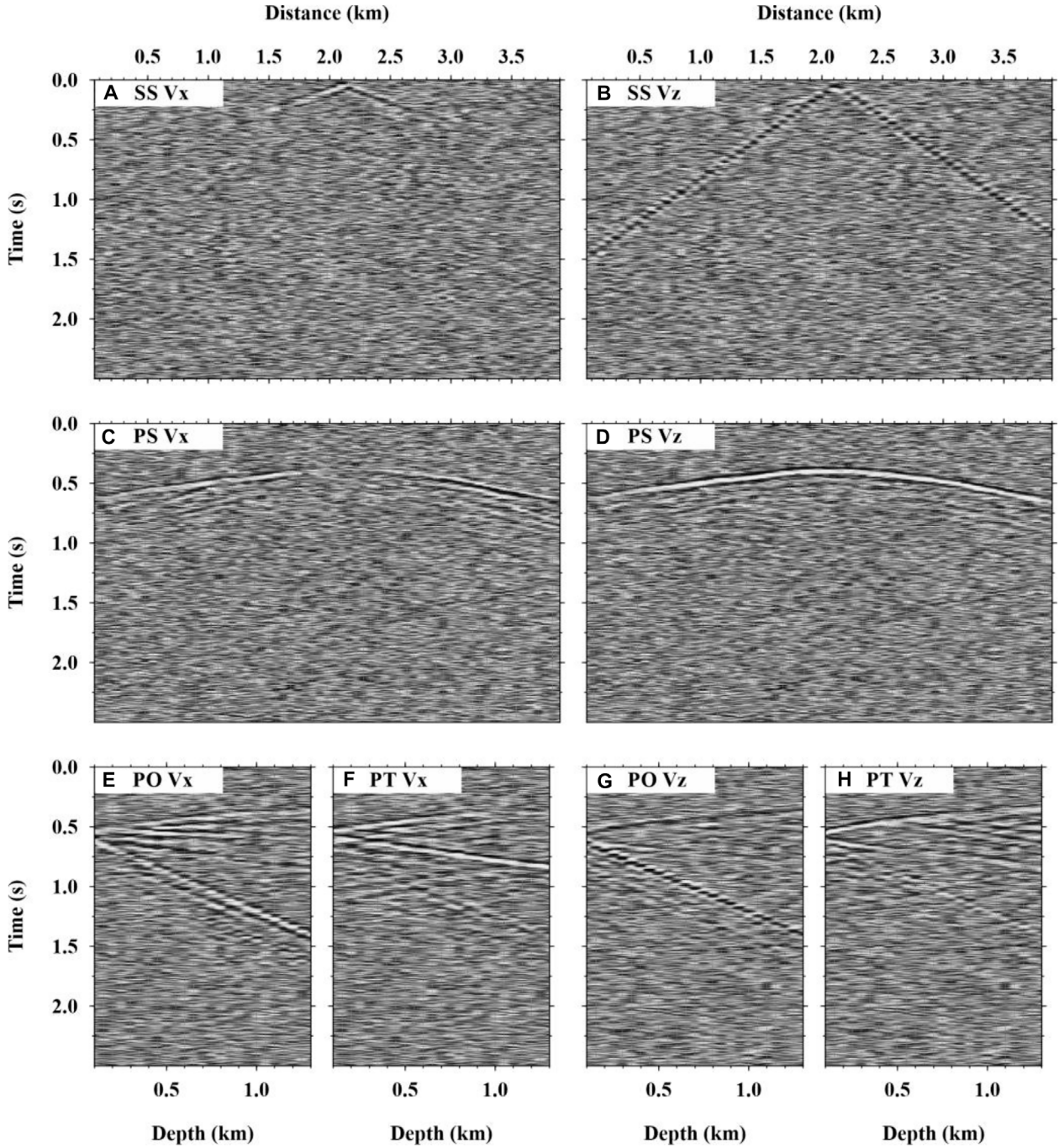

FIGURE 10 | Noisy data with S/N = 2.0 synthesized by adding Gaussian to the Vx and Vz seismograms of SS (Plots **A** and **B**), PS (Plots **C** and **D**), PO (Plots **E** and **G**), and PT (Plots **F** and **H**), as shown in **Figure 2**. The seismograms of PT were recorded using the array deployed on the vertical well on the right-hand side of the model.

Anti-Noise Performance

The conclusions above are based on the experiment using noise-free data. Considering that field seismic data usually contain a certain degree of noise, we use noisy data to test the validity of the conclusions.

The first experiment concerns Gaussian noise, which is generated and added into the seismogram (**Figure 2**) to synthesis noisy seismic data with S/N = 2.0 (**Figure 10**). The S/N used is defined as the ratio of the root-mean-square (RMS) amplitude of noise-free data (shown in **Figure 2**) to random noise for each trace. Comparing **Figure 10** with **Figure 2**, most of the signals of SS (a and b), PS (c and d), PO (e and g), and PT (f and h) are submerged in noise.

The noisy data, as shown in **Figure 10**, were then used for the FWI inversion in the same way as the previous inversion

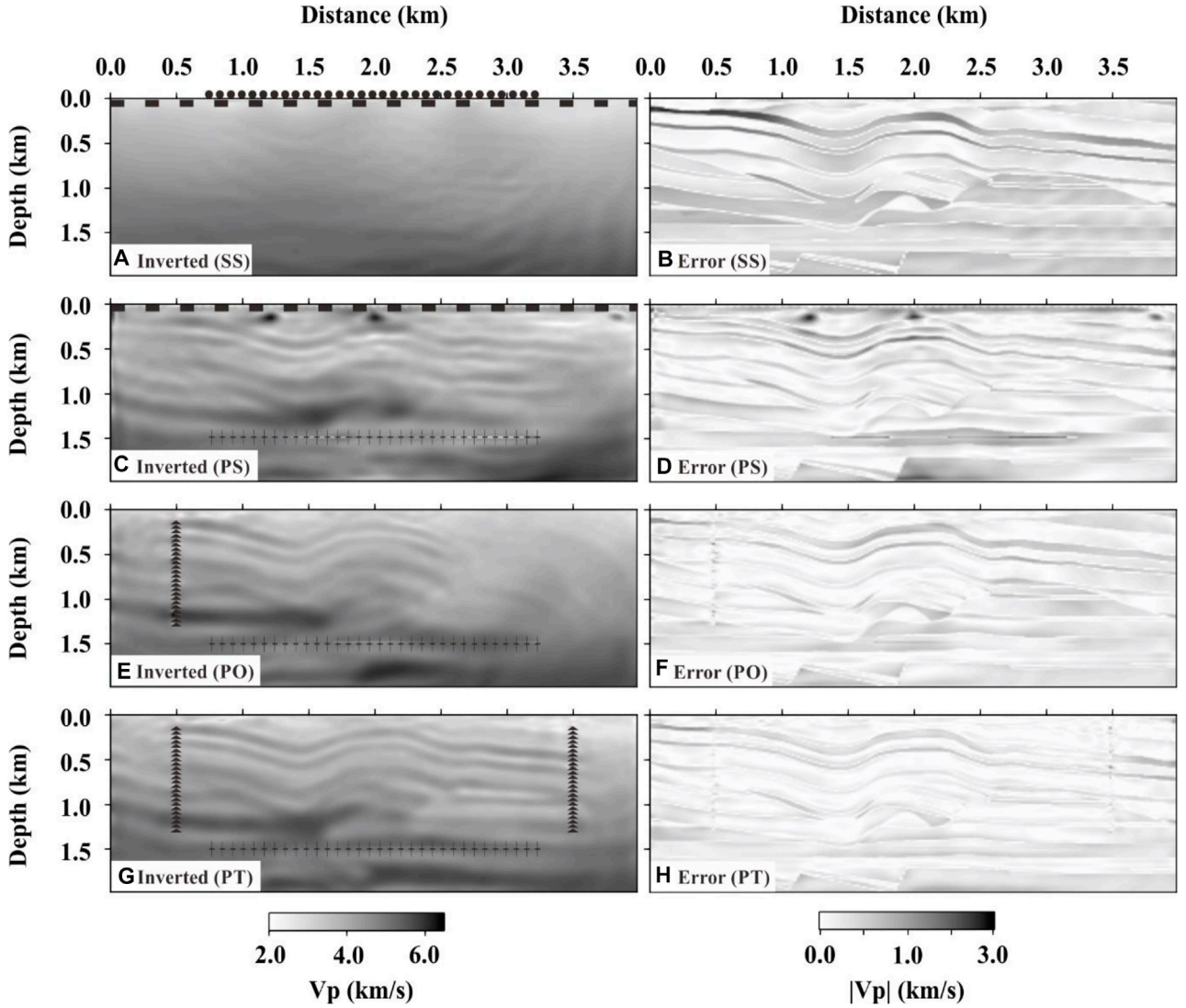

FIGURE 11 | Inversion results (Blocks **A**, **C**, **E** and **G** in the column on the left-hand side) of data contaminated with Gaussian noise (S/N = 2.0) and the absolute velocity error (Blocks **B**, **D**, **F** and **H** in the column on the right-hand side) relative to the actual velocity model. The results of SS, PS, PO, and PT data are marked in the bottom left corner of each block.

experiment. The results alongside their absolute errors from the actual velocity model are shown in **Figure 11**. Compared with the noise-free results (**Figures 4**–**7**), the structural characterization accuracy of the final inversion results of the noisy data is deteriorated for all data of SS, PS, PO, and PT (**Figures 11A,C,E,G**). The final inversion results of SS data only show the outline shape of the shallow folded strata (**Figure 11A**). The complex structures near the horizontal well are obscured. Moreover, the overall velocity error of SS is large (**Figure 11B**). The inversion results of PS data recover the general shape of the nappe structures near the horizontal well (**Figure 11C**), but there are very large errors in the shallow part (**Figure 11D**). By using PO data, the inversion can recover the structure near the observation well (**Figure 11E**) with small errors (**Figure 11F**). The reconstructed structures using the PT data (**Figure 11G**) are in good agreement with the exact model (**Figure 1**). Compared with SS, PS, and PO, PT has the smallest overall velocity error (**Figure 11H**). These results confirm that the previous conclusions from the noise-free data are valid for data deteriorated by Gaussian noise.

The second experiment concerns field noise. The Gaussian noise was replaced by the field noise recorded from the Upper Yangtze area of China. This field noise includes not only the natural random noise but also human activities and machine operations on site. Before adding the field noise to the synthetic data (**Figure 2**), a frequency band pass filtering is processed to keep it consistent with the data. The noise is added in such a proportion that the resultant noisy data are of S/N = 2.0. As seen from **Figure 12**, the noisy seismic records contain large amplitude noise randomly distributed in the profiles.

Using the same inversion procedures as for the previous experiments concerning Gaussian noise, we obtained the

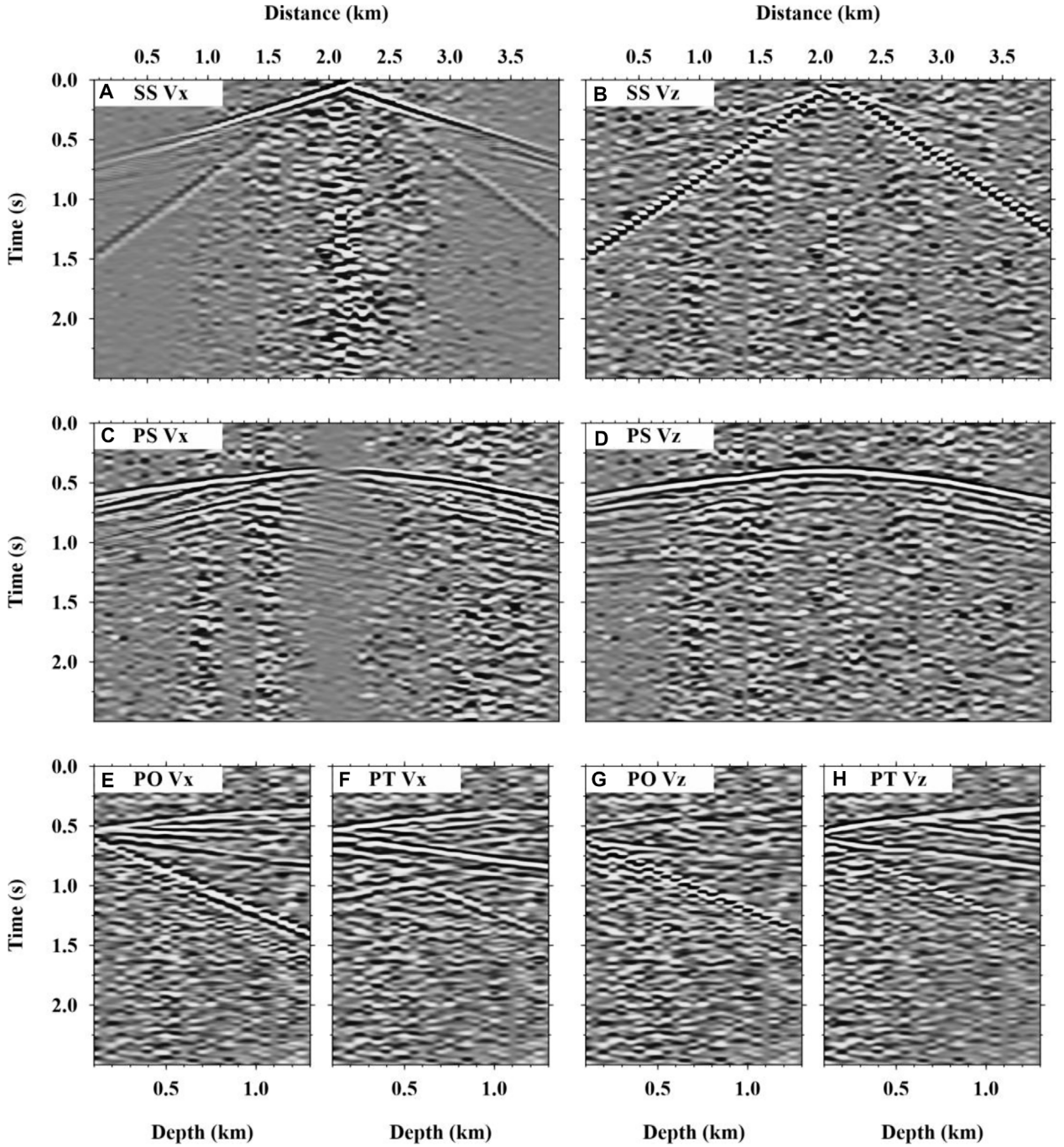

FIGURE 12 | Noisy data with S/N = 2.0 synthesized by adding field noise to the Vx and Vz seismograms of SS (Plots **A** and **B**), PS (Plots **C** and **D**), PO(Plots **E** and **G**), and PT (Plots **F** and **H**), as shown in **Figure 2**. The seismograms of PT are recorded using the array on the vertical well on the right-hand side of the model.

inversion results and their velocity errors against the actual model (**Figure 13**). From the structures near the horizontal wells, the results of **Figure 13** are consistent with that of the Gaussian noise shown in **Figure 12**. The inversion result of SS (**Figure 13A**) cannot clearly reflect the complex structure near the horizontal well and the error is the largest (**Figure 13B**). The results of PO (**Figure 13E**) recover most of the overthrust structures above the horizontal well. Its velocity error is much smaller than that of SS (**Figure 13F**). The results of PS (**Figures 13C,D**) are similar to those of PT (**Figures 13G,H**), but PT has the best agreement with the exact velocity model. It further confirms that the previous conclusions obtained from the noise-free data hold valid not only for data deteriorated by Gaussian noise but also by random field noise.

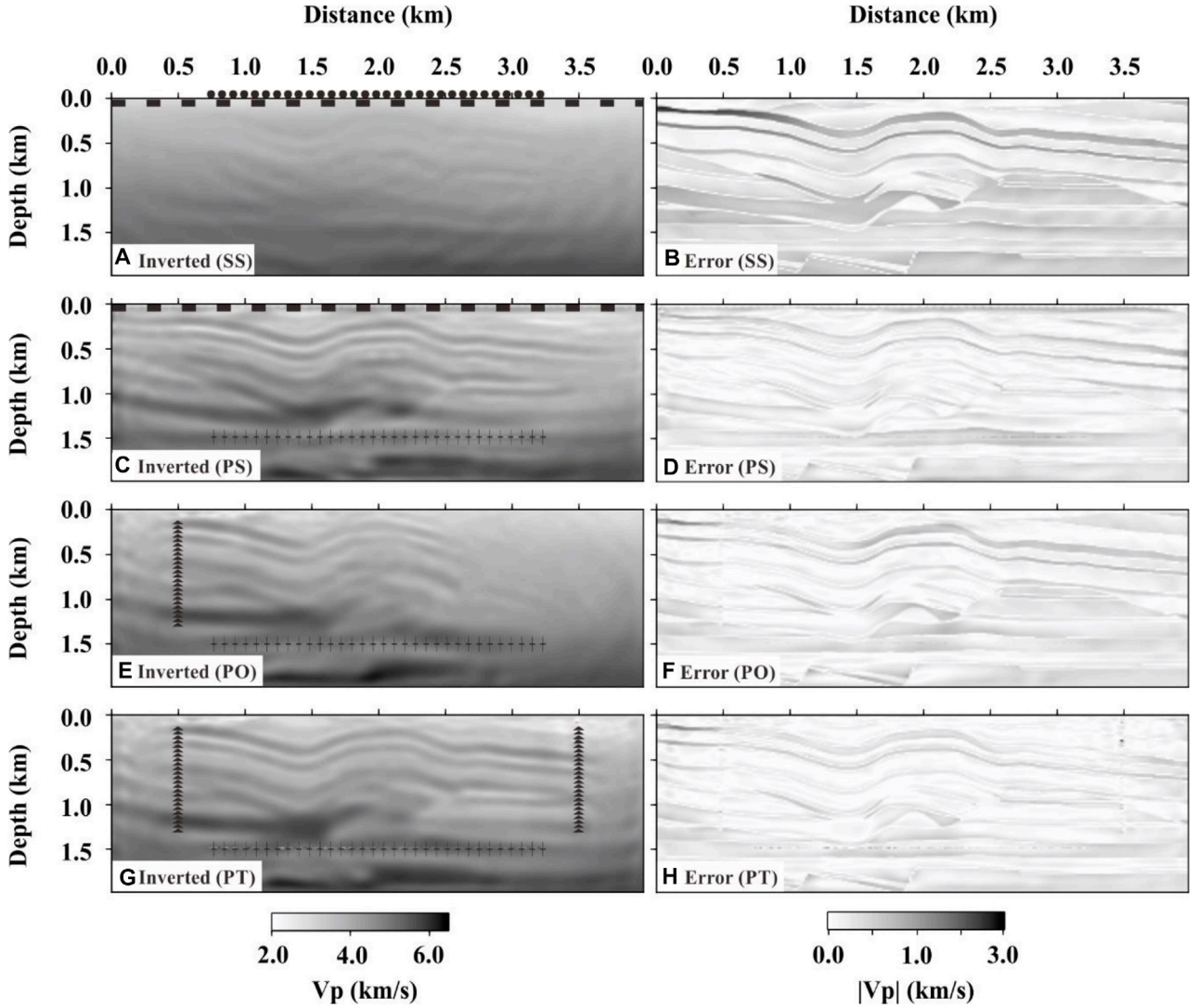

FIGURE 13 | Inversion results (left) and absolute velocity error (right) of SS, PS, PO, and PT data with field noise (S/N = 2). **(A)** Result of SS. **(B)** Absolute error between the inverted velocity in **(A)** and the exact velocity **(Figure 2)**. Similarly, **(C,D)** are from PS, **(E,F)** from PO, and **(G,H)** from PT. The results of SS, PS, PO, and PT data are marked in the lower left corner of each block and presented in order from the top to the bottom.

Fault Imaging

To achieve the goals of a hydraulic fracturing operation, it is desirable to image the faults around a horizontal hydraulic fracturing well. In the previous modeling experiments, there are complex fault structures around the horizontal hydraulic fracturing well (arrows in **Figure 14A**). To demonstrate the ability of FWI to image these faults using perforation seismic data, a comparison of the FWI results of SS, PS, PO, and PT data contaminated by the field noise (S/N = 2.0) is shown in **Figure 14**. No sign of the faults is seen in the FWI results of SS (**Figure 14B**). This means the faults cannot be imaged using conventional ground surface seismic data. On the contrary, the faults are successfully recovered in the FWI results of PS, PO, and PT data (*See* the red arrows in **Figures 14C–E**, respectively). Among the results of PS, PO, and PT, the ability of using PS data to image faults is limited (black arrows in **Figure 14C**). In addition, PO produces a sharper image of the fault structures near the receiving array (red arrows in **Figure 14D**), while the image of the faults far away from the receiving array is poor. In contrast, the PT image showed the most accurate shapes and locations of all the faults (red arrows of **Figure 14E**).

It is worth to pointing out that the strategy given in this article mainly focuses on the inversion of macroscopic structures. It is theoretically possible to image micro-scale fractures under ideal conditions. However, this would require a very dense array of observation systems capable of receiving very effective frequency data, which would be very challenging technically and unbearable economically.

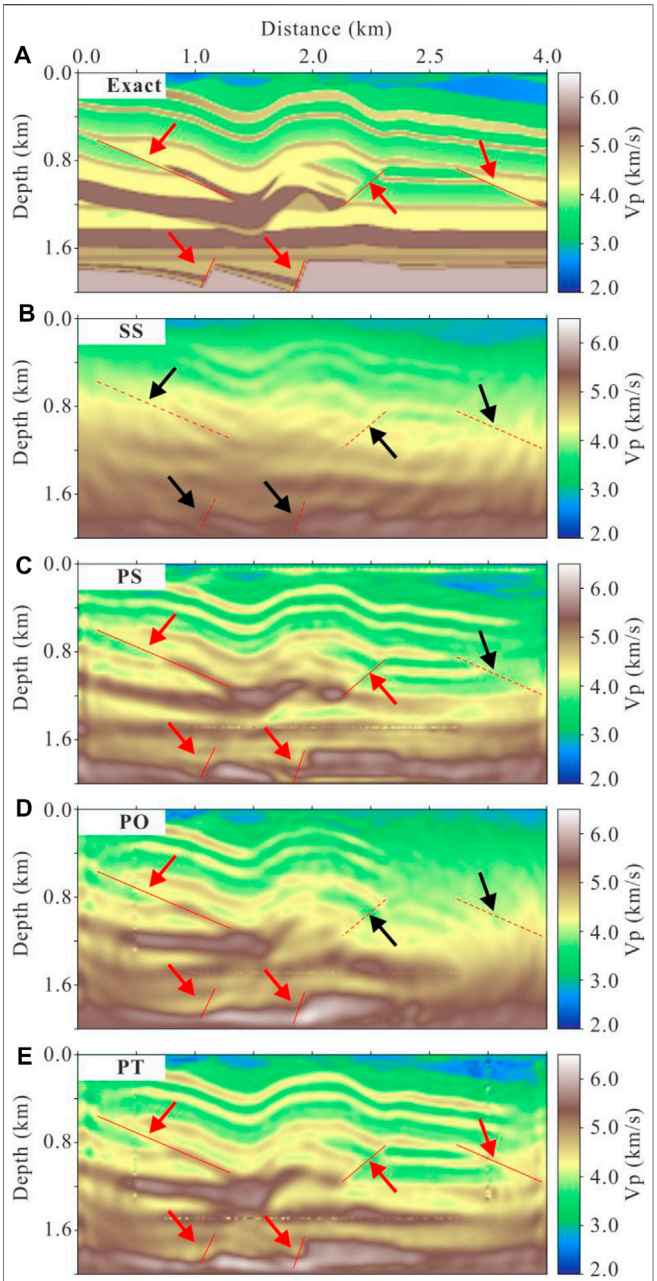

FIGURE 14 | Comparison of fault structures from the exact velocity model **(A)**. Inversion results of SS **(B)**, PS **(C)**, PO **(D)**, and PT **(E)**. Red arrows in **(A)** indicate the location of complex fault structures (solid red lines). **(B–E)** Red arrows indicate the successfully imaged fault structures (solid red lines), while the black arrows indicate fault structures that failed to recover (dashed red lines).

CONCLUSIONS

In this article, we proposed an FWI strategy for the inversion of concealed complex structures around a horizontal well using perforation seismic data. Numerical experiments were used to test the feasibility of the strategy. Perforation seismic data recorded from the ground surface and the observation wells were separately used in the inversion. As a benchmark, inversion is also performed using conventional reflection seismic data from the ground surface. The results show that:

(1) The FWI inversion of using perforation seismic data to image the concealed complex structures around horizontal wells is successful. The inversion images of perforation data showed clear details of the structures that cannot be imaged clearly with conventional reflection seismic data.
(2) The validity of this FWI strategy was further proved by the anti-noise performance experiments using data heavily contaminated with Gaussian or field noise. Inversions using perforation data from observation wells outperformed using data from the ground surface.
(3) The experiments also demonstrated that FWI using perforation seismic data could image the faults around a horizontal hydraulic fracturing well, while this was unable to achieved using conventional ground surface seismic data.

In summary, the modeling experiments demonstrate that the proposed FWI strategy for imaging concealed complex structures around a horizontal well using perforation seismic data is feasible. Compared with using conventional seismic data from the ground surface, this strategy has significant advantages in imaging resolution and anti-noise performance.

DATA AVAILABILITY STATEMENT

The original contributions presented in the study are included in the article/supplementary material, further inquiries can be directed to the corresponding author.

AUTHOR CONTRIBUTIONS

GQ, JLY and XF are responsible for the experiments, of which the plan was designed together with JSY, and the initial draft of the manuscript, which was later rewritten by JSY with further analysis of experiment results.

FUNDING

This work was funded by the Open Fund (PLC2020060) of the State Key Laboratory of Oil and Gas Reservoir Geology and Exploitation (Chengdu University of Technology), China and the National Natural Science Foundation of China (Grant Number 41774059).

REFERENCES

Aminzadeh, F., Burkhard, N., Nicoletis, L., Rocca, F., and Wyatt, K. (1994). SEG/EAEG 3-D Modeling Project: 2nd Update. *The Leading Edge* 13 (9), 949–952. doi:10.1190/1.1437054

Atkinson, G. M., Eaton, D. W., Ghofrani, H., Walker, D., Cheadle, B., Schultz, R., et al. (2016). Hydraulic Fracturing and Seismicity in the Western Canada Sedimentary Basin. *Seismological Res. Lett.* 87 (3), 631–647. doi:10.1785/0220150263

Bao, X., and Eaton, D. W. (2016). Fault Activation by Hydraulic Fracturing in Western Canada. *Science* 354 (6318), 1406–1409. doi:10.1126/science.aag2583

Bardainne, T., and Gaucher, E. (2010). Constrained Tomography of Realistic Velocity Models in Microseismic Monitoring Using Calibration Shots. *Geophys. Prospecting* 58 (5), 739–753. doi:10.1111/j.1365-2478.2010.00912.x

Clarke, H., Eisner, L., Styles, P., and Turner, P. (2014). Felt Seismicity Associated with Shale Gas Hydraulic Fracturing: The First Documented Example in Europe. *Geophys. Res. Lett.* 41, 8308–8314. doi:10.1002/2014gl062047

Dai, Y. H., and Yuan, Y. (1999). A Nonlinear Conjugate Gradient Method with a strong Global Convergence Property. *SIAM J. Optim.* 10 (1), 177–182. doi:10.1137/s1052623497318992

De Pater, C., and Baisch, S. (2011). Geomechanical Study of Bowland Shale Seismicity. *Synth. Rep.* 57.

Edwards, R. W. J., and Celia, M. A. (2018). Shale Gas Well, Hydraulic Fracturing, and Formation Data to Support Modeling of Gas and Water Flow in Shale Formations. *Water Resour. Res.* 54 (4), 3196–3206. doi:10.1002/2017wr022130

Edwards, R. W. J., Doster, F., Celia, M. A., and Bandilla, K. W. (2017). Numerical Modeling of Gas and Water Flow in Shale Gas Formations with a Focus on the Fate of Hydraulic Fracturing Fluid. *Environ. Sci. Technol.* 51 (23), 13779–13787. doi:10.1021/acs.est.7b03270

Ellsworth, W. L. (2013). Injection-induced Earthquakes. *Science* 341 (6142), 1225942. doi:10.1126/science.1225942

Flewelling, S. A., and Sharma, M. (2014). Constraints on Upward Migration of Hydraulic Fracturing Fluid and Brine. *Groundwater* 52 (1), 9–19. doi:10.1111/gwat.12095

Green, K. W., Jr., Zelbst, P. J., Meacham, J., and Bhadauria, V. S. (2012). Green Supply Chain Management Practices: Impact on Performance. *Supply Chain Manag. Int. J.* 17 (3), 290–305. doi:10.1108/13598541211227126

Hennings, P., Allwardt, P., Paul, P., Zahm, C., Reid, R., Alley, H., et al. (2012). Relationship between Fractures, Fault Zones, Stress, and Reservoir Productivity in the Suban Gas Field, Sumatra, Indonesia. *Bulletin* 96 (4), 753–772. doi:10.1306/08161109084

Hestenes, M., and Stiefel, E. (1952). *Methods of Conjugate Gradients for Solving Linear Systems*. NBS, 33–38.

Köhn, D., De Nil, D., Kurzmann, A., Przebindowska, A., and Bohlen, T. (2012). On the Influence of Model Parametrization in Elastic Full Waveform Tomography. *Geophys. J. Int.* 191 (1), 325–345.

Köhn, D. (2011). *Time Domain 2D Elastic Full Waveform Tomography. PhD Thesis*. Kiel University.

Ladevèze, P., Rivard, C., Lavoie, D., Séjourné, S., Lefebvre, R., and Bordeleau, G. (2019). Fault and Natural Fracture Control on Upward Fluid Migration: Insights from a Shale Gas Play in the St. Lawrence Platform, Canada. *Hydrogeology J.* 27 (1), 121–143.

Li, J., Zhang, H., Rodi, W. L., and Toksoz, M. N. (2013). Joint Microseismic Location and Anisotropic Tomography Using Differential Arrival Times and Differential Backazimuths. *Geophys. J. Int.* 195 (3), 1917–1931. doi:10.1093/gji/ggt358

Li, L., Tan, J., Wood, D. A., Zhao, Z., Becker, D., Lyu, Q., et al. (2019). A Review of the Current Status of Induced Seismicity Monitoring for Hydraulic Fracturing in Unconventional Tight Oil and Gas Reservoirs. *Fuel* 242, 195–210. doi:10.1016/j.fuel.2019.01.026

Li, Y., Zhou, D.-H., Wang, W.-H., Jiang, T.-X., and Xue, Z.-J. (2020). Development of Unconventional Gas and Technologies Adopted in China. *Energ. Geosci.* 1 (1–2), 55–68. doi:10.1016/j.engeos.2020.04.004

Mair, R., Bickle, M., Goodman, D., Koppelman, B., Roberts, J., Selley, R., et al. (2012). *Shale Gas Extraction in the UK: A Review of Hydraulic Fracturing*. The Royal Society, 112–122.

Maxwell, S., Jones, M., Parker, R., Miong, S., Leaney, S., Dorval, D., et al. (2009). *Fault Activation during Hydraulic Fracturing*. SEG Technical Program Expanded Abstracts, 1552–1556.

Nocedal, J., and Wright, S. (2006). *Numerical Optimization*. Springer Science & Business Media, 17–22.

Operto, S., Miniussi, A., Brossier, R., Combe, L., Métivier, L., Monteiller, V., et al. (2015). Efficient 3-D Frequency-Domain Mono-Parameter Full-Waveform Inversion of Ocean-Bottom cable Data: Application to Valhall in the Visco-Acoustic Vertical Transverse Isotropic Approximation. *Geophys. J. Int.* 202 (2), 1362–1391. doi:10.1093/gji/ggv226

Pei, D., Quirein, J., Cornish, B., Quinn, D., and Warpinski, N. (2009). Velocity Calibration for Microseismic Monitoring: A Very Fast Simulated Annealing (VFSA) Approach for Joint-Objective Optimization. *Geophysics* 74 (6), 47–55. doi:10.1190/1.3238365

Pei, D., Quirein, J., Cornish, B., Zannoni, S., and Ay, E. (2008). "Velocity Calibration Using Microseismic Hydraulic Fracturing Perforation and String Shot Data," in 49th Annual Logging Symposium, 181–189.

Plessix, R.-E., and Mulder, W. A. (2004). Frequency-domain Finite-Difference Amplitude-Preserving Migration. *Geophys. J. Int.* 157 (3), 975–987. doi:10.1111/j.1365-246x.2004.02282.x

Plessix, R. (2006). A Review of the Adjoint-State Method for Computing the Gradient of a Functional with Geophysical Applications. *Geophys. J. Int.* 167 (24), 495–503. doi:10.1111/j.1365-246x.2006.02978.x

Rutqvist, J., Rinaldi, A., and Cappa, F. (2017). Fault Reactivation and Seismicity Associated with Shale-Gas Fracturing and Geologic Carbon Storage - A Comparison from Recent Modeling Studies. *Poromechanics VI* 2000-2007. doi:10.1061/9780784480779.248

Schultz, R., Atkinson, G., Eaton, D. W., Gu, Y. J., and Kao, H. (2018). Hydraulic Fracturing Volume Is Associated with Induced Earthquake Productivity in the Duvernay Play. *Science* 359 (6373), 304–308. doi:10.1126/science.aao0159

Schultz, R., Stern, V., Novakovic, M., Atkinson, G., and Gu, Y. J. (2015). Hydraulic Fracturing and the Crooked Lake Sequences: Insights Gleaned from Regional Seismic Networks. *Geophys. Res. Lett.* 42 (8), 2750–2758. doi:10.1002/2015gl063455

Shin, C., Jang, S., and Min, D.-J. (2001). Improved Amplitude Preservation for Prestack Depth Migration by Inverse Scattering Theory. *Geophys. Prospecting* 49 (5), 592–606. doi:10.1046/j.1365-2478.2001.00279.x

Sirgue, L., Barkved, O., Dellinger, J., Etgen, J., Albertin, U., and Kommedal, J. (2010). Thematic Set: Full Waveform Inversion: The Next Leap Forward in Imaging at Valhall. *First Break* 28 (4), 65–70. doi:10.3997/1365-2397.2010012

Tan, Y., Chai, C., and Engelder, T. (2014). Use of S-Wave Attenuation from Perforation Shots to Map the Growth of the Stimulated Reservoir Volume in the Marcellus Gas Shale. *The Leading Edge* 33 (10), 1090–1096. doi:10.1190/tle33101090.1

Vidic, R. D., Brantley, S. L., Vandenbossche, J. M., Yoxtheimer, D., and Abad, J. D. (2013). Impact of Shale Gas Development on Regional Water Quality. *Science* 340, 1235009. doi:10.1126/science.1235009

Virieux, J., Asnaashari, A., Brossier, R., Métivier, L., Ribodetti, A., and Zhou, W. (2017). *Encyclopedia of Exploration Geophysics*, R1–R1.An Introduction to Full Waveform Inversion

Virieux, J., and Operto, S. (2009). An Overview of Full-Waveform Inversion in Exploration Geophysics. *Geophysics* 74 (6), 1–26. doi:10.1190/1.3238367

Warpinski, N., Sullivan, R., Uhl, J., Waltman, C., and Machovoie, S. (2005). Improved Microseismic Fracture Mapping Using Perforation Timing Measurements for Velocity Calibration. *SPE J.* 10 (1), 14–23. doi:10.2118/84488-pa

Witten, B., and Shragge, J. (2017). Microseismic Image-Domain Velocity Inversion: Marcellus Shale Case Study. *Geophysics* 82 (6), KS99–KS112. doi:10.1190/geo2017-0263.1

Zhang, H., Sarkar, S., Toksöz, M., Kuleli, H., and Al-Kindy, F. (2009). Passive Seismic Tomography Using Induced Seismicity at a Petroleum Field in Oman. *Geophysics* 74 (6), 57–69. doi:10.1190/1.3253059

Zhang, Q., Zhou, H., Li, Q., Chen, H., and Wang, J. (2016). Robust Source-independent Elastic Full-Waveform Inversion in the Time Domain Robust Source-independent Elastic FWI. *Geophysics* 81 (2), 29–44. doi:10.1190/geo2015-0073.1

Zheng, H., Zhang, J., and Qi, Y. (2020). Geology and Geomechanics of Hydraulic Fracturing in the Marcellus Shale Gas Play and Their Potential Applications to the Fuling Shale Gas Development. *Energ. Geosci.* 1 (1–2), 36–46. doi:10.1016/j.engeos.2020.05.002

Conflict of Interest: The authors declare that the research was conducted in the absence of any commercial or financial relationships that could be construed as a potential conflict of interest.

Publisher's Note: All claims expressed in this article are solely those of the authors and do not necessarily represent those of their affiliated organizations, or those of the publisher, the editors, and the reviewers. Any product that may be evaluated in this article, or claim that may be made by its manufacturer, is not guaranteed or endorsed by the publisher.

frontiers in Earth Science

ORIGINAL RESEARCH
published: 30 March 2022
doi: 10.3389/feart.2022.870332

Study on Pore Structure and the Microscopic Mechanism of the Difference in Petrophysical Properties of Tight Sandstone: A Case Study of the Chang 3 Member of Weibei Oilfield, Ordos Basin

Ying Tang[1,2], Jingchao Lei[3]*, Haoran Dong[1], Shihao Tan[1], Duanyue Ma[1], Nan Zhang[1] and Mingxian Wang[4]*

[1]College of Petroleum Engineering, Xi'an Shiyou University, Xi'an, China, [2]Beijing Key Laboratory of Unconventional Natural Gas Geological Evaluation and Development Engineering, Beijing, China, [3]Exploration Department of PetroChina Changqing Oilfield Company, Xi'an, China, [4]School of Earth Sciences and Engineering, Xi'an Shiyou University, Xi'an, China

OPEN ACCESS

Edited by:
Hu Li,
Southwest Petroleum University, China

Reviewed by:
Jun Wu,
China University of Geosciences, China
Wenjie Feng,
Yangtze University, China

***Correspondence:**
Jingchao Lei
364666192@qq.com
Ying Tang
tangying330@126.com

Specialty section:
This article was submitted to Economic Geology, a section of the journal Frontiers in Earth Science

Received: *09 February 2022*
Accepted: *07 March 2022*
Published: *30 March 2022*

Citation:
Tang Y, Lei J, Dong H, Tan S, Ma D, Zhang N and Wang M (2022) Study on Pore Structure and the Microscopic Mechanism of the Difference in Petrophysical Properties of Tight Sandstone: A Case Study of the Chang 3 Member of Weibei Oilfield, Ordos Basin. Front. Earth Sci. 10:870332. doi: 10.3389/feart.2022.870332

Tight sandstone reservoirs have complex pore throat structures and poor and large differences in petrophysical properties. In this study, taking the Chang 3 Member of Weibei Oilfield, Ordos Basin, China as an example, the microscopic mechanism of the differences in petrophysical properties of tight sandstone reservoirs was systematically studied by thin section observation, scanning electron microscope, whole-rock X-ray diffraction, and high-pressure mercury intrusion experiments. The research results show that the reservoir types of the Chang 3 Member are mainly feldspar lithic sandstone and lithic feldspar sandstone; the pore types include intergranular, intragranular dissolution pores, and a small amount of residual intergranular pores. Taking the permeability of 0.3×10^{-3} and 0.5×10^{-3} μm^2 as the boundary, we divided the samples involved in high-pressure mercury intrusion into three categories according to the permeability from high to low: Type I, Type II, and Type III. Their proportions were 31.4, 20.0, and 48.6%, respectively. The study found that the smaller the sorting coefficient, the poorer the petrophysical properties of the samples; the pore throat distribution of different samples gradually changed to a uniform double peak–dominated type. The permeability of tight sandstone reservoirs is contributed by a small part of pore throats with a large radius, while the reservoir space is mainly contributed by a large number of pores connected with small throats. The porosity is negatively and positively correlated with the median pressure and mercury injection tortuosity, respectively. In addition, the pore throat radius corresponding to the maximum permeability contribution rate, maximum pore throat radius, and sorting coefficient are all positively correlated with the permeability. In general, the areas with larger pore throat radius, lower pore throat tortuosity, and larger pore throat sorting coefficient can be regarded as favorable areas for Chang 3 tight sandstone reservoirs.

Keywords: Ordos Basin, tight sandstone, high-pressure mercury intrusion, difference in petrophysical properties, microscopic mechanism

1 INTRODUCTION

Conventional oil resources are decreasing day by day, and tight sandstone oil has become an important part of China's oil resources. Tight oil resources in major basins in China range from 8 to 10 billion tons. At present, China has built a highly industrialized tight oil–producing area in the Ordos Basin, and the producing layer is located in the Upper Triassic Yanchang Formation. Tight sandstone reservoirs are characterized by tight lithology, poor petrophysical properties, and strong microscopic heterogeneity (Yin et al., 2018; Yin and Ding, 2019; Dong et al., 2020; Hong et al., 2020; Santosh and Feng., 2020; Chen et al., 2021; Xue et al., 2021). Pore throats with different radii are obviously affected by complex capillary action and gravity, which lead to huge differences in seepage laws within different pore throat radii (Yin and Wu, 2020; Yoshida and Santosh., 2020; Zhang et al., 2020; Ding et al., 2021). Reservoir petrophysical properties are the final response of the microscopic pore throat structures (Yin et al., 2020a; Mohammed et al., 2021; Qie et al., 2021).

In recent years, the research methods of reservoir micro-heterogeneity have been continuously improved. For example, its development has gradually transitioned from conventional methods such as microscope observation and mercury intrusion to advanced methods such as nuclear magnetic resonance, high-pressure mercury intrusion, three-dimensional CT scanning, and laser focusing microscopy (Yin et al., 2020b; Hower and Groppo., 2021; Mirzaei-Paiaman and Ghanbarian., 2021; Wang and Wang., 2021). These methods directly or indirectly reflect the microscopic heterogeneity of the reservoir. The previous methods usually use the water displacement experiment to analyze the seepage characteristics of tight sandstone reservoirs, but there are few studies on the microscopic mechanism of the difference in petrophysical properties of tight sandstone reservoirs (Sun and Tang., 2006; Askarinezhad, 2010; Li et al., 2020; Mahmud et al., 2020; Lan et al., 2021). There is no doubt that the petrophysical properties of tight sandstone reservoirs are the key factors affecting oil content, oil saturation, production rate, and ultimate recovery factor of the reservoir (Barsotti et al., 2016; Fan et al., 2019; Yang et al., 2021). Therefore, an in-depth micro-mechanism study of the differences in petrophysical properties of tight sandstone reservoirs is necessary, which is of great significance to improve the accuracy of high-quality reservoir prediction (Zhang et al., 2019; Zuo et al., 2019).

In this study, taking the Chang 3 Member of Weibei Oilfield, Ordos Basin, China as an example, the microscopic mechanism of the difference in petrophysical properties of tight sandstone reservoirs was systematically studied by thin section observation, scanning electron microscope, whole-rock X-ray diffraction, and high-pressure mercury intrusion experiments. This study can provide a reliable basis for sweet spot prediction of tight sandstone reservoirs.

2 GEOLOGICAL BACKGROUND

The Ordos Basin in China has a total area of 370,000 km^2. The Upper Triassic Yanchang Formation has a monoclinic structure that is low in the northwest and high in the southeast. In addition, the slope of the Yanchang Formation is 8–20 m/km, and the formation dip is 1–2°. Affected by the tectonic activities of the Weibei Uplift Belt, some small-scale faults with small fault throws developed in this area (Nabawy et al., 2009; Li et al., 2016; Wang A. et al., 2018; Wang et al., 2020).

The study area, Weibei Oilfield, is located at the intersection part of the Weibei Uplift and Yishan Slope in the Ordos Basin, with an area of about 2028.9 km^2. The oil resources of the Yanchang Formation in the study area are 1.46×10^8t. According to the regionally developed stratigraphic correlation markers such as tuff, shale, and coal lines, the Upper Triassic Yanchang Formation is divided into Chang 10–Chang 1 Members from bottom to top (Gier et al., 2008; Gao et al., 2011; Dai et al., 2016; Cui et al., 2019). The Chang 10 to 7 Members (hereinafter referred to as C10–C7 in figures) were deposited in a lake transgression stage during which the lacustrine basin is formed and developed. During the deposition of the Chang 7 Member, the lacustrine basin was at its peak, and dark mudstone and interbedded oil shales of shallow and semi-deep lacustrine facies were developed. The deposition of Chang 6 to Chang 1 Members occurred during the delta construction in the lacustrine basin, followed by lake shrunk, and disappeared (Jia et al., 2012; Kwak et al., 2017). Among them, the Chang 3 Member (C3) is the main oil-bearing formation with an average burial depth of 550 m (**Figure 1**). The Chang 3 Member of Weibei Oilfield belongs to the front facies of braided river delta and develops underwater distributary channel, interdistributary bay, and mouth bar microfacies. Underwater distributary channel sand bodies are the main reservoirs (Li et al., 2019; Hong et al., 2020). The sand bodies are distributed in a north–south direction (**Figure 2**).

3 DATA AND METHODS

In this study, we completed thin section observation, scanning electron microscope test, particle size analysis, high-pressure mercury injection, whole-rock X-ray diffraction (XRD) analysis, and XRD clay mineral measurement of core samples from Chang 3 Member reservoirs in Weibei Oilfield.

A total of 234 cast thin sections were observed, and the mineral composition, pore type, particle sorting, and surface porosity parameters of the thin sections were determined using a Zeiss metallographic microscope (Axio Imager A2m) under the conditions of an indoor temperature of 25°C and a relative humidity of 50%. The detection basis is SY/T 5368-2000 "Rock Thin Section Identification". In addition, a total of 42 samples were observed by using an FEI QUANTA 250 environmental scanning electron microscope. The detection is based on GB/T 18295-2001 "Scanning Electron Microscope Analysis Method for Sandstone Samples of Oil and Gas Reservoirs".

The particle size distribution of 38 reservoir rock samples was tested by using an SFY-B2000 sonic vibration sieve particle size analyzer. Furthermore, reservoir rock grain size, percentage of different grain sizes, sorting coefficients, and kurtosis were obtained.

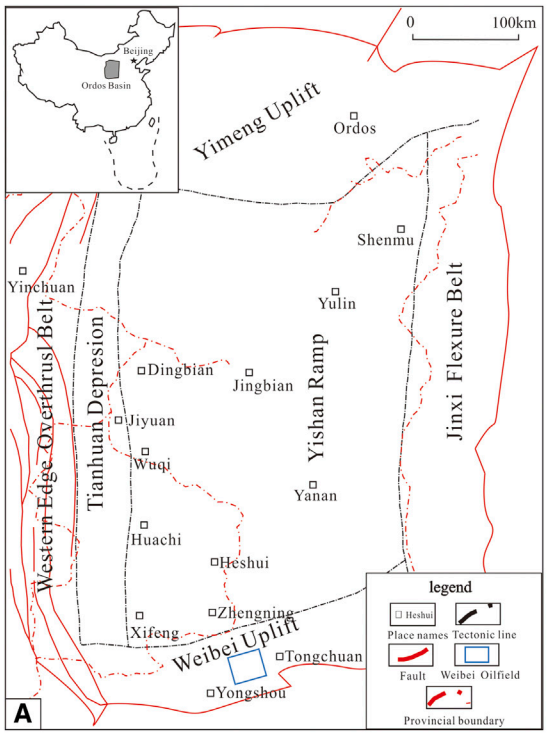

Erathem	System	Formation	Member	Thickness (m)	Evolution of the basin
Cenozonic	Quaternary			50-90	
Mesozoic	Lower Cretaceous			10-50	
	Jurassic	Zhiluo Formation		20-60	
		Yanan Formation		20-180	Lake basin filling Development stage of river and lake deltas
	Upper Triassic	Yan chang Formation	C2	0-165	Stable depression, lake basin shrinkage
			C3	100-165	
			C4+5	110-170	
			C6	100-150	
			C7	100-140	Strong depression
			C8	65-120	Lake basin expansion
			C9	90-110	The initial depression formed the lake basin
			C10	160-260	

B

FIGURE 1 | Location of the Weibei Oilfield **(A)** and stratigraphic column of the Yanchang Formation in the Ordos Basin **(B)** (modified from Wang et al., 2022).

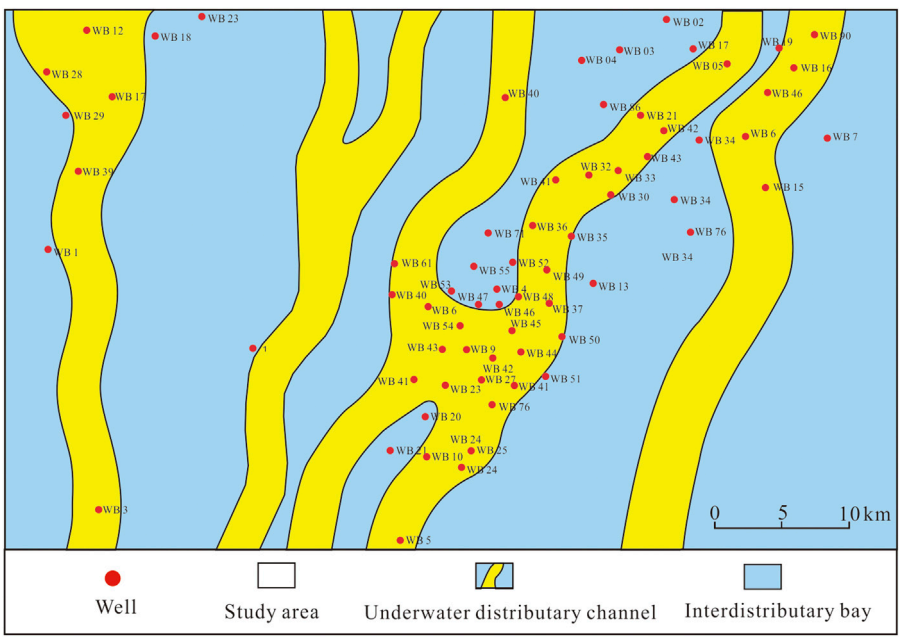

FIGURE 2 | Planar distribution of sedimentary facies in the Chang 3 Member of Weibei Oilfield.

An AutoPore IV 9505 automatic mercury porosimeter was used to complete the high-pressure mercury porosimetry of 35 tight sandstone sample gates at a temperature of 18°C and a relative humidity of 30%. The detection basis is SY/T 5346-2005 "Determination of Rock Capillary Pressure Curve". Furthermore, the porosity–permeability, mercury intrusion curves, and

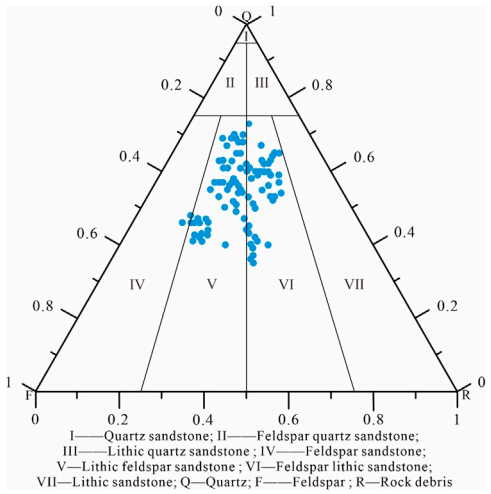

FIGURE 3 | Lithologic triangular diagram of sandstone in the Chang 3 Member in Weibei Oilfield.

characteristic parameters of pore throat structures of the samples were obtained.

Whole-rock X-ray diffraction (XRD) analysis and XRD clay mineral measurement were performed on 29 rock samples using a D/max-2600 X-ray diffractometer, and the contents of different types of minerals and clay minerals were obtained. The detection basis is SY/T 5163-2010 "X-ray Diffraction Analysis Method of Clay Minerals and Common Non-clay Minerals in Sedimentary Rocks".

4 RESULTS

4.1 Lithologies and Pore Types

The oil-bearing reservoirs in the Chang 3 Member are gray and gray–brown fine sandstones, with particle sizes mainly ranging from 0.06 to 0.25 mm. In addition, the clastic particles are mostly subangular to sub-round with moderate sorting and roundness. The lithologies of the reservoir are mainly feldspar lithic sandstone and lithic feldspar sandstone (**Figure 3**). Among the mineral components, the content of quartz is the largest (55.54%), followed by feldspar (24.09%) and debris (19.31%) (**Figures 4A,B**). According to the observation of microscopic thin sections, the composition of the Chang 3 Member comprises magmatic, metamorphic, and sedimentary rock debris. In the detrital composition, Q/F is 2.30 and Q/(F+R) is 1.29, indicating that the Chang 3 reservoir has high compositional maturity. In addition, the interstitials are dominated by carbonate cement and muddy matrix, with an average content of 8.28 and 3.80%, respectively; the content of clay minerals is low (average content of 3.8%) and dominated by kaolinite and illite (**Figures 4C,D**).

According to the observation results of the cast thin sections, the average face ratio of the Chang 3 Member is 7.61%, and its surface area is relatively low (the average value is 0.32 μm^{-1}). Statistics show that the shape factor of the target layer is relatively low (average 0.46), indicating that the pores are regular in shape. Moreover, the average coordination number of pore throats is 0.48 and the sorting coefficient is 9.78, indicating that the number of throats connected to pores is large and the pore heterogeneity is strong (**Table 1**). In addition, the proportions of three types of pores, namely, intergranular, intragranular dissolution pores, and residual intergranular pores, are 76.15, 18.15 and 5.7%, respectively. This shows that the pore types of the tight sandstone in the target layer are mainly intergranular and intragranular dissolution pores, and the proportion of residual intergranular pores is the lowest (**Figures 4C,D**).

4.2 Petrophysical Characteristics and Pore Structure Parameters

The petrophysical properties and pore structure parameters of the samples obtained based on the high-pressure mercury intrusion experiment are shown in **Table 2**. The porosity of the samples ranges from 2.20 to 14.97%, with an average value of 10.17%; the permeability ranges from 0.09×10^{-3} to 1.58×10^{-3} μm^2, with an average value of $0.44 \times 10^{-3} \mu m^2$. Referring to the classification criteria for ultra-low permeability reservoirs proposed by Yang and Fu (2012), we divided the samples into three categories with permeability (K) of 0.3×10^{-3} and 0.5×10^{-3} μm^2 as the boundaries: (Type I) $K \geq 0.5 \times 10^{-3}$ μm^2, (Type II) $0.5 \times 10^{-3} \mu m^2 > K \geq 0.3 \times 10^{-3}$ μm^2, and (Type III) $K < 0.3 \times 10^{-3}$ μm^2.

According to statistics, the proportions of Types I, II, and III samples in the Chang 3 Members are 31.4, 20.0, and 48.6%, respectively (**Figure 5**). From Type I to Type III reservoirs, with the decrease of the petrophysical properties of the samples, the average value of the maximum pore throat radius, median pore throat radius, and mercury withdrawal efficiency gradually decreased; and the average value of displacement pressure, median pressure, and residual mercury saturation gradually increased. Among them, the mercury withdrawal efficiency corresponds to the recovery factor in oilfield development, and the residual mercury saturation is the mercury saturation that remains in the rock sample when the injection pressure drops to a minimum value (Fan et al., 2020). It shows that the smaller the pore throat radius of the sample the greater the capillary resistance and the worse the petrophysical properties. Such reservoirs will show low recovery and high residual oil content in the actual development process.

From the correlation between permeability and porosity (**Figure 6**), it can be seen that there is a certain positive correlation between porosity and permeability, but the correlation is poor and the correlation coefficient R^2 is only 0.33. Some samples with less porosity can also obtain larger permeability, indicating that the porosity–permeability relationship of tight sandstone is significantly different from that of conventional sandstone. The research on the differences in petrophysical properties of this type of tight reservoirs should start from the perspective of microscopic pore throat structures (Nelson, 2009; Ryazanov, et al., 2014; Li et al., 2020).

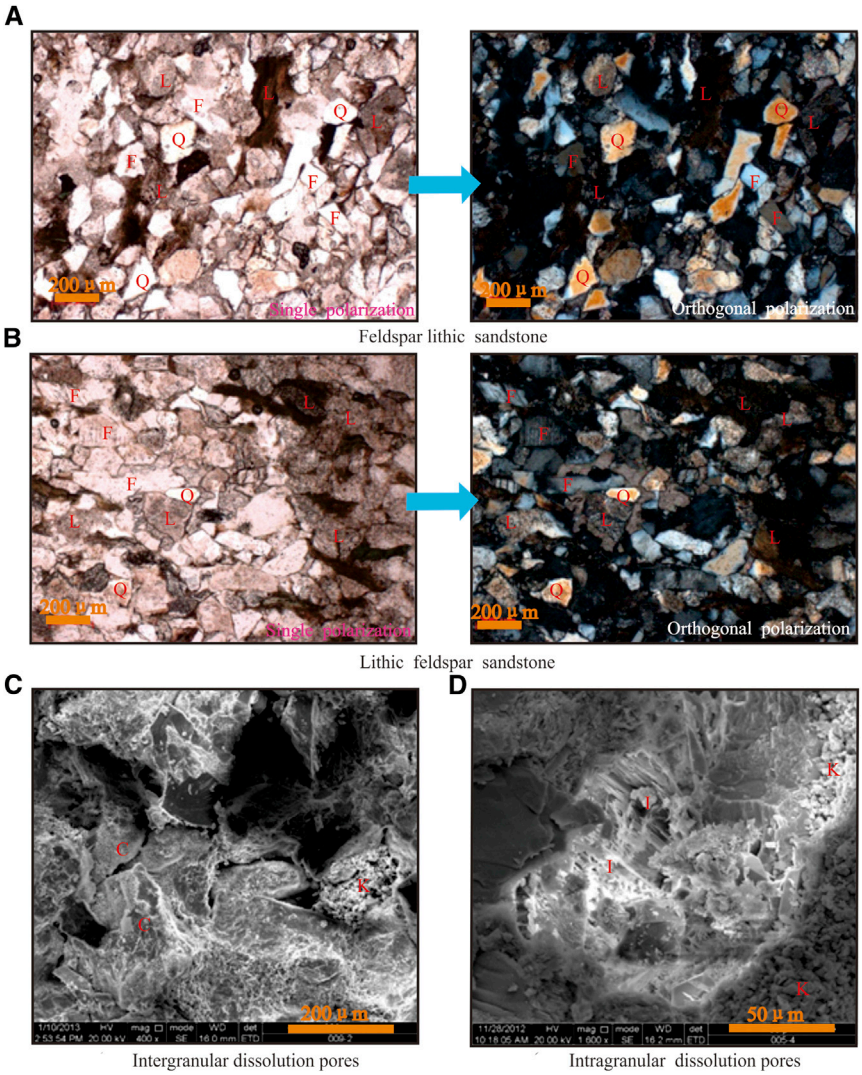

FIGURE 4 | Photomicrographs and scanning electron microscopy (SEM) images of the Chang 3 sandstone. Images on the left of **(A)** and **(B)** were test results under plane-polarized light, and images on the right of **(A)** and **(B)** were test results under cross-polarized light. **(A)** Well WB2, 544.60 m, ×50; **(B)** Well WB2, 547.71 m, ×50; **(C)** Well WB11, 395.84 m, intergranular pores with chlorite film on the surface of the particles. In addition, the pores are filled with book-like authigenic kaolinite; **(D)** Well WB15, 226.17 m; intragranular dissolution pores; and the pores are filled with kaolinite and illite. Q: quartz; R: rock debris; F: feldspar; C: chlorite; K: kaolinite; I: illite.

TABLE 1 | Types and characteristic parameters of pores analyzed for samples in the Chang 3 Member.

Horizon	Average face ratio	Average surface area (μm^{-1})	Average shape factor	Average coordination number	Sorting coefficient	Average pore throat ratio	Pore composition (%)		
							Residual intergranular pore	Intergranular dissolution pore	Intragranular dissolution pore
C3	7.61	0.32	0.46	0.48	9.78	9.50	5.70	76.15	18.15

5 DISCUSSION

5.1 Influence of Pore Throat Structures on Petrophysical Properties

The capillary pressure curve is the relationship between capillary pressure and mercury saturation, and a certain capillary pressure corresponds to a certain pore throat radius. From the perspective of pore structure, the capillary pressure curve can reflect the distribution of the pore and throats of the rock (Wang, 2008; Qiao et al., 2020). The shape of the capillary pressure curve is mainly controlled by the sorting of the pore throats and size of the throats. Sortability refers to the degree of dispersion of throat size

TABLE 2 | Petrophysical properties and pore structure parameters of the Chang 3 tight sandstone samples.

Type	Pore throat radius distribution	Well name	No	H(m)	ϕ (%)	k ($10^{-3}\mu m^2$)	Mercury intrusion parameters						
							P_d (MPa)	P_m (MPa)	S_{max} (%)	W_e (%)	S_r (%)	r_{max} (μm)	r_m (μm)
I	SP	WB11	WB11-15	397.45	13.14	1.58	0.35	4.47	82.20	41.36	48.20	2.17	0.17
I	SP	WB2	WB2-2	543.81	14.97	0.58	1.06	7.84	100.00	36.47	63.53	0.70	0.09
I	SP	WB2	WB2-39	550.88	13.79	1.16	0.64	4.57	100.00	37.15	63.80	1.15	0.16
I	DP	WB6	WB6-5	299.67	11.90	0.68	0.88	9.45	89.40	25.62	66.50	0.86	0.08
I	DP	WB9	WB9-19	509.18	2.20	0.63	1.11	41.06	60.00	18.67	48.80	0.67	0.02
I	DP	WB2	WB2-13	545.45	12.91	0.52	1.06	7.84	100.00	37.15	61.79	0.69	0.09
I	DP	WB7	WB7-2	409.23	14.56	0.91	0.35	4.37	90.80	37.15	69.40	2.12	0.17
I	DP	WB2	WB2-8	544.75	13.08	0.55	1.06	8.76	100.00	37.15	62.85	0.70	0.08
I	DP	WB2	WB2-23	547.15	14.27	0.94	0.62	6.41	100.00	37.15	61.06	1.18	0.12
I	DP	WB2	WB2-27	547.71	13.88	0.82	0.62	6.34	100.00	37.15	61.82	1.18	0.12
I	DP	WB2	WB2-47	553.68	11.89	0.94	0.48	4.70	100.00	37.15	65.13	1.53	0.16
Average					12.42	0.84	0.75	9.62	92.95	34.74	61.17	1.18	0.11
II	SP	WB11	WB11-4	394.91	8.93	0.38	0.75	8.45	88.20	33.33	58.80	1.00	0.09
II	SP	WB7	WB7-15	411.53	11.73	0.45	0.50	3.78	92.50	21.95	72.20	1.50	0.20
II	SP	WB2	WB2-43	551.75	5.78	0.33	5.04	26.22	100.00	37.15	52.18	0.15	0.03
II	SP	WB15	WB15-17	233.80	11.58	0.36	0.79	2.96	90.00	26.67	66.00	0.95	0.25
II	DP	WB6	WB6-52	306.43	10.66	0.49	0.70	7.63	92.80	18.97	75.20	1.07	0.10
II	DP	WB9	WB9-11	506.60	13.41	0.32	1.58	7.79	88.30	28.77	62.90	0.47	0.10
II	DP	WB2	WB2-17	546.12	3.89	0.34	6.42	31.93	100.00	37.15	56.73	0.12	0.02
II	DP	WB2	WB2-33	549.07	12.42	0.43	1.06	7.18	100.00	37.15	62.09	0.70	0.10
Average					9.80	0.39	2.10	11.99	93.98	30.14	63.26	0.74	0.11
III	SP	WB15	WB15-34	236.69	8.36	0.17	1.27	5.02	88.00	29.55	62.00	0.59	0.15
III	DP	WB15	WB15-4	225.99	7.90	0.12	2.01	10.44	86.00	32.56	58.00	0.37	0.07
III	DP	WB15	WB15-46	238.37	7.10	0.13	2.35	12.33	83.00	30.12	58.00	0.32	0.06
III	DP	WB15	WB15-55	246.74	8.71	0.17	1.30	6.02	89.00	21.35	70.00	0.58	0.12
III	DP	WB6	WB6-18	301.60	10.90	0.29	0.88	12.08	91.20	23.25	70.00	0.85	0.06
III	DP	WB6	WB6-31	303.69	12.56	0.25	1.30	10.71	93.50	23.74	71.30	0.58	0.07
III	DP	WB6	WB6-61	307.41	9.46	0.18	1.98	19.42	86.60	25.17	64.80	0.38	0.04
III	DP	WB6	WB6-44	305.46	8.42	0.22	1.70	9.45	91.20	19.08	73.80	0.44	0.08
III	DP	WB9	WB9-27	511.55	10.31	0.24	3.02	24.15	86.70	39.56	52.40	0.25	0.03
III	DP	WB9	WB9-5	504.62	10.21	0.23	2.78	11.24	89.50	33.85	59.20	0.27	0.07
III	DP	WB11	WB11-28	399.68	7.33	0.12	3.14	15.20	87.70	28.05	63.10	0.24	0.05
III	DP	WB11	WB11-37	401.41	7.51	0.13	2.92	15.11	85.20	26.29	62.80	0.26	0.05
III	DP	WB7	WB7-27	414.36	8.67	0.14	3.37	14.74	91.30	15.44	77.20	0.22	0.05
III	DP	WB7	WB7-35	416.88	10.07	0.14	3.31	16.47	92.80	17.46	76.60	0.23	0.05
III	DP	WB7	WB7-46	419.51	7.41	0.29	4.65	24.27	90.00	29.89	63.10	0.16	0.03
III	DP	WB13	WB13-2	309.25	6.30	0.09	4.81	19.99	90.00	24.22	68.20	0.16	0.04
Average					8.83	0.18	2.55	14.16	88.86	26.22	65.66	0.37	0.06

Notes: SP, single peak; DP, double peak; ϕ, porosity; k, permeability; P_d, displacement pressure; P_m, median pressure; S_{max}, maximum mercury saturation; W_e, mercury withdrawal efficiency; S_r, residual mercury saturation; r_{max}, maximum pore throat radius; r_m, median pore throat radius.

(Wang L. et al., 2018; Zhou et al., 2021). The more concentrated the distribution of throat size, the better the sorting, the longer the flat section in the middle of the capillary pressure curve, and the closer it is to parallel with the abscissa (Yang and Fu., 2012).

Moreover, the distribution interval and distribution shape of pore throat radius represent the proportion of the corresponding pore throat radius and strength of seepage capacity, respectively, and the pore structures represented by different peak shapes are also different (Yang et al., 2017). A single peak indicates that the pore type is relatively single, such as intergranular dissolution pores, intragranular dissolution pores, residual intergranular pores, or microcracks. The double peaks indicate that there are two main pore types combined, which together control the storage and permeability of the rock (Wang et al., 2017; Zhong, 2017; Wang R. et al., 2018). Due to the differences in the dominant pore type, the reservoir and percolation capacities of single peak–type or double peak–type reservoirs are also different.

The pore throat distribution of the Chang 3 Member reservoir is in the form of single peak and double peak, and double peak is dominant, with double peak samples accounting for 74% (**Figure 7**). A single peak–type pore throat distribution represents a single pore–type reservoir. The pore types of the single peak samples are mainly intergranular or intragranular dissolution, and the pore throat sorting is better and the average sorting coefficient is low (0.86). When the pore throat distribution is bimodal, it means that

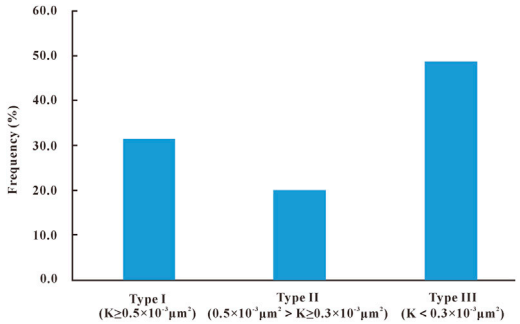

FIGURE 5 | Division of reservoir types in the Chang 3 Member.

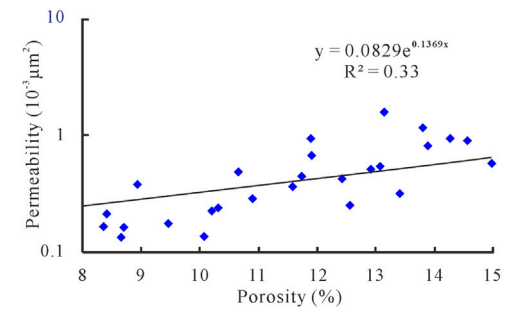

FIGURE 6 | Relationship between porosity and permeability of the tight sandstone samples in the Chang 3 Member.

the Chang 3 reservoir mainly develops pore throat spaces with two pore diameter ranges. This type of reservoir mainly develops intergranular and intragranular dissolution pores, which are poorly sorted and have a high average sorting coefficient (1.44). In addition, the average petrophysical properties of the double peak samples are worse than those of the single peak samples, indicating that tight reservoirs with a single pore type have better petrophysical properties.

Comparing the typical capillary pressure curves of the abovementioned three types of samples (**Figure 8**), it can be found that the capillary curves of the samples of Types I, II, and III are getting more and more smoother, indicating that the sorting of pore throats is gradually getting better. The sorting coefficients corresponding to these three types of reservoirs also decreased gradually from 0.3427 to 0.1018. That is, the smaller the pore throat sorting coefficient (the better the sorting), the worse the petrophysical properties of the samples. In addition, with the gradual improvement of the sorting properties of the samples, the pore throat radius distribution of the samples gradually changed to a single double peak shape. The double peak samples contain two pore types: intergranular and intragranular dissolution pores.

In addition, the lower limit of the pore throat radius of these three types of samples is about 0.0013 μm. However, only when the pore throat radius is greater than 0.004 μm, a certain amount of mercury exists in the pore throat. Mercury in Type I samples mainly exists in the pore throats controlled by the radius of 0.004–3.25 μm, and the permeability is the highest. Mercury in Type II samples mainly exists in the pore throats controlled by the radius of 0.004–1.3 μm, and the permeability is moderate. Mercury in Type III samples mainly exists in the pore throats controlled by the radius of 0.004–0.21 μm, and the permeability is the lowest. Samples with larger large pore throats have the best percolation performance.

Comparing the relationship among mercury injection amount, permeability contribution, and pore throat radius, it is found that as the pore throat radius decreases, the pore throat radius corresponding to the peak of permeability contribution is always larger than the pore throat radius corresponding to the

Horizon	Distribution of pore throat radius	Number of samples	Correlation diagram between mercury injection amount / permeability contribution rate and pore throat radius	Average porosity (%)	Average permeability (10^{-3}μm²)	Average sorting coefficient
Chang3	Single peak	8	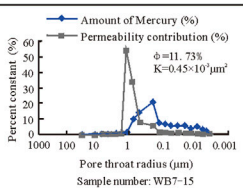	**11.04**	0.63	0.86
	Double peak	27	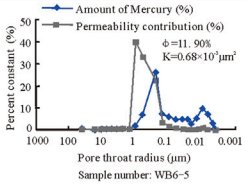	9.75	0.36	1.44

FIGURE 7 | Average of porosity, permeability, and sorting coefficient of single and double peak of the Chang 3 Member in the study area.

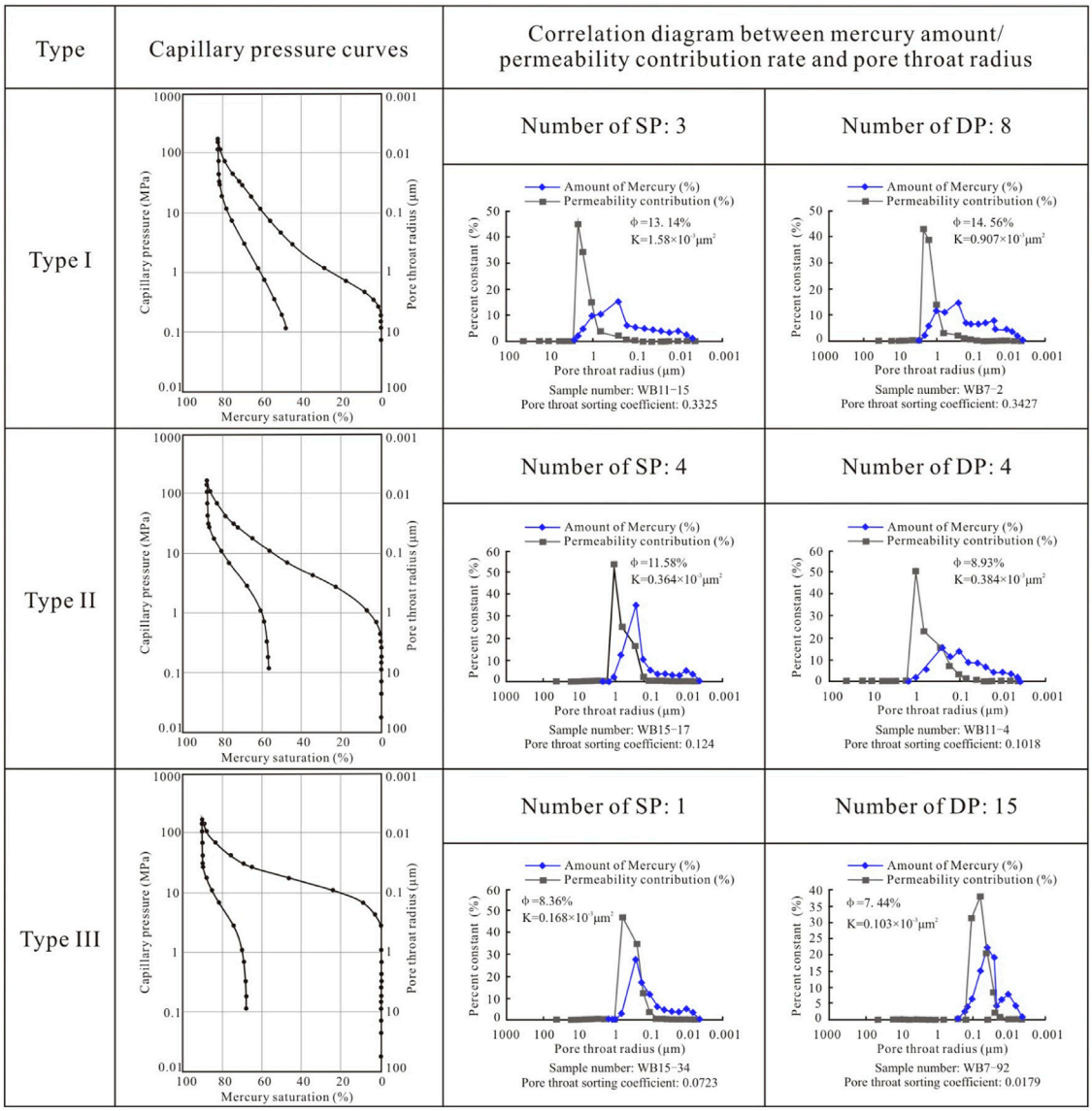

FIGURE 8 | Comparison of capillary pressure curves and mercury intrusion parameters of different types of samples in the Chang 3 Member. Notes: SP, single peak; DP, double peak.

peak mercury injection amount. Moreover, the pore throat radius covered by the peak mercury injection amount is larger. This shows that the reservoir permeability is contributed by a small part of pore throats with large radius, while the reservoir space is mainly contributed by a large number of pores connected with small throats.

5.2 Correlation Between Characteristic Parameters of Pore Structure and Petrophysical Properties

In this study, the high-pressure mercury intrusion experiments were used to obtain not only the petrophysical properties and pore throat structure parameters of the reservoir but also parameters such as structure coefficient and geometric factor (**Table 3**). Among them, the microscopic homogeneity coefficient represents the concentration degree of pore throats, and the pore structure coefficient represents the detour degree of fluid seepage in the pores. The larger the pore structure coefficient, the stronger the degree of bending and tortuousness of the pores (Zhong, 2017; Ren et al., 2019; Liu et al., 2020). Mercury injection and withdrawal tortuosity reflect the tortuosity of the pore throat morphology experienced by the nonwetting phase (mercury) when it enters and exits the cores, respectively (Song and Kovscek., 2016; Zhu et al., 2018; Shi et al., 2019). From the range of these characteristic parameters

TABLE 3 | Characteristic parameters of pore structures of the Chang 3 reservoirs.

Pore throat structure characteristic parameters	Chang 3 member		
	Minimum	Average	Maximum
Porosity (%)	2.20	10.18	14.97
Permeability ($10^{-3}\mu m^2$)	0.09	0.44	1.58
Pore throat radius corresponding to the maximum permeability contribution rate (μm)	0.10	0.45	1.60
Pore throat radius corresponding to the maximum mercury injection (μm)	0.04	0.18	0.25
Mercury injection tortuosity	0.30	1.20	2.93
Mercury withdrawal tortuosity	0.88	3.38	5.89
Relative sorting coefficient	0.77	1.01	1.41
Geometric factor	0.28	0.46	0.67
Maximum pore throat radius (μm)	0.12	0.71	2.17
Average pore throat radius (μm)	0.03	0.10	0.31
Median pore throat radius (μm)	0.02	0.09	0.25
Sorting coefficient	0.02	0.09	0.34
Displacement pressure (MPa)	0.35	1.88	6.42
Microscopic homogeneity coefficient	0.07	0.14	0.19
Pore structure coefficient	0.44	6.09	38.90

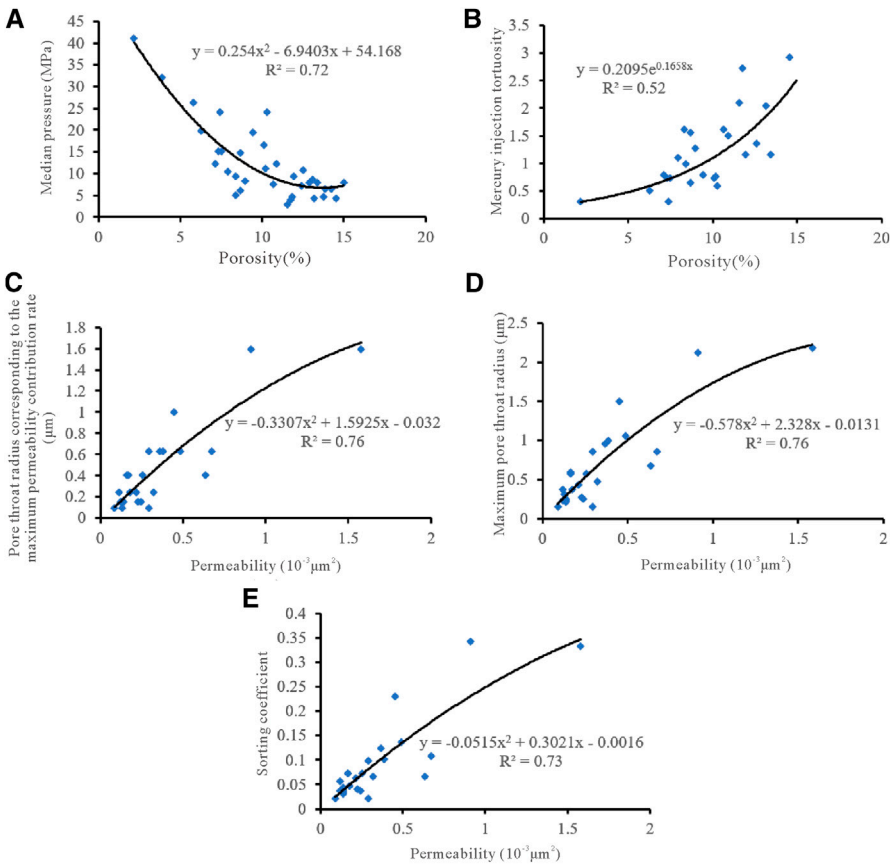

FIGURE 9 | Relationship between petrophysical properties and characteristic parameters of the pore structure of tight sandstone reservoirs in the Chang 3 Member.

and the relationship between the mercury injection amount/permeability contribution value and pore throat distribution (**Figures 7**, **8**), it can be found that due to the severe densification of the Chang 3 reservoir, the pore structure parameters are not much different, so the reservoir has good sorting. Because the pore throat radius tends to be small as a

whole, the number of effective throats in the reservoir is relatively small. The permeability of tight sandstone reservoirs is mainly contributed by a small fraction of larger pore throats. Ultimately, it is difficult for mercury to enter into the core and even more difficult to exit the core (the tortuosity of mercury withdrawal is greater than that of mercury injection).

From the correlation between the characteristic parameters of the pore structure of the Chang 3 Member and the petrophysical properties, it is found that the characteristic parameters of the pore structure that have a good correlation with the petrophysical properties include median pressure, mercury injection tortuosity, pore throat radius corresponding to the maximum permeability contribution rate, maximum pore throat radius, and sorting coefficient. Among them, the porosity is negatively and positively correlated with the median pressure and mercury injection tortuosity, respectively (**Figure 9**). This is because when the pore throat space is small, the capillary resistance is large, and the median pressure is also large. Mercury injection tortuosity reflects the degree of tortuosity of the pore throat morphology experienced by the nonwetting phase (mercury) when entering the core. When the tortuosity of mercury injection is large to a certain extent, the connectivity of pore throats will be impaired, but the increase of pore space will not be affected. The pore throat radius, maximum pore throat radius, and sorting coefficient corresponding to the maximum permeability contribution rate are positively correlated with the permeability (**Figure 9**). This is because the larger pore throat radius corresponding to the maximum permeability contribution rate and larger maximum pore throat radius are beneficial to the fluid flow in the pore throat space. The larger the sorting coefficient, the higher the probability of pore throats with larger radius and the higher the rock permeability.

6 CONCLUSION

1) In this study, taking the Chang 3 Member of Weibei Oilfield, Ordos Basin, China as an example, the microscopic mechanism of the difference in petrophysical properties of tight sandstone reservoirs was systematically studied by thin section observation, scanning electron microscope, whole-rock X-ray diffraction, and high-pressure mercury intrusion experiments.
2) The reservoir types of the Chang 3 Member are mainly feldspar lithic sandstone and lithic feldspar sandstone; the pore types include intergranular, intragranular dissolution pores, and a small amount of residual intergranular pores. Taking the permeability of 0.3×10^{-3} and 0.5×10^{-3} μm^2 as the boundary, we divided the samples involved in high-pressure mercury intrusion into three categories according to the permeability from high to low: Type I, Type II, and Type III. Their proportions were 31.4, 20.0, and 48.6%, respectively. Analysis of the three types of samples of high-pressure mercury injection data found that the smaller the sorting coefficient (sorting coefficient, the better, pore throat radius were similar to each other, the greater pore throat radius of low probability), sample properties, mercury injection dense sandstone core to overcome larger capillary force (expulsion pressure), and mercury withdrawal when residual mercury saturation is larger.
3) The study found that the smaller the sorting coefficient, the poorer the petrophysical properties of the samples and the pore throat distribution of different samples gradually changed to a uniform double peak–dominated type.
4) The permeability of tight sandstone reservoirs is contributed by a small part of pore throats with large radius, while the reservoir space is mainly contributed by a large number of pores connected with small throats. The porosity is negatively and positively correlated with the median pressure and mercury injection tortuosity, respectively. In addition, the pore throat radius corresponding to the maximum permeability contribution rate, maximum pore throat radius, and sorting coefficient are all positively correlated with the permeability. In general, the areas with larger pore throat radius, lower pore throat tortuosity, and larger pore throat sorting coefficient can be regarded as favorable areas for Chang 3 tight sandstone reservoirs.

DATA AVAILABILITY STATEMENT

The original contributions presented in the study are included in the article/Supplementary Material, further inquiries can be directed to the corresponding authors.

AUTHOR CONTRIBUTIONS

YT and JL contributed to the method and writing of the manuscript. HD, ST, DM, NZ, and MW contributed to experiments.

FUNDING

This research was supported by the PetroChina Innovation Foundation (No. 2020D-5007-0202), the Opening Foundation of Provincial and Ministerial Key Laboratory of China University of Geosciences (Beijing) (No. 20210102), the Natural Science Basic Research Plan in Shaanxi Province of China (No. 2021JQ-598), and the National Natural Science Foundation of China (No. 52104031).

REFERENCES

Askarinezhad, R. (2010). A New Statistical Approach to Pore/throat Size Distribution of Porous media Using Capillary Pressure Distribution Concept. *J. Pet. Sci. Eng.* 75 (1-2), 100–104. doi:10.1016/j.petrol.2010.10.011

Barsotti, E., Tan, S. P., Saraji, S., Piri, M., and Chen, J.-H. (2016). A Review on Capillary Condensation in Nanoporous media: Implications for Hydrocarbon Recovery from Tight Reservoirs. *Fuel* 184, 344–361. doi:10.1016/j.fuel.2016.06.123

Bukar, M., Worden, R. H., Bukar, S., and Shell, P. (2021). Diagenesis and its Controls on Reservoir Quality of the Tambar Oil Field, Norwegian North Sea. *Energ. Geosci.* 2 (1), 10–31. doi:10.1016/j.engeos.2020.07.002

Chen, G. B., Li, T., Yang, L., Zhang, G. H., Li, J. W., and Dong, H. J. (2021). Mechanical Properties and Failure Mechanism of Combined Bodies with Different Coal-Rock Ratios and Combinations. *J. Mining Strata Control. Eng.* 3 (2), 023522. doi:10.13532/j.jmsce.cn10-1638/td.20210108.001

Cui, J., Zhu, R., Mao, Z., and Li, S. (2019). Accumulation of Unconventional Petroleum Resources and Their Coexistence Characteristics in Chang7 Shale Formations of Ordos Basin in central China. *Front. Earth Sci.* 13 (3), 575–587. doi:10.1007/s11707-019-0756-x

Dai, Q., Luo, Q., Chen, Z., Lu, C., Zhang, Y., Lu, S., et al. (2016). Pore Structure Characteristics of Tight-Oil sandstone Reservoir Based on a New Parameter Measured by NMR experiment: A Case Study of Seventh Member in Yanchang Formation, Ordos Basin. *Acta Petrolei Sinica* 37 (7), 887–897. doi:10.7623/syxb201607007

Ding, F., Xie, C., Zhou, X., Jiang, C., Li, K., Wan, L., et al. (2021). Defining Stratigraphic Oil and Gas Plays by Modifying Structural Plays: A Case Study from the Xihu Sag, east China Sea Shelf Basin. *Energ. Geosci.* 2 (1), 41–51. doi:10.1016/j.engeos.2020.08.002

Dong, S., Zeng, L., Lyu, W., Xia, D., Liu, G., Wu, Y., et al. (2020). Fracture Identification and Evaluation Using Conventional Logs in Tight Sandstones: A Case Study in the Ordos Basin, China. *Energ. Geosci.* 1 (3–4), 115–123. doi:10.1016/j.engeos.2020.06.003

Fan, C., Li, H., Qin, Q., Shang, L., Yuan, Y., and Li, Z. (2020). Formation Mechanisms and Distribution of Weathered Volcanic Reservoirs: A Case Study of the Carboniferous Volcanic Rocks in Northwest Junggar Basin, China. *Energy Sci. Eng.* 8 (8), 2841–2858. doi:10.1002/ese3.702

Fan, C., Zhong, C., Zhang, Y., Qin, Q., and He, S. (2019). Geological Factors Controlling the Accumulation and High Yield of Marine-Facies Shale Gas: Case Study of the Wufeng-Longmaxi Formation in the Dingshan Area of Southeast Sichuan, China. *Acta Geologica Sinica - English Edition* 93 (3), 536–560. doi:10.1111/1755-6724.13857

Gao, H., Xie, W., Yang, J., Zhang, C., and Sun, W. (2011). Pore Throat Characteristics of Extra -ultra Low Permeability sandstone Reservoir Based on Constant-Rate Mercury Penetration Technique. *Pet. Geology. Exp.* 33, 206–214. doi:10.1007/s12182-011-0123-3

Gier, S., Worden, R. H., Johns, W. D., and Kurzweil, H. (2008). Diagenesis and Reservoir Quality of Miocene Sandstones in the Vienna Basin, Austria. *Mar. Pet. Geology.* 25 (8), 681–695. doi:10.1016/j.marpetgeo.2008.06.001

Hong, D., Cao, J., Wu, T., Dang, S., Hu, W., and Yao, S. (2020). Authigenic clay Minerals and Calcite Dissolution Influence Reservoir Quality in Tight Sandstones: Insights from the central Junggar Basin, NW China. *Energ. Geosci.* 1 (1–2), 8–19. doi:10.1016/j.engeos.2020.03.001

Hower, J. C., and Groppo, J. G. (2021). Rare Earth-Bearing Particles in Fly Ash Carbons: Examples from the Combustion of Eastern Kentucky Coals. *Energ. Geosci.* 2 (2), 90–98. doi:10.1016/j.engeos.2020.09.003

Jia, C., Zou, C., Li, J., Li, D., and Zheng, M. (2012). Assessment Criteria, Main Types, Basic Features and Resource Prospects of the Tight Oil in China. *Acta Petrolei Sinica* 33 (3), 343–350. doi:10.1016/0031-9384(73)90235-7

Kwak, D., Han, S., Han, J., Wang, J., Lee, J., and Lee, Y. (2018). An Experimental Study on the Pore Characteristics Alteration of Carbonate during Waterflooding. *J. Pet. Sci. Eng.* 161, 349–358. doi:10.1016/j.petrol.2017.11.051

Lan, S. R., Song, D. Z., Li, Z. L., and Liu, Y. (2021). Experimental Study on Acoustic Emission Characteristics of Fault Slip Process Based on Damage Factor. *J. Mining Strata Control. Eng.* 3 (3), 023038. doi:10.13532/j.jmsce.cn10-1638/td.20210510.002

Li, G., Qin, Y., Shen, J., Wu, M., Li, C., Wei, K., et al. (2019). Geochemical Characteristics of Tight sandstone Gas and Hydrocarbon Charging History of Linxing Area in Ordos Basin, China. *J. Pet. Sci. Eng.* 177, 198–207. doi:10.1016/j.petrol.2019.02.023

Li, H., Li, Y., Chen, S., Guo, J., Wang, K., and Luo, H. (2016). Effects of Chemical Additives on Dynamic Capillary Pressure during Waterflooding in Low Permeability Reservoirs. *Energy Fuels* 30 (9), 7082–7093. doi:10.1021/acs.energyfuels.6b01272

Li, Y., Zhou, D., Wang, W., Jiang, T., and Xue, Z. (2020). Development of Unconventional Gas and Technologies Adopted in China. *Energ. Geosci.* 1 (1–2), 55–68. doi:10.1016/j.engeos.2020.04.004

Liu, Y., Gao, M., and Zhao, H. (2020). Detection of Overlying Rock Structure and Identification of Key Stratum by Drilling and Logging Technology. *J. Mining Strata Control. Eng.* 2 (2), 81–89. doi:10.13532/j.jmsce.cn10-1638/td.2020.02.004

Mahmud, H. B., Bin Muhammad Hisham, M. H., Mahmud, W. M., Leong, V. H., and Shafiq, M. U. (2020). Petrophysical Interpretations of Subsurface Stratigraphic Correlations, Baram Delta, Sarawak, Malaysia. *Energ. Geosci.* 1 (3–4), 100–114. doi:10.1016/j.engeos.2020.04.005

Mirzaei-Paiaman, A., and Ghanbarian, B. (2021). A New Methodology for Grouping and Averaging Capillary Pressure Curves for Reservoir Models. *Energ. Geosci.* 2 (1), 52–62. doi:10.1016/j.engeos.2020.09.001

Nabawy, B. S., Géraud, Y., Rochette, P., and Bur, N. (2009). Pore-throat Characterization in Highly Porous and Permeable Sandstones. *Bulletin* 93 (6), 719–739. doi:10.1306/03160908131

Nelson, P. H. (2009). Pore-throat Sizes in Sandstones, Tight Sandstones, and Shales. *Bulletin* 93 (3), 329–340. doi:10.1306/10240808059

Qiao, J., Zeng, J., Jiang, S., and Wang, Y. (2020). Impacts of Sedimentology and Diagenesis on Pore Structure and Reservoir Quality in Tight Oil sandstone Reservoirs: Implications for Macroscopic and Microscopic Heterogeneities. *Mar. Pet. Geology.* 111, 279–300. doi:10.1016/j.marpetgeo.2019.08.008

Qie, L., Shi, Y. N., and Liu, J. S. (2021). Experimental Study on Grouting Diffusion of Gangue Solid Filling Bulk Materials. *J. Mining Strata Control. Eng.* 3 (2), 023011. doi:10.13532/j.jmsce.cn10-1638/td.20201111.001

Ren, D., Zhou, D., Liu, D., Dong, F., Ma, S., and Huang, H. (2019). Formation Mechanism of the Upper Triassic Yanchang Formation Tight sandstone Reservoir in Ordos Basin-Take Chang 6 Reservoir in Jiyuan Oil Field as an Example. *J. Pet. Sci. Eng.* 178, 497–505. doi:10.1016/j.petrol.2019.03.021

Ryazanov, A. V., Sorbie, K. S., and van Dijke, M. I. J. (2014). Structure of Residual Oil as a Function of Wettability Using Pore-Network Modelling. *Adv. Water Resour.* 63, 11–21. doi:10.1016/j.advwatres.2013.09.012

Santosh, M., and Feng, Z. Q. (2020). New Horizons in Energy Geoscience. *Energ. Geosci.* 1 (1–2), A1. doi:10.1016/j.engeos.2020.05.005

Shi, B., Chang, X., Yin, W., Li, Y., and Mao, L. (2019). Quantitative Evaluation Model for Tight sandstone Reservoirs Based on Statistical Methods - A Case Study of the Triassic Chang 8 Tight Sandstones, Zhenjing Area, Ordos Basin, China. *J. Pet. Sci. Eng.* 173, 601–616. doi:10.1016/j.petrol.2018.10.035

Song, W., and Kovscek, A. R. (2016). Direct Visualization of Pore-Scale Fines Migration and Formation Damage during Low-Salinity Waterflooding. *J. Nat. Gas Sci. Eng.* 34, 1276–1283. doi:10.1016/j.jngse.2016.07.055

Sun, W., and Tang, G. Q. (2006). Visual Study of Water Injection in Low Permeable sandstone. *J. Can. Pet. Techn.* 45 (11), 21–26. doi:10.2118/06-11-02

Wang, A., Zhong, D., Zhu, H., Guo, L., Li, Z., Jiang, Y., et al. (2018a). Depositional and Diagenetic Controls on the Reservoir Quality of Upper Triassic Chang-7 Tight Oil Sandstones, Southwestern Ordos basin, China. *Geosci. J.* 23 (3), 471–488. doi:10.1007/s12303-018-0042-z

Wang, E., Liu, G., Pang, X., Wu, Z., Li, C., Bai, H., et al. (2020). Sedimentology, Diagenetic Evolution, and Sweet Spot Prediction of Tight sandstone Reservoirs: A Case Study of the Third Member of the Upper Paleogene Shahejie Formation, Nanpu Sag, Bohai Bay Basin, China. *J. Pet. Sci. Eng.* 186, 106718. doi:10.1016/j.petrol.2019.106718

Wang, J., and Wang, X. L. (2021). Seepage Characteristic and Fracture Development of Protected Seam Caused by Mining Protecting Strata. *J. Mining Strata Control. Eng.* 3 (3), 033511. doi:10.13532/j.jmsce.cn10-1638/td.20201215.001

Wang, L., Zhao, N., Sima, L., Meng, F., and Guo, Y. (2018b). Pore Structure Characterization of the Tight Reservoir: Systematic Integration of Mercury

Injection and Nuclear Magnetic Resonance. *Energy Fuels* 32 (7), 7471–7484. doi:10.1021/acs.energyfuels.8b01369

Wang, R., Chi, Y., Zhang, L., He, R., Tang, Z., and Liu, Z. (2018c). Comparative Studies of Microscopic Pore Throat Characteristics of Unconventional Superlow Permeability sandstone Reservoirs: Examples of Chang 6 and Chang 8 Reservoirs of Yanchang Formation in Ordos Basin, China. *J. Pet. Sci. Eng.* 160, 72–90. doi:10.1016/j.petrol.2017.10.030

Wang, R. (2008). *Microscopic Characteristics of Ultra-low Permeability sandstone Reservoir*. Beijing: Petroleum Industry Press.

Wang, R., Xu, G., Wu, X., Liu, Z., and Chi, Y. (2017). Comparative Studies of Three Nonfractured Unconventional Sandstone Reservoirs with Superlow Permeability: Examples of the Upper Triassic Yanchang Formation in the Ordos Basin, China. *Energy Fuels* 31 (1), 107–118. doi:10.1021/acs.energyfuels.6b01616

Wang, S. L., Li, H., Lin, L. F., and Yin, S. (2022). Development Characteristics and Finite Element Simulation of Fractures in Tight Oil Sandstone Reservoirs of Yanchang Formation in Western Ordos Basin. *Front. Earth Sci.* 9, 1–10. doi:10.3389/feart.2021.823855

Xue, F., Liu, X. X., and Wang, T. Z. (2021). Research on Anchoring Effect of Jointed Rock Mass Based on 3D Printing and Digital Speckle Technology. *J. Mining Strata Control. Eng.* 3 (2), 023013. doi:10.13532/j.jmsce.cn10-1638/td.20201020.001

Yang, H., and Fu, J. (2012). *Exploration Theory and Technology for Ultra-low Permeability Reservoirs*. Beijing: Petroleum Industry Press.

Yang, H., Liang, X., Niu, X., Feng, S., and You, Y. (2017). Geological Conditions for continental Tight Oil Formation and the Main Controlling Factors for the Enrichment: A Case of Chang7 Member, Triassic Yanchang Formation, Ordos Basin, NW China. *Pet. Exploration Dev.* 44 (1), 12–20. doi:10.1016/S1876-3804(17)30003-4

Yang, J. X., Luo, M. K., Zhang, X. W., Huang, N., and Hou, S. J. (2021). Mechanical Properties and Fatigue Damage Evolution of Granite under Cyclic Loading and Unloading Conditions. *J. Mining Strata Control. Eng.* 3 (3), 033016. doi:10.13532/j.jmsce.cn10-1638/td.20210510.001

Yin, S., and Ding, W. (2019). Evaluation Indexes of Coalbed Methane Accumulation in the strong Deformed Strike-Slip Fault Zone Considering Tectonics and Fractures: A 3D Geomechanical Simulation Study. *Geol. Mag.* 156 (6), 1052–1068. doi:10.1017/s0016756818000456

Yin, S., Dong, L., Yang, X., and Wang, R. (2020b). Experimental Investigation of the Petrophysical Properties, Minerals, Elements and Pore Structures in Tight Sandstones. *J. Nat. Gas Sci. Eng.* 76 (1), 103189–103214. doi:10.1016/j.jngse.2020.103189

Yin, S., Lv, D., and Ding, W. (2018). New Method for Assessing Microfracture Stress Sensitivity in Tight sandstone Reservoirs Based on Acoustic Experiments. *Int. J. Geomechanics* 18 (4), 1–11. doi:10.1061/(ASCE)GM.1943-5622.0001100

Yin, S., Tian, T., Wu, Z., and Li, Q. (2020a). Developmental Characteristics and Distribution Law of Fractures in a Tight sandstone Reservoir in a Low-amplitude Tectonic Zone, Eastern Ordos Basin, China. *Geol. J.* 55 (2), 1546–1562. doi:10.1002/gj.3521

Yin, S., and Wu, Z. (2020). Geomechanical Simulation of Low-Order Fracture of Tight sandstone. *Mar. Pet. Geology.* 117, 104359–104410. doi:10.1016/j.marpetgeo.2020.104359

Yoshida, M., and Santosh, M. (2020). Energetics of the Solid Earth: An Integrated Perspective. *Energ. Geosci.* 1 (1–2), 28–35. doi:10.1016/j.engeos.2020.04.001

Zhang, B., Shen, B., and Zhang, J. (2020). Experimental Study of Edge-Opened Cracks Propagation in Rock-like Materials. *J. Mining Strata Control. Eng.* 2 (3), 033035. doi:10.13532/j.jmsce.cn10-1638/td.20200313.001

Zhang, J., Ju, Y., and Zhang, Q. (2019). Low Ecological Environment Damage Technology and Method in Coal Mines. *J. Mining Strata Control. Eng.* 1 (1), 013515. doi:10.13532/j.jmsce.cn10-1638/td.2019.02.005

Zhong, D. (2017). Micro-petrology, Pore Throat Characteristics and Genetic Mechanism of Tight Oil Reservoirs – A Case from the 6^{th} and 7^{th} Members of Triassic Yanchang Formation in the Ordos Basin. *Oil Gas Geology.* 38 (1), 49–61. doi:10.11743/ogg20170106

Zhou, N., Lu, S., Wang, M., Huang, W., Xiao, D., Jiao, C., et al. (2021). Limits and Grading Evaluation Criteria of Tight Oil Reservoirs in Typical continental Basins of China. *Pet. Exploration Dev.* 48 (5), 1089–1100. doi:10.1016/S1876-3804(21)60093-9

Zhu, H., Zhong, D., Zhang, T., Liu, G., Yao, J., and He, C. (2018). Diagenetic Controls on the Reservoir Quality of fine-grained "tight" Sandstones: a Case Study Based on NMR Analysis. *Energy Fuels* 32 (2), 1612–1623. doi:10.1021/acs.energyfuels.7b03734

Zuo, J., Yu, M., and Hu, S. (2019). Experimental Investigation on Fracture Mode of Different Thick Rock Strata. *J. Mining Strata Control. Eng.* 1 (1), 013007. doi:10.13532/j.jmsce.cn10-1638/td.2019.02.008

Conflict of Interest: Author JL was employed by the Exploration Department of PetroChina Changqing Oilfield Company.

The authors declare that the research was conducted in the absence of any commercial or financial relationships that could be construed as a potential conflict of interest.

frontiers | Frontiers in Earth Science

ORIGINAL RESEARCH
published: 08 April 2022
doi: 10.3389/feart.2022.865355

Characteristics, Main Controlling Factors and Prediction of Complex Fracture–Cavity Reservoirs of Buried Carbonate Hills in the Weixinan Depression, Western South China Sea

Chong Zhang[1,2]*, *Wen Zhou*[1]*, *Chang Liu*[3], *Xinguang Wang*[2] and *Hao Xu*[1]*

[1]College of Energy, Chengdu University of Technology, Chengdu, China, [2]CNOOC China Limited, Hainan Branch, Haikou, China, [3]CNOOC Research Institute Limited, Beijing, China

Buried hill oil reservoirs have become a key area for offshore oil and gas exploration. In this paper, a typical oil field in the western South China Sea is used as the research object, and a study on the characterization, cause of formation and prediction of the fracture–cavity reservoir distribution is carried out. The reservoir in the study area is a complex fracture–cavity reservoir that developed due to weathering and leaching, tectonic movement and dissolution reconstruction on the limestone skeleton. The reservoir spaces are composed of karst caves, fractures and pores. The main controlling factors include lithological changes, karst landforms, tectonic deformation and faulting. To address the controlling mechanisms of the lithological changes on the formation of fracture–cavity reservoirs, a new parameter, the lithology standard deviation, to evaluate lithological changes is proposed based on the characteristics of the lithological changes, and the distribution of these lithological changes is portrayed in combination with the seismic attributes. The tectonic deformation principal curvature inversion algorithm is used to simulate the distribution of the tectonic principal curvature at the top of the Carboniferous. The larger the tectonic principal curvature is, the stronger the deformation of the rock formation and the more favorable the conditions are for fracture formation. The karst geomorphology controls the overall reservoir distribution, and the karst highlands and karst slope areas are the zones with the most–developed secondary pore space (or fractures and karst caves). The faulting control area is the fracture and dissolution pore development area, major faults control the distribution of the karst cave reservoirs, and secondary faults influence the formation of fractures in the faulted area. The study predicts and evaluates the distribution of fracture–cavity reservoirs from the perspective of fracture–cavity genesis quantification, and by gridding and normalizing the four major genesis quantification evaluation parameters and fusing the geological factors that control the formation of fractures and karst caves by using Back–Propagation neural network deep learning algorithms, a method for predicting the distribution of fracture–cavity reservoirs constrained by geological genesis analysis is developed.

Keywords: fracture-cavity reservoirs, carbonate, buried hill, main controlling factors, distribution prediction, weixinan depression

OPEN ACCESS

Edited by:
Shuai Yin,
Xi'an Shiyou University, China

Reviewed by:
Xie Runcheng,
Chengdu University of Technology, China
Kesai Li,
Chengdu University of Technology, China
Wenlong Ding,
China University of Geosciences, China
Qilin Wu,
Guangdong University of Petrochemical Technology, China

***Correspondence:**
Chong Zhang
zchlsqw@163.com
Wen Zhou
zhouw62@cdut.edu.cn
Hao Xu
haoxu777@qq.com

Specialty section:
This article was submitted to Structural Geology and Tectonics, a section of the journal Frontiers in Earth Science

Received: *29 January 2022*
Accepted: *25 February 2022*
Published: *08 April 2022*

Citation:
Zhang C, Zhou W, Liu C, Wang X and Xu H (2022) Characteristics, Main Controlling Factors and Prediction of Complex Fracture–Cavity Reservoirs of Buried Carbonate Hills in the Weixinan Depression, Western South China Sea. Front. Earth Sci. 10:865355. doi: 10.3389/feart.2022.865355

INTRODUCTION

Buried hill reservoirs have become key areas for offshore oil and gas exploration in recent years and have very high resource potential (Lu and Cai., 2010; Du et al., 2011). As exploration progresses, the exploration potential for tectonic reservoirs, such as anticlines and fault blocks, decreases (Jiang et al., 2014; Yin et al., 2018a; Yin et al., 2018b; Guo et al., 2020; Kang, 2020; Santosh and Feng., 2020; Chen et al., 2021). The buried carbonate hills in the Beibuwan Basin and buried granite hills in the deep water area of the Qiongdongnan Basin are gradually highlighted by their high resource potential as the focus of future oil and gas research in the western South China Sea (Yang, 2016; Zhao et al., 2019; Li et al., 2020; Xue et al., 2021).

The Weixinan Depression is located in the most hydrocarbon–rich depression that is indicated in the Beibuwan Basin of the western South China Sea (Ma et al., 2014; Li et al., 2015). The buried carbonate hills are mainly located between two major faults within the depression, and the current level of exploration is relatively low. However, drilling has revealed active oil and gas displays in the area (Zhang et al., 2015), with high tested production amounts per well (up to thousands of cubic meters per day).

Several buried carbonate hill reservoirs or oil–bearing formations have been discovered in the area, which demonstrate that the area has broad exploration and development prospects in the buried–hill field (Zhao et al., 2018). At present, several buried carbonate hill reservoirs or oil–bearing structures have been found in this area, which indicate that this area has broad prospects for the exploration and development of buried hills.

The buried carbonate hills in the Weixinan Depression consist of a set of thick light gray microcrystalline–fine grained carbonate strata. The Weizhou 1–N oilfield is a representative buried–hill carbonate reservoir in the Weixinan Depression (**Figure 1**). During the drilling process, most wells experienced mud and sea water loss and drilling tool cavitation, which indicate that buried–hill fractures and karst caves are well developed in this area. The oilfield has a high production capacity, but the reservoir distribution is extremely complex. Only five out of 11 wells obtained industrial oil flows, and the results of the later adjustment wells did not reach expectations. This occurred mainly because the distributions of fractures and karst caves are complex, and the development of fracture–cavity reservoirs is highly random. The formation of fracture–cavity reservoirs is controlled by factors such as lithology, tectonic movement, weathering and denudation time, paleoclimate and paleolandscape location in the area where buried hills developed. Even in the same area, the fracture cavity development characteristics of the drilled wells are not consistent, which make it difficult to predict the quality of reservoirs. The development of seam holes is the key to the formation of high–quality reservoirs. Understanding the development characteristics and formation mechanisms of

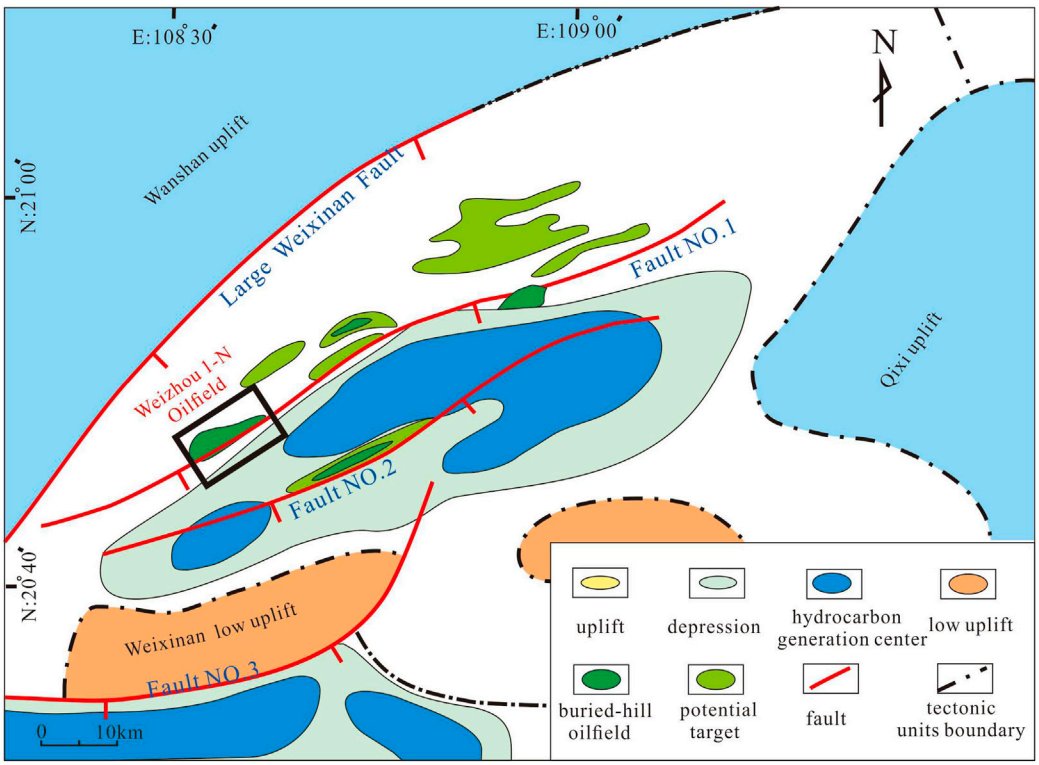

FIGURE 1 | Buried–hill distribution and tectonic location of the Weizhou 1–N oilfield in the Weixinan Depression.

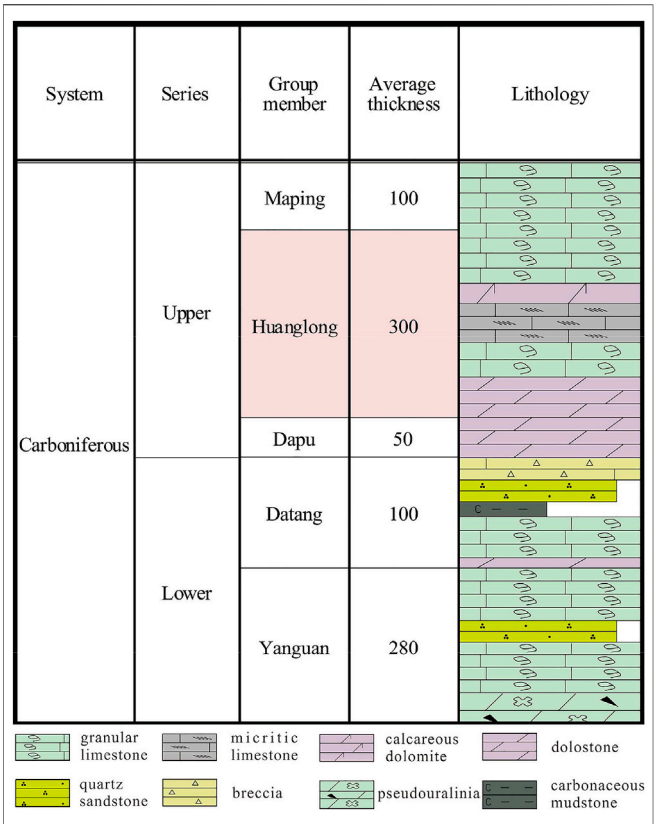

FIGURE 2 | Stratigraphic and lithology profiles of the Carboniferous strata in the Weixinan Depression.

seam holes in this area is an important basis for understanding the development law of high–quality reservoirs in buried carbonate hills (Yan, 2002; Xiao J et al., 2003), which is of great significance to the development and adjustment of buried carbonate hills in the Weixinan Depression.

GEOLOGICAL SETTING

The buried hill in the Weixinan Depression is mainly composed of marine Carbon–iferous strata (Xiao J et al., 2003). After the Carboniferous deposition, the area mainly experienced three major tectonic cycles, including the Indosinian tectonic movement, Yanshan and Himalayan Movement (Zhao et al., 2018). In the late Hercynian Movement, the Carboniferous strata were uplifted and exposed at the surface and were altered by weathering and formed carbonate weathering crust reservoirs. During the Indosinian and Yanshan Movements, a series of large NE–trending faults were generated, and the Weixinan large fault succession resulted in a series of NE–trending extensional faults (Tong et al., 2018), of which fault No. One was one, which thus formed the rudimentary shape of the current buried hill. In the third stage of the Himalayan movement, the buried hill was formed, the Beibuwan Basin also entered a depression development stage from a fault depression stage, and the strata changed from a differential uplift movement to large–area subsidence movement stage (Li, 2012; Sun et al., 2014; Gan et al., 2017).

The buried hill of the Weizhou 1–N oilfield limestone is located on the upthrown side of the No. One fault in the northern Weixinan Depression, which consists of an uplifted basement and ancient buried–hill trap that were buried after denudation. The relatively high part of the structure developed in a zonal pattern from southwest to northwest, the buried–hill shape is complete, and the buried hill is distributed in a northeast direction along fault No. 1 (**Figure 1**). The target strata were reached by each well in the Carboniferous Huangliu Formation, and the lithologies mainly consist of light gray and gray granular biological limestone, micritic biological limestone, and calcareous silt–crystal dolomite (**Figure 2**). From the Permian to Cretaceous, the buried hill was exposed to the surface for a long period and experienced strong weathering and erosion, which created favorable conditions for the development of fractures and karst caves (Zhao et al., 2019, 2018).

MATERIALS AND METHODS

Core Description and Casting Section Identification

The core observations are based on core wells that were drilled to encounter the Carboniferous Huanglong Formation, with a total observed core length of 40.06 m and core harvest rate of 72.5%. A total of 290 cast thin sections were taken from rock chips or from the cores of four wells. Core and cast body thin section observations can clarify the lithology, filling characteristics of the small–scale fractures and cavities, fracture opening degrees, and dissolution pore development, which can be used as constraints for seam hole analyses and reservoir predictions.

Method for Characterization of Lithological Changes

The standard deviation (STD DEV) is a statistical term used in mathematics to measure the degree to which a data distribution of is scattered and quantifies the degree to which the data values deviate from the arithmetic mean (Wang, 2009; Chen et al., 2013; Mahmud et al., 2020; Qie et al., 2021). The smaller the standard deviation, the less these values deviate from the mean, and vice versa (Zhang and Song., 1981; Gu., 2006; Dong et al., 2020; Yoshida and Santosh., 2020; Wang and Wang., 2021).

From the above definition, it can be seen that the standard deviation reflects the degree of dispersion of the numerical values relative to the mean value. Therefore, this paper proposed defining a standard deviation value that reflects the dispersion degree of the single–layer thicknesses and average thicknesses of the strata in the longitudinal direction of a reservoir as the lithology standard deviation. The specific expression is as follows:

$$LSD = \sqrt{\frac{\sum\left(h_i - \bar{h}\right)^2}{N-1}} \quad (1)$$

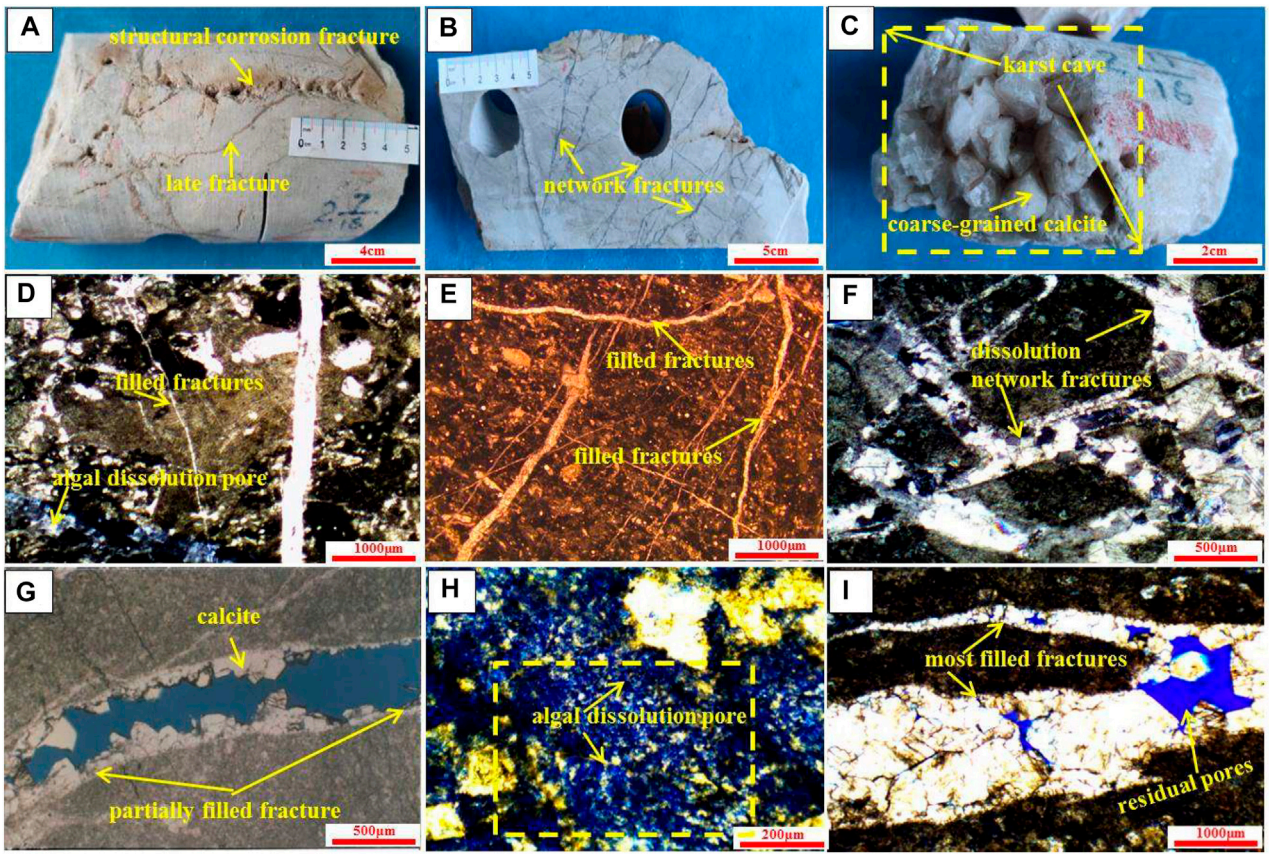

FIGURE 3 | Carbonate reservoir space characteristics in the buried hills of the Weixinan Depression. **(A)** W1–N1, 1,553 m, grainy biological limestone, and the tectonic fractures cut and restrict each other. The early fractures are filled with medium–coarse calcite, the width of the fractures is 0.4 mm, there are a few dissolution pores along the fractures, and the growth of the late fractures is restricted by the early fractures. **(B)** W1–N1, 1,554 m, grain–white biological limestone with reticulated weathering fractures, which are generally filled with fine–grained calcite. **(C)** W1–N1, 1,556 m, karst caves filled with horse–tooth–shaped giant calcite crystals, the karst cave diameter is 6 cm, and light crude oil flows out of the core. **(D)** W1–N2, 1,587 m, algal limestone, with a tectonic fracture with a width of 160 μm and several tectonic and weathering fractures with widths of less than 10 μm are all filled with sparry calcite. **(E)** W1–N3, 1,612 m, bioclastic limestone, the weathering fractures and tectonic fractures cut each other, and the fractures are filled with sparry calcite. **(F)** W1–N3, 1,615 m, bioclastic limestone with obvious recrystallization and dissolved network fractures filled with medium–coarse grain calcite with only a few residual pores. **(G)** W1–N1, 1,555.65, residual pores in the semifilled fractures with good connectivity. **(H)** W1–N3, biological algal limestone, local red algae dissolved into pores and relatively developed pores. **(I)** Well W1–N1, 1,555.8 m, bioclastic limestone with residual pores in the fractures.

where *LSD*–lithology standard deviation, dimensionless; h_i–single layer thickness, m; $\bar{h}$ – average layer thickness of a single well, m; and *N*–number of layers, layers.

The lithologies in this area change rapidly, and these lithology changes will cause differences in the thickness of a single rock layer in the formation. Therefore, the new parameter, lithology standard deviation, can be used to describe the change characteristics of the longitudinal lithology of the buried hill reservoir in this area. The smaller the lithology standard deviation is, the more dramatic the thickness changes are.

Tectonic Principal Curvature Simulation

Numerical simulations of the deformation process of rock formations by using mathematical physical methods have been used to obtain the distribution of the ancient strain field during rock deformation to evaluate the fracture development and are an important research direction in fracture research (Cao and Liu., 2008; Chen et al., 2020; Lan et al., 2021; Mirzaei-Paiaman and Ghanbarian., 2021). The simulation method using the tectonic principal curvature was first proposed by Murray, which applies the combination of trend surface analysis and the difference method to calculate the principal curvatures of tectonic surfaces by using discrete data at the tectonic level (Zhou., 1998; Yin et al., 2020a; Hong et al., 2020; Yin and Wu., 2020; Yang et al., 2021).

By mathematically describing an abstractly constructed surface as a mathematical surface, S, and by establishing a fixed reference system; then, the surface S can be uniquely determined by the Equation $z = f(x, y)$. Then, tectonic trend surface fitting was carried out for the top tectonic surface of a certain stratum (Kong et al., 2011; Liu et al., 2012; Hu, 2018; Yin et al., 2020b; Zhang et al., 2020). When the fitting degree exceeds 85%, the trend surface equation is obtained as follows:

$$f(x,y) = Ax^3 + By^3 + Cx^2y + Dxy^2 + Exy + Fx^2 + Gy^2 + Hx + Iy + J \quad (2)$$

Based on the above tectonic surface trend equation, we can calculate the principal curvature values by using the following equation:

$$1/R_{1,2} = \left(\frac{1}{r_x} + \frac{1}{r_y}\right) \pm \sqrt{\frac{1}{4}\left(\frac{1}{r_x} - \frac{1}{r_y}\right)^2 + \frac{1}{r_{xy}}} \quad (3)$$

Where:

$$\frac{1}{r_x} = \frac{\partial^2 f(x,y)}{\partial x^2},\ \frac{1}{r_y} = \frac{\partial^2 f(x,y)}{\partial y^2},\ \frac{1}{r_{xy}} = \frac{\partial^2 f(x,y)}{\partial x \partial y} \quad (4)$$

According to the calculation results, the maximum principal curvature of a point on the plane is plotted to obtain the curvature distribution, which can be used to evaluate the distribution characteristics of fractures that are caused by tectonic deformation.

Neural Network Deep Learning Method

Neural network deep learning algorithms have been widely used in various research fields (Kaba, 2018; Yin et al., 2019a; Yin et al., 2019b; Shen, 2019; Taesic et al., 2019; Zhang et al., 2019). The neural network training process generally uses a learning sample set, which is as known as the error back propagation (BP) algorithm for training, by calculating the errors between the output values and the expected values (E). If this process cannot achieve the desired outputs in the output layer, then back propagation occurs by adjusting the connection weights among the output layer, hidden layer and input layer and the values of the hidden layer and output layer until the error signal is minimized.

For the neurons that are in the input layer of the BP model, the output is the same as the input, while the calculation formula for the neurons in the hidden middle layer and for the output layer is as follows:

$$net_{Pj} = \sum_i W_{ji} O_{Pi} \quad (5)$$

$$O_{Pj} = f_j\left(net_{Pj}\right) \quad (6)$$

where p is the current input sample number, W_{ji} is the connection weight from Neuron I to Neuron J, O_{pi} is the current input of Neuron J, and O_{PJ} is its output. When the BP network uses the steepest descent method, the transformation function uses the sigmoid function. The function is expressed as follows:

$$f(x) = \frac{1}{1 + e^{-x}} \quad (7)$$

The network output error is set as follows:

$$E_P = \frac{1}{2}\sum_n \left(t_{Pj} - O_{Pj}\right)^2 \quad (8)$$

Then, the error generated by all samples in the entire training set is calculated as follows:

$$E = \sum E_P \quad (9)$$

$$\frac{\partial E_P}{\partial w_{ji}} = \frac{\partial E_P}{\partial net_{Pj}} \frac{\partial net_{Pj}}{\partial w_{ji}} \quad (10)$$

$$\frac{\partial net_{Pj}}{\partial W_{ji}} = \frac{\partial}{\partial w_{ji}} \sum_k w_{jk} O_{Pk} = O_{Pi} \quad (11)$$

$$\delta_{Pj} = -\frac{\partial E_P}{\partial net_{pj}} \quad (12)$$

$$\frac{\partial E_P}{\partial w_{ji}} = -\delta_{Pj} O_{Pj},\ \Delta_P w_{ji} = \eta \delta_j O_{Pi} \quad (13)$$

If j is the output node, then:

$$\delta_{jk} = -\left(t_{Pj} - O_{Pj}\right) f_j\left(net_{Pj}\right) \quad (14)$$

If J is not an output node, then:

$$\delta_{jk} = f'\left(net_{jk}\right) \sum_m \delta_{mk} W_{mj} \quad (15)$$

The unified weight adjustment formula for the BP network is as follows:

$$\Delta_n W_{ij}(t+1) = \eta \cdot \delta_{nj} + a \cdot \Delta_n W_{ij}(t) \quad (16)$$

When the error signal is at a minimum, the connection power and threshold between the networks no longer change, which thus predicts the unknown information with similar input conditions as the training information.

RESULTS

Characteristics of Fracture–cavity Reservoirs

The buried carbonate hills in the study area were exposed to the surface over long geological periods and experienced severe weathering, denudation and karstification and formed many secondary pore spaces. According to the analysis of the drilling and core testing data, three types of carbonate reservoir spaces are present in the buried hills: karst caves, fractures and pores (**Figure 3**).

(1) Karst cave.

This term mainly refers to those karst caves that were formed by dissolution or col–lapse, which usually include unfilled, half–filled and fully filled caves. Karst caves are well developed in this area. There are 11 wells in total, nine of which exhibited cavitation phenomena and a total of 28 karst caves (18 of which are in the reservoir section), while the cave heights are 0.1–10 m. These caves are unfilled or half–filled karst caves, which are the most favorable reservoirs in this area. The core and logging data indicate that the karst caves are fully filled with chemical precipitation. The filling minerals are coarse–giant crystal calcite–coarse crystals and can be produced in the shape of horse teeth (**Figure 3C**). Light oil can be seen flowing from

TABLE 1 | Carbonate rock type classification standard (Zhou, 1998).

	Rock types	Calcite content (%)	Dolomite content (%)
Limestone	Limestone	100–95	0–5
	dolomite–bearing limestone	95–75	5–25
dolostone	dolomitic limestone	75–50	25–50
	lime–bearing dolostone	50–25	50–75
	Lime dolostone	25–5	75–95
	dolostone	5–0	95–100

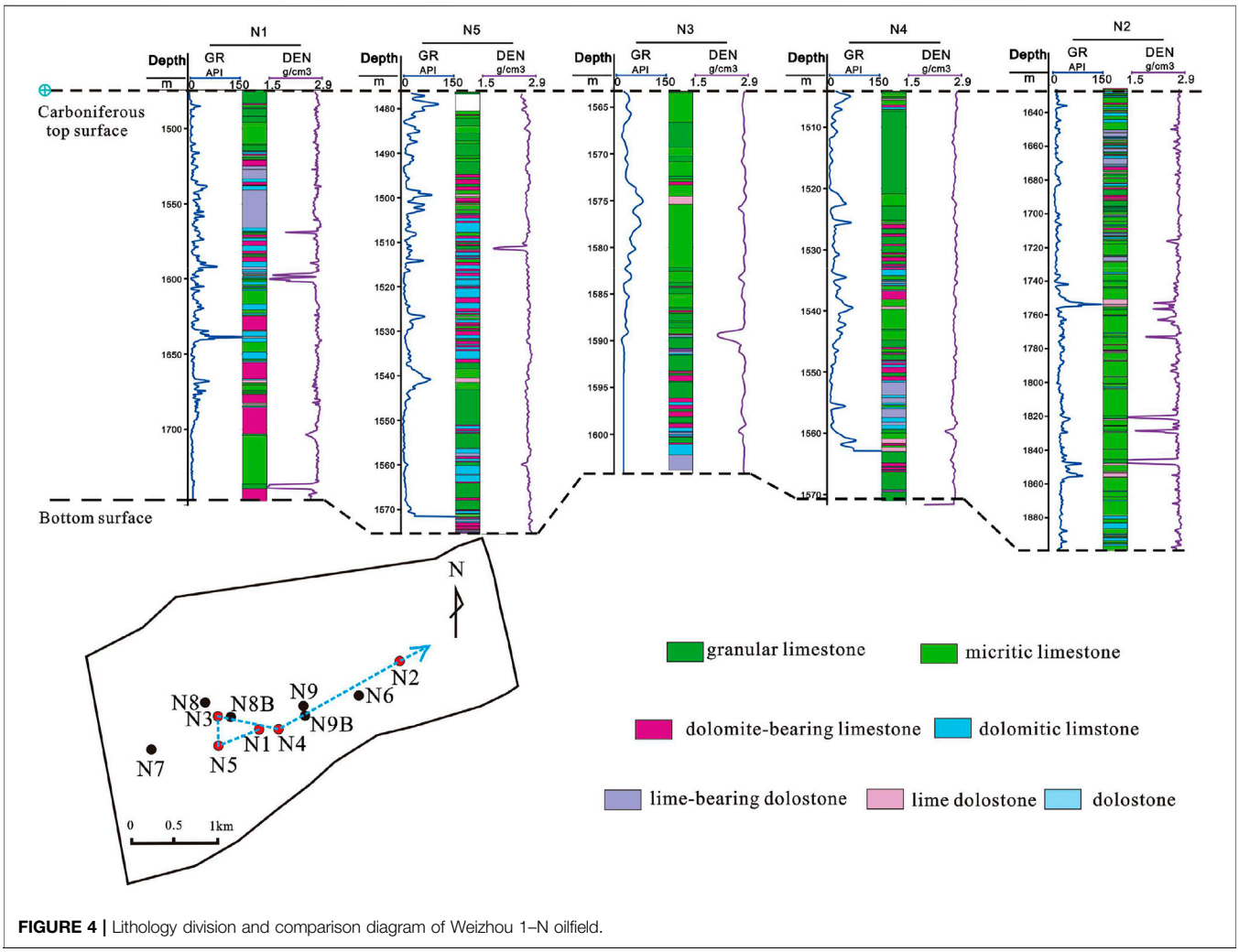

FIGURE 4 | Lithology division and comparison diagram of Weizhou 1–N oilfield.

between the crystals, which indicates that small amounts of pore space can still be reserved in the chemically filled karst caves in this area.

(2) Fractures.

The fractures are generally developed and are mainly vertically oriented with high–angle fractures (**Figure 3A**), the fracture densities in a single well range from 10 to 20 fractures/m, and the fracture density at the core surface is 0.56 fractures/cm^2. Fractures are also extremely developed in the microscopic rock thin sections, fractures are present in each of the 40 core thin sections, with an average of 11.4 fractures per thin section, and the effective fractures (e.g., semifilled and unfilled fractures) account for approximately 27% of the total number of fractures. The fractures in buried hill reservoirs are often formed by multiple geological factors. Observations of the rock thin sections and cores identify the presence of both weathering fractures and tectonic fractures in this area, which developed in roughly equal proportions. The tectonic fractures

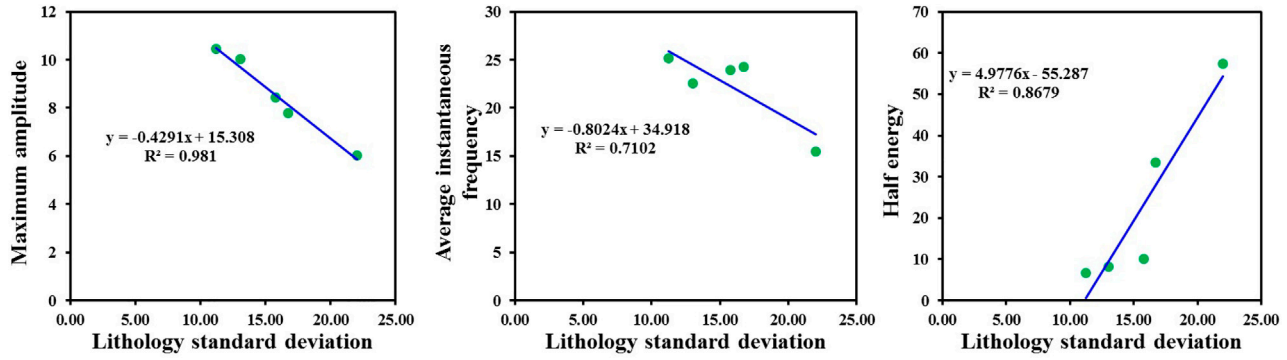

FIGURE 5 | Correlation analysis between seismic attributes and lithology standard deviation.

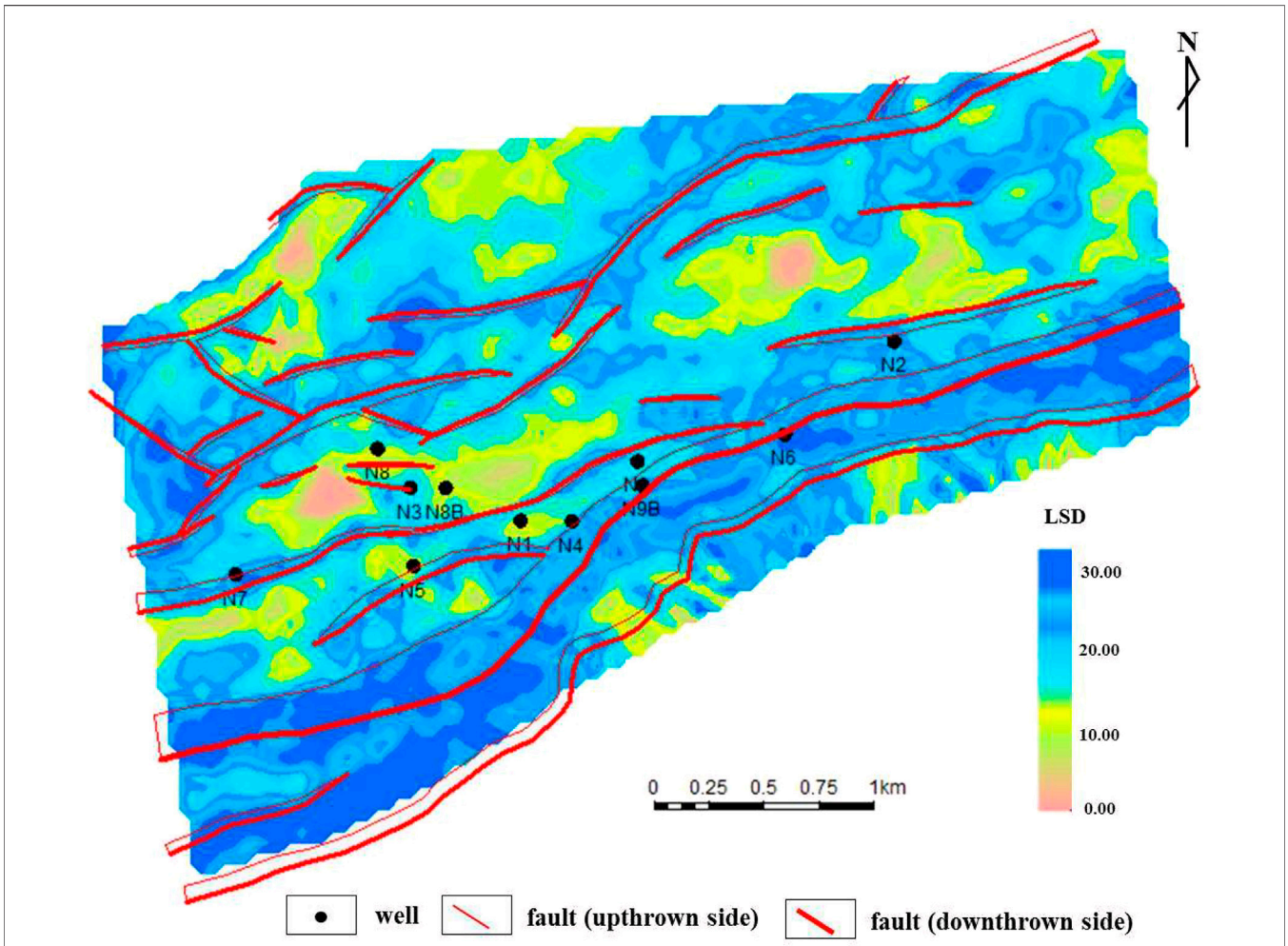

FIGURE 6 | Lithology standard deviation (LSD) plane distribution of the Weizhou 1–N oilfield.

tend to extend over large scales, with dissolution occurring along the fracture faces, the fracture openings are generally large (**Figure 3A**), and the fracture faces are often partially filled or fully filled with medium–to coarse–crystalline calcite (**Figures 3B–F**). The relationship between the fracture filling rates and fracture cutting surfaces suggests that the tectonic fractures in the area can be divided into at least three periods of formation (**Figure 3E**), the early stage fractures are fully filled with

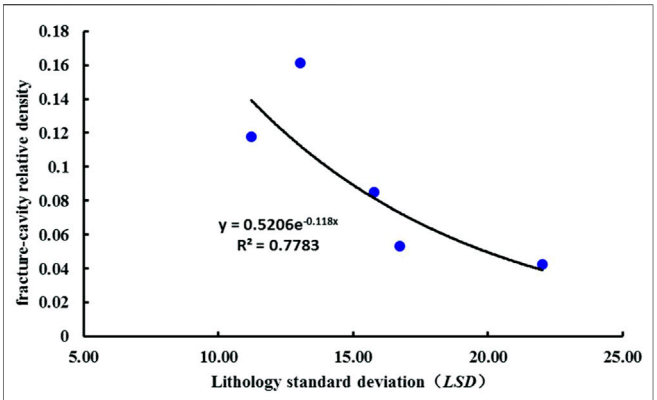

FIGURE 7 | Relationship between lithology standard deviation (LSD) and fracture–cavity relative density.

calcite; the middle stage fractures are semifilled with calcite, while small crystal cavities are often developed in the fractures; and the late stage fractures are slightly filled or unfilled. The weathering fractures are curved, are mostly reticulate or dendritic, and are mostly filled with fine or powdered calcite (**Figure 3B**), with only a few residual intergranular pores, which are less effective than tectonic fractures.

(3) Pores.

The reservoir pores consist mainly of intercrystalline pores and microdissolved pores, which are mainly developed in algal limestone (**Figure 3H**), and residual pores in the fractures can also be seen (**Figures 3G, I**). According to the statistics of the 40 core thin sections, the face rate is generally in the range of 1.5–3%, and the maximum rate can be up to 8%.

In summary, the formation of karst caves, fractures and pores is closely related. The dissolution pores that develop in rocks can reduce the mechanical strength of these rocks, and it is easier to form fractures under the action of the same stress. Fracture formation is often accompanied by the additional occurrence of dissolution, and the formation of karst caves often results from the further dissolution of fractures and pores. The fractures cut each other, dissolution pores and fractures accompany each other, karst caves are formed in fractures, and the karst caves and fractures are connected to each other, which form complex storage spaces in this area.

Lithology Changes Rate Distribution

Since rocks are the basis for the formation of carbonate reservoir space, the formation of seam holes is closely related to the lithology, and frequent lithological changes cause the non–homogeneity of seam hole development (Zhao W et al., 2011; Li et al., 2012; Tian et al., 2012; Zuo et al., 2019). The lithology of this area is based on bioclastic limestone, which was later modified by strong diagenesis. In the shallow burial period of the Upper Carboniferous, the bioclastic limestone and crystalline limestone permeated and reflow dolomitization occurred under the action of evaporative brine produced by local tidal flat and lagoon environment, which resulted in extremely complex lithologies in this area. To better characterize such complex lithology change characteristics, the lithologies in this area are classified based on to changes in the relative dolomite contents in the rocks through thin section and well logging calibration. According to the differences in dolomite contents, the lithologies can be divided into limestone, dolomite–bearing limestone, dolomitic limestone, lime–bearing dolostone, lime dolostone and dolostone (**Table 1**). The pure limestones are subdivided into granular limestone and micritic limestone according to its structure.

To characterize the lithology change characteristics between wells, the thickness of each single rock layer was calculated, and the degree of dispersion between the thickness of each single rock layer and the mean thickness of the single rock layers in the reservoir were calculated by using the mathematical representation method based on the lithology standard deviation; thus, the longitudinal lithology changes were described. The smaller the lithology standard deviation is, the more drastic are thickness changes between the different lithologies. **Figure 4** shows the connected well comparison diagram of the Weizhou 1–N oilfield. From left to right are the N1, N2, N3, N4 and N5 wells of the Weizhou 1–N oilfield. The calculated lithology standard deviations for each well are 16.72, 22.01, 15.78, 13.04 and 11.21. The standard deviation of the lithology in well N5 is the smallest, and the lithology changes the fastest.

To describe the distribution of the lithology changes in plane and space, a variety of seismic attributes that are related to lithology changes were extracted by using the Schlumberger Petrel seismic interpretation platform, and the seismic attributes that can reflect lithology changes were chosen by analyzing the correlations among the seismic attributes and the lithology standard deviations. The seismic attributes that were chosen, which include the maximum amplitude, average instantaneous frequency and half energy, have obvious correlations with the lithology standard deviation, and the correlation coefficients are 0.9810, 0.7102, and 0.8679, respectively (**Figure 5**). The BP neural network deep learning algorithm is used to fit the lithology standard deviation values of the wells with the seismic attributes that can reflect lithology changes, and the calculation model for the lithology standard deviation is then established. Finally, the plane distribution characteristics of the lithology standard deviation are simulated. **Figure 6** shows that the lithology standard deviations in the fault clamping area of the Weizhou 1–N oilfield are small, which reflect the rapid changes in lithology.

DISCUSSION

The Main Controlling Factors of Fracture–cavity Formation

Due to the influences of multiple geological effects, such as leaching, dissolution, tectonics and filling, the buried hill reservoir in the study area developed numerous empty caves, mechanically filled these caves with clastic rocks, mineral

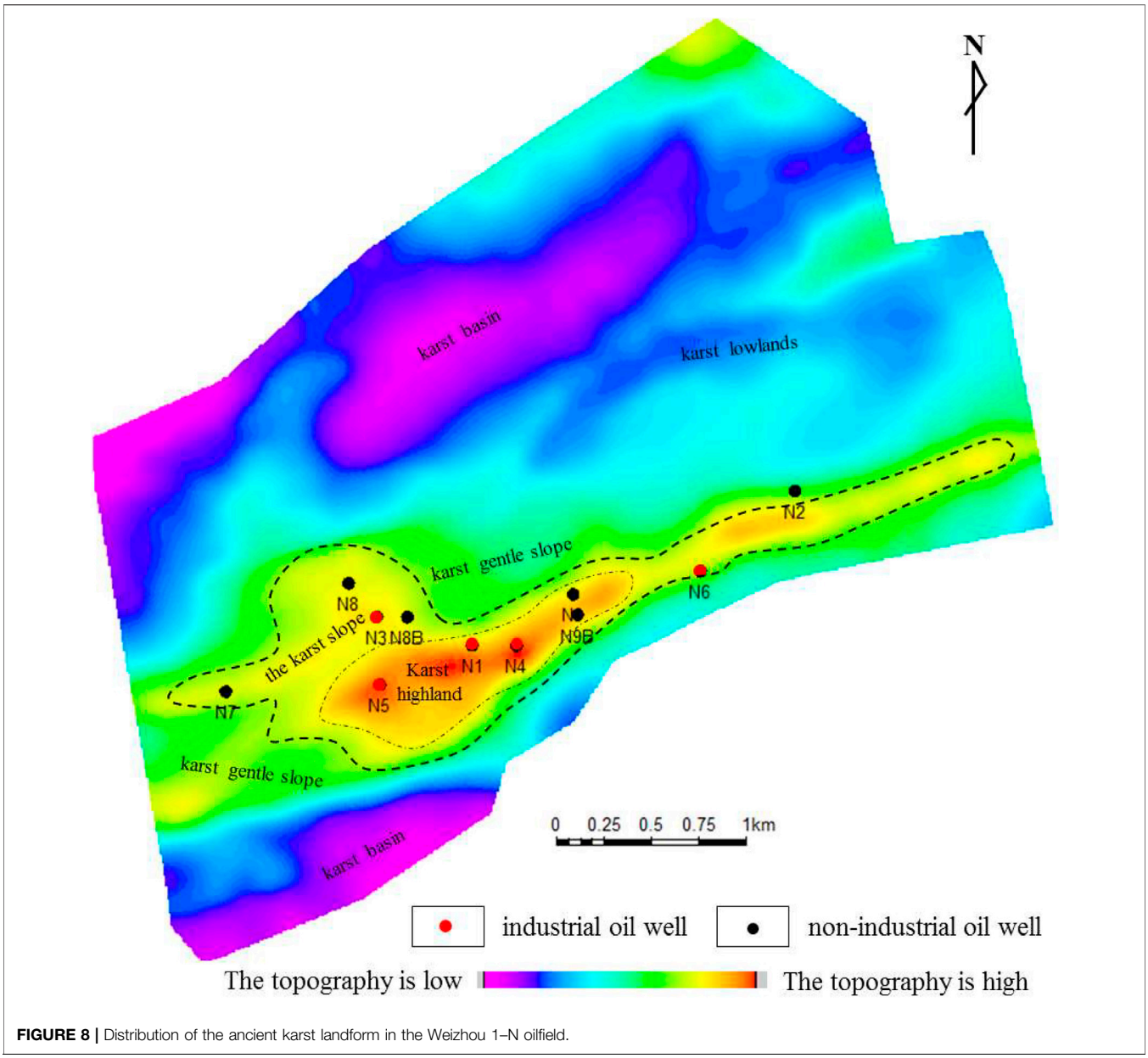

FIGURE 8 | Distribution of the ancient karst landform in the Weizhou 1–N oilfield.

precipitation–filled caves, fractures and dissolution pores on the basis of limestone being the main rock skeleton, and have formed an extremely complex system of fracture–cavity systems. The seismic imaging data in this area are poor, and it is difficult to characterize and identify the small and medium–sized fractures and caves. Analysis of the main geological factors that controlled the formation of fractures and caves is of great significance for predicting fracture–cavity reservoirs (Makeen et al., 2021; Radwan et al., 2020; Yin et al., 2019c). Combined with drilling in the exploration stage and production, it is considered that the formation of high–quality fracture–cavity reservoirs in this area was mainly affected by four factors: lithology changes, karst landforms, tectonic deformations and faulting.

(1) Lithology changes.

Rocks with similar lithologies and certain thicknesses often have similar rock mechanics properties (Saein and Riahi., 2017; Yin et al., 2019a; Zen et al., 2010). Rocks with different lithologies vary greatly in their rock strengths, have different mechanical properties, and therefore vary in their ease of fracturing (Hower and Groppo., 2021). The changes in rock properties show the changes in rock thicknesses in the longitudinal direction. Under the same stress, thin rock layers are more prone to fracture under similar burial depths, structural positions and lithologies. The density of fracture development is significantly negatively correlated with the rock thickness; that is, the fracture density decreases with increasing rock thickness, which was also confirmed by a number of studies (Fan et al., 2008; Li and Fan., 2011; Liu et al., 2020; Mohammed et al., 2021). The buried limestone hill reservoir in the Weixinan Depression has been subjected to different degrees

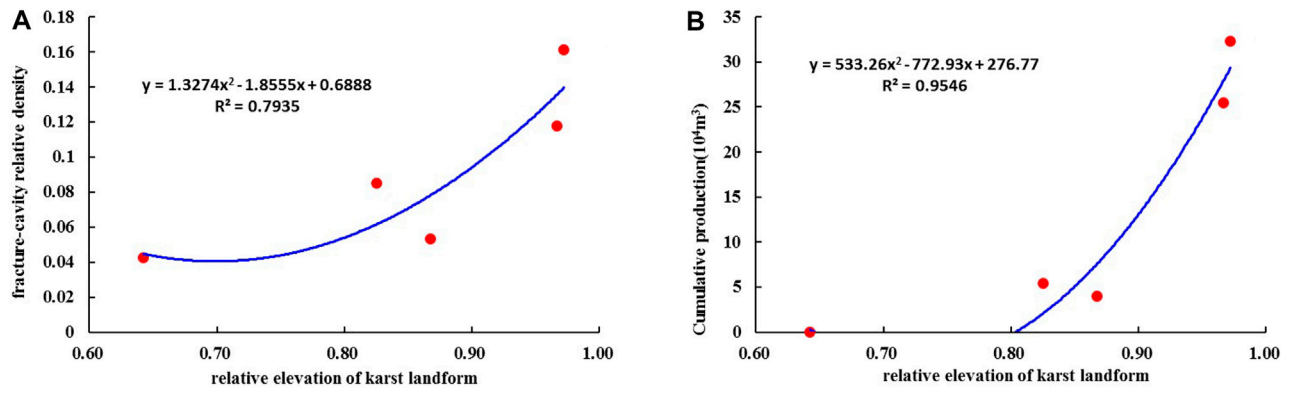

FIGURE 9 | (A) Relationships between the relative elevations of the karst landform and the fracture–cavity relative densities. **(B)** Relationships between the relative elevations of the karst landform and the cumulative yields.

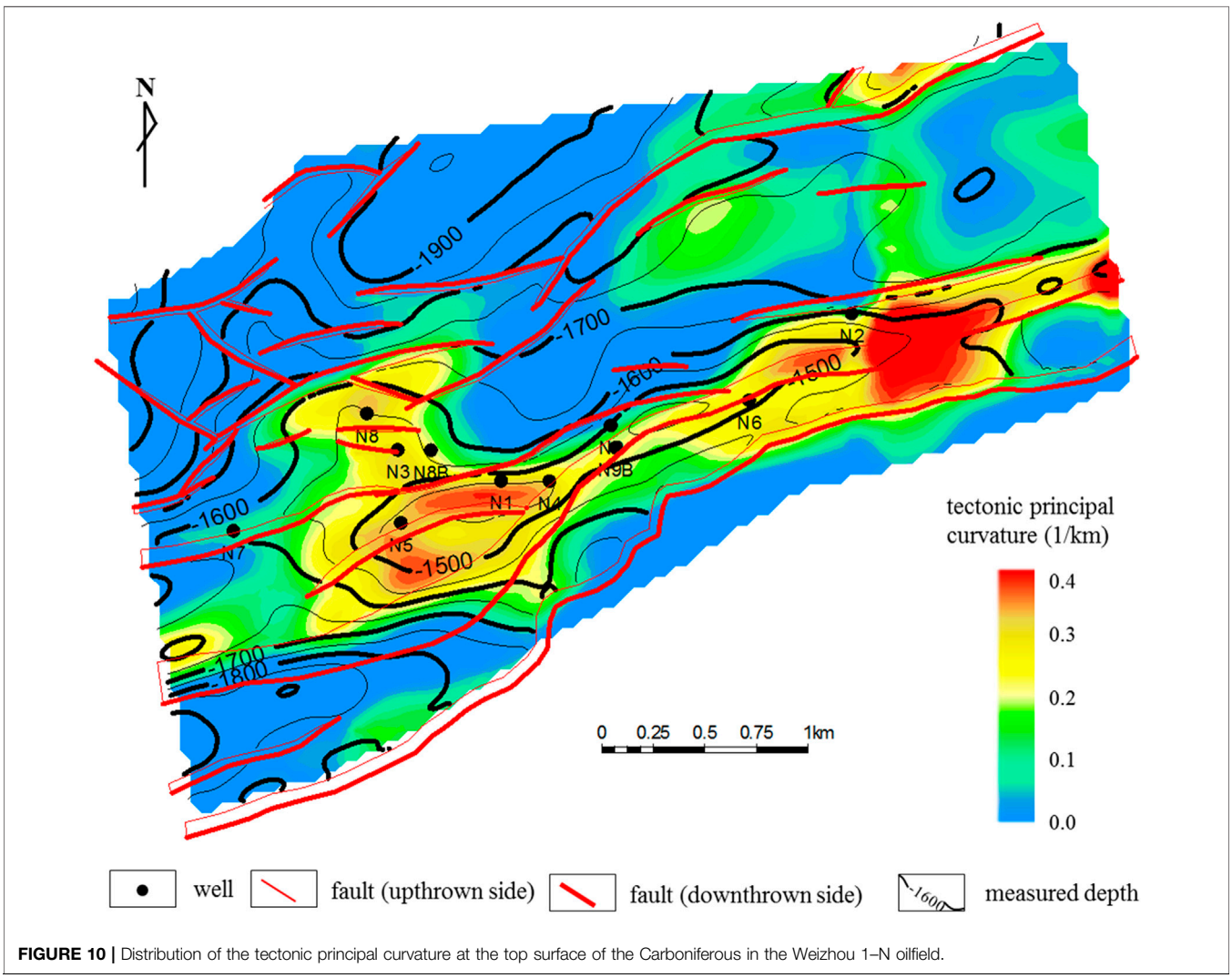

FIGURE 10 | Distribution of the tectonic principal curvature at the top surface of the Carboniferous in the Weizhou 1–N oilfield.

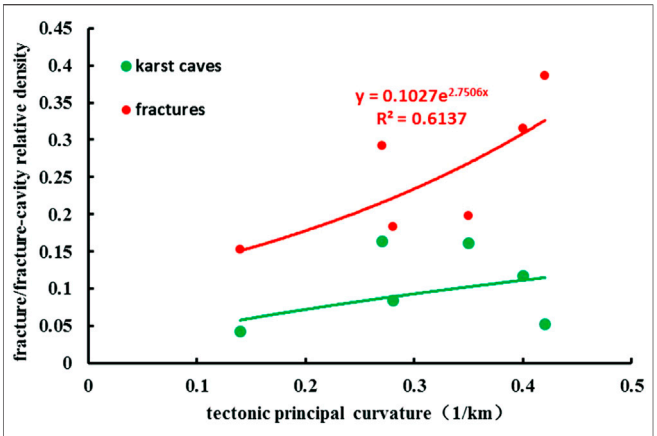

FIGURE 11 | Relationship between the tectonic principal curvature and relative density of fractures or karst caves.

of dolomitization. Due to the large differences in crystallization intensity, the mechanical strengths of the rocks also changed. Affected by the uneven crystallization intensities, there are weak surfaces between the crystals and original rock, and the rock is more prone to fracturing. In summary, lithology changes should be an important factor for influencing the differences in fracture cavity development. The correlation between the fracture–cavity relative density which is the ratio of fracture–cavity thickness to thickness of target stratum in well profile and lithology standard deviation of a single well in the study area is statistically analyzed (**Figure 7**). The results show that the smaller the lithology standard deviation is, the higher the fracture–cavity relative density is, and the more intense the lithology changes are, the more likely a fracture cavity is to be formed.

(2) The ancient karst landform.

The ancient karst landform in the study area formed under humid climate conditions. The scales of buried karst hills are small and are similar to the modern karst in Guilin. Due to the influence of a humid climate, atmospheric precipitation is frequent and surface runoff is high, which caused erosion and leaching in the upper and slope parts of the buried hill over a long period. The intensity of these factors is also high, which easily causes the development of dissolution holes (Fu et al., 2001; Kang and Wu., 2003; Xu et al., 2005; He et al., 2010; Zhang et al., 2021). The production wells in this area are located in karst highlands and karst slope areas (**Figure 8**). The drilling results have also revealed that these areas are those with the strongest leaching and most developed secondary pores (or fractures and karst caves). The time thicknesses of the described karst landform are normalized. The larger the relative elevation of the karst landform is, the higher the ancient landform position was, and the higher the fracture cavity relative density and cumulative oil production are (**Figure 9**), which indicate that the ancient karst landform had an important controlling effect on the development of fractures and karst caves and on the reservoir output capability.

(3) Tectonic deformation strength.

The tectonic principal curvature distribution usually determines the development law of tectonic fractures, and the formation of tectonic fractures is an important channel for the expansion and dissolution of secondary fractures and cavities (Atkinson and Meredith., 1987; Ma, 2005). The tectonic principal curvature distribution of the top surface of the Carboniferous in the Weizhou 1–N oilfield is simulated (**Figure 10**). Based on the results of single–well fracture and fracture–cavity identifications, the control of tectonic deformation on fracture–cavity formation is comprehensively analyzed (**Figure 11**). The study shows that there is a significant positive correlation between the tectonic principal curvature and relative density of fractures, and the larger the tectonic deformation intensity is, the more developed the fracturing is. However, the relationship between the tectonic principal curvature and relative development density of karst caves is obviously poor, which indicates that the formation of fracture–cavity reservoirs is a complex process, but most formed by further dissolution and expansion along the early fracture network system. Therefore, the relative development density of karst caves has no obvious corre–lation with the tectonic principal curvature distribution, but fracture cavities are often developed in areas with relatively high intensities of tectonic deformation.

(4) Faulting.

Faults are the macroscopic manifestations of formation fractures. Faults and fractures coexist and promote each other. Fracture formation promotes the formation of dissolved pores and holes in soluble rocks (Ren et al., 2018; Zhao et al., 2018; Ding et al., 2021). Based on the analysis of the fault system in the study area, the faults in this area can be divided into two types: major faults and secondary faults. The fault directions are mainly NNE, which represent normal faults. The faults in the study area have obvious controlling effects on the distributions of fractures and karst caves. It is evident from the thickness proportion distribution of the karst cave reservoir that faults control the formation of karst cave reservoirs (**Figure 12**). The controlling effect for large faults is strong and that for small faults is relatively weak. The fracture densities and relative densities of karst cave development in each well were calculated, and the faults were classified according to the fault sizes. The curves showing the relationships of the fracture density and karst cave density of each well with the distance of the major fault and F4 secondary fault were fitted. **Figure 13A** shows that there is no obvious relationship between the karst cave density and distance from the fault, which indicates that secondary faults such as F4 have a weak level of control on the formation of karst caves, but the fracture density has a good relationship with the distance from the fault. The closer the distance from the fault, the more developed a fracture is. **Figure 13B** shows that the major fault has a significant controlling effect on the formation of karst caves. The closer to the major fault, the greater the density of karst caves. However, the fracture density has no obvious relationship with the distance from the major fault. It is speculated that this is because the fractures that formed near the major fault are more likely to dissolve to form larger–scale karst caves, which result in the fracture

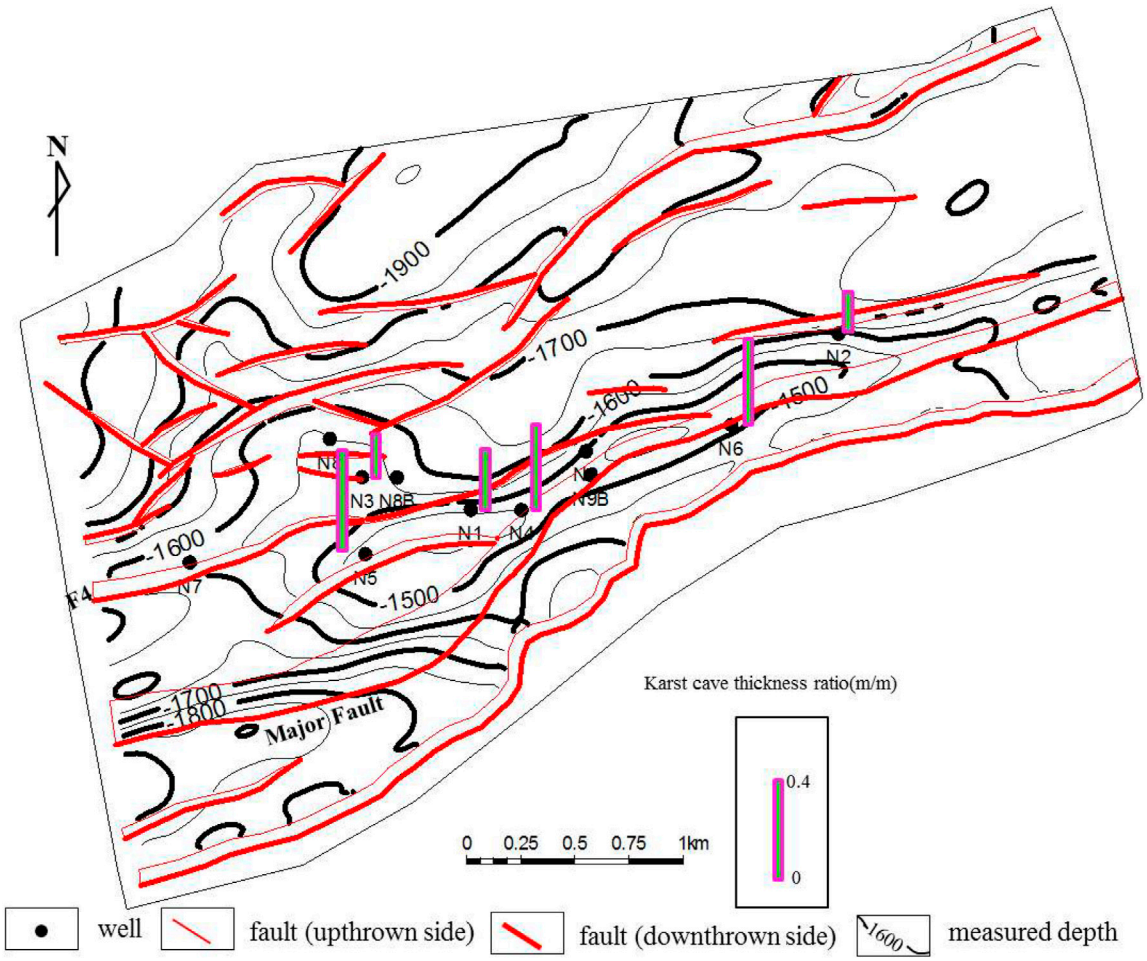

FIGURE 12 | Faults distribution in the Weizhou 1–N oilfield.

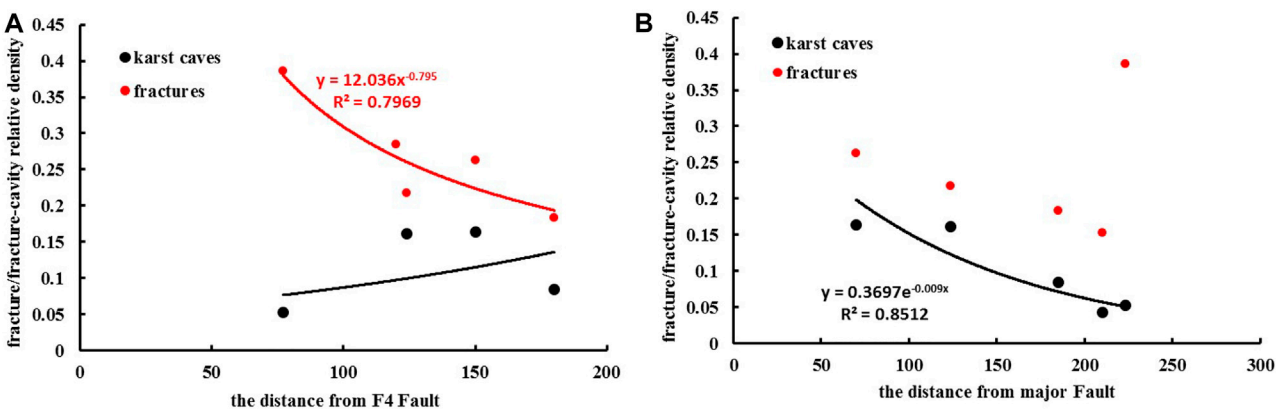

FIGURE 13 | (A) Relationship between fracture–cavity density and distance from the F4 secondary fault. **(B)** Relationship between fracture–cavity density and distance from the major fault.

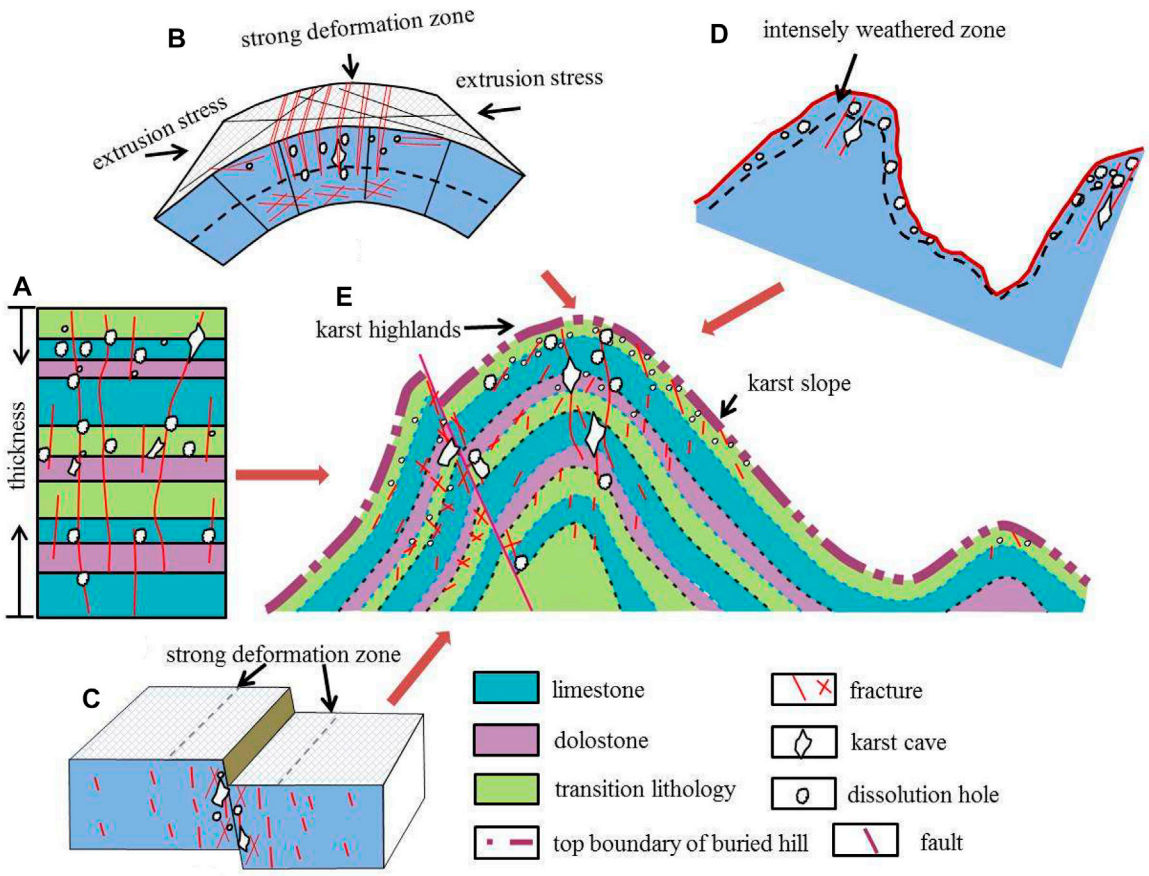

FIGURE 14 | (A) The controlling patern of lithology on fracture formation. **(B)** The controlling patern of structural deformation on fracture formation. **(C)** The controlling patern of faulting on fracture–cave reservoirs formation. **(D)** The controlling patern of the ancient karst landform on fracture–cave reservoirs formation. **(E)** The fracture– cave development patern of Weizhou 1-N oilfield.

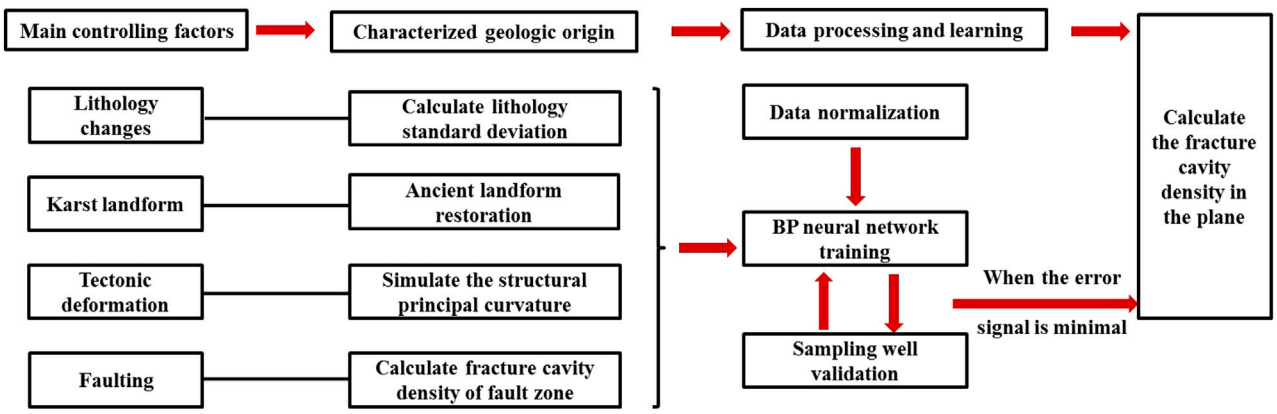

FIGURE 15 | Flowchart of fracture–cavity reservoir prediction.

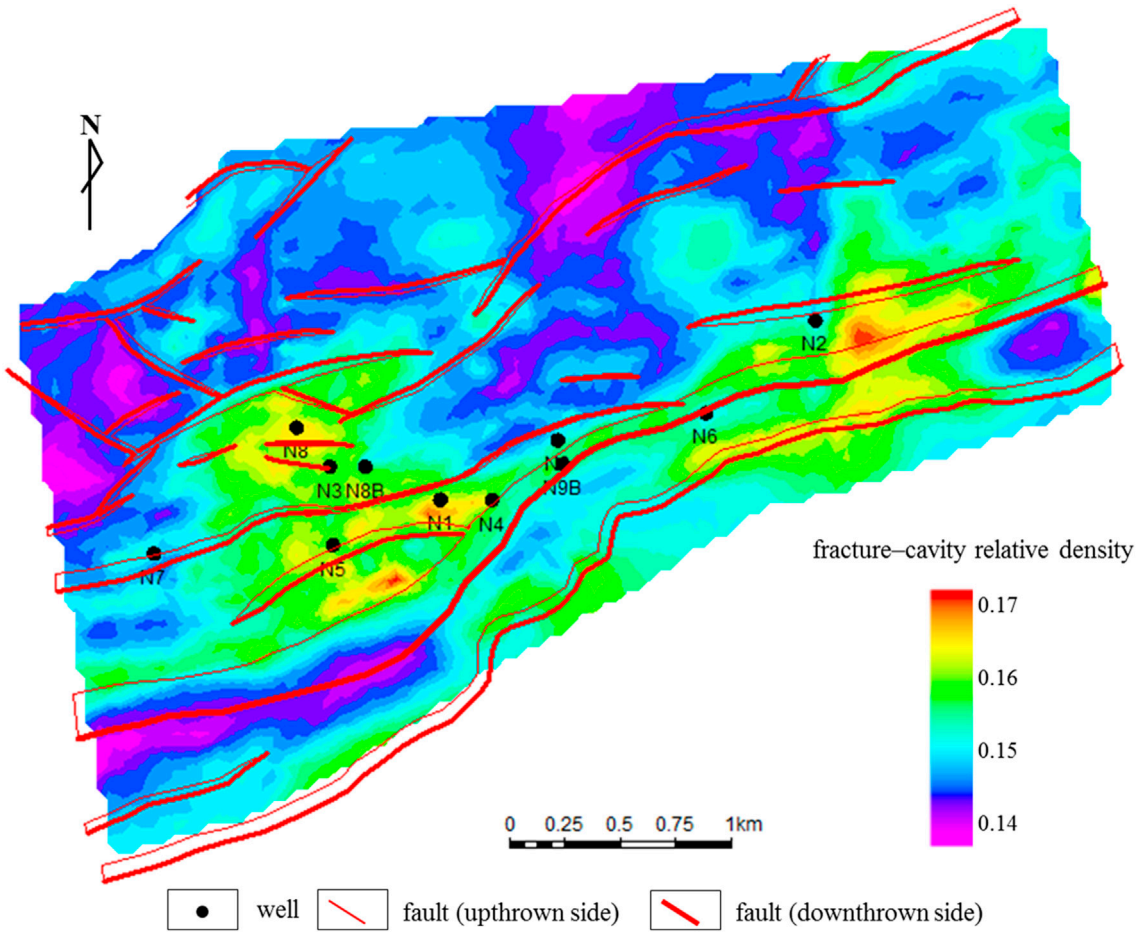

FIGURE 16 | Distribution prediction diagram of the fracture–cavity relative density in the Weizhou 1–N oilfield.

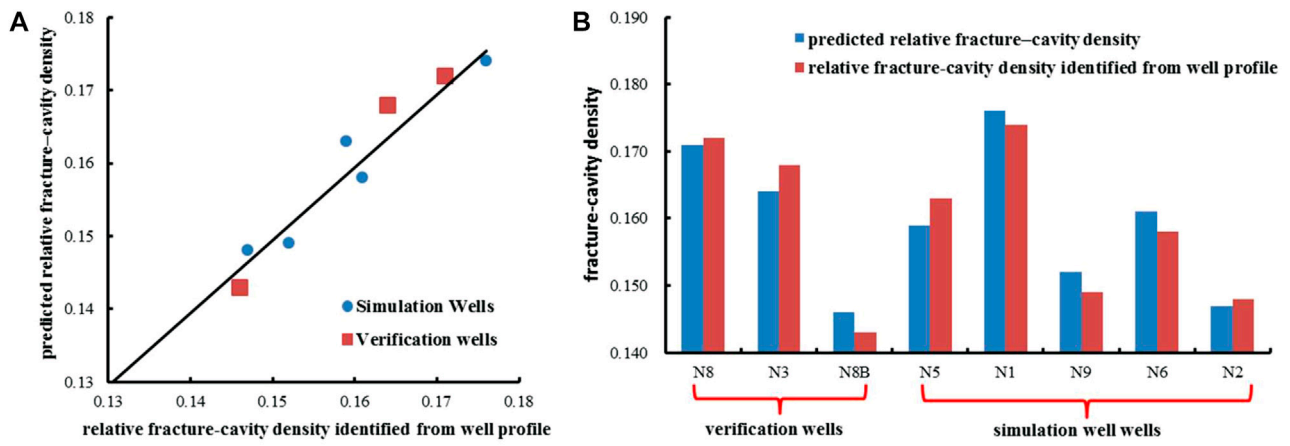

FIGURE 17 | (A) Relationships between the relative fracture-cavity density identified from well profile and the predicted relative fracture–cavity density. **(B)** The error comparison of the relative fracture-cavity density identified from well profile and the predicted relative fracture-cavity density.

information being obscured. **Figures 13A, B** also show that the range of control of the secondary fault on fracture formation is within 150 m from the fault. The range of control of the major fault on karst cave formation is within 200 m from the fault.

(5) Evolution pattern of fracture–cave reservoirs

The dolomites in this area formed mainly by metasomatism in the late quasi–contemporaneous period. Mud crystal calcareous sediments were exposed at the surface, and freshwater and seawater mixed to dolomitize the sediments. Sea level changed many times, which resulted in the formation of rocks with different dolomitization intensities and complex lithology combinations (**Figure 14A**). In the Middle Triassic, regional uplift occurred in the early Indosinian movement, missing the Middle Triassic. Folding and faulting resulted in large numbers of structural fractures in the Huanglong Formation. The Late Jurassic and Yanshan movements uplifted the area again, which resulted in folds, faults and weathering erosion. Until the Early Tertiary, the area was subjected to weathering erosion and corrosion leaching, and large numbers of karst caves and dissolved pores developed. Due to the uplift of the region, folds and faults occurred in the strata. The folds caused bending deformation of the strata, and the derived local tensile stresses ruptured the strata and resulted in vertical structural fractures. The greater the deformation intensity of the strata is, the more developed the fractures are (**Figure 14B**). Faulting can form shear stress fields near fault zones and result in new fractures. A strong deformation zone is located near the fault, the fractures are highly developed, and the development level of the fractures far from the fault is lower (**Figure 14C**). The buried hill has been exposed to the surface for a long time. Before the deposition of the Early Tertiary Changliu Formation, many large, medium and small pores and dissolution joints developed due to weathering leaching and dissolution over a long geological period. The weathering zone exhibited undulations along the paleotopographic surface (**Figure 14D**). The strata with different dolomitization intensities in the Weizhou 1–N buried hill were affected by paleokarst weathering, fold deformation and faulting, which formed a complex fracture–cavity reservoir development pattern (**Figure 14E**). The zones with smaller rock thicknesses, stronger tectonic folding, faults and higher paleotopography are the most developed zones.

The Prediction of Fracture–cavity Reservoirs

Evaluations of favorable fracture–cavity carbonate reservoirs often focus on fracture–cavity evaluations, and the key is to dig deeper into the fracture–cavity information and determine the main factors that control the formation of fracture–cavity reservoirs. In this study, the fracture–cavity distribution is predicted and evaluated from the perspective of quantitative fracture–cavity genesis. First, it is clear that the formation of fractures and karst caves is mainly controlled by four geological factors: lithology changes, tectonic deformations, karst landforms and faulting. We used the mathematical characterization method to establish a new parameter to evaluate the lithology changes and combined it with seismic attributes to predict the distribution of the lithology standard deviations to obtain a quantitative characterization of the lithology changes. To characterize the con–trolling mechanism of tectonic deformation, the principal curvature inversion method of tectonic deformation was used to simulate the principal curvature distribution of tectonic deformation for the target layer in the study area, and a quantitative characterization of the tectonic deformation factors was achieved. The relative elevations of the karst land–forms were normalized to achieve a quantitative characterization of the karst landforms as a geological factor. According to **Figures 13A, B**, the density distribution function of the karst caves or fractures near the fault can be fitted, and the plane distribution of the densities of the fractures and karst caves that are affected by the fault can be determined by calculating the function equation. In this way, a spatial quantitative characterization of four geological genetic factors that control the formation and distribution of fractures and karst caves in the study area was carried out. The concepts used in fracture–cavity distribution prediction technology consist of to gridding the four geological factors in the same gridding step and normalize the data, which is followed by integrating the geological factors that can quantitatively reflect the karst landforms, lithology changes, faulting and tectonic deformations. The BP neural network deep learning algorithm is used to fit and calculate the four genetic factors with the fracture–cavity relative density that was identified by the results of single–well logging data. When the required prediction accuracy is satisfied, the numerical simulation calculation is carried out over the whole plane to evaluate the plane fracture–cavity distribution.

Figure 15 shows the process for predicting the fracture–cavity distribution. **Figure 16** is the fracture–cavity reservoir distribution map of the Carboniferous buried hill reservoir in the Weizhou 1–N oilfield, as predicted by the above evaluation method. To verify whether the evaluation results are reasonable, we compared these from two perspectives. First, we compared the relative densities of the fracture–cavities in the three wells that were not involved in the simulation calculations with the predicted result (**Figure 17**), and the error in the predicted fracture–cavity relative density was less than 5%. The second aspect was verified from a drilling and production perspective. The production performance of five industrial wells in the Weizhou 1–N oilfield reflects the characteristics of dual–pore medium flow. These five wells can be roughly divided into two types. One type is when the reservoir spaces are dominated by rock blocks, small fractures, karst caves and pores, and the wells that encountered only emptying in the drilling process are called pore and cave oil wells, such as wells N4 and N5. The reservoir spaces of the other well type are dominated by fractures. Wells with serious leakage during drilling are called fracture wells, such as wells N1, N3 and N6. The above five wells confirmed the development of fractures or karst caves from their production performances, and these five production wells were also located in the high–value area of the fracture–cavity density prediction in this evaluation. The

drilling results of wells N2, N8B and N9 suggested that the fractures and karst caves were clearly not developed, and the evaluation results were also located in the low–density area of predicted fractures and karst caves. This shows that the quantitative prediction method of fractured–cavity reservoir development zones that is based on genesis is reliable and can guide the adjustment and exploitation of oilfields.

CONCLUSION

(1) Owing to the intense epigenetic transformations, the buried Carboniferous carbonate hill formed complex reservoir spaces in which the karst caves, fractures and pores were associated with and communicated with each other. The main controlling factors include lithology changes, karst landforms, tectonic deformation and faulting.

(2) The buried limestone hill has been seriously reformed and dolomitized to varying degrees. To characterize the distribution characteristics of the lithology changes, a new parameter, the lithology standard deviation, which can reflect the longitudinal lithology changes of the reservoir, is proposed. The smaller the lithology standard deviation is, the more dramatic are the longitudinal thickness changes. Lithological changes form the basis for the formation of fractures and karst caves. The relative density of a single well fracture cavity has a significant negative correlation with the lithology standard deviation. The smaller the lithology standard deviation is, the higher the relative density of the fracture cavity is, and the more intense the lithology change is, and the more likely a fracture cavity is to be formed.

(3) The degrees of fracture development in the buried hill are closely related to the local tectonic deformations. The larger the tectonic principal curvature is, the more developed the fractures are. Faulting is also a key geological factor for the formation of fractures and karst caves. The closer the area is to the secondary fault, the more developed the fractures, but there is no obvious relationship between the density of karst caves and the distance to the secondary fault. The major fault obviously controls the formation of karst caves. The closer the drilling is to the major fault, the higher the density of karst caves. The range of control of the secondary faults on fracture formation is within 150 m from the fault. The range of control of major faults on karst cave formation is within 200 m from the fault.

DATA AVAILABILITY STATEMENT

The original contributions presented in the study are included in the article/Supplementary Material, further inquiries can be directed to the corresponding author.

AUTHOR CONTRIBUTIONS

CZ contributed the writing and paper preparation, WZ and HX contributed to the conception of the study and supported the experiments of the study; CL contributed to the sampling and the data analyses; XW helped perform the analysis with constructive discussions.

FUNDING

This work is granted by the National Science and Technology Major Projects of China (Grant No. 2016ZX05024–006).

REFERENCES

Atkinson, B., and Meredith, P. (1987). "Experimental Fracture Mechanics Data for Rocks and Minerals," in *Fracture Mechanics of Rock*. Editor B. K. Atkinson (London, England: Academic Press), 76–80. doi:10.1016/b978-0-12-066266-1.50016-8

Bukar, M., Worden, R. H., Bukar, S., and Shell, P. (2021). Diagenesis and its Controls on Reservoir Quality of the Tambar Oil Field, Norwegian North Sea. *Energ. Geosci.* 2 (1), 10–31. doi:10.1016/j.engeos.2020.07.002

Cao, R. R., and Liu, Z. Y. (2008). Application of Curvature of Face–Trend Surface Fit–Ting Method in Fracture Prediction. *Comput. Appl. Pet.* 16 (3), 12–14.

Chen, G. B., Li, T., Yang, L., Zhang, G. H., Li, J. W., and Dong, H. J. (2021). Mechanical Properties and Failure Mechanism of Combined Bodies with Different Coal-Rock Ratios and Combinations. *J. Mining Strata Control. Eng.* 3 (2), 023522. doi:10.13532/j.jmsce.cn10-1638/td.20210108.001

Chen, Q., Liu, D. Y., Chen, Y. J., Shen, X. H., Jiang, J. J., Li, X., et al. (2013). Comparative Analysis of Grade–Standard Deviation Method and Factors Analysis Method for Environmental Sensitive Factor Analysis. *Earth Environ.* 41 (3), 319–325.

Chen, Z. G., Ma, W. J., Zhao, H. Z., Xu, F., Cui, Q. Z., Ma, H., et al. (2020). A Technical Workflow of Fracture Prediction with Curvature–Related Attributes and its Applications. *Geophys. Geochemical Exploration* 44 (5), 1201–1207.

Ding, F., Xie, C., Zhou, X., Jiang, C., Li, K., Wan, L., et al. (2021). Defining Stratigraphic Oil and Gas Plays by Modifying Structural Plays: A Case Study from the Xihu Sag, east China Sea Shelf Basin. *Energ. Geosci.* 2 (1), 41–51. doi:10.1016/j.engeos.2020.08.002

Dong, S., Zeng, L., Lyu, W., Xia, D., Liu, G., Wu, Y., et al. (2020). Fracture Identification and Evaluation Using Conventional Logs in Tight Sandstones: A Case Study in the Ordos Basin, China. *Energ. Geosci.* 1 (3–4), 115–123. doi:10.1016/j.engeos.2020.06.003

Du, J. H., He, H. Q., Pi, X. J., Guo, X. J., Hu, S. Y., Zhang, Y. J., et al. (2011). Petroleum Exploration Progress and Future Exploring Succeeding Areas of PetroChina. *Lithologic Reservoirs* 23 (1), 1–16.

Fan, Z. J., Liu, J. H., and Zhang, W. F. (2008). Log Interpretation and Evaluation of the Ordovician Carbonate Rock Reservoirs in Tahe Oilfield. *Oil Gas Geology.* 29 (1), 61–65.

Fu, L. X., Hu, R. B., Liu, S. Z., Hu, J. Y., and Liang, D. G. (2001). Paleokarst in the Ordovician Carbonate Rocks in Huanghua Depression: the Evolution and Dominant Roles of it in Hydrocarbon Accumulation in Buried–hills. *Mar. Origin Pet. Geology.* 6 (2), 21–27.

Gan, J., Zhao, S. L., Luo, W., and Hu, C. H. (2017). Hydrocarbon Accumulation Conditions and Models of Stratigraphic Oil and Gas Reservoirs in Weixinan Sag. *Spec. Oil Gas Reservoirs* 24 (2), 40–44.

Gu, X. E. (2006). The Dicussion of the Standard Error and Standard Deviation. *Phys. Exp. Coll.* 19 (3), 66–67.

Guo, X. S., Hu, D. F., and Duan, J. B. (2020). Problems and Suggestions on marine Petroleum Exploration in South China. *Pet. Geology. Exp.* 42 (5), 675–686.

He, Z. L., Peng, S. T., and Zhang, T. (2010). Controlling Factors and Genetic Pattern of the Ordovician Reservoirs in the Tahe Area. *Oil Gas Geology.* 31 (6), 743–752.

Hong, D., Cao, J., Wu, T., Dang, S., Hu, W., and Yao, S. (2020). Authigenic clay Minerals and Calcite Dissolution Influence Reservoir Quality in Tight Sandstones: Insights from the central Junggar Basin, NW China. *Energ. Geosci.* 1 (1–2), 8–19. doi:10.1016/j.engeos.2020.03.001

Hower, J. C., and Groppo, J. G. (2021). Rare Earth-Bearing Particles in Fly Ash Carbons: Examples from the Combustion of Eastern Kentucky Coals. *Energ. Geosci.* 2 (2), 90–98. doi:10.1016/j.engeos.2020.09.003

Hu, B. (2018). Application of Curvature–Based fine Interpretation Technique in Complex Fault Area. *Offshore Oil* 38 (1), 22–27.

Jian, E. O. M. A., and Fan, D. (2021). Sedimentology, Petrography, and Reservoir Quality of the Zarga and Ghazal Formations in the Keyi Oilfield, Muglad Basin, Sudan. *scientific Rep.* 11 (1), 743.

Jiang, Z. R., Lu, Z. Y., Lv, Z. G., and Yang, J. (2014). Distribution of Carbonate Fractured and Vuggy Reservoirs of Maokou Formation in Luzhou Paleo–Uplift during Dongwu Movement, Sichuan Basin. *Pet. Geology. Exp.* 36 (4), 411–415.

Kaba, K., Sarıgül, M., Avcı, M., and Kandırmaz, H. M. (2018). Estimation of Daily Global Solar Radiation Using Deep Learning Model. *Energy* 162, 126–135. doi:10.1016/j.energy.2018.07.202

Kang, Y. Z. (2020). Potential and Exploration Direction of Oil and Gas Resources in the Uplift Regions of Southern China. *Fault–Block Oil and Gas Field* 27 (04), 409–411.

Kang, Z. H., and Wu, M. D. (2003). Technology of Recovering Ancient Geomorphy Though Sequence Stratigraphy: A Case Study in Tahe 6th Reservoir, Tarim basin. *Xinjiang Geology.* 21 (3), 290–292.

Kong, X. L., Tang, J. M., and Xu, T. J. (2011). Application of Seismic Curvature Attribute to Fracture Prediction in Xinchang Area, Western Sichuan Depression. *Geophys. Prospecting Pet.* 50 (5), 517–520.

Lan, S. R., Song, D. Z., Li, Z. L., and Liu, Y. (2021). Experimental Study on Acoustic Emission Characteristics of Fault Slip Process Based on Damage Factor. *J. Mining Strata Control. Eng.* 3 (3), 033024. doi:10.13532/j.jmsce.cn10-1638/td.20210510.002

Li, C. R., Zhang, G. C., Liang, J. S., Zhao, Z. G., and Xu, J. Y. (2012). Characteristics of Fault Structure and its Control on Hydrocarbons in the Beibuwan Basin. *Acta Petrolei Sinica* 33 (2), 195–203.

Li, S. J. (2020). Some Developments of Estimation Procedures of Mechanical Model Parameter Based on Deep Learning Neural Network. *Artif. Intelligence Robotics Res.* 9 (2), 100–109.

Li, X. S., Gan, J., Zhang, Y. Z., Zhang, J. X., Yang, X. B., Deng, Y., et al. (2015). Hydrocarbon Accumulation Regularity and Exploration Prospects of Fault Lacustrine Basins in Western South China Sea. *China Offshore Oil and Gas* 27 (4), 22–29.

Li, Y. (2012). Ordovician Carbonate Fracture–Cavity Reservoirs Identification and Quantitative Characterization in Tahe Oilfield. *J. China Univ. Pet.* 36 (1), 1–7.

Li, Y. T., and Fan, Z. H. (2011). Developmental Pattern and Distribution Rule of the Fracture–Cavity System of Ordovician Carbonate Reservoirs in the Tahe Oilfield. *Acta Petrolei Sinica* 32 (1), 101–106.

Li, Y., Zhou, D.-H., Wang, W.-H., Jiang, T.-X., and Xue, Z.-J. (2020). Development of Unconventional Gas and Technologies Adopted in China. *Energ. Geosci.* 1 (1–2), 55–68. doi:10.1016/j.engeos.2020.04.004

Liu, Y., Gao, M., and Zhao, H. (2020). Detection of Overlying Rock Structure and Identification of Key Stratum by Drilling and Logging Technology. *J. Mining Strata Control. Eng.* 2 (2), 023038. doi:10.13532/j.jmsce.cn10-1638/td.2020.02.004

Liu, Z. F., Qu, S. L., and Sun, J. G. (2012). Progress of Seismic Fracture Characterization Technology. *Geophys. Prospecting Pet.* 51 (2), 191–198.

Lu, X. B., and Cai, Z. X. (2010). A Study of the Paleokarst System in the Fractured–Vuggy Carbonate Reservoirs and Oil/Gas Development–Taking the Reservoirs in Tahe Oilfield as an Example. *Oil Gas Geology.* 31 (1), 22–27.

Ma, R. H. (2005). Fracture Prediction of Tight sandstone Reservoir. *Nat. Gas Industry* 25 (10), 36–37.

Ma, Y., Li, S. Z., Liu, X., Zhao, S. J., Yu, S., Wang, X. F., et al. (2014). Formation Machanism of the Beibuwan Basin, South China. *J. Jilin Univ. Earth Sci. Edition* 44 (6), 1727–1736.

Mahmud, H. B., Bin Muhammad Hisham, M. H., Mahmud, W. M., Leong, V. H., and Shafiq, M. U. (2020). Petrophysical Interpretations of Subsurface Stratigraphic Correlations, Baram Delta, Sarawak, Malaysia. *Energ. Geosci.* 1 (3–4), 100–114. doi:10.1016/j.engeos.2020.04.005

Makeen, Y. M., Shan, X., Ayinla, H. A., Adepehin, E. J., Ayuk, N. E., Yelwa, N. A., et al. (2021). Sedimentology, Petrography, and Reservoir Quality of the Zarga and Ghazal Formations in the Keyi Oilfield, Muglad Basin, Sudan. *Sci. Rep.* 11 (1), 743. doi:10.1038/s41598-020-80831-y

Mirzaei-Paiaman, A., and Ghanbarian, B. (2021). A New Methodology for Grouping and Averaging Capillary Pressure Curves for Reservoir Models. *Energ. Geosci.* 2 (1), 52–62. doi:10.1016/j.engeos.2020.09.001

Qie, L., Shi, Y. N., and Liu, J. S. (2021). Experimental Study on Grouting Diffusion of Gangue Solid Filling Bulk Materials. *J. Mining Strata Control. Eng.* 3 (2), 023011. doi:10.13532/j.jmsce.cn10-1638/td.20201111.001

Radwan, A. E., Trippetta, F., Kassem, A. A., and Kania, M. (2020). Multi–scale Characterization of Unconventional Tight Carbonate Reservoir: Insights from October Oil Filed, Gulf of Suez Rift basin, Egypt. *J. Pet. Sci. Eng.*, 107968.

Ren, C., Gao, X., Jiang, H., Li, J., and He, F. (2018). Characteristics and Favorable Area Prediction of Ordovician Buried-hill Carbonate Reservoirs in the Bozhong 21-2 Tectonic belt, Bohai Bay Basin, China. *Pet. Sci. Technol.* 36, 1374–1381. doi:10.1080/10916466.2018.1474222

Saein, A., and Riahi, Z. (2017). Controls on Fracture Distribution in Cretaceous Sedimentary Rocks from the Isfahan Region, Iran. *Geol. Mag.* 154, 1–13. doi:10.1017/s0016756817000346

Santosh, M., and Feng, Z. Q. (2020). New Horizons in Energy Geoscience. *Energ. Geosci.* 1 (1–2), A1–A2. doi:10.1016/j.engeos.2020.05.005

Shen, S. (2019). A Deep Learning Method for Online Capacity Estimation of Lithium–Ion Batteries. *J. Energ. Storage* 25, 1–13. doi:10.1016/j.est.2019.100817

Sun, X., Zhang, X., Zhang, G., Lu, B., Yue, J., and Zhang, B. (2014). Texture and Tectonic Attribute of Cenozoic basin Basement in the Northern South China Sea. *Sci. China Earth Sci.* 57, 1199–1211. doi:10.1007/s11430-014-4835-2

Taesic, L., Juwon, K., Young, U., and Hyunju, L. (2019). Deep Neural Network for Estimating Low Density Lipoprotein Cholesterol. *Clinica Chim. Acta* 489, 35–40.

Tian, F., Jing, Q., Li, Y., Zhang, H. F., and Zhang, W. B. (2012). Identification of Small Fracture–Vugs and Their Fillings through Log Interpretation in Fractured–Vuggy Ordovician Reservoirs in Tahe Oilfield. *Oil Gas Geology.* 33 (6), 900–908.

Tong, H. M., Fan, C. W., Meng, L. J., Zhao, B. Y., and Fan, J. Y. (2018). Manifestation and Origin Mechanism of the Fault System Complexity in Rift Basins in Eastern–Southern China:Case Study of the Nanbu and Weixinan Sags. *Acta geologica sinica* 92 (9), 1753–1765.

Wang, J., and Wang, X. L. (2021). Seepage Characteristic and Fracture Development of Protected Seam Caused by Mining Protecting Strata. *J. Mining Strata Control. Eng.* 3 (3), 033511. doi:10.13532/j.jmsce.cn10-1638/td.20201215.001

Wang, Z. J. (2009). A Polarization SAR Image Fusion Algorithm Based on the Product of Local Energy and Regional Standard Deviation in Contourlet Domain. *J. Image Graphics* 14 (3), 514–519.

Xiao, J., Wang, H., Ma, L. J., Gan, H. J., Liu, J. R., and Chen, L. (2003). Characteristics of Buried hill Oil Pool of W61 Area in Weixi'nan Depression, Beibu Gulf basin. *J. Xinjiang Pet. Inst.* 15 (4), 30–37.

Xiao Y. R, Y. R., He, F. Y., and Sun, Y. M. (2003). Reservoir Characteristics of Paleocave Carbonates a Case Study of Ordovician Paleocave in Tahe Oilfield, Tarim Basin. *Oil Gas Geology.* 24 (1), 75–80.

Xu, G. S., Liu, S. G., Wu, H. Z., Li, Z. W., and Sun, W. (2005). The Relationship between Sea Level Change and Cave Formation Sequence. *Acta Sedimentologica Sinica* 23 (2), 316–322.

Xue, F., Liu, X. X., and Wang, T. Z. (2021). Research on Anchoring Effect of Jointed Rock Mass Based on 3D Printing and Digital Speckle Technology. *J. Mining Strata Control. Eng.* 3 (2), 023013. doi:10.13532/j.jmsce.cn10-1638/td.20201020.001

Yan, X. B. (2002). Characteristics of Ordovician Carbonate Rock Reservoirs inTahe Oilfield. *Oil Gas Geology.* 23 (3), 262–265.

Yang, J. X., Luo, M. K., Zhang, X. W., Huang, N., and Hou, S. J. (2021). Mechanical Properties and Fatigue Damage Evolution of Granite under Cyclic Loading and Unloading Conditions. *J. Mining Strata Control. Eng.* 3 (3), 033016. doi:10.13532/j.jmsce.cn10-1638/td.20210510.001

Yang, X. B. (2016). Hydrocarbon Accumulation Conditions in Beibu Gulf Basin, Northern South China Sea. *China Pet. Exploration* 21 (4), 85–92.

Yin, S., Dong, Li., Yang, Xia., and Wang, Ruyue. (2020a). Experimental Investigation of the Petrophysical Properties, Minerals, Elements and Pore Structures in Tight Sandstones. *J. Nat. Gas Sci. Eng.* 76 (1), 1–14. doi:10.1016/j.jngse.2020.103189

Yin, S., Han, C., Wu, Z., and Li, Q. (2019c). Developmental Characteristics, Influencing Factors and Prediction of Fractures for a Tight Gas sandstone in a Gentle Structural Area of the Ordos Basin, China. *J. Nat. Gas Sci. Eng.* 72 (12), 1–14. doi:10.1016/j.jngse.2019.103032

Yin, S., Lv, D., and Ding, W. (2018a). New Method for Assessing Microfracture Stress Sensitivity in Tight sandstone Reservoirs Based on Acoustic Experiments. *Int. J. Geomechanics* 18 (4), 1–10. doi:10.1061/(asce)gm.1943-5622.0001100

Yin, S., Tian, T., and Wu, Z. (2019a). Developmental Characteristics and Distribution Law of Fractures in a Tight sandstone Reservoir in a Low–Ampli–Tude Tectonic Zone, Eastern Ordos Basin, China. *Geol. J.* 54, 1–16.

Yin, S., Tian, T., Wu, Z., and Li, Q. (2020b). Developmental Characteristics and Distribution Law of Fractures in a Tight sandstone Reservoir in a Low-amplitude Tectonic Zone, Eastern Ordos Basin, China. *Geol. J.* 55, 1546–1562. doi:10.1002/gj.3521

Yin, S., and Wu, Z. (2020). Geomechanical Simulation of Low-Order Fracture of Tight sandstone. *Mar. Pet. Geology.* 100, 1–10. doi:10.1016/j.marpetgeo.2020.104359

Yin, S., Xie, R., Wu, Z., Liu, J., and Ding, W. (2019b). *In Situ* stress Heterogeneity in a Highly Developed Strike-Slip Fault Zone and its Effect on the Distribution of Tight Gases: A 3D Finite Element Simulation Study. *Mar. Pet. Geology.* 99 (1), 75–91. doi:10.1016/j.marpetgeo.2018.10.007

Yin, S., Zhao, J., Wu, Z., and Ding, W. (2018b). Strain Energy Density Distribution of a Tight Gas sandstone Reservoir in a Low-Amplitude Tectonic Zone and its Effect on Gas Well Productivity: A 3D FEM Study. *J. Pet. Sci. Eng.* 170, 89–104. doi:10.1016/j.petrol.2018.06.057

Yoshida, M., and Santosh, M. (2020). Energetics of the Solid Earth: An Integrated Perspective. *Energ. Geosci.* 1 (1–2), 28–35. doi:10.1016/j.engeos.2020.04.001

Zeng, L., Jiang, J., and Yang, Y. (2010). Fractures in the Low Porosity and Ultra-low Permeability Glutenite Reservoirs: A Case Study of the Late Eocene Hetaoyuan Formation in the Anpeng Oilfield, Nanxiang Basin, China. *Mar. Pet. Geology.* 27, 1642–1650. doi:10.1016/j.marpetgeo.2010.03.009

Zhang, B., Shen, B., and Zhang, J. (2020). Experimental Study of Edge-Opened Cracks Propagation in Rock-like Materials. *J. Mining Strata Control. Eng.* 2 (3), 033035. doi:10.13532/j.jmsce.cn10-1638/td.20200313.001

Zhang, H., Xu, G., Liu, M., and Wang, M. (2021). Formation Environments and Mechanisms of Multistage Paleokarst of Ordovician Carbonates in Southern North China Basin. *Sci. Rep.* 11 (1), 819. doi:10.1038/s41598-020-80878-x

Zhang, J., Ju, Y., and Zhang, Q. (2019). Low Ecological Environment Damage Technology and Method in Coal Mines. *J. Mining Strata Control. Eng.* 1 (1), 013515. doi:10.13532/j.jmsce.cn10-1638/td.2019.02.005

Zhang, J. Z., and Song, L. Y. (1981). On the Method of Estimating B–Value and its Standard Error–The Monte Carlo Method of Estimating the Accuracy of B–Valve. *Acta Seismologica Sinica* 3 (3), 292–301.

Zhang, P., Zheng, J., Xi, M. H., Wang, W. J., Huang, J. J., and Wang, X. P. (2015). Hydrocarbon Accumulation Conditions and Patterns in the Southwestern Margin of Weixinan Sag, Beibuwan Basin. *Pet. Geology. Exp.* 37 (2), 157–163.

Zhao, S. L., Yang, X. B., Chen, L., Zhou, G., Jiao, L. B., and Zhao, Y. Z. (2019). Hydrocarbon Accumulation Conditions and Exploration Potential of Carbonate Buried hills in Weixinan Sag in Western South China Sea. *China Offshore Oil and Gas* 31 (2), 51–61.

Zhao, S. L., Zhao, Y. Z., Yang, X. B., Jiao, L. B., and Chen, C. F. (2018). An Analysis on the Characteristics and Main Controlling Factors of Reservoir in Carbonate Buried hill in the Weixi'nan Sag,Beibuwan Basin. *Acta Oceanologica Sinica* 40 (9), 43–53.

Zhao Z, Z., Deng, H., and Liu, H. (2011). The Characteristics, Classification and Appraisal of the Reservoirs at Carboniferous Isolated Carbonate Platform Margin in Kenjiyak Oil Field. *Mar. Geology. Quat. Geology.* 31 (2), 111–120. doi:10.3724/sp.j.1140.2011.02111

Zhou W, W., Li, X. H., J, W. H., Zhao, Z. C., and Zhou, Q. M. (2011). The Control Action of Fault to Paleokarst in View of Ordovician Reservoir in Tahe Area. *Acta Petrologica Sinica* 27 (8), 2339–2348.

Zhou, W. (1998). *Evaluation Methods of Fracture Reservoir in Oil and Gas Pool*. Chengdu: Publishing House of Sichuan Science and Technology. (in Chinese).

Zuo, J., Yu, M., and Hu, S. (2019). Experimental Investigation on Fracture Mode of Different Thick Rock Strata. *J. Mining Strata Control. Eng.* 1 (1), 013007. doi:10.13532/j.jmsce.cn10-1638/td.2019.02.008

Conflict of Interest: Authors CZ and XW were employed by CNOOC China Limited, Hainan Branch, CL was employed by CNOOC Research Institute Limited.

The remaining authors declare that the research was conducted in the absence of any commercial or financial relationships that could be construed as a potential conflict of interest.

The reviewers (KL and XR) declared a shared affiliation with the authors (WZ and HX) to the handling editor at the time of review.

Publisher's Note: All claims expressed in this article are solely those of the authors and do not necessarily represent those of their affiliated organizations, or those of the publisher, the editors and the reviewers. Any product that may be evaluated in this article, or claim that may be made by its manufacturer, is not guaranteed or endorsed by the publisher.

frontiers | Frontiers in Earth Science

ORIGINAL RESEARCH
published: 12 April 2022
doi: 10.3389/feart.2022.889067

Process and Controlling Factors of Pore Evolution in Marine-Continental Transitional Black Shale—An Example From Permian Shanxi Formation in the Eastern Margin of Ordos Basin

Jin Wu[1,2], *Xiaowei Zhang*[1,2]*, *Hao Xu*[3]*, *Yufeng Xiao*[1,2], *Guiying Liu*[3], *Lingfeng Jiang*[3], *Naier Deng*[3] *and Zihe Ren*[3]

[1]PetroChina Research Institute of Petroleum Exploration and Development, Beijing, China, [2]National Energy Shale Gas R & D Experimental Center, Beijing, China, [3]State Key Laboratory of Oil and Gas Reservoir Geology and Exploitation, Chengdu University of Technology, Chengdu, China

OPEN ACCESS

Edited by:
Wenlong Ding,
China University of Geosciences, China

Reviewed by:
Rui Liu,
Southwest Petroleum University, China
Wei Zhao,
China University of Mining and Technology, China

***Correspondence:**
Xiaowei Zhang
zhangxw69@petrochina.com.cn
Hao Xu
haoxu777@qq.com

Specialty section:
This article was submitted to Structural Geology and Tectonics, a section of the journal Frontiers in Earth Science

Received: *03 March 2022*
Accepted: *28 March 2022*
Published: *12 April 2022*

Citation:
Wu J, Zhang X, Xu H, Xiao Y, Liu G, Jiang L, Deng N and Ren Z (2022) Process and Controlling Factors of Pore Evolution in Marine-Continental Transitional Black Shale—An Example From Permian Shanxi Formation in the Eastern Margin of Ordos Basin. Front. Earth Sci. 10:889067. doi: 10.3389/feart.2022.889067

Pore and pore network evolution of shale is critical for the evaluation the pore system in shale gas reservoirs. Thermal maturation effect acts as an indispensable role in porosity evolution. In this paper, high-temperature and high-pressure *in-situ* thermal simulation experiments were conducted to investigate the process and controlling factors of pore evolution in marine-continental transitional shale. Multiple methods, including scanning electron microscopy (SEM), X-ray diffraction, helium porosimetry and low-pressure N2 and CO2 adsorption were used to investigate the evolution of mineral composition and pore structure at different stages of thermal maturity. The results showed that type III organic matter (OM) generated petroleum with the thermal maturity increasing. The total organic carbon (*TOC*) decreased by 13.3% when temperature reached 607°C. At the same time, it produced numerous organic and mineral pores during hydrocarbon generation. Besides, some changes in mineral composition have occurred, especially in illite (from 11% to 31%) and kaolinite (from 89% to 69%). In general, it can divide into 3 stages (maturity, high maturity and over maturity) for shale pore system evolution with the thermal maturity increasing. In the low maturity period, large amounts of pyrolytic bitumen and oil generated to fill the pores, causing the pore system to diminish; in the high maturity period, a large number of pores were generated when oil is cracked into gas, resulting in a rapid expansion of the pore system; in the over-maturity period, the cracking of pyrolysis and hydrocarbon slowed down, allowing the pore system to stabilize. Shale pore evolution is primarily controlled by the thermal evolution of OM, and the conversion of inorganic minerals contributes less to pore evolution compared to organic matter. The high maturity period (1.2% < Ro < 2.0%) was the period when extensive pyrolysis and hydrocarbon generated in the Shanxi Formation shale, which contributed mostly for the pores generation and accumulation of shale gas.

Keywords: porosity evolution, thermal simulation, marine-continental transitional shale, shanxi formation, ordos basin

INTRODUCTION

Marine, marine-continental transitional, and continental shales are widely distributed in China, and contributed 15% of the total natural gas production (Zou et al., 2019). Recently, marine shale is already being effectively developed in Sichuan Basin, with annual production of 200 × 10^8 m^3 in 2020.And many researches on shale pore system evolution and shale gas accumulation in marine shales have been systematic analyzed (Liu Y. et al., 2020; Xu et al., 2020). Marine-continental transitional shale gas, which accounts for about a quarter of total stock of shale gas, represents a new strategic substitute resource for the China's natural gas industry (Bhatti et al., 2020; Chen et al., 2020; Abouzar and Ghanbarian., 2021; Gao, 2021; Guo et al., 2021; Wu et al., 2021). And the unconventional resource in upper Paleozoic Carboniferous-Permian units in the Ordos Basin is rich (Yin et al., 2020). However, researchers pay small attention to the marine-continental transitional shale. There are few works for Permian Shanxi Formation shale and the enrichment mechanism of this type of shale are still unknown.

The pore system is very complex and many factors may influence the pores generation and evolution, such as total organic content, thermal maturity, maceral type, overburden/tectonic compaction (Chen and Xiao, 2014; Zargari et al., 2015; Ko et al., 2016; Liu Y. et al., 2020; Liu et al., 2020b; Dong et al., 2020; Hower and Groppo., 2021; Wang and Wang., 2021; Xue et al., 2021). Apart from the diagenetic process, the hydrocarbon generation of OM also constitutes a key influencing factor for shale pore evolution (Jarvie et al., 2007; Zhang et al., 2020; Hou et al., 2022). For the marine-continental transitional shale, the OM mostly comes from terrestrial higher plants and the type of OM is type III (Qiu et al., 2021). In the recent research of the typical marine-continental transitional shales such as Permian Longtan Formation, some researchers concluded that almost no pore developed in type III OM (Jiang et al., 2017; Li et al., 2020; Zhao W et al., 2020). Some others discovered that some type III OM contains hydrocarbon-generating gas pores, but these pores were inhomogeneous (Liu et al., 2020c; Kuang et al., 2020; Qie et al., 2021). Some researchers also hold different opinions toward the pore development degree of type III OM. Some believed that vitrinite tends to have poor pore development (Dong et al., 2015); and some previous researchers reported that large numbers of micropores smaller than 2 nm were observed in vitrinite (Mastalerz et al., 2013). Obviously, the pore system of type III OM is insufficiently understood, especially the pore evolution inside OM.

Thermal simulation experiment of hydrocarbon generation is one of the most important way to investigate source rocks and evaluate shale gas reservoirs (He et al., 2020; Santosh and Feng., 2020; Wang et al., 2020). Thermal simulation experiment can be used to examine the hydrocarbon dynamics during hydrocarbon generation-expulsion of source rocks, and now it has also been frequently used to investigate the pore dynamics in shale reservoirs (Shi et al., 2018; Wang et al., 2021; Zhang et al., 2021; Zhao et al., 2021). Through extensive thermal evolution simulation on low maturity shale, previous researchers have demonstrated that maturity is the main controlling factor for the development of organic pores in shale (Klaver et al., 2012; Löhr et al., 2015; Zargari et al., 2015; Sun et al., 2021). Besides, the shale inhomogeneity, experiment development degree, and water-bearing condition also have some impacts on the development degree of organic pores in shale (Sun et al., 2015; Li and Li., 2021; Zhang et al., 2022). In addition, due to the limitations of design purpose, sample selection and experimental equipment, it is difficult to match the simulation evolution stage and experimental conditions with the real underground conditions. However, previous researchers have tried to investigate the shale diagenetic history and organic pore evolution in different ways. Dong et al. (2015) controlled the simulation temperature by assuming a short action and without considering the effect of formation pressure, and the porosity after experiments could be a little larger than that of the real geological sample. Chen and Xiao performed an anhydrous pyrolysis experiment on three low maturity shale samples with different kerogen types or *TOC* contents at a wide range of temperatures and applied N2 adsorption, CO2 adsorption to characterize the micro-nano pore systems. (Chen and Xiao, 2014). Ji et al. (2017). designed high-temperature and high-pressure simulation experiments for constant temperature and constant pressure, respectively, to explore how temperature and pressure control shale pore evolution. The results showed that large numbers of micropores can form in OM, pyrite, and dolomite matrices.

Identifying the process and controlling factors of pore evolution is the basis for understanding the genesis and enrichment mechanism of shale gas (Cavelan et al., 2020). However, there are still few researches on pore structure evolution for marine-continental transitional shale. So in this paper, the Shanxi Formation shales were collected to conduct the thermal simulation experiment to analysis the pore evolution and shale gas accumulation. High-temperature, high-pressure thermal simulation experiments were performed on low maturity marine-continental transitional shale from Ordos Basin. And the pore system of shale samples were characterized before and after simulation, respectively. Besides, the rock pyrolysis, X-ray diffraction (XRD), and gas adsorption results were quantitatively compared to explore the process and controlling factors of pore evolution. The findings could provide some clues for examining the enrichment mechanism of marine-continental transitional shale gas.

SAMPLES AND EXPERIMENTS

Experiment Samples and Experiments

In this paper, dozens of marine-continental transitional shale samples were collected from Permian Shanxi Formation shale across the Palougou section in Baode, Ordos Basin (**Figure 1**). The shale samples from Permian Shanxi Formation are a typical marine-continental transitional shale. The selected shale samples were cut into several similar groups to conduct the thermal simulation experiments. Multiple techniques were used in this

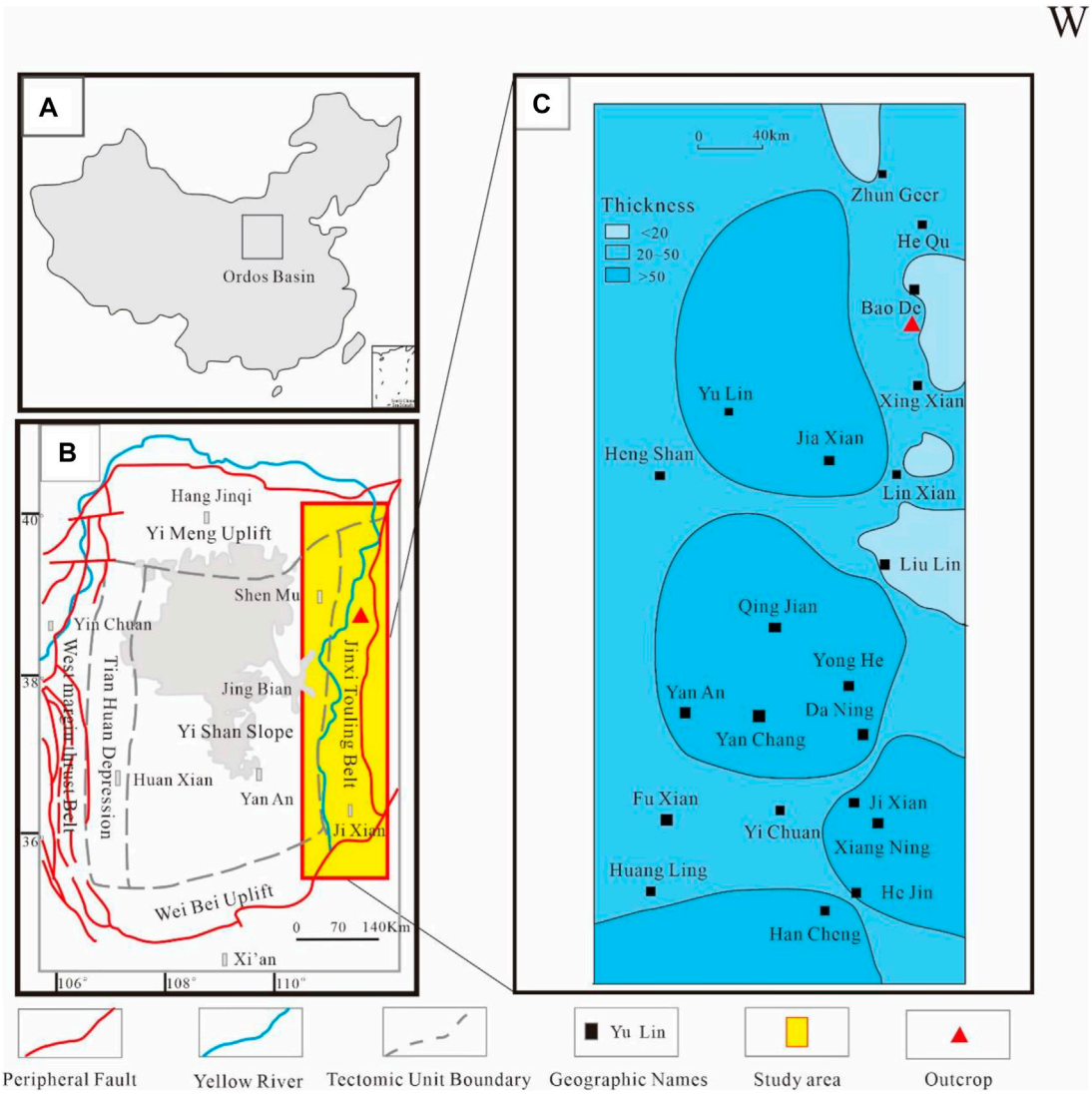

FIGURE 1 | (A) Locations of the Ordos Basin. **(B)** Sketch map of Ordos Basin, the study area, and gas resource distribution. **(C)** Thickness distribution of Shanxi Formation shale and well location.

paper, XRD and SEM were used to obtain microscopic petrological and mineralogy characteristics; Rock-Eval and vitrinite reflectance analysis were used to get the geochemical characteristics of the shales; and SEM, low pressure N2 and CO2 adsorption were conducted to obtain the pore structure of the shale.

TOC, rock-Eval and XRD analyses were completed at the Key Laboratory of Petroleum Geochemistry of CNPC, using a LECCO CS230 carbon-sulfur analyzer and Rigaku TTR III automatic X-ray diffractometer. Low-temperature CO2 and N2 adsorption experiments were completed at Beijing Center for Physical & Chemical Analysis, using an Autosorb-IQ-MP specific surface and porosity analyzer. The test pore size interval was 0.35–200 nm. Pore structure parameters were calculated with Dubinin-Radushkevich (DR) model and Barrett-Johner-Halenda (BJH) model. All experiments were run in strict accordance with the national and industry specifications for experiment.

Thermal Simulation Experiments

Thermal simulation experiment was carried out at the Key Laboratory of Oil and Gas Reservoir of CNPC, using a diagenesis physical simulation system. Closed system thermal simulation method was applied. The experiment was completed in a split reactor system. The temperature of each reactor can be separately controlled by the program set on the computer. The maximum experiment temperature was 550°C; the maximum static rock pressure was 275 MPa. The main body of the instrument is an autoclave that contains the massive samples needed for simulation. The autoclave cavity is 2 cm in diameter and 40 cm deep. Two-dimensional FE-SEM images of the samples before and after simulation was completed with an

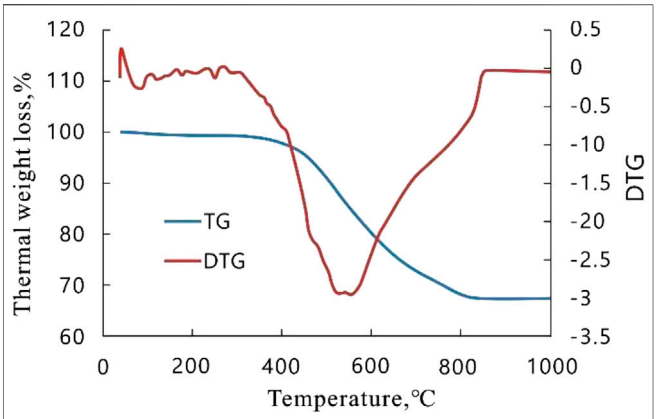

FIGURE 2 | Thermal gravimetry (TG) and differential thermal gravimetry (DTG) curves of the samples.

Apreo dual-probe low vacuum FE-SEM. The experiment procedure was as follows: 1) The sample was divided into four parallel samples, which were separately prepared into four FE-SEM samples and four 100-mesh powder samples; 2) FE-SEM imagery characterization was performed on the four SEM samples to obtain pore structure information of the original samples; 3) The four samples were separately placed into four reactors, the desired simulation temperatures were set, the experiment pressure was set to 60 MPa, the temperature increase rate was set to 20°C/h; 4) The four samples after thermal simulation were taken out, naturally cooled after 8 h of constant temperature, before.

FE-SEM imagery characterization was performed at the same position as in step (2) to obtain their pore structure information under the simulation temperature; (5) The four powder samples were placed into four respective reactors and thermally treated at the same temperature point as set in step (3); (6) Organic geochemical, XRD, and gas adsorption analyses were performed on the thermally treated powder samples.

Thermal decomposition experiment was carried out with a synchronous thermal analyzer, using air as the reaction gas. High-purity N_2 was injected as the protective gas. The sample was heated at the temperature increase rate of 10°C/min to obtain its DG curve from normal temperature to 1,000°C (**Figure 2**). Thermal gravimetric analysis was proceeded in two stages: from normal temperature to 308°C, the mass of the sample reduced from 255.72 to 253.91 g, with weight loss rate of 0.71%; from 308 to 600°C, the mass of the sample reduced from 253.91 to 172.05 g, with weight loss rate of 32%. The experiment result indicated that the OM thermal decomposition temperature of Shanxi Formation shale is between 308 and 600°C, with maximum DTG corresponding to approximately 550°C. The *Ro* of the original sample is 0.78%. The four temperature points set for the simulation were: 400°C, 450°C, 500°C, and 550°C; the corresponding Ro levels were approximately 1.0%–1.2%, 1.4%–1.6%, 1.8%–2.0%, and 2.2%–2.5%. It can be classified into three evolution stages according to the different Ro size: low maturity, high maturity and high over-maturity stage.

EXPERIMENT RESULTS

Organic Geochemistry, Petrology and Mineralogy

The marine-continental transitional shale in the Shanxi Formation has been cut and preserved as 5 samples with the same characteristics. The original shale samples were selected from the original samples of organic geochemistry, petrology and mineralogy, and then thermal simulation experiments were performed on the remaining 4 shale samples. Geochemical parameters, mineral composition and gas adsorption experimental results of the original samples and thermal simulation experimental samples at different temperatures were shown in **Table 1**. It can be obtained from the data: original shale vitrinite reflectance (*Ro*) = 0.78%, total organic carbon (*TOC*) = 19.47%, free hydrocarbon content = 1.7 mg/g, pyrolysis hydrocarbon content = 60.46 mg/g, the maximum Pyrolysis peak temperature = 436°C. According to the analysis of microscopic components, the types of OM were mainly chitinite and vitrinite, and the type of kerogen is type III; the mineral components were mainly clay minerals and quartz, with a small amount of feldspar; the clay minerals were mainly kaolinite, Illite content is less (**Table 1**).

FE-SEM Observation

A small amount of clay mineral interlayer pores, organic pores, dissolution pores and micro-fractures developed in the original samples. The observation results of nearly 500 observation layers show that with the increase of thermal simulation temperature, the pore system of the sample first decreases and then increases (**Figure 3**). Using FE-SEM observation, it was found that some microcracks appeared in the sample at 400°C (**Figure 3B**), but the OM had melted, the surface softened and folded, and the oil spilled out of the pyrolyzed asphalt, which was an intermediate product of the pyrolysis of the OM (**Figure 3C**). The pyrolyzed bitumen is highly plastic and can fill the original pores, resulting in a reduced pore system (**Figure 3F**). From 450 to 500°C, the liquid hydrocarbon products produced in the early stage were continuously consumed by secondary pyrolysis, resulting in the formation of organic pores or the expansion of the original organic pores, and the organic micro-cracks also continue to be generated or expanded (**Figures 3G–N**). Besides, some bar OM (ligneous OM) also begins to generate large numbers of singular organic pores. These circular or elliptical pores spread in a dispersed manner, generally smaller than 20 nm in size (**Figures 3O,P**).

For samples at 550°C, organic pores and micro-cracks continued to increase, but the increase was smaller (**Figures 3U–X**). Although micro-fractures were likely to appear at the edges of inorganic minerals and OM, the inorganic mineral pores and fractures have little change before and after the thermal simulation experiment (**Figures 3I,R,T**).

Gas Adsorption

Low-temperature CO_2 adsorption and low-temperature N_2 adsorption experiments were carried out to quantitatively compare the structural characteristics of micro-pores ($d < 2$ nm) and mesopores ($2\text{ nm} < d < 50$ nm) in the samples

TABLE 1 | Shale sample parameters under different simulation temperatures.

Geochemical parameters				Mineral composition							N_2 adsorption		CO_2 adsorption	
Simulation Temp/°C	*TOC*/ %	*Ro*/%	Tmax/ °C	S_1 (mg/ g)	S_2 (mg/ g)	Quartz/ %	Feldspar/ %	Clay/ %	Illite/ %	Kaolinite/ %	BET Specific Suface Area (m^2/g)	BJH Pore Volume (cm^3/g)	DR Specific Surface Area (m^2/g)	DR Micropore Volume (cm^3/g)
Original Sample	19.5	0.78	436	1.7	60.46	44.9	1.5	53.6	11	89	4.12	0.0154	27.97	0.0112
400	18.1	1.0–1.2	453	7.53	23.7	42.8	1.0	56.2	23	77	1.00	0.004	23.88	0.0096
450	17.5	1.4–1.6	565	1.07	6.01	36.1	/	63.9	20	80	1.39	0.0043	39.68	0.0159
500	17.2	1.8–2.0	606	0.83	1.48	47.7	/	52.3	22	78	1.55	0.0045	52.99	0.0213
550	16.9	2.2–2.5	607	0.12	0.40	46.8	/	53.2	31	69	2.65	0.0063	63.34	0.0254

Note: TOC, *total organic carbon; maturity of OM; Tmax—maximum pyrolysis temperature;* S_1*—hydrocarbon monastery;* S_2*—pyrolysis hydrocarbon content.*

before and after thermal simulation experiments. The experimental results show that with the increase of the temperature of the thermal simulation experiment, the structural parameters of the micropores and mesopores show a trend of first decreasing and then increasing. The BET mesopore specific surface area first decreased from 4.12 m^2/g of the original sample to 1.0 m^2/g (400°C), and then increased to 1.3 m^2/g (450°C), 1.55 m^2/g (500°C) and 2.65 m^2/g (550°C). Correspondingly, the BJH mesopore volume first decreased from 0.0154 cm^3/g in the original sample to 0.004 cm^3/g (400°C), and then increased to 0.0043 cm^3/g (450°C), 0.0045 cm^3/g (500°C) and 0.0063 cm^3/g (550°C) (**Table 1**). Similarly, the specific surface area of DR micro-pores first decreased from 27.97 m^2/g of the original sample to 23.88 m^2/g (400°C), and then increased to 39.68 m^2/g (450°C), 52.99 m^2/g (500°C) and 63.34 m^2/g (550°C). In addition, the volume of DR micro-pores decreased from 0.0112 cm^3/g of the original sample to 0.0096 cm^3/g (400°C), and then increased to 0.0159 cm^3/g (450°C), 0.0213 cm^3/g (500°C), and 0.0254 cm^3/g (550°C) (**Table 1**). It can be obtained from the experimental data that the higher the temperature of the thermal simulation experiment, the higher the degree of micro-pore development of the sample. For example, under the temperature condition of 550°C, the micro-porous structure parameters of the samples are more than twice that of the original samples.

Figure 4 showed the comparison of low-temperature CO_2 adsorption isotherms of samples at different temperatures. As can be seen from the figure, under the temperature condition of 400°C, the adsorption capacity of the sample is the smallest, even lower than that of the original sample. After that, with the increase of the temperature of the thermal simulation experiment, the adsorption amount of the sample also began to increase, and reached the highest level at 550°C. The size distribution of the DFT micropores (**Figure 5**) also supports this observation. But it is worth noting that, compared with the original samples, two new peaks at 0.55 and 0.65 nm appeared in the pore size distribution of the samples at 450°C, 500°C and 550°C, which indicated that during the thermal evolution, the new micro Pore diameters may appear between 0.5 and 0.7 nm.

Figures 6, **7** show the low-temperature N_2 adsorption curves and mesopore distributions of the samples under different temperature conditions. It can be seen that the N_2 adsorption-desorption curve of the original sample is similar to the H_3 curve under the IUPAC classification. With the increase of relative pressure, the adsorption curve rises slowly; when approaching the saturated vapor pressure, the adsorption curve rises sharply and the desorptioncurve falls sharply due to capillary condensation. This experimental phenomenon indicated that there were groove pores around. The N_2 adsorption-desorption curves of the thermal simulation samples were similar to the H_4 curve, and also show some characteristics of the H_3 curve. The adsorption-desorption loop was narrow. As the relative pressure increased, the adsorption curve firstly rose slowly. And then the curve became a steep rise due to capillary coalescence when the pressure near the saturation vapour pressure. The desorption curve dropped fast, which indicating the existence of slit pores and slot pores open on four sides. With the increase of the temperature of the thermal simulation experiment, the mesopores and micropores changed from mainly slot pores to coexistence of slit pores and slot pores.

The mesoporous structure parameters of the thermal simulation experimental samples are significantly smaller than those of the original samples. From 400 to 550°C, the structural parameters increased, but were still smaller than the original samples. The BET specific surface area decreased from 4.12 m^2/g of the original sample to 1.0 m^2/g (400°C), then increased to 1.39 m^2/g (450°C), 1.55 m^2/g (500°C) and 2.65 m^2/g (550°C). The BJH mesopore volume reduces from 0.015 cm^3/g for the original sample to 0.004 cm^2/g, then increases to 0.0043 cm^3/g (450 °C), 0.0045 cm^3/g (500°C), and 0.0063 cm^3/g (550°C).

DISCUSSION

Process of Pore Evolution

Previous researchers have found that nanopores were related to the petroleum generation and OM reshape through heating experiments and SEM observation (Ko et al., 2016). Similar to previous pyrolysis experiments on type I kerogen, the results of thermal simulation experiments for type III kerogen showed that porosity were associated with the stages of OM. From the

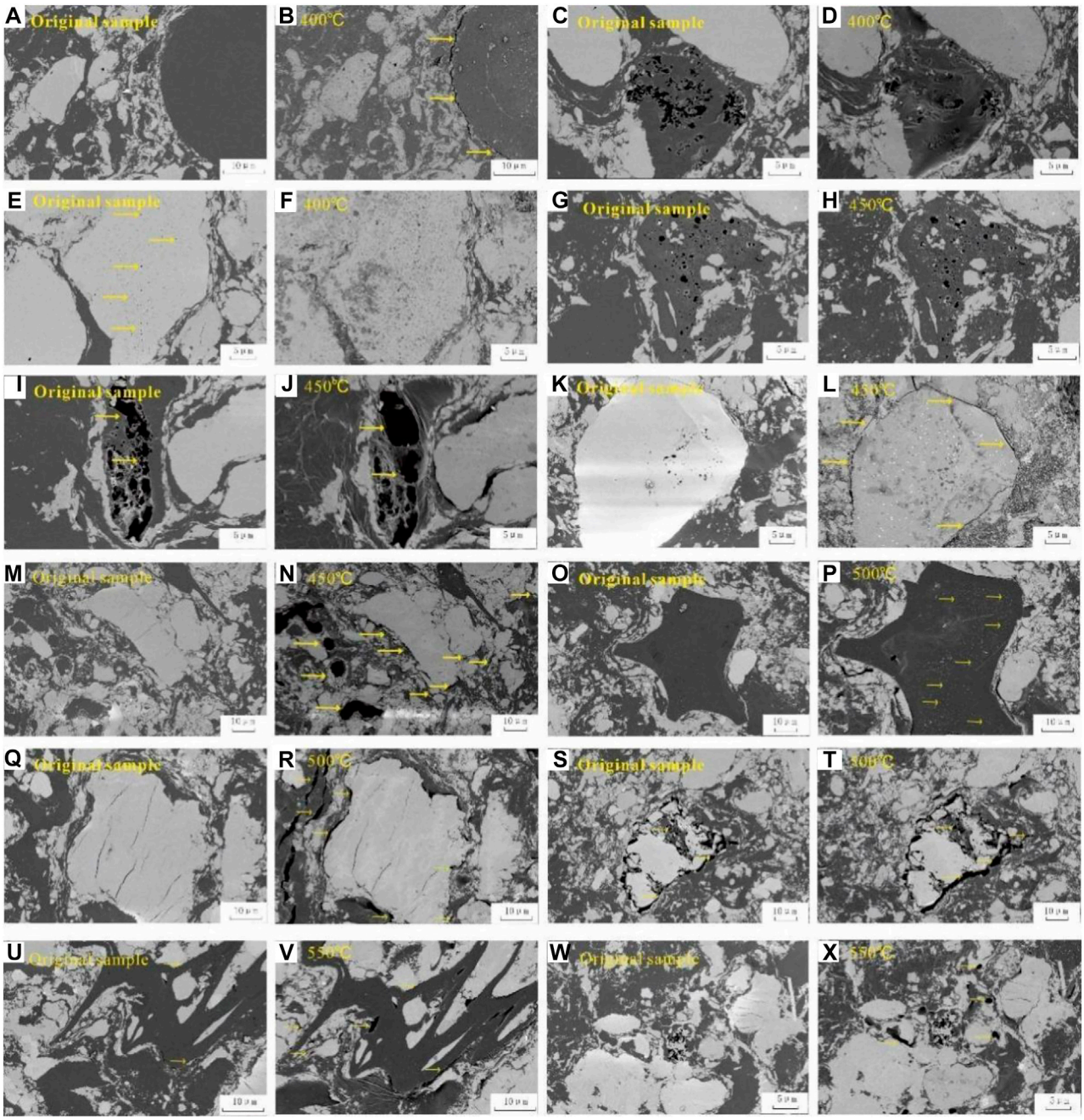

FIGURE 3 | Evolution of OM and inorganic minerals under different temperatures. **(A)** Original sample, where no pore was developed; **(B)** 400°C simulation sample, where microfactures appeared on the edge of OM and minerals; **(C)** Original sample, a few biogenic air pores were developed; **(D)** 400°C simulation sample, OM melted to produce pyrolytic bitumen that fills the original pores; **(E)** A few original pores developed in the inorganic minerals; **(F)** 400°C simulation sample, where the original pores were filled; **(G)** OM pores were developed in the original sample; **(H)** 450°C simulation sample, micropores emerged; **(I)** OM pores developed in the original sample; **(J)** 450°C simulation sample, the OM pores enlarged; **(K)** Very few microfractures emerged on the edge of minerals in the original sample; **(L)** 450°C simulation sample, the microfractures on the edge of minerals increased and broadened; **(M)** No pore developed in the original sample; **(N)** 450°C simulation sample, OM pores and fractures developed; **(O)** Original sample, pores were not developed on the edge of massive OM; **(P)** 500°C simulation sample, large numbers of singular pores emerged in the OM; **(Q)** A few inorganic mineral pores and fractures developed in the original sample; **(R)** 500°C simulation sample, where inorganic mineral pores and fractures have not changed visibly, large numbers of pores and fractures emerged inside the OM; **(S)** Intergranular pores and fractures developed in the OM and inorganic minerals in the original sample; **(T)** 500°C simulation sample, where the intergranular pores and fractures increased and enlarged; **(U)** No pore developed in the original sample; **(V)** 550°C simulation sample, OM pores and fractures are developed; **(W)** A few OM pores were present in the original sample; **(X)** 550°C simulation sample, OM increased and enlarged.

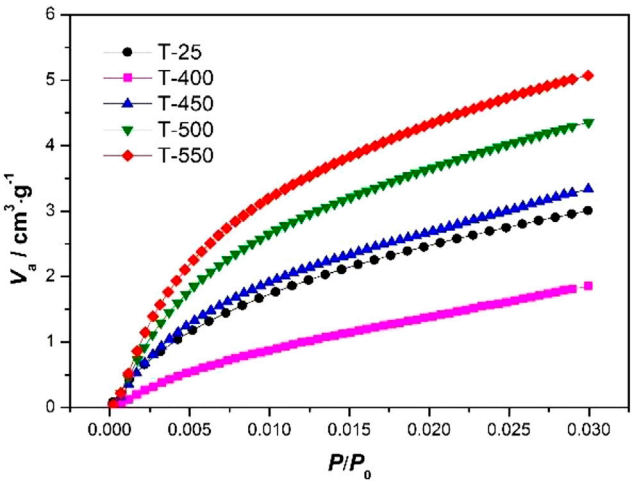

FIGURE 4 | Low-temperature CO_2 adsorption isotherms of the samples at different temperatures.

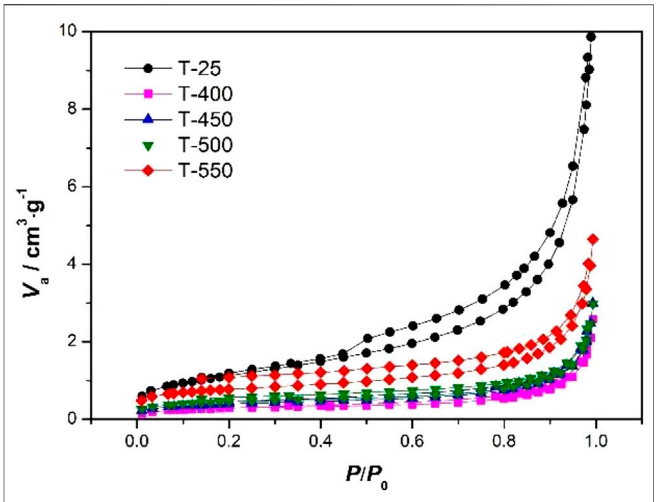

FIGURE 6 | Low-temperature N_2 adsorption curves of the samples at different temperature points.

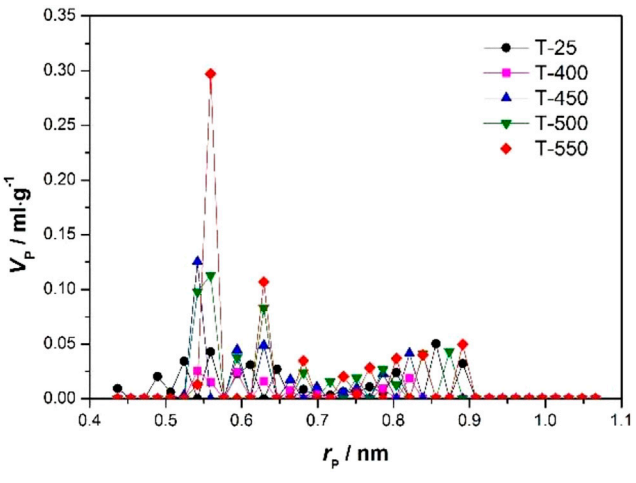

FIGURE 5 | Pore size distribution of micro-pores in the samples at different temperature points.

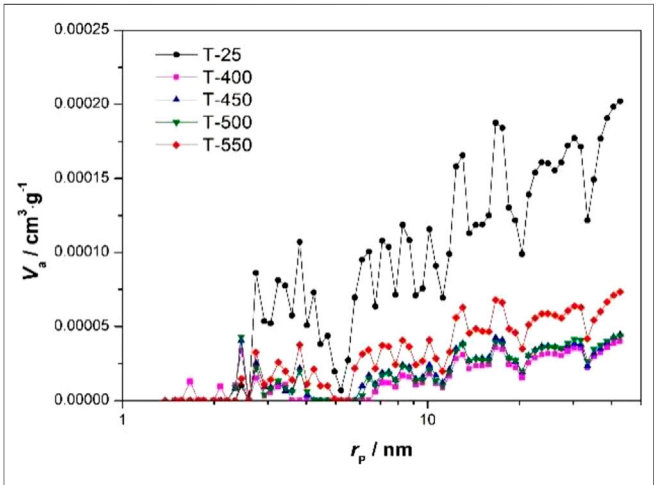

FIGURE 7 | Pore size distribution of mesopores in the samples at different temperature points.

observation for the shale samples during the process of the artificial heating experiments, it is found that there were distinct changes for shale pores during the thermal evolution, so the shale evolution process can divide into four stages as follows (**Figure 8**):

Stage 1 (1.0% < *Ro* < 1.2%),the maturity stage. It is corresponding to the simulated temperature of 400°C. The porosity decreased rapidly in this stage. During this period, the pyrolysis of OM produced a large amount of pyrolysis asphalt, the *TOC* decreased and the hydrocarbon generation capacity (S_1+S_2) decreased from 62.16 mg/g to 31.23 mg/g. Micro-pores and micro-cracks appeared in the interior or edges of OM. Most of these new pores were observed to be mainly slit pores. In addition, the high plasticity hot asphalt filled the pores in a large area, resulting in a sharp reduction of the pore system, especially the mesopores.

Stage 2 (1.2% < *Ro* < 2.0%), the high maturity stage, the corresponding simulated temperature was 400–500°C. The pore system developed rapidly in the stage. During this period, the pyrolysis of OM produced a large amount of gaseous hydrocarbons, and the (S_1+S_2) level decreased from 31.23 mg/g to 2.31 mg/g. The formation of a large number of organic pores resulted that the pore system expanded rapidly. Additionally, a large amount of organic acid also produced when OM generated hydrocarbons. It leaded to the transformation of feldspar minerals and many dissolution pores were observed. High temperature and pressure conditions in this stage stimulated the transformation of clay minerals such as kaolinite and illite as well, which leading to an increment of the inorganic mineral pore system. So both organic and inorganic pores increased rapidly in this stage. In the late of this period (2.0% < *Ro* < 2.5%), it is also in the high maturity stage, while the formation of

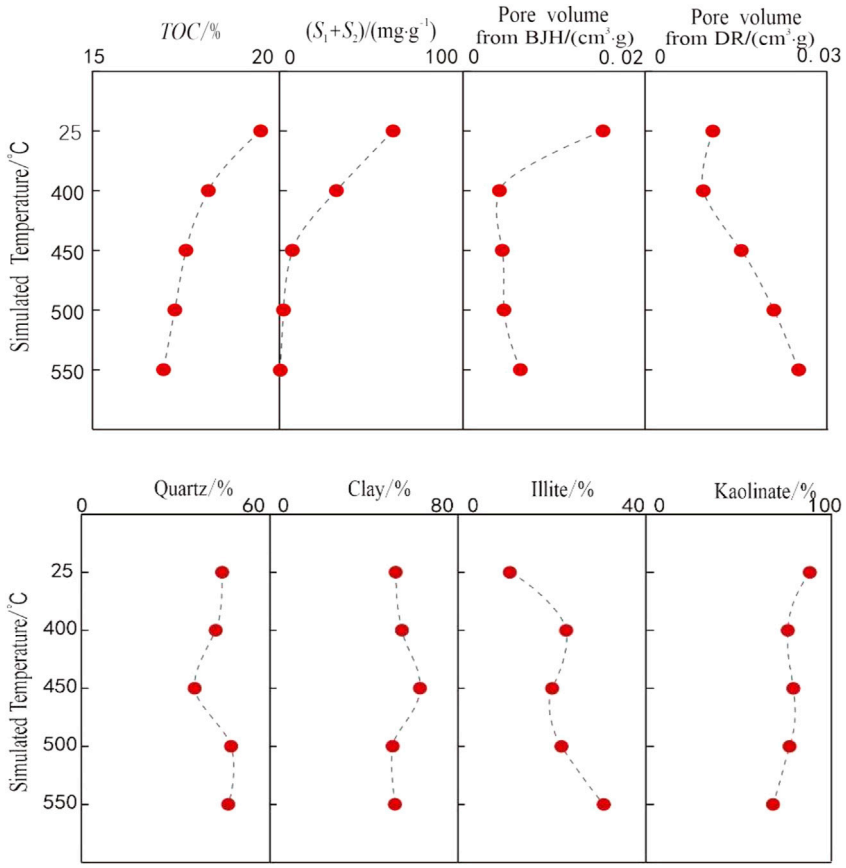

FIGURE 8 | Parameters variation trend for the simulated samples at different temperatures.

new pores speeded down. The corresponding simulated temperature is around 550°C. During this period, OM contents continued to decrease, with (S_1+S_2) levels dropping from 2.31 mg/g to 0.52 mg/g. The organic minerals tended to stabilize, the conversion rate decreased. The pore space contribution from this period to whole porosity was much smaller than last period.

Stage 3 (Ro > 2.5%), over-mature stage. And the pore system was trend to stable. At this period, (S_1+S_2) level was 0.52 mg/g, a small amount of OM was pyrolyzed and a small amount of organic pores were generated. At this time, the rock was in the late diagenetic stage and had good compression resistance and stability. Mineral particles and OM particles existed alternately to form an interconnected organic-inorganic pore network system, which kept the entire pore system relatively stable.

In conclusion, the whole process of porosity evolution during the thermal simulation was roughly divided into 3 stages (maturity, high maturity and over maturity) as the thermal maturity increases. The porosity first decreased, then increased, and finally stabilized. The high maturity period (1.2 %< Ro<2.0%) was the period when extensive hydrocarbon generated in the Shanxi Formation shale.

Summarily, the high maturity period (1.2% < Ro < 2.0%) is the period of OM maturity. At this time, the shale of the Shanxi Formation was extensively pyrolyzed to generate hydrocarbons, and the pore system was greatly expanded. This period is the best period for pore evolution.

Controlling Factors of Pore Evolution

Hydrocarbon generation and diagenesis were key controlling factors for shale pore evolution (Cavelan et al., 2020; Liu et al., 2017; Zhao Z. et al., 2020). From the results of thermal simulation experiments: with the increase of simulated temperature, *TOC* decreased from 19.47% to 16.92%; (S_1+S_2) level decreased from 62.16 mg/g to 0.52 mg/g (**Table 1**; **Figure 8**). This indicated that strong pyrolysis hydrocarbon generation occurred in the OM. In our observations, maturity and OM type affect the pore system. In immature shale, organic pores were not developed; in mature shale, pores were mainly developed in OM. Therefore, maturity is a key factor affecting the development of shale pores (Sun et al., 2015). In shale samples, the pore system does not increase linearly with the increase of maturity, and secondly, it showed a trend of first decreasing and then increasing rapidly. Obviously, in the low maturity stage, the OM loses some pores; in the high maturity stage, a large number of pores regenerated. In the low maturity stage, a large amount of pyrolysis asphalt produced by the pyrolysis of OM fills the pores in a large area, resulting in a smaller pore system, and the volume of mesopores decreases from

0.0154 cm^3/g to 0.004 cm^3/g; the volume of micropores decreases from 0.0112 cm^3/g to 0.0096 cm^3/g. In the high over-maturity stage, OM undergoes structural rearrangement, pyrolysis cyclization, aromatization polycondensation or cross-linking to generate small molecular hydrocarbons, resulting in a large number of pores. The pyrolyzed bitumen produced in the early stage also began to undergo a second pyrolysis, resulting in a large number of organic pores and the rapid expansion of the pore system. Micropore volume increased from 0.0096 cm^3/g to 0.0254 cm^3/g; mesopore volume increased from 0.004 cm^3/g to 0.0063 cm^3/g. In addition, the type of organic pores changed with increasing maturity. The original sample is at an immature stage, affected by shallow biological processes, resulting in a small amount of biogas and a small number of slots. In the thermal simulation experimental samples, a large number of pores and cracks generated in the OM, and the pores were mainly slits.

The type of OM also plays a role in pore development. Compared with type I and type II kerogen, type III kerogen is more prone to a large number of micro-pores (Jia et al., 2020). The OM of our experimental samples is type III, and a large number of micro-pores and a small amount of mesopores were generated during the thermal simulation experiment, further confirming that type III OM has the potential to generate a large number of pores and cracks (**Figure 3**). In the high maturity stage (400–500°C), a large number of micro-pores were formed, and the pore volume increases from 0.0096 cm^3/g to 0.0159 cm^3/g, an increase of 1.2 times; a small amount of mesopores develops, and the pore volume increases from 0.004 cm^3/g to 0.0045 cm^3/g. In the high over-maturity period (500–550°C), a large number of mesopores were formed, and the pore volume increased from 0.0045 cm^3/g to 0.0063 cm^3/g, an increase of 0.4 times; the micro-pores also developed continuously, and the pore volume increased by 0.2 times, resulting in an increase of 0.4 times. The micro-pores were interconnected to form mesopores. Previous studies have demonstrated that rock micro-pores containing vitrinite components were very developed (Ji et al., 2017). Our FE-SEM observation also revealed that singular pores were developed in bar OM, with pore size smaller than 20 nm. This result is consistent with the organic pore development characteristics of the high-maturity shale in the Shanxi Formation, which further verifies the reliability of our thermal simulation results. However, given the limited resolution of FE-SEM, we likely did not observe many pores smaller than 10 nm.

The inorganic minerals in the Shanxi Formation shale samples were mainly clay minerals and quartz, with less feldspar. XRD analysis showed that with the increase of simulation temperature, the content of clay minerals first increased and then decreased; the content of kaolinite decreased; the content of illite increased; the content of quartz decreased first and then increased; the content of feldspar decreased to zero (**Table 1**; **Figure 8**), the result indicated that inorganic minerals were transformed during diagenesis. When the simulated temperature reached to 450°C, the inherently acidic diagenetic conditions of coal measure formations resulted in the transformation of feldspar to kaolinite (Kuila et al., 2014), which increased the content of clay minerals. The potassium ions released by the feldspar alteration also caused the continuous transformation of kaolinite to illite. When the simulated temperature exceeds 450°C, the high temperature and high pressure conditions further stimulate the transformation of clay minerals, and the released siliceous precipitates were transformed into authigenic quartz, thereby reducing the content of clay minerals and increasing the content of quartz (Peltonen et al., 2009; Xu et al., 2021). The range of 400–500°C was the main transformation period of clay minerals, and the corresponding Ro was 1.0%–2.0%. After this, the degree of transformation and the contribution to the storage space decreased. The acidic fluid generated by organic hydrocarbon generation can dissolve soluble minerals and generate dissolution pores. From the FE-SEM observation, the feldspar dissolution cracked in the simulated samples tended to enlarge (**Figure 3I**). In addition, increased or enlarged micropores and microfractures can also be observed inside the quartz mineral, but at a limited rate of increase (**Figure 3T**). Overall, from the XRD results, the inorganic minerals in the shale were transformed with the increase of temperature; but from the FE-SEM results, no obvious mineral pores were observed in the samples before and after the thermal simulation experiment. One possible explanation was that the high-pressure conditions generated by the closed system used for the experiments inhibited the development of pores to some extent, especially for inorganic minerals that cannot generate hydrocarbons.

In summary, as the temperature of the thermal simulation experiment increased, both organic hydrocarbon generation and inorganic mineral transformation played a certain role in the development of shale pores, but the former had a much greater impact on the development of pores. The type of OM determined the type of pore development; the maturity of OM controlled the degree of pore development. In addition, in the closed-system thermal simulation experiments, the pressure inhibited the development of shale pores to a certain extent. In other words, under high pressure conditions, there were fewer pores and smaller pore sizes.

Geological Implication

The production tests from several wells from the eastern Ordos Basin have shown that the Permian continental and marine transitional shale has great potential and broadly exploration prospects (Kuang et al., 2020). The previous research has shown that organic-rich shale in the Shanxi Formation has the characteristics of high continuous thickness, high organic carbon content, and wide distribution range (Wu et al., 2021). So it has received extensive attention in the study of marine-continental transitional shale gas in recent years. But there is still a debate about the effectiveness for pore system of the Shanxi Formation. Some researchers believe that the pore system in Type III OM is not sufficient to form shale gas reservoir (Jiang et al., 2017). To reveal the effectiveness and evolution process for shale pores system, the artificial pyrolysis or thermal simulation experiments play a key factor. Many existing experiments, such as gold tube pyrolysis experiments, artificial high-pressure and high-temperature simulation experiments can explore the stepwise changes in pores shape and size in the process of thermal maturity (Chen and Xiao, 2014; Ko et al.,

2016; Dong et al., 2020; Hower and Groppo., 2021).And then the experiments results can show the potential and effectiveness of the shale. So, for this study, we tried to use thermal simulation experiments to reveal the pore evolution process and controlling factors of marine-continental shale, and finally come to the conclusion that 1) the pore system of the Shanxi Formation shale is sufficient enough to accumulate shale gas and 2) whether the Type III OM has the capacity to generate the enough hydrocarbon for shale gas.

Through thermal simulation experiments and careful analysis during the process of the thermal simulation, two main understandings can be drawn: 1) Type III OM has good hydrocarbon generation potential, though the capacity of hydrocarbon generation for Type III OM is weaker than that of type I. 2) complex, stable and sufficient pore system in Shanxi Formation shale formed in the process of hydrocarbon generation and the high maturity stage (1.2% < *Ro* < 2.0%) is the extensive pyrolysis of OM in the Shanxi Formation shale to generate hydrocarbons period. The findings from high-pressure and high-temperature simulation experiments can guide to explore the "sweet-spots" for shale gas for this kind of shale. Based on our previous research, the regional maturity of the Shanxi Formation in the eastern Ordos Basin varies greatly, with *Ro* distribution ranging from 0.6% to 2.8%, and the maturity increases from northeast to southwest. The Ro of the shale in the northern Baode-Xingxian-Linxian line is 0.6%–1.2%, which is in the low maturity stage; the shale in the southern part is deeply buried and the maturity is high, and the Ro of the shale along the Shilou-Daning-Jixian line is 1.2%–2.2%, the *Ro* value along the Fuxian-Yichuan line is as high as 2.8% (Wu et al., 2021). Based on these findings, maturity can be used as a key indicator for finding the most favorable zones for shale gas in the Shanxi Formation. Based on the high-pressure and high-temperature simulation experiments and Ro distribution for the shale, it can roughly conclude that the most potential area for the Shanxi shale is around along the Shilou-Daning-Jixian line. However, due to the significant differences in temperature, pressure and fluid between actual formation conditions and thermal simulation experiments, this research work is only a preliminary exploration of pore evolution. The Ro can play a key factor for the exploration for the marine continental transitional shale, and TOC, depth, fracturity and other parameters also act the important role.

CONCLUSION

(1) The results from artificial high-temperature and high pressure thermal simulation experiments showed that the type III OM shale from Shanxi Formation has good hydrocarbon generation potential though smaller than type I OM. It produced large numbers of micropores (<2 nm) and small numbers of mesopores (2–50 nm) during hydrocarbon generation. And maturity can be used as a key indicator for finding the most favorable zones for shale gas in the Shanxi Formation.

(2) The key factor influenced the shale pore system evolution during the thermal simulation is the generation and adjustment of organic pores. The organic pores from conversion of inorganic minerals (kaolinite into illite) contribute less to pore volume than organic pores.

(3) The evolution of the shale pore system can be divided into 3 stages (maturity, high maturity and over maturity) as the thermal maturity increases. The porosity first decreased, then increased, and finally stabilized. The high maturity period (1.2%< *Ro* <2.0%) was the period when extensive hydrocarbon generated in the Shanxi Formation shale, which contributed mostly for the pores generation and accumulation of shale gas.

DATA AVAILABILITY STATEMENT

The original contributions presented in the study are included in the article/Supplementary Material, further inquiries can be directed to the corresponding authors.

AUTHOR CONTRIBUTIONS

JW, XZ, and HX contributed to the conception of the study; YX contributed to drafting the discussion; JW and HX contributed significantly to analysis and manuscript preparation; GL, LJ, ND, and ZR, performed the data analyses and figure preparation. YX, XZ, and HX performed the constructive discussions and revised the manuscript. All authors contributed to the article and approved the submitted version.

ACKNOWLEDGMENTS

We want to thank National Natural Science Foundation of China (Grant No. 42002157), Sichuan Science and Technology Support Project (2021YJ0349), PetroChina Research Institute of Petroleum Exploration & Development and National Energy Shale Gas R&D (Experimental) Center for this research. We greatly acknowledge Associate Editor and all the reviewers for their insightful and thorough reviews to contribute greatly to this special issue.

REFERENCES

Abouzar, M., and Ghanbarian, B. (2021). A New Methodology for Grouping and Averaging Capillary Pressure Curves for Reservoir Models. *Energ. Geosci.* 2, 52–62. doi:10.1016/j.engeos.2020.09.001

Bhatti, A. A., Ismail, A., Raza, A., Gholami, R., Rezaee, R., Nagarajan, R., et al. (2020). Permeability Prediction Using Hydraulic Flow Units and Electrofacies Analysis. *Energ. Geosci.* 1, 81–91. doi:10.1016/j.engeos.2020.04.003

Cavelan, A., Boussafir, M., Le Milbeau, C., Delpeux, S., and Laggoun-Défarge, F. (2020). Influence of Experimental Temperature and Duration of Laboratory Confined thermal Maturation Experiments on the Evolution of the Porosity of

Organic-Rich Source Rocks. *Mar. Pet. Geology.* 122, 104667. doi:10.1016/j.marpetgeo.2020.104667

Chen, J., and Xiao, X. (2014). Evolution of Nanoporosity in Organic-Rich Shales during thermal Maturation. *Fuel* 129, 173–181. doi:10.1016/j.fuel.2014.03.058

Chen, Y., Wang, Y., Guo, M., Wu, H., Li, J., Wu, W., et al. (2020). Differential Enrichment Mechanism of Organic Matters in the marine-continental Transitional Shale in Northeastern Ordos Basin, China: Control of Sedimentary Environments. *J. Nat. Gas Sci. Eng.* 83, 103625. doi:10.1016/j.jngse.2020.103625

Dong, S., Zeng, L., Lyu, W., Xia, D., Liu, G., Wu, Y., et al. (2020). Fracture Identification and Evaluation Using Conventional Logs in Tight Sandstones: A Case Study in the Ordos Basin, China. *Energ. Geosci.* 1 (3–4), 115–123. doi:10.1016/j.engeos.2020.06.003

Dong, T., Harris, N. B., Ayranci, K., Twemlow, C. E., and Nassichuk, B. R. (2015). Porosity Characteristics of the Devonian Horn River Shale, Canada: Insights from Lithofacies Classification and Shale Composition. *Int. J. Coal Geology.* 141-142, 74–90. doi:10.1016/j.coal.2015.03.001

Gao, F. Q. (2021). Influence of Hydraulic Fracturing of strong Roof on Mining-Induced Stress Insight from Numerical Simulation. *J. Mining Strata Control. Eng.* 3 (2), 023032. doi:10.13532/j.jmsce.cn10-1638/td.20210329.001

Guo, L. L., Zhou, D. W., Zhang, D. M., and Zhou, B. H. (2021). Deformation and Failure of Surrounding Rock of a Roadway Subjected to Mining-Induced Stresses. *J. Mining Strata Control. Eng.* 3 (2), 023038. doi:10.13532/j.jmsce.cn10-1638/td.20200727.001

He, X., Zhang, P., He, G., Gao, Y., Liu, M., Zhang, Y., et al. (2020). Evaluation of Sweet Spots and Horizontal-Well-Design Technology for Shale Gas in the basin-margin Transition Zone of southeastern Chongqing, SW China. *Energ. Geosci.* 1, 134–146. doi:10.1016/j.engeos.2020.06.004

Hou, L., Cui, J., and Zhang, Y. (2022). Evolution Mechanism of Dynamic thermal Parameters of Shale. *Mar. Pet. Geology.* 138, 105423. doi:10.1016/j.marpetgeo.2021.105423

Hower, J. C., and Groppo, J. G. (2021). Rare Earth-Bearing Particles in Fly Ash Carbons: Examples from the Combustion of Eastern Kentucky Coals. *Energ. Geosci.* 2 (2), 90–98. doi:10.1016/j.engeos.2020.09.003

Jarvie, D. M., Hill, R. J., Ruble, T. E., and Pollastro, R. M. (2007). Unconventional Shale-Gas Systems: The Mississippian Barnett Shale of north-central Texas as One Model for Thermogenic Shale-Gas Assessment. *Bulletin* 91 (4), 475–499. doi:10.1306/12190606068

Ji, L., Su, L., Wu, Y., and He, C. (2017). Pore Evolution in Hydrocarbon-Generation Simulation of Organic Matter-Rich Muddy Shale. *Pet. Res.* 2 (2), 146–155. doi:10.1016/j.ptlrs.2017.07.002

Jia, A., Hu, D., He, S., Guo, X., Hou, Y., Wang, T., et al. (2020). Variations of Pore Structure in Organic-Rich Shales with Different Lithofacies from the Jiangdong Block, Fuling Shale Gas Field, SW China: Insights into Gas Storage and Pore Evolution. *Energy Fuels* 34 (10), 12457–12475. doi:10.1021/acs.energyfuels.0c02529

Jiang, S., Tang, X., Cai, D., Xue, G., He, Z., Long, S., et al. (2017). Comparison of marine, Transitional, and Lacustrine Shales: A Case Study from the Sichuan Basin in China. *J. Pet. Sci. Eng.* 150, 334–347. doi:10.1016/j.petrol.2016.12.014

Klaver, J., Desbois, G., Urai, J. L., and Littke, R. (2012). BIB-SEM Study of the Pore Space Morphology in Early Mature Posidonia Shale from the Hils Area, Germany. *Int. J. Coal Geology.* 103, 12–25. doi:10.1016/j.coal.2012.06.012

Ko, L. T., Loucks, R. G., Zhang, T., Ruppel, S. C., and Shao, D. (2016). Pore and Pore Network Evolution of Upper Cretaceous Boquillas (Eagle Ford-equivalent) Mudrocks: Results from Gold Tube Pyrolysis Experiments. *Bulletin* 100 (11), 1693–1722. doi:10.1306/04151615092

Kuang, L., Dong, D., He, W., Wen, S., Sun, S., Li, S., et al. (2020). Geological Characteristics and Development Potential of Transitional Shale Gas in the East Margin of the Ordos Basin, NW China. *Pet. Exploration Dev.* 47 (3), 471–482. doi:10.1016/s1876-3804(20)60066-0

Kuila, U., McCarty, D. K., Derkowski, A., Fischer, T. B., Topór, T., and Prasad, M. (2014). Nano-scale Texture and Porosity of Organic Matter and clay Minerals in Organic-Rich Mudrocks. *Fuel* 135, 359–373. doi:10.1016/j.fuel.2014.06.036

Li, L., and Li, S. J. (2021). Evolution Rule of Overlying Strata Structure in Repeat Mining of Shallow Close Distance Seams Based on Schwarz Alternating Procedure. *J. Mining Strata Control. Eng.* 3 (2), 023515. doi:10.13532/j.jmsce.cn10-1638/td.20210225.001

Li, Y., Zhou, D.-H., Wang, W.-H., Jiang, T.-X., and Xue, Z.-J. (2020). Development of Unconventional Gas and Technologies Adopted in China. *Energ. Geosci.* 1 (1–2), 55–68. doi:10.1016/j.engeos.2020.04.004

Liu, B., Schieber, J., and Mastalerz, M. (2017). Combined SEM and Reflected Light Petrography of Organic Matter in the New Albany Shale (Devonian-Mississippian) in the Illinois Basin: A Perspective on Organic Pore Development with thermal Maturation. *Int. J. Coal Geology.* 184, 57–72. doi:10.1016/j.coal.2017.11.002

Liu, R., Hao, F., Engelder, T., Zhu, Z., Yi, J., Xu, S., et al. (2020b). Influence of Tectonic Exhumation on Porosity of Wufeng-Longmaxi Shale in the Fuling Gas Field of the Eastern Sichuan Basin, China. *Bulletin* 104 (4), 939–959. doi:10.1306/08161918071

Liu, R., Zheng, J., Hao, F., Nie, Z., Heng, D., Tan, X., et al. (2020c). Variation in Pore Systems with Tectonic Stress in the Overthrust Wufeng-Longmaxi Shale of the Southern Sichuan Basin, China. *J. Nat. Gas Sci. Eng.* 83, 103617. doi:10.1016/j.jngse.2020.103617

Liu, Y., Gao, M., and Zhao, H. (2020a). Detection of Overlying Rock Structure and Identification of Key Stratum by Drilling and Logging Technology. *J. Mining Strata Control. Eng.* 2 (2), 023038. doi:10.13532/j.jmsce.cn10-1638/td.2020.02.004

Löhr, S. C., Baruch, E. T., Hall, P. A., and Kennedy, M. J. (2015). Is Organic Pore Development in Gas Shales Influenced by the Primary Porosity and Structure of Thermally Immature Organic Matter? *Org. Geochem.* 87, 119–132. doi:10.1016/j.orggeochem.2015.07.010

Mastalerz, M., Schimmelmann, A., Drobniak, A., and Chen, Y. (2013). Porosity of Devonian and Mississippian New Albany Shale across a Maturation Gradient: Insights from Organic Petrology, Gas Adsorption, and Mercury Intrusion. *Bulletin* 97 (10), 1621–1643. doi:10.1306/04011312194

Peltonen, C., Marcussen, Ø., Bjørlykke, K., and Jahren, J. (2009). Clay mineral Diagenesis and Quartz Cementation in Mudstones: The Effects of Smectite to Illite Reaction on Rock Properties. *Mar. Pet. Geology.* 26 (6), 887–898. doi:10.1016/j.marpetgeo.2008.01.021

Qie, L., Shi, Y. N., and Liu, J. S. (2021). Experimental Study on Grouting Diffusion of Gangue Solid Filling Bulk Materials. *J. Mining Strata Control. Eng.* 3 (2), 023011. doi:10.13532/j.jmsce.cn10-1638/td.20201111.001

Qiu, Z., Song, D., Zhang, L., Zhang, Q., Zhao, Q., Wang, Y., et al. (2021). The Geochemical and Pore Characteristics of a Typical marine-continental Transitional Gas Shale: A Case Study of the Permian Shanxi Formation on the Eastern Margin of the Ordos Basin. *Energ. Rep.* 7, 3726–3736. doi:10.1016/j.egyr.2021.06.056

Santosh, M., and Feng, Z. Q. (2020). New Horizons in Energy Geoscience. *Energ. Geosci.* 1 (1–2), A1–A2. doi:10.1016/j.engeos.2020.05.005

Shi, M., Yu, B., Zhang, J., Huang, H., Yuan, Y., and Li, B. (2018). Evolution of Organic Pores in marine Shales Undergoing Thermocompression: A Simulation experiment Using Hydrocarbon Generation and Expulsion. *J. Nat. Gas Sci. Eng.* 59, 406–413. doi:10.1016/j.jngse.2018.09.008

Sun, J., Xiao, X., Wei, Q., Cheng, P., and Tian, H. (2021). Occurrence of Irreducible Water and its Influences on Gas-Bearing Property of Gas Shales from Shallow Longmaxi Formation in the Xishui Area, Guizhou, Southern China. *Front. Earth Sci.* 9, 654136. doi:10.3389/feart.2021.654136

Sun, L., Tuo, J., Zhang, M., Wu, C., Wang, Z., and Zheng, Y. (2015). Formation and Development of the Pore Structure in Chang 7 Member Oil-Shale from Ordos Basin during Organic Matter Evolution Induced by Hydrous Pyrolysis. *Fuel* 158, 549–557. doi:10.1016/j.fuel.2015.05.061

Wang, H., Qiao, L., Lu, S., Chen, F., Fang, Z., He, X., et al. (2021). A Novel Shale Gas Production Prediction Model Based on Machine Learning and its Application in Optimization of Multistage Fractured Horizontal Wells. *Front. Earth Sci.* 9, 726537. doi:10.3389/feart.2021.726537

Wang, J., and Wang, X. L. (2021). Seepage Characteristic and Fracture Development of Protected Seam Caused by Mining Protecting Strata. *J. Mining Strata Control. Eng.* 3 (3), 033511. doi:10.13532/j.jmsce.cn10-1638/td.20201215.001

Wang, P., Zhang, C., Li, X., Zhang, K., Yuan, Y., Zang, X., et al. (2020). Organic Matter Pores Structure and Evolution in Shales Based on the He Ion Microscopy (HIM): A Case Study from the Triassic Yanchang, Lower Silurian Longmaxi and Lower Cambrian Niutitang Shales in China. *J. Nat. Gas Sci. Eng.* 84, 103682. doi:10.1016/j.jngse.2020.103682

Wu, J., Wang, H., Shi, Z., Wang, Q., Zhao, Q., Dong, D., et al. (2021). Favorable Lithofacies Types and Genesis of marine-continental Transitional Black Shale: A Case Study of Permian Shanxi Formation in the Eastern Margin of Ordos Basin, NW China. *Pet. Exploration Dev.* 48 (6), 1315–1328. doi:10.1016/s1876-3804(21)60289-6

Xu, H., Zhou, W., Hu, Q., Yi, T., Ke, J., Zhao, A., et al. (2021). Quartz Types, Silica Sources and Their Implications for Porosity Evolution and Rock Mechanics in the Paleozoic Longmaxi Formation Shale, Sichuan Basin. *Mar. Pet. Geology.* 128, 105036. doi:10.1016/j.marpetgeo.2021.105036

Xu, S., Gou, Q., Hao, F., Zhang, B., Shu, Z., and Zhang, Y. (2020). Multiscale Faults and Fractures Characterization and Their Effects on Shale Gas Accumulation in the Jiaoshiba Area, Sichuan Basin, China. *J. Pet. Sci. Eng.* 189, 107026. doi:10.1016/j.petrol.2020.107026

Xue, F., Liu, X. X., and Wang, T. Z. (2021). Research on Anchoring Effect of Jointed Rock Mass Based on 3D Printing and Digital Speckle Technology. *J. Mining Strata Control. Eng.* 3 (2), 023013. doi:10.13532/j.jmsce.cn10-1638/td.20201020.001

Yin, S., Dong, L., Yang, X., and Wang, R. (2020). Experimental Investigation of the Petrophysical Properties, Minerals, Elements and Pore Structures in Tight Sandstones. *J. Nat. Gas Sci. Eng.* 76, 103189. doi:10.1016/j.jngse.2020.103189

Zargari, S., Canter, K. L., and Prasad, M. (2015). Porosity Evolution in Oil-Prone Source Rocks. *Fuel* 153, 110–117. doi:10.1016/j.fuel.2015.02.072

Zhang, Y., Hu, S., Shen, C., Liao, Z., Xu, J., and Zhang, X. (2022). Factors Influencing the Evolution of Shale Pores in Enclosed and Semi-enclosed thermal Simulation Experiments, Permian Lucaogou Formation, Santanghu Basin, China. *Mar. Pet. Geology.* 135, 105421. doi:10.1016/j.marpetgeo.2021.105421

Zhang, Y., Yu, B., Pan, Z., Hou, C., Zuo, Q., and Sun, M. (2020). Effect of thermal Maturity on Shale Pore Structure: A Combined Study Using Extracted Organic Matter and Bulk Shale from Sichuan Basin, China. *J. Nat. Gas Sci. Eng.* 74, 103089. doi:10.1016/j.jngse.2019.103089

Zhang, Z., Zhang, K., Song, Y., Jiang, Z., Jiang, S., Wang, P., et al. (2021). Study on the Formation Mechanism of Shale Roof, Floor Sealing, and Shale Self-Sealing: A Case of Member I of the Upper Ordovician Wufeng Formation-Lower Silurian Longmaxi Formation in the Yangtze Region. *Front. Earth Sci.* 9, 764287. doi:10.3389/feart.2021.764287

Zhao, W., Wang, K., Liu, S., Ju, Y., Zhou, H., Fan, L., et al. (2020). Asynchronous Difference in Dynamic Characteristics of Adsorption Swelling and Mechanical Compression of Coal: Modeling and Experiments. *Int. J. Rock Mech. Mining Sci.* 135, 104498. doi:10.1016/j.ijrmms.2020.104498

Zhao, W., Wang, K., Wang, L., Cheng, Y., Dong, H., Li, B., et al. (2021). Influence of Matrix Size and Pore Damage Path on the Size Dependence of Gas Adsorption Capacity of Coal. *Fuel* 283, 119289. doi:10.1016/j.fuel.2020.119289

Zhao, Z., Wu, K., Fan, Y., Guo, J., Zeng, B., and Yue, W. (2020). An Optimization Model for Conductivity of Hydraulic Fracture Networks in the Longmaxi Shale, Sichuan basin, Southwest China. *Energ. Geosci.* 1, 47–54. doi:10.1016/j.engeos.2020.05.001

Zou, C., Zhu, R., Chen, Z.-Q., Ogg, J. G., Wu, S., Dong, D., et al. (2019). Organic-matter-rich Shales of China. *Earth-Science Rev.*, 189: 51–78.doi:10.1016/j.earscirev.2018.12.002

Conflict of Interest: JW, XZ, and YX were employed by PetroChina Research Institute of Petroleum Exploration and Development.

The remaining authors declare that the research was conducted in the absence of any commercial or financial relationships that could be construed as a potential conflict of interest.

Publisher's Note: All claims expressed in this article are solely those of the authors and do not necessarily represent those of their affiliated organizations, or those of the publisher, the editors and the reviewers. Any product that may be evaluated in this article, or claim that may be made by its manufacturer, is not guaranteed or endorsed by the publisher.

frontiers | Frontiers in Earth Science

ORIGINAL RESEARCH
published: 12 April 2022
doi: 10.3389/feart.2022.882499

Quantitative 3-D Model of Carbonate Reef and Shoal Facies Based on UAV Oblique Photogrammetry Data: A Case Study of the Jiantanba Outcrop in West Hubei, China

Senlin Yin[1]*, *Lei Zhao*[2]*, *Yu Lin*[3], *Baiyu Zhu*[1], *Junwei Zhao*[1] and *Leli Cheng*[1]

[1]Institute of Mud Logging Technology and Engineering, Yangtze University, Jingzhou, China, [2]Petroleum Exploration and Production Research Institute, SINOPEC, Beijing, China, [3]China National Petroleum Corp Bureau of Geophysical Prospecting Inc., Zhuozhou, China

OPEN ACCESS

Edited by:
Hu Li,
Southwest Petroleum University, China

Reviewed by:
Hui Han,
Southwest Petroleum University, China
Nan Xin Yin,
Chongqing University of Science and Technology, China

***Correspondence:**
Senlin Yin
yinxiang_love@qq.com
Lei Zhao
ray-zhao@163.com

Specialty section:
This article was submitted to Structural Geology and Tectonics, a section of the journal Frontiers in Earth Science

Received: 23 February 2022
Accepted: 11 March 2022
Published: 12 April 2022

Citation:
Yin S, Zhao L, Lin Y, Zhu B, Zhao J and Cheng L (2022) Quantitative 3-D Model of Carbonate Reef and Shoal Facies Based on UAV Oblique Photogrammetry Data: A Case Study of the Jiantanba Outcrop in West Hubei, China. Front. Earth Sci. 10:882499. doi: 10.3389/feart.2022.882499

Aiming at the problem of insufficient data acquisition for steep carbonate outcrops, we used unmanned aerial vehicle oblique photogrammetry to quantitatively evaluate Jiantianba outcrops from a global perspective. This method can quickly and flexibly acquire, process and interpret outcrop data, establish the three-dimensional digital outcrop model and quantitative reservoir geological knowledge database. Through the fine analysis and comparative study of multiple outcrop sections, we use lithofacies combination, hierarchical interface, sequential indicator stochastic simulation and multiple-point geostatistical simulation methods to establish a three-dimensional multi-point statistical model of the outcrop area. The results show that the model of the Jiantianba carbonate outcrop has three-dimensional coordinates that correspond to oblique photograph image data, allowing for both the accurate location of any point and the measurement of the rock body, and thus providing a base for studying the stratigraphic architecture of the outcrop. Through fine-scale geological and statistical analyses of the geological parameters of three geologic sections, we established a database and model of a typical outcrop, including the types, continuity and scale of lithology, as well as different lithological combinations and the geological evolution of the region. And we established a geological model and quantitative geological database via sequential indicator simulation, using virtual well location, lithological combination, stratigraphic correlation, three-dimensional stratigraphic and lithological models of a typical outcrop. Subsequently, we analyzed the training images of different microfacies based on these models combined with the outcrop geometry. Finally, we established a three-dimensional geological model of reef–shoal facies that is more in line with our current understanding of the geology of the outcrop area by multi-point geostatistical simulations.

Keywords: UAV, 3-D model, outcrop, carbonate reef, shoal facies

INTRODUCTION

Reef–shoal deposits serve as important carbonate oil and gas reservoirs, and large-scale gas fields, such as Puguang, Longgang and Yuanba, have been discovered in Permian bioherm reservoirs in China (Ma et al., 2006, 2014; Fan et al., 1996, 1982). The petrological characteristics of reefs (Fan and Wu, 2002; Jody et al., 2004), their genesis, distribution and the characteristics of reef reservoir development (Wang et al., 1997; Robert, 2002; Abbey et al., 2013; Zhu et al., 2013; Ji et al., 2016; Xu et al., 2017) and the generative mechanism of reef gas reservoirs (Ma et al., 2005) has previously been explored via outcrop surveys (Hu et al., 2012; Qin et al., 2018; Li et al., 2019; Martin et al., 2005; Rong et al., 2009; Shen and Chen, 2001), reservoir predictions based on seismic data (Cai, 2011; Long et al., 2015; Wu et al., 2017), three-dimensional (3-D) geological modelling (Zhang et al., 2017; Zhou et al., 2018; Hao et al., 2019; Hu et al., 2002) and well logging (Yang et al., 2017; Wang et al., 2019). However, the use of traditional manual photography, stratigraphic scale measurements, sampling and two-dimensional (2-D) irregular sections to characterize outcrops are gradually being replaced by more accurate instruments (Guo, 2001; Hu et al., 2012). Gamma meters that characterise outcrop lithology and large-scale geological analyses *via* Google Earth (Shi et al., 2012; Zhang et al., 2017), as well as small-scale field outcrop structural characterisation based on 3-D laser scanning (Zhu et al., 2013; Fan et al., 2020) are now being employed.

In order to better understand the internal architecture of sand bodies, more advanced technologies, such as ground-penetrating radar, have been widely used (Woodward, et al., 2003; Yan et al., 2018; Yu et al., 2017; Zhang et al., 2015; Zhang et al., 2017). Constant technological updates have enabled researchers to obtain increasingly rich and accurate geological information. However, even as the data acquisition, transmission, processing and interpretation continue to develop rapidly, the methods remain limited. For example, 3-D laser scanning technology is an important method to study the internal architecture of sandy outcrops, but many carbonate outcrops located in large difference of elevation (>500 m), long profile (>1,000 m) and irregular profile surfaces. Additionally, trees and protruding rocks in some outcrop areas can block laser transmission, rendering the measurement from laser scanners inaccurate. In essence, laser scanning still only provides irregular, 2-D profile measurements. These indicate that outcrop characterization is not a complete 3-D digital outcrop.

Surveying field work from outcrops is the foundation of geological research, and the partitioning of outcrops has the advantages of directness and high precision. Compared with many clastic rock profiles, carbonate outcrops are commonly seen in high mountains and valleys with rugged terrain, making them more difficult to characterise. Meanwhile, 3-D geological modelling technologies have progressed greatly, evolving from deterministic to stochastic models and more recently, to multi-point geostatistical simulations (MPSs) (Wu and Li, 2005; Feng et al., 2019), which integrate multidisciplinary information and algorithms to build models approaching geological reality (Zhao et al., 2017). However, the amount of data information needed in this process has been a key factor in determining the accuracy of such models.

Even though the amount of data in field outcrop profiles is abundant, the lack of accurate profile locality information with which to quantitatively characterise 2-D, non-regularly associated outcrop sections make it difficult to fully utilise the data. The traditional method of outcrop characterisation is observation, description, 2-D representation and modelling of typical sections (Yin et al., 2013; Picke et al., 2015; Wang et al., 2001). For reef–flat outcrops, it is more difficult to convert profile information into planar and there has been no millimetre or centimetre-scale, 3-D geological model for reef flats available so far (Yin et al., 2011; Yang et al., 2017; Duan et al., 2019; Zhang et al., 2020; Qie et al., 2017).

Some researchers have tried to characterise and build genetic models of clastic reservoirs based on unmanned aerial vehicle (UAV) oblique photogrammetry (Yin et al., 2018a; 2018b, 2021); however, such characterisation of carbonate reef–shoal reservoirs have rarely been reported. Oblique photogrammetry has been proposed to develop georeferenced panoramic images and 3-D models using panoramic image projection algorithms. With the continued development of UAV capabilities, larger, higher and steeper slope sections have been captured than in previous terrestrial photogrammetric studies (Buckley et al., 2008; Jamie et al., 2019). Generally, there are three steps involved in dealing with oblique photogrammetry data, including obtaining a dense point cloud, generating 3-D reconstructions in real scenes and a digital surface model (DSM) (Remondino and Gerke, 2015; Svennevig et al., 2015; Carvajal-Ramírez et al., 2019). Owing to the advancement of spatial data acquisition (Buckley et al., 2008; Jamie, et al., 2019; Shan et al., 2021), oblique photogrammetric technologies have been applied in many studies of chalky sea cliffs, Hellenistic architecture, the identification of ruts and potholes and landslide processes, among other issues (Jamie, et al., 2019; Azri and Khairul, 2019; Mirko et al., 2019; Yahya et al., 2020).

In view of the shortcomings of more traditional for reef-flat outcrops, digital outcrop characterisation via oblique photogrammetry technology (OPT) was introduced in this study. Thus far, OPT has been used effectively in military (Bao and Wang, 2017), agricultural and forestry (Yang, et al., 2017), urban planning (Mi, et al., 2017) and other application (Bi et al., 2015; Wang, 2017). Here, we applied OPT to understand the stratigraphic architecture of an area of reef–shoal outcrops in China.

GEOLOGIC SETTING

The field outcrop area is located in Lichuan Prefecture, Enshi City in western Hubei Province (**Figures 1A,B**). During the late Permian period, the Jiantianba area was located at the north-eastern margin of the Yangtze Block, with the Exi Rift to the east and the Guangwang–Liangping Trough to the west. The Changxing Formation is complete in this section and exhibits a thickness of ~250 m. The sequence divisions in this area are

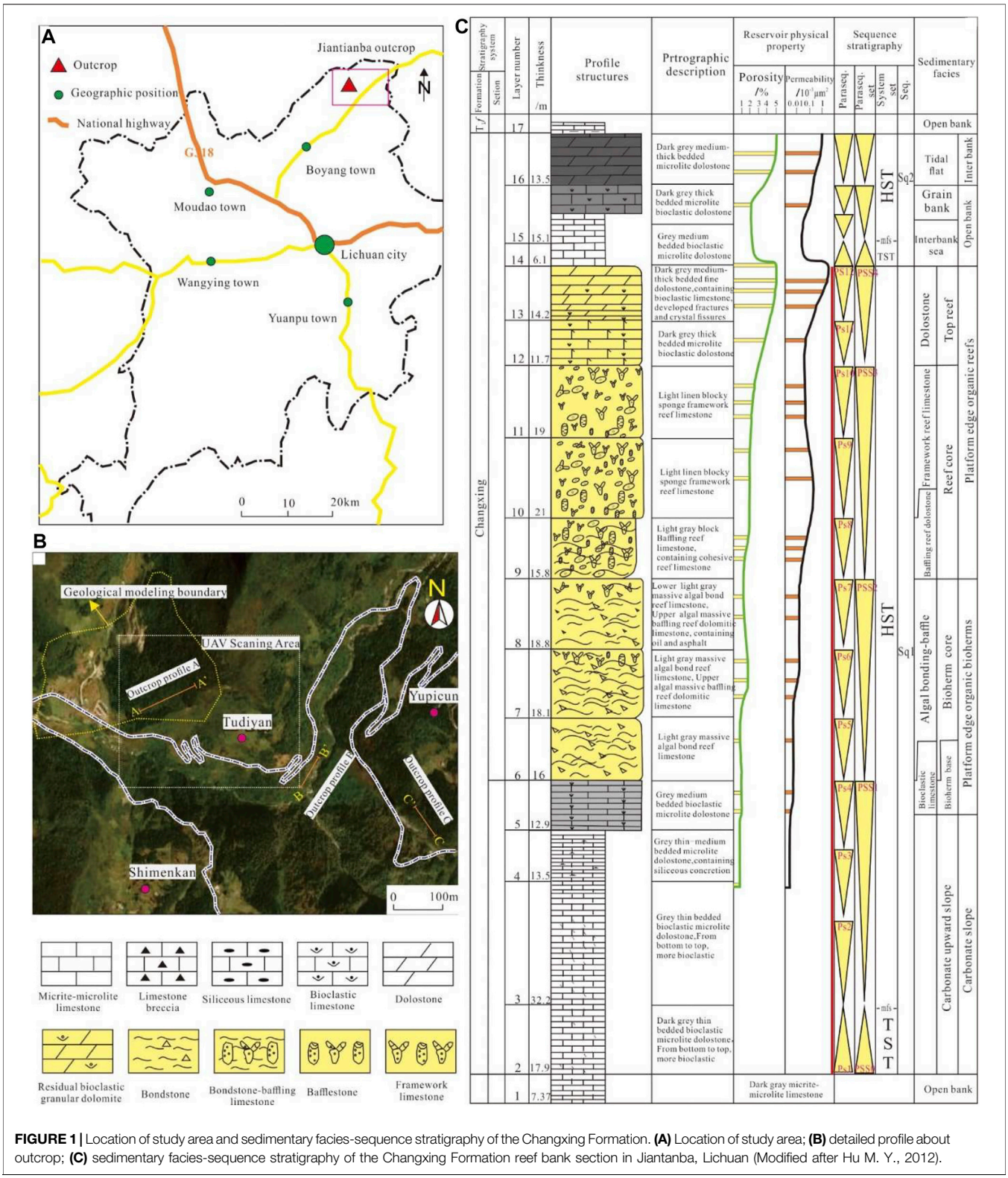

FIGURE 1 | Location of study area and sedimentary facies-sequence stratigraphy of the Changxing Formation. **(A)** Location of study area; **(B)** detailed profile about outcrop; **(C)** sedimentary facies-sequence stratigraphy of the Changxing Formation reef bank section in Jiantanba, Lichuan (Modified after Hu M. Y., 2012).

closely related to the development of the reef body. The Changxing Formation here conformably contacts the underlying Longtan Formation and the overlying upper Triassic Feixianguan Formation (**Figure 1C**).

The Changxing Formation is divided into two third-order sequences; the bottom surface of Sq1 lies between the upper Permian Longtan Formation and the Changxing Formation. Below this surface is the grey, thinly bedded micritic limestone

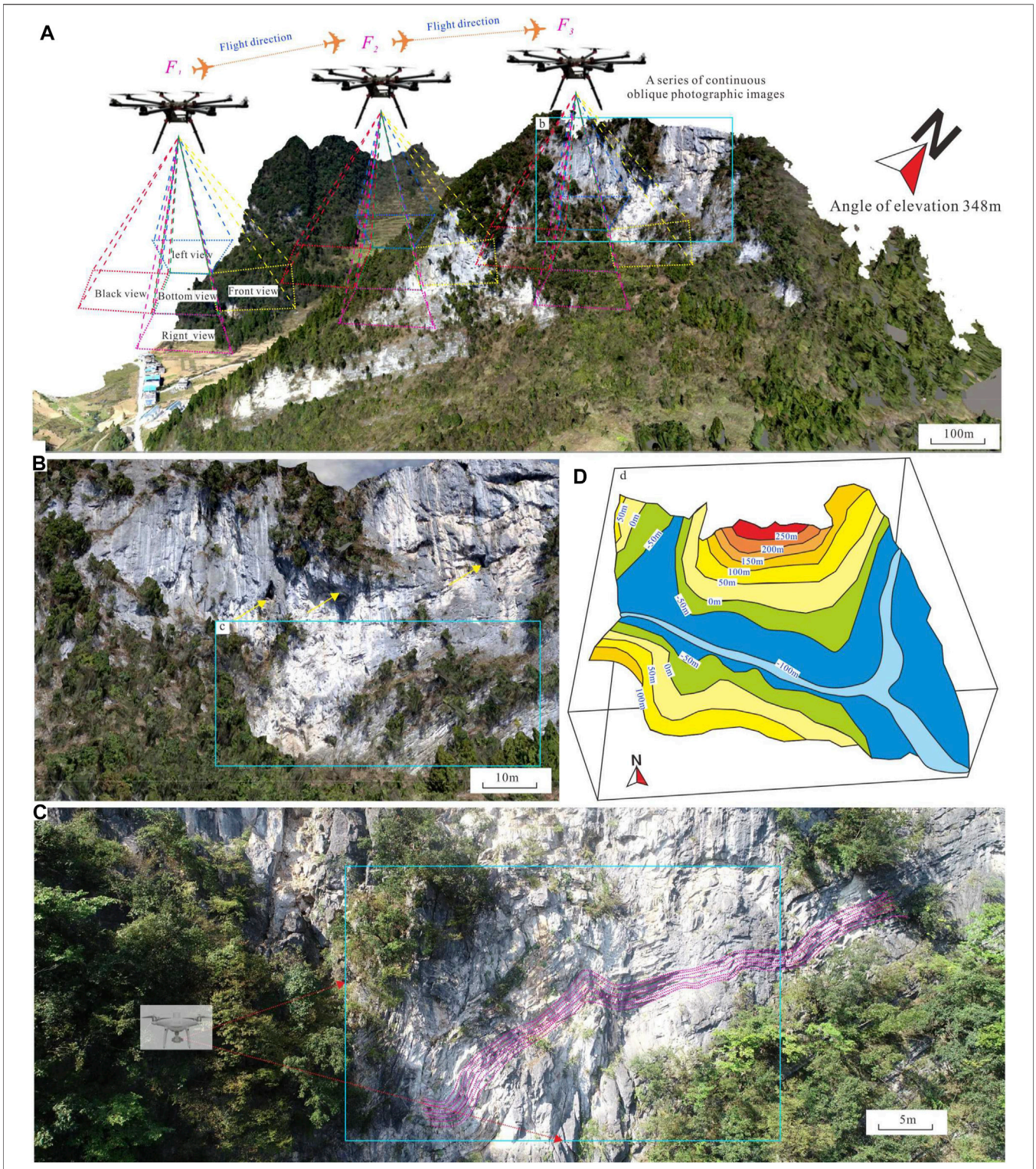

FIGURE 2 | Technology of UAV oblique photographic and outcrop area elevation contour map. **(A)** A series of continuous oblique photographic images; **(B)** pictures obtained by UAV oblique photographic; **(C)** pictures obtained by UAV oblique photographic with deposition details; **(D)** elevation contour map obtained by UAV.

of the Longtan Formation, while above is the dark grey, thinly bedded, bioclast-micritic limestone of the slope facies at the bottom of the Changxing Formation (**Figure 1C**). The bottom surface of Sq2 is located within the Changxing Formation. Below it lies a set of light grey, medium–thickly bedded, fine-grained dolomite and residual bioclastic grey dolomite. Above this surface

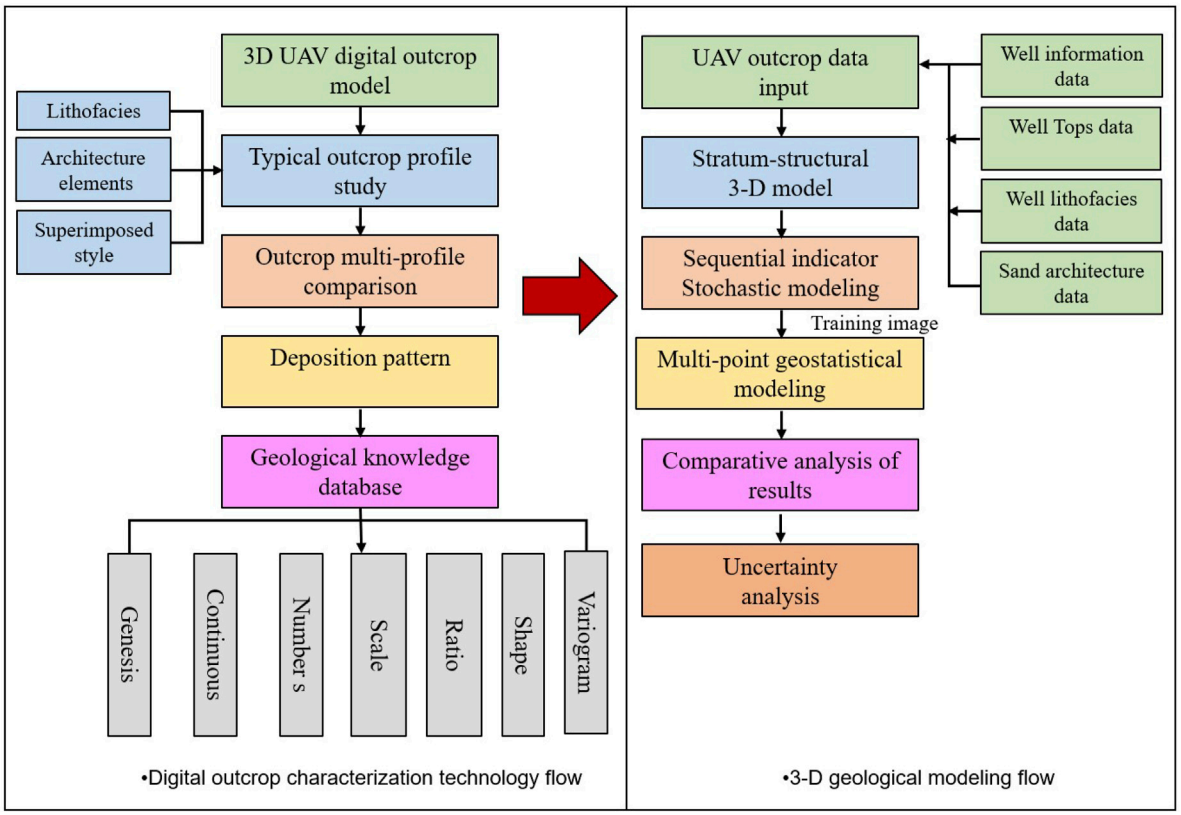

FIGURE 3 | Digital outcrop characterization technology and 3-D geological modeling flow chart.

is a grey, medium–thickly bedded micritic limestone and there are signs of local exposure dissolution near the surface (**Figure 1C**). The high stand systems tract (HSST) of Sq1 of the Changxing Formation in the study area is a complete set of reefs–shoal sediments, including five microfacies (reef base, reef core, reef beach, reef top beach and reef top tidal flat) (**Figure 1C**), which are the foci of this study.

MATERIALS AND METHODS

This study is based on traditional field work and outcrop data collection via UAV OPT, processing and interpretation. Approximately 20 field sites were surveyed, among which typical outcrop sections of six key sites were surveyed manually, and ~200 photos of the outcrops were taken. Additionally, the Jiantianba outcrop area was scanned using five UAV-mounted photo sensors (**Figures 2A,B**), with 1.5 km^2 of 3-D outcrop data of the study area collected. The maximum elevation difference is nearly 300 m (**Figure 2C**). The collected data included 3-D point cloud data and a large amount of oblique photo data (~5,000 images). Subsequently, the collected data were processed using Context Capture v. 2.0 (Bentley System, Inc., United States) and a 3-D digital model of a typical field outcrop with coordinates corresponding to the images was established.

Making use of a global, systematic and continuous 3-D digital model of the outcrop, 17 virtual wells were established in the processed model of Jiantianba to analyze the geologic structure of the reef flat in combination with another two outcrop profiles of the study area (**Figure 1B**). A 3-D geological model of the outcrop area with data collected by UAV was then constructed. The main 3-D geological modelling process included skeletal mesh and grid model establishment, the random simulation of a lithological variogram and MPS. The model employed sequential indicator simulation (SIS) to explore the distribution of lithologies across the outcrop area before attempting to convert the profile data of the outcrop area into planar data. Based on the contour map of the lithological composition of the reef flat outcrop, a lithological plane constraint range was established, and different facies belts were used in different training images to perform MPSs of the study area (**Figure 3**).

GEOLOGICAL ANALYSIS OF TYPICAL OUTCROP

Lithology of Field Outcrops

In the typical outcrop profiles of the Jiantianba area, a variety of lithologies may be identified, including:

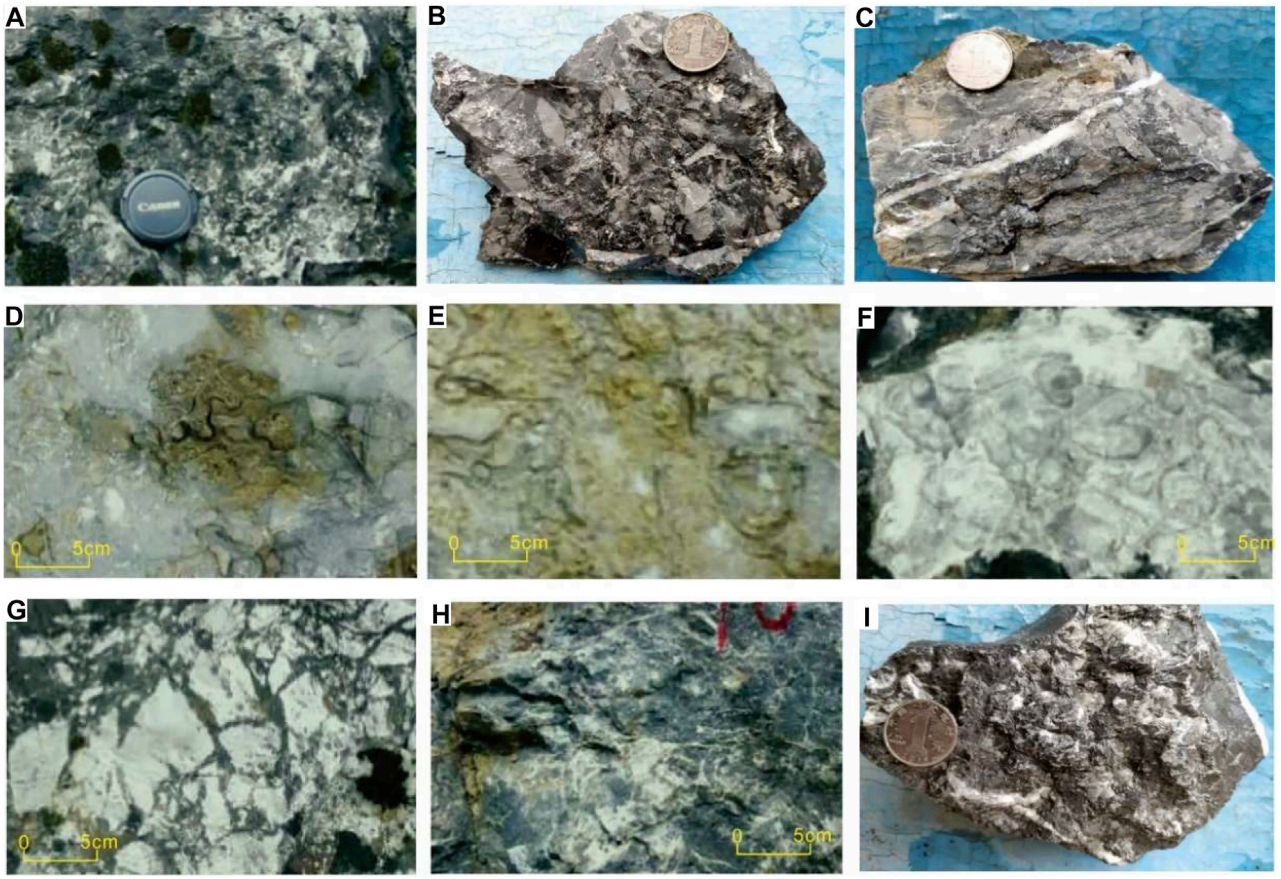

FIGURE 4 | Lithology and biology of Changxing Formation reef in outcrop of Jiantianba. **(A,B)** Algal reef limestone, mainly composed of blue-green algae, content up to 65%; **(C,D)** algal bonded sponge reef limestone, with about 25% sponge content and 35% blue-green algae content, has obvious algal bonded—barrier structure; **(E)** sponge skeleton reef limestone, with obvious barrier—skeleton structure, reef-building organisms are mainly string sponges and fiber sponges, the content of which is about 60%; **(F)** skeleton reef limestone, with biological skeleton structure, reef-building organisms are mainly string sponges, fiber sponges, etc., **(G)** limestone breccia, breccia for angular, for the collapse of the reef formation; **(H,I)** light grey blocky dolomitic reef limestone, fracture and dissolution of the geode is developed well.

- Algal-bound reef limestones primarily composed of 65% blue-green algae (**Figures 4A,B**);
- Algal-bound sponge reef limestone with a 25% sponge content, 35% blue-green algae and a conspicuously algal-bound structure (**Figures 4C,D**);
- Algal-bound limestone and algal-bound sponge bafflestone with poor layering at the top;
- Sponge reef limestone, with an obvious skeletal structure in which reef-building organisms mainly include ~60% string sponge and fiber sponge reef (**Figure 4E**).

Different stratigraphic positions are dominated by different species, with blue-green algae dominating at the bottom of the section and sponges at the top. The structure of the skeletal reef limestone is mainly composed of string sponges and fiber sponges reef as reef-building organisms (**Figure 4F**); in the lateral extension of the bottom of the Jiantianba section, a large amount of skeletal reef limestone was found. Limestone breccia, which was formed due to the collapse of the reef (**Figure 4G**); dark grey, thickly bedded dolomite, with visible cracks and dissolution vugs (**Figures 4H,I**) and caves that exceeded 10 m were also observed.

Different types of lithologies corresponded to different sedimentary microfacies in the study area. Bioclastic reef limestone, shoal facies and sand debris constituted the reef-based microfacies, while sponge skeletal and algal-bound rocks comprised the block reef core. Dolomite was interbedded with echinoderm limestone, micritic dolostone and stratified dolomite, in which there were abundant epigenetic dissolution pores in a layered distribution. Some of these pores have been filled by asphaltene and calcite. The reef top microfacies, which undulates and protrudes upward, is a favourable reservoir.

Lithologic Distribution of Field Outcrops

Several outcrop sections were surveyed and analysed in this study. The A–A' section of Jiantianba was in the eastern part of the study area (**Figure 1B**). The section is ~300-m-long from north to south, 400-m-long from east to west and has a strike of N70°E. The exposed part of the profile corresponds to the

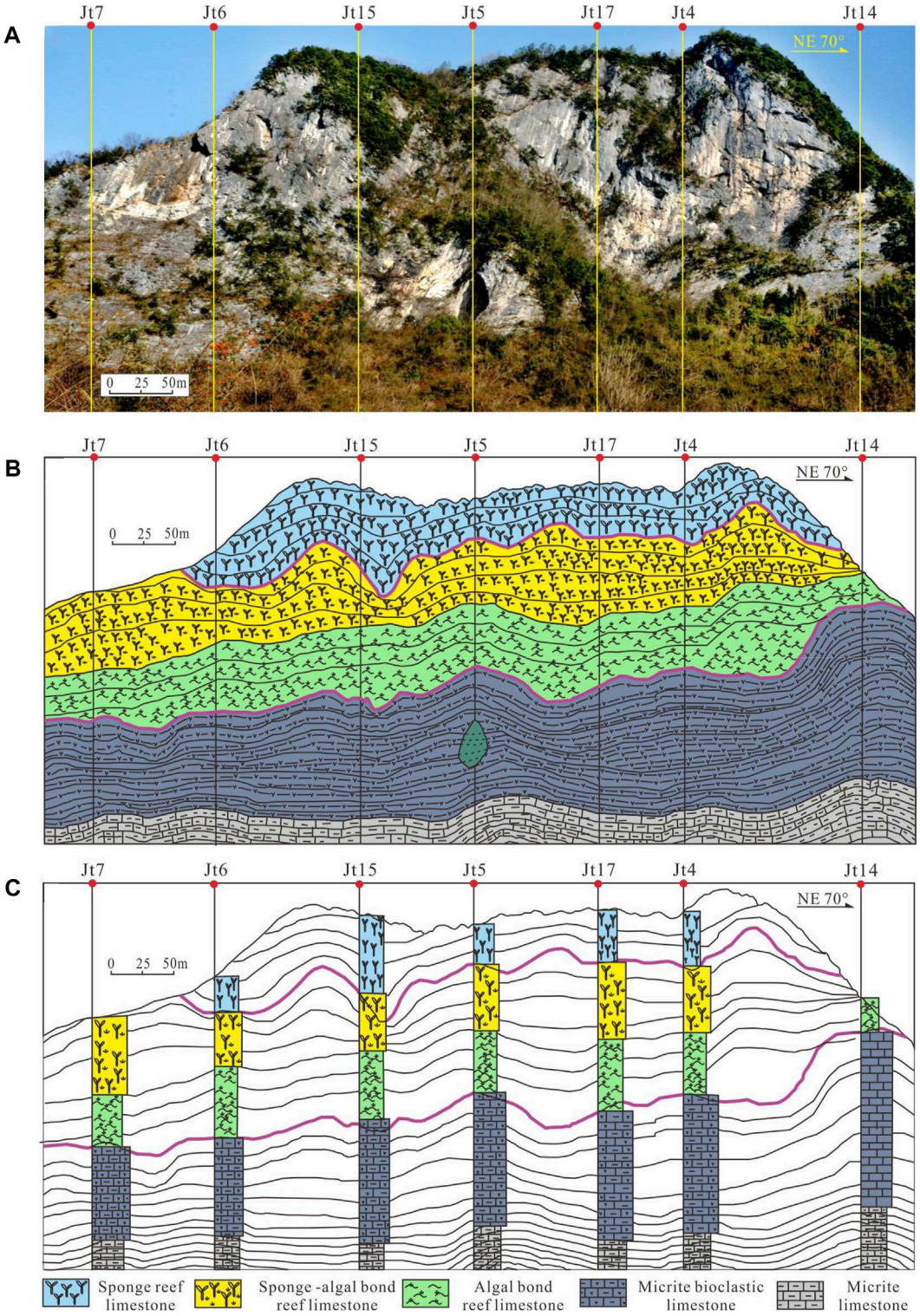

FIGURE 5 | Architecture geological model of Jiantianba AA' section, Lichuan. **(A)** Field outcrop picture; **(B)** outcrop profile sketch; **(C)** architecture geological model.

reef core and reef base microfacies and to the PSS2 and PSS1 quasi-sequence groups in the stratigraphic sequence (**Figure 5A**). At the bottom of the section, there is an ~75-m-thick, dark grey, thin–medium bedded micritic limestone, in which single layers are ~0.15-m-thick and ~0.1 m at a minimum. The micritic limestone transitions upward into

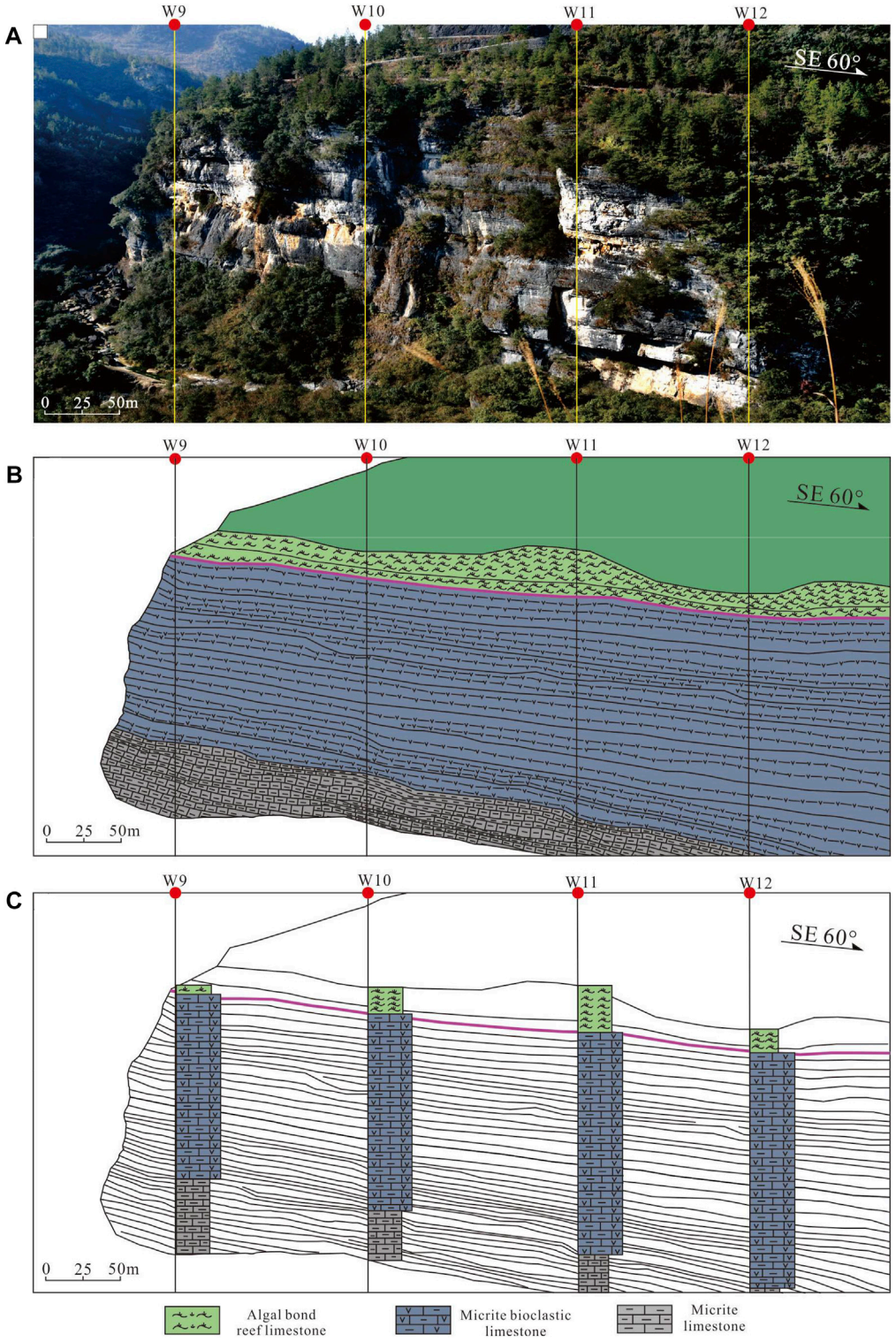

FIGURE 6 | Architecture geological model of Jiantianba BB' section, Lichuan. **(A)** Field outcrop picture; **(B)** outcrop profile sketch; **(C)** architecture geological model.

bioclast–micritic limestone that is ~150-m-thick, with layers of ~0.2 m and at least 0.15 m in thickness. The bioclast content gradually increases from the bottom to the top and there are local occurrences of grey, medium-bedded bioclast–micritic limestone. There are only a few types of organisms represented, mainly brachiopods, echinoderms and algae,

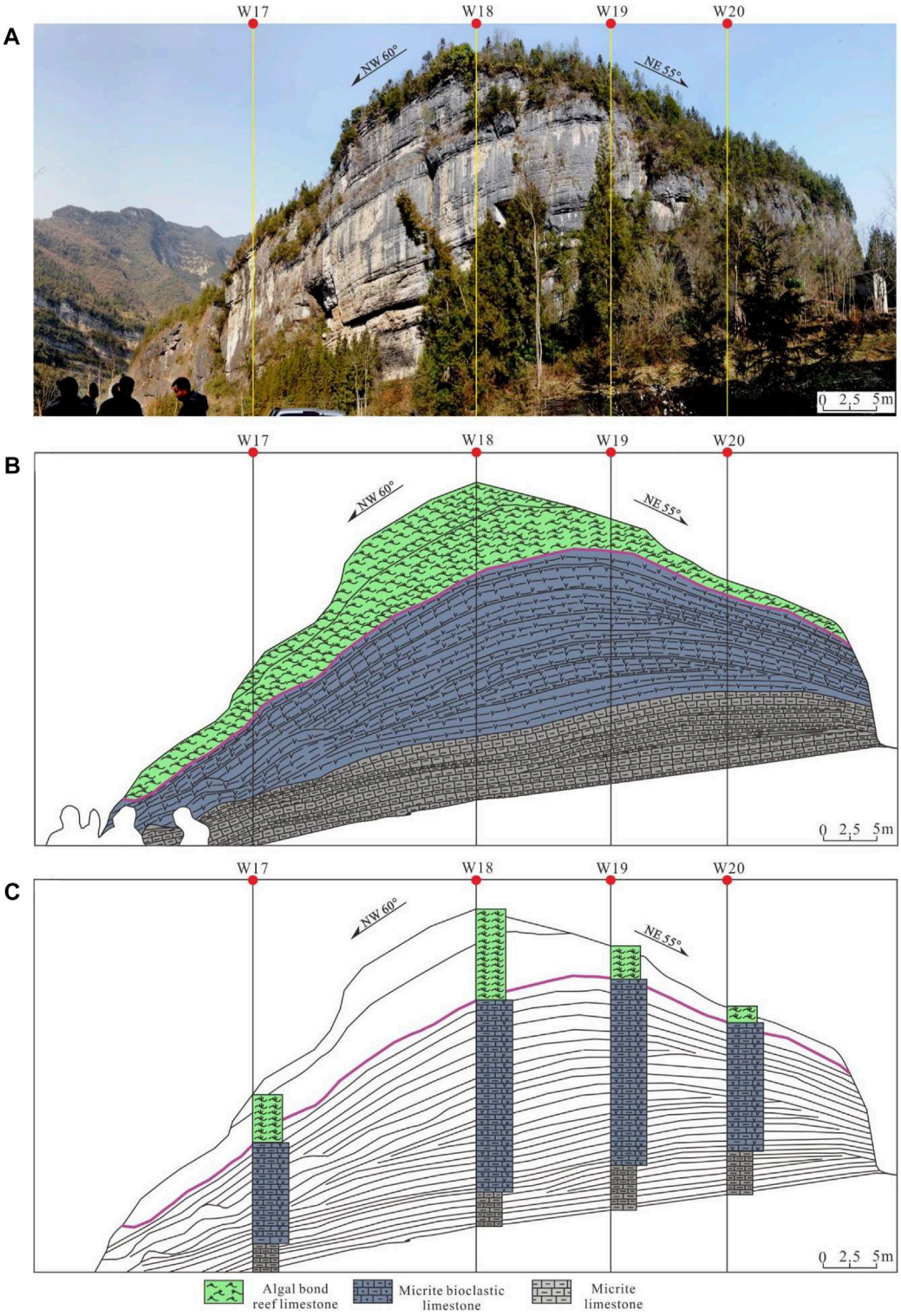

FIGURE 7 | Architecture geological model of Jiantianba CC' section, Lichuan. **(A)** Field outcrop picture; **(B)** outcrop profile sketch; **(C)** architecture geological model.

none of which are abundant. The chrysanthemum reef is visible at the bottom, indicating a deep-water low-energy environment at the time of its deposition. In the middle of the section, the lithology transition from a micritic limestone to an algal-bound reef limestone that is ~43-m-thick; the mean thickness of individual layers is ~2–3 m.

TABLE 1 | Quantitative parameters of lithofacies architecture in the outcrop area.

No.		J_Out.001	J_Out.002	J_Out.003	J_Out.004	J_Out.005	J_Out.006
Fine dolomite	Vertical thickness/m	75 m	70 m	2.5 m	50 m	40 m	15 m
	Lateral scale/m	2000m	1700 m	85 m	650 m	700 m	120 m
	Layer thickness and variation	Thin-medium, uniformity	Thin, uniformity	Thin, uniformity	Thin-medium, uniformity	Thin-medium, uniformity	Thin, uniformity
Biomicrite	Vertical thickness/m	150 m	100 m	15 m	200 m	200 m	25 m
	Lateral scale/m	1500 m	800 m	80 m	650 m	700 m	85 m
	Layer thickness and variation	Thin-medium, uniformity	Thin-medium, uniformity	Thin-medium, uniformity	Thin-medium, uniformity	Thin-medium, uniformity	medium, uniformity
Algal reef limestone	Vertical thickness/m	43 m	25 m	12 m	35 m	25 m	15 m
	Lateral scale/m	800 m	170 m	65 m	600 m	600 m	65 m
	Layer thickness and variation	Massive structure, disorderly deposits	Massive structure, disorderly deposits	Massive structure, disorderly deposits	Massive structure, disorderly deposits	Massive structure, disorderly deposits	Massive structure, disorderly deposits
Algal bonded sponge reef limestone	Vertical thickness/m	35 m	18 m	15 m	—	—	—
	Lateral scale/m	600 m	150 m	60 m	—	—	—
	Layer thickness and variation	Massive structure, disorderly deposits	Massive structure, disorderly deposits	Massive structure, disorderly deposits	—	—	—
Spongy reef limestone	Vertical thickness/m	25 m	—	14 m	—	—	—
	Lateral scale/m	450 m	—	30 m	—	—	—
	Layer thickness and variation	Massive structure, disorderly deposits	—	Massive structure, disorderly deposits	—	—	—

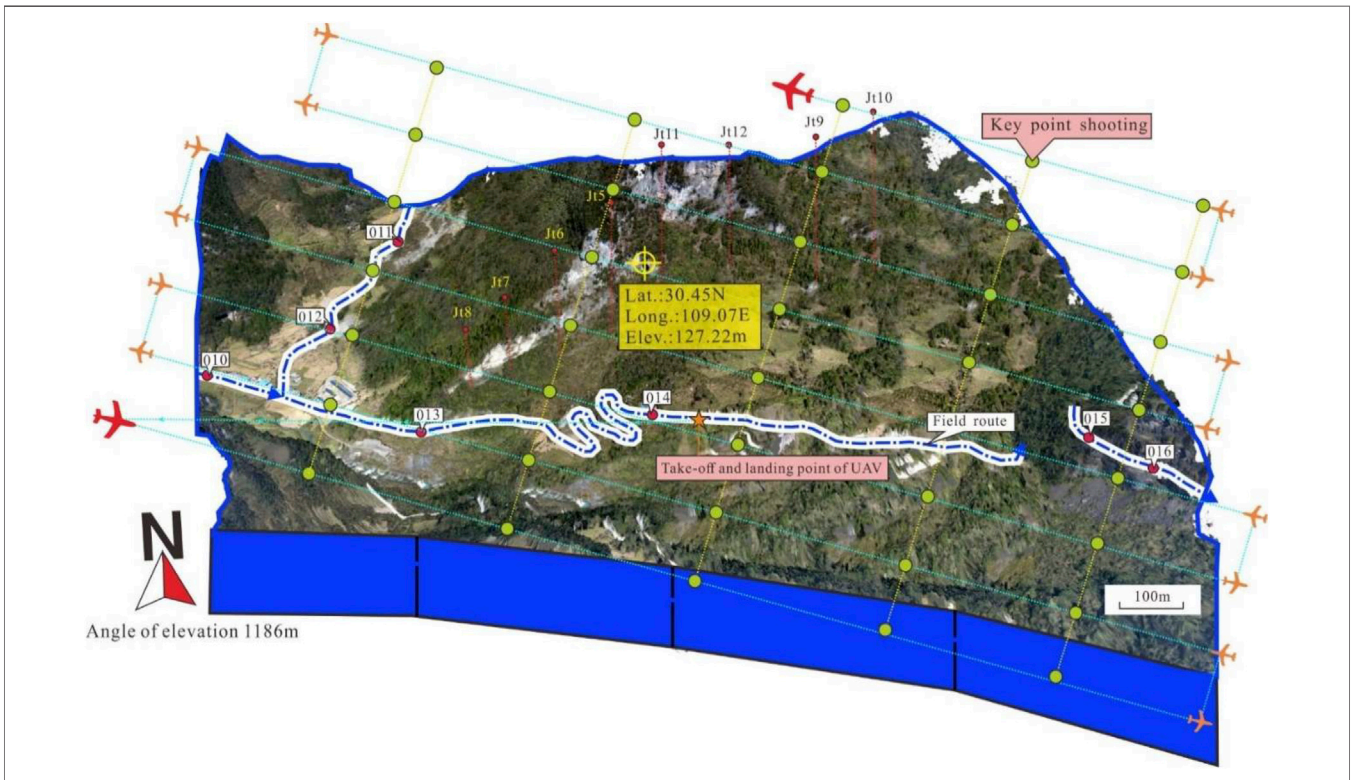

FIGURE 8 | 3D digital outcrop model processed by UAV oblique photography, outcrop of Jiantianba. The maximum resolution of a local image was ~10–20 cm. Cruise line automatic set-up by POS system. The UAV take off from start point to the end then achieved outcrop scanning and taking pictures.

TABLE 2 | Coordinate data information of virtual wells of outcrop, Jiantianba.

Well number	X-coodinate	Y-coodinate	Vertical depth/m
Jt1	19,315,875.91	3,372,239.384	300
Jt2	19,315,803.17	3,372,671.984	300
Jt3	19,315,747.19	3,372,518.875	300
Jt4	19,315,660.86	3,372,150.599	300
Jt5	19,315,580.8	3,372,151.959	300
Jt6	19,315,526.9	3,372,122.063	300
Jt7	19,315,473.53	3,372,122.97	300
Jt8	19,315,365.22	3,372,032.376	300
Jt9	19,315,873.82	3,372,116.172	300
Jt10	19,315,819.4	3,372,055.472	300
Jt11	19,315,633.12	3,372,089.446	300
Jt12	19,315,606.44	3,372,089.899	300
Jt13	19,315,850.27	3,372,301.442	300
Jt14	19,315,795.33	3,372,209.939	300
Jt15	19,315,475.1	3,372,215.379	300
Jt16	19,315,369.41	3,372,278.8	300
Jt17	19,315,636.26	3,372,274.264	300

On the algal-bound limestone, a set of sponge reef limestones is ~35-m-thick and exhibits poor layering. A set of sponge skeletal bafflestones also occur at the top of the section, in which the main reef-building organisms are string sponges and fiber sponge reef. These rocks contain abundant algae and sponge but extremely poor layering, exhibiting a massive structure, with a small amount of visible asphaltene (**Figure 5B**). The profile worsens in layering from the bottom to the top and the fine, horizontal strata are mostly concentrated in the bottom of the outcrop area, with good continuity and characteristics typical of reef base sediments (**Figure 5C**).

The B–B' section in Jiantianba (**Figure 1B**) is located in the southeast of a typical outcrop area, Yupi Village, with a strike of S60°E. The vertical sequence mainly corresponds to the PSS1 quasi-sequence group, on which the reef base microfacies in the sedimentary facies belt crops out, and the bioherm core microfacies is visible at the top. Except for the top, which is covered by vegetation, the rock mass is fully exposed (**Figure 6A**). At the bottom of the section is an ~40-m-thick micritic limestone, which appears in evenly distributed layers of ~0.25 m and at least 0.15 m in thickness. This limestone has localised silicate nodules and is lithological stable overall and large in its lateral extent. Above this layer is am ~200-m-thick bioclast–micritic limestone. This rock comes contains layers of ~0.3 m in thickness (minimum: ~0.2 m) and has local silicate nodules. At the top of the section is a small amount of algal-bound limestone (~25-m-thick), with poor layering, but a blocky structure and clustered distribution (**Figure 6B**). From the bottom to the top of the profile, micritic limestone, bioclast–micritic limestone and algal-bound limestones appear sequentially. The lithological transition between the bioclast–micritic limestone and algal-bound limestone corresponds to the boundary between the quasi-sequence groups PSS1 and PSS2. Having been subjected to later geological reworking, the top of the reef limestone varies in thickness at different locations (**Figure 6C**).

The C–C' section in Jiantianba (**Figure 1B**) is 500 m southeast of the typical outcrop area in Village. The section exhibits a "V" shape in top view, stretching from the middle to both sides, with the rock walls on two sides striking N60°W and N55°E, respectively. The section has a middle bulge and is small in scale. The reef base, bioherm and reef core microfacies in the reef facies are completely exposed and the vertical sequence corresponds to three quasi-sequence groups (PS S3, PSS2, and PSS1) (**Figure 7A**). At the bottom of the section is am ~15-m-thick micritic limestone distributed in even layers of ~0.2 m and at minimum 0.1 m in thickness. Above the micritic limestone is a layer of bioclast–micritic limestone that is ~25-m-thick, with layers of ~0.3 m and a minimum of 0.2 m in thickness. Overlying the bioclast–micritic limestone lies a set of algal-bound reef limestones that are generally ~15-m-thick and poorly layered at the top (**Figure 7B**). From the bottom to the top of the section, micritic limestone, bioclast–micritic limestone and algal-bound limestone occur in succession. Mudrocks are laterally consistent in content and stable. The lithologic transition between the bioclast–micritic limestone and algal-bound limestone corresponds to the boundary between the PSS1 and PSS2 quasi-sequence groups. Having been affected by later geological reworking, the top reef limestone is large in scale in the middle of the section and smaller in on the two flanks. The reef varies somewhat in thickness at different locations (**Figure 7C**). Based on the field survey and comparison of the sections, the quantitative parameters of the stratigraphic architecture of the aforementioned five sections were analysed (**Table 1**).

TABLE 3 | 3-D modeling lithology data and input code which used in simulation software, Jiantianba.

Lithology	Input code of software
Fine dolomite (FD)	0
Bioclastic dolomite-limestone (BDL)	1
Spongy reef limestone (SRL)	2
Algal bonded sponge reef limestone (ABSRL)	3
Algal reef limestone (ARL)	4
Biomicrite (B)	5
Marls (M)	6

CONVERSION OF UNMANNED AERIAL VEHICLE DATA TO GEOLOGICAL INFORMATION

Processing of Unmanned Aerial Vehicle Data

The UAV, combined with OPT, allowed for the rectangular spatial coordinates of any point on the image to be accurately obtained. In this survey, an eight-rotor UAV (Tiantu, China) was flown in parallel according to the planned cruising route. The aerial folding range was ~40%. During flight, a Share-200 (Motoar Sky, China) oblique camera carried by the UAV continuously acquired image information from five angles according to the set exposure mode (**Figure 2A**, **Figure 8**).

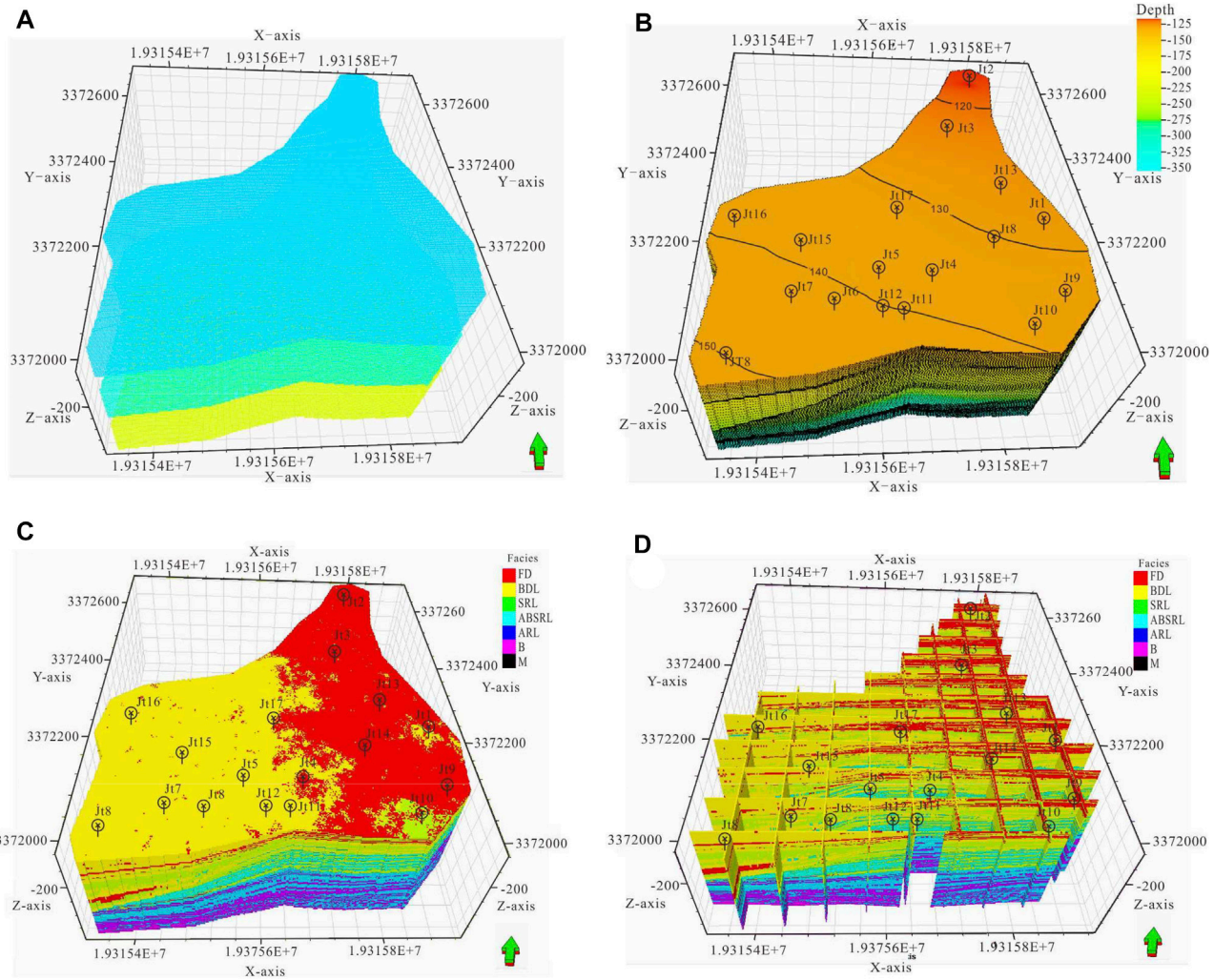

FIGURE 9 | 3-D stratigraphic structural model of typical outcrop area of Jiantianba. **(A)** 3-D griding model; **(B)** 3-D stratigraphic structural model; **(C)** 3-D lithological model; **(D)** palisade 3-D grids display about lithological model.

The UAV was also equipped with a positioning and orientation system (POS) that accurately recorded the real-time rectangular spatial coordinates of each point during flight. The POS and image information were continuously accepted by the ground sensor and imported into the ground terminal operating platform. After aerial photography, the ground terminal platform was used to guide the vehicle to return safely and data collection in the study area was completed.

The data were integrated using Context Capture v. 2.0 (Bentley System, Inc., United States) to construct a 3-D model of the Jiantianba outcrop area with coordinates (**Figure 1B**, **Figure 5**), which can reflect the real geological conditions in the field very well. The coordinates of any point can be obtained directly and the spatial distributions of the geological bodies in the model were well expressed. The scanning model built can satisfy 360° observation and can zoom in and display local parts of an image. The maximum resolution of a local image was ~10–20 cm. By changing camera or adjusting the flying height, the resolution can be further improved (**Figure 8**). The model had a large range, covering many remote and dangerous areas that cannot be safely reached by humans; this kind of data acquisition is much more efficient than manual inspection. The data acquired also provides a solid geological foundation for quantitative modelling.

Acquisition of 3-D Geological Modelling Data

Virtual well data. Traditional outcrop investigations cannot connect the information from continuous points, limiting the interpretability of the research to some extent, especially when the geographical coordinates of the research block cannot be continuously obtained. The UAV OPT accurately matches the image and geographic coordinate information of any point in the study area. In this study, we selected the *x*-coordinates, *y*-coordinates and elevation, *z* (**Table 2**), of 17 wells in the

TABLE 4 | Part of well tops data about virtual wells of outcrop, Jiantanba.

Well no	Well tops	Depth/m	Well no	Well tops	Depth/m
Jt1	PSS4	129.53	Jt7	PSS0	359.72
Jt1	PSS3	155.33	Jt8	PSS1	304.83
Jt1	PSS2	215.53	Jt8	PSS0	355.73
Jt1	PSS1	273.53	Jt9	PSS1	278.3
Jt1	PSS0	351.23	Jt9	PSS0	358.1
Jt2	PSS4	117.48	Jt10	PSS1	277.27
Jt2	PSS3	143.48	Jt10	PSS0	351.27
Jt2	PSS2	199.18	Jt11	PSS1	296.58
Jt2	PSS1	252.58	Jt11	PSS0	356.48
Jt2	PSS0	350.88	Jt12	PSS1	303.75
Jt3	PSS4	122.97	Jt12	PSS0	357.75
Jt3	PSS3	149.77	Jt13	PSS3	233.15
Jt3	PSS2	207.77	Jt13	PSS2	252.85
Jt3	PSS1	266.17	Jt13	PSS1	300.85
Jt3	PSS0	351.67	Jt13	PSS0	358.35
Jt4	PSS4	136.85	Jt14	PSS3	197.59
Jt4	PSS3	155.25	Jt14	PSS2	225.39
Jt4	PSS2	212.25	Jt14	PSS1	286.59
Jt4	PSS1	272.95	Jt14	PSS0	359.09
Jt4	PSS0	350.95	Jt15	PSS4	162.88
Jt5	PSS4	132.62	Jt15	PSS3	170.38
Jt5	PSS3	157.92	Jt15	PSS2	234.48
Jt5	PSS2	217.42	Jt15	PSS1	289.08
Jt5	PSS1	278.12	Jt15	PSS0	354.48
Jt5	PSS0	353.22	Jt16	PSS3	237.63
Jt6	PSS4	161.52	Jt16	PSS2	249.93
Jt6	PSS3	169.72	Jt16	PSS1	292.63
Jt6	PSS2	233.92	Jt16	PSS0	355.83
Jt6	PSS1	289.22	Jt17	PSS4	131.23
Jt6	PSS0	352.32	Jt17	PSS3	158.03
Jt7	PSS3	222.62	Jt17	PSS2	218.23
Jt7	PSS2	248.82	Jt17	PSS1	278.13
Jt7	PSS1	299.52	Jt17	PSS0	357.13

outcrop field, which laid the foundation for 3-D geological modelling.

Lithological data. After determining the coordinates of well positions, by analysing the collected rock samples, combined with the aforementioned field analysis and lithological calibration results, the lithologies of different depth sections of atypical outcrop of Jiantianba was calibrated. In consideration of the subsequent modelling, lithotypes, including crystal–fine-grained dolomite, bioclast–dolomitic limestone, sponge skeletal reef limestone, algal-bound sponge reef limestone, algal-bound reef limestone, bioclast–micritic limestone and mudstone, were identified and represented by corresponding codes. The lithotypes and corresponding codes for different well depths were determined and taken as input data during modelling (**Table 3**).

Well top data. According to the field research, there are typical reef base, bioherm core, reef core and reef top sedimentary microfacies from the bottom to the top of the Jiantianba outcrop, with obvious lithological interfaces. Therefore, in the subsequent 3-D geological model, the section was divided into five single layers (PSS0, PSS1, PSS2, PSS3 and PSS4) based on the top bedding plane. The stratigraphic divisions for the five layers in the corresponding wells were obtained from UAV elevation data to lay a foundation for 3-D reservoir modelling.

Establishment of a Gridding Model

After inputting the converted geological information (i.e., wells, seven lithologies and well top data) into Petrel V.2009 (Schlumberger, United States), the 3-D gridding model (**Figure 9A**) and stratigraphic model of the study area were built using Pillar gridding, horizon and layering modules (**Figure 9B**). The model was composed of 637,880 grids sized 1 m × 1 m × 0.25 m.

Primary Lithology Sequential Indicator Simulation of the Outcrop

Based on the field research and UAV OPT data, including the thickness, spatial relationships and extensional direction of various lithofacies, and using lithological, well and well top data as constraints (**Table 4**), geological modelling was carried out using the "Data Analysis" and "Facies Modeling" modules in Petrel V.2009 (Schlumberger, United States). An SIS algorithm based on a variogram function was used to run 50 random simulations of the lithology of the Jiantianba outcrop area. The geological models obtained were compared and the reasonable model was finally selected (**Figure 9C**). This model was in line with the known geological understanding of the area. Based on the SIS model of the lithofacies, a map of the planar distribution of lithofacies was obtained using the "properties" function in Petrel (**Figure 9D**). Analysing the facies distribution, the sedimentary units generally show a lithological transition from micritic limestone to reef limestone to limy dolomite from the bottom to the top.

3-D MULTI-POINT GEOSTATISTICAL SIMULATION MODELLING

Training Image Generation

The contour map showing the lithological distribution from the SIS was combined with the geological outcrop profile analyses as the prototype model for the 3-D training image and MPS was carried out. The geometric shape of the training image in the study area was obtained from the lithological contour map. A darker colour (purple) and larger mean numerical code indicated that the lithology of the region was closer to that of the reef base. Conversely, a lighter (orange) colour and smaller numerical code indicated that the lithology of the area was closer to that of the reef top, if at the top of the reef, a higher degree of dolomite development was observed.

The lithofacies distribution shows that the sedimentary units evolved from a micritic limestone to a reef limestone to a limy dolomite from the bottom to the top. The dolomitic limestone in the reef top transitioned from a continuous distribution to an

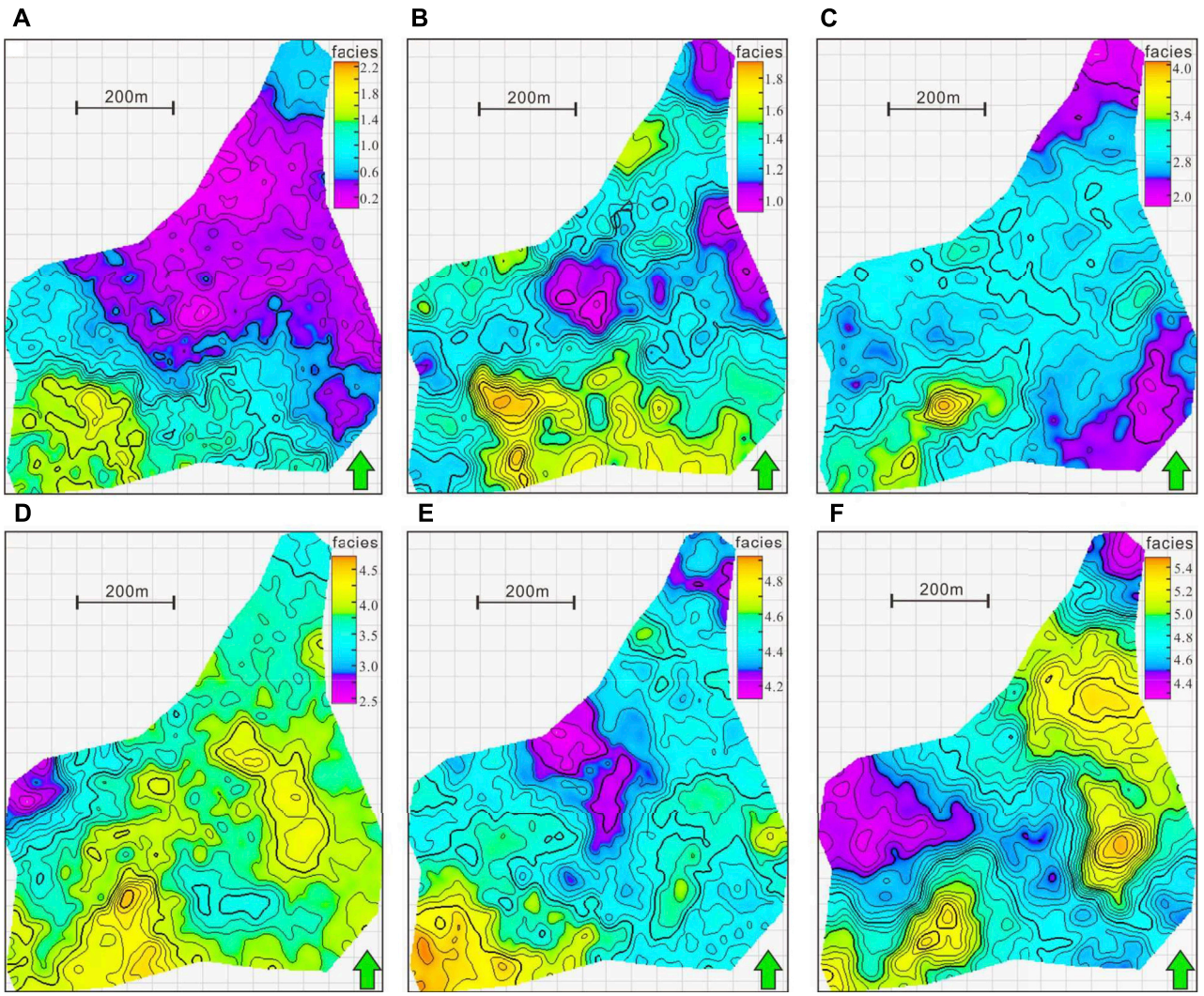

FIGURE 10 | Pattern of lithological distribution realized by the first SIS modeling. **(A–B)** local point-like distribution reef limestone; **(C)** rich algal reef limestone; **(D)** high content locally; **(E)** point-like distribution in the northwest; **(F)** point-like distribution in the southwest.

isolated, point-like distribution. In contrast, the reef limestone exhibited good overall continuity and a local point-like distribution (**Figures 10A,B**). Observing the reef core microfacies reveals that the reef-forming facies mainly occur in isolated points, and the algal-bound reef limestone is more abundant in content in the southwest (**Figure 10C**). Observation of the bioherm microfacies further reveals that the reef-forming facies were in the northwest region. Algal-bound and bioclast–micritic limestones occurred in layers, with high content locally (**Figure 10D**). By observing the reef base microfacies, it was found that the algal-bound reef limestone and bioclast–micritic limestone were continuous. The reef core microfacies, which are mainly algal-bound and bioclast–micritic limestones exhibit isolated, point-like distributions. The main reef base bodies (yellow) are in the northeast and southwest of the area (**Figures 10E,F**).

In order to improve the accuracy and quantitative capacity of the training images, the four single layers controlled by the five lithological interfaces were processed in detail. According to the vertical and planar facies sequences, the functions of the "Facies" module in Petrel were used to re-adjust the spatial distributions and quantitative relationships of various lithologies, and to obtain 3-D models of different reef shoal microfacies, including reef base, bioherm, reef core and reef top (**Figures 11A–D**). The results of the first depositional SIS were edited in Petrel. It can be seen from the 3-D grid diagram that the spatial contacts between the facies belts maintained the results of the original deposit and the mesh size of the training image matched that in the subsequent MPS, ensuring the accuracy and precision of the 3-D spatial search. The 3-D training image model reflects the variations of various lithologies in the vertical and horizontal directions quite well.

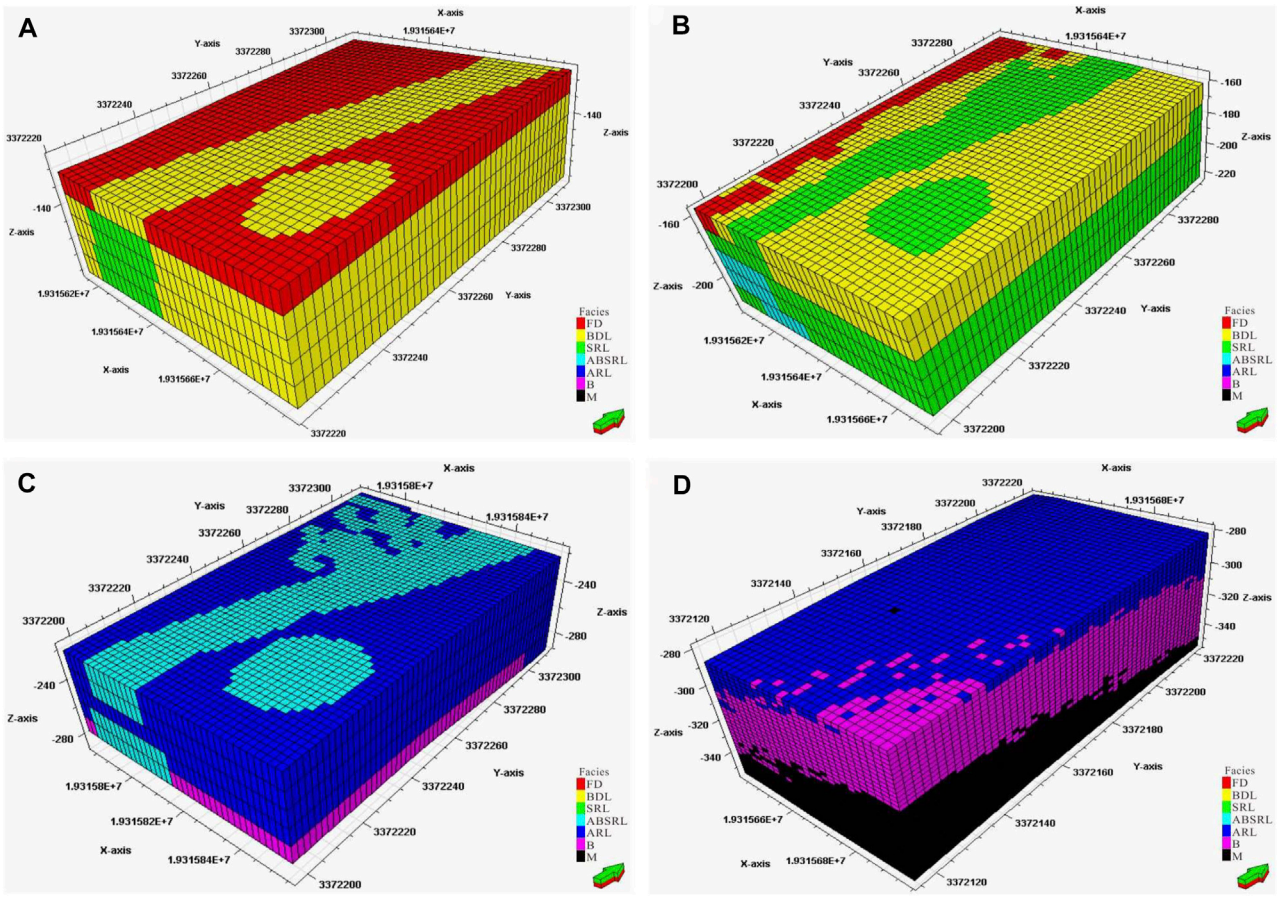

FIGURE 11 | 3-D training image model of each lithological microfacies. **(A)** Reef crest; **(B)** reef core; **(C)** bioherm; **(D)** reef base.

3-D Model Realization *via* Multi-Point Geostatistical Simulation

Multi-point geostatistical simulations were based on the Petrel software platform, using the fairly mature single normal equation simulation (SNESIM) algorithm. Based on the well lithofacies data, MPSs under the constraint of lithofacies was conducted to simulate the distribution of six lithologies in different layers of the reef base, bioherm, reef core and reef top microfacies. The SIS method was used to simulate the 3-D sedimentary microfacies of the reef base (**Figure 12B**), which was composed of argillaceous limestone, bioclast–micritic limestone and a small amount of algal-bound limestone. The results of the primary SIS showed that the micritic limestone and bioclastic limestone were unevenly distributed, while also existing as continuous pieces, with no geometric regularity. After MPS under the constraint of the training image (**Figure 12A**), it was found that the micritic limestone and bioclast–micritic limestone alternated. That is, the bioclasts exhibited multi-period distributions that roughly paralleled the direction of the coastline. The geological connotation of the training image is well expressed and the lithological relationships are more in line with the understanding of the reef base microfacies (**Figures 12C,D**).

The bioherm was mainly composed of bioclast–micritic limestone, algal-bound limestone and a small amount of sponge skeletal rock with an algal-bound structure. The results of primary SIS revealed that the algal-bound limestone and sponge skeletal rock were in a continuous piece with no obvious geometric distribution (**Figure 13B**). In the secondary MPS, under the constraint of the training image (**Figure 13A**), the planar trend and vertical variation in lithologies were strongly regulated. The results of MPS showed that the bioclastic limestone and algal-bound limestone were interbedded, largely in layers, but also as discrete points. The stratigraphic sequence was also more in line with our understand of bioherm core microfacies (**Figures 13C, D**).

The main lithologies of the reef core microfacies included a sponge reef limestone with an algal-bound structure, sponge skeletal bafflestone, bioclastic limestone and a small amount of fine-grained dolomite. The results of primary SIS showed that the contacts between the different lithologies were irregular, and the fine-grained dolomite at the reef top was continuously distributed (**Figure 14B**). After the secondary MPS, under the constraint of the training image (**Figure 14A**), it was found the bioclast–dolomitic limestone and the sponge skeletal reef

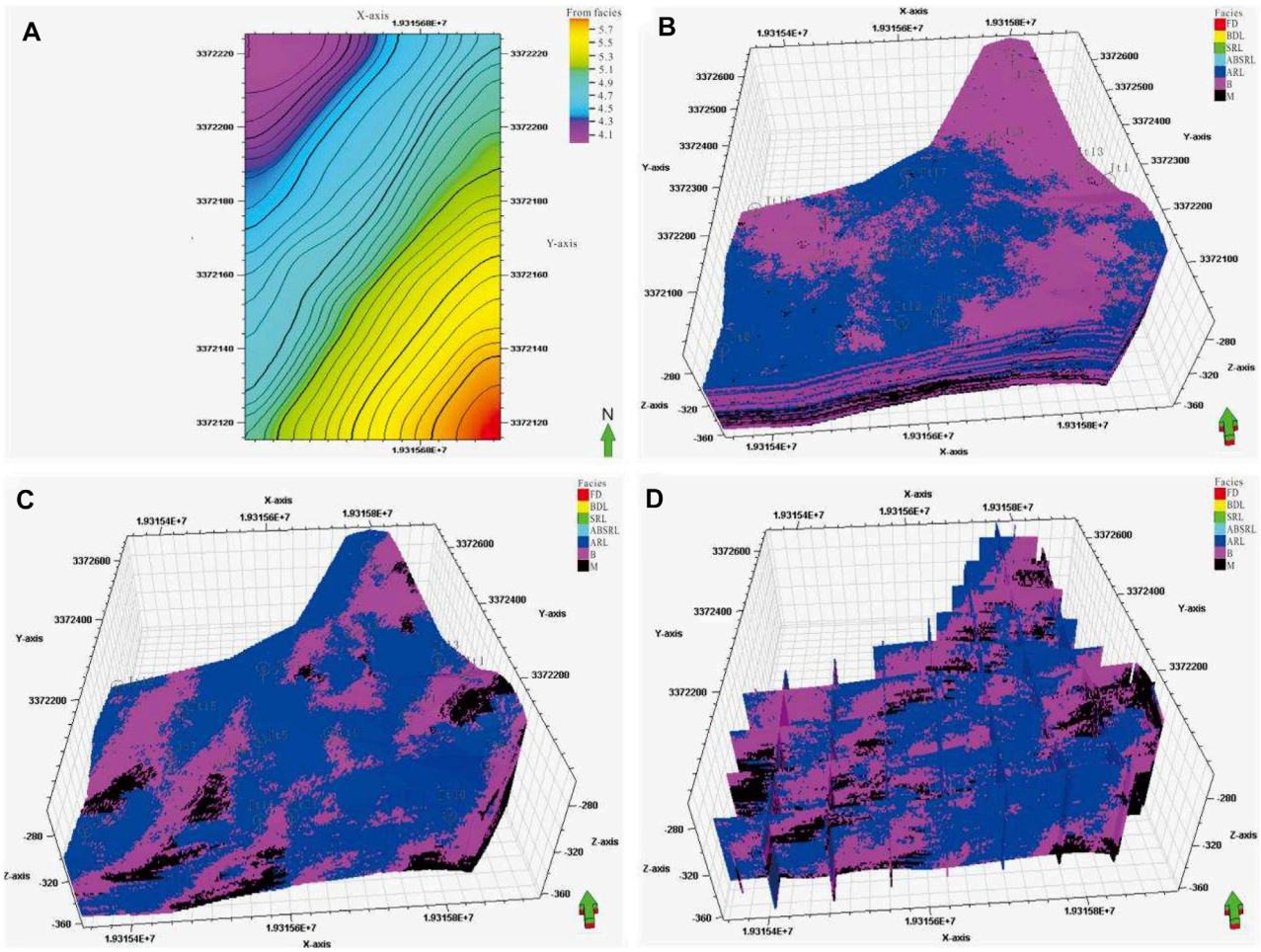

FIGURE 12 | 3-D outcrop modeling of reef base microfacies, which are restraint by training image pattern. **(A)** Reef base training image obtained by SIS, which deposited carbonate lithofacies gradually to bioherm; **(B)** the SIS Lithological modeling; **(C)** MPS realization; **(D)** palisade 3-D grids display about the multipoint geostatistics model.

limestone were heterogeneous in distribution. Overall, the algal-bound limestone was scattered and evenly distributed, while the sponge skeletal limestone appeared in layers in striking northeast–southwest, which is more consistent with the geospatial distribution of a linear reef. Locally, the content of the reef increased, which is presumed to represent single-point reefs on the seaward side. The lithologic relationships are also more in line with the understanding of reef core microfacies (**Figures 14C, D**).

The main lithologies of the reef top microfacies included a sponge reef limestone with an algal-bound structure, sponge skeletal bafflestone, bioclast–dolomitic limestone and a small amount of fine-grained dolomite. The SIS results showed that the fine-grained dolomite was concentrated in the eastern part of the model and was continuously distributed, while the bioclast–dolomitic limestone was concentrated in the west (**Figure 15B**). The planar distribution differs from the lithologic distribution of the reef–shoal facies considerably. The MPS, under the constraints of the training image, showed that the fine-grained dolomite and bioclastic limy dolomite were well regulated (**Figure 15A**). The amount of fine-grained dolomite was greatly reduced and shifted to the northwest. The sponge skeletal reef limestone appeared in layers approximately parallel to the coastline. The stratigraphic relationships observed are more consistent with the understanding of the reef top microfacies (**Figures 15C,D**).

Comprehensive Evaluation

Through comparing the morphologies and lithological distributions of different microfacies in the models, we found that in the MPS under the constraint of lithofacies, the training image controlled the spatial distribution of the lithofacies quite well. Compared with the SIS, the lithologies of the MPS displayed better regularity in both vertical and lateral distributions, which is more in line with the current geological understanding of the reef–shoal facies in the Jiantianba outcrop area. Combining field

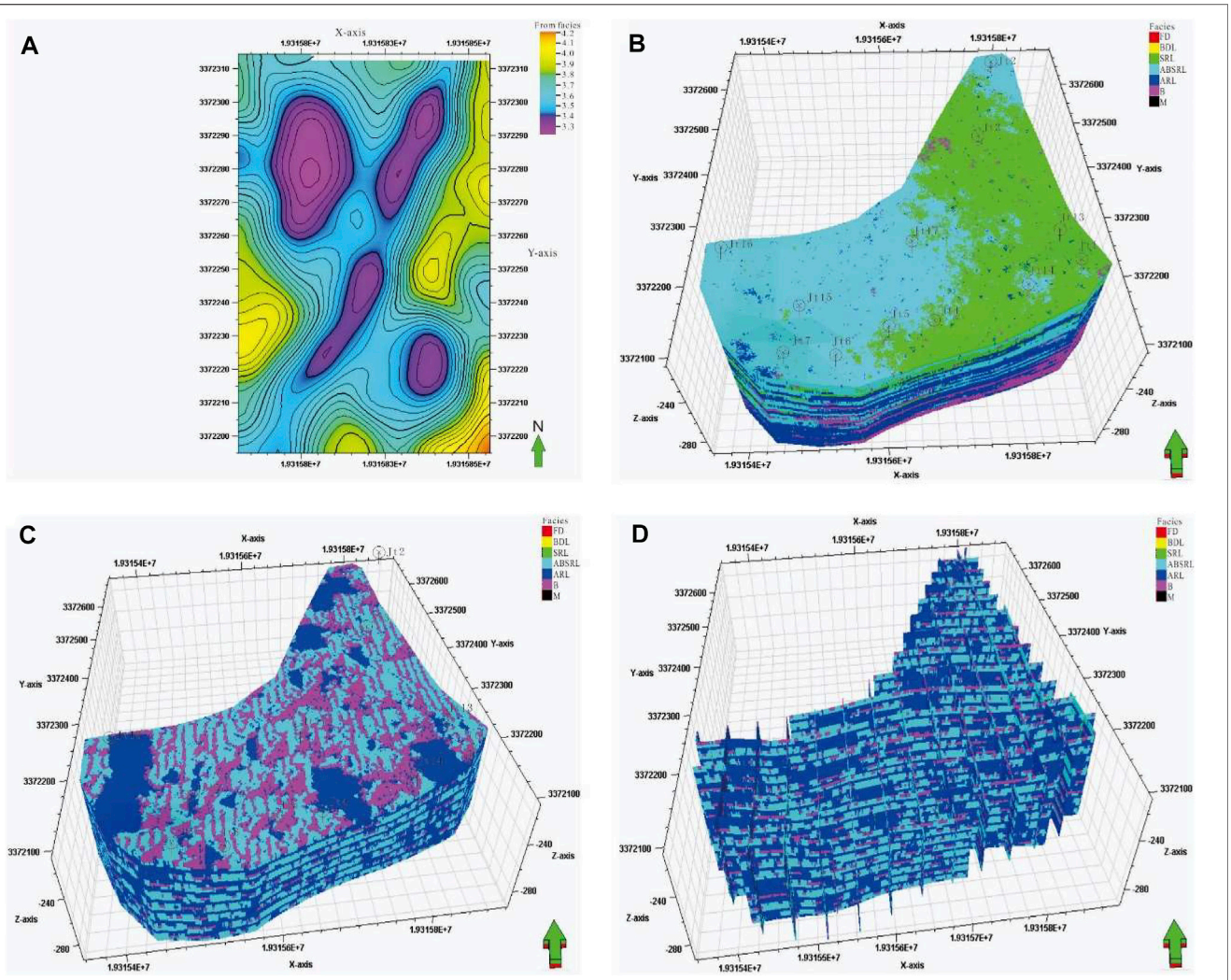

FIGURE 13 | 3-D outcrop modeling of bioherm microfacies, which are restraint by training image pattern. **(A)** Bioherm training image obtained by SIS, which deposited carbonate lithofacies suddenly to reef core; **(B)** the SIS lithological modeling; **(C)** MPS realization; **(D)** palisade 3-D grids display about the multipoint geostatistics model.

research and modelling, the parameters of the SIS and MPS were statistically compared. It was found that the geological knowledge effectively constrained the data for each lithofacies in the MPS. The difference between the results of the MPS parameters and the statistical results from the geological knowledge based on field surveys was small (**Table 5**), with the difference in lithology reaching a maximum of 15.2% and a minimum of 0%, which indicates that the model is generally reliable.

DISCUSSION

The improvement of current geological knowledge and 3-D geologic modelling-based data collected via UAV can be promoted in similar reservoirs in this and other study areas. Under the same sedimentary system, based on the OPT of the UAV, an outcrop can be used as a prototype model (Zhang et al., 2017; Zhao et al., 2017). The 3-D geological model of the outcrop can then be established, which can guide the oil development and production and reduce the risks of developing similar reservoirs (Yin et al., 2018a; 2018b, 2021).

To make the 3-D geological model established approach reality, modelers aim to have planar geological information to assist the 3-D simulation by acting as a constraint (Wu and Li, 2005). However, it is difficult to realise the conversion of geologically associated irregular profile data into planar data via traditional field-based approaches, which greatly impair the application of high-precision and visual data of the field outcrops in 3-D geological models (Yin et al., 2013; Picke et al., 2015). Meanwhile, the accuracy of the model is closely related to the modeler's experience with the geological setting of the study area. In recent years, our geological

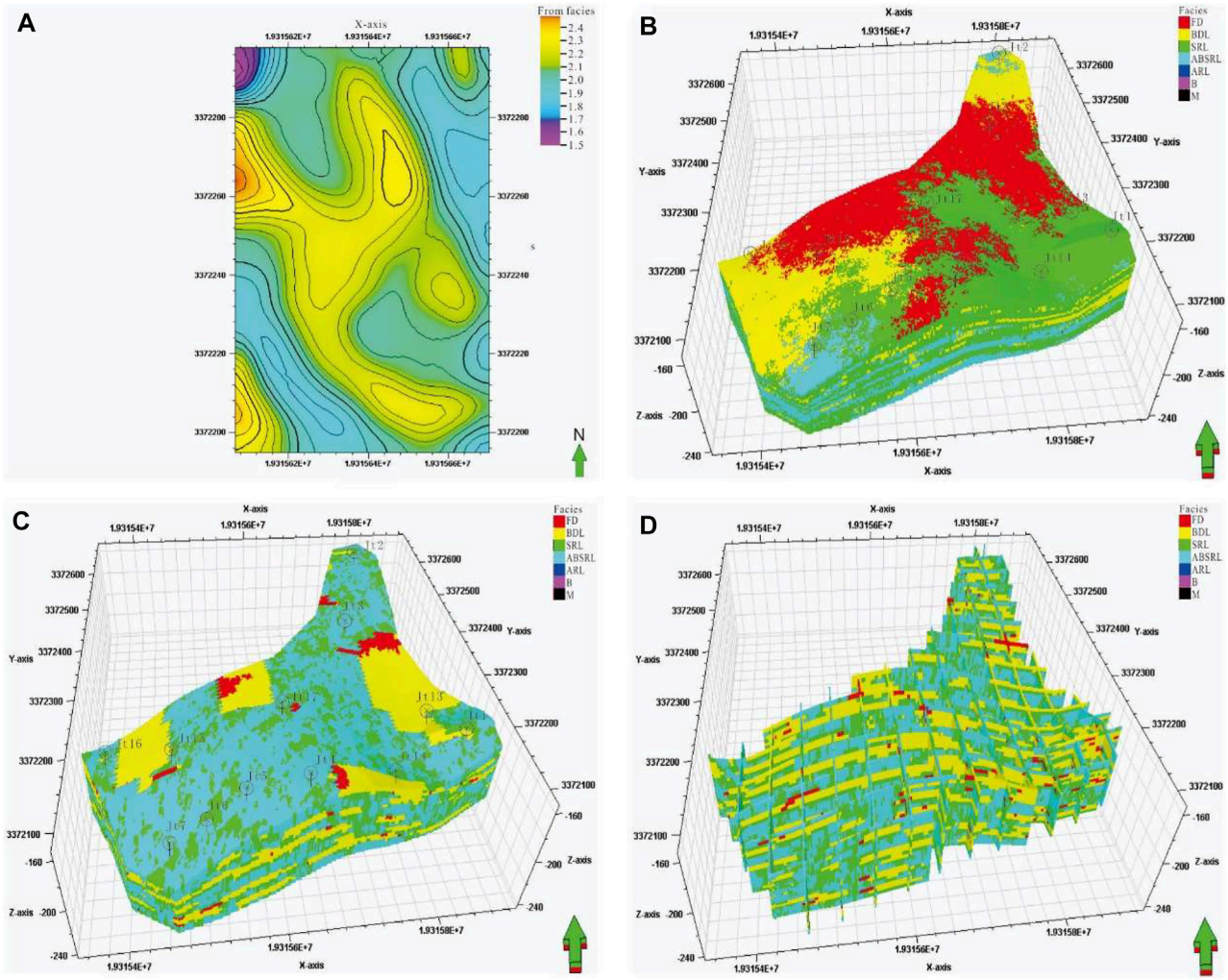

FIGURE14 | 3-D outcrop modeling of reef core microfacies, which are restraint by training image pattern. **(A)** Reef core training image obtained by SIS, which deposited carbonate lithofacies but poor continuity; **(B)** the SIS lithological modeling; **(C)** MPS realization; **(D)** palisade 3-D grids display about the multipoint geostatistics model.

knowledge has made great progresses in two aspects: the acquisition technologies used for quantitative data in geological databases and the algorithm of inter-well reservoir predictions (Duan et al., 2019). In particular, the MPS method has developed rapidly. How to obtain training images more reasonably and lay the foundation for establishing model libraries has become an important research topic (Zhao et al., 2017; Yin et al., 2021). The essence of this is still to quantify geological knowledge. The UAV with OPT opens a new window for data acquisition of training images.

The results of this study show that outcrop 3-D modelling based on UAV OPT has following advantages compared to conventional surveys:

It enhances the quantification of data and provides a spatial framework for 3-D outcrop modelling; Coordinates and lithology may be unfed in the 3-D digital outcrop model, improving upon the original manual recording mode of outcrop surveys, providing quantitative data for the continuous characterisation of the geological body and making it possible to display the irregular shape of such units more vividly and the prototype model more reliable; Transforming profiles into planar information and enhancing the input data of the model, provide an important and reliable constraint.

The outcrop 3-D modelling technology based on UAV oblique photogrammetry should be improved. Specifically, the image and automatic lithological conversion and recognition technology should be enhancing, as the field outcrop data acquired by UAV cruise are large in volume and it is unrealistic to manually calibrate the lithologies and stratigraphic contacts. Therefore, it is necessary to further improve the automatic conversion of images to lithotypes to

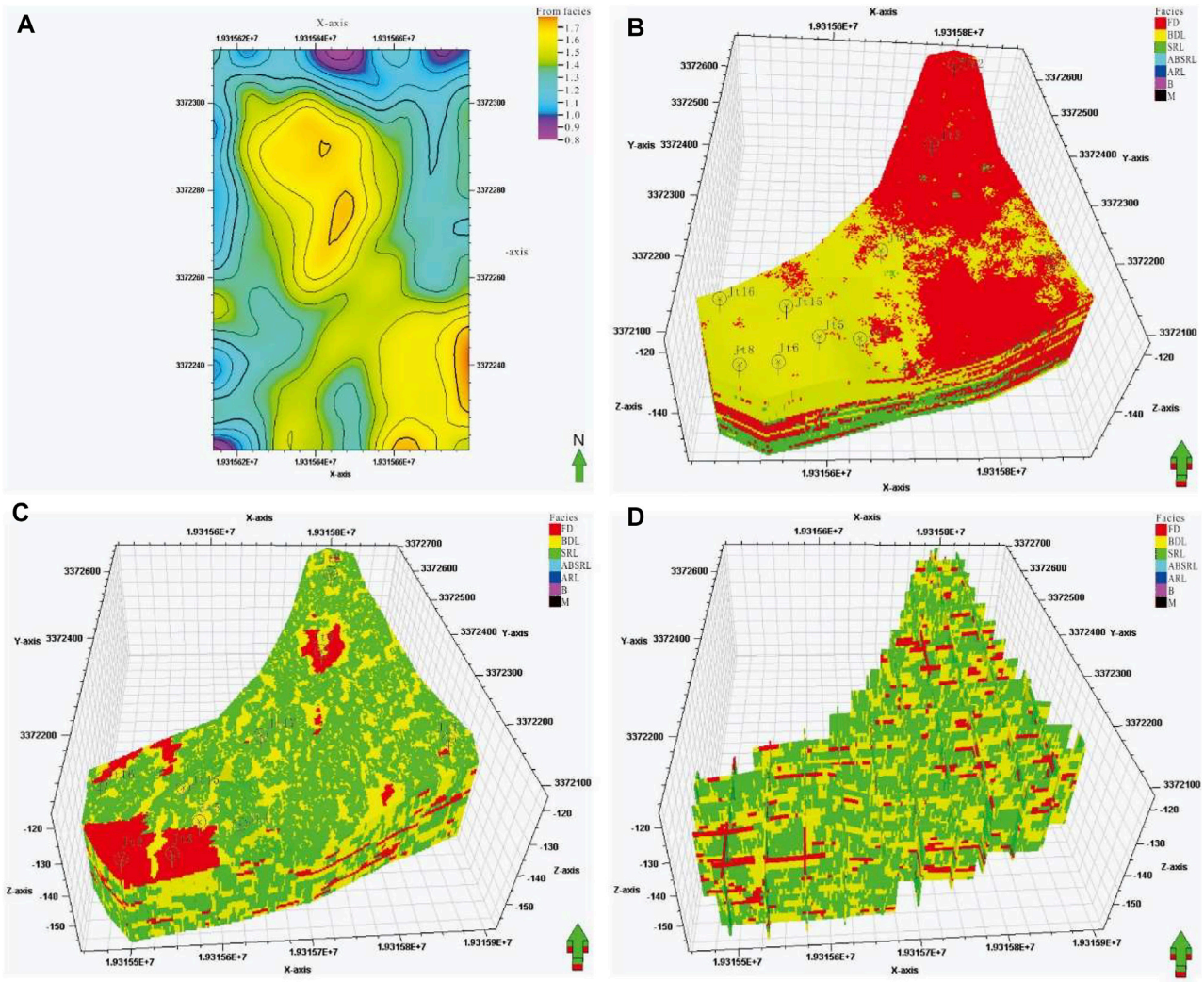

FIGURE15 | 3-D outcrop modeling of reef crest microfacies, which are restraint by training image pattern. **(A)** Reef crest training image, which deposited carbonate lithofacies but very poor continuity; **(B)** the SIS lithological modeling; **(C)** MPS realization; **(D)** palisade 3-D grids display about the multipoint geostatistics model.

TABLE 5 | Comparison of lithology model data to input.

Lithofacies code microfacies		0	1	2	3	4	5	6
Reef base	Input data/%	—	—	—	—	31.3	48.4	20.3
	MPS realization/%	—	—	—	—	31.1	49.1	19.9
	Difference	—	—	—	—	–0.64%	1.45%	–1.97%
Bioherm	Input data/%	—	—	12.8	29.2	36.1	21.9	—
	MPS realization/%	—	—	11.3	31.4	38.6	18.8	—
	Difference	—	—	–11.70%	7.53%	6.93%	–14.20%	—
Reef core	Input data/%	1.4	21.7	44.7	31.7	0.6	—	—
	MPS realization/%	1.2	20.3	48.6	31	0.6	—	—
	Difference	–14.30%	–6.45%	8.72%	–2.21%	0	—	—
Reef crest	Input data/%	43.8	43.1	13.1	—	—	—	—
	MPS realization/%	43	45.9	11.1	—	—	—	—
	Difference	–1.86%	6.50%	–15.20%	—	—	—	—

quickly identify the lithology of the 3-D digital outcrop area. Additionally, the nature of the UAV OPT outcrop model is only a 2-D irregular surface model and the model must to be transformed into a 3-D mesh to realise the characterisation of geological features in the outcrop area at an arbitrary precision. Finally, the training images of the study area must be improved by enhancing model algorithms and making use of the quantification and visualisation advantages of data acquisition; the MPS theory and methods must also be deepened.

CONCLUSION

A model of the carbonate outcrop data of Jiantianba has been generated from UAV OPT; the 3-D coordinates and corresponding image information of the model are highly accurate, making it possible to locate and measure the coordinates of any position accurately. This lays a base for researching the stratigraphic architecture of carbonate deposits and establishing an accurate reservoir database.

Meanwhile,the type, continuity and scale of lithofacies, vertical lithological sequences and evolutionary characteristics of typical outcrops in the field were compared, and the model parameters included an algal-bound reef limestone, algal-bound sponge reef limestone, sponge skeletal reef limestone, skeletal reef limestone, limestone breccia, and crystal–fine-grained dolomite, making up the reef top, reef core, bioherm core and reef base microfacies in the reef flat facies of the study area. The micritic limestone was stably distributed for 800–2000 m across and 15–40 m thick in thin layers. Bioclast–micritic limestone was distributed stably for 650–1,500 m across and 100–200 m in thickness, with uniform thin–medium bedded layers. Finally, the algal-bound reef limestone, sponge–algal-bound reef limestone and sponge skeletal reef limestone were similar in their unstable distributions, which ranged from 600 to 800 m across about 15–35 m in thickness, and exhibited a blocky structure.

Based on geological analyses, a 3-D stratigraphic model and two lithologic models of the typical outcrop section were established. Comparison of the models revealed that the MPS included reefs in different facies zones, which was essentially consistent with our understanding based on field surveys and better shows the combination and stratigraphic succession of different reef flat microfacies.

DATA AVAILABILITY STATEMENT

The original contributions presented in the study are included in the article/Supplementary Material, further inquiries can be directed to the corresponding author.

AUTHOR CONTRIBUTIONS

Conceptualization, SY; methodology, LZ validation, BZ; formal analysis, JZ; investigation, BZ; data curation LC; writing—original draft preparation, SY.

FUNDING

This study was supported by the Open Foundation of Top Disciplines in Yangtze University (Grant No. 2019KFJJ0818022), the National Natural Science Foundation of China (Grant No. 41502126) and the National Science and Technology Major Project (Grant No. 2017ZX05008-006-004-002).

REFERENCES

Abbey, E., Webster, J. M., Braga, J. C., Jacobsen, G. E., Thorogood, G., Thomas, A. L., et al. (2013). Deglacial Mesophotic Reef Demise on the Great Barrier Reef. *Palaeogeogr. Palaeoclimatol. Palaeoecol.* 392, 473–494. doi:10.1016/j.palaeo.2013.09.032

Azri, M. S., and Khairul, N. T. (2019). Identification of Rut and Pothole by Using Multirotor Unmanned Aerial Vehicle (UAV). *Measurement* 137, 647–654. doi:10.1016/j.measurement.2019.01.093

Bao, Z., and Wang, S. W. (2017). Research on Generating the Cooperative Operational Ability of the Manned/Unmanned Aerial Vehicles. *Natl. Defense Sci. Technology* 38 (3), 76–79. doi:10.13943/j.issn1671-4547.2017.03.12

Bi, K., Li, Y. C., Ding, X. B., and Liu, F. (2015). Aerial Photogrammetric Technology of Light Small UAV: Status and Trend of Development. *Bull. Surv. Mapp.* 60 (3), 27–31. doi:10.13474/j.cnki.11-2246.2015.0068

Buckley, S. J., Howell, J. A., Enge, H. D., and Kurz, T. H., 2008, Terrestrial Laser Scanning in Geology: Data Acquisition, Processing and Accuracy Considerations: *J. Geol. Soc.*, 165, 625–638.doi:10.1144/0016-76492007-100

Cai, X. Y. (2011). The Subtly Method of Reservoir and Exploration Effects on the Organic Reef-beach Body of Changxing Formation. *Yuanba Area, Northeast. Sichuan: Eng. Sci.* 13 (10), 28–33.

Carvajal-Ramírez, F., Navarro-Ortega, A. D., Agüera-Vega, F., Martínez-Carricondo, P., and Mancini, F. (2019). Virtual Reconstruction of Damaged Archaeological Sites Based on Unmanned Aerial Vehicle Photogrammetry and 3D Modelling. Study Case of a southeastern Iberia Production Area in the Bronze Age. *Measurement* 136, 225–236. doi:10.1016/j.measurement.2018.12.092

Duan, T. Z., Wang, G. F., Lian, P. Q., and Zhang, W. B. (2019). *Quantitative Geological Modeling of Oil and Gas Reservoirs and Application*. Beijing, China: Petroleum Industry Press, 1–20.

Fan, C., Li, H., Qin, Q., He, S., and Zhong, C. (2020). Geological Conditions and Exploration Potential of Shale Gas Reservoir in Wufeng and Longmaxi Formation of southeastern Sichuan Basin, China. *J. Pet. Sci. Eng.* 191, 107138. doi:10.1016/j.petrol.2020.107138

Fan, J. R. (1996). *Reef and Oil & Gas in China*. Beijing: Beijing Ocean Press, 326–329.

Fan, J. S., and Wu, Y. S. (2002). Restudies on Permian Reefs in Eastern Sichuan, China. *Oil Gas Geology*. 23 (1), 12–18.

Fan, J. S., Zhang, W., Ma, X., and Zhang, Y. B. (1982). The Upper Permian Reefs in Lichuan Area West Hubei. *Scientia Geologica Sinica* 17 (3), 274–282.

Feng, W. J., Yin, Y. S., Zhang, C. M., Duan, T. Z., Zhang, W. B., Hou, G., et al. (2019). A Training Image Optimal Selecting Method Based on Composite Correlation Coefficient Ranking for Multiple-point Geostatistics. *J. Pet. Sci. Eng.* 179, 321–327. doi:10.1016/j.petrol.2019.04.046

Guo, Z. H. (2001). Some Problems of Height Surveying and Setting-Out with Total Station. *Bull. Surv. Mapp.* 12, 39–40.

Hao, T., Kershaw, S., Tan, X. C., Liu, H., Li, F., Shen, C., et al. (2019). Sedimentology of Reefal Buildups of the Xiannüdong Formation (Cambrian Series 2):SW China. *J. Palaeogeogr.* 8 (2), 170–180. doi:10.1186/s425010190022x

Hu, M., Hu, Z., Qiu, X., Zhao, E., and Wang, D. (2012). Platform Edge Reef and Bank Structure and Depositional Model of Changxing Formation in Panlongdong Section, Xuanhan, Northeastern Sichuan. *J. Earth Sci.* 23 (4), 431–441. doi:10.1007/s12583-012-0266-1

Hu, M. Y., D Zhu, Z., He, P., Zhang, J., and Wang, Q. C. (2002). Ordovician Reef in Lunan-Bachu Area and Their Reservoir Characteristics. *Oil Gas Geology*. 23 (2), 179–182.

Hu, M. Y., Wei, H., Qiu, X. S., and Zhao, E. Z. (2012). Reef Composition and Their Forming Models of Changxing Formation in Jiantianba Section of Lichuan, Western Hubei. *Acta Sedimentologica Sinica* 30 (1), 33–42.

Jamie, G., Barlow, J., and Moore, R. (2019). Detection and Analysis of Mass Wasting Events in Chalk Sea Cliffs Using UAV Photogrammetry. *Eng. Geology*. 250, 101–112. doi:10.1016/j.enggeo.2019.01.013

Ji, X. J., Hou, J. G., Liu, H. L., Chen, J., and Liu, X. (2016). Quantitative Characterization of Plane Heterogeneity of Reef Bank Reservoir. *Geol. Rev.* 62 (5), 1315–1328. doi:10.16509/j.georeview.2016.05.015

Jody, M. W., Wallace, L., Silver, E., Potts, D., Bragac, J. C., Renema, W., et al. (2004). Coralgal Composition of Drowned Carbonate Platforms in the Huon Gulf, Papua New Guinea: Implications for Lowstand Reef Development and Drowning. *Mar. Geology*. 204, 59–89. doi:10.1016/S0025-3227(03)00356-6

Leinfelder, R. R., Schlagintweit, F., Werner, W., et al. (2005). Significance of Stromatoporoids in Jurassic Reefs and Carbonate Platforms—Concepts and Implications. *Facies* 51 (1), 288–326. doi:10.1007/s10347-005-0055-8

Li, H., Tang, H., Qin, Q., Zhou, J., Qin, Z., Fan, C., et al. (2019). Characteristics, Formation Periods and Genetic Mechanisms of Tectonic Fractures in the Tight Gas Sandstones Reservoir: A Case Study of Xujiahe Formation in YB Area, Sichuan Basin, China. *J. Pet. Sci. Eng.* 178, 723–735. doi:10.1016/j.petrol.2019.04.007

Long, S. X., You, Y. C., Liu, G. P., and Feng, Q. (2015). Fine Characterization of Ultra-deep Reef-Shoal Reservoirs of Ramp-type in Changxing Formation in Yuanba Gas field,Sichuan Basin. *Oil Gas Geology*. 36 (6), 994–1000. doi:10.11743/ogg20150614

Ma, Y. S., Cai, X. Y., and Zhao, P. R. (2014). Characteristics and Formation Mechanisms of Reef-Shoal Carbonate Reservoirs of Changxing-Feixianguan Formation, Yuanba Gas Field. *Acta Petrolei Sinica* 35 (6), 1001–1011.

Ma, Y. S., Fu, Q., Guo, T. L., Yang, F. L., and Zhou, Z. Y. (2005). Pool Forming Pattern and Process of the Upper Permian-Lower Triassic, Puguang Gas Field, Northeast Sichuan Basin, China. *Pet. Geology. Exp.* 27 (5), 455–460.

Ma, Y. S., Mu, C. L., Guo, X. S., and Zhao, P. Y. (2006). Characteristic and Framework of the Changxingian Sedimentation in the Northeastern Sichuan Basin. *Geol. Rev.* 52 (1), 25–29. doi:10.16509/j.georeview.2006.01.006

Mi, Y. H., Zhang, X. P., and Li, Y. J. (2017). Research on 3D City Modeling Based on Oblique Photography. *Geomatics Spat. Inf. Technology* 40 (1), 215–217.

Mirko, F., Simone, M., Stead, D., Sciarra, N., Mataloni, G., and Calamita, F. (2019). A New Fast and Low-Cost Photogrammetry Method for the Engineering Characterization of Rock Slopes. *Remote Sensing* 11 (11), 1267–1290. doi:10.3390/rs11111267

Picke, A., Frechette, J. D., Comunian, A., and Weissmann, G. S. (2015). Building a Training Image with Digital Outcrop Models. *J. Hydrol.* 531, 5–361. doi:10.1016/j.jhydrol.2015.08.049

Qie, L., Shi, Y. N., and Liu, J. G. (2021). Experimental Study on Grouting Diffusion of Gangue Solid Filling Bulk Materials. *J. Min. Strata Control Eng.* 3 (2), 023011. doi:10.13532/j.jmsce.cn10-1638/td.20201111.001

Qin, P., Hu, Z. G., Wu, S. Y., Zuo, M. T., and Han, L. (2018). Vertical Heterogeneity and Formation Mechanism of the Platform Edge Reef and Bank Reservoir in Changxing Formation of Eastern Sichuan Basin. *Acta Petrologica et Mineralogica* 37 (1), 61–74.

Remondino, F., and Gerke, M. (2015). "Oblique Aerial Imagery - a Review," in *Photogrammetric Week 2015* (Stuttgart, Germany: Wichmann/VDE Verlag), 75–83.

Robert, R. (2002). Structure and Composition of Organic Reefs and Carbonate Mud mounds: Concepts and Categories. *Earth-Science Rev.* 58, 163–231. doi:10.1016/S0012-8252(01)00089-7

Rong, H., Jiao, Y. Q., Wu, L. Q., Li, R., Wang, R., Wang, S. H., et al. (2009). Organic Bioherms and Their Forming Models of Changxing Formation in Manyue-Ganquan Section of Kaix-Ian, Northeast Sichuan. *Acta Sedimentologica Sinica* 27 (1), 9–17.

Shan, S. C., Wu, Y. Z., Fu, Y. K., and Zhou, P. H. (2021). Shear Mechanical Properties of Anchored Rock Mass under Impact Load. *J. Min. Strata Control.Eng.* 3 (4), 043034. doi:10.13532/j.jmsce.cn10-1638/td.20211014.001

Shen, A. J., and Chen, Z. E. (2001). Genetic Type of Permian Reefs and its Application to Prediction of Buried Reefs in Nanpanjiang. *Pet. Exploration Development* 28 (3), 29–34.

Shi, S. Y., Hu, S. Y., Feng, W. J., and Liu, W. (2012). Building Geological Knowledge Database Based on Google Earth Software. *Acta Sedimentologica Sinica* 30 (5), 869–878. doi:10.14027/j.cnki.cjxb.2012.05.003

Svennevig, K., Guarnieri, P., and Stemmerik, L. (2015). From Oblique Photogrammetry to a 3D Model - Structural Modeling of Kilen, Eastern North Greenland. *Comput. Geosciences* 83, 120–126. doi:10.1016/j.cageo.2015.07.008

Wang, H. (2017). *Research on the Path Planning and Positioning Navigation System of UAV*. Hangzhou, China: Master's thesis of Zhejiang University, 20–35.

Wang, L. X., Yin, Y. S., Feng, W. J., Duan, T. Z., Zhao, L., and Zhang, W. B. (2019). Training Image Optimization Method in Multipoint Geostatistics and its Application in Geological Modeling. *Pet. Exploration Development* 46 (3), 1–7. doi:10.1016/s1876-3804(19)60231-4

Wang, Y. B., Xu, G. R., Lin, Q. X., and Gong, S. Y. (2001). Depositional Model of Early Per-Mian Reef-Island in Eastern Kunlun. *Sci. China: Ser. D* 31 (3), 243–249. doi:10.1007/BF02907093

Wang, Y. B., Xu, G. R., and Lin, Q. X. (1997). Paleoecological Relations between Coral Reef and Sponge Reef of Late Permian in Cili Area, West Hunan Province. *Earth Sci. J. China Univ. Geosciences* 22 (2), 135–138.

Woodward, J., Ashworth, P. J., Best, J. L., Sambrook Smith, G. H., and Simpson, C. J. (2003). The Use and Application of GPR in sandy Fluvial Environments: Methodological Considerations. *Geol. Soc. Lond. Spec. Publications* 211, 127–142. doi:10.1144/gsl.sp.2001.211.01.11

Wu, H. Z., Wu, Y. J., and Ke, G. M. (2017). Bioherm Development Model and Reservoir Prediction of Changxing Formation in Yuanba Area, Northeastern Sichuan Basin. *Oil Gas Geology*. 38 (4), 645–657.

Wu, S. H., and Li, W. K. (2005). Multiple-point Geostatistics :theory , Application and Perspective. *J. Palaeogeogr.* 7 (1), 137–144.

Xu, S. C., Li, G. R., Zhang, X. Q., Wu, Y. J., Jing, X. Y., and Liu, Y. Y. (2017). Genetic Mechanism of Reefal Dolostones of the Changxing Formation in Yuanba Area, Northeastern Sichuan Basin. *Oil Gas Geology*. 38 (4), 729–740.

Yahya, A., El-Khalili, M., Almasri, E., Bala'awi, F., and Al-Massarweh, A. (2020). Heritage Documentation Using Laser Scanner and Photogrammetry: The Case Study of Qasr Al-Abidit, Jordan. *Digital Appl. Archaeology Cult. Heritage* 16, e00133. doi:10.1016/j.daach.2019.e00133

Yan, Z. L., Xing, F. C., Duan, J. B., Hu, H. R., and Wu, S. Y. (2018). Sedimentary Texture and Reservoir Distribution of Platform Margin Reef Flat Zone in Changxing Formation of Northeastern Sichuan Basin. *Xinjiang Pet. Geology*. 39 (3), 311–317.

Yang, L. B., Den, W. L., Xu, S. C., Wang, J., Liu, Y. Y., and Ke, G. M. (2017). Geological Characteristics of Sedimentary Microfacies in Reef Flat of Changxin Formation in Guangyuan Gas Reservoir and its Well Logging Identification Method. *Well Logging Technology* 41 (5), 538–543. doi:10.16489/j.issn.1004-1338.2017.05.008

Yang, L. Q., Guo, L., Zhu, J. F., Gao, Z. C., Zhou, T. Q., Yu, Z. R., et al. (2017). The Development Situation and prospect of Agricultural UAV in China. *J. Agric. Mechanization Res.* 8, 6–11. doi:10.13427/j.cnki.njyi.2017.08.002

Yin, S. L., Chen, G. Y., Liu, Z. L., Feng, W., and Liu, Y. (2018a). 3D Digital Outcrop Characterization Technology Based on Unmanned Aerial Vehicle Oblique Photography. *Acta Sedimentologica Sinica* 36 (1), 72–80. doi:10.3969/j.issn.1000-0550.2018.009

Yin, S. L., Gao, Y., Hu, Z. M., Xiong, T., Feng, W. J., Zhao, J. W., et al. (2021). Multiple-point Geostatistical Simulation of Outcrop Based on UAV Oblique Photographic Data: a Case Study of Shihezi Formation in Pingtou Township, Lvliang City, Shanxi. *Acta Petrolei Sinica* 42 (2), 198–216. doi:10.7623/syxb202102005

Yin, S. L., Tan, Y. Y., Zhang, L., Feng, W., Liu, S. Y., and Jing, J. (2018b). 3D Outcrop Geological Modeling Based on UAV Oblique Photography Data: A Case Study of Pingtouxiang Section in Lüliang City, Shanxi Province. *J. Paleogeography* 20 (5), 909–924.

Yin, S. L., Wu, S. H., Feng, W. J., Tang, W., Hu, Z. M., and Ren, X. (2013). Variogram Analysis and Simulation on Sedimentary Outcrop Profile of Braided

River. *J. Cent. South Univ. (Science Technology)* 44 (12), 4988–4994. doi:10.1016/j.injury.2013.09.005

Yin, Y. S., Zhang, C. M., Li, J. Y., and Shi, S. Y. (2011). Progress and prospect of Multiple-point Geostatistics. *J. Palaeogeogr.* 13 (2), 245–252. doi:10.7605/gdlxb.2018.05.064

Yu, S. Y., Li, S. H., Wang, D. P., Wang, J., Zhang, Y. G., and Yu, J. B. (2017). Multipoint Geo-Statistical Modeling Algorithm Based on P-Stable LSH. *Acta Petrolei Sinica* 38 (12), 1425–1433.

Zhang, C. M., Zhu, R., Zhao, K., Hu, W., Yin, Y. S., Li, S. H., et al. (2017). From End Member to Continuum: Review of Fluvial Facies Model Research. *Acta Sedimentologica Sinica* 35 (5), 926–944.

Zhang, W. B., Duan, T. Z., Zheng, L., Liu, Z. Q., Xu, H. M., and Zhao, L. (2015). Generation and Application of Three-Dimensional MPS Training Images Based on Shallow Seismic Data. *Oil Gas Geology*. 36 (6), 1030–1037.

Zhang, W. B., Duan, T. Z., Liu, Y. F., Xu, R., Yang, Z. C., and Zhang, D. M. (2017). Integrated Sedimentary Forward Modeling and Multipoint Geostatistics in Carbonate Platform Simulation : a Case Study of Jupiter Oilfield in Brazil. *Acta Petrolei Sinica* 38 (8), 925–934.

Zhang, X., Zhao, P., Hu, Q., Ai, M., Hu, D., and Li, J. (2020). A UAV-Based Panoramic Oblique Photogrammetry (POP) Approach Using Spherical Projection. *ISPRS J. Photogrammetry Remote Sensing* 159, 198–219. doi:10.1016/j.isprsjprs.2019.11.016

Zhao, L., Ke, L., Shang, X. F., and He, T. T. (2017). The Alluvial Fan Reservoir Modeling Based on Seismic Inversion Data and Multiple Information Constraint. *J. Northeast Pet. Univ.* 41 (1), 63–72.

Zhou, J. N., Tian, J. H., Fan, T. E., Cai, W. T., and Ni, J. E. (2018). Velocity Modeling Method in Reef Reservoir. *Prog. Geophys.* 33 (1), 347–352.

Zhu, R, K., Bai, B., Yuan, X. J., Luo, Z., Wang, P., Gao, Z. Y., et al. (2013). A New Approach for Outcrop Characterization and Geostatistical Analysis of Meandering Channels Sandbodies within a delta plain Setting Using Digital Outcrop Models: Upper Triassic Yanchang Tight sandstone Formation, Yanhe Outcrop, Ordos Basin. *Acta Sedimentologica Sinica* 31 (5), 867–877.

Conflict of Interest: YL was employed by the company China National Petroleum Corp Bureau of Geophysical Prospecting Inc.

The remaining authors declare that the research was conducted in the absence of any commercial or financial relationships that could be construed as a potential conflict of interest.

Publisher's Note: All claims expressed in this article are solely those of the authors and do not necessarily represent those of their affiliated organizations, or those of the publisher, the editors and the reviewers. Any product that may be evaluated in this article, or claim that may be made by its manufacturer, is not guaranteed or endorsed by the publisher.

frontiers | Frontiers in Earth Science

ORIGINAL RESEARCH
published: 19 April 2022
doi: 10.3389/feart.2022.890084

Study on Stress Sensitivity of Ultra-Low Permeability Sandstone Reservoir Considering Starting Pressure Gradient

Xiang Luo[1], Xiujuan Wang[2], Zhonghu Wu[3], Tongtong He[2], Xiangliang Qiu[1], Fang Yuan[2] and Chengqian Tan[4]**

[1]Xi'an Shiyou University, School of Petroleum Engineering, Xi'an, China, [2]Geological Research Institute of No. 9 Oil Production Plant, Changqing Oilfield, CNPC, Xi'an, China, [3]College of Civil Engineering, Guizhou University, Guiyang, China, [4]Xi'an Shiyou University, School of Earth Science and Engineering, Xi'an, China

OPEN ACCESS

Edited by:
Wenlong Ding,
China University of Geosciences, China

Reviewed by:
Peng Dai,
Chinese Academy of Geological Science, China
Chong Zhang,
Chengdu University of Technology, China

***Correspondence:**
Zhonghu Wu
wuzhonghugzu@163.com
Chengqian Tan
1098364810@qq.com

Specialty section:
This article was submitted to Structural Geology and Tectonics, a section of the journal Frontiers in Earth Science

Received: *05 March 2022*
Accepted: *01 April 2022*
Published: *19 April 2022*

Citation:
Luo X, Wang X, Wu Z, He T, Qiu X, Yuan F and Tan C (2022) Study on Stress Sensitivity of Ultra-Low Permeability Sandstone Reservoir Considering Starting Pressure Gradient. Front. Earth Sci. 10:890084. doi: 10.3389/feart.2022.890084

When studying the influence of nonlinear seepage on the water flooding development of ultra-low permeability reservoirs, it is difficult to accurately characterize the nonlinear seepage state of ultra-low permeability reservoirs using conventional reservoir numerical simulation methods. A large number of field development and tests in the oil fields show that there are indeed starting pressure gradients and stress sensitivity effects in ultra-low permeability sandstone reservoirs. In this study, taking the tight sandstone of the Chang 6 Member in the Yanchang Formation as an example, the rock displacement vector was utilized to equivalently characterize the stress-sensitive effect of the reservoir based on a novel numerical simulation software tNavigator. Furthermore, the starting pressure gradient and the feasibility of a new stress-sensitive equivalent characterization method were verified combining the poroelastic media physics equations. In addition, we systematically studied the impact of stress-sensitive effects on oil well productivity under the influence of starting pressure gradient and considering petrophysical properties. The results show that the existence of the starting pressure gradient can improve the stress sensitivity of the matrix reservoir. Considering the starting pressure gradient, when the rock shear modulus is 14.29 GPa, the cumulative oil production decreases by 4.1%; when the rock shear modulus is 11.36 GPa, the cumulative oil production decreases by 11.2%. Finally, a numerical simulation was conducted with Block B in the Zhouwan-Wugucheng area, and the model can accurately predict the reservoir stress sensitivity based on the starting pressure gradient. When both the starting pressure gradient and stress sensitivity are considered, the crude oil recovery degree of the target layer decreases by 11.7%; when only the starting pressure gradient is considered, the crude oil recovery degree decreases by 8.8%; and when only the stress sensitivity is considered, the crude oil recovery degree decreases by 0.5%.

Keywords: starting pressure gradient, stress sensitivity, equivalent characterization, ultra-low permeability reservoir, numerical simulation

1 INTRODUCTION

In recent years, the proportion of ultra-low permeability tight sandstone reserves in China's newly-added proven oil-in-place reserves has reached 60% (Meng and Li., 2013; Chen et al., 2019; Qian et al., 2021). Tight sandstone oil and gas has become the main energy field in the future utilization and exploitation of oil and gas resources (Kuuskraa., 1996; Lu and Wang., 1999; Ruan., 2002). Therefore, the efficient development of ultra-low permeability sandstone reservoirs is of great significance to the sustainable development of oil industry (Hansbo., 1960; Geng et al., 2017; Gao., 2021; Wu et al., 2021). Non-Darcy seepage problems are often involved in actual reservoir development (Francesconi., 1995; Shi et al., 1999; Wang et al., 1999; Dong et al., 2015; Zhao et al., 2021). If the fluids seep very slowly, they do not satisfy Darcy's law.

Previous studies have systematically studied the effect of stress sensitivity on rock porosity and permeability (Hu et al., 2006; Jiao et al., 2011; Xu et al., 2021; Xue et al., 2021). These studies showed that with the increase of effective stress, rock porosity and permeability decreased to varying degrees (Mitchell, 1967; Von E and Tunn, 1995; Lei et al., 2007; Tian, 2014). Moreover, there are several studies showing that the initial displacement pressure required for oil flow increases as the permeability becomes effective (Liu et al., 2001; Cai et al., 2017; Li et al., 2020; Mahmud et al., 2020; Li and Li., 2021).

At present, existing commercial softwares cannot effectively simulate stress-sensitive effects in low-permeability reservoirs by setting the minimum pressure for fluid percolation (Todd., 2016; Maksim., 2019; Wu et al., 2020). The limitation of fluid flow simulation technology is that it cannot accurately characterize the non-Darcy flow state of low permeability reservoirs (Lv et al., 2002; Hong et al., 2020; Zheng et al., 2020). Fluid-structure interaction is currently recognized worldwide as an equivalent characterization method for stress-sensitive effects (Xu et al., 2014; Wang et al., 2016; He et al., 2020; Guo et al., 2021; Hower and Groppo., 2021; Mohammed et al., 2021). Most of the current commercial numerical simulation software only considers the pressure sensitivity of permeability and porosity, and does not consider the rock physical parameters (elastic modulus, Poisson's ratio, etc.) under high temperature and pressure conditions (Shang., 2004; Song., 2012; Wang et al., 2012; Ren et al., 2020; Chen et al., 2021). In this study, taking the tight sandstone of the Chang 6 Member in the Yanchang Formation as an example, the rock displacement vector was utilized to equivalently characterize the stress-sensitive effect of the reservoir based on a novel numerical simulation software tNavigator. It can introduce rock mechanics parameters into the simulation of ultra-low permeability sandstone reservoir. In addition, a new generation of numerical simulator, the calculation kernel is optimized, the parallel computing efficiency and acceleration ratio are improved. The GPU was used to accelerate the calculation, which significantly reduces the time cost of numerical simulation. By applying this technology to actual oil reservoirs, the non-Darcy flow conditions of low permeability reservoirs can be simulated more accurately.

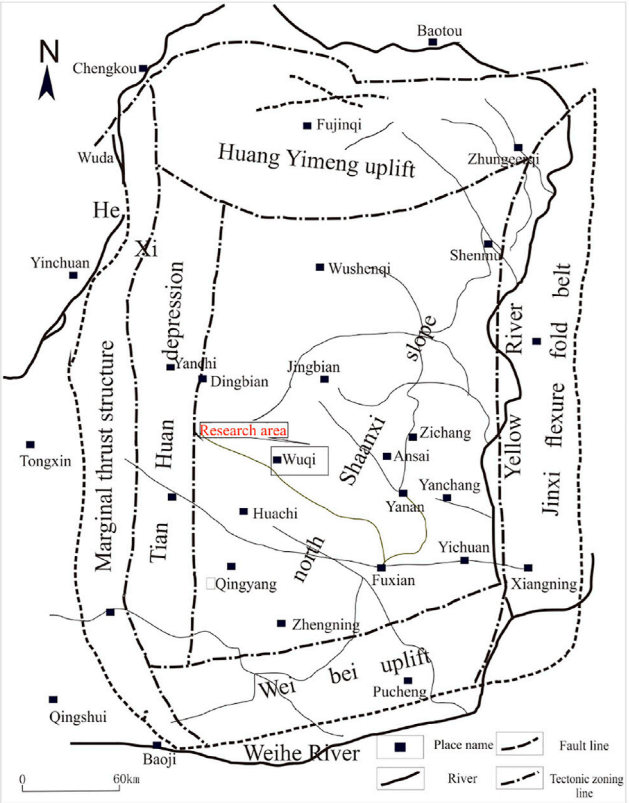

FIGURE 1 | Regional overview of the study area.

2 MATERIALS AND METHODS

2.1 Geological Background and Reservoir

The Triassic strata in the Ordos Basin have experienced complex evolutionary stages of lake basin expansion and eventual shrinkage and extinction. The study area is located in the Zhouwan-Wugucheng area (**Figure 1**), where tight sandstone reservoirs are developed in the Lower Triassic Yanchang Formation. Moreover, the main reservoir is the Chang 6 Member. The Chang 6 Member belongs to the delta front subfacies deposition, and the underwater distributary channel, channel flanks and inter-distributary bay microfacies are developed.

The experimental procedure of casting thin section: low viscosity epoxy resin impregnated with pigment, casting agent and dyeing agent are injected into the pores of rock under certain temperature and pressure, and the linear epoxy resin is crosslinked into huge molecules with network structure by curing reaction to form hard solid epoxy resin. Then the cast thin sections are made by sticking and grinding procedures. According to the identification results of thin sections and SEM (scanning electron microscope) of 107 sandstone samples taken from 27 wells, the pore types of Chang 6 reservoirs in the study area mainly include intergranular pores, feldspar dissolved pores, and detrital dissolved pores. Intergranular pores are the

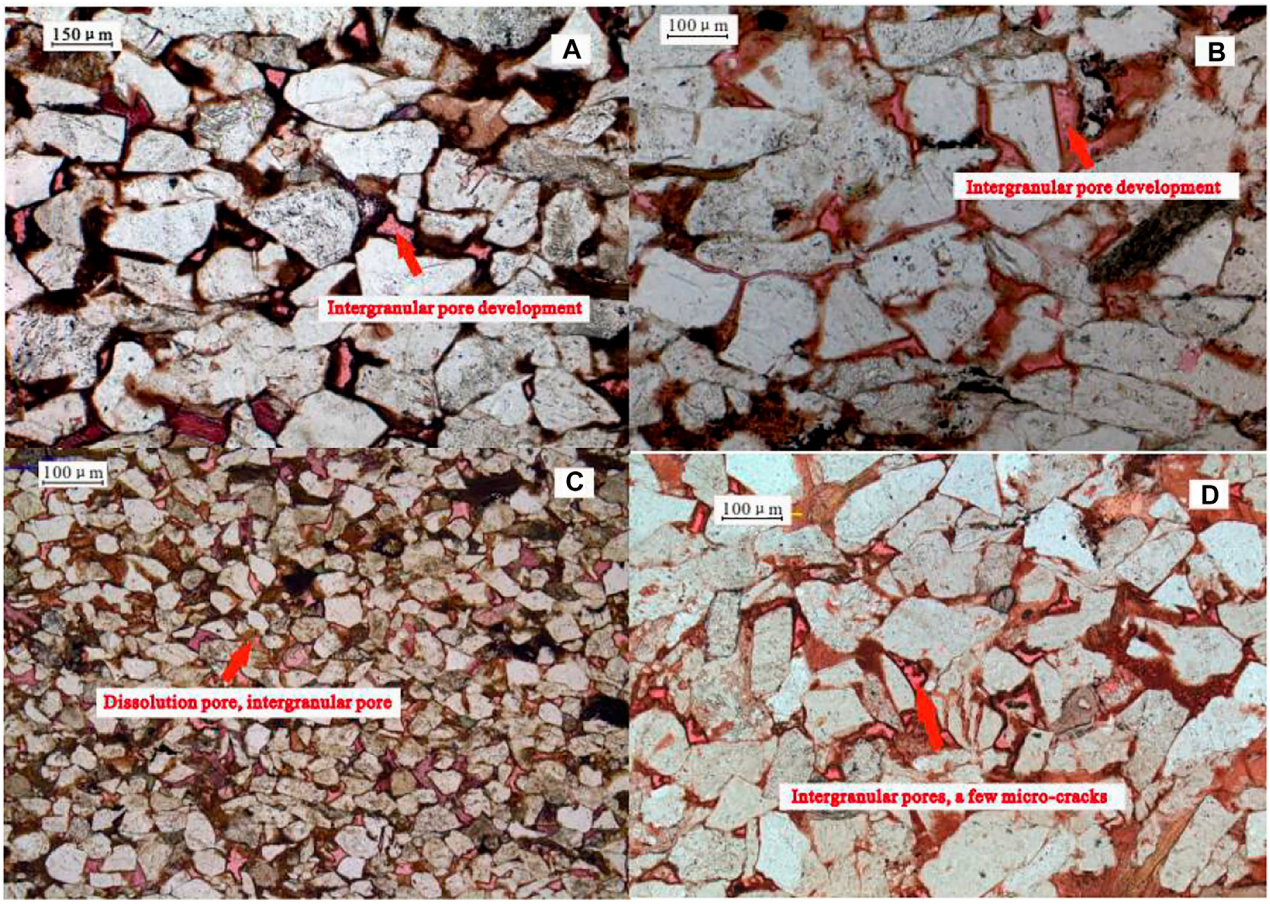

FIGURE 2 | Identification of typical sandstone thin sections of the Chang 6 reservoir in the Zhouwan-Wugucheng area. **(A)** Well B282, Chang 6 Member, 1852.75 m, isolated intergranular pores are developed; **(B)** Well B516, Chang 6 Member, 1785.94 m, intergranular pores are well-developed; **(C)** Well B513, Chang 6 Member, 1825.42 m, dissolution and intergranular pores; **(D)** Well B286, Chang 6 Member, 1773.97 m, intergranular pores and micro-cracks are developed.

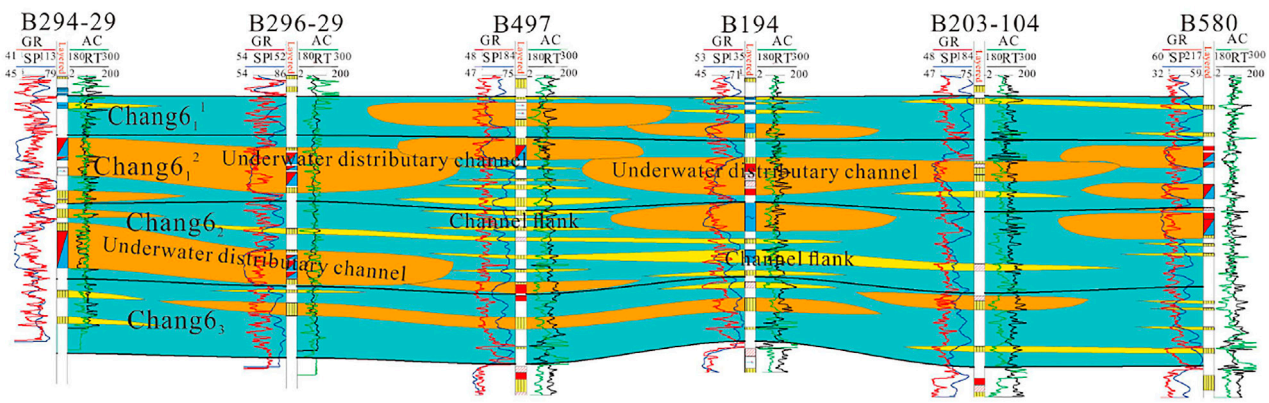

FIGURE 3 | Profile of sedimentary microfacies in the Chang6 Member in the study area (SW-NE direction).

main type of pores, followed by feldspar dissolved pores, and detrital dissolved and intercrystalline pores are locally visible. The shapes of these pores are mostly triangular and quadrilateral, and the pores are mostly connected by narrow and short throats (**Figure 2**). Affected by the stress-sensitivity effect, the radius of some narrow and short throats

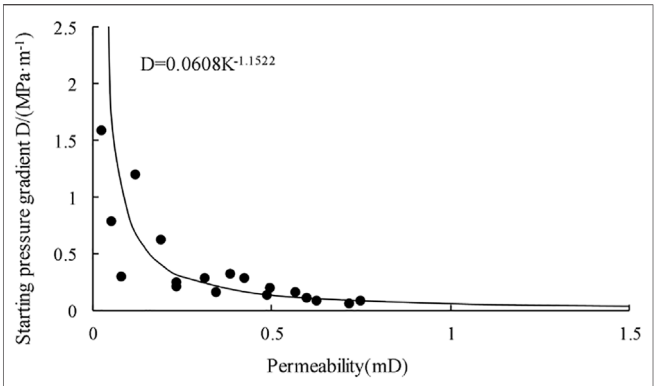

FIGURE 4 | Relationship between permeability and starting pressure gradient of the Chang 6 reservoir in Block **(B).**

will gradually decrease during the waterflooding development process.

In the study, the profile of the Chang 6 Member shows that the subaqueous distributary channel has well continuity and long extension distance in the SW-NE direction, and multi-staged superposed channels are developed. In the NW-SE direction, the underwater distributary channel is cut by interdistributary bay and has poor sand body continuity (**Figure 3**).

2.2 Equivalent Simulation of Starting Pressure Gradient

2.2.1 Equivalent Simulation of Starting Pressure Gradient

The simulation of the starting pressure gradient in the ECLIPSE Software is based on the equilibrium partitions to achieve the minimum pressure setting for fluid percolation between adjacent partitions (Wu et al., 2017). If we set a separate partition for each grid, it will result in a huge number of partitions, the software cannot obtain results through normal operations, and the computational workload is also huge (Xiong et al., 2009; Wang et al., 2020; Yang et al., 2021). However, the tNavigator Software can assign the grids in the work area through the keywords PTHRESHI, PTHRESHJ, and PTHRESHK, and then calibrate the starting pressure gradients in the three directions of I, J, and K. This method can be used to study the variation law of the production index in the work area under different starting pressure gradients (Yang et al., 2010).

The starting pressure gradient of the target layer of the work area measured by the experiment is 0.04 MPa/m, the grid size of the work area is 100 × 80 × 30, and the total number of grids is 240,000. In addition, the starting pressure gradient in the I, J, and K directions between grids in the work area is 0.04 MPa/m, and the keywords are PTHRESHI 240000*0.04, PTHRESHJ 240000*0.04, and PTHRESHK 240000*0.04, respectively.

2.2.2 Optimization of Starting Pressure Gradient

The tNavigator Software can realize the setting of different starting pressure gradients in the I, J and K directions of each grid in the work area according to the reservoir properties and the keyword ARITHMETIC. This technology can restore the seepage states of the fluids inside the reservoir as realistically as possible, thereby greatly improving the simulation accuracy. **Figure 4** shows the relationship between the permeability under the condition of the starting pressure gradient and the threshold pressure gradient of the Chang 6 reservoir in the Zhouwan-Wugucheng area obtained from the core experiments. We can get $D = 0.0608\ K^{-1.1522}$. The keywords are:

ARITHMETIC PTHRESHI = 0.0608*PERMX$^{-1.1522}$;
ARITHMETIC PTHRESHJ = 0.0608*PERMY$^{-1.1522}$;
ARITHMETIC PTHRESHK = 0.0608*PERMZ$^{-1.1522}$.

Notes: PERMX, PERMY and PERMZ are the permeability in *x*, *y* and *z* directions, respectively. The ARITHMETIC PTHRESHI, the ARITHMETIC PTHRESHJ, and the ARITHMETIC PTHRESHK are the starting pressure gradient values in the *x*, *y*, and *z* directions, respectively.

Furthermore the pressure differential flow method was adopted in the experiment. The basic principle is: after different displacement pressure differences are stabilized, the flow rate of fluid through the core is measured, the relationship between flow rate and pressure gradient is drawn, and the starting pressure gradient is calculated by regression curve (**Table 1**).

The starting pressure gradient values for each grid in three dimensions can be obtained, based on the different permeability assignments on each grid throughout the model.

2.3 Equivalent Simulation of Stress-Sensitive Effects

Subsurface porous media rocks are composed of rock particles and pore fluids. During the development stage of the reservoir, the compression of the rock will generate compound stress, which will lead to the deformation and displacement of the rock skeleton (**Figure 5**). When the pore fluid migrates with the rock skeleton, relative seepage will also occur (Wang et al., 2019).

As shown in **Figure 5**, the reservoir rock can be equivalently regarded as a single hexahedral unit. (Dai., 2006; Ewing et al., 1980; Feng et al., 2018). The opposite sides of the regular hexahedral elements are parallel to each other. And, along the *x*, *y*, and *z* axes, the lengths of each side of the hexahedral unit correspond to d*x*, d*y*, and d*z*, respectively. The nine components on the reservoir rock are shown in **Eq. 1**. Moreover, the size of the nine components is not only related to the direction of the coordinate axis, but also to the force of the point. The stress state at a certain point inside the rock can be represented in the form of a matrix:

$$\sigma_{ij} = \begin{bmatrix} \sigma_x & \tau_{xy} & \tau_{xz} \\ \tau_{yz} & \sigma_y & \tau_{yx} \\ \tau_{zx} & \tau_{zy} & \sigma_z \end{bmatrix} \quad (1)$$

Chen and Ewing., 1999 used the elastic physical equation of porous media is used to describe the relationship between the effective stress and strain of rock, and its general expression is:

TABLE 1 | Oil phase starting pressure gradient under different water saturations.

Core number	Length (cm)	Perm-plug method (mD)	Water saturation (%)	Starting pressure gradient ($MPa \cdot m^{-1}$)
B1	5.089	0.566	58.3	0.1595
B2	4.926	0.022	69.6	1.5875
B3	5.553	0.121	63.7	1.2100
B4	5.628	0.343	61.5	0.1685
B5	4.831	0.627	56.9	0.0926
B6	5.436	0.737	51.6	0.0890
B7	5.211	0.601	55.2	0.1179
B8	4.933	0.191	62.8	0.6250

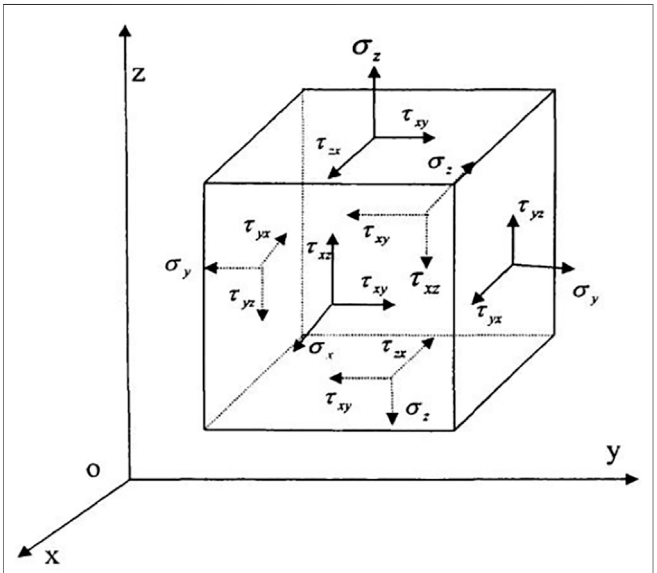

FIGURE 5 | Schematic diagram of forces acting on a rock element (Dai., 2006). Notes: σ_x, σ_y, σ_z are normal stresses in x, y, and z directions; τ_{xy} and τ_{yx} are shear stresses on x and y planes; τ_{xz}, τ_{zx} are shear stresses on x and z planes; τ_{yz} and τ_{zy} are shear stresses on y and z planes.

$$\left\{\sigma_{eff}\right\} = f\left(\{\varepsilon\}\right) \tag{2}$$

Where $\{\sigma_{eff}\}$ is the stress vector of the rock skeleton, m; $\{\varepsilon\}$ is the strain vector of the rock skeleton, m.

For isotropic elastic media, the generalized Hooke's law satisfies:

$$\begin{cases} \varepsilon_x = \dfrac{\left(\sigma_{eff}\right)_x}{E_h} - \mu_{hh}\dfrac{\left(\sigma_{eff}\right)_y}{E_h} - \mu_{vh}\dfrac{\left(\sigma_{eff}\right)_z}{E_v} \\ \varepsilon_y = \dfrac{\left(\sigma_{eff}\right)_y}{E_h} - \mu_{hh}\dfrac{\left(\sigma_{eff}\right)_x}{E_h} - \mu_{vh}\dfrac{\left(\sigma_{eff}\right)_z}{E_v} \\ \varepsilon_z = \dfrac{\left(\sigma_{eff}\right)_z}{E_v} - \mu_{hv}\dfrac{\left(\sigma_{eff}\right)_x}{E_h} - \mu_{vh}\dfrac{\left(\sigma_{eff}\right)_y}{E_h} \\ \gamma_{xy} = \dfrac{\left(\tau_{eff}\right)_{xy}}{G_h} \quad \gamma_{yz} = \dfrac{\left(\tau_{eff}\right)_{yz}}{G_v} \quad \gamma_{zx} = \dfrac{\left(\tau_{eff}\right)_{zx}}{G_h} \end{cases} \tag{3}$$

Where E_h and E_v are the elastic moduli of the rock skeleton in the horizontal and vertical directions, respectively, GPa; G_h and G_v are the horizontal and vertical shear moduli of the rock skeleton, GPa, respectively; μ_{hh} and μ_{hv} are the Poisson's ratios in the horizontal and vertical directions, respectively; μ_{hv} is the Poisson's ratio of the horizontal deformation caused by the stress in the vertical direction; τ_{eff} is the effective shear stress, MPa.

Equation 3 regards the rock skeleton as a plane isotropic medium (homogeneous rock), with $E_h = E_v = E$, $\mu_{hv} = \mu_{hh} = \mu_{vh} = \mu$, $G_h = G_v = G$.

Then the physical equation is:

$$\begin{cases} \varepsilon_x = \dfrac{1}{E}\left[\left(\sigma_{eff}\right)_x - \mu\left(\left(\sigma_{eff}\right)_y + \left(\sigma_{eff}\right)_z\right)\right] \\ \varepsilon_y = \dfrac{1}{E}\left[\left(\sigma_{eff}\right)_y - \mu\left(\left(\sigma_{eff}\right)_x + \left(\sigma_{eff}\right)_z\right)\right] \\ \varepsilon_z = \dfrac{1}{E}\left[\left(\sigma_{eff}\right)_z - \mu\left(\left(\sigma_{eff}\right)_x + \left(\sigma_{eff}\right)_y\right)\right] \\ \gamma_{xy} = \dfrac{\left(\tau_{eff}\right)_{xy}}{G} \quad \gamma_{yz} = \dfrac{\left(\tau_{eff}\right)_{yz}}{G} \quad \gamma_{zx} = \dfrac{\left(\tau_{eff}\right)_{zx}}{G} \end{cases} \tag{4}$$

This physical equation can be written in matrix form:

$$\left\{\sigma_{eff}\right\} = [D_e]\{\varepsilon\} \tag{5}$$

Where $[D_e]$ is the elastic matrix:

$$[D_e] = \begin{bmatrix} d_1 & 0 & 0 & 0 & 0 & 0 \\ d_2 & d_1 & 0 & 0 & 0 & 0 \\ d_2 & d_2 & d_1 & 0 & 0 & 0 \\ 0 & 0 & 0 & d_3 & 0 & 0 \\ 0 & 0 & 0 & 0 & d_3 & 0 \\ 0 & 0 & 0 & 0 & 0 & d_3 \end{bmatrix} \tag{6}$$

Of which:

$$\begin{cases} d_1 = E_s = \dfrac{E(1-\mu)}{(1+\mu)(1-2\mu)} = \lambda + 2G \\ d_2 = \dfrac{\mu}{1-\mu}E_s = \dfrac{E(1-\mu)}{(1+\mu)(1-2\mu)} = \lambda \\ d_3 = G = \dfrac{E}{2(1+\mu)} \end{cases} \tag{7}$$

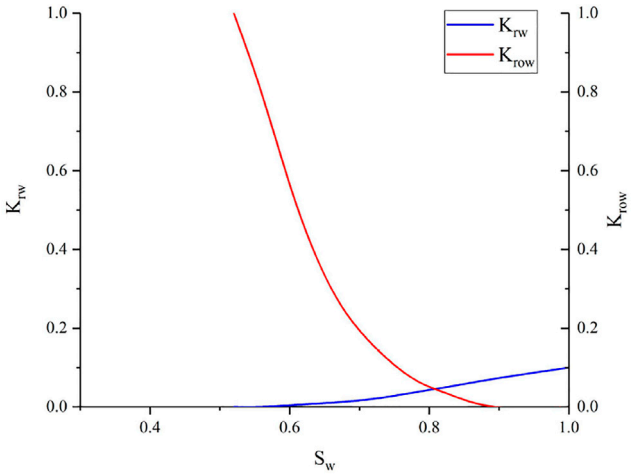

FIGURE 6 | Relative permeability curves of oil-water two-phase.

Where E, μ, G, E_s, and λ are the elastic modulus, Poisson's ratio, shear modulus, compressive modulus and Lame constant of the homogeneous rock skeleton, respectively.

It can be seen from **Eq. 4** that in the development stage of low-permeability reservoirs, the effective stress on the formation rock in the x, y, and z directions remains unchanged when the same pressure drop is maintained. With the increase of rock elastic modulus E and Poisson's ratio μ, the displacement vectors of rock unit body in x, y and z directions decrease.

In the stress-sensitive simulation based on tNavigator Software, it is necessary to consider the influence of the stress-sensitive effect on the oil well productivity and the swept range of the water injection well. By introducing the elastic modulus E and Poisson's ratio μ of the rock, the one-way coupling method is used to couple the stress sensitivity and geomechanics to equivalently characterize the rock displacement vectors. This method can be used to analyze the production variation law of different lithologic reservoirs, and visually present the variation of rock displacement vectors on each grid.

3 RESULTS

3.1 Parameter Settings

The numerical simulation model is established with reference to the reservoir and fluid properties and development status of the Chang 6 Member of Block B in the study area. The basic parameters of the mechanism model are as follows:

(1) Grid number, NX = NY = 90, NZ = 5;
(2) Geometric size of the model, 900 m × 900 m × 50 m;
(3) Permeability, K_x = K_y = 0.5 mD, K_z = 0.05 mD;
(4) Porosity: 12%;
(5) Top depth: 1,950 m;
(6) Formation pressure: 28.9 MPa;
(7) Edge and bottom water are not considered;
(8) The oil-water relative permeability curves under different oil-water viscosity ratios were measured by the steady-state method. The relative permeability curves of oil and water are shown in **Figure 6**. The Chang 6 reservoir in the study area is a high water-saturated reservoir with low porosity and low permeability. The larger the reservoir porosity, the better the petrophysical properties and the higher the water saturation. In addition, the Chang 6 Member reservoir has strong heterogeneity, complex pore structures, and large two-phase seepage disturbance. Due to the large capillary resistance and weak seepage capacity, the irreducible water saturation of the Chang 6 reservoir is high.

3.2 Equivalent Method Validation

The seepage velocity expression of the quasi-start pressure gradient model is:

$$\begin{cases} V = 0 & \frac{\Delta P}{L} < c \\ V = \frac{K}{\mu}\left(\frac{\Delta P}{L} - c\right) & \frac{\Delta P}{L} \geq c \end{cases} \tag{8}$$

Where v is the seepage velocity, m/s; K is the reservoir matrix permeability, mD; μ is the crude oil viscosity, mPa s; c is the pseudo starting pressure gradient, MPa/m; Δp is the pressure difference between the two ends of the grid at distance L, MPa.

According to the theory of limit well spacing, Douglas et al. (1983) used the pressure gradient out of the maximum flowable distance should be greater than the starting pressure gradient. The pressure difference Δp satisfies:

$$L < \frac{\Delta p}{c} \tag{9}$$

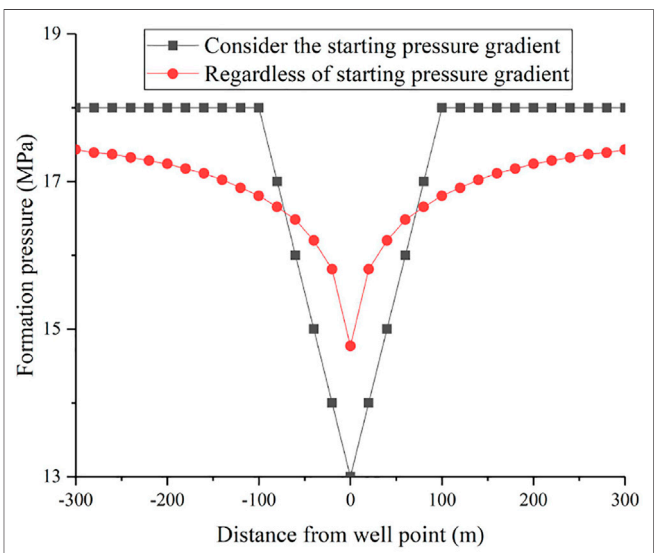

FIGURE 7 | Variation characteristics of formation pressure around wellbore.

TABLE 2 | Test results of mineral composition and rock mechanical parameters.

Number	Burial depth (m)	Horizon	Mineral content (%)				Elastic modulus (GPa)	Poisson's ratio
			Quartz	Orthoclase	Pagioclase	Eruptive rock		
B1	1929.5	Chang 6	33.00	15.00	15.00	12.33	28.42	0.296
B2	1937.1	Chang 6	35.00	19.50	16.75	11.25	30.80	0.289
B3	1876.4	Chang 6	30.00	20.00	20.00	15.00	23.84	0.318
B4	1900.0	Chang 6	36.50	17.00	20.00	9.00	25.93	0.294
B5	1872.6	Chang 6	35.33	15.33	15.00	7.00	24.07	0.299
B6	1807.5	Chang 6	34.83	15.67	14.17	3.33	20.75	0.292
B7	1830.2	Chang 6	37.50	19.50	18.00	2.50	25.46	0.285
B8	1816.4	Chang 6	39.00	25.00	20.00	7.00	21.29	0.308

For a reservoir with a matrix permeability of 1 mD, when the production pressure difference is 4.5 MPa, the maximum production range when the starting pressure gradient is considered is 100 m. Furthermore, the limit production range predicted by the model set by this method is also 100 m. Thus, the accuracy of this method is verified. When the starting pressure gradient is not considered, the production range predicted by the model is more than 300 m, which has a large error (**Figure 7**).

Rock mechanics parameter experiment: a solid cylindrical specimen with the same height and diameter is subjected to a relative compressive linear load in the diameter direction to fracture along the plane controlled by the load. Then, the tensile strength of the rock is obtained according to the elastic theory. In this study, a total of 8 standard cores were used to verify the effect of rock brittleness on reservoir stress sensitivity. Through rock mechanics experiments, the Poisson's ratio and mineral composition of eight groups of samples were measured (**Table 2**).

It can be seen from **Table 2** that the elastic moduli of the rock samples are distributed in the range of 20.75–30.80 GPa, and the Poisson's ratio is distributed in the range of 0.285–0.318. The internal components of the tight sandstone in the target layer are mainly quartz, potassium feldspar, plagioclase and eruptive rocks.

The strain characteristics of matrix reservoirs can be analyzed according to the stress-deformation method of the fluid-solid dual medium model (Wu et al., 2014). Then, the changes of permeability and porosity caused by rock mass deformation are:

$$\begin{cases} \varphi_m = \varphi_{mi}\left(\sigma_M^{'}\right) \\ k_m = k_{mi}\left(\sigma_M^{'}\right) \end{cases} \tag{10}$$

Among them, φ_{mi} and k_{mi} are the original porosity and permeability, respectively.

The mean effective stress is:

$$\sigma_M^{'} = \sigma_x + \sigma_y + \sigma_z \big/ 3 \tag{11}$$

The existence of stress-sensitive effect makes oil well production decrease (Liu., 2014). The formula for calculating the oil recovery index considering the stress-sensitive effect is:

$$J_o = \frac{2\pi h k_{mi}\left(\sigma_M^{'}\right)}{\mu B_o In\left(\frac{r_e}{r_w}\right)} \tag{12}$$

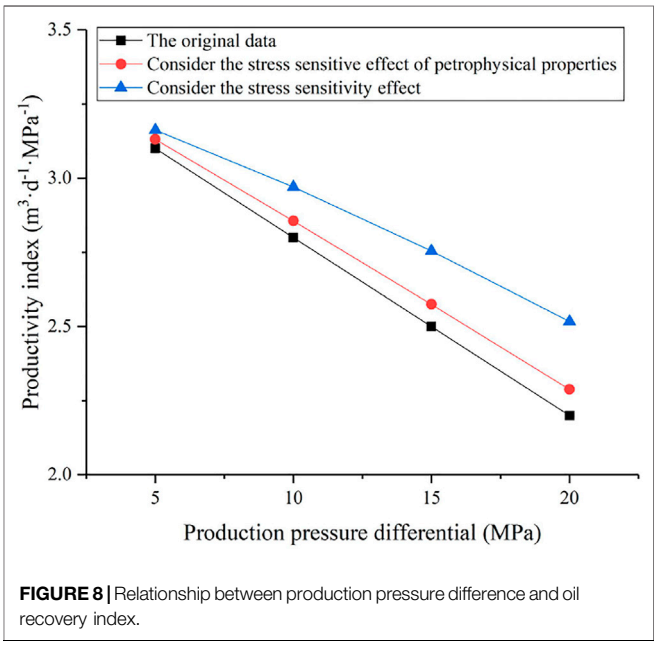

FIGURE 8 | Relationship between production pressure difference and oil recovery index.

Among them, J_o is the oil production index, $m^3\ day^{-1}\ MPa^{-1}$; h is the effective reservoir thickness, m; B_o is the coefficient of crude oil formation volume; r_e is the oil supply radius, m; r_w is the wellbore radius, m; k_{mi} is the original permeability, mD.

The relationship between the production pressure difference and the change in permeability is:

$$k_m = k_{mi} e^{-\alpha\left(p_e - p_w\right)} \tag{13}$$

Where α is the stress sensitivity coefficient.

Affected by stress sensitivity, the reservoir matrix undergoes elastic deformation as the production pressure difference increases. Compared with the conventional stress-sensitive

TABLE 3 | Young's modulus and Poisson's ratio of different types of sandstones.

Sandstone type	Elastic modulus (E/GPa)	Poisson's ratio μ
Fine sandstone	27.900–47.622	0.15–0.52
Medium sandstone	24.056–38.296	0.10–0.22
Coarse sandstone	16.642–40.306	0.10–0.45

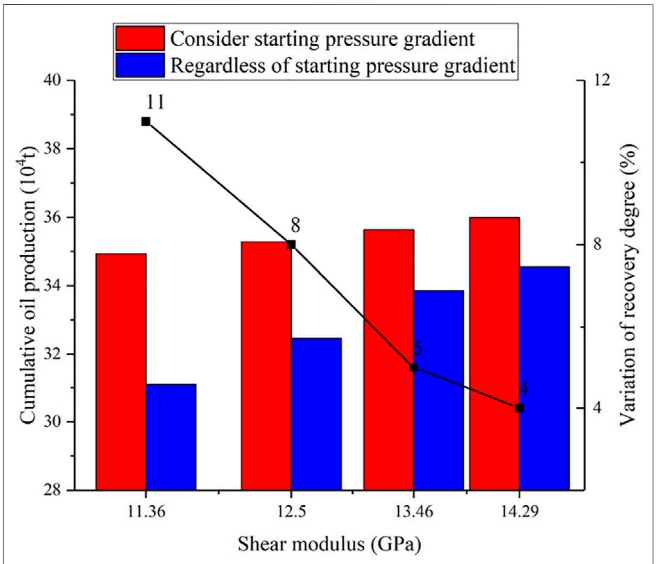

FIGURE 9 | Cumulative oil production under different shear modulus conditions.

equivalent characterization method, it can be seen that the oil recovery index obtained by the method used in this study is closer to the actual data, and the model accuracy is significantly improved (**Figure 8**). It is also known from **Eqs 10** and **13** that when the permeability change value is constant, the production pressure difference is negatively correlated with the average effective stress.

4 DISCUSSION

In this study, we established two numerical simulation models: a homogeneous and a heterogeneous permeability model, and they both adopted a diamond-shaped inverse nine-spot well pattern. The influence of stress-sensitive effects on the productivity of ultra-low permeability reservoirs has been systematically studied, taking into account the starting pressure gradient. The rock is sensitive to stress, and the larger the elastic modulus value E, the smaller the deformation of the rock under stress. Poisson's ratio expresses the ratio of the strain ε_1 in the vertical direction to that in the loading direction. Within the elastic deformation of the rock, μ is a coefficient that measures the lateral strain capacity of the rock.

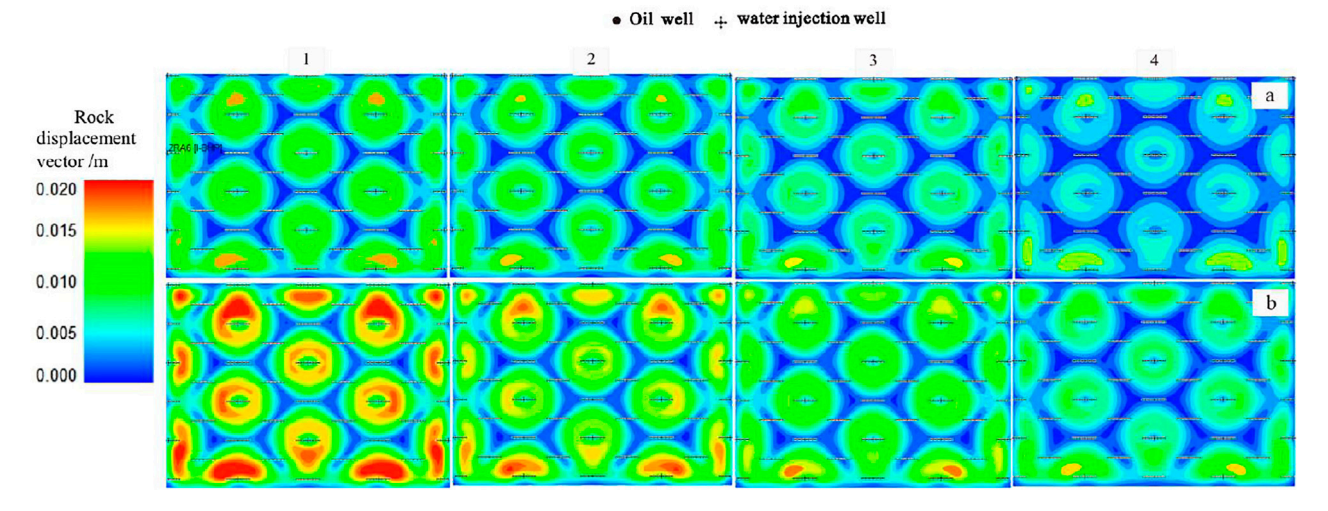

FIGURE 10 | Rock displacement vector diagrams based on different shear modulous values considering starting pressure gradient: **(A)** Pressure gradient is not considered, **(B)** Starting pressure gradient is considered.

TABLE 4 | The results of mechanical parameters in the Chang 6 reservoir.

Number	Shear modulus (GPa)	Elastic modulus (GPa)	Poisson's ratio μ
1	11.36	2.5	0.10
2	12.50	3.0	0.20
3	13.46	3.5	0.30
4	14.29	4.0	0.40

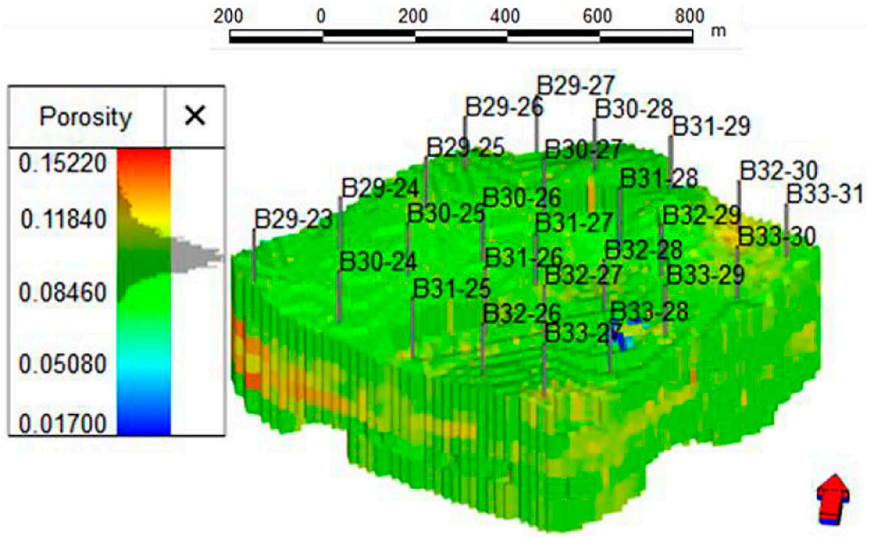

FIGURE 11 | Schematic diagram of geological model of the target layer in the study area.

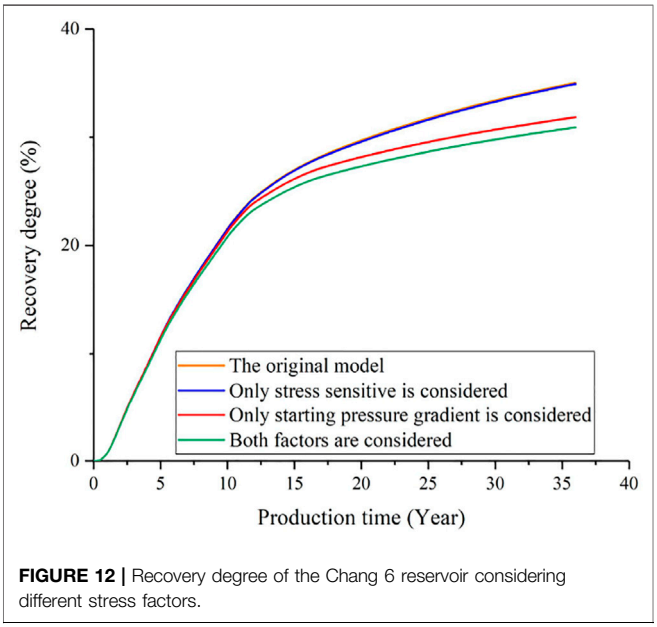

FIGURE 12 | Recovery degree of the Chang 6 reservoir considering different stress factors.

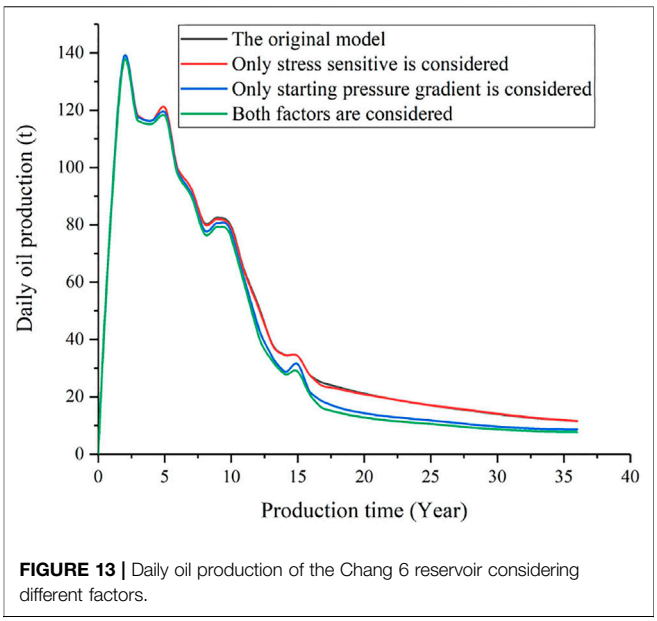

FIGURE 13 | Daily oil production of the Chang 6 reservoir considering different factors.

Therefore, under the same elastic modulus of rock, the larger the Poisson's ratio, the weaker the stress-sensitive effect of the rock.

4.1 Effects of Stress Sensitivity on Reservoir Development

In this study, a shear modulus $G = E/[2(1+\mu)]$ was introduced. The value ranges of elastic modulus and Poisson's ratio of different types of sandstone are shown in **Table 3**. The shear modulus is used to characterize the stiffness of the rock in the numerical model. The larger the shear modulus value, the smaller the deformation of the rock during compression or tension. The results of rock mechanics parameters are shown in **Table 4**.

Under different shear modulus conditions (**Figure 9**), the reservoir stress sensitivity is weaker when the starting pressure gradient is not considered. Affected by the starting pressure gradient, the reservoir stress sensitivity is strong, and the production range of the oil well is reduced. In addition, the formation pressure changes sharply during constant liquid production, the rock displacement vector increases, the matrix permeability decreases, and the difference in cumulative oil production increases as well.

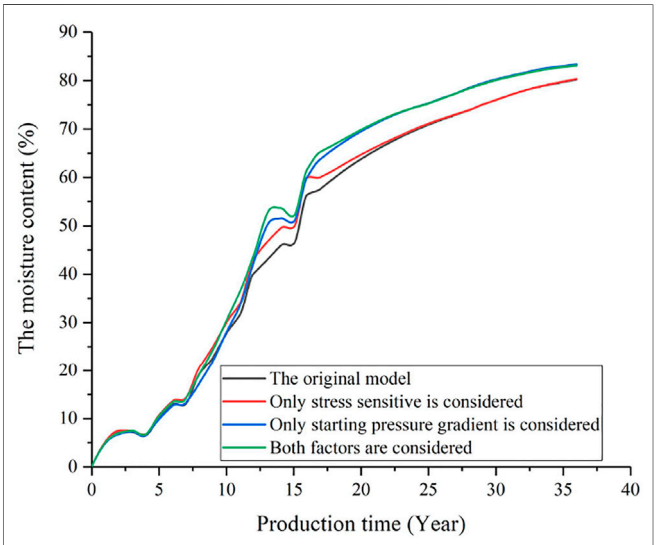

FIGURE 14 | Water cut curves of the Chang 6 reservoir considering different factors.

Figure 10 different degrees of starting pressure gradient exist in the development process of ultra-low permeability oil and gas fields. Therefore, the increase of rock shear modulus G is accompanied by the change of bottom hole pressure. The rock displacement vector and variation range near the wellbore of the oil wells are reduced, which has a strong impact on the productivity of ultra-low permeability reservoirs with starting pressure gradients. It can be seen from **Figure 9** that when the rock shear modulus is 14.29 GPa, the cumulative oil production decreases by 4.1%; when the rock shear modulus is 11.36 GPa, the cumulative oil production decreases by 11.2%.

4.2 Case Analysis

The main producing layer of the Chang 6 reservoir in the study area is Chang 6_1, the reservoir is buried at a depth of 1,950 m, the average reservoir thickness is 28.2 m, and the original formation pressure is 28.9 MPa. In addition, the Chang 6 reservoir has an average porosity of 11.1%, an average permeability of 0.59 mD, and a crude oil density of 0.8225 g/cm^3. The model contains four layers from top to bottom: chang 6_1^1 (model layer 1), chang 6_1^2 (model layer 2), chang 6_2 (model layer 3–4), chang 6_3 (model layer 5–6). **Figure 11** is the planar distribution of the three-dimensional porosity of the target layer.

Figures 12–14 show the comparisons of daily oil production, water cut and recovery degree of the non-Darcy seepage model equivalently characterized by the method in this study under the condition of diamond reverse nine-spot well pattern. When the two factors of stress sensitivity and starting pressure gradient are not considered, the recovery degree of the target layer is 35.0%. When only stress sensitivity is considered, the pressure of the well group remains relatively stable in the early stage of development; however, as the development period increases, the pressure drop of the well group begins to become significant, which in turn leads to a decrease in reservoir permeability. Furthermore, the daily oil production of the oil well gradually decreased, and the recovery degree was 34.8%. Usually, it is affected by differences in oil and water viscosity, when only the starting pressure gradient is considered, it is difficult for crude oil to break through its own seepage resistance. However, the impact of the starting pressure gradient on the formation water is relatively small, and the water cut rises rapidly, resulting in water channeling. At this time, the production capacity of oil wells declined, and the recovery rate of daily oil production was only 31.9%. When both factors are considered, the reservoir stress sensitivity effect is strong due to the influence of the starting pressure gradient. In addition, the rock displacement vectors in the plane increase, and the permeability decreases greatly. At this time, the daily oil production of the oil well decreased significantly, and the recovery degree was 30.9%. Therefore, comparing the results of different factors, when only the starting pressure gradient is considered, the recovery degree of the target layer decreases by 8.8%; when only the stress-sensitive effect is considered, the recovery degree of the target layer decreases by 0.5%; when

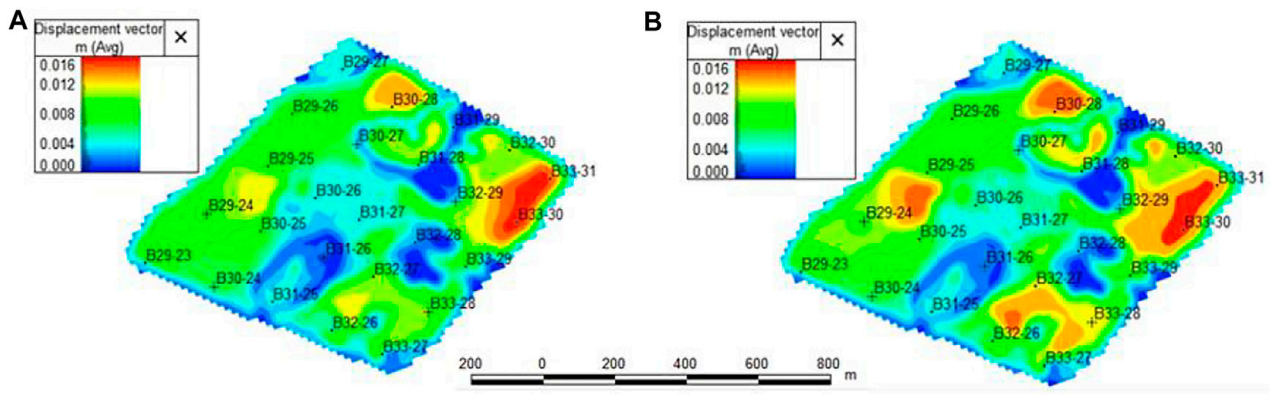

FIGURE 15 | Plane distribution of displacement vector of the target layer in the study area: **(A)** Only stress sensitive is considered, **(B)** Both starting pressure gradients and stress-sensitive effects are considered.

both factors are considered, the recovery degree of the target layer decreases by 11.7%.

Comparing **Figures 15A,B**, it can be seen that when both factors are considered, due to the influence of the starting pressure gradient, the crude oil in the reservoir cannot break through its own seepage resistance, and the pressure variation range near the wellbore of some oil wells expands. Furthermore, it leads to an increase in the swept range of the variation of the reservoir rock displacement vector, and the target layer exhibits relatively strong stress sensitivity.

Based on this study, it can be seen that in the development process of ultra-low permeability sandstone reservoirs, the simulation results have higher accuracy when the stress-sensitive effects considering rock properties and starting pressure gradients are introduced. However, in low-permeability sandstone reservoirs, the influence of natural fractures is usually taken into account, which is a current research difficulty in reservoir numerical simulation. The method in this study can also be applied to the numerical simulation study of ultra-low permeability sandstone reservoirs considering natural fractures.

5 CONCLUSION

(1) For ultra-low permeability sandstone reservoirs, the elastic modulus and Poisson's ratio of rock are used to equivalently characterize the stress-sensitive effect in this study, and a new method for equivalently characterizing stress-sensitivity in numerical simulation is proposed. Through verification, the calculation results of this model are consistent with the actual situation.

(2) When the starting pressure gradient is considered, with the increase of the shear modulus of the rock, the deformation resistance of the rock increases, the reservoir stress sensitivity decreases, and the cumulative oil production increases. Considering the starting pressure gradient, when the rock shear modulus is 14.29 GPa, the cumulative oil production decreases by 4.1%; when the rock shear modulus is 11.36 GPa, the cumulative oil production decreases by 11.2%.

(3) A numerical simulation was conducted with Block B in the Zhouwan-Wugucheng area as an example. The model can accurately predict the reservoir stress sensitivity based on the starting pressure gradient. When both the starting pressure gradient and stress sensitivity are considered, the crude oil recovery degree of the target layer decreases by 11.7%; when only the starting pressure gradient is considered, the crude oil recovery degree decreases by 8.8%; and when only the stress sensitivity is considered, the crude oil recovery degree decreases 0.5%.

DATA AVAILABILITY STATEMENT

The original contributions presented in the study are included in the article/Supplementary Material, further inquiries can be directed to the corresponding authors.

AUTHOR CONTRIBUTIONS

XL is responsible for the idea and writing of this paper and XW, ZW, TH, XQ, FY and CT are responsible for the data interpretation.

REFERENCES

Cai, J., W., Wei, X., Hu, R, Liu., and Wang, J. (2017). Fractal Characterization of Dynamic Fracture Network Extension in Porous media. *Fractals* 25 (02). 1750023. doi:10.1142/s0218348x17500232

Chen, G. B., Li, T., Yang, L., Zhang, G. H., Li, J. W., and Dong, H. J. (2021). Mechanical Properties and Failure Mechanism of Combined Bodies with Different Coal-Rock Ratios and Combinations. *J. Mining Strata Control. Eng.* 3 (2), 023522. doi:10.13532/j.jmsce.cn10-1638/td.20210108.001

Chen, Z., and Ewing, R. (1999). Mathematical Analysis for Reservoir Models. *SIAM J. Math. Anal.* 30 (2), 431–453. doi:10.1137/s0036141097319152

Chen, Z., Liao, X., Yu, W., and Sepehrnoori, K. (2019). Pressure-Transient Behaviors of Wells in Fractured Reservoirs with Natural- and Hydraulic-Fracture Networks. *SPE J.* 24 (01), 375–394. doi:10.2118/194013-pa

Dai, P. (2006). *Experiment and Numerical Simulation of Low Permeability Stress Sensitive Reservoir*. Chengdu. Southwest Petroleum University, 70–73.

Dong, L. F., Yue, X. A., Xu, X., Su, Q., and Song, W. X. (2015). Experimental Study on Stress Sensitivity of Reservoirs with Different Permeability. *Geol. Sci. Technol. Inf.* 34 (06), 155–158. doi:10.1021/acsomega.1c00259

Douglas, J. J., Jr., Ewing, R. E., and Wheeler, M. F. (1983). The Approximation of the Pressure by a Mixed Method in the Simulation of Miscible Displacement. *RAIRO. Anal. Numér.* 17 (1), 17–33. doi:10.1051/m2an/1983170100171

Ewing, R. E., and Wheeler, M. F. (1980). Galerkin Methods for Miscible Displacement Problems in Porous media. *SIAM J. Numer. Anal.* 17 (3), 351–365. doi:10.1137/0717029

Feng, Y. L., Liu, Y. T., and Ding, Z. P. (2018). Deformation Characteristics and Dynamic Permeability Model of a Group of Parallel Fractures. *Fault-block oil & gas field* 25 (6), 736–741. doi:10.6056/dkyqt201806010

Francesconi, A. (1995). Sand Body Geometry and Permeability Areal Distribution in Fluvial Sandstones Reservoir. *AAPG Bull.* 79 (8), 199512. doi:10.1306/8d2b273b-171e-11d7-8645000102c1865d

Gao, F. Q. (2021). Influence of Hydraulic Fracturing of strong Roof on Mining-Induced Stress Insight from Numerical Simulation. *J. Mining Strata Control. Eng.* 3 (2), 023032. doi:10.13532/j.jmsce.cn10-1638/td.20210329.001

Geng, Y., Tang, D., Xu, H., Tao, S., Tang, S., Ma, L., et al. (20172017). Experimental Study on Permeability Stress Sensitivity of Reconstituted Granular Coal with Different Lithotypes. *Fuel* 202, 12–22. doi:10.1016/j.fuel.2017.03.093

Guo, L. L., Zhou, D. W., Zhang, D. M., and Zhou, B. H. (2021). Deformation and Failure of Surrounding Rock of a Roadway Subjected to Mining-Induced Stresses. *J. Mining Strata Control. Eng.* 3 (2), 023038. doi:10.13532/j.jmsce.cn10-1638/td.20200727.001

Hansbo, S. (1990). Consolidation of clay, Eith Special Reference to Influence of Vertical Sanddrains. Swedish Geotech. *Inst. Proc.* 18, 41.

He, X., Zhang, P., He, G., Gao, Y., Liu, M., Zhang, Y., et al. (2020). Evaluation of Sweet Spots and Horizontal-Well-Design Technology for Shale Gas in the basin-margin Transition Zone of southeastern Chongqing, SW China. *Energ. Geosci.*, 1(3–4), 134–146. doi:10.1016/j.engeos.2020.06.004

Hong, D., Cao, J., Wu, T., Dang, S., Hu, W., and Yao, S., (2020). Authigenic clay Minerals and Calcite Dissolution Influence Reservoir Quality in Tight

Sandstones: Insights from the central Junggar Basin, NW China. *Energ. Geosci.*, 1(1–2), 8–19. doi:10.1016/j.engeos.2020.03.001

Hower, J. C., and Groppo, J. G., (2021). Rare Earth-Bearing Particles in Fly Ash Carbons: Examples from the Combustion of Eastern Kentucky Coals, *Energ. Geosci.*, 2(2), 90–98. doi:10.1016/j.engeos.2020.09.003

Hu, Z. M., Ba, Z. B., and Xiong, W. (2006). Analysis of Micro-pore Structure in Low Permeability Reservoirs. *J. A Pet. Inst.* 30 (3), 51–53. doi:10.3969/j.issn.2095-4107.2006.03.016

Jiao, C. Y., He, S. L., and Xie, Q. (2011). An Experimental Study on Stress-dependent Sensitivity of Ultra-low Permeability sandstone Reservoirs. *Acta Pet. Sin* 32 (3), 489–494. doi:10.7623/syxb201103018

Kuuskraa, V. A. (1996). Advances Benefit Tight Gas Sands Development. *Oil Gas* 94 (15), 6–7.

Lei, Q., Xiong, W., Yuang, J., Cui, Y., and Wu, Y. S. (2007). *Analysis of Stress Sensitivity and its Influence on Oil Production from Tight Reservoirs*. Lexington: Eastern Regional Meeting, 34–36.

Li, L., and Li, S. J. (2021). Evolution Rule of Overlying Strata Structure in Repeat Mining of Shallow Close Distance Seams Based on Schwarz Alternating Procedure. Journal of Mining and Strata Control. *Engineering* 3 (2), 023515. doi:10.13532/j.jmsce.cn10-1638/td.20210225.001

Li, Y., Zhou, D.-H., Wang, W.-H., Jiang, T.-X., and Xue, Z.-J., (2020). Development of Unconventional Gas and Technologies Adopted in China, *Energ. Geosci.*, 1(1–2), 55–68. doi:10.1016/j.engeos.2020.04.004

Liu, J. J., Liu, X. G., and Zeng, L. F. (2001). Dynamic Simulation of Permeability Change in Low Permeability Fractured Reservoir. *J. liaoning Tech. Univ. (natural science)* 20 (4), 543–545. doi:10.3969/j.issn.1008-0562.2001.04.058

Liu, S. D. (2014). Analysis of Productivity Factors Affecting Low Permeability Stress Sensitive Reservoir. *Sci. Tech. Enterprise* (10), 287–288. doi:10.13751/j.cnki.kjyqy.2014.10.269

Lu, J. F., and Wang, D. (1999). Kemper. Intrinsic Permeability of clay as Affected Byclay-Water Interaction. *Soil Sci.* 88 (2), 83.

Lv, C. Y., Wang, J., and Sun, Z. G. (2002). An Experimental Study on Starting Pressure Gradient of Fluids Flow in Low Permeability Sandstone Porous Media. *Pet. Exploration Dev.* 29 (2), 86–89. doi:10.3321/j.issn:1000-0747.2002.02.023

Mahmud, H. B., Bin Muhammad Hisham, M. H., Mahmud, W. M., Leong, V. H., and Shafiq, M. U., (2020). Petrophysical Interpretations of Subsurface Stratigraphic Correlations, Baram Delta, Sarawak, Malaysia. *Energ. Geosci.*, 1, (3–4), 100–114. doi:10.1016/j.engeos.2020.04.005

Maksim, E. (2019). *Numerical Simulation of Multiphase Non-darcy Flows Generalized Approach*. Calgary, Alberta, Canada: SPE, 199769. doi:10.2118/199769-STU

Meng, Z., and Li, G. (2013). Experimental Research on the Permeability of High-Rank Coal under a Varying Stress and its Influencing Factors. *Eng. Geology.* 162, 108–117. doi:10.1016/j.enggeo.2013.04.013

Mitchell, J. K. (1967). Younger. Abnormalities in Hydraulic Flow Throughfine-Grained Soils. *ASTM Spech* 417, 106–141.

Mohammed, B., Richard, H. W., Shettima, B., and Philip, S., (2021). Diagenesis and its Controls on Reservoir Quality of the Tambar Oil Field, Norwegian North Sea. *Energ. Geosci.*, 2(1), 10–31. doi:10.1016/j.engeos.2020.07.002

Qian, G. B., Jiang, X. H., and Zhang, H. M. (2021). *Numerical Simulation Study of Water Injection Development in an Extra-low Permeability Fractured Reservoir*. Beijing, China: XG Oilfield, SPE, 64794. doi:10.2118/64794-MS

Ren, J. W., Wang, X. J., and Zhang, X. M. (2020). Refracturing and Fracture Parameters Optimization Simulation for Horizontal Well in Daqing Tight Oil Reservoir. *Fault Z. Block Oil Gas Field* 27 (5), 638–642. doi:10.6056/dkyqt202005018

Ruan, M., and Wang, L. G. (2002). Low-permeability Oilfield Development and Pressure-Sensitivity Effect. *Acta Pet. Sin* 23 (3), 73–76. doi:10.7623/syxb200203016

Shang, G. H. (2004). *Study on Nonlinear Seepage Law of Low Permeability*. Beijing: Institute of Seepage Fluid Mechanics, Chinese Academy of Sciences, 23–26.

Shi, L. J., Chen, J. G., and Jia, Z. Q. (1999). Low Non-darcy Percolation Characteristics of Single Phase Fluids in A Eastern Low Permeability Reservoirs. *J. A Pet. Inst.* 23 (2), 82. doi:10.3969/j.issn.2095-4107.1999.02.027

Song, C. T. (2012). Numerical Reservoir Simulation Considering Threshold Pressure Gradient and Stress Sensitive Phenomenon. *Sci. Technol. Eng.* 25 (12), 6319–6327. doi:10.3969/j.issn.1671-1815.2012.25.014

Tian, Y. (2014). *Experimental Study on Stress Sensitivity of Naturally Fractured Reservoirs*. Amsterdam: SPE Annual Technical Conference and Exhibition, 23–25.

Todd, M. R., O'Dell, P. M., and Hirasaki, G. J. (2016). Methods for Increased Accuracy in Numerical Reservoir Simulators. *Soc. Pet. Eng.* 3516 (6), 515–530.

Von E, W., and Tunn, W. L. M. (1995). The Flow of Fluids through Sandstones. *Stategeol. Surv.* 194, 1–17.

Wang, G. C., Li, L. K., and Wang, P. (2012). A New Method for Equivalent Simulation of Starting Pressure in Numerical Simulation Software. *Sci. Technol. Eng.* 12 (1), 165–167. doi:10.3969/j.issn.1671-1815.2012.01.039

Wang, H., Shi, Z., Zhao, Q., Liu, D., Sun, S., Guo, W., et al. (2020). Stratigraphic Framework of the Wufeng-Longmaxi Shale in and Around the Sichuan Basin, China: Implications for Targeting Shale Gas. *Energ. Geosci.*, 1(3–4), 124–133. doi:10.1016/j.engeos.2020.05.006

Wang, L., Yang, X. Y., Gong, P. Z., Zhang, J. T., and Zhang, B. (2019). Study on Stress Sensitivity of Middle-Deep Reservoirs in Bohai Sea: A Case Study of Kenli A Oilfield. *Pet. Geology. Eng.* 35 (03), 50–54. doi:10.3969/j.issn.1673-8217.2021.03.010

Wang, S., Ji, T., Tan, X. H., Wang, L., and Zhang, S. H. (2016). Permeability Limits of Advanced Water Injection Technology in Low Permeability Reservoirs. SPE-182431-MS, Paper Presented at the Asia Pacific Oil & Gas Conference and Exhibition, Perth, Australia. October 2016. 25–27. doi:10.2118/182431-ms

Wang, X., Thauvin, F., and Mohanty, K. K. (1999). Non-Darcy Flow through Anisotropic Porous media. *Chem. Eng. Sci.* 54, 1859–1869. doi:10.1016/s0009-2509(99)00018-4

Wu, D., Ju, B., Wu, S., Brantson, E. T., Fu, Y., and Lei, Z. (2017). Investigation of Productivity Decline in Inter-salt Argillaceous Dolomite Reservoir Due to Formation Damage and Threshold Pressure Gradient: Laboratory, Mathematical Modeling and Application. *Energy Exploration & Exploitation* 35 (1), 33–53. doi:10.1177/0144598716684308

Wu, H. Q., Peng, X. L., and Zhu, S. Y. (2021). Economic Decision of Shale Reservoir Based on Numerical Simulation and Integration of Reservoir Development and Management. *Pet. Reservoir Eval. Dev.* 11 (3), 404–413. doi:10.13809/j.cnki.cn32-1825/te.2021.03.016

Wu, J. L., Liu, Y. T., and Luo, J. (2014). Numerical Simulation of Fluid-Structure Interaction in Fractured Stress-Sensitive Reservoir. *Chin. J. Comput. Phys.* 31 (04), 455–464. doi:10.3969/j.issn.1001-246X.2014.04.011

Wu, Y. Z., Wang, Y., and Ma, D. (2020). Reservoir Simulation of Waterflooding under the Influence of Dynamic Fractures for Tight Oil Reservoir. *Sci. Tech. Eng.* 20 (27), 11059–11066. doi:10.3969/j.issn.1671-1815.2020.27.012

Xiong, W., Lei, Q., and Liu, X. G. (2009). Pseudo Threshold Pressure Gradient to Flow for Low-Permeability Reservoirs. *Pet. Explor* 36 (2), 232–235. doi:10.3321/j.issn:1000-0747.2009.02.015

Xu, J. C., Jiang, R. Z., Xie, L. S., Wang, R. H., and Shan, L. J. (2021). *Non-Darcy Flow Numerical Simulation for Low-Permeability Reservoirs SPE*, 154890.

Xu, T., Huang, H. L., Xiu, D. Y., Kang, H. J., and Sun, H. T. (2014). A New Method for Stress Sensitivity Evaluation of Low Permeability Reservoirs. *Spec. oil gas reservoirs* 21 (06), 126–129. doi:10.3969/j.issn.10066535.2014.06.031

Xue, F., Liu, X. X., and Wang, T. Z. (2021). Research on Anchoring Effect of Jointed Rock Mass Based on 3D Printing and Digital Speckle Technology. *J. Mining Strata Control. Eng.* 3 (2), 023013. doi:10.13532/j.jmsce.cn10-1638/td.20201020.001

Yang, X. F., Lei, Q. H., and Wang, R. F. (2021). Comparative Analysis of Start-Up Pressure Gradient of Tight Oil Reservoir in Ordos Basin. *Chin. J. Geophys.* 36 (1), 310–317. doi:10.6038/pg2021DD0412

Yang, Z. M., Yu, R. Z., and Su, Z. X. (2010). Numerical Simulation of Nonlinear Seepage Flow in Ultra-low Permeability Reservoir. *Pet. exploration Dev.* 37 (1), 94–98. doi:10.7623/syxb201102017

Zhao, K. K., Jiang, P. F., Feng, Y. J., Sun, X. D., Cheng, L. X., and Zheng, J. W. (2021). Investigation of the Characteristics of Hydraulic Fracture Initiation by

Using Maximum Tangential Stress Criterion. *J. Mining Strata Control. Eng.* 3 (2), 023520. doi:10.13532/j.jmsce.cn10-1638/td.20201217.001

Zheng, H., Zhang, J., and Qi, Y., (2020). Geology and Geomechanics of Hydraulic Fracturing in the Marcellus Shale Gas Play and Their Potential Applications to the Fuling Shale Gas Development. *Energ. Geosci.* 1(1–2), 36–46. doi:10.1016/j.engeos.2020.05.002

Conflict of Interest: XW, TH and FY were employed by the Geological Research Institute of No. 9 Oil Production Plant, Changqing Oilfield, CNPC.

The remaining authors declare that the research was conducted in the absence of any commercial or financial relationships that could be construed as a potential conflict of interest.

Publisher's Note: All claims expressed in this article are solely those of the authors and do not necessarily represent those of their affiliated organizations, or those of the publisher, the editors and the reviewers. Any product that may be evaluated in this article, or claim that may be made by its manufacturer, is not guaranteed or endorsed by the publisher.

frontiers | Frontiers in Earth Science

ORIGINAL RESEARCH
published: 27 April 2022
doi: 10.3389/feart.2022.911504

Comprehensive Evaluation of Rock Mechanical Properties and *in-situ* Stress in Tight Sandstone Oil Reservoirs

Mingliyang Cai[1], *Ming Li*[2]*, *Xiaoshuan Zhu*[3], *Hao Luo*[4] and *Qiang Zhang*[5]

[1]Chengdu University of Technology, College of Geophysics, Chengdu, China, [2]Chengdu University of Technology, College of Ecology and Environment, Chengdu, China, [3]County Planning and Natural Resources Bureau of Chongqing Dianjiang, Chongqing, China, [4]County Planning and Natural Resources Bureau of Chongqing Fuling, Chongqing, China, [5]Sichuan Nine One Five Engineering Survey and Design Limited Company, Meishan, China

Comprehensive research on reservoir rock mechanics and *in-situ* stress properties combined with petrophysical experiments, logging models and numerical simulation is an important means to achieve efficient development of tight sandstone oil reservoirs. In this study, a large number of rock mechanics and acoustic experiments, full-wave train array acoustic wave tests, hydraulic fracturing data and three-dimensional finite element simulations were used to study the rock mechanical properties and *in-situ* stress characteristics of continental tight oil reservoirs in the Yanchang Formation. The results show that under uniaxial conditions, the tight sandstone samples mainly suffer from tensional ruptures. With the increase of confining pressure, the tight sandstone samples undergo obvious shear ruptures. When the confining pressure is loaded to 35 MPa, a typical vertical shear fracture will be formed. The hydraulic fracturing calculation results show that the *in-situ* stress state of the target layer satisfies σ_v (vertical principal stress)>σ_H (maximum horizontal principal stress)>σ_h (minimum horizontal principal stress). Based on the results of rock mechanics and acoustic tests, we have constructed the dynamic and static mechanical parameter conversion models of tight oil reservoirs and the logging interpretation model of current *in-situ* stress. Furthermore, the finite element method is used to simulate the three-dimensional structural stress field of the target layer. The simulations show that the horizontal principal stress distribution in the work area is consistent with the applied environmental stress. The σ_H of the target layer is mainly distributed in 32–50 MPa, and the σ_h is mainly distributed in 20–34 MPa. Both σ_H and σ_h are relatively high in the southern uplift of the work area; among them, σ_H is usually greater than 44 MPa, and σ_h is usually greater than 24 MPa. The northern part of the study area developed several grooved areas with relatively low stress values. The regions with high stress values are often distributed in bands, which may be related to the compression caused by the deformation of the strata. For shear stress, left-handed and right-handed regions usually alternate with each other. However, the extent of the left-handed area in the southern uplift area is larger than that of the right-handed area, indicating that the tight oil reservoirs in the study area are mainly affected by left-handed activities.

Keywords: tight oil reservoir, triaxial experiment, rock mechanical properties, *in-situ* stress, numerical simulation

OPEN ACCESS

Edited by:
Shuai Yin,
Xi'an Shiyou University, China

Reviewed by:
Peng Wang,
Yibin University, China
Teng Zhao,
China University of Geosciences, China
Ying Tang,
Xi'an Shiyou University, China

***Correspondence:**
Ming Li
liming3775@126.com

Specialty section:
This article was submitted to Structural Geology and Tectonics, a section of the journal Frontiers in Earth Science

Received: *02 April 2022*
Accepted: *13 April 2022*
Published: *27 April 2022*

Citation:
Cai M, Li M, Zhu X, Luo H and Zhang Q (2022) Comprehensive Evaluation of Rock Mechanical Properties and in-situ Stress in Tight Sandstone Oil Reservoirs. Front. Earth Sci. 10:911504. doi: 10.3389/feart.2022.911504

INTRODUCTION

Continental tight oil reservoirs are developed in the Upper Triassic Yanchang Formation in the Ordos Basin. In the process of oil and gas exploitation, the determination of rock mechanics and *in-situ* stress properties of tight reservoirs can provide a basis for fracturing plan and production pressure difference design (Borgia et al., 1996; Hong et al., 2020; Lan et al., 2021). In addition, during drilling, rock mechanics and *in-situ* stress properties of tight reservoirs are also necessary for wellbore stability analysis (Baecher., 1983; Fan et al., 2014; Chen et al., 2021). At present, the methods to obtain rock mechanics parameters mainly include rock mechanics experiments and calculation using logging data (Li Y. et al., 2020; Cui and Radwan., 2021; Li., 2022). Rock mechanics experiment is the most basic and direct method to determine rock mechanics parameters (Li., 2022). However, the core experimental data is limited and discrete, which cannot reflect the changing trend of rock strength in the whole well section (Chitrala et al., 2013; Lommatzsch et al., 2015; Dong et al., 2018; Li Y. et al., 2020). Using logging data to predict rock strength parameters can lead to continuous stratigraphic rock strength profiles. However, the rock mechanical properties obtained from logging data are dynamic results, which need to be corrected to static values when applied to engineering constructions (Huang et al., 2019; Zuo et al., 2019; Li H. et al., 2020; Gao., 2021).

Continental tight sandstone reservoirs are characterized by low porosity, low permeability, strong heterogeneity and anisotropy. Therefore, the comprehensive study of reservoir rock mechanics and *in-situ* stress properties combined with experimental testing, logging model and 3D simulation method is an important means for efficient development of tight sandstone oil reservoirs (Gurocak et al., 2012; He et al., 2015; Mahmoodi et al., 2019; Yin and Wu., 2020). The petrophysical properties and fluid occurrence states of tight reservoirs are affected by rock mechanical properties and current *in-situ* stresses. The study area is located in the western part of the Ordos Basin. In the past, there were few studies on the rock mechanical properties and *in-situ* stress of the Yanchang Formation in this area, which restricted the efficient exploration and development of tight oil and gas in the Yanchang Formation. In this study, a large number of rock mechanics and acoustic experiments, full-wave train array acoustic wave tests, hydraulic fracturing data and three-dimensional finite element simulations were used to systematically study the rock mechanical properties and *in-situ* stress characteristics of continental tight oil reservoirs. This study has important reference value for efficient exploration and development of tight oil reservoirs.

GEOLOGICAL BACKGROUND

The study area is located in the western part of the Yishan Slope in the Ordos Basin (**Figure 1**). The stratigraphic structure in this area is a west-dipping monocline (Cui and Radwan., 2021). The Ordos inland lake basin was formed in the Late Triassic. The basement of the basin is composed of metamorphic rocks and crystalline rock series, which is a rigid basement of cratons. The tectonic movement is mainly manifested in the up-and-down movement inside the basin, the stratum is gentle, and the structure is simple. Some low-amplitude structures developed locally in the study area (Shuai et al., 2013). The direction of the present maximum principal stress in the study area is NE45° (Yin and Wu., 2020).

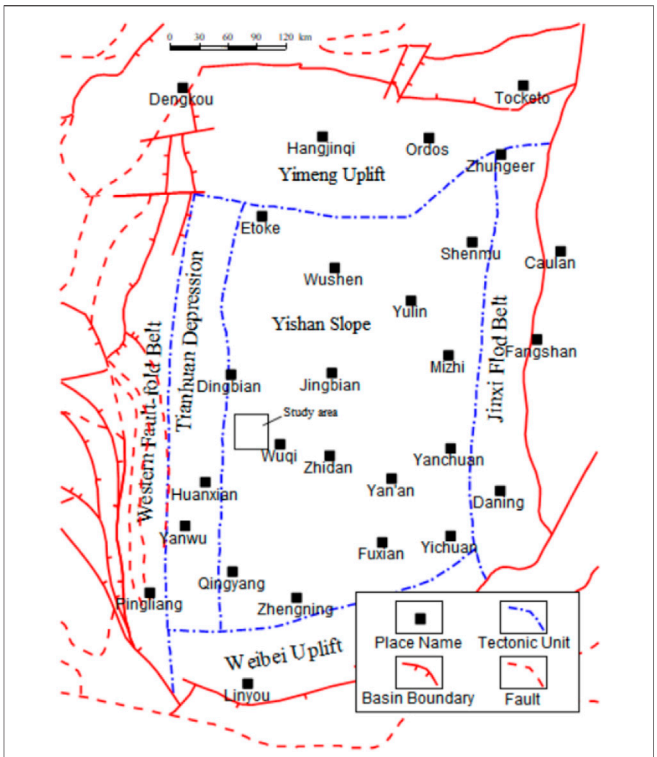

FIGURE 1 | The study area is located in the west part of the Yishan Slope in the Ordos Basin.

The target layers in the study area are the Chang 6, Chang 7 and Chang 8 Members (C6, C7 and C8) of the Yanchang Formation, which belong to the delta front sedimentary facies. The sedimentary microfacies developed in the target layer are mainly distributary channels and inter-channel bays. The grain size of the channel sand body is usually coarse, and the lithology is mainly fine sandstone, which gradually transitions upward to siltstone and silty mudstone; while the interdistributary bay is mainly composed of silty mudstone and mudstone.

MATERIALS AND METHODS

In this study, uniaxial and triaxial rock mechanics and acoustic experiments and full-wave train array acoustic wave tests of tight oil reservoirs were conducted. At the same time, the basic fracturing parameters and fracturing curve data of 38 groups of fracturing intervals were collected, and then the *in-situ* stresses of the work area were calculated using the fracturing data.

FIGURE 2 | Rock physics test system in rock mechanics experiment.

The instrument for triaxial rock mechanics and acoustic testing is a rock physics testing system (**Figure 2**). There are 10 groups of rock mechanics test samples, and each group have four samples. The sample size is a small cylinder with a diameter of 2.5 cm and a height of 5 cm. The test confining pressures are 0, 10, 20, and 35 MPa, respectively; the acoustic test results are the rock compressional and shear wave velocities under the condition of 35 MPa confining pressure, and the samples are all saturated with formation water. The design of confining pressure takes into account the burial depth and pore pressure of the formation. The average formation depth is 2,500 m, and the formation pressure is 1, so the effective pressure is 35 MPa. Moreover, the pressure sensor error of rock mechanics test is less than 1%, the displacement sensor range is between ±50 mm, and the displacement range resolution is 0.000 1 mm. The high test accuracy ensures the reliability of the experimental results.

The full-wave train array acoustic wave testing well interval is from the Chang 6 to Chang 8 Members. Full-wave train array acoustic logging can measure the full wave train information of the formation, with high signal-to-noise ratio, and can obtain high-quality formation shear wave data. At the same time, it overcomes the shortcomings of formation shear waves that cannot be measured by ordinary acoustic wave instruments in soft formations (mudstone formations) or formations with higher toughness. The test results are completed on the LEAD software platform, which uses the completion natural gamma ray as the reference curve for depth calibration.

Using fracturing construction data to determine *in-situ* stress is one of the most direct and reliable methods at present. When applying this method, the fracturing well interval with complete formation should be selected, that is, the fracturing well with the rupture point can be clearly identified in the fracturing operation curve. Finally, 38 groups of fracturing interval data in the study area were selected for *in-situ* stress calculation.

RESULTS

Reservoir Petrological Characteristics

The main components of terrigenous clasts in the target layers (C6, C7 and C8) of the Yanchang Formation are quartz and feldspar, while the content of lithic debris and other minerals is less. There is no significant difference in the components of terrigenous detritus among the three layers. In addition, there was no significant difference in feldspar content between C6, C7 and C8. Feldspar is composed of potassium feldspar and plagioclase, of which the plagioclase content is slightly higher than that of potassium feldspar. For debris component, the content of debris in the three layers is dominated by metamorphic rocks. The debris components of the three layers are mainly eruptive rocks and granites, and the content of eruptive rocks is higher than that of granites. Among them, the granite content of the C6 and C7 Members is obviously higher than that of the C8 Member, but there is no significant difference between the granite content of the C6 and C7 Members. Statistics show that the eruptive rock content of the C6 Member is higher than that of the C7 and C8 Members, and the eruptive rock content of the C7 Member is slightly lower than that of the C8 Member.

The relationship between the cement and various framework mineral components and the face ratio of the rock samples is shown in **Figure 3**. There is a good negative correlation between the cement components (mainly siliceous, carbonate and clay cements) and face ratio and average pore size. This indicates that cement plays a certain role in destroying the petrophysical properties of the Yanchang Formation tight sandstone reservoirs. Furthermore, the correlation between quartz content and face ratio is not significant. However, there is a good positive correlation between feldspar component content and face ratio, which is related to the development of a large number of dissolved pores and fractures in the feldspar minerals.

Rock Rupture Characteristics

Typical stress-strains of the samples in rock mechanics tests are shown in **Figure 4**. Under uniaxial conditions, the rock has a relatively obvious compaction process, and then transitions to an elastic deformation process, and the main failure mode is exhibited with brittle failures. Under triaxial conditions (35 MPa confining pressure), the rock exhibits elastic-plastic deformation. The higher the confining pressure, the greater the proportion of plastic deformation before failure (Liu et al., 2020; Xu et al., 2021). The main failure mode under triaxial conditions is compression-shear failure, and the plastic segment is significantly extended (Kang et al., 2010; He et al., 2020). Due to the internal mineral composition, micro-cracks or edge damage, the strength values of some samples under high confining pressure conditions are lower than those under low confining pressure conditions.

The study found that under uniaxial conditions, the samples had obvious tensile rupture patterns. With the addition and increase of confining pressure, the rupture of rock has obvious shear rupture pattern. When the confining pressure is loaded to 35 MPa, a vertical shear fracture is formed.

Changes of Rock Mechanical Parameters Under Different Confining Pressures

The rock mechanics test results show that the compressive strength and Young's modulus of tight reservoirs are very low

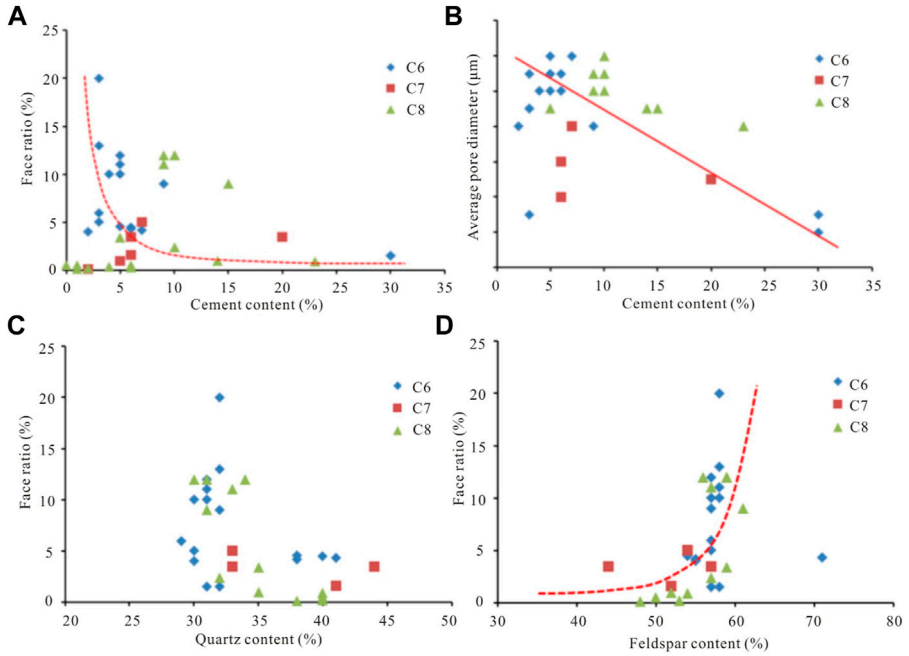

FIGURE 3 | Effects of different types of mineral components on petrophysical properties of tight oil reservoirs. **(A)** Relationship between cement content and face ratio; **(B)** Relationship between cement content and average pore diameter; **(C)** Relationship between quartz content and face ratio; **(D)** Relationship between feldspar content and face ratio.

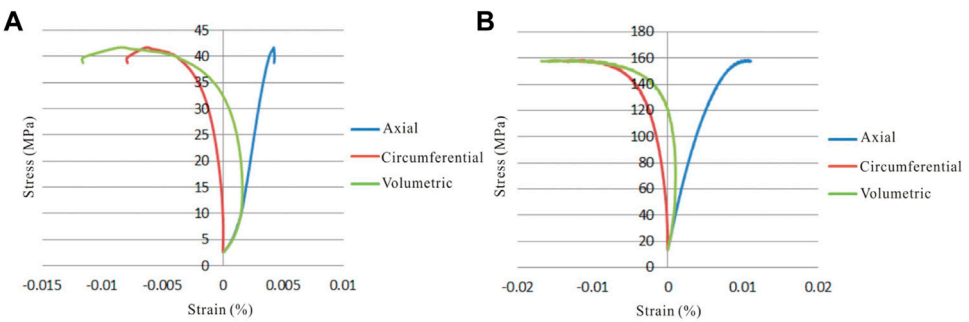

FIGURE 4 | Stress and strain curves of Lc-1 sample in rock mechanics experiments. **(A)** Uniaxial condition; **(B)** Confining pressure 35 MPa condition.

under uniaxial conditions. The strength and Young's modulus of the C7 Member are slightly higher than those of the C6 and C8 Members. The Poisson's ratios of the C6, C7 and C8 Members are not very different. The difference in rock strength under triaxial conditions is small, and the overall strength of the C6 and C7 Members is slightly higher than that of the C8 Member. Under triaxial conditions, the Young's modulus of rocks has little difference, and the overall Young's modulus of the C6 and C7 Members is slightly higher than that of the C8 Member. There is little difference in the Poisson's ratio of rocks under triaxial conditions. Under the condition of low confining pressure (10 MPa), the Poisson's ratio of the C6 Member is slightly higher. Under the condition of high confining pressure, the Poisson's ratio of the C6 and C7 Members is slightly lower than that of the Chang 8 Member.

The variation law of rock mechanical parameters of the samples under different confining pressure conditions is shown in **Figure 5**. On the whole, as the confining pressure increases, the rock is gradually compacted, and at this time, the compressive strength of the samples gradually increases (Li., 2022). With the increase of confining pressure, the Young's modulus of rock will gradually increase. However, the sample 2# is abnormal, and the Young's modulus under the condition of confining pressure of 10 MPa shows a high abnormal value (**Figure 5A**). Analysis of the reasons found that the sample has an extremely fine-grained sand-like

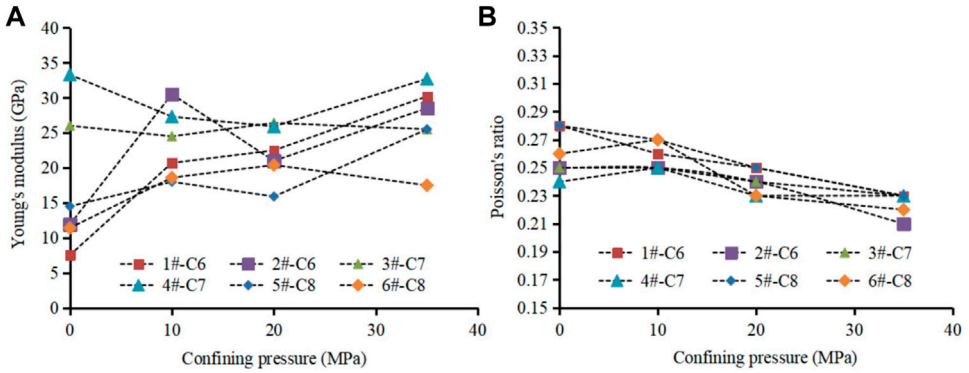

FIGURE 5 | Variation of rock mechanical parameters of samples under different confining pressures. **(A)** Young's modulus; **(B)** Poisson's ratio.

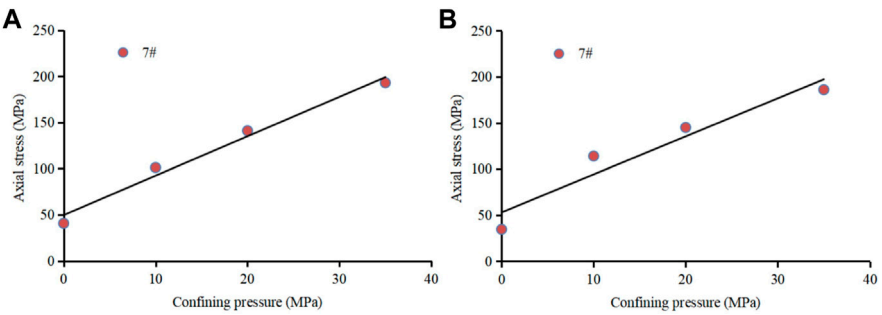

FIGURE 6 | Relationship between axial stress and confining pressure of the sandstone samples. **(A)** Sample 7#; **(B)** Sample 7#.

structure and a high content of volcanic debris, resulting in an abnormally high modulus value. For the Poisson's ratio, with the increase of confining pressure, the Poisson's ratio has a slightly decreasing trend, which means that the rock hardness gradually increases and the lateral strain amount gradually decreases (**Figure 5B**).

The cohesive force (C) represents the mutual force between the particles inside the rock, and the internal friction angle (φ) represents the direction of rupture of the particles inside the rock. According to the linear Mohr-Coulomb criterion, the rock C and φ are calculated according to the relationship between the axial stress σ_1 and the confining pressure σ_3 at failure.

$$\sigma_1 = \frac{2C \times \cos\phi}{1 - \sin\phi} \frac{\sigma_3(1 + \sin\phi)}{1 - \sin\phi} \quad (1)$$

where σ_1 is the axial stress when the rock sample fails, MPa; σ_3 is the confining pressure, MPa.

The relationship between axial stress and confining pressure of some test samples is shown in **Figure 6**. According to the slope and intercept of this straight line, the cohesion and internal friction angle of the sample can be calculated. The test results show that the cohesion of the C7 Member sand body is relatively high, which represents a high degree of consolidation between grains. The cohesion values of the C6 and C8 Members have little difference. In addition, the internal friction angles of the C6 to C8 sand bodies are mainly distributed between 36.6° and 46.5°. The internal friction angle of the C6 sand body is slightly higher than that of the C7 and C8 Members, while the internal friction angle of the C7 and C8 Members has little difference.

DISCUSSION

Logging Interpretation of Rock Mechanical Parameters

When using logging data to extract rock mechanical parameters, the longitudinal and shear wave time differences are required. Based on the full-wave train array acoustic wave test of the target layer, reliable longitudinal and shear wave velocity data were obtained for the C6 to C8 oil groups. Using the **Eq. 2**, the shear wave time difference of the formation rock can be predicted.

$$\Delta t_p = 2.02\Delta t_s - 12.14\,(R = 0.98) \quad (2)$$

where Δt_p is the longitudinal wave time difference, Δt_s is the shear wave time difference, and R is the correlation coefficient.

The interpretation of rock Young's modulus and Poisson's ratio adopts the following physical equations (**Eqs 3**, **4**).

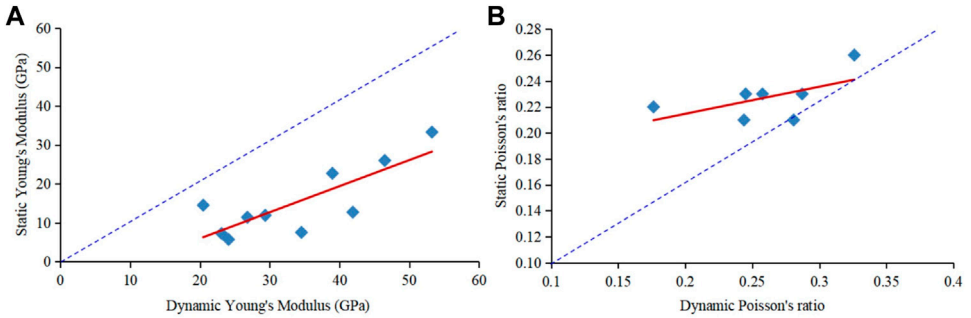

FIGURE 7 | Conversion relationship between dynamic and static rock mechanics parameters of the target layer in the study area. **(A)** Dynamic and static Young's modulus; **(B)** Dynamic and static Poisson's ratio.

$$E_d = \frac{\rho_b}{\Delta t_s^2} \frac{3\Delta t_s^2 - 4\Delta t_p^2}{\Delta t_s^2 - \Delta t_p^2} \tag{3}$$

$$v_d = \frac{1}{2}\left(\frac{\Delta t_s^2 - 2\Delta t_p^2}{\Delta t_s^2 - \Delta t_p^2}\right) \tag{4}$$

In the formula, E_d is the dynamic Young's modulus, GPa; v_d is the dynamic Poisson's ratio; Δt_p is the longitudinal wave time difference, μs·ft^{-1}; Δt_s is the shear wave time difference, μs·ft^{-1}; ρ_b is the bulk density, g·cm^{-3}.

There are differences between the dynamic and static elastic parameters of rocks. On the one hand, it is related to factors such as micro-fractures, pore fluids, mineral components and micro-fabric differences in the rock, and on the other hand, it is related to the strain amplitude and frequency of the loads. Generally, the value of dynamic elastic parameters of rock is larger than its static value, but the parameters of static mechanical properties of rock are more in line with the actual geological situation. The conversion relationships between the dynamic and static Young's modulus and the Poisson's ratio of the target layer are shown in **Figure 7**. Poisson's ratio is the ratio of the lateral strain to the longitudinal strain of a sample, which is affected by the combined effects of different mineral compositions and tiny sample processing dimensions. Therefore, the dynamic and static Poisson's ratio usually has a certain degree of dispersion. We think the test results in **Figure 7** can satisfy the logging interpretation of mechanical parameters.

The logging interpretation formula of cohesion is as follows (**Eq. 5**):

$$C = 4.69 \times 10^7 \rho_b^2 \left(\frac{1+v_d}{1-v_d}\right)(1-2v_d)\frac{(1+0.78V_{sh})}{\Delta t_p^4} \tag{5}$$

Based on the empirical formula, the least squares method is used to fit the cohesion, and the final cohesion fitting formula is as follows:

$$C = 10.26 + 1.86 \times 10^7 \rho_b^2 \left(\frac{1+v_d}{1-v_d}\right)(1-2v_d)\frac{(1+0.78V_{sh})}{\Delta t_p^4} \tag{6}$$

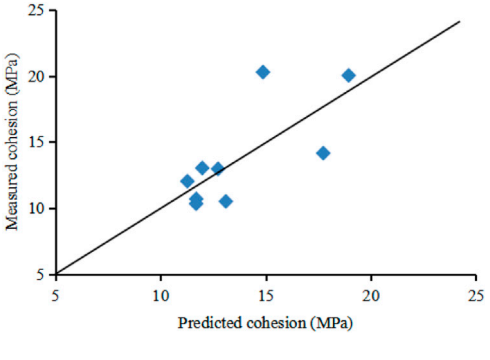

FIGURE 8 | Comparison of the tested and predicted values of the cohesion of the samples.

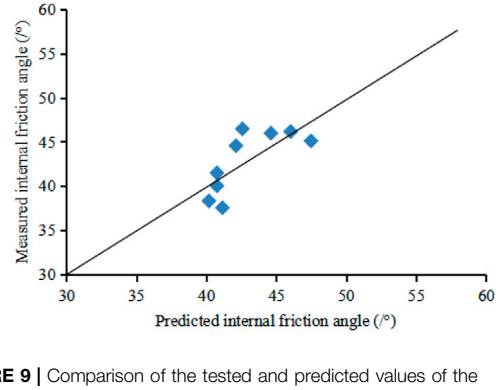

FIGURE 9 | Comparison of the tested and predicted values of the internal friction angle of the samples.

The average absolute error of the prediction results of the cohesion of the rock samples is 1.9 MPa, and the prediction accuracy is high (**Figure 8**).

The internal friction angle is explained by **Equations 7**, **8**:

$$\varphi = \mathrm{alg}\left[M + \left(M^2+1\right)^{1/2}\right] + \mathrm{b} \tag{7}$$

$$M = A - B \cdot C \tag{8}$$

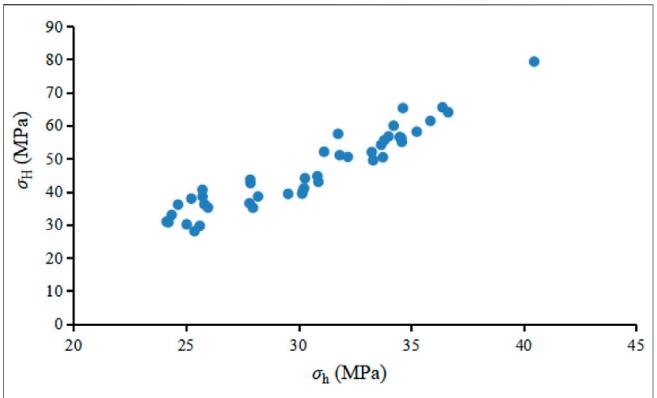

FIGURE 10 | Relationship between the maximum and minimum horizontal principal stresses of the target layer in the study area.

In the formula, M, A and B are intermediate process variables, dimensionless.

Based on the empirical formula, the least squares method is used to fit the internal friction angle, and the fitting formula of the internal friction angle of the samples is obtained (**Eqs 9**, **10**):

$$\varphi = -37.49\lg\left[M + \left(M^2 + 1\right)^{1/2}\right] + 16.24 \quad (9)$$

$$M = 0.16 - 0.2 \cdot C \quad (10)$$

The comparison between the predicted and the measured values of the internal friction angle of the rock samples is shown in **Figure 9**. It can be seen that the average absolute error of the overall internal friction angle is 2.9°, and the interpretation accuracy is high.

Logging Interpretation of In-Situ Stresses

During the fracturing process, the fracturing pressure (P_f) of the rock can be obtained directly from the fracturing test curve (Jaeger and Cook, 1976; Kirmani et al., 2021). Furthermore, the maximum horizontal principal stress (σ_H) can be determined by the theoretical formula: $\sigma_H = 3\sigma_h - P_f - P_p + \sigma_t$. P_p is the formation pressure, and the average pressure coefficient of the target layer is 0.74. σ_t represents the tensile strength, which is usually 10% of the rock's compressive strength for tight sandstones (Zoback et al., 2003; Yin et al., 2018).

The relationship between the horizontal maximum and horizontal minimum principal stresses of the target layer in the study area is shown in **Figure 10**. It can be seen that σ_H is mainly distributed in 30–60 MPa, and σ_h is mainly distributed in 25–37 MPa. With the increase of burial depth, each principal stress value increases. The state of *in-situ* stress satisfies: vertical principal stress (σ_v) >horizontal maximum principal stress (σ_H) >horizontal minimum principal stress (σ_h). It shows that the current *in-situ* stress of the target layer basically presents a relatively relaxed normal stress state.

In-situ stress refers to the internal stress existing in the crustal rock mass. It is the force on the unit area inside the medium caused by the force of vertical motion and horizontal motion inside the crust and the force of other factors (Li and Zhang 1997; Li et al., 2012; Shuai et al., 2013; Yin et al., 2020). The rock formations in sedimentary basins are under triaxial stress state, and the stress sources are complex. It is generally believed that the stress they are subjected to is composed of the gravity of the overlying rock, the formation pressure, and the tectonic activity. Because the geological situation is very complex, each factor is not independent, but interacts and influences each other (McBride., 1989; Santosh and Feng., 2020; Zheng et al., 2020; Xue et al., 2021).

In this study, an improved Newberry model based on the principle of anisotropy was used to calculate the *in-situ* stress of tight oil reservoirs. The calculation method has been described in detail by Cui and Radwan (2021). Finally, the comparison between the calculated and the measured results of *in-situ* stress of some fracturing intervals in the study area is shown in **Figure 11**. Overall, the mean absolute error of σ_H of the target layer in the study area is 5.7 MPa, and the mean absolute error of σ_h is 1.9 MPa. The overall error is small, indicating that the prediction results are reliable.

In-situ Stress Field Simulation

To establish a tectonic stress field simulation geological model, a series of geological parameters need to be determined. These parameters include the direction of the tectonic stress field, the magnitude of the tectonic stress value, and the mechanical parameters of the deformed medium rock (Zou et al., 2013; Zhao et al., 2017). They are not only the basis for the tectonic

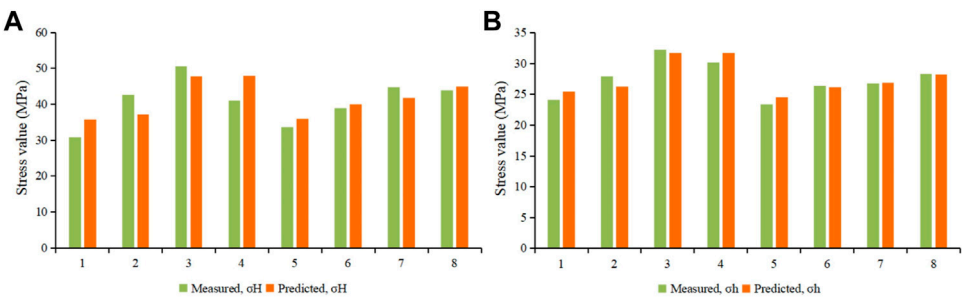

FIGURE 11 | Calculated and measured results of the *in-situ* stresses of some fracturing intervals in the study area. **(A)** σ_H; **(B)** σ_h.

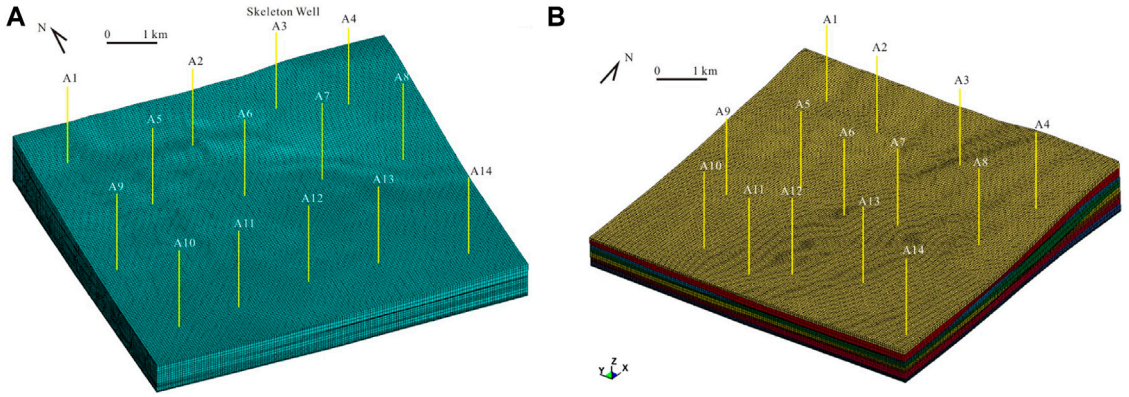

FIGURE 12 | 3D finite element model of the target layer in Block **(A)** Overall mesh model; **(B)** Layered mesh model.

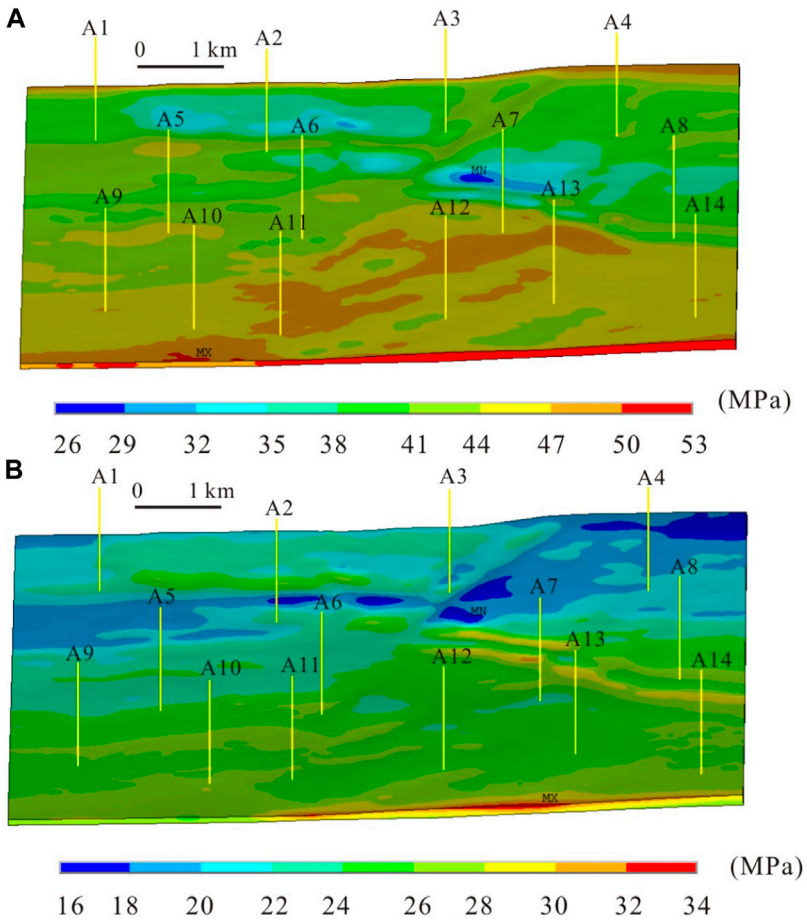

FIGURE 13 | Planar distribution of the horizontal principal stresses of the target layer. **(A)** Maximum horizontal principal stress; **(B)** Minimum horizontal principal stress.

stress field simulation, but also the constraint conditions to test the results of the tectonic stress field simulation. According to the triaxial rock mechanics experiment, the Young's modulus of the target layer is 23 GPa, the Poisson's ratio is 0.23, the cohesive force is 15 MPa, and the internal friction angle is 42°. Generally, the finer the division of the geological body unit, the higher the

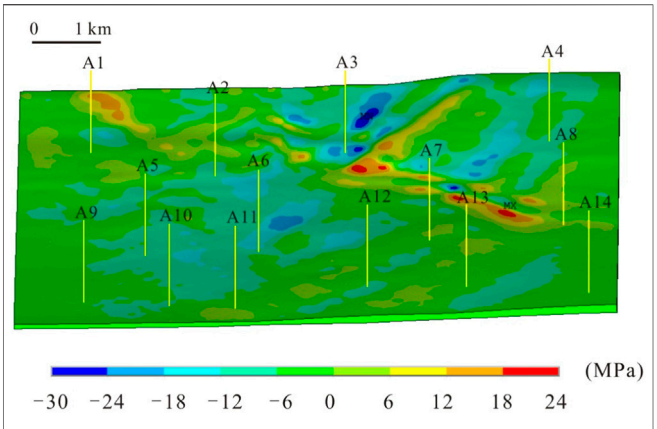

FIGURE 14 | Planar distribution of shear stress in the target layer.

calculation accuracy of the mathematical model. There are no faults in the study area, and only low-amplitude structures are developed in local areas. Thus, the mesh density is increased in the low-amplitude uplift regions. The finite element simulation of the established target layer is meshed with hexahedral elements, and a total of 134,213 elements are obtained. The area of the study area is 70 km^2, and the size of the grid is 30 m.

A three-dimensional finite element model is constructed according to the main geological structural features of the target layer. The current principal stress direction of the target layer in the study area is the NE direction, so the maximum horizontal principal stress direction is set to the NE direction. Similarly, the minimum horizontal principal stress direction is set to the NW direction. The NE direction stress value is set to 50 MPa, and the NW direction stress value is set to 30 MPa. This boundary condition is reasonable.

In the process of mathematical simulation, according to the law of statics, the resultant force of the external force on the model must be equal to zero, and the resultant moment of the external force must also be equal to zero. That is, the external force system must be balanced to ensure that the calculated model does not move and rotate as a whole. After each force system is balanced, the elasto-plastic incremental method is used to construct the stress field numerical simulation software for *in-situ* stress calculation and output. If the difference between the calculated value and the measured value is large, it is needed to continue to adjust the boundary force, re-compile the input data body, and then carry out the balance debugging of the force system. Furthermore, it is needed to repeat adjustment→calculation→verification until the principal stress direction calculated by simulation is the same as the measured one. The calculation is not stopped until the differential stress value is quite close to the measured differential stress value of each well point. In this study, the error of the principal stress in the horizontal direction of the simulation results is less than 3 MPa, so the simulation results are reliable.

The finite element mesh model of the study area A is shown in **Figure 12A**. The model covers the C6 to C8 Members, the C6 Member contains $C6^1$ to $C6^4$ sublayers, the C7 Member contains $C7^1$ to $C7^3$ sublayers, and the C8 Member contains $C8^1$ to $C8^2$ sublayers. Thus, the target layer contains nine sublayers (**Figure 12B**).

In this study, the $C8^1$ sublayer was taken as an example to illustrate the simulation results of the tectonic stress field (**Figure 13**). The simulation results show that the horizontal maximum principal stress is distributed along the NE direction, while the horizontal minimum principal stress is distributed along the NW direction (**Figure 13**). Thus, the stress distribution in the target layer of the work area matches the direction of the applied environmental stress. The values in **Figure 13** are all positive, representing compression. In the target layer, σ_H is mainly distributed in 32–50 MPa, while σ_h is mainly distributed in 20–34 MPa. Both σ_H and σ_h are relatively high in the southern uplift, and the σ_H is usually greater than 44 MPa, while the σ_h is usually greater than 24 MPa. The northern part of the study area developed several grooves with relatively low stress values. High stress values are usually banded, which may be related to compression caused by formation deformation.

The distribution characteristics of shear stress in the target layer were further analyzed, and the results are shown in **Figure 14**. It can be seen that the shear stress of the target layer is mainly distributed between −24 and 24 MPa. Typically, negative values represent left-handed, and positive values represent right-handed. The shear stress of the target layer also presents a band-like distribution. Moreover, the left-handed regions and the right-handed regions are usually alternately distributed. However, the extent of the left-handed area in the southern uplift area is larger than that of the right-handed area, indicating that the tight oil reservoirs in the study area are mainly affected by left-handed activities.

CONCLUSION

1) Under uniaxial conditions, the tight sandstone samples mainly suffer from tensional ruptures. With the increase of confining pressure, the tight sandstone samples undergo obvious shearing ruptures. When the confining pressure is loaded to 35 MPa, a typical vertical shear fracture will be formed in a certain sample.
2) The hydraulic fracturing results show that the *in-situ* stress state of the target layer satisfies $\sigma_v > \sigma_H > \sigma_h$. Based on the results of rock mechanics and acoustic tests, we have constructed the dynamic and static mechanical parameter conversion models of tight oil reservoirs and the logging interpretation model of current *in-situ* stress.
3) The finite element method is used to simulate the three-dimensional structural stress field of the target layer. The horizontal principal stress distribution in the work area is consistent with the applied environmental stress. The σ_H of the target layer is mainly distributed in 32–50 MPa, and the σ_h is mainly distributed in 20–34 MPa. Both σ_H and σ_h are relatively high in the southern uplift of the work area;

among them, σ_H is usually greater than 44 MPa, and σ_h is usually greater than 24 MPa.

4) The northern part of the study area developed several grooved areas with relatively low stress values. The regions with high stress values are often distributed in bands, which may be related to the compression caused by the strong deformation of the strata. Left-handed and right-handed regions usually alternate with each other. However, the extent of the left-handed area in the southern uplift area is larger than that of the right-handed area, indicating that the tight oil reservoirs in the study area are mainly affected by left-handed activities.

DATA AVAILABILITY STATEMENT

The original contributions presented in the study are included in the article/Supplementary Material, further inquiries can be directed to the corresponding author.

AUTHOR CONTRIBUTIONS

MC and ML are responsible for the idea and writing of this paper and XZ, HL, and QZ are responsible for the data preparation and analysis.

REFERENCES

Baecher, G. B. (1983). Statistical Analysis of Rock Mass Fracturing. *Math. Geology.* 15 (2), 329–348. doi:10.1007/bf01036074

Borgia, G. C., Bortolotti, V., Brancolini, A., Brown, R. J., and Fantazzini, P. (1996). Developments in Core Analysis by NMR Measurements. *Magn. Reson. Imaging* 14 (7-8), 751–760. doi:10.1016/s0730-725x(96)00160-9

Chen, G. B., Li, T., Yang, L., Zhang, G. H., Li, J. W., and Dong, H. J. (2021). Mechanical Properties and Failure Mechanism of Combined Bodies with Different Coal-Rock Ratios and Combinations. *J. Mining Strata Control. Eng.* 3 (2), 023522. doi:10.13532/j.jmsce.cn10-1638/td.20210108.001

Chitrala, Y., Moreno, C., Sondergeld, C., and Rai, C. (2013). An Experimental Investigation into Hydraulic Fracture Propagation under Different Applied Stresses in Tight Sands Using Acoustic Emissions. *J. Pet. Sci. Eng.* 108, 151–161. doi:10.1016/j.petrol.2013.01.002

Cui, X., and Radwan, A. E. (2021). Coupling Relationship between Current *In-Situ* Stress and Natural Fractures of continental Tight sandstone Oil Reservoirs. *Interpretation* 12, 1–53. doi:10.1190/int-2021-0200.1

Dong, S., Zeng, L., Dowd, P., Xu, C., and Cao, H. (2018). A Fast Method for Fracture Intersection Detection in Discrete Fracture Networks. *Comput. Geotechnics* 98, 205–216. doi:10.1016/j.compgeo.2018.02.005

Fan, X. Y., Gong, M., Zhang, Q. Z., Wang, J. R., Bai, L., and Chen, Y. J. (2014). Prediction of the Horizontal Stress of the Tight sandstone Formation in Eastern Sulige of China. *J. Pet. Sci. Eng.* 113, 72. doi:10.1016/j.petrol.2013.11.016

Gao, F. Q. (2021). Influence of Hydraulic Fracturing of strong Roof on Mining-Induced Stress Insight from Numerical Simulation. *J. Mining Strata Control. Eng.* 3 (2), 023032. doi:10.13532/j.jmsce.cn10-1638/td.20210329.001

Gurocak, Z., Solanki, P., Alemdag, S., and Zaman, M. M. (2012). New Considerations for Empirical Estimation of Tensile Strength of Rocks. *Eng. Geology.* 145-146, 1–8. doi:10.1016/j.enggeo.2012.06.005

He, S. M., Wang, W., and Shen, H. (2015). Factors Influencing Wellbore Stability during Underbalanced Drilling of Horizontal wells when Fluid Seepage Is Considered. *J. Nat. Gas Sci. Eng.* 23, 80~–89. doi:10.1016/j.jngse.2015.01.029

He, X., Zhang, P., He, G., Gao, Y., Liu, M., Zhang, Y., et al. (2020). Evaluation of Sweet Spots and Horizontal-Well-Design Technology for Shale Gas in the basin-margin Transition Zone of southeastern Chongqing, SW China. *Energ. Geosci.* 1 (3–4), 134–146. doi:10.1016/j.engeos.2020.06.004

Hong, D., Cao, J., Wu, T., Dang, S., Hu, W., and Yao, S. (2020). Authigenic clay Minerals and Calcite Dissolution Influence Reservoir Quality in Tight Sandstones: Insights from the central Junggar Basin, NW China. *Energ. Geosci.* 1 (1–2), 8–19. doi:10.1016/j.engeos.2020.03.001

Huang, X., Li, A., Li, X., and Liu, Y. (2019). Influence of Typical Core Minerals on Tight Oil Recovery during CO_2 Flooding Using the Nuclear Magnetic Resonance Technique. *Energy Fuels* 33 (8), 7147–7154. doi:10.1021/acs.energyfuels.9b01220

Jaeger, J. C., and Cook, N. G. W. (1976). *Fundamentals of Rock Mechanics*. London: Chapman & Hall, 128

Kang, H., Zhang, X., and Si, L. (2010). *In-situ* Stress Measurements and Stress Distribution Characteristics in Underground Coal Mines in China. *Eng. Geology.* 116, 333– 345. doi:10.1016/j.enggeo.2010.09.015

Kirmani, F. U. D., Raza, A., Gholami, R., Haidar, M. Z., and Fareed, C. S. (2021). Analyzing the Effect of Steam Quality and Injection Temperature on the Performance of Steam Flooding. *Energ. Geosci.* 2 (1), 83–86. doi:10.1016/j.engeos.2020.11.002

Lan, S. R., Song, D. Z., Li, Z. L., and Liu, Y. (2021). Experimental Study on Acoustic Emission Characteristics of Fault Slip Process Based on Damage Factor. *J. Mining Strata Control. Eng.* 3 (3), 033024. doi:10.13532/j.jmsce.cn10-1638/td.20210510.002

Li, D. Y., Wong, L. N. Y., Liu, G., and Zhang, X. P. (2012). Influence of Water Content and Anisotropy on the Strength and Deformability of Low Porosity Meta-Sedimentary Rocks under Triaxial Compression. *Eng. Geology.* 126, 46––66. doi:10.1016/j.enggeo.2011.12.009

Li, H., Qin, Q., Zhang, B., Ge, X., Hu, X., Fan, C., et al. (2020b). Tectonic Fracture Formation and Distribution in Ultradeep Marine Carbonate Gas Reservoirs: A Case Study of the Maokou Formation in the Jiulongshan Gas Field, Sichuan Basin, Southwest China. *Energy Fuels* 34 (11), 14132–14146. doi:10.1021/acs.energyfuels.0c03327

Li, H. (2022). Research Progress on Evaluation Methods and Factors Influencing Shale Brittleness: A Review. *Energ. Rep.* 8, 4344–4358. doi:10.1016/j.egyr.2022.03.120

Li, Y., Zhou, D., Wang, W., Jiang, T., and Xue, Z. (2020a). Development of Unconventional Gas and Technologies Adopted in China. *Energ. Geosci.* 1 (1–2), 55–68. doi:10.1016/j.engeos.2020.04.004

Li, Z. M., and Zhang, J. C. (1997). *Crustal Stress and Hydrocarbon Exploration and Development*. Beijing: Petroleum Industry Press, 138– 140.

Liu, Y., Gao, M., and Zhao, H. (2020). Detection of Overlying Rock Structure and Identification of Key Stratum by Drilling and Logging Technology. *J. Mining Strata Control. Eng.* 2 (2), 023038. doi:10.13532/j.jmsce.cn10-1638/td.2020.02.004

Lommatzsch, M., Exner, U., Gier, S., and Grasemann, B. (2015). Dilatant Shear Band Formation and Diagenesis in Calcareous, Arkosic Sandstones, Vienna Basin (Austria). *Mar. Pet. Geology.* 62, 144–160. doi:10.1016/j.marpetgeo.2015.02.002

Mahmoodi, S., Abbasi, M., and Sharifi, M. (2019). New Fluid Flow Model for Hydraulic Fractured wells with Non-uniform Fracture Geometry and Permeability. *J. Nat. Gas Sci. Eng.* 68, 1–14. doi:10.1016/j.jngse.2019.102914

McBride, E. F. (1989). Quartz Cement in Sandstones: A Review. *Earth- Sci. Rev.* 26, 69~112. doi:10.1016/0012-8252(89)90019-6

Santosh, M., and Feng, Z. Q. (2020). New Horizons in Energy Geoscience. *Energ. Geosci.* 1 (1–2), 1–3. doi:10.1016/j.engeos.2020.05.005

Shuai, Y., Zhang, S., Mi, J., Gong, S., Yuan, X., Yang, Z., et al. (2013). Charging Time of Tight Gas in the Upper Paleozoic of the Ordos Basin, central China. *Org. Geochem.* 64, 38–46. doi:10.1016/j.orggeochem.2013.09.001

Xu, Y., Zhang, H., and Guan, Z. (2021). Dynamic Characteristics of Downhole Bit Load and Analysis of Conversion Efficiency of Drill String Vibration Energy. *Energies* 14, 228–229. doi:10.3390/en14010229

Xue, F., Liu, X. X., and Wang, T. Z. (2021). Research on Anchoring Effect of Jointed Rock Mass Based on 3D Printing and Digital Speckle Technology. *J. Mining Strata Control. Eng.* 3 (2), 023013. doi:10.13532/j.jmsce.cn10-1638/td.20201020.001

Yin, S., Dong, L., Yang, X., and Wang, R. (2020). Experimental Investigation of the Petrophysical Properties, Minerals, Elements and Pore Structures in Tight Sandstones. *J. Nat. Gas Sci. Eng.* 76 (1), 1–14. doi:10.1016/j.jngse.2020.103189

Yin, S., Lv, D., and Ding, W. (2018). New Method for Assessing Microfracture Stress Sensitivity in Tight sandstone Reservoirs Based on Acoustic Experiments. *Int. J. Geomechanics* 18 (4), 1–10. doi:10.1061/(asce)gm.1943-5622.0001100

Yin, S., and Wu, Z. (2020). Geomechanical Simulation of Low-Order Fracture of Tight sandstone. *Mar. Pet. Geology.* 100, 1–10. doi:10.1016/j.marpetgeo.2020.104359

Zhao, J., Tang, D., Qin, Y., Xu, H., Lv, Y., Tao, S., et al. (2017). Evaluation of Fracture System for Coal Marcolithotypes in the Hancheng Block, Eastern Margin of the Ordos Basin, China. *J. Pet. Sci. Eng.* 159, 799–809. doi:10.1016/j.petrol.2017.09.031

Zheng, H., Zhang, J., and Qi, Y. (2020). Geology and Geomechanics of Hydraulic Fracturing in the Marcellus Shale Gas Play and Their Potential Applications to the Fuling Shale Gas Development. *Energ. Geosci.* 1 (1–2), 36–46. doi:10.1016/j.engeos.2020.05.002

Zoback, M. D., Barton, C. A., and Brudy, M. (2003). Determination of Stress Orientation and Magnitude in Deep wells. *Int. J. Rock Mech. Mining Sci.* 40, 1049~–1076. doi:10.1016/j.ijrmms.2003.07.001

Zou, C. N., Yang, Z., Tao, S. Z., Yuan, X. J., Zhu, R. K., Hou, L. H., et al. (2013). Continuous Hydrocarbon Accumulation over a Large Area as a Distinguishing Characteristic of Unconventional Petroleum: The Ordos Basin, North-Central China. *Earth-Science Rev.* 126, 358–369. doi:10.1016/j.earscirev.2013.08.006

Zuo, J., Yu, M., and Hu, S. (2019). Experimental Investigation on Fracture Mode of Different Thick Rock Strata. *J. Mining Strata Control. Eng.* 1 (1), 013007. doi:10.13532/j.jmsce.cn10-1638/td.2019.02.008

Conflict of Interest: XZ was employed by the company County Planning and Natural Resources Bureau of Chongqing Dianjiang and HL was employed by the company County Planning and Natural Resources Bureau of Chongqing Fuling and QZ was employed by the company Sichuan Nine One Five Engineering Survey and Design Limited Company.

The remaining authors declare that the research was conducted in the absence of any commercial or financial relationships that could be construed as a potential conflict of interest.

frontiers | Frontiers in Earth Science

METHODS
published: 16 May 2022
doi: 10.3389/feart.2022.903588

Study on the Microscopic Pore Structures of Coal Measure Reservoirs in the Shanxi Formation, Eastern Ordos Basin

Jiao Pengfei[1,2], *Wang Pengwan*[2]*, *Zhou Shangwen*[1,3], *Wang Huaichang*[4] and *Chen Xiangyang*[5]

[1]PetroChina Research Institute of Petroleum Exploration and Development, Beijing, China, [2]PetroChina Hangzhou Institute of Petroleum Geology, Hangzhou, China, [3]PetroChina Key Laboratory of Unconventional Oil and Gas, Langfang, China, [4]Exploration and Development Research Institute, Changqing Oilfield, PetroChina, Xi'an, China, [5]Tuha Branch Office, China Petroleum Logging Co.LTD., Shangshan, China

OPEN ACCESS

Edited by:
Wenlong Ding,
China University of Geosciences, China

Reviewed by:
Changan Shan,
Xi'an Shiyou University, China
Bing Zhang,
Chengdu University of Technology, China

***Correspondence:**
Wang Pengwan
wangpw_hz@petrochina.com.cn

Specialty section:
This article was submitted to Economic Geology, a section of the journal Frontiers in Earth Science

Received: 24 March 2022
Accepted: 28 April 2022
Published: 16 May 2022

Citation:
Pengfei J, Pengwan W, Shangwen Z, Huaichang W and Xiangyang C (2022) Study on the Microscopic Pore Structures of Coal Measure Reservoirs in the Shanxi Formation, Eastern Ordos Basin. Front. Earth Sci. 10:903588. doi: 10.3389/feart.2022.903588

The Carboniferous-Permian coal measures in China contain abundant natural gas resources. Shale, coal and tight sandstone reservoirs are developed in coal measures, and the quantitative characterization of the pore structures of different types of reservoirs can provide scientific guidance for the sweet spot prediction of tight reservoirs. In this study, taking the Shan 2 Member coal measure of the Shanxi Formation in the eastern Ordos Basin as an example, the pore structures of shale, coal rock and tight sandstone were systematically studied based on organic geochemistry, scanning electron microscopy, high-pressure mercury injection, and low-temperature N_2 and CO_2 adsorption experiments. The results show that the microscopic pore structures of different types of reservoirs in the Shan 2 Member coal measures are quite different. Shale and tight sandstone mainly develop clay mineral pores at mesopore scale, followed by intragranular and dissolution pores developed in quartz and feldspar minerals, while organic pores are rarely developed. A large number of macro-scale clay mineral pores and micro-fractures are developed in tight sandstone, meanwhile the pore connectivity of tight sandstone is better than that of shale. A large number of micro to nano-scale organic pores are developed in coal, and the specific surface area of micropores in coal is much larger than that of mesopores in shale and tight sandstone. Sandstone, shale, and coal are frequently interbedded in coal measure strata. Tight sandstone provide the main storage space for free gas, and pores in shale and coal absorb a large amount of natural gas. Sandstone-shale-coal assemblages and sandstone-coal assemblages are the key targets for the exploration of hydrocarbons in the Shanxi Formation coal measures in the study area.

Keywords: coal measure, Ordos Basin, Shan 2 Member, pore structure, clay mineral pores

INTRODUCTION

The Carboniferous-Permian coal measures in the Ordos Basin of China contain abundant natural gas resources, including conventional sandstone gas and unconventional natural gas (coalbed methane, shale gas, and tight sandstone gas) (Dong et al., 2016; Sun et al., 2017; Wang and Wang., 2021). Coal measures refer to sedimentary systems with similar symbiotic relationship in terms of genesis (Qin et al., 2018; Qin, 2018). Generally, the source rocks in coal measures are mainly Type III kerogen developed in coal seams, dark shales and oil shales. Furthermore, different types of natural gas generated through thermal evolution are called coal measure gas (Xue et al., 2021; Yi et al., 2018), for example, free tight sandstone gas, adsorbed coalbed methane, and both free and adsorbed shale gas (Cheng M. et al., 2018; Yao et al., 2018; Yin et al., 2018). Affected by complex depositional conditions, different types of reservoirs exhibit interbedded and cyclical characteristics in space (Liang, 2016; Yin et al., 2019; Zhang et al., 2019). The coal-measure source rocks of the Upper Paleozoic in the Ordos Basin are mainly coal seams, shale and mud-bearing biological limestone, of which coal and shale are the main gas source rocks. In addition, various types of superimposed source rocks have stable thickness and wide coverage. These factors provide a good material basis for the accumulation of coal-measure gas.

In the past, there were many examples of exploration and development of a single type of coal-measure gas. For example, the Sulige and Daniudi Gas Fields mainly develop tight sandstone gas (He et al., 2022; Qu et al., 2015); the commercial development of Upper Paleozoic gas reservoirs in the eastern margin of the Ordos Basin is mainly for coalbed methane resources (Yi et al., 2018); China's first marine-continental transitional shale gas demonstration project will be conducted in the Daning—Jixian Block. Some scholars believe that the development of a single coal measure gas will cause waste for other types of natural gas. Furthermore, the idea of co-exploration and co-production of three types of coal measure tight gas (coalbed methane, shale gas, and tight sandstone gas) is proposed (Chen et al., 2021; Li and Li., 2021; Qin et al., 2018; Qin, 2018; Yi et al., 2018; Yin et al., 2020). The co-exploration and co-production of different types of natural gas requires a fine study of the properties of the entire coal-measure reservoirs, especially the systematic study of the gas-bearing properties and microscopic pore structures of the reservoirs (Zhang et al., 2015; Wu et al., 2017; Wu et al., 2022). High-pressure mercury intrusion experiments are usually used to analyze the microscopic pore structures of tight sandstone reservoirs. Coal rock has the characteristics of easy crushing and high ash content, so low-temperature N_2 adsorption experiments are often used to study its microscopic pore structures. Pores of different scales are developed in shale reservoirs. Therefore, high-pressure mercury intrusion, low-temperature N_2 and CO_2 adsorptions are often combined to quantitatively characterize pore structures of different scales (Xu et al., 2020). In this study, taking the Shan 2 Member coal measure of the Shanxi Formation in the eastern Ordos Basin as an example, the pore structures of shale, coal rock and tight sandstone were systematically studied based on organic geochemistry, scanning electron microscopy, high-pressure mercury injection, and low-temperature N_2 and CO_2 adsorption experiments. Through this study, the dominant pore types and combinations of different types of coal-measure strata reservoirs have been clarified, which can provide a scientific basis for the co-exploration and co-production of three gases (tight sandstone gas, shale gas and coalbed methane).

GEOLOGICAL BACKGROUND

The study area is located in the eastern margin of the Ordos Basin (**Figure 1**). More than 600 wells have been drilled in the study area, and the main exploration horizon is the Shan 2 Member of the Permian Shanxi Formation. The Permian in the study area belongs to the marine-continental transitional facies sediments. Among them, the lithologies of the Taiyuan Formation include quartz sandstone, shale, interbeded limestone and coal seam; while the lithologies of the Shanxi Formation include quartz sandstone, lithic quartz sandstone, medium to coarse-grained or unequal-grained lithic sandstone, while interbeded black shale, sandstone and coal seams can be seen locally. The Shan 2 Member generally has 3-5 coal-forming periods, and its lithological assemblage is mainly gray, dark gray or gray-brown medium-fine-grained sandstone and siltstone intercalated with black shale, with a thickness of about 40–60 m. According to coal measure assemblages and sedimentary cycles, the Shan 2 Member is divided into three sub-layers, Shan 2_1, Shan 2_2 and Shan 2_3 sub-members. Coal 4# and 5# are the boundary marker layers of Shan 2_1 and Shan 2_2, and Shan 2_2 and Shan 2_3, respectively.

MATERIALS AND METHODS

Samples

In this study, 20 samples were collected from the Shan 2 Member of Shanxi Formation in Well M5 in the study area, including 3 coal samples, 4 shale and 13 tight sandstone samples. The sample depth and specific lithology (including color, particle size and approximate composition content) are shown in **Table 1**. The particle size of tight sandstone changes frequently, and shale and coal are interspersed, which is enough to explain the rapid change of sedimentary environment. Targeted experiments were carried out on all samples.

Experimental Methods

Field gas content tests were conducted for different lithologies of coal measure strata in the Shan 2 Member of M5 well. Both decomposed and residual gases can be completed at the drilling site. The cores out of the barrel are immediately put into the desorption tank to be sealed and heated to the reservoir

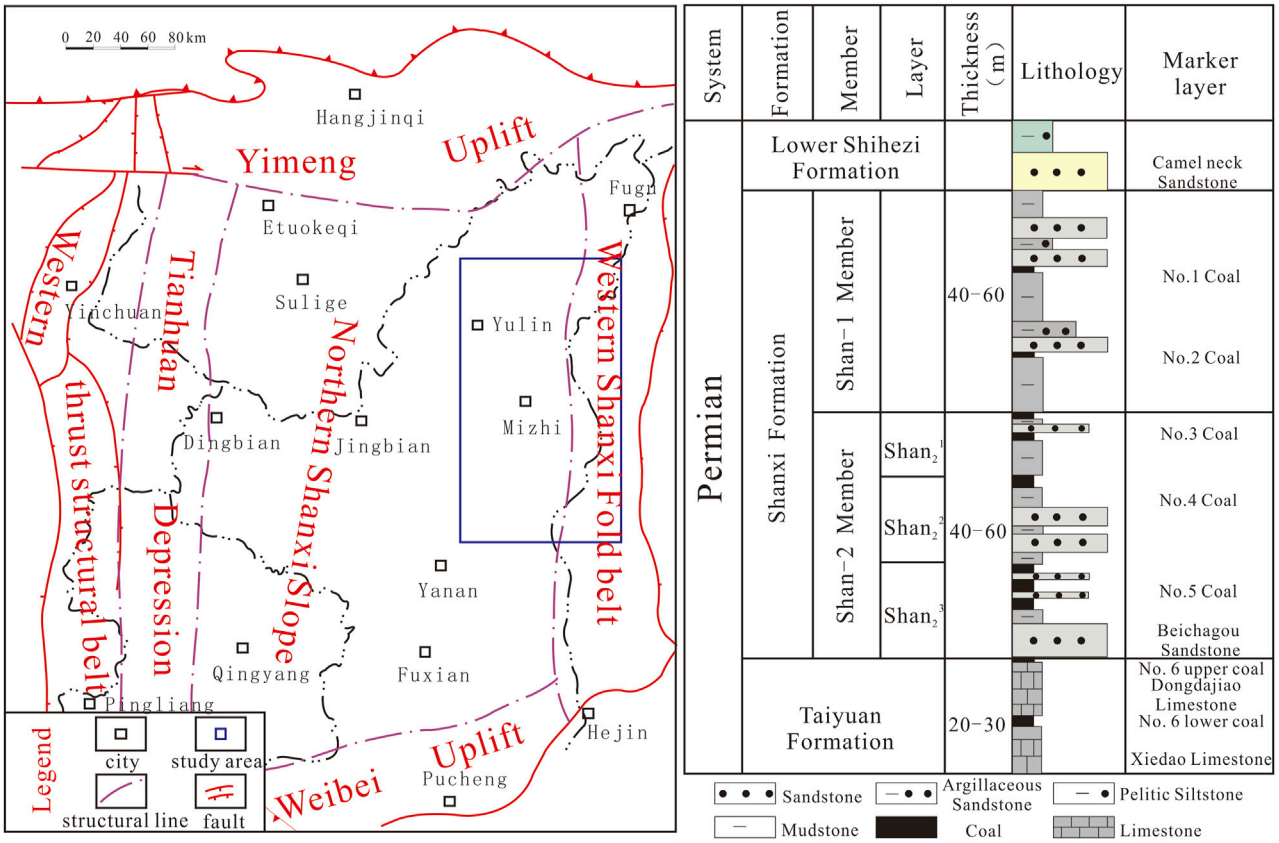

FIGURE 1 | Location of the study area and lithologic histogram of the Shanxi Formation.

TABLE 1 | Test results of organic geochemical parameters and gas-bearing properties of coal-measure samples collected from the Shanxi Formation in the study area.

Sample number	Depth (m)	Lithology	TOC (%)	R_o (%)	Gas content (m^3/t)
M5-1	1962.80	Dark gray silty shale	0.54	1.37	0.19
M5-2	1965.30	Black carbonaceous shale	1.91	1.36	0.35
M5-3	1968.70	Coal	77.3	1.40	6.52
M5-4	1979.30	Grey medium-grained detrital sandstone	0.39	1.25	0.09
M5-5	1981.90	Coal	81.60	1.39	6.31
M5-6	1983.00	Black argillaceous coarse sandstone	1.06	1.29	0.40
M5-7	1986.07	Dark grey fine-grained detrital sandstone	1.19	1.35	0.50
M5-8	1987.57	Grey medium-grained detrital sandstone	0.32	1.38	0.47
M5-9	1995.38	Grey fine-grained detrital sandstone	2.59	1.42	0.35
M5-10	1997.60	Grey coarse-grained detrital sandstone	0.61	1.44	0.20
M5-11	2001.05	Coal	76.7	1.40	6.96
M5-12	2002.85	Black fine-grained detrital sandstone	0.73	1.41	0.18
M5-13	2003.75	Gray-black coarse silt-bearing shale	2.53	1.47	0.07
M5-14	2008.05	Gray coarse silt-bearing shale	1.80	1.39	0.14
M5-15	1962.80	Grey fine-grained detrital sandstone	0.59	1.36	0.26
M5-16	1965.30	Grey fine-grained detrital sandstone	7.18	1.40	0.30
M5-17	1968.70	Grey coarse-grained detrital sandstone	2.37	1.39	0.27
M5-18	2010.81	Grey medium-grained detrital sandstone	6.12	1.44	0.08
M5-19	2014.55	Grey medium-grained detrital sandstone	11.10	1.37	0.16
M5-20	2018.15	Grey unequal-grained detrital sandstone	8.58	1.40	0.31

temperature. Then, a gas flow meter is used to record the analytical gas volume. The analytical gas volume test ends when the average analytical volume per day is less than or equal to 10 ml. Furthermore, the last recorded value is corrected in the standard state to obtain the analytical gas content (Zhou et al., 2019a). After the natural desorption is completed, a part of the sample is taken out, weighed, ground to below 60 mesh, and decomposed again at the reservoir temperature until the desorption amount is no more than 10 ml per day. This part of the analytical quantity is the residual gas content (National Energy Board, 2014). The time when the coring barrel is raised to half the depth of the wellbore and the time when the core enters the tank seal is recorded, and the difference between the two times is the lost time. Finally, the USBM method is used to calculate the lost gas content (Xue et al., 2013), and the sum of the analytical gas, residual gas and lost gas content is the on-site gas content.

The prepared bulk samples were polished (4 h) and carbon-plated (20 min) with a PECS II 685 argon ion polisher to enhance the flatness and conductivity of the samples. Furthermore, two-dimensional images of rock samples were performed using FEI Helios 650 dual-beam scanning electron microscope (FIB-SEM) in backscattering mode (BSE) and secondary electron mode (SE), respectively, and different minerals, organic matter and pores were distinguished (Zhou et al., 2016). A specific area on the 2D image is selected for ion beam cutting, and the electron beam is imaged for each cut. In addition, an Avizo software was utilized to perform digital core analysis on several hundred consecutively cut images, and data such as porosity, pore size, and coordination number were obtained (Zhou et al., 2018a).

A Micromeritics Instrument IV 9510 mercury porosimeter was used to perform high-pressure mercury porosimetry experiments with a maximum pressure of 60,000 psia (413 MPa). The pore throat diameter can be obtained from the relationship between the recorded injection pressure and mercury saturation, and using the Washburn equation (Washburn, 1921). Moreover, the Young-Duper equation (Guan et al., 2020) was used to obtain pore specific surface area and average pore size data. These data can be used to quantitatively characterize the microstructural features of macropores and micropores.

The Surface Area and Porosity Analyzer 2420 from Micromeritics Company was used to perform low temperature N_2 and CO_2 adsorption experiments on rock samples below 200 mesh. The low-temperature N_2 adsorption experiments were conducted at 77 K. At this temperature, the saturated vapor pressure p_0 of N_2 is 0.11117 MPa, the maximum equilibrium pressure p of the experiment is atmospheric pressure (0.1013 MPa), and the relative pressure of adsorption varies from 0.0095 to 0.995. In addition, the BJH method (Barrett et al., 1951) can be used to analyze the distribution characteristics of mesopore pore size and calculate the average pore size and total pore volume; the specific surface area of the samples can be calculated by the BET equation (Brunauer et al., 1938; Zhou et al., 2019b). At this temperature, the saturated vapor pressure p_0 of CO_2 is 3.48 MPa. The maximum equilibrium pressure p of the experiment is consistent with the N_2 adsorption, so the relative pressure of CO_2 adsorption varies from 0.00001 to 0.03.

In this study, we also compared nanopore diameter, total pore volume, and specific surface area data for the shale, tight sandstone, and coal samples. The adsorption gas content of coal rock is higher than that of tight sandstone and shale. Therefore, the CO_2 adsorption experiment at 273.15 K temperature was carried out on the coal rock samples. The NLDFT method (Liu et al., 2018; Zhang et al., 2017) was used to analyze the pore size distribution characteristics of coal rock micropores and was used to obtain the micropore volume, and the DR method (Dubinin and Astakhov, 1971) was used to obtain the coal rock micropore specific surface area. Furthermore, the pore volume and specific surface area of mesopores and micropores in coal rocks were compared. The above results are an important basis for judging the type of reservoir space in the rock.

RESULTS

TOC, Maturity, Gas Content, and Mineral Compositions

The TOC content of coal-measure shale samples is between 0.54% and 2.53%, with an average value of 1.69%; the TOC content of coal samples is between 76.70% and 81.60%, with an average value of 78.53%; and the TOC value of tight sandstone samples is between 0.32% and 11.10%, with an average value of 3.29%. The organic matter maturity is between 1.25% and 1.47%, with an average value of 1.38%. The coal measure samples are in the high maturity stage, and the organic matter type is mainly type III, which mainly produces gas. The gas content of shale is between 0.07 m^3/t and 0.35 m^3/t, with an average value of 0.19 m^3/t; the gas content of coal is between 6.31 m^3/t and 6.96 m^3/t, with an average value of 6.60 m^3/t; and the gas content of tight sandstone is between 0.08 m^3/t and 0.50 m^3/t, with an average value of 0.27 m^3/t (**Table 1**).

The TOC content of the coal samples from the Shan 2 Member in the study area is extremely high, and organic matter is the main component, followed by clay minerals, and there are almost no brittle minerals. The clay mineral content in the shale samples is higher than that in the tight sandstone, with an average value of 55.2%. However, the quartz mineral content in the shale samples is lower than that of the tight sandstone, with an average value of 40%. The content of clay minerals in the sandstone samples is not much different from that of quartz minerals. The average content of clay minerals and quartz minerals is 44.9% and 45.4%, respectively. In addition, a small amount of feldspar minerals and siderite are also developed in the sandstone samples, but pyrite is not developed (**Figure 2A**).

The clay minerals of shale and dense sandstone less than 2000 m mainly develop illite/smectite mixed layer and illite, but the content of illite/smectite mixed layer is higher; In

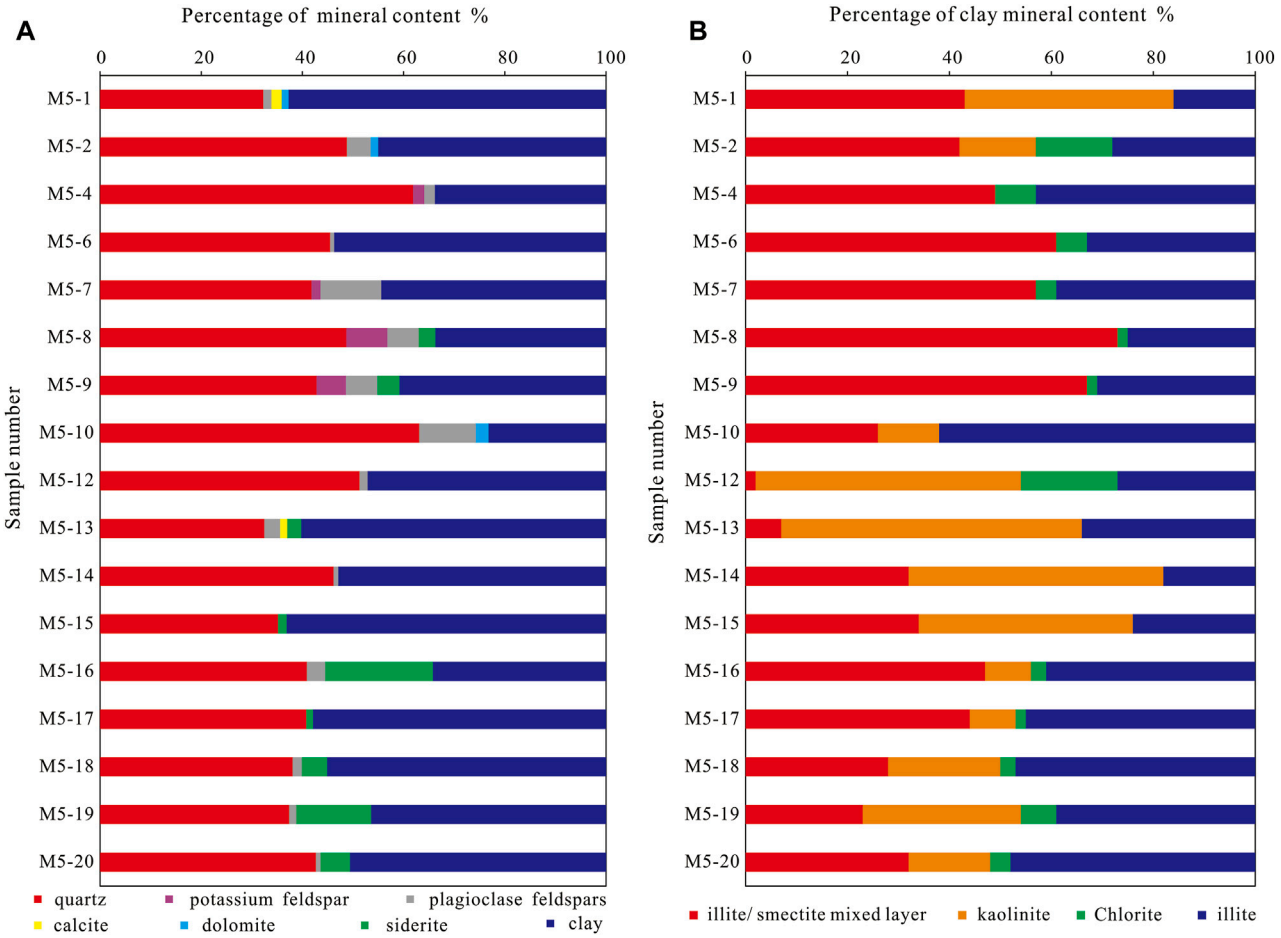

FIGURE 2 | Content of mineral components in samples with different lithologies. **(A)** percentage of mineral content; **(B)** percentage of clay mineral content.

addition to the development of illite/smectite mixed layer and illite, the content of kaolinite is also high in shale and dense sandstone with a buried depth of more than 2000 m, but the content of illite is higher than that of Yimeng mixed layer. Most samples contain a small amount of chlorite (**Figure 2B**).

Scanning Electron Microscope Observations

Observing a large number of SEM images, it is found that, unlike the marine shales of the Wufeng Formation-Longmaxi Formation in the Sichuan Basin with high organic matter content, only a small amount of organic matter can be observed in the shale and tight sandstone samples of the Shan 2 Member in the study area. A small amount of organic matter pores developed at the edge of organic matter and its contact with clay minerals (**Figure 3A**, **Figure 3F**). The organic matter edge fractures are easily formed at the parts where the organic matter is in contact with the brittle minerals (**Figure 3H**). Some organic matter edge fractures cut through the organic matter, thus effectively connecting the pore clusters in different parts. Unlike shale and tight sandstone, the coal rock in the target layer has a high content of organic matter, and a large area of organic matter can be seen on the SEM image of the coal rock (**Figure 3K**). The study found that organic pores in coal rocks are not well developed (**Figure 3L**), but there are a large number of micro-fractures in the edges and interiors of organic matter in coal rocks. In addition, no organic bubble pores were found in the coal measure strata. The reason is that the type of organic matter in the Shan 2 Member coal-measure strata is mainly type III, which mainly produces gas and hardly produces liquid hydrocarbons. At the same time, the reflectivity of vitrinite is less than 1.5%, and it is in a high maturity stage. There is no liquid hydrocarbon cracking and gas generation process, and organic matter bubble pores cannot be formed.

Clay mineral pores (**Figures 3C,H,L**) are the most common type of mineral matrix pores within different lithologies in coal measure strata. Smectite and Aemon mixed layer clay minerals are dominated by slit-like pores. The pores of montmorillonite clay minerals are book-like (**Figure 3L**), and the long axis of the pore diameter is very long; while the pores of clay minerals with higher illite content are hair-like and the long axis of the pore diameter is short (**Figure 3C**). Clay minerals are mostly

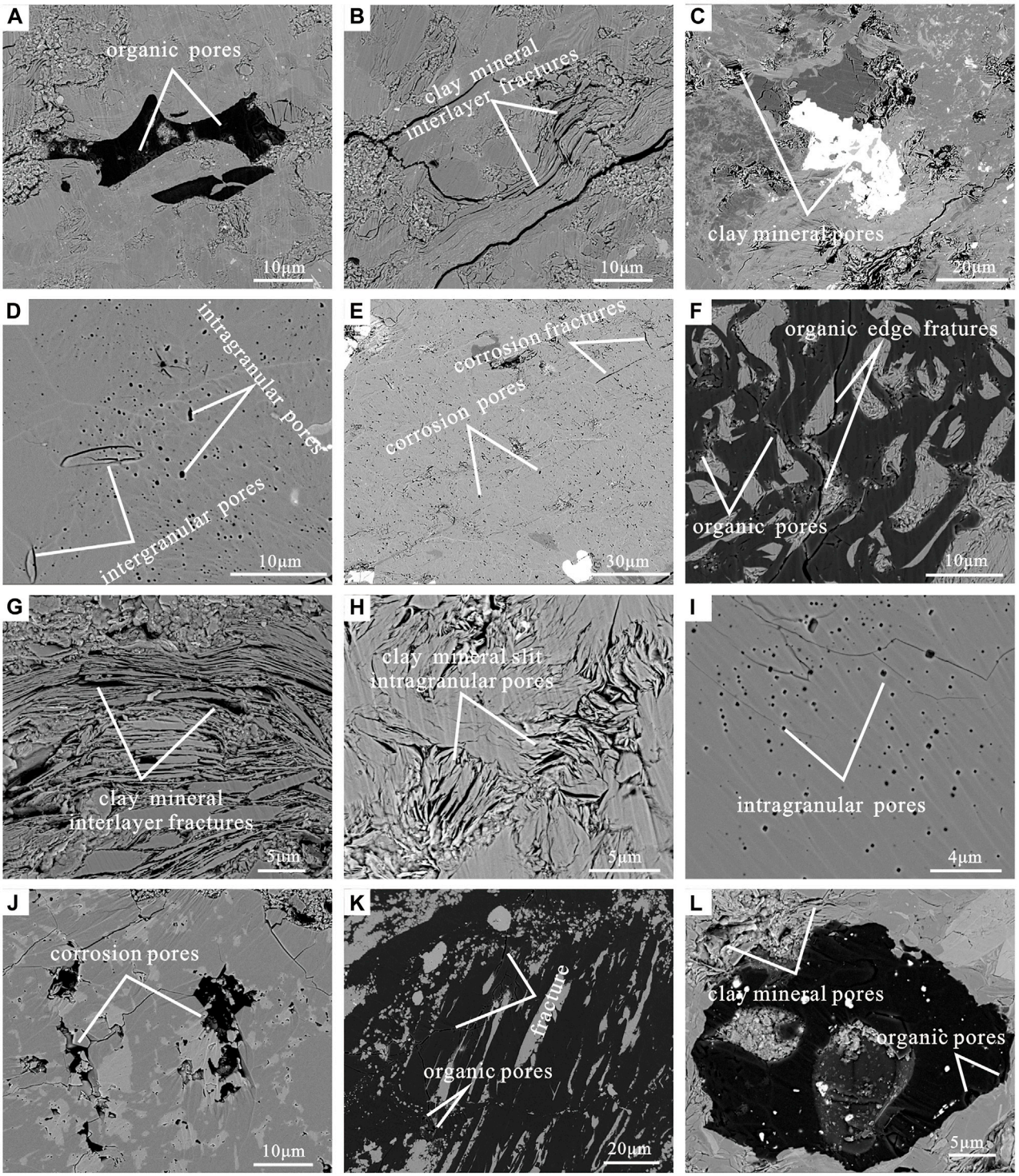

FIGURE 3 | Development characteristics of different types of pores of the coal measure samples collected from the M5 well in the Shan 2 Member. Notes: **(A)** M5-1, Organic pores in shale; **(B)** M5-1 and **(C)** M5-14, Interlayer micro-fractures and pores in clay minerals in shale; **(D)** M5-14 Intragranular and intergranular pores in shale; **(E)** M5-13, Feldspar dissolution pores and micro-fractures in shale; **(F)** M5-16, Organic pores and organic edge micro-fractures in tight sandstones; **(G)** M5-7 and **(H)** M5-9, Interlayer micro-fractures and micropores in clay minerals in tight sandstone; **(I)** M5-7, Quartz intragranular pores in tight sandstone; **(J)** M5-4, Feldspar dissolution pores in tight sandstone; **(K)** M5-3, Organic pores and micro-fractures developed in coal; **(L)** M5-11, Clay mineral pores in coal.

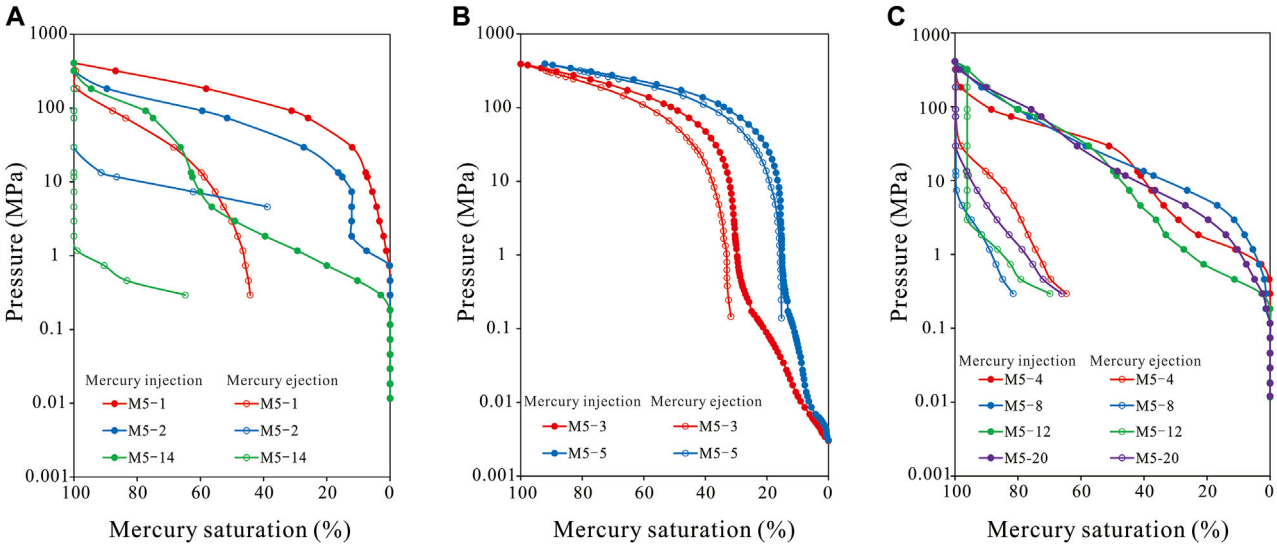

FIGURE 4 | High pressure mercury intrusion curves of typical samples collected from the Shan 2 Member. **(A)** Shale; **(B)** Coal; **(C)** Tight sandstone.

sheet-like structures, and the hydrodynamic conditions under which they are deposited are very weak. Layered clay minerals are formed by gravitational accumulation in a suspended state. Therefore, the interlayer fractures of clay minerals in the Shan 2 Member coal measure strata are very developed (**Figures 3B,G**), which increases the connectivity with other pores. A large number of round or elliptical intragranular pores are developed in brittle minerals in the Shan 2 Member shale and tight sandstone (**Figures 3D,I**). Feldspar and calcite minerals are easily dissolved by formation fluids to form dissolution pores (**Figures 3E,J**), and they are easily eroded to form dissolution micro-fractures under strong extrusion. In addition, a small number of slit-like intergranular pores are visible in the brittle minerals (**Figure 3D**). Compared with tight sandstone, the dissolution pores of shale have smaller pore size, more regular shape, and a certain fixed expansion direction.

High Pressure Mercury Intrusion Results

The high-pressure mercury intrusion curves of the three samples with different lithologies in the coal measure strata are quite different (**Figure 4**). It shows that there are great differences in the development of pores and the connectivity between pores among the samples. The mercury injection pressure of coal-measure shale is about 1 MPa. When the mercury injection pressure is less than 1 MPa, there is almost no mercury injection, indicating that pores larger than 1 μm are not developed. Moreover, the amount of mercury injected in the pressure range of 1–10 MPa is less, indicating that the pores of 100 nm–1 μm are less developed. However, when the pressure is between 10 and 100 MPa, the mercury injection rate increases rapidly, and pores of 10–100 nm are well-developed. When the pressure is greater than 100 MPa, the mercury injection amount quickly reaches the maximum value, indicating that the pores smaller than 10 nm in the shale are extremely developed. Compared with shale, there are few pores with pore size larger than 1 μm in the Shan 2 Member coal rock, and pores with pore size in the range of 50 nm–1 μm are hardly developed, but pores with pore size less than 50 nm are very developed. In the coal-measure strata, the pores with pore size larger than 1 μm are less developed in the tight sandstone, and the pores smaller than 1 μm are very developed. The mercury removal efficiency of tight sandstone is between 20% and 40%, indicating that its pore connectivity is poor. The mercury removal efficiency of shale and coal is much higher than that of tight sandstone. Due to the excessive pressure in the coal rock and shale in the later stage of the mercury injection process, the opening of micro-fractures can allow the mercury to exit quickly.

High-pressure mercury intrusion can characterize the pore structures of microscopic pores in the range of 3 nm–410 μm. According to the pore size distribution curve of shale samples (**Figure 5A**), it can be judged that pores smaller than 10 nm and larger than 20 μm are relatively developed, and pores between 10 nm and 20 μm are basically not developed; pores larger than 20 μm may be caused by micro-fractures formed by excessive injection pressure. The mercury intrusion pore size distribution curve of coal rock (**Figure 5B**) shows that pores below 100 nm are very developed, and pores or micro-fractures with pore size larger than 1 μm are developed as well. For tight sandstones (**Figure 5C**), the mercury intrusion pore size distribution curve results show that the pores with full pore size from 3 nm to 410 μm are relatively developed, and the pores smaller than 1 μm are more developed than those in other intervals, and the pores or micro-fractures larger than 1 μm are also more well-developed.

Low Temperature N_2 Adsorption Results

The nitrogen adsorption isotherms of shale, coal and tight sandstone samples taken from the Shan 2 Member coal

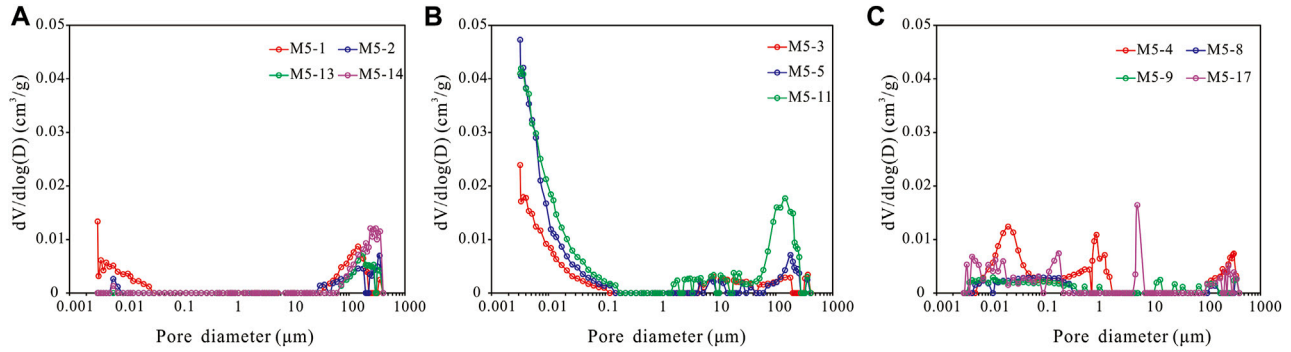

FIGURE 5 | Typical mercury intrusion pore size distribution curves for samples with different lithologies that collected from the Shan 2 Member. **(A)** Shale; **(B)** Coal; **(C)** Tight sandstone.

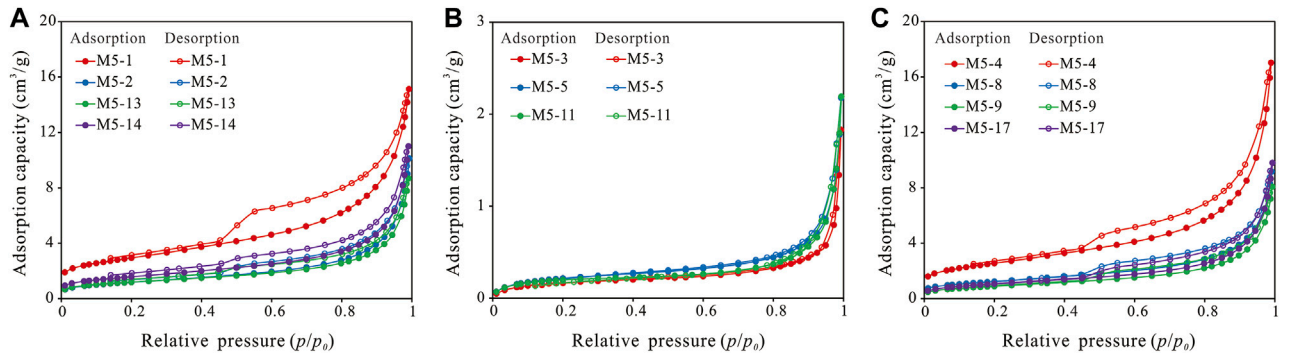

FIGURE 6 | N_2 adsorption curves of different samples. **(A)** Shale; **(B)** Coal; **(C)** Tight sandstone.

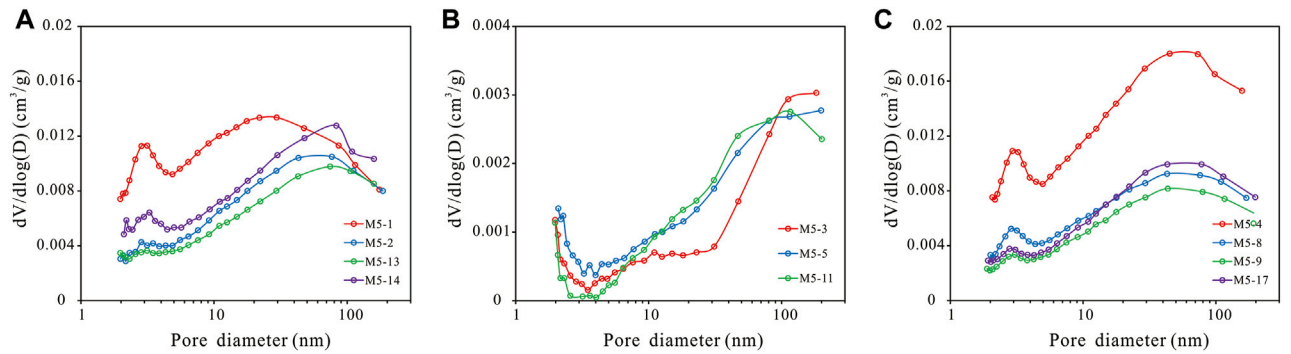

FIGURE 7 | Nitrogen adsorption pore size distribution curves of different samples. **(A)** Shale; **(B)** Coal; **(C)** Tight sandstone.

measures are all S-type, that is, typical IV-type isotherms (Xi et al., 2016; Zhou et al., 2018b) (**Figure 6**). The shale and tight sandstone samples in the coal measure have similar nitrogen adsorption capacity, and their hysteresis loop is obvious (H3 type), which means that the mesopores are relatively developed. And their desorption branches all experienced sudden evaporation when p/p_0 = 0.45. It shows that there are fine neck-shaped pores or ink bottle-shaped pores (Liu et al., 2018) in both shale and tight sandstone in coal measures. The nitrogen adsorption capacity of the coal rock in the Shan 2 Member is very low, and the hysteresis loop is very small. The adsorption and desorption curves almost coincided. This shows that the coal rock mainly develops semi-open pores, which are favorable for natural gas adsorption, but not conducive to gas flow. The adsorption branches of the three types of rocks in the marine-continental transitional coal

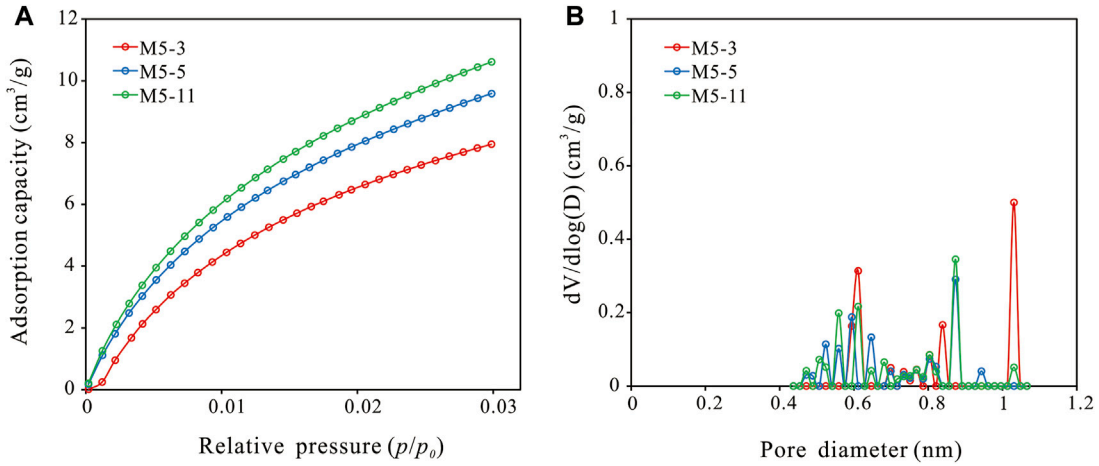

FIGURE 8 | CO_2 adsorption characteristics and micropore size distribution of coal samples. **(A)** Low temperature carbon dioxide isotherm adsorption curves; **(B)** Pore size distribution.

measure have obvious capillary condensation when the p/p_0 is about 0.9. That is, the amount of adsorption increases sharply and does not reach saturation. This shows that the shale, coal and tight sandstone in the coal measures all develop micro-fractures or parallel plate-like pores.

The nitrogen adsorption curves of shale and tight sandstone in coal measures are similar, and the pore size distribution curves obtained by the BJH method are also similar (**Figure 7**). There is a lower peak at the pore size between 2 and 4 nm, and the pore volume change rate increases rapidly in the pore size range of 5–40 nm, and then a wider peak appears. Although the first peak with a pore size between 2 and 4 nm is relatively low, because the single pore size is very small, the micropores at the peak position are very developed. On the contrary, the broad peak after 40 nm has a large single pore volume, but the number of pores is small. By comparison, it is found that pores between 2 and 10 nm in shale and tight sandstone in coal measures are well developed, pores between 10 and 50 nm are also well developed, and pores with pore diameter larger than 50 nm are rare. The broad peak of the tight sandstone is wider than that of the shale, indicating that the pore size of the tight sandstone is larger than that of the shale. The pore size distribution curve of coal is quite different from that of shale and tight sandstone, and the two peaks are not obvious. In addition, the pore volume change rate of coal is an order of magnitude smaller than that of shale and tight sandstone, indicating that pores with a pore size larger than 2 nm are less developed in coal.

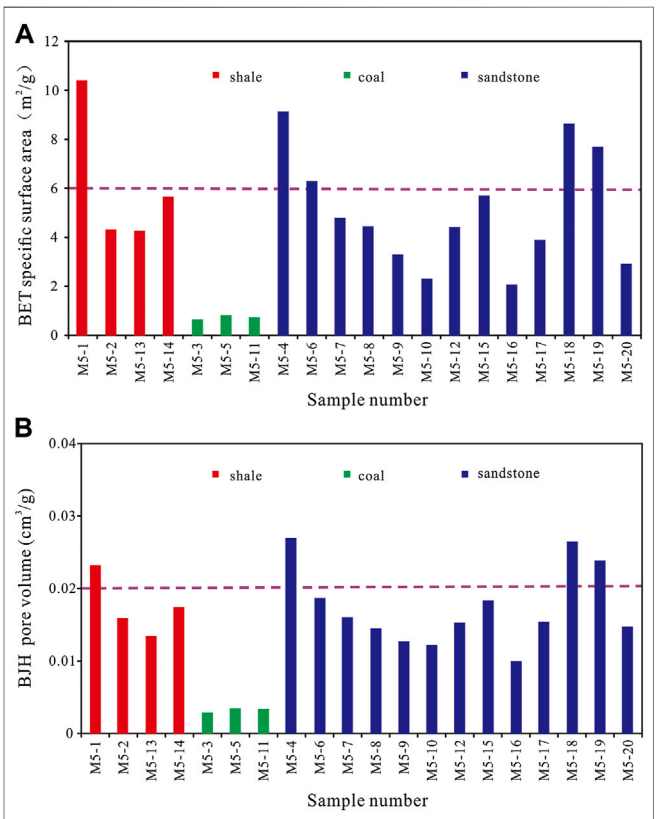

FIGURE 9 | Comparison of BET specific surface area and BJH pore volume of different kinds of samples. **(A)** BET specific surface area; **(B)** BJH pore volume.

Low Pressure CO_2 Adsorption Results

The pore size distribution characteristics of macropores show that pores with pore diameters less than 100 nm are more developed in coal rocks than in shale and tight sandstones. This result is consistent with the gas content of coal generally higher than that of shale and tight sandstone. However, the distribution of mesopore size shows that pores with a pore size larger than 2 nm are not well developed in coal rocks. The natural gas in the coal rock mainly exists in the form of adsorption, and the coal rock mainly develops micropores

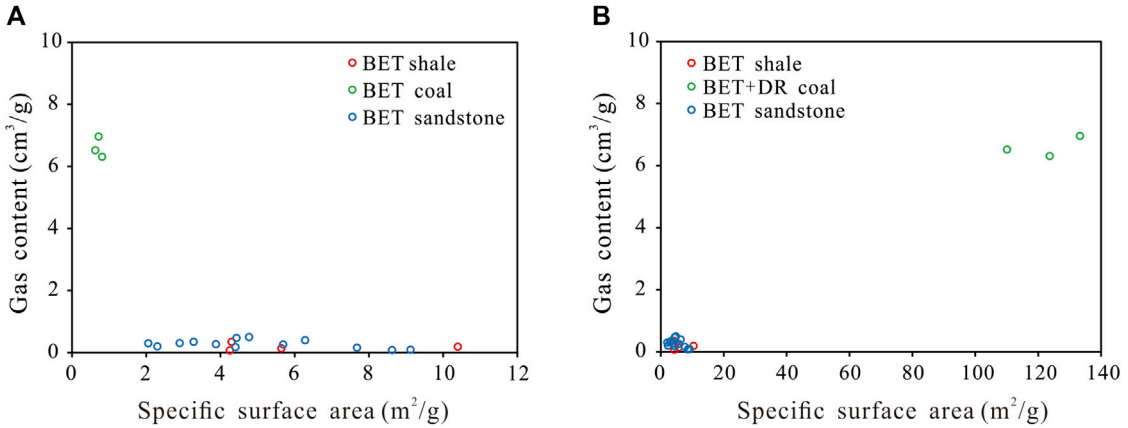

FIGURE 10 | Correlation analysis between specific surface area and gas content. **(A)** Correlation analysis between BET specific surface area and gas content. **(B)** On the basis of Panel A, the BET specific surface area of coal is added with Dr specific surface area.

with a diameter of less than 2 nm. Therefore, we conducted the low-temperature CO_2 adsorption experiment of coal rock for its special pore size. Comparing the CO_2 and N_2 adsorption curves of coal rocks in coal measures (**Figure 8A**), it can be seen that the maximum adsorption capacity of CO_2 adsorption is about 5 times that of N_2 adsorption. It is almost equal to the N_2 adsorption capacity of shale and tight sandstone, indicating that there is a larger actual total specific surface area in coal. The study also found that the pore volume change rate of micropores inside coal rocks in coal measures is an order of magnitude larger than that of mesopores in shale and tight sandstone (**Figure 8B**). This indicates that the actual total pore volume of the coal rock is relatively large, and the micropores in the two intervals of 0.5–0.7 nm and 0.8–0.9 nm are extremely developed.

DISCUSSION

Comparison of Specific Surface Area and Pore Volume

In this study, BET specific surface area and BJH pore volume were used to compare the differences in the microscopic pore structures of shale, coal and tight sandstone in coal measures. The BET specific surface area of shale ranges from 4.25 m^2/g to 10.40 m^2/g, with an average value of 6.15 m^2/g; the total pore volume of BJH ranges from 0.0134 ml/g to 0.0232 ml/g, with an average value of 0.0174 ml/g; the average pore diameter is 12.82 nm. The BET specific surface area of coal rock is in the range of 0.63 m^2/g–0.81 m^2/g, with an average value of 0.72 m^2/g; the total pore volume of BJH is in the range of 0.0028 ml/g–0.0034 ml/g, with an average value of 0.0032 ml/g; the average pore diameter is 20.93 nm. The BET specific surface area of tight sandstone ranges from 2.05 m^2/g to 9.12 m^2/g, with an average value of 5.03 m^2/g; the total pore volume of BJH ranges from 0.0099 ml/g to 0.0269 ml/g, with an average value of 0.0173 ml/g; the average pore diameter is 14.20 nm.

The pore characteristics of shale and tight sandstone in the Shan 2 Member coal measures are similar. Most shale and tight sandstones have BET specific surface areas below 6 m^2/g (**Figure 9A**) and BJH pore volumes within 0.02 ml/g (**Figure 9B**). This shows that the development of pores in the mesopore range of shale and tight sandstone is similar. However, due to the rapid changes in the sedimentary environment of the marine-continental transition facies reservoir, and the different hydrodynamic conditions, the sedimentary particle size and arrangement of the tight sandstone are different, resulting in a large heterogeneity of its own pore structures. On the other hand, the shale sedimentary water body is calm and the sedimentary particle size is uniform, so the pore structure heterogeneity of shale is small.

The BET specific surface area and BJH pore volume of coal in the Shan 2 Member are much smaller than those of shale and tight sandstone. Comparing the relationship between the BET specific surface area and gas content (**Figure 10A**), it is found that the coal rock has a small BET specific surface area and a high gas content, which is not in line with common sense. Using the DR equation, the micropore specific surface area in the coal sample is 121.63 m^2/g, which is much higher than the BET specific surface area of the shale and tight sandstone samples in the coal measure. It further proves that the micropores of coal rocks in coal measure are extremely developed. It can be seen from **Figure 10B** that the high specific surface area of coal is matched with its high gas content. Previous studies have found that the DR specific surface area and DR pore volume of shale are far less than those of coal, and it is also proved that the specific surface area of coal and shale is positively correlated with gas content (Zhou et al., 2019c).

Development Degree and Connectivity of Pores

Scanning electron microscope image analysis shows that clay mineral pores and clay mineral interlayer fractures are mainly

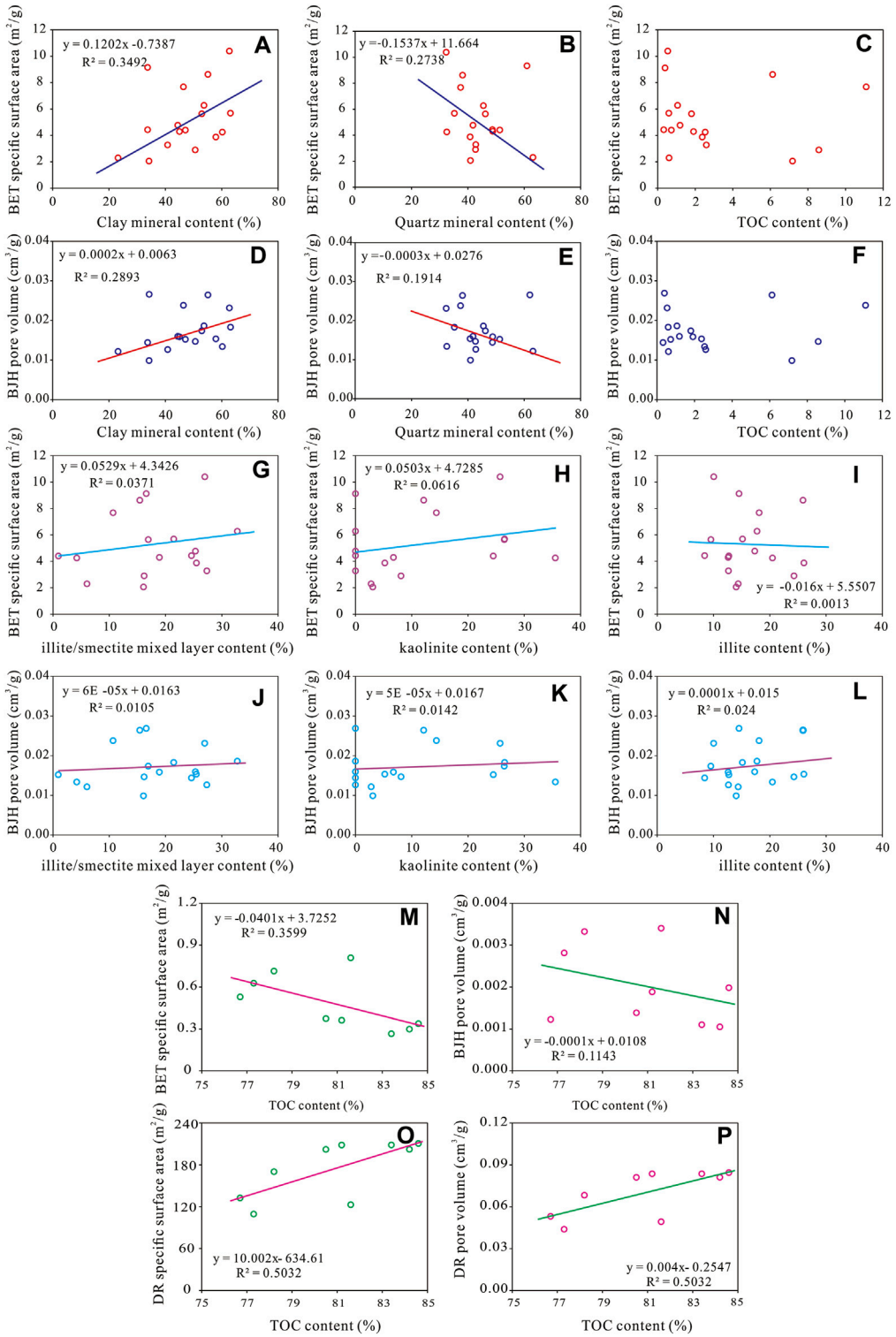

FIGURE 11 | Correlation analysis of factors influencing pore development. **(A–C)** Correlation between clay, quartz, organic carbon and BET specific surface area in shale and tight sandstone. **(D–F)** Correlation between clay, quartz, organic carbon and BJH pore volume in shale and tight sandstone. **(G–I)** Correlation between illite/smectite mixed layer, kaolinite, illite and BET specific surface area in shale and tight sandstone. **(J–L)** Correlation between illite/smectite mixed layer, kaolinite, illite and BJH pore volume in shale and tight sandstone. **(M)** Correlation between TOC and BET specific surface area in coal. **(N)** Correlation between TOC and BJH pore volume in coal. **(O)** Correlation between TOC and DR specific surface area in coal. **(P)** Correlation between TOC and DR pore volume in coal.

developed in the shale and tight sandstone of the Shan 2 Member. Followed by a large number of round or angular intragranular pores and irregular dissolution pores developed in quartz and feldspar minerals. However, organic matter bubble pores do not develop. The pore size distribution analysis shows that the mesopores in the shale and tight sandstone in the coal measures are relatively developed, that is, the pores with the pore diameter of 2–10 nm are developed, and the pores with the pore diameter of 10–50 nm are also relatively developed. Pores with a pore size larger than 50 nm are more developed in tight sandstone than in shale. In addition, shale and tight sandstone in coal measures are mainly composed of clay minerals and quartz minerals, and clay mineral pores and clay mineral interlayer micro-fractures are the main types of pores. Therefore, the content of clay minerals is the main factor affecting the development of pores; the pores of organic matter are hardly developed, and it is speculated that the content of organic matter has little effect on the development of pores.

In order to verify the accuracy of the inference, the clay mineral content, quartz mineral content and TOC content of shale and tight sandstone were linearly fitted with the BET specific surface area and BJH pore volume, respectively. The analysis found that clay mineral content had a good positive correlation with BET specific surface area (**Figure 11A**) and BJH pore volume (**Figure 11D**). This indicates that the increase of clay mineral content makes clay mineral pores and clay mineral interlayer fractures more developed. The content of quartz minerals has a relatively obvious negative correlation with them (**Figures 11B,E**). An increase in the content of quartz minerals resulted in a decrease in the content of clay minerals. Although there are many intragranular pores developed in quartz minerals, the content of intragranular pores cannot be compared with that of clay minerals, so the total number of pores will decrease. There was no obvious correlation between organic carbon content and BET specific surface area (**Figure 11C**) and BJH pore volume (**Figure 11F**). This is because organic pores are not well developed in shale and tight sandstone in coal measures.

In order to clarify which clay mineral is the most important factor affecting the pore development of coal measure shale and tight sandstone, the content of different types of clay minerals is regressed with the specific surface area and volume of mesopores. Because the content of chlorite is low and chlorite is not developed in some samples, chlorite is not analyzed. The results show that none of the three clay minerals has a very obvious effect on pore development. The increase of illite/smectite mixed layer and kaolinite content has a weak promoting effect on BET specific surface area and BJH pore volume (**Figures 11G,H,J,K**), while the illite content has no obvious correlation with mesopore specific surface area (**Figure 11I**), but has a weak positive effect on mesopore volume (**Figure 11L**). Therefore, it is inferred that the pores developed by a single clay mineral do not play a key role in the increase of BET specific surface area and BJH pore volume, but the development of pores of a variety of clay minerals jointly promote the growth of mesoporous reservoir space.

The main component of coal rock in the Shan 2 Member coal measures is organic matter. At the same time, the analysis of pore size distribution shows that there are mainly micropores smaller than 2 nm in the coal rock, while there are few mesopores. Therefore, the content of organic matter is the main factor affecting the development of pores. Due to the limited number of data points, we added the coal samples of Taiyuan Formation and Benxi Formation in the same well, which belong to the coal measure strata of marine-continental transitional. The correlations between BET specific surface area (**Figure 11M**), BJH pore volume (**Figure 11N**), DR specific surface area (**Figure 11O**) and DR pore volume (**Figure 11P**) and organic matter content were compared respectively. It can be clearly seen from the figure that the TOC content of coal samples is negatively correlated with the specific surface area and volume of mesopores, but opposite to the specific surface area and volume of micropores. It shows that the organic matter in coal mainly develops micropores, and the development of micropores has an obvious inhibitory effect on mesopores.

The 2D SEM image can be used to clearly observe the structure of a certain section of the pore, and it can also be used to extract the equivalent circle diameter of the pore and calculate the surface porosity based on image analysis software (Bai et al., 2018; Cheng Z. H. et al., 2018; Jiao et al., 2014). Surface porosity data can only be equivalent to porosity when the formation is homogeneous. However, coal measures have strong heterogeneity, so it is impossible to accurately analyze the pore microstructure using only two-dimensional image analysis data.

A large number of clay mineral pores are developed in the shale and tight sandstone in the target layer. Therefore, areas with well-developed clay mineral pores were selected for section imaging, from a black carbonaceous shale sample (M5-2) and a dark grey fine-grained detrital sandstone sample (M5-7). Furthermore, 3D digital core simulation was performed using Avizo software (Wang et al., 2021) (**Figures 12A,D**), and clay mineral pores were extracted separately for analysis (**Figures 12B,E**). 2878 clay mineral pores were extracted from the coal measure shale sample. The pore diameter is between 6.57 and 504.56 nm, with an average value of 29.92 nm; and 3217 clay mineral pores were extracted from the tight sandstone sample. The pore size is in the range of 7.28–960.97 nm, with an average value of 54.20 nm. This indicates that the clay mineral pores in the tight sandstone sample in the Shan 2 Member coal measures are more developed than those in the shale. In addition, we calculated the porosity of two rock samples, 1.08% for the shale sample and 4.04% for the tight sandstone sample. Tight sandstone can provide more storage space for natural gas.

The pore network models of clay minerals in shale and tight sandstone in the Shan 2 Member are shown in **Figure 12C** and **Figure 12F**. The pore coordination numbers of the extracted samples are shown in **Figure 13**. Pore coordination number refers to the number of throats connecting a single pore to other pores. The greater the frequency of high coordination number, the better the connectivity between pores. The comparison shows that the

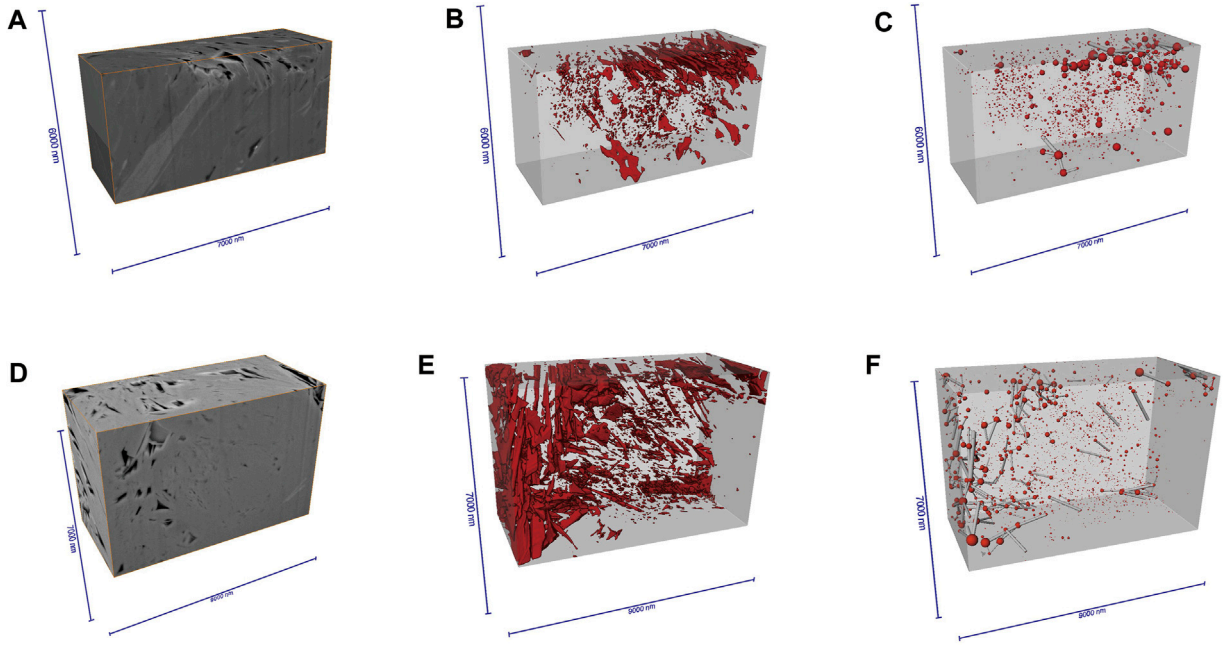

FIGURE 12 | Digital cores of shale and tight sandstone samples. **(A)**, **(B)** and **(C)** M5-2 well, black carbonaceous shale; **(D)**, **(E)** and **(F)** M5-7 well, Dark grey fine-grained detrital sandstone.

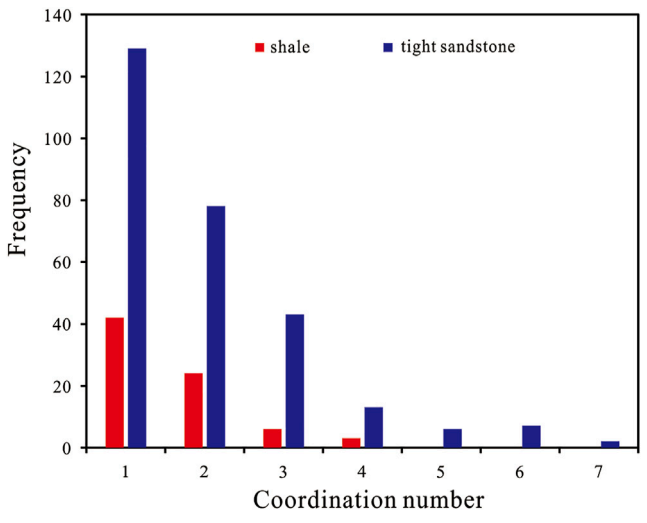

FIGURE 13 | Histograms of frequency distributions of coordination numbers for shale and tight sandstone samples.

coordination numbers of shale and tight sandstone are mainly between 1 and 2, indicating that their pore connectivity is poor. However, the frequency of tight sandstone coordination numbers between 1 and 2 is about three times that of shale, and there are coordination numbers in the range of 3–7. It shows that the connectivity of pores in the tight sandstone in the Shan 2 Member is higher than that in shale, which is beneficial to the flow of natural gas.

Pore Assemblages of Coal Measures

A large number of organic matter nanopores are developed in the marine shale of the Wufeng-Longmaxi Formation in the Sichuan Basin (Zou et al., 2018; Ma et al., 2020a; Ma et al., 2020b). Micropores and mesopores provide the main storage space for adsorbed and free gases. At the same time, most of the free gas occurs in macropores larger than 50 nm. Various scales of organic pores are developed in marine shale (Zou et al., 2017; Dong et al., 2018; Hu et al., 2017), and both free gas and adsorbed gas account for a large proportion. Therefore, marine shale gas wells can achieve high production in the early stage of production, and can maintain stable production for a long time. Considering the whole coal measure of the Shan 2 Member as a gas-bearing whole, the coal rock develops a large number of micropores less than 2 nm, which can absorb a large amount of natural gas. The organic pores in shale and tight sandstone are not well developed, but a large number of mesoporous clay mineral pores and quartz mineral intragranular pores are developed. The pore surface of clay minerals has strong adsorption capacity and can absorb a large amount of natural gas. Intragranular pores of quartz minerals can provide storage space for free gas. There are also a large number of micron-scale clay mineral interlayer micro-fractures and pores in the tight sandstone, which can store a large amount of free gas.

The pore assemblage of the entire coal measure is similar to the pore system of different scales inside the marine shale (**Figure 14**). Sandstone, shale and coal are frequently interbedded in the marine-continental transitional coal measures, and the natural gas generated from shale and coal

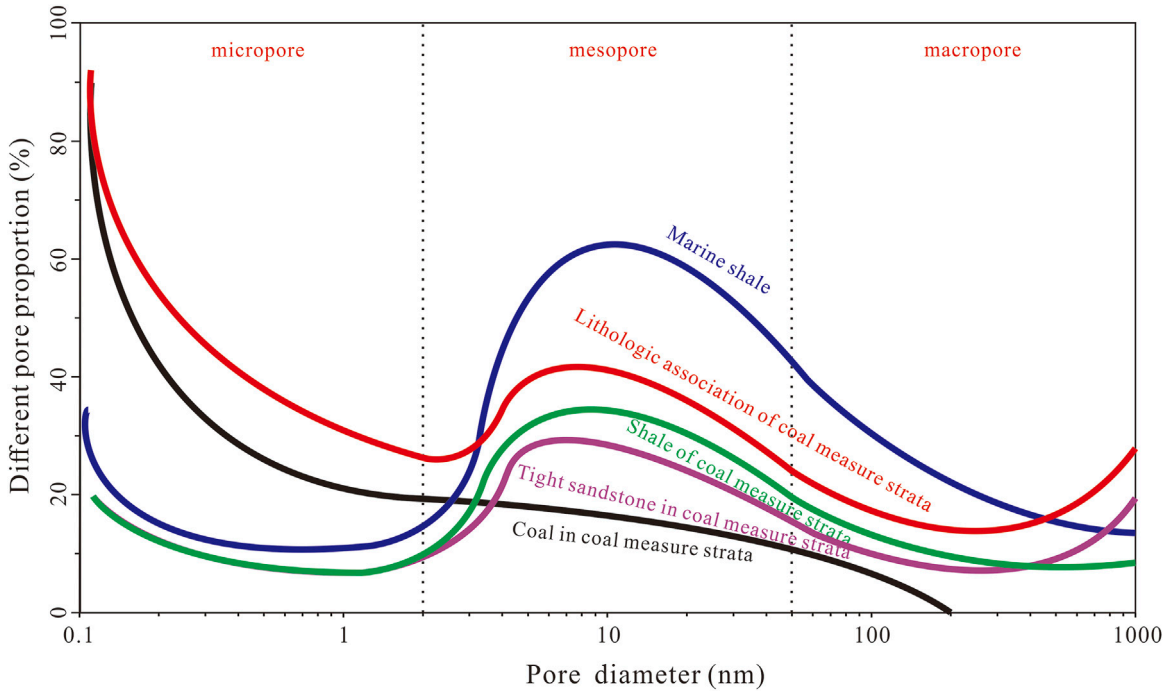

FIGURE 14 | Proportion of pores of different scales in different types of coal measure reservoirs.

can quickly migrate to the nearby tight sandstone through the interlayer fractures of clay minerals, and can also be adsorbed in the pores of clay minerals and coal. Free gas in tight sandstone can achieve high initial production, and adsorbed gas in coal and shale can ensure long-term stable production. Therefore, a better interbed combination of sandstone, shale and coal is expected to achieve high-efficiency three-gas commingled production. Among coal measures, interbedded sandstone and coal assemblages are also a good combination for coal measure gas exploitation, and sandstone and coal assemblages are extremely common.

CONCLUSION

In this study, taking the Shan 2 Member coal measure of the Shanxi Formation in the eastern Ordos Basin as an example, the pore structures of shale, coal rock and tight sandstone were systematically studied based on organic geochemistry, scanning electron microscopy, high-pressure mercury injection, and low-temperature N_2 and CO_2 adsorption experiments. The conclusions are as follows:

1) The microscopic pore structures of different types of reservoirs in Shan 2 Member coal measures are quite different. Shale and tight sandstone mainly develop clay mineral pores at mesopore scale, followed by intragranular pores and dissolution pores developed in quartz and feldspar minerals, while organic pores are rarely developed. A large number of macro-scale clay mineral pores and micro-fractures are developed in tight sandstone, so its pore connectivity is better than that of shale. A large number of micropore-scale organic nano-pores are developed in coal, and the micropore specific surface area of coal is much larger than the mesopore specific surface area of shale and tight sandstone.
2) The content of clay minerals is the main factor affecting the development of pores in coal-measure shale and tight sandstone. The content of clay minerals is significantly positively correlated with BET specific surface area and BJH pore volume, but negatively correlated with quartz mineral content. There was no obvious correlation between TOC content and BET specific surface area and BJH pore volume.
3) Sandstone, shale, and coal are frequently interbedded in coal measure strata. Tight sandstone can provide the main storage space for free gas, and pores in shale and coal can absorb a large amount of natural gas. Sandstone-shale-coal assemblages and sandstone-coal assemblages are the key targets for hydrocarbon exploration in the Shanxi Formation coal measures in the study area.

DATA AVAILABILITY STATEMENT

The original contributions presented in the study are included in the article/Supplementary Materials, further inquiries can be directed to the corresponding author.

AUTHOR CONTRIBUTIONS

JP: experiment, data analysis and interpretation, writing papers WP: provide theoretical guidance ZS: experimental theory and operation guidance WH: provide some information CX: provide some information.

FUNDING

This study was jointly funded by the National Natural Science Foundation of China (Grant No. 2020YFA0710601-01-01) and the science and technology project of CNPC (Grant No. kt2021-06-03).

REFERENCES

Bai, M, G., Xia, X. H., Zhang, C., Meng, F-Y, Yang, Y-R, Zhang, C-H, et al. (2018). Study on Shale Organic Porosity in the Longmaxi Formation, AnYe - 1 Well Using Field Emission-Scanning Electron Microscopy and PerGeos System. *Rock Mineral Analysis* 37 (03), 225–234. doi:10.15898/j.cnki.11-2131/td.201803260030

Barrett, E. P., Joyner, L. G., and Halenda, P. P. (1951). The Determination of Pore Volume and Area Distributions in Porous Substances. I. Computations from Nitrogen Isotherms. *J. Am. Chem. Soc.* 73 (73), 373–380. doi:10.1021/ja01145a126

Brunauer, S., Emmett, P. H., and Teller, E. (1938). Adsorption of Gases in Multimolecular Layers. *J. Am. Chem. Soc.* 60 (60), 309–319. doi:10.1021/ja01269a023

Chen, G. B., Li, T., Yang, L., Zhang, G. H., Li, J. W., and Dong, H. J. (2021). Mechanical Properties and Failure Mechanism of Combined Bodies with Different Coal-Rock Ratios and Combinations. *J. Min. Strata Control Eng.* 3 (2), 023522. doi:10.13532/j.jmsce.cn10-1638/td.20210108.001

Cheng, M., Fu, X. H., Zhang, M., Cheng, W-P, and Qu, L-Z, (2018a). Comparative Study on Porosjity and Permeability in Net Confining Stress of Three Natural Gases in Coal Series Reservoirs in Guxian County, Qinshui Basin. *Nat. Gas. Geosci.* 29 (08), 1163–1171. doi:10.11764/j.issn.1672-1926.2018.05.013

Cheng, Z., Xue, H., Li, W., Lu, S., and Zhou, N, (2018b). Quantitative Characterization of Reservoir Space of Tight Sandsto;nes Based on a Large-View FE-SEM Splicing Technology: a Case Study on the Hetaoyuan Formation in Biyang Sag. *China Pet. Explor.* 23 (05), 79–87. doi:10.3969/j.issn.1672-7703.2018.05.010

Dong, D., Wang, Y., Li, X., Zou, C., Guan, Q., Zhang, C., et al. (2016). Breakthrough and Prospect of Shale Gas Exploration and Development in China. *Nat. Gas. Ind.* 36 (01), 19–32. doi:10.1016/j.ngib.2016.02.002

Dong, D., Shi, Z., Giang, Q., Jiang, S., Zhang, M., Zhang, C., et al. (2018). Progress, Challenges and Prospects of Shale Gas Exploration in the Wufeng-Longmaxi Reservoirs in the Sichuan Basin. *Nat. Gas. Ind.* 38 (04), 67–76. doi:10.1016/j.ngib.2018.04.011

Dubinin, M. M., and Astakhov, V. A. (1971). Description of Adsorption Equilibria of Vapors on Zeolites over Wide Ranges of Temperature and Pressure. *Adv. Chem.* 102, 69–85. doi:10.1021/ba-1971-0102.ch044

Guan, M., Liu, X., Jin, Z., and Lai, J. (2020). The Heterogeneity of Pore Structure in Lacustrine Shales: Insights from Multifractal Analysis Using N2 Adsorption and Mercury Intrusion. *Mar. Petroleum Geol.* 114, 104150. doi:10.1016/j.marpetgeo.2019.104150

He, D. B., Ji, G., and Jiang, Q. F. (2022). Differential Development Technological Measures for High-Water-Cut Tight Sandstone Gas Reservoirs in Western Area of Sulige Gas Field. *Nat. Gas. Ind.* 42 (1), 73–82. doi:10.3787/j.issn.1000-0976.2022.01.007

Hu, H., Hao, F., Lin, J., Lu, Y., Ma, Y., and Li, Q. (2017). Organic Matter-Hosted Pore System in the Wufeng-Longmaxi (O 3 W-S 1 1) Shale, Jiaoshiba Area, Eastern Sichuan Basin, China. *Int. J. Coal Geol.* 173, 40–50. doi:10.1016/j.coal.2017.02.004

Jiao, K., Yao, S. P., Wu, H., Li, M., and Tang, Z (2014). Advances in Characterization of Pore System of Gas Shales. *Geol. J. China Univ.* 20 (01), 151–161. doi:10.16108/j.issn1006-7493.2014.01.009

Li, L., and Li, S. J. (2021). Evolution Rule of Overlying Strata Structure in Repeat Mining of Shallow Close Distance Seams Based on Schwarz Alternating Procedure. *J. Min. Strata Control Eng.* 3 (2), 023515. doi:10.13532/j.jmsce.cn10-1638/td.20210225.001

Liang, B., Shi, Y. S., Sun, W. J., and Liu, Q (2016). Reservoir Forming Characteristics of "The Three Gases" in Coal Measure and the Possibility of Commingling in China. *J. China Coal Soc.* 41 (01), 167–173. doi:10.13225/j.cnki.jccs.2015.9016

Liu, K., Ostadhassan, M., and Kong, L. (2018). Multifractal Characteristics of Longmaxi Shale Pore Structures by N2 Adsorption: A Model Comparison. *J. Petroleum Sci. Eng.* 168, 330–341. doi:10.1016/j.petrol.2018.04.072

Ma, X. H., Xie, J., and Yong, R. (2020a). Geological Characteristics and High Production Control Factors of Shale Gas in Silurian Longmaxi Formation, Southern Sichuan Basin, SW China. *Petroleum Explor. Dev.* 47 (05), 1–15. doi:10.1016/s1876-3804(20)60105-7

Ma, X., Li, X., Liang, F., Wan, Y, Shi, Q, Wang, Y, et al. (2020b). Key Control Factors of Well Performance and Development Strategies Optimization in the Weiyuan Shale Gas Play, Sichuan Basin, SW China. *Petroleum Explor. Dev.* 47 (03), 1–9. doi:10.1016/s1876-3804(20)60076-3

National Energy Board. (2014). *SY/T6940-2013 Shale Gad Content Determination Method[S]*. Beijing: Petroleum Industry Press.

Qin, Y., Wu, J. G., and Shen, J. (2018). Frontier Research of Geological Technology for Coal Measure Gas Joint-Mining. *J. China Coal Soc.*, 43(6): 1504–1516. doi:10.13225/j.cnki.jccs.2018.4034

Qin, Y. (2018). Research Progress of Symbiotic Accumulation of Coal Measure Gas in China. *Nat. Gas. Ind.* 38 (04), 26–36. doi:10.1016/j.ngib.2018.04.013

Qu, X. Y., Chen, X., and Qiu, L. W. (2015). Genesis of Secondary Pore of Quartz Dissolution Type and its Influences on Reservoir: Taking the Tight Sandstone Reservoir in the Upper Paleozoic of Daniudi Gas Field as an Example. *Oil Gas Geol.* 36 (5), 804–813. doi:10.11743/ogg20150512

Sun, Z. P., Wang, Y. L., and Wei, Z. F. (2017). Shale Gas Content and Geochemical Characteristics of Marine-Continental Transitional Shale: A Case from the Shanxi Formation of Ordos Basin. *J. China Univ. Min. Technol.* 46 (04), 859–868. doi:10.13247/j.cnki.jcumt.000663

Wang, J., and Wang, X. L. (2021). Seepage Characteristic and Fracture Development of Protected Seam Caused by Mining Protecting Strata. *J. Min. Strata Control Eng.* 3 (3), 033511. doi:10.13532/j.jmsce.cn10-1638/td.20201215.001

Wang, G., Qin, X., Han, D., and Liu, Z. (2021). Study on Seepage and Deformation Characteristics of Coal Microstructure by 3D Reconstruction of CT Images at High Temperatures. *Int. J. Min. Sci. Technol.* 31, 175–185. doi:10.1016/j.ijmst.2020.11.003

Washburn, E. W. (1921). Note on a Method of Determining the Distribution of Pore Sizes in a Porous Material. *Proc. Natl. Acad. Sci. U. S. A.* 7 (7), 115–116. doi:10.1073/pnas.7.4.115

Wu, J., Tang, D. Z., and Li, S. (2017). Characteristics and Influence Factors of Pore Structure of Coal Reservoirs in the Eastern Margin of Ordos Basin. *Coal Geol. Explor.* 45 (05), 58–65. doi:10.3969/j.issn.1001-1986.2017.05.011

Wu, P., Gao, L. J., and Li, Y. (2022). An Evaluation Method for Shale Gas Potential of Marine-Continent Transitional Facies with Frequent Interbedded Lithology: A Case Study on the Lower Permian Shanxi Formation in Linxing Block of the Ordos Basin. *Nat. Gas. Ind.* 42 (2), 28–39. doi:10.3787/j.issn.1000-0976.2022.02.004

Xi, Z. D., Tian, Z. B., and Tang, S. H. (2016). Characteristics and Main Controlling Factors of Shale Gas Reservoirs in Transitional Facies on the Eastern Margin of Ordos Basin. *Geol. China* 43 (6), 2059–2069. doi:10.12029/gc20160616

Xu, Z., Shi, W., Zhai, G., Peng, N., and Zhang, C. (2020). Study on the Characterization of Pore Structure and Main Controlling Factors of Pore Development in Gas Shale. *J. Nat. Gas Geoscience* 5, 255–271. doi:10.1016/j.jnggs.2020.09.003

Xue, X. H., Yue, X. J., and Wei, W. (2013). Some Suggestions in Shale Gas Content Measuring Process. *Coal Geol. China* 25 (04), 27–29. doi:10.3969/j.issn.1674-1803.2013.04.07

Xue, F., Liu, X. X., and Wang, T. Z. (2021). Research on Anchoring Effect of Jointed Rock Mass Based on 3D Printing and Digital Speckle Technology. *J. Min. Strata Control Eng.* 3 (2), 023013. doi:10.13532/j.jmsce.cn10-1638/td.20201020.001

Yi, T. S., and Gao, W. (2018). Reservoir Formation Characteristics as Well as Co-exploration and Co-mining Orientation of Upper Permian Coalbearing Gas in Liupanshui Coalfield. *J. China Coal Soc.* 43 (06), 1553–1564. doi:10.13225/j.cnki.jccs.2018.4018

Yin, S., and Wu, Z. (2020). Geomechanical Simulation of Low-Order Fracture of Tight Sandstone. *Mar. Petroleum Geol.* 117, 104359–104416. doi:10.1016/j.marpetgeo.2020.104359

Yin, S., Lv, D. W., and Ding, W. L. (2018). New Method for Assessing Microfracture Stress Sensitivity in Tight Sandstone Reservoirs Based on Acoustic Experiments. *Int. J. Geomechanics* 18 (4), 1–16. doi:10.1061/(ASCE)GM.1943-5622.0001100

Yin, S., Xie, R., Wu, Z., Liu, J., and Ding, W. (2019). *In Situ* stress Heterogeneity in a Highly Developed Strike-Slip Fault Zone and its Effect on the Distribution of Tight Gases: A 3D Finite Element Simulation Study. *Mar. Petroleum Geol.* 99 (1), 75–91. doi:10.1016/j.marpetgeo.2018.10.007

Zhang, J. Z., Li, X. Q., and Wang, Y. (2015). Accumulation Conditions and Reservoir Characteristics of Marine-Terrigenous Facies Coal Measures Shale Gas from Longtan Formation in South Sichuan Basin. *J. China Coal Soc.* 40 (08), 1871–1878. doi:10.13225/j.cnki.jccs.2015.0320

Zhang, L., Xiong, Y., Li, Y., Wei, M., Jiang, W., Lei, R., et al. (2017). DFT Modeling of CO 2 and Ar Low-Pressure Adsorption for Accurate Nanopore Structure Characterization in Organic-Rich Shales. *Fuel* 204, 1–11. doi:10.1016/j.fuel.2017.05.046

Zhang, J., Ju, Y., and Zhang, Q. (2019). Low Ecological Environment Damage Technology and Method in Coal Mines. *J. Min. Strata Control Eng.* 1 (1), 013515. doi:10.13532/j.jmsce.cn10-1638/td.2019.02.005

Zhou, S., Yan, G., Xue, H., Guo, W., and Li, X. (2016). 2D and 3D Nanopore Characterization of Gas Shale in Longmaxi Formation Based on FIB-SEM. *Mar. Petroleum Geol.* 73, 174–180. doi:10.1016/j.marpetgeo.2016.02.033

Zhou, G. Z., Xu, S. Y., and Ran, X. J. (2018a). Pore Structure Characteristics and Control Factors of Shale in the Da'anzhai Formation Centrale of Sichuan Basin. *J. Northwest Univ. Nat. Sci. Ed.* 48 (05), 718–728. doi:10.16152/j.cnki.xdxbzr.2018-05-014

Zhou, S., Ning, Y., Wang, H., Liu, H., and Xue, H. (2018b). Investigation of Methane Adsorption Mechanism on Longmaxi Shale by Combining the Micropore Filling and Monolayer Coverage Theories. *Adv. Geo-Energy Res.* 2 (3), 269–281. doi:10.26804/ager.2018.03.05

Zhou, S. W., Wang, H. Y., and Liu, H. (2019a). A New Calculation Method for Lost Gas Content of Shale Based on Arps Production Decline Analysis Model. *Nat. Gas. Geosci.* 30 (01), 102–110. doi:10.11764/j.issn.1672-1926.2018.10.021

Zhou, S., Zhang, D., Wang, H., and Li, X. (2019b). A Modified BET Equation to Investigate Supercritical Methane Adsorption Mechanisms in Shale. *Mar. Petroleum Geol.* 105, 284–292. doi:10.1016/j.marpetgeo.2019.04.036

Zhou, S., Liu, H., Chen, H., Wang, H., Guo, W., Liu, D., et al. (2019c). A Comparative Study of the Nanopore Structure Characteristics of Coals and Longmaxi Shales in China. *Energy Sci. Eng.* 7 (6), 2768–2781. doi:10.1002/ese3.458

Zou, C., Zhao, Q., Dong, D., Yang, Z., Qiu, Z., Liang, F., et al. (2017). Geological Characteristics, Main Challenges and Future Prospect of Shale Gas. *Nat. Gas. Geosci.* 28 (12), 1781–1796. doi:10.1016/j.jnggs.2017.11.002

Zou, C., Yang, Z., He, D., Wei, Y., Li, J., Jia, A., et al. (2018). Theory, Technology and Prospects of Conventional and Unconventional Natural Gas. *Petroleum Explor. Dev.* 45 (04), 1–13. doi:10.1016/s1876-3804(18)30066-1

Conflict of Interest: The authors JP and ZS are employed by PetroChina Research Institute of Petroleum Exploration and Development. The author WP is employed by PetroChina Hangzhou Institute of Petroleum Geology. The author ZS is employed by PetroChina Key Laboratory of Unconventional Oil and Gas. The author WH is employed by Changqing Oilfield, PetroChina. The author CX is employed by China Petroleum Logging Co.LTD.

Publisher's Note: All claims expressed in this article are solely those of the authors and do not necessarily represent those of their affiliated organizations, or those of the publisher, the editors and the reviewers. Any product that may be evaluated in this article, or claim that may be made by its manufacturer, is not guaranteed or endorsed by the publisher.

frontiers | Frontiers in Earth Science

ORIGINAL RESEARCH
published: 16 May 2022
doi: 10.3389/feart.2022.906782

Types and Eruption Patterns of the Carboniferous Volcanic Edifices in the Shixi Area, Junggar Basin

Abulimiti Yiming[1], *Baoli Bian*[1], *Longsong Liu*[1], *Hailong Chen*[1], *Xuanlong Shan*[2], *Ang Li*[2]* *and Jian Yi*[2]

[1]Research Institute of Exploration and Development, Xinjiang Oilfield Company, PetroChina, Karamay, China, [2]College of Earth Sciences, Jilin University, Changchun, China

The types of volcanic edifices and volcanic eruption patterns control the accumulation and distribution of oil and gas. By means of drillings, seismic data, and geochemical analysis, the types and distribution of the Carboniferous volcanic edifices in the Shixi area of Junggar Basin were studied, the formation mechanism of magma was clarified, and the eruption patterns of volcanoes were investigated. The results show that the types of the Carboniferous volcanic edifices in the Shixi area mainly include stratovolcanic edifices, shield basic volcanic edifices, and mound superimposed volcanic edifices. Stratovolcanic edifices and mound superimposed volcanic edifices are developed around the Shixi fault, while single stratovolcanic edifices are developed around the Mobei fault. Shield basic volcanic edifices are only developed in the south of the Shixi area. Vertically, volcanic edifices are mainly developed on the hanging walls of the faults. When the faults develop, the volcanic vents are dendritic, forming mound superimposed volcanic edifices in space. On the plane, there are more volcanic edifices in the Shixi salient than in the Mobei salient. Intermediate-acid volcanic edifices are distributed in beaded shapes along one side of the Shixi fault and the Mobei fault, while basic volcanic edifices are distributed in sheet shapes on both sides of the Dinan fault. In the early Carboniferous, the Shixi area was in the island arc environment under the subduction of the oceanic crust. The basic magma came from the melting of the subduction plate, and the intermediate-acid magma came from the partial melting of the crust. In the late Carboniferous, the extensional environment formed by the retraction of the subduction plate led to the formation of large-scale volcanic eruptions. The extensional environment formed by the retreat of the subduction plate in the later stage resulted in large-scale volcanic eruptions.

Keywords: Junggar Basin, Shixi area, Carboniferous, volcanic edifices, eruption patterns, magma source

OPEN ACCESS

Edited by:
Hu Li,
Southwest Petroleum University, China

Reviewed by:
Jianhua He,
Chengdu University of Technology, China
Saipeng Huang,
University of Barcelona, Spain

***Correspondence:**
Ang Li
liang2020@jlu.edu.cn

Specialty section:
This article was submitted to Structural Geology and Tectonics, a section of the journal Frontiers in Earth Science

Received: *29 March 2022*
Accepted: *13 April 2022*
Published: *16 May 2022*

Citation:
Yiming A, Bian B, Liu L, Chen H, Shan X, Li A and Yi J (2022) Types and Eruption Patterns of the Carboniferous Volcanic Edifices in the Shixi Area, Junggar Basin. Front. Earth Sci. 10:906782. doi: 10.3389/feart.2022.906782

1 INTRODUCTION

Volcanic oil and gas, as an important unconventional source of oil and gas, has effectively alleviated the energy shortage in China and become a realistic replacement field for oil and gas exploration (Chen et al., 2015; Ma et al., 2019). Since the 1980s, China's onshore volcanic oil and gas exploration has entered a stage of rapid development, and the proved geological reserves have been greatly improved. Industrial oil and gas flows have been found in the Carboniferous-Permian volcanic rocks in Songliao Basin, Bohai Bay Basin, Junggar Basin, and Santanghu Basin (Zou et al., 2008; He et al.,

2009; Meng et al., 2021). In 2008, the Xinjiang oilfield discovered the Kelamili gas field with resources of 100 billion cubic meters in the Carboniferous volcanoes in the central Junggar Basin, which opened a new prospect of volcanic oil and gas exploration and development in the Junggar Basin. Previous studies have focused on the tectonic setting, chronological characteristics, and hydrocarbon accumulation mechanism of volcanic rocks in the Junggar Basin, which has played an important supporting role in promoting the exploration and development of volcanic oil and gas reservoirs in the Junggar Basin (Zhang et al., 2015; Huang et al., 2020; You et al., 2021).

The Shixi area is located in the Luliang uplift, and the proven petroleum reserves of the Carboniferous system are 38.94 million tons. The high-quality volcanic reservoirs are mainly volcanic breccia, volcanic agglomerate, and blowhole lava. The volcanic edifice controls the scale and distribution of volcanic lithologies and lithofacies, so it is very important to find out the eruption patterns and distribution laws of volcanic edifices for the exploration and development of volcanic oil and gas. Based on magma properties, lithological associations, volcanic edifice structures, and eruption patterns, previous studies have divided a variety of classification schemes of volcanic edifices. Tang et al. (2012) divided the volcanic edifices of the Yingcheng formation in the southern Songliao basin into rhyolitic lava volcanic edifices, rhyolitic clastic volcanic edifices, composite volcanic edifices, dacite lava volcanic edifices, and andesitic clastic volcanic edifices according to the magma properties and lithology. The Carboniferous volcanic edifices in the Ludong-Wucaiwan area of the Junggar Basin are divided into shield volcanic edifices, stratovolcanic edifices, calderas, lava domes, and cinder cones according to the structure and shape of volcanic edifices (Zhao and Shi, 2012). Huang et al. (2007) further divided conical volcanic edifices into single conical volcanic edifices, multi-conical volcanic edifices, and stacked conical volcanic edifices. At present, the research on volcanic eruption patterns mainly analyzes the relationships between volcanic eruptions and faults. Volcanic eruptions mainly include central eruptions, fissure eruptions, and fissure-central eruptions. The Permian magma erupted in the fissure type along the NE-trending faults in the southern Jianyang area of the Sichuan Basin (Xia et al., 2020). Qu (2019) divided the volcanic eruption patterns of the Yingcheng formation in the Xushen gasfield of the Songliao basin into central eruptions and fissure-central eruptions distributed along faults.

The Carboniferous volcanic rocks in the Shixi area are deeply buried and have undergone multiple stages of tectonic movements and weathering, resulting in hard-to-identify volcanic edifices due to serious deformation. By means of field geological survey, observation and description of drilling cores, and geophysical techniques, researchers have a deep understanding of the lithologies, lithofacies, and identification methods of volcanic edifices in this area (Yin et al., 2019; Dai et al., 2020; Lan et al., 2021; Li H. et al., 2021; Li, 2022). However, the research studies on volcanic edifice types and volcanic eruption patterns are a little insufficient. On the basis of summarizing previous achievements, drillings, seismic data, and geochemical analysis are used in this article to investigate the types and distribution of the Carboniferous volcanic edifices, the formation mechanism of magma, and the eruption patterns of volcanoes in the Shixi area. The results provide a geological basis for increasing oil and gas reserves and production in this area.

2 GEOLOGICAL BACKGROUND

The Shixi area is located in the Shixi salient and Mobei salient in the south of the Luliang uplift in the central Junggar Basin and adjacent to the west sag of the Pen 1 well and Shinan sag, respectively, in the north and south, which has superior oil and gas geological conditions (**Figure 1**). NE-trending and NW-trending faults are developed in this area, of which two NE-trending large basement faults (Shixi fault and Mobei fault) control the development of nose-shaped salients (Ma et al., 2013). In the early Carboniferous, the Luliang island arc was affected by oceanic crust subduction, resulting in large-scale volcanic eruptions and the development of a huge thickness of volcanic rock strata with a buried depth of more than 4,000 m (Wang L. et al., 2020). There are three eruption cycles in the upper Carboniferous in the Shixi area, of which the third cycle includes four stages of volcanic activities. Most wells are drilled in the third cycle, and the lithofacies are mainly characterized by overflow facies and explosive facies, which appear alternately and are dominated by overflow facies. The rock types of overflow facies mainly include basalt, andesite, dacite, and rhyolite. The explosive facies mainly develop volcanic breccia and tuff (**Figure 2**). The upper Carboniferous volcanic reservoirs are connected with hydrocarbon generation sags through basement faults, forming large-scale oil and gas reservoirs.

3 VOLCANIC EDIFICE TYPES

The upper Carboniferous volcanic rocks in the Shixi area are mainly intermediate-acid rocks, and a small number of basic rocks are developed in the south. Based on the lithology, structure, and shape, the volcanic edifices in the study area can be divided into various types. Intermediate-acid lavas are mostly interbedded with pyroclastic rocks to form mound-like stratovolcanic edifices. When volcanic vents are well developed in a certain region, mound superimposed volcanic edifices can be formed. In addition, the basic lava develops into large shield volcanic edifices.

3.1 Stratovolcanic Edifice

A stratovolcanic edifice, an interbedded volcanic structure composed of eruptive pyroclasts and overflow lavas, is formed by periodic central eruptions (Gao et al., 2019; Gong et al., 2019). The lavas of the stratovolcanic edifice in the Shixi area are mainly intermediate-acid lavas such as andesite, dacite, and rhyolite, which play the role of the framework of volcanic edifices (**Figure 3A**). The upper subfacies of lava develop blowhole belts, which can be regarded as favorable reservoirs for oil and gas (**Figure 4**). The eruptive pyroclasts are mainly volcanic

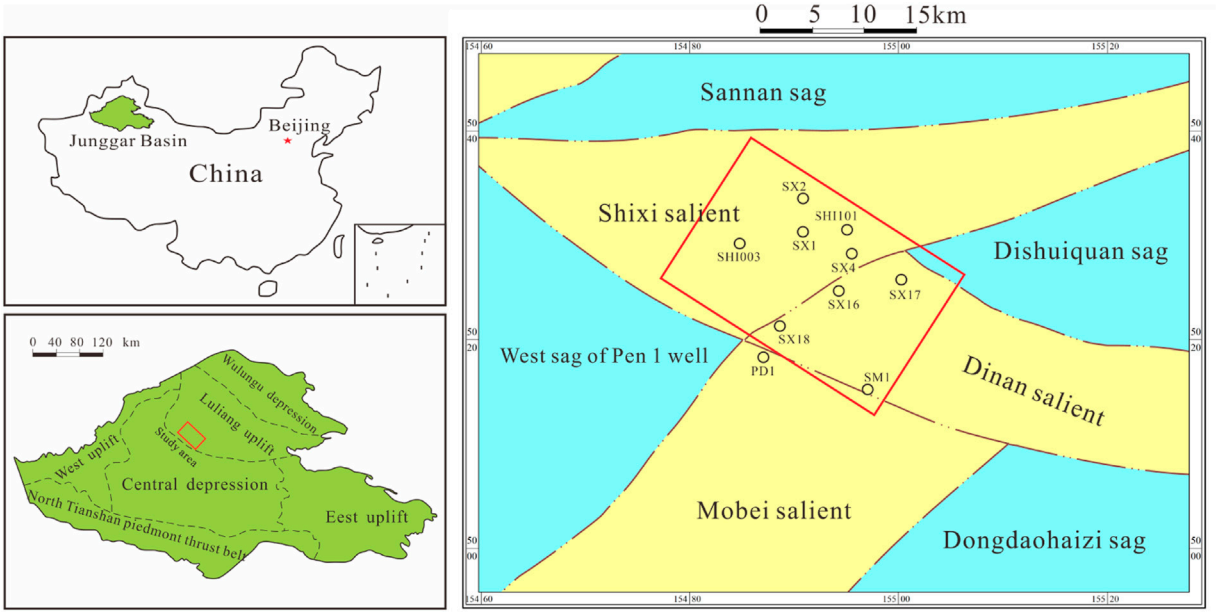

FIGURE 1 | Tectonic unit of the Junggar Basin and studying area.

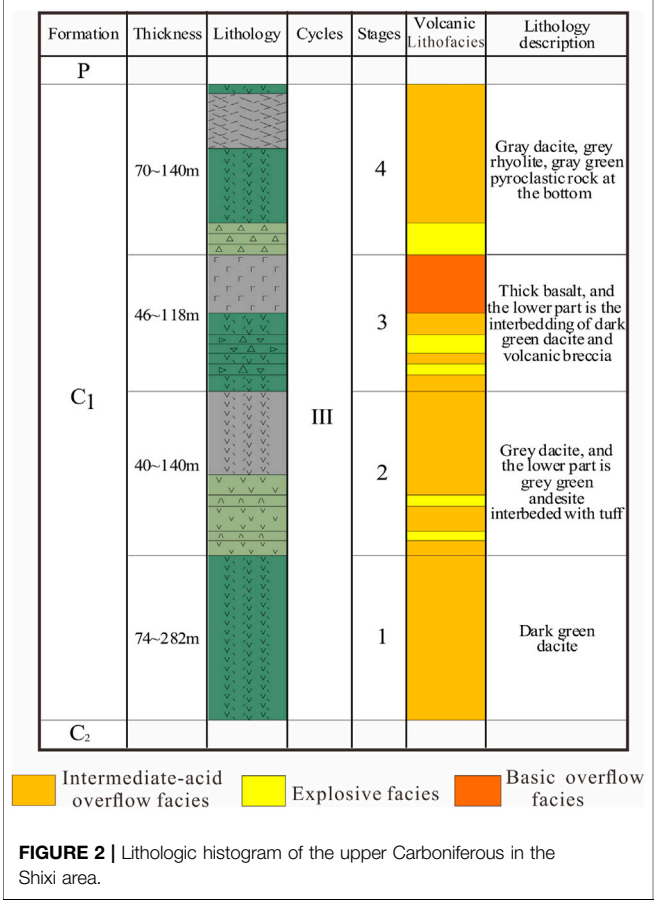

FIGURE 2 | Lithologic histogram of the upper Carboniferous in the Shixi area.

breccia, volcanic agglomerate, and a small amount of tuff. The thickness of lavas and pyroclasts is controlled by the intensity of eruption. Due to the high viscosity of intermediate-acid magma, stratovolcanic edifices usually have a large aspect ratio, showing the shapes of cones or mounds.

The stratovolcanic edifice is the most developed type of volcanic edifice in the Shixi area. In the seismic profile, it shows a mound-shaped seismic reflection shape and strong amplitude chaotic reflection and continuous reflection interbedding in the interior due to the lithology difference. The volcanic vent is located in the middle of the volcanic edifice. The interior of the volcanic vent shows disordered or blank seismic reflection, and the strata on both sides of the volcanic vent are inclined to both sides. Wells SX16 and SX18 in the study area were drilled into the proximal facies of volcanic edifices. The interbedded volcanic breccia with volcanic lava (andesite and dacite) can be seen in the SX16 well, which is a typical stratovolcanic edifice. The upper part of the SX18 well is volcanic breccia, and the lower part is dacite. Due to the influence of formation thickness and drilling depth, the interbedded structure of volcanic breccia and volcanic lava is not shown in the SX18 well.

3.2 Shield Basic Volcanic Edifice

Basic magma is characterized by low viscosity and high fluidity and forms shield volcanic edifices with a small aspect ratio and wide distribution (Hu et al., 2018). Basic magma often presents fissure eruptions along large faults, so basic volcanic edifices are distributed in a belt around the faults. When the magma flow is large or close to the volcanic vent, the shear stress is generated by

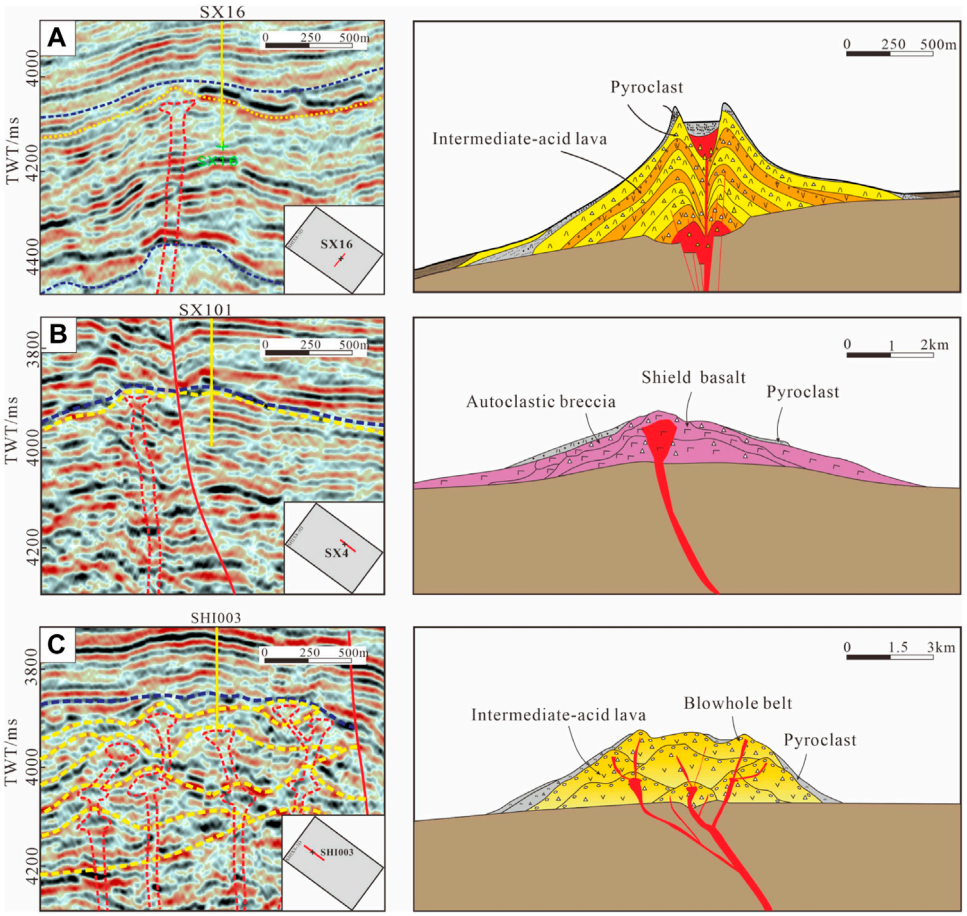

FIGURE 3 | Types and development models of Carboniferous volcanic edifices in the Shixi area.

the velocity difference between the top and bottom due to the fast condensation rate and slow flow speed at the top and the slow condensation rate and fast flow speed at the bottom, which leads to the formation of autoclastic breccia belts at the top of the magma (Luo et al., 2013; Li H. et al., 2020; Tang et al., 2020).

There are few shield basic volcanic edifices in the study area. It is only found that the Dinan fault in the south of the study area is a basic magmatic vent, and basalt is distributed in sheet shapes on both sides of the fault (**Figure 3B**). In the seismic profile, basalt shows a large thickness near the Dinan fault and gradually thinning far away from the fault, and the whole volcanic edifice is a shield. The seismic reflection axis has a strong amplitude, a moderate frequency, and good continuity. Thick basalt was drilled in wells SX101, SX4, and SX17 in the south of the study area. Multiple sets of basaltic autoclastic breccia belts were developed in the SX101 well close to the volcanic vent. However, wells SX4 and SX17 are far away from the volcanic vents, so there are no autoclastic breccia belts, and the lithology of these two wells is thick basalt with blowholes at the top (**Figure 4**).

3.3 Mound Superimposed Volcanic Edifice

When volcanic vents are well developed in a certain region, a composite volcanic edifice with multiple volcanic mounds superimposed on each other can be formed. Volcanic vents are inherited and extend in tree shapes in space. Cryptoexplosive breccia belts are often developed in mound superimposed volcanic edifices (Yi et al., 2011; Wang X. Y. et al., 2020). The mound superposed volcanic edifice in the study area is dominated by intermediate-acid overflow facies, intercalated with explosive facies (**Figure 3C**). The scale of a single volcanic mound is small, but the thickness of a composite volcanic edifice is large. Because the upper subfacies of the overflow facies often developed blowhole belts, there were several sets of blowhole lavas in the vertical direction of this volcanic edifice, which is regarded as a high-quality volcanic reservoir and conducive to the enrichment of oil and gas. In the study area, the mound superposed volcanic edifices mainly occur in the area where faults are developed, and the large basement faults and secondary faults provide channels for the upwelling magma. In the seismic profile, the volcanic mounds are obviously superposed vertically, which has the characteristics of multi-stage volcanic eruptions. Seismic reflection is disordered because of the development of faults and volcanic vents. The interface between the lava and pyroclast is characterized by discontinuous strong reflection. Well SHI003 was drilled into the shallow layer

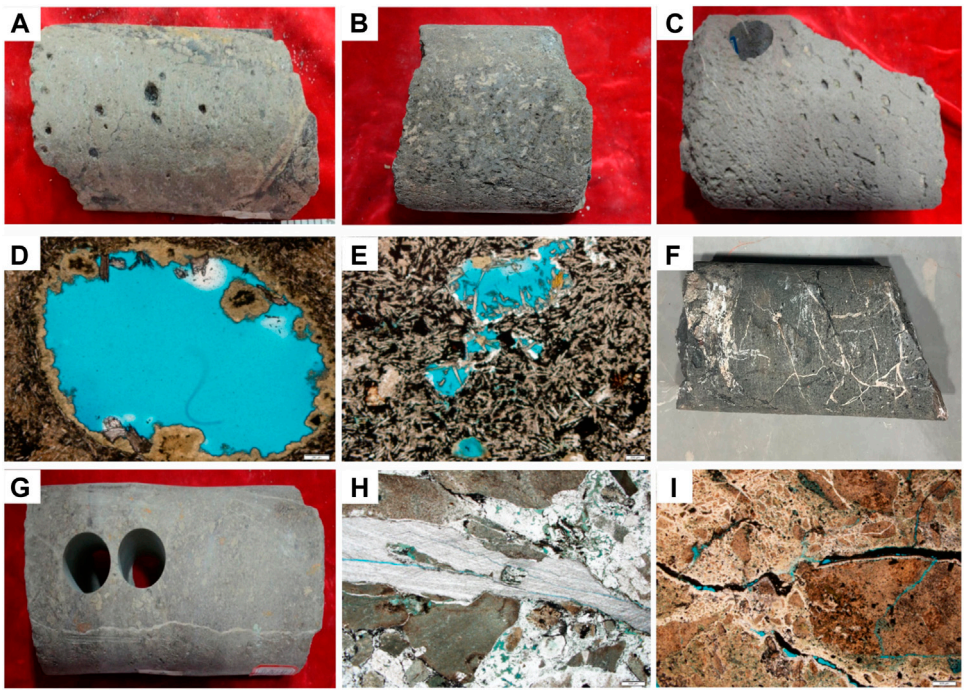

FIGURE 4 | Blowholes in upper subfacies of the lava and fractures in volcanic rocks. **(A, B)** Blowholes in andesite, SX16, 4805.5 m and SX4, 4822.4 m; **(C)** blowholes in basalt, SX4, 4720.2 m; **(D)** microscopic characteristics of blowholes in andesite, SX16, 4805.5 m; **(E)** microscopic characteristics of blowholes in basalt, SX4, 4720.8 m; **(F, G)** volcanic rock fractures, SX18, 5179.6 m and SX3, 4720.8 m; **(H, I)** microscopic characteristics of volcanic rock fractures, SX3, 4721.06 m and SX3, 3867.5 m.

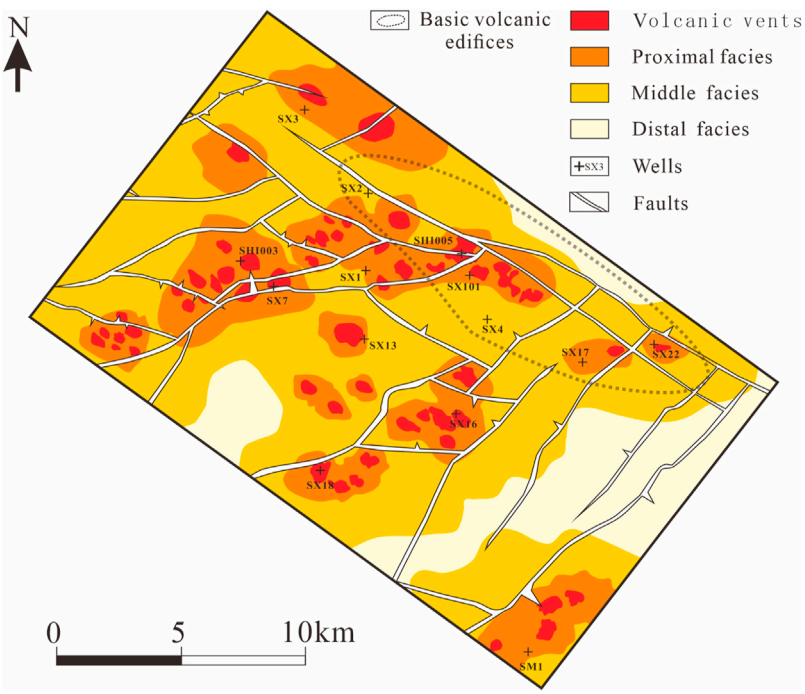

FIGURE 5 | Distribution of upper Carboniferous volcanic edifices in the study area.

of mound superimposed volcanic edifices, and the lithology was a set of thick andesite because this well was far away from the volcanic vents.

4 VOLCANIC EDIFICES AND FAULTS

As the channels for magma, faults control the eruption of volcanoes. The Shixi fault, the Mobei fault, and the Dinan fault are three large basement faults which control the development of nose-shaped salients in the Shixi area and are also channels of magma eruption. Through the interpretation of seismic data, the volcanic edifice distribution of the upper Carboniferous in the Shixi area is shown in **Figure 5**. Faults not only control the types of volcanic edifices but also affect the distribution of volcanic edifices.

4.1 Relationships Between Volcanic Edifice Types and Faults

Volcanic eruptions mainly include central eruptions and fissure eruptions. The intermediate-acid magma with high viscosity upwelled along the Shixi fault and Mobei fault in the way of "squeezing toothpaste" to form the central eruption and accumulated with the pyroclast to form the volcanic mounds. Therefore, the volcanic edifices developed around the Shixi fault and the Mobei fault are stratovolcanic edifices and mound superimposed volcanic edifices. In addition, the development degree of fault controls the types of volcanic edifices in the study area. The structure conditions of the Shixi salient in the west of the Shixi area are relatively complicated. The development degree of NW-trending faults in the Shixi salient is significantly higher than that of the Mobei salient, and the NW-trending faults are intersected with the Shixi faults, resulting in the development of secondary faults near the basement faults, which are conducive to the formation of volcanic vents (Li, 2019). Therefore, the mound superimposed volcanic edifices are well developed in the Shixi salient, while there is no such volcanic edifice in the Mobei salient and there are mostly single stratovolcanic edifices. In addition, the scale of a mound superimposed volcanic edifice formed by multi-stage eruptions is larger than that of a single stratovolcanic edifice. Fractures in volcanic rocks are well developed in the areas where faults are well developed and complex (**Figure 4**). The viscosity of basic magma is less than that of intermediate-acid magma, which makes it easier to form fissure eruptions along the fault. The Dinan fault is a banded volcanic vent with basic magma overflow, and the shield basic volcanic edifice is distributed in the NW direction along the Dinan fault. The distribution of basic volcanic edifices on the plane is significantly larger than that of stratovolcanic edifices and mound superimposed volcanic edifices.

4.2 Relationships Between Volcanic Edifice Distribution and Faults

Deep magma usually erupts, overflows, or emplaces along weak zones of the strata, and these weak zones are the basement faults and associated faults with long-term succession activities (Shan et al., 2011; Lu et al., 2019; Fan et al., 2020; Lan et al., 2021; Meng et al., 2021). The Shixi fault, Mobei fault, and Dinan fault, as three large basement faults in the Shixi area, are the main magma channels and control the distribution of volcanic edifices. Vertically, the volcanic edifice is mainly developed on the hanging walls of the faults (Shixi salient and Mobei salient), which results in the thickness of volcanic rocks on the salients being obviously larger than that on the sags. After rising along the main channel, the intermediate-acid magma erupted from the surface by the secondary faults or strata melt-through. When the secondary faults are well developed near the basement fault, dendritic volcanic vents are easily formed, and multiple volcanic edifices are superimposed in space. Conversely, when secondary faults are not developed, a single or small number of volcanic edifices are formed (**Figure 6**). In the plane, intermediate-acid volcanic edifices are distributed in beads along one side of the Shixi fault and Mobei fault (**Figure 7**). The number of volcanic edifices in the Shixi salient is more than that in the Mobei salient. The proximal facies and middle facies of volcanic edifices are mainly developed in the Shixi salient, while there are proximal facies, middle facies, and distal facies of volcanic edifices in the Mobei salient. Some small faults such as the east fault of well SX17 and the west fault of the SM1 well do not cut deep into the basement and are far away from the Mobei fault, so these faults cannot become volcanic vents. It can also be seen from the distribution map of volcanic edifices that the volcanic edifices around small faults are not developed. In general, the development of volcanic edifices in the west of the Shixi area is significantly stronger than that in the east, and the volcanic edifices between the two salients are not developed. The basic volcanic edifices are distributed in sheet shapes on both sides of the Dinan fault. There are few intermediate-acid volcanic edifices near the Dinan fault, and only a few volcanic vents are developed at the intersection with the Shixi fault. Therefore, according to the relationship between volcanic edifices and faults, the Shixi area can be divided into three volcanic belts: the Shixi fault intermediate-acid volcanic belt, Mobei fault intermediate-acid volcanic belt, and Dinan fault basic volcanic belt.

5 VOLCANIC ERUPTION

5.1 Magma Formation Mechanism

In order to study the formation and evolution of magma in the Shixi area, the volcanic rocks were systematically sampled, and the major and trace element analysis and Sr-Nb isotope tests were carried out. In the Total Alkali and Silica (TAS) diagram and Nb/Y-Zr/TiO_2 diagram, most samples are in the andesite and dacite area, two samples are in the rhyolite area, and one sample is in the basalt area (**Figure 8**). In this study, whole-rock geochemical data (**Figure 9**) and Sr-Nd isotopic data (**Figure 10**) were used to discuss the magma formation mechanism of the three types of volcanic rocks with different geochemical properties.

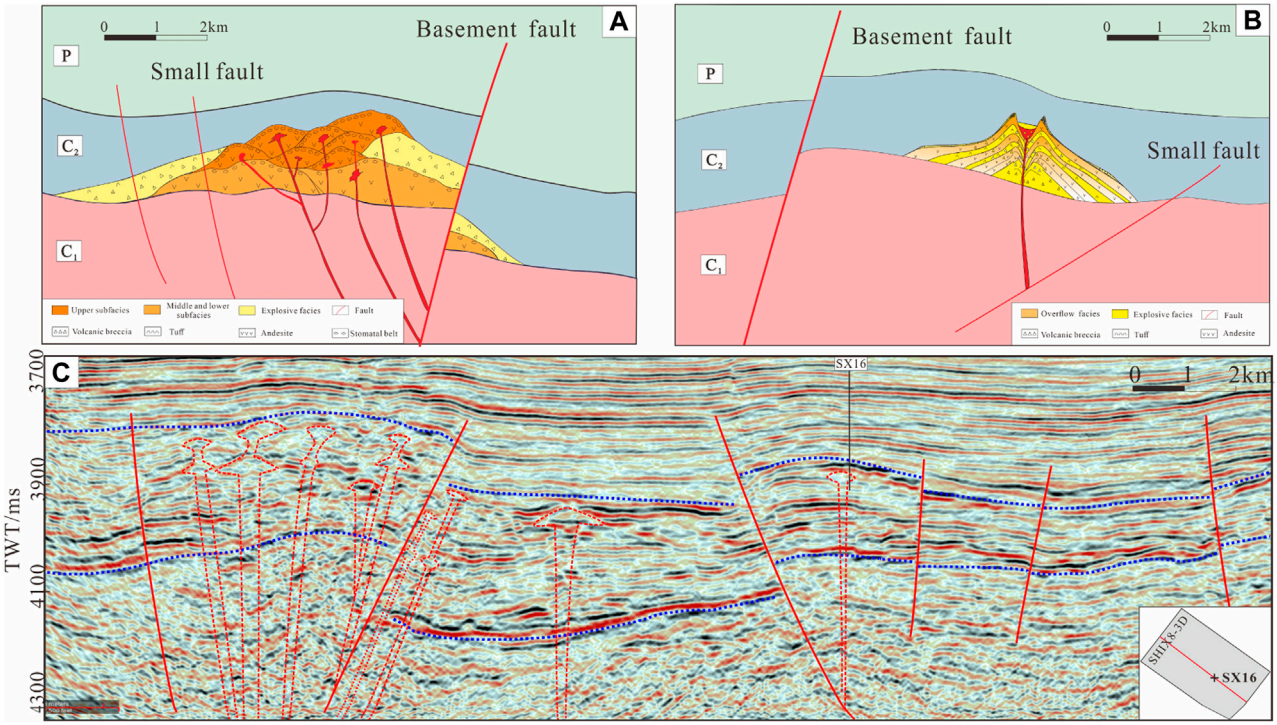

FIGURE 6 | Relationship between faults and volcanic edifices in the Shixi area. **(A)** When faults develop, mound superimposed volcanic edifices are developed; **(B)** when faults are not developed, single stratovolcanic edifices are developed; **(C)** seismic profile through well SX16.

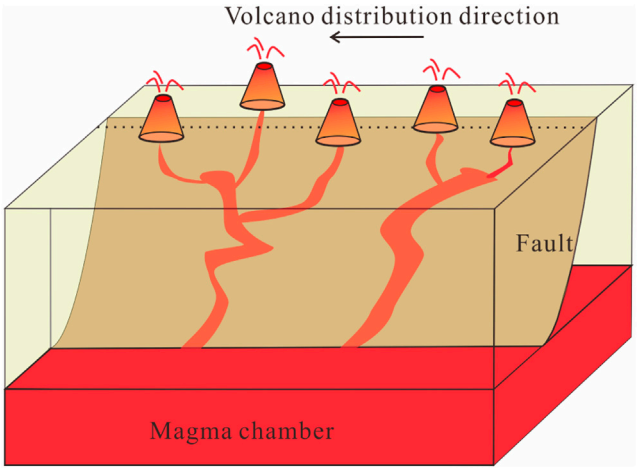

FIGURE 7 | Beaded distribution of intermediate-acid volcanic edifices along faults.

5.1.1 Formation Mechanism of Basic Magma

The Mg# (0.443) of basalt samples is relatively low, which reflects that the basalt underwent a very weak degree of fractional crystallization. At the same time, these samples have the characteristics of a low Th/Ce value (0.038) and a low Th/La value (0.080), indicating that the assimilation and contamination of the continental crust during the evolution of basic magma are very little. The low $(^{87}Sr/^{86}Sr)_i$ value (0.70448) and the high εNd(t) value (6.31) of the basic samples also prove that the evolution of the basalt has nothing to do with the contamination of the crust. The isotopic composition indicates that the magma originated from the depleted mantle. There are no obvious negative anomalies of Nb and Ta, and the trace element composition model is similar to that of oceanic island basalt (OIB). Combined with the characteristics of $(Th/Nb)_N$ less than 1 and the depleted Sr-Nd isotope, it is speculated that the basic magma originated from the asthenosphere mantle (Aldanmaz et al., 2000; Tamura et al., 2014; Li et al., 2019; Zhu et al., 2019; Li S. B. et al., 2021).

5.1.2 Formation Mechanism of Intermediate Magma

Andesite and dacite samples are characterized by low MgO contents (0.314–3.14), indicating that they are not caused by partial melting of subduction plate materials from the enriched mantle. There are relatively few basic volcanic rocks in the upper Carboniferous in the Shixi area, and their petrographic characteristics do not contain ferromagnetic inclusions, so it is ruled out that the intermediate magma came from the mixing of basic magma and acid magma. The La/Sm values of the samples increase gradually with the increase of La contents, reflecting that the magma was derived from partial melting rather than fractional crystallization (Geng et al., 2011; Safonova et al., 2015; Li L. et al., 2020). The samples are enriched in large ion

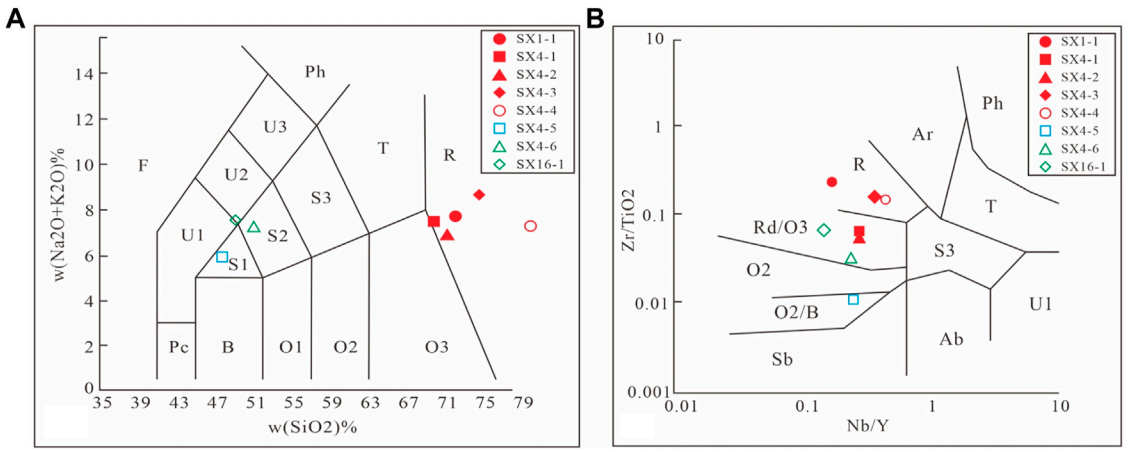

FIGURE 8 | TAS diagram **(A)** and Nb/Y-Zr/TiO_2 lithology classification diagram **(B)** of Carboniferous volcanic rocks in the Shixi area (Pc-Picrite; B-Basalt; O1-Basaltic Andesite; O2-Andesite; O3-Dacite; R-Rhyolite; S1-Trachybasalt; S2-Basaltic Trachyandesite; S3-Trachyandesite; T-Trachyte and Trachydacite; F-Feldspathoidite; U1-Tephrite and Basanite; U2-Phonolitic Tephrite; U3-Tephritic Phonolite; Ph-Phonolite; Ab-Alkaline basalt; Ar-Alkaline rhyolite; and Sb-Subalkaline basalt).

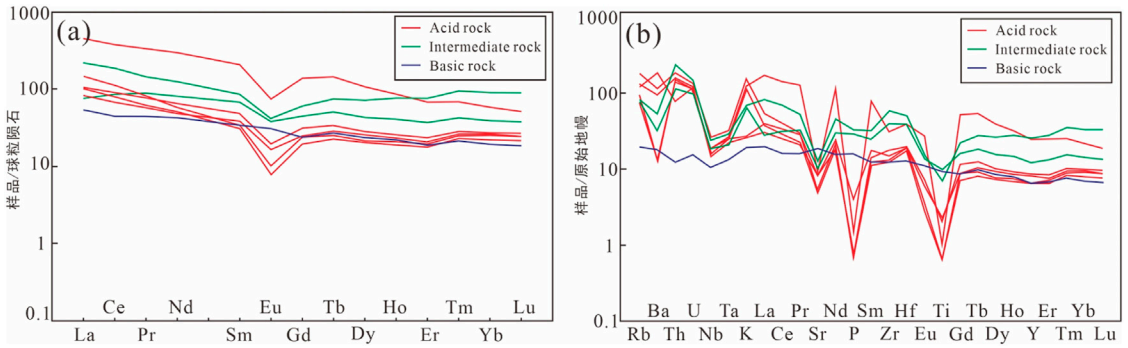

FIGURE 9 | Chondrite-normalized REE patterns **(A)** and primitive mantle-normalized trace element patterns **(B)** for the Carboniferous volcanic rocks in the Shixi area.

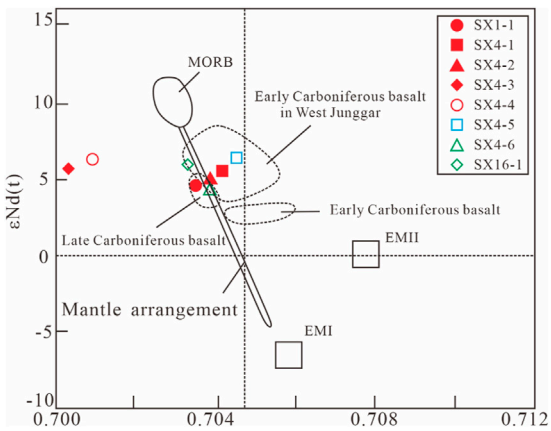

FIGURE 10 | Sr-Nd isotopic characteristics of Carboniferous volcanic rocks in the Shixi area.

lithophile elements and depleted in high-field-strength elements. In addition, the samples have obvious negative Nb and Ta anomalies, positive Pb anomalies, no obvious fractionation of heavy rare earth elements, and high εNd(t) values, which also indicates that the intermediate magma came from the partial melting of the young basic lower crust.

5.1.3 Formation Mechanism of Acid Magma

On the basis of excluding the origin of basic magma fractional crystallization, the low Sr/Y values of acid volcanic rocks indicate that they are not derived from the enriched lithospheric mantle. Low Mg# values (0.19–0.27), low Nb contents (9.98–17.8 ppm), low Nb/La values (0.1648–0.5207), and low $(Ce/Pb)_N$ values (0.088–0.43) indicate that the acid magma is the product of crust melting. The high εNd(t) values (4.87–5.95) indicate that acid magma originated from the young lower crust. Therefore, the acid magma in the Shixi area was formed by partial melting of the young lower crust.

5.2 Volcanic Eruption Pattern

The Carboniferous Junggar basin was formed and developed in the process of subduction and closing of the Paleo-Asian Ocean (Zheng M. L. et al., 2019; Zheng Z. H. et al., 2019; Hou et al., 2020; Xu and Gao, 2020; Wang et al., 2021). In the early Early Carboniferous, the Junggar Basin inherited the Devonian oceanic crust subduction pattern, which was characterized by several ocean basins separated by island arcs. The Kalamiri Ocean was subducted toward the Luliang island arc, and the subduction plate dehydrated and melted to form basic magma. Basic magma rose into the mantle wedge and was retained at the bottom of the crust to form basic magma chambers. In addition, basic magma baked the overlying crust causing partial melting of crustal materials, which then rose to the shallow layer and accumulated into intermediate-acid magma chambers. In the late Early Carboniferous, the retreat of the subduction plate formed an extensional environment in the Luliang island arc, resulting in the development of rifting in the island arc (Tang et al., 2015; He et al., 2018; Yin and Ding, 2019). At this point, volcanic activities began to increase. In the early to middle of the Late Carboniferous, the further retreat of the subduction plate prompted the reactivation of the previous faults, resulting in more intense volcanic activities than in the Early Carboniferous. Intermediate-acid magma upwelled along the Shixi fault and Mobei fault and then formed central eruptions along the secondary faults or melt-through strata, and beaded volcanic edifices along the strike of the faults were developed on the hanging walls of the faults. Affected by fault development, the Shixi fault volcanic belt developed intermediate-acid stratovolcanic edifices and mound superimposed volcanic edifices, while the Mobei fault volcanic belt was dominated by stratovolcanic edifices. The Dinan fault connected with the basic magma chambers. As a banded volcanic vent, the Dinan fault led to fissure eruption, forming widely distributed shield basic volcanic edifices.

6 CONCLUSION

1) The types of Carboniferous volcanic edifices in the Shixi area of the Junggar Basin mainly include stratovolcanic edifices, shield basic volcanic edifices, and mound superimposed volcanic edifices. Stratovolcanic edifices are the most developed in the Shixi area, shield basic volcanic edifices are the least and only distributed in the south of the Shixi area, and the autoclastic breccia belts are developed near the volcanic vents. The volcanic vents extend in tree shapes in space and are well developed in the mound superimposed volcanic edifices. Moreover, cryptoexplosive breccia belts and blowhole lavas are well developed in mound superimposed volcanic edifices.

2) The intermediate-acid magma mainly erupted in a center type along the Shixi and Mobei faults in the study area. The faults control the types and numbers of volcanic edifices. The types of volcanic edifices around the Shixi fault are mainly stratovolcanic edifices and mound superimposed volcanic edifices, while mound superimposed volcanic edifices around the Mobei fault are not developed; only stratovolcanic edifices are developed. The number of volcanic edifices in the Shixi salient is more than that of the Mobei salient. The volcanic edifices are mainly developed on the hanging walls of the faults, which leads to the thicker volcanic strata on the hanging walls. The intermediate-acid volcanic edifices are beaded along one side of the Shixi fault and Mobei fault. The shield basic volcanic edifices are distributed in the northwest direction along both sides of the Dinan fault.

3) The Junggar Basin inherited the oceanic crust subduction pattern of the Devonian, which was characterized by several ocean basins separated by island arcs. The subduction plate dehydrated and melted to form basic magma, and basic magma rose into the mantle wedge and retained at the bottom of the crust to form basic magma chambers. The basic magma baked the overlying crust, causing partial melting of the crustal materials, which then rose to the shallow layer and accumulated into intermediate-acid magma chambers. In the late Early Carboniferous, the extensional environment caused by the retreat of the subduction plate resulted in the development of a large number of faults in the Shixi area. The late tectonic movements reactivated the basement faults, resulting in large-scale volcanic eruptions.

DATA AVAILABILITY STATEMENT

The raw data supporting the conclusions of this article will be made available by the authors, without undue reservation.

AUTHOR CONTRIBUTIONS

AY and AL are responsible for the idea, writing, and revision of this article. BB, LL, and HC are responsible for the data analysis and drawing. XS and JY are responsible for reviewing and editing.

FUNDING

This article is supported by the 14th Five-year Major Project of CNPC “Continental Deep and Ultra-Deep Oil and Gas Enrichment Law and Exploration Evaluation Research” (2021DJ0206).

REFERENCES

Aldanmaz, E., Pearce, J. A., Thirlwall, M. F., and Mitchell, J. G. (2000). Petrogenetic Evolution of Late Cenozoic, Post-collision Volcanism in Western Anatolia, Turkey. *J. Volcanol. Geotherm. Res.* 102, 67–95. doi:10.1016/S0377-0273(00)00182-7

Chen, S. M. (2015). Hydrocarbon Migration and Accumulation Mechanism of Volcanic Reservoirs in Eastern and Western China. *Nat. Gas. Ind.* 35 (4), 16–24. doi:10.3787/j.issn.1000-0976.2015.04.003

Dai, J. J., Luo, J. L., He, X. Y., Ma, S. W., Wang, C., and Xu, X. L. (2020). Oil and Gas Characteristics and Petrogenetic Evolution of the Carboniferous Volcanic Lava in Xiquan Area, Junggar Basin. *Geol. China* 47 (3), 742–754. doi:10.12029/gc20200313

Fan, C., Li, H., Qin, Q., He, S., and Zhong, C. (2020). Geological Conditions and Exploration Potential of Shale Gas Reservoir in Wufeng and Longmaxi Formation of Southeastern Sichuan Basin, China. *J. Pet. Sci. Eng.* 191, 107138. doi:10.1016/j.petrol.2020.107138

Gao, F. (2019). Use of Numerical Modeling for Analyzing Rock Mechanic Problems in Underground Coal Mine Practices. *J. Min. Strata Control Eng.* 1 (1), 013004. doi:10.13532/j.jmsce.cn10-1638/td.2019.02.009

Geng, H., Sun, M., Yuan, C., Zhao, G., and Xiao, W. (2011). Geochemical and Geochronological Study of Early Carboniferous Volcanic Rocks from the West Junggar: Petrogenesis and Tectonic Implications. *J. Asian Earth Sci.* 42, 854–866. doi:10.1016/j.jseaes.2011.01.006

Gong, W. C., Zhang, X. G., Shi, C., Duan, X. X., and Liu, J. S. (2019). Seismic Identification and Analysis of the Volcanic Mechanism of the Huoshiling Formation in the Yingshan Sag, Northern Songliao Basin. *Contemp. Chem. Ind.* 48 (4), 791–794. doi:10.13840/j.cnki.cn21-1457/tq.2019.04.034

He, D. F., Zhang, L., Wu, S. T., Li, D., and Zhen, Y. (2018). Tectonic Evolution Stages and Features of the Junggar Basin. *Oil Gas Geol.* 39 (5), 845–848. doi:10.11743/ogg20180501

He, D., Li, J. H., Liu, S. J., and Han, L. (2009). Research on the Types of Volcanic Structures and Eruption Patterns of the Lower Cretaceous Yingcheng Formation in the Xujiaweizi Fault Depression in the Northern Songliao Basin. *Acta Petrol. Sin.* 25 (3), 659–666. doi:10.1007/s12182-012-0227-4

Hou, E., Cong, T., and Xie, X. (2020). Ground Surface Fracture Development Characteristics of Shallow Double Coal Seam Staggered Mining Based on Particle Flow. *J. Min. Strata Control Eng.* 2 (1), 013521. doi:10.13532/j.jmsce.cn10-1638/td.2020.01.002

Hu, J., Wang, L. W., Zhang, S. J., Pi, X., Chi, H. Z., Xing, C., et al. (2018). Establishment Method and Application of Geological Model of Volcanic Institutions in the Basin: Taking Yingcheng Formation Volcanic Rocks in Southern Songliao Basin as an Example. *J. Xi'an Shiyou Univ. (Natural Science Edition)* 33 (6), 18–26. doi:10.3969/j.issn.1673-064X.2018.06.003

Huang, W. L., Wang, P. J., Feng, Z. Q., Shao, R., Guo, Z. H., and Xu, Z. J. (2007). Analogy of Volcanic Edifices between Modern Volcanoes and Ancient Remnant Volcanoes in Songliao Basin. *J. Jilin Univ. (Earth Science Edition)* 37 (1), 65–72. doi:10.13278/j.cnki.jjuese.2007.01.011

Huang, Y., Liang, S. Y., Jia, C. M., Gu, X. P., Mao, H. B., and Fu, X. P. (2020). Identification of Palaeovolcanic Structures and Practice of Oil and Gas Exploration in the Reconstruction of the Junggar Basin. *Nat. Gas. Ind.* 40 (3), 30–37. doi:10.3787/j.issn.1000-0976.2020.03.004

Lan, S. R., Song, D. Z., Li, Z. L., and Liu, Y. (2021). Experimental Study on Acoustic Emission Characteristics of Fault Slip Process Based on Damage Factor. *J. Min. Strata Control Eng.* 3 (3), 033024. doi:10.13532/j.jmsce.cn10-1638/td.20210510.002

Li, H., Li, J., Xu, X. Y., Yang, G. X., Wang, Z. P., Xu, Q., et al. (2021). Petrogenesis and Tectonic Implications of Alkali Basalts in Kalamaili Area, East Junggar, Xinjiang (NW China): Constraints from Petrology, Geochronology and Geochemistry. *Acta Geol. Sin.* 95 (11), 3282–3300. doi:10.19762/j.cnki.dizhixuebao.2020281

Li, H., Qin, Q., Zhang, B., Ge, X., Hu, X., Fan, C., et al. (2020a). Tectonic Fracture Formation and Distribution in Ultradeep Marine Carbonate Gas Reservoirs: A Case Study of the Maokou Formation in the Jiulongshan Gas Field, Sichuan Basin, Southwest China. *Energy Fuels* 34 (11), 14132–14146. doi:10.1021/acs.energyfuels.0c03327

Li, H. (2022). Research Progress on Evaluation Methods and Factors Influencing Shale Brittleness: A Review. *Energy Rep.* 8, 4344–4358. doi:10.1016/j.egyr.2022.03.120

Li, H., Tang, H., Qin, Q., Zhou, J., Qin, Z., Fan, C., et al. (2019). Characteristics, Formation Periods and Genetic Mechanisms of Tectonic Fractures in the Tight Gas Sandstones Reservoir: A Case Study of Xujiahe Formation in YB Area, Sichuan Basin, China. *J. Pet. Sci. Eng.* 178, 723–735. doi:10.1016/j.petrol.2019.04.007

Li, L., Zhang, X., and Deng, H. (2020b). Mechanical Properties and Energy Evolution of Sandstone Subjected to Uniaxial Compression with Different Loading Rates. *J. Min. Strata Control Eng.* 2 (4), 043037. doi:10.13532/j.jmsce.cn10-1638/td.20200407.001

Li, S. B., Guo, X. G., Zheng, M. L., Wang, Z. S., and Liu, X. L. (2021). Lithology Identification of Carboniferous Volcanic Rocks in Xiquan Area, Eastern Junggar Basin. *Lithol. Reserv.* 33 (1), 258–266. doi:10.12108/yxyqc.20210124

Li, Z. (2019). *Study on Reservoir Characteristics of Carboniferous Volcanic Weathering Crust in Shixi Oilfield, Central Junggar Basin*. Chengdu: Southwest Petroleum University, 22–36. doi:10.27420/d.cnki.gxsyc.2019.000185

Lu, J. L., Zuo, Z. X., Shi, Z., Dong, X., Wu, Q., and Wu, Q. J. (2019). Characteristics of Permian Volcanism and Natural Gas Exploration Potential in Western Sichuan Basin. *Nat. Gas. Ind.* 39 (2), 46–53. doi:10.3787/j.issn.1000-0976.2019.02.006

Luo, B., Xia, M. L., Wang, H., Fan, Y., Xu, L., Liu, R., et al. (2013). Hydrocarbon Accumulation Conditions of Permian Volcanic Gas Reservoirs in the Western Sichuan Basin. *Nat. Gas. Ind.* 39 (2), 9–16. doi:10.3787/j,issn.1000-0976.2019.02.002

Ma, L. M., Li, Z. P., Lin, C. Y., Dong, B., Bu, L. X., and Cui, L. (2013). Jurassic Structural Style and its Oil Control Rule in Dzungar Basin Field. *Petroleum Geol. Xinjiang* 34 (1), 27–29. doi:10.1080/10916466.2019.1702688

Ma, X. H., Yang, Y., Zhang, J., and Xie, J. R. (2019). A Major Discovery in Permian Volcanic Rock Gas Reservoir Explorationin the Sichuan Basin and its Implications. *Nat. Gas. Ind.* 39 (2), 1–8. doi:10.1016/j.ngib.2019.02.001

Meng, F. C., Zhou, L. H., Wei, J. Y., Cui, Y., Lou, D., Chen, S. Y., et al. (2021). Characteristics and Formation Mechanism of Mesozoic Volcanic Reservoirsfrom Buried Hills in Huanghua Depression, Bohai Bay Basin. *J. Central South Univ. Sci. Technol.* 52 (3), 859–875. doi:10.11817/j.issn.1672-7207.2021.03.019

Qu, Y. (2019). Structural Fractures and Geostress in Volcanic Rocks of Yingcheng Formation, D Block, Xushen Gasfield, Songliao Basin. *Nat. Gas Explor. Dev.* 42 (1), 28–34. doi:10.12055/gaskk.issn.1673-3177.2019.01.005

Safonova, I., Kojima, S., Nakae, S., Romer, R. L., Seltmann, R., Sano, H., et al. (2015). Oceanic Island Basalts in Accretionary Complexes of SW Japan: Tectonic and Petrogenetic Implications. *J. Asian Earth Sci.* 113, 508–523. doi:10.1016/j.jseaes.2014.09.015

Shan, X. L., Chen, Y. P., Tang, L. M., and Yi, J. (2011). Comprehensive Evaluation Method for Volcanic Rock Reservoirs and its Application: Taking Songnan Gas Field for Example. *J. Shandong Univ. Sci. Technol.* 30 (3), 1–6. doi:10.16452/j.cnki.sdkjzk.2011.03.001

Tamura, Y., Ishizuka, O., Stern, R. J., Nichols, A. R. L., Kawabata, H., Hirahara, Y., et al. (2014). Mission Immiscible: Distinct Subduction Components Generate Two Primary Magmas at Pagan Volcano, Mariana Arc. *J. Petrology* 55 (1), 63–101. doi:10.1093/petrology/egt061

Tang, H. F., Wang, P. J., Bian, W. H., Huang, Y. L., Gao, Y. F., and Dai, X. J. (2020). Review of Geological Research on Volcanic Rock Reservoirs. *Chin. J. Petroleum* 32 (5), 1744–1773. doi:10.7623/syxb202012026

Tang, H. F., Wang, P. J., Li, R. L., Huang, C., and Bai, B. (2012). Classification of Volcanic Edifices and its Characteristics of Gas Pool in Faulted Sequence of the Songliao Basin, NE China. *J. Jilin Univ. (Earth Science Edition)* 42 (3), 583–589. doi:10.13278/j.cnki.jjuese.2012.03.001

Tang, Y., Wang, G., Zheng, M, L., Chen, L., Feng, L., Kong, Y. H., et al. (2015). Carboniferous Basin Evolution and its Hydrocarbon Accumulation in the North of Xinjiang. *Earth Sci. Front.* 22 (3), 241–253. doi:10.13745/j.esf.2015.03.021

Wang, L., Xu, Y. D., Zhang, Y. J., Liu, Z. C., and Shang, F. K. (2020). Main Controlling Factors and Development Model of Carboniferous Reservoirs in Chepaizi Uplift, Junggar Basin. *J. Northeast Petroleum Univ.* 44 (2), 79–90. doi:10.3969/j.issn.2095-4107.2020.02.008

Wang, X. J., Song, Y., Zheng, M. L., Ren, H. J., Wu, H. S., He, W. J., et al. (2021). Composite Petroleum System and Multi-Stage Hydrocarbon Accumulation in Junggar Basin. *China Pet. Explor.* 26 (4), 29–43. doi:10.3969/j.issn.1672-7703.2021.04.003

Wang, X. Y., Liu, Q. H., Zhu, H. T., Hou, G. W., and Qin, L. Z. (2020). Three-dimensional Sculpture and Genetic Mechanism Analysis of Volcanic Structures in the Tiantai Slope Zone of Xihu Sag. *Bull. Geol. Sci. Technol.* 40 (4), 72–80. doi:10.19509/j.cnki.dzkq.2021.0406

Xia, M. L., Wen, L., Li, Y., Luo, B., He, K. L., Liu, R., et al. (2020). Permian Volcanic Eruption Cycle, Environment and Model in the Jianyang Area of the Sichuan Basin. *Nat. Gas. Ind.* 40 (9), 11–22. doi:10.3787/j.issn.1000-0976.2020.09.002

Xu, N., and Gao, C. (2020). Study on the Special Rules of Surface Subsidence Affected by Normal Faults. *J. Min. Strata Control Eng.* 2 (1), 011007. doi:10.13532/j.jmsce.cn10-1638/td.2020.01.011

Yi, J., Shan, X. L., Tang, H. F., Zhang, Y. Y., and Chen, Y. P. (2011). The Geological-Geophysical Two-Dimensional Dissection of Basin Buried Volcanic Edifices-Take the First Member of Yingcheng Formation in Yaoyingtai Region of Southern Songliao Basin as an Example. *Chin. J. Geophys.* 54 (2), 587–596. doi:10.3969/j.issn.0001-5733.2011.02.038

Yin, S., and Ding, W. L. (2019). Evaluation Indexes of Coalbed Methane Accumulation in the Strong Deformed Strike-Slip Fault Zone Considering Tectonics and Fractures: A 3D Geomechanical Simulation Study. *Geol. Mag.* 156 (6), 1–17. doi:10.1017/s0016756818000456

Yin, S., Xie, R., Wu, Z., Liu, J., and Ding, W. (2019). *In Situ* stress Heterogeneity in a Highly Developed Strike-Slip Fault Zone and its Effect on the Distribution of Tight Gases: A 3D Finite Element Simulation Study. *Mar. Petroleum Geol.* 99 (1), 75–91. doi:10.1016/j.marpetgeo.2018.10.007

You, X. C., Gao, G., Wu, J., Zhao, J. Y., Liu, S. J., and Duan, Y. J. (2021). Differences of Effectivity and Geochemical Characteristics of the Fengcheng Formation Source Rock in Ma'nan Area of the Junggar Basin. *Nat. Gas. Geosci.* 32 (11), 1697–1708. doi:10.11764/j.issn.1672-1926.2021.08.002

Zhang, S. Y., Zhu, J., Wen, G., Liu, S. Q., Lu, X. C., Zhang, S. C., et al. (2015). Significant of Volcanic Eruption Spatiotemporal Sequence in Batamayineishan Formation, Ludong Region, Junggar Basin. *J. Central South Univ. Sci. Technol.* 46 (1), 199–207. doi:10.11817/j.issn.1672−7207.2015.01.027

Zhao, N., and Shi, Q. (2012). Characteristics of Fractured and Porous Volcanic Reservoirs and the Major Controlling Factors of Their Physical Properties: A Case Study from the Carboniferous Volcanic Rocks in Ludong-Wucaiwan Area, Junggar Basin. *Nat. Gas. Ind.* 32 (10), 14–23. doi:10.3787/j.issn.1000-0976.2012.10.004

Zheng, M. L., Fan, X. D., He, W. J., Yang, T. Y., Tang, Y., Ding, J., et al. (2019a). Superposition and Evolution of Deep Geological Structure and Hydrocarbon Accumulation in Junggar Basin. *Earth Sci. Front.* 26 (1), 22–32. doi:10.13745/j.esf.sf.2019.1.2

Zheng, Z. H., Du, S. K., Liao, J. B., Chen, H. Y., and Yu, H. G. (2019b). Drops of West Region in Junggar Basin Carboniferous Igneous Rock Gas Reservoir Capacity Main Control Factors. *J. China Univ. Min.* 13 (3), 604–615. doi:10.13247/j.cnki.jcumt.000955

Zhu, W., Niu, L., and Li, S. (2019). Creep-impact Test of Rock: Status-Of-The-Art and Prospect. *J. Min. Strata Control Eng.* 1 (1), 013003. doi:10.13532/j.jmsce.cn10-1638/td.2019.02.007

Zou, C.-N., Zhao, W.-Z., Jia, C.-Z., Zhu, R.-K., Zhang, G.-Y., Zhao, X., et al. (2008). Formation and Distribution of Volcanic Hydrocarbon Reservoirs in Sedimentary Basins of China. *Petroleum Explor. Dev.* 35 (3), 257–271. doi:10.1016/s1876-3804(08)60071-3

Conflict of Interest: The authors AY, BB, LL, and HC were employed by the PetroChina Xinjiang Oilfield Company.

The remaining authors declare that the research was conducted in the absence of any commercial or financial relationships that could be construed as a potential conflict of interest.

frontiers | Frontiers in Earth Science

ORIGINAL RESEARCH
published: 31 May 2022
doi: 10.3389/feart.2022.922683

Influence of Water Saturation Time on Microstructure and Mechanical Properties of Jointed Limestone

Huigui Li[1], Jun Wang[1,2]*, Xiaohe Wang[2], Wanliang Liang[2], Guosheng Xu[1] and Yingchun Kang[3]*

[1]College of Mining Engineering, Guizhou University of Engineering Science, Bijie, China, [2]School of Energy and Mining, China University of Mining and Technology, Beijing, China, [3]China Mining Products Safety Approval and Certification Center, Beijing, China

In order to study the influence of water saturation time on the mechanical properties of jointed limestone, the joint limestone samples with a crack length of 20 mm and a crack angle of 30° are saturated with water for 0, 1, 3, 5 and 7 days and tested with the RMT-150C mechanical test machine. The results show that the water saturation time has a significant effect on the stress-strain curve, peak strength, elastic modulus, crack development and failure characteristics of the jointed limestone. There is a step rise or fall phenomenon near the peak stress. The peak strength and elastic modulus of the joint limestone are significantly negatively correlated with the saturated time. Compared with that of the saturated 0-day sample, the peak compressive strength of the saturated 1-day, 3-day, 5-day and 7-day samples was decreased by 16.5%, 24.7%, 43.6%, and 47.7%, respectively, and the elastic modulus decreased by 11.0%, 32.0%, 45.0%, and 67.9%, respectively. Saturated water cracks the skeleton particles of the limestone samples, and the length of the microscopic pores and fissures increased gradually. The phenomenon that the number and length of cracks increase with the increase of the water saturation time will weaken the mechanical properties of the jointed limestone. The physical and chemical reactions, lubrication, and pore water pressure produced by water-saturated water-rock interactions make it easier for the Mohr stress circle to reach the limit equilibrium state. Saturated water reduces the degree of fragmentation of the sample, and the integrity of the fracture surface is higher after failure. The findings in this paper are helpful to further reveal the mechanism of the crushing of supports and the frequent occurrence of water gushing accidents at the working face in the Xinhua region of northwestern Guizhou.

Keywords: water saturation time, jointed limestone, mechanical properties, uniaxial compression, microstructure

OPEN ACCESS

Edited by:
Hu Li,
Southwest Petroleum University, China

Reviewed by:
Dezhong Kong,
Guizhou University, China
Zhenhua Jiao,
Anhui University of Science and Technology, China

****Correspondence:***
Huigui Li
lihuigui1221@163.com
Jun Wang
wang_jun1107@163.com

Specialty section:
This article was submitted to Economic Geology, a section of the journal Frontiers in Earth Science

Received: *18 April 2022*
Accepted: *09 May 2022*
Published: *31 May 2022*

Citation:
Li H, Wang J, Wang X, Liang W, Xu G and Kang Y (2022) Influence of Water Saturation Time on Microstructure and Mechanical Properties of Jointed Limestone. Front. Earth Sci. 10:922683. doi: 10.3389/feart.2022.922683

INTRODUCTION

There are many discontinuities such as joints, fissures and interlayers in the rock mass, which will greatly weaken the stability of the rock mass. For the rock mass in the roof of the coal seam, in addition to a large number of discontinuous surfaces, there is often a large amount of water in the discontinuous surfaces. The presence of water will promote the further development of the discontinuity, resulting in the fracture of the rock mass. In particular, due to the long-term action of water, the physical and mechanical properties of the rock in the aquifer will change, which has a great impact on the stability of the overlying rock and the surrounding rock of the

roadway (Deng et al., 2017a; Duan and Ren, 2019; Wang et al., 2019). The mechanical model has played an important role in the study of jointed rock formation and rock mechanics. Many scientists have carried out related research on the mechanical model of jointed rock. Zhao et al. (2020) used the discrete element software 3DEC to establish a numerical model to analyze the mechanical and failure characteristics of jointed rocks under uniaxial tension. Meng et al. (2019) proposed a modeling method based on homogenization to study the influence of columnar joint structure on the mechanical properties of rock mass. Yang et al. (2019) used the theory of damage mechanics to explore multiple groups of joints distributed in the rock mass, and established a damage mechanics model. Liu et al. (2016) studied non-penetrating jointed rock mass and developed a dynamic damage constitutive model under uniaxial compression. Li H. G. et al., (2020), Li et al. (2021), Li et al. (2020b) use siltstone, medium grained sandstone, coarse-grained sandstone and coal in the strata of Bulianta coal mine and Buertai coal mine in Shendong mining area as the research object, and analyzed the influence of interlayer thickness on the mechanical properties of jointed rock. They found that the thickness of the interlayer has a significant effect on the mechanical properties of the jointed coal rock and the interlayer thickness has a significant influence on the mechanical properties of the jointed coal rock. Li et al. (2019), Fan et al. (2020), Li et al. (2020a), Li (2022) used finite element simulation and structural mechanics to investigate the positive correlation effect of fracture occurrence state on rock failure degree, and the influence of structural joints, etc. on the occurrence state of shale gas. 3D printing technology is increasingly applied to the study of jointed rock mass. Huang et al. (2020) combined Voronoi diagram stochastic simulation and 3D printing technology to prepare an irregular columnar joint network model and analyze the mechanical properties of irregular columnar joint rock mass. The results show that the columnar joints have a significant effect on the uniaxial compressive strength. Xia et al. (2020) used 3D printing technology to produce three-dimensional irregular columnar jointed rock mass, and analyzed the influence of irregular columnar joints on the mechanical behavior of jointed rock mass.

To study the physical and mechanical properties of water-saturated rocks, Vasarhelyi (2005) examined the negative correlation between water content and limestone strength by using statistical methods. Yilmaz (2010) studied the deterioration effect of water content on gypsum strength and deformation. Niu et al. (2018) analyzed the mechanical characteristics and energy evolution mechanism of water-saturated sandstone through post-peak cyclic loading and unloading tests on coarse sandstone samples, and found that water saturation reduced the total absorbed energy, dissipated energy and elastic strain of rock samples. Su et al. (2017) carried out uniaxial tests on the natural water-filled roof sandstone of coal seams. The results showed that the strength and deformation parameters of the sandstone samples are weakened by saturated water to varying degrees. Li et al. (2018) conducted a study on the influence of water saturation time on the deterioration of physical and mechanical properties of slate, and quantitatively evaluated the degree of damage and deterioration of slate from a macroscopic perspective through mass and strength variables. Zhang et al. (2019) took argillaceous siltstone as the research object, and obtained the damage and deterioration laws of argillaceous siltstone affected by water content, such as strength, deformation characteristics and failure mode. Wang et al. (2016), Wang et al. (2017), Wen et al. (2017), and Zheng et al. (2017) studied the mechanical parameters of coal and sandstone in their saturated state by using the combined dynamic and static loading method. They found that the saturated state had a significant effect on the dynamic mechanical parameters of coal and sandstone. Yang et al. (2018) adopted a similar simulation method, conducted a similar single-fissure rock mass freezing triaxial test, and concluded that the mechanism of increasing rock mass strength with decreasing temperature led to an increase of the freezing of rock mass pore water and fissure water into ice. Moreover, the inclination angle of the fracture affected the initial position of the fracture surface, the trace length affected the expansion scale of the fracture surface, and the confining pressure affected the extension direction of the fracture surface. It was concluded that the dip angle had the greatest influence on the strength of the rock mass, followed by the trace length, and the temperature had the least influence. Deng et al. (2017b) reported that the influence of water content on the tensile strength of layered sandstone was the deterioration of macroscopic mechanical properties caused by the change in microstructure. Li B. et al. (2020) analyzed the unloading confining pressure characteristics of shale with different water contents, and believed that the deformation parameters and strength parameters of shale were significantly affected by water. When the shale is saturated with water, the inter-particle cementation is loose, which improves the crack propagation ability and reduces the weakening of its macro-mechanical properties such as strength and deformation. Li J. et al. (2020) took the weathered granite from Mount Tianshan in Xinjiang as the research object, analyzed the strength and deformation characteristics of water-saturated weathered granite at different temperatures and different confining pressures, and pointed out that when the temperature decreased, the saturated water further increased the friction and improved the rock strength.

In summary, researchers have conducted a number of studies on the influence of joints and fissures on the physical and mechanical properties of rocks, and have also carried out related research on sandstone, argillaceous siltstone, granite, slate, etc. Systematic laws have been revealed in the influence of water on the physical and mechanical characteristics of sandstone and the influence of joints and fissures on the physical and mechanical properties of rock. However, there is little research on the changing laws of physical and mechanical properties of rocks in their water saturated state. There are a large number of aquifers with joints and fissures in the overlying strata of the coal seam. Therefore, it is particularly important to study the influence of saturated water on the physical and mechanical properties of the jointed strata. Since April 2016, there have been 22 water gushing accidents at the working face caused by the mining of the M9 coal seam in Xinhua District. One of the main reasons for the accidents was the limestone fault of the Changxing

FIGURE 1 | Dry rock samples.

Formation overlying the M9 coal seam. The limestone of the Changxing Formation is an aquifer and is the main source of water for the water influx accidents at the working face. Water has a great impact on the physical and mechanical properties of the limestone in this group, and also has a great influence on the breaking form of the overlying rock at the working face, especially after the rainy season. Therefore, it is urgent to study the physical and mechanical properties of the Changxing Formation limestone in this area under different water-saturated states. In this paper, with the limestone from the limestone fault in the Changxing Formation in northwestern Guizhou as the research object, the relationship between the uniaxial compressive strength, elastic modulus and other parameters of the jointed limestone and the water saturation time is studied.

SAMPLE PREPARATION AND EXPERIMENTAL SCHEME

Sample Preparation

The limestone samples were collected from the Xinhua region in northwest Guizhou, and transported to the university laboratory. According to the requirements of the specification Ministry of Coal Industry of the Peoples Republic of China, (1988), the limestone was cored, cut and ground to make standard samples with Φ×H of 50 mm × 100 mm sample. After the samples were made, a 4 mm circular hole was drilled in the center of each sample, and then a crack with a length of 20 mm, a width of 2 mm, and an angle of 30° angle to the bottom was cut by hydraulic slitting. The joint angle is consistent with that observed on site. The samples are divided into 5 groups. The samples in Group A are dry samples, and the sample numbers are A1 to A3. The samples in Group B, Group C, Group D and Group E are soaked samples, soaked for 1 day, 3 days, 5 days, respectively. They are numbered B1-B3, C1-C3, D1-D3 and E1-E3, respectively. There are 3 samples in each group. The group of dry samples prepared is shown in **Figure 1**, and the parameters of all groups of samples are listed in **Table 1**.

Sample Preparation

The mechanical experiment was carried out by using the RMT-150C mechanical test system designed by Wuhan Institute of Geomechanics, China. In this experiment, the displacement controlled loading method is adopted. The loading rate during the experiment was 0.002 mm/s. The experiment was repeated 3 times for each group of samples.

INFLUENCE OF WATER SATURATION TIME ON MECHANICAL PROPERTIES OF JOINTED LIMESTONE

Characteristic Analysis of Stress-Strain Curve

To study the influence of water saturation time on the mechanical properties of jointed limestone, uniaxial compression tests were carried out on the jointed limestone samples saturated with water for 0, 1, 3, 5, and 7 days by using the RMT-150C mechanical testing machine. **Table 2** shows the mechanical parameters of the jointed limestone with different water saturation times under uniaxial compression. **Figures 2A–E** are the stress-strain relationship curves of the jointed limestone with different

TABLE 1 | Basic parameters of jointed limestone samples.

Sample No.	Crack angle/°	Crack length/mm	Height/mm	Diameter/mm	Saturation time/day
A1	30	20	100.70	49.76	0
A2	30	20	100.84	49.47	0
A3	30	20	99.98	49.53	0
B1	30	20	97.68	49.47	1
B2	30	20	100.73	49.49	1
B3	30	20	101.07	49.50	1
C1	30	20	99.93	49.54	3
C2	30	20	100.77	49.46	3
C3	30	20	100.55	49.51	3
D1	30	20	99.73	49.55	5
D2	30	20	100.90	49.41	5
D3	30	20	100.10	49.59	5
E1	30	20	100.41	49.52	7
E2	30	20	101.24	49.49	7
E3	30	20	100.68	49.48	7

TABLE 2 | Mechanical parameters of jointed limestone with different water saturation time under uniaxial compression.

No.	Crack angle/°	Crack length/mm	Saturation time/day	σ_c/ MPa	σ_p/ MPa	E/ GPa	E_p/ GPa	Notes
A1	30	20	0	71.06		42.10		
A2	30	20	0	70.13	72.77	41.14	45.15	
A3	30	20	0	77.11		52.21		
B1	30	20	1	68.87		32.03		
B2	30	20	1	58.25	60.74	45.51	40.20	
B3	30	20	1	55.10		43.07		
C1	30	20	3	58.25		34.47		
C2	30	20	3	56.24	54.82	29.69	30.72	
C3	30	20	3	49.97		28.00		
D1	30	20	5	40.32		23.45		
D2	30	20	5	42.36	41.01	23.42	24.84	
D3	30	20	5	40.36		27.65		
E1	30	20	7	37.08		14.02		
E2	30	20	7	—	38.07		14.51	Failure
E3	30	20	7	39.06		14.99		

water saturation times under uniaxial compression. The stress-strain curve of the uniaxial compression of the E2 specimen is missing in **Figure 2E**. During the experiment, the power supply of the computer was suddenly cut off, so that this group of data was not recorded. However, since the samples in this experiment were all collected from the same location, there were no remaining samples, so no supplements were made. experiment. **Figures 2A, E** indicate that the water saturation time has a significant effect on the stress-strain curve of the jointed limestone. When the water saturation time is 0, 1, 3, 5, and 7 days, the stress-strain curve basically presents three stages, namely: initial compaction stage, linear elastic stage, and plastic deformation failure stage. None of the samples have residual strength. They all break suddenly after the peak stress, because limestone is a relatively brittle rock. However, with the increase of the water saturation time, the characteristics of the stress-strain curve show a difference. The strain in the initial compaction period is larger, the curve becomes gentler, the slope of the curve in the linear elastic stage gradually decreases, and there is a step-up phenomenon in the peak stress stage.

Analysis of Influence of Water Saturation Time on the Strength of Jointed Limestone

Table 2 shows the mechanical parameters of the jointed limestone with different water saturation times under uniaxial compression, where σ_c is the uniaxial compressive strength, E is the elastic modulus, σ_p and Ep are the average uniaxial compressive strength and the average elastic modulus, respectively. With **Table 2** and **Figure 3** combined, it can be found that the saturation time has a significant effect on the peak compressive strength of the jointed limestone. The uniaxial compressive strengths of the jointed limestone at water saturation times of 0, 1, 3, 5, and 7 days are 72.77, 60.74, 54.82, 41.01 and 38.07 MPa, respectively, which are lower than that with no water saturation by 16.5%, 24.7%, 43.6%, and 47.7%, respectively. These data indicated that there is an obvious negative correlation between the uniaxial compressive strength of the sample and the saturated time. Comparison of the strength of the saturated sample for 1 day and the dry sample shows that water has a significant effect on the strength of limestone. The uniaxial compressive strength of limestone decreases greatly when the water saturation time is 3–5 days, and the negative correlation effect of water content on limestone is obviously slowed down after saturated for 5 days, which shows that when the joints are saturated for about 5 days in the natural state, the moisture content of limestone reaches relative saturation. **Figure 3** shows the relationship between the peak compressive strength of the jointed limestone and the water saturation time. With the above analysis and **Figure 3** combined, it can be found that the peak compressive strength of the jointed limestone has a negative correlation with the water saturation time. With the increase of the water saturation time the peak compressive strength decreases gradually. The relationship is fitted by curve fitting. The fitting equation is shown in **Eq. 1**, and the correlation coefficient is 0.94, which indicates that the correlation is good.

$$\sigma_c = 71.32 - 7.86t + 0.43t^2 \quad (1)$$

where σ_c is the peak compressive strength, MPa; t is the water saturation time, d.

Analysis of influence of water saturation time on elastic modulus of jointed limestone.

To investigate the influence of water saturation time on the elastic modulus of the jointed limestone, the relationship between the elastic modulus of the jointed limestone and the saturation time was analysed. **Figure 4** shows the relationship between the elastic modulus and the saturation time. It can be seen from **Table 2** and **Figure 4** that when the jointed limestone is saturated with water for 0 day, 1 day, 3, 5, and 7 days, the variation range of the elastic modulus is 41.14 ~ 52.21 GPa, 32.03 ~ 45.51 GPa, 28.00 ~ 34.47 GPa, 23.42 ~ 27.65 GPa, 14.02 ~ 14.99 GPa, and the average elastic modulus is 45.15, 40.20, 30.72, 24.84, 14.51 GPa,

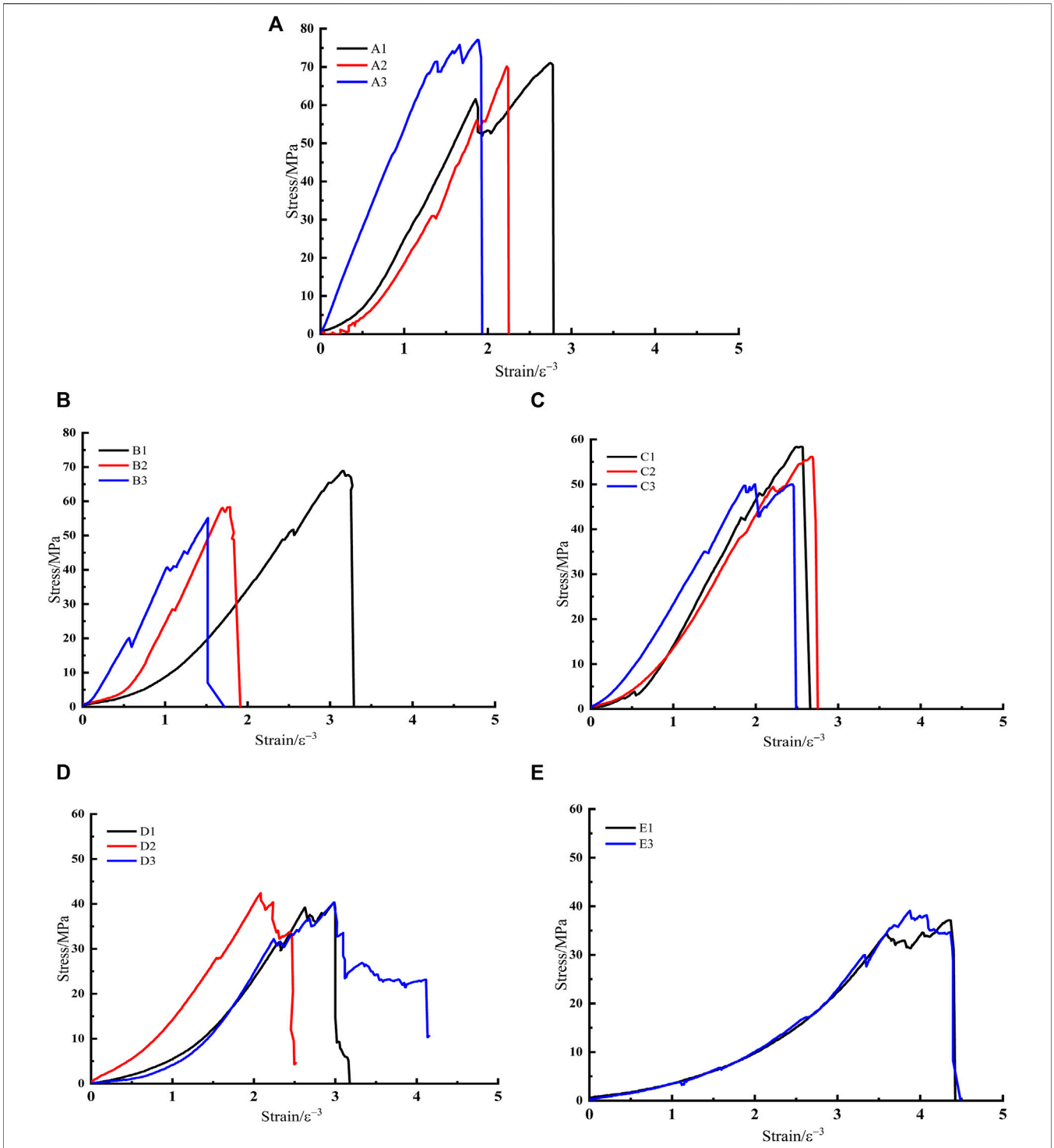

FIGURE 2 | Stress strain curves of jointed limestone with different water saturation times. **(A)** Dry. **(B)** 1 day. **(C)** 3 days. **(D)** 5 days. **(E)** 7 days.

respectively. These data indicated that the saturated time not only has a significant impact on the peak compressive strength of the jointed limestone, but also has a significant impact on the elastic modulus of the jointed limestone. Furthermore, the elastic modulus of the jointed limestone is also negatively correlated with the saturation time. Compared with that for 0 day, the elastic modulus of the jointed limestone saturated with water for 1 day, 3, 5 and 7 days is decreased by 4.95, 14.43, 20.31, and 30.64 GPa, with a decrease rate of 11.0% and 32.0 %, 45.0%, 67.9%, respectively. Through the above analysis, the relationship is

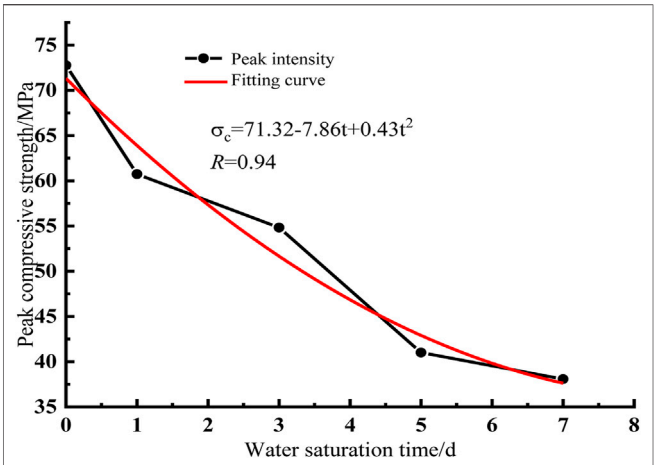

FIGURE 3 | Relationship between peak strength of jointed limestone and water saturation time.

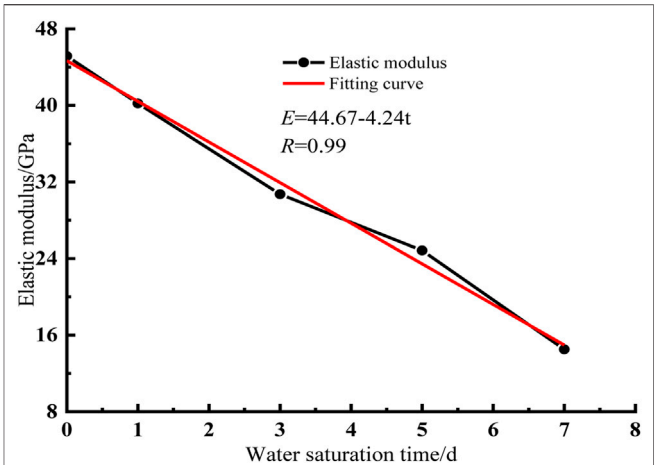

FIGURE 4 | Relationship between elastic modulus of jointed limestone and water saturation time.

fitted by linear fitting, the fitting equation is shown in **Eq. 2**, and the correlation coefficient is 0.99, which indicates that the correlation is good.

$$E = 44.67 - 4.24t \quad (2)$$

where E is the elastic modulus of the jointed limestone, GPa; t is the saturation time, d.

EFFECT OF WATER SATURATION TIME ON MICROSTRUCTURE OF JOINTED LIMESTONE

To study the effect of water saturation time on the microstructure of the jointed limestone, the microstructure of the limestone samples dried, saturated with water for 1, 3, 5 and 7 days was observed on an environmental scanning electron microscope (FEI-SEM) in the Institute of Geochemistry, Chinese Academy of Sciences. The limestone samples were magnified 5000 times and 10,000 times, respectively. Moreover, to study the influence of water saturation time on the length and width of pores and fissures and the number of pores and fissures in the microstructure of limestone, the professional processing software Smileview was used to measure the length and width of microcracks of five limestone samples with different water saturation times, as shown in **Figure 5**. **Figure 5** indicates that the number of micropores and cracks in the dried sample is very small, and the cracks mainly exist between the particles. However, with the increase of the water saturation time, the number of micropores and fractures in the limestone samples gradually increases, and fractures began to appear in the grains, resulting in the fracture of the skeleton grains. **Figure 5** shows that a large number of microscopic cracks appear in the limestone sample saturated with water for 7 days, mainly in the interior of the particles. The length of microcracks in the limestone samples increases significantly with the increase of the water saturation time.

Table 3 is a statistical table of the lengths and widths of microscopic pores and fissures of the limestone samples dried and saturated with water for 1, 3, 5 and 7 days. There are differences in the lengths and widths of microscopic pores and fissures of the samples, and the water saturation time has a significant effect on the length and width of the microscopic pores and fissures of the limestone samples, especially the length of the microscopic pores and fissures of the limestone samples. The length gradually increases with the increase of the water saturation time. The length ranges of the microscopic pores and fissures of the limestone samples dried and saturated with water for 1, 3, 5 and 7 days are 0.11 ~ 5.57 μm, 0.50 ~ 5.98 μm, 0.60 ~ 7.97 μm, 0.70 ~ 8.20 μm and 1.11 ~ 9.32 μm, respectively. This indicates that with the gradual increase of the water saturation time, the minimum and maximum lengths of the microscopic pores and fissures in limestone gradually increase, showing a positive correlation. The average lengths of the microscopic pores and fissures of the limestone samples dried and saturated with water for 1, 3, 5 and 7 days are 1.62, 2.05, 2.52, 2.79 and 4.23 μm, respectively. Compared with that of the dried samples, the microcrack lengths of the samples saturated with water for 1, 3, 5 and 7 days are increased by 26.5%, 55.6%, 72.2%, and 161.1%, respectively. Furthermore, with the increase of the saturation time, the number of cracks increases significantly, and most of the cracks appear in the middle of the particles, which is one of the main reasons for the change of macroscopic mechanical parameters. In addition, the width ranges of the microscopic pores and fissures of the limestone samples dried and saturated with water for 1, 3, 5 and 7 days are 0.08 ~ 0.80 μm, 0.10 ~ 1.32 μm, 0.14 ~ 1.65 μm, 0.17 ~ 0.97 μm and 0.25 ~ 2.55 μm, respectively, and the average values of the microscopic pore and fissure widths are 0.45, 0.41, 0.40, 0.74 μm, respectively. The minimum value of the pore and fissure width increases gradually with the increase of the water saturation time, and the maximum value also fluctuates.

Figure 6 shows the characteristic diagram of the microscopic pore and fracture parameters of the limestone samples dried and saturated with water for 1 day, 3, 5 and 7 days. As indicated in **Figure 6**, there are significant

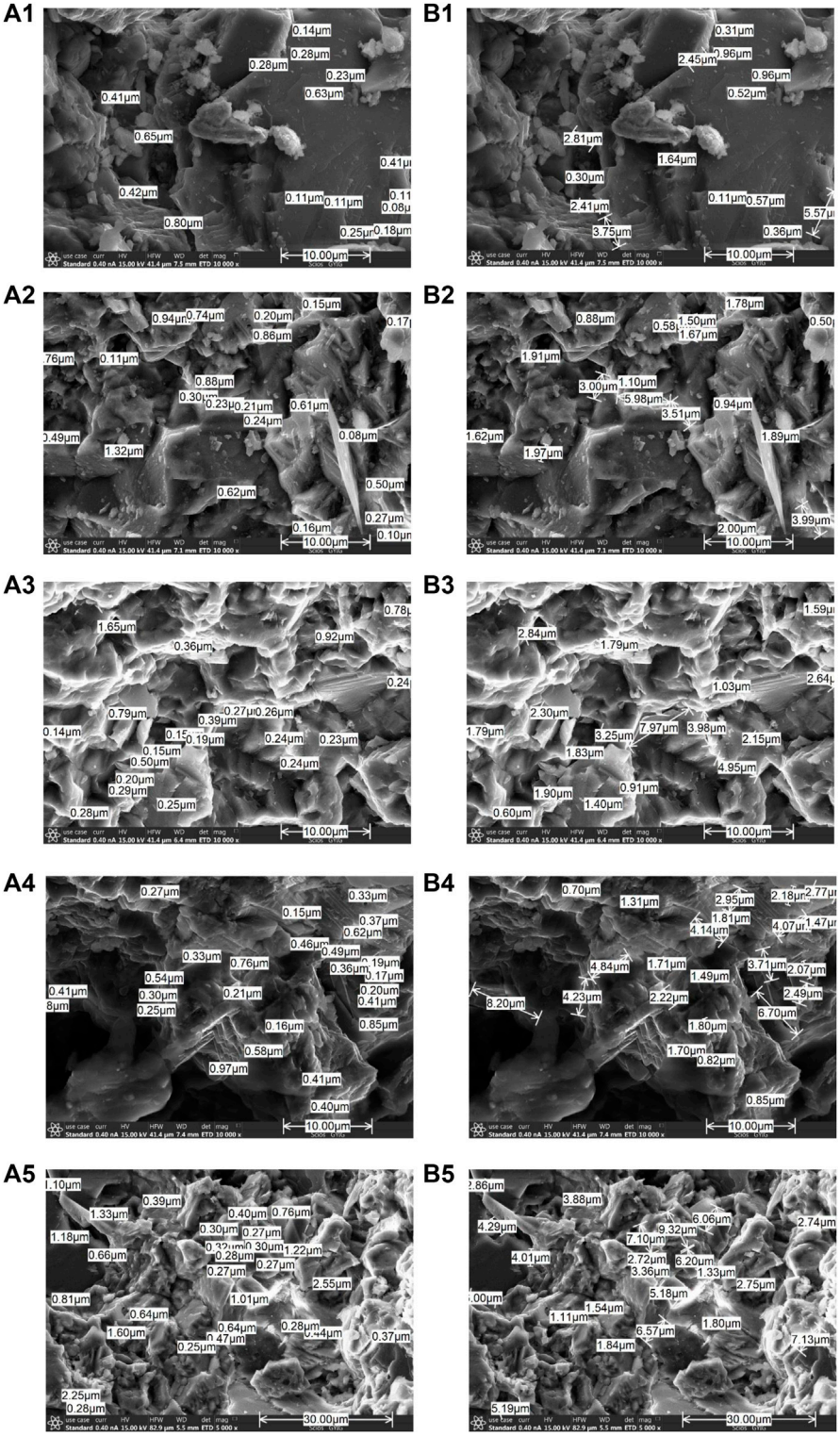

FIGURE 5 | Microstructure of jointed limestone with different water saturation times. **(A1–A5)**: Crack width of limestone samples dried and saturated for 1, 3, 5 and 7 days. **(B1–B5)**: Crack length of limestone samples dried and saturated for 1, 3, 5 and 7 days.

differences in the main ranges of microscopic pores width and length of the limestone samples with different water saturation times. The width of pores and cracks in dry samples is mainly concentrated in 0 ~ 0.30 μm, and the number of cracks measured accounts for 60% of the total number of cracks. And the width of pores and cracks is mainly concentrated in

TABLE 3 | Characteristics of limestone pores and fissures at different water saturation times.

Water saturation time	Length of pores and fissures/um		Width of pores and fissures/um	
	Average value	Standard deviation	Average value	Standard deviation
Dry	1.62	1.60	0.32	0.22
1 Day	2.05	1.39	0.45	0.34
3 Days	2.52	1.79	0.41	0.36
5 Days	2.79	1.89	0.40	0.22
7 days	4.23	2.25	0.74	0.61

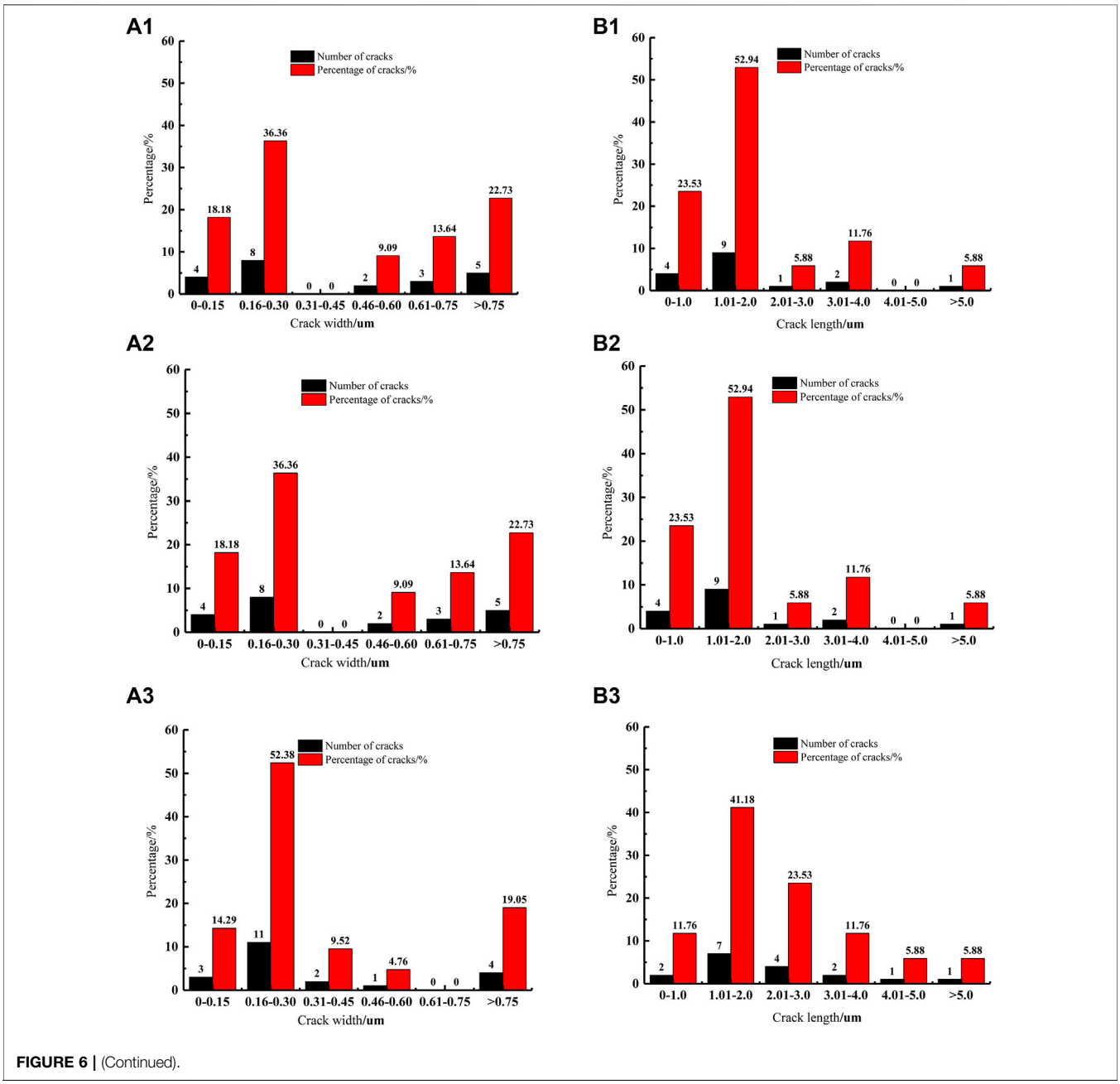

FIGURE 6 | (Continued).

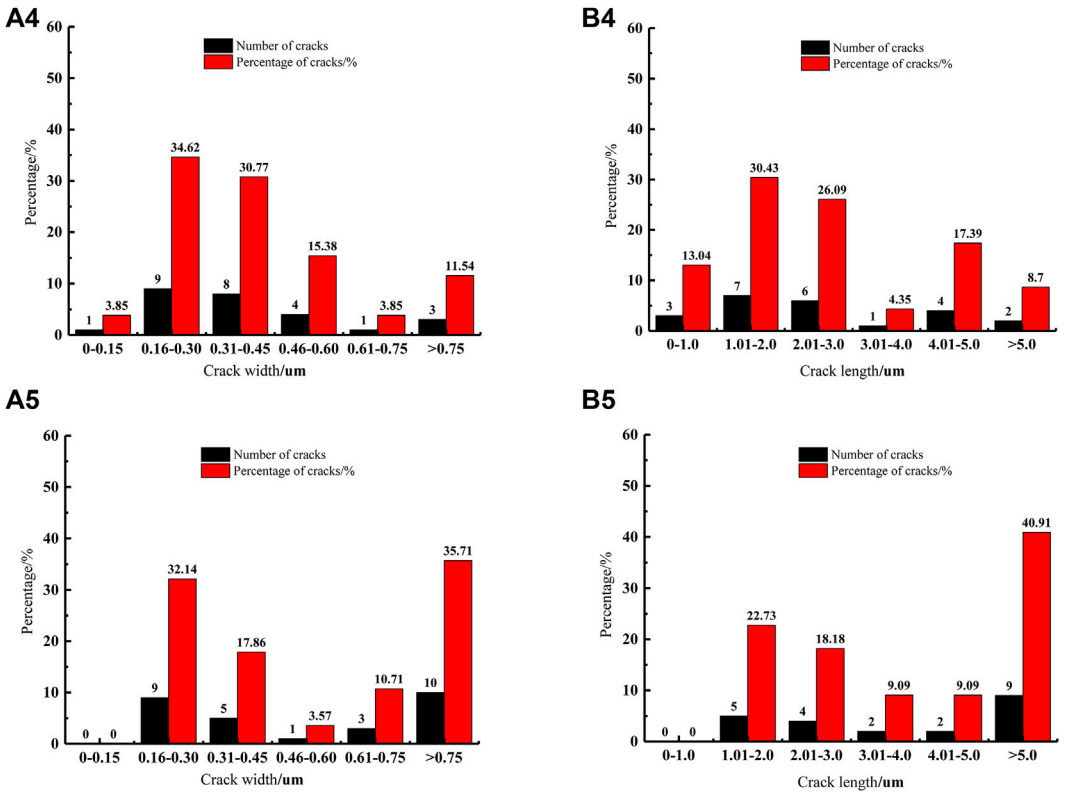

FIGURE 6 | (Continued). Characteristics of micro pores and cracks in limestone at different water saturation times. (A1–A5): Crack width of limestone samples dried and saturated for 1 day, 3, 5 and 7 days. (B1–B5): Crack length of limestone samples dried and saturated for 1, 3, 5, and 7 days

0 ~ 1.00 μm, and the number of cracks measured accounts for 57.14% of the total number of cracks. The width of pores and cracks in the sample after being saturated for 1 day is mainly concentrated in 0.16 ~ 0.30 μm and greater than 0.75 μm, and the number of cracks measured accounts for 59.09% of the total number of cracks. And the width of pores and cracks is mainly concentrated in 0 ~ 2.00 μm, the number of cracks measured accounted for 53.53% of the total number of cracks. The width of pores and cracks in the samples saturated with water for 3 days is mainly concentrated in 0.16 ~ 0.30 μm, and the number of cracks measured accounts for 52.38% of the total number of cracks. The width of pores and cracks in the sample after 5 days of water saturation is mainly concentrated in 0.16 ~ 0.45 μm, and the number of cracks measured accounts for 65.39% of the total number of cracks. The width of pores and cracks in the samples saturated with water for 7 days is mainly concentrated in 0.16 ~ 0.30 μm and greater than 0.75 μm, and the number of cracks measured accounts for 67.85% of the total number of cracks. And the width of pores and cracks is mainly concentrated in 1.00 ~ 2.00 μm and greater than 5.0 μm, the number of cracks measured accounts for 63.64% of the total number of cracks. Based on the above analysis, it can be found that with the gradual increase of the water saturation time, the main concentration range of the width and length of the pores and fractures gradually increases, indicating that water saturation time has a promoting effect on the development of microscopic pores and fractures in limestone.

WEAKENING MECHANISM OF MECHANICAL PROPERTIES OF WATER BEARING JOINTED LIMESTONE

In the process of water saturation, the jointed limestone undergoes water-rock interaction. In the process of water-rock interaction, water mainly degrades the mechanical properties of jointed limestone from two aspects. First of all, after the jointed limestone is saturated with water, the original pores and fissures will be filled with water. The water in the pores and fissures will gradually increase with time, and will physically and chemically react with nearby hydrophilic minerals to generate new joints and fissures. The clay minerals will expand, resulting in an internal expansion force σ_p. Secondly, after the jointed limestone is saturated with water, lubrication is produced during uniaxial compression, reducing the internal friction angle inside the rock. After water saturation, the internal friction angle can be reduced by 6%~28% (Barton. 1973; Erguler and Ulusay, 2009; Alejano et al., 2012; Vilarrasa et al., 2019; Zhao, 2021). According to the Mohr-Coulomb theory (Yang et al., 2019; Zhao et al., 2020), in the process of water saturation of jointed limestone, the internal friction angle in **Eq. 3** will decrease and become φ_w, and the

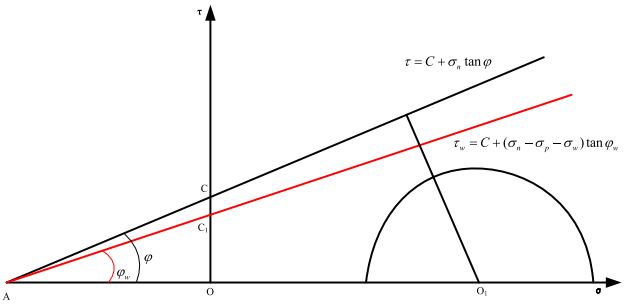

FIGURE 7 | Mohr circle analysis of stress in water bearing jointed limestone.

normal stress on the shear plane will be affected by the expansion forces σ_p and σ_w. After the jointed limestone is saturated with water, the modified Mohr-Coulomb formula is shown in **Eq. 4**. When the stress Mohr circle analysis (as shown in **Figure 7**) is applied, it can be found that after the jointed limestone is saturated with water, the stress Mohr circle is more likely to reach the limit equilibrium state, and the compressive strength of the jointed limestone will decrease.

$$\tau = C + \sigma_n tan\varphi \tag{3}$$

Where τ is the shear stress, C is the cohesion, σ_n is the normal stress, and φ is the internal friction angle.

$$\tau_w = C + \left(\sigma_n + \sigma_p - \sigma_w\right)tan\varphi_w \tag{4}$$

Where τ_w is the corrected shear stress, σ_p is the expansion force, σ_w is the pore water pressure, and φ_w is the internal friction angle after water saturation.

EFFECT OF WATER SATURATION TIME ON THE MACROSCOPIC FAILURE CHARACTERISTICS OF JOINTED LIMESTONE

To understand the influence of water saturation time on the macroscopic failure characteristics of jointed limestone, the macroscopic characteristics of jointed limestone with different water saturation times were analyzed. **Figure 8** shows that the macroscopic characteristics of the jointed limestone saturated for 0, 1, 3, 5 and 7 days. As indicated in the figure, the water saturation time has a certain influence on the macroscopic failure characteristics of the jointed limestone. The destruction levels of the samples saturated with water for 0 day is obviously higher than those of the samples saturated with water for 1, 3, 5, and 7 days. The integrity of the failure surface is worse, and the failure degree tends to decrease gradually with the increase of the water saturation time. The failure of jointed limestone is dominated by tension and shear failure. The failure of the sample basically starts from the vicinity of the joint, gathers and penetrates, and there is a certain number of secondary cracks

FIGURE 8 | Failure modes of jointed limestone at different water saturation times. **(A)** Dry. **(B)** 1 day. **(C)** 3 days. **(D)** 5 days. **(E)** 7 days.

near it. However, with the increase of the water saturation time, the crack propagation tends to weaken.

CONCLUSION

To reveal the influence of water saturation time on the mechanical properties of jointed limestone, the stress-strain curve, compressive strength and elastic modulus of the limestone from northwest Guizhou are studied. After analysis and discussion, the main conclusions are drawn as follows:

(1) The water saturation time has an influence on the stress-strain curve of the jointed limestone. With the gradual increase of the water saturation time, the stress-strain curve changes significantly. The initial compaction period becomes significantly longer, the slope of the curve in the linear elastic stage gradually decreases, and there is a step rise or fall near the peak stress.
(2) There is a negative correlation between the peak compressive strength and elastic modulus of the jointed limestone and the water saturation time. The peak compressive strength and elastic modulus of the jointed limestone gradually decreases with the increase of the water saturation time.
(3) With the increase of the water saturation time, the skeleton particles of limestone samples are fractured and cracks

appear, and the length of microscopic pores and cracks gradually increases. The number and length of cracks are positively correlated with the water saturation time. In addition, the main concentration range of the microscopic pore and fracture length of limestone gradually increases. The phenomenon that the number of cracks and the length of cracks increase with the increase of the water saturation time is one of the reasons for the deterioration of the mechanical properties of the jointed limestone.

(4) In the process of water-rock interaction of jointed limestone, water mainly destroys the mechanical properties of jointed limestone from three aspects: physical and chemical reactions, lubrication, and formation of certain pore water pressure. Therefore, after the jointed limestone is saturated with water, the stress molar circle is more likely to reach the limit equilibrium state, and the compressive strength of the jointed limestone will decrease.

(5) When the jointed limestone samples are damaged, they basically start to crack from the vicinity of the joints, gather and penetrate, and a certain number of cracks will appear in the vicinity. The main failures are tension and tension shear, the degree of fracture is lower during failure, and the integrity of the failure surface is higher after failure.

DATA AVAILABILITY STATEMENT

The original contributions presented in the study are included in the article/supplementary material, further inquiries can be directed to the corresponding authors.

AUTHOR CONTRIBUTIONS

HL, JW, and GX conducted experiments and collected experimental data; the full text was co-authored by HL and JW. XW is responsible for the data analysis and graphics rendering in **Section 3**. WL is responsible for the data analysis and graphics drawing in **Section 4**; YK is responsible for the editing of the article.

FUNDING

This research was funded by Natural Science Foundation of Guizhou Education Department (Qianjiaohe KY Zi [2019] 166), Research Initiation Fund for High-Level Talents (YKHZG2018011), and the Natural Science Foundation Project of Bijie Science and Technology Bureau (Bikelianhezi NO.G[2019]5).

REFERENCES

Alejano, L. R., González, J., and Muralha, J. (2012). Comparison of Different Techniques of Tilt Testing and Basic Friction Angle Variability Assessment. *Rock Mech. Rock Eng.* 45, 1023–1035. doi:10.1007/s00603-012-0265-7

Barton, N. (1973). Review of a New Shear-Strength Criterion for Rock Joints. *Eng. Geol.* 7 (4), 287–332. doi:10.1016/0013-7952(73)90013-6

Coal Industry Ministry of the Peoples Republic of China (1988). *Measuring Methods of Physics-Mechanic Property for Coal and Rock*. Beijing: Criterion Press of China, 32–33.

Deng, H. F., Fang, J. C., and Li, J. L. (2017a). Mechanical Properties of Red-Bed Soft Rock on Saturated State. *J. China Coal Soc.* 42 (8), 1994–2002. doi:10.13225/j.cnki.jccs.2016.1735

Deng, H. F., Zhang, Y. C., and Li, J. L. (2017b). Effect of Moisture Content on Splitting Tensile Strength of Layered Sandstone. *Chin. J. Rock Mech. Eng.* 36 (11), 2778–2787. doi:10.13722/j.cnki.jrme.2017.1175

Duan, T. Z., and Ren, Y. P. (2019). Study on Uniaxial Compression Mechanical Properties of Sandstone with Different Moisture Content and Wave Velocity Method. *Coal Geol. Explor.* 47 (4), 153–158. doi:10.3969/j.issn.1001-1986.2019.04.023

Erguler, Z. A., and Ulusay, R. (2009). Water-Induced Variations in Mechanical Properties of Clay-Bearing Rocks. *Int. J. Rock Mech. Min. Sci.* 46 (2), 355–370. doi:10.1016/j.ijrmms.2008.07.002

Fan, C., Li, H., Qin, Q., He, S., and Zhong, C. (2020). Geological Conditions and Exploration Potential of Shale Gas Reservoir in Wufeng and Longmaxi Formation of Southeastern Sichuan Basin, China. *J. Petroleum Sci. Eng.* 191, 107138. doi:10.1016/j.petrol.2020.107138

Huang, W., Xiao, W. M., and Tian, M. T. (2020). Model Test Research on the Mechanical Properties of Irregular Columnar Jointed Rock Masses. *Rock Soil Mech.* 41 (7), 2349–2359. doi:10.16285/j.rsm.2019.1493

Li, T., Zhao, J. J., and Xie, M. L. (2018). Experimental Study on the Effect of Slate Rock Mechanics Properties Degradation by the Saturation-Time. *Sci. Tech. Eng.* 18 (6), 217–222.

Li, H., Tang, H., Qin, Q., Zhou, J., Qin, Z., Fan, C., et al. (2019). Characteristics, Formation Periods and Genetic Mechanisms of Tectonic Fractures in the Tight Gas Sandstones Reservoir: A Case Study of Xujiahe Formation in YB Area, Sichuan Basin, China. *J. Petroleum Sci. Eng.* 178, 723–735. doi:10.1016/j.petrol.2019.04.007

Li, B., Liu, J., and Liu, Z. P. (2020). The Unloading Mechanical Properties of Shale with Different Water Saturation. *Rock Soil Mech.* 41 (Suppl. 2), 1–11. doi:10.16285/j.rsm.2019.1837

Li, H., Qin, Q., Zhang, B., Ge, X., Hu, X., Fan, C., et al. (2020a). Tectonic Fracture Formation and Distribution in Ultradeep Marine Carbonate Gas Reservoirs: A Case Study of the Maokou Formation in the Jiulongshan Gas Field, Sichuan Basin, Southwest China. *Energy fuels.* 34 (11), 14132–14146. doi:10.1021/acs.energyfuels.0c03327

Li, H. G., Yang, Z. K., and Li, H. M. (2020). Mechanical Characteristics and Failure Mechanism of Siltstone with Different Joint Thickness. *Adv. Civ. Eng.* 2020, 3824538. doi:10.1155/2020/3824538

Li, H., Wei, L., and Li, H. M. (2020b). Analysis of the Influence of Coal Thickness on the Physical and Mechanical Characteristics of Coal and Rock Mass. *Min. Safe. Environ. Prot.* 47 (6), 48–53. doi:10.19835/j.issn.1008-4495

Li, J., Li, G. Y., and Peng, W. L. (2020). The Strength and Deformation Characteristics of Saturated Weathered Granite under Freezing and Thawing Conditions. *J. Glaciol. Geo.* 42 (2), 1–9. doi:10.7522/j.issn.1000-0240.2020.0011

Li, H. G., Li, H. M., and Gao, B. B. (2021). Study on Acoustic Emission Characteristics in the Process of Fracture of Coal-Rock Combination Body with Different Thickness of Coal. *J. Henan Polytech. Univ. Nat. Sci. Ed.* 40 (5), 30–37. doi:10.16186/j.cnki.1673-9787.2019120077

Li, H. (2022). Research Progress on Evaluation Methods and Factors Influencing Shale Brittleness: A Review. *Energy Rep.* 8, 4344–4358. doi:10.1016/j.egyr.2022.03.120

Liu, H. Y., Wang, X. S., and Zhang, L. M. (2016). A Dynamic Damage Constitutive Model for Rock Mass with Non-persistent Joints under Uniaxial Compression. *Chin. J. Geo. Eng.* 38 (3), 426–436. doi:10.11779/CJGE201603005

Meng, Q.-X., Wang, H.-L., Xu, W.-Y., and Chen, Y.-L. (2019). Numerical Homogenization Study on the Effects of Columnar Jointed Structure on the Mechanical Properties of Rock Mass. *Int. J. Rock Mech. Min. Sci.* 124, 104127. doi:10.1016/j.ijrmms.2019.104127

Niu, S.-j., Ge, S.-s., Yang, D.-f., Dang, Y.-h., Yu, J., and Zhang, S. (2018). Mechanical Properties and Energy Mechanism of Saturated Sandstones. *J. Cent. South Univ.* 25 (6), 1447–1463. doi:10.1007/s11771-018-3839-z

Su, C. D., Sun, Y. N., and Zhang, Z. H. (2017). On the Effect of Water-Saturated State on Failure Energy of Sandstone from Coal Seam Roof Subjected to Uniaxial Compression. *J. Exp. Mech.* 32 (2), 223–231. doi:10.7520/1001-4888-16-118

Vasarhelyi, B. (2005). Statistical Analysis of the Influence of Water Content on the Strength of the Miocene Limestone. *Rock Mech. Rock Engng.* 38 (1), 69–76. doi:10.1007/s00603-004-0034-3

Vilarrasa, V., Carrera, J., Olivella, S., Rutqvist, J., and Laloui, L. (2019). Induced Seismicity in Geologic Carbon Storage. *Solid Earth.* 10, 871–892. doi:10.5194/se-10-871-2019

Wang, W., Li, H. M., and Yuan, R. F. (2016). Micromechanics Analysis and Mechanical Characteristics of Water-Saturated Coal Samples under Coupled Static-Dynamic Loads. *J. China Coal Soc.* 41 (3), 611–617. doi:10.13225/j.cnki.jccs.2015.0558

Wang, W., Li, H. M., and Gu, H. L. (2017). Experimental Study of Strength Characteristics of Water-Saturated Coal Specimens under 3D Coupled Static-Dynamic Loadings. *Chin. J. Rock Mech. Eng.* 36 (10), 2406–2414. doi:10.13722/j.cnki.jrme.2017.0545

Wang, C., Liu, C. W., and Liu, D. F. (2019). Experimental Study on Volume Effect of Saturated Fractured Sandstone under Uniaxial Compression. *Chin. J. Undergr. Space Eng.* 15 (5), 1331–1340.

Wen, M., Chen, Z., and Xu, J. Y. (2017). Static-dynamic Split Tensile Tests and Micro Analysis on Red-Sandstone with Different Moisture Contents. *Chin. J. Undergr. Space Eng.* 13 (1), 86–92.

Xia, Y., Zhang, C., Zhou, H., Hou, J., Su, G., Gao, Y., et al. (2020). Mechanical Behavior of Structurally Reconstructed Irregular Columnar Jointed Rock Mass Using 3D Printing. *Eng. Geol.* 268, 105509. doi:10.1016/j.enggeo.2020.105509

Yang, H., Zhang, J. X., and Shan, R. L. (2018). Experimental Study on Mechanical Properties of Frozen Saturated Single Fractured Rock Mass. *Rock Soil Mech.* 39 (4), 1245–1255. doi:10.16285/j.rsm.2016.0989

Yang, W., Zhang, Q., Ranjith, P. G., Yu, R., Luo, G., Huang, C., et al. (2019). A Damage Mechanical Model Applied to Analysis of Mechanical Properties of Jointed Rock Masses. *Tunn. Undergr. Space Technol.* 84, 113–128. doi:10.1016/j.tust.2018.11.004

Yilmaz, I. (2010). Influence of Water Content on the Strength and Deformability of Gypsum. *Int. J. Rock Mech. Min. Sci.* 47 (2), 342–347. doi:10.1016/j.ijrmms.2009.09.002

Zhang, E. F., Yang, G. S., and Tang, L. Y. (2019). Study on Influence of Water Content to Damage and Degradation Laws of Argillaceous Siltstone. *Coal Sci. Tech.* 47 (2), 14–20. doi:10.13199/j.cnki.cst.2019.02.003

Zhao, Y., Wu, Y., Xu, Q., Jiang, L., Huang, W., Zhang, P., et al. (2020). Numerical Analysis of the Mechanical Behavior and Failure Mode of Jointed Rock under Uniaxial Tensile Loading. *Adv. Civ. Eng.* 2020, 1–13. doi:10.1155/2020/8811282

Zhao, Z. H. (2021). Study on Water-Rock Interaction Mechanisms and Mechanical Behaviors of Single Rock Fractures. *Chin. J. Rock Mech. Eng.* 40 (Suppl. 2), 3063–3073. doi:10.13722/j.cnki.jrme.2021.0553

Zheng, G. H., Xu, J. Y., and Wang, P. (2017). A Dynamic/Static Experiment Research on the Red-Sandstone Mechanical Property under Different Saturated Degree. *J. Air Force Eng. Uni. Na. Sci. Ed.* 18 (1), 99–104. doi:10.3969/j.issn.1009-3516.2017.01.017

Conflict of Interest: The authors declare that the research was conducted in the absence of any commercial or financial relationships that could be construed as a potential conflict of interest.

Publisher's Note: All claims expressed in this article are solely those of the authors and do not necessarily represent those of their affiliated organizations, or those of the publisher, the editors and the reviewers. Any product that may be evaluated in this article, or claim that may be made by its manufacturer, is not guaranteed or endorsed by the publisher.

frontiers | Frontiers in Earth Science

ORIGINAL RESEARCH
published: 01 June 2022
doi: 10.3389/feart.2022.916475

Genetic Types of the tp12cx Strike-Slip Fault Segments and Their Role in Controlling Reservoirs in the Tarim Basin

Yanping Lv, Hailong Ma, Zhen Wang, Guangxiao Deng and Huan Wen*

Sinopec Northwest Oilfield Company, Urumqi, China

The change of motion mode of multistage active strike-slip faults controls the segmentary types of strike-slip faults, which is seldom studied.Based on high-precision 3D seismic data and the principle of structural analysis, this paper defines the structural evolution characteristics of the tp12cx strike-slip fault in the key structural period and identifies the fault segmentation types. Combined with the statistical results of drilling production data and fault width, and fault width, it is demonstrated that different fault segments display various reservoir architecture and hydrocarbon potential. The tp12cx strike-slip fault experienced two phases of tectonic activity controlling reservoir development: the middle Caledonian and the late Caledonian to early Hercynian. During the middle Caledonian period, a left-lateral and left-step strike-slip fault was formed. The overlapping segments of the left steps were transtension zones, and the rest were pure strike-slip segments. From the late Caledonian to the early Hercynian, the movement mode changed from left-lateral to right-lateral, and the arrangement of left steps remained unchanged, forming right-lateral and left-step strike-slip faults. That is, as a weak zone, the transtension zones of all the preexisting overlapping segments took the lead in moving into many pure strike-slip segments and maintained the transtensional property. During the right-lateral slipping process of all the original pure strike-slip segments along the fault, they were blocked and squeezed by the surrounding rocks on both sides, forming a series of “positive” flower-shaped fault anticlines, which became overlapping segments, and the fault property became transpressional. Under the continuous action of the right-lateral slipping, a regional right-lateral and right-step strike slip fault formed. The interiors of the right-step-arranged faults were composed of the left-step arranged faults. Among them, the right-step overlapping segments were weakly step overlapping segments were weakly transtensional, and the larger the fault width of the internal left step pure strike slip and overlapping segments, the stronger the dissolution. The deformation of the right-step pure strike-slip segments was weak and basically maintained the characteristics of the previous stage. According to the evolution and superposition of pure strike-slipped and overlapped segments and the changes in fault properties, four types of strike-slip fault segments and corresponding reservoir models are divided. Type I: left-step pure strike-slip segment + left-step transpressional segment + right-step transtensional segment; Type II: left-step

OPEN ACCESS

Edited by:
Hu Li,
Southwest Petroleum University, China

Reviewed by:
Jianhua He,
Chengdu University of Technology, China
Heng Zhang,
China University of Geosciences Wuhan, China

***Correspondence:**
Hailong Ma
297048455@qq.com

Specialty section:
This article was submitted to Economic Geology, a section of the journal Frontiers in Earth Science

Received: *09 April 2022*
Accepted: *02 May 2022*
Published: *01 June 2022*

Citation:
Lv Y, Ma H, Wang Z, Deng G and Wen H (2022) Genetic Types of the tp12cx Strike-Slip Fault Segments and Their Role in Controlling Reservoirs in the Tarim Basin. Front. Earth Sci. 10:916475. doi: 10.3389/feart.2022.916475

transtensional segment + left-step pure strike-slip segment + right-step transtensional segment; Type III: left-step pure strike-slip segment + left-step transpressional segment; and Type IV: left-step transtensional segment + left-step pure strike-slip segment. The fault width and oil production of type II and type IV with transtensional properties are much larger than those of type I and type III with transpressional properties.

Keywords: strike-slip fault, structural evolution, fault segment type, movement mode, reservoir mode

INTRODUCTION

Petroleum exploration in the Tabei Tazhong area of the Tarim Basin in China shows that strike-slip faults not only are important oil migration pathways but also play an important role in controlling the development of fractured vuggy reservoirs in carbonate karst and hydrocarbon accumulation (Deng et al., 2018; Lu et al., 2018; Qiu et al., 2019; Deng et al., 2021; Zhang et al., 2021). The control of carbonate reservoirs by strike-slip faults is mainly reflected in the following aspects: first, fault activity creates a certain range of fracture zones, and many fractures near the fault surface improve reservoir quality (Stefanov and Bakeev, 2014; Lu et al., 2017; Ramadhan et al., 2018; Neng et al., 2018; Zhao et al., 2020; Jiang et al., 2020). second, the network channel formed by faults is conducive to atmospheric freshwater leaching and deep hydrothermal fluid corrosion transformation of the fracture network and surrounding rock, thus forming a large number of corrosion holes (Lu et al., 2017; Yin et al., 2019; Yin et al., 2018b; Li et al., 2019; Li et al., 2020; Li, 2022). A strong-amplitude seismic reflection anomaly is well matched with the fault development area, which indicates that the fault transformation area is the dominant area for the development of dissolution pores (Li et al., 2020; Zhao et al., 2020). A strike-slip fault is composed of multiple pure strike-slip segments and overlapping segments, which can be divided into two types: transpressional and transtensional (Yin et al., 2019; Yin et al., 2020). The left-step overlapping segments of a left-lateral strike-slip fault or the right-step overlapping segments of a right-lateral strike-slip fault are in a state of transtensional stress and develop tension and fault depressions. the right-step segments of a left-lateral strike-slip fault or the left-step segments of a right-lateral strike-slip fault are in a state of compressive stress and develop transpression and fault uplift (Aydin and Nur, 1985; Wang et al., 1999; Mcclay et al., 2001; Cunningham et al., 2007). An transtensional fault has an oblivious effect on fluid migration. In particular, a strike-slip fault overlapping a transtensional segment reservoir is well developed, and oil are enriched (Stefanov and Bakeev, 2014; Deng et al., 2020; Fan et al., 2020). The segmentation of strike-slip faults is of great importance to the deployment of development plans, the construction of well patterns and the selection of drilling technology (Lu et al., 2017; Qie et al., 2021; Shan et al., 2021).

In addition to the differences between structural styles and stress states, the relationship between faults and reservoirs is also considered (Li et al., 2018; Ma et al., 2019; Li et al., 2021; Yin et al., 2019; Yin et al., 2020; Zhou et al., 2022). However, due to the vertical dip angle, small fault distance and narrow deformation zone of a small-scale strike-slip fault, it is difficult to restore the fault style and evolution characteristics of each stage due to the high degree of fracturing in the narrow fault zone, complex structure and accuracy of seismic data identification (He et al., 2020; Zheng et al., 2020; Chen et al., 2021; Zhao et al., 2021; Lan et al., 2021; Zhu et al., 2022; Liu et al., 2022). Changes in the stress state and movement mode of multistage strike-slip faults lead to changes in the fault style, nature, width and quantity (de Joussineau and Aydin, 2007; Mitchell et al., 2009; Kim et al., 2003; Chemenda et al., 2016; Davis et al., 2000; Dooley et al., 2012; Swanson, 2005; Yin and Ding, 2019) and control the reservoir scale and distribution. In the Tabei area, a NE strike-slip fault in the oil enrichment zone has not yet been restored, and the pattern of changes in structural style and its reservoir control function in the key structural period have not been determined. This would be helpful to the further study and understanding of the mechanism of multistage strike-slip faults controlling reservoirs in the Tabei area. The changes in structural style and reservoir control during the key structural period of NE strike-slip fault restoration in the oil enrichment zone in the Tabei area need to be further studied.

In this paper, using high-precision 3D seismic data and structural analysis methods, the NE-trending tp12cx strike-slip fault in the Tabei area is optimized. Combining this information with the regional geological background, the changes in the fault movement mode and structural style in the key tectonic period are reconstructed, and the fault genetic segmentation types are established. The fault properties, width, reservoir development scale, oil production, analysis of reservoir control, and reservoir control are determined. An oil enrichment model corresponding to the genetic segment types of the tp12cx strike-slip fault is established. This study is expected to provide a certain guiding importance for the exploration and development of karst fracture cave reservoirs related to strike-slip faults.

GEOLOGICAL SETTINGS

The large NE-trending tp12cx strike-slip fault is located in the Tabei uplift of the Tarim Basin (**Figure 1**). The planar length of the 3D seismic study area is 67 km (actually more than 88 km), and NW-trending strike-slip faults form multiple groups of "X"-type conjugate faults in map view. By the end of 2020, the fault zone had accumulated oil production of 12.64 million tons, accumulated water production of 1.31 million tons, and average oil production of a single well of 87000 tons. This area is one of the most important oil production reservoirs in the Middle and Lower Ordovician. Its burial depth is more than 6000 m, indicating deep-ultradeep oil exploration. The strata in the study area are well developed, including the Sinian, Cambrian, Ordovician, Silurian, Devonian,

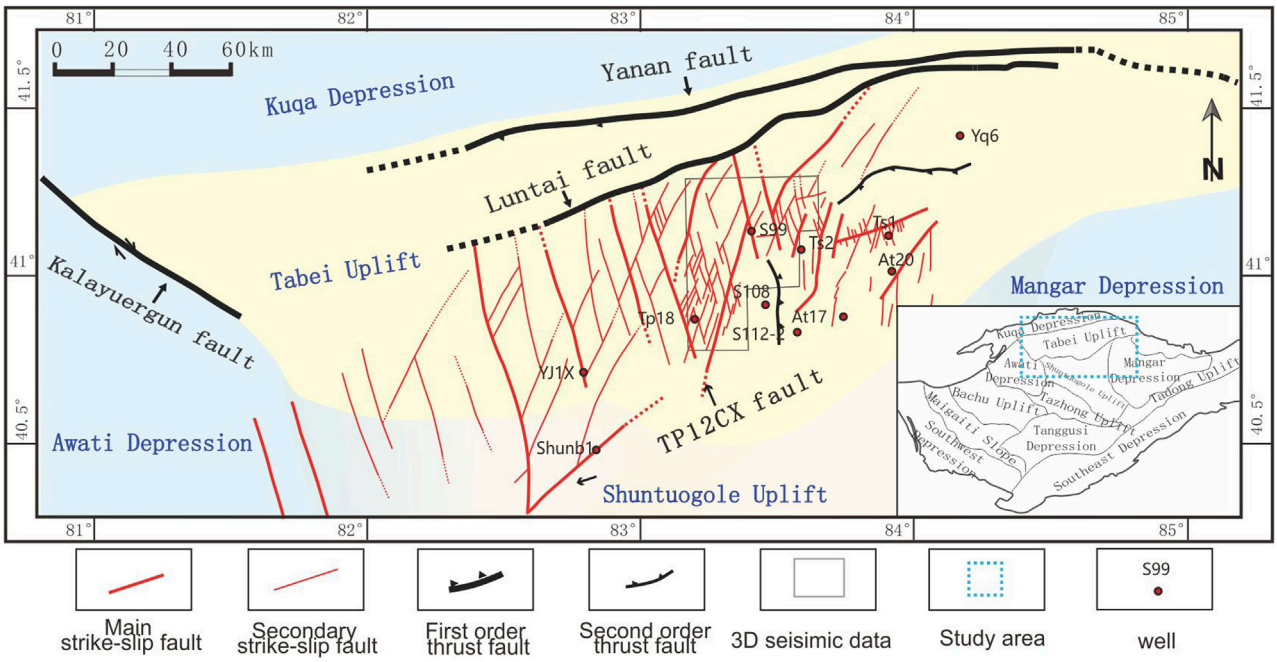

FIGURE 1 | Location map of TP12CX fault structure unit.

Carboniferous, Permian, Triassic, Jurassic, Cretaceous, Paleogene, Neogene and Quaternary systems. The Ordovician system can be subdivided into the upper Sangtamu Formation (O_{3s}), Lianglitage Formation (O_{3l}) and Qiarbak Formation (O_{3q}) from top to bottom. The middle Yijianfang Formation (O_{2yj}), the middle to lower Yingshan Formation ($O_{1\text{-}2y}$), and the lower Ordovician Penglaiba Formation (O_{1p}). From south to north, the Sangtamu Formation and Lianglitage Formation were eroded and pinched out (**Figure 2**).

The study area underwent multiple main tectonic episodes, including the middle to late Caledonian, early Hercynian, late Hercynian, Indosinian, Yanshanian and Himalayan movements (Chen et al., 2019; He et al., 2013; Zhang et al., 2011a; Wu et al., 2020; Wu et al., 2016). The tp12cx fault experienced multistage tectonic movements and continued to move, retaining the signs of each stage of movement. Thus, the tp12cx fault is representative for studying the structural characteristics of each stage in the evolution of strike-slip faults in the Tarim Basin. Since the strike-slip fault zone played an important role in controlling the development of the Ordovician karst reservoir and hydrocarbon accumulation from the middle Caledonian to the early Hercynian period, this paper mainly discusses the segmentation characteristics of the strike-slip fault from the middle Caledonian to the early Hercynian and its control on hydrocarbon accumulation.

DATA AND METHODS

The data used in this paper include high-precision 3D seismic volume data, drilling logging data distributed along the fault zone, and drilling production data. The 3D seismic data are high-precision prestack depth migration data processed in Tahe in 2020, with a total stacking area of 1600 km^2, bin of 15 m × 15 m, sampling rate of 1 m, and two-way travel time of 7 s. Drilling logging data are used to identify the seismic horizon, drilling vent and leakage segment to demarcate the fault boundary, and drilling production data are used to analyze the oil enrichment pattern.

The research ideas and methods are as follows: 1) Combined with the changes in the movement mode of the tp12cx strike-slip fault caused by regional stress changes, the structural evolution characteristics of the top of the Ordovician Yingshan Formation in the key structural period of the tp12cx strike-slip fault are restored. Based on the segmentation of the tp12cx strike-slip fault, the fault genetic segmentation types under the changes in movement mode are divided (Zhang et al., 2011b; Wu et al., 2016; Wu et al., 2020). 2) The width of each fault zone and drilling production of the tp12cx strike-slip fault are counted to verify the rationality of the genetic segmentation type. The distribution of strike-slip faults in key structural layers can be identified by the properties of coherence, tensor and dip angle. Since the northern part of tp12cx fault is a buried hill area jointly controlled by paleogeomorphology and faults, the role of fault in controlling reservoir is weakened compared with the southern covering area; thus, the width and nature of the fault zone in the fault-controlled karst area only in the southern part of the tp12cx fault are assessed. Among the faults, the top fault in the Ordovician Yingshan Formation dolomitic limestone (seismic reflection group T_7^6) is used to calculate the width of the fault zone to avoid the illusion of widening of the fault zone caused by dissolution. The width of the fault zone is determined by the ratio of the area of the fault zone to the approximate length of the fault zone. 3) The relationship between the genetic segmentation type and the reservoir is analyzed, and a corresponding reservoir model is established. First, using the root mean square amplitude change

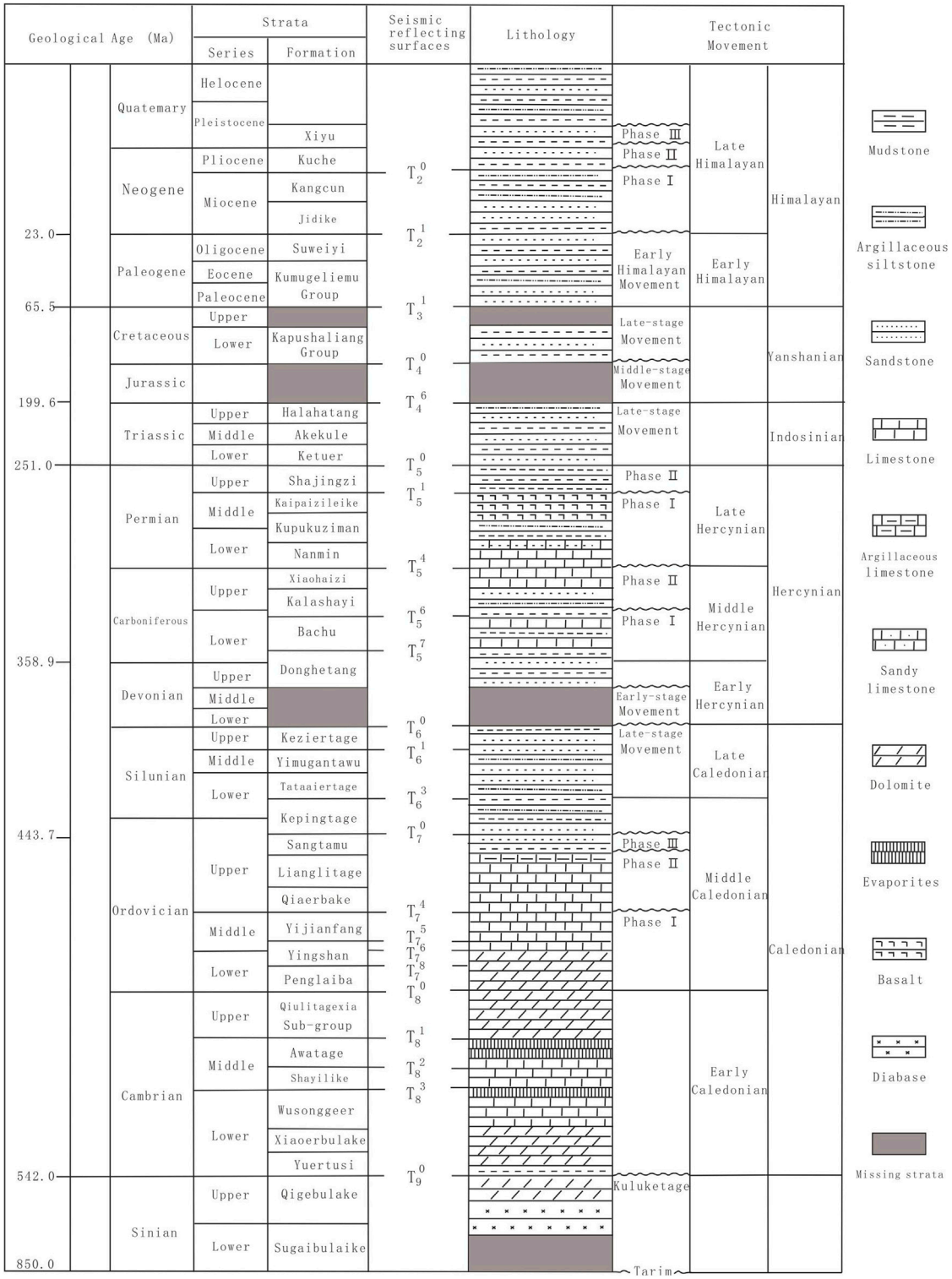

FIGURE 2 | Chart showing the Tarim Basin stratigraphy, the seismic reflecting surfaces, and timing of regionl tectonic movements.

rate attribute of the Ordovician Yijianfang Yingshan Formation is a relatively mature method (Ma et al., 2019; Wang et al., 2019) to predict the karst fracture vuggy reservoir in the study area. Through the superposition of the strike-slip fault and fracture vuggy reservoir and the width of the fault zone, the impacts of the movement mode, genesis and segmentation type on the fracture vuggy reservoir are

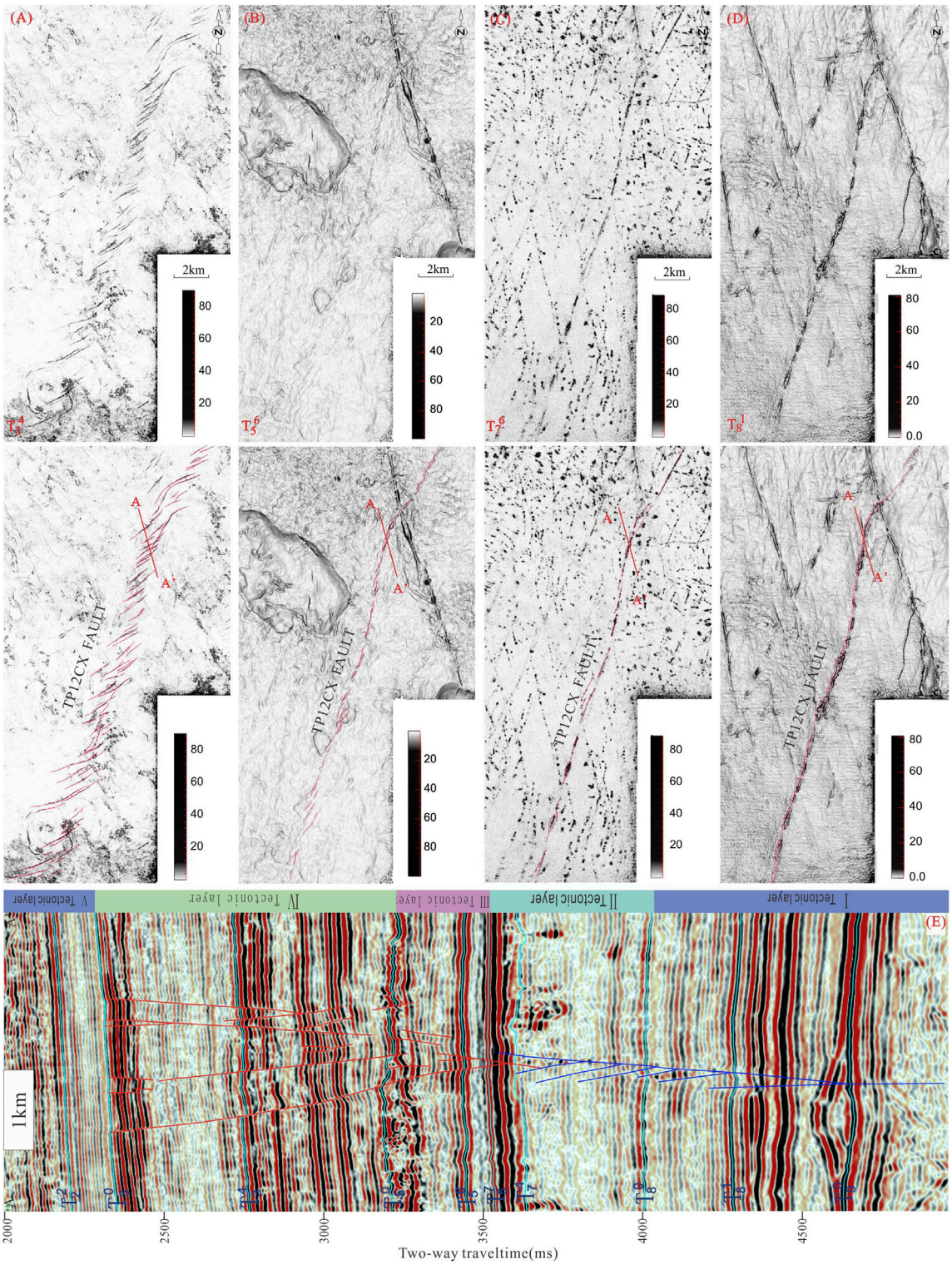

FIGURE 3 | Uninterpreted coherence slices(top images in **(A–D)**) and interpreted coherence slices (middle images in **(A–D)**), The middle image, AA ′, shows the location of the seismic section located at the bottom. **(A)** coherence slice of surface T34. **(B)** coherence slice of surface T56. **(C)** coherence slice of surface T76. **(D)** coherence slice of surface T81 and **(E)** AA' section of TP12CX fault.

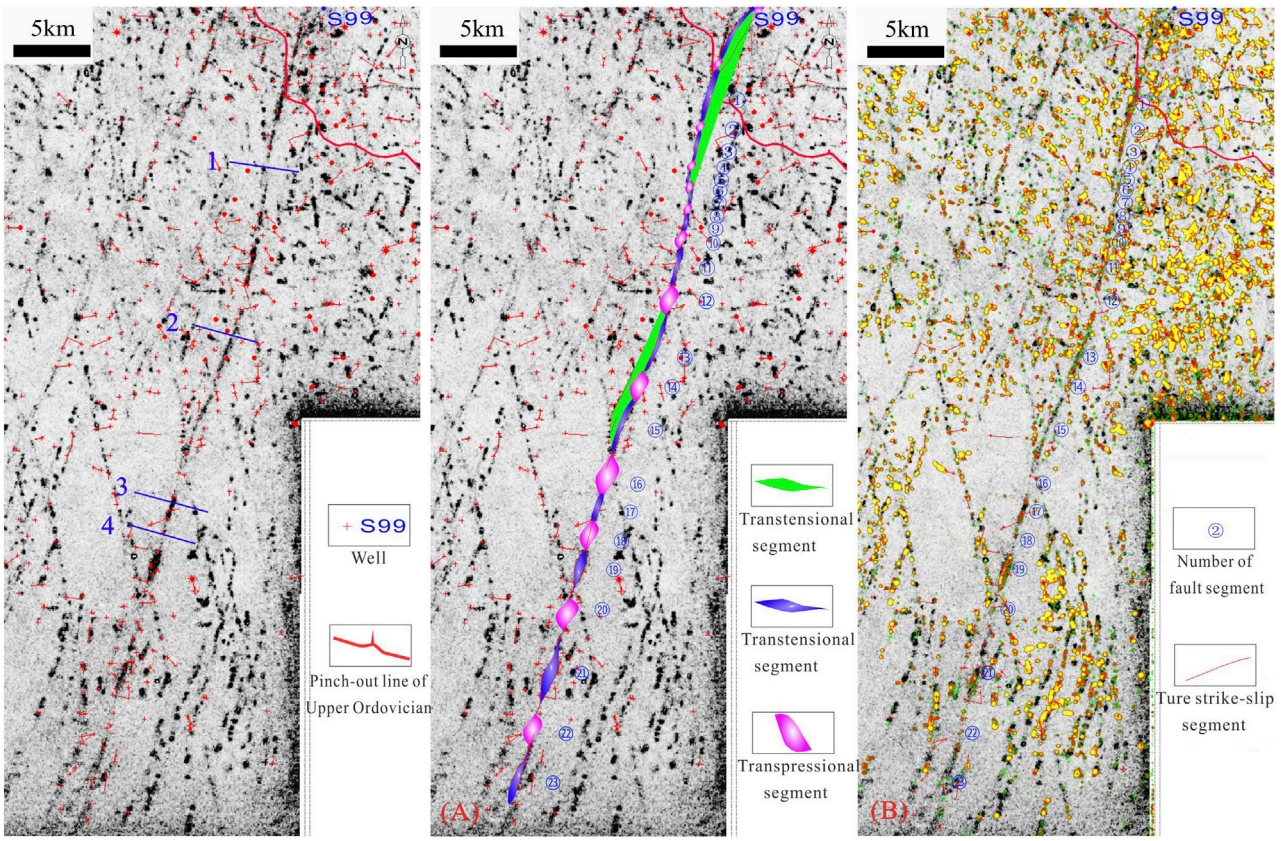

FIGURE 4 | (A) Segmented results of TP12CX fault **(B)** Amplitude rate of T74 and coherence of T76

analyzed. The second step is to analyze the differences in oil enrichment of the segmented types through drilling oil production and to establish the oil enrichment model corresponding to the genetically segmented types of Ordovician movement modes.

RESULTS

Structural Stratification

Vertically, the study area is divided into five structural layers (**Figure 3**). Structural layer I (ϵ_{2a} ~ basement) developed normal faults. The second structural layer (D_{3d}~ϵ_{2a}) is the most developed fault layer, which contains mainly NE-trending and NW-trending flower-like strike-slip faults. Some of the main NE- and NW-trending strike-slip faults of structural layer III (P ~ D_{3d}) continued to move. The fourth structural layer (P ~ E) consists of grabens and half-grabens controlled by tensional torsional left-lateral normal faults. In structural layer V (above E), faults are underdeveloped.

Geometry Characteristics of Fault

The TP12CX strike-slip fault zone can be divided into 23 segments, 12 segments of transtension segment, 11 segments of transpression segment (**Figure 4**) in mudstone covered area of The Sangtamu Formation, and the pure strike-slip segment is missing.

Transpression segment: fault anticlines or anticlines characterized by transpression in the segment (**Figures 5A,C**), which break down through the middle and lower Cambrian strata and spread upward in the face of T80 reflection layer to form fault anticlines or anticlines. Different degrees of faults are developed along the axis of the fault anticline, and the number and connectivity of faults are greatly different. Most of the seismic reflection characteristics are chaotic weak reflection, and the strong reflection of the string of beads is underdeveloped. There are strong reflections on the two wings of the fault anticline and continuous weak reflections on the two wings of the anticline. The reflection characteristics of faults are continuous downward, and the faults in the T80-T74 seismic reflection layer become discontinuous and appear intermittently.The number of faults is less than that of transtensional segmental faults, the fault grade is smaller and the connectivity between upper and lower faults is poor. The width of the fault zone ranges from 0 to 110m, and the oil production ranges from 0 to 57,300 tons (**Figure 6** and **Table 1**). **Figure 4B** shows the overall underdevelopment of the reservoir.

Transtension segment: the segment is characterized by vertical tensional half-graben or graben, and the fault zone is chaotic, beadlike strong reflection is generally developed, with high fracture degree and good connectivity above and below the fault (**Figures 5A,C**). In plane, the fault is rhomboid and

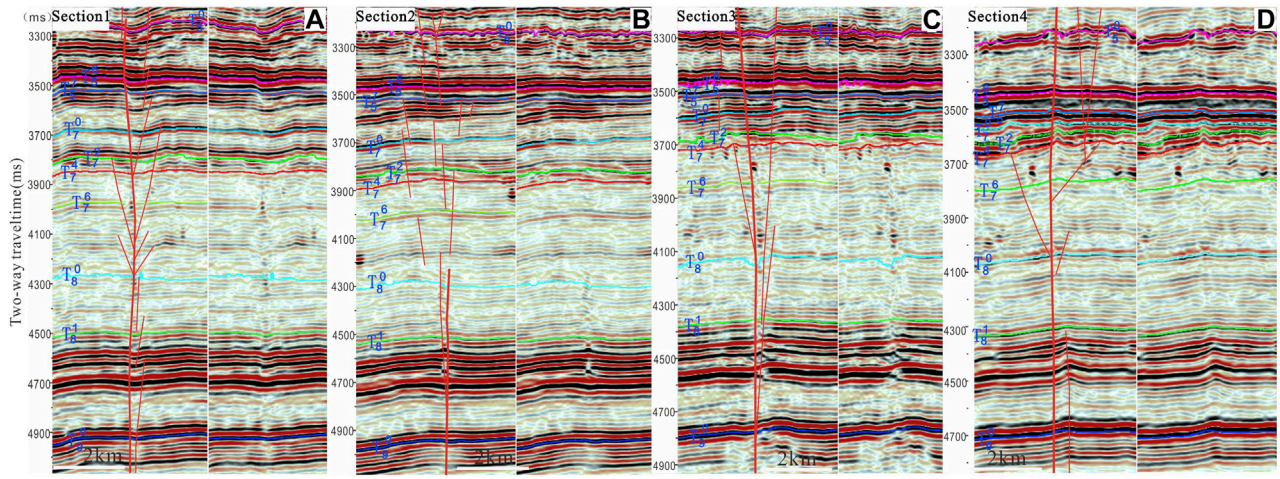

FIGURE 5 | Fault interpretations of cross sections 1–4 oriented perpendicularly to fault TP12CX. **(A)** Section 1. **(B)** Section 2. **(C)** Section 3. **(D)** Section 4. **(A–D)** The uninterpreted right images are shown for comparison and cropped as the central part of the left images where fault zones occur; see **Figure 4** for the locations of the sections.

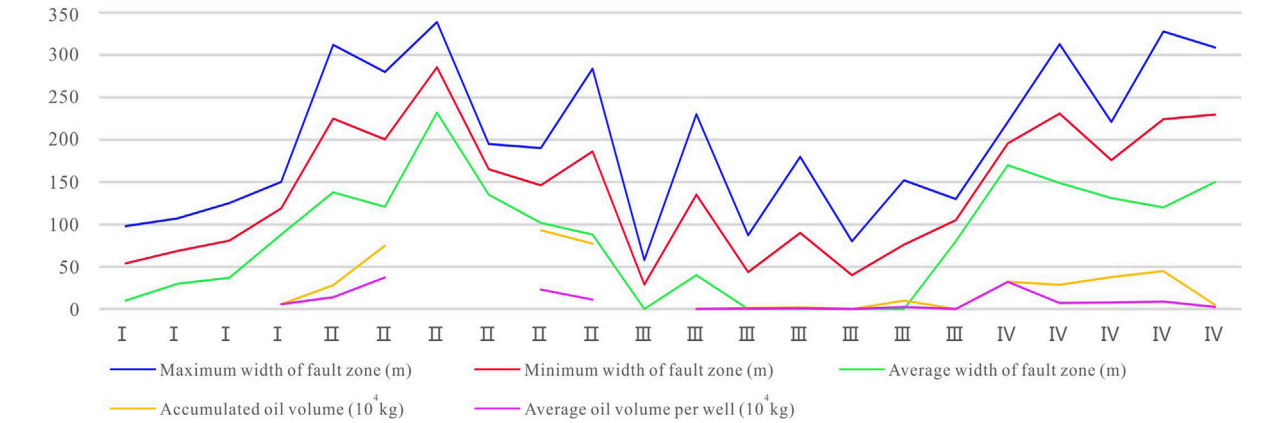

FIGURE 6 | Fault width and oil and gas production of the tp12cx strike slip fault.

banded. Compared with the transpression segment, the number of faults is larger, and the connectivity between upper and lower faults is better. The width of the fault zone ranges from 110 to 345 m, with oil production ranging from 24,700 to 374,400 tons (**Figure 6** and **Table 1**). **Figure 4B** shows that the reservoir is more developed as a whole.

DISCUSSION

Tectonic Evolution of the tp12cx Fault in a Key Tectonic Period

Given the regional geological background of the Tabei uplift (Zhang et al., 2011a; Wu et al., 2020; Wu et al., 2016), the tp12cx fault mainly experienced the early Caledonian, middle to late Caledonian, early Hercynian, late Hercynian, Indosinian, Yanshanian and Himalayan movements. During these movements, the NE-trending tp12cx strike-slip fault did not develop along the NE-trending (**Figure 2**) transtensional faults formed in the early Caledonian period, so the influence of tectonic activity in this period is not considered. The South Tianshan orogeny lasted until the end of the Triassic and then entered the postorogenic stress relaxation stage from the Jurassic to the Early Cretaceous. Regional tectonic transtension occurred along the early large-scale strike-slip faults, forming a series of en echelon left-step transtensional faults. Therefore, the influence of Indosinian and Yanshanian tectonic movements is not considered. This paper mainly focuses on the relationship between the movement mode transformation and fault segmentation of the (Wu et al., 2020) strike-slip fault in the middle to late Caledonian, early Hercynian and late Hercynian.

In the middle Caledonian stage I-III movements, the Tabei area was under the action of a N-S-trending compressive tectonic stress field, forming a series of NW- and NE-trending "X"-type

TABLE 1 | Characteristics and oil and gas production of each segment of the tp12cx strike slip fault.

Number of Fault Segment	Types of Fault Segments	Structural Properties	Maximum Width of Fault Zone (m)	Minimum Width of Fault Zone (m)	Average Width of Fault Zone (m)	Accumulated Oil Volume (10^4 Kg)	Average Oil Volume per Well (10^4 Kg)	Number of Wells
1	II	Extension	292	138	210	28.2	14.1	2
2	I	Compression	98	10	30	0	0	0
3	II	Extension	220	121	160	74.88	37.44	2
4	I	Compression	107	30	63	Reservoir nature reserve, unable to drill		
5	II	Extension	339	232	243			
6	I	Compression	125	37	82			
7	II	Extension	165	125	155			
8	III	Compression	58	0	14			
9	IV	Extension	251	200	219	32.23	32.23	1
10	III	Compression	230	40	110	0.23	0.23	1
11	IV	Extension	343	169	255	28.48	7.12	4
12	III	Compression	87	0	10	1.34	0.67	2
13	II	Extension	190	92	155	93	23.25	4
14	I	Compression	150	88	110	5.73	5.73	1
15	II	Extension	284	80	172	77.35	11.05	7
16	III	Compression	180	0	20	2.07	1.035	2
17	IV	Extension	225	138	180	37.79	7.558	5
18	IV	Compression	80	0	30	0	0	0
19	IV	Extension	442	120	345	44.81	8.962	5
20	III	Compression	152	0	40	10.02	2.505	4
21	IV	Extension	329	150	212	4.94	2.47	2
22	III	Compression	130	80	110	0	0	0
23	IV	Extension	320	150	275	80.18	11.45429	7

conjugate shear fault systems (**Figure 7A**). The NW-trending faults are dominated by right-lateral motion and left steps, while the NE-trending faults are dominated by left-lateral motion and left steps. The overlapping segments of the left step of the NW-trending fault are compressive. The overlapping segments of the left step of the NE-trending fault are mainly pulled apart, and the pure strike-slip segments are vertical linear faults.

From the late Caledonian to early Hercynian, under the NNE or NE shear stress produced by NW-SE transpression, the tp12cx fault moved again, and its mode changed from left-lateral to right-lateral strike-slip movement. The left-lateral and left-step faults, which resulted in the formation of early left-lateral strike-slip motion, disappeared in the process of right-lateral strike reverse strike-slip motion, and their formation and evolution experienced two stages. In the first stage (**Figure 7B**), the left-lateral left-step segment is transformed into a right-lateral left-step fault segment. The original left-step overlapping transtensional segment is undergoing pure strike-slip motion. In the process of right-lateral strike-slip movement, the left-step pure strike-slip segment is compressed and closes to form a positive flower-like deformation with transpressional uplift. In the second stage, with continuous right-lateral strike-slip activity, a regional arc-shaped right-lateral and right-step fault composed of several left-step faults forms (**Figure 7C**).

In the late Hercynian period, influenced by the southwestern Tarim orogenic belt, the tp12cx fault moved in the form of right-lateral motion under long-distance transpression from south to north. This interpretation further confirms that the arcuate faults in the right-lateral right-step region include small left-lateral left-step faults.

Genetic Segmentation Type

From the above fault evolution characteristics, it can be seen that the segmented characteristics of TP12CX strike-slip faults are due to the transformation of fault motion mode, which leads to the continuous change of fault arrangement and fracture properties. The tp12cx strike-slip fault is divided into four genetic segmentation types according to the mutual superposition of overlapping segments and pure strike-slip segments, the change characteristics of fault properties, and the statistical data characteristics of reservoir development (**Figure 4**), drilling production data and fault width (**Table 1**).

Type I: left-step pure strike-slip segment + left-step transpressional segment + right-step transtensional segment.

In the middle Caledonian, this type of segment is a left-step pure strike-slip segment. From the late Caledonian to early Hercynian, after transformation from left-lateral to right-lateral strike-slip motion, this type of segment appears as a right-lateral and left-step overlapping segment, showing a positive flower-like structural style. Under the continuous action of right-lateral strike-slip motion, only a few more faults form in the transtensional zone of the right-lateral right-step segments in the region, and the pattern of normal flower transpression remains unchanged (**Figure 5B**, **Figure 8**). The fault breaks downward through the middle and lower Cambrian strata, displaces the anticline upward and deforms, with faults on both limbs and a few small faults on the axis of the anticline.

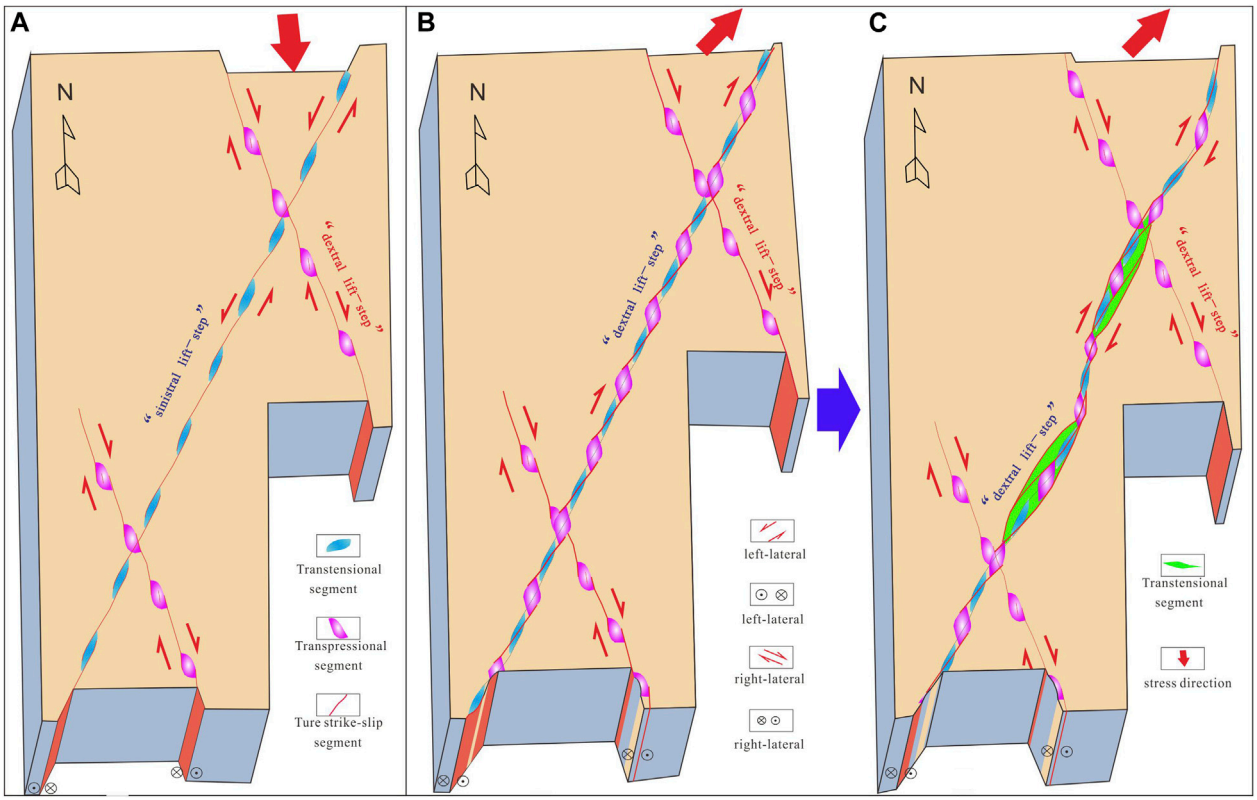

FIGURE 7 | Structural evolution model of Ordovician in key structural period of tp12cx strike slip fault. **(A)** Middle Caledonian **(B)** late Caledonian Early Hercynian stage I **(C)** late Caledonian Early Hercynian stage II.

Against the background of disordered weak reflections, only beaded strong reflections are developed along the fault, the number of faults is small, and the width of the fault zone is 30–110 m. At least one well is drilled, and the average oil production capacity of each segment is 57300 tons. The average oil production of a single well is 57300 tons. The average oil production of a single well is equal to the ratio of the cumulative production sum to the sum of wells.

Type II: left-step transtensional segment + left-step pure strike-slip segment + right-step transtensional segment.

In the middle Caledonian, this type of segment is a left-step transtensional overlapping segment, and it then becomes a left-step pure strike-slip segment under the action of right-lateral strike-slip motion and still retains the negative flower-like structural style. Under the continuous action of right-lateral strike-slip, it is in the regional right-lateral and right-step transtensional zone, the number of faults increases, and the transtensional range is larger. The overall result is a rhombic and banded transtensional zone (**Figures 5A**, **8**), which is broken up and down with a high degree of fragmentation. In the fault zone, disordered and beaded strong reflections are widely developed. The number of faults is the highest, and the width of the fault zone ranges from 110 to 243 m. The number of drilling wells is up to 11. The oil production capacity of each segment ranges from 110500 to 374400 tons, and the average oil production of a single well is approximately 182300 tons.

Type III: left-step pure strike-slip segment + left-step transpressional segment + right-step pure strike-slip segment.

In the middle Caledonian period, this type of segment is a left-lateral left-step pure strike-slip segment, and a right-lateral strike-slip segment then becomes a right-lateral left-step overlapping segment, which is blocked in a transpression normal flower structure style (**Figures 5D**, **8**). This type is very similar to type I, except that the axial fault of the anticline is underdeveloped and the strong reflection of the anticline is not developed. The number of faults is the lowest, the width of the fault zone is 0–80 m, and 9 wells are drilled. The oil production capacity of each segment is 0–25000 tons, and the average oil production of a single well is approximately 15200 tons. The benefit of a single well is low, and few wells are deployed.

Type IV: left-step transtensional segment + left-step pure strike-slip segment + right-step pure strike-slip segment.

In the middle Caledonian period, this type of segment is a left-lateral left-step transtension overlap segment, and a right-lateral strike-slip segment then becomes a right-lateral left-step pure strike-slip segment, which still retains the negative flower-like structural style and is of transtensional nature as a whole (**Figures 5C**, **8**). The target layer is characterized by

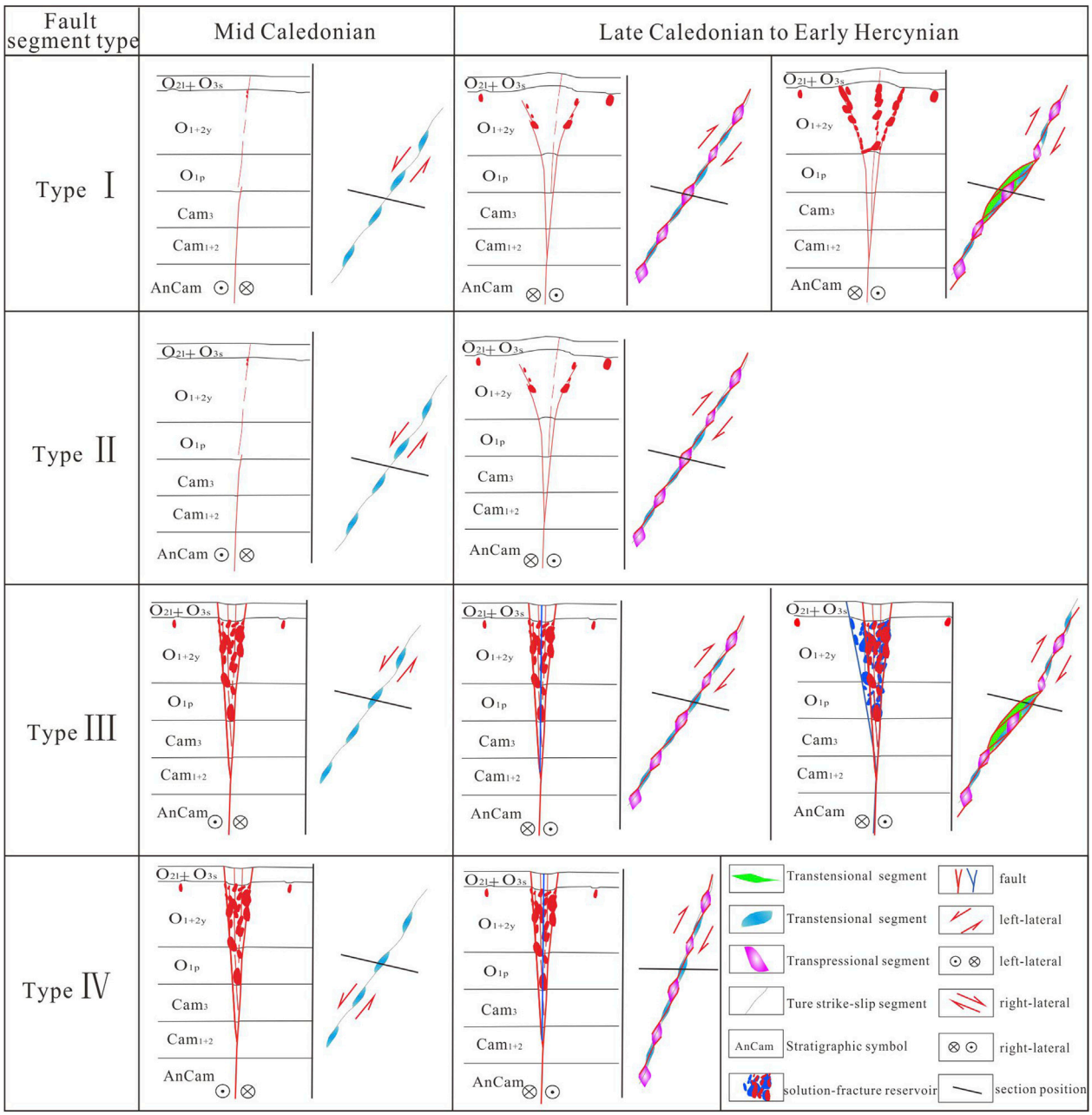

FIGURE 8 | Segment-type diagram of a NE-trending strike-slip fault based on the evolution characteristics.

disordered strata, abundant strong seismic reflection anomalies, obvious fault extent and good communication between the upper and lower layers. The width of the fault zone is 180–345 m, and up to 23 wells have been drilled. The average oil production capacity of each segment is 24700–322300 tons, and the average oil production of a single well is approximately 95200 tons.

According to the statistical results (**Figure 6**), 1) the number of wells indicates that the regional right-lateral and right step transtensional segment is only locally developed. 2) The number of faults, the width of the fault zone, the size of the reservoir and the oil production in the transtensional segment are larger than those in the transpressional segment. 3) The larger the number of faults and the width of the fault zone are, the larger the reservoir scale and oil production. 4) The width of the fault zone, reservoir scale and reservoir quality are ordered as type II > type IV > type I > type III. The reservoirs in the transpressional segment are developed along strike-slip faults on a large scale, and the reservoirs far from the fault zone are weakly developed. The fracture cavity bodies in the

transpression segment are scattered, isolated or undeveloped along the strike-slip fault zone.

Development Model of Fault-Solution Reservoir

The distribution and scale of Ordovician reservoirs in the tp12cx strike-slip fault zone are controlled by the segmentation type of strike-slip faults, and the segmentation type of strike-slip faults is controlled by the multistage superposition and transformation of overlapping and pure strike-slip segments caused by the movement mode of strike-slip faults.

In the middle Caledonian period, under the action of left-lateral strike-slip motion, left-step arranged strike-slip faults formed. The overlapping segment of the left step has the property of transtension, and the pure strike-slip segment is a vertical linear fault. Regardless of whether the number and width of faults in the transtension area of the overlapping segment are much larger than those in the pure strike-slip segment, the karstification and dissolution degree along the fault zone are much greater than those along the pure strike-slip segment, and the reservoir scale is correspondingly better than that along the pure strike-slip segment.

From the late Caledonian to the early Hercynian, the tp12cx fault reversed to right-lateral strike slip, and the original left lateral and left step fault styles were transformed. First, the arrangement of the left step fault did not change, but only the fault style and local properties changed. That is, the left step transtensional segment is most easily transformed as a weak zone due to more developed faults and fractures, a higher degree of fragmentation and a wider fault zone and is transformed into a right-lateral and left step pure strike-slip segment, retaining the transtensional property. Due to the vertical plane shape of the fault and weak fracture network fragmentation, the original left step pure strike-slip segment is not easily transformed by the later tectonic activities. Under the action of later tectonic activities, it gradually changes into a right lateral and left step overlapping area and forms a “positive” flower-shaped transpression segment of the fault anticline under the action of extrusion pressure. In the early stage, the scale of the karst stage and the right-lateral displacement fracture network are better, and the properties of the left and right displacement fractures are better preserved. In the right lateral and left step overlapping segment, the original fault is compressed and partially closed, and the fracture cave reservoir becomes worse. The two newly formed wing faults of the anticline experience karstification in this period and develop fracture cave reservoirs, and the scale of the reservoirs is relatively limited.Second, under the action of continuous right-lateral strike slip, the bending effect occurs, and a regional arc right-lateral strike-slip fault is gradually formed. The interior is composed of faults arranged on the left step. The overlapping segment of the right lateral and right step in the region is generally weakly pulled apart, and the number, width and reservoir development scale of faults in the transpression segments and transtension segments are relatively better than those in the pure strike-slip segments. Among them, the number and degree of fractures in the transtension segments of the left step are greater, the karstification is stronger, and the reservoir is more developed. The transpression segment is compacted, the faults on both wings of the anticline are opened, the karstification becomes stronger, and the reservoir becomes better. Since the late Hercynian karstification has made little contribution to the Ordovician carbonate cave reservoir, the fractured reservoir formed by the fault itself has limited reservoir capacity (Zhang et al., 2011b; Zhou et al., 2011a; Zhang et al., 2012; Han et al., 2016). The right lateral and right step overlapping transtension segment, regardless of the reservoir scale and reservoir scale, is larger than the right lateral and right step pure strike-slip segment. The main reservoir-forming period in the study area was the late Caledonian Indosinian period (Zhu et al., 2010), indicating that the regional arc right lateral and right step strike-slip faults formed before the late Hercynian period, and the reservoir scale was controlled by the pre-Hercynian correlation.

It can be seen from the above that the scale of the reservoir is jointly controlled by the number and nature of faults and corresponding karstification, but the strength of karstification is controlled by the segmented type of strike-slip faults. Therefore, in the final analysis, the scale of the reservoir is controlled by the number and nature of strike-slip faults, especially the nature of strike-slip faults.

Fault Solution Reservoir Model

The structure of the fault fracture network and matched karst reservoir jointly determine the development characteristics of the reservoir. Four types of strike-slip fault segments correspondingly form four types of fault solution reservoir models (**Figure 9**):

Type I reservoir model, corresponding to the type I structure. The evolution process of fault properties is first transpression, then transtension. The whole area is characterized by fault anticline transpression, obvious fault distance in the deep part, positive flower-shaped fault anticline deformation in the shallow part, and beaded strong reflection reservoirs developed along the two wings and axis faults of the anticline. After the left-lateral changes to right-lateral strike slip, it translates and slides in the formed left-lateral strike-slip zone, and then the sliding in the left-lateral strike-slip segment is blocked to form a flower-shaped fault anticline and then form a regional right-lateral strike-slip fault. This stress gradient transmission mode does not make the whole fault anticline disappear; that is, the scale of the bending effect in the late stage is small, which is not enough to change the whole right-lateral strike-slip segment into an transtension zone. Only the faults and fractures are more developed, the reservoir connectivity is better, and the reservoir scale is better than that of the type III extrusion segment. The average oil production of a single well is lower, reaching 57300 tons.

Type II reservoir model, corresponding to the type II structure type. The evolution process of fault properties is: first transtension, then transtension. A wide graben is formed by vertical faults as a whole. The plane is in a continuous banded and rhombic shape. The fault width is large. The beaded strong reflection reservoir is developed along the whole fault zone. The average oil production of a single well is the largest, up to 182300 tons.

The reservoir model of the type III segment corresponds to the type III structure type. and the evolution of fault properties has

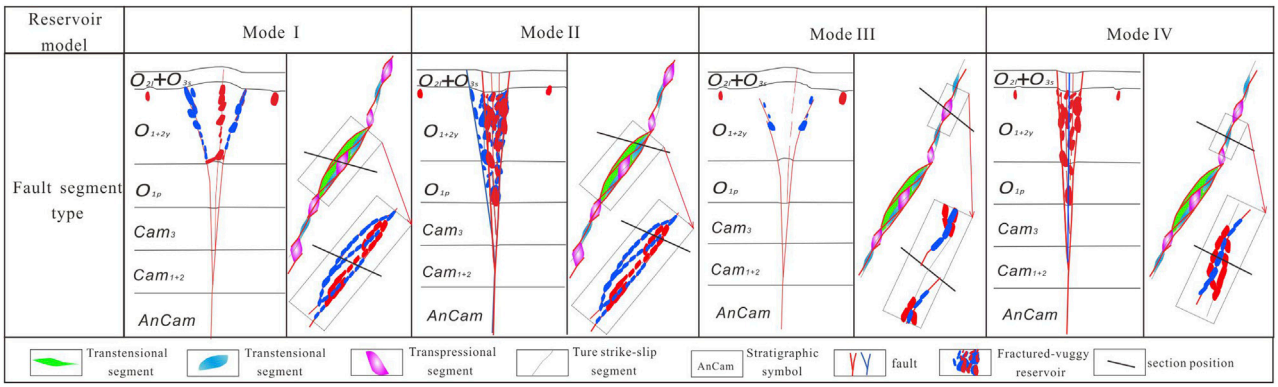

FIGURE 9 | TP12CX fault segmentation type and reservoir model.

only experienced transpression. It is very similar to the type I transpression mode, but the difference is that the anticline axis fault is underdeveloped, and the beaded strong reflection reservoir is also underdeveloped. The average oil production of this type of single well is the lowest, only 15200 tons. This is because this type of segment is a translational segment in the middle Caledonian period, and karstification developed along the line-like faults. Under the action of transpression and torsion from the late Caledonian to the early Hercynian, the lithology was dense, and the physical properties of the original reservoir worsened. At the same time, the weak faults along the two wings of the anticline were dissolved to form a limited reservoir with a small scale.

Type IV reservoir model, corresponding to the type IV reservoir structure. The evolution of fracture properties only experienced tension. Narrow symmetrical grabens or asymmetric half grabens are formed by vertical faults, with relatively continuous linear planes and narrow widths. Strong amplitude reflection reservoirs are developed along the whole fault zone. The average oil production of a single well is more than once, reaching 95200 tons.

CONCLUSION

The tp12cx strike-slip fault experienced two key stages of tectonic movement determining segmentation: middle Caledonian and late Caledonian to early Hercynian. In the middle Caledonian period, right-lateral and right-step faults form. The overlapping left-step segment is a transtensional zone, and the remainder is a linear pure strike-slip segment. From the late Caledonian to early Hercynian, the mode changes from left-lateral strike-slip to right-lateral strike-slip movement. The left-step tension fracture zone first ruptures and retains the property of being transtensional, while the left-step linear pure strike-slip segment is transformed into a left-step overlapping segment with transpression. With continuous right-lateral movement, a regional right-lateral right-step strike-slip fault composed of several left-step faults is formed.

Four structure types of strike-slip faults and corresponding reservoir models are divided based on the structural evolution process. The left-step pure strike-slip segment + left-step transpressional segment + right-step transtensional segment is type I, the left-step transtensional segment + left-step pure strike-slip segment + right-step transtensional segment is type II, the right-step translation + left-step pure strike-slip segment left-step pure strike-slip segment + left-step transpressional segment is type III, and the left-step transtensional segment + left-step pure strike-slip segment is type IV. The fault width and oil production of type II and type IV fractures with transtensional properties are much larger than those of transpression types I and III.

DATA AVAILABILITY STATEMENT

The original contributions presented in the study are included in the article/Supplementary Material, further inquiries can be directed to the corresponding author.

AUTHOR CONTRIBUTIONS

YL: Provide research ideas; HM: The structural analysis and genetic type of TP12cx strike-slip fault are summarized; ZW Reservoir type summary and analysis; GD: Statistical analysis of data; HW: Statistical analysis and mapping of data.

ACKNOWLEDGMENTS

We thank all editors and reviewers for their helpful comments and suggestions.

REFERENCES

Aydin, A., and Nur, A. (1982). Evolution of Pull-Apart Basins and Their Scale Independence. *Tectonics* 1 (1), 91–105. doi:10.1029/tc001i001p00091

Aydin, A., and Nur, A. The Types and Role of Stepovers in Strike-Slip Tectonics. 1985,.37:35–44 doi:10.2110/pec.85.37.0035

Chemenda, A. I., Cavalié, O., Vergnolle, M., Bouissou, S., and Delouis, B. (2016). Numerical Model of Formation of a 3-D Strike-Slip Fault System. *Comptes Rendus Geosci.* 348 (1), 61–69. doi:10.1016/j.crte.2015.09.008

Chen, G. B., Li, T., and Yang, L. (2021). Mechanical Properties and Failure Mechanism of Combined Bodies with Different Coal-Rock Ratios and Combinations. *J. Min. Strata Control Eng.* 3 (2), 023522. doi:10.13532/j.jmsce.cn10-1638/td.20210108.001

Chen, J. J., He, D. F., and Sun, F. Y. (2019). Three Dimensional Geological Structure of Tabei Paleouplift and Related Problems. *Geosci. Front.* 26 (01), 121–133. doi:10.13745/j.esf.sf.2019.1.8

Cunningham, W. D., and Mann, P. (2007). Tectonics of Strike-Slip Restraining and Releasing Bends. *Geol. Soc. Lond. Spec. Publ.* 290 (1), 1–12. doi:10.1144/sp290.1

Davis, G. H., Bump, A. P., Garcıia, P. E., and Ahlgren, S. G. (2000). Conjugate Riedel Deformation Band Shear Zones. *J. Struct. Geol.* 22 (2), 169–190. doi:10.1016/s0191-8141(99)00140-6

de Joussineau, G., and Aydin, A. (2007). The Evolution of the Damage Zone with Fault Growth in Sandstone and its Multiscale Characteristics. *John Wiley Sons, Ltd* 112 (B12), 6. doi:10.1029/2006jb004711

Deng, S., Li, H., Zhang, Z., Zhang, J., and Yang, X. (2018). Structural Characterization of Intracratonic Strike-Slip Faults in the Central Tarim Basin. *AAPG Bull.* 103 (1)109-137. doi:10.1306/06071817354

Deng, S., Liu, Y. Q., and Liu, J. (2021), Development and Evolution of Strike Slip Faults in the Inner Craton Basin and Their Petroleum Geological Significance: a Case Study of Shunbei Area. *Tarim Basin. Geotect. metallogeny*, 1–16. [2021-05-15]. doi:10.16539/j.ddgzyckx

Dooley, T. P., and Schreurs, G. (2012). Analogue Modelling of Intraplate Strike-Slip Tectonics: A Review and New Experimental Results. *Tectonophysics* 574-575, 1–71. doi:10.1016/j.tecto.2012.05.030

Fan, C., Li, H., Qin, Q., He, S., and Zhong, C. (2020). Geological Conditions and Exploration Potential of Shale Gas Reservoir in Wufeng and Longmaxi Formation of Southeastern Sichuan Basin, China. *J. Petroleum Sci. Eng.* 191, 107138. doi:10.1016/j.petrol.2020.107138

Han, C. C., Lin, C. Y., and Ren, L. H. (2016). Characteristics of Ordovician Fault in the Block 10 of Tahe Oilfield, Tarim Basin and its Controlling Effect on Karst Reservoirs. *Nat. Gas. Geosci.* 27 (5), 790–798. doi:10.11764/j.issn.1672-1926.2016.05.0790

He, B. Z., Jiao, C. L., and Xu, Z. Q. (2013). Response of Tectonic Unconformity in the Middle Late Caledonian Period of Tarim Basin to the Tectonism of Peripheral Orogenic Belt. *Acta Geol. Sin.* 87 (S1), 34. doi:10.1111/1755-6724.12148_4

He, X., Zhang, P., He, G., Gao, Y., Liu, M., Zhang, Y., et al. (2020). Evaluation of Sweet Spots and Horizontal-Well-Design Technology for Shale Gas in the Basin-Margin Transition Zone of Southeastern Chongqing, SW China. *Energy Geosci.* 1 (3–4), 134–146. doi:10.1016/j.engeos.2020.06.004

Hong, D., Cao, J., Wu, T., Dang, S., Hu, W, and Yao, S. (2020). Authigenic Clay Minerals and Calcite Dissolution Influence Reservoir Quality in Tight Sandstones: Insights from the Central Junggar Basin, NW China. *Energy Geosci.* 1 (1–2), 8–19. doi:10.1016/j.engeos.2020.03.001

Jiang, T. W., Han, J. F., Wu, G. H., Yu, H., Su, Z, Xiong, C, et al. (2020). Differences and Controlling Factors of Composite Hydrocarbon Accumulations in the Tazhong Uplift, Tarim Basin, NW China. *Petroleum Explor. Dev. Online* 47 (2): 229-241. doi:10.1016/s1876-3804(20)60042-8

Kim, Y.-S., Peacock, D. C. P., and Sanderson, D. J. (2003). Mesoscale Strike-Slip Faults and Damage Zones at Marsalforn, Gozo Island, Malta. *J. Struct. Geol.* 25 (5), 793–812. doi:10.1016/s0191-8141(02)00200-6

Lan, S. R., Song, D. Z., Li, Z. L., and Liu, Y. (2021). Experimental Study on Acoustic Emission Characteristics of Fault Slip Process Based on Damage Factor. *J. Min. Strata Control Eng.* 3 (3), 033024. doi:10.13532/j.jmsce.cn10-1638/td.20210510.002

Li, H., Qin, Q., Zhang, B., Ge, X., Hu, X., Fan, C., et al. (2020). Tectonic Fracture Formation and Distribution in Ultradeep Marine Carbonate Gas Reservoirs: A Case Study of the Maokou Formation in the Jiulongshan Gas Field, Sichuan Basin, Southwest China. *Energy fuels.* 34 (11), 14132–14146. doi:10.1021/acs.energyfuels.0c03327

Li, H. (2022). Research Progress on Evaluation Methods and Factors Influencing Shale Brittleness: A Review. *Energy Rep.* 8, 4344–4358. doi:10.1016/j.egyr.2022.03.120

Li, H., Tang, H., Qin, Q., Zhou, J., Qin, Z., Fan, C., et al. (2019). Characteristics, Formation Periods and Genetic Mechanisms of Tectonic Fractures in the Tight Gas Sandstones Reservoir: A Case Study of Xujiahe Formation in YB Area, Sichuan Basin, China. *J. Petroleum Sci. Eng.* 178, 723–735. doi:10.1016/j.petrol.2019.04.007

Li, W., Meng, M. F., and Chen, X. P. (2021). Quantitative Characterization of Extension and Compression Derived from Bending Strike Slip Faults in the Eastern Bohai Sea Area and its Petroleum Geological Significance. *J. China Univ. Petroleum Nat. Sci. Ed.* 45 (05), 23–32.

Li, X. W., Feng, X. K., and Liu, Y. L. (2018). Anatomy of Ordovician Strike Slip Fault System and Analysis of its Reservoir Controlling Characteristics in Tazhong Area. *Pet. Geophys. Prospect.* 57 (05), 764–774.

Li, Y., Zhou, D., Wang, W., Jiang, T., and Xue, Z. (2020). Development of Unconventional Gas and Technologies Adopted in China. *Energy Geosci.* 1 (1–2), 55–68. doi:10.1016/j.engeos.2020.04.004

Liu, J., Yang, H., Xu, K., Wang, Z., Liu, X., Cui, L., et al. (2022). Genetic Mechanism of Transfer Zones in Rift Basins: Insights from Geomechanical Models. *GSA Bull.*, doi:10.1130/B36151.1

Lu, X. B., Rong, Y. S., and Li, X. B. (2017). Injection Production Well Pattern Construction and Development Significance of Carbonate Fractured Vuggy Reservoir: a Case Study of Tahe Oilfield. *Petroleum Nat. gas Geol.* 38 (04), 658–664. doi:10.11743/ogg20170403

Lu, X. B., Wang, Y., Tian, F., Li, X., Yang, D., Li, T., et al. (2017). New Insights into the Carbonate Karstic Fault System and Reservoir Formation in the Southern Tahe Area of the Tarim Basin. *Mar. Petroleum Geol.* 86: 587-605. doi:10.1016/j.marpetgeo.2017.06.023

Lu, X. B., Yang, M., and Wang, Y. (2018). Characteristics of "stratabound" and "fault Controlled" Reservoirs in Northern Tarim Basin: a Case Study of Ordovician Reservoirs in Tahe Oilfield. *Pet. Exp. Geol.* 40 (04), 461–469.

Ma, D. B., Tong, G. H., and Zhu, Y. F. (2019). Segmentation Characteristics of Deep Strike-Slip Faults in Tarim Basin and Their Control on Oil and Gas Enrichment: Taking Ordovician Strike-Slip Faults in Halahatang Oilfield in Tabei Area as an Example. *Earth Sci. Front.* 26 (01), 225–237.

Mcclay, K., and Massim Bonora, M. (2001). Analog Models of Restraining Stepovers in Strike-Slip Fault Systems. *Aapg Bull.* 85 (2), 233–260. doi:10.1306/8626c7ad-173b-11d7-8645000102c1865d

Mitchell, T. M., and Faulkner, D. R. (2009). The Nature and Origin of Off-Fault Damage Surrounding Strike-Slip Fault Zones with a Wide Range of Displacements: A Field Study from the Atacama Fault System, Northern Chile. *J. Struct. Geol.* 31 (8), 802–816. doi:10.1016/j.jsg.2009.05.002

Neng, Y., Yang, H. J., and Deng, X. L. (2018). Structural Patterns of Fault Damage Zones in Carbonate Rocks and Their Influences on Petroleum Accumulation in Tazhong Paleo-Uplift, Tarim Basin, NW China. *Petroleum Explor. Dev. Online* 45 (1). doi:10.1016/s1876-3804(18)30004-1

Qie, L., Shi, Y. N., and Liu, J. G. (2021). Experimental Study on Grouting Diffusion of Gangue Solid Filling Bulk Materials. *J. Min. Strata Control. Eng.* 3 (2), 023011. doi:10.13532/j.jmsce.cn10-1638/td.20201111.001

Qiu, H. B., Deng, S., Cao, Z., Yin, T, and Zhang, Z (2019). The Evolution of the Complex Anticlinal Belt with Crosscutting Strike-Slip Faults in the Central Tarim Basin, NW China. *Tectonics* 38 (6), 2087–2113. doi:10.1029/2018TC005229

Ramadhan, Aldis., Samudra, A. B., Puji Lestari, E, Saputro, J, Hirosiadi, Y, and Amrullah, I (2018). Strike-Slip Fault Deformation and its Control in Hydrocarbon Trapping in Ketaling Area, Jambi Subbasin, Indonesia. *IOP Conf. Ser. Earth Environ. Sci.* 132 (1). doi:10.1088/1755-1315/132/1/012025

Shan, S. C., Wu, Y. Z., Fu, Y. K., and Zhou, P. H. (2021). Shear Mechanical Properties of Anchored Rock Mass under Impact Load. *J. Min. Strata Control. Eng.* 3 (4), 043034. doi:10.13532/j.jmsce.cn10-1638/td.20211014.001

Stefanov, Y. P., and Bakeev, R. A. (2014). *Deformation and Fracture Structures in Strike-Slip Faulting.* Engineering Fracture Mechanics, 129, 102–111. doi:10.1016/j.engfracmech.2014.05.019

Swanson, M. T. (2005). Geometry and Kinematics of Adhesive Wear in Brittle Strike-Slip Fault Zones. *J. Struct. Geol.* 27, 871–887. doi:10.1016/j.jsg.2004.11.009

Wang, Y. T., and Li, J. L. (1999). Related Structures of Strike Slip Faulting. *Geol. Sci. Technol. Inf.* (03), 30–34.

Wang, Z., Wen, H., Deng, G., Ding, W., and Wang, X (2019). Fault-karst Charaterization Technology in the Tahe Oilfield, China. *Geophys. Prospect. Petroleum* 58 (1), 149–154. doi:10.3969/j.issn.1000-1441.2019.01.017

Wu, G. H., Kim, Y-S., Su, Z, Yang, P, Ma, D, and Zheng, D (2020). Segment Interaction and Linkage Evolution in a Conjugate Strike-Slip Fault System from the Tarim Basin, NW China. *Mar. Petroleum Geol.*, 112. doi:10.1016/j.marpetgeo.2019.104054

Wu, G. H., Yang, H. J., He, S., et al. (2016). Effects of Structural Segmentation and Faulting on Carbonate Reservoir Properties: A Case Study from the Central Uplift of the Tarim Basin, China. *Mar. Petroleum Geol.*, 71. doi:10.1016/j.marpetgeo.2015.12.008

Yin, S., and Ding, W. L. (2019). Evaluation Indexes of Coalbed Methane Accumulation in the Strong Deformed Strike-Slip Fault Zone Considering Tectonics and Fractures: A 3D Geomechanical Simulation Study. *Geol. Mag.* 156 (6), 1–17. doi:10.1017/s0016756818000456

Yin, S., Dong, L., Yang, X., and Wang, R. (2020). Experimental Investigation of the Petrophysical Properties, Minerals, Elements and Pore Structures in Tight Sandstones. *J. Nat. Gas Sci. Eng.* 73, 1–14. doi:10.1016/j.jngse.2020.103189

Yin, S., and Gao, Z. (2019). Numerical Study on the Prediction of "sweet Spots" in a Low Efficiency-Tight Gas Sandstone Reseroirv Based on a 3D Strain Energy Model. *IEEE Access* 7 (6), 1–12. doi:10.1109/access.2019.2933450

Yin, S., Lv, D. W., and Ding, W. L. (2018b). New Method for Assessing Microfracture Stress Sensitivity in Tight Sandstone Reservoirs Based on Acoustic Experiments. *Int. J. Geomechanics* 18 (4), 1–16. doi:10.1061/(asce)gm.1943-5622.0001100

Yin, S., and Wu, Z. (2020). Geomechanical Simulation of Low-Order Fracture of Tight Sandstone. *Mar. Petroleum Geol.* 100, 1–16. doi:10.1016/j.marpetgeo.2020.104359

Yin, S., Xie, R., Wu, Z., Liu, J., and Ding, W. (2019). *In Situ* stress Heterogeneity in a Highly Developed Strike-Slip Fault Zone and its Effect on the Distribution of Tight Gases: A 3D Finite Element Simulation Study. *Mar. Petroleum Geol.* 99 (1), 75–91. doi:10.1016/j.marpetgeo.2018.10.007

Yin, S., Zhao, J., Wu, Z., and Ding, W. (2018a). Strain Energy Density Distribution Of A Tight Gas Sandstone Reservoir In A Low-Amplitude Tectonic Zone And Its Effect On Gas Well Productivity: A 3D Fem Study. *J. Petroleum Sci. Eng.* 170, 89–104. doi:10.1016/j.petrol.2018.06.057

Zhang, X. B., Lv, H. T., and Zhao, X. K. (2011a). Paleostructural Evolution of Lower-Middle Ordovician Top and its Relationship with Hydrocarbon in Tahe Oilfield. *Petroleum Geol. Exp.* 33 (3), 233–238.

Zhang, X. B., Lv, H. T., and Zhao, X. K. (2011b). Paleotectonic Evolution and Oil-Gas Relationship at the Top of Middle Lower Ordovician in Tahe Oilfield. *Pet. Exp. Geol.* 33 (03), 233–238.

Zhang, X. F., Li, M., and Chen, Z. Y. (2012). Characteristics and Karstification of the Ordovician Carbonate Reservoir, Halahatang Area, Northern Tarim Basin. *Acta Petrol. Sin.* 28 (3), 815–826.

Zhang, Z. P., Kang, Y., Lin, H., Han, J, Zhao, R, Zhu, X, et al. (2021). A Study on the Reservoir Controlling Characteristics and Mechanism of the Strike Slip Faults in the Northern Slope of Tazhong Uplift, Tarim Basin, China. *Arabian J. Geosciences* 14 (8). doi:10.1007/s12517-021-07076-5

Zhao, K. K., Jiang, P. F., and Feng, Y. J. (2021). Investigation of the Characteristics of Hydraulic Fracture Initiation by Using Maximum Tangential Stress Criterion. *J. Min. Strata Control Eng.* 3 (2), 023520. doi:10.13532/j.jmsce.cn10-1638/td.20201217.001

Zhao, R., Deng, S., Yun, L., Lin, H., Zhao, T., Yu, C, et al. (2020). Description of the Reservoir along Strike-Slip Fault Zones in China T-Sh Oilfield, Tarim Basin. *Carbonates Evaporites* 36 (1). doi:10.1007/s13146-020-00661-x

Zheng, H., Zhang, J., and Qi, Y. (2020). Geology and Geomechanics of Hydraulic Fracturing in the Marcellus Shale Gas Play and Their Potential Applications to the Fuling Shale Gas Development. *Energy Geosci.* 1 (1–2), 36–46. doi:10.1016/j.engeos.2020.05.002

Zhou, B. W., Chen, H. H., and Yun, L. (2022). Relationship between Fault Offset Segmentation Difference and Fault Width of Lower Paleozoic Strike Slip Fault Zone in Shunbei Area of Tarim Basin. *Earth Sci.* 47 (02), 437–451.

Zhou, W., Li, X. H., and Jin, W. H. (2011). The Control Action of Fault to Paleokarst in View of Ordovician Reservoir in Tahe Area. *Acta Petrol. Sin.* 27 (8), 2339–2348.

Zhu, G. Y., Yang, H. J., and Zhu, Y. F. (2010). Study on Petroleum Geological Characteristics and Accumulation of Carbonate Reservoirs in Hanilcatam Area, Tarim Basin. *Acta Petrol. Sin.* 27 (3), 827–844.

Zhu, Q. Y., Dai, J., Yun, F. F., Zhai, H. H., Zhang, M., and Feng, L. R. (2022). Dynamic Response and Fracture Characteristics of Granite under Microwave Irradiation. *J. Min. Strata Control. Eng.* 4 (1), 019921. doi:10.13532/j.jmsce.cn10-1638/td.20210926.001

Conflict of Interest: YL, HM, ZW, GD, and HW were employed by Sinopec Northwest Oilfield Company.

The author declares that the research was conducted in the absence of any commercial or financial relationships that could be construed as a potential conflict of interest.

frontiers | Frontiers in Earth Science

ORIGINAL RESEARCH
published: 01 June 2022
doi: 10.3389/feart.2022.857343

Characteristics of Lithofacies in Deep Shale Gas Reservoirs in the Southeast Sichuan Basin and Their Influence on Pore Structure

Jiang He[1], Songyue Zhu[1], Xuewen Shi[2], Shengxian Zhao[2], Lieyan Cao[2], Shulin Pan[1], Feng Wu[1] and Meng Wang[3,4]**

[1]School of Geoscience and Technology, Southwest Petroleum University, Chengdu, China, [2]Shale Gas Research Institute of PetroChina Southwest Oil and Gas Field Company, Chengdu, China, [3]School of Chemistry and Chemical Engineering, Chongqing University of Science & Technology, Chongqing, China, [4]Key Laboratory of Shale Gas Exploration, Ministry of Natural Resources, Chongqing Institute of Geology and Mineral Resources, Chongqing, China

The characteristics of lithofacies in the shale reservoir of the Wufeng and Longmaxi formations located in the Luzhou gas field were studied using the three-end-member method (mineralogical components). In addition, the microscopic characteristics and pore genesis of different lithofacies were studied and compared using TOC, FESEM, and digital core images. The results of the present study showed the development of five lithofacies: 1) quartz-rich argillaceous shale; 2) quartz/clay-mixed shale; 3) calcareous/clay-mixed shale; 4) calcium-rich argillaceous shale; and 5) clay-rich siliceous shale. The degree of pore development between lithofacies was highly heterogeneous. In addition, data indicated that total shale porosity increased with the increase in TOC. Thus, the pores were mainly related to organic matter. The enrichment of framboidal pyrite in quartz-rich shale (S1, S-3) and mixed shale facies (M-2, M-3) is essential during the formation of high-quality reservoirs. On the other hand, the content of organic matter in clayey shale was low, which does not favor the development of high-quality reservoirs. The differences in lithofacies pore structures are controlled by the sedimentary environment. The strong retention and reduction environment are the most favorable features for the formation of organic-rich siliceous shale lithofacies, which promote the preservation of organic matter and the development of reservoirs.

Keywords: shale, lithofacies, Ordovician Wufeng formation, Silurian Longmaxi formation, Luzhou field, Sichuan Basin

OPEN ACCESS

Edited by:
Shuai Yin,
Xi'an Shiyou University, China

Reviewed by:
Bo Jiu,
China University of Geosciences, China
Weiming Wang,
China University of Petroleum, China

****Correspondence:***
Jiang He
hejiang_swpu@126.com
Meng Wang
wangmeng_cqust@126.com

Specialty section:
This article was submitted to Economic Geology, a section of the journal Frontiers in Earth Science

Received: *19 January 2022*
Accepted: *21 April 2022*
Published: *01 June 2022*

Citation:
He J, Zhu S, Shi X, Zhao S, Cao L, Pan S, Wu F and Wang M (2022) Characteristics of Lithofacies in Deep Shale Gas Reservoirs in the Southeast Sichuan Basin and Their Influence on Pore Structure. Front. Earth Sci. 10:857343. doi: 10.3389/feart.2022.857343

1 INTRODUCTION

Shale gas resources play an important role in the world energy supply (Dong et al., 2011). With the development of unconventional oil and gas exploration and production, the study of shale pore structure has attracted extensive attention (Zou et al., 2010; Zou et al., 2015). As a result of commercial development of shale gas in North America, differences in mineralogical composition, gas-bearing storage, and compressibility of several lithofacies have been documented (Abouelresh and Slatt, 2012). These variations indicate that potential development of the lithofacies will also be different. The marine shale of the Wufeng and

Longmaxi formations in the Sichuan Basin is an important shale gas exploration and development succession in China. Its lithofacies division and the genesis of high-quality reservoir intervals have attracted significant attention (Chen et al., 2015; Zhao et al., 2016).

Lithofacies is a component of sedimentary facies. The study of lithofacies is essential during shale reservoir characterization and shale oil and gas reservoir evaluation (Wang and Carr, 2012). Shale lithofacies types are divided according to their characteristics using petrological, geochemical, and geophysical methods, which consider mineral composition, paleontology, structural strength, mineral content, and distribution. Among them, the most widely used method includes the three-end elements: clay minerals; carbonate rocks; and quartz and feldspar (Allix et al., 2010). The proper characterization of shale lithofacies includes the relationship between micropore structure and macro-sedimentary facies, mineral structure, and reservoir characteristics, as well as gas bearing and geomechanical properties of the reservoir. This information is extremely helpful for decision-making purposes during exploration and production of shale gas.

Considering different factors including climate change, material supply, and sea-level change, among others, different lithofacies are subjected to dissimilar sedimentary environments. For this reason, their mineral composition, organic matter content, and sedimentary structure display variability. In general, the shale reservoirs present low porosity and ultra-low permeability, as well as various pore types and wide pore size distribution, which results from an extremely complex pore structure (Liu et al., 2022). Different types of pore bodies are formed in different diagenetic stages and have various genetic types. Sedimentation, structure, and diagenetic evolution have an important impact on the evolution, preservation, and buried depth of shale reservoirs. These features determine the temporal and spatial distribution of high-quality shale reservoirs (Li et al., 2019; Li et al., 2020). Marine shale is highly heterogeneous. Different lithofacies display significant differences in pore structures. In silica shale, the degree of organic matter filling intergranular pores on large-scale is high. The clayey shale is affected by TOC content and organic matter clay complex structure. Organic pores present a wide pore size distribution, with a high average pore size; however, the total amount of organic pores is small (Fan et al., 2020). The organic pores are mainly developed in organic-rich shale facies of the shale gas reservoir. Several publications have reported on the influencing factors of organic matter abundance on the micropore structure. It has been found that organic carbon content determines the specific surface area and pore volume of micropores. In shales with elevated organic matter content, the higher the content of clay minerals, the higher the proportion of macropores (Li et al., 2019). This mainly occurs because of the large number of interlayer pores of nano-clay minerals, which promote the development of macropores.

Luzhou shale gas field, which formed in the southeast of the Sichuan Basin during the deposition of the first member of the Wufeng formation, can be divided into two parts: 1) shallow and 2) deep-water shelf parts (Ma et al., 2020). Since this is a new shale gas exploration block, little is known about its shale lithofacies and pore space characteristics. In addition, the control of lithofacies on reservoir pore type and the genetic mechanism of high-quality shale gas reservoirs is not clear. This restricts the evaluation and prediction of high-quality shale gas strata (Wang et al., 2017). For this reason, in order to provide a proper guidance for shale gas production, in the present study, we analyzed the relationship between shale lithofacies characteristics and pore type and structure.

2 SAMPLING AND METHODS

A total of 270 core samples were collected from 5 wells in the Lu203 well block located in the Wufeng and Longmaxi formations at depths between 3,892 m and 4051.15 m.

First, the rock type, mineralogical composition, particle shape, size and quantity, morphology, and size of pores and microcracks of 270 shale thin sections were analyzed using an Axioskop 40 polarizing microscope and FEI QUANTA 250 field emission scanning electron microscope (FESEM). PerGeos software was used to extract and segment pores from the images obtained by SEM, and the pore size and distribution characteristics of shale samples were quantitatively evaluated. In order to determine the mineralogical composition and lithofacies change in the vertical direction, the mineralogical composition and clay mineral type and content of 120 samples were quantitatively tested by using a PanalyticalX'Pert PRO MPD X-ray diffractometer, and the shale lithofacies types were classified according to the quantitative analysis results.

The total organic carbon (TOC) of 150 samples was analyzed using a LECO CS-200 carbon/sulfur analyzer to evaluate hydrocarbon generation potential. The plunger core porosity tester and STL—II high pressure permeability tester were used to determine the porosity and permeability of 140 core plug samples.

3 RESULTS

3.1 Mineralogical Composition of Shale

The X-ray diffraction results showed that the main mineral components were quartz, feldspar, calcite, dolomite, pyrite, and clay. The content of quartz and clay minerals accounted for more than 60% of the total, and the clay minerals consisted of illite, a mixed layer of illite/montmorillonite, and chlorite–kaolinite. The content of brittle minerals was between 31.8 and 97.0%, with an average of 64.1%, and a median of 62.0%. In addition, the content of clay minerals was 3.0%–59%, with an average of 29.5%, and a median of 28.0% (**Figure 1**).

The analysis of 256 samples from the Wufeng and Longmaxi formations showed a TOC between 0.1% and 9.3%, with an average of 2.1%. Among them, the TOC of gas reservoir samples was between 1.1% and 9.3%, with an average value of 2.9%. TOC varied between 2.0% and 4.0%, accounting for 63% of the total. According to the microscopic examination of kerogen in the core samples of Longmaxi formation, the average content of the sapropel group was more than 90%. The organic matter of the Wufeng and Longmaxi formations' organic-rich shale was mainly of type I kerogen.

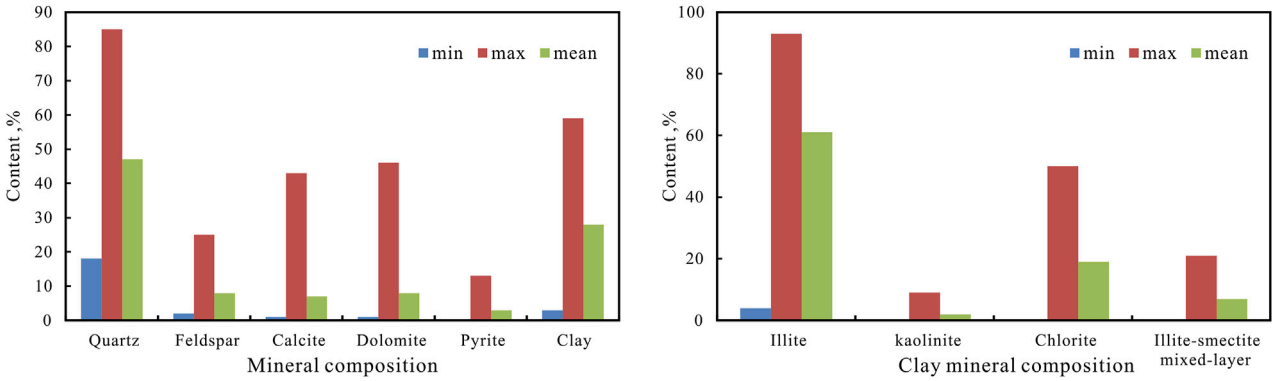

FIGURE 1 | Mineral composition histogram of the shale reservoir; **(A)** mineral composition and **(B)** clay mineral composition. min: minimum content value; max : maximum content value; mean: mean content value.

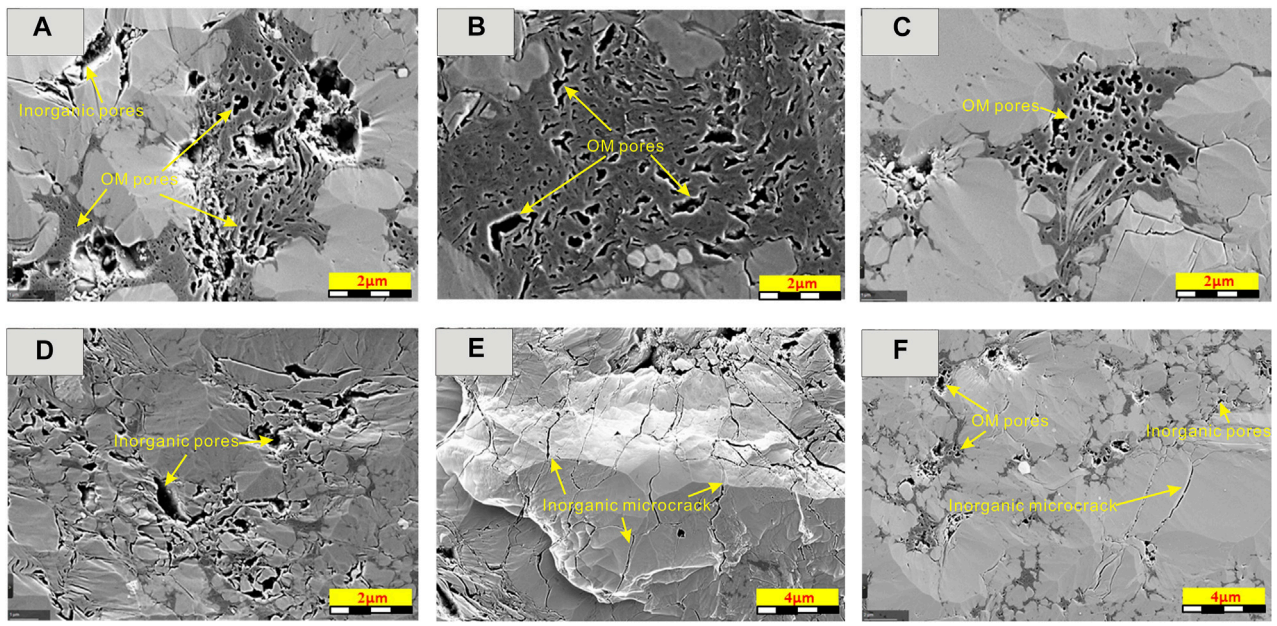

FIGURE 2 | Photographs of scanning electron microscopy (SEM) of the Wufeng–Longmaxi Formation shale; **(A)** inorganic pores and organic matter pores from L203 well, **(B)** organic matter pores from L205 well, **(C)** organic matter pores from L207well, **(D)** inorganic pores from L209 well, **(E)** inorganic microcrack from L206 well, and **(F)** inorganic pores, microcracks, and organic matter pores from L208 well.

3.2 Shale Gas Reservoir Characteristics

3.2.1 Types and Characteristics of Pore Spaces

According to the SEM and composition results, the shale pores in the study area can be divided into four basic types: organic pores (**Figures 2A–C**), organic cracks, inorganic pores (**Figures 2D,F**), and inorganic cracks (**Figures 2E,F**). Among them, the organic pores are subdivided into two subclasses: organic matter evolution pores (intra-OM pores) and pores between organic matter. The organic cracks can be divided into two subclasses: internal cracks in organic matter and cracks between organic matter. In addition, the inorganic pores are subdivided into two subclasses: mineral intragranular pores and mineral intercrystalline pores. Also, the inorganic cracks are divided into inorganic cracks and mineral grain boundary cracks. The organic and inorganic pores represent the main reservoir spaces. The organic matter pores generally exist in the form of bubbles and pores, and the primary organic matter pores are less developed.

3.2.2 Physical Properties of the Shale Reservoir

According to the analysis of 140 core samples from the shale gas interval of the L203 block, the porosity varied between 2.19% and 5.65%, with an average of 3.74%, and a median of 3.79%. Among them, the samples with porosity of 2%–4% are generally typified as low-porosity reservoirs, which in the present study accounted for 57.9% of the total. According to the analysis of 77 samples

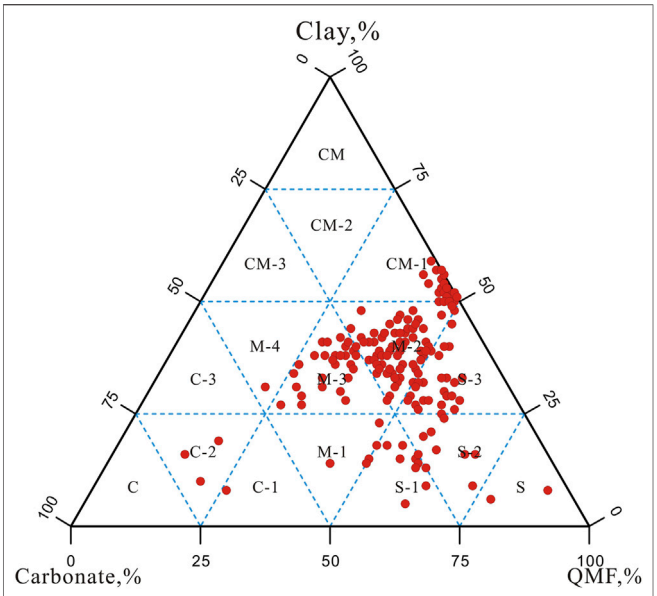

FIGURE 3 | Ternary lithofacies diagram of the Wufeng–Longmaxi Formation in the L203 well area SE Sichuan Basin. CM, mudstone facies; CM-1, silicon-rich argillaceous shale facies; CM-2, mixed argillaceous shale facies; and CM-3, calcium-rich argillaceous shale facies; S, siliceous facies; S-1, calcium-rich argillaceous shale facies; S-2, mixed siliceous shale facies; and S-3, mud-rich siliceous shale facies; C, limestone facies; C-1, silica-rich calcareous shale facies; C-2, mixed calcareous shale facies; and C-3, mud-rich calcareous shale facies; and M-1, calcareous/silica-mixed shale facies; M-2, silica/mud-mixed shale facies; M-3, calcareous/mud-mixed shale facies; and M-4, mixed shale.

from shale gas intervals of 2 wells, the matrix permeability varied between 3.98×10^{-5} mD and 9.81×10^{-2} mD, with an average of 1.12×10^{-2} mD. Thus, data indicated the presence of an ultra-low permeability reservoir.

The grain density of shale samples of different lithofacies varied from 2.4 g/cm^3 to 2.67 g/cm^3.

3.3 Lithofacies Division and Comparison of Shale Characteristics

The mineralogical composition measured by X-diffraction showed that this shale is mainly composed of quartz and clay minerals, with a small amount of carbonate minerals, feldspar, and pyrite. According to the division scheme proposed by Allix, the main types of lithofacies are divided by the relative contents of quartz, feldspar, clay minerals, and carbonate minerals (**Figure 3**).

The Wufeng and Longmaxi shale in the study area generally contains less than 50% clay and 25%–50% silica. Five types of lithofacies developed including silicon/mud mixed shale (M-2), calcareous/mud mixed shale (M-3), quartz-rich argillaceous shale (CM-1), mud-rich siliceous shale (S-3), and calcium-rich argillaceous shale (S-1) (**Figure 4**). Because of the high shale content, CM-1, M-2, and S-3 lithofacies reflect long-term stable sedimentation. Thus, they can be used as the unique lithofacies in deep-water sedimentary environments. M-3 represents the main shallow-water shelf lithofacies. In addition, S-1 corresponds to the common lithofacies in shallow-deep water sedimentary environments.

Clayey shales mostly contain clay mineral interlayer pores, intercrystalline pores, and organic matter pores, as well as a low content of organic matter. On the other hand, mixed shales display a high content of calcite and dolomite. In addition, the edge-dissolved pores and intercrystalline-dissolved pores of calcite and dolomite are relatively developed, with larger pore sizes as compared to those observed in the organic matter pores and clay intercrystalline pores. Moreover, most of the dissolution pores are filled with migrating organic matter (Wang et al., 2018). The sedimentary environment of siliceous shale presents an anoxic deep-water environment. In this case, pyrite is relatively developed, and the intercrystalline pores of framboidal pyrite aggregates are almost filled with migrating organic matter (Loucks and Ruppel, 2007).

4 DISCUSSION

4.1 Genetic Mechanism of Shale Lithofacies

Dissimilar sedimentary environments result in differences in lithofacies. With respect to shale lithofacies, different mineral compositions, organic matter content, and sedimentary structures formed in various sedimentary environments result in different types of rocks.

Vertically, the Wufeng Formation of the Upper Ordovician developed a medium carbon siliceous shale with high carbonate content. Data indicated that a thin-layer of pyrite was developed along the bedding surface of the shale.

The sedimentary period of the lower member of the Longmaxi formation corresponds to a stagnant deep-water sedimentary environment, which developed a siliceous shelf. The shale facies correspond to thin-layer mixed shale and thick siliceous shale, with high organic carbon content.

During the sedimentary period of the middle Longmaxi formation, the water depth decreased, the sedimentary facies mostly corresponded to mixed and sandy shelf, the shale lithofacies were comprised of thin and mixed shale, and the organic carbon content displayed a medium level.

Moreover, the water depth of the upper member of the Longmaxi formation further decreased, and argillaceous shelves were mostly present in sedimentary lithofacies. In addition, thin-layer mixed shale and clayey shale formed the shale lithofacies, and a low organic carbon content was present.

From bottom to top, the content of organic matter and quartz gradually decreased, and the content of silt particles and clay gradually increased. In addition, sandy nodules and sandy strips were observed in the top core. Pyrite structures presented gradual transitions from thick-layered in the lower part to scattered-layered in the upper part. It was also observed that the input of terrigenous debris gradually increased from bottom to top, the hydrodynamic conditions gradually increased, the sedimentary water body decreased, and the characteristics of the sedimentary environment changed from strong retention and strong reduction to a weak reduction environment.

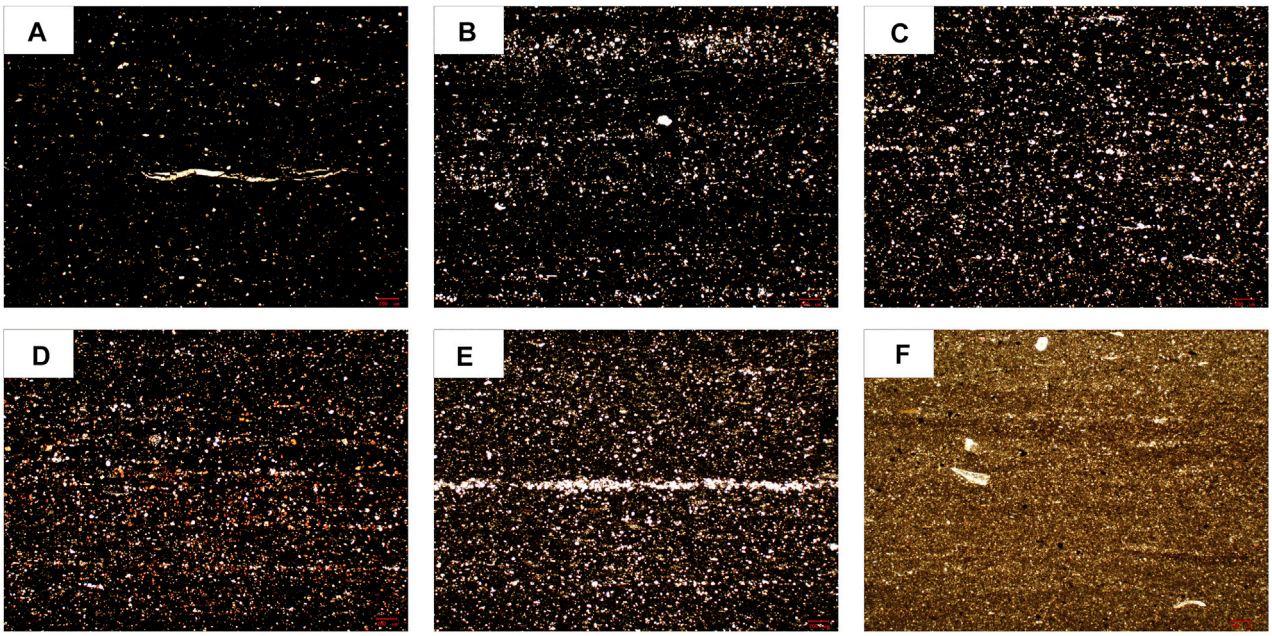

FIGURE 4 | Characteristics of shale of different lithofacies under polarizing microscope. **(A)** CM-1 lithofacies, 2983.78 m, well L205; **(B)**M-2 lithofacies, 4016.32 m, well L205; **(C)** M-3 lithofacies, 4026.12 m, well L205; **(D)**S-3 lithofacies, 4029.97 m, well L205; **(E)** S-2 lithofacies, 4032.58 m, well L205; and **(F)** S-1 lithofacies, 4041.67 m, well L205.

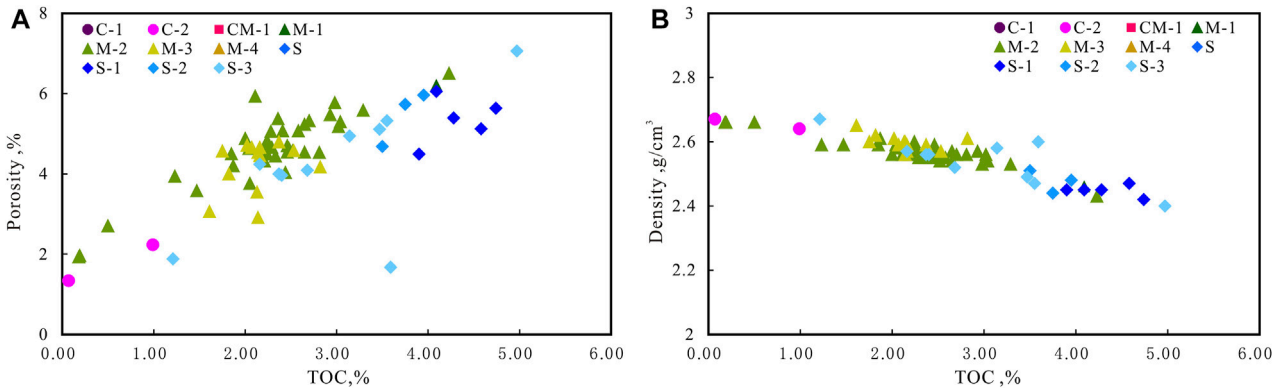

FIGURE 5 | TOC versus porosity **(A)** and density **(B)** of shale samples from Wufeng–Longmaxi Formation in the L203 well area.

With respect to the main shale facies, the mineral composition in the siliceous shale facies was relatively pure and contained pyrite. This indicated that the sedimentary environment was a relatively quiet and anoxic reduction environment. In the mixed siliceous shale facies, the clay minerals and carbonate mineral contents were less than 25%. In this case, foliation developed. It was also observed that micro-characteristic quartz was evenly distributed and scattered pyrite, and relatively developed silty laminae were distributed along the layers. These data indicated that a gradual change from an early strong reduction environment to a weak reduction environment occurred. In clay-bearing siliceous shale facies, clay mineral content increased. Silty strips as well as a progressive bedding development were observed in the core. This result suggested the enhanced supply of terrigenous debris and the transition of the sedimentary environment from a weak reduction environment to an oxidation environment.

4.2 Influence of Lithofacies on Organic Geochemical Characteristics

The enrichment of organic matter is usually related to the paleoenvironment (Xie et al., 2008). Generally, the anaerobic environment has a strong reduction ability, which promotes the preservation and enrichment of organic matter. The organic

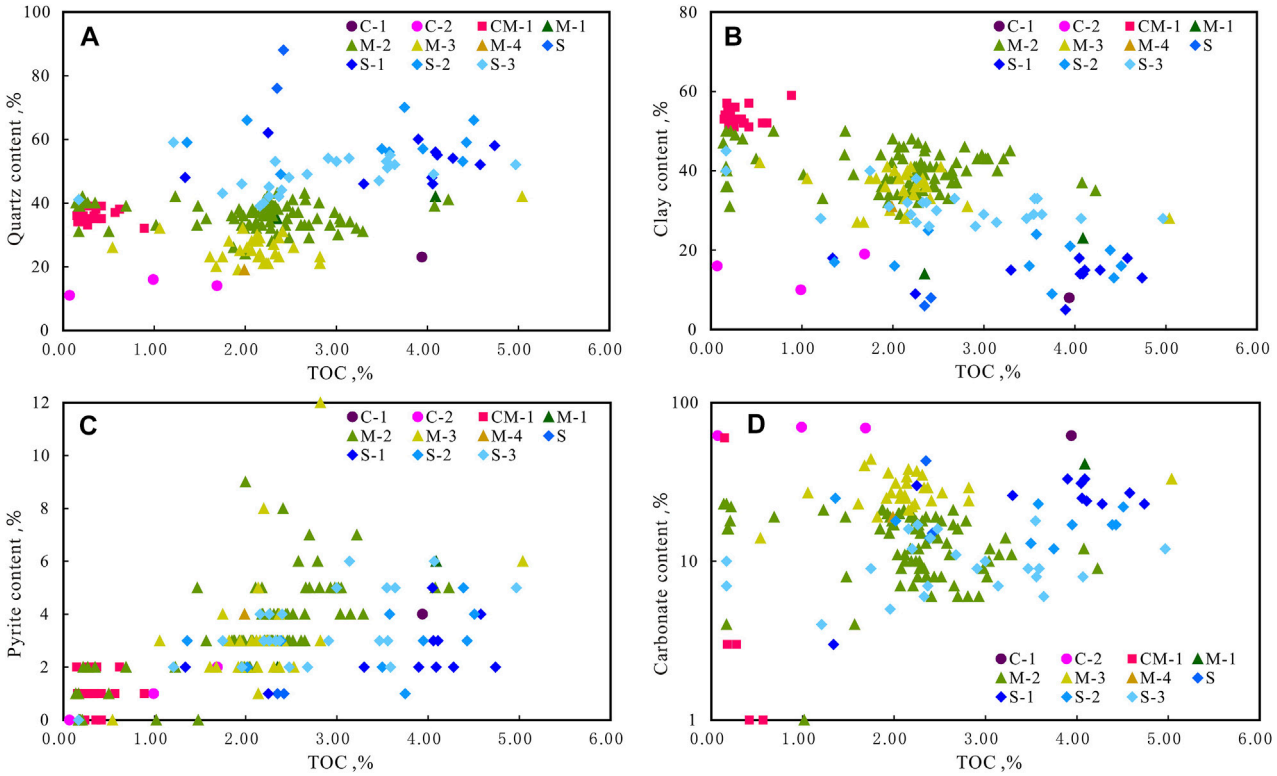

FIGURE 6 | TOC versus quartz content **(A)**, clay content **(B)**, pyrite content **(C)**, and carbonate content **(D)** of the shale samples from Wufeng–Longmaxi Formation in the L203 well area.

matter present in the deep shale reservoir significantly contributes to permeability, especially in the interval dominated by organic matter pores where the porosity is greatly affected by TOC. The results indicated good correlation coefficients between TOC-porosity and TOC-density, with values of 0.68 and 0.82, respectively (**Figure 5**). The highest TOC, porosity, and density correlations corresponded to those in mixed lithofacies. According to these results, the organic matter in mixed lithofacies is the main parameter controlling pore development. It was also observed that shale density decreased with the increase in TOC, and the total porosity increased with the increase in TOC. These data indicated that in the deep shale reservoir, organic matter pores were mostly present (Schlanser et al., 2016; Wang et al., 2018).

The relationship between clay minerals, quartz, and TOC content shows that TOC is positively correlated with quartz content (**Figure 6A**) but negatively correlated with clay mineral content (**Figure 6B**). These results indicated that siliceous shale was mainly derived from biogenic silicon, which also suggests that organic matter content in shale rich in clay minerals is relatively low. The relationship between pyrite, carbonate minerals, and TOC concentrations showed that TOC was positively correlated with pyrite content (**Figure 6C**) but not with carbonate mineral content (**Figure 6D**). Thus, pyrite influences the formation of organic pores to a certain extent (Wang et al., 2020).

The TOC in shale samples of main lithofacies varied from 0.07% to 5.04%. The data indicated that the siliceous shale displayed the highest TOC content. In the S-1 and S-3 shale facies, TOC varied from 1.36% to 4.97%, while in M-2 and M-3 facies, the TOC values were between 0.54% and 4.23%. The lowest TOC values were observed in CM-1 facies with numbers varying from 0.15% to 0.89%.

Clay shale displays high clay mineral content and low TOC content. Compared with mixed shale and siliceous shale, organic matter accounts for a relatively low proportion. The present study demonstrated that the development of organic matter pores controls the pore space of siliceous shale and mixed shale, while the pore space of clayey shale is mainly affected by the pore development of clay minerals. Quartz in siliceous shale mostly comes from the dissolution and reprecipitation of siliceous organisms such as radiolaria and siliceous sponges. Some pores between microcrystalline authigenic quartz particles provide a storage space for migrating organic matter. In addition, the bubble pores and sponge pores can be formed in organic matter. The TOC content in the mixed shale was slightly lower than that in siliceous shale and its micropores and mesopores were

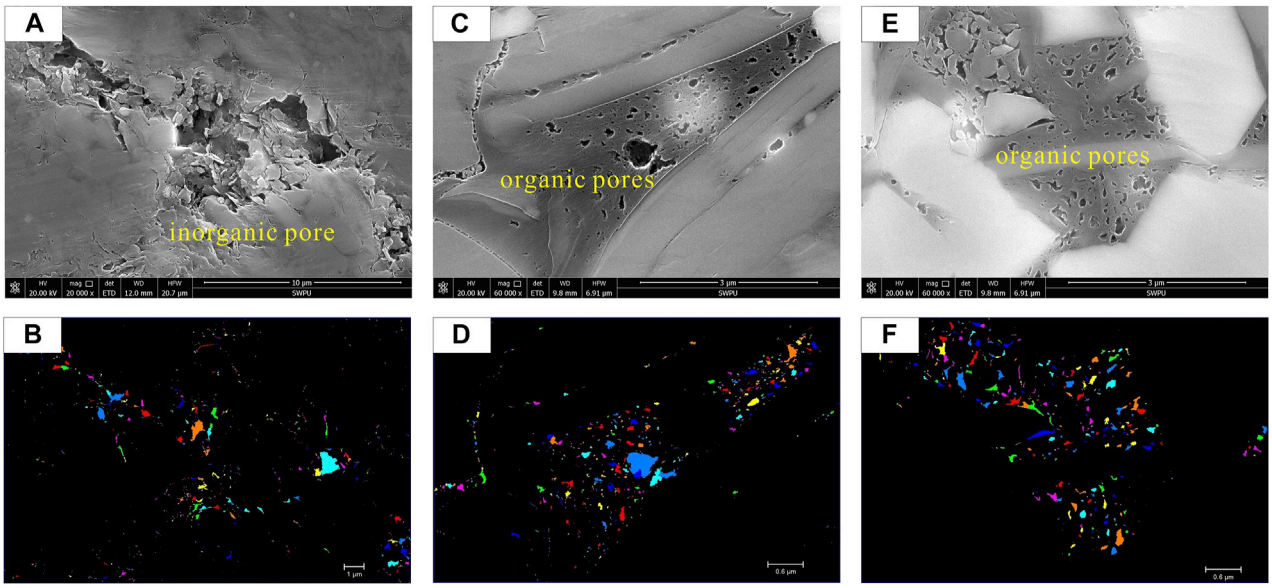

FIGURE 7 | Microphotographs showing main pore types and distribution characteristics of shale reservoir. **(A)** Inorganic pores, 3939.25 m, L206 well; **(B)** pore morphology and distribution of graph a; **(C)** organic pores and grain boundary pores, 3967.62 m, L206 well; **(D)** pore morphology and distribution of graph c; **(E)** pyrite intercrystalline pores and organic pores between pyrite crystals, 3980.96 m, L206 well; **(F)** pore morphology and distribution of graph **(E)**.

mostly composed of clay mineral-related pores, quartz intercrystalline pores, and organic matter pores. In addition, the increase in carbonate mineral content can provide dissolution pores for the preservation of migrating organic matter to a certain extent.

4.3 Origin of Different Pores in Deep Shale Reservoirs

Differences in the genesis of organic pores, inorganic pores, and inorganic cracks in the main spaces of deep shale reservoirs have been observed (Chen et al., 2015; Zhang et al., 2018).

Inorganic pores can be divided into intragranular and intercrystalline pores. The inorganic intragranular pores of black shale in the Luzhou area mainly developed in quartz, clay, feldspar, pyrite, and carbonate minerals. In addition, quartz grains contain primary pores. The transformation from montmorillonite to illite during the burial of clay minerals may also result in the formation of intragranular pores. Also, dissolution pores are easily formed in unstable minerals such as feldspar and carbonates. Intragranular dissolution pores exist in single-crystal pyrite or framboidal pyrite. On the other hand, intragranular pores mostly display spherical, grooved, or honeycomb morphologies. The pore sizes vary from tens of nanometers to tens of microns, and the connectivity is relatively poor (**Figure 7A**). Shale intercrystalline pores are mainly formed by mutual support of the same or multiple minerals. Interparticle pores are formed between grains or crystals such as quartz, clay minerals, feldspar, and dolomite in which pore size is larger than that of intragranular pores.

The inorganic pores developed in shales where an abundance of organic matter is relatively low. They present smooth edges, oval shape, uniform individual size, and relatively large pore diameter. On the other hand, the organic pores develop in relatively high organic matter shales, display irregular edges, mostly flat shapes, as well as certain directionality and relatively small pore diameter. The organic pores are formed during hydrocarbon maturation. The organic pores are mostly found in gas generation window (RO > 1.2%), and a few of them are also observed in oil generation windows (RO between 0.6% and 1.0%) (Jarvie et al., 2007; Mastalerz et al., 2013). The black shale from the Wufeng and Longmaxi formations has reached the mature stage. Thus, kerogen and early oil pyrolysis asphalt will produce organic matter evolution pores (Zhao et al., 2016). During thermal evolution, kerogen is often mixed with clay, quartz, feldspar, carbonate, and other minerals to form spherical or porous honeycomb structures. The most common honeycomb-shaped organic pores are formed in mixtures of quartz and clay minerals (**Figures 7C,E**).

The shales contain different types of pores, which are mostly developed in organic matter, brittle minerals, and clay minerals, among others. Organic matter pores represent the main type of pore space. They are formed in organic siliceous shales and organic mixed shale lithofacies (Tang et al., 2015; Wang et al., 2016; Li, 2022). The organic matter pores in organic-rich siliceous shales are highly developed and present a nearly circular shape, good connectivity, and a pore diameter higher than 150 nm. Medium to high organic siliceous shales contain microcracks at the edge of organic matter and rigid minerals and dissolution pores in the rigid particles. The pores in organic matter are developed and present a small pore size and slightly poor connectivity. The organic matter-rich mixed shales show low organic matter content, intergranular pores, and locally developed microfractures.

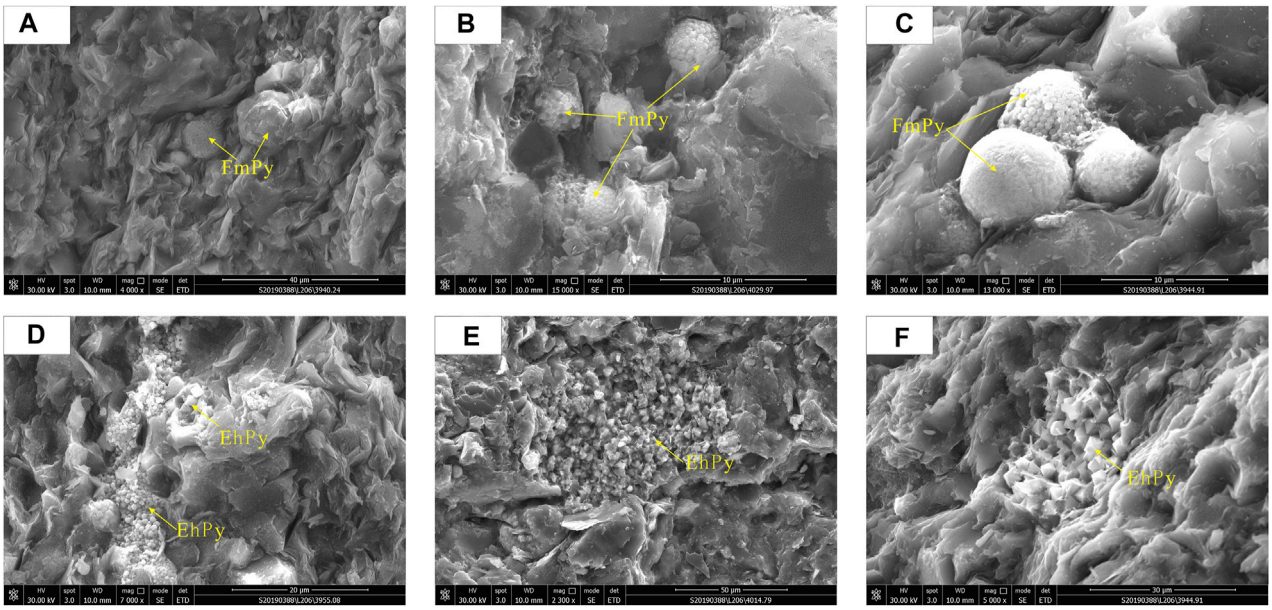

FIGURE 8 | Microphotographs showing different types of pyrites. **(A)** Framboidal pyrite (FmPy) associated with illite, 3940.24 m, L206; **(B)** framboidal pyrite (FmPy), 4029.97 m, L206; **(C)** framboidal pyrite (FmPy), 3944.96 m, L206; **(D)** lamellar euhedral pyrite aggregate (EhPy), 3955.08 m, L206; **(E)** euhedral pyrite aggregate (EhPy), 4014.79 m, L206; and **(F)** euhedral pyrite (EhPy), 3944.96 m, L206.

Gas-bearing property is an important index to measure the productivity of shale reservoirs. Organic matter is the material source of shale gas. In the process of hydrocarbon generation by organic matter, high-pressure protective pores and organic pores are formed. The higher the organic carbon content and the larger the total volume of micropores, the larger the surface area available for adsorption of adsorbed gas. Thus, total gas content increases (Hubbert, 1953; England et al., 1987). TOC presents a positive correlation with total gas content and porosity. Among siliceous shales, high carbon siliceous shales are the ones with the highest content of gas, which is usually more than 6.5 cm^3/g, followed by medium carbon siliceous shale, with a gas content of 4.2 cm^3/g. The organic matter content of low-carbon siliceous shales is similar to that found in mixed shales. Because of the large difference in porosity, the gas content in low-carbon siliceous shales is higher than that of mixed shale. However, in both cases, the values are lower than 4.0 cm^3/g.

4.4 Influence of Pyrite on the Formation of High-Quality Reservoirs

Figure 8 indicated the presence of many types of framboidal, lamellar, and nodular pyrite in the study area (**Figure 8**). In addition, it was found that framboidal pyrite is composed of microcrystals (**Figures 8A–C**), which are generally polygonal, octahedral, or cubic with uniform sizes. Nodular pyrite is mostly distributed on the sedimentary surface of the laminated shale in the form of cubic euhedral single crystals. If these crystals are enriched to a certain extent, they will show fine macroscopical strips produced along the layer (**Figure 8D**). Euhedral pyrite exists in octahedral, cubic, and spherical shapes (**Figures 8E,F**). This type usually appears as isolated and aggregated particles, often as euhedral or semi-euhedral crystals with large variations in particle size. Euhedral pyrite usually coexists with clay particles or clay lamellae, in which the pyrite particles between clay lamellae are usually surrounded by organic matter. In general, heteromorphic pyrite does not present regular shapes. Compared with framboidal pyrite, heteromorphic crystals and aggregates of pyrite are usually irregular monomer particles or irregular aggregates.

Framboidal pyrites with high organic matter content reflects the reduction conditions of stable water bodies. In the study area, the increased pyrite content was accompanied by an increase in organic matter content. High-quality shales with high organic carbon content are also formed under this sedimentary condition. Pyrite is an indicator of organic matter content in a shale, which is consistent with the positive correlation between pyrite content and TOC (**Figure 6C**).

Shale pore type and pore structure directly affect the adsorption and flow capacity of shale gas. Pyrite structures present various pore types. Microcrystalline and intercrystalline pores are developed in the raspberry-like pyrite aggregates with the highest content in the shale (**Figure 9A**). At the same time, the special shape of raspberry-like pyrite crystals causes most of the voids between the internal grains to be filled with organic matter to form an organic/pyrite complex. In addition, a great number of organic matter pores are developed in the organic matter structure (**Figure 9B**). Microscopic observations have shown that most organic

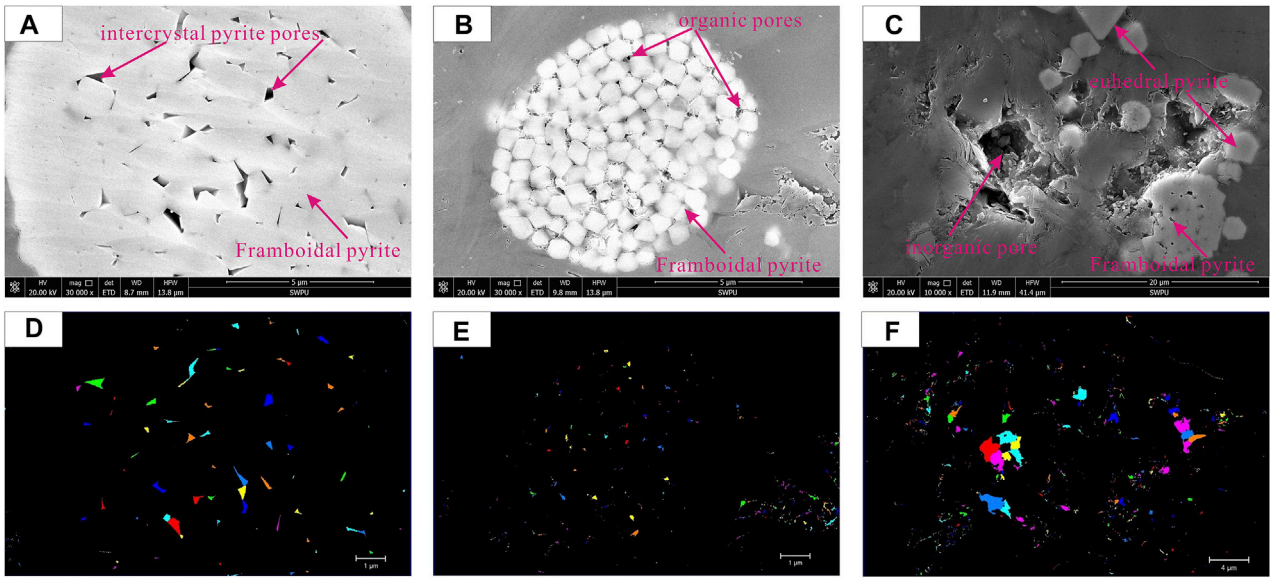

FIGURE 9 | Microphotographs showing pyrite and micropore development characteristics. **(A)** Intercrystal pyrite pores are developed in framboidal pyrite (FmPy), 3786.85 m, L208 well; **(B)** intercrystal pyrite pores and organic pores are developed in framboidal pyrite, 3830.40 m, L208 well; **(C)** inorganic pores, euhedral pyrite, and framboidal pyrite, 3840.43 m, L208 well; **(D)** pore morphology and distribution of graph a; **(E)** pore morphology and distribution of graph b; **(F)** pore morphology and distribution of graph **(C)**

matter pores are irregular and develop between organic matter or around the grain edge. Due to the support and protection of pyrite aggregates and the role of catalytic organic matter in hydrocarbon and gas generation, the number of pores in pyrite is more than that in surrounding organic matter (Han and Li, 2019). In addition, some mold pores are formed by the effect of crystals falling off the surface of the aggregate (**Figure 9C**). The pore size is generally larger than that in the internal organic matter pore, and the shape depends on the morphology of exfoliated crystals, which mostly display honeycomb shapes. Since they contain large pore sizes, they represent the main enrichment site of free gas.

A significant amount of space for the storage of oil and gas is provided by intercrystalline pores present in framboidal pyrite and pores formed by intercrystalline pyrite filled with organic matter (Zhao et al., 2016; Han and Li, 2019; Wang et al., 2020). The high content of pyrite results in the development of high-quality reservoirs. Among various lithofacies, the highest pyrite content corresponds to that of siliceous shale (S-2 and S-3) and mixed shale (M-2 and M-1), with average values of more than 3.3%. The average pyrite content in M-3 facies is 2.9% and that in other lithofacies is less than 2%.

The shale in the study area was divided into three categories: siliceous shale, calcareous shale, and mixed shale. Comparing different lithofacies, the type and content of pyrite are quite different. The highest pyrite content was found in the mixed shale, where pyrite was distributed in strips. The second highest pyrite content was determined in siliceous shale, which was scattered along the layer. Finally, the smallest amounts of pyrite were found in the calcareous shale. Our results were consistent with those reported in previous studies (Wu et al., 2016). The supporting framework composed of quartz in the shale provides a good space for kerogen preservation. The development of clay minerals has a catalytic effect on kerogen. Pyrite was mainly found in strawberry-like structures and irregular non-idiomorphic arrangements.

The time framework for the formation of pyrite is the same as that of early diagenetic formation. Pyrite, one of the common minerals present in shale reservoirs, plays a certain role in controlling the enrichment and production of shale gas.

Three different types of organic pores developed in organic matter migrate into pyrite minerals: 1) pyrite is associated and developed next to the migrated organic matter, and the formation period of pyrite occurs earlier with respect to that of organic matter. Pyrite plays a catalytic role in the formation of organic pores. 2) The transported organic matter fills the spaces between pyrite particles, and organic matter pores develop. Similar single-grain sizes and shapes of pyrite are formed in the same period, and some single crystals are formed in inorganic minerals. This occurs earlier with respect to the transport of organic matter. 3) The transported organic matter fills the spaces in pyrite particles, and organic matter pores develop. Pyrite obviously preceded the formation of organic matter.

The number and size of organic pores developed in the presence of pyrite are significantly better than those formed without pyrite. This indicates that pyrite has a very positive impact on the formation of organic pores. In the latter two types, pyrite not only catalyzes but also supports and protects organic pores. Most pyrite in shale exists in the form of strawberry-like pyrite structures. The best degree of pore development corresponds to the second type of organic pore.

5 CONCLUSION

1) The shale reservoir of the Wufeng and Longmaxi formations in the Luzhou block is characterized by low porosity and ultra-low permeability. Vertically, the development degree of organic pores and inorganic pores is highly heterogeneous. According to mineralogical composition, the main lithofacies in the study area were identified as quartz-rich argillaceous shale facies, silica/mud-mixed shale facies, calcareous/mud-mixed shale facies, calcium-rich argillaceous shale facies, and mud-rich siliceous shale facies.
2) Total shale porosity increases with the increase in TOC. In addition, in deep shale, mainly organic matter pores are present. Siliceous shale (S1 and S-3) and mixed shale (M-2 and M-3) contain a significant amount of intercrystalline pores in framboidal pyrite and pores generated by pyrite intergranular filling organic matter, which promote the formation of high-quality reservoirs. The pore space in clay shale is mainly affected by the organic pore development in clay minerals.
3) The differences in the sedimentary environment control the pore structure in lithofacies. The strong retention and reduction environment provide the conditions needed for the enrichment and preservation of organic matter. The organic-rich siliceous shale facies formed in this environment favor the formation of pores with large diameters in the organic matter structures. Thus, organic matter displays high porosity and gas content. In conclusion, organic-rich siliceous shale facies represent the most favorable lithofacies for the development of shale reservoirs.

DATA AVAILABILITY STATEMENT

The original contributions presented in the study are included in the article/Supplementary Material; further inquiries can be directed to the corresponding author.

AUTHOR CONTRIBUTIONS

JH contributed as the major author of the manuscript. SZ, XS, and SZ conceived the project. LC and SP collected the samples. FW and MW analyzed the samples. All authors contributed to the manuscript and approved the submitted version.

FUNDING

This study received support from the Science and Technology Cooperation Project of the CNPC-SWPU Innovation Alliance (2020CX020000), the China Postdoctoral Science Foundation (2017M623059), the General Project of Chongqing Natural Science Foundation (No.cstc2021jcyj-msxmX0897) the Major Scientific and Technological Project of Sichuan Province (2020YFSY0039), and the Opening Foundation of Key Laboratory of Shale Gas Exploration, Minisitry of Natural Resources (KLSGE-202102).

ACKNOWLEDGMENTS

We would like to thank reviewers for their suggestions.

REFERENCES

Abouelresh, M. O., and Slatt, R. M. (2012). Lithofacies and Sequence Stratigraphy of the Barnett Shale in East-Central Fort Worth Basin, Texas. *Bulletin* 96 (1), 1–22. doi:10.1306/04261110116

Allix, P., Burnham, A., Fowler, T., and Herron, M. (2010). Coaxing Oil from Shale. *Oilfield Rev.* 22 (4), 4–15.

Chen, L., Lu, Y., Jiang, S., Li, J., Guo, T., and Luo, C. (2015). Heterogeneity of the Lower Silurian Longmaxi Marine Shale in the Southeast Sichuan Basin of china. *Mar. Petroleum Geol.* 65, 232–246. doi:10.1016/j.marpetgeo.2015.04.003

Dong, D. Z., Zou, C. N., and Li, J. Z. (2011). Resource Potential, Exploration and Development Prospect of Shale Gas in the Whole World. *Geol. Bull. China* 30 (2), 324–336. doi:10.3969/j.issn.1671-2552.2001.02.18 (in Chinese with English abstract).

England, W. A., Mackenzie, A. S., Mann, D. M., and Quigley, T. M. (1987). The Movement and Entrapment of Petroleum Fluids in the Subsurface. *J. Geol. Soc.* 144 (2), 327–347. doi:10.1144/gsjgs.144.2.0327

Fan, C., Li, H., Qin, Q., He, S., and Zhong, C. (2020). Geological Conditions and Exploration Potential of Shale Gas Reservoir in Wufeng and Longmaxi Formation of Southeastern Sichuan Basin, China. *J. Petroleum Sci. Eng.* 191, 107138. doi:10.1016/j.petrol.2020.107138

Han, S., and Li, W. (2019). Study on the Genesis of Pyrite in the Longmaxi Formation Shale in the Upper Yangtze Area. *Nat. Gas. Geosci.* 30 (11), 1608–1618.

Hubbert, M. H. (1953). Entrapment under Hydrodynamic Conditions. *AAPG Bull.* 37 (8), 1954–2026. doi:10.1306/5ceadd61-16bb-11d7-8645000102c1865d

Jarvie, D. M., Hill, R. J., Ruble, T. E., and Pollastro, R. M. (2007). Unconventional Shale-Gas Systems: The Mississippian Barnett Shale of North-Central Texas as One Model for Thermogenic Shale-Gas Assessment. *Bulletin* 91 (4), 475–499. doi:10.1306/12190606068

Li, H., Qin, Q., Zhang, B., Ge, X., Hu, X., Fan, C., et al. (2020). Tectonic Fracture Formation and Distribution in Ultradeep Marine Carbonate Gas Reservoirs: A Case Study of the Maokou Formation in the Jiulongshan Gas Field, Sichuan Basin, Southwest China. *Energy fuels.* 34 (11), 14132–14146. doi:10.1021/acs.energyfuels.0c03327

Li, H. (2022). Research Progress on Evaluation Methods and Factors Influencing Shale Brittleness: A Review. *Energy Rep.* 8, 4344–4358. doi:10.1016/j.egyr.2022.03.120

Li, H., Tang, H., Qin, Q., Zhou, J., Qin, Z., Fan, C., et al. (2019). Characteristics, Formation Periods and Genetic Mechanisms of Tectonic Fractures in the Tight Gas Sandstones Reservoir: A Case Study of Xujiahe Formation in YB Area, Sichuan Basin, China. *J. Petroleum Sci. Eng.* 178, 723–735. doi:10.1016/j.petrol.2019.04.007

Liu, J., Yang, H., Xu, K., Wang, Z., Liu, X., Cui, L., et al. (2022). Genetic Mechanism of Transfer Zones in Rift Basins: Insights from Geomechanical Models. *GSA Bull.* doi:10.1130/B36151.1

Loucks, R. G., and Ruppel, S. C. (2007). Mississippian Barnett Shale: Lithofacies and Depositional Setting of a Deep-Water Shale-Gas Succession in the Fort Worth Basin, Texas. *Bulletin* 91 (4), 579–601. doi:10.1306/11020606059

Ma, X., Xie, J., Yong, R., and Zhu, Y. (2020). Geological Characteristics and High Production Control Factors of Shale Gas Reservoirs in Silurian Longmaxi Formation, Southern Sichuan Basin, SW China. *Petroleum Explor. Dev.* 47 (5), 841–855. doi:10.1016/s1876-3804(20)60105-7

Mastalerz, M., Schimmelmann, A., Drobniak, A., and Chen, Y. (2013). Porosity of Devonian and Mississippian New Albany Shale across a Maturation Gradient: Insights from Organic Petrology, Gas Adsorption, and Mercury Intrusion. *Bulletin* 97, 1621–1643. doi:10.1306/04011312194

Schlanser, K., Grana, D., and Campbell-Stone, E. (2016). Lithofacies Classification in the Marcellus Shale by Applying a Statistical Clustering Algorithm to Petrophysical and Elastic Well Logs. *Interpretation* 4 (2), E31–E49. doi:10.1190/int-2015-0128.1

Tang, X., Jiang, Z., Li, Z., Gao, Z., Bai, Y., Zhao, S., et al. (2015). The Effect of the Variation in Material Composition on the Heterogeneous Pore Structure of High-Maturity Shale of the Silurian Longmaxi Formation in the Southeastern Sichuan Basin, China. *J. Nat. Gas Sci. Eng.* 23, 464–473. doi:10.1016/j.jngse.2015.02.031

Wang, C., Zhang, B. Q., Lu, Y. C., Shu, Z. H., Lu, Y. Q., Bao, H. Y., et al. (2018). Lithofacies Distribution Characteristics and Main Development Controlling Factors of Shale in Wufeng Formation-Member 1 of Longmaxi Formation in Jiaoshiba Area. *Acta Pet. Sin.* 39 (6), 631–644. doi:10.7623/syxb201806003

Wang, G., and Carr, T. R. (2012). Methodology of Organic-Rich Shale Lithofacies Identification and Prediction: A Case Study from Marcellus Shale in the Appalachian Basin. *Comput. Geosciences* 49, 151–163. doi:10.1016/j.cageo.2012.07.011

Wang, M., Tang, H., Zhao, F., Liu, S., Yang, Y., Zhang, L., et al. (2017). Controlling Factor Analysis and Prediction of the Quality of Tight Sandstone Reservoirs: a Case Study of the He8 Member in the Eastern Sulige Gas Field, Ordos Basin, china. *J. Nat. Gas Sci. Eng.* 46, 680–698. doi:10.1016/j.jngse.2017.08.033

Wang, P., Jiang, Z., Ji, W., Zhang, C., Yuan, Y., Chen, L., et al. (2016). Heterogeneity of Intergranular, Intraparticle and Organic Pores in Longmaxi Shale in Sichuan Basin, South China: Evidence from SEM Digital Images and Fractal and Multifractal Geometries. *Mar. Petroleum Geol.* 72, 122–138. doi:10.1016/j.marpetgeo.2016.01.020

Wang, Z., Chen, L., Chen, D., Lai, J., Deng, G., Liu, Z., et al. (2020). Characterization and Evaluation of Shale Lithofacies within the Lowermost Longmaxi-Wufeng Formation in the Southeast Sichuan Basin. *J. Petroleum Sci. Eng.* 193 (1), 107353. doi:10.1016/j.petrol.2020.107353

Wu, L., Hu, D. F., Lu, Y. C., and Ruobing, L. I. U. (2016). Advantageous Shale Lithofacies of Wufeng Formation-Longmaxi Formation in Fuling Gas Field of Sichuan Basin, SW China. *Petroleum Explor. Dev.* 43 (2), 189–197. doi:10.1016/s1876-3804(16)30024-6

Xie, X. N., Li, H. J., Xiong, X., Huang, J., Yan, J., and Wu, L. (2008). Main Controlling Factors of Organic Matter Richness in a Permian Section of Guangyuan, Northeast Sichuan. *J. Earth Sci.* 19 (5), 507–517. doi:10.1016/s1002-0705(08)60056-4

Zhang, L., Lu, S., Jiang, S., Xiao, D., Chen, L., Liu, Y., et al. (2018). Effect of Shale Lithofacies on Pore Structure of the Wufeng-Longmaxi Shale in Southeast Chongqing, china. *Energy fuels.* 32, 6603–6618. doi:10.1021/acs.energyfuels.8b00799

Zhao, J., Jin, Z., Wen, X., Geng, Y., and Nie, H. (2016). Lithofacies Types and Sedimentary Environment of Shale in Wufeng-Longmaxi Formation, Sichuan Basin. *Acta Pet. Sin.* 37 (5), 572–586. doi:10.7623/syxb201605002

Zou, C., Dong, D., Wang, S., Li, J., Li, X., Wang, Y., et al. (2010). Geological Characteristics and Resource Potential of Shale Gas in China. *Petroleum Explor. Dev.* 37 (6), 641–653. doi:10.1016/s1876-3804(11)60001-3

Zou, C., Dong, D., Wang, Y., Li, X., Huang, J., Wang, S., et al. (2015). Shale Gas in China: Characteristics, Challenges and Prospects (I). *Petroleum Explor. Dev.* 42 (6), 753–767. doi:10.1016/s1876-3804(15)30072-0

Conflict of Interest: SX, ZS, and CL were employed by the Shale gas Research Institute of PetroChina Southwest Oil and Gas Field Company.

The remaining authors declare that the research was conducted in the absence of any commercial or financial relationships that could be construed as a potential conflict of interest.

frontiers | Frontiers in Earth Science

ORIGINAL RESEARCH
published: 07 June 2022
doi: 10.3389/feart.2022.938765

Development Characteristics of Silurian Strike-Slip Faults and Fractures and Their Effects on Drilling Leakage in Shunbei Area of Tarim Basin

*Haiying Li**

Exploration and Development Research Institute, Sinopec Northwest Oilfield Branch, Urumqi, China

In recent years, the Ordovician fault-controlled fracture-cavity reservoirs developed in the basement strike-slip fault zone in the Shunbei area of the Tarim Basin has achieved major breakthroughs. However, during the drilling process of the strike-slip fault zone in the Shunbei area, the problem of mud leakage in the frequently interbedded Silurian sandstone and mudstone strata overlying the Ordovician target layer is very significant, and it has seriously affected the normal drilling and wellbore stability. In this study, taking the Silurian of the No. A Strike-slip Fault Zone in the Shunbei area as an example, the development characteristics of strike-slip faults and fractures, the strength of the *in-situ* stress field, and the influence of these factors on the drilling mud leakage were systematically studied using 3D seismic, logging, drilling, logging, well log, and engineering construction data. The results show that the mud leakage in strata S_{1t} is significantly larger than that in S_{1k}, and the leakage amount in sandy mudstone is the largest; the strong strike-slip extension developed the negative flower-shaped normal faults and the right-order swan-type faults and caused serious stratigraphic fragmentation. The amount of mud leakage increases with the increase of fault distance. Moreover, the closer to the fault, the higher the frequency and amount of mud leakage. When the distance between the wellbore and the fault exceeds 300 m, the possibility of mud leakage decreases significantly. The Silurian S_{1t} is dominated by high-angle and vertical tension-shear fractures with good opening; while the S_{1k} is dominated by low-angle structural and horizontal bedding fractures. The differences in fracture type cause the mud leakage in S_{1t} to be significantly larger than that of S_{1k}. In addition, the fracture development intervals identified by the R/S-FD method are in good agreement with the mud leakage intervals, which further indicates that the degree of fracture development is the key factor leading to the drilling mud leakage. The study also found that the degree of fracture development and the difference in horizontal principal stresses are the dominant factors leading to high Silurian mud leakage.

Keywords: tarim basin, shunbei area, silurian, strike-slip fault, fracture characteristics, drilling leakage analysis

OPEN ACCESS

Edited by:
Shuai Yin,
Xi'an Shiyou University, China

Reviewed by:
Teng Zhao,
China University of Geosciences, China
Li Ang,
Jilin University, China

****Correspondence:***
Haiying Li
lihaiying202205@163.com

Specialty section:
This article was submitted to Structural Geology and Tectonics, a section of the journal Frontiers in Earth Science

Received: *08 May 2022*
Accepted: *13 May 2022*
Published: *07 June 2022*

Citation:
Li H (2022) Development Characteristics of Silurian Strike-Slip Faults and Fractures and Their Effects on Drilling Leakage in Shunbei Area of Tarim Basin. Front. Earth Sci. 10:938765. doi: 10.3389/feart.2022.938765

INTRODUCTION

Basement strike-slip fault zones in petroliferous basins are an important type of high-yield hydrocarbon enrichment zone (Jiao, 2017; Jiao, 2018; Santosh and Feng, 2020; Qi et al., 2021). Controlled by the action of basement strike-slip structures, the deformation of strike-slip structures is usually confined to a narrow strip along the main fault strike. Furthermore, most of them are linear, belt-shaped, geese-shaped, S-shaped or reverse-S-shaped on the plane, and have a flower-like structure on the cross-section. In three-dimensional space, the main faults often show the phenomenon of "ribbon effect" and "dolphin effect", and indirectly cause the strike-slip fault zone to have obvious segmentation differences. Then, "strike-slip extension", "strike-slip overhang" and "strike-slip translation" can be identified (Deng, et al., 2019a; Li et al., 2019; Fan et al., 2020; Ding et al., 2021; Li, 2022). Moreover, they are affected by multi-stage tectonic movements and multiple sets of detachment layers, so that the deformation styles of strike-slip faults in different tectonic layers have obvious stratification differences (Li et al., 2020; Xue et al., 2021).

Strike-slip fault zones often exhibit the characteristics of "planar segmentation, vertical stratification, multi-period superposition, and variable stress" (Deng et al., 2018; Deng et al., 2019b; He et al., 2020; Hower and Groppo., 2021; Zhan Zhao et al., 2021). They are also the internal mechanism of the "reservoir and hydrocarbon-controlling effect" of strike-slip faults. The multi-stage activities of strike-slip faults have an important impact on the formation of fracture systems and the improvement of petrophysical properties in carbonate rock, shale, and tight sandstone reservoirs (Han et al., 2016; Zhao et al., 2019; Mohammed et al., 2021). In addition, fault activity can also cause the wellbore instability of drilling near the strike-slip fault zone (such as mud loss, wellbore collapse, falling blocks and sticking, etc.) (Al-Ajmi and Zimmerman., 2006; Chen et al., 2014; Yin et al., 2015; Yan and Zhao, 2018; Yin et al., 2018; Zheng et al., 2020; Chen et al., 2021; Gao, 2021).

The Paleozoic and Mesozoic Cenozoic sedimentary strata in Shunbei area of Tarim Basin are well developed, and Permian volcanic rocks and upper Ordovician intrusive dolerite bodies are also developed. Among them, the carbonate rocks of the Middle and Lower Ordovician are the target layers for oil and gas exploration, while the overlying Silurian sand-mudstone interbedded strata, Permian volcanic rocks, and Upper Ordovician diabase strata have serious wellbore instability. Especially in the Silurian sand-mudstone interbedded strata, the leakage of drilling mud is the most serious, and the phenomenon of "nine leakages in ten wells" is remarkable. Therefore, with the continuous expansion of the oil and gas exploration scope of the strike-slip fault zone in the Shunbei area, studies have found that the Silurian sand-mudstone strata overlying the Ordovician target layer have low stress bearing capacity, developed faults, and developed a large number of complex open and closed fracture systems (Yin et al., 2020). Therefore, the random multi-point mud leakage in the whole well section is very serious, which has seriously affected the normal drilling and wellbore stability. *In-situ* stress is the key factor of leakage (Li et al., 2011).

In this study, taking the Silurian of the No. A Strike-slip Fault Zone in the Shunbei area as an example, the theory of reservoir geomechanics was used to analyze the development characteristics of strike-slip faults and fractures, as well as the distribution characteristics of *in-situ* stress fields, and their relationship with drilling mud leakage (Yin and Wu., 2020; Zhao et al., 2020; Li and Li., 2021; Zhao et al., 2021). This study can provide scientific guidance for revealing the wellbore instability mechanism of strike-slip fault zones in similar areas (Jin et al., 1999; Chen et al., 2013; Chen et al., 2015; Gao et al., 2016; Wang et al., 2020; Guo et al., 2021).

GEOLOGICAL SETTING

The Shunbei area is located on the Shuntuoguole Uplift in the central part of the Tarim Basin (**Figure 1**). The structural characteristics of this area are high in the north and low in the south, and high in the east and low in the west. It is a relatively stable ancient tectonic unit in the Tarim Basin. Affected by the

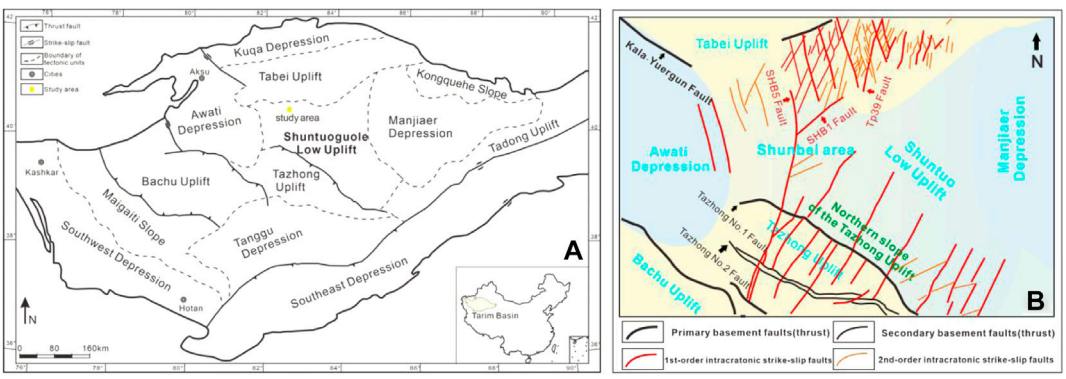

FIGURE 1 | Tectonic location and regional tectonic characteristics of the No. **(A)** Fault Zone in the Shunbei area of Tarim Basin. **(B)** Distribution of faults in the study area.

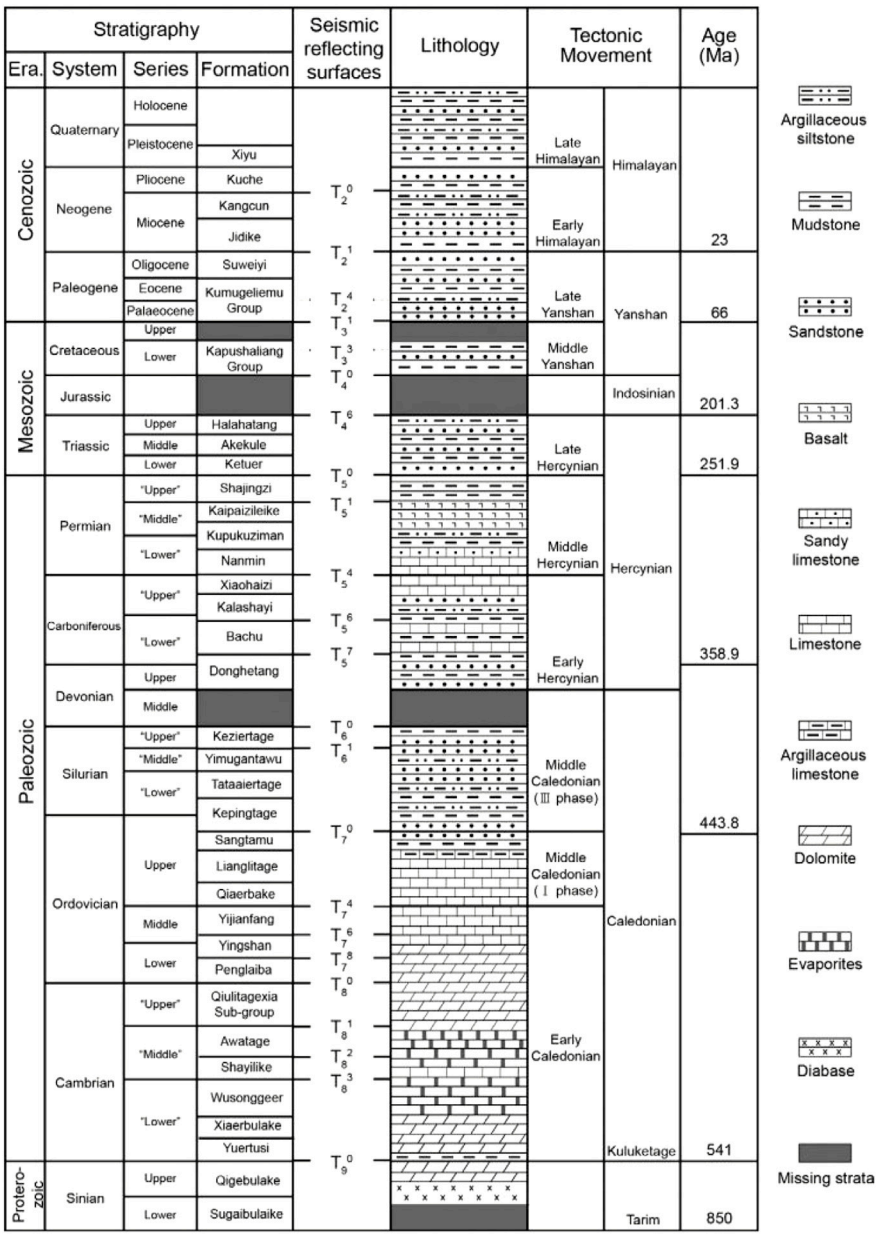

FIGURE 2 | Division of stratigraphic units in the Tarim Basin.

Caledonian, Hercynian, Indosinian, Yanshanian and Himalayan Movements, 18 strike-slip faults in the Shunbei area and its adjacent areas developed in a nearly SN-NE trend. In addition, fault-fracture-type oil and gas reservoirs developed in ultra-deep Ordovician carbonate rocks, and it has been confirmed that these strike-slip fault belts are rich in oil and gas. The Jurassic strata in the Shunbei area are missing; the Cretaceous, Permian, Triassic and Carboniferous strata are partially missing; and other strata are normally developed. From bottom to top, the study area develops Cambrian, Ordovician, Silurian, Devonian, Carboniferous, Permian, Triassic, Cretaceous, Paleogene, Neogene, and Quaternary (**Figure 2**). Among them, the Silurian is the stratum with interbedded sand and mudstone, and the layers with serious leakage of drilling mud are the Lower Silurian Kepingtag Formation and Tata Ertag Formation.

MATERIALS AND METHODS

Materials and Experiments

The data in this study include the Silurian drilling mud leakage data for 19 wells near the strike-slip fault zone in the study area. The specific data include the geological layer at the time of leakage, the section of the leakage well (m), and the lithology; the latter includes

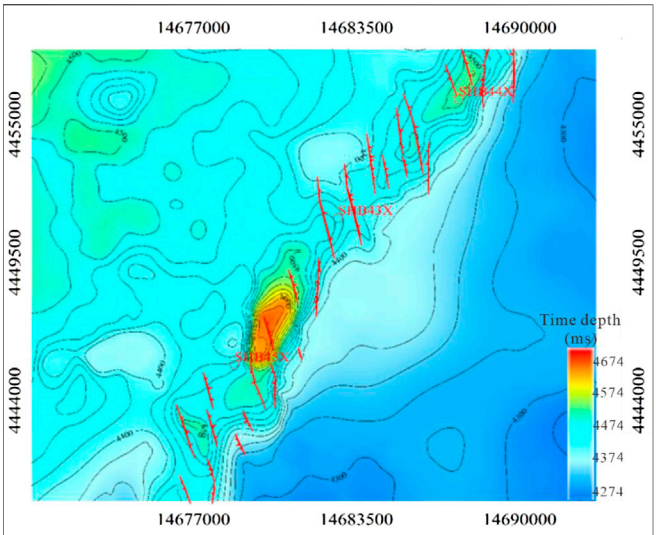

FIGURE 3 | T_6^3 structural contour map of the Silurian in the Shunbei A Strike-Slip Fault Zone in the Tarim Basin.

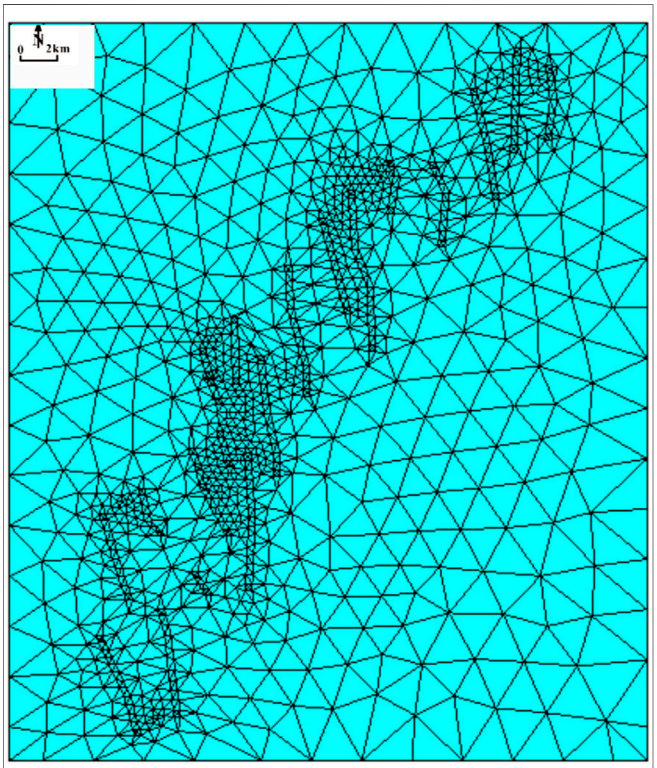

FIGURE 4 | Grid model of Silurian in Shunbei A Strike-Slip Fault Zone in Tarim Basin.

the rate of mud leakage, the cumulative amount of mud leakage (m^3), the density of drilling leakage (g/m^3), and the construction work at the time of mud leakage. In addition, there are three-dimensional (3D) seismic data and interpretation results of the No. A strike-slip fault zone in the Shunbei area. The experimental data includes rock mechanics experiments and acoustic emission (AE) tests.

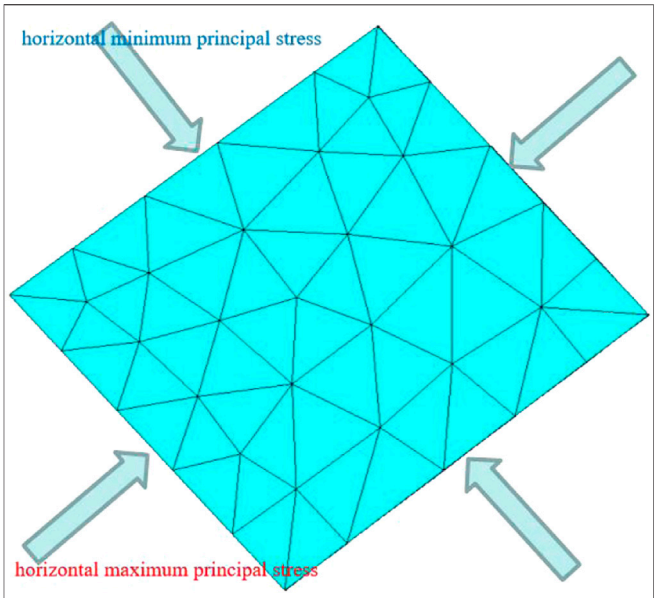

FIGURE 5 | Boundary constraints of numerical simulation of Silurian stress field in Shunbei No. a fault zone.

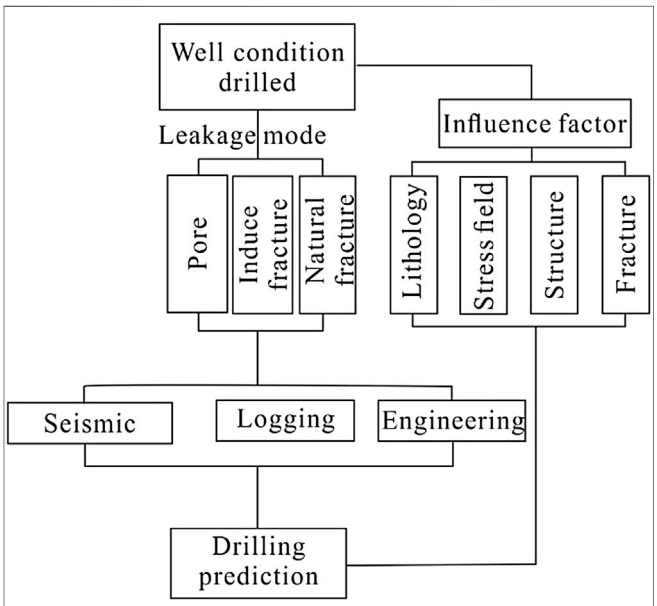

FIGURE 6 | Technical roadmap of strike-slip faults and fractures and their influence on drilling leakage.

Finite Element Method

In this study, the finite element method was used to simulate the tectonic stress field (Ding., et al., 2010; Ding et al., 2012; Jiu et al., 2013; Zeng., et al., 2013; Ding et al., 2016; Liu., et al., 2018). The structural geological model of the northern segment of the Strike-Slip Fault Zone A in the Shunbei area is shown in **Figure 3**, which is subdivided into a series of node and unit grids, including 40,187 nodes and 20,926 grid units (**Figure 4**).

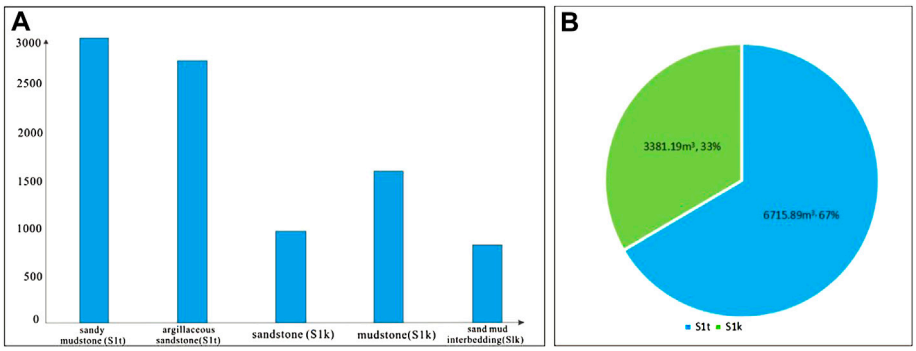

FIGURE 7 | The histogram of the leakage of different layers and lithologies in the Silurian in Shunbei area. **(A)** Leakage of different lithologies; **(B)** Leakage of different strata.

According to the experimental test results of acoustic emission *in-situ* stress, the pressure gradient of the overlying rock of the target layer is 0.0256 MPa/m, the maximum horizontal *in-situ* stress gradient is 0.0234 MPa/m, and the minimum horizontal *in-situ* stress gradient is 0.0187 MPa/m. Finally, we determined that the direction of the maximum horizontal principal stress during the main rupture formation period of the Silurian sand-mudstone stratum was NE-SW, and the direction of the minimum horizontal principal stress was NW-SE (**Figure 5**).

To facilitate the calculation process, the tensile rupture rate I_t and the shear rupture rate I_n are introduced:

$$I_t = \sigma_T/\sigma_t \tag{1}$$

where σ_T is the effective tensile stress, MPa; σ_t is the tensile strength of the rock, MPa. When $I_t \geq 1$, the rock undergoes tension fracture.

$$I_n = \tau_n/|\tau| \tag{2}$$

where τ_n is the effective shear stress, MPa, and $|\tau|$ is the shear strength of the rock, MPa. When $I_n \geq 1$, the rock undergoes shear fracture.

The fracture mode of rock is a comprehensive reflection of tensile stress and shear stress, and a comprehensive fracture coefficient is introduced.

$$I_z = (aI_t + bI_n)/2 \tag{3}$$

In the formula, a and b are the proportions of tension fractures (including tension-shear fractures) and shear fractures obtained from core and electron microscope observations, respectively. In this study a:b = 6:4. Similarly, when $I_z \geq 1$, the rock reaches a fractured state, and the higher the comprehensive fracture rate value, the greater the fracture degree.

R/S-FD Method

R/S analysis, also known as rescaled range analysis or variable scale analysis. This method was originally proposed by British hydrologist Hurst on the basis of long-term research on the relationship between water volume and storage capacity of reservoirs (Hurst, 1951). Through the processing of conventional logging curves by R/S analysis method, the fracture development interval can be preliminarily determined by manually identifying abnormal positions on the R/S curve (Rangarajan and Sant., 2004; Xiao et al., 2019).

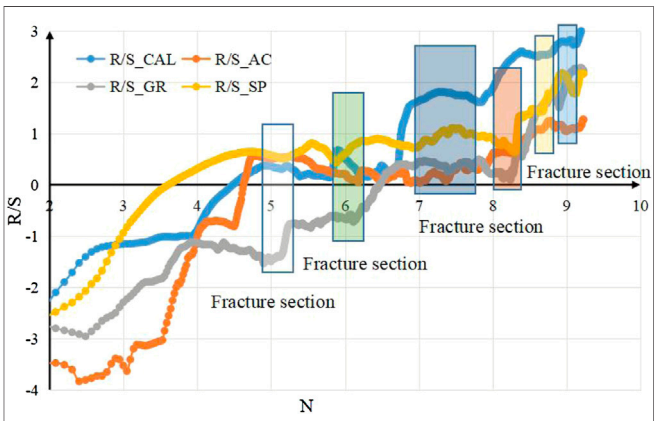

FIGURE 8 | Fracture interval identification based on R/S-FD method in Silurian of Well X in the study area.

In the *R/S* analysis method, *R* is the range, which is the difference between the maximum value and the minimum value, indicating the fluctuation range and complexity of the time series; *S* is called the standard deviation, indicating the average trend of the time series. *R/S* is a dimensionless time series representing fluctuation strength. The calculation methods of *R* and *S* are shown in **formula 4** and **formula 5** respectively:

$$\mathrm{R}(n) = \max_{0<u<n}\left\{\sum_{i=1}^{u} Z(i) - \frac{u}{n}\sum_{i=1}^{u} Z(j)\right\} - \min_{0<u<n}\left\{\sum_{i=1}^{u} Z(i) - \frac{u}{n}\sum_{i=1}^{u} Z(j)\right\} \tag{4}$$

$$\mathrm{S}(n) = \sqrt{\frac{1}{n}\sum_{i=1}^{u} Z^2(i) - \left[\frac{1}{n}\sum_{j=1}^{u} Z(j)\right]^2} \tag{5}$$

$$D = 2 - \frac{\partial LOG\left\{\left[\frac{R(n)}{S(n)}\right], 10\right\}}{\partial n} \tag{6}$$

Among them, Z is a logging curve for *R/S* analysis; n is the number of sampling points in the logging analysis interval (one

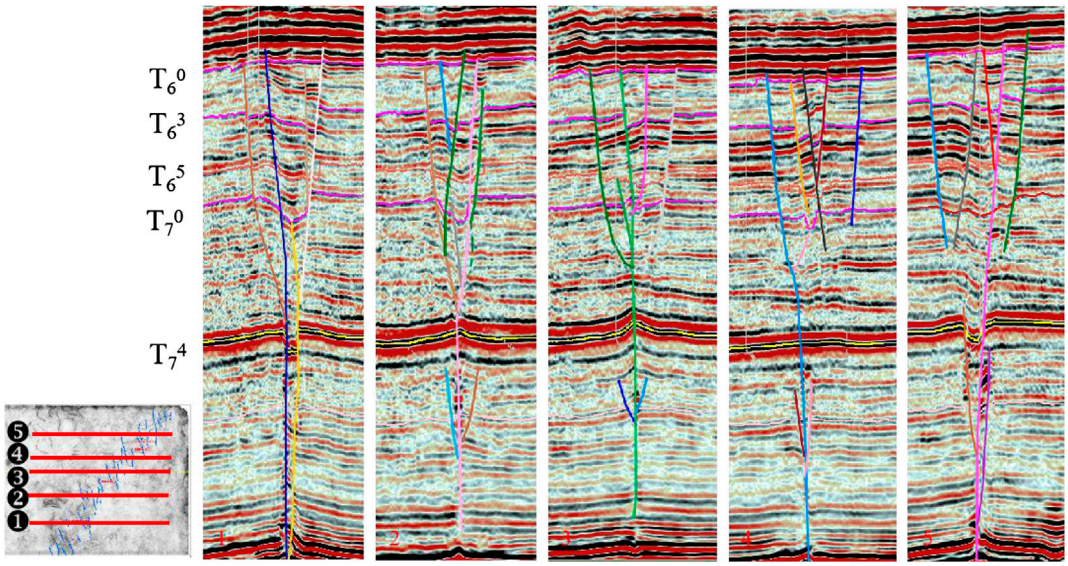

FIGURE 9 | Seismic interpretation profile of the Silurian (T_7^0-T_6^0) negative flower-shaped fault in Shunbei A Fault Zone.

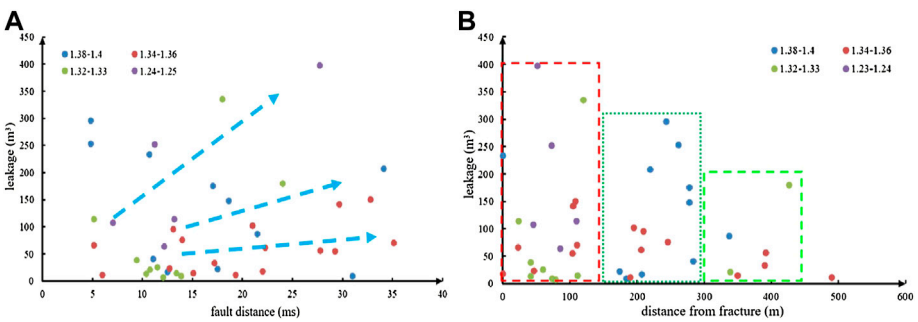

FIGURE 10 | Relationship between Silurian mud leakage and fault throw and its distance from wellbore to fault. **(A)** Relationship between leakage and fault distance; **(B)** Relationship between leakage and distance to fracture.

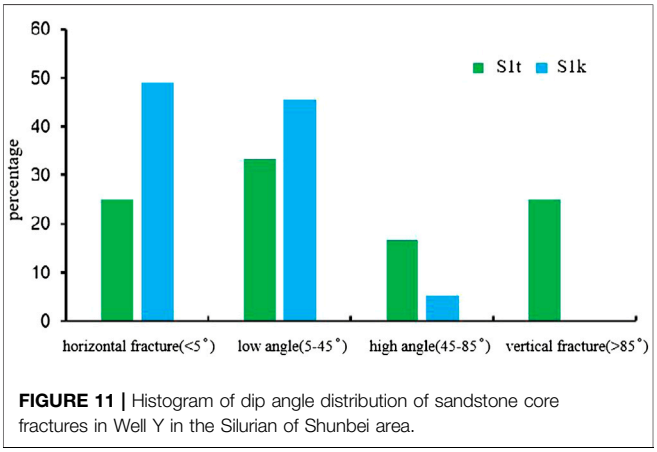

FIGURE 11 | Histogram of dip angle distribution of sandstone core fractures in Well Y in the Silurian of Shunbei area.

sample is taken every 0.125 m), and each n has a corresponding $R(n)/S(n)$ value; u is the number of sampling points increased each time since the beginning; i and j represent variables; D is the fractal dimension, dimensionless, **formula (6)**. Technical roadmap of strike-slip faults and fractures and their influence on drilling leakage is shown in **Figure 6**.

RESULTS

Mud Leakage Characteristics

Statistics on the Silurian mud loss data of 19 wells in the Shunbei area show that in general, the mud loss in S_{1t} is significantly larger than that in S_{1k}. The leakage of sand-bearing mudstone is the largest, followed by mud-bearing sandstone and mudstone layers (**Figure 7**). The mud leakage of each well in different lithologic sections varies greatly.

Log Identification Results of Fractures

R(n)/S(n) is the R/S value corresponding to the nth sampling point. The R/S value and n of each interval are plotted as a logarithmic scatter plot. If the relative change of the two is observed as a densely distributed fitting curve, it indicates that

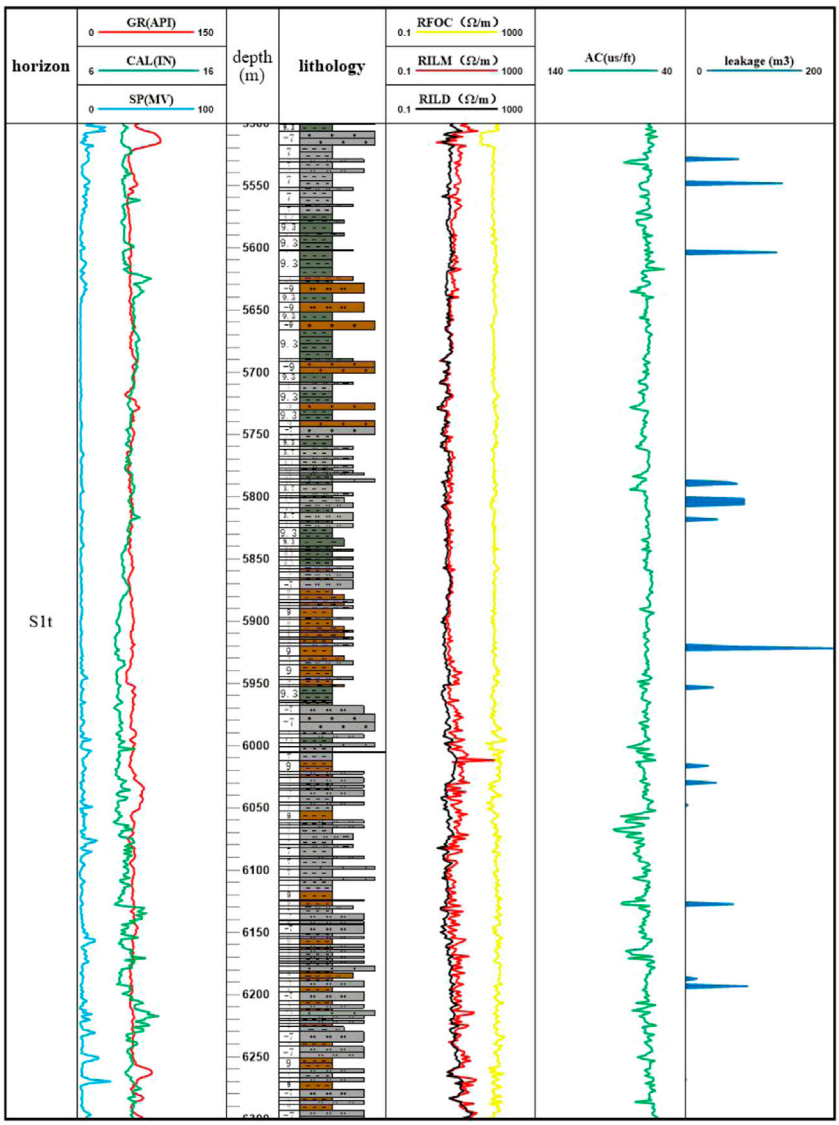

FIGURE 12 | Fracture log identification based on R/S-FD method in target layer of Well Z.

the sequence has good fractal characteristics. The slope H of the R(n)/S(n) curve is called the Hurst exponent. The fractal dimension D of a certain interval can be calculated by **formula (6)**, and its value reflects the heterogeneity of carbonate reservoirs. When some scholars use fractal theory to study the degree of fracture development, they believe that the larger the fractal dimension D, the more developed the fractures (Qie et al., 2021; Wang and Wang., 2021; Wen et al., 2004). The existence of fractures in the formation will lead to a great increase in the complexity of the formation, which corresponds to a higher fractal position value D and a smaller Hurst exponent. The R(n)/S(n) curve shows a decreasing slope segment, which is specifically characterized by the downward shift of the R(n)/S(n) curve. From this, it can be concluded that morphologically, the down-concave segment of the R(n)/S(n) curve can be considered as a potential fracture development segment (**Figure 8**).

Based on the above methods and theories, this paper comprehensively conducts R/S analysis and calculation on five conventional logging curves (CAL, AC, GR, SP and RD) of the Silurian drilling in Shunbei area. If most of the R(n)/S(n) curves show depression in a certain section at the same time, it can indicate that this section is a fracture-developed section. Large errors are usually introduced when manually identifying the concave section of the R(n)/S(n) curve. In order to solve the shortcomings of this method, the second derivative of the function in advanced mathematics is introduced to improve the method. Since the value of R(n)/S(n) is discrete data, this paper uses the finite difference method (FD) to approximate the derivative operation. The logging fracture identification results show that the fracture identification accuracy based on the R/S-FD analysis method can reach 78%.

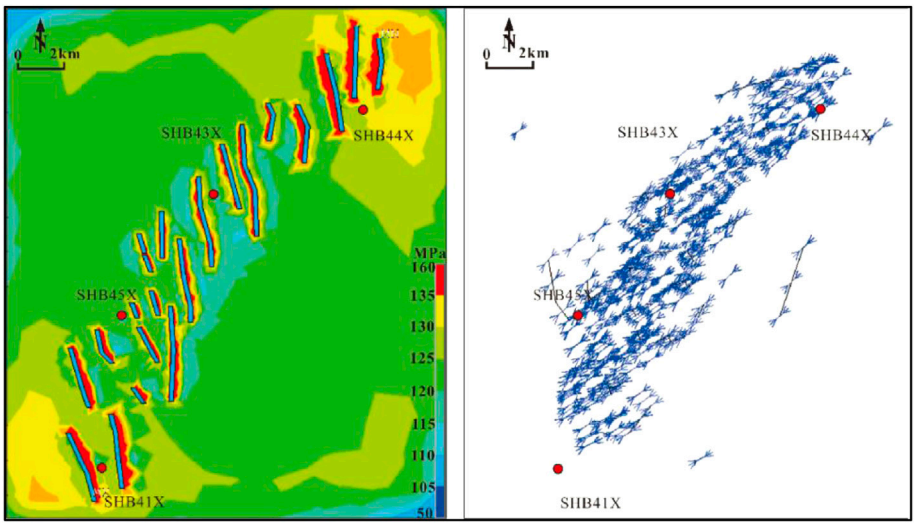

FIGURE 13 | Planar distribution of the maximum principal stress and direction at the T_6^3 interface of the Shunbei No. A Fault Zone.

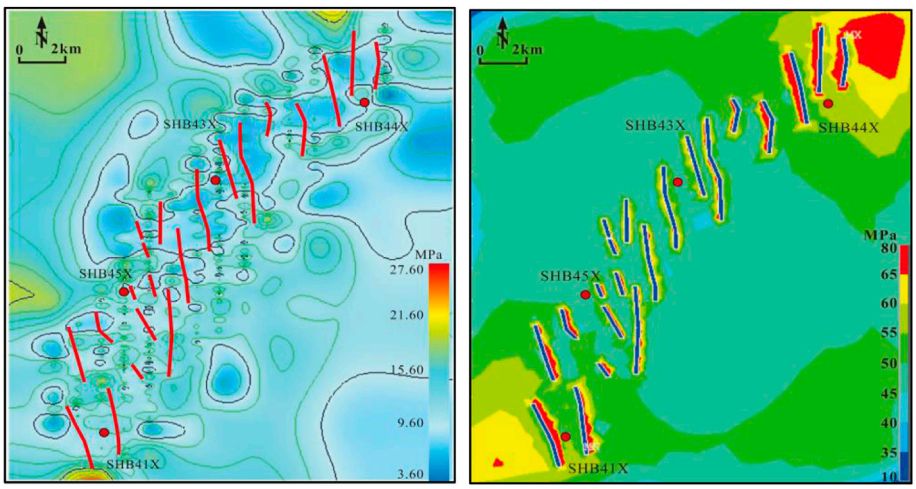

FIGURE 14 | Planar distribution of shear stress and horizontal stress difference at T_6^3 interface of Shunbei No. A Fault Zone.

DISCUSSION

Relationship Between Fault and Mud Leakage

The three-dimensional seismic data can well reflect the fault distribution characteristics of the Silurian system in both vertical and horizontal directions. The faults appear as flower-like structures on the seismic profiles, with obvious strike-slip fault characteristics. The Silurian tectonic layer is an asymmetric negative flower-like tectonic style, with a large number and well-developed strike-slip extensional branch normal faults. The vertical fault throws of main and branch faults are small, reflecting weak extension (**Figure 9**). In addition, the Silurian fault system is mainly arranged in a geese-type normal fault combination pattern on the plane, with a small extension length, and some of them exist in pairs (**Figure 3**).

Nearly north-south extensional negative flower-like branch normal faults are well developed in the study area, which are distributed in a right-order geese pattern, and a few local high points are developed. These features indicate that the Silurian strike-slip extension is strong in the Shunbei area, and the stratum is severely fractured. According to the statistical data of 20 wells, the mud leakage increases with the increase of the fault distance, and the frequency and the leakage volume are the highest when the distance is closer to the fault. Moreover, the leakage frequency is the highest when the wellbore is within 150 m of the fault, followed by 150–300 m. When the wellbore is more than 300 m away from the fault, the likelihood of leakage is lowest (**Figure 10**). The development of negative

TABLE 1 | Criteria for judging the development degree of Silurian fractures in Shunbei area.

Fracture Development Grade	A	B	C
Comprehensive rupture rate IF	IF > 1.4	1.0 < IF < 1.4	IF < 1.0
Fracture development degree	Developed	Relatively developed	Undeveloped

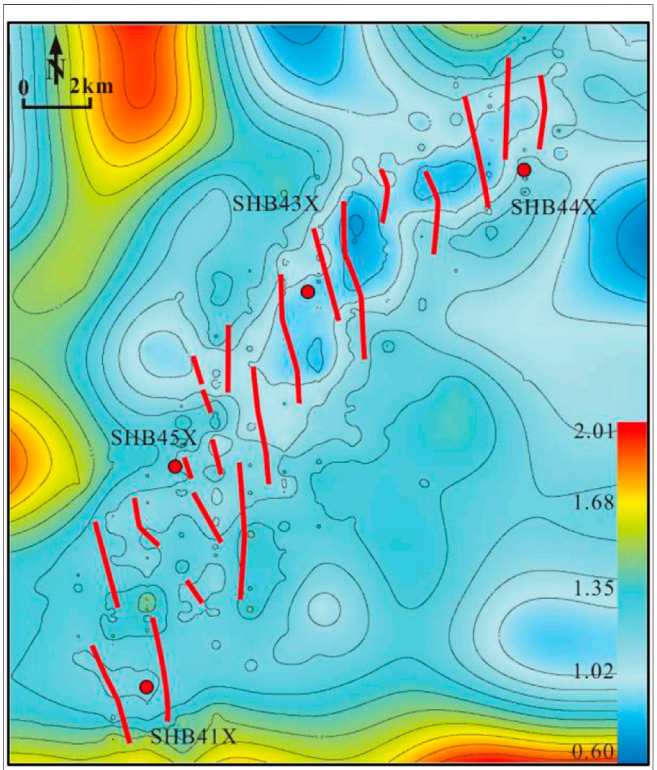

FIGURE 15 | Prediction results of the distribution of Silurian fracture development coefficients in the northern segment of the Shunbei No. A fault zone.

flower-like branch normal faults is the macro-controlling factor of Silurian sand-mudstone formation leakage. The deep tectonic pattern in the study area is shown on the seismic section as a large-angle or near-upright strike-slip fault breaking into the basement, which is mainly developed at the T_7^4 interface (top surface of the middle-lower Ordovician unified Yijianfang Formation) and underlying strata. These faults are formed in one stage.

Relationship Between Fracture Occurrence and Mud Leakage

In Well Shunbei Y, medium and high-angle tension-shear fractures are mainly developed in the sandstone section of the Silurian Tata Ertag Formation (S_{1t}), and low-angle fractures are prone to occur at the sand-mudstone interface. The residues of the invading mud during drilling can be seen on the fracture surfaces of the opened fractures. In addition, Well Shunbei Y mainly developed low-angle fractures in the sandstone section of the Silurian Kalpintag Formation (S_{1k}), and the fractures were mainly generated along weak planes such as horizontal or oblique bedding.

Statistics show that fractures of different dip angles are developed in Silurian S_{1t}, mainly high-angle and vertical fractures. In S_{1k}, low-angle and horizontal fractures are the main factors (**Figure 11**), which is also the main factor causing the mud loss in S_{1t} to be significantly larger than that in S_{1k}.

Relationship Between Vertical Development Characteristics of Fractures and Mud Leakage

Based on the R/S-FD analysis method, this paper uses four logging curves (AC, CAL, SP, GR) to calculate the fractures. Most of the R(n)/S(n) curves show a fracture development segment in the concave curve segment (**Figure 8**, **Figure 12**). And the study found that the fracture development section is in good agreement with the mud leakage section, indicating that the Silurian fracture development is the key factor leading to the leakage.

Tectonic Stress Field and Fracture Distribution and Their Relationship With Mud Leakage

In this study, the finite element method was used to simulate the tectonic stress field and predict the fracture distribution of the Silurian in the Shunbei No. A Fault Zone in the Shunbei area. The maximum principal stress of Shunbei No. A Fault Zone is mainly compressive stress, and its value is concentrated between 115–130 MPa, and it is greatly affected by the fault zone. The stress inside the fault zone is relatively small, and the stress is relatively large near the fault zone (**Figure 13**). The shear stress value of Shunbei No. A Fault Zone is generally positive, ranging from 3.6 to 21.6 MPa. It is reflected that it is dominated by the counterclockwise left-handed shear stress field. In addition, the shear stress values along the main fault zone and its vicinity are larger, and the simulation results are consistent with the deformation characteristics of the compressive-torsional strike-slip structure in the Shunbei area. In addition, the horizontal stress difference range is relatively small (45–60 MPa) within the fault zone, while it is relatively large near the fault zone (**Figure 14**).

In this study, the finite element method was used to calculate the planar distribution of the fracture development coefficient I_F of the Silurian strata in the northern segment of the No. A Fault Zone in the Shunbei area (**Figure 13**). The fracture development coefficient I_F of the Silurian strata in this fault zone is distributed between 0.61 and 2.01. When the I_F of the formation is less than 1, it can be considered that the rock is not fractured. When the I_F of

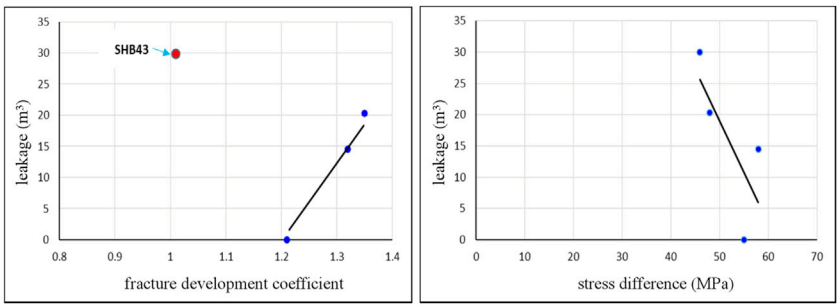

FIGURE 16 | Relationship between Silurian fracture development coefficient, horizontal stress difference and mud leakage in the northern segment of Shunbei No. A fault zone.

the formation is greater than 1, the rocks are fractured to different degrees. The larger the value of I_F, the greater the probability of rock fracture. According to the distribution range of I_F value of Silurian in Shunbei area, it can be divided into three grades A, B and C (**Table 1**). The larger the I_F value and the higher the classification, the easier the rock is to be fractured and the more developed the fractures. In the main fault zone and its vicinity, the fracture development coefficient is between 1.0 and 1.35 (**Figure 15**).

For the four wells drilled on the No. A fault zone in the Shunbei area, we calculated the fracture development coefficient, horizontal stress difference, and their relationship with mud leakage (**Figure 16**). The Silurian as a whole shows that the higher the degree of fracture development, the greater the mud leakage, and the horizontal stress difference is negatively correlated with the mud leakage. For example, Well W3 has a large leakage and a small fracture development coefficient, but the stress difference is small, 46 MPa, which is 2–12 MPa smaller than other stress differences. It shows that the leakage of this well is mainly controlled by *in-situ* stress. The degree of fracture development and the difference in horizontal stress in the Silurian sand-mudstone formation are the main factors leading to high mud leakage.

Through the correlation analysis between the mud leakage and the horizontal stress difference, distance from the fault, and fault distance, it is concluded that the horizontal stress difference is the most direct cause of the mud leakage.

CONCLUSION

(1) In this study, based on 3D seismic, logging, drilling, logging, well log, and engineering construction data, development characteristics of strike-slip faults and fractures, the strength of the *in-situ* stress field, and the influence of these factors on the drilling mud leakage were systematically studied.
(2) The mud leakage in S_{1t} is significantly larger than that in S_{1k}, and the leakage amount in sandy mudstone is the largest; the strong strike-slip extension developed the negative flower-shaped normal faults and the right-order swan-type faults and caused serious stratigraphic fragmentation. The amount of mud leakage increases with the increase of fault distance. Moreover, the closer to the fault, the higher the frequency and amount of mud leakage. When the distance between the wellbore and the fault exceeds 300 m, the possibility of leakage decreases significantly.
(3) The Silurian S_{1t} is dominated by high-angle and vertical tension-shear fractures with good opening; while the S_{1k} is dominated by low-angle structural and horizontal bedding fractures. The difference in fracture type causes the mud leakage in S_{1t} to be significantly larger than that of S_{1k}.
(4) The fracture development intervals identified by the R/S-FD method are in good agreement with the mud leakage intervals, which further indicates that the degree of fracture development is the key factor leading to the drilling mud leakage.
(5) The degree of fracture development and the difference in horizontal principal stresses are the dominant factors leading to high Silurian mud leakage. Mud leakage has significant positive and negative correlations with the fracture development coefficient and the horizontal stress difference, respectively.

DATA AVAILABILITY STATEMENT

The original contributions presented in the study are included in the article/supplementary material further inquiries can be directed to the corresponding author.

AUTHOR CONTRIBUTIONS

HL is responsible for the idea, seismic/logging data interpretation and writing of this paper.

FUNDING

This research was supported by the National Natural Science Foundation of China (Grant No. 42072173) and the scientific research project (KY2020-S-030) of Sinopec Northwest Oilfield Company.

REFERENCES

Al-Ajmi, A. M., and Zimmerman, R. W. (2006). Stability Analysis of Vertical Boreholes Using the Mogi-Coulomb Failure Criterion. *Int. J. Rock Mech. Min. Sci.* 43 (8), 1200–1211. doi:10.1016/j.ijrmms.2006.04.001

Chen, Z., Zhang, H., Shen, B., Yin, G., and Wang, X. (2013). A Study on Safe and Dangerous Drilling Azimuths of Horizontal Well. *Acta Pet. Sin.* 34 (1), 164–168. doi:10.7623/syxb201301021

Chen, P., Ma, T., and Xia, H. (2014). A Collapse Pressure Prediction Model of Horizontal Shalegas Wells with Multiple Weak Planes. *Nat. Gas. Ind.* 34 (12), 87–93. doi:10.3787/j.issn.1000-0976.2014.12.012

Chen, P., Ma, T., and Fan, X. (2015). Well Path Optimization Based on Wellbore Stability Analysis. *Nat. Gas. Ind.* 35 (10), 84–92. doi:10.3787/j.issn.1000-0976.2015.10.011

Chen, G. B., Li, T., Yang, L., Zhang, G. H., Li, J. W., and Dong, H. J. (2021). Mechanical Properties and Failure Mechanism of Combined Bodies with Different Coal-Rock Ratios and Combinations. *J. Min. Strata Control Eng.* 3 (2), 023522. doi:10.13532/j.jmsce.cn10-1638/td.20210108.001

Ding, W., Fan, T., Huang, X., and Liu, C. (2010). Paleo-structural Stress Field Simulation for Middle-Lower Ordovician in Tazhong Area and Favorable Area Prediction of Fractured Reservoirs. *J. China Univ. Petroleum* 34 (5), 1–6. doi:10.3969/j.issn.1673-5005.2010.05.001

Ding, W., Fan, T., Yu, B., Huang, X., and Liu, C. (2012). Ordovician Carbonate Reservoir Fracture Characteristics and Fracture Distribution Forecasting in the Tazhong Area of Tarim Basin, Northwest China. *J. Petroleum Sci. Eng.* 86-87, 62–70. doi:10.1016/j.petrol.2012.03.006

Ding, W., Zeng, W., Wang, R., Jiu, K., Wang, Z., Sun, Y., et al. (2016). Method and Application of Tectonic Stress Field Simulation and Fracture Distribution in Shale Reservoir. *Earth Sci. Front.* 23 (2), 63–74. doi:10.13745/j.esf.2016.02.008

Deng, S., Li, H., Zhang, Z., Wu, X., and Zhang, J. (2018). Characteristics of Differential Activities in Major Strike-Slip Fault Zones and Their Control on Hydrocarbon Enrichment in Shunbei Area and its Surroundings, Tarim Basin. *Oil Gas Geol.* 39 (05), 878–888. doi:10.11743/ogg20180503

Deng, S., Li, H., Zhang, Z., Zhang, J., and Yang, X. (2019a). Structural Characterization of Intracratonic Strike-Slip Faults in the Central Tarim Basin. *Bulletin* 103 (1), 109–137. doi:10.1306/06071817354

Deng, S., Li, H., Han, J., Cui, D., and Zou, R. (2019b). Characteristics of the Central Segment of Shunbei 5 Strike-Slip Fault Zone in Tarim Basin and its Geological Significance. *Oil Gas Geol.* 40 (05), 990–998+1073. doi:10.11743/ogg20190504

Ding, F., Xie, C., Zhou, X., Jiang, C., Li, K., Wan, L., et al. (2021). Defining Stratigraphic Oil and Gas Plays by Modifying Structural Plays: A Case Study from the Xihu Sag, East China Sea Shelf Basin. *Energy Geosci.* 2 (1), 41–51. doi:10.1016/j.engeos.2020.08.002

Fan, C., Li, H., Qin, Q., He, S., and Zhong, C. (2020). Geological Conditions and Exploration Potential of Shale Gas Reservoir in Wufeng and Longmaxi Formation of Southeastern Sichuan Basin, China. *J. Petroleum Sci. Eng.* 191, 107138. doi:10.1016/j.petrol.2020.107138

Gao, F. Q. (2021). Influence of Hydraulic Fracturing of Strong Roof on Mining-Induced Stress Insight from Numerical Simulation. *J. Min. Strata Control Eng.* 3 (2), 023032. doi:10.13532/j.jmsce.cn10-1638/td.20210329.001

Gao, J., Deng, J., Yan, W., Feng, Y., Wang, H., and Li, Y. (2016). Establishment of Apredіction Model for the Borehole Trajactory Optimization Based on Controlling Wellbore Stability. *Acta Pet. Sin.* 37, 1179–1186. doi:10.7623/syxb201609013

Guo, L. L., Zhou, D. W., Zhang, D. M., and Zhou, B. H. (2021). Deformation and Failure of Surrounding Rock of a Roadway Subjected to Mining-Induced Stresses. *J. Min. Strata Control Eng.* 3 (2), 023038. doi:10.13532/j.jmsce.cn10-1638/td.20200727.001

Han, J., Kuang, A., Neng, Y., Huang, C., Li, Q., Chen, P., et al. (2016). Vertical Layered Structure of Shunbei No.5 Strike-Slip Fault Zone and its Significance on Hydrocarbon Accumulation. *Xingjiang Pet. Geol.* 42 (02), 152–160. doi:10.7657/XJPG20210204

He, X., Zhang, P., He, G., Gao, Y., Liu, M., Zhang, Y., et al. (2020). Evaluation of Sweet Spots and Horizontal-Well-Design Technology for Shale Gas in the Basin-Margin Transition Zone of Southeastern Chongqing, SW China. *Energy Geosci.* 1 (3–4), 134–146. doi:10.1016/j.engeos.2020.06.004

Hower, J. C., and Groppo, J. G. (2021). Rare Earth-Bearing Particles in Fly Ash Carbons: Examples from the Combustion of Eastern Kentucky Coals. *Energy Geosci.* 2 (2), 90–98. doi:10.1016/j.engeos.2020.09.003

Hurst, H. E. (1951). Long-term Storage Capacity of Reservoirs. *Trans. Am. Soc. Civ. Eng.* 116 (1), 770–799. doi:10.1061/TACEAT.0006518

Jiao, F. (2017). Significance of Oil and Gas Exploration in NE Strike-Slip Fault Belts in Shuntuoguole Area of Tarim Basin. *Oil Gas Geol.* 38 (05), 831–839. doi:10.11743/ogg20170501

Jiao, F. (2018). Significance and Prospect of Ultra-deep Carbonate Fault-Karst Reservoirs in Shunbei Area, Tarim Basin. *Oil Gas Geol.* 39 (02), 207–216. doi:10.11743/ogg20180201

Jin, Y., Chen, M., Liu, G., and Chen, Z. (1999). Wellbors Stability Analysis of Extended Reach Wells. *J. Geomechanics* 5 (1), 1–4. doi:10.3969/j.issn.1006-6616.1999.01.002

Jiu, K., Ding, W., Huang, W., You, S., Zhang, Y., and Zeng, W. (2013). Simulation of Paleotectonic Stress Fields within Paleogene Shale Reservoirs and Prediction of Favorable Zones for Fracture Development within the Zhanhua Depression, Bohai Bay Basin, East China. *J. Petroleum Sci. Eng.* 110, 119–131. doi:10.1016/j.petrol.2013.09.002

Li, D., Kang, Y., Liu, S., Zeng, Y., and Du, C. (2011). Leakage Pressure Model of Carbonate Formation Based on Leakage Mechanism. *ACTA PET. SIN.* 32 (5), 5. doi:10.7623/syxb201105026

Li, H., Tang, H., Qin, Q., Zhou, J., Qin, Z., Fan, C., et al. (2019). Characteristics, Formation Periods and Genetic Mechanisms of Tectonic Fractures in the Tight Gas Sandstones Reservoir: A Case Study of Xujiahe Formation in YB Area, Sichuan Basin, China. *J. Petroleum Sci. Eng.* 178, 723–735. doi:10.1016/j.petrol.2019.04.007

Li, H., Qin, Q., Zhang, B., Ge, X., Hu, X., Fan, C., et al. (2020). Tectonic Fracture Formation and Distribution in Ultradeep Marine Carbonate Gas Reservoirs: A Case Study of the Maokou Formation in the Jiulongshan Gas Field, Sichuan Basin, Southwest China. *Energy fuels..* 34 (11), 14132–14146. doi:10.1021/acs.energyfuels.0c03327

Li, H. (2022). Research Progress on Evaluation Methods and Factors Influencing Shale Brittleness: A Review. *Energy Rep.* 8, 4344–4358. doi:10.1016/j.egyr.2022.03.120

Li, L., and Li, S. J. (2021). Evolution Rule of Overlying Strata Structure in Repeat Mining of Shallow Close Distance Seams Based on Schwarz Alternating Procedure. *J. Min. Strata Control Eng.* 3 (2), 023515. doi:10.13532/j.jmsce.cn10-1638/td.20210225.001

Liu, J., Ding, W., Dai, J., Wu, Z., and Yang, H. (2018). Quantitative Prediction of Lower Order Faults Based on the Finite Element Method: A Case Study of the M35 Fault Block in the Western Hanliu Fault Zone in the Gaoyou Sag, East China. *Tectonics* 37 (10), 3479–3499. doi:10.1029/2017TC004767

Mohammed, B., Richard, H. W., Shettima, B., and Philip, S. (2021). Diagenesis and its Controls on Reservoir Quality of the Tambar Oil Field, Norwegian North Sea. *Energy Geosci.* 2 (1), 10–31. doi:10.1016/j.engeos.2020.07.002

Qi, L., Yun, L., Cao, Z., Li, H., and Huang, C. (2021). Geological Reserves Assessment and Petroleum Exploration Targets in Shunbei Oil & Gas Field. *Xingjiang Pet. Geol.* 42 (02), 127–135. doi:10.7657/XJPG20210201

Qie, L., Shi, Y. N., and Liu, J. S. (2021). Experimental Study on Grouting Diffusion of Gangue Solid Filling Bulk Materials. *J. Min. Strata Control Eng.* 3 (2), 023011. doi:10.13532/j.jmsce.cn10-1638/td.20201111.001

Rangarajan, G., and Sant., D. A. (2004). Fractal Dimensional Analysis of Indian Climatic Dynamics. *Chaos, Solit. Fractals* 19 (2), 285–291. doi:10.1016/S0960-0779(03)00042-0

Santosh, M., and Feng, Z. Q. (2020). New Horizons in Energy Geoscience. *Energy Geosci.* 1 (1–2), 1–2. doi:10.1016/j.engeos.2020.05.005

Wang, H., Shi, Z., Zhao, Q., Liu, D., Sun, S., Guo, W., et al. (2020). Stratigraphic Framework of the Wufeng-Longmaxi Shale in and Around the Sichuan Basin, China: Implications for Targeting Shale Gas. *Energy Geosci.* 1 (3–4), 124–133. doi:10.1016/j.engeos.2020.05.006

Wang, J., and Wang, X. L. (2021). Seepage Characteristic and Fracture Development of Protected Seam Caused by Mining Protecting Strata. *J. Min. Strata Control Eng.* 3 (3), 033511. doi:10.13532/j.jmsce.cn10-1638/td.20201215.001

Wen, H., Xiao, C., Li, R., Yang, B., and Wang, H. (2004). On Multifractal Analysis Method in Well Logging Interpretation. *Well Logging Technol.* 28 (5), 381–385. doi:10.16489/j.issn.1004-1338.2004.05.004

Xiao, Z., Ding, W., Liu, J., Tian, M., Yin, S., Zhou, X., et al. (2019). A Fracture Identification Method for Low-Permeability Sandstone Based on R/S Analysis and the Finite Difference Method: A Case Study from the Chang 6 Reservoir in

Huaqing Oilfield, Ordos Basin. *J. Petroleum Sci. Eng.* 174, 1169–1178. doi:10.1016/j.petrol.2018.12.017

Xue, F., Liu, X. X., and Wang, T. Z. (2021). Research on Anchoring Effect of Jointed Rock Mass Based on 3D Printing and Digital Speckle Technology. *J. Min. Strata Control Eng.* 3 (2), 023013. doi:10.13532/j.jmsce.cn10-1638/td.20201020.001

Yan, C., and Zhao, K. (2018). *New Technology for Evaluating Wellbore Stability in Complex Strata*. Beijing: Sinopec Press, 1–2.

Yin, S., Ding, W., Yang, W., Zhao, W., Zhang, M., and Cong, S. (2015). Progress of Borehole Stability Considering Strata Anisotropy. *Adv. Earth Sci.* 30, 13–25. doi:10.11867/j.issn.1001-8166.2015.11.1218

Yin, S., Lv, D. W., and Ding, W. L. (2018). New Method for Assessing Microfracture Stress Sensitivity in Tight Sandstone Reservoirs Based on Acoustic Experiments. *Int. J. Geomechanics* 18 (4), 1–16. doi:10.1061/(asce)gm.1943-5622.0001100

Yin, S., Dong, L., Yang, X., and Wang, R. (2020). Experimental Investigation of the Petrophysical Properties, Minerals, Elements and Pore Structures in Tight Sandstones. *J. Nat. Gas Sci. Eng.* 73, 1–14. doi:10.1016/j.jngse.2020.103189

Yin, S., and Wu, Z. (2020). Geomechanical Simulation of Low-Order Fracture of Tight Sandstone. *Mar. Petroleum Geol.* 100, 1–16. doi:10.1016/j.marpetgeo.2020.104359

Zeng, W., Ding, W., Zhang, J., Zhang, Y., Guo, L., Jiu, K., et al. (2013). Fracture Development in Paleozoic Shale of Chongqing Area (South China). Part Two: Numerical Simulation of Tectonic Stress Field and Prediction of Fractures Distribution. *J. Asian Earth Sci.* 75, 267–279. doi:10.1016/j.jseaes.2013.07.015

Zhan Zhao, Z., Liu, J., Ding, W., Yang, R., and Zhao, G. (2021). Analysis of Seismic Damage Zones: A Case Study of the Ordovician Formation in the Shunbei 5 Fault Zone, Tarim Basin, China. *J. Mar. Sci. Eng.* 9 (6), 630. doi:10.3390/JMSE9060630

Zhao, R., Zhao, T., Li, H., Deng, S., and Zhang, J. (2019). Fault-Controlled Fracture-Cavity Reservoir Characterization and Main-Controlling Factors in the Shunbei Hydrocarbon Field of Tarim Basin. *Special Oil Gas Reservoirs* 26 (05), 8–13. doi:10.3969/j.issn.1006-6535.2019.05.002

Zhao, Z., Wu, K., Fan, Y., Guo, J., Zeng, B., and Yue, W. (2020). An Optimization Model for Conductivity of Hydraulic Fracture Networks in the Longmaxi Shale, Sichuan Basin, Southwest China. *Energy Geosci.* 1 (1–2), 47–54. doi:10.1016/j.engeos.2020.05.001

Zhao, K. K., Jiang, P. F., Feng, Y. J., Sun, X. D., Cheng, L. X., and Zheng, J. W. (2021). Investigation of the Characteristics of Hydraulic Fracture Initiation by Using Maximum Tangential Stress Criterion. *J. Min. Strata Control Eng.* 3 (2), 023520. doi:10.13532/j.jmsce.cn10-1638/td.20201217.001

Zheng, H., Zhang, J., and Qi, Y. (2020). Geology and Geomechanics of Hydraulic Fracturing in the Marcellus Shale Gas Play and Their Potential Applications to the Fuling Shale Gas Development. *Energy Geosci.* 1 (1–2), 36–46. doi:10.1016/j.engeos.2020.05.002

Conflict of Interest: Author HL was employed by the Sinopec Northwest Oilfield Branch.

The remaining author declares that the research was conducted in the absence of any commercial or financial relationships that could be construed as a potential conflict of interest.

Publisher's Note: All claims expressed in this article are solely those of the authors and do not necessarily represent those of their affiliated organizations, or those of the publisher, the editors and the reviewers. Any product that may be evaluated in this article, or claim that may be made by its manufacturer, is not guaranteed or endorsed by the publisher.

frontiers | Frontiers in Earth Science

ORIGINAL RESEARCH
published: 09 June 2022
doi: 10.3389/feart.2022.910666

Links of Hydrogen Sulfide Content With Fluid Components and Physical Properties of Carbonate Gas Reservoirs: A Case Study of the Right Bank of Amu Darya, Turkmenistan

Youyou Cheng[1,2], Zhao Feng[1], Chunqiu Guo[3], Pengyu Chen[3], Chengqian Tan[1,2], Haidong Shi[3] and Xiang Luo[1]*

[1]School of Earth Sciences and Engineering, Xi'an Shiyou University, Xi'an, China, [2]Shaanxi Key Lab of Petroleum Accumulation Geology, Xi'an, China, [3]PetroChina Research Institute of Petroleum Exploration and Development, Beijing, China

OPEN ACCESS

Edited by:
Wenlong Ding,
China University of Geosciences, China

Reviewed by:
Heng Wang,
Chengdu University of Technology, China
Mingjun Chen,
Southwest Petroleum University, China

***Correspondence:**
Youyou Cheng
charmingx2u@126.com

Specialty section:
This article was submitted to Economic Geology, a section of the journal Frontiers in Earth Science

Received: *04 April 2022*
Accepted: *22 April 2022*
Published: *09 June 2022*

Citation:
Cheng Y, Feng Z, Guo C, Chen P, Tan C, Shi H and Luo X (2022) Links of Hydrogen Sulfide Content With Fluid Components and Physical Properties of Carbonate Gas Reservoirs: A Case Study of the Right Bank of Amu Darya, Turkmenistan. Front. Earth Sci. 10:910666. doi: 10.3389/feart.2022.910666

Hydrogen sulfide (H_2S) in carbonate gas reservoirs shows strong relevance with the natural gas components and has an obvious impact on reservoir types and their petrophysical properties. In this work, core and fluid samples were collected from the Right Bank of Amu Darya reservoirs, Turkmenistan. Then, fluid composition analysis and flash evaporation experiments were performed to investigate the components of reservoir fluid. Petrophysical properties, that is, porosity and permeability, and micropore structures of cores were determined by permeameter–porosimeter and scanning electron microscope (SEM) analysis, respectively. Results in this work indicate that the H_2S content shows obvious relevance to fluid components in carbonate gas reservoirs. With the increase of H_2S content, the total heavy hydrocarbons and potential condensate content decrease, while the condensate density increases. In addition, at higher H_2S content, larger pore and vug porosity was observed. However, in reservoirs with lower H_2S content, the matrix pores are relatively tight and prone to develop fractures. Furthermore, sulfate thermochemical reduction (TSR) is found to be the dominant contributor to high H_2S content in carbonate reservoirs through material and thermodynamic condition analysis. The Gibbs free energy and normalized hydrocarbon content show that the consumption of heavy hydrocarbons generally increases with carbon numbers during TSR, but reaches a minimum at the components of C_7 to C_9. Finally, the relationship between TSR and rock petrophysical properties was discussed, indicating that pore volume enlargement and the dissolution effect of acidic gases are the main mechanisms for TSR to improve carbonate reservoir property. Results in this study present comprehensive analyses of the links between H_2S content and fluid components and petrophysical properties in carbonate gas reservoirs.

Keywords: carbonate gas reservoir, hydrogen sulfide, heavy hydrocarbon, TSR, fracture

1 INTRODUCTION

Currently, carbonate gas reservoirs, accounting for about 45% of the world's total gas reserves, is one of the most significant gas field types (Skrebowski, 1996; Wei et al., 2020). Accompanied by different sizes of pores, fractures, and vugs, carbonate rocks are featured with strong reservoir heterogeneity and anisotropy (Hu et al., 2019; Zhu et al., 2019; Liu D. et al., 2020; Lan et al., 2021; Xue et al., 2021). Hence, carbonate gas reservoirs show significant differences in reservoir characteristics, flow capabilities, and production performances (Cheng et al., 2017; Liu L.-l. et al., 2020; Chen et al., 2021; Zhao et al., 2021). On the other hand, natural gas containing hydrogen sulfide (H_2S) is mostly presented in carbonate reservoirs. Fei et al. (2010) investigated 52 H_2S-bearing oil and natural gas fields all over the world, 48 of which are limestone or dolomite reservoirs. As a consequence, numerous works on the generation and distribution of H_2S and its effect on reservoir features have been done to reveal the relationship between H_2S and the carbonate reservoir (Zhang et al., 2008; He et al., 2019; Liao et al., 2020).

At present, thermal decomposition of sulfur compounds (TDS), bacterial sulfate reduction (BSR), and sulfate thermochemical reduction (TSR) have been regarded as the most significant origins of H_2S in natural gas reservoirs (Basafa and Hawboldt, 2019; Zhao et al., 2019). Due to the toxic effect of H_2S on bacteria, the amount of H_2S from the BSR process is negligible generally (Machel, 2001; Xiao et al., 2021). As for the TDS, the required sulfur compounds such as thiol, thioether, and thiophene are rather scarce in natural gas reservoirs. Besides, the temperature threshold for sufficient thermal decomposition is commonly considered to be not lower than 150°C (Shi and Wu, 2021). Therefore, TSR is regarded as the main contribution to the H_2S in carbonate gas reservoirs (Li et al., 2019; Jia et al., 2021). The favorable conditions of the TSR progress have been widely discussed. In general, the material condition and the thermodynamic condition are believed to be the fundamental preconditions to progress TSR in the underground formation. Morad et al. (2019) concluded that the existence of gypsum rock is the basic precondition to providing sufficient sulfate for TSR. Furthermore, the development of matrix pores, the content of sulfate ions in formation water, formation temperature, gas-water contact, hydrocarbon composition, and so on have been studied on the generation of H_2S (Qu et al., 2019; Liu D. et al., 2020). In addition, Liu et al. (2022) conducted a physical simulation to depict the reaction between anhydrite and organic matters for the generation process of H_2S. Tian et al. (2020) have performed TSR simulations under different temperatures in a closed system to investigate the effect of temperature on the reaction.

The impact of H_2S on the composition of natural gas has been another concerned topic. In the early 1990s, Manzano et al. (1997) noticed the effect of H_2S on oil and gas composition for the first time. Since then, to figure out the component variation of natural gas, a variety of datasets such as petrography, fluid inclusions, and stable isotopes have been used (Deng et al., 2020; Torghabeh et al., 2021). It has been declared that acidic gases like H_2S and CO_2 can increase the drying coefficient of natural gas (Alawi et al., 2020). Up to now, the consumption characteristic of hydrocarbon components during TSR has become the bottleneck for the explanation of the relation between H_2S and hydrocarbon components. Hu et al. (2021) introduced activation energy to distinguish the hydrocarbon loss during TSR and found that the consumption of heavy hydrocarbons would increase along with the carbon numbers. However, the priorities of different hydrocarbon components during the TSR process and the relevance of H_2S content to the fluid components are still unclear.

Actually, the effect of H_2S on the reservoir property should be an integrant part of related research. Some academics have revealed the controlling function of H_2S on the reservoir types and physical properties (Zhao et al., 2019; Liu Y. et al., 2020). Zhang et al. (2005) noticed that the H_2S-rich natural gas is commonly distributed in the porous reservoirs. Cai et al. (2015) declared that the generation of H_2S requires sufficient pore space and connectivity, and the porosity should not be less than 3.5% for H_2S-bearing carbonate reservoirs. From the perspective of TSR, the positive relationship between reservoir porosity and H_2S content has been confirmed by many reports (Mayrhofer et al., 2014; Wu et al., 2022). Accordingly, the good connectedness of the matrix can facilitate the TSR progress for producing H_2S; meanwhile, the metasomatism and dissolution effect of acidic gases can promote the development of high-quality carbonate reservoirs (Lai et al., 2021). Therefore, it is legitimate to declare that TSR plays a positive role in the improvement of carbonate reservoir properties. On basis of this, the study can be furthered by performing a systemic analysis of the pore structure and petrophysical properties of carbonate reservoirs within different H_2S content and figuring out the mechanism involved.

The purpose of this research is to illustrate the links between H_2S content on fluid components and reservoir properties of carbonate gas fields. Core and fluid samples collected from the Right Bank of Amu Darya carbonate reservoirs were used to investigate fluid compositions, microscopic pore structure, and reservoir physical property. Then, the influences of H_2S content on fluid composition and reservoir characteristics were studied in detail. Finally, based on the mechanism of TSR, the priority of hydrocarbon consumption was studied, and its effect on carbonate rock properties was discussed.

2 GEOLOGICAL SETTING

2.1 Fundamental Geological Characteristics

The gas fields of the Right Bank of Amu Darya, Turkmenistan, are located in the northeast portion of the Amu Darya Basin and close to Uzbekistan in the north. It is shaped like a narrow strip and can be divided into six different tectonic units (**Figure 1**). The Callovian–Oxfordian carbonate rocks developed in the Middle–Upper Jurassic Series are the most significant pay zone. The overlying Kimmeridgian–Tithonian Stage is regarded as the giant salt–gypsum formation, with a maximum thickness of 1,600 m (**Figure 2**). The development of salt-gypsum caprocks can provide guarantees for sufficient gas supply and preservation. The sedimentary facies of Callovian–Oxfordian carbonate rocks are

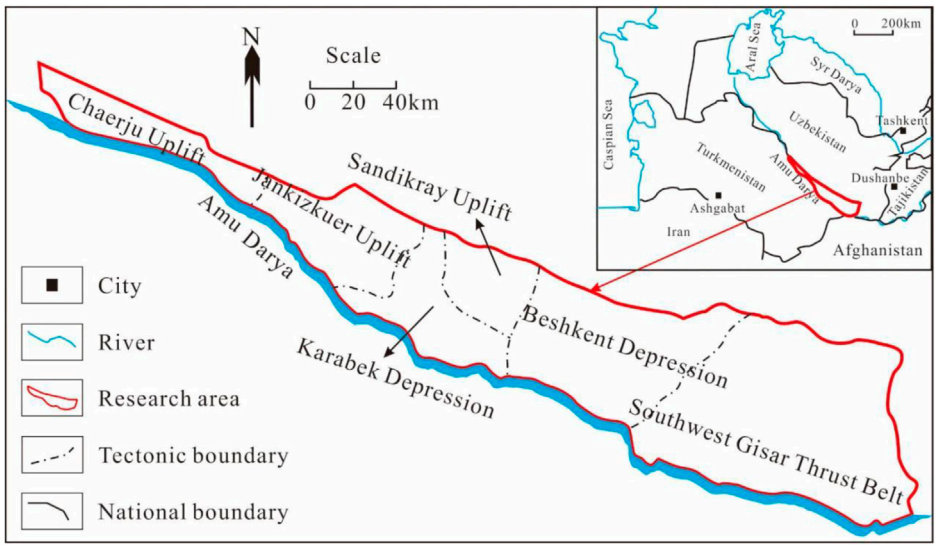

FIGURE 1 | Location of the research area.

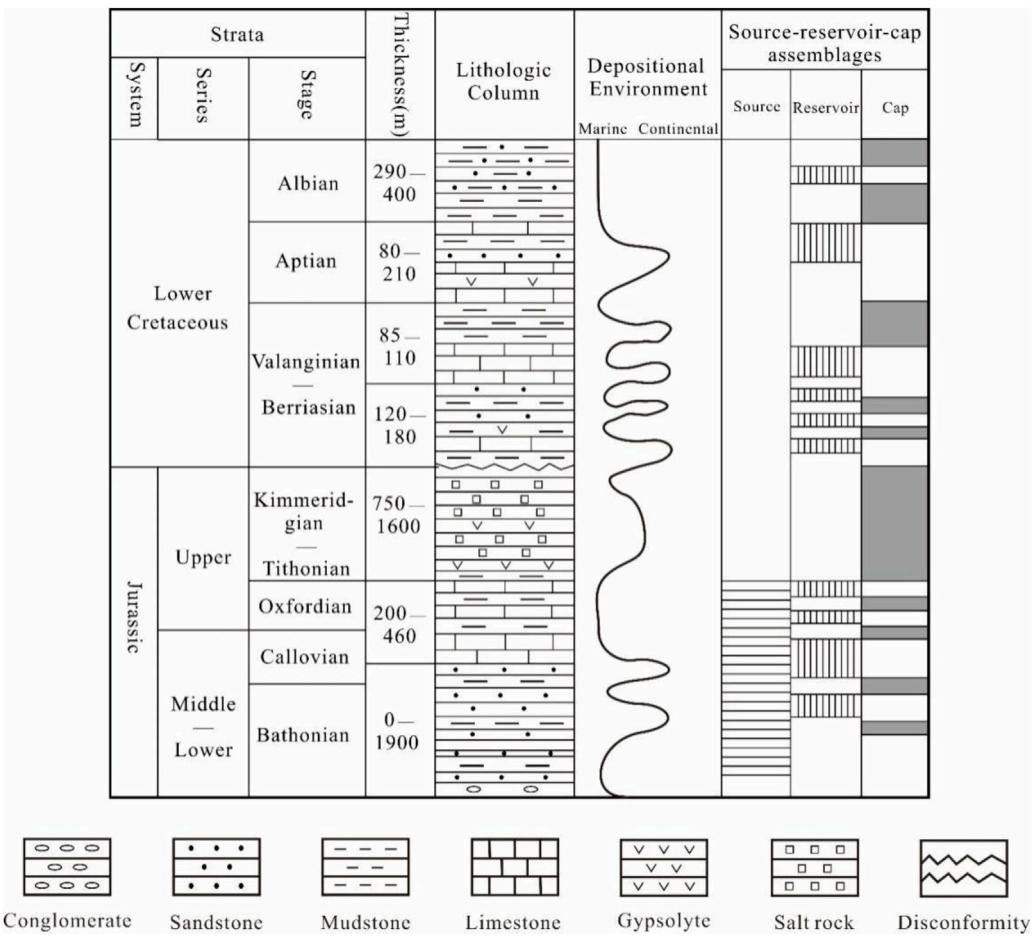

FIGURE 2 | The stratigraphic column of the Right Bank of the Amu Darya reservoirs.

TABLE 1 | H_2S content of different gas fields.

Gas field	H_2S content (%)	Type	Gas field	H_2S content (%)	Type
MJ	5.1084	High H_2S content	YC	0.2903	Low H_2S content
SM	4.2211		UZ	0.0767	
DY	2.0526		KS	0.0541	
YL	0.6254	Medium H_2S content	JR	0.0535	
YJ	0.5048		BP	0.0279	
JD	0.5029		HJ	0.0213	
AK	0.3586		AG	0.0178	
AJ	0.3090		JL	0.0022	

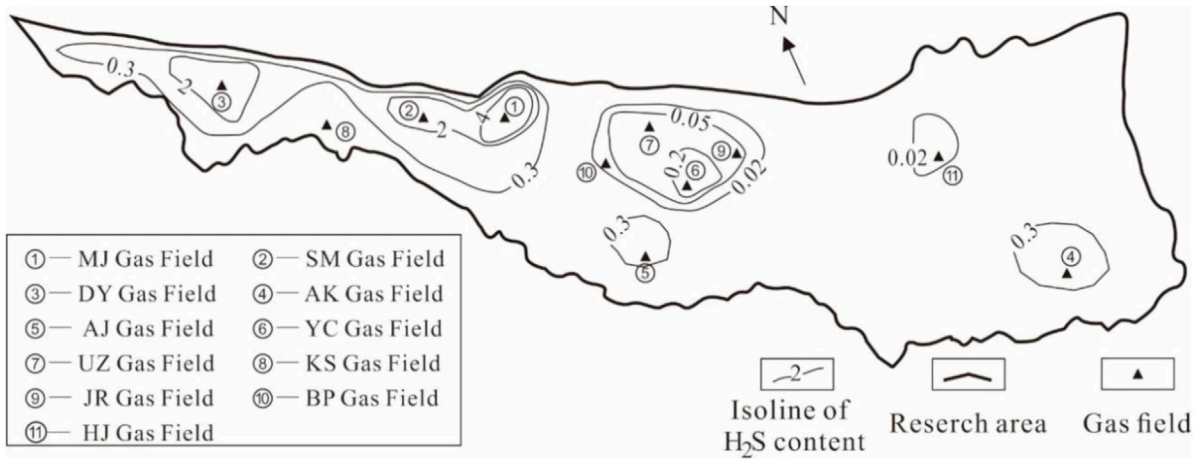

FIGURE 3 | H_2S distribution map of gas fields in the Right Bank of the Amu Darya.

gradually transforming eastward from evaporative platform-open platform to platform margin. Dissolved pores and fractures are widely developed within the reef–shoal bodies.

Currently, sixteen gas fields are being developed in the Right Bank of Amu Darya. All gas fields involved are featured by the marine carbonate reservoir with low porosity and strong heterogeneity. According to core description results, the porosity of the gas fields is 3.43~11.27% in general and 6.37% on average, and permeability is 0.02~18.92 mD in general and 0.77 mD on average. Fractures, especially the high-angled ones, are extensively developed in the pay zone. Reservoir conditions of those gas fields vary notably with the position. Reservoirs in the western region are with large thicknesses and good physical properties with an average porosity of 10%. Conversely, formation thickness decreases for reservoirs in the middle and eastern region, and their flow capability is greatly affected by the natural fractures and vugs.

2.2 H_2S Content

H_2S content of the gas fields of the Right Bank of Amu Darya generally ranges from 0.0022% to 5.1084% (shown in **Table 1**), including classifications of a high content (>2%), medium content (0.3–2%), and low content (<0.3%). **Figure 3** plots the isoline of H_2S content, and it can be observed that gas fields with high H_2S content are distributed in the western regions; while H_2S content of the middle and eastern regions are mostly categorized as medium and low content, especially for reservoirs like BP, HJ, and AG, whose H_2S content are lower than 0.05% in general.

There also exists a certain relation between H_2S content and the burial depth: The H_2S content showed a decreasing trend with the increase of depth. It is the distance from the overlying gypsum rock that provides the explanation for the H_2S content variation with depth. Considering the generation process of H_2S in carbonate reservoirs, the gypsum plays crucial role despite the different reaction mechanisms involved there. As a result, for gas reservoirs in the Right Bank of Amu Darya, the H_2S content experiences an obvious rise with the distance closer to the overlying gypsum rock (**Figure 4**).

3 MATERIALS AND METHODS

3.1 Materials

The gas and condensate samples from 10 reservoirs in the Right Bank of the Amu Darya were collected from the wellhead separator, with an average operating pressure and temperature

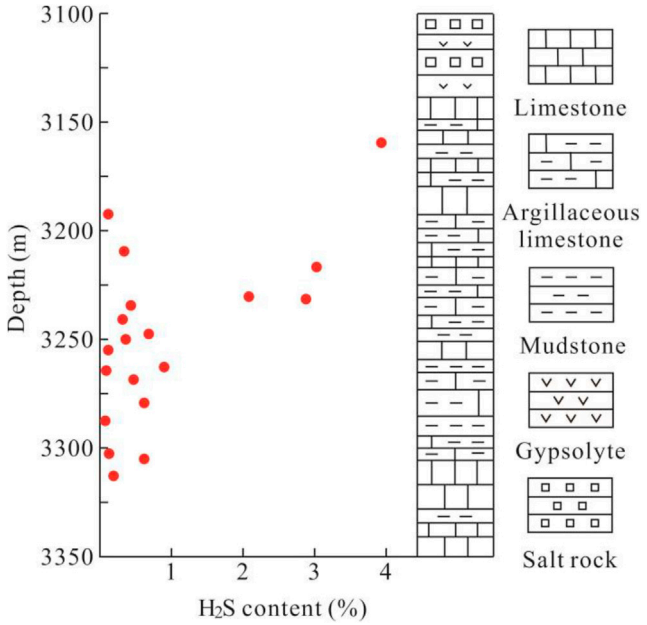

FIGURE 4 | The relation between H_2S content and the burial depth.

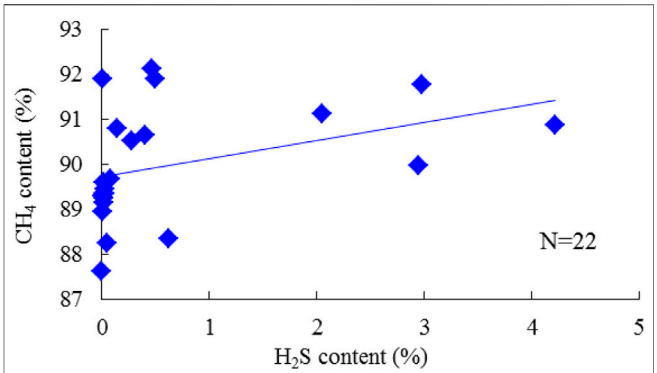

FIGURE 5 | Relationship between CH_4 and H_2S content.

of 1.82 MPa and 32°C, respectively. All fluid samples were immediately sealed into sampling bottles to avoid component loss. Basic information and properties of the gas and condensate samples are shown in **Table 2**. To characterize the petrophysical properties and microscopic pore structure of the reservoir rocks, ten core samples were collected, with three cores from the western region and the rest from the middle and east.

3.2 Experimental Methods

3.2.1 Fluid Composition Analysis

The composition of gas and condensate samples was analyzed by the chromatograph Agilent 7890A, abiding by the Industrial Standard "Analysis of natural gas composition: Gas chromatographic method (GB/T 13610-2014)." The hydrocarbons were determined from methane (C_1) to icosane (C_{20}) for the gas samples and from C_1 to tetratriacontane (C_{34}) for the condensate, respectively. The main nonhydrocarbon components, referring to H_2S, nitrogen (N_2), and carbon dioxide (CO_2), were also detected. Each component was expressed with its mole fraction in the gas and condensate sample.

3.2.2 Flash Evaporation Experiment

Flash evaporation experiments of the condensate samples were performed at the standard temperature and pressure using a flash tank to separate flash gas and volatile oil from the condensate. The gas–oil ratio (GOR) and formation volume factor (FVF) of the condensate and the composition of the gas, flash gas, and volatile oil were determined. Then, the well production fluid components under formation conditions were calculated following the "Test method for reservoir fluid physical properties (GB/T 26981-2011)."

3.2.3 Core Sample Analysis

The porosity of the core samples was measured based on Boyle–Mariotte's law *via* a Core Porosimeter OFITE 350, while, an *in situ* N_2 displacement experiment was launched to obtain the Klinkenberg permeability of the core with a core flooding device STL-II. All the test procedures abide by the "Core Analysis Method (SY/T 5336-2019)." Furthermore, the ultrahigh resolution scanning electron microscope (SEM) device QUANTA 400 was involved to characterize the structure of the pores and microfractures within the gold-coated core slice.

4 EXPERIMENTAL RESULTS

4.1 Relationships Between Fluid Component With H_2S Content

4.1.1 Hydrocarbon Components

Methane (CH_4) is the dominant component of natural gas. The measured CH_4 content varies from 87.617% to 92.779%, with an average of 95.308% in the gas phase. The cross-plot of CH_4 and H_2S content was plotted to investigate their relationships, as shown in **Figure 5**. However, the positive correlation is weak. Heavy hydrocarbons, that is, the C_{2+} component, mainly appear in the condensate phase; for gas and condensate samples, the C_{2+} content

TABLE 2 | Basic information and physical properties of samples.

Type	Formation information			Operating condition			Sample property	
	Depth (m)	Pressure (MPa)	Temperature (°C)	Sampling position	Pressure (MPa)	Temperature (°C)	Numbers	Relative density
Gas	3,150–3,570	53–62	107–121	Wellhead separator	0.45–3.46; 1.82 average	24–36; 32 average	22	0.64
Condensate							22	0.78

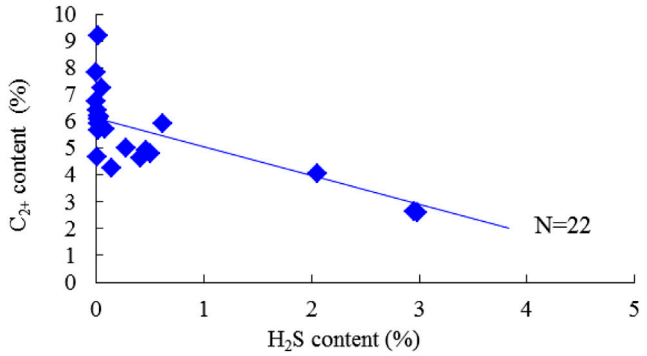

FIGURE 6 | Relationship between C_{2+} and H_2S content.

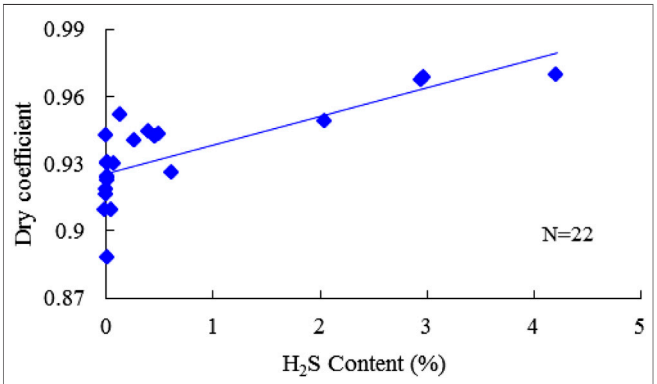

FIGURE 7 | Relationship between dry coefficient and H_2S content.

was 4.459% and 87.984%, respectively. The C_{2+} content generally presents a negative correlation with the increase of H_2S content, especially for samples with medium and high H_2S content (**Figure 6**). Correspondingly, the dry coefficient, referring to the ratio of the CH_4 content to the C_{2+} content in natural gas, shows a positive trend with the H_2S content (**Figure 7**).

To investigate the relationship between condensate and H_2S content, the potential condensate contents were calculated from the flash evaporation results of the well production fluids. The potential content decreases and the density increases with the H_2S content as shown in **Figure 8**, indicating that the heavy hydrocarbons could act as reactants in the production of H_2S, but their consumption would not increase monotonously with the carbon number.

4.1.2 Nonhydrocarbon Components

N_2 is relatively scarce in the Right Bank of Amu Darya and its content varies slightly within the limit of 0.271%–0.516% in the well production fluid. The studied gas fields can be defined as medium CO_2 content reservoirs, whose content ranges from 0.917% to 4.556%, according to "The classification of the gas pool (SY/T 6168-2009)." As shown in **Figure 9**, CO_2 content is independent of H_2S at low and medium content ranges, while a positive correlation can be found between CO_2 and H_2S at high H_2S content. In addition, CO_2 content is greater than H_2S content within all samples despite the H_2S degree.

4.2 Reservoir Characteristics With H_2S Content

4.2.1 Porosity and Permeability

Similar to most carbonate reservoirs with fractures, the porosity and permeability of studied reservoirs do not show a clear positive correlation (**Figure 10**). As shown in **Figure 11**, the porosity increases with the increase of H_2S content, and the same trend can be found for the permeability of core samples without fractures. However, for core samples with fractures, there is no clear correlation observed between permeability and H_2S content as permeability is mainly affected by fractures. Actually, due to the lower aperture and higher permeability of fractures, the Poro–Perm Relation would somehow overturn in fractured reservoirs, which explains the differences in porosity and permeability with H_2S content. Therefore, porosity should be an intrinsic factor to figure out the effect of H_2S on reservoir physical properties.

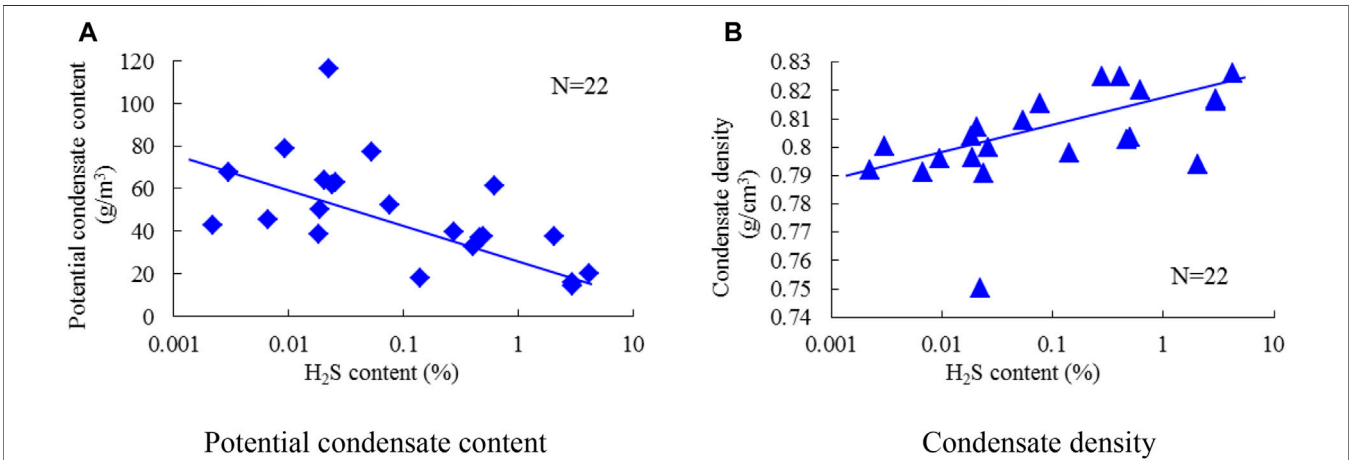

FIGURE 8 | Relationship between condensate property and H_2S content. **(A)** Potential condensate content. **(B)** Condensate density.

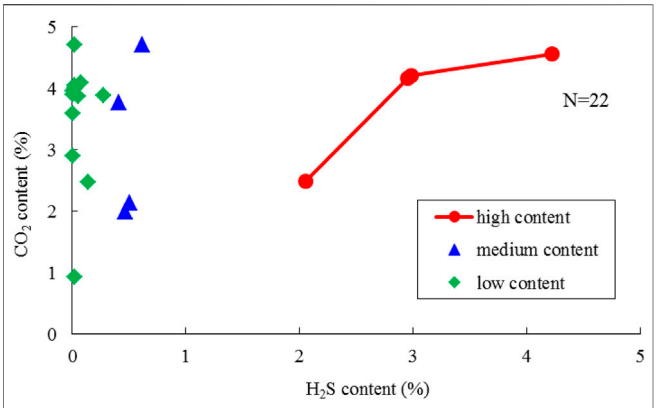

FIGURE 9 | Relationship between CO_2 and H_2S content.

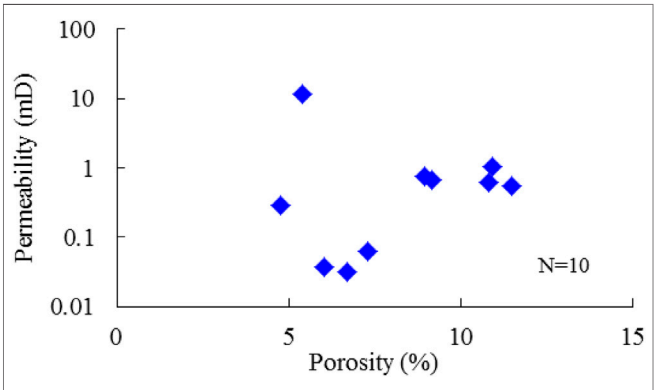

FIGURE 10 | Porosity and permeability of core samples.

4.2.2 Reservoir Types

The Right Bank of Amu Darya experienced multistage tectonic movement, and a large number of structural fractures were generated during that process. Meanwhile, the dissolution of the carbonate rocks caused by acidic gases can result in a large number of dissolved pores and vugs. As a consequence, diverse reservoir types have been discriminated in this area, among which pore, pore-fracture, pore-vug, and fracture are the most representative types.

The SEM analysis facilitates the connections between H_2S and reservoir microstructures. As can be seen in **Figure 12**: 1) Well DY-21, whose H_2S content was measured to be 2.0526%, was classified as the pore-vug type. The porosity and permeability were 11.47% and 0.55 mD, respectively. The SEM slice can observe a distinct moldic vug associated with the primary pores. 2) Well AJ-21, whose H_2S content was measured to be 0.3090%, was classified as the pore type. The porosity and permeability were 7.31% and 0.062 mD, respectively. The pore structure showed great homogeneity and intercrystal pores were commonly distributed. 3) BL-22 well, whose H_2S content was measured to be 0.0279%, was classified as the pore-fracture type. The porosity and permeability were 6.41% and 11.64 mD, respectively. The SEM slice was penetrated by a dissolved fracture, while the surrounding pores in the matrix are rather tight. This indicates that the H_2S could be regarded as one of the evidence to characterize the reservoir property for the gas fields in the Right Bank of Amu Darya. With higher H_2S content, the porosity would be larger and the reservoir types mainly consist of pore and pore-vug. Yet, for reservoirs with low H_2S content, the matrix pore could be relatively tight and prone to develop with fractures.

To further expand this knowledge, H_2S content, porosity, and brief reservoir descriptions of 10 major gas fields from different regions of the Right Bank of Amu Darya are summarized in **Table 3**. It shows that gas fields in the western region can be characterized as high H_2S content and high porosity reservoirs. However, H_2S content rarely exceeds 0.07% in the middle and east where fractures are well developed. In particular, for gas field JL with H_2S content of 0.0022%, the porosity almost reaches the lower limit of the effective pore, and the field is thus defined as a pure fractured reservoir.

5 DISCUSSION

5.1 H_2S Origin of Gas Fields in the Right Bank of Amu Darya

With respect to the TDS and BSR, TSR has been regarded as the most significant H_2S origin. TSR refers to a series of reduction reactions between sulfates and hydrocarbons, and the sulfates are consequently reduced into acidic gases, that is,

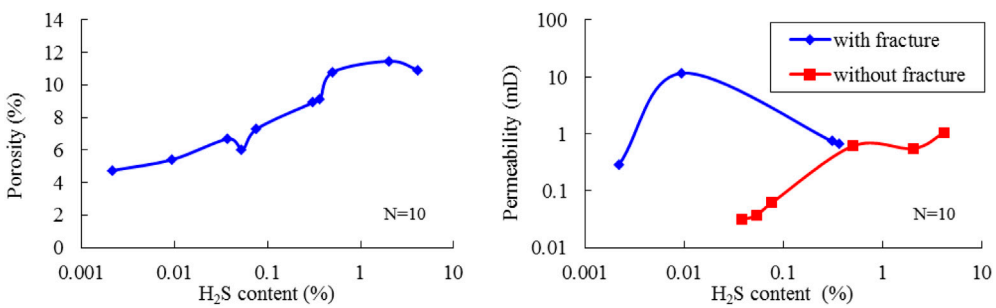

FIGURE 11 | Relationship between reservoir physical properties and H_2S contents.

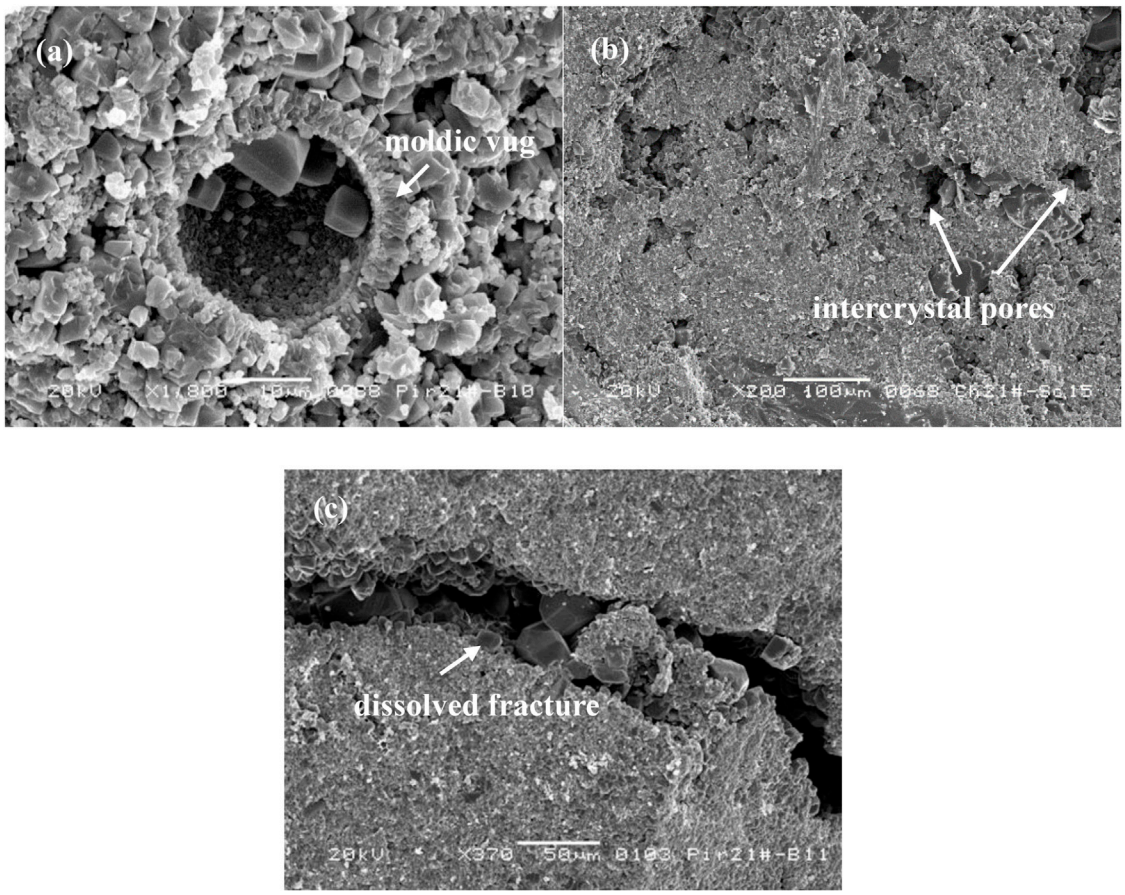

FIGURE 12 | The SEM images of core samples. **(A)** Well DY-21, showing a moldic vug; **(B)** Well AJ-21, developing with intercrystal pores; **(C)** BL-22 Well, showing a dissolved fracture.

TABLE 3 | H_2S content and reservoir characteristics of typical fields.

Gas field	Region	H_2S content (%)	Porosity (%)	Reservoir description	Reservoir type
DY	West	2.0526	9.27–13.66	Brownish gray silty limestone, light gray micritic limestone; primary pores are well developed, along with subsize vugs	Pore-vug
SM	West	4.2211	8.89–14.85	Brownish gray limestone, fine quality; the whole reservoir is of good physical properties with medium–high porosity	Pore-vug
JD	West	0.5029	9.37–12.81	Light gray silty dolomite, with good physical properties	Pore
YJ	Middle	0.5048	7.46–11.16	Light gray silty limestone; high porosity and permeability, low water saturation	Pore-vug
BP	Middle	0.0279	4.61–9.81	Dark gray and brownish gray micritic limestone, with high fracture development degree	Pore-fracture
UZ	Middle	0.0767	6.37–10.13	Grayish brown and light gray micritic limestone or silty limestone; microfractures are well developed	Pore-fracture
JR	Middle	0.0535	5.72–7.53	Brownish gray silty limestone; high angle fractures are developed	Pore-fracture
AJ	Middle	0.3090	8.62–9.93	Light gray bioclastic limestone; dissolved fracture pores and vugs are developed	Pore-vug
AG	East	0.0178	5.16–7.03	Brownish gray silty limestone; medium-scale fractures intensively are developed	Pore-fracture
JL	East	0.0022	3.53–5.04	Gray, brownish-gray micritic limestone; tight matrix pores, fractures are well developed	Fracture

H_2S and CO_2. The reaction process can be summarized in **Eq. 1** (Zhang et al.,2008; He et al., 2019):

$$C_nH_{2n+2} + n\mathrm{CaSO_4} \rightarrow n\mathrm{CaCO_3} + \mathrm{H_2S} + n\mathrm{H_2O} \pm \mathrm{CO_2} \pm \mathrm{S} \quad (1)$$

It is generally believed that the TSR requires the following preconditions: hydrocarbons, sulfate (material conditions), and high temperature (thermodynamic condition). Because the TSR can hardly advance with the anhydrite, the reaction rate depends on the dissolution of calcium sulfate ($CaSO_4$) in the formation water. Therefore, higher connectivity is essential to allow adequately mixing between dissolved sulfate with hydrocarbons.

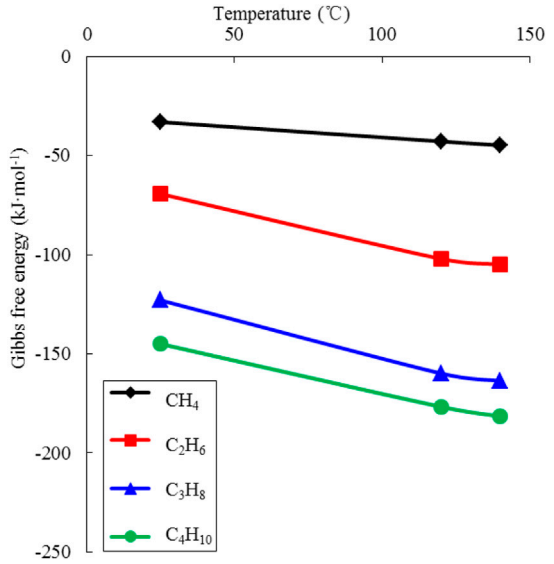

FIGURE 13 | The Gibbs free energy of C_2H_6 to C_4H_{10} during TSR at different temperatures.

For the carbonate gas reservoirs in the Right Bank of Amu Darya, the material conditions, that is, hydrocarbons and sulfate, have undoubtedly met the requirement of TSR. Furthermore, the overlying gypsum-salt rock and the interbedded limestone-gypsum layers, dispersing in the upper section of the Callovian-Oxfordian Stage, provide direct contact for hydrocarbons and $CaSO_4$ to complete the reaction in the pay zone. The current formation temperature of the Amu Darya Basin ranges from 100 to 130°C. In view of the tectonic movement in the Himalayan period, the formation experienced higher temperatures. According to the inclusions homogenization temperature, the paleo–geotemperature of the reservoir had once reached 140°C, which exceeds the temperature threshold of TSR. Therefore, TSR is the dominant origin of H_2S in carbonate gas reservoirs in the Right Bank of Amu Darya. Ma et al. (2021) confirm that TSR is the principal producer of H_2S in the Right Bank of Amu Darya and also the contributor to the development of secondary pores.

5.2 Hydrocarbon Consumptions in the TSR Process

To clarify the relation between hydrocarbons and H_2S content, the priority of different hydrocarbon components involved in the TSR should be studied. According to the Van't Hoff isothermal formula (Atkins and De, 2006), the Gibbs free energy of each component can be determined with **Eq. 2**.

$$\Delta_r G_{\mathbf{m}} = \Delta_r G_{\mathbf{m}}^{\Theta} + RT \ln Q \tag{2}$$

where $\Delta_r G_{\mathrm{m}}$ is the Gibbs free energy, kJ/mol; $\Delta_r G_{\mathrm{m}}^{\Theta}$ is the standard formation free energy at 298.15 K, kJ/mol; R is the thermodynamic constant, 8.314 J/(mol·K); T is the reaction temperature, K; Q is the reaction quotient.

Figure 13 shows the calculated Gibbs free energy of CH_4 to C_4H_{10} involved in TSR at different temperatures. It can be seen that: 1) The Gibbs free energy is decreasing dramatically with the increased temperature, which elucidates the necessity of high temperature for activating the reaction. 2) The Gibbs free energy of CH_4 stays at a high level despite the rising temperature, indicating that CH_4 is difficult to participate in the TSR reaction. This coincides with the statement mentioned in **Section 4.1** that "no clear relation observed between CH_4 and H_2S content." 3) For heavy hydrocarbons from C_2H_6 to C_4H_{10}, all calculated Gibbs free energy are less than −100 kJ/mol at the temperature of 120–140 °C, which demonstrates that these components are available in TSR at the reservoir conditions. In addition, the Gibbs free energy decreases with the increase of carbon numbers, indicating a rising trend of the consumption from C_2H_6 to C_4H_{10}.

Furthermore, to investigate the relative decrement of each hydrocarbon component along with per unit H_2S content growth, the normalized hydrocarbon content was used in this study. With well production fluid composition given, regressions between the normalized content of each hydrocarbon component and the H_2S content can be established. The correlation slope can thus be employed to describe the consumption involved in TSR. Considering that the slope showed a negative value, the absolute value of the slope was adopted and named the "relative consumption." The definition of the normalized content and the regression results for each component is attached in **Supplementary Appendix**.

The relative consumptions of different heavy hydrocarbon components are shown in **Figure 14**. It was found that there is a V-shaped relationship between relative consumption and carbon number. The consumptions reach the minimum value at C_7 and then increase with carbon numbers; as a consequence, the consumptions of C_7 to C_9 are relatively low among all heavy hydrocarbon components except for C_2. This provides a reasonable interpretation for the variation of condensate content and density with H_2S content. The decrease of potential condensate content is caused by the consumption of total heavy hydrocarbons; while the remnant of intermediate components, typified by C_7 to C_9, would lead to an increase in condensate density.

To sum up, heavy hydrocarbons act as the reactant in TSR, while CH_4 can hardly take part in the reaction. The consumption of heavy hydrocarbons generally increases with carbon numbers but reaches a minimum at C_7~C_9. The relative consumption method facilitates the reveal of hydrocarbon consumption and explains the dynamic of gas and condensate features with H_2S content.

5.3 Influence of TSR on Nonhydrocarbon Components

As mentioned earlier, inert gases like N_2 are merely affected by H_2S content, whereas the CO_2 content shows a positive correlation with H_2S content at higher concentrations. This is because CO_2 is also one of the products of TSR. In addition, H_2S dissolution in formation water can form hydrosulfuric acid, which will further react with carbonate minerals to produce CO_2. It explains the content of CO_2 is higher than that of H_2S, which can be regarded as one of the symbols of carbonate reservoirs emerging TSR.

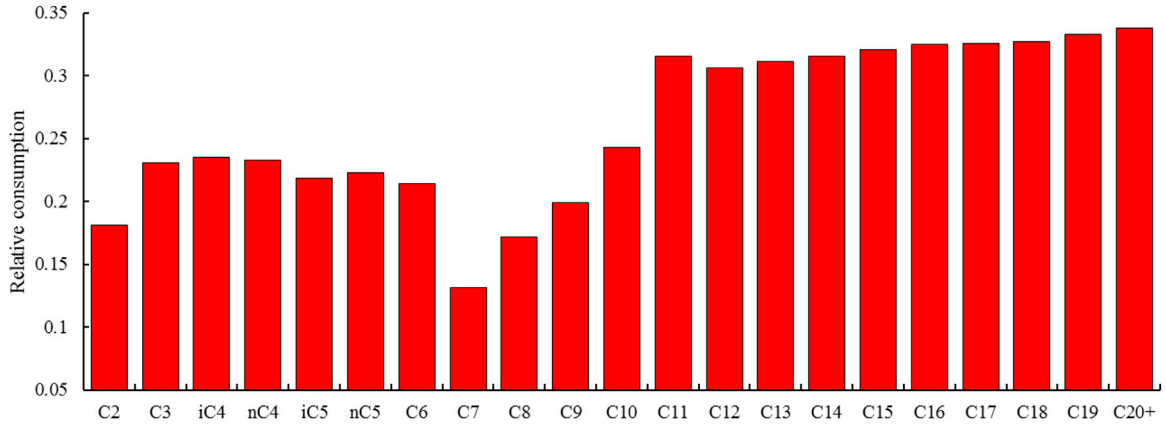

FIGURE 14 | The relative consumption of heavy hydrocarbon components in TSR.

5.4 Improvement of Reservoir Property Through TSR

From the perspective of TSR, the contribution of H_2S to the improvement of porosity can then be discerned. The controlling factor of TSR on reservoir physical properties and reservoir types can be manifested in the following aspects:

1) Compared to the fractured reservoirs, pore and pore-vug typed reservoirs are of higher connectedness and larger storage capacity, which not only provide space for the mutual contact of the reactants but also ensure a continuous supply of reactants and transfer of products. This prompts the TSR in the right direction. It explains why H_2S-bearing natural gas fields are generally discovered in large porous reservoirs.
2) It can be noticed from **Eq. 1** that 1 mol of calcite ($CaCO_3$) can be generated with 1 mol of anhydrite ($CaSO_4$). The molar volume of $CaCO_3$ and $CaSO_4$ are 37 cm^3/mol and 47 cm^3/mol, respectively. Therefore, after 1 mol of anhydrite is involved in the reaction, the pore volume of the reservoir rock would increase by about 10 cm^3. This process is usually called the "pore volume enlargement" effect of the TSR.
3) As the products of TSR, large amounts of H_2S and CO_2, which are acidic gases and soluble in formation water, played a significant role in the growth of secondary pores and vugs in carbonate rock. It is also an important mechanism to improve the porosity of carbonate reservoirs.

6 CONCLUSION

1) The H_2S content shows obvious relevance to fluid components in carbonate gas reservoirs. With the increase of H_2S content, the total content of heavy hydrocarbons decreases, causing the reduction of potential condensate content, while the condensate density is increasing with the H_2S content. In high H_2S content reservoirs, a positive correlation was observed between CO_2 content and H_2S content.
2) With higher H_2S content, the porosity would be larger and the reservoir rock mainly consists of pores and vugs; while for reservoirs with low H_2S content, the matrix pores could be relatively tight and prone to develop with fractures.
3) TSR is the dominant hydrogen sulfide origin for H_2S-rich carbonate reservoirs resembling the Right Bank of Amu Darya. The consumption of heavy hydrocarbons during TSR generally increases with carbon numbers but would reach a minimum at the components of C_7 to C_9. The pore volume enlargement and the dissolution effect of acidic gases can be regarded as the main mechanisms for the improvement of the reservoir property of TSR.

DATA AVAILABILITY STATEMENT

The raw data supporting the conclusion of this article will be made available by the authors, without undue reservation.

AUTHOR CONTRIBUTIONS

YC is responsible for the idea and writing of the manuscript; ZF, PC, CT, and HS are responsible for the experiments; CG and XL are responsible for the analysis and interpretation of data.

FUNDING

This work is financially supported by the Scientific Research and Technology Development Project of CNPC (2021DJ3301) and the General Special Scientific Research Plan of the Shaanxi Provincial Department of Education (20JK0848).

SUPPLEMENTARY MATERIAL

The Supplementary Material for this article can be found online at https://www.frontiersin.org/articles/10.3389/feart.2022.910666/full#supplementary-material

REFERENCES

Atkins, P., and De, P. J. (2006). *Physical Chemistry 8th*. New York: W.H. Freeman and Company.

Ba Alawi, M., Hassan, A., Aljawad, M. S., Kamal, M. S., Mahmoud, M., and Al-Nakhli, A. (2020). A Novel Approach to Improve Acid Diversion in Carbonate Rocks Using Thermochemical Fluids: Experimental and Numerical Study. *Molecules* 25, 2976. doi:10.3390/molecules25132976

Basafa, M., and Hawboldt, K. (2019). Reservoir Souring: Sulfur Chemistry in Offshore Oil and Gas Reservoir Fluids. *J. Petrol Explor Prod. Technol.* 9, 1105–1118. doi:10.1007/s13202-018-0528-2

Cai, C., Hu, G., Li, H., Jiang, L., He, W., Zhang, B., et al. (2015). Origins and Fates of H_2S in the Cambrian and Ordovician in Tazhong Area: Evidence from Sulfur Isotopes, Fluid Inclusions and Production Data. *Mar. Petroleum Geol.* 67, 408–418. doi:10.1016/j.marpetgeo.2015.05.007

Chen, G. B., Li, T., Yang, L., Zhang, G. H., Li, J. W., and Dong, H. J. (2021). Mechanical Properties and Failure Mechanism of Combined Bodies with Different Coal-Rock Ratios and Combinations. *J. Min. Strata Control Eng.* 3 (2), 023522. doi:10.13532/j.jmsce.cn10-1638/td.20210108.001

Cheng, Y., Mu, L., Zhu, E., Zhang, P., Guo, C., Leng, Y., et al. (2017). Water Producing Mechanisms of Carbonate Reservoirs Gas Wells: A Case Study of the Right Bank Field of Amu Darya, Turkmenistan. *Petroleum Explor. Dev.* 44, 89–96. doi:10.1016/s1876-3804(17)30011-3

Deng, Q., Zhang, T., Zhao, F., Wang, H., and Yin, J. (2020). The Influence of Hydrogeology to Generation of Hydrogen Sulfide of Low-Rank Coal in the Southeast Margin of Junggar Basin, China. *Geofluids* 2020, 1–10. doi:10.1155/2020/8859100

Fei, A. G., Zhu, G. Y., Zhang, S., Hu, J., Chen, S., Zhang, B., et al. (2010). Global Distribution Hydrogen Sulphide-Bearing Natural Gas and the Major Factors Controlling its Formation. *Earth Sci. Front.* 17, 350–360. doi:10.3724/SP.J.1231.2010.06586

He, K., Zhang, S., Mi, J., Ma, Q., Tang, Y., and Fang, Y. (2019). Experimental and Theoretical Studies on Kinetics for Thermochemical Sulfate Reduction of Oil, C2-5 and Methane. *J. Anal. Appl. Pyrolysis* 139, 59–72. doi:10.1016/j.jaap.2019.01.011

Hu, A., Shen, A., Yang, H., Zhang, J., Wang, X., Yang, L., et al. (2019). Dolomite Genesis and Reservoir-Cap Rock Assemblage in Carbonate-Evaporite Paragenesis System. *Petroleum Explor. Dev.* 46, 969–982. doi:10.1016/S1876-3804(19)60253-3

Hu, Y., Cai, C., Liu, D., Peng, Y., Wei, T., Jiang, Z., et al. (2021). Distinguishing Microbial from Thermochemical Sulfate Reduction from the Upper Ediacaran in South China. *Chem. Geol.* 583, 120482. doi:10.1016/j.chemgeo.2021.120482

Jia, L., Cai, C., Zhang, J., Liu, L., Luo, Q., and Li, K. (2021). Effect of Thermochemical Sulfate Reduction on Carbonate Reservoir Quality: Cambrian and Ordovician Oilfield, Tazhong Area, Tarim Basin, China. *Mar. petroleum Geol.* 123, 104745. doi:10.1016/j.marpetgeo.2020.104745

Lai, J., Liu, S., Xin, Y., Wang, S., Xiao, C., Song, Q., et al. (2021). Geological-petrophysical Insights in the Deep Cambrian Dolostone Reservoirs in Tarim Basin, China. *Bulletin* 105, 2263–2296. doi:10.1306/03122119135

Lan, S. R., Song, D. Z., Li, Z. L., and Liu, Y. (2021). Experimental Study on Acoustic Emission Characteristics of Fault Slip Process Based on Damage Factor. *J. Min. Strata Control Eng.* 3 (3), 033024. doi:10.13532/j.jmsce.cn10-1638/td.20210510.002

Li, K., George, S. C., Cai, C., Gong, S., Sestak, S., Armand, S., et al. (2019). Fluid Inclusion and Stable Isotopic Studies of Thermochemical Sulfate Reduction: Upper Permian and Lower Triassic Gasfields, Northeast Sichuan Basin, China. *Geochimica cosmochimica acta* 246, 86–108. doi:10.1016/j.gca.2018.11.032

Liao, J., Wang, T., Lu, H., Greenwood, P. F., Peng, P. a., and Samuel Hsu, C. (2020). Effects of Mississippi Valley-type Minerogenetic Metal Sulfates on Thermochemical Sulfate Reduction, Studied by Hydrous Pyrolysis. *Org. Geochem.* 150, 104128. doi:10.1016/j.orggeochem.2020.104128

Liu, D., Li, J., Liu, J.-q., and Zhang, L. (2020). Modeling Hydrocarbon Accumulation Based on Gas Origin and Source Rock Distribution in Paleozoic Strata of the Ordos Basin, China. *Int. J. Coal Geol.* 225, 103486. doi:10.1016/j.coal.2020.103486

Liu, L.-l., Cui, Z.-h., Wang, J.-j., Xia, Z.-h., Duan, L.-j., Yang, Y., et al. (2020). Pore Size Distribution Characteristics of High Rank Coal with Various Grain Sizes. *ACS Omega* 5, 19785–19795. doi:10.1021/acsomega.0c02569

Liu, Y., Gao, M., and Zhao, H. (2020). Detection of Overlying Rock Structure and Identification of Key Stratum by Drilling and Logging Technology. *J. Min. Strata Control Eng.* 2 (2), 023038. doi:10.13532/j.jmsce.cn10-1638/td.2020.02.004

Liu, Y., Zhang, C., Ding, K., Yu, Z., and Wu, Y. (2022). Thermochemical Sulfate Reduction by Pyrobitumen: Review and Experiments. *ACS Earth Space Chem.* 6, 308–321. doi:10.1021/acsearthspacechem.1c00291

Ma, W. X., Ou, C. Y., Liao, Y. B., Xu, Q. K., Chen, R. J., Wang, X., et al. (2021). Characteristics and Genesis of Oxford Stage Microbial Limestone Reservoir in Eastern Amu Darya Basin. *Lithol. Reserv.* 33 (5), 59–69. doi:10.12108/yxyqc.20210506

Machel, H. G. (2001). Bacterial and Thermochemical Sulfate Reduction in Diagenetic Settings — Old and New Insights. *Sediment. Geol.* 140 (1), 143–175. doi:10.1016/S0037-0738(00)00176-7

Manzano, B. K., Fowler, M. G., and Machel, H. G. (1997). The Influence of Thermochemical Sulphate Reduction on Hydrocarbon Composition in Nisku Reservoirs, Brazeau River Area, Alberta, Canada. *Org. Geochem.* 27, 507–521. doi:10.1016/S0146-6380(97)00070-3

Mayrhofer, C., Niessner, R., and Baumann, T. (2014). Hydrochemistry and Hydrogen Sulfide Generating Processes in the Malm Aquifer, Bavarian Molasse Basin, Germany. *Hydrogeol. J.* 22, 151–162. doi:10.1007/s10040-013-1064-2

Morad, D., Nader, F. H., Morad, S., Rossi, C., Gasparrini, M., Alsuwaidi, M., et al. (2019). Limited Thermochemical Sulfate Reduction in Hot, Anhydritic, Sour Gas Carbonate Reservoirs: The Upper Jurassic Arab Formation, United Arab Emirates. *Mar. petroleum Geol.* 106, 30–41. doi:10.1016/j.marpetgeo.2019.04.023

Qu, X., Chen, S., Yang, X., You, L., and Zhong, J. (2019). Study on Hydrocarbon Accumulation Period in Deep Water Areas of the South China Sea: An Example from the Miocene Reservoir of the Ledong-Lingshui Sag in the Qiongdongnan Basin. *J. Coast. Res.* 94, 112–116. doi:10.2112/SI94-021.1

Shi, Q., and Wu, J. (2021). Review on Sulfur Compounds in Petroleum and its Products: State-Of-The-Art and Perspectives. *Energy fuels.* 35 (18), 14445–14461. doi:10.1021/acs.energyfuels.1c02229

Skrebowski, C. (1996). *World Oilfields and World Gasfields Series*. South America: The Petroleum Economist Ltd.

Tian, J., Li, J., Kong, H., Zeng, X., Wang, X., Dong, L., et al. (2021). Genesis of Hydrogen Sulfide in Natural Gas Reservoirs in the Western Qaidam Basin. *Interpretation* 9, T223–T233. doi:10.1190/INT-2020-0120.1

Torghabeh, A. K., Kalantariasl, A., Kamali, M., and Akbarifard, M. G. (2021). Reservoir Gas Isotope Fingerprinting and Mechanism for Increased H2S: An Example from Middle East Shanul Gas Field. *J. petroleum Sci. Eng.* 199, 108325. doi:10.1016/j.petrol.2020.108325

Wei, G., Du, J., Zou, C., Xu, C., Yang, W., Xie, W., et al. (2020). The Anyue Giant Gas Field in the Sichuan Basin as the Largest Gas Field in Marine Carbonate Deposits from Domestic China. *Russ. Geol. Geophys.* 61, 1015–1027. doi:10.15372/RGG2020127

Wu, X. L., Xu, W. L., Li, R. X., Li, N. X., Liu, Q., Zhao, D., et al. (2022). Genesis of Hydrogen Sulfide in Ordovician Majiagou Formation ,mid-Eastern Ordos Basin:evidence from Fluid Inclusions[J]. *Acta Pet. Sin.* 43 (2), 250–261. doi:10.7623/syxb202202007

Xiao, Q., Cai, S., and Liu, J. (2021). Microbial and Thermogenic Hydrogen Sulfide in the Qianjiang Depression of Jianghan Basin: Insights from Sulfur Isotope and Volatile Organic Sulfur Compounds Measurements. *Appl. Geochem.* 126, 104865. doi:10.1016/j.apgeochem.2020.104865

Xue, F., Liu, X. X., and Wang, T. Z. (2021). Research on Anchoring Effect of Jointed Rock Mass Based on 3D Printing and Digital Speckle Technology. *J. Min. Strata Control Eng.* 3 (2), 023013. doi:10.13532/j.jmsce.cn10-1638/td.20201020.001

Zhang, S. C., Zhu, G. Y., Dai, J. X., Xiong, Y., and Liang, Y. B. (2005). TSR and Sour Gas Accumulation: A Case Study in the Sichuan Basin, SW China. *Geochimica Cosmochimica Acta* 69, 562. doi:10.1016/j.gca.2005.03.033

Zhang, S., Shuai, Y., and Zhu, G. (2008). TSR Promotes the Formation of Oil-Cracking Gases: Evidence from Simulation Experiments. *Sci. China Ser. D-Earth Sci.* 51, 451–455. doi:10.1007/s11430-008-0009-4

Zhao, H., Liu, W., Borjigin, T., Zhang, J., Luo, H., and Wang, X. (2019). Study of Thermochemical Sulfate Reduction of Different Organic Matter: Insight from Systematic TSR Simulation Experiments. *Mar. Petroleum Geol.* 100, 434–446. doi:10.1016/j.marpetgeo.2018.11.009

Zhao, K. K., Jiang, P. F., Feng, Y. J., Sun, X. D., Cheng, L. X., and Zheng, J. W. (2021). Investigation of the Characteristics of Hydraulic Fracture Initiation by Using Maximum Tangential Stress Criterion. *J. Min. Strata Control Eng.* 3 (2), 023520. doi:10.13532/j.jmsce.cn10-1638/td.20201217.001

Zhu, D., Liu, Q., Zhang, J., Ding, Q., He, Z., and Zhang, X. (2019). Types of Fluid Alteration and Developing Mechanism of Deep Marine Carbonate Reservoirs. *Geofluids* 2019, 1–18. doi:10.1155/2019/3630915

Conflict of Interest: The authors declare that the research was conducted in the absence of any commercial or financial relationships that could be construed as a potential conflict of interest.

Publisher's Note: All claims expressed in this article are solely those of the authors and do not necessarily represent those of their affiliated organizations or those of the publisher, the editors, and the reviewers. Any product that may be evaluated in this article, or claim that may be made by its manufacturer, is not guaranteed or endorsed by the publisher.

frontiers | Frontiers in Earth Science

ORIGINAL RESEARCH
published: 13 June 2022
doi: 10.3389/feart.2022.916326

Determination of Favorable Lithofacies for Continental Shale Gas: A Case Study of the Shahezi Formation, Changling Fault Depression, Songliao Basin

Wen Xu[1], *Guoqiao Yang*[2,3]*, *Ang Li*[1]*, *Zhenxiang Song*[2,3] *and Wenhui Hu*[4]

[1]College of Earth Sciences, Jilin University, Changchun, China, [2]Wuxi Research Institute of Petroleum Geology, RIPEP, SINOPEC, Wuxi, China, [3]State Key Laboratory of Shale Oil and Gas Enrichment Mechanisms and Effective Development, Wuxi, China, [4]Institute of Earth Sciences and Resources, China University of Geosciences, Beijing, China

OPEN ACCESS

Edited by:
Hu Li,
Southwest Petroleum University, China

Reviewed by:
Xinlu Yan,
Taiyuan University of Technology, China
Ma Xiao,
China University of Petroleum, Beijing, China

***Correspondence:**
Guoqiao Yang
yangguoqiao.syky@sinopec.com
Ang Li
liang2020@jlu.edu.cn

Specialty section:
This article was submitted to Structural Geology and Tectonics, a section of the journal Frontiers in Earth Science

Received: 09 April 2022
Accepted: 09 May 2022
Published: 13 June 2022

Citation:
Xu W, Yang G, Li A, Song Z and Hu W (2022) Determination of Favorable Lithofacies for Continental Shale Gas: A Case Study of the Shahezi Formation, Changling Fault Depression, Songliao Basin. Front. Earth Sci. 10:916326. doi: 10.3389/feart.2022.916326

In order to determine the optimum lithofacies for continental shale, the reservoir characteristics of different lithofacies types were studied based on a series of experiments. The lacustrine organic-rich shale of the Shahezi Formation is divided into siliceous (ORS), argillaceous (ORA), calcareous (ORC), and mixed (ORM) shales. The ORS, ORA, ORC, and ORM shales all carried out comprehensive reservoir comparative analysis. The results showed that the moderate content of clay minerals (45%) can significantly improve porosity, and high and low clay mineral contents are not conducive to the improvement of porosity. The ORM shale tends to have better pore connectivity than the ORS and ORA shales, and the ORC shale has the poorest pore-throat connectivity in micron-size. Internal pores in bitumen and clay shrinkage cracks are the dominant pore type and are well developed in ORS and ORM shales. The two types of pores are less developed in the ORA shale; however, dissolution pores are better developed than those of ORS and ORM shales. Inorganic pores are well-developed in the ORC shale, but organic pores are not. Organic and inorganic pores tend to be better connected in the ORM shale than those of the other three types, which could help improve the gas storage capacity. The ORM shale may have more irregular surfaces and lower liquid/gas surface tension. The higher capillary condensation on pore surfaces is more likely to occur in the ORA shale. The ORS shale offers fewer adsorption sites for CH_4 and has lower adsorption capacity. The ORC shale has weak heterogeneity of the pore structure. Therefore, the ORM shale may be the most favorable lithofacies for shale gas enrichment and development, which has high porosity, good pore connectivity, moderate brittleness, and strong gas adsorption and storage capacity, followed by the ORS and ORA shales. The ORC shale is the worst.

Keywords: Shahezi Formation, pore structure, continental shale, shale lithofacies, shale gas

1 INTRODUCTION

Shale gas is commercially exploited in both China and North America. The shale in China can be divided into three types: marine, transitional, and continental. Only the Paleozoic marine shale realized commercial exploitation of shale gas in the Sichuan Basin (Zou et al., 2010; Zhao et al., 2020; Li, 2021). However, continental shale gas has not made a major breakthrough for a long time, especially because of its strong heterogeneity; shale lithofacies is very different. Current research on shale gas mostly focuses on marine shale and lacks research reports on terrestrial shale.

Generally, the determination of favorable intervals is crucial and can directly affect the effect of further exploration and development of shale gas. At present, total organic carbon (TOC), thermal evolution, development of organic pores, brittleness index, gas content, preservation conditions, and burial depth are often considered the main factors for evaluating the favorable area of marine shale gas (Zhao et al., 2016). However, compared with marine shale, the mineral composition and sedimentary laminae of terrestrial shale are more complex. Multiple sources in different directions in the same lake basin at the same time and lateral migration of the depositional center in different periods lead to frequent intercalation and rapid change of the shale lithofacies. Different shale lithofacies have different pore structure characteristics, which can affect both the gas storage capacity and even further shale gas development (Wang and Carr, 2012; Nie et al., 2020). Therefore, understanding the reservoir characteristics of different types of lithofacies can provide significant guidance for evaluating and selecting favorable intervals.

A lot of studies have carried out lithofacies characteristics analysis for marine shale. Hu et al. (2019) found that lithofacies controls many reservoir parameters, such as the total organic carbon (TOC), porosity, pore size, shape, and volume. The siliceous and high TOC-mixed lithofacies are thought to be the best for shale gas exploration and development. Wang et al. (2017) analyzed the effects of shale lithofacies on the pore structure for the Niutitang shale. They found that the organic-rich siliceous shale has a strong gas storage capacity with a large pore surface area; however, the organic-poor calcareous shale has unsatisfied gas storage capacity with a poor pore volume and surface area. Wu et al. (2016) established that the favorable shale lithofacies of the Wufeng–Longmaxi Formation are mixed siliceous shale lithofacies and clay-rich siliceous shale lithofacies. Tang et al. (2016) indicated that the organic-rich argillaceous shale shows a strong methane adsorption capacity, and organic-rich siliceous shale generally has high gas desorption content *in situ*. Compared to the marine shale lithofacies, the proportion of the siliceous shale is lower and that of the argillaceous shale is higher for the continental shale lithofacies (Chen L. et al., 2016). The sedimentary environments and sediment provenances may affect the pore structure characteristics. However, there are few studies that investigated detailed reservoir characteristics of different lithofacies types for continental shale and their impact on shale gas enrichment.

Paleoclimate and provenance have an important influence on terrestrial shale deposition (Wang et al., 2020; Lin et al., 2021). The organic matter abundance, mineral composition, and scale of lamination are three primarily considered parameters to classify the lithofacies of terrestrial shale (Chen S. Y. et al., 2016; Liu et al., 2018; Yin and Wu, 2020). TOC determines the material basis for gas formation and also provides storage space. Mineral composition has an important influence on shale gas storage capacity and brittleness. The laminae are an important factor affecting the pore structure of terrestrial shales and can increase the heterogeneity of lithofacies (Chalmers et al., 2012; Mathia et al., 2016; Liang et al., 2018). However, the laminae in lacustrine shales are difficult to identify and predict based on conventional logging data in the well with no cores. A specific sedimentary environment has specific mineral composition and sedimentary structure. Therefore, due to the data limitations and the difficulties of lamina identification in the actual application process for production well, only the TOC and mineral composition were considered as the basis for the division of lithofacies in this research.

The Songliao Basin is an important petroliferous basin with abundant continental shale gas resources and is one of the basins most likely to achieve commercial exploitation of continental shale gas. In recent years, the Shahezi Formation has attracted extensive attention from researchers because of its developing thick organic-rich shale with high gas content. Gao et al. (2018) have studied the shale reservoir characteristics of the Shahezi Formation and discussed controlling factors of the pore structure; however, the comparison of pore structure characteristics for different lithofacies types is insufficient, and further analysis is needed to provide guidance for the optimization of intervals and target areas. In this study, a series of reservoir testing and analysis were carried out on shale core samples of the Shahezi Formation in the fault depression of the southern Songliao Basin. The reservoir characteristics of different shale lithofacies types were compared, and the most favorable lithofacies type is determined, which could provide an important reference for selecting favorable intervals.

2 GEOLOGICAL SETTING

The Songliao Basin, located in northeast China, is one of the largest continental petroliferous basins with a large Mesozoic–Cenozoic deposition (Shu et al., 2003). The Songliao Basin can be divided into the north depression, the northeast uplift, the west slope, the central depression, the south uplift, the southwest uplift, and the south depression (**Figure 1C**). The Changling Fault Depression is located in the middle and south of the central fault depression area and is the largest fault basin in the south of the Songliao Basin (Wang H. et al., 2015; Gao et al., 2018). The Songliao Basin has experienced four tectonic stages, i.e., extensional faulting, subsidence, tectonic inversion, and Cenozoic faulting (Hu et al., 2005; Li et al., 2017). Paleozoic metamorphic, volcanic, and magmatic rocks formed the

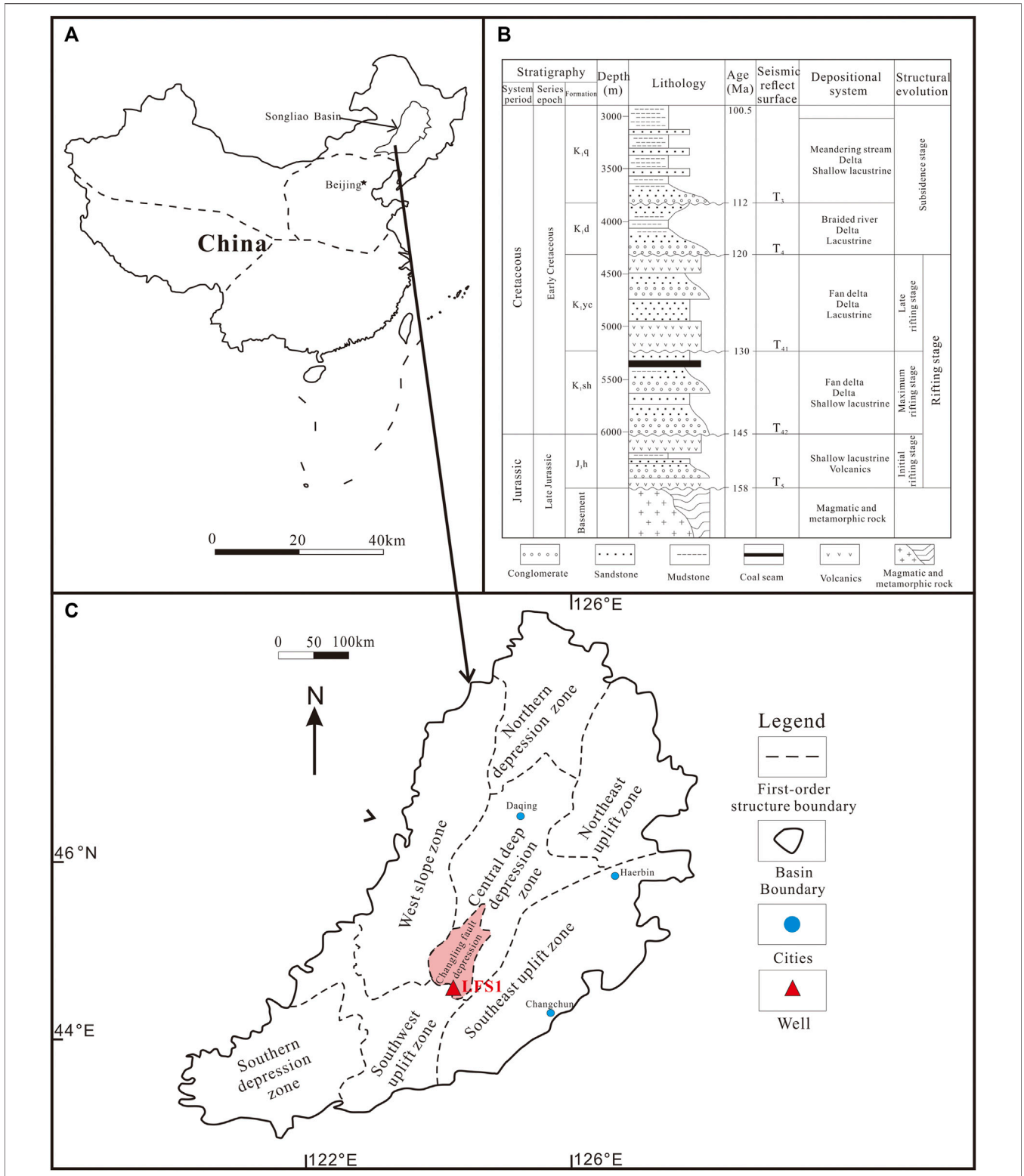

FIGURE 1 | (A) Location of the Songliao Basin within China. **(B)** Stratigraphic column of the Changling Fault Depression. J_3h, Huoshiling Formation; K_1sh, Shahezi Formation; K_1yc, Yingcheng Formation; K_1d, Denglouku Formation; and K_1q, Quantou Formation (modified after Cai et al., 2017).**(C)** Location of the Changling Fault Depression and sampling well (modified from Wang M. et al., 2015).

TABLE 1 | Measurements for 51 shale samples of the Shahezi Formation of the LFS1 well.

Sample ID	Depth (m)	Formation	Organic geochemistry				Mineralogy	Microscopy	Petrophysics				Gas content
			Ro	TOC	MC	CIK	XRD	FE-SEM	HP	MI	N_2	CO_2	
LFS1-1	3,576.18	Shahezi		√			√		√				√
LFS1-2	3,578.52	Shahezi	√	√	√	√	√		√				√
LFS1-3	3,580.19	Shahezi		√			√		√				√
LFS1-4	3,581.65	Shahezi		√			√		√				√
LFS1-5	3,582.41	Shahezi		√			√	√	√	√	√	√	√
LFS1-6	3,583.31	Shahezi		√			√		√				√
LFS1-7	3,584.42	Shahezi	√	√	√	√	√		√				√
LFS1-8	3,586.28	Shahezi		√			√		√				√
LFS1-9	3,586.79	Shahezi		√			√	√	√	√	√	√	√
LFS1-10	3,588.8	Shahezi		√			√		√				√
LFS1-11	3,589.5	Shahezi	√	√	√	√	√		√				√
LFS1-12	3,590.76	Shahezi		√			√		√				√
LFS1-13	3,591.38	Shahezi		√			√	√	√	√	√	√	√
LFS1-14	3,592.95	Shahezi		√			√		√				√
LFS1-15	3,594.41	Shahezi		√			√		√				√
LFS1-16	3,595.95	Shahezi	√	√	√	√	√		√				√
LFS1-17	3,596.69	Shahezi		√			√		√				√
LFS1-18	3,598.54	Shahezi		√			√		√				√
LFS1-19	3,599.81	Shahezi		√			√		√				√
LFS1-20	3,601.03	Shahezi	√	√	√	√	√	√	√	√	√	√	√
LFS1-21	3,602.5	Shahezi		√			√		√				√
LFS1-22	3,603.72	Shahezi		√			√	√	√	√	√	√	√
LFS1-23	3,605.14	Shahezi		√			√		√				√
LFS1-24	3,606.3	Shahezi		√			√		√				√
LFS1-25	3,607.9	Shahezi		√			√		√				√
LFS1-26	3,608.92	Shahezi	√	√	√	√	√		√				√
LFS1-27	3,610.7	Shahezi		√			√		√				√
LFS1-28	3,611.7	Shahezi		√			√		√				√
LFS1-29	3,611.99	Shahezi		√			√		√				√
LFS1-30	3,612.5	Shahezi		√			√		√				√
LFS1-31	3,615.58	Shahezi	√	√	√	√	√		√				√
LFS1-32	3,618.83	Shahezi		√			√		√				√
LFS1-33	3,619.5	Shahezi		√			√		√				√
LFS1-34	3,621.3	Shahezi	√	√	√	√	√		√				√
LFS1-35	3,622.35	Shahezi		√			√		√				√
LFS1-36	3,623.3	Shahezi		√			√		√				√
LFS1-37	3,624.75	Shahezi		√			√		√				√
LFS1-38	3,626.49	Shahezi		√			√		√				√
LFS1-39	3,627.5	Shahezi	√	√	√	√	√		√				√
LFS1-40	3,630.74	Shahezi		√			√		√				√
LFS1-41	3,631.1	Shahezi		√			√		√				√
LFS1-42	3,632.08	Shahezi		√			√		√				√
LFS1-43	3,634.91	Shahezi	√	√	√	√	√		√				√
LFS1-44	3,635.36	Shahezi		√			√		√				√
LFS1-45	3,636.1	Shahezi		√			√		√				√
LFS1-46	3,637.35	Shahezi		√			√	√	√	√	√	√	√
LFS1-47	3,638.2	Shahezi		√			√		√				√
LFS1-48	3,639.04	Shahezi	√	√	√	√	√		√				√
LFS1-49	3,640.1	Shahezi		√			√		√				√
LFS1-50	3,641.2	Shahezi		√			√		√				√
LFS1-51	3,644.7	Shahezi		√			√	√	√	√	√	√	√

Ro, vitrinite reflectance values; TOC, total organic carbon; MC, maceral composition; CIK, stable carbon isotopes of kerogen; XRD, X-ray diffraction; FE-SEM, field emission scanning electron microscope; HP, helium porosity; MI, mercury intrusion; N_2, nitrogen adsorption; CO_2, carbon dioxide adsorption.

basement of the basin, which is overlain by Jurassic, Cretaceous, and Cenozoic sedimentary rocks (Wang et al., 2013).

The Cretaceous strata are the main sedimentary cover in the Songliao Basin and can be divided into upper and lower series. The lower Cretaceous strata have great potential for oil and gas exploration and, from the bottom to the top, it developed the Huoshiling, Shahezi, Yingcheng, Denglouku, and Quantou formations (**Figure 1B**) (Han et al., 2021). The Shahezi Formation and Yingcheng Formation are the main source rocks in the deep petroleum system of the fault depression, which are also the main continental shale gas development layers. The dark shale of the Shahezi Formation in the Longfengshan sag of the Changling Fault Depression is a potential stratum for current exploration and research. The

lithology of the Shahezi Formation is mainly black, gray-black mudstone and siltstone, intercalated with gray sandstone and glutenite, and develops thin layers of acid tuff, fused tuff, and tuff breccia at the bottom. The sedimentary facies is mainly shore-shallow lake subfacies.

3 SAMPLES AND METHODS

3.1 Samples

Continuous shale coring was carried out for the Shahezi Formation in well LFS1 in the south of the Changling Fault Depression, with a total length of 69 m. For this study, 51 lacustrine shale core samples were collected continuously from the bottom to the top in this core section. Each sample was split into several aliquots for different tests. The field gas content, total organic carbon (TOC) content and X-ray diffraction (XRD), and helium porosity were carried out for all samples. Kerogen isolation, maceral component determination, vitrinite reflectance (Ro), and kerogen stable carbon isotope ($\delta^{13}C_{P\ DB}$) analysis were performed for 11 shale samples. According to the results of TOC and XRD, seven samples were selected for field emission scanning electron microscopy (FE-SEM), low-temperature gas adsorption (CO_2 and N_2), and the mercury injection capillary pressure (MICP) measurements. **Table 1** lists the detailed test items on each shale sample. The samples are selected and numbered from LFS1-1 to LFS1-51, considering the burial depth variation.

3.2 Methods

3.2.1 Organic Geochemistry

The TOC content was determined using a Leco CS230 carbon/sulfur analyzer, according to GB/T 19145-2003. The shale samples were first ground to a particle diameter less than 200 mesh in size and weighed about 10 g and then dealt with 5% hydrochloric acid at 80°C in a porous crucible for 2 h to remove inorganic carbon. Before combustion, all samples were cleaned with deionized water, neutralized, dried, and reweighed. The TOC content was measured according to Littke (1993).

The maceral compositions are determined based on kerogen isolation which was conducted for all shale samples. The detailed experimental procedure can be found in Dang et al. (2016). Identification of kerogen macerals was conducted using a DM4500P polarizing microscope, according to SY/T5125-2014. The types of kerogen were determined according to the results of maceral composition and stable carbon isotopes of kerogen. The Finnigan DELTA plus V stable isotope mass spectrometer was used to measure the stable carbon isotopes of kerogen, according to GB/T18340.2-2010. The test results were relative to the V-PDB standard ($\delta^{13}C_{PDB}$) with a measurement precision of ±0.5%.

Thermal maturity is commonly evaluated using Ro. Ro was measured with an MSP200 microphotometer, according to SY/T5124-2012. The readings of Ro were obtained with white light by using an oil immersion objective lens (Ma et al., 2021). The final value of Ro for each sample was an average of 40 measurements.

3.2.2 X-Ray Diffraction Analysis

The mineral composition was tested using a Bruker D8 A25 X-ray diffractometer, according to SY/T 5163-2018. The shale samples were ground to a particle diameter of less than 300 mesh. The shale powder was mixed with ethanol and smeared onto glass slides for XRD analysis. The instrument worked at 40 kV and 40 mA with Cu Kα-radiation.

3.2.3 Field Emission Scanning Electron Microscope

The Helios 650-focused ion beam scanning electron microscopy instrument was used to observe pore types and pore structure visually. FE-SEM has broken through the resolution limit of optical microscopes because of its secondary electronic imaging technique. FE-SEM has a strong three-dimensional imaging sense and is more intuitive in the observation of pore morphology characteristics. The pore surroundings are highlighted in response to secondary electrons which exhibit the pore morphology well (Loucks et al., 2012; Milliken et al., 2013; Wang et al., 2017). The samples were cut into regular shapes of 10 mm × 10 mm × 4 mm and pre-polished using hand sandpaper. Then, the shale samples were polished under vacuum conditions using an ion gun. Generally, the polishing time can last 3–4 h to obtain a high-quality surface, and then, the sample is coated with a 3-nm thick carbon film. The samples were observed in a vacuum.

3.2.4 Porosity

The effective porosity measurements of shale samples were performed using an Ultrapore-200AH helium porosimeter, according to GB/T 34533-2017. Cylindrical shape samples with a diameter and length of 2.5 cm were drilled from the shale. The cylindrical samples were ground flat at both ends and then placed in an oven and dried at 105°C to a constant weight. The porosity of the samples was determined from the difference between bulk density and skeletal density (Chalmers et al., 2012; Xi et al., 2018a).

3.2.5 Low-Pressure N_2 and CO_2 Physisorption

N_2 and CO_2 adsorption experiments were performed using a Micromeritics ASAP 2460 and JWBK-200C analyzer, respectively. The shale samples were crushed to a grain size of 60–80 mesh. Adsorbed moisture and capillary water were removed by drying the shale sample at 200°C for at least 2 h. The dehydrated samples for N_2 and CO_2 adsorption analysis were vacuum degassed for 24 h at 383.15 K. The experiments of N_2 isothermal adsorption and desorption were conducted at 77.35 K and less than 760 mmHg. The isothermal adsorption experiments of CO_2 were carried out at 273.15 K. All tests followed the standard of SY/T 6154-2019.

Based on the adsorption branch of the N_2 isotherms, the Barrett–Joyner–Halenda (BJH) method and the Brunauer–Emmett–Teller (BET) model were used to obtain the pore size distribution (PSD) of mesopore (2–50 nm) and the specific surface area, respectively (Brunauer et al., 1938; Barrett et al., 1951; Yin et al., 2020b). The density functional theory (DFT) method was used to determine the PSD of

micropores (<2 nm) with the CO_2 isotherms (Gregg and Sing, 1982).

3.2.6 Mercury Injection Capillary Pressure

MICP measurements were performed using an Autopore 9520 microporous structure analyzer, according to GB/T 29171-2012. Shale samples were weighed out to 8–10 g. Before mercury injection, samples were dried in an oven for 24 h at 105°C under vacuum. According to the Washburn equation, a pore size of 6 nm can be detected as the mercury injection pressure in this experiment can reach up to 410 Mpa (Washburn, 1921).

3.2.7 Gas Content Measurement

The gas content was tested with a shale gas field desorption apparatus developed by the Wuxi Research Institute of Petroleum Geology, RIPEP, SINOPEC. The test process for 51 shale samples was according to the standard of SY/T 6940-2020. The lost gas, desorbed gas, and residual gas determined the final gas content. The lost gas was speculated with the data on desorption gas volume and desorption time adopted by the United States Bureau of Mines (USBM) method (Diamond and Schatzel, 1998). The desorbed gas and residual gas can be directly measured by sealing shale samples in a desorption canister, and shale samples were crushed when measuring the residual gas content. The experimental process was described in detail in Diamond and Schatzel (1998) and Chen L. et al. (2016).

4 RESULTS

4.1 Organic Matter Abundance and Maturity

TOC and Ro are two basic and important evaluation parameters of hydrocarbon generation potential; 51 shale samples were tested for TOC, and 11 of which were tested for thermal maturity at the same time. The TOC content of shale varies from 0.26% to 5.16%, with an average of 2.02%, showing a good hydrocarbon generating material base (**Figure 5H**). The Ro values of the shale range from 1.48% to 1.67%, with an average of 1.55%. The analysis of the Ro suggests that the shale of the Shahezi Formation evolved into the humid gas and thermal cracking gas window as the organic matter has reached the high maturation stage (Tissot, 1984). The Shahezi Formation was in a high thermodynamic environment due to volcanic thermal events, and thus, the shale reached a high maturity.

4.2 Organic Matter Type

Kerogen has three major types: humic (type I), humic-sapropelic mixed (type II), and sapropelic (type III). Kerogen types determine the hydrocarbon generation characteristics, where type I has the strongest ability to generate oil, type III has the strongest ability to generate gas, and type II falls somewhere in between (Batten, 1996; Tang et al., 2019). Two methods are used to determine the types of organic matter, including type index (TI) analysis based on maceral compositions and carbon stable isotope analysis. TI values of 11 shale samples were calculated according to the maceral composition of the kerogen. The calculated TI values for the Shahezi Formation ranged from −37 to 17.5 with an average of −10 (**Table 2**). The $\delta^{13}C_{PDB}$ values of the kerogen of these 11 shale samples ranged from −23.8% to −22.3% with an average of−22.76% (**Table 2**). The results of carbon stable isotope analysis were consistent with the TI analysis aforementioned, except for four shale samples. In general, the kerogen types of shale samples from the Shahezi Formation were primarily Type II and Type III kerogen and tend to produce gas in the high maturation stage.

4.3 Lithofacies Types

The gas content has an obvious positive correlation with TOC (**Figure 5H**), indicating the TOC plays an important role in shale gas enrichment. Previous studies have shown that the TOC content of at least 2.0% is necessary for the formation and enrichment of shale gas (Tan et al., 2014; Chen et al., 2015). The TOC content of two-thirds of the shale samples is greater than 2.0%. XRD analysis suggests that the shale of the Shahezi Formation is mainly composed of quartz, clay minerals, feldspar, carbonates (calcite and dolomite), and pyrite. The total content of quartz and feldspar ranged from 13.9% to 55.3%, with an average of 41.7%. The content of clay ranged from 15.3% to 69.8%, with an average of 45.7%. The total content of calcite and dolomite ranged from 0.2% to 63.9%, with an average of 4.0%. The shale of the Shahezi Formation in the study area shows high brittle mineral content. Combined with the mineral composition, the organic-rich shale (TOC>2%) is further classified into four types: organic-rich siliceous (ORS) shale (quartz and feldspar >50%), organic-rich argillaceous (ORA) shale (clay >50%), organic-rich calcareous (ORC) shale (carbonate >50%), and organic-rich mixed (ORM) shale (quartz and feldspar <50%, clay <50%, and carbonate <50%). The results showed that the lithofacies of organic-rich shale samples in the well LFS1 are mostly mixed, followed by siliceous and argillaceous shales and a few calcareous shale samples (**Figure 2**). For the ORS shale, the total content of quartz and feldspar is between 50% and 75%, the clay content is between 25% and 50%, and the carbonate content is less than 25%. For the ORA shale, the clay content is between 50% and 75%, the total content of quartz and feldspar is between 25% and 50%, and the carbonate content is less than 25%. For the ORC shale, the carbonate content is between 50% and 75%, the clay content is less than 25%, and the total content of quartz and feldspar is less than 25%. For the ORM shale, the total content of quartz and feldspar is between 25% and 50%, the clay content is between 25% and 50%, and the carbonate content is less than 25%. Seven shale samples of different lithofacies types were selected for detailed analysis of reservoir characteristics and to identify favorable lithofacies types. The basic parameters of the seven samples are shown in **Table 3**.

4.4 Porosity and the Gas Content

The porosity of the selected seven organic-rich shale samples of four lithofacies types is compared. The porosity values of the seven samples are all larger than the limits (around 1%) for a shale gas reservoir (Nie et al., 2011). The ORS and ORM shales have obviously higher porosity than the ORA shale. Also, the porosity of the ORM shale seems to be relatively higher than the ORS shale as the clay mineral content of the two ORM shale samples is about 45% (**Table 3**). The only one ORC shale sample shows a low

TABLE 2 | Geochemical data on shale samples for the Shahezi Formation.

Sample ID	Depth (m)	Formation	TOC (%)	Ro (%)	Maceral composition (%)				TI	$\delta^{13}C_{PDB}$ (‰)
					Sapropelinite	Liptinite	Virtrinite	Inertinite		
LFS1-2	3,578.52	Shahezi	0.48	1.48		38	54	8	-29.50	-22.4
LFS1-7	3,584.42	Shahezi	4.02	1.50	25	40	30	5	17.50	-23.0
LFS1-11	3,589.5	Shahezi	2.61	1.52	16	44	34	6	6.50	-22.3
LFS1-16	3,595.95	Shahezi	2.33	1.49	12	42	39	7	-3.25	-23.3
LFS1-20	3,601.03	Shahezi	3.88	1.52		42	52	6	-24.00	-23.8
LFS1-26	3,608.92	Shahezi	0.84	1.61		32	60	8	-37.00	-22.9
LFS1-31	3,615.58	Shahezi	0.91	1.51	7	55	32	6	4.50	-22.6
LFS1-34	3,621.3	Shahezi	2.22	1.63		34	58	8	-34.50	-22.3
LFS1-39	3,627.5	Shahezi	1.00	1.67		68	28	4	9.00	-22.3
LFS1-43	3,634.91	Shahezi	0.70	1.56	10	44	40	6	-4.00	-22.3
LFS1-48	3,639.04	Shahezi	4.01	1.58		48	44	8	-17.00	-23.2

*TI, type index; TI, 100 * % sapropelinite + 50 * % liptinite + (-75) * % virtrinite + (-100) * % inertinite. Type I, TI > 80 and $\delta^{13}C_{PDB}$ shifting from –35% to –30%; type II, TI is between 80 and 40 and $\delta^{13}C_{PDB}$ shifting from –30% to –27.5%; type II–III, TI is between 40 and 0 and $\delta^{13}C_{PDB}$ shifting from –27.5% to –25%; type III, TI < 0 and $\delta^{13}C_{PDB}$ is higher than –25% (Meyers, 1994).*

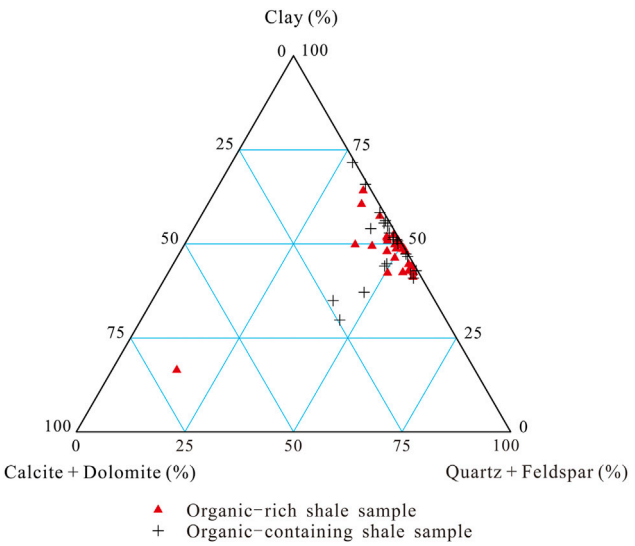

FIGURE 2 | Ternary diagram of mineral components for shale samples from the Shahezi Formation based on XRD.

porosity, with a value of 2.1%, similar to the ORA shale (an average of 2.3%).

The ORM shale shows the highest gas content (with an average of 3.7 m^3/t) in these seven shale samples, followed by the ORS and ORA shales with an average of 2.5 and 2.3 m^3/t, respectively (**Table 3**). The ORC shale has poor gas content, with a value of only 1.5 m^3/t.

4.5 N_2 Adsorption

N_2 adsorption is commonly used to analyze mesoporous (2–50 nm) characteristics. The N_2 adsorption–desorption isotherms for all shale samples were of type IV with a hysteresis loop, according to the classification of physisorption isotherms by Sing, 1985. N_2 adsorption isotherms of shale samples rise rapidly at low pressure and then increase slowly, showing an anti-S shape. The shape shows a transition process of adsorption from monolayer to multilayer. N_2 adsorption curves show that the adsorbed volumes of ORM shale samples are less than those of ORS and ORA shale samples (**Figure 3**), indicating that the ORM shale has lower mesopore volumes than the ORS and ORA shale. The ORC shale has a much lower mesopore volume than the other three lithofacies.

TABLE 3 | Basic parameters of the selected seven samples.

Lithofacies	Sample ID	Depth (m)	Mineral composition				Brittleness (%)	TOC (wt%)	Gas content (m^3/t)	Porosity (%)
			Q + F (%)	Clay (%)	C + D (%)	Other minerals (%)				
ORS	LFS1-22	3,603.72	54.2	40.7	1.1	4.0	57.6	2.9	2.6	2.6
	LFS1-9	3,586.79	53.5	41.5	2.0	3.0	57.2	2.3	2.4	3.1
	Mean		53.9	41.1	1.6	3.5	57.5	2.6	2.5	2.9
ORM	LFS1-51	3,644.70	48.1	44.3	3.4	4.2	53.8	5.2	4.2	3.7
	LFS1-5	3,582.41	46.1	47.4	1.7	4.8	50.2	2.6	3.1	2.8
	Mean		47.1	45.9	2.6	4.5	52.0	3.9	3.7	3.2
ORA	LFS1-20	3,601.03	32.7	61.7	1.8	3.8	35.9	3.9	2.0	3.0
	LFS1-13	3,591.38	34.2	58.4	3.9	3.5	39.5	3.0	2.6	1.5
	Mean		33.5	60.1	2.9	3.7	37.7	3.4	2.3	2.3
ORC	LFS1-46	3,637.35	13.9	15.3	63.9	6.9	83.6	3.0	1.5	2.1

ORS, organic-rich siliceous shale; ORM, organic-rich mixed shale; ORA, organic-rich argillaceous shale; ORC, organic-rich calcareous shale; Q + F, quartz + feldspar; C + D, calcite + dolomite; brittleness, (Q + F + C + D)/(Q + F + clay + C + D).

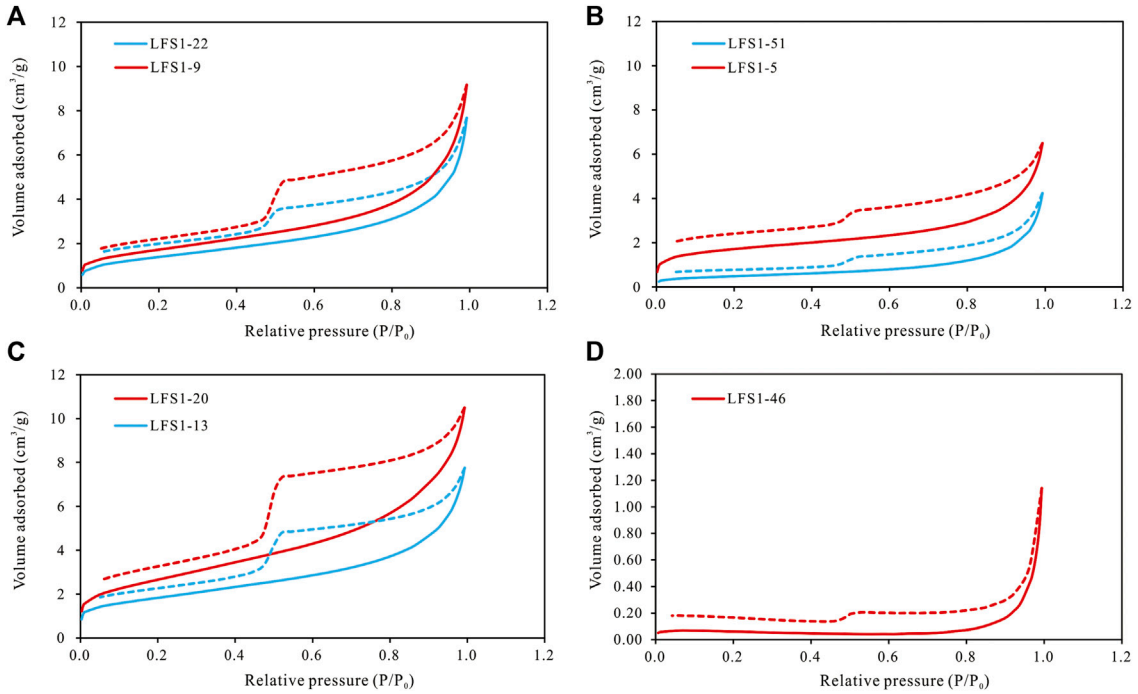

FIGURE 3 | N_2 adsorption isotherms of four types of lithofacies for shale samples in the Shahezi Formation. **(A)** ORS shale; **(B)** ORM shale; **(C)** ORA shale; and **(D)** ORC shale.

The pore shape of the shale can be characterized according to the N_2 adsorption–desorption isotherms (Xi et al., 2017; 2018b). The hysteresis loops were classified into four types based on De Boer's categories by IUPAC. In general, the type H2 hysteresis loop is often associated with pores that have narrow necks and wide bodies (defined as inkbottle-shaped pores), and the type H3 hysteresis loop represents slit-shaped or wedge-shaped pores. The slit-shaped or wedge-shaped pores can have a better connectivity than the inkbottle-shaped pores. The shapes of the hysteresis loop for the shale samples varied between types H2 and H3, indicating a combination of several typical pore types (**Figure 3**). At low pressure ($P/P_0 < 0.2$), the unclosed hysteresis loops for all shale samples suggest the existence of ultra-micropores as N_2 diffuses at a very slow velocity (Bertier et al., 2016). There are obvious differences in the shape of the hysteresis loop among the four types of lithofacies. The hysteresis loops of the ORM shale are smaller and flatter than those of the ORS and ORA shale, and the desorption curve is closer to the adsorption curve than that of the ORS and ORA shale (**Figure 3**). In addition, the desorption curves of the ORS and argillaceous shale are steeper at a relative pressure of 0.4–0.6 than that of the ORM shale. Furthermore, the hysteresis loops of the ORA shale are larger than those of the ORS shale. Also, for ORA shale, the distance between desorption and adsorption curves is further than that of the ORS shale at the relative pressure of 0.5–1.0. The results show that slit-shaped or wedge-shaped pores are better developed in the organic-rich mixed shale than those in ORS and ORA shales. The development degree of inkbottle-shaped pores is higher in the ORA shale and followed by the ORS shale, and the ORM shale seems to have a relatively low proportion of inkbottle-shaped pores. The hysteresis loop of ORC shale is similar to that of ORM shale, showing that the pores may be dominated by slit-shaped or wedge-shaped pores.

4.6 High-Pressure Mercury Intrusion Porosimetry

The mercury intrusion–extrusion curves are generally used to elucidate the characteristics of macropores (>50 nm), such as the distribution of micron-size pores and pore-throat connectivity (Rezaee et al., 2012). In this study, in order to eliminate the effects of the filling of fractures and surface irregularities, the surface roughness is corrected by subtracting injection volumes of the mercury intrusion porosimetry (MIP) data below 0.07 MPa (10 PSI) (Giesche, 2006; Gao and Hu, 2016). The mercury intrusion–extrusion curves of accumulated mercury saturation are similar among the ORS shale, ORM shale, and ORA shale (**Figure 4**). The cumulative intrusion curves increase stability when the capillary pressure is below 100 Mpa, and the mercury saturation increased with pressure, showing a slit-shaped pore structure consisting mainly of mineral matrix pores. Also, the slope of cumulative intrusion curves for the ORM shale is little higher than that of the ORS shale and ORA shale, indicating a better development degree of slit-shaped pores. When the capillary pressure exceeds 100 Mpa, the slope of cumulative intrusion curves increases distinctly, indicating that mercury breaks through the pores with narrow necks and enters the pores with wide bodies, which are mainly affected by the organic and clay mineral pores (Cai et al., 2013).

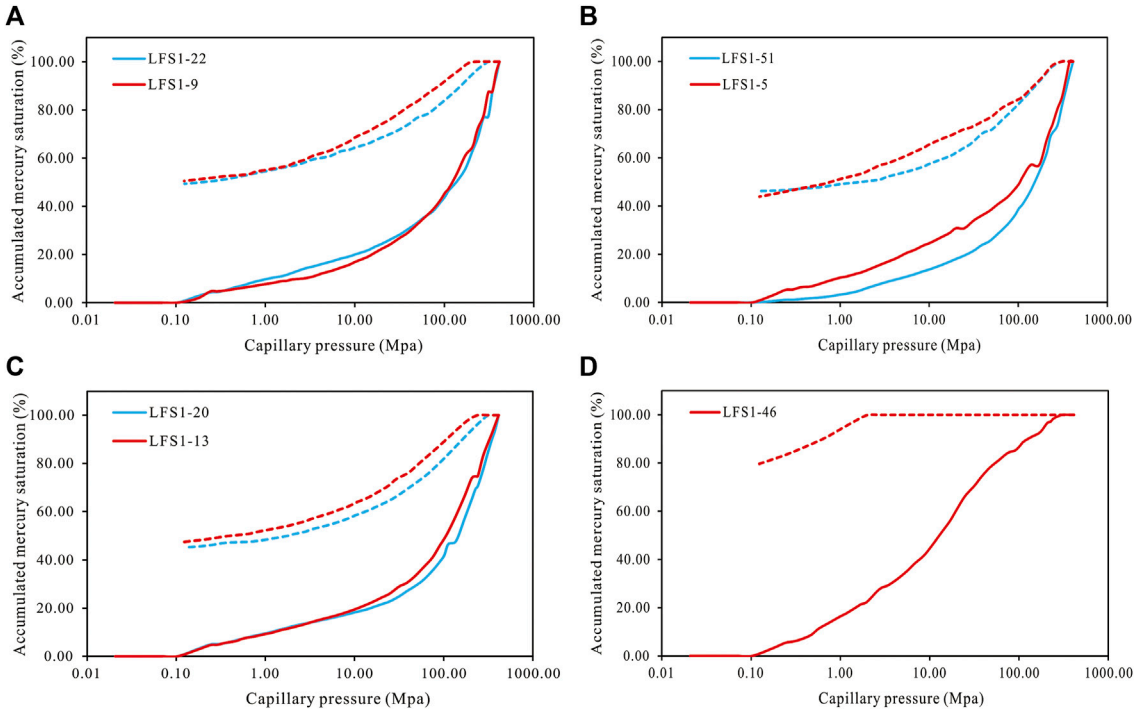

FIGURE 4 | Curves of mercury intrusion–extrusion from different lithofacies for shale samples in the Shahezi Formation. **(A)** ORS shale; **(B)** ORM shale; **(C)** ORA shale; and **(D)** ORC shale.

The cumulative mercury extrusion curves have a platform in the initial stage at high pressure for the ORS shale, ORM shale, and ORA shale, and then, the curves gradually decrease (**Figure 4**). The platform of the ORS shale and ORA shale seems to be bigger than that of the ORM shale, indicating that the mercury in the ORS shale and ORA shale is more difficult to extrude from pores at high pressure than that in the ORM shale. The results suggest that the ORM shale may have better pore connectivity than the ORS shale and ORA shale. The average value of the mercury withdrawal efficiency for the ORM shale is 54.9% and is slightly higher than that for the ORS shale and ORA shale with an average of 50.1% and 53.7%, respectively.

The mercury intrusion–extrusion curve of the ORC shale is quite different from the other three (**Figure 4**). The slope of the intrusion curve increases when the capillary pressure exceeds 10 Mpa, showing a breakthrough of pore throat, and gradually decreases when the capillary pressure is higher than 60 Mpa. The extrusion curve has a large platform at a capillary pressure of 2–450 Mpa, and the final mercury withdrawal efficiency is only 20.4%. The results suggest the ORC shale may have poor pore-throat connectivity in micron-size pores.

5 DISCUSSION

5.1 Factors Affecting Porosity and the Gas Content

Porosity is a key parameter to evaluate reservoirs, which provides a measure of the potential shale gas capacity. The weak correlation between porosity and TOC suggests that the organic pore may account for a low proportion of total porosity, and the inorganic pore is the main type (**Figure 5D**). Siliceous minerals are positively correlated with porosity (**Figure 5A**). Argillaceous minerals seem to be positively correlated with porosity when the content is lower than 45% and negatively correlated with porosity when the content exceeds 45% (**Figure 5B**). However, calcareous minerals have no correlation with porosity (**Figure 5C**). Therefore, the siliceous and argillaceous minerals are the key factors influencing the porosity. Siliceous minerals have a greater effect on porosity than argillaceous minerals. The siliceous minerals which have strong rigidity could shield the pores from compaction. Also, the combination of siliceous and argillaceous shales in a suitable proportion may be contributed to increasing the porosity. A high content of argillaceous minerals could decrease the porosity as it lacks the support from rigid minerals. The calcareous minerals may decrease the porosity due to re-precipitation within pore spaces.

TOC is positively correlated with the gas content (**Figure 5H**), and there is a slight positive correlation between siliceous minerals and the gas content (**Figure 5E**). The relationship between the gas content and porosity and gas content and calcareous minerals is not obvious (**Figures 5G,I**). Argillaceous minerals seem to be positively correlated with the gas content when the content is lower than 45% and negatively correlated with the gas content when the content exceeds 45% (**Figure 5F**). The results indicated that material basis is the key factor affecting

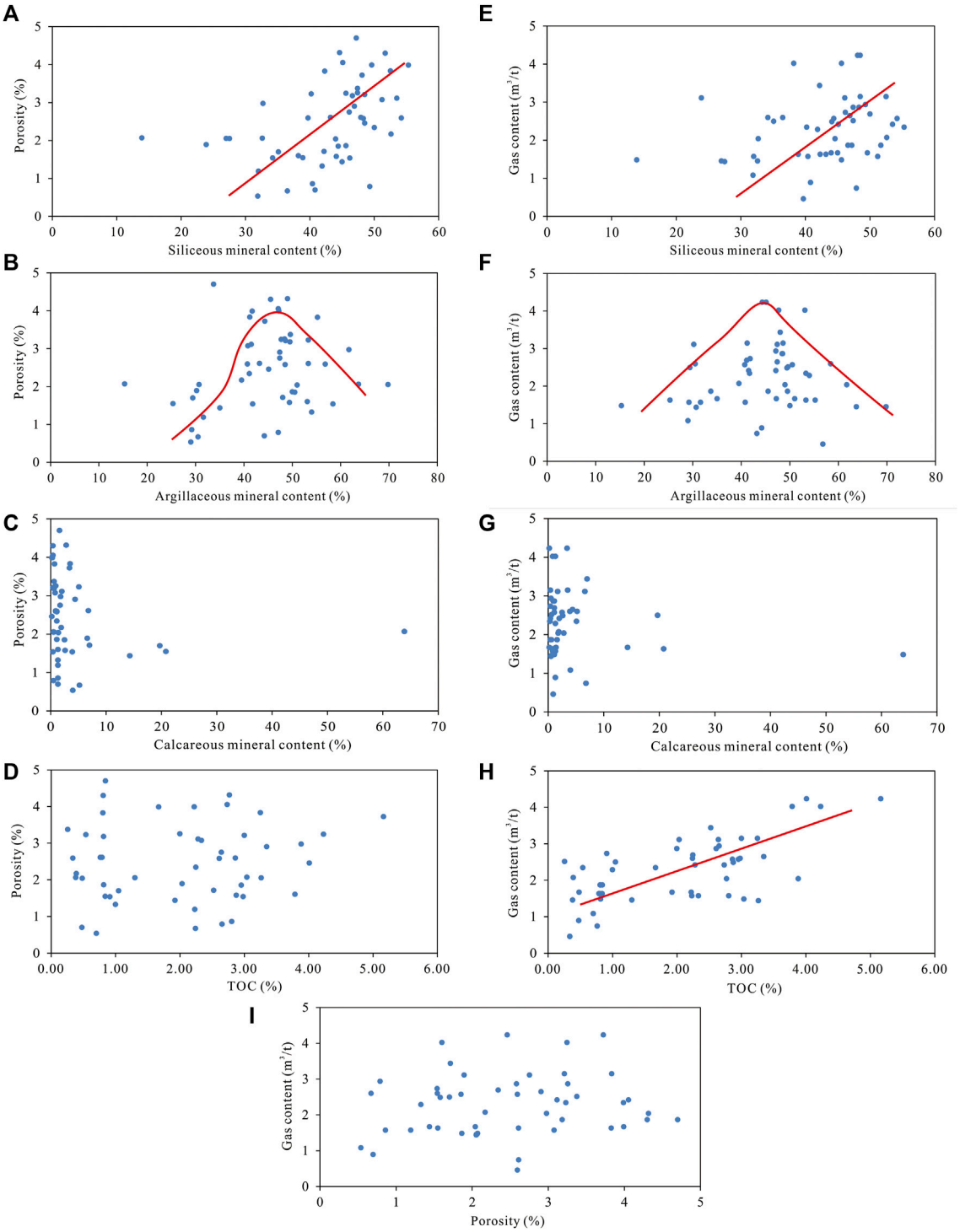

FIGURE 5 | Relationship between porosity and **(A)** siliceous minerals, **(B)** argillaceous minerals, **(C)** calcareous minerals, **(D)** TOC; relationship between the gas content and **(E)** siliceous minerals, **(F)** argillaceous minerals, **(G)** calcareous minerals, **(H)** TOC; and **(I)** relationship between porosity and gas content.

the gas content, and the moderate argillaceous mineral content (45%) can contribute to the form of favorable reservoir space and increase the gas content. The influence of other factors on the gas content is relatively limited.

5.2 Pore Size Distribution

The PSD of shale of four lithofacies types was calculated on the basis of CO_2 and N_2 adsorption and MICP data. The micropores (0–2 nm), mesopores (2–50 nm), and macropores (>50 nm) were

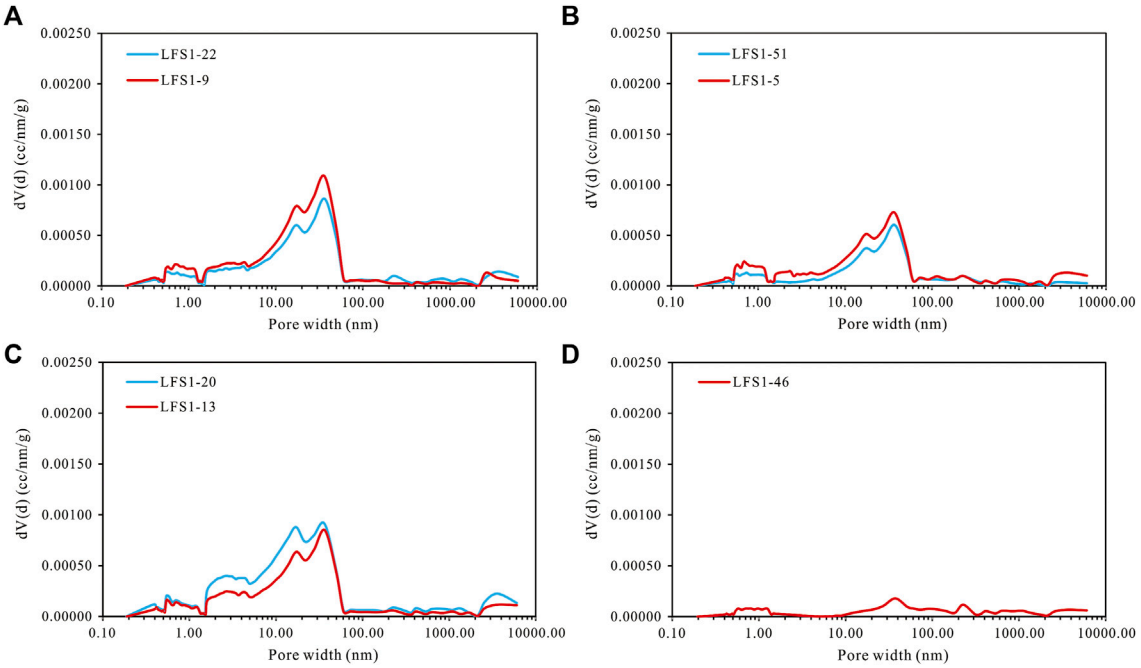

FIGURE 6 | PSD of four types of lithofacies for shale samples in the Shahezi Formation. **(A)** ORS shale; **(B)** ORM shale; **(C)** ORA shale; and **(D)** ORC shale. Note: 0–2 nm, CO_2 DFT model; 2–50 nm, N_2 BJH model; >50 nm, mercury intrusion.

TABLE 4 | Pore volume of all size pores in the shale of different lithofacies types from the Shahezi Formation.

Category	Sample ID	Pore volume (ml/g)				Percentage (%)			Specific surface area
		Micropore	Mesopore	Macropore	Total	Micropore	Mesopore	Macropore	(m^2/g)
ORS	LFS1-22	0.0019	0.0073	0.0012	0.0104	18.63	70.13	11.24	5.01
	LFS1-9	0.0029	0.0094	0.0008	0.0132	22.25	71.64	6.11	6.13
	Mean	0.0024	0.0084	0.0010	0.0118	20.44	70.89	8.67	5.57
ORM	LFS1-51	0.0018	0.0038	0.0008	0.0065	28.47	58.43	13.11	1.70
	LFS1-5	0.0031	0.0058	0.0012	0.0102	30.94	57.01	12.05	5.85
	Mean	0.0025	0.0048	0.0010	0.0083	29.70	57.72	12.58	3.78
ORA	LFS1-20	0.0026	0.0124	0.0015	0.0166	15.79	75.09	9.12	9.54
	LFS1-13	0.0021	0.0084	0.0009	0.0114	18.28	73.40	8.31	6.43
	Mean	0.0024	0.0104	0.0012	0.0140	17.04	74.25	8.72	7.99
ORC	LFS1-46	0.0011	0.0006	0.0011	0.0028	39.67	22.06	38.27	0.18

characterized with CO_2 adsorption (DFT model), N_2 adsorption (BJH model), and MICP (Washburn equation) data, respectively. The results showed that mesopores contribute mostly to the total pore volume in the ORS, ORM, and ORA shale (**Figure 6**). The average pore volume of mesopores in the ORM shale (0.0048 ml/g) is much smaller than that in the ORS shale (0.0084 ml/g) and the ORA shale (0.0104 ml/g) (**Table 4**). The average pore volume of micropores and macropores is similar among the ORS, ORM, and ORA shale. The development degree of pores for the ORC shale is weak compared with the other three types of shale.

For the ORM shale, the proportion of micropores and macropores (29.70% and 12.58%) in the total pore volume is higher than that of the ORS (20.44% and 8.67%) and ORA shale (17.04% and 8.72%). The proportion of mesopores (57.72%) in the ORM shale is much lower than that of the ORS (70.89%) and ORA shale (74.25%). The results indicate that for the ORM shale, the higher proportion of micropores may contribute to increasing the adsorption capacity, and the higher proportion of macropores may help promote pore connectivity.

The ORM shale has the highest specific surface area with an average value of 9.54 m^2/g, followed by ORA shale and ORS shale with an average value of 7.99 and 5.57 m^2/g, respectively (**Table 4**). The high specific surface area of ORM shale may be contributed by the moderately developed organic pores that were protected by the rigid minerals and clay-related pores. On the contrary, the ORC shale has the minimum specific surface area, with a value of 0.18 m^2/g. The ORC shale shows a poor adsorption capacity as the pores are poorly developed.

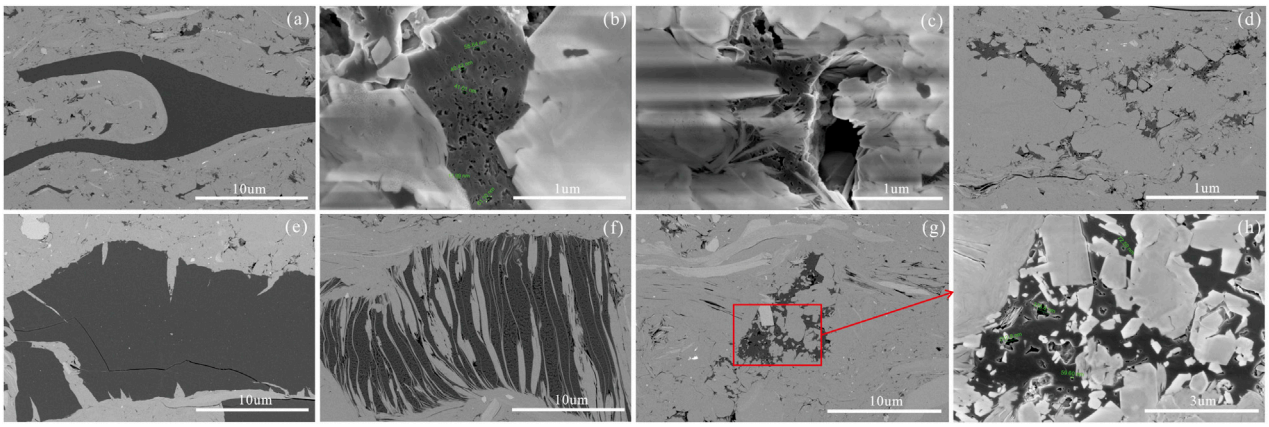

FIGURE 7 | SEM images of ORS shale samples in the Shahezi Formation. **(A–D)** LFS1-22; **(E–H)** LFS1-9. **(A)** Organic debris with little internal pores; **(B)** micropores developed in the bitumen; **(C)** intergranular pores are well developed, and the micropores in the edge of bitumen are well developed; **(D)** quartz intergranular pores and clay shrinkage cracks are well developed; **(E)** organic debris with little pores; **(F)** bitumen is filled between clay layers; **(G)** clay shrinkage cracks; **(H)** micropores are developed in the bitumen which is filled between quartz.

5.3 Microscopic Pore Characteristics

For the two ORS shale samples, the matrix is dominated by quartz and clay. The organic matter mainly consists of higher plant detritus and bitumen filling between grains. The pores in the organic detritus are not developed (**Figures 7A,E**), but sometimes shrinkage cracks are developed (**Figure 7E**). Bitumen is usually filled between quartz grains or between layers of clay (**Figures 7B,C,F,H**), and some of the micropores in the bitumen are well developed, as protected by siliceous minerals or rigid grains. The big pore cavity can sometimes be observed in the bitumen (**Figure 7C**). The organic matter pore shapes are from elongated to irregular polygons, and pore sizes range from several to hundreds of nanometers (**Figures 7B,C,F,H**). The inorganic pores are mainly quartz intergranular pores and clay shrinkage cracks (**Figures 7D,G**). The organic matter pores appear to be interconnected with each other; however, most of the inorganic pores seem to be disconnected from the organic matter pores.

For the two ORM shale samples, similar to the ORS shale, the matrix is dominated by clay and quartz, and the organic matter mainly consists of scattered higher plant detritus and bitumen filling between grains. The pores in the organic detritus are poorly developed (**Figures 8E,G**). Bitumen pores are generally unevenly developed (**Figures 8B,D**), and pore sizes can range from several to hundreds of nanometers (**Figures 8B,D,F**). The big pore cavity can also be observed in the bitumen (**Figure 8D**), and sometimes the shape of bitumen pores is honeycomb (**Figure 8F**). Inorganic pores are mainly contact gaps between quartz particles, shrinkage gaps between clay minerals, and gaps between clay mineral layers (**Figures 8C,G**). Different from the ORS shale, organic and inorganic pores in the two ORM shale tend to be interconnected by the microfractures, including structural microfractures and organic shrinkage fractures (**Figures 8A–C, E,G**). The moderate content of clay minerals seems to contribute to increasing the occurrence probability of longer shrinkage fractures. The interconnection between organic and inorganic pores contributes to providing more effective storage space as gas generated from organic matter can flow into the inorganic pores through connected microfractures.

For the two ORA shale samples, the internal pores of organic clasts are poorly developed (**Figure 9A**). The internal pores of bitumen are generally not developed (**Figure 9B**) but can sometimes be observed locally (**Figures 9E,F**). The pores in bitumen vary in size and are irregular polygon shapes. The pores developed in bitumen seem to be bigger than those in the other types of shale (**Figure 9F**). Inorganic pores are mainly shrinkage cracks of clay minerals and dissolution pores in feldspar. The shrinkage cracks of clay minerals are less developed than those of ORS and ORM shale (**Figure 9C**) and generally developed locally (**Figures 9D,H**). The phenomenon shows that the ORA shale has a stronger compaction effect than ORS and ORM shales due to the reduction in the content of rigid minerals. Dissolution pores in feldspar are observed in the ORA shale (**Figure 9G**), which are rarely found in the ORS and ORM shale. In the process of hydrocarbon generation from organic matter, the clay minerals, as a favorable catalyst, promote the transformation of organic matter and the formation of organic acids, which results in the development of dissolution pores in feldspar. Higher clay contents in the ORA shale than those in the ORS and ORM shale may contribute to increased organic acid content and form a strong dissolution effect.

For the ORC shale sample, the pores in organic detritus and bitumen are less developed, and only a few pores can be observed (**Figures 10A,B**). The poor development of organic pores may be caused by alkaline diagenetic conditions that inhibit the pore development of organic matter. Also, the low clay mineral content may decrease the rate of hydrocarbon generation of organic matter as clay minerals are effective catalysts for hydrocarbon generation from organic matter. Inorganic pores are well developed, including intergranular pores and shrinkage gaps between clay minerals (**Figures 10C,D**). In addition, a few dissolution pores inside the mineral particles can be observed

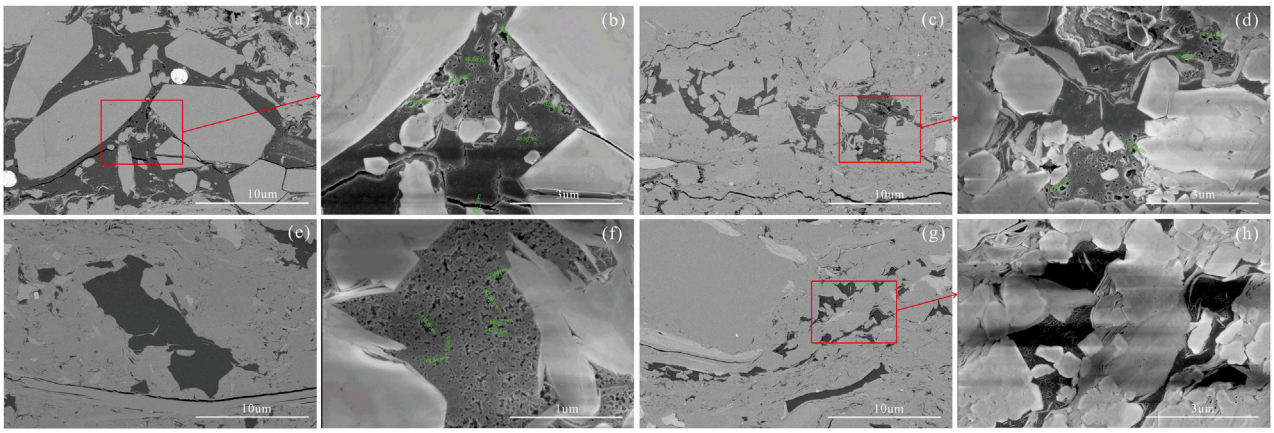

FIGURE 8 | SEM images of ORM shale samples in the Shahezi Formation. **(A–D)** LFS1-5; **(E–H)** LFS1-51. **(A)** Structural microfractures and organic shrinkage fractures; **(B)** micropores developed in the bitumen; **(C)** contact gaps between quartz particles and shrinkage gaps between clay minerals; **(D)** unevenly developed bitumen pores; **(E)** organic debris with little internal pores; **(F)** cellular pores in bitumen; **(G)** gaps between clay mineral layers; **(H)** micropores are developed in the bitumen which is filled between quartz.

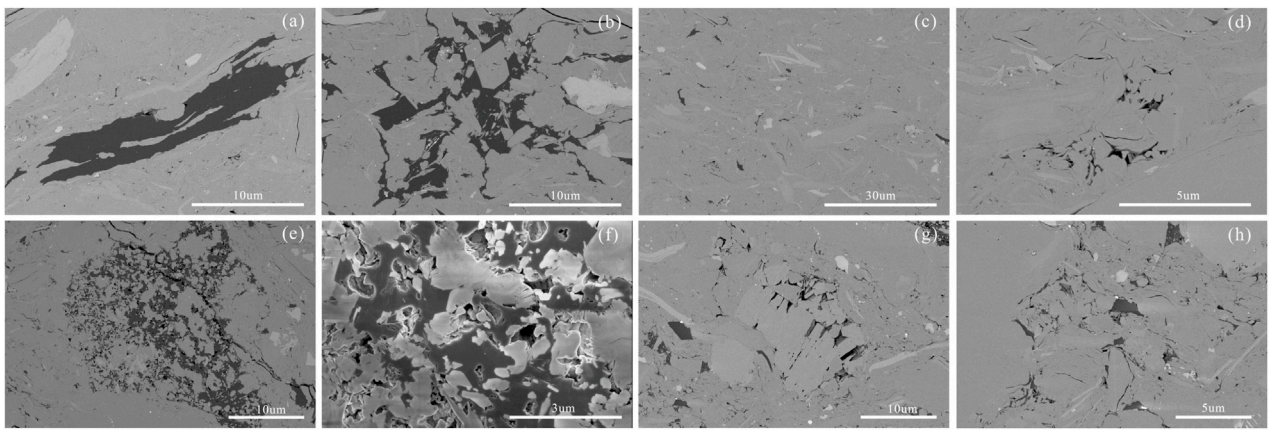

FIGURE 9 | SEM images of ORA shale samples in the Shahezi Formation. **(A–D)** LFS1-13; **(E–H)** LFS1-20. **(A)** Organic debris with little internal pores; **(B)** bitumen with little internal pores; **(C)** shrinkage gaps between clay minerals are undeveloped; **(D)** shrinkage gaps between clay minerals and intergranular pores; **(E)** internal pores developed locally in bitumen; **(F)** internal and marginal pores in bitumen; **(G)** dissolution pores in feldspar grains; **(H)** shrinkage cracks of clay minerals.

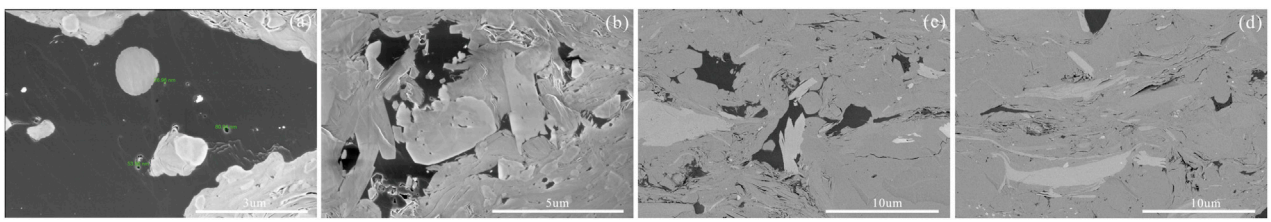

FIGURE 10 | SEM images of ORA shale samples in the Shahezi Formation. **(A–D)** LFS1-46. **(A)** Organic debris with little internal pores; **(B)** bitumen with little internal pores; **(C,D)** a few dissolution pores inside the mineral particles, intergranular pores, and shrinkage gaps between clay minerals.

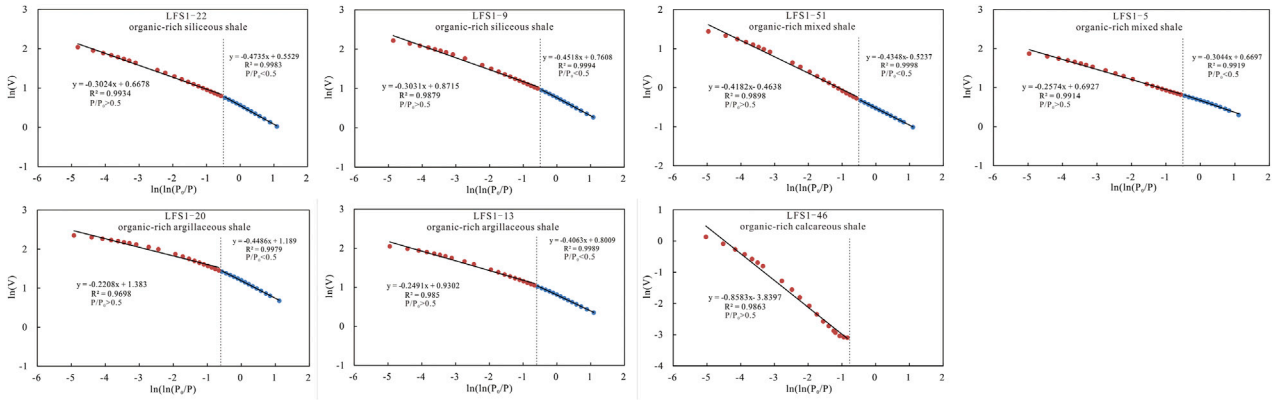

FIGURE 11 | Scatter diagram of ln (V) vs. ln (ln (P_0/P)) from N_2 adsorption data for shale samples from the Shahezi Formation.

TABLE 5 | Fractal dimensions of four types of lithofacies.

Lithofacies type	Samples	P/P0 = 0.5–1.0			P/P0 = 0–0.5		
		Fitting equation	D2	R^2	Fitting equation	D1	R^2
ORS	3,603.72 m and TOC = 2.86%	y = −0.3024x + 0.6678	2.6976	0.9934	y = −0.4735x + 0.5529	2.5265	0.9983
	3,586.79 m and TOC = 2.28%	y = −0.3031x + 0.8715	2.6969	0.9879	y = −0.4518x + 0.7608	2.5482	0.9994
	Mean		2.6973			2.5374	
ORM	3,644.7 m and TOC = 5.16%	y = −0.4182x − 0.4638	2.5818	0.9898	y = −0.4348x −0.5237	2.5652	0.9998
	3,582.41 m and TOC = 2.64%	y = −0.2574x + 0.6927	2.7426	0.9914	y = −0.3044x + 0.6697	2.6956	0.9919
	Mean		2.6622			2.6304	
ORA	3,601.03 m and TOC = 3.88%	y = −0.2208x + 1.383	2.7792	0.9698	y = −0.4486x + 1.189	2.5514	0.9979
	3,591.38 m and TOC = 2.98%	y = −0.2491x + 0.9302	2.7509	0.9850	y = −0.4063x + 0.8009	2.5937	0.9989
	Mean		2.7651			2.5726	
ORC	3,637.35 m and TOC = 3.04%	y = −0.8583x − 3.8397	2.1417	0.9863			

(**Figures 10B–D**). Most of the inorganic pores seem to be disconnected from organic matter, which may not be conducive to shale gas storage and enrichment.

5.4 Fractal Dimensions From the Analysis of N_2 Gas Adsorption Isotherms

Fractal theory can describe the heterogeneity of a porous material and has been proven to be a useful tool to characterize the roughness of the pore surface and the complexity of the pore structure for porous media such as shale (Yao et al., 2009; Mishra et al., 2018). The fractal dimension (D) is a key parameter that is commonly used to quantitatively describe the heterogeneity of shale surfaces and pores. In general, the fractal dimension values range between 2 and 3, and the larger the fractal dimension, the rougher is the pore surface or the more complex is the pore structure. The values 2 and 3 for surface fractal dimension indicate a perfect flat pore surface and a very rough pore surface, respectively. The fractal BET (Brunauer–Emmett–Teller), fractal Frenkele–Halseye–Hill (FHH), and thermodynamic methods are three available methods to obtain the value of D based on gas adsorption isotherms (Avnir and Jaroniec 1989; Yao et al., 2008; Cai et al., 2013). Among these, the FHH model is the most commonly used and most effective. According to FHH, the fractal dimension can be calculated with the results of nitrogen adsorption, according to the following equation:

$$\ln(V) = K\left[\ln\left(\ln\left(\frac{P_0}{P}\right)\right)\right] + constant, \quad (1)$$

where V represents the adsorbed volume (cm^3) at equilibrium pressure P (MPa); K is the power-law exponent that is dependent on D and the mechanism of adsorption; and P_0 (MPa) is the saturation pressure of the gas. Fractal dimension D can be derived from the expression "K = (D−3)," which can provide realistic results.

Scatter diagrams of ln (V) versus ln (ln (P_0/P)) for these shale samples were drawn using the original low-temperature N_2 adsorption isotherm data. The plots all show a good linear relationship (**Figure 11**), indicating that the pores of the shale sample are fractal. The two distinct linear segments can be observed at a relative pressure (P/P_0) of 0–0.55 and 0.55–1, indicating that the pores in shale have different fractal characteristics in these two regions, and the fractal dimension D1 at a lower relative pressure (P/P_0) of 0–0.55 and fractal dimension D2 at a higher relative pressure (P/P_0) of 0.55–1 can be obtained. Previous studies have researched the discrepancies of D1 and D2 and their contributions to the CH_4 adsorption capacity (Li et al., 2016). The pore structure

fractal dimension and the surface fractal dimension are the two conventional definitions in describing fractality (Pyun and Rhee, 2004). At a lower relative pressure (P/P_0) of 0–0.55, with the increasing pressure, gas molecules gradually adsorb on the whole pore surfaces from monolayer to multilayer until the smoothing effect appears. In this region, micropore filling mainly occurs, and van der Waals forces between gas and solid control the gas/solid interface. The fractal dimension D1 corresponds to the surface fractal dimension. A higher value of D1 means a more irregular surface of the shale sample, which can have more adsorption sites for CH_4 and increase the adsorption capacity of shale. At a higher relative pressure (P/P_0) of 0.55–1, the increasing adsorbed layers lead to the occurrence of smoothing effects as van der Waals forces between gas and solid become weak, and the capillary condensation of gas clumps in the shale pores takes more effects (Qi et al., 2002; Mahnke and Mögel, 2003; Sing, 2004). The fractal dimension D2 corresponds to the pore structure fractal dimension; a greater pore structure fractal dimension D2 indicates that the shale has a higher capillary condensation on pore surfaces, which causes the decrease of CH_4 adsorption.

The values of fractal dimensions D1 and D2 for four lithofacies types of shale are calculated by $D = K + 3$, and the results are shown in **Table 5**. Compared with the ORS and ORA shale, the ORM shale has the highest fractal dimension D1 and lowest fractal dimension D2, with the mean values of 2.6304 and 2.6622, respectively. This suggests that the ORM shale may have a more irregular surface which could provide more space for CH_4 adsorption and have lower liquid/gas surface tension that can enhance CH_4 adsorption capacity. Also, this may be an important reason for explaining that the ORM shale has higher gas content than the ORS and ORA shale. The ORA shale has a higher fractal dimension D2 (a mean value of 2.7651) than that of the ORS and ORM shale (a mean value of 2.6973 and 2.6622), indicating that higher capillary condensation on pore surfaces is more likely to occur in the ORA shale, which causes the decrease of CH_4 adsorption and lower gas content than that of the ORS and ORM shale. The ORS shale has a lower fractal dimension D1 (a mean value of 2.5374) than that of the ORA and ORM shale (a mean value of 2.5726 and 2.6304), showing that the ORS shale offers fewer adsorption sites for CH_4 and has lower adsorption capacity. For the ORC shale, at a lower relative pressure (P/P_0) of 0–0.55, it has very weak gas adsorption, and the fractal dimension D1 is unrealistic. The fractal dimension D2 of the ORC shale is much lower than the ORS, ORM, and ORA shale, with a value of 2.1417, indicating that the ORC shale has weak heterogeneity of the pore structure and is unlikely to occur in the capillary condensation of gas clumps.

6 CONCLUSION

Based on the multi-methods, including organic geochemical analysis, XRD analysis, porosity tests, FE-SEM, N_2 and CO_2 adsorption, and MIP experiments, reservoir characteristic differences among ORS, ORA, ORC, and ORM shales from the Shahezi Formation are comprehensively analyzed, and the favorable lithofacies is determined. The following conclusions can be drawn:

1) The ORM shale may be the most favorable lithofacies for shale gas enrichment and development, which has high porosity, good pore connectivity, moderate brittleness, and strong gas adsorption and storage capacity, followed by the ORS and ORA shale; the ORC shale is the worst.
2) The moderate content of clay minerals (45%) can significantly improve porosity, and high and low clay mineral contents are not conducive to the improvement of porosity. The ORM shale tends to have better pore connectivity than the ORS shale and ORA shale, and the ORC shale has the poorest pore-throat connectivity in micron-size. The ORM shale is dominated by slit-shaped or wedge-shaped pores; however, ORS and ORA shales mainly develop inkbottle-shaped pores. The ORC shale shows low mercury withdrawal efficiency.
3) Internal pores in bitumen and clay shrinkage cracks are the dominant pore type. The two types of pores are likely interconnected in the ORM shale as structural microfractures and organic shrinkage fractures are well developed. However, they are generally disconnected for the ORS and ORA shale. The bitumen pores and shrinkage cracks of clay minerals for ORA shale are less developed than those of the ORS and mixed shale; however, dissolution pores are better developed than that of them. Inorganic pores are well developed in the ORC shale, but organic pores are not.
4) The ORM shale may have a more irregular surface which could provide more space for CH_4 adsorption and have lower liquid/gas surface tension which can enhance the CH_4 adsorption capacity. The higher capillary condensation on pore surfaces is more likely to occur in the ORA shale, which causes the decrease of CH_4 adsorption. The ORS shale offers fewer adsorption sites for CH_4 and has lower adsorption capacity. The ORC shale has weak heterogeneity of the pore structure and is unlikely to occur in the capillary condensation of gas clumps.

DATA AVAILABILITY STATEMENT

The original contributions presented in the study are included in the article/Supplementary Material; further inquiries can be directed to the corresponding authors.

AUTHOR CONTRIBUTIONS

WX and GY are responsible for the idea, writing, and revision of this manuscript. AL is responsible for the data analysis and review. ZS and WH are responsible for drawing and editing.

FUNDING

This work was supported by the National Natural Science Foundation of China (Grant No. 42072156) and the Project of Sinopec Science and Technology Department (P21035-2).

REFERENCES

Avnir, D., and Jaroniec, M. (1989). An Isotherm Equation for Adsorption on Fractal Surfaces of Heterogeneous Porous Materials. *Langmuir* 5, 1431–1433. doi:10.1021/la00090a032

Barrett, E. P., Joyner, L. G., and Halenda, P. P. (1951). The Determination of Pore Volume and Area Distributions in Porous Substances. I. Computations from Nitrogen Isotherms. *J. Am. Chem. Soc.* 73, 373–380. doi:10.1021/ja01151a04610.1021/ja01145a126

Batten, D. J. (1996). Sedimentary Organic Matter. Organic Facies and Palynofacies. *Mar. Petroleum Geol.* 13 (5), 595–596. doi:10.1016/0264-8172(96)88335-8

Bertier, P., Schweinar, K., Stanjek, H., Ghanizadeh, A., Clarkson, C. R., Busch, A., et al. (2016). On the Use and Abuse of N2 Physisorption for the Characterization of the Pore Structure of Shales. *CMS Workshop Lect.* 21, 151–161. doi:10.1346/CMS-WLS-21.12

Brunauer, S., Emmett, P. H., and Teller, E. (1938). Adsorption of Gases in Multimolecular Layers. *J. Am. Chem. Soc.* 60, 309–319. doi:10.1021/ja01269a023

Cai, Q., Hu, M., Ngia, N. R., and Hu, Z. (2017). Sequence Stratigraphy, Sedimentary Systems and Implications for Hydrocarbon Exploration in the Northern Xujiaweizi Fault Depression, Songliao Basin, NE China. *J. Petroleum Sci. Eng.* 152, 471–494. doi:10.1016/j.petrol.2017.02.022

Cai, Y., Liu, D., Pan, Z., Yao, Y., Li, J., and Qiu, Y. (2013). Pore Structure and its Impact on CH4 Adsorption Capacity and Flow Capability of Bituminous and Subbituminous Coals from Northeast China. *Fuel* 103, 258–268. doi:10.1016/j.fuel.2012.06.055

Chalmers, G. R., Bustin, R. M., and Power, I. M. (2012). Characterization of Gas Shale Pore Systems by Porosimetry, Pycnometry, Surface Area, and Field Emission Scanning Electron Microscopy/transmission Electron Microscopy Image Analyses: Examples from the Barnett, Woodford, Haynesville, Marcellus, and Doig Units. *Bulletin* 96, 1099–1119. doi:10.1306/10171111052

Chen, L., Jiang, Z., Liu, K., Wang, P., Ji, W., Gao, F., et al. (2016). Effect of Lithofacies on Gas Storage Capacity of Marine and Continental Shales in the Sichuan Basin, China. *J. Nat. Gas Sci. Eng.* 36, 773–785. doi:10.1016/j.jngse.2016.11.024

Chen, S. Y., Zhang, S., Wang, Y. S., and Tan, M. Y. (2016). Lithofacies Types and Reservoirs of Paleogene Fine-Grained Sedimentary Rocks in Dongying Sag, Bohai Bay Basin. *Petroleum Explor. Dev.* 43 (2), 198–208. (in Chinese with English abstract). doi:10.1016/S1876-3804(16)30025-8

Chen, Y., Wei, L., Mastalerz, M., and Schimmelmann, A. (2015). The Effect of Analytical Particle Size on Gas Adsorption Porosimetry of Shale. *Int. J. Coal Geol.* 138, 103–112. doi:10.1016/j.coal.2014.12.012

Dang, W., Zhang, J., Tang, X., Chen, Q., Han, S., Li, Z., et al. (2016). Shale Gas Potential of Lower Permian Marine-Continental Transitional Black Shales in the Southern North China Basin, Central China: Characterization of Organic Geochemistry. *J. Nat. Gas Sci. Eng.* 28, 639–650. doi:10.1016/j.jngse.2015.12.035

Diamond, W. P., and Schatzel, S. J. (1998). Measuring the Gas Content of Coal: a Review. *Int. J. Coal Geol.* 35, 311–331. doi:10.1016/s0166-5162(97)00040-2

Gao, F., Song, Y., Li, Z., Xiong, F., Chen, L., Zhang, Y., et al. (2018). Lithofacies and Reservoir Characteristics of the Lower Cretaceous Continental Shahezi Shale in the Changling Fault Depression of Songliao Basin, NE China. *Mar. Petroleum Geol.* 98, 401–421. doi:10.1016/j.marpetgeo.2018.08.035

Gao, Z., and Hu, Q. (2016). Wettability of Mississippian Barnett Shale Samples at Different Depths: Investigations from Directional Spontaneous Imbibition. *Bulletin* 100 (1), 101–114. doi:10.1306/09141514095

Giesche, H. (2006). Mercury Porosimetry: a General (Practical) Overview. *Part. Part. Syst. Charact.* 23 (1), 9–19. doi:10.1002/ppsc.200601009

Gregg, S. J., and Sing, K. S. W. (1982). *Adsorption, Surface Area, and Porosity*. New York: Academic Press, 303.

Han, H., Dai, J., Guo, C., Zhong, N., Pang, P., Ding, Z., et al. (2021). Pore Characteristics and Factors Controlling Lacustrine Shales from the Upper Cretaceous Qingshankou Formation of the Songliao Basin, Northeast China: A Study Combining SEM, Low-temperature Gas Adsorption and MICP Experiments. *Acta Geol. Sin. - Engl. Ed.* 95 (2), 585–601. doi:10.1111/1755-6724.14419

Hu, H., Hao, F., Guo, X., Yi, J., Shu, Z., Bao, H., et al. (2019). Effect of Lithofacies on the Pore System of Over-mature Longmaxi Shale in the Jiaoshiba Area, Sichuan Basin, China. *Mar. Petroleum Geol.* 109, 886–898. doi:10.1016/j.marpetgeo.2019.06.050

Hu, W., Lü, B., Zhang, W., Mao, Z., Leng, J., and Guan, D. (2005). An Approach to Tectonic Evolution and Dynamics of the Songliao Basin. *Sci. Geol. Sin.* 1, 16–31. (in Chinese with English abstract). doi:10.3321/j.issn:0563-5020.2005.01.002

Li, A., Ding, W., He, J., Dai, P., Yin, S., and Xie, F. (2016). Investigation of Pore Structure and Fractal Characteristics of Organic-Rich Shale Reservoirs: a Case Study of Lower Cambrian Qiongzhusi Formation in Malong Block of Eastern Yunnan Province, South China. *Mar. Petroleum Geol.* 70, 46–57. doi:10.1016/j.marpetgeo.2015.11.004

Li, S., Zhang, J., Gong, F., Zhu, H., and Bai, Y. (2017). The Seven Properties Characteristics of Mudstone in the First and Second Member of Upper Cretaceous Qingshankou Formation and Favorable Area Optimization of Shale Oil in the North of Songliao Basin. *Geol. Rev.* 63 (Suppl. p), 71–72. (in Chinese with English abstract). doi:10.16509/j.georeview.2017.s1.035

Li, Y. (2021). Mechanics and Fracturing Techniques of Deep Shale from the Sichuan Basin, SW China. *Energy Geosci.* 2 (1), 1–9. doi:10.1016/j.engeos.2020.06.002

Liang, C., Cao, Y., Liu, K., Jiang, Z., Wu, J., and Hao, F. (2018). Diagenetic Variation at the Lamina Scale in Lacustrine Organic-Rich Shales: Implications for Hydrocarbon Migration and Accumulation. *Geochimica Cosmochimica Acta.* 229, 112–128. doi:10.1016/j.gca.2018.03.017

Lin, L., Liu, S., Xu, Y., and Li, F. (2021). Lithofacies and Pore Structure of Fine-grained Sedimentary Rocks of Qing-1 Member of Cretaceous in the Southern Songliao Basin. *Acta Geol. Sin. - Engl. Ed.* 95 (2), 570–584. doi:10.1111/1755-6724.14657

Littke, R. (1993). Deposition, Diagenesis and Weathering of Organic Matter-Rich Sediments. *Lect. Notes Earth Sci.* 47. doi:10.1007/bfb0009988

Liu, B., Shi, J. X., Fu, X. F., Lv, Y. F., Sun, X. D., Gong, L., et al. (2018). Petrological Characteristics and Shale Oil Enrichment of Lacustrine Fine-Grained Sedimentary System: A Case Study of Organic-Rich Shale in First Member of Cretaceous Qingshankou Formation in Gulong Sag, Songliao Basin, NE China. *Petroleum Explor. Dev.* 45 (5), 1–11. doi:10.1016/S1876-3804(18)30091-0

Loucks, R. G., Reed, R. M., Ruppel, S. C., and Hammes, U. (2012). Spectrum of Pore Types and Networks in Mudrocks and a Descriptive Classification for Matrix-Related Mudrock Pores. *Bulletin* 96 (6), 1071–1098. doi:10.1306/08171111061

Ma, Z., Tan, J., Zheng, L., Shen, B., Wang, Z., Shahzad, A., et al. (2021). Evaluating Gas Generation and Preservation of the Wufeng-Longmaxi Formation Shale in Southeastern Sichuan Basin, China: Implications from Semiclosed Hydrous Pyrolysis. *Mar. Petroleum Geol.* 129, 105102. doi:10.1016/j.marpetgeo.2021.105102

Mahnke, M., and Mögel, H. J. (2003). Fractal Analysis of Physical Adsorption on Material Surfaces. *Colloids Surfaces A Physicochem. Eng. Aspects.* 216, 215–228. doi:10.1016/S0927-7757(02)00577-0s

Mathia, E. J., Bowen, L., Thomas, K. M., and Aplin, A. C. (2016). Evolution of Porosity and Pore Types in Organic-Rich, Calcareous, Lower Toarcian Posidonia Shale. *Mar. Petroleum Geol.* 75, 117–139. doi:10.1016/j.marpetgeo.2016.04.009

Meyers, P. A. (1994). Preservation of Elemental and Isotopic Source Identification of Sedimentary Organic Matter. *Chem. Geol.* 114 (3), 289–302. doi:10.1016/0009-2541(94)90059-0

Milliken, K. L., Rudnicki, M., Awwiller, D. N., and Zhang, T. (2013). Organic Matter-Hosted Pore System, Marcellus Formation (Devonian), Pennsylvania. *Bulletin* 97 (2), 177–200. doi:10.1306/07231212048

Mishra, S., Mendhe, V. A., Varma, A. K., Kamble, A. D., Sharma, S., Bannerjee, M., et al. (2018). Influence of Organic and Inorganic Content on Fractal Dimensions of Barakar and Barren Measures Shale Gas Reservoirs of Raniganj Basin, India. *J. Nat. Gas Sci. Eng.* 49, 393–409. doi:10.1016/j.jngse.2017.11.028

Nie, H., Li, D., Liu, G., Lu, Z., Hu, W., Wang, R., et al. (2020). An Overview of the Geology and Production of the Fuling Shale Gas Field, Sichuan Basin, China. *Energy Geosci.* 1 (3–4), 147–164. doi:10.1016/j.engeos.2020.06.005

Nie, H., Zhang, J., and Li, Y. (2011). Accumulation Conditions of the Lower Cambrian Shale Gas in the Sichuan Basin and its Periphery. *Acta Pet. Sin.* 32, 959–967. doi:10.1007/s12182-011-0123-3

Pyun, S.-I., and Rhee, C.-K. (2004). An Investigation of Fractal Characteristics of Mesoporous Carbon Electrodes with Various Pore Structures. *Electrochimica Acta.* 49, 4171–4180. doi:10.1016/j.electacta.2004.04.012

Qi, H., Ma, J., and Wong, P.-z. (2002). Adsorption Isotherms of Fractal Surfaces. *Colloids Surfaces A Physicochem. Eng. Aspects.* 206, 401–407. doi:10.1016/S0927-7757(02)00063-8

Rezaee, R., Saeedi, A., and Clennell, B. (2012). Tight Gas Sands Permeability Estimation from Mercury Injection Capillary Pressure and Nuclear Magnetic Resonance Data. *J. Petroleum Sci. Eng.* 88-89, 92–99. doi:10.1016/j.petrol.2011.12.014

Shu, L. S., Mu, Y. F., and Wang, B. C. (2003). The Oil-Gas-Bearing Strata and the Structural Features in the Songliao Basin, NE China. *J. Stratigr.* 27 (4), 340–347. (in Chinese with English abstract). doi:10.1016/S0955-2219(02)00073-0

Sing, K. S. W. (2004). Characterization of Porous Materials: Past, Present and Future. *Colloids Surfaces A Physicochem. Eng. Aspects.* 241, 3–7. doi:10.1016/j.colsurfa.2004.04.003

Sing, K. S. W. (1985). Reporting Physisorption Data for Gas/solid Systems with Special Reference to the Determination of Surface Area and Porosity (Recommendations 1984). *Pure Appl. Chem.* 57 (4), 603–619. doi:10.1351/pac198557040603

Tan, J., Weniger, P., Krooss, B., Merkel, A., Horsfield, B., Zhang, J., et al. (2014). Shale Gas Potential of the Major Marine Shale Formations in the Upper Yangtze Platform, South China, Part II: Methane Sorption Capacity. *Fuel* 129, 204–218. doi:10.1016/j.fuel.2014.03.064

Tang, X., Jiang, Z., Huang, H., Jiang, S., Yang, L., Xiong, F., et al. (2016). Lithofacies Characteristics and its Effect on Gas Storage of the Silurian Longmaxi Marine Shale in the Southeast Sichuan Basin, China. *J. Nat. Gas Sci. Eng.* 28, 338–346. doi:10.1016/j.jngse.2015.12.026

Tang, Y., Yang, R., Zhu, J., Yin, S., Fan, T., Dong, L., et al. (2019). Analysis of Continental Shale Gas Accumulation Conditions in a Rifted Basin: A Case Study of Lower Cretaceous Shale in the Southern Songliao Basin, Northeastern China. *Mar. Petroleum Geol.* 101, 389–409. doi:10.1016/j.marpetgeo.2018.12.002

Tissot, B. P.(1984). Recent Advances in Petroleum Geochemistry Applied to Hydrocarbon Exploration. *Bulletin* 68 (5), 545–563. doi:10.1306/ad461336-16f7-11d7-8645000102c1865d

Wang, C., Feng, Z., Zhang, L., Huang, Y., Cao, K., Wang, P., et al. (2013). Cretaceous Paleogeography and Paleoclimate and the Setting of SKI Borehole Sites in Songliao Basin, Northeast China. *Palaeogeogr. Palaeoclimatol. Palaeoecol.* 385, 17–30. doi:10.1016/j.palaeo.2012.01.030

Wang, G., and Carr, T. R. (2012). Methodology of Organic-Rich Shale Lithofacies Identification and Prediction: a Case Study from Marcellus Shale in the Appalachian Basin. *Comput. Geosciences.* 49, 151–163. doi:10.1016/j.cageo.2012.07.011

Wang, H., Fan, T., and Wu, Y. (2015). The Subsurface Structure and Stratigraphic Architecture of Rift-Related Units in the Lishu Depression of the Songliao Basin, China. *J. Asian Earth Sci.* 99, 13–29. doi:10.1016/j.jseaes.2014.11.026

Wang, H., Shi, Z., Zhao, Q., Liu, D., Sun, S., Guo, W., et al. (2020). Stratigraphic Framework of the Wufeng-Longmaxi Shale in and Around the Sichuan Basin, China: Implications for Targeting Shale Gas. *Energy Geosci.* 1 (4), 124–133. doi:10.1016/j.engeos.2020.05.006

Wang, M., Xue, H., Tian, S., Wilkins, R. W. T., and Wang, Z. (2015). Fractal Characteristics of Upper Cretaceous Lacustrine Shale from the Songliao Basin, NE China. *Mar. Petroleum Geol.* 67, 144–153. doi:10.1016/j.marpetgeo.2015.05.011

Wang, P., Jiang, Z., Yin, L., Chen, L., Li, Z., Zhang, C., et al. (2017). Lithofacies Classification and its Effect on Pore Structure of the Cambrian Marine Shale in the Upper Yangtze Platform, South China: Evidence from FE-SEM and Gas Adsorption Analysis. *J. Petroleum Sci. Eng.* 156, 307–321. doi:10.1016/j.petrol.2017.06.011

Washburn, E. W. (1921). Note on a Method of Determining the Distribution of Pore Sizes in a Porous Material. *Proc. Natl. Acad. Sci. U.S.A.* 7 (4), 115–116. doi:10.1073/pnas.7.4.115

Wu, L., Hu, D., Lu, Y., Liu, R., and Liu, X. (2016). Advantageous Shale Lithofacies of Wufeng Formation-Longmaxi Formation in Fuling Gas Field of Sichuan Basin, SW China. *Petroleum Explor. Dev.* 43 (2), 208–217. doi:10.1016/S1876-3804(16)30024-6

Xi, Z., Tang, S., Wang, J., Yang, G., and Li, L. (2018a). Formation and Development of Pore Structure in Marine-Continental Transitional Shale from Northern China across a Maturation Gradient: Insights from Gas Adsorption and Mercury Intrusion. *Int. J. Coal Geol.* 200, 87–102. doi:10.1016/j.coal.2018.10.005

Xi, Z., Tang, S., Wang, J., Yi, J., Guo, Y., and Wang, K. (2018b). Pore Structure and Fractal Characteristics of Niutitang Shale from China. *Minerals* 8 (4), 163. doi:10.3390/min8040163

Xi, Z., Tang, S., Zhang, S., and Li, J. (2017). Nano-Scale Pore Structure of Marine-Continental Transitional Shale from Liulin Area, the Eastern Margin of Ordos Basin, China. *J. Nanosci. Nanotechnol.* 17 (9), 6109–6123. doi:10.1166/jnn.2017.14501

Yao, Y., Liu, D., Tang, D., Tang, S., and Huang, W. (2008). Fractal Characterization of Adsorption-Pores of Coals from North China: An Investigation on CH4 Adsorption Capacity of Coals. *Int. J. Coal Geol.* 73, 27–42. doi:10.1016/j.coal.2007.07.003

Yao, Y., Liu, D., Tang, D., Tang, S., Huang, W., Liu, Z., et al. (2009). Fractal Characterization of Seepage-Pores of Coals from China: An Investigation on Permeability of Coals. *Comput. Geosciences.* 35, 1159–1166. doi:10.1016/j.cageo.2008.09.005

Yin, S., Dong, L., Yang, X., and Wang, R. (2020b). Experimental Investigation of the Petrophysical Properties, Minerals, Elements and Pore Structures in Tight Sandstones. *J. Nat. Gas Sci. Eng.* 76, 103189. doi:10.1016/j.jngse.2020.103189

Yin, S., and Wu, Z. (2020). Geomechanical Simulation of Low-Order Fracture of Tight Sandstone. *Mar. Petroleum Geol.* 117, 104359. doi:10.1016/j.marpetgeo.2020.104359

Zhao, W. Z., Li, J. Z., Yang, T., Wang, S. F., and Huang, J. L. (2016). Geological Difference and its Significance of Marine Shale Gases in South China. *Petroleum Explor. Dev.* 43 (4), 499–510. (in Chinese with English abstract). doi:10.1016/S1876-3804(16)30065-9

Zhao, Z., Wu, K., Fan, Y., Guo, J., Zeng, B., and Yue, W. (2020). An Optimization Model for Conductivity of Hydraulic Fracture Networks in the Longmaxi Shale, Sichuan Basin, Southwest China. *Energy Geosci.* 1 (1–2), 47–54. doi:10.1016/j.engeos.2020.05.001

Zou, C., Dong, D., Wang, S., Li, J., Li, X., Wang, Y., et al. (2010). Geological Characteristics and Resource Potential of Shale Gas in China. *Petroleum Explor. Dev.* 37 (6), 641–653. doi:10.1016/S1876-3804(11)60001-3

Conflict of Interest: Authors GY and ZS were employed by the company RIPEP, SINOPEC.

The remaining authors declare that the research was conducted in the absence of any commercial or financial relationships that could be construed as a potential conflict of interest.

Publisher's Note: All claims expressed in this article are solely those of the authors and do not necessarily represent those of their affiliated organizations, or those of the publisher, the editors, and the reviewers. Any product that may be evaluated in this article, or claim that may be made by its manufacturer, is not guaranteed or endorsed by the publisher.

frontiers | Frontiers in Earth Science

ORIGINAL RESEARCH
published: 13 June 2022
doi: 10.3389/feart.2022.885602

Effect of Diagenesis on the Quality of Sandstone Reservoirs Exposed to High-Temperature, Overpressure, and CO_2-Charging Conditions: A Case Study of Upper Miocene Huangliu Sandstones of Dongfang District, Yinggehai Basin, South China Sea

Xiaowei Lv[1,2,3], Meiyan Fu[1,2]*, Shaonan Zhang[4], Xianghao Meng[1,2], Yi Liu[5], Xiaoqi Ding[1,2], Ya Zhang[6] and Tengjiao Sun[1,2]*

[1]College of Energy Resource, Chengdu University of Technology, Chengdu, China, [2]State Key Laboratory of Oil and Gas Geology and Exploitation, Chengdu, China, [3]The Research Institute of Henan Oilfield Company, SINOPEC, Zhengzhou, China, [4]College of Geosciences and Technology, Southwest Petroleum University, Chengdu, China, [5]The Research Institute of Zhanjiang Branch of CNOOC, Zhanjiang, China, [6]Southwest Oil and Gas Field Company of Petro China Company Limited, Chengdu, China

OPEN ACCESS

Edited by:
Wenlong Ding,
China University of Geosciences, China

Reviewed by:
Lanpu Chen,
China University of Geosciences Wuhan, China
Duan Wei,
China University of Geosciences, China

***Correspondence:**
Xiaowei Lv
lxwcdut@163.com
Meiyan Fu
fumeiyan08@cdut.cn

Specialty section:
This article was submitted to Structural Geology and Tectonics, a section of the journal Frontiers in Earth Science

Received: 28 February 2022
Accepted: 03 May 2022
Published: 13 June 2022

Citation:
Lv X, Fu M, Zhang S, Meng X, Liu Y, Ding X, Zhang Y and Sun T (2022) Effect of Diagenesis on the Quality of Sandstone Reservoirs Exposed to High-Temperature, Overpressure, and CO_2-Charging Conditions: A Case Study of Upper Miocene Huangliu Sandstones of Dongfang District, Yinggehai Basin, South China Sea. Front. Earth Sci. 10:885602. doi: 10.3389/feart.2022.885602

The Upper Miocene Huangliu sandstones of the Dongfang district are currently regarded as an important exploration target in the Yinggehai Basin. Affected by the anomalous diagenetic environments of high temperature, overpressure, and CO_2 fillings, the diagenetic evolution of the Huangliu sandstones appear complicated characteristics and subsequently exert a significant influence on reservoir development. Integrated methods employed in this study include an electron microscope, cathode luminescence, X-ray diffraction, scanning electron microscope, electron microprobe, stable isotope analysis, homogenization temperature, and physical property tests. By the comparative researches between the AF-1 and AF-2 areas of the Dongfang district, the aim of this study is to investigate the complex diagenetic modifications and their controlling effects on reservoir quality and development mechanism. With similar sedimentary features, the reservoirs in the AF-1 area exhibit slightly higher porosity than those of the AF-2 area. The permeability in the AF-1 area shows one or two orders of magnitude lower than that of the AF-2 area, and throats size distribution act as a critical factor to cause distinct diversities of permeability. In the AF-1 area, the later appearance of overpressure contributed to stronger compaction intensity and more loss of primary porosity. The dissolution induced by CO_2-rich thermal fluids in late stage enhanced the secondary porosity significantly and improved the total porosity. However, extensive dissolution cause abundant precipitation including carbonate cement and authigenic illite in a closed diagenetic system, which lead to the decrease of reservoirs' permeability. As for the AF-2 area, earlier occurrence of overpressure restrained mechanical compaction obviously and further retarded corrosion of organic acid, which preserved high proportions of primary porosity. Due to lesser impact by CO_2 filling, the AF-2 area had a poor intensity of

dissolution and cementation, and the authigenic illitization was also restrained significantly, which effectively prevented heavy damage on reservoir quality, and especially for permeability. Based on the diagenetic evolution pathways, two types of porosity evolution patterns are established. The effect degree on diagenesis by high temperature, overpressure, and CO_2 filling vary significantly between the AF-1 and AF-2 areas. The two areas show different pathways of diagenetic evolution, forming two development patterns and exhibiting different reservoir types.

Keywords: Huangliu sandstones, high temperature, overpressure, CO_2 dissolution, diagenetic evolution

1 INTRODUCTION

As most of hydrocarbon resources in shallow layers have been discovered and exploration technologies progress continuously, the exploration transferring to deeply buried and complex reservoirs become an inevitable choice, and deepening understandings on the impact for reservoir quality by high pressure, high temperature (HPHT), and CO_2 injection are considered to be even more significant for diminishing prospecting risk in deeper targets (Taylor et al., 2010; Stricker et al., 2016; Duan et al., 2020). Being different from normal pressure coefficient and geothermal gradient, the sandstones exposed in anomalous settings of HPHT and CO_2 filling present a wide variety of diagenetic modifications and complex diagenetic evolution, and consequently exert a battery of crucial controls on reservoir quality and development mechanism (Di Primio and Neumann, 2008; Nguyen et al., 2013; Grant et al., 2014; Fu et al., 2016; Duan et al., 2020; Li et al., 2020).

The important influence of overpressure on reservoir development have been widely studied across the overpressed petroliferous basins worldwide in the last few decades (e.g., Taylor et al., 2010; Grant et al., 2014; Sathar and Jones, 2016; Lai et al., 2017; Santosh and Feng, 2020). The opinion of reducing vertical effective stress (VES) toward intergranular and cement-grain contacts by overpressure is generally accepted, which plays a significant role in primary porosity preservation and subsequently results in anomalously high porosity in deeply buried reservoirs (Osborne and Swarbrick, 1999; Bloch et al., 2002; Tingay et al., 2009; Sathar and Jones, 2016; Li, 2021). Furthermore, considerable studies indicate that overpressure has a non-ignorable influence on several diagenetic aspects mainly as follow: protecting dissolved porosities (Taylor et al., 2015; Zhang et al., 2020; Wang and Wang, 2021), indirectly controlling dissolution efficiency of organic acids and CO_2 (Jansa and Noguera Urrea, 1990; Wilkinson et al., 1997; Duan et al., 2018), retarding clay minerals transformation (Colten-Bradley, 1987; Meng et al., 2012), and affecting cementation intensity such as quartz overgrowth and carbonate cements (Osborne and Swarbrick, 1999; Bloch et al., 2002; Duan et al., 2018).

Temperature is also one of critical factors for reservoir evolution by altering the rate of water–rock reaction and intensity of diagenesis (Schmoker and Gautier, 1988; Di Primio and Neumann, 2008; Yoshida and Santosh., 2020; Zheng et al., 2020; Yang et al., 2021). Previous practical studies show that the high-temperature setting, especially higher geothermal gradient or anomalously thermal events caused by thermal fluid activities, are mostly suggested to have significant effect on enhancing compaction rate, strengthening cementation and dissolution, and accelerating transformation efficiency of clay minerals, which are of great significance to deepen the understanding for formation mechanism of reservoir (Stricker et al., 2016; Dong et al., 2020; Lan et al., 2021; Li, 2022).

In recent years, interest has been increasing on exploring the diagenetic evolution and formation mechanism of sandstone reservoirs influenced by fillings of CO_2-rich thermal fluid (Wilkinson et al., 2009; Fu et al., 2016; Duan et al., 2018; Zhang et al., 2019; Zhao et al., 2020). The CO_2 charging correlated with thermal fluid cause exceptional diagenetic alteration of dissolution and precipitation exert a non-negligible influence on and diagenetic modifications and reservoir development (Watson et al., 2004; Higgs et al., 2007; Zuo et al., 2019; Duan et al., 2020).

There is no single diagenetic element that is solely or dominantly governing the porosity evolution (Mansurbeg et al., 2008; Wang et al., 2020). Most previous studies assessed the effect of diagenesis on reservoir development influenced by one or two of abnormal diagenetic elements including HPHT and CO_2 injection. Fewer work synthetically documented the combined effects for reservoirs quality controlled by multivariate overlapped extreme conditions of HPHT and CO_2 filling in spatial and temporal scale, and the integrated effects controlled by the extreme conditions are barely investigated and poorly understood. The Dongfang district is located at the northern of the central depression in the Yinggehai Basin (**Figure 1A**), of which the Huangliu Formation (N_1h) is a critical exploration target (Xie et al., 2012; Duan et al., 2020). Exposed in anomalous environments characterized by higher pressure coefficient, higher thermal gradient, and CO_2 filling, the Huangliu sandstones have undergone complicated diagenetic history and evolution processes, which provide an excellent opportunity to investigate the complex formation mechanism of reservoirs controlled by HPHT and CO_2 charging. The effect of high temperature, high pressure, and CO_2 filling are studied individually by several published studies in the Dongfang district, yet the integrated impact of the anomalous environments are rarely explored. Utilizing integrated methods of reservoir geology and geochemistry, this study aims to investigate various diagenetic modifications controlled by HPHT and CO_2 charging and unravel the formation mechanisms for the reservoirs of the Huangliu sandstones. By

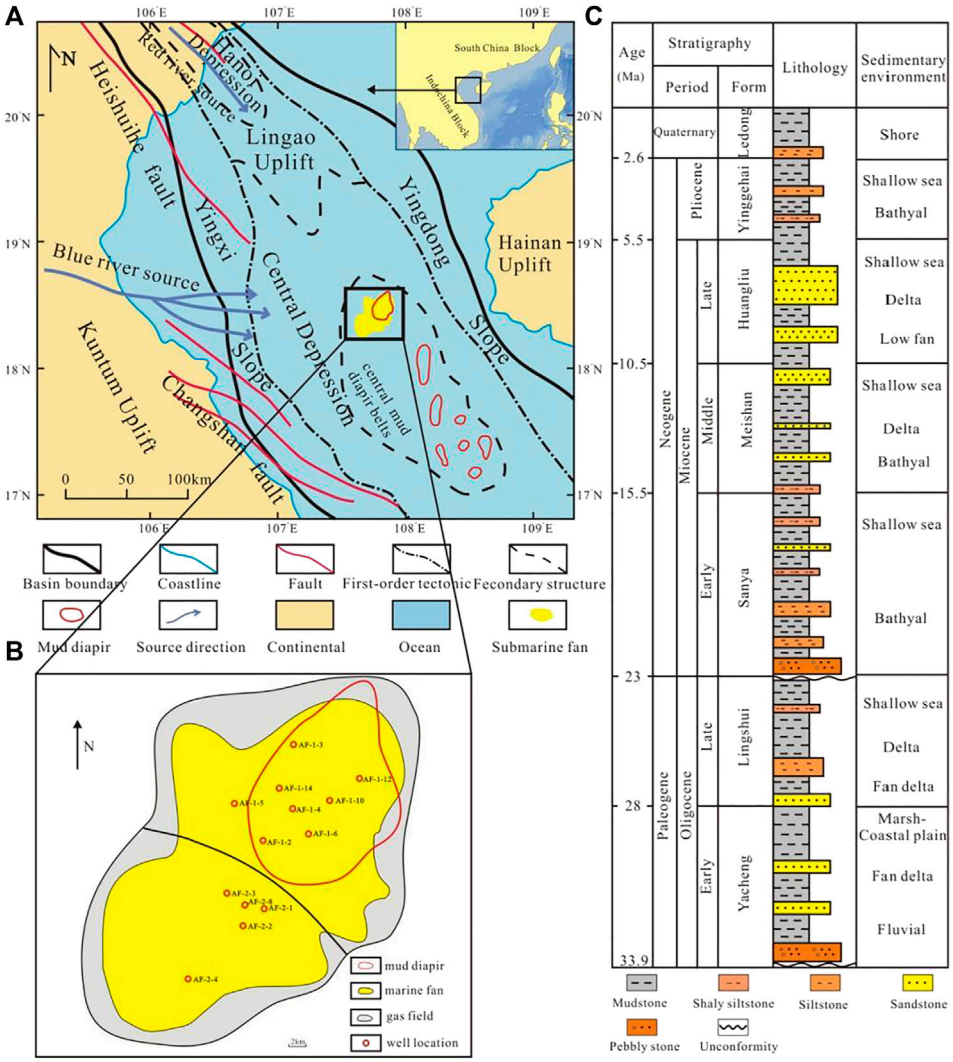

FIGURE 1 | (A) Geographic location of the Yinggehai Basin and the study area. **(B)** Distribution of prospecting wells in the Dongfang district. **(C)** Stratum system of the Dongfang district. (Panel 1A and Panel 1B are modified from Huang et al., 2017; Panel 1C is modified from Duan et al., 2020).

comparative study between the AF-1 and AF-2 areas, the evolution history of porosity and the origin of different distribution tendency of permeability are also discussed. This study case provides valuable insights for understanding the evolution of reservoir quality in the Yinggehai Basin, as well as for similar plays worldwide.

2 GEOLOGICAL SETTING

The Yinggehai Basin is a Cenozoic petroliferous basin developing on the basement of northwestern continental shelf of the South China Sea, with an area of approximate 12×10^4 km^2 (Huang et al., 2017) (**Figure 1A**). With a transform-extensional origin, the basin evolved in accordance with regional lithosphere extension induced by strike-slip movement of the Red River Fault zone (Luo et al., 2003). The basin is generally segmented into three first-order tectonic units: the Yingxi Slope, the Central Depression, and the Yingdong Slope (**Figure 1A**). The Yinggehai Basin is dominated by rapid subsidence and sedimentation rates and accumulates thick-bedded sediments up to 17-km thick (Hao et al., 2000). From bottom to top, the stratigraphic system of the basin mainly contain the Oligocene Yacheng and Lingshui formations; the Miocene Sanya, Meishan, and Huangliu formations; the Pliocene Yinggehai Formation; and the Quaternary Ledong Formation (**Figure 1C**) (Duan et al., 2020). The main source rocks layers are made up of dark gray marine mudstone from supper Sanya Formation and Lower Meishan Formation (Xie et al., 2012). The sandstone- or siltstone-dominated layers associated with deltic or gravity flow deposits in the Huangliu and Yinggehai formations constitute the principal reservoirs (Xie et al., 2012). The basin-scale thick mudstone sequences of overlying Yinggehai Formation mainly act as effective gas-bearing seal (Xie et al., 2012).

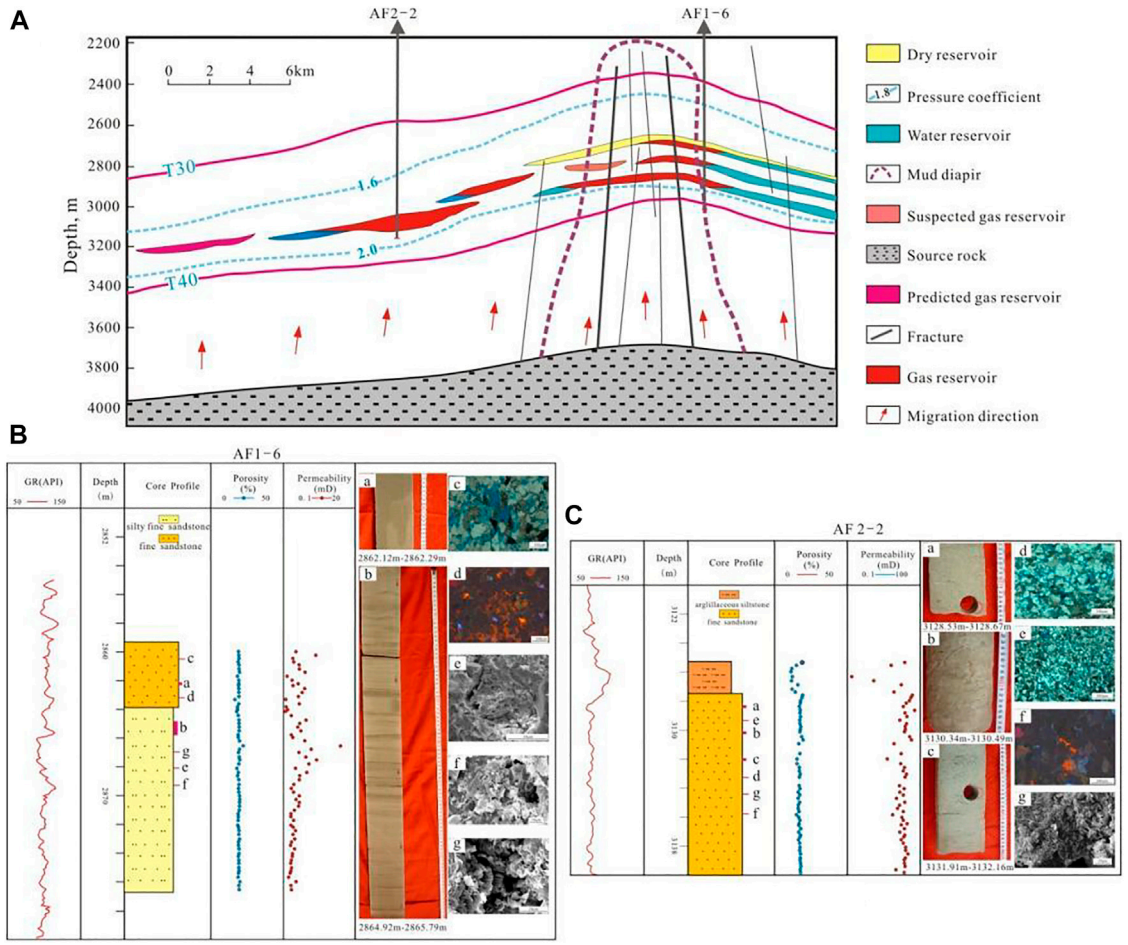

FIGURE 2 | Accumulation model of natural gas accumulation related to mud diapir in the Dongfang district in the Yinggehai Basin **(A)** (modified from Xie et al., 2012). The comprehensive profile comprising logging characteristics, lithology, physical properties, and photographs of cores and diagenetic alterations in well AF-1–6 **(B)** and well AF-2–2 **(C)** in the Dongfang district.

In the Yinggehai Basin, the intensive extension of lithosphere and simultaneous upwelling of asthenosphere are mainly responsible for high geothermal gradient, with an average geothermal gradient of 4.6°C/100 m (Hao et al., 2000). The extensive undercompaction of thick-bedded accumulation of mudrock caused by rapid deposition rate contributes to the generation of overpressure in medium–deep layers (Fu et al., 2016). The hydrocarbon generation and thermal expansion of pore fluids further enhance overpressure (Hao et al., 2000), and the allogenic transmission conducted by episodic fracture opening is also considered as a non-negligible mechanism for heightening overpressure (Luo et al., 2003). The overpressure prevails mostly in the central depression with maximum pressure coefficient of 2.2, and the depth of top boundary of overpressure zone increase from the center to the margin of the basin (Duan et al., 2018). Triggered by extensional stress from strike-slip movement and overpressured plastic mudstone, multicolumn diapirs were developed in the central depression (Hao et al., 2000). With diapir intrusion, the thermal fluid invaded toward the overlying strata, accordingly heightening the geothermal field and pressure field (Hao et al., 2000).

The Dongfang district is one of the principal gas fields in the Yinggehai Basin, with an area of about 2,400 km^2 (**Figure 1B**). The fine-grained sandstones and silty sandstones of the Huangliu Formation are main gas-bearing in the Dongfang Gas Field, which are identified to derive from shallow marine gravity flow with main provenance from Blue River (Huang et al., 2019). Multiple sets of sandy lobes serve as the principal bodies of the Huangliu sandstones, which deposit as multi-period alterations of gravity flow (Huang et al., 2019) (**Figures 2B,C**). The minor part of the eastern AF-1 area with very fine-grained sandstones is determined as neritic sandbar deposition with main source from the Hainan Uplift (Huang et al., 2019). Located around the diapir zone, the AF-1 area suffered multi-period episodic injection of CO_2-rich thermal fluid severely (**Figure 2A**) (Fu et al., 2016). In contrast, the AF-2 area lied far away from the diapir and underwent minimal interference from thermal fluid intrusion (**Figure 1B**) (Fu et al., 2016). The present-day formation temperature of Huangliu sandstones

TABLE 1 | Results of natural gas compositions, stable isotope, formation pressure and temperature of wells from drilling tests in the Huangliu sandstones. MDT: modular formation dynamics tester; DST: drill stem testing.

Well	Depth (m)	Testing methods	Natural gas composition (%)			$\delta^{13}C_1$/‰	$\delta^{13}C_{CO2}$/‰	Pressure factor	Temperature(°C)
			CH_4	C_nH_m ($2 \leq n \leq 5$)	CO_2				
AF-1–12	2,792.6–2,806.3	DST	30.36–34.54	0.62–0.96	53.84–56.38	–30.57	–2.67	1.96–2.07	127.4–140.3
AF-1–14	2,914.0–2,959.0	MDT&DST	65.43–73.59	1.66–1.73	18.38–23.46	–31.76	–3.87	1.89–1.92	132.8–143.6
AF-1–2	2,977.3–3,054.6	MDT	—	—	—	—	—	1.87–1.89	129.5–140.7
AF-1–4	2,833.6–2,879.0	MDT&DST	35.18–64.26	1.31–1.39	23.60–53.62	–32.47	–6.19	1.92–1.95	124.0–137.8
AF-1–6	2,815.8–2,863.0	MDT&DST	18.73–22.31	0.34–0.82	71.26–73.85	–35.54	–4.55	1.95–1.98	136.4–137.3
AF-2–1	2,973.2–3,125.3	MDT	88.83–94.26	2.51–3.36	1.36–5.78	–32.34	–15.24	1.75–1.83	129.4–142.1
AF-2–2	3,035.6–3,142.9	MDT	92.53–93.65	2.83–2.89	2.64–3.18	–32.97	–19.66	1.72–1.78	131.8–142.4
AF-2–4	3,215.3–3,441.8	MDT	96.26–97.93	0.14–0.28	1.42–3.43	–32.54	–18.58	1.66–1.72	135.6–148.6

present minor distinction (**Table 1**), but the homogenization temperature of fluid inclusion indicate that the AF-1 area has experienced anomalously higher temperature (112–193°C) than the AF-2 area (66–131°C) in diagenetic history (Hao et al., 2000; Duan et al., 2020). The AF-1 area shows a higher pressure coefficient (1.87–2.07) than that of the AF-2 area (1.66–1.83) (**Table 1**). The CO_2 contents of wells intervals in the AF-1 area (18.38–73.85 vol%) are obviously higher than that of the AF-2 area (1.36–5.78 vol%) (**Table 1**).

3 SAMPLES AND METHODS

To investigate lithofacies and sedimentary structures, 46-m core intervals were observed and depicted from eight wells in total (Wells AF-1–12, AF-1–2, AF-1–3, AF-1–4, AF-1–6, AF-2–1, AF-2–2, and AF-2–8, shown in **Figure 1B**), from which all core plugs and cutting samples were collected and processed to study the petrological feature, diagenetic alteration, and physical properties. All of experiments and analyses were conducted at the State Key Laboratory of Oil and Gas Reservoir Geology and Exploitation, Chengdu, China.

The thin sections (163 samples) were impregnated with blue epoxy resin and stained with alizarin red S and K-ferricyanide to examine pores structure and recognize carbonate cements. A DMAX-3C X-ray diffraction (Rigaku Corporation, Tokyo, Japan) was employed to measure the composition of clay minerals with 118 cutting samples. The cathode luminescence (CL) examinations for 47 samples of polished thin sections were finished using a MK5-2 stage (CITL, Hertfordshire, England), with a voltage of 14 kV, an electric current of 380 μA. To distinguish the genesis of carbonate cements, 15 sandstone samples were examined for stable carbon and oxygen isotope composition, which were completed by a MAT253 isotope ratio mass spectrometer (Thermo Fisher Scientific, Waltham, MA, United States), with a precision of 0.0037‰ for $\delta^{13}C$ and 0.013‰ for $\delta^{18}O$. The results were reported with respect to the Vienna Pee Dee Belemnite (VPDB). The measurements of homogenization temperature fluid inclusions from 22 samples were conducted by a cooling–heating stage of THM600 (Linkam Scientific, Surrey, England). To upgrade the accuracy, every sample analysis was repeated at least three times, with a precision of ± 1°C. To clearly detect the texture of cements and clay minerals, 45 samples were selected with carbon coated for scanning electron microscope (SEM) observation, which were completed by an apparatus of Quanta 250 FEG (FEI Company, Hillsboro, OR, United States) under an acceleration voltage of 20 kV and a filament current of 240 mA. The determinations of elemental composition of cements (12 samples) were conducted by an EPMA-1720 H Series electron probe (Shimadzu Corporation, Kyoto, Japan), with an acceleration voltage of 15 kV and an electric current of 10 nA.

For physical properties investigation, 135 core plugs and 112 core plugs were collected from the AF-1 area and the AF-2 area, respectively. The porosity tests were conducted by a helium porosimeter (UltraPore-300) and permeability analyses were completed by an air-permeability instrument (UltraPerm-400). This study selected five core plugs and two core plugs from the AF-1 area and the AF-2 area, respectively, to research reservoir microstructure. The constant-rate mercury injection was employed to analyze pore-throat size, and an automatic pore structure tester (ASPE-730) was adopted to accomplish the test with a parameter accuracy of 0.001 μm.

4 RESULTS

4.1 Reservoir Characteristics

4.1.1 Petrology Feature

The Huangliu sandstones of the AF-1 area are dominated by very fine- and fine-grained sandstones, mostly classified as lithic quartz sandstones according to classification scheme proposed by Folk (1980) and averaged as $Q_{79.3}$ $F_{6.1}$ $L_{14.6}$. By contrast, the AF-2 area is featured predominantly by feldspar lithic sandstones and slightly coarser grain size, with an average compositional value of $Q_{74.6}$ $F_{9.1}$ $L_{16.3}$. The contents of monocrystalline quartz (av. 51.3%) evidently surpass that of polycrystalline quartz (av. 4.8%), and the proportion of K-feldspar (av. 5.4%) is higher than that of plagioclase (av. 1.2%), and metamorphic lithic fragments (av. 7.7%) is much more richer than volcanic lithic fragments (av. 0.9%). As a whole, the interstitial materials are dominated by detrital and authigenic clay minerals and carbonate cements, with minor siliceous cements. Generally, the Huangliu sandstones are

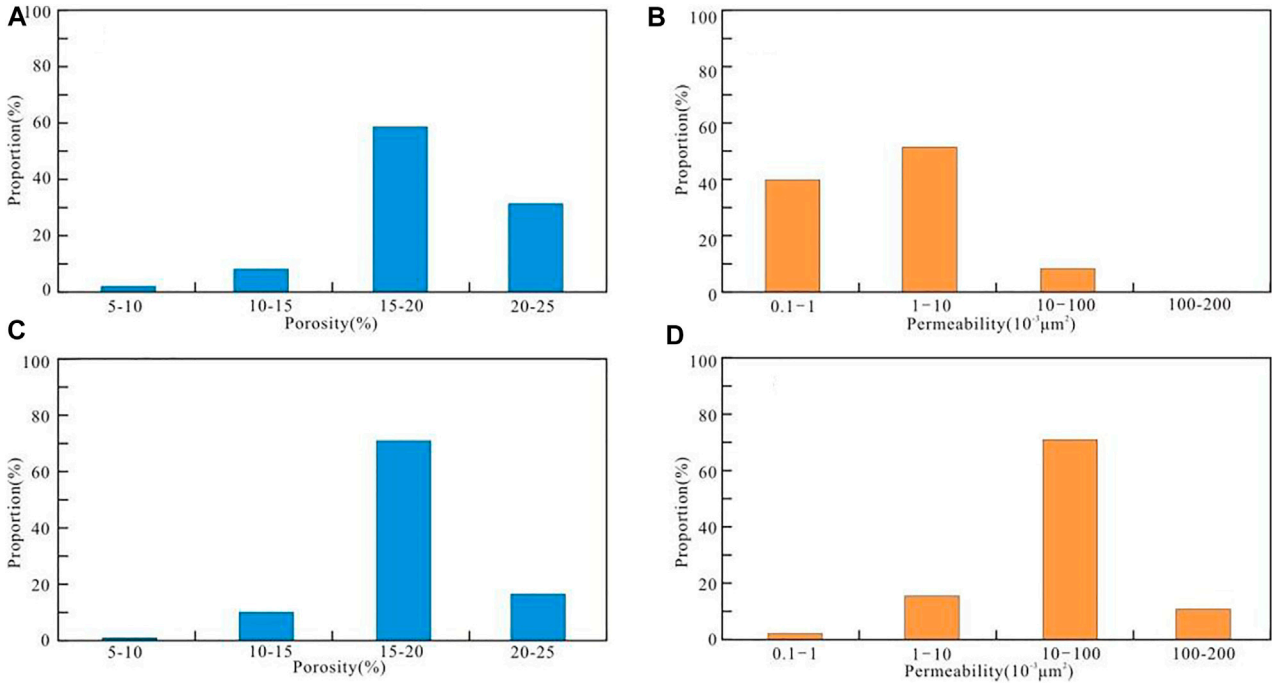

FIGURE 3 | Distribution characteristics of **(A)** the porosity in the AF-1 area, **(B)** permeability in the AF-1 area, **(C)** porosity in the AF-2 area, and **(D)** permeability in the AF-2 area in the Huangliu sandstones.

moderately to well sorted, mainly grain supported, and subangular to subround.

4.1.2 Porosity and Permeability

The average value of porosity in the AF-1 area (18.4%) is slightly higher than that of the AF-2 area (17.9%), with a median distribution span from 14.6% to 22.4% (**Figure 3**). However, the permeability of the Huangliu sandstones in the AF-2 area is dramatically higher than that of the AF-1 area (**Figure 3**). The values of permeability range from 0.1 to 10 mD (81% of total samples) in the AF-1 area and from 10 to 100 mD (72% of total samples) in the AF-2 area (**Figure 3**). Most intervals of the Huangliu sandstones in the AF-1 area belong to medium-porosity and low-permeability reservoirs, while that of the AF-2 area are mainly ranked as medium-porosity and medium-permeability reservoirs.

4.1.3 Microscopic Pore Structures

The measurements by constant-rate mercury injection show that the distribution tendency of pore radii presents a smaller difference between the samples of the AF-1 area and the AF-2 area (**Figure 4A**). However, the performance of pore-throats radii distribution reveals prominent distinction: the dominated extent of samples from the AF-1 area range from 0.5 to 2.3 μm while that of the AF-2 area range from 4.2 to 5.5 μm (**Figure 4B**). Correspondingly, from the perspective of physical properties, the samples from the AF-1 area show low permeability, and those of the AF-2 area display medium permeability.

4.2 Diagenesis

In the Dongfang district, the combinations of anomalous geothermal field, pressure, and thermal fluid, present considerable heterogeneous distributions in time and space, which control diagenetic alterations significantly and result in a wide variety of responses on authigenic minerals and pore-throat microstructure.

4.2.1 Compaction

The mechanical compaction can be observed ubiquitously in the Huangliu sandstones, which are visibly confirmed with bended strip-shaped minerals and deformation of ductile fragments (**Figures 5A,B**). The types of grains contacts mostly center on planar and spot-line and concavo-convex contacts is subordinate, whereas the pressure solution of framework grains is almost unobservable (**Figures 5A,B**). The measured porosities can still maintain 19–23% than expected at the equivalent buried depth of 2800–3000 m. The anomalous variations of porosity–depth trend deviating from routine situation indicate that compaction degree is relatively weaker, which facilitate the preservation of primary porosity.

4.2.2 Cementation

4.2.2.1 Carbonate cements

The carbonate cements in the Huangliu sandstones mainly consist of siderite, calcite, ferrocalcite, dolomite, and ankerite, and present multistage geneses and regional variations. The total amounts of carbonate cements in the AF-1 area are significantly higher than that of the AF-2 area (**Table 2**). The carbonate

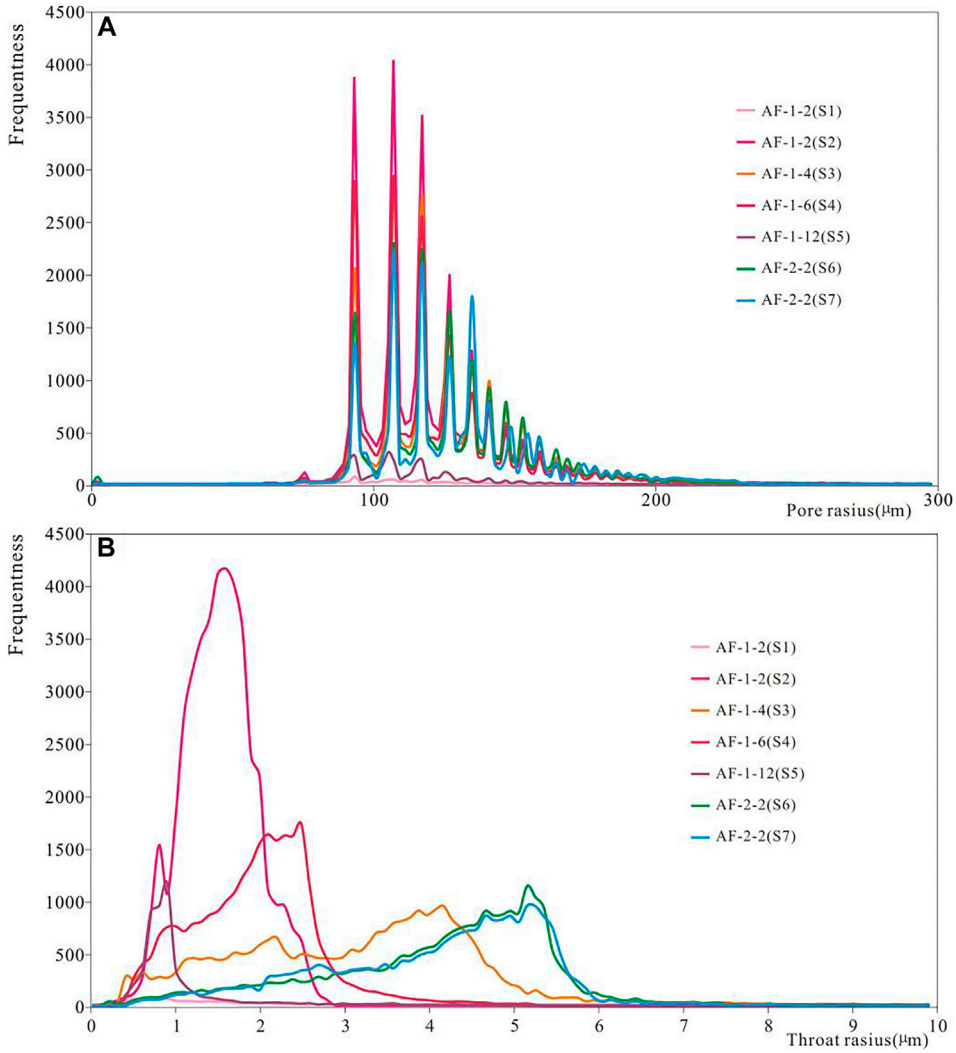

FIGURE 4 | Distribution curves of **(A)** pore radius and **(B)** throat radius from seven samples of the Huangliu sandstones in five wells from the AF-1 area and the AF-2 area, respectively.

cements in the AF-1 area mainly are composed of ankerite and siderite, while that of the AF-2 area are dominated by ferrocalcite and calcite (**Table 2**).

Early carbonate cements containing siderite, calcite, and dolomite mainly occur around grains as discontinuous coating and replace calcareous bioclastic (**Figure 5C**). A considerable amount of cements fill the intergranular pores as assemblage texture, or partly replace feldspar grains (**Figures 5D,E**; **Figure 6E**). The precipitation of ferrocalcite, symbolizing mesogenetic cements, are detected as glow dull red under CL and present as pore-filling and replacing grains (**Figures 5D,E**; **Figure 6D**), with a content of 0.3–1.0 vol% and 1.2–2.3 vol% in the AF-1 area and the AF-2 area, respectively (**Table 2**). The late carbonate cements principally include ankerite and siderite and are mostly distributed in the AF-1 area (**Table 2**). With coarser crystallinity and rhombohedron shape, ankerite generally fill intergranular pores and dissolved pores, or replace early cements (**Figure 6A**), with a fraction up to 7.1 vol% in the AF-1 area (**Table 2**). Unlike early analogue, late siderite exhibit better crystallinity and is relatively abundant in the AF-1 area, occurring as pore-filling constituent in dissolved pores or intermixing with clay minerals as hybrid agglomerate (**Figure 6C**). The coarser crystallinity implies an indicator of high-temperature genesis for siderite and ankerite.

4.2.2.2 Siliceous Cements

By observation of SEM, the overgrowth of euhedral microquartz can be detected on the surface of quartz grains (**Figure 6B**), and pore-filling aggregates of authigenic microquartz coexisting with authigenic filiform illite or I/S mixed-layer are also found (**Figures 7C,D**). Macroquartz cements and well-developed overgrowth are rarely observed, which indicate that the intensity of siliceous cementation is fairly weaker in the

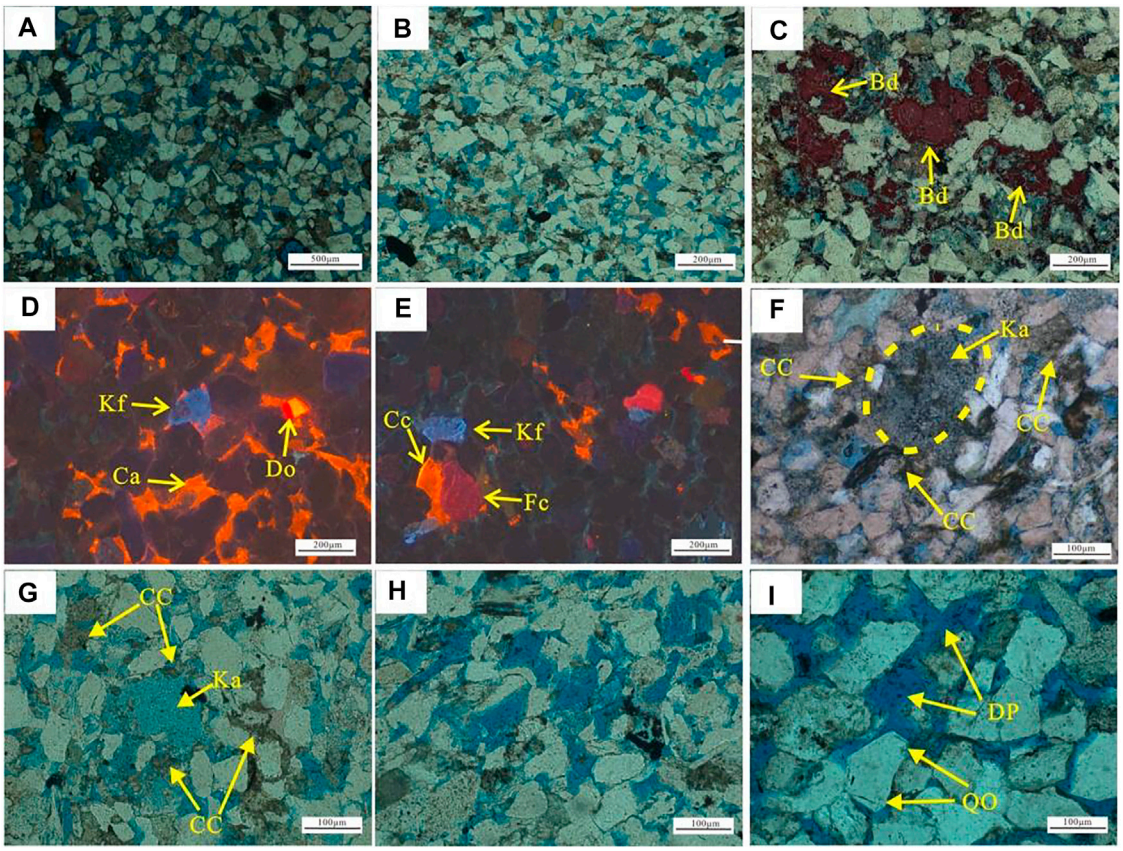

FIGURE 5 | Photomicrographs showing diagenetic characteristics of the Huangliu sandstones. **(A)** Well AF-2–1, 2,977.15 m, primary pores are well developed, and the types of particles contacts are dominated by line-point and planar. **(B)** Well AF-1–2, 3,040.96 m, weak compaction and dissolution pores are distributed widely. **(C)** Well AF-1–2, 2,992.16 m, biodetritus (Bd) are replaced by early carbonate cements. **(D)** Well AF-2–2, 3,134.16 m, calcite (Ca), dolomite (Do), and K-feldspar (Kf) fill intergranular pores. **(E)** Well AF-2–2, 3,067.64 m, the ferrocalcite (Fc) replace calcite (Ca) partly, and K-feldspar (Kf) are dissolved to some extent. **(F)** Well AF-1–2, 2,981.15 m, kaolinite (Ka) caused by feldspar dissolution exist in dissolved pores, and carbonate cements (CC) block pores and throats. **(G)** Well AF-1–2, 2,987.93 m, sandstones encounter strong dissolution, and related residual kaolinite and carbonate precipitation disperse in pore-throats. **(H)** Well AF-1–2, 3,047.09 m, feldspar grains are strongly dissolved to form large pores and enlarge intergranular pores. **(I)** Well AF-2–4, 3,215.5 m, fewer residues are left in dissolution pores (DP), and quartz overgrowth (QO) develops on detrital quartz.

TABLE 2 | Volume fraction of carbonate cements in the Huangliu sandstones.

Well	Calcite	Ferrocalcite	Dolomite	Ankerite	Siderite	Carbonate cements
	Average value (minimum to maximum value) φ_B/%					
AF-1–12	0.2 (0.1–0.3)	0.3 (0.1–0.5)	0.7 (0.5–1.0)	4.8 (2.5–6.3)	1.9 (1.2–3.6)	8.1 (6.2–11.1)
AF-1–14	0.3 (0.1–0.4)	0.3 (0.1–0.4)	0.6 (0.5–0.9)	3.4 (2.2–4.9)	1.7 (1.0–2.2)	6.9 (4.4–8.6)
AF-1–2	0.2 (0.1–0.5)	0.4 (0.1–0.6)	0.8 (0.5–1.5)	4.4 (2.2–5.3)	1.8 (0.9–2.5)	7.8 (5.1–9.8)
AF-1–4	0.2 (0.1–0.4)	0.7 (0.2–1.0)	0.7 (0.6–0.9)	5.1 (3.6–6.2)	1.4 (0.8–2.1)	8.8 (5.8–10.1)
AF-1–6	0.2 (0.1–0.5)	1.0 (0.2–1.4)	0.9 (0.6–1.7)	5.8 (4.6–7.1)	1.7 (1.0–2.4)	9.5 (7.3–12.2)
AF-2–1	0.2 (0.1–0.3)	1.3 (0.4–1.7)	0.6 (0.2–0.9)	0.5 (0.1–0.8)	0.8 (0.6–1.4)	3.2 (1.8–4.9)
AF-2–2	0.3 (0.1–0.4)	2.3 (1.1–3.5)	0.3 (0.1–0.5)	0.4 (0.2–0.7)	0.5 (0.2–0.8)	3.6 (1.9–5.1)
AF-2–4	0.2 (0.1–0.5)	2.2 (0.8–4.7)	0.2 (0.1–0.3)	0.2 (0.1–0.4)	0.2 (0.1–0.3)	2.8 (1.6–5.7)
AF-2–8	0.3 (0.1–0.4)	1.2 (0.5–1.5)	0.8 (0.3–1.2)	0.4 (0.2–0.6)	0.6 (0.2–1.0)	3.1 (1.9–4.5)

Huangliu sandstones. Conventionally, siliceous cementation shows higher sensibility to high temperature (Osborne and Swarbrick, 1999); nevertheless, the authigenic quartz and quartz overgrowth are determined in trace amount (<0.5 vol %) to minor amount (0.5–1.2 vol%). Previous studies demonstrate that weaker quartz overgrowth is closely related to the restriction of overpressure (Osborne and Swarbrick, 1999; Bloch et al., 2002).

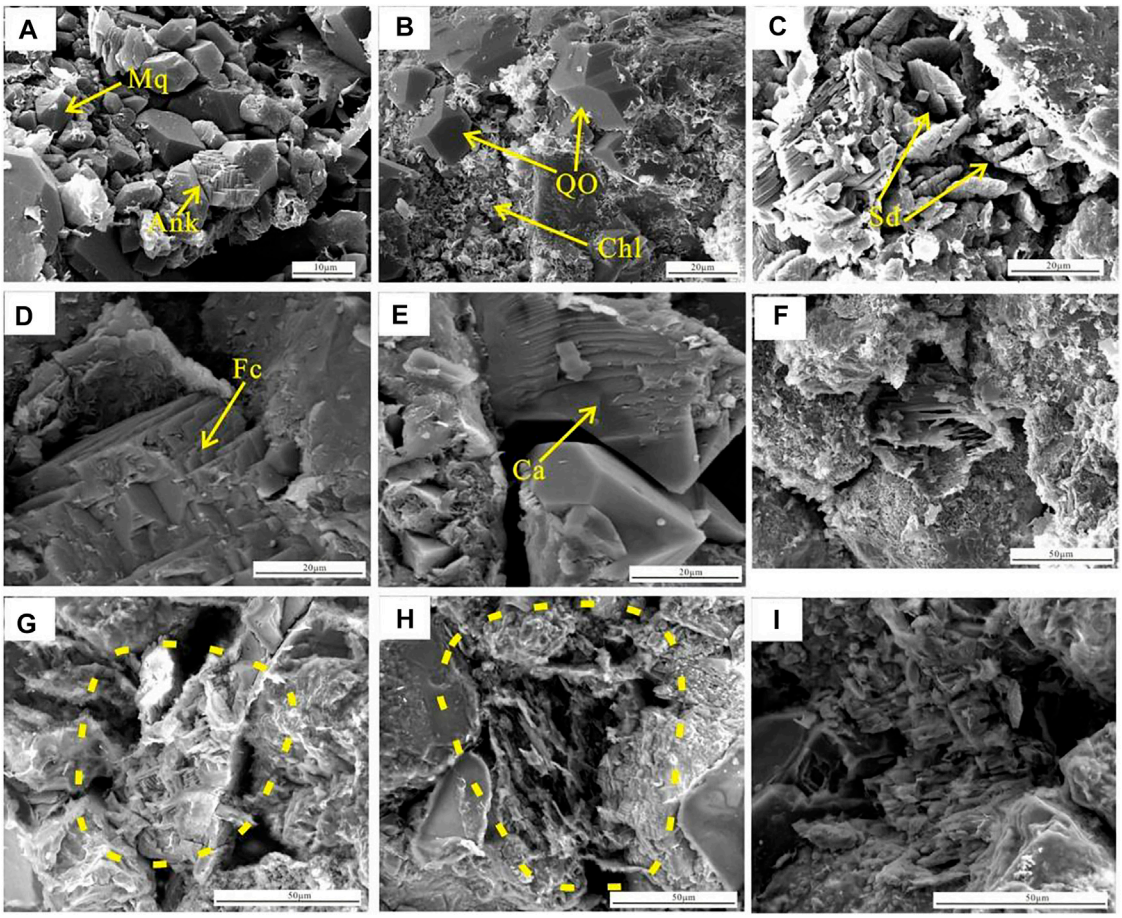

FIGURE 6 | Typical SEM photographs of diagenetic alterations in the Huangliu sandstones. **(A)** Well AF-1–6, 2,875.68 m, ankerite (Ank) and microquartz (Mq) exist in intergranular pores. **(B)** Well AF-1–12, 2,710.46 m, microquartz overgrowth develop on quartz grain with authigenic chlorite (Chl). **(C)** Well AF-1–6, 2,874.82 m, discus shape siderite (Sd) fill in dissolved pores. **(D)** Well AF-2–1, 3,004.12 m, ferrocalcite generate between particles and replace feldspar. **(E)** Well AF-2–1, 2,996.28 m, the intergranular space is taken up by calcite, and the cementation is partly corroded. **(F)** Well AF-1–4, 2,869.85 m, feldspar is subjected to heavy dissolution. **(G)** Well AF-1–2, 2,990.78 m, K-feldspar is dissolved and filiform illite exsit in pores and throats. **(H)** Well AF-1–3, 2,907.12 m, the feldspar is corroded and complex micropores develop. **(I)** Well AF-2–1, 3,110.38 m, K-feldspar is leached partly.

4.2.3 Authigenic Clay Minerals

The examination of XRD and SEM indicate that authigenic clay minerals in the Huangliu sandstones mainly contain illite, kaolinite, chlorite, and I/S mixed-layer. The AF-1 area presents higher relative contents of illite and kaolinite but extremely lower relative content of chlorite (**Figure 8**). The AF-2 area is dominated by higher relative fraction of chlorite and relatively lower relative proportion of kaolinite and illite (**Figure 8**).

The content of illite in the AF-1 area (51–62 wt% of total clay fraction) is obviously higher than that of the AF-2 area (18–31 wt% of total clay fraction) (**Figure 8**). The illite chiefly occur as filling-pores and blocking throats with a fibrous or pore-bridging form (**Figures 6G, 7D**), and in some places, surround grains as a flocculent grain-coating (**Figure 7C**). Controlled by high geothermal gradient, smectite disappear at a shallower burial depth, and thus can be rarely detected. The samples close to diapir show higher proportion of illite (90–95%) within a well-ordered I/S mixed-layer.

As identified by XRD, the kaolinite of the AF-1 area occurs with a fairly higher content (21–26% of total clay fraction) than that of the AF-2 area (12–16% of total clay fraction) (**Figure 8**). Detected by SEM, authigenic kaolinite commonly occur as pore-filling nature with vermiform or booklet texture (**Figures 7E,F**). In some cases, the kaolinite interlace with authigenic illite and chlorite, implying that they may have a genesis link. The extensive replacements of feldspar by authigenic kaolinite demonstrate that the dissolution acts as a significant developing mechanism for authigenic kaolinite (**Figures 5F,G**).

The chlorite contents in the AF-1 area range from trace to 8% of total clay fraction (**Figure 8**). By contrast, the chlorite in the AF-2 area presents obviously well-developed, accounting for 27–32%, total clay fraction (**Figure 8**). The authigenic chlorite display as needle-shaped or leaf-like platelets and generally surround particles as coating, or exist in intergranular pores (**Figures 7A,B**). The authigenic

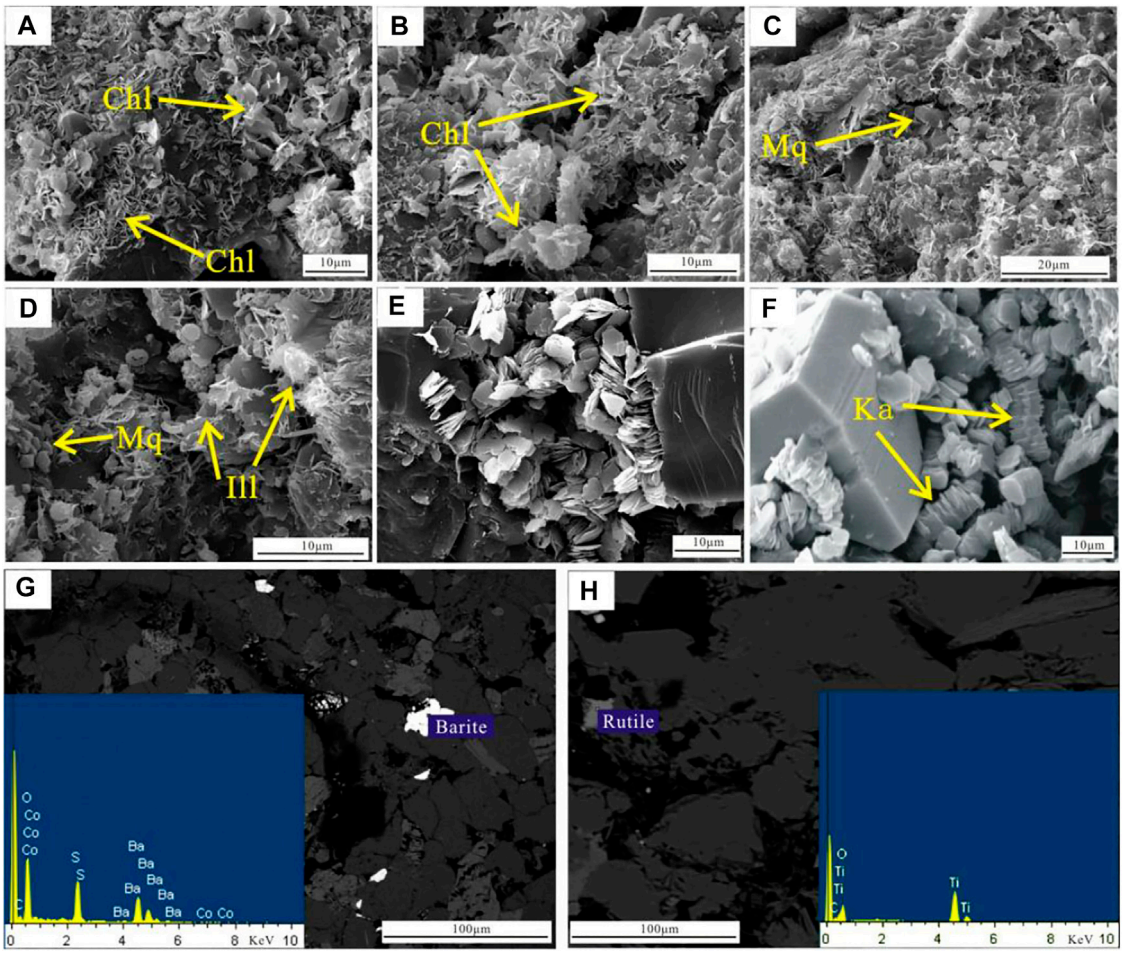

FIGURE 7 | Images of SEM and EMPA of authigenic clay minerals and hydrothermal minerals in the Huangliu sandstones. **(A)** Well AF-2–1, 3,042.12 m, needle-shaped and foliated chlorite present on particle surface. **(B)** Well AF-2–8, 3,082.65 m, needle-shaped chlorite wrap the surface of particle. **(C)** Well AF-1–12, 2,712.75 m, filamentous and foliaceous illite cover feldspar grain and microquartz (Mq) are encircled by illite and chlorite aggregate. **(D)** Well AF-1–12, 2,706.58 m, foliaceous and threadlike illite fill intergranular pores, and microquartz grains are surrounded by authigenic illite and chlorite. **(E)** Well AF-1–6, 2,861.32 m, abundant plate shape authigenic kaolinite fill interparticle space. **(F)** Well AF-1–4, 2,867.44 m, vermiform authigenic kaolinite exist in dissolved pore. **(G)** Well AF-1–6, 2,861.54 m, authigenic hydrothermal mineral of barite is detected. **(H)** Well AF-1–12, 2,709.71 m, hydrothermal mineral of rutile is found.

micoquartz partly develop on chlorite coating (**Figure 6B**), implying that chlorite rim formed before early quartz overgrowth. In addition, some microquartz are enclosed by pore-filling chlorite in dissolved pores, indicating that authigenic chlorite also has a late-period genesis (**Figures 7C,D**). Authigenic chlorite exert a non-negligible control on reservoir quality, and the significance of chlorite grain-coating on preserving primary porosity has been documented by numerous publications (Bloch et al., 2002; Taylor et al., 2010).

4.2.4 Dissolution

Based on thin section and SEM, the Huangliu sandstones have experienced severe dissolution, especially in the AF-1 area (**Figures 6F–I**). K-feldspar, plagioclase, and unstable lithic fragments constitute main material basis for multistage corrosion caused by multiple medium including mixed water, organic acids and CO_2-rich fluid (**Figures 5G–I**). Abundant moldic pores and oversized dissolved pores are mostly filled with vermicular stacked pseudohexagonal kaolinite (**Figures 7E,F**) and mixed assemblage of late-stage carbonate cements (**Figures 6A,C**), evidently revealing strong intensity of corrosion. By pore-count data from casting thin section, the visual dissolved porosities account for 46–48% of total porosities in the AF-1 area. In the AF-2 area, the dissolution strength appears relatively weaker, with a secondary porosity proportion of 19–22%. The honeycomb texture of partially dissolved feldspar, the marginal erosion with poorly defined boundaries of particles, and the incomplete corrosion for early cements all support a scenario of moderately to poorly dissolved status for investigated sandstones in the AF-2 area (**Figure 6I**), simultaneously with minor residues in the dissolved cavities (**Figure 5I**).

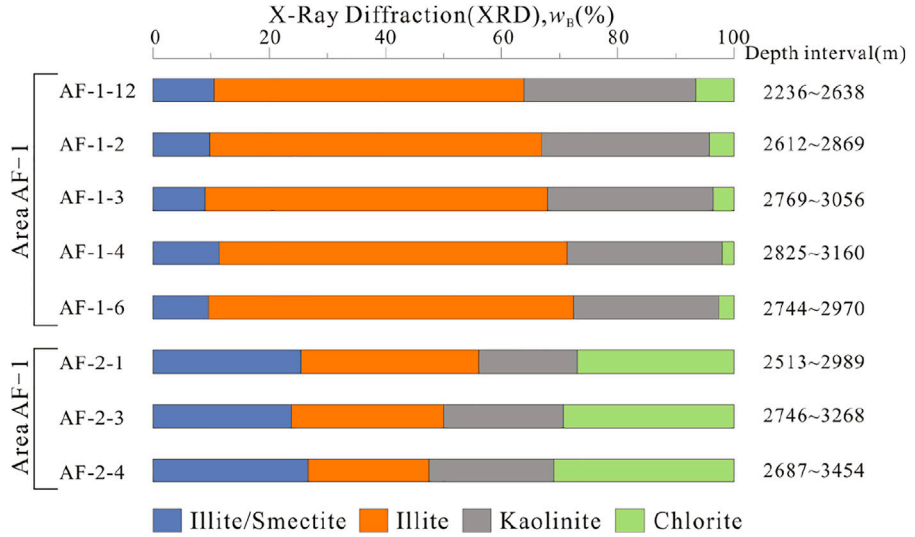

FIGURE 8 | Relative contents of clay minerals within the Huangliu sandstones from eight wells in the AF-1 area and the AF-2 area.

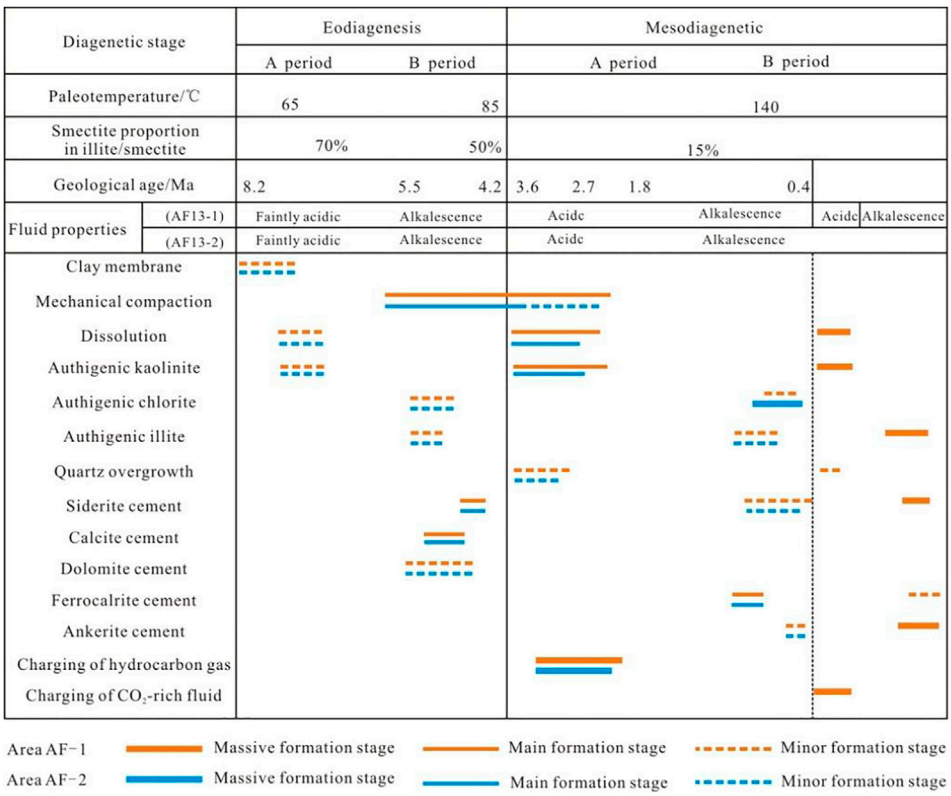

FIGURE 9 | Diagenetic sequence of the Huangliu sandstones in the AF-1 area and the AF-2 area.

4.2.5 Authigenic Hydrothermal Minerals

Determined by EPMA, the authigenic hydrothermal minerals of barite ($BaSO_4$) and rutile (TiO_2) are recognized in some intervals of the AF-1 area, and account for trace to 0.3 vol% of whole rock composition, with euhedral crystals mainly existing in intergranular pores (**Figures 7G,H**). Although exerting a minor influence on reservoir quality, the barite and rutile are suggested as an important indicator for occurrence of thermal fluid activity under high-temperature setting (Shi et al., 2014).

5 DISCUSSION

5.1 Heterogeneity of Diagenetic Phase and Paragenesis Sequence

The integrated analyses of authigenic minerals, petrologic structure and pore microstructure suggest that the AF-1 area mainly reach B-period of mediate diagenetic stage, while the AF-2 area mostly are maintained in the A-period of mediate diagenetic stage (**Figure 9**), as defined by Ying et al. (2003). This is also evidenced by thermal evolution indicators: 1) the AF-1 area present higher R_o value (0.88–1.4%) than that of the AF-2 area (0.58–1.05%); 2) the homogenization temperatures of fluid inclusion in the AF-1 area are higher than that in the AF-2 area on the whole; 3) the fraction of illite in I/S mixed-layer is 90–95% in the AF-1 area, with a lower range of 80–90% in the AF-2 area.

The intervals of the Huangliu sandstones in the AF-1 area (2700–2900 m) are shallower than that of the AF-2 area (2900–3100 m), whereas the diagenetic stages are contradictory to the equivalent depths. Previous studies suggest that the Huangliu sandstones have experienced overpressure, which can restrict diagenetic intensity to some extent (Duan et al., 2018). In addition, the AF-1 area suffered multistage thermal fluid activity, which elevated geothermal gradient dramatically and contributed to advanced diagenetic stage in the AF-1 area (Hao et al., 2000).

According to petrographic texture relationship, sequential order of authigenic minerals and burial history, the paragenetic sequence of the Huangliu sandstones are summarized as **Figure 9**. The AF-1 and AF-2 areas experience analogous paragenetic sequence of eodiagenesis and early stage of mesogenesis, and the relative onset timing are reconstructed as **Figure 9**. In addition, during late mesogenetic stage, the AF-1 area suffered multistage CO_2 charging, which caused significant modifications of paragenesis in the AF-1 area: 1) large-scale dissolution of feldspar particles; 2) extensive conversion of clay minerals, and 3) major precipitation of carbonate cements.

5.2 Overpressure Intensity and Occurring Timing

The effect of overpressure on preservation of primary porosity has been evidenced by considerable a few of literature (Gluyas and Cade, 1997; Bloch et al., 2002; Taylor et al., 2010). Fluid overpressure decreases VES to various extent, and therefore lightens the load of sediments during ongoing compaction, which acts as a chief mechanism for resisting mechanical compaction and maintaining intergranular porosity (Bloch et al., 2002; Nguyen et al., 2013). Under parallel depositing setting and buried depth, the potential of porosity preservation have positive correlation with the magnitude of overpressure (Gluyas and Cade, 1997). In addition, the early occurring timing of fluid overpressure is generally favorable for the capacity against compaction (Paxton et al., 2002).

Overpressure prevails in the Huangliu sandstones and play a significant role in compaction trend and primary porosity preservation. In this study, the contacting index (CI), as defined by Liang et al. (2011) and illustrated by **Formula 1**, is adopted to quantitatively assess the potential of overpressure on resistance to compaction, which is calculated by a function related to the various grain contact patterns conducted by thin section counting (Liang et al., 2011).

$$CI = (a + 1.5ab + 2b + 3c + 4d)/(a + ab + b + c + d) \quad (1)$$

(Liang et al., 2011) Notation: a-number of points contact; ab-number of point-line contacts; b-number of line contacts; c-number of concave and convex contacts; d-number of suture contacts.

According to Liang et al. (2011), CI is classified by three categories: weak compaction (1.0–1.5), medium compaction (1.5–2.5), strong compaction (>2.5). For detailed comparison, this research further subdivides medium compaction into grade I medium compaction (CI ~ 1.5–1.8) and grade II medium compaction (CI ~ 1.8–2.5). The CI values calculated show that the AF-1 area are dominated by grade I medium compaction and that of the AF-2 area almost fall into the scope of grade II, showing that the compaction of the AF-1 area is stronger than that of the AF-2 area (**Figure 10**). The tests data show the present-day strata pressure of the AF-1 area exceeds that of the AF-2 area (**Table 1**), which is inconsistent with the trend of compaction degree. Given the similar depositing environments, the occurring timing of overpressure should be considered to interpret the anomalous trend.

Considering the origin of overpressure, the modeling of interval transit time (ITT) for mudstone is suitable to estimate the occurring timing of the overpressure (Duan et al., 2018). The

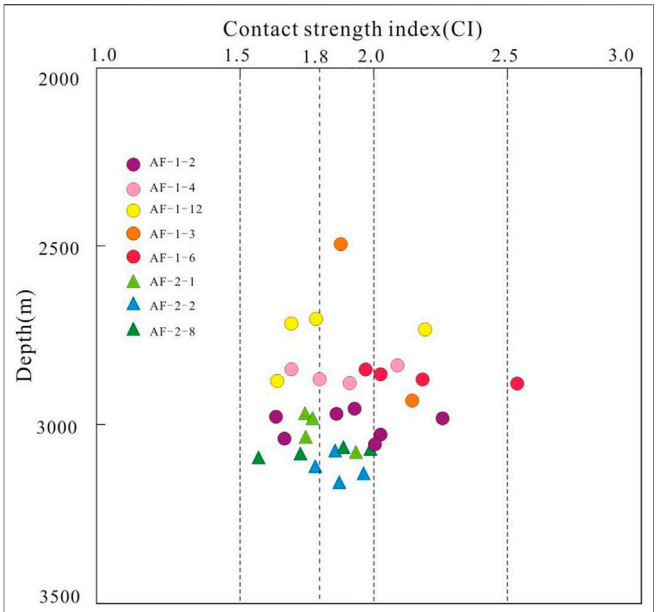

FIGURE 10 | The relationships of contact strength index (CI) vs. depth in eight wells from the AF-1 area and the AF-2 area.

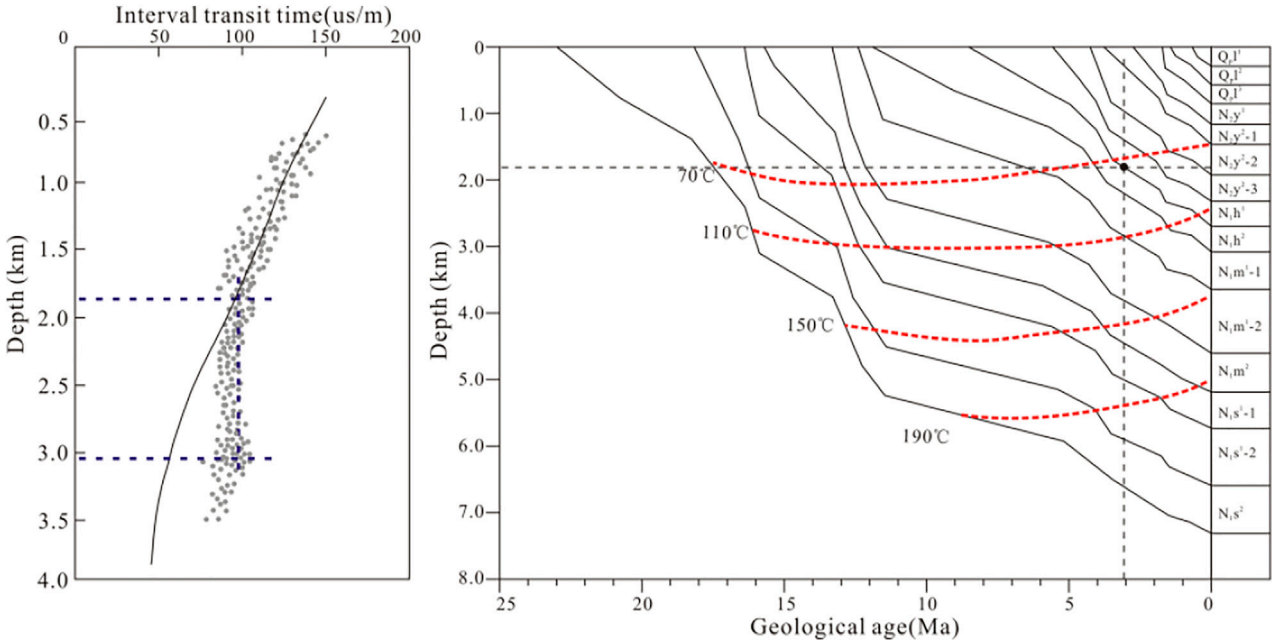

FIGURE 11 | Schematic diagram of the calculation theory about onset timing for overpressure in well AF-1–2.

ITT deviating toward normal compaction curve indicate that compacting process start to suffer overpressure, at which depth the overpressure occurred (Fu and Zhang, 1998). The depth of deviating point is projected on the corresponding burial history, and synchronously the occurring timing of overpressure is determined (**Figure 11**). With the computed results, the occurring time of overpressure in the AF-2 area (2.8–3.0 Ma) are earlier than the AF-1 area (2.7–2.8 Ma), which is considered as the significant reason to explain weaker compaction in the AF-2 area. During late diagenetic stage, the multiphase episodic intrusion of CO_2 enhance the pressure field and geothermal gradient in the AF-1 area, which is mainly responsible to higher present-day strata pressure. The overpressure can work for preserving primary porosity only at the moment when grains are still bearing ongoing compaction (Paxton et al., 2002), and therefore a late-period strengthening of overpressure subsequent to fully compacted status has only minor contribution to preserving primary porosity. This argument provides a more valuable insight into elucidating a higher ratio of primary porosity and weaker compaction degree but with deeper burial depth in the AF-2 area compared with the AF-1 area.

5.3 Multi-Phase Cementation and Dissolution in Diverse Diagenetic System

During dissolution–reprecipitation reactions, the diagenetic system exhibiting open or closed geochemical constrains determine the scale of mass transport, resulting in various by-products and authigenic minerals assemblages, and profoundly influencing reservoir quality (Bjørlykke and Jahren, 2012; Yuan et al., 2015).

In early diagenesis, the near-surface dissolution of silicate minerals induced by mixed marine and meteoric waters commonly occur in open geological system, which are mainly controlled by the flowing rate of pore fluid and undersaturation degree of solution (Bjørlykke and Jahren, 2012). The Huangliu sandstones deposit in lowstand systems tract (Huang et al., 2019), which provide preferable conditions for mixed water dissolution (Morad et al., 2000). Although the early dissolution is weaker and lasts a short duration because of lower temperature and H^+ concentration, the open geochemical system contribute to enhancing dissolved porosity.

With abnormally high geothermal gradient, the thermal decarboxylation of adjacent mudstone began to generate organic acids at an earlier time in the Dongfang district (Barth and Bjørlykke, 1993; Hao et al., 2000). Fluid inclusion geochemistry and kinetics simulation of hydrocarbon generation indicate that initial timing of hydrocarbon charging occurred at 3.7 Ma approximately in the Huangliu sandstones (Xie et al., 2012), and the expulsion of accompanying organic acids generally are proposed to arise before or during hydrocarbon charging (Surdam et al., 1989). The above research show that the overpressure of the Huangliu sandstones formed at 2.7–3.0 Ma, and appeared posterior to organic acids filling, implying that organic acids dissolution predated overpressure. Before overpressure forming, the progressive compaction provided driving force for advective and diffusive mass transport of pore fluids, which served as an open or semi-open geochemical system for mass transport (Bjørlykke, 2014). Consequently, the residual by-products induced by organic acid leaching can be discharged to various

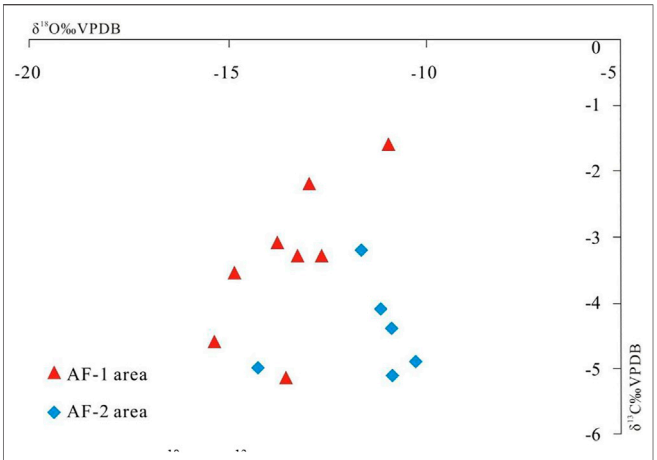

FIGURE 12 | Scatter diagram of δ18 O vs. δ13C for calcite cements in the Huangliu sandstones.

degree, which enhanced dissolved porosities to some extent for the Huangliu sandstones (Yuan et al., 2015).

The overpressure is evidenced as a significant event for kinetically restricting the producing efficiency of organic acids and forming a geochemically closed diagenetic system (Hao et al., 2007; Bjørlykke, 2014). Therefore, the dissolution was constrained and became weaker gradually. The previous publication documented that overpressure could restrain clay minerals transformation, causing that the yield of metal cations acting as the reactant for precipitation of carbonate cements were restricted (Meng et al., 2012). In addition, overpressure can enhance the solubility of carbonate in aqueous solution, and thus hinder the precipitation of carbonate cements (Duan et al., 2018). These factors proposed above are mainly responsible for the lower contents of carbonate cements in the AF-2 area (**Table 2**). The fluid inclusions of ferrocalcite cements in the AF-2 area show a range of homogenization temperature of 72–98°C, implying that the carbonate cements of the AF-2 area mainly formed during the mesodiagenesis and were consistent with the main temperature span (80–120°C) of organic acids expulsion proposed by Surdam et al. (1989). A lighter value of $\delta^{13}C$ suggest that the ferrocalcite cements mainly belong to the precipitation induced by organic acids dissolution (**Figure 12**).

Earlier research revealed that CO_2-rich thermal fluid from the underlying beds invaded the AF-1 area (Hao et al., 2000), which occurred as a pattern of multiphase episodic vertical injection from about 0.4 Ma (Xie et al., 2012) and was evidenced by high content of CO_2 (**Table 1**). The AF-1 area suffer extreme influence from CO_2 filling, and rarely affected traces are found in the AF-2 area (Duan et al., 2020).

The CO_2 charging exert serious control on diagenetic evolution and reservoir quality and thus raise more concern from petroleum geologists (Fu et al., 2016; Duan et al., 2020). The dissolution of unstable minerals induced by CO_2 charging was widely reported (Watson et al., 2004; Wigley et al., 2012). When expelling into saline aquifers, the CO_2 dissolved in pore fluid and broke geochemical equilibrium, resulting in a weak-acid setting (Wigley et al., 2012). In the Huangliu sandstones, the overpressure enhanced the solubility of CO_2 and thus increased the acidity, and thermal fluid migration induced anomalously high temperature, which greatly facilitated dissolution (Fu et al., 2016). The dissolved pores natures characterized by abundant oversized pores and high-proportioned secondary porosity visibly indicate large-scale dissolution in the AF-1 area.

The potential of enhancing porosity by dissolution mainly depend on the byproduct distribution released from feldspar grains, which are constrained by the properties of geochemically diagenetic system (Yuan et al., 2015). Based on material equilibrium, the most effective dissolution for enhancing net porosity is therefore expected in sandstones which are exposed to a geochemically open system and can freely discharge by-products and authigenic minerals (Nedkvitne and Bjørlykke, 1992). With the sealed effect by overpressure, the diagenetic environment is generally considered to be a geochemically closed system and removing large quantities of solute become extreme difficulty (Wilkinson et al., 1997). The hydraulic fracture was demonstrated to be a pressure leak-off point in the overpressure strata of the Central Graben in the North Sea, from which the fluid could migrate through the top seal (Wilkinson et al., 1997). The leak-off point induced an open system and allowed dissolution products to migrate dynamically, which was beneficial to enhance secondary porosity (Wilkinson et al., 1997).

In the diapir, steep-dipping fractures associated with diapir evolution act as significant channels for fluid migration and mass transfer, from which the reactive material and production can discharge (Hao et al., 2000; Yuan et al., 2019) (**Figure 2A**). Based on gas accumulation and diagenetic progress, the thermal fluid migration in diapir was proposed to have an episodic nature (Hao et al., 2000). When CO_2-rich thermal fluid injected the Huangliu sandstones along fractures, the feldspar, lithic fragments and carbonate cements suffered extensive dissolution. The dissolution products can be transferred out of reservoir by fluid migration, which can enhance storage potential (Qie et al., 2021). During the intervals of thermal fluid upwelling, the diagenetic system was in a semi-closed or even closed state, and the flow rate of pore fluid decelerated drastically and the efficiency of mass transfer became extremely lower (Yuan et al., 2015). In addition, the temperature and pressure of formation decreased accordingly (Hao et al., 2000). The extensive dissolution and advanced conversion of clay minerals provided abundant Ca^{2+}, Mg^{2+} and Fe^{2+}, which combined with high content of CO_3^{2-} to form a large amount of late-period carbonate cements (Duan et al., 2018), damaging permeability seriously (**Figure 13C**). The heavier $\delta^{13}C$ value of ankerite and siderite in the AF-1 area indicated the carbonate cements were mainly associated with inorganic CO_2 (**Figure 12**).

The multistage thermal fluid induced cumulative diagenetic process characterized by the overlap of multiphase dissolution and subsequent precipitation (Jansa and Noguera Urrea, 1990; Xue et al., 2021). During the expulsion of CO_2-rich fluid, the diagenetic system was relatively open and the dissolution had a constructive effect for porosity, which was suggested the main

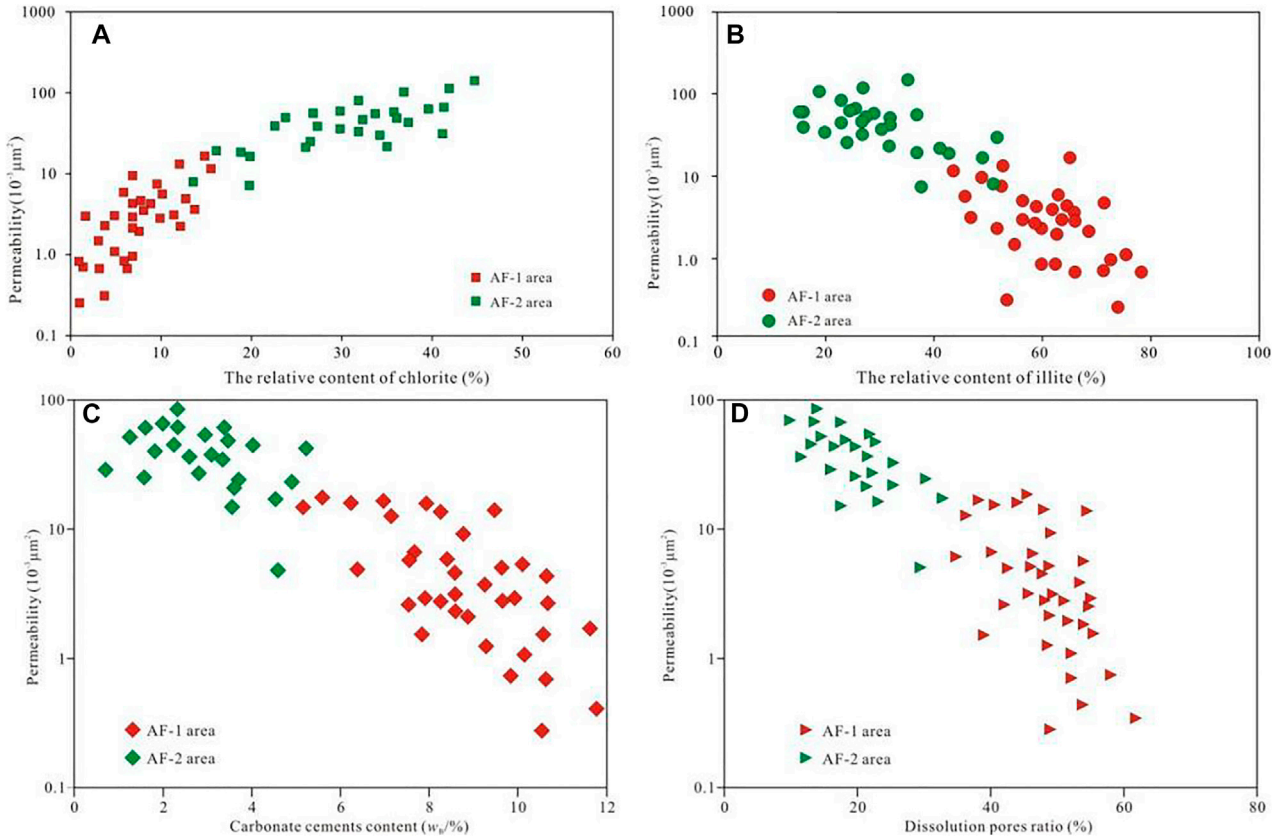

FIGURE 13 | Correlation between permeability and **(A)** relative content of chlorite, **(B)** relative content of illite, **(C)** carbonate cements content, and **(D)** dissolution pores ratio in the Huangliu sandstones.

mechanism to interpret higher total porosities of the AF-1 area than that of the AF-2 area despite experiencing stronger compaction.

In some case, considerable amount of dissolved pores are poorly connected to pores network due to the blocking of remnants and cements (Lai et al., 2017; Liu et al., 2020). The multiphase, the high contents of carbonate cements act as occluding material to block pore-throats (**Figures 5F,G**), resulting in a set of microstructures characterized by smaller throats size and poor interconnectivity (**Figure 6H**), which is one of main reasons for low permeability in the AF-1 area (**Figure 13D**). Moreover, the massive dissolution and the assemblage of authigenic minerals can modify pore-size distribution, minerals surface feature and pores geometry, complicating the seepage regime and decreasing penetrability significantly (Dutton and Loucks, 2010; Chen et al., 2021).

Well-connected primary pores tend to have large throat size contributing to permeability, whereas secondary pores and micropores connected by confined pore-throats are disadvantageous to permeability (Dutton and Loucks, 2010). The AF-2 area suffered little effect from intensive dissolution of CO_2 charging. As a result, the lower contents of carbonate cements and weaker dissolution intensity protect more primary pores and present a higher proportion of primary porosity and medium-permeability (**Figure 13D**).

5.4 Different Evolution Tendency of Clay Minerals

Clay minerals in sandstone reservoirs occur with varied assembling patterns and relative amounts, which are mainly controlled by transformation process influenced by combined factors including temperature, pressure and fluid properties (Bjørlykke, 1998; Meng et al., 2012). For the Huangliu sandstones, the complicated diagenetic setting with HTHP and thermal fluid exert considerable control on clay transformation and distribution.

Temperature is a crucial factor for illitization of smectite, and furthermore, the compositional trends in I/S mixed-layer are taken as an indicator of geothermal distribution (Bühmann, 1992). Generally, the illitization of smectite presents an increasing rate with rising geothermal gradient (Meng et al., 2012). Influenced by thermal anomaly induced by thermal fluid in the AF-1 area, the illitization of smectite accelerated markedly (Hao et al., 2000). In contrast, with the effect of suppressing dehydration for smectite by increasing pressure, the overpressure can restrain the transformation from smectite

to illite (Colten-Bradley, 1987). Furthermore, overpressure can limit the source of K^+ by restricting dissolution of K-feldspar, which also act as a retarder for transformation of smectite to illite by limiting reacting materials (Chuhan et al., 2001). In addition, with an earlier onset timing of overpressure, the AF-2 area experienced stronger restraint and had lower intensity of illitization of smectite accordingly.

The distribution of authigenic chlorite is controlled by thermal history, fluid property, and ferromagnesian grains (Bahlis and De Ros, 2013). With similar depositional setting and burial experience, the AF-2 area present obviously higher contents of authigenic chlorite than the AF-1 area, implying differential transformation process. Authigenic chlorite in the Huangliu sandstones occur predominately as pore-lining and rosette pattern, which are similar to the Santos sandstones in eastern Brazil described by Bahlis and De Ros (2013). Different from progressive transformation of smectite coatings in the Santos sandstones, smectite coatings and volcanic rock fragments are absent in the Huangliu sandstones, indicating that smectitic precursor rarely act as dominating source for authigenic chlorite (Bahlis and De Ros, 2013). With weak alkaline environment, the transformation of kaolinite integrated ferroan carbonates to chlorite is considered as a significant way to form chlorite (Meng et al., 2012). From thermodynamics perspective, chlorite is unstable and particularly prone to transforming to kaolinite under high temperature and acidic condition (Meng et al., 2012) **(Eq. 2)**. During the late period, weakly acidic and high temperature conditions caused by a thermal fluid induced major dissolution of chlorite (Meng et al., 2012; He et al., 2020). Therefore, the key diagenetic event of late-stage transformation mainly contributes to reducing chlorite in the AF-1 area, which is consistent with the measured results. As verified by quite a few of papers, chlorite coating and pore-lining chlorite play a positive role in inhibiting quartz cementation and restraining compaction (Bloch et al., 2002; Taylor et al., 2010; Mohammed et al., 2021). The measured permeability of the Huangliu sandstones are positively correlated with the amount of chlorite, indicating constructive significance of authigenic chlorite on reservoir quality (**Figure 13A**).

With massive dissolution of feldspar induced by CO_2 charging, a considerable amount of authigenic kaolinite are still detained in the AF-1 area, despite a part of authigenic kaolinite are transported out of dissolved pores by fluid expulsion and consumed by illitization of kaolinite (Chuhan et al., 2001; Yuan et al., 2019). As one of major pore-filling constituents, the residual kaolinite with vermicular and booklets habits develop abundant micropores (Lai et al., 2015). The micropores apparently add a lesser amount of total storage volume, and nevertheless, the microporous texture intertwining with pseudomatrix can enhance the tortuosity of seepage channels and tend to have poor interconnectivity, which also exacerbate permeability in the AF-1 area (Worden and Morad, 2003; Lai et al., 2015).

Apart from illitization of smectite, the illitization of kaolinite is also a major genesis for authigenic illite (Chuhan, et al., 2000). In the AF-2 area, the overpressure suppressed the dissolution of K-feldspar, which distinctly decreased the concentration of K^+. In addition, the closed diagenetic system limit the transfer of K^+ (Yuan et al., 2019). In a closed system, the appropriate thermodynamic condition for precipitation of authigenic illite is a temperature range of 120–140°C (Chuhan, et al., 2001). The homogenization temperature of fluid inclusion shows a mainstream interval of 85–115°C. The conditions mentioned above restrict the reactants and diagenetic setting for illite precipitation in the AF-2 area. In the AF-1 area, the significant diagenetic event of thermal fluid expulsion caused intensive dissolution of K-feldspar and thus provided abundant K^+ and kaolinite for illite precipitation **Eq. (3)** (Chuhan, et al., 2001). Furthermore, the thermal fluid activities can evoke vertical transfer of potassium along fractures in overpressure sequence, therefore enhancing illitization of kaolinite (Yuan et al., 2019). The thermal anomaly heightened the formation temperature in the AF-1 area with a paleogeothermal interval of 123–165°C, improving illitization of kaolinite largely (Duan, et al., 2020). Consequently, the favorable geochemical and thermodynamic conditions yielded abundant authigenic illite in the AF-1 area which exceeded the AF-2 area obviously. As for the AF-1 area, the widespread fibrous and pore-bridging illite aggregation blocked throats and damaged permeability significantly (Lai et al., 2017) (**Figure 13B**). More seriously, in a deeply buried sequence with high temperature, fibrous illite decrease permeability by several orders of magnitude (Ajdukiewicz and Lander, 2010). Based on data of physical properties, the permeability presented a negative correlation with the amount of illite (**Figure 13B**). In contrast, the poorly developed authigenic illite in the AF-2 area contributed to seepage behavior and permeability.

$$\begin{aligned} Fe_{3.5}Mg_{3.5}Al_6Si_6O_{20}(OH)_{16}\ (\text{Chloride}) + 14\,H^+ \\ = 3\,Al_2Si_2O_5(OH)_4\,(\text{Kaolinite}) + 3.5\,Fe^{2+} \\ + 3.5\,Mg^{2+} + 9H_2O, \end{aligned} \tag{2}$$

$$\begin{aligned} Al_2Si_2O_5(OH)_4\,(\text{Kaolinite}) + KAlSiO_3 \\ = KAl_3Si_3O_{10}(OH)_2\ (\text{Illite}) + 2\,SiO_2 + H_2O. \end{aligned} \tag{3}$$

5.5 Two Different Mechanisms of Reservoirs Development

The physical properties of reservoir are generally governed by integrated attributes of depositional characteristics and subsequent diagenetic modifications (Mansurbeg et al., 2008). The elements relevant to deposition including detrital composition, sedimentary structure, grain size and amount of matrix determine original pores system (Ozkan et al., 2011). After depositing, a wide variety of diagenetic modifications of compaction, dissolution and cementation significantly control reservoirs quality and heterogeneity (Morad et al., 2000). In particular, exceptional diagenetic modifications induced by extreme diagenetic setting such as HPHT and CO_2 charging can even obscure the depositional imprints (Ozkan et al., 2011). As for

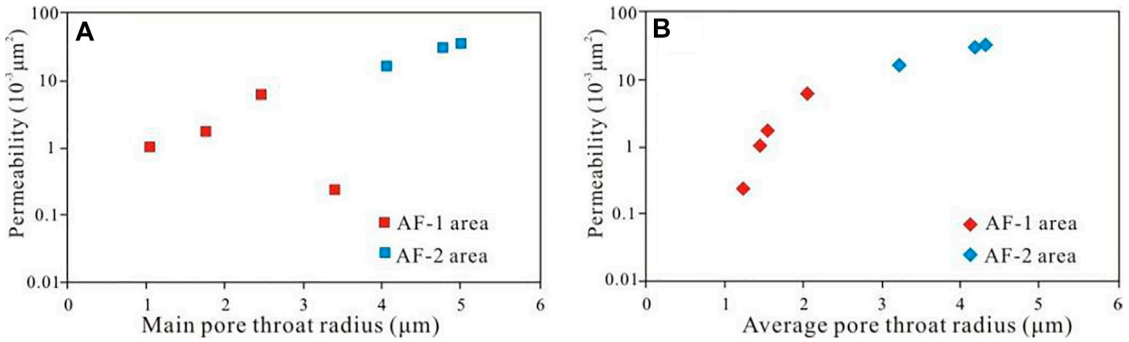

FIGURE 14 | Cross plot of permeability vs. main throat radius **(A)** and average throat radius **(B)** in the Huangliu sandstones.

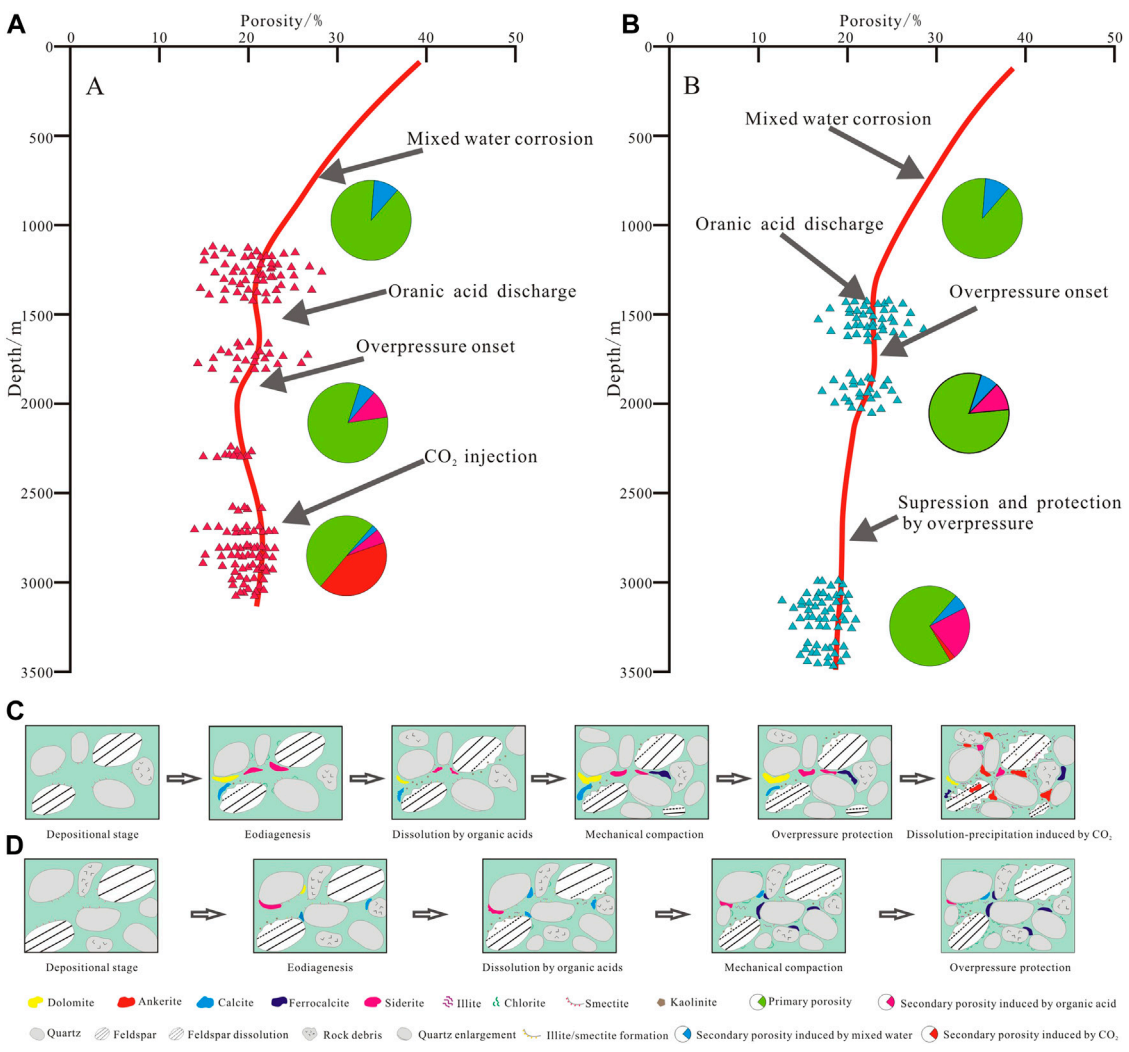

FIGURE 15 | Trend of porosity evolution with depth in the AF-1 area **(A)** and the AF-2 area **(B)**, and diagenetic evolution of the Huangliu sandstones in the AF-1 area **(C)** and the AF-2 area **(D)** in the Dongfang district.

the Huangliu sandstones, it appeared analogous depositional features between the AF-1 and AF-2 areas. However, controlled by different diagenetic environments, the AF-1 area and the AF-2 area presented variable diagenetic histories, resulting in a wide variety of spatial and temporal distribution of diagenetic alterations across the two areas (Ozkan et al., 2011).

As a routinely employed method for porosity prediction, porosity versus depth curves tend to have considerable limitation in greater depths where sandstones experience stronger diagenetic degree, such as extensive dissolution and cementation (Taylor et al., 2010). Especially, in the extreme cases exposed to HPHT and CO_2 dissolution, the conventional porosity versus depth trends are essentially meaningless for porosity prediction (Taylor et al., 2010). Therefore, for such diagenetically heterogeneous sandstones, the porosity modeling dependent on depths variation should be revalued based on extreme diagenetic events.

Based on synthetical analysis of diagenetic alterations, we establish two patterns of porosity evolution for the Huangliu sandstones to deepen understanding of development mechanism of reservoirs (**Figure 15**). Previous to overpressure occurrence, considerable amount of intergranular volumes were lost due to progressive compaction. In early period, the dissolution associated with mixed water increased porosity slightly. The medium-term corrosion by organic acid can add a certain number of dissolved porosities. The mechanical compaction was retarded when overpressure occurred, and thus more primary porosities were preserved and the downward trend of porosity became slower, especially in the AF-2 area with an earlier onset timing of resistance to compaction (**Figure 15**). Restrained by overpressure, the dissolution derived by organic acids was limited and so was cementation strength, which restricted secondary porosity but retained more primary porosities. During late diagenetic stage in the AF-1 area, dissolved porosities were improved dramatically by CO_2 injection, resulting in higher proportion of secondary pores and abnormal rise of average porosity (**Figure 15**). With lesser influence from CO_2 dissolution and chiefly suppressed by overpressure, the AF-2 area had a gentle variation of porosity–depth curve and higher primary porosity, though showed marginally lower porosity than the AF-1 area in the mass.

As a critical factor to characterize seepage performance, permeability is considered as a function of porosity and connectivity of individual pore and predominantly controlled by pore-throat size (Dutton and Loucks, 2010). While causing a wide variation of porosities, diagenetic modifications also act as a crucial factor for reconstructing original pores network, controlling pore-throat size and consequently determining permeability (Dutton and Loucks, 2010). An evident positive relationship existing between throat size and permeability, indicated that the variations of permeability were dominantly controlled by the distribution of throat size (**Figure 14**). The higher contents of carbonate cements and authigenic illite caused by CO_2 injection under anomalously high temperature blocked throats severely, resulting in a rapid loss of permeability for the Huangliu sandstones in the AF-1 area (**Figures 13B,C**). With stronger influence by unremitting overpressure and lesser impact from CO_2 charging in the AF-2 area, the authigenic illite and kaolinite were suppressed largely, and the cementation intensity of carbonate cements was also restricted, which prevented serious damage for permeability (**Figures 13B,C**).

With intensive diagenetic modifications, the AF-1 area present higher average porosity due to massive dissolution. However, the redistribution of secondary porosities and simultaneous authigenic minerals deteriorated permeability with one or two orders of magnitude lower than the AF-2 area restricted effectively by overpressure (Aase et al., 1996) (**Figure 13**). As for the Huangliu sandstones with similar depositional features, the spatial and temporal differentiation of diagenetic settings resulted in two obviously diverse patterns of diagenesis-driven evolution pathways and development mechanisms, and formed two categories of reservoirs (**Figure 15**). Considering significant impact by anomalous diagenetic environments, it is quite essential to link the combined modes of anomalous diagenetic conditions with diagenetic evolution and development mechanism for the sandstones characterized by HPHT and CO_2 injection. This study enhances our understanding on the formation mechanism of sandstone reservoirs under anomalous diagenetic conditions, and provides important geological reference for reservoirs prediction in HPHT sequences in the Yinggehai Basin and other basins worldwide with similar geological conditions.

6 CONCLUSION

1) The reservoir characteristics of the Huangliu sandstones present regional diversity. The AF-1 area is characterized by high proportion of secondary porosity and medium porosity to low permeability, while the AF-2 area is dominated by primary porosity and medium porosity to medium permeability. The determination of rate-controlled porosimetry indicate that the AF-1 area show distinctly lower throat sizes than that of the AF-2 area overall, which is mainly responsible for low permeability in the AF-1 area.
2) In the AF-1 area, the later occurrence time of overpressure cause stronger compaction intensity and major loss of primary porosity. The multistage invasion of CO_2-rich thermal fluids in the late stage induced intense corrosion of feldspar grains and enhanced secondary porosity significantly, and therefore improved total porosity. Meanwhile, extensive CO_2 dissolution caused abundant precipitations including carbonate cements and authigenic illite in a closed diagenetic system, which leaded to the blocking of throats and lowering of seepage capacity.
3) For the AF-2 area, earlier onset of overpressure restrained mechanical compaction obviously, and further retarded the corrosion of organic acid, which preserved more primary porosities. Rarely influenced by CO_2 filling, the CO_2 dissolution and carbonate cementation were markedly weaker. The conversions of clay minerals were restrained significantly because of overpressure and lesser impact by thermal fluids. The weaker diagenetic strength prevented heavy deterioration for reservoir quality, especially for permeability.
4) The onset timing of overpressure, the distribution trend of high temperature and the scope of influence by CO_2 filling vary significantly between the AF-1 and AF-2 areas. The diagenesis strength and diagenetic modifications show distinct difference due to the integrated impact of anomalous diagenetic environments, which cause two types of diagenetic evolution

pathways, forming two development patterns and exhibiting different reservoir types for the Huangliu sandstones.

DATA AVAILABILITY STATEMENT

The original contributions presented in the study are included in the article/Supplementary Material; further inquiries can be directed to the corresponding authors.

AUTHOR CONTRIBUTIONS

XL and MF are responsible for the idea and writing of this manuscript; SZ, XM, YL, XD, YZ, and TS are responsible for the data interpretations.

FUNDING

The author(s) disclosed receipt of the following financial support for the research, authorship, and/or publication of this article: National Science and Technology Major Project (Grant No. KJ125ZDXM07LTD02ZJ11).

ACKNOWLEDGMENTS

We would like to acknowledge staff of the State Key Laboratory of Oil and Gas Reservoir Geology and Development, Zhanjiang Branch Company of CNOOC, for their contribution of data and valuable discussion, which significantly improved the quality of the manuscript.

REFERENCES

Ajdukiewicz, J. M., and Lander, R. H. (2010). Sandstone Reservoir Quality Prediction: The State of the Art. *Bulletin* 94 (8), 1083–1091. doi:10.1306/intro060110

Aase, N. E., Bjørkum, P. A., and Nadeau, P. H. (1996). The Effect of Grain-Coating Microquartz on Preservation of Reservoir Porosity. *Bulletin* 80 (10), 1654–1673. doi:10.1306/64EDA0F0-1724-11D7-8645000102C1865D

Bahlis, A. B., and De Ros, L. F. (2013). Origin and Impact of Authigenic Chlorite in the Upper Cretaceous Sandstone Reservoirs of the Santos Basin, Eastern Brazil. *Pet. Geosci.* 19, 185–199. doi:10.1144/petgeo2011-007

Barth, T., and Bjørlykke, K. (1993). Organic Acids from Source Rock Maturation: Generation Potentials, Transport Mechanisms and Relevance for Mineral Diagenesis. *Appl. Geochem.* 8, 325–337. doi:10.1016/0883-2927(93)90002-X

Bjørlykke, K. (1998). Clay Mineral Diagenesis in Sedimentary Basins - a Key to the Prediction of Rock Properties. Examples from the North Sea Basin. *Clay Min.* 33, 15–34. doi:10.1180/000985598545390

Bjørlykke, K., and Jahren, J. (2012). Open or Closed Geochemical Systems during Diagenesis in Sedimentary Basins: Constraints on Mass Transfer during Diagenesis and the Prediction of Porosity in Sandstone and Carbonate Reservoirs. *Bulletin* 96 (12), 2193–2214. doi:10.1306/04301211139

Bjørlykke, K. (2014). Relationships between Depositional Environments, Burial History and Rock Properties. Some Principal Aspects of Diagenetic Process in Sedimentary Basins. *Sediment. Geol.* 301, 1–14. doi:10.1016/j.sedgeo.2013.12.002

Bloch, S., Lander, R. H., and Bonnell, L. (2002). Anomalously High Porosity and Permeability in Deeply Buried Sandstone Reservoirs: Origin and Predictability. *Bulletin* 86 (2), 301–328. doi:10.1306/61EEDABC-173E-11D7-8645000102C1865D

Bühmann, C. (1992). Smectite-to-illite Conversion in a Geothermally and Lithologically Complex Permian Sedimentary Sequence. *Clays Clay Minerals* 40 (1), 53–64. doi:10.1346/CCMN.1992.0400107

Bukar, M., Worden, R. H., Bukar, S., and Shell, P. (2021). Diagenesis and its Controls on Reservoir Quality of the Tambar Oil Field, Norwegian North Sea. *Energy Geosci.* 2 (1), 10–31. doi:10.1016/j.engeos.2020.07.002

Chen, G. B., Li, T., Yang, L., Zhang, G. H., Li, J. W., and Dong, H. J. (2021). Mechanical Properties and Failure Mechanism of Combined Bodies with Different Coal-Rock Ratios and Combinations. *J. Min. Strata Control Eng.* 3 (2), 023522. doi:10.13532/j.jmsce.cn10-1638/td.20210108.001

Chuhan, F. A., Bjorlykke, K., and Lowrey, C. J. (2001). Closed-system Burial Diagenesis in Reservoir Sandstones: Examples from the Garn Formation at Haltenbanken Area, Offshore Mid-Norway. *J. Sediment. Res.* 71 (1), 15–26. doi:10.1306/041100710015

Chuhan, F. A., Bjørlykke, K., and Lowrey, C. (2000). The Role of Provenance in Illitization of Deeply Buried Reservoir Sandstones from Haltenbanken and North Viking Graben, Offshore Norway. *Mar. Petroleum Geol.* 17, 673–689. doi:10.1016/S0264-8172(00)00014-3

Colten-Bradley, V. A. (1987). Role of Pressure in Smectite Dehydration--Effects on Geopressure and Smectite-To-Illite Transformation. *Bulletin* 71 (11), 1414–1427. doi:10.1306/703C8092-1707-11D7-8645000102C1865D

Di Primio, R., and Neumann, V. (2008). HPHT Reservoir Evolution: a Case Study from Jade and Judy Fields, Central Graben, UK North Seafields, Central Graben, UK North Sea. *Int. J. Earth Sci. Geol. Rundsch)* 97, 1101–1114. doi:10.1007/s00531-007-0206-y

Dong, S., Zeng, L., Lyu, W., Xia, D., Liu, G., Wu, Y., et al. (2020). Fracture Identification and Evaluation Using Conventional Logs in Tight Sandstones: A Case Study in the Ordos Basin, China. *Energy Geosci.* 1 (3–4), 115–123. doi:10.1016/j.engeos.2020.06.003

Duan, W., Li, C.-F., Chen, X.-G., Luo, C.-F., Tuo, L., and Liu, J.-Z. (2020). Diagenetic Differences Caused by Gas Charging with Different Compositions in the XF13 Block of the Yinggehai Basin, South China Sea. *Bulletin* 104 (4), 735–765. doi:10.1306/06191917331

Duan, W., Li, C.-F., Luo, C., Chen, X.-G., and Bao, X. (2018). Effect of Formation Overpressure on the Reservoir Diagenesis and its Petroleum Geological Significance for the DF11 Block of the Yinggehai Basin, the South China Sea. *Mar. Petroleum Geol.* 97, 49–65. doi:10.1016/j.marpetgeo.2018.06.033

Dutton, S. P., and Loucks, R. G. (2010). Diagenetic Controls on Evolution of Porosity and Permeability in Lower Tertiary Wilcox Sandstones from Shallow to Ultradeep (200-6700m) Burial, Gulf of Mexico Basin, U.S.A. *Mar. Petroleum Geol.* 27, 69–81. doi:10.1016/j.marpetgeo.2009.08.008

Folk, R. L. (1980). *Petrology of Sedimentary Rocks*. Austin, TX: Hemphill Publishing Company, 182.

Fu, G., and Zhang, F. Q. (1998). A Method for Analyzing the Paleo-Pressure Sealing Ability of Poorly Compacted Shale Barrier with the Use of Acoustic Logging Data. *Oil Geophys. Prospect.* 33 (6), 812–818. doi:10.13810/j.cnki.issn.1000-7210.1998.06.014

Fu, M.-y., Song, R.-c., Xie, Y.-h., Zhang, S.-n., Gluyas, J. G., Zhang, Y.-z., et al. (2016). Diagenesis and Reservoir Quality of Overpressured Deep-Water Sandstone Following Inorganic Carbon Dioxide Accumulation: Upper Miocene Huangliu Formation, Yinggehai Basin, South China Sea. *Mar. Petroleum Geol.* 77, 954–972. doi:10.1016/j.marpetgeo.2016.08.005

Gluyas, J., and Cade, C. A. (1997). Prediction of Porosity in Compacted Sands. *Reserv. Qual. Predict. Sandst. carbonatesAAPG Mem.* 69, 19–27. doi:10.1306/M69613C2

Grant, N. T., Middleton, A. J., and Archer, S. (2014). Porosity Trends in the Skagerrak Formation, Central Graben, United Kingdom Continental Shelf: The Role of Compaction and Pore Pressure History. *Bulletin* 98 (6), 1111–1143. doi:10.1306/10211313002

Hao, F., Li, S. T., and Gong, Z. S. (2000). Thermal Regime, Interreservoir Compositional Heterogeneities, and Reservoir-Filling History of the Dongfang Gas Field, Yinggehai Basin, South China Sea: Evidence for Episodic Fluid Injections in Overpressured Basins? *Bulletin* 84 (5), 607–626. doi:10.1306/C9EBCE69-1735-11D7-8645000102C1865D

Hao, F., Zou, H., Gong, Z., Yang, S., and Zeng, Z. (2007). Hierarchies of Overpressure Retardation of Organic Matter Maturation: Case Studies from

Petroleum Basins in China. *Bulletin* 91 (10), 1467–1498. doi:10.1306/05210705161

He, X., Zhang, P., He, G., Gao, Y., Liu, M., Zhang, Y., et al. (2020). Evaluation of Sweet Spots and Horizontal-Well-Design Technology for Shale Gas in the Basin-Margin Transition Zone of Southeastern Chongqing, SW China. *Energy Geosci.* 1 (3–4), 134–146. doi:10.1016/j.engeos.2020.06.004

Higgs, K. E., Zwingmann, H., Reyes, A. G., and Funnell, R. H. (2007). Diagenesis, Porosity Evolution, and Petroleum Emplacement in Tight Gas Reservoirs, Taranaki Basin, New Zealand. *J. Sediment. Res.* 77, 1003–1025. doi:10.2110/jsr.2007.095

Huang, Y., Yao, G., and Fan, X. (2019). Sedimentary Characteristics of Shallow-Marine Fans of the Huangliu Formation in the Yinggehai Basin, China. *Mar. Petroleum Geol.* 110, 403–419. doi:10.1016/j.marpetgeo.2019.07.039

Huang, Y., Yao, G., Zhou, F., and Wang, T. (2017). Impact Factors on Reservoir Quality of Clastic Huangliu Formation in Overpressure Diapir Zone, Yinggehai Basin, China. *J. Petroleum Sci. Eng.* 154, 322–336. doi:10.1016/j.petrol.2017.04.044

Jansa, L. F., and Noguera Urrea, V. H. (1990). Geology and Diagenetic History of Overpressured Sandstone Reservoirs, Venture Gas Field, Offshore Nova Scotia, Canada (1). *Bulletin* 74 (10), 1640–1658. doi:10.1306/0C9B2551-1710-11D7-8645000102C1865D

Lai, J., Wang, G., Chai, Y., Ran, Y., and Zhang, X. (2015). Depositional and Diagenetic Controls on Pore Structure of Tight Gas Sandstone Reservoirs: Evidence from Lower Cretaceous Bashijiqike Formation in Kelasu Thrust Belts, Kuqa Depression in Tarim Basin of West China. *Resour. Geol.* 65 (2), 55–75. doi:10.1111/rge.12061

Lai, J., Wang, G., Chai, Y., Xin, Y., Wu, Q., Zhang, X., et al. (2017). Deep Burial Diagenesis and Reservoir Quality Evolution of High-Temperature, High-Pressure Sandstones: Examples from Lower Cretaceous Bashijiqike Formation in Keshen Area, Kuqa Depression, Tarim Basin of China. *Bulletin* 101 (6), 829–862. doi:10.1306/08231614008

Lan, S. R., Song, D. Z., Li, Z. L., and Liu, Y. (2021). Experimental Study on Acoustic Emission Characteristics of Fault Slip Process Based on Damage Factor. *J. Min. Strata Control Eng.* 3 (3), 033024. doi:10.13532/j.jmsce.cn10-1638/td.20210510.002

Li, H. (2022). Research Progress on Evaluation Methods and Factors Influencing Shale Brittleness: A Review. *Energy Rep.* 8, 4344–4358. doi:10.1016/j.egyr.2022.03.120

Li, Y. (2021). Mechanics and Fracturing Techniques of Deep Shale from the Sichuan Basin, SW China. *Energy Geosci.* 2 (1), 1–9. doi:10.1016/j.engeos.2020.06.002

Li, Y., Zhou, D.-H., Wang, W.-H., Jiang, T.-X., and Xue, Z.-J. (2020). Development of Unconventional Gas and Technologies Adopted in China. *Energy Geosci.* 1 (1–2), 55–68. doi:10.1016/j.engeos.2020.04.004

Liang, J. S., Wang, Q., Hao, L. W., Tang, J., Liao, P., et al. (2011). Application of Diagenetic Facies Analysis to Reservoir Prediction in Deep Water Area of the Northern South China Sea: a Case Study from Baiyun Sag, Zhujiangkou Basin. *Acta Sedimentol. Sin.* 29 (3), 503–511. doi:10.14027/j.cnki.cjxb.2011.03.002

Liu, Y., Gao, M., and Zhao, H. (2020). Detection of Overlying Rock Structure and Identification of Key Stratum by Drilling and Logging Technology. *J. Min. Strata Control Eng.* 2 (2), 023038. doi:10.13532/j.jmsce.cn10-1638/td.2020.02.004

Luo, X., Dong, W., Yang, J., and Yang, W. (2003). Overpressuring Mechanisms in the Yinggehai Basin, South China Sea. *Bulletin* 87 (4), 629–642. doi:10.1306/10170201045

Mansurbeg, H., Morad, S., Salem, A., Marfil, R., El-ghali, M. A. K., Nystuen, J. P., et al. (2008). Diagenesis and Reservoir Quality Evolution of Palaeocene Deep-Water, Marine Sandstones, the Shetland-Faroes Basin, British Continental Shelf. *Mar. Petroleum Geol.* 25, 514–543. doi:10.1016/j.marpetgeo.2007.07.012

Meng, F. J., Xiao, L. H., Xie, Y. H., Wang, Z. F., Liu, J. H., Tong, C. X., et al. (2012). Abnormal Transformation of the Clay Minerals in Yinggehai Basin and its Significances. *Acta Sedimentol. Sin.* 30 (3), 469–476. doi:10.14027/j.cnki.cjxb.2012.03.005

Morad, S., Ketzer, J. M., and De Ros, L. F. (2000). Spatial and Temporal Distribution of Diagenetic Alterations in Siliciclastic Rocks: Implications for Mass Transfer in Sedimentary Basins. *Sedimentology* 47 (Suppl. 1), 95–120. doi:10.1046/j.1365-3091.2000.00007.x

Nedkvitne, T., and Bjørlykke, K. (1992). Secondary Porosity in the Brent Group (Middle Jurassic), Huldra Field, North Sea: Implication for Predicting Lateral Continuity of Sandstones? *Sepm Jsr* 62 (1), 23–34. doi:10.1306/D426787A-2B26-11D7-8648000102C1865D

Nguyen, B. T. T., Jones, S. J., Goulty, N. R., Middleton, A. J., Grant, N., Ferguson, A., et al. (2013). The Role of Fluid Pressure and Diagenetic Cements for Porosity Preservation in Triassic Fluvial Reservoirs of the Central Graben, North Sea. *Bulletin* 97 (8), 1273–1302. doi:10.1306/01151311163

Osborne, M. J., and Swarbrick, R. E. (1999). Diagenesis in North Sea HPHT Clastic Reservoirs - Consequences for Porosity and Overpressure Prediction. *Mar. Petroleum Geol.* 16, 337–353. doi:10.1016/S0264-8172(98)00043-9

Ozkan, A., Cumella, S. P., Milliken, K. L., and Laubach, S. E. (2011). Prediction of Lithofacies and Reservoir Quality Using Well Logs, Late Cretaceous Williams Fork Formation, Mamm Creek Field, Piceance Basin, Colorado. *Bulletin* 95 (10), 1699–1723. doi:10.1306/01191109143

Paxton, S. T., Szabo, J. O., and Ajdukiewicz, J. M. (2002). Construction of an Intergranular Volume Compaction Curve for Evaluating and Predicting Compaction and Porosity Loss in Rigid-Grain Sandstone Reservoirs. *Bulletin* 86 (12), 2047–2067. doi:10.1306/61EEDDFA-173E-11D7-8645000102C1865D

Qie, L., Shi, Y. N., and Liu, J. S. (2021). Experimental Study on Grouting Diffusion of Gangue Solid Filling Bulk Materials. *J. Min. Strata Control Eng.* 3 (2), 023011. doi:10.13532/j.jmsce.cn10-1638/td.20201111.001

Surdam, R. C., Crossey, L. J., Hagen, E. S., and Heasler, H. P. (1989). Organic-inorganic Interactions and Sandstone Diagenesis. *Bulletin* 73 (1), 1–23. doi:10.1306/703C9AD7-1707-11D7-8645000102C1865D

Santosh, M., and Feng, Z. Q. (2020). New Horizons in Energy Geoscience. *Energy Geosci.* 1 (1–2), A1–A2. doi:10.1016/j.engeos.2020.05.005

Sathar, S., and Jones, S. (2016). Fluid Overpressure as a Control on Sandstone Reservoir Quality in a Mechanical Compaction Dominated Setting: Magnolia Field, Gulf of Mexico. *Terra nova.* 28 (3), 155–162. doi:10.1111/ter.12203

Schmoker, J. W., and Gautier, D. L. (1988). Sandstone Porosity as a Function of Thermal Maturity. *Geol* 16, 1007–1010. doi:10.1130/0091-7613(1988)016<1007:spaafo>2.3.co;2

Shi, Z. Q., Wang, Y., and Jin, X. (2014). The Silurian Hydrothermal Clastic Reservoirs in Tarim Basin: Evidences, Mineral Assemblages and its Petroleum Geological Implications. *Oil Gas Geol.* 35 (6), 903–913. doi:10.11743/ogg20140617

Stricker, S., Jones, S. J., Sathar, S., Bowen, L., and Oxtoby, N. (2016). Exceptional Reservoir Quality in HPHT Reservoir Settings: Examples from the Skagerrak Formation of the Heron Cluster, North Sea, UK. *Mar. Petroleum Geol.* 77, 198–215. doi:10.1016/j.marpetgeo.2016.02.003

Taylor, T. R., Giles, M. R., Hathon, L. A., Diggs, T. N., Braunsdorf, N. R., Birbiglia, G. V., et al. (2010). Sandstone Diagenesis and Reservoir Quality Prediction: Models, Myths, and Reality. *Bulletin* 94 (8), 1093–1132. doi:10.1306/04211009123

Taylor, T. R., Kittridge, M. G., Bryndzia, L. T., and Fibonnell, L. M. (2015). Reservoir Quality and Rock Properties Modeling - Triassic and Jurassic Sandstones, Greater Shearwater Area, UK Central North Sea. *Mar. Petroleum Geol.* 65, 1–21. doi:10.1016/j.marpetgeo.2015.03.020

Tingay, M. R. P., Hillis, R. R., Swarbrick, R. E., Morley, C. K., and Damit, A. R. (2009). Origin of Overpressure and Pore-Pressure Prediction in the Baram Province, Brunei. *Bulletin* 93 (1), 51–74. doi:10.1306/08080808016

Wang, H., Shi, Z., Zhao, Q., Liu, D., Sun, S., Guo, W., et al. (2020). Stratigraphic Framework of the Wufeng-Longmaxi Shale in and Around the Sichuan Basin, China: Implications for Targeting Shale Gas. *Energy Geosci.* 1 (3–4), 124–133. doi:10.1016/j.engeos.2020.05.006

Wang, J., and Wang, X. L. (2021). Seepage Characteristic and Fracture Development of Protected Seam Caused by Mining Protecting Strata. *J. Min. Strata Control Eng.* 3 (3), 033511. doi:10.13532/j.jmsce.cn10-1638/td.20201215.001

Watson, M. N., Zwingmann, N., and Lemon, N. M. (2004). The Ladbroke Grove-Katnook Carbon Dioxide Natural Laboratory: A Recent CO2 Accumulation in a Lithic Sandstone Reservoir. *Energy* 29, 1457–1466. doi:10.1016/j.energy.2004.03.079

Wigley, M., Kampman, N., Dubacq, B., and Bickle, M. (2012). Fluid-mineral Reactions and Trace Metal Mobilization in an Exhumed Natural CO2 Reservoir, Green River, Utah. *Geology* 40, 555–558. doi:10.1130/G32946.1

Wilkinson, M., Darby, D., Haszeldine, R. S., and Couples, G. D. (1997). Secondary Porosity Generation during Deep Burial Associated with Overpressure Leak-Off: Fulmar Formation, United Kingdom Central Graben. *Bulletin* 81 (5), 803–813. doi:10.1306/522B484D-1727-11D7-8645000102C1865D

Wilkinson, M., Haszeldine, R. S., Fallick, A. E., Odling, N., Stoker, S. J., and Gatliff, R. W. (2009). CO2-Mineral Reaction in a Natural Analogue for CO2 Storage--Implications for Modeling. *J. Sediment. Res.* 79, 486–494. doi:10.2110/jsr.2009.052

Worden, R. H., and Morad, S. (2003). Clay Minerals in Sandstones: Controls on Formation, Distribution and Evolution. *Int. Assoc. Sedimentol. Spec. Publ.* 34, 1–41. doi:10.1002/9781444304336.ch1

Xie, Y. H., Zhang, Y. Z., Li, X. S., Zhu, J. C., Tong, C. X., Zhong, Z. H., et al. (2012). Main Controlling Factors and Formation Models of Natural Gas Reservoirs with High-Temperature and Overpressure in Yinggehai Basin. *Acta Pet. Sin.* 33 (4), 601–609. doi:10.7623/syxb201204009

Xue, F., Liu, X. X., and Wang, T. Z. (2021). Research on Anchoring Effect of Jointed Rock Mass Based on 3D Printing and Digital Speckle Technology. *J. Min. Strata Control Eng.* 3 (2), 023013. doi:10.13532/j.jmsce.cn10-1638/td.20201020.001

Yang, J. X., Luo, M. K., Zhang, X. W., Huang, N., and Hou, S. J. (2021). Mechanical Properties and Fatigue Damage Evolution of Granite under Cyclic Loading and Unloading Conditions. *J. Min. Strata Control Eng.* 3 (3), 033016. doi:10.13532/j.jmsce.cn10-1638/td.20210510.001

Ying, F. X., He, D. B., Long, Y. M., Wang, K. Y., Long, Y. M., Lin, X. S., et al. (2003). *SY/T5477, the Division of Diagenetic Stages in Clastic Rocks (Petroleum Industry Criterion in P.R.C.)*. Beijing: Petroleum Industry Press. (in Chinese).

Yoshida, M., and Santosh, M. (2020). Energetics of the Solid Earth: An Integrated Perspective. *Energy Geosci.* 1 (1–2), 28–35. doi:10.1016/j.engeos.2020.04.001

Yuan, G., Cao, Y., Gluyas, J., Li, X., Xi, K., Wang, Y., et al. (2015). Feldspar Dissolution, Authigenic Clays, and Quartz Cements in Open and Closed Sandstone Geochemical Systems during Diagenesis: Typical Examples from Two Sags in Bohai Bay Basin, East China. *Bulletin* 99 (11), 2121–2154. doi:10.1306/07101514004

Yuan, G., Cao, Y., Schulz, H.-M., Hao, F., Gluyas, J., Liu, K., et al. (2019). A Review of Feldspar Alteration and its Geological Significance in Sedimentary Basins: From Shallow Aquifers to Deep Hydrocarbon Reservoirsficance in Sedimentary Basins: From Shallow Aquifers to Deep Hydrocarbon Reservoirs. *Earth-Science Rev.* 191, 114–140. doi:10.1016/j.earscirev.2019.02.004

Zhang, B., Shen, B., and Zhang, J. (2020). Experimental Study of Edge-Opened Cracks Propagation in Rock-like Materials. *J. Min. Strata Control Eng.* 2 (3), 033035. doi:10.13532/j.jmsce.cn10-1638/td.20200313.001

Zhang, J., Ju, Y., and Zhang, Q. (2019). Low Ecological Environment Damage Technology and Method in Coal Mines. *J. Min. Strata Control Eng.* 1 (1), 013515. doi:10.13532/j.jmsce.cn10-1638/td.2019.02.005

Zhao, Z., Wu, K., Fan, Y., Guo, J., Zeng, B., and Yue, W. (2020). An Optimization Model for Conductivity of Hydraulic Fracture Networks in the Longmaxi Shale, Sichuan Basin, Southwest China. *Energy Geosci.* 1 (1–2), 47–54. doi:10.1016/j.engeos.2020.05.001

Zheng, H., Zhang, J., and Qi, Y. (2020). Geology and Geomechanics of Hydraulic Fracturing in the Marcellus Shale Gas Play and Their Potential Applications to the Fuling Shale Gas Development. *Energy Geosci.* 1 (1–2), 36–46. doi:10.1016/j.engeos.2020.05.002

Zuo, J., Yu, M., and Hu, S. (2019). Experimental Investigation on Fracture Mode of Different Thick Rock Strata. *J. Min. Strata Control Eng.* 1 (1), 013007. doi:10.13532/j.jmsce.cn10-1638/td.2019.02.008

Conflict of Interest: XL was employed by the the research institute of Henan Oilfield Company, YL was employed by the research institute of Zhanjiang Branch of CNOOC, and YZ was employed by the Southwest Oil and Gas field Company of Petro China Company Limited.

The remaining authors declare that the research was conducted in the absence of any commercial or financial relationships that could be construed as a potential conflict of interest.

Publisher's Note: All claims expressed in this article are solely those of the authors and do not necessarily represent those of their affiliated organizations, or those of the publisher, the editors, and the reviewers. Any product that may be evaluated in this article, or claim that may be made by its manufacturer, is not guaranteed or endorsed by the publisher.

frontiers | Frontiers in Earth Science

ORIGINAL RESEARCH
published: 22 June 2022
doi: 10.3389/feart.2022.914383

Classification and Evaluation of Volcanic Rock Reservoirs Based on the Constraints of Energy Storage Coefficient

Wen-Tie Sun[1,2,3], *Yi-Shan Lou*[1,2], *Arnaud Regis Kamgue Lenwoue*[1,2], *Zhong-Hui Li*[1,2]*, *Liang Zhu*[1,2] *and Hui-Mei Wu*[1,2]

[1]*Department of Petroleum Engineering, Leak Resistance and Sealing Technology Research Department National Engineering Laboratory of Petroleum Drilling Technology, Yangtze University, Wuhan, China,* [2]*Key Laboratory of Drilling and Production Engineering for Oil and Gas, Wuhan, China,* [3]*Exploration and Development Research Institute of Jilin Oil Field Company, PetroChina, Songyuan, China*

OPEN ACCESS

Edited by:
Hu Li,
Southwest Petroleum University, China

Reviewed by:
Cunhui Fan,
Southwest Petroleum University, China
Kun Zhang,
Southwest Petroleum University, China

***Correspondence:**
Zhong-Hui Li
lizc577@126.com

Specialty section:
This article was submitted to Structural Geology and Tectonics, a section of the journal Frontiers in Earth Science

Received: *06 April 2022*
Accepted: *02 May 2022*
Published: *22 June 2022*

Citation:
Sun W-T, Lou Y-S, Kamgue Lenwoue AR, Li Z-H, Zhu L and Wu H-M (2022) Classification and Evaluation of Volcanic Rock Reservoirs Based on the Constraints of Energy Storage Coefficient. Front. Earth Sci. 10:914383. doi: 10.3389/feart.2022.914383

The current classification and evaluation methods of volcanic rock reservoirs have low accuracy and cannot effectively provide guidance for the selection of volcanic rock gas reservoirs, which have efficient properties for gas production. In this research, we have analyzed the lithology, lithofacies, reservoir space type, pore combination mode, and reservoir microscopic characteristics of volcanic reservoirs using the energy storage coefficient as a constraint. Then, the method of reservoir classification was proposed. The results showed the following: 1) The energy storage coefficient can better characterize the single-layer productivity of gas wells. The volcanic rock reservoirs in the Wangfu gas field can be subdivided into three categories by considering the energy storage coefficient. 2) Type I reservoirs mainly develop structural fractures–matrix dissolution pores, structural fractures–intercrystalline micropores, and matrix dissolution pores. Type II reservoirs mainly develop matrix dissolution pores and residual intergranular pores, and Type III reservoirs are dominated by structural fractures. From Type I to Type III reservoirs, the skewness of the mercury intrusion curve and the sorting coefficient deteriorated, and the physical properties of the reservoir and the maximum mercury saturation and other parameters also decreased, whereas the displacement pressure and the median saturation pressure increased. 3) The characteristics of conventional and special logging curves of typical reservoirs were comprehensively analyzed, and the combination of sensitivity parameters reflecting gas-bearing properties and logging curves was optimized. Furthermore, a reservoir classification chart was established, and the results enabled to confirm the choice of the reservoir and demonstrated that the standard classification has high accuracy. 4) The diagenesis processes such as weathering, leaching, and dissolution improved the physical properties of the reservoir. The research results can effectively provide guidance for the evaluation of the “sweet spot” of volcanic rock reservoirs.

Keywords: reservoir classification, energy storage factor, volcanic rocks, wangfu gas field, diagenesis

1 INTRODUCTION

With the increasing global demand for oil and natural gas resources, unconventional oil and gas resources, such as volcanic gas reservoirs, have become a new field for global oil and gas exploration and development (Stagpoole et al., 2001; Polyansky et al., 2003; Feng et al., 2006; Wu et al., 2006; Shi B. et al., 2020). China has become the main subject for the global volcanic rock oil and gas reservoir exploration practice and has made major breakthroughs in the exploration of volcanic rocks in the Songliao basin, Sichuan basin, and Junggar basin (Feng et al., 2008; Feng et al., 2014; Gao, 2019; Li, 2022; Mao et al., 2015; Chang et al., 2019; Wen et al., 2019). In the Songliao basin, a number of volcanic rock oil and gas reservoirs have been discovered, which showed great potential for oil and gas. The results of gas testing and production have confirmed that volcanic gas reservoirs have large differences in gas well productivity.

Reservoir characteristics are mainly studied in terms of lithology, lithofacies, reservoir space types, pore combinations, pore structures, and reservoir classification scheme (Lan et al., 2021; Pola et al., 2012; Wang et al., 2015; Li et al., 2019; Gao, 2019; Li, 2022; Sruoga and Rubinstein, 2007; Shi et al., 2020b; Zheng et al., 2018b). The lithology identifications of volcanic rock mainly include three methods: gravity-magnetic-electric method identification, geological-log data identification, and seismic identification method (Ran et al., 2005; Chen et al., 2010; Gong et al., 2012). Wang et al. (2006) stipulated that volcanic rocks can be divided into basic, neutral, and acidic volcanic rocks according to the differences in the mineral composition. According to the diagenetic method, the rocks are divided into lava, clastic lava, and pyroclastic rocks; Wang et al. (2003a), Luo et al. (2008), Mou et al. (2010) divided the volcanic lithofacies into 5 types and 15 subfacies according to the volcanic eruption modes, rock types, and volcanic rock output forms. Ren and Jin (1999), Wang et al. (2014), and Luo et al. (2008) divided the reservoir space into primary pores and fractures, and secondary pores and fractures according to the morphological characteristics. Yu et al. (2004) pointed out that in the volcanic rock reservoir space, there are various combinations of pores and fractures. The main technical means for studying the microstructures of the volcanic reservoir space include the capillary pressure curve method, cast thin section, scanning electron microscope, CT scanning, resistivity logging, and nuclear magnetic resonance logging methods (Sruoga and Rubinstein, 2007; Shi et al., 2020b; Zheng et al., 2018b; Hou et al., 2020; Tian et al., 2013; Ma et al., 2017; Yin and Wu., 2020). Sruoga et al. (2004) studied the controlling effect of diagenesis on porosity and permeability in volcanic rock reservoirs by taking the Neuque'n basin in southern Argentina as an example; Pang et al. (2007) analyzed the microscopic pore structures of acid volcanic rock reservoirs and used mercury intrusion data to divide the pore structures of the Yingcheng Formation volcanic rocks in the northern Songliao basin into coarse and fine types.

At present, the classification and evaluation standards of volcanic rock reservoirs are not uniformized. Liu et al. (2003) applied the principle of fuzzy mathematics to select three parameters of energy storage abundance, permeability, and median pore-throat radius that reflect the macroscopic and microscopic characteristics of the reservoir and established the reservoir selection on the basis of core analysis and test data. Evaluation criteria of volcanic rock reservoirs and reasonable structural membership functions included calculating weights and selecting appropriate fuzzy synthesis. Shan et al. (2011) selected seven key parameters for reservoir evaluation based on the factors affecting the quality of volcanic rock reservoirs. They assigned parameters based on expert experience and conducted a single-well reservoir quantitative evaluation. Jin et al. (2007), Chen et al. (2016), and Huang et al. (2019) established the classification and evaluation standards of volcanic rock reservoirs by considering the lithology, storage space combination, physical, electrical, and gas-bearing properties. At present, the accuracy of classification of volcanic rock reservoirs is not high. In fact, compared with clastic rock reservoirs, volcanic rock reservoirs have strong reservoir heterogeneity and are mainly characterized by multi-layer production. In the process of fracturing and production, low-efficiency layers lead to increasing investment costs and low production of gas wells. This paper carries out quantitative and qualitative descriptions of volcanic rock reservoirs and establishes a set of evaluation criteria for effective reservoir classification, and the research results can effectively provide guidance for the evaluation of the "sweet spot" of volcanic rock reservoirs.

2 REGIONAL OVERVIEW, EXPERIMENTAL EQUIPMENT, AND METHODS

2.1 Geological Background

The Wangfu gas field is located in the northwest of the southeast uplift area in the southern Songliao basin. The exploration area is 2,100 km^2. The overall structural form is characterized by steep in the west and gentle in the east. Seismic data and drilling parameters revealed that the Paleozoic Carboniferous–Permian strata are developed from bottom to top in the study area, including the upper Jurassic Huoshiling Formation, lower Cretaceous Shahezi Formation, Yingcheng Formation, Denglouku Formation, and Quantou Formation. The first and second sets of strata are presented in **Figure 1**.

The research horizons are the Shahezi and Huoshiling Formations. A total of 29 wells in the study area revealed that the thickness of the formation is 160–1,223 m. The study area has experienced four stages of volcanic eruption (**Figure 2**). The eruption stages I to III were formed in the period of the Huoshiling Formation and were formed by central-fissure volcanic eruptions. It is mainly composed of rock, trachoic breccia and submerged volcanic breccia, and andesite, and basalt, which are locally developed; the eruption stage IV was formed in the Shahezi Formation, and it is only developed in the structural high of the CS6 well area. The lithology is submerged by volcanic breccia, and the scale of the volcanic body is small.

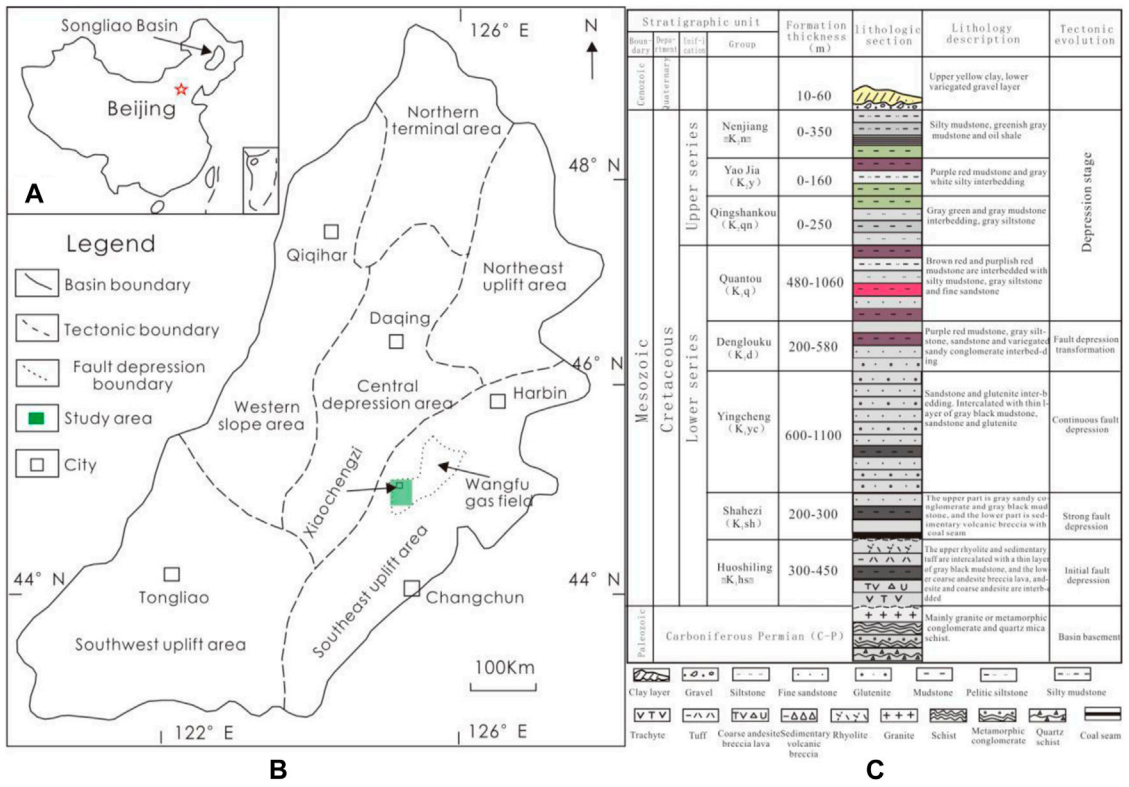

FIGURE 1 | (A) Geographical location map of the Songliao basin, **(B)** regional structural location map of the Wangfu gas field, and **(C)** comprehensive stratigraphic bar map of the Wangfu gas field.

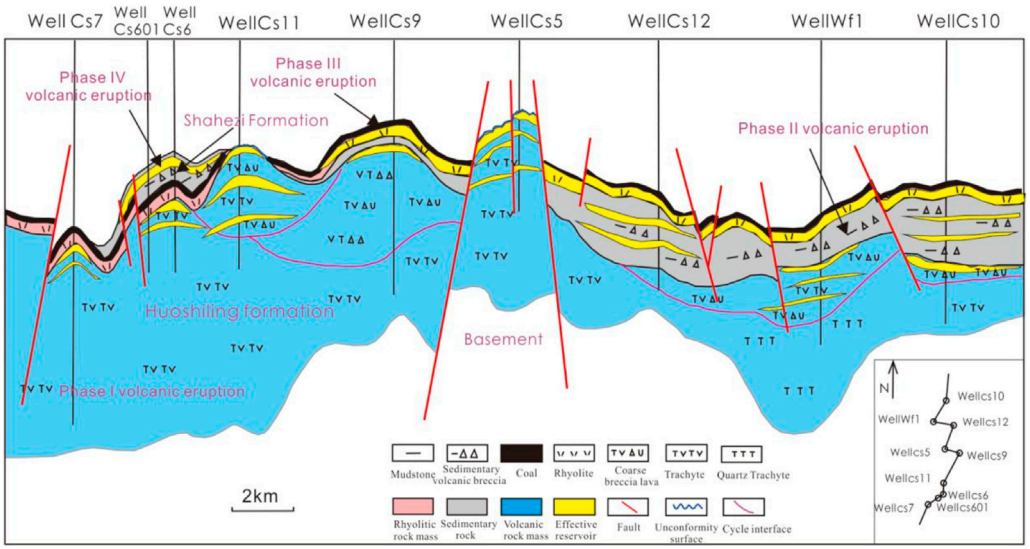

FIGURE 2 | Contrastive profile of volcanic rocks in the Wangfu gas field through wellCs7 to wellCs10.

2.2 Experiments and Methods

During the exploration of this area, seismic, logging, drilling, and test data were obtained. The lithology of volcanic rocks in 29 wells was identified using 271 m cores, 124 cast thin sections, and 4,030 m full borehole imaging logging data (FMI–Formation MicroScanner Image); the lithofacies of volcanic rocks were identified by a combination of geological and logging data. The types of reservoir spaces and pores were observed through resin-impregnated core

samples and cast thin sections. The pore structure characteristics of the volcanic rock reservoirs were analyzed using the data of 26 ordinary mercury injection experiments. This study selected a core sample that has good representativeness. The high-quality volcanic rock reservoir is mainly formed in the weathering crust at the top of volcanic eruption period. The diagenesis of weathering forest filtration and dissolution has a great influence on the reservoir physical property, while the burial depth has a little influence on the reservoir. Meanwhile, in order to further eliminate the influence of burial depth, core samples are mainly selected from the weathered crust, as detailed in **Section 5.2**.

Porosity and permeability tests were performed at the Physics Laboratory of Jilin University, Changchun City, Jilin Province, using the AP608 instrument through helium (helium) injection. The test temperature was 220°C, and the test was carried out in accordance with the standard method of petroleum industry of the People's Republic of China (SY/T 5336–2006, "Core Analysis Method").

The capillary pressure was measured by mercury porosimetry using an automated IV 9505 porosity analyzer in the Fluid Mechanics Laboratory of the Daqing Oilfield Research Institute. The test temperature was 19.10°C, and the humidity was 39% RH. The test adopts the petroleum industry standard method of the People's Republic of China (SY/T 5346-2005: "Measurement of the capillary pressure curve of rocks").

The reservoirs' characteristics of intrusive rocks were analyzed by the integration analysis of petrology, logging, and 3D seismic. The void spaces were assessed through a combination of megascopic observations, thin section of resin-impregnated studies of samples from 8.5 m core of intrusive rocks of the Huoshiling Formation of the Wangfu gas field.

3 CHARACTERISTICS OF VOLCANIC RESERVOIRS

3.1 Lithology and Lithofacies

Lithology is the basic parameter for evaluation of volcanic reservoirs (Sun et al., 2019). The Wangfu gas field volcanic rocks have complex lithology and rock types. On the basis of identifications of cores and cast thin sections, the three-level classification principle of "genesis + composition + structure" is adopted. The volcanic rocks have been divided into four categories: volcanic lava, pyroclastic rock, volcanic lava–volcanic clastic rock, and pyroclastic rock–sedimentary rock.

The volcanic lava reservoirs include six lithologies: trachyandesite, andesite, trachyte, basalt, dacite, and rhyolite. Among them, trachyandesite and andesite are the most developed accounting for 43.74%, while the other lithologies are relatively few, accounting for less than 10%. Pyroclastic reservoirs are mainly present in coarse andesitic (tuff) volcanic breccia, andesitic volcanic breccia (tuff), rhyolitic (tuff) volcanic breccia, and trachytic (tuff) volcanic breccia. Among them, coarse andesitic (tuff) volcanic breccia and andesitic volcanic breccia (tuff) are moderately present, accounting for 12.78 and 8.48%, respectively. The volcanic clastic rock reservoirs are mainly encountered in coarse andesitic (tuff) breccia lava and andesitic (tuff) breccia lava, accounting for 7.88 and 4.37%, respectively. The clastic rock–sedimentary rock reservoirs are mainly composed of sedimentary pyroclastic rock, accounting for 10.56% (**Figure 3**).

The study area mainly includes four types of volcanic lithofacies: explosive facies, overflow facies, volcanic channel facies, and volcanic sedimentary facies. The results in **Figure 4** show that the upper, middle, and lower subfacies of the overflow facies are encountered in the whole area, accounting for 67.4%; the proportion of pyroclastic flow in explosive facies is 19.6%, and there are few empty falling subfacies. Volcanic neck subfacies and re-transported pyroclastic sedimentary rocks are relatively few.

3.2 Types of Storage Space

According to the classification scheme of storage space types by Wang et al. (2003b), He et al. (2016), and Tang et al. (2020), the storage space of volcanic rocks in the Wangfu gas field can be divided into primary and secondary categories: Combined with the structure and morphology of the reservoir space, it can be further subdivided into four subtypes: primary pores, primary fractures, secondary pores, and secondary fractures. There are 10 types of specifically identified reservoir spaces, including primary pores, intergranular pores, intercrystalline micropores, explosion fractures, phenocryst pores, matrix corrosion pores, dissolution fractures, and structural fractures (**Table 1**; **Figure 5**).

4 CLASSIFICATION AND EVALUATION OF VOLCANIC RESERVOIR

4.1 Analysis on Influencing Factors of Volcanic Reservoir

Reservoir classification is an important part of high-quality reservoir screening and is also a key step in establishing high-quality reservoir identification criteria (Zhao et al., 2007; Wang et al., 2021). There are many factors that affect the productivity of gas wells. The geological parameters used to classify the volcano reservoir sweet spot are reasonable and easy to operate. Therefore, the test data of 10 wells in the Wangfu gas field (**Table 2**) are obtained for effective thickness (H), effective thickness * porosity (h.Φ), formation coefficient (h.k), and energy storage coefficient ($h.\Phi.S_{g_i}$). The relationship between other parameters and unblocked flowrate is studied, and the sensitive parameters to reservoir characteristics are implemented.

4.1.1 Single Layer Production Splitting (Q_i)

The volcanic reservoir is characterized by strong reservoir heterogeneity and "thin and multi-layer" lithologic combination. In the production process, in order to achieve a certain output of a single gas well, it is necessary to increase the productivity by multi-layer joint investment. In order to distinguish the contribution of single-layer natural gas production, it is necessary to split the production volume (Wang et al., 2016; Kadavi et al., 2018; Yang et al., 2018; Faizan et al., 2019). In this study, the parameter method is used to split the output. The formula is as follows:

$$Q_i = Q_0 . \frac{h_i . \Phi_i . S_{g_i}}{\sum_i^n h . \Phi . S_g}, \quad (1)$$

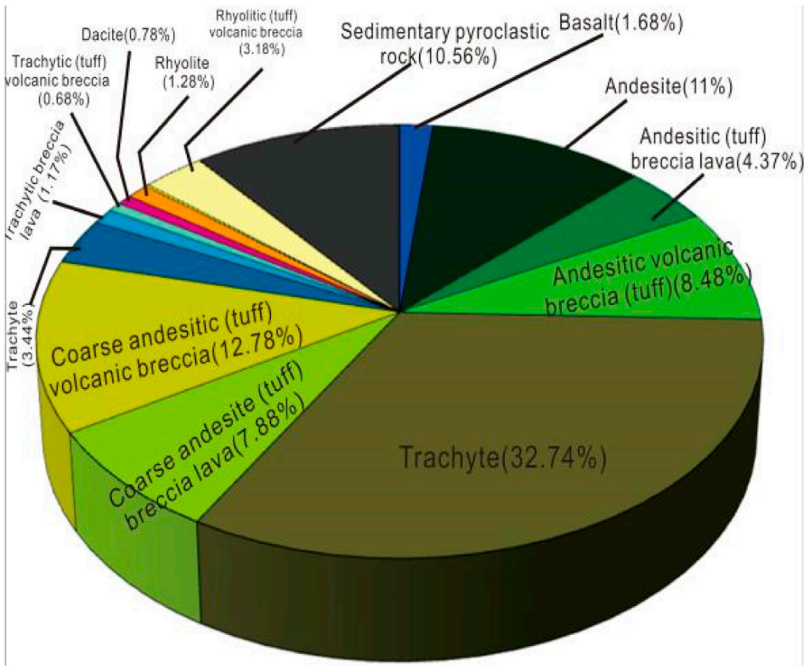

FIGURE 3 | Pie chart of volcanic rock lithology distribution in the Wangfu gas field.

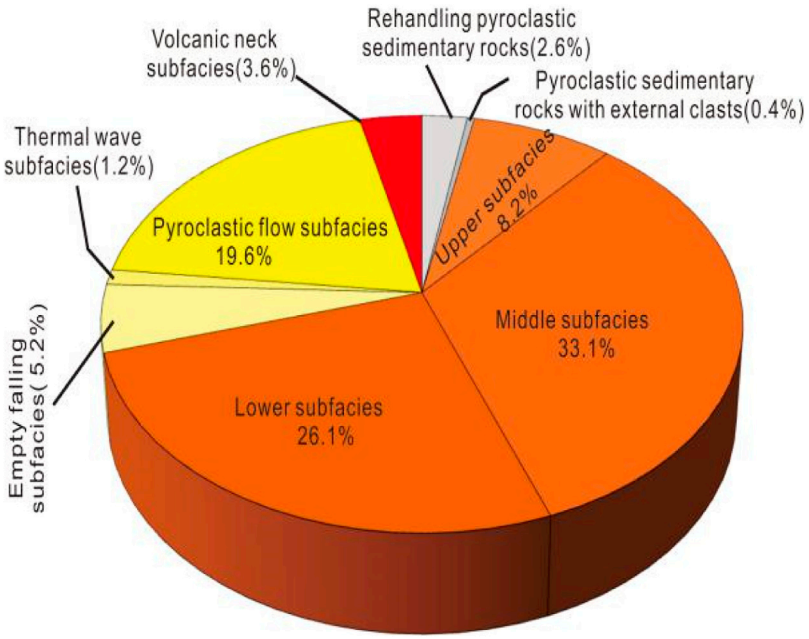

FIGURE 4 | Pie chart of volcanic lithofacies distribution in the Wangfu gas field.

where Q_0—test production (10^4 m^3), Q_i—level i test production (10^4 m^3), h—average effective thickness (m), Φ—average effective porosity (%), S_g—average original gas saturation (%), h_i—average effective thickness of layer i (m), Φ_i—average effective porosity of layer i (%), and S_{g_i}—average original gas saturation of layer i (%).

4.1.2 Effective Thickness (H)

Effective thickness refers to the thickness of the gas reservoir with gas production capacity under the production differential pressure allowed by the existing process technology. Generally, the effective thickness is directly proportional to the gas well

TABLE 1 | Reservoir space types and characteristics of the volcanic rocks in the Huoshiling Formation of the Wangfu gas field in the Songliao basin.

Type of Storage Space			Genesis Mechanism	Characteristics	Distribution	Representative Legend
Primary	Pores	Primary pore	Formation of volatile gas escape	The shapes of stomata are round, oval, and irregular, with different sizes, and some of them are unconnected independent pores	It is mostly found in rhyolite and trachyte in the upper and lower subfacies of eruptive facies	**Figure 5A**
		Intergranular pore	Residual pores after compaction of pyroclastic particles	Irregular shape, usually distributed along the edge of debris, with good connectivity	Volcano clastic rocks are mainly pyroclastic subfacies and subsurface facies	**Figure 5B**
		Intercrystalline pore	Residual space after crystallization	It develops between lava matrix and microcrystalline minerals and can be seen under the microscope	Trachyte and andesite, the middle part of the eruption facies	**Figure 5C**
	Fracture	Explosion fracture	Phenocryst fissure caused by magmatic eruption	The crystal plane is irregular or cleavage like	Rhyolitic clastic rocks of explosive facies are common	**Figure 5D**
Secondary	Pores	Phenocryst pore	Formed by hydrothermal solution, groundwater dissolution, and weathering leaching	The pore shape is irregular, the minerals are completely dissolved, and the original crystal illusion is retained	All kinds of volcanic rocks, cycle times, top, fault zone, and uplift area	**Figure 5E**
		Matrix corrosion pore	Formed by hydrothermal solution, groundwater dissolution, and weathering leaching	The pore morphology is mostly small sieve pore with certain connectivity	All kinds of volcanic rocks, cycle times, top, fault zone, and uplift area	**Figure 5F**
	Fracture	Dissolution fracture	Formed by hydrothermal solution, water dissolution, and weathering leaching	It has no directionality, the fracture wall is irregular, and it often dissolves along the early cracks. Developed in various volcanic rocks	They are developed in volcano rocks, secondary cycles, fault zones, and uplift zones	**Figure 5G**
		Structural fracture	Formation of tectonic stress	Directional, multi-stage cross cutting, penetrating crystals, or pyroclastic particles, communicating with other primary pores	All kinds of volcanic rocks, near faults, and uplift areas	**Figure 5H**

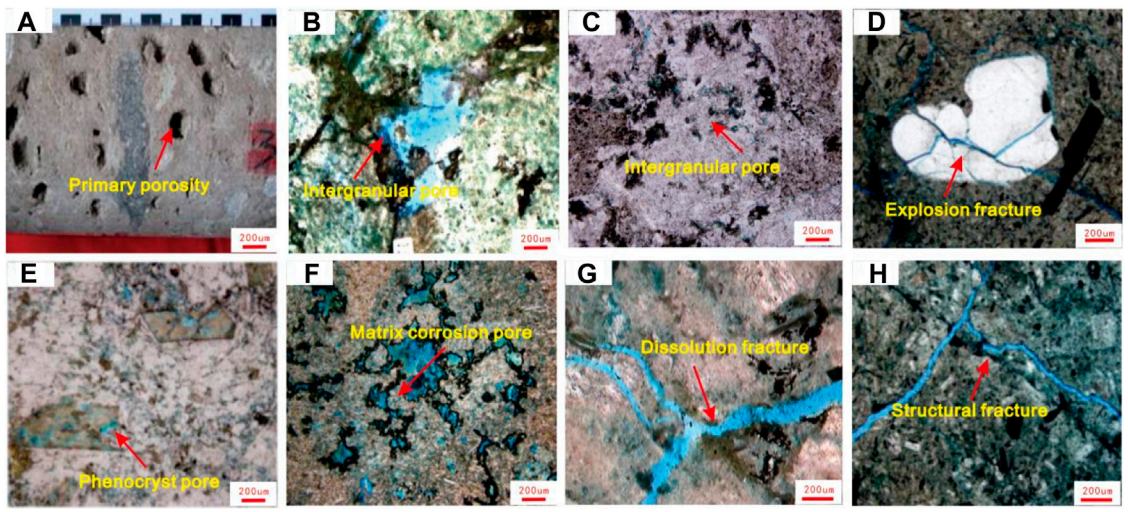

FIGURE 5 | Genetic types of volcanic rock reservoir space in the Wangfu gas field. **(A)** Primary pores, rhyolite, wellCs14, 2,997.75 m, core; **(B)** intergranular pores, rhyolite breccia, wellCs13, 2232mm, single polarized light×10; **(C)** intergranular pores, gray andesite, wellWf1, 3130m, single polarized light ×10; **(D)** explosion fracture, trachycere breccia lava, well Cs11, 3043m, single polarized light ×10; **(E)** porphyry pores, trachyandesite, wellWf1, 3230 m, single polarized light×10; **(F)** matrix corrosion pore, volcanic breccia, wellCs602, 2,614.8 m, single polarized light×10; **(G)** dissolution fracture, trachyandesite, wellCs11, 2720 m, single polarized light×10; and **(H)** structural fracture, trachoic breccia lava, wellCs11, 3043m, single polarized light×10.

production. Usually, the greater the effective thickness, the higher the gas well production (Zhou et al., 2007; Hasan et al., 2018). **Figure 6A** shows that there is a certain correlation between the effective thickness of volcanic reservoir and open flow, but the correlation coefficient R^2 is low, only 0.1548. This conclusion is quite different from the understanding of clastic reservoir. There

TABLE 2 | Statistics of the production capacity and sensitivity parameters of the Wangfu gas field reservoir.

Well Number	Test Production	Layer Number	Split Test Production Q_i ($\times 10^4$ m^3/d)	Porosity (%)	Permeability (mD)	Gas Saturation (%)	Effective Thickness (m)	Energy Storage Coefficient
WF1	8.9	219	0.373	4.6	0.15	45.0	2.6	0.05
		220	2.525	6.5	0.25	55.0	10.2	0.36
		240	5.050	5.5	0.15	60.0	22.1	0.73
		241	0.952	5.0	0.14	50.0	5.5	0.14
CS4	5.5	171	2.937	6.3	0.22	55.0	2.8	0.10
		172	0.839	5.7	0.17	40.5	1.2	0.03
		176	0.997	4.2	0.17	39.2	2	0.03
		179	0.728	3.8	0.21	45.2	1.4	0.02
CS5	12.8	78	0.452	8.7	0.80	38.7	1.3	0.04
		79	3.977	9.8	1.24	56.2	7	0.39
		80	8.371	8.2	0.63	53.2	18.6	0.81
CS6	16.2	148	10.329	13.8	3.83	65	11.6	1.04
		153	5.871	10.2	1.43	38	11	0.43
CS7	1.2	207	0.406	4	0.18	40	14.7	0.24
		208	0.587	4.5	0.15	46	16.4	0.34
		209	0.207	4.5	0.15	38	7	0.12
CS9	10.6	117	1.365	12.2	2.61	31.2	2.9	0.11
		116	4.722	16.1	5.96	50.6	4.7	0.38
		115	4.513	12.8	3.04	58.2	4.9	0.37
CS11	4.6	121	2.418	11.3	2.04	66.1	9.1	0.68
		107	2.182	8.4	0.69	58.6	12.5	0.61
CS601	3.5	161	1.509	5.0	0.14	62.7	14.7	0.46
		145	1.991	10.0	1.34	38.0	16	0.61
CS606	2.2	165	1.504	11.1	1.92	48.1	10.6	0.57
		163	0.696	8.3	0.66	38.0	8.3	0.26
CS608	1.9	175	1.900	18.0	8.17	50.0	6	0.54

are two main reasons: First, the formation of volcanic reservoir has a certain suddenness from the formation mechanism, and the distribution scale, lithology, physical properties, and pore structure characteristics of the volcanic reservoir have a strong non-mean, and it is difficult to determine the plane and longitudinal distribution law. At present, there is no corresponding research report, and this field will be the focus of further research. Second, compared with clastic reservoirs, the production of gas wells is not only related to the effective thickness of volcano reservoirs but is also highly influenced by the physical properties (porosity and permeability) of gas reservoirs. Therefore, the effective thickness of the volcanic rock reservoir has poor correlation with productivity.

4.1.3 Effective Thickness * Porosity (H.Φ)

Porosity is a parameter to measure the ability of the rock reservoir to contain fluids. The larger the porosity of reservoir, the larger the pore space in rock. Only the interconnected pores have practical significance from the practical point of view of gas reservoir research because they cannot only store natural gas but also allow gas to percolate therein. Therefore, the effective thickness of volcano reservoir * porosity (H.) is established. Φ) And open flow (**Figure 6B**).

From **Figure 6B**, it can be seen that when H Φ is greater than 0.43, the open flow is greater than $1.62 \times 10^4 m^3/d$, When H Φis close to or greater than 1.04, the open flow is greater than $3.74 \times 10^4 m^3/d$. h Φ. There is a certain positive correlation with the open flow, but the correlation coefficient R^2 is only 0.4915, which is still not ideal, and the correlation coefficient is still relatively low.

4.1.4 Formation Coefficient (H.K)

Permeability is the ability of rocks to allow fluids to pass through their pores. It plays an important role in studying and evaluating oil and gas reservoirs and production capacity (Farquharson et al., 2015). Therefore, the relationship between the formation coefficient (H.K) and open flow of volcanic reservoir in the Wangfu gas field is established. **Figure 6C** shows that the gas test production increases with the formation coefficient (H.K). When the local formation coefficient (H.K) is greater than 1.06, the open flow is greater than $1.62 \times 10^4 m^3/d$. However, the correlation coefficient R^2 between the formation coefficient and open flow is relatively low, only 0.3407, which is not ideal. The main reason is that the volcanic reservoir is dense and heterogeneous, and the production of gas wells is not only related to the effective thickness and physical properties, and it is also closely related to the gas bearing property of the gas reservoir. If there is a gas reservoir with large thickness and good physical properties, but with little gas or even water filled in it, the gas saturation will be low and the gas test will not obtain high production.

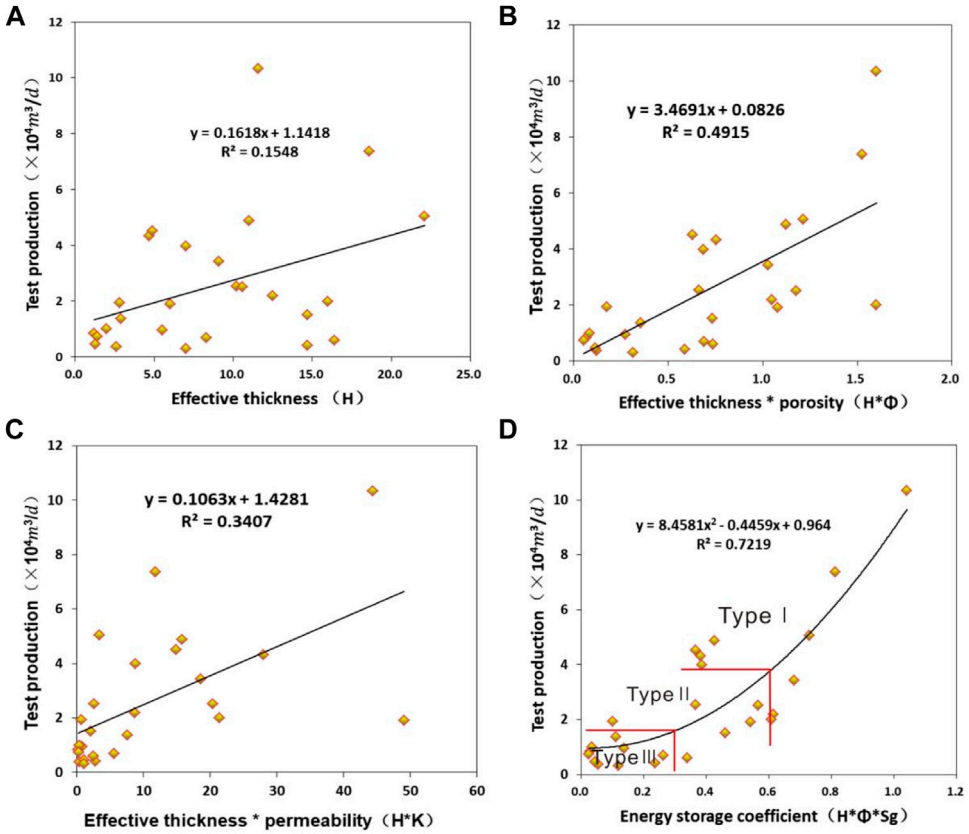

FIGURE 6 | Relationship between sensitive parameters and productivity of volcanic reservoir in the Wangfu gas field. Note: **(A)** Relationship between the effective thickness and production capacity, **(B)** relationship between effective thickness * porosity and productivity, **(C)** relationship between the formation coefficient and productivity; and **(D)** relationship between the energy storage coefficient and productivity.

4.1.5 Energy Storage Coefficient ($h.\Phi.S_{g_i}$)

As we all know, the reserve calculation formula using the volumetric method is

$$G = 0.01A_g.h.\Phi.S_{g_i}\frac{P_i.T_{SC}}{P_{SC}.T.Z_i}, \quad (2)$$

where G—natural gas original geological reserves (10^8 m^3), A_g—gas bearing area (km^2), h—average effective thickness (m), Φ—average effective porosity (%), S_{g_i}—average original gas saturation (%), T—average formation temperature (K), T_{SC}—ground standard temperature T (K), P_i—average initial formation pressure (MPa), P_{SC}—surface standard pressure (MPa), and Z_i—original gas deviation coefficient, a dimensionless quantity.

It can be seen from the formula that the energy storage coefficient ($h.\Phi.S_{g_i}$) is a factor of G, which better reflects the gas enrichment degree of a single horizon. **Figure 6D** shows that the energy storage coefficient has a good correlation with the gas well productivity. With the increase of energy storage coefficient, the gas well productivity increases in a polynomial relationship, and the correlation coefficient R^2 reaches 0.7219. Therefore, the energy storage coefficient can well reflect the productivity characteristics of the monolayer. When the energy storage coefficient is between 0.0 and 0.3, the open flow of the gas well is less than $1.62 \times 10^4 m^3/d$ (Class III). When the energy storage coefficient is between 0.3 and 0.6, the open flow of the gas well is in the range of $1.62 - 3.74 \times 10^4 m^3/d$(class II). When the energy storage coefficient is greater than 0.6, the open flow is more than $3.74 \times 10^4 m^3/d$ (class I) (**Figure 6D** and **Table 2**).

The gas test and production data of 10 wells in the study area were utilized to investigate the energy storage coefficient. Based on previous research and considering the energy storage coefficient as the constraint condition, the volcanic reservoir is divided into three categories according to the boundary of energy storage coefficient greater than 0.6, 0.6–0.3, and less than 0.3. The rock samples from different reservoirs were selected to complete the indoor experiments such as casting thin section and conventional mercury injection.

Based on the characteristics of conventional and special logging curves, the reservoir space combination characteristics were analyzed, the micro-pore structure and logging response characteristics of different types of reservoirs were evaluated, and the sensitive parameters such as the reflecting gas bearing property was optimized. Furthermore, the reservoir classification standards were established, and a guidance for the classification and evaluation of volcanic reservoirs was provided.

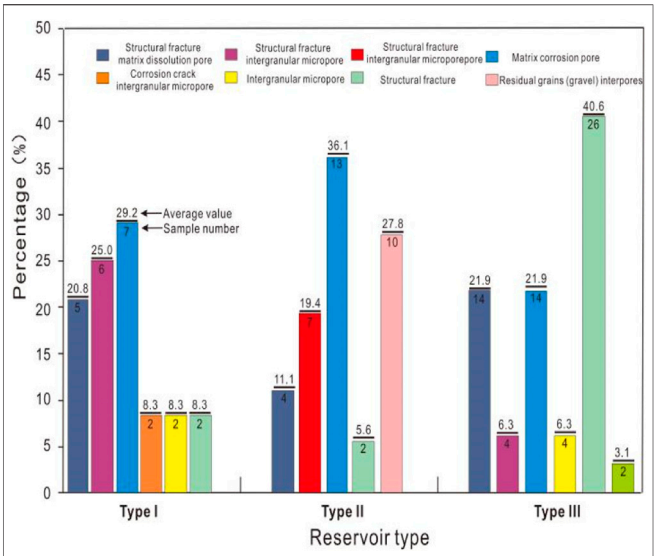

FIGURE 7 | Histogram of various reservoir spatial combinations of the volcanic reservoir in the Wangfu gas field.

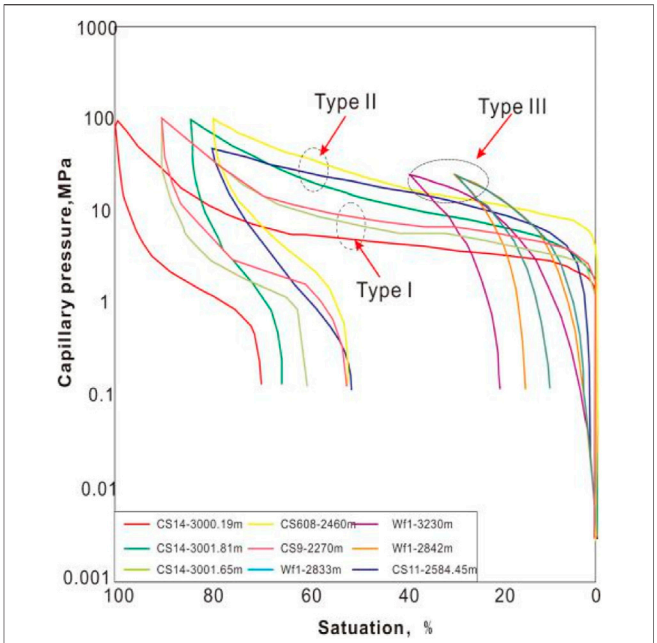

FIGURE 8 | Classification diagram of the mercury injection curve of the typical volcanic reservoir in the Wangfu gas field.

4.2 Reservoir Space Combination Characteristics

Generally, the reservoir space of volcanic rock reservoir does not exist alone but appears in some combination form (Zheng et al., 2018a; Wang et al., 2020). Therefore, using the data of 124 cast thin sections, the characteristics of the reservoir space combination are analyzed through image pore throat analysis and measurement technology, and the characteristics of reservoir space combination of three types of reservoirs are evaluated based on the dominant reservoir space combination (**Figure 7**).

Type I: This type is mainly composed of structural fracture matrix dissolution pores, structural fracture intergranular micropores, and matrix dissolution pores. Structural fracture matrix dissolution pores and structural fracture intergranular pores are common in andesite and rhyolite reservoirs of volcanic lava. Fractures play a connecting role between pores, and the reservoir space is greatly affected by the strength of dissolution and the magnitude of structural stress. Intergranular dissolution pores are often found in the andesite of volcanic lava reservoirs. The pores have good connectivity and strong seepage capacity and are generally good reservoir spaces.

Type II: Matrix dissolution pores and residual intergranular pores are mainly presented. The matrix dissolution pores and residual grains' interpores are mainly developed in the volcano clastic sedimentary rocks and volcano breccia reservoirs, which are affected by diagenesis and tectonics; the connectivity between pores is poor; the percolation ability is generally; and most of them are general reservoir spaces.

Type III: This type is mainly composed of structural fractures, followed by structural fractures' matrix dissolution pores and matrix dissolution pores. The type of structural fracture reservoir space is mostly the residual fractures after the structural fractures are filled with carbonate. The combination mode of reservoir space is single. This kind of pore structure is common in the pyroclastic rock reservoir and volcanic lava pyroclastic rock reservoir. The physical properties of the reservoir are poor, and most of them are poor reservoirs.

TABLE 3 | Typical mercury injection curves and characteristic parameters of volcano rocks with different pore throat types.

Classification of Pore Structure	Type I	Type II	Type III
PD (MPa)	<2.0	2.0–6.0	>6.0
Pc-50 (MPa)	<20.0	20.0–36.0	/
Maximum mercury saturation (%)	89.9–99.2	75.2–85.5	25–35
Porosity (%)	>8.0	4.0–8.0	<4.0
Permeability (mD)	>0.1	0.01–0.1	<0.01
Test production (× $10^4 m^3/d$)	<1.30	1.3–3.9	>3.9

4.3 Distribution Characteristics of Micro-Pore Structure

The genesis of volcanic reservoir throat is more complex than sedimentary rock, and the reservoir has different micro-pore structure characteristics. Based on the mercury injection data of 26 blocks, the micro-pore structure characteristics and seepage capacity of volcanic rock reservoir are analyzed. According to the pore structure and curve shape, the pore structure of the volcanic rock reservoir is divided into three categories (**Figure 8** and **Table 3**):

Type I: The curve shape is characterized by closing to the left and down and concave to the right, with coarse skewness and good sorting; The characteristic parameters are low displacement pressure (PD < 2 MPa), low mercury saturation median pressure (PD <

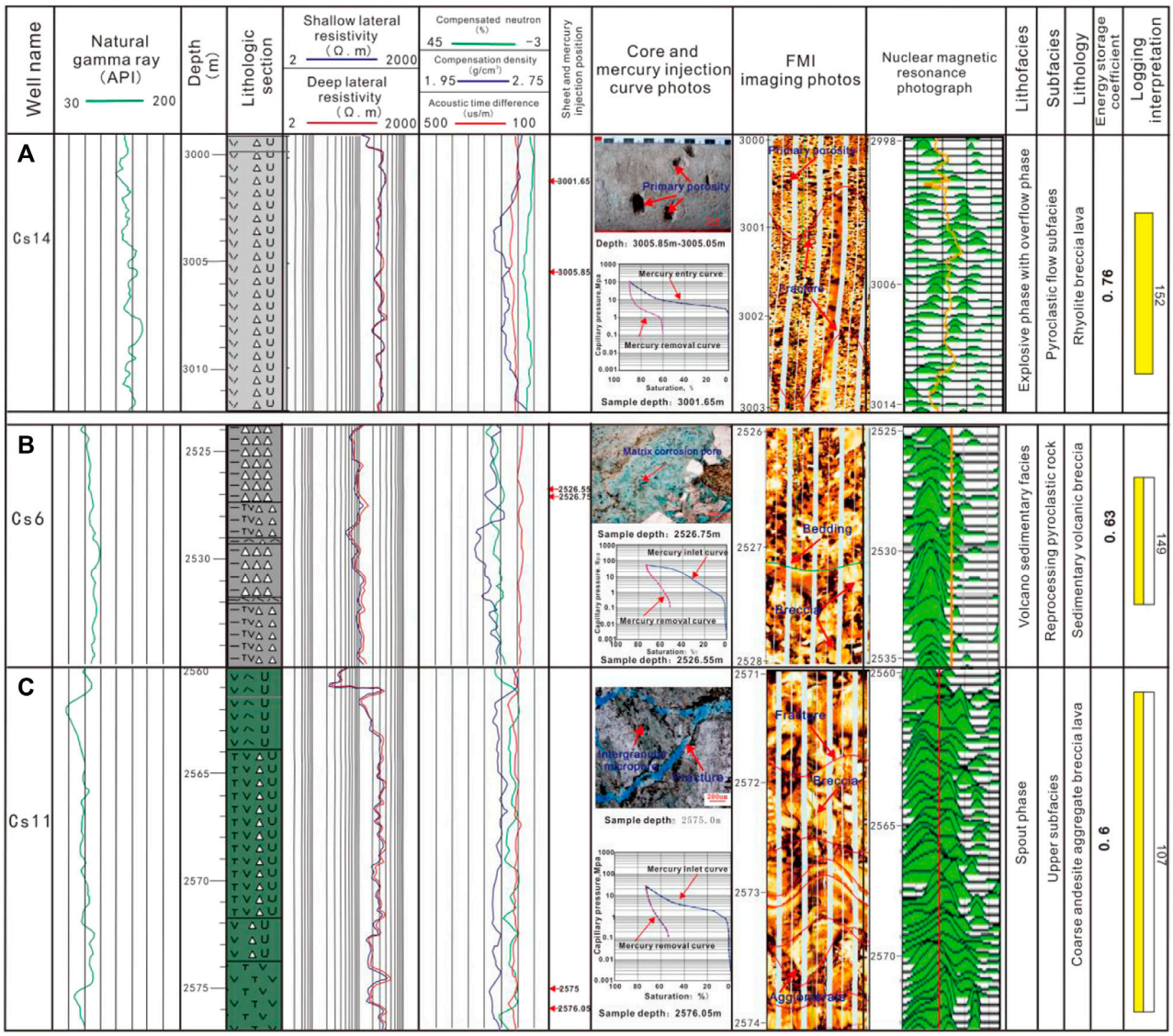

FIGURE 9 | Typical logging evaluation map of Type I volcano reservoir in the Wangfu Gas Field. Notes: **(A)** Well Cs14; **(B)** Well Cs6; **(C)** Well Cs11.

20 MPa), and high maximum mercury saturation (89.9–99.2%). The reservoir has good physical properties, porosity ranging between 8–12% and permeability more than 0.1 mD.

Type II: The curve shape range is a straight line with a slope angle between 45° and 60°. The platform section is not developed, medium skewness and general sorting. The characteristic parameters are higher displacement pressure (PD is 2 ~ 6 MPa), higher median pressure of mercury saturation (PD is 20–36 MPa), and lower maximum mercury saturation (75.2–85.5%). The physical properties of the reservoir are general, with porosity between 4 and 8% and permeability between 0.01 and 0.1 mD.

Type III: The curve shape is close to the right and up, the skewness is very fine, and the sorting is poor; the characteristic parameters are high displacement pressure (PD > 6 MPa), no median mercury saturation, and extremely low maximum mercury saturation (25–35%). The reservoir property is low, the porosity is less than 4%, and the permeability is less than 0.01 mD.

4.4 Logging Response Characteristics of Typical Reservoirs

The logging response characteristics of typical reservoirs are investigated in order to realize the reservoir classification evaluation of the whole well section, comprehensively analyze

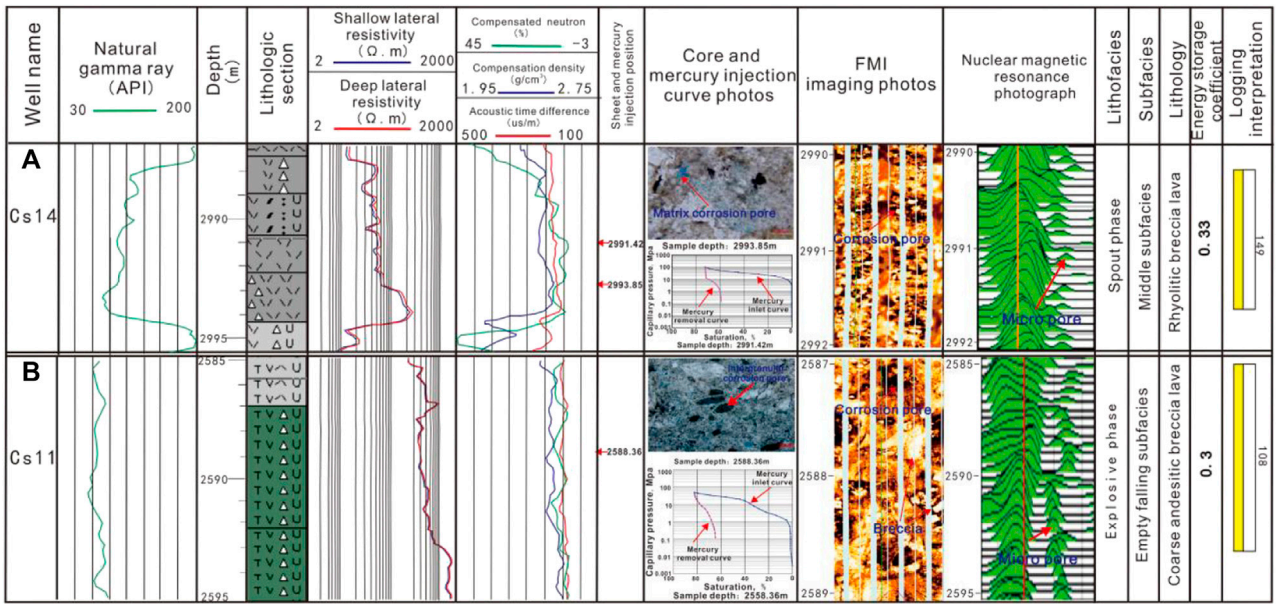

FIGURE 10 | Typical logging evaluation map for Type II volcano reservoir in the Wangfu Gas Field. Notes: **(A)** Well Cs14; **(B)** Well Cs11.

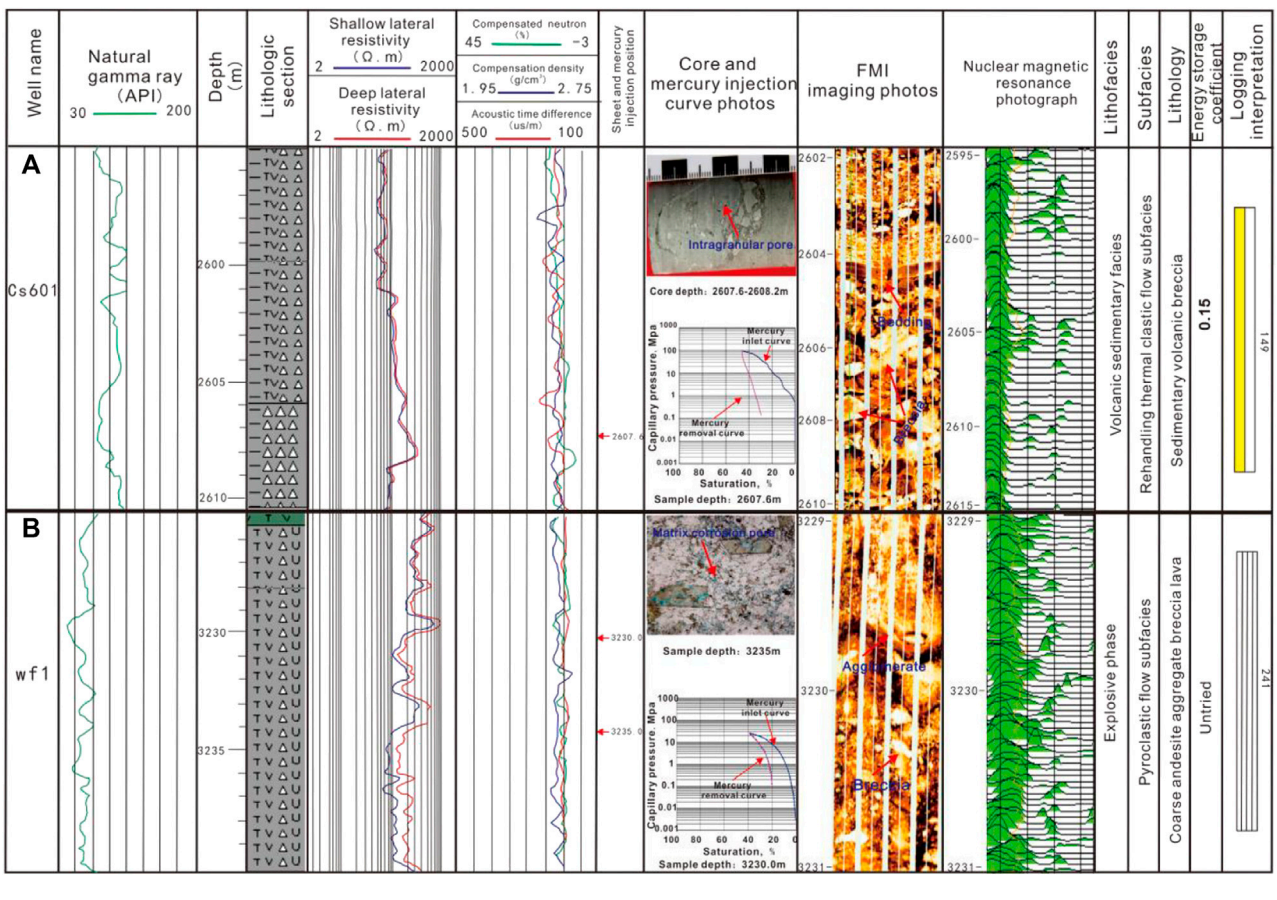

FIGURE 11 | Typical logging evaluation map of Type III volcano reservoir in the Wangfu Gas Field. Notes: **(A)** Well Cs601; **(B)** Well wf1.

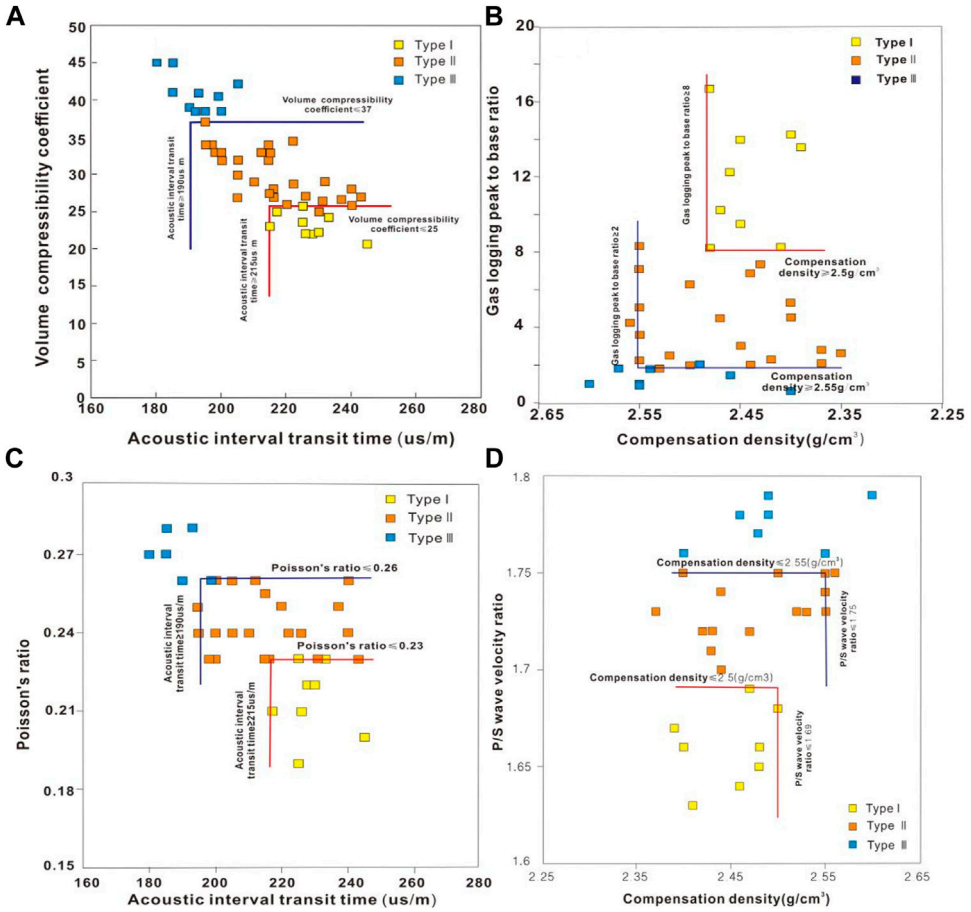

FIGURE 12 | Classification and identification chart of effective reservoir logging in the Wangfu gas field. Note: **(A)** Crossplot of the acoustic time difference and volume compressibility coefficient. **(B)** Compensated density-gas logging peak to base ratio crossplot. **(C)** Acoustic interval transit time Poisson's ratio crossplot. **(D)** Compensating density-P/S wave velocity ratio crossplot.

the conventional and special logging response characteristics, and summarize the logging response characteristics of different types of volcanic reservoirs.

Type I: Volcano lava reservoirs: Logging curves are characterized by high gamma ray (100–120 API), medium high resistivity (200–300 Ω m), high acoustic transit time, low density, and low neutron. FMI imaging shows the characteristics of stomata and high conductivity joints. NMR logging has common multi peak characteristics, and its free peaks develop. The T_2 spectrum is tailed obviously, as shown in **Figure 9A**. For the pyroclastic sedimentary rock reservoir, the logging curve shows low natural gamma (70–90API), medium resistivity (100–200 Ω m), low density, medium and low neutrons, an obvious excavation effect, a narrow strip shape, and a high acoustic time difference. FMI imaging shows the characteristics of agglomerates and breccia and certain bedding and fractures. Nuclear magnetic logging often shows double peak characteristics, and the amplitude of the free peak is large. The tailing phenomenon of the T_2 spectrum is obvious, as shown in **Figure 9B** and **Figure 9C**.

Type II: Volcano lava reservoirs: Logging curves are characterized by high gamma ray (90-115API), low resistivity (50–100 Ω m), low density, low neutron, a low acoustic time difference, and no obvious excavation effect. FMI imaging shows relatively less obvious dissolution characteristics, no cracks, and bedding characteristics. Nuclear magnetic logging is mostly unimodal, its free peaks are not developed, and the T_2 spectrum is not obvious, as shown in **Figure 10A**. For the volcanic lava reservoir, the logging curve shows high natural gamma (70–90API), medium and high resistivity (200–400 Ω m), low density, medium and low neutrons, and a low acoustic wave time difference, and the excavation effect is not obvious. Some breccia characteristics can be seen in FMI Imaging, but the breccia boundary is fuzzy, with certain fusion characteristics, no fracture, and bedding characteristics, and the nuclear magnetic logging mostly shows single peak characteristics, the free peak is not developed, and the tailing phenomenon of the T_2 spectrum is not obvious, as shown in **Figure 10B**.

Type III: The logging curve shows medium and low natural gamma (50–90 API). Due to the difference of breccia size and composition, the resistivity changes greatly (80–500 Ω m). The density ranges between high and medium, and almost no obvious excavation effect and low acoustic wave time

TABLE 4 | Classification standard of volcano reservoir in the Wangfu Gas Field.

Series & Category	Lithology and lithofacies		Reservoir physical properties		Microscopic characteristics			Conventional logging curve		Logging and logging data derived parameters				Special logging series		Productivity characteristics
	Lithology	lithofacies	Porosity (%)	Permeability (mD)	Displacement pressure (MPa)	Throat mean (m)	Median pressure (MPa)	AC (us/m)	Den (g/cm^3)	Gas logging peak to base ratio	Volume compressibility coefficient	P / S wave velocity ratio	Poisson's ratio	Nuclear magnetic logging	Imaging logging	
Type I	Volcanic lava, pyroclastic sedimentary rock	Explosive phase and overflow phase	>8	>0.1	<2	<12	<20	>215	<2.5	>8	<25	<1.69	<0.23	Common multimodal characteristics, free peak development, and T_2 spectrum tail phenomenon are obvious.	Pores, breccias and high guide fractures can be seen, and a small amount of bedding can be seen locally	The energy storage coefficient is greater than 0.6 and has a certain stable production capacity, with a daily gas output of more than 3.74 × 10^4m^3/d
Type II	Volcanic lava pyroclastic rock, pyroclastic rock sedimentary rock	Explosive facies, volcanic sedimentary facies	4–8	0.01–0.1	2–6	12–16	20–36	190–215	2.5–2.55	2–8	25–37	1.69–1.75	0.23–0.26	There is a single peak character, the free peak is not developed, and the T_2 spectrum is not obvious.	Relatively insignificant dissolution features can be seen, no fracture and bedding features are found, and some breccia boundaries are fuzzy	The energy storage coefficient is between 0.3–0.6, stable production capacity is poor, Nissan 1.62 – 3.74 × 10^4m^3/d
Type III	Volcanic lava, pyroclastic rock, volcanic lava pyroclastic rock, pyroclastic sedimentary rock	Explosive facies, overflow facies and volcanic sedimentary facies	<4	<0.01	>6	>16	>36	<190	>2.55	<1.8	>37	>1.75	>0.26	Nuclear magnetic logging is mostly characterized by single peak, and there is no tailing phenomenon of T_2 spectrum	Obvious characteristics of agglomerates and breccia can be seen, and the boundary of agglomerates or breccia is fuzzy	The energy storage coefficient is less than 0.3, the gas production is less, and the daily gas production is less than 1.62 × 10^4m^3/d

TABLE 5 | effective reservoir thickness, fracturing parameters, and process data table of Block CS6 in the Wangfu gas field.

Well Number	Effective Reservoir Thickness (m)				Fracturing Technology	Fracturing Parameters			Gas Volume (× $10^4 m^3/d$)
	Type I	Type II	Type III	Total Thickness		Number of Segments	Sand Quantity (m^3)	Liquid volume (m^3)	
CS6	11.6	19.2	18.2	49	Vertical well multi-stage fracture pattern fracturing	2	140	824.6	3.0
CS601	8.0	14.8	26.8	49.6	Vertical well multi-stage fracture pattern fracturing	2	110	763	0.58

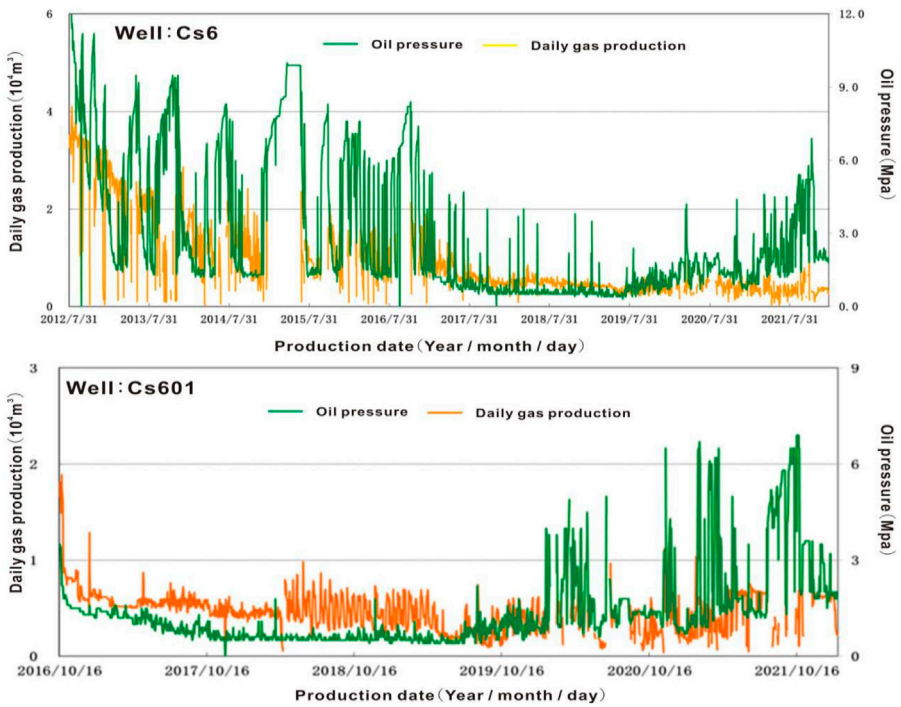

FIGURE 13 | production curve of wells CS6 and cs601 in the Wangfu gas field.

difference are observed; FMI imaging shows obvious lump and breccia characteristics. The blocks or breccia boundaries are fuzzy. They have certain melting characteristics, which reflect the tight characteristics of the reservoir. The nuclear magnetic logging is mostly single peak, as shown in **Figures 11A,B**.

4.5 Classification and Identification of Volcanic Reservoirs

The aim of this part is to summarize the logging response characteristics of the reservoir (**Figure 9**, **Figure 10** and **Figure 11**), analyze the corresponding relationship between logging and logging response characteristics of different types of reservoirs and physical properties and gas bearing properties, optimize the parameters such as the P/S wave velocity ratio (eliminate lithology lithologic effects, considering the difference of fluid on the influence of the longitudinal wave, shear wave velocity, and identification of reservoir hydrocarbon content), gas logging peak to base ratio (during logging, the ratio of the gas measurement peak value to base value is used to judge the reservoir gas content), volume compressibility coefficient (the difference in gas content leads to the change of the ratio of compressibility to compressibility, which is derived from the ratio of compressibility to compressibility), Poisson's ratio (the ratio of axial strain to radial strain indirectly reflects the gas bearing property of the reservoir, and this parameter is derived from the aspect ratio), acoustic interval transit time, and compensation density, establish the intersection chart of reservoir classification (**Figure 12**), and then determine the reservoir classification standard (**Table 4**).

The study equally comprehensively analyzes the laboratory and logging data, the reservoir classification chart (**Table 3** and **Table 4**) is established, and finally, a new set of volcanic reservoir classification standards is determined, as shown in **Table 4**.

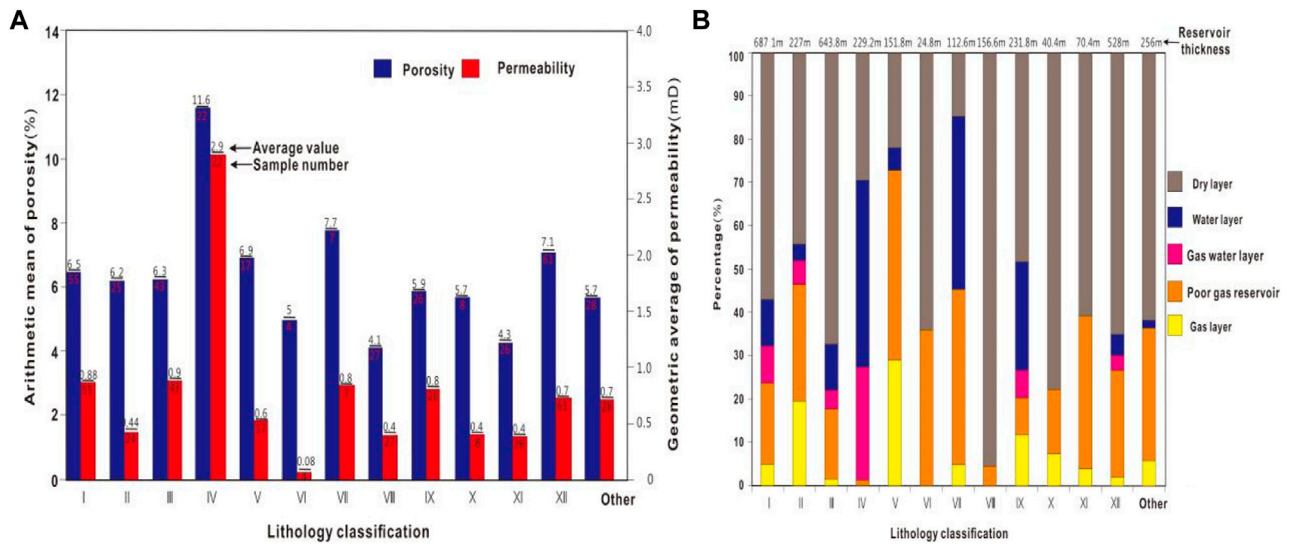

FIGURE 14 | Relationship between volcanic reservoir physical properties, effective reservoir distribution, and rock types. Notes: I—coarse andesite, II—coarse andesitic breccia lava, III—coarse andesitic volcanic breccia, IV—coarse andesitic tuff, V—rhyolite, VI—rhyolitic tuff lava, VII—trachyte, VIII—andesite, IX—andesitic volcanic breccia, X—andesitic tuff, XI—sedimentary tuff, and XII—sedimentary breccia. **(A)** Histogram of the lithology physical property relationship of the volcanic reservoir. **(B)** Histogram of the lithology effective reservoir relationship of the volcanic reservoir.

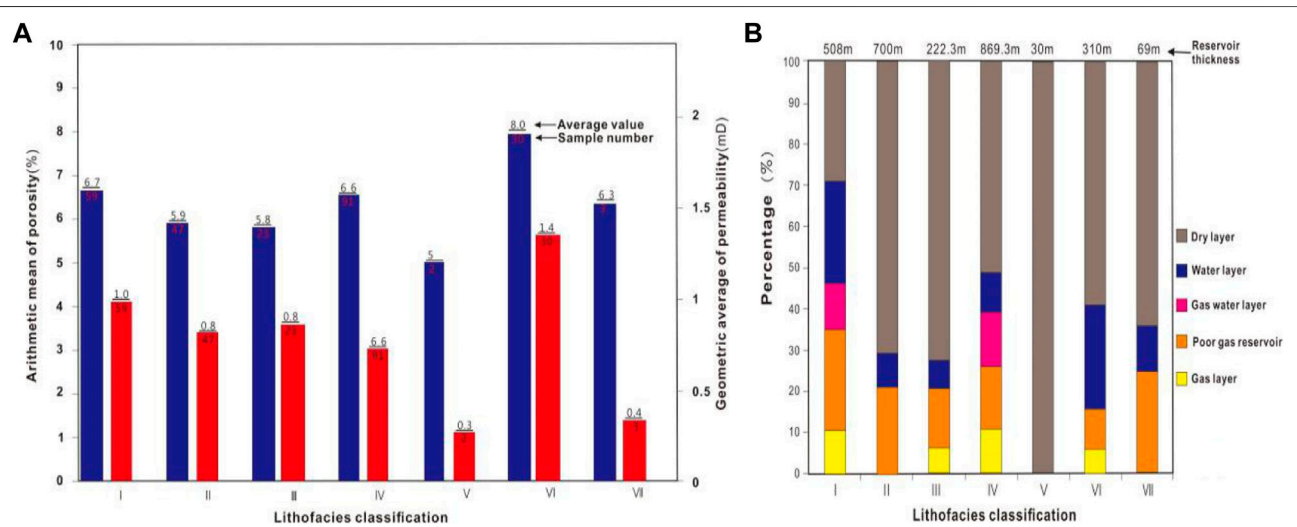

FIGURE 15 | Relationship between volcanic reservoir physical properties, effective reservoir distribution, and lithofacies type. Notes: I—upper subfacies, II—middle subfacies, III—lower subfacies, IV—thermal clastic flow subfacies, V—thermal wave subfacies, VI—air fall subfacies, and VII—volcanic neck subfacies. **(A)** Histogram of the lithofacies physical property relationship of the volcanic reservoir. **(B)** Histogram of the lithofacies effective reservoir relationship of the volcanic reservoir.

4.6 Result Verification

According to the above criteria, 29 wells are classified, and the accuracy of reservoir classification results is verified by gas test and production data. Wells CS6 and cs601 are two wells located in the same trap (**Figure 2**). The effective reservoir thickness produced is 49 and 49.6 m. It is approximately considered that the effective reservoir thickness produced is the same. The fracturing process and fracturing parameters adopted are basically the same, but the production effect is quite different (**Table 5** and **Figure 13**). The main reason for the analysis is that the thickness of type I and II reservoirs is relatively large in the CS6 well, which are 11.6 and 19.2 m, respectively, accounting for 62.8% of the total applied thickness. The type III reservoirs are relatively few, so the output of the CS6 well is relatively high. The reason for the low production of the CS601 well is mainly due to the use of type III reservoirs. The effective thickness of type I and II reservoirs is relatively thin, and the contribution of reservoir productivity is relatively small. Therefore, the results of the

operation confirm that the classification methods and results are relatively accurate.

5 DISCUSSION

5.1 Relationship Between Lithology, Lithofacies, and Effective Reservoir

5.1.1 Lithology, Physical Property, and Effective Reservoir

The volcano reservoir has strong heterogeneity, and different volcanic rocks have different properties such as density, composition, and structure, which lead to different physical properties of volcano rocks with different lithology. According to the measured physical property data, logging interpretation results, and gas test data, statistics are made on the reservoir physical properties and effective reservoir distribution of 12 main volcanic rocks developed in the Wangfu gas field. The results showed that the lithology with good physical properties is coarse andesite tuff, trachyte, and sedimentary breccia, followed by coarse andesite breccia lava, coarse andesite volcanic breccia, and rhyolite, and the lithology with poor physical properties is rhyolite tuff lava, andesite, andesite volcanic breccia, andesite tuff, and sedimentary tuff (**Figure 14A**). According to the comprehensive analysis of effective reservoir proportion and development thickness, effective reservoirs are mainly distributed in rhyolite, coarse andesite breccia lava, and trachyte, followed by coarse andesite, rhyolite tuff lava, tuff, and breccia, and effective reservoirs of other lithology are less developed (**Figure 14B**).

Forming two points: 1) The corresponding relationship between physical properties and gas bearing properties of reservoirs with the same lithology is poor. For example, coarse andesitic tuff has good physical properties, but its gas bearing properties are poor, and most of the effective reservoirs are class III reservoirs. Therefore, the development of effective reservoirs is greatly affected not only by reservoir physical properties but also by reservoir forming conditions and other factors. 2) The effective reservoirs of rhyolite, coarse andesite breccia lava, trachyte, and sedimentary breccia are relatively developed, especially the rhyolite reservoir. Class I and class II reservoirs account for more than 75% of the rhyolite reservoirs revealed in the whole region.

5.1.2 Lithofacies, Physical Properties, and Effective Reservoir

The physical characteristics of volcano facies are very different. According to the measured physical property data, logging interpretation results, and gas test data, the reservoir physical properties and effective reservoir distribution of the volcano facies reservoir developed in the Wangfu gas field are statistically analyzed. The results showed that the lithofacies with good physical properties are upper subfacies (I), thermal clastic flow subfacies (IV), and empty subfacies (VI), followed by middle subfacies (II) and lower subfacies (III) (**Figure 15A**). Thermal wave subfacies (V) and volcanic neck subfacies (VII) have poor reservoir physical properties. Effective reservoirs are mainly distributed in the upper subfacies, empty fall subfacies, and thermal clastic flow subfacies, followed by the middle subfacies, lower subfacies, volcanic neck subfacies, and thermal base wave subfacies (**Figure 15B**).

Forming two conclusions: 1) The physical properties and effective reservoir development degree of the same lithofacies reservoir correspond well, and the high-quality lithofacies type corresponds to good physical properties and gas bearing properties; 2) The upper subfacies, air drop subfacies, and thermal clastic flow subfacies are the dominant facies belt types of effective reservoirs.

5.2 Relationship Between Diagenesis Such as Weathering, Leaching, and Dissolution, and Effective Reservoir

5.2.1 Weathering and Leaching

Weathering and leaching have a great impact on the physical properties of the volcanic reservoir (Heap et al., 2014; Colombier et al., 2017). The analysis shows that the volcanic reservoir of the Wangfu gas field is mainly affected by weathering forest filtration in the following two aspects:

1) The weathering crust formed at the top of volcanic rock eruption cycle and eruption interval is a high-quality reservoir development area (**Figure 2**). For example, in the well section 2560–2576 m at the top of volcanic rock cycle of well CS11, coarse andesite aggregate breccia lava, andesite, andesite tuff lava, and other reservoirs in this well section are affected by weathering and leaching, with good physical properties and excellent reservoir forming conditions, and class I and II reservoirs are developed. Under the influence of atmosphere and surface water, the volcanic reservoir in the weathering crust development area is broken to form a series of micro-fractures. At the same time, chemical weathering such as dissolution, oxidation, hydration, and carbonation leads to the development of source dissolution pores (matrix dissolution pores and micro-fractures) in the volcanic reservoir, which greatly improves the reservoir performance of volcanic rocks (**Figure 9C**).
2) Under the influence of weathering and denudation, the volcanic reservoir in the high part of the structure accumulates rapidly to the trough area to form a high-quality sedimentary pyroclastic reservoir. According to the cast thin section and imaging data of the coring section of well CS6, the volcanic breccia in the sedimentary volcanic breccia reservoir is mostly supported by clastic particles, and the breccia is poorly sorted. It can be seen that the volcanic breccia has certain rounding characteristics locally, and the matrix dissolution pores, phenocryst dissolution pores, and other secondary pores are developed (**Figure 2**, **Figure 9B**, **Figures 5E,F**). The physical properties of the reservoir are good. Class I, II, and III reservoirs are developed, with the porosity of 5–10% and the permeability of 0.01–1.17 mD. Weathering and denudation are the key to the formation of effective reservoirs of sedimentary pyroclastic rocks in high parts and control the distribution of sedimentary pyroclastic reservoirs in low parts.

5.2.2 Dissolution

The volcano reservoir has deep buried and long reservoir forming time, and most of them have experienced severe dissolution. Dissolution plays a significant role in improving

volcano reservoir formation (Li et al., 2014; Zhang et al., 2015). Core description and microscopic thin section identification show that the dissolution is mainly manifested in the dissolution of volcanic phenocrysts and matrix, and the dissolution of fillings in primary pores and fractures (**Figure 5E–G**). Dissolution pores are an important part of volcanic reservoir space in the study area. Class I, class II, and class III reservoirs are developed.

The dissolution of the volcano reservoir in this area has two advantages: 1) volcano rock forming stage experienced multi-stage tectonic movement, and faults and microfractures developed, providing channels for the migration of underground hydrothermal and acidic fluids. 2) Two sets of high-quality source rocks are developed at the interval of the volcanic eruption cycle and the bottom of the Shahezi Formation. In the thermal evolution stage, a large number of organic acid solutions can be formed, which is the key to dissolution. Therefore, there are secondary dissolution pore development zones formed by dissolution near the fault, the lower part of the unconformity and the top of the cycle.

6 CONCLUSION

1) The parameters such as effective thickness, effective thickness * porosity, formation coefficient, and energy storage coefficient are relatively sensitive to the productivity of gas wells, and the energy storage coefficient can better characterize the productivity of single wells of gas wells than other parameters, According to the boundary of energy storage coefficient greater than 0.6, 0.6–0.3, and less than 0.3, the volcano reservoir in the Wangfu gas field is subdivided into three types.
2) Taking the classification of the reservoir coefficient as the constraint condition, a series of experimental analysis work such as core observation, cast thin section, and conventional mercury injection are carried out for different types of reservoirs and the characteristics of different types of reservoirs are defined. In terms of reservoir space combination characteristics, the Type I reservoir is mainly composed of structural fracture matrix dissolution pores, structural fracture matrix micropores, and matrix dissolution pores. Type II reservoir matrix dissolution pores and residual intergranular pores are relatively developed, and the Type III reservoir is mainly composed of structural fractures. In terms of micro-pore structure characteristics, from Type I to Type III reservoirs, the porosity, permeability, and maximum mercury saturation decreased, the displacement pressure and median saturation pressure increased. From class I to class III reservoirs, the shape skewness and sorting coefficient of mercury injection curve deteriorated.
3) There are some differences in the logging curve characteristics of different typical reservoirs. Among them, the derived parameters such as P-and S-wave velocity, peak to base ratio of gas logging, volume compressibility coefficient, acoustic time difference, and density are relatively sensitive to reservoir characteristics. Based on the above parameters, four sets of reservoir classification charts were established, and 29 reservoirs in the whole area were classified and evaluated. The results of gas well test in Cs6, Cs601, and other wells confirmed that the classification standards were accurate and reliable.
4) Weathering, leaching, dissolution, and other diagenesis have improved the physical properties of the reservoir. The corresponding relationship between lithology, physical property, and gas bearing property is poor, which shows that the development degree of the effective reservoir is not only controlled by lithology but also affected by reservoir space type, diagenesis, and other factors. Lithologic facies correspond well with physical properties and gas bearing properties of reservoirs. Rhyolitic, coarse, and stable breccia lava, trachyte, and sedimentary breccia are relatively effective lithologic reservoirs. The lithofacies of Kobe Aso, air fall subfacies, and thermal clastic flow are the dominant facies belts of effective reservoirs.

DATA AVAILABILITY STATEMENT

The original contributions presented in the study are included in the article/Supplementary Material; further inquiries can be directed to the corresponding author.

AUTHOR CONTRIBUTIONS

W-TS: The leading author of this article. Z-HL: Funding provider. Y-SL: Guide teachers and provide overall thinking. LZ: funding provider, experimental operator and drawing personnel. H-MW: Data analyst and article checker. AK: data analyst and article checker.

FUNDING

This work was completed with the support of China's major national special project "development of large oil and gas fields and coalbed methane" special topic "effective development technology of deep tight gas in the south of Songliao Basin" (2016zx05047005-006).

ACKNOWLEDGMENTS

We thank Professor Lou Yishan and Professor Li Zhonghui for their technical guidance. At the same time, the author thanks Professor Tang Huafeng's team of Jilin University for their analytical and laboratory equipment and their professionals for their useful advice, discussion, and help. We also thank the reviewers for their comments.

REFERENCES

Chang, X., Wang, Y., Shi, B., and Xu, Y. (2019). Charging of Carboniferous Volcanic Reservoirs in the Eastern Chepaizi Uplift, Junggar Basin (Northwestern China) Constrained by Oil Geochemistry and Fluid Inclusion. *Bulletin* 103 (7), 1625–1652. doi:10.1306/12171818041

Chen, H. Q., Hu, Y. L., Yan, L., Zhang, J., and Tong, M., (2016). Comprehensive Quantitative Evaluation of Yingchengl Volcanic Reservoirs in Xudong. *Special oil gas Reserv.* 23 (01), 21–24. doi:10.3969/j.issn.1006-6535.2016.01.005

Chen, K. Y., Duan, X. G., Zhang, X. B., and Song, R. C. (2010). Lithology Identification and Prediction of Igneous Rock Based on 3D Lithofacies Simulation. *Joumal Southwest Petrolerm Univ. Sci. Technopgy Ed.* 32 (02), 19–24. doi:10.3863/j.issn.1674-5086.2010.02.004

Colombier, M., Wadsworth, F. B., Gurioli, L., Scheu, B., Kueppers, U., Di Muro, A., et al. (2017). The Evolution of Pore Connectivity in Volcanic Rocks. *Earth Planet. Sci. Lett.* 462, 99–109. doi:10.1016/j.epsl.2017.01.011

Faizan, N., Löffler, A., Heininger, R., Utesch, M., and Krcmar, H. (2019). Classification of Evaluation Methods for the Effective Assessment of Simulation Games: Results from a Literature Review. *Int. Assoc. Online Eng.* Retrieved from. www.learntechlib.org/p/207576/ March 4, 2022. 9(1), doi:10.3991/ijep.v9i1.9948

Farquharson, J., Heap, M. J., Varley, N. R., Baud, P., and Reuschlé, T. (2015). Permeability and Porosity Relationships of Edifice-Forming Andesites: a Combined Field and Laboratory Study. *J. Volcanol. Geotherm. Res.* 297, 52–68. doi:10.1016/j.jvolgeores.2015.03.016

Feng, Z. Q. (2006). Exploration Prospect of Qingshen Large Gas Field in Songliao Basin. *Nat. Gas. Ind.* 25 (06), 1–5.

Feng, Z. Q. (2008). Volcanic Rocks as Prolific Gas Reservoir: A Case Study from the Qingshen Gas Field in the Songliao Basin, NE China. *Mar. Petroleum Geol.* 25 (4-5), 416–432. doi:10.1016/j.marpetgeo.2008.01.008

Feng, Z., Yin, C., Liu, J., Zhu, Y., Lu, J., and Li, J. (2014). Formation Mechanism of In-Situ Volcanic Reservoirs in Eastern China: A Case Study from Xushen Gasfield in Songliao Basin. *Sci. China Earth Sci.* 57, 2998–3014. doi:10.1007/s11430-014-4969-2

Gao, F. (2019). Use of Numerical Modeling for Analyzing Rock Mechanic Problems in Underground Coal Mine Practices. *J. Min. Strata Control Eng.* 1 (1), 013004. doi:10.13532/j.jmsce.cn10-1638/td.2019.02.009

Gong, Q. S., Huang, G. P., Meng, X. C., Zhu, C., and Ni, G. H. (2012). Methods for Lithology Discrimination of Volcanics in Santanghu Basin. *China pet. Explor.* 17 (03), 37–41+6. doi:10.3969/j.issn.1672-7703.2012.03.006

Hasan, A., Baroudi, B., Elmualim, A., and Rameezdeen, R. (2018). Factors Affecting Construction Productivity: a 30 Year Systematic Review. *Ecam* 25 (7), 916–937. doi:10.1108/ecam-02-2017-0035

He, H., Li, S. M., Kong, C. X., Jiang, Q. P., Zhou, T. Y., Jia, J. F., et al. (2016). Characteristics and Quantitative Evaluation of Volcanic Effective Reservoir in Jiamuhe Formation of Permian, Northwestern Margin of Junggar Basin. *J. China Univ. Petroleum Nat. Sci.* 40 (02), 1–12. doi:10.3969/j.issn.1673-5005.2016.02.001

Heap, M. J., Xu, T., and Chen, C. F. (2014). The Influence of Porosity and Vesicle Size on the Brittle Strength of Volcanic Rocks and Magma. *Bull. Volcanol.* 76 (9), 1–15. doi:10.1007/s00445-014-0856-0

Hou, E., Cong, T., Xie, X., and Wei, J. B. (2020). Ground Surface Fracture Development Characteristics of Shallow Double Coal Seam Staggered Mining Based on Particle Flow. *J. Min. Strata Control Eng.* 2 (1), 013521. doi:10.13532/j.jmsce.cn10-1638/td.2020.01.002

Huang, Y. X., Hu, W. S., Yuan, B. T., Zhang, G. Y., and Bai, L. D. (2019). Evaluation of Pore Structures in Volcanic Reservoirs: a Case Study of the Lower Cretaceous Yingcheng Formation in the Southern Songliao Basin, NE China. *Environ. Earth Sci.* 78 (4), 1–14. doi:10.1007/s12665-019-8055-0

Jin, C. Z., Yang, S. L., Shu, P., and Wang, G. J. (2007). Comprehensive Research on Relationship between Productivity and Pore Structure Characteristics of Volcanic Reservoir in Shengping Developing Area. *Petroleum Geol. Oilfield Dev. Daqing* 26 (2), 38–45. doi:10.3969/j.issn.1000-3754.2007.02.010

Kadavi, P. R., and Lee, C.-W. (2018). Land Cover Classification Analysis of Volcanic Island in Aleutian Arc Using an Artificial Neural Network (ANN) and a Support Vector Machine (SVM) from Landsat Imagery. *Geosci. J.* 22 (4), 653–665. doi:10.1007/s12303-018-0023-2

Lan, S. R., Song, D. Z., Li, Z. L., and Liu, Y. (2021). Experimental Study on Acoustic Emission Characteristics of Fault Slip Process Based on Damage Factor. *J. Min. Strata Control Eng.* 3 (3), 033024. doi:10.13532/j.jmsce.cn10-1638/td.20210510.002

Li, G. R., Wu, H. Z., Ye, B., Li, Z. Z., Peng, B., and Wu, Y. J. (2014). Stages and Mechanism of Dissolution in Changhsing Reservoir, Yuanba Area. *Acta Petrol. Sin.* 30 (03), 709–717. doi:10.3787/j.issn.1000-0976.2017.02.007

Li, H. (2022). Research Progress on Evaluation Methods and Factors Influencing Shale Brittleness: A Review. *Rep.* 8, 4344–4358. doi:10.1016/j.egyr.2022.03.120

Li, X., Song, M., Lin, H., Zhang, K., Shi, H., Zhang, Y., et al. (2019). Characteristics of Carboniferous Volcanic Reservoirs in the Chun-Feng Oilfield of the Junggar Basin, China. *Arabian J. Geosciences* 12 (16), 1–13. doi:10.1007/s12517-019-4663-y

Liu, W. F., and Kuang, H. W. (2003). Comprehensive Evaluation of Volcanics Reservoir by Fuzzy Mathematics. *Oil Gas Recovery Technol* 10 (2), 1–5. doi:10.13673/j.cnki.cn37-1359/te.2003.02.003

Luo, J. L., Lin, T., Yang, Z. S., Liu, X. H., Zhang, J., and Liu, S. Y. (2008). Lithofacies and Reservoir Quality Control Factors of Volcanics in the YingchengFormation in the Shengping Gas Field in the Songliao Basin. *Oil & Gas Geol.* 29 (06), 748–757. doi:10.3321/j.issn:0253-9985.2008.06.007

Ma, S. W., Luo, J. l., Chen, C. Y., He, X. Y., Dai, J. J., Xu, X. L., et al. (2017). Classification and Evaluation of Micro Pore Structure of Volcanic Rock Reservoirs :A Case Study of the Carboniferous Volcanic Reservoirs in Xiquan Area, Eastern Junggar Basin. *Pet. geology & Exp.* 39 (05), 647–654. doi:10.11781/sysydz201705647

Mao, Z.-G., Zhu, R.-K., Luo, J.-L., Wang, J.-H., Du, Z.-H., Su, L., et al. (2015). Reservoir Characteristics, Formation Mechanisms and Petroleum Exploration Potential of Volcanic Rocks in China. *Pet. Sci.* 12 (1), 54–66. doi:10.1007/s12182-014-0013-6

Mou, Z. H., Liu, J. S., and Xu, J. (2010). Lithofacies of Volcanic Rock at the Top of Upper Carboniferous Stratigraphy in Luxi Area of Junggar Basin. *Nat. Gas. Geosci.* 21 (01), 47–53.

Pang, Y. M., Zhang, F. Q., Qiu, H. F., and Zhan, J. F. (2007). Characteristics of Microscopic Pore Structure and Physical Property Parameter in Acidic Volcanic Reservoir. *Acta Pet. Sin.* 28 (6), 72–77. doi:10.3321/j.issn:0253-2697.2007.06.014

Pola, A., Crosta, G., Fusi, N., Barberini, V., and Norini, G. (2012). Influence of Alteration on Physical Properties of Volcanic Rocks. *Tectonophysics,* 566-567, 67–86. doi:10.1016/j.tecto.2012.07.017

Polyansky, O. P., Reverdatto, V. V., Khomenko, A. V., and Kuznetsova, E. N. (2003). Modeling of Fluid Flow and Heat Transfer Induced by Basaltic Near-Surface Magmatism in the Lena-Tunguska Petroleum Basin (Eastern Siberia, Russia). *J. Geochem. Explor.* 78, 687–692. doi:10.1016/s0375-6742(03)00079-7

Ran, Q. Q., Hu, Y. L., and Ren, B. S. (2005). A Lithologic Identification Method of Igneous Rocks and its Application: a Case of the Igneousreservoir in Block Zao-35. *China offshore oil gas* 23 (3), 25–30. doi:10.3969/j.issn.1673-1506.2005.01.006

Ren, Z. W., and Jin, C. S. (1999). Reservoir Space Feature of the Volcanic Rocks in the Area of WellWa-609, Liaohe Sag. *Petroleum Explor. Dev.* 26 (04), 54–56 + 5. doi:10.1006/mcpr.1998.0211

Shan, X. L., Chen, Y. P., Tang, L. M., and Yi, J. (2011). Comprehensive Evaluation Method for Volcanic Rock Reservoirs and Its Application: Taking Songnan Gas Field for Example. *J. Shandong Univ. Sci. Technol. Nat. Sci.* 30 (03), 1–6. doi:10.3969/j.issn.1672-3767.2011.03.001

Shi, B., Chang, X., Xu, Y., Mao, L., Zhang, J., and Li, Y. (2020). Charging History and Fluid Evolution for the Carboniferous Volcanic Reservoirs in the Western Chepaizi Uplift of Junggar Basin as Determined by Fluid Inclusions and Basin Modelling. *Geol. J.* 55 (4), 2591–2614. doi:10.1002/gj.3527

Shi, X. L., Cui, Y. J., Xun, W. K., Zhang, J. S., and Guan, Y. Q. (2020). Formation Permeability Evaluation and Productivity Prediction Based on Mobility from Pressure Measurement while Drilling. *Petroleum Explor. Dev.*, 47(1), 146–153. doi:10.1016/S1876-3804(20)60013-1

Sruoga, P., Rubinstein, N., and Hinterwimmer, G. (2004). Porosity and Permeability in Volcanic Rocks: a Case Study on the Serie Tobífera, South Patagonia, Argentina. *J. Volcanol. Geotherm. Res.*, 132(1), 31–43. doi:10.1016/S0377-0273(03)00419-0

Sruoga, P., and Rubinstein, N. (2007). Processes Controlling Porosity and Permeability in Volcanic Reservoirs from the Austral and Neuquén Basins, Argentina. *Bulletin* 91 (1), 115–129. doi:10.1306/08290605173

Stagpoole, V., and Funnell, R. (2001). Arc Magmatism and Hydrocarbon Generation in the Northern Taranaki Basin, New Zealand. *Pet. Geosci.* 7(3), 255–267. doi:10.1144/petgeo.7.3.255

Sun, H., Zhong, D., and Zhan, W. (2019). Reservoir Characteristics in the Cretaceous Volcanic Rocks of Songliao Basin, China: A Case of Dynamics and Evolution of the Volcano-Porosity and Diagenesis. *Energy Explor. Exploitation*, 37(2), 607–625. doi:10.1177/0144598718812546

Tang, H. F., Wang, P. J., and Bian, W. H. (2020). Review of Volcanic Reservoir Geology. *Acta Pet. Sin.* 41 (12), 1744–1773. doi:10.7623/syxb202012026

Tian, J., Sun, X., Zhang, X., and Shou, Y. (2013). Reservoir Space Types and the Factors Influencing the Characteristics of Spherulite in Rhyolite. *Sci. China Earth Sci.* 56(5), 748–755. doi:10.1007/s11430-013-4599-0

Wang, L., He, Y., Peng, X., Deng, H., Liu, Y., and Xu, W. (2020). Pore Structure Characteristics of an Ultradeep Carbonate Gas Reservoir and Their Effects on Gas Storage and Percolation Capacities in the Deng IV Member, Gaoshiti-Moxi Area, Sichuan Basin, SW China. *Mar. Petroleum Geol.* 111, 44–65. doi:10.1016/j.marpetgeo.2019.08.012

Wang, L., Li, J. H., Shi, Y. M., Zhao, Y., and Ma, Y. S. (2014). Analysis of the Reservoir Spaces and Their Main Controlling Factors of Carboniferous Volcanic Rocks in Dixi Area, Junggar Basin. *Earth. Sci. Front.* 21 (1), 205.

Wang, P., and Chen, S. (2015). Cretaceous Volcanic Reservoirs and Their Exploration in the Songliao Basin, Northeast China. *Bulletin*, 99(3), 499–523. doi:10.1306/09041413095

Wang, P. J., Chen, S. M., Liu, W. Z., Shan, X. L., Cheng, R. H., Zhang, Y., et al. (2003b). Relationship between Volcanic Facies and Volcanic Reservoirs in Songliao Basin. *Oil Gas Geol.* 24 (1), 18–23. doi:10.3969/j.issn.1671-5888.2003.04.011

Wang, P. J., Chi, Y. L., Liu, W. Z., Cheng, R. H., Shan, X. L., and Ren, Y. G. (2003a). Volcanic Facies of the Songliao Basin: Classification, Characteristics and Reservoir Significance. *J. Jilin Univ. (Earth Sci. Ed.)* 33 (4), 449–456. doi:10.3969/j.issn.1671-5888.2003.04.011

Wang, P. J., Wu, H. Y., Pang, Y. M., Men, G. T., Ren, Y. G., Liu, W. Z., et al. (2006). Volcanic Facies of the Songliao Basin: Sequence, Model and the Quantitative Relationship with Porosity & Permeability of the Volcanic Reservoir. *J. Jilin Univ. (Earth Sci. Ed.)* 36 (5), 805–812. doi:10.3969/j.issn.1671-5888.2006.05.016

Wang, Y., Gao, Y., and Fang, Z. (2021). Pore Throat Structure and Classification of Paleogene Tight Reservoirs in Jiyang Depression, Bohai Bay Basin, China. *Petroleum Explor. Dev.*, 48(2), 308–322. doi:10.1016/S1876-3804(21)60025-3

Wang, Z. S., Liu, Z. C., Du, Y. L., Tan, Z. H., Hu, J. G., Yang, S. H., et al. (2016). A Splitting Method of Oil and Gas Production in Multiple Completion Wells of Multi Layered Reservoir. *Nat. Gas. Geosci.* 27 (10), 1878–1882. doi:10.11764/j.issn.1672-1926.2016.10.1878

Wen, L., Li, Y., Yi, H., Liu, X., Zhang, B., Qiu, Y., et al. (2019). Lithofacies and Reservoir Characteristics of Permian Volcanic Rocks in the Sichuan Basin. *Nat. Gas. Ind. B*, 6(5), 452–462. doi:10.1016/j.ngib.2019.02.003

Wu, C., Gu, L., Zhang, Z., Ren, Z., Chen, Z., and Li, W. (2006). Formation Mechanisms of Hydrocarbon Reservoirs Associated with Volcanic and Subvolcanic Intrusive Rocks: Examples in Mesozoic-Cenozoic Basins of Eastern China. *Bulletin* 90 (1), 137–147. doi:10.1306/07130505004

Yang, Z. P., Yue, S. J., Zheng, C. L., Liu, X. Z., and Chen, G. X. (2018). Production Split Method Restricted Synthetically by Multi-Factors in Thin Interbed Sandstone Reservoirs. *Lithol. Reserv.* 30 (06), 117–124. doi:10.12108/yxyqc.20180614

Yin, S., and Wu, Z. (2020). Geomechanical Simulation of Low-Order Fracture of Tight Sandstone. *Mar. Petroleum Geol.* 117, 104359. doi:10.1016/j.marpetgeo.2020.104359

Yu, C. M., Zheng, J. P., Tang, Y., Yang, Z., and Qi, X. F. (2004). Reservoir Properties and Effect Factors on Volcanic Rocks of Basement beneath Wucaiwan Depression, Junggar Basin. *Earth Sci.* 29 (5), 303–308. doi:10.3321/j.issn:1000-2383.2004.03.007

Zhang, K. H., Lin, H. X., Zhang, G. L., and Xu, W. L. (2015). Characteristics and Controlling Factors of Volcanic Reservoirs of Hala' Alate Mountains Tectonic Belt. *J. China Univ. Petroleum Nat. Sci.* 39 (02), 16–22. doi:10.3969/j.issn.1673-5005.2015.02.003

Zhao, J. Z., Wu, S. B., and Wu, F. L. (2007). The Classification and Evaluation Criterion of Low Permeability Reservoir: An Example from Ordos Basin. *Lithol. Reserv.* 19 (03), 28–31. doi:10.3969/j.issn.1673-8926.2007.03.005

Zheng, H., Sun, X., Wang, J., Zhu, D., and Zhang, X. (2018a). Devitrification Pores and Their Contribution to Volcanic Reservoirs: A Case Study in the Hailar Basin, NE China. *Mar. Petroleum Geol.*, 98, 718–732. doi:10.1016/j.marpetgeo.2018.09.016

Zheng, H., Sun, X., Zhu, D., Tian, J., Wang, P., and Zhang, X. (2018b). Characteristics and Factors Controlling Reservoir Space in the Cretaceous Volcanic Rocks of the Hailar Basin, NE China. *Mar. Petroleum Geol.*, 91, 749–763. doi:10.1016/j.marpetgeo.2018.01.038

Zhou, X. M., and Tang, Y. H. (2007). Productivity Characteristics and Influential Factors Analysis of Volcanic Gas Reservoirof Xushen Gas Field. *Nat. Gas. Ind.* 27 (01), 90–92. doi:10.3321/j.issn:1000-0976.2007.01.027

Conflict of Interest: W-TS was employed by the Company Exploration and Development Research Institute of Jilin Oil Field Company.

The remaining authors declare that the research was conducted in the absence of any commercial or financial relationships that could be construed as a potential conflict of interest.

frontiers | Frontiers in Earth Science

ORIGINAL RESEARCH
published: 29 June 2022
doi: 10.3389/feart.2022.919923

Genetic Mechanism of Pyrite in the Shale of the Longmaxi Formation and Its Influence on the Pore Structure: A Case Study of the Changning Area, South Sichuan Basin of SW China

Jiang He[1], Lan Yang[1], Xuewen Shi[2], Shengxian Zhao[2], Lieyan Cao[2], Shulin Pan[1], Feng Wu[1] and Meng Wang[3,4]**

[1]School of Geoscience and Technology, Southwest Petroleum University, Chengdu, China, [2]Shale gas Research Institute of PetroChina Southwest Oil and gas Field Company, Chengdu, China, [3]School of Chemistry and Chemical Engineering, Chongqing University of Science and Technology, Chongqing, China, [4]Key Laboratory of Shale Gas Exploration, Ministry of Natural Resources, Chongqing Institute of Geology and Mineral Resources, Chongqing, China

OPEN ACCESS

Edited by:
Wenlong Ding,
China University of Geosciences, China

Reviewed by:
Zhu Baiyu,
Yangtze University, China
Lei Liu,
Chengdu University of Technology, China

***Correspondence:**
Jiang He
hejiang_swpu@126.com
Meng Wang
wangmeng_cqust@126.com

Specialty section:
This article was submitted to Economic Geology, a section of the journal Frontiers in Earth Science

Received: 14 April 2022
Accepted: 23 May 2022
Published: 29 June 2022

Citation:
He J, Yang L, Shi X, Zhao S, Cao L, Pan S, Wu F and Wang M (2022) Genetic Mechanism of Pyrite in the Shale of the Longmaxi Formation and Its Influence on the Pore Structure: A Case Study of the Changning Area, South Sichuan Basin of SW China. Front. Earth Sci. 10:919923. doi: 10.3389/feart.2022.919923

Pyrite is a mineral that is commonly found in shale gas reservoirs. Its genetic mechanism and impact on pore and organic matter in shale gas reservoirs are critical for shale gas exploration. This study selects the Longmaxi shale (Lower Silurian) in the Changning area of the southern Sichuan Basin by comprehensively using a scanning electron microscope (SEM), X-ray diffraction (XRD), total organic carbon (TOC), and image processing technology. The type and characteristics of pyrite in shale reservoirs are studied, the sedimentary environment and genetic mechanism of pyrite are analyzed, and the influence of pyrite formation on organic matter enrichment and reservoir formation is evaluated. The results showed that pyrite in shale primarily forms framboidal pyrite, euhedral pyrite, and subhedral pyrite, with particle sizes ranging from 1 to 15 μm. The maximum framboid diameter (MFD) is less than 20 μm, with the average particle size distribution of 3–5 μm. These parameters indicate the vulcanization and blocking environment. The reducing environment promotes organic matter enrichment and preservation. Framboidal pyrite has two genetic sequences: rich organic matter and poor organic matter. The development of organic matter will limit the continuous radial growth of pyrite and is conducive to the protection of pores, and the formation of pyrite can reduce the activation energy of kerogen reaction and catalyze the hydrocarbon generation of organic matter, resulting in higher gas content. The framboidal pyrite content can be used to predict high-quality shale gas reservoirs.

Keywords: framboidal pyrite, shale gas reservoir, sedimentary environment, Longmaxi Formation, Sichuan Basin

1 INTRODUCTION

In recent years, there has been a growing interest in the mechanism of shale gas accumulation, migration, and storage, as well as the pore structure and sedimentary environment of the reservoir (Zou et al., 2011). As a characteristic mineral in an organic-rich shale formation, pyrite plays a positive role in shale gas development due to its structural characteristics, environmental significance, and impact on shale reservoirs and shale gas development (Han and Li, 2019).

Authigenic pyrite is the main product of sulfate reduction in an anoxic marine environment and widely occurs in marine sediments on the continental margin. The main factors controlling the formation of pyrite are the degradation of organic matter and the anaerobic oxidation of methane. Pyrite has mostly bedding distribution, lenticular structures, and some linear structures, but under the microscope, it has framboidal, massive, euhedral, nodular, and fissure filling shapes (Wilkin et al., 1996; Wei et al., 2016). Different forms indicate different formation processes, each representing a distinct formation environment, particularly framboidal pyrite, which can be classified as quasi syngenetic or diagenetic. The former occurs in sulfide water bodies, while the latter occurs in anoxic void water in sediments beneath oxidized or oxygen-depleted water bodies. They differ in shape, particle size, and sulfur isotope (Wei et al., 2016).

The surrounding environment limits the microcrystal of framboidal pyrite aggregate during its growth and its particle size change, which correlates well with the degree of hypoxia in the water body. It is a reliable index to distinguish the redox conditions of paleo-sedimentary water bodies (Wilkin et al., 1996; Wilkin and Barnes, 1997; Chang et al., 2009,2011; Wei et al., 2016), which has great significance in judging the sedimentary environment of shale reservoir. Chang and Chu (2011) and Zhou and Jiang (2009) refined the sedimentary environment into three oxidation levels, weak oxidation and sulfidic, using framboidal pyrite. Cui et al. (2013) proposed that pyrite has a positive impact on oil and gas reservoirs, hydrocarbon generation, and expulsion. Nie and Zhang (2012) concluded that pyrite plays a vital role in shale gas accumulation by studying the controlling factors of shale gas accumulation conditions. Cao et al. (2018) concluded that pyrite contributes to organic matter hydrocarbon generation and shale gas development by examining pyrite in different horizons in the Yangtze region and combined it with previous research results. Zhu et al. (2018) believed that pyrite can affect oil and gas accumulation in the reservoir and promote oil and gas accumulation and hydrocarbon generation and expulsion of organic matter.

The contribution of pyrite developed in shale to the pore system is now widely accepted (Li et al., 2019; Li et al., 2020; Liu et al., 2022), but there are still some disputes about its porosity development degree and the importance of pores related to pyrite. The contribution of pore development characteristics related to the pyrite of a shale reservoir cannot be quantified (Fan et al., 2020). From the perspective of diagenesis, pyrite cementation will occupy a portion of the primary pore space, but its particles have rigid characteristics that can effectively inhibit the influence of the compaction of particles and adjacent areas (Wang et al., 2017). Simultaneously, large-scale pyrite will induce the formation of microcracks and maintain a moderate opening, while irregular granular pyrite is more cemented between clay mineral flakes. Effective support is formed to prevent intergranular pores from becoming completely compacted, allowing for the filling and storage of liquid hydrocarbons (Li, 2022). Furthermore, the organic pores formed by liquid hydrocarbon cracking can be effectively preserved due to pyrite's "pillared" protection. In general, the earlier the pyrite cementation is formed, the higher the degree of development and the more conducive to mechanical compaction, formation, and preservation of organic pores in the later stage (Wang et al., 2019; Lu et al., 2022).

There have been few successes in analyzing the sedimentary environment of pyrite in the Longmaxi Formation shale in the upper Yangtze region. Although many researchers have made clear the impact relations between the two in terms of the indicative significance of pyrite on shale gas energy storage, there is no significant amount of theoretical data support. The present research defines the origin of pyrite, restores the shale sedimentary environment, and analyzes the impact of pyrite formation on the evolution of organic matter and the transformation of reservoir properties, providing a reference for the prediction of organic shale reservoirs through a comprehensive analysis of the structure, content, and particle size of pyrite in the shale of the Longmaxi Formation.

2 GEOLOGICAL SETTING

The Sichuan Basin is an essential part of the upper Yangtze plate and the most promising area for oil and gas exploration in southern China. The Changning main anticline structure is situated at the intersection of the Sichuan Basin and the Yunnan Guizhou Plateau, between the low and steep structural area of the ancient depression middle uplift in the South Sichuan and the Loushan fold belt (**Figure 1A**) (Chen et al., 2014; Huang et al., 2018).

The Longmaxi Formation of Silurian is the main target interval for shale gas exploration in the study area. The black shale of the Longmaxi Formation is in integrated contact with the black siliceous and calcareous shale of the Upper Ordovician Wufeng Formation, containing the Hirnantia–Dalmanitina fauna. The Longmaxi Formation has a thickness of 0 m 373 m, and it can be further subdivided into two lithologic sections: the first member of the Longmaxi Formation (S_1L_1) and the second member of the Longmaxi Formation (S_1L_2) (Zhu et al., 2018).

The rhythmic boundary is found between the gray–black shale at the bottom of the second member of the S_1L_2 formation and the black shale gray silty shale in the overlying S_1L_1 member. According to the secondary cycles and lithologic characteristics, it can be divided into two subsegments from the bottom ($S_1L_1^1$ and $S_1L_1^2$). The lithologic interface is the dark gray shale at the bottom of the $S_1L_1^2$ member and the gray-black shale of the underlying $S_1L_1^1$ member.

The $S_1L_1^1$ sub-member is a set of black carbonaceous shale rich in organic matter. Many graptolite groups with different shapes

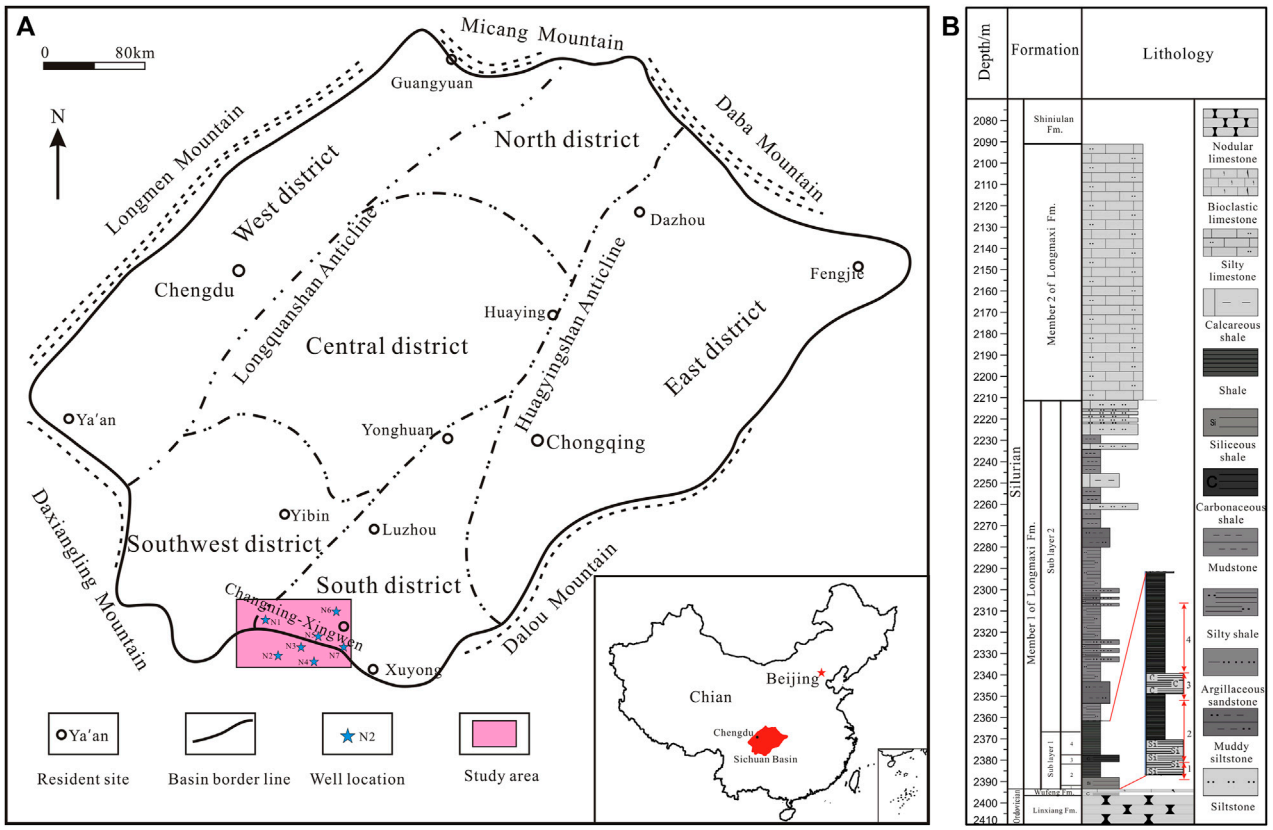

FIGURE 1 | (A) Location of the study area in the Sichuan Basin (Modified from Chen et al. (2014)); **(B)** stratigrapy of the Longmaxi Formation in well N3.

are developed, belonging to the calcareous outer shelf facies. It can also be subdivided into four sub-layers ($S_1 L_1^{1-1}$, $S_1 L_1^{1-2}$, $S_1 L_1^{1-3}$, and $S_1 L_1^{1-4}$) (**Figure 1B**).

3 METHODS

The data of Longmaxi Formation conventional logging, elemental capture spectroscopy (ECS), XRD (whole rock analysis), and porosity of seven wells were collected systematically. Mineral and pore structure characteristics, XRD (whole rock minerals), and total organic carbon (TOC) tests were carried out on 80 core samples from 7 wells.

Quanta 450 ESEM was used to examine the minerals and pore characteristics of shale samples. The pores in the SEM images were extracted and measured using PerGeos software from the FEI.

XRD analysis was performed using the PANalytical X'Pert PRO. The particle sizes of the shale powder were measured at less than 200 mesh.

The TOC content was measured using a LECO CS230 carbon/sulfur analyzer according to the national standard GB/T 19145–2003 after the samples were crushed into small particles of less than 0.2 mm in size and were treated with hydrochloric acid to remove the carbonates at 60–80°C.

The pyrite particle size and pore diameter of the shale sample were measured using Corephic v2.1 measurement software. More than 100 pyrite particle size data were collected for each shale sample. The sedimentary environment characteristics of pyrite formation were studied using the maximum particle size method (MFD) (Wignall et al., 2005), box-and-whisker plot (Wignall et al., 2005), and binary graphic method after data collection (Wilkin et al., 1996). The box-and-whisker plot can intuitively reflect the variation of lithology along with the depth, maximum and minimum particle sizes of framboidal pyrite, the middle particle size, and the distribution characteristics of particle concentration or dispersion (Wilkin et al., 1996; Wei et al., 2016; Wignall et al., 2016). The binary diagram of average particle size, standard deviation, and skewness also serves as potential methods for analyzing the redox conditions of sedimentary water (Wilkin et al., 1996; Chang et al., 2009).

4 RESULTS

4.1 Morphology and Particle Size Characteristics of Pyrite

SEM image shows that pyrite in the Longmaxi Formation of the study area is well developed and distributed in shale in different forms.

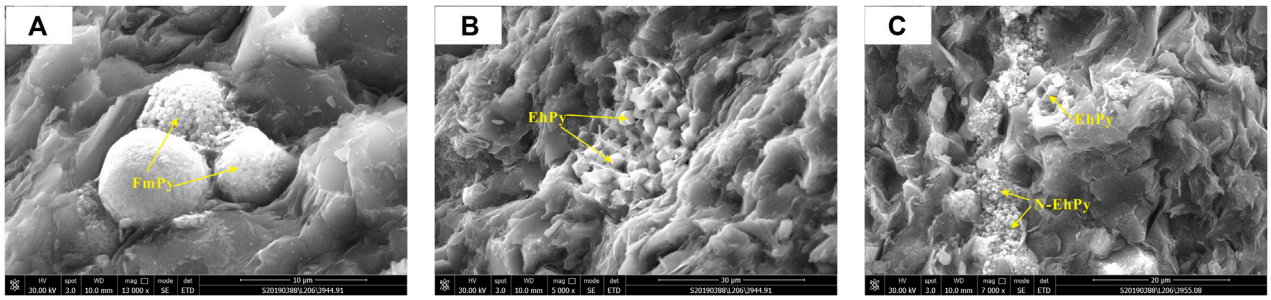

FIGURE 2 | Photomicographs of authigenic pyrite morphologies. **(A)** SEM image of typical framboidal pyrite of the Longmaxi Formation, **(B)** SEM image of euhedral pyrite of the Longmaxi Formation **(C)**. SEM image of banded shape and non-euhedral pyrite of the Longmaxi Formation.

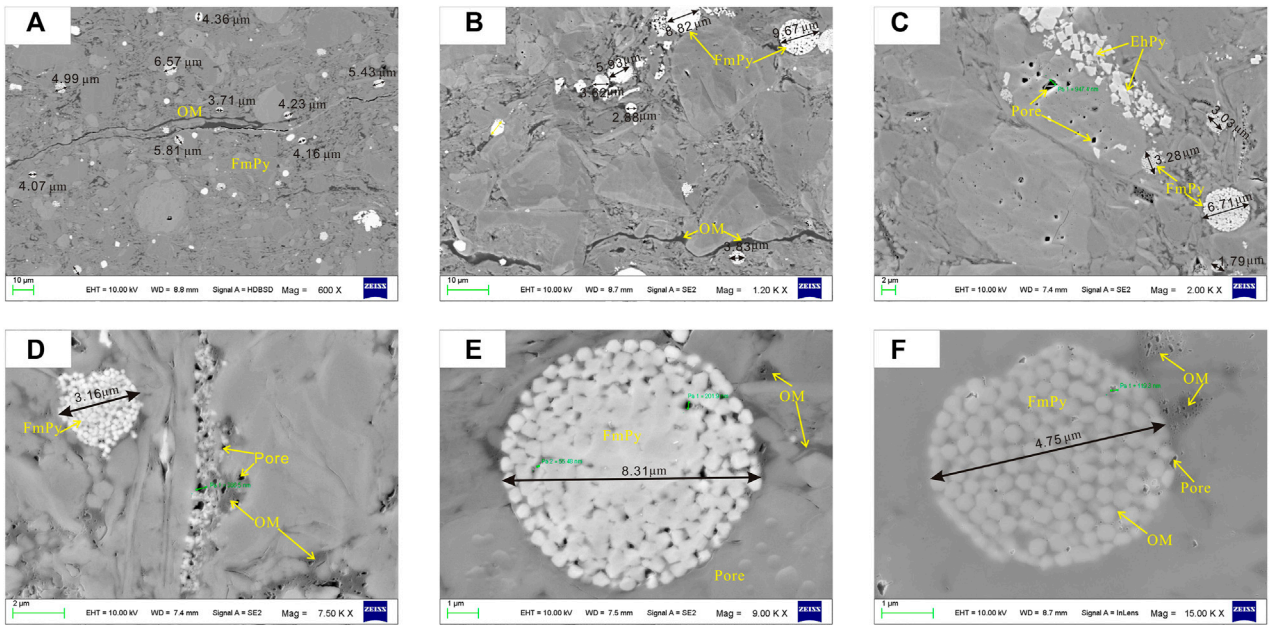

FIGURE 3 | Measurement of framboidal pyrite diameters *via* Corephic v2.1 software. Pyrite from samples of the Longmaxi Formation. OM = organic matter; FmPy = framboidal pyrite; Ehpy = euhedral pyrite.

Aggregating multiple granular microcrystals form framboidal pyrite in the form of spheres and sub spheres (**Figure 2A**). The diameter of a single crystal is generally 0.1–1 μm; most of the pyrite structures are well preserved, with a small number of pyrite microcrystals having secondary growth. The morphology of microcrystals changes from spherical to euhedral irregular shapes. A few framboidal pyrites recrystallize and lose their framboid structure. This is the most common type of pyrite in the study area.

The crystal structure of euhedral pyrite is octahedral, cubic, and spherical. It typically manifests as isolated crystals and aggregates (**Figure 2B**). It is frequently euhedral or semi-euhedral crystals with significant variation in the particle size. In general, euhedral pyrite aggregates form near organic matter and framboidal pyrite aggregates or marginal gaps.

Banded pyrite, which belongs to non-euhedral pyrite, is slender banded with an obvious directional arrangement and is mainly distributed at the junction of organic matter, mineral particles, and intergranular pores (**Figure 2C**).

Pyrite is primarily found in areas where organic matter is abundant. It is distributed in a long strip along the direction of organic matter development or concentrated in areas where organic matter and clay minerals coexist. Pyrite will form in small amounts near inorganic minerals or between mineral particles and in mineral particles.

The test characteristics of particle size of pyrite in shale show that the particle size distribution of framboidal pyrite in $S_1L_1^2$ members is 2.077–6.045 μm, with an average of 4.34 μm, 1.027–10.277 μm in $S_1L_1^1$ member, with an average of 4.31 μm. The particle size of $S_1L_1^{1-2}$ and $S_1L_1^{1-3}$ in the lower part is larger than that of pyrite in the shale at the top and bottom layers. In the deep Wufeng Formation, the particle size distribution of pyrite is 1.424–12.97 μm, with an average value

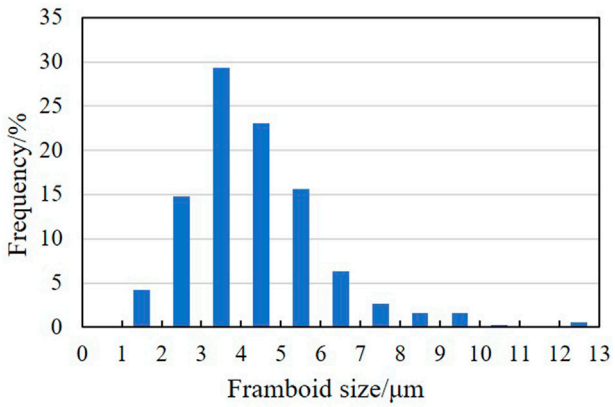

FIGURE 4 | Pyrite framboid size distribution histogram.

of 4.4 μm (**Figure 3**). In general, the particle size of framboidal pyrite is a single peak distributed from 1 to 13 μm, with a peak value of 3–5 μm (**Figure 4**). The particle size of pyrite increases first and then decreases from bottom to top, with the peak value of particle size distribution in the $S_1L_1^{1-2}$ (**Table.1**).

4.2 Vertical Distribution Characteristics of Pyrite and TOC

Considering N1 wells as an example, the vertical distribution characteristics and depth changes of pyrite, S element, and TOC are drawn (**Figure 5**).

The vertical variation of the pyrite content is more evident than that of the particle size. The pyrite content is distributed from 0.3 to 7.9%, with an average of 2.31%. Among them, the average content of Wufeng formation is 0.6%, the content of $S_1L_1^2$ is 0.8–7.9%, with an average of 1.8%; and the content of $S_1L_1^1$ is 1–5.9%, with an average of 3.0% The content of $S_1L_1^{1-2}$ and $S_1L_1^{1-3}$ layer sections is the highest, with average values of 2.6 and 3.9%, respectively; the content of pyrite increased first and then decreased.

The TOC of shale in the Longmaxi Formation is 0.23–4.93%, with an average of 1.78%. ECS logging data show that the content of the S element in the Longmaxi Formation is 0.001 kg/kg to 0.03 kg/kg, with an average of 0.01 kg/kg. Overall, TOC and S values show a positive correlation trend. After a sharp increase from the Wufeng formation to the bottom of the Longmaxi Formation, these two parameters maintain high values in $S_1L_1^1$. According to the fitting between the logging curve and the test TOC results, the predicted TOC value ranges from 2.8 to 6.7%, with an average value of 3.75%. Notably, higher TOC corresponds to higher porosity. In this interval, the average porosity of shale is greater than 4.8% and can reach up to 6.28%, indicating good reservoir capacity.

The vertical characteristics of TOC and S values indicate that the bottom of the Longmaxi Formation lies in an occluded reduction environment, whereas the top lies in an oxygen-deficient/reduction environment. The TOC content has strong compliance with the S element. The changing trend is basically the same, reflecting the dependence of organic matter enrichment in shale on sulfide sedimentary environment, which is closely related to the S element. The more reductive the sedimentary environment is, the more conducive it is to enriching organic matter (Wu C. et al., 2014; Han and Li, 2019).

TABLE 1 | Pyrite framboid size distributions *via* SEM images and Corephic v2.1 software measurement. SD = standard deviation; MFD = maximum framboid diameter; SK = skewness.

Samples	SD (μm)	Min (μm)	Mean (μm)	MFD (μm)	SK
$S_1L_1^2$	2.246	2.077	4.34	6.045	2.322
$S_1L_1^{1-4}$	1.374	1.027	2.51	4.043	0.696
$S_1L_1^{1-4}$	1.226	1.403	3.43	5.495	0.133
$S_1L_1^{1-3}$	1.824	1.235	4.31	9.738	1.094
$S_1L_1^{1-3}$	1.463	1.514	4.14	8.974	0.971
$S_1L_1^{1-2}$	1.553	2.027	4.79	9.745	0.635
$S_1L_1^{1-2}$	2.513	2.514	5.15	10.277	1.275
$S_1L_1^{1-1}$	1.196	1.852	3.66	5.879	0.205
Wufeng Formation	3.890	1.424	4.69	12.97	2.000
Wufeng Formation	1.406	2.493	4.35	9.924	1.904

5 DISCUSSION

5.1 Formation Environment of Pyrite

Framboidal pyrite can retain its original shape and size after burial; thus, it is frequently used to indicate the redox conditions of the water environment in modern marine sediments (Wilkin et al., 1996). Pyrite is the most commonly found near the chemical alteration layer. When the bottom water body is euxinic, pyrite is rapidly deposited on the sediment surface after formation, with large quantities and a small variation range of particle sizes. Under reduction conditions, pyrite with small particle sizes and a large amount will form near the interface between the sediment and water body in an environment with a lack of H_2S and oxygen, dominated by framboidal pyrite (Wignall and Newton, 1998; Bond and Wignall, 2010; Zhou et al., 2017). Pyrite grows in the pore water between oxygen-poor sediment particles below the sedimentary interface in the oxygen and oxygen-poor environment. The oxidant in the sediment is gradually consumed due to bacterial sulfate reduction. Once the sulfide environment is formed, framboidal pyrite is formed; Fe^{2+}, H_2S, and elemental sulfur are continuously and slowly supplied, resulting in a long growth time and a slow growth rate of pyrite; framboidal and euhedral pyrite will then appear with large and different sizes (Wilkin et al., 1996,1997). With increasing oxidation degree, larger particle size euhedral pyrite can form at the interface between the sediment and water, whereas oxidation produces only a small amount of euhedral pyrite (Wignall and Newton, 1998; Bond and Wignall, 2010).

The final formation of pyrite is controlled by the local microenvironment (Chang et al., 2020), and the process results from the combined influence of several factors (Berner, 1984). 1) Sulfate reduction and pyrite burial rates are significantly positively correlated with organic carbon burial rates (Lin et al., 2000). Therefore, the content and activity of organic matter become the primary factors limiting the formation of

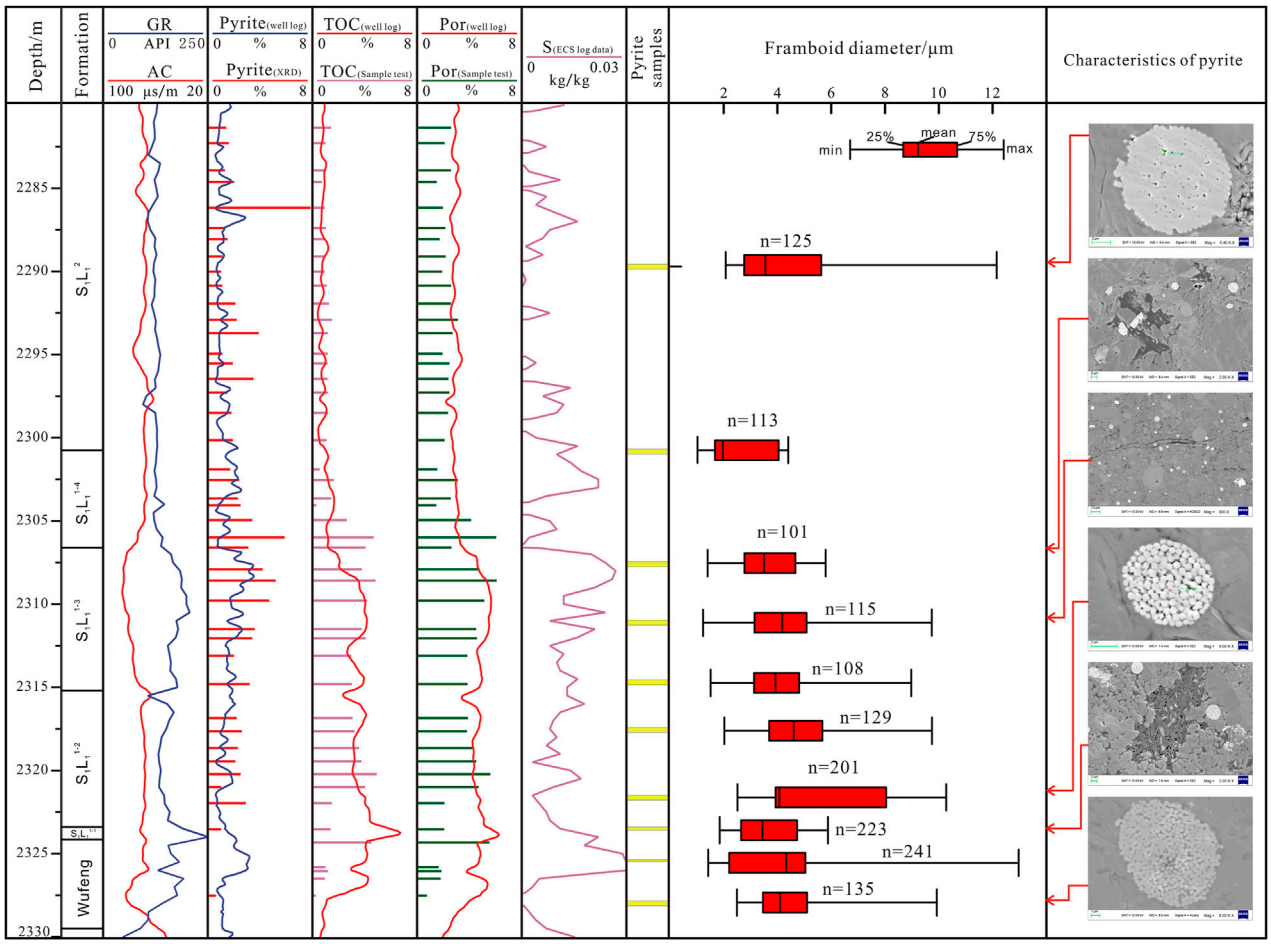

FIGURE 5 | Comprehensive comparison of geochemistry, reservoir physical properties and pyrite distribution characteristics of shale in the Longmaxi Formation.

authigenic pyrite. Terrestrial organic matter is relatively difficult to decompose and is not conducive to sulfate reduction reaction. 2) The diagenetic system gradually transits from open to closed with an increased water depth. The sulfate content in pore water is gradually consumed and limited, controlling the formation and burial of authigenic pyrite (Gomes and Hurtgen, 2013). According to the vertical variation of the sulfate content, soluble sulfur, and pyrite sulfur isotope signal in pore water, the formation of pyrite can be divided into four stages: 1) rapid reduction of sulfate, acid-soluble volatile sulfur yield is higher than that of pyrite; 2) the sulfate reduction rate and the yield of acid-soluble volatile sulfur began to decrease, and pyrite formed slowly; 3) sulfate content began to decrease, indicating the formation of the closed environment; 4) if organic carbon remains after sulfate is exhausted, authigenic pyrite enriched with ^{34}S will continue to be generated with SO_4^{2-} in the adjacent horizon (Chang et al., 2020). The closed diagenetic environment is conducive to the formation of pyrite; 3) in the redox sequence, organic carbon is buried and utilized by methanogens to generate CH_4, which diffuses upward in the sulfate methane transition zone, causing intense microbial sulfate reduction activity, leading to the enrichment of pyrite and the decomposition of natural gas hydrate (Zhang and Wu, 2019); 4) the deposition rate affects the formation of pyrite by changing other limiting factors. A high deposition rate is accompanied by the high organic matter content. However, when the deposition rate is too high, it will dilute the organic matter in the sediment (Tyson, 2001), reduce the residence time of sulfide at the redox interface, and lead to the incomplete conversion of acid-soluble volatile sulfur to pyrite (Chang et al., 2020).

Wilkin et al. (1996) proposed restoring the sedimentary environment using the box-and-whisker diagram of framboidal pyrite. The diagram in **Figure 3** shows the median, average, distribution range, and quartile of the particle size, which can intuitively reflect the distribution characteristics of maximum and minimum particle sizes, intermediate particle size, and particle concentration or dispersion of framboidal pyrite with depth (Wei et al., 2016; Wignall et al., 2016). The binary diagram of average particle size, standard deviation, and skewness can also be used to assess deposition redox conditions (Wilkin et al., 1996; Chang et al., 2009).

The oxygen and hydrogen sulfide concentrations in modern marine water can be divided into four categories: oxic, suboxic, anoxic, and euxinic (Tribovillard et al., 2006). The parameter

TABLE 2 | Characteristics of framboids used to define oxygen-related depositional conditions and facies (Bond and Wignall, 2010).

Conditions	Framboid parameters
Euxinic (persistently sulfidic lower water column)	Small (mean 3–5 μm), abundant, with narrow size range. Framboids dominate pyrite fraction
Anoxic (no oxygen in bottom waters for long periods)	Small (mean 4–6 μm), abundant, with a few, larger framboids. Framboids dominate pyrite fraction
Lower dysoxic (weakly oxygenated bottom waters)	Mean 6–10 μm, moderately common, with a few, larger framboids and some crystalline pyrite
Upper dysoxic (partial oxygen restriction in bottom waters)	Moderately common to rare, broad range of sizes, only a small proportion <5 μm. Majority of pyrite as crystals
Oxic (no oxygen restriction)	No framboids, rare pyrite crystals

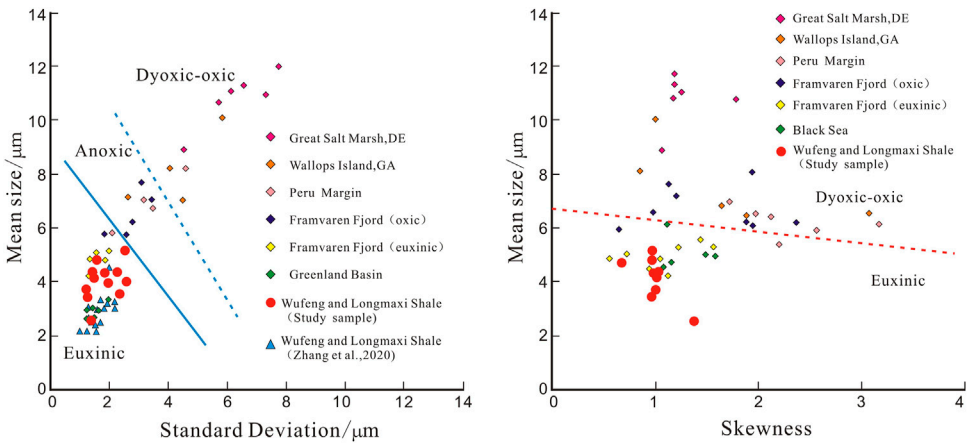

FIGURE 6 | Plot of the mean vs. the standard deviation (after Zhou et al., 2017; Zhang et al., 2020) and the mean vs. the skewness of the framboid size distribution (after Zhou et al., 2017).

characteristics of framboidal pyrite under different redox conditions are proposed (**Table.2**), which can be widely applied to the restoration of paleoenvironmental conditions in the sediments of various strata. The particle size distribution range of framboidal pyrite is narrow in the closed water environment (euxinic), but it tends to widen as the oxygen content increases.

The average particle size and skewness of framboidal pyrite can also identify the redox conditions for sediment formation (**Figure 6**) (Wilkin et al., 1996; Wei et al., 2016). Skewness is a good indicator of the heterogeneity of particle size distribution. When the variation range of framboidal pyrite particle size is small, it indicates a closed or semi-closed environment (**Figure 6**) (Wilkin et al., 1996).

The average particle size and standard deviation of the samples in this study are compared with the previous data. The sedimentary environment of Longmaxi formation samples in the study area is a euxinic environment (**Table.1**). Combined with the data in **Figure 6**, it can be inferred that the shale sedimentary environment of the Longmaxi Formation is the euxinic environment, which has strong reducibility, poor water fluidity, and a closed state. Pyrite cannot grow fully due to rapid settlement and burial after crystallization, resulting in generally small particle size characteristics due to an insufficient supply of materials, reducing agents, and energy required during the grain growth period of pyrite under poor hydrodynamic conditions. However, this closed euxinic environment with low long-term hydrodynamic force boosts organic matter deposition, accumulation, and preservation in Longmaxi Formation shale (Han and Li, 2019).

In sedimentation, shale is comprehensively controlled by the basin structure, water environment, sediment supply, and other factors, forming lithofacies that can reflect different environmental characteristics. According to the mineral composition, the shale in the study area can be divided into three lithofacies types: siliceous shale, calcareous shale, and mixed shale facies (Wang et al., 2016). The content and type of pyrite in different lithofacies are significantly different. The bottom of the Longmaxi Formation is dominated by siliceous shale, and mixed shale is occasionally seen. The development of banded pyrite and intermittent sandy lamina in the shale indicates a relatively quiet deep-water reduction environment in the sedimentary period, with the most pyrite content (Sun et al., 2019). The lithofacies in the middle and lower part of Longmaxi changed from siliceous shale to mixed shale, with scattered pyrite and relatively developed silty laminae, reflecting that the sedimentary environment changed from an early strong reduction environment to a weak reduction environment and decreased the pyrite content. Siliceous shale and mixed shale are more conducive to pyrite formation than calcareous shale (Lu et al., 2021).

5.2 Genetic Mechanism of Pyrite

Sedimentary pyrite is formed by reducing Fe^{3+} ions in sediments to Fe^{2+} ions in a strong reduction environment. Fe^{2+} ions react

with a large amount of H_2S produced by bacteria that decompose organic matter or sulfate-reducing bacteria. Reducing sulfate in sediments to form hydrometeorite pyrite ($FeS{\cdot}nH_2O$) or monosulfide iron, hydrometeorite pyrite reacts with elemental sulfur to form colloidal pyrite ($FeS_2{\cdot}nH_2O$), colloidal pyrite crystallizes and dehydrates to form pyrite (FeS_2) (Zhu and Geng, 2002).

Pyrite can be formed in two cases. The first is that it can be formed and precipitated directly from the solution under low in-situ active iron concentration. The second is to form mackinawite, greigite, framboidal pyrite, and euhedral pyrite under the high solubility of in-situ active iron. The formation stage of pyrite can be divided into the sedimentary and diagenetic types (Liu et al., 2016).

Sedimentary pyrite was formed in the synsedimentary period and early diagenetic stage. Sulfate-reducing bacteria reduce sulfate ions in the reducing water environment to produce H_2S or HS^-. Sulfide reacts with active iron Fe^{2+} to form tetragonal pyrite Fe_9S_8. (Bontognali et al., 2008; Heywood et al.,1990) Tetragonal pyrite is further transformed into pyrite Fe_3S_4. Pyrite particles are then aggregated under the influence of magnetic force to form framboidal pyrite (Wilkin et al., 1996).

$$2\,(CH_2O) + SO_4^{2-} \rightarrow 2HCO^{3-} + HS^-$$
$$CH_4 + SO_4^{2-} \rightarrow HS^- + HCO^{3-} + H_2O$$
$$S^{2-} + Fe^{2+} \rightarrow FeS_2$$

Diagenetic pyrite is formed in the stage of deep burial. In closed water with insufficient material supply (Wang, 2013), the concentration of active iron is low. Affected by the difference in pH value, pyrite can be formed either by crystallization directly from the water body or by forming FES first and then by some series of reactions (Cao and Wei, 2015). If the material supply and growth space are sufficient, framboidal pyrite with a large particle size will be formed. In contrast, self-shaped pyrite with small particles will be formed (Liu et al., 2016).

$$SO_4^{2-} + 1.33\,(CH_2) + 2H^+ \rightarrow H_2S + 1.33CO_2 + 1.33H_2O$$
$$S^{2+} + Fe^{2+} \rightarrow FeS_2$$

There is a small amount of lamellar and nodular pyrite in the Longmaxi Formation. At the formation stage, sediments are relatively loose, the supply of sulfur and iron is sufficient, and the pyrite microcrystals formed in the pores will gradually grow and increase until they fill the pore space. Following diagnoses such as compaction, pressure dissolution, and cementation, pyrite microcrystals in the space continue to grow and aggregate in the pores to form lumpy pyrite, which eventually forms euhedral, laminar, and nodular pyrites. This pyrite indicates the acidic sulfide reduction environment, which is conducive to the preservation and enrichment of organic matter.

The framboidal pyrite with the highest content in the Longmaxi formation is considered to have formed during a quasi syngenetic stage or early diagenesis in sedimentation (Marynowski and Zatoń, 2008). Barnes and Wilkin (1997). Framboidal pyrite is thought to have evolved through four continuous processes: 1) the formation of microcrystalline nuclei of ferrous sulfide, 2) the nucleation of colloidal pyrite (Fe_2S), 3) the gathering of colloidal pyrite crystallites to form a spherical strawberry body, and 4) the transformation of colloidal pyrite into framboidal pyrite (Cao and Wei, 2015; Zhou et al., 2017).

There has always been controversy about the organic or inorganic origin of pyrite. The view of biogenesis was put forward as early as 1923. Zhou and Jiang (2009) showed that framboidal pyrite is the illusion that cell aggregates or spherical organisms could be replaced by pyrite. Schouten (1946) once proposed that the framboidal structure has an inorganic origin. Yang and Gong (2011) opposed this inorganic origin of the biogenic view as framboidal pyrite was found in ores unrelated to the biological action (Lowenstam, 1981). In recent years, researchers have successfully synthesized strawberry pyrite in a vacuum anhydrous and aqueous solution. Sweeney believed that amorphous iron sulfide is formed in the initial stage of the reaction and then further reacts into equiaxed pyrite (Sweeney and Kaplan, 1973). Thus, the spherical structure is inherited when iron monosulfide is transformed into framboidal pyrite.

The authigenic pyrite in this sample has the general shape of a raspberry ball, and some balls develop octahedral microcrystals with very automorphic shapes. This is due to pyrite pellet nucleation, which crystallizes many microcrystals and transforms the pellets into raspberry balls. As a result, the formation of pyrite in the study area is more of inorganic nature. However, the genetic sequences, both organic-rich and organic-poor pyrites, could be established based on the degree of organic matter enrichment.

SEM images (**Figure 7**) depict the relationship between pyrite and organic matter, consistent with previous research: 1) organic matter is filled around or inside framboidal pyrite, indicating that its formation time is earlier than the kerogen massive oil generation period (Lu et al., 2021). 2) The aggregation of some framboidal pyrite microcrystals occurs in the space limited by the structure of organic matter. When pyrite grows to a certain extent, it is limited by organic matter and cannot continue to increase (MacLean et a1., 2008). 3) Euhedral pyrite aggregates often exist near the edge gaps of organic matter and framboidal pyrite aggregates.

The genetic sequence of organic-rich framboidal pyrite in the study area is established: 1) pyrite microcrystals nucleate and begin to aggregate and grow in the space limited by the structure of organic matter during the sulfate reduction stage of organic matter decomposition; 2) growing pyrites and microcrystals congregate to fill the remaining space in the cubic crystal form or the ubiquitous pentagonal dodecahedron. At the same time, it will cause many microspheres to form. These tiny pellets eventually evolved into euhedral pyrite crystals; 3) it extends and grows into framboidal pyrite through automorphic growth; 4) when there is little or no organic matter between the microcrystals in framboidal pyrite, the microcrystal particles fuse with each other under the condition of close aggregation so that the inclusions in the microcrystals and the organic matter mixed between the microcrystals disappear or are pushed out to form subhedral and subhedral shape pyrite crystals (**Figure 7**).

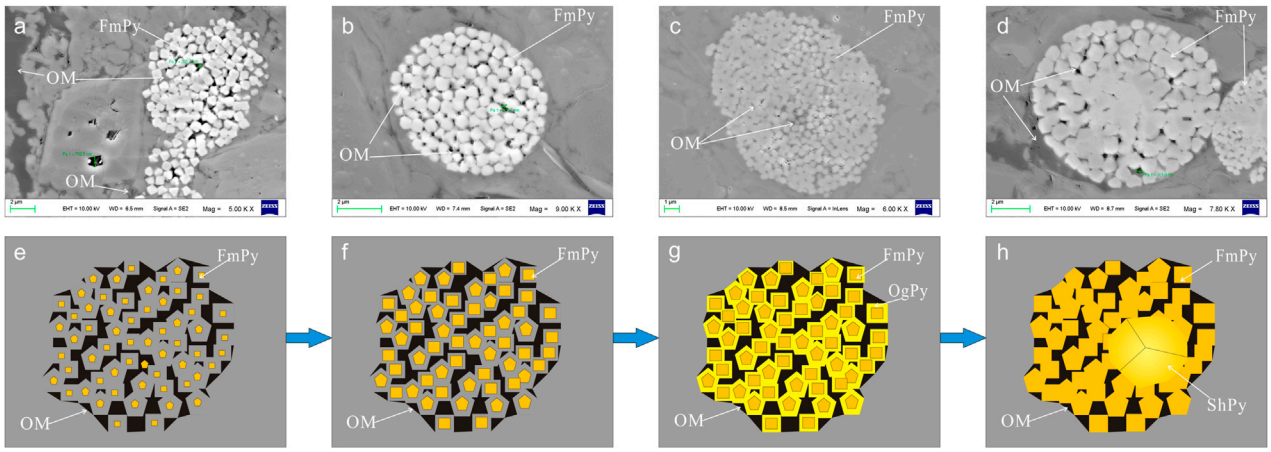

FIGURE 7 | Genetic model of framboidal pyrite in organic-rich shale. OM = organic matter; FmPy= framboidal pyrite; OgPy= pyrite overgrowth; ShPy = subhedral pyrite.

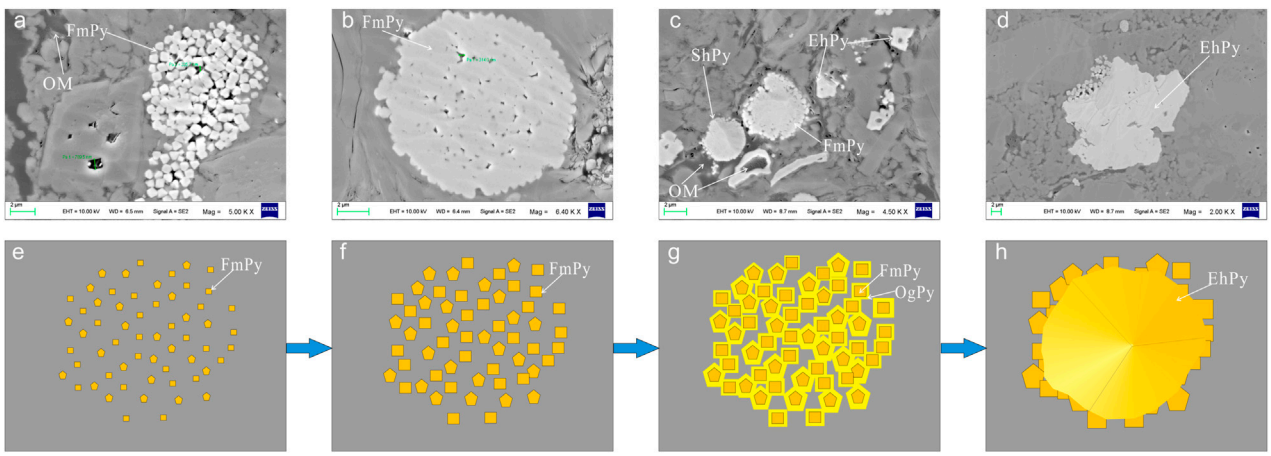

FIGURE 8 | Genetic model of framboidal pyrite in organic-poor shale. OM = organic matter; FmPy= framboidal pyrite; OgPy= pyrite overgrowth; EhPy= euhedral pyrite.

More experiments have confirmed the inorganic genesis of framboidal pyrite compared to the complex genesis affected by organic matter (Zuo et al., 2021). According to the microscopic characteristics, the inorganic genetic sequence is established: 1) the pyrite microcrystals continue to grow after nucleation, and the microcrystals increase and form cubic crystals or pentagonal dodecahedrons to gather and fill in the pore space; 2) after the microcrystal particles grow in their shape, they grow radially around the pyrite nodules to form raspberry pyrite; 3) due to the lack of organic matter and other substances, framboidal pyrite continues to grow and recrystallize, and finally fill the gap between single crystals to form self-shaped pyrite (**Figure 8**).

Notably, the saturation degree of the solution determines the crystal morphology of pyrite during the process of crystal growth. The appearance of self-shaped crystals indicates that the sulfur concentration in the sedimentary environment presents a long-term low saturation, and the sedimentary environment is conducive to the enrichment of organic matter.

5.3 Effect of Pyrite on Organic Matter

TOC (total organic carbon) is the total organic carbon in sediments (Canfield, 1994; Schoepfer et al., 2015). High marine primary productivity and reduced water environment are conducive to high TOC values in sediments. Pyrite generally exists in the shallow surface sediments of the continental margin sea. As the degradation product of organic matter and stable solid reduced sulfur, pyrite is preserved in the anoxic environment. The burial and decomposition conditions of organic matter in various sedimentary environments lead to significant differences in the contents of total organic carbon and pyrite sulfur (Wu L. et al., 2014).

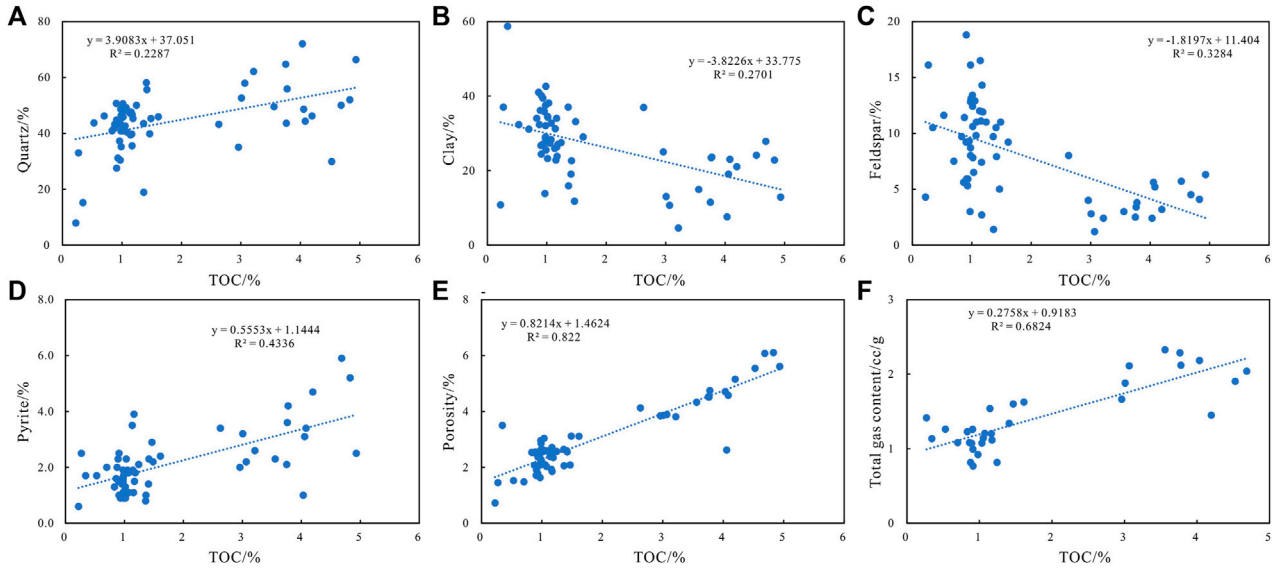

FIGURE 9 | Correlation diagram between TOC, shale mineral components, porosity, and total gas content. Quartz: quartz content, Clay: clay content, Feldspar: feldspar content, Pyrite: pyrite content of the shale samples.

Cao et al. (2018) proposed that the sedimentary environment restricts the type of organic matter and pyrite, and they are closely related. Organic matter provides a reductant and energy source during the formation of pyrite (Li et al., 2018). The organic parent material biofilm provides a necessary chemical environment for the structure and growth of pyrite. After sulfate-reducing bacteria degrade the initial organic matter, the generated H_2S reacts with iron to form pyrite (Wacey et al., 2015). Sulfur-rich kerogen takes a relatively lower time to generate hydrocarbon, and its C–S bond energy is lower, making it easier to decompose and generate hydrocarbon. In marine shale, sulfur mainly exists in the form of pyrite (Huang et al., 2017), and the formation of pyrite can reduce the activation energy of kerogen reaction and catalyze the hydrocarbon generation of organic matter (Zhang and Zhang, 1996). During diagenesis and diagenetic evolution, pyrite can weaken the compaction effect on organic matter and protect and support organic matter pores (Sun and Guo, 2017).

The sulfide reduction environment for the enrichment of framboidal pyrite is conducive to the enrichment and preservation of organic matter. The higher the iron content in water, the more conducive to the generation and enrichment of organic matter (Zhang et al., 2020). In the same sedimentary stage, the concentration of active iron and sulfur ions in the sedimentary environment controls the formation of pyrite. Framboidal pyrite positively correlates with the shale organic matter content and adsorbed gas content (Shu, 2015). Therefore, pyrite can indicate the enrichment of organic matter in shale. In the burial diagenetic stage, framboidal pyrite is formed in the sulfide reduction environment. The higher the pyrite content, the stronger the seawater reduction environment, and the shallower the redox interface. This is more conducive to organic matter enrichment, consistent with the positive correlation between synsedimentary pyrite and TOC (Li et al., 2018). The enrichment of pyrite also reflects the excellent water reduction environment in the sedimentary period, conducive to the enrichment and preservation of organic matter.

Generally, the content of organic matter is high, and the mineralization degree of pyrite is also high. If the organic matter is insufficient, the formed FeS remains at a particular stage of monosulfide. In order to convert FeS to FeS_2, there must be an oxidant. Experimental research shows that elemental sulfur is the only possible oxidant causing this transformation.

$$3\,FeS + S \rightarrow Fe_3S_4$$
$$Fe_3S_4 + 2S \rightarrow 3FeS_2$$

Quartz in shale can also form a siliceous support framework, providing a good space for kerogen preservation. Inorganic minerals such as clay minerals also have a specific catalytic effect on kerogen (**Figures 9A–C**). Under the reduction condition of pyrite development, shale has a high TOC value, leading to a high degree of pore development and the total gas content of shale (**Figure 9F**). In the study area, the Longmaxi Formation is in a reducing sedimentary environment with rapid material exchange; thus, there is an apparent positive correlation between organic carbon in shale and sulfur content in pyrite that is significantly stronger than that of quartz, clay, and feldspar (**Figure 9**). However, the TOC content is not the highest in some samples, but there is an abnormally high pyrite content. The unusually high abundance of pyrite is difficult to explain by the causes of organic matter, so the correlation between the two is not absolute.

5.4 Effect of Pyrite on the Porosity of Shale Reservoir

The reservoir space types of organic-rich shale mainly include fractures, inorganic pores, and organic pores, among which the pores related to pyrite include organic pores and inorganic pores.

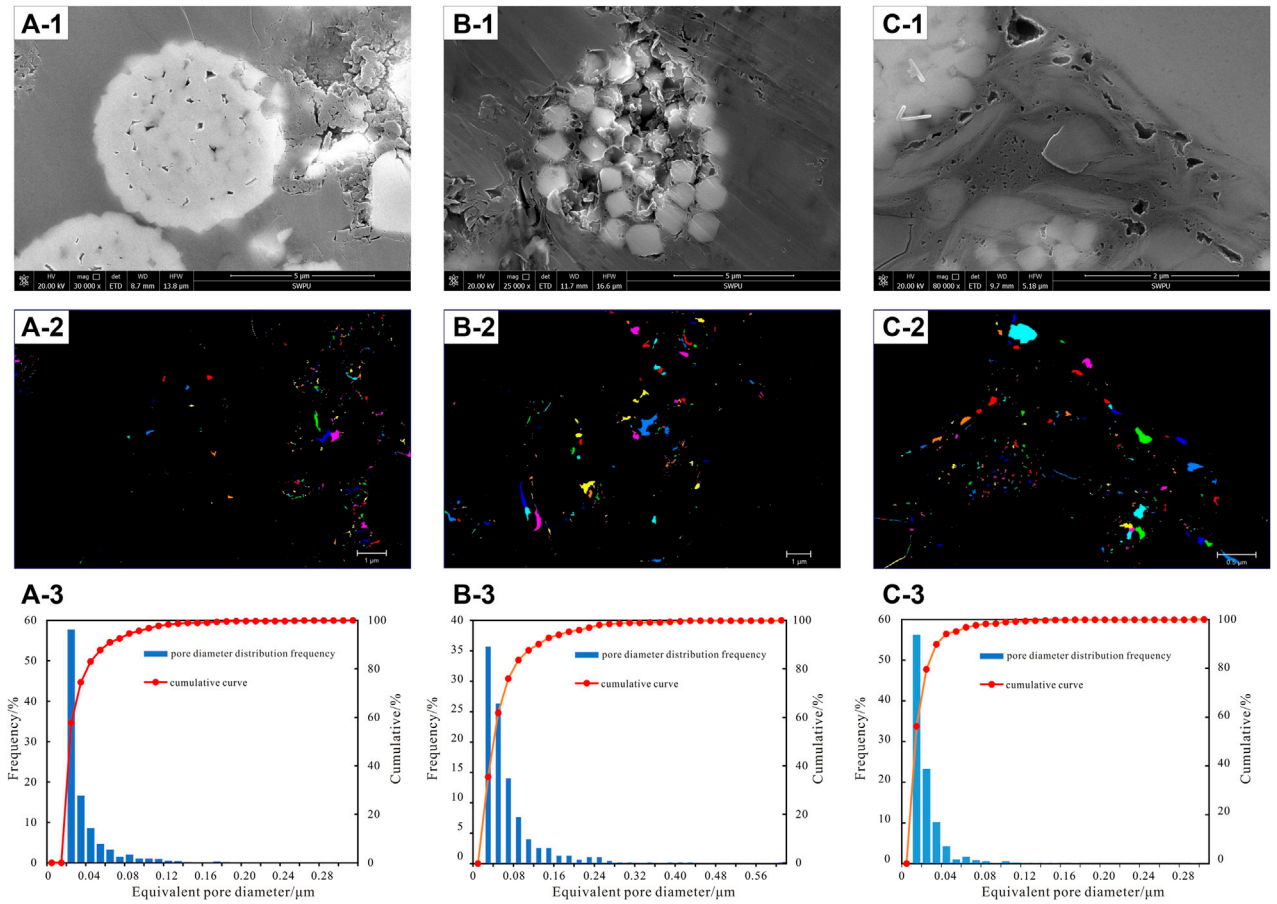

FIGURE 10 | Comparison of the pore structure characteristics of shale related to pyrite, (a-1, b-1, c-1 microscopic characteristics of shale, a-2, b-2, c-1 pore extraction characteristics, and a-3, b-3, c-3 equivalent pore diameter distribution), **(A)** 2326.45 m, well N2; **(B)** 2405.25 m, well N3; **(C)** 2215.36 m, well N4.

The inorganic pores are mainly the pores between the microcrystals of framboidal pyrite aggregate poor in organic matter and the mold pores formed by crystals falling off on the surface of the aggregate. In the former, the pores are often small, mostly isolated, and the pore diameter ranges from 0.02 to 0.04 μm due to the lack of restrictions on the radial growth of pyrite (**Figure 10**). The shape of the latter depends on the shape of the falling-off crystal, which is mostly honeycomb. The mold hole has good connectivity with the hole of organic matter in the crystal, and the pore diameter is large, which is the prominent enrichment place of free gas (Han and Li, 2019).

According to the relationship between pyrite and organic matter, organic pores can be divided into organic matter pores filling the interior of pyrite particles and organic matter pores between framboidal pyrite particles. The organic matter that fills the spaces between the grains of framboidal pyrite has mostly irregular pore morphology (Cao et al., 2018). Pyrite intergranular pores and organic matter pores are developed due to the limitation of organic matter. Intergranular pyrite pores will not expand after growing to a certain extent, and these pores are mainly organic matter pores, with the pore sizes ranging from 0.02 to 0.08 μm. The growth of pyrite affects the organic matter between pyrite particles, and the pore size of organic matter preserved under reduction conditions is generally 0.02–0.04 μm

There are numerous intergranular pores in framboidal pyrite and pores formed by pyrite intergranular filling organic matter, which provide storage space for gas accumulation. However, the influence of pyrite on the two types of pores differs. During the reservoir diagenesis process, the skeleton structure formed by stacking raspberry pyrite microcrystals can protect the development of nanopores between microcrystals by forming a “triangular stress protection structure” for the inorganic pores between pyrite grains (Zhao et al., 2018). The pores developed inside the organic matter contained in pyrite microcrystals. Pyrite aggregation protects the development of organic matter (Liu et al., 2017) and promotes the hydrocarbon generation and gas generation of organic matter by catalysis (Zhang and Zhang, 1996). Compared to shale without pyrite, the number of pores in pyrite is greater than that of the surrounding organic matter, and the number and size of organic pores in pyrite-enriched shale are larger.

The area ratio of framboidal pyrite aggregate is between 1.5 and 3.2%, and the average value is 1.8%. The face rate of framboidal pyrite aggregate is 3.5 ~ 9.5%, with an average

value of 5.8%, which is higher than the average face rate of the shale matrix. Therefore, pyrite pores have a positive contribution to the reservoir pore system. The pore contribution parameters of framboidal pyrite are obtained using the pyrite area ratio, the average face rate of pyrite, and the average face rate of the matrix, with the parameters ranging from 0.5 to 8%. Framboidal pyrite aggregate positively contributes to the reservoir pore system, and the pore diameter is small, primarily adsorption pores. Organic matter pores with diameters ranging from 10 to 50 nm in the framboidal pyrite aggregate are the most developed, accounting for more than 90% of the pores.

6 CONCLUSION

Framboidal pyrite, euhedral pyrite, and banded shape pyrite are all formed in the Longmaxi Formation shale, with framboidal pyrite being the most developed. The average particle size distribution of framboidal pyrite in the $S_1L_1^1$ member of the main reservoir is 3–5 μm, with the characteristics of a sulfidic environment. The average particle size of pyrite in a few shales is 4–6 μm, and it is oxygen-deficient in an anaerobic environment. The particle size of the sample in the lower part of the Longmaxi formation is between 1 and 15 μm, and the maximum particle size (MFD) is less than 20 μm, according to the box-and-whistler method. It is associated with an occluded reduction environment.

Two genetic sequences of framboidal pyrite are established based on the enrichment degree of shale organic matter and its associated relationship with pyrite. The formation of organic matter between pyrite microcrystalline particles will limit the continuous growth of pyrite, resulting in semi-euhedral and euhedral pyrite.

The sedimentary environment restricts the type of organic matter and pyrite. The reductive sedimentary environment of the Longmaxi Formation is conducive to the enrichment of organic matter, where the TOC value ranges from 0.23 to 4.93%, with an average value of 1.78%. There is a strong positive correlation between the pyrite content and TOC value. The TOC value of $S_1L_1^{1-2}$ and $S_1L_1^{1-3}$ members with the strongest reducibility is the highest, with the degree of pore development and total gas content are the strongest.

The pores related to pyrite in shale are mainly inorganic pores between microcrystals of framboidal pyrite aggregate, mold pores formed by crystals falling off on the surface of pyrite aggregate, organic matter pores inside pyrite particles, and organic matter pores between framboidal pyrite particles, organic pores are the main reservoir space. Also, pores are the main body of reservoir space. The enrichment of pyrite promotes the development of organic pores, and the number of pores in pyrite exceeds that of surrounding organic matter.

DATA AVAILABILITY STATEMENT

The original contributions presented in the study are included in the article/Supplementary Material; further inquiries can be directed to the corresponding authors.

AUTHOR CONTRIBUTIONS

JH and MW contributed in writing, reviewing, and editing, data curation, and writing—original draft preparation; LY, XS, SZ, LC, SP, and FW contributed in data analysis, mineral analysis, and graphic drawing.

FUNDING

This study received support from the Science and Technology Cooperation Project of the CNPC-SWPU Innovation Alliance (2020CX020000), China Postdoctoral Science Foundation (2017M623059), General Project of Chongqing Natural Science Foundation (No. cstc2021jcyj-msxmX0897), the Major Scientific and Technological Project of Sichuan Province (2020YFSY0039), and the Opening Foundation of Key Laboratory of Shale Gas Exploration, Minisitry of Natural Resources (KLSGE-202102).

ACKNOWLEDGMENTS

The authors would like to thank the PetroChina Southwest Oil and Gasfield Company for providing shale samples and experimental data. They appreciate the reviewers' suggestions.

REFERENCES

Berner, R. A. (1984). Sedimentary Pyrite Formation: An Update. *Geochimica Cosmochimica Acta* 48 (4), 605–615. doi:10.1016/0016-7037(84)90089-9

Bond, D. P. G., and Wignall, P. B. (2010). Pyrite Framboid Study of Marine Permian-Triassic Boundary Sections: A Complex Anoxic Event and its Relationship to Contemporaneous Mass Extinction. *Geol. Soc. Am. Bull.* 122 (7-8), 1265–1279. doi:10.1130/B30042.1

Bontognali, T. R. R., Vasconcelos, C., Warthmann, R. J., Dupraz, C., Bernasconi, S. M., and McKenzie, J. A. (2008). Microbes Produce Nanobacteria-like Structures, Avoiding Cell Entombment. *Geol* 36 (8), 663–666. doi:10.1130/G24755A.1

Canfield, D. E. (1994). Factors Influencing Organic Carbon Preservation in Marine Sediments. *Chem. Geol.* 114 (3/4), 315–329. doi:10.1016/0009-2541(94)90061-2

Cao, F., and Wei, H. (2015). Two Causes for the Low Abundance of Framboidal Pyrite in the Permian in Enshi Area in Hubei Province. *J. East China Inst. Technol. Nat. Sci.* 38 (2), 158–166. doi:10.3969/j.issn.1674-3504.2015.02.004

Cao, T., Deng, M., Song, Z., Liu, G. -X., Huang, Y. -R., Andrew, S. H., et al. (2018). Study on the Effect of Pyrite on the Accumulation of Shale Oil and Gas. *Nat. Gas. Geosci.* 29 (3), 404–414. doi:10.11764/j.issn.1672-1926.2017.12.006

Chang, H., Chu, X., Feng, L., Huang, J., et al. (2009). Framboidal Pyrites in Cherts of the Laobao Formation, South China: Evidence for Anoxic Deep Ocean in the Terminal Ediacaran. *Acta Petrol. Sin.* 25 (4), 1001.

Chang, H., and Chu, X. (2011). Pyrite Framboids and Palaeo Ocean Redox Condition Reconstruction. *Adv. Earth Sci.* 26 (5), 475. doi:10.12017/dzkx.2017.016

Chang, X., Zhang, M., Gu, Y., Wang, H., Liu, X., et al. (2020). Formation Mechanism and Controlling Factors of Authigenic Pyrite in Mud Sediments

on the Shelf of the Yellow Sea and the East China Sea. *Adv. Earth Sci.* 35 (12), 1306–1320. doi:10.11867/j.issn.1001-8166.2020.105

Chen, S., Zhu, Y., Qin, Y., Wang, h., Liu, H., and Fang, J. (2014). Reservoir Evaluation of the Lower Silurian Longmaxi Formation Shale Gas in the Southern Sichuan Basin of china. *Mar. Petroleum Geol.* 57, 619–630. doi:10.1016/j.marpetgeo.2014.07.008

Cui, J., Zhu, R., and Wu, S. (2013). The Effect of Pyrite on the Accumulation of Organic Matter, Hydrocarbon Generation and Expulsion, and Accumulation of Oil in Shale. *Geol. Review.59(supplement)* 1, 783.

Fan, C., Li, H., Qin, Q., He, S., and Zhong, C. (2020). Geological Conditions and Exploration Potential of Shale Gas Reservoir in Wufeng and Longmaxi Formation of Southeastern Sichuan Basin, China. *J. Petroleum Sci. Eng.* 191, 107138. doi:10.1016/j.petrol.2020.107138

Gomes, M. L., and Hurtgen, M. T. (2013). Sulfur Isotope Systematics of a Euxinic, Low-Sulfate Lake: Evaluating the Importance of the Reservoir Effect in Modern and Ancient Oceans. *Geology* 41 (6), 663–666. doi:10.1130/G34187.1

Han, S., and Li, W. (2019). Study on the Genesis of Pyrite in the Longmaxi Formation Shale in the Upper Yangtze Area. *Nat. Gas. Geosci.* 30 (11), 1608–1618. doi:10.11764/j.issn.1672-1926.2019.11.010

Heywood, B. R., Bazylinski, D. A., Garratt-Reed, A., Mann, S., and Frankel, R. B. (1990). Controlled Biosynthesis of Greigite (Fe_3S_4) in Magnetotactic Bacteria. *Naturwissenschaften* 77 (11), 536–538. doi:10.1007/BF01139266

Huang, H., He, D., Li, Y., Li, J., and Zhang, L. (2018). Silurian Tectonic-Sedimentary Setting and Basin Evolution in the Sichuan Area, Southwest china: Implications for Palaeogeographic Reconstructions. *Mar. Petroleum Geol.* 92, 403–423. doi:10.1016/j.marpetgeo.2017.11.006

Huang, Y., Zhang, X., Xiong, T., and Zhang, T. (2017). Profiling of Relationship between Shale Organic Matter Enrichment Mechanism and Gas-Bearing Property-A Case Study of Well QQ No. 1. *Coal Geol. China* 29 (12), 5–11. doi:10.3969/j.issn.1674-1803.2017.12.02

Li, D., Ou, C. H., Ma, Z. G., Jin, P. P., Ren, Y. J., and Zhao, Y. F. (2018). Pyrite-shale Interaction in Shale Gas Enrichment and Development. *Geophys. Prospect. Petroleum* 57 (3), 332–343. doi:10.3969/j.issn.1000-1441.2018.03.002

Li, H., Qin, Q., Zhang, B., Ge, X., Hu, X., Fan, C., et al. (2020). Tectonic Fracture Formation and Distribution in Ultradeep Marine Carbonate Gas Reservoirs: A Case Study of the Maokou Formation in the Jiulongshan Gas Field, Sichuan Basin, Southwest China. *Energy fuels.* 34 (11), 14132–14146. doi:10.1021/acs.energyfuels.0c03327

Li, H. (2022). Research Progress on Evaluation Methods and Factors Influencing Shale Brittleness: A Review. *Energy Rep.* 8, 4344–4358. doi:10.1016/j.egyr.2022.03.120

Li, H., Tang, H., Qin, Q., Zhou, J., Qin, Z., Fan, C., et al. (2019). Characteristics, Formation Periods and Genetic Mechanisms of Tectonic Fractures in the Tight Gas Sandstones Reservoir: A Case Study of Xujiahe Formation in YB Area, Sichuan Basin, China. *J. Petroleum Sci. Eng.* 178, 723–735. doi:10.1016/j.petrol.2019.04.007

Lin, S., Huang, K.-M., and Chen, S.-K. (2000). Organic Carbon Deposition and its Control on Iron Sulfide Formation of the Southern East China Sea Continental Shelf Sediments. *Cont. Shelf Res.* 20, 619–635. doi:10.1016/S0278-4343(99)00088-6

Liu, J., Yang, H., Xu, K., Wang, Z., Liu, X., Cui, L., et al. (2022). Genetic Mechanism of Transfer Zones in Rift Basins: Insights from Geomechanical Models. *GSA Bull.* doi:10.1130/B36151.1

Liu, Z. B., Gao, B., Hu, Z. Q., Du, W., Nie, H. K., and Jiang, T. (2017). Reservoir Characteristics and Pores Formation and Evolution of High Maturated Organic Rich Shale: a Case Study of Lower Cambrian Jiumenchong Formation, Southern Guizhou Area. *Acta Pet. Sin.* 38 (12), 1381–1389. doi:10.7623/syxb201712005

Liu, Z., Zhang, J., Liu, Y., Yu, W., He, W., and Li, B. (2016). The Particle Size Characteristics of Pyrite in Western Hunan and Hubei Areas' Wufeng-Longmaxi Formation Shale. *Sci. Technol. Eng.* 16 (26), 8. doi:10.3969/j.issn.1671-1815.2016.26.005

Lowenstam, H. A. (1981). Minerals Formed by Organisms. *Science* 211, 1126–1131. doi:10.1126/science.7008198

Lu, L., Liu, W., and Wei, Z. (2022). Diagenesis of the Silurian Shale, Sichuan Basin: Focus on Pore Development and Preservation. *Acta Sedimentol. Sin.* 40 (1), 73–87. doi:10.14027/j.issn.1000-0550.2021.125

Lu, Z., Tang, X., Zhang, T., Yufang, W., Jiazhcng, Z., Qingqiang, M., et al. (2021). Existence and Geological Significance of Pyrite in the Organic-Rich Shale of Lower Cambrian Niutitang Formation in Upper Yangtze Region. *Pet. Geology&Experiment* 43 (4), 599–610. doi:10.11781/sysydz202104599

MacLean, L. C. W., Tyliszczak, T., Gilbert, P. U. P. A., Zhou, D., Pray, T. J., Onstott, T. C., et al. (2008). A High-Resolution Chemical and Structural Study of Framboidal Pyrite Formed within a Low-Temperature Bacterial Biofilm. *Geobiology* 6 (5), 471–480. doi:10.1111/j.1472-4669.2008.00174.x

Marynowski, L., and Zatoń, M. K. (2008). Early Diagenetic Conditions during Formation of the Callovian (Middle Jurassic) Carbonate Concretions from Lukow (Eastern Poland): Evidence from Organic Geochemistry, Pyrite Framboid Diameters and Petrographic Study. *njgpa* 247, 191–208. doi:10.1127/0077-7749/2008/0247-0191

Nie, H., and Zhang, J. (2012). Shale Gas Accumulation Conditions and Gas Content Calculation:A Case Study of Sichuan Basin and its Periphery in the Lower Paleozoic. *Acta Geol. Sin.* 86 (2), 349–361. doi:10.3969/j.issn.0001-5717.2012.02.013

Schoepfer, S. D., Shen, J., Wei, H., Tyson, R. V., Ingall, E., and Algeo, T. J. (2015). Total Organic Carbon, Organic Phosphorus, and Biogenic Barium Fluxes as Proxies for Paleomarine Productivity. *Earth-Science Rev.* 149, 23–52. doi:10.1016/j.earscirev.2014.08.017

Shu, L. (2015). Geological Significance and Controlling Factors of Nonhydrocarbon Fluid of Jiufotang Formation in Naiman Sag. *Lithol. Reserv.* 27 (3), 75–81. doi:10.3969/j.issn.1000-1441.2018.03.002

Sun, C., Nie, H., Liu, G., et al. (2019). Quartz Type and its Control on Shale Gas Enrichment and Production:a Case Study of the Wufeng-Longmaxi Formations in the Sichuan Basin and its Surrounding Areas, China. *Earth Sci.* 44 (11), 3692–3704. doi:10.3799/dqkx.2019.203

Sun, Y. S., and Guo, S. B. (2017). Characteristics of Microscopic Pores of Shale from Upper Sinian Doushantuo Formation in the Western of Hunan and Hubei, China and the Main Controlling Factors. *J. Earth Sci. Env.* 39 (1), 114–125. doi:10.3969/j.issn.0001-5717.2012.02.013

Sweeney, R. E., and Kaplan, I. R. (1973). Pyrite Framboid Formation; Laboratory Synthesis and Marine Sediments. *Econ. Geol.* 68 (5), 618–634. doi:10.2113/gsecongeo.68.5.618

Tribovillard, N., Algeo, T. J., Lyons, T., and Riboulleau, A. (2006). Trace Metals as Paleoredox and Paleoproductivity Proxies: an Update. *Chem. Geol.* 232 (1-2), 12–32. doi:10.1016/j.chemgeo.2006.02.012

Tyson, R. V. (2001). Sedimentation Rate, Dilution, Preservation and Total Organic Carbon: Some Results of a Modelling Study. *Org. Geochem.* 32, 333–339. doi:10.1016/S0146-6380(00)00161-3

Wacey, D., Kilburn, M. R., Saunders, M., Cliff, J. B., Kong, C., Liu, A. G., et al. (2015). Uncovering Framboidal Pyrite Biogenicity Using Nano-Scale CNorg Mapping. *Geology* 43 (1), 27–30. doi:10.1130/G36048.1

Wang, M., Tang, H., Tang, H., Liu, S., Zhang, L., Zeng, M., et al. (2019). Impact of Differential Densification on the Pore Structure of Tight Gas Sandstone: Evidence from the Permian Shihezi and Shanxi Formations, Eastern Sulige Gas Field, Ordos Basin, china. *Geofluids* 2019 (2), 1–25. doi:10.1155/2019/4754601

Wang, M., Tang, H., Zhao, F., Liu, S., Yang, Y., Zhang, L., et al. (2017). Controlling Factor Analysis and Prediction of the Quality of Tight Sandstone Reservoirs: a Case Study of the He8 Member in the Eastern Sulige Gas Field, Ordos Basin, china. *J. Nat. Gas Sci. Eng.* 46, 680–698. doi:10.1016/j.jngse.2017.08.033

Wang, P., Huang, Y., Wang, C., Feng, Z., and Huang, Q. (2013). Pyrite Morphology in the First Member of the Late Cretaceous Qingshankou Formation, Songliao Basin, Northeast China. *Palaeogeogr. Palaeoclimatol. Palaeoecol.* 385 (5), 125–136. doi:10.1016/j.palaeo.2012.09.027

Wang, Y., Wang, S., Dong, D., Li, X., Huang, J., Zhang, C., et al. (2016). Lithofacies Characterization of Longmaxi Formation of the Lower Silurian, Southern Sichuan. *Earth Sci. Front.* 23 (1), 119–133. doi:10.13745/j.esf.2016.01.011

Wei, H., Wei, X., Qiu, Z., Song, H., and Shi, G. (2016). Redox Conditions across the G-L Boundary in South China: Evidence from Pyrite Morphology and Sulfur Isotopic Compositions. *Chem. Geol.* 440, 1–14. doi:10.1016/j.chemgeo.2016.07.009

Wignall, P. B., Bond, D. P. G., Sun, Y., Grasby, S. E., Beauchamp, B., Joachimski, M. M., et al. (2016). Ultra-shallow-marine Anoxia in an Early Triassic Shallow-Marine Clastic Ramp (Spitsbergen) and the Suppression of Benthic Radiation. *Geol. Mag.* 153 (2), 316–331. doi:10.1017/S0016756815000588

Wignall, P. B., Newton, R., and Brookfield, M. E. (2005). Pyrite Framboid Evidence for Oxygen-Poor Deposition during the Permian-Triassic Crisis in Kashmir. *Palaeogeogr. Palaeoclimatol. Palaeoecol.* 216 (3-4), 183–188. doi:10.1016/j.palaeo.2004.10.009

Wignall, P. B., and Newton, R. (1998). Pyrite Framboid Diameter as a Measure of Oxygen Deficiency in Ancient Mudrocks. *Am. J. Sci.* 298 (7), 537–552. doi:10.2475/ajs.298.7.537

Wilkin, R. T., Arthur, M. A., and Dean, W. E. (1997). History of Water-Column Anoxia in the Black Sea Indicated by Pyrite Framboid Size Distributions. *Earth Planet. Sci. Lett.* 148 (3-4), 517–525. doi:10.1016/S0012-821X(97)00053-8

Wilkin, R. T., Barnes, H. L., and Brantley, S. L. (1996). The Size Distribution of Framboidal Pyrite in Modern Sediments: an Indicator of Redox Conditions. *Geochimica cosmochimica acta* 60 (20), 3897–3912. doi:10.1016/0016-7037(96)00209-8

Wilkin, R. T., and Barnes, H. L. (1997). Formation Processes of Framboidal Pyrite. *Geochimica Cosmochimica Acta* 61 (2), 323–339. doi:10.1016/S0016-7037(96)00320-1

Wu, C., Zhang, M., Ma, W., Liu, Y., Xiong, D., Sun, L., et al. (2014a). Organic Matter Characteristic and Sedimentary Environment of the Lower Cambrian Niutitang Shale in Southeastern Chongqing. *Nat. Gas. Geosci.* 25 (8), 1267–1274. doi:10.11764/j.issn.1672-1926.2014.08.1267

Wu, L., Lei, H. Y., Ou, W. J., and Han, C. (2014b). Distribution Characteristic and Crystal Form of Pyrite from the Sediment Cores on Northern South China Sea. *J. Appl. Oceanogr.* 33 (1), 21–28. doi:10.3969/J.ISSN.2095-4972.2014.01.003

Yang, X., and Gong, Y. (2011). Pyrite Framboid: Indicator of Environments and Life. Diqiu Kexue - Zhongguo Dizhi Daxue Xuebao. *Earth Sci. - J. China Univ. Geosciences* 36 (4), 643–658. doi:10.3799/dqkx.2011.066

Zhang, G. R., Nie, H. K., Tang, X., Du, W., Sun, C. X., and Chen, S. (2020). Pyrite Type and its Effect on Shale Gas Accumulation: a Case Study of Wufeng-Longmaxi Shale in Sichuan Basin and its Periphery. *Pet. Geology&Experiment* 42 (3), 459–466. doi:10.11781/sysydz202003459

Zhang, J., and Zhang, P. (1996). A Discussion of Pyrite Catalysis on the Hydrocarbon Generation Process. *Adv. Earth Sci.* 11 (3), 282–287. doi:10.3321/j.issn:1001-8166.1996.03.009

Zhang, Y., and Wu, Z. (2019). Sedimentary Organic Carbon Mineralization and its Contribution to the Marine Carbon Cycle in the Marginal Seas. *Adv. Earth Sci.* 34 (2), 202–209. doi:10.11867/j.issn.1001-8166.2019.02.0202

Zhao, D. F., Guo, Y. H., Zhu, Y. M., Wang, G., Liu, J., Chong, X., et al. (2018). Micropore Characteristics and Geological Significance of Pyrite in Shale Rocks of Longmaxi Formation. *Acta Sedimentol. Snica* 36 (5), 864–876. doi:10.14027/j.issn.1000-0550.2018.077

Zhou, C., and Jiang, S.-Y. (2009). Palaeoceanographic Redox Environments for the Lower Cambrian Hetang Formation in South China: Evidence from Pyrite Framboids, Redox Sensitive Trace Elements, and Sponge Biota Occurrence. *Palaeogeogr. Palaeoclimatol. Palaeoecol.* 271 (3-4), 279–286. doi:10.1016/j.palaeo.2008.10.024

Zhou, J., Qiu, Z., Wang, H., Lu, B., and Jiang, Z. (2017). Formation Mechanism of Pyrite Framboid and its Research Significance. *Chin. J. Geol.* 52 (1), 242–253. doi:10.12017/dzkx.2017.016

Zhu, D., Liu, Q., Zhou, B., Jin, Z., and Li, T. (2018). Sulfur Isotope of Pyrite Response to Redox Chemistry in Organic Matter-Enriched Shales and Implications for Components of Shale Gas. *Interpretation* 6 (4), SN71–SN83. doi:10.1190/int-2018-0023.1

Zhu, Y. H., and Geng, J. J. (2002). Analysis on Causes of Depositional Pyrite under Different Environment. *Hebei Coal* 1, 11–12. doi:10.3969/j.issn.1007-1083.2002.01.006

Zou, C., Dong, D., Yang, H., Wang, Y., Huang, J., Wang, S., et al. (2011). Conditions of Shale Gas Accumulation and Planning Practices in China. *Nat. Gas. Ind.* 31 (12), 26–39. doi:10.3787/j.issn.1000-0976.2011.12.005,

Zuo, Q., Xu, Y., Yu, B., Zhang, C., Zhang, Y., Hou, C., et al. (2021). NanoSIMS Sulfur Isotope Studies of Pyrite from the Early Paleozoic Marine Shale: Implications for the Sedimentary Environment. *Mar. Petroleum Geol.* 124, 104802. doi:10.1016/j.marpetgeo.2020.104802

Conflict of Interest: XS, SZ and LC were employed by the Shale Gas Research Institute of PetroChina Southwest Oil and Gasfield Company.

The remaining authors declare that the research was conducted in the absence of any commercial or financial relationships that could be construed as a potential conflict of interest.

Publisher's Note: All claims expressed in this article are solely those of the authors and do not necessarily represent those of their affiliated organizations, or those of the publisher, the editors, and the reviewers. Any product that may be evaluated in this article, or claim that may be made by its manufacturer, is not guaranteed or endorsed by the publisher.

frontiers | Frontiers in Earth Science

TYPE Original Research
PUBLISHED 19 August 2022
DOI 10.3389/feart.2022.935508

OPEN ACCESS

EDITED BY
Shuai Yin,
Xi'an Shiyou University, China

REVIEWED BY
Xinghua Wang,
SINOPEC Petroleum Exploration and Production Research Institute, China
Yaxiong Sun,
SINOPEC Petroleum Exploration and Production Research Institute, China

*CORRESPONDENCE
Xuanlong Shan,
shanxl@jlu.edu.cn

SPECIALTY SECTION
This article was submitted to Structural Geology and Tectonics, a section of the journal Frontiers in Earth Science

RECEIVED 04 May 2022
ACCEPTED 19 July 2022
PUBLISHED 19 August 2022

CITATION
Wang W, Yi J, Shan X, Zhang X, Liu X, Liu P and Ren S (2022), Characteristics of fractures development and its controlling factors within the buried hill reservoirs from the Archaean metamorphic basement in the Bozhong Sag, Bohai Bay Basin, Eastern China. *Front. Earth Sci.* 10:935508. doi: 10.3389/feart.2022.935508

Characteristics of fractures development and its controlling factors within the buried hill reservoirs from the Archaean metamorphic basement in the Bozhong Sag, Bohai Bay Basin, Eastern China

Wei Wang[1], Jian Yi[1], Xuanlong Shan[1]*, Xintao Zhang[2], Xiaojian Liu[2], Pengcheng Liu[1] and Shuyue Ren[1]

[1]College of Earth Sciences, Jilin University, Changchun, China, [2]Tianjin Branch of China National Offshore Oil Corporation Ltd., Tianjin, China

Metamorphic rocks have almost no primary pore space, and their formation of large-scale reservoirs depends on fractures and related secondary pore space formed by tectonic and fluid activities. The BZ19-6 block in the Bozhong Sag, Bohai Bay Basin, is the largest and deepest buried basement condensate field of buried-hill in the world, and its reservoirs are characterized by strong heterogeneity. In this paper, we systematically summarize the characteristics of fracture development, explore the main factors controlling fracture development, establish a fracture development model and clarify the influence of fractures on reservoir quality by using core and microscopic thin section observations, physical property data, imaging logging data and 3D seismic data analysis. The results show that the major types of fractures in the study area are tectonic fractures and dissolution fractures. In particular, the tectonic fractures are widely developed, accounting for 71.7% of the total number of fractures. Migmatization controls the lithological distribution of Archean metamorphic rocks. The migmatitic granite, having the highest degree of migmatization, is the dominant lithology for fracture development because it is rich in brittle minerals, such as feldspar and quartz. Strong compressional orogeny occurred during Indosinian period when many fractures initially developed, which become dominant among the tectonic fractures. Compression-tension-compression multistage tectonic movements characterized the Yanshanian period. During this period, fractures of different degrees formed. The Himalayan period, critical for fracture reconstruction, reactivated the early fractures and promoted the positive influence of atmospheric freshwater and organic acids on fracture reconstruction. Fractures are distributed unevenly in the vertical direction, and fracture-intensive zones are the main development sites for favourable reservoirs because they enhance the porosity and permeability of Archean metamorphic rocks. It means that these fractures can provide effective storage

space for oil and gas, which is key for the formation of large-scale reservoirs. In addition, fractures can provide migration channels for organic acids and atmospheric freshwater, which lead to later dissolution, and connect various dispersed dissolution pores to improve the effectiveness of reservoir space.

KEYWORDS

Archean metamorphic rocks, buried hill, fracture characteristics, controlling factor, metamorphic reservoir, Bohai Bay basin

1 Introduction

With the continuous vertical development of oil and gas exploration, basement buried hills have become increasingly important targets in the exploration of hydrocarbon-bearing basins (Hou et al., 2019). To date, several medium to large oil and gas fields in buried hills of metamorphic rocks have been discovered worldwide, such as the Bach Ho oil field in the Cuu Long Basin, Vietnam (Cuong and Warren, 2009); the La Paz-Mara gas field in Venezuela (Nelson et al., 2000); the Aryskum oil and gas field in the South Turgay Basin, Kazakhstan (Han et al., 2020); the buried hill in the Bongor Basin, Chad (Dou et al., 2015; Li et al., 2017); and the Xinglongtai buried hill in the Liaohe Depression, China (Song et al., 2011). The Bohai Bay Basin is an important hydrocarbon-bearing basin in China, and important achievements and breakthroughs have been made in the exploration of buried hills of metamorphic rocks for oil and gas in the past 50 years, including the discovery of JZ25-1S, CFD18-1/2, BZ26-2, BZ19-6, BZ13-2, JZ25-3 and other oil and gas fields (Li et al., 2012; Zhao et al., 2015; Ye et al., 2021b). In particular, the discovery of the BZ19-6 gas field, which is the largest and deepest buried basement condensate field of buried hill in the world, shows the great exploration potential of deep buried hill of metamorphic rocks in the Bohai Bay Basin (Xie et al., 2018).

Buried hills of metamorphic rock have unique characteristics, such as a weak influence of burial depth, large reservoir thickness and strong physical heterogeneity (Luo et al., 2005; Liu et al., 2020). Metamorphic rocks have almost no primary pore space (Ni et al., 2011, 2013), and the formation of large-scale reservoirs in such rocks depends on fractures and related secondary pore space formed by tectonic activity, so fractures play an important role in reservoirs (Ameen et al., 2010; Carvalho et al., 2013; Guo et al., 2017; Hou et al., 2019). A large number of drilling records have shown that there are abundant hydrocarbons within the fractures in the Archean buried hills of metamorphic rocks in the Bohai Bay Basin (Yang et al., 2016; Xue and Li, 2018), indicating that fractures not only are effective pathways for hydrocarbon migration and enhance the permeability of reservoirs (Carvalho et al., 2013; Liu et al., 2016; Ye et al., 2020b), but also serve as the main storage space for the accumulation of hydrocarbons (Luo et al., 2005; Parnell, 2010; Ding et al., 2013; Shen et al., 2015; Guo et al., 2016). Hence, for dense metamorphic rocks, the degree of fracture development determines the scale and production of reservoirs (Tong et al., 2012).

At present, many scholars have carried out studies on fractures in buried hills of metamorphic rocks (Fu et al., 2003; Eig and Bergh, 2011; Zou et al., 2013; Achtziger-Zupančič et al., 2017; Li et al., 2020; Ye et al., 2021b). It is believed that the distribution and development of fractures are controlled by lithology, strata thickness, weathering intensity, stress and other factors (Bazalgette et al., 2010; Zeng et al., 2013; Wang et al., 2016; Yin et al., 2019; Chen et al., 2021; Zhao et al., 2021). Under the same tectonic stress conditions, rocks rich in brittle minerals, such as felsic minerals, are more likely to produce fractures (Ye et al., 2021b). Weathering and eluviation can cause irregular fractures of different scales to form near the surface of rocks, resulting in a high degree of rupture and well-developed fractures (Salah and Alsharhan, 1998; Yue et al., 2014). Tectonics is a key factor contributing to fracture generation in rocks. The intensity of active faults is strongly correlated with fracture density (Maerten et al., 2018). In addition, faults control the development of fractures by affecting the local tectonic stress around them, and the closer fractures are to faults, the more intense the fractures are (Ye et al., 2021a). In the vertical direction, folds can be divided from top to bottom into tensile strain zones, transition zones and shortening zones according to stress changes. In the tensile strain zone, tensile fractures develop, while shear fractures develop in the shortening zone (Li et al., 2018).

Some scholars have studied the fractures of buried hills of metamorphic rocks in the Bohai Bay Basin (Tong et al., 2012; Ye et al., 2020b), and they have mostly focused on reservoir descriptions, identifying tectonic fractures and dissolution fractures as the main reservoir spaces (Zhou et al., 2005; Hou et al., 2019). However, no clear fracture development model is available that can comprehensively illustrate the development of fractures and accurately predict buried hills of metamorphic rocks reservoirs. To address this limitation, taking the Bozhong Sag in the Bohai Sea area as an example, we integrate core and microscopic thin section observations, physical property data, imaging logging data and 3D seismic data analysis to systematically summarize the characteristics of fracture development, explore the main controlling factors of fracture development, and establish a fracture development model to clarify the impact of fractures on reservoir quality. These research results are of great importance to fracture prediction and the effective development of buried hill in the study area, and provide insight that can guide the future exploration of buried hill reservoirs.

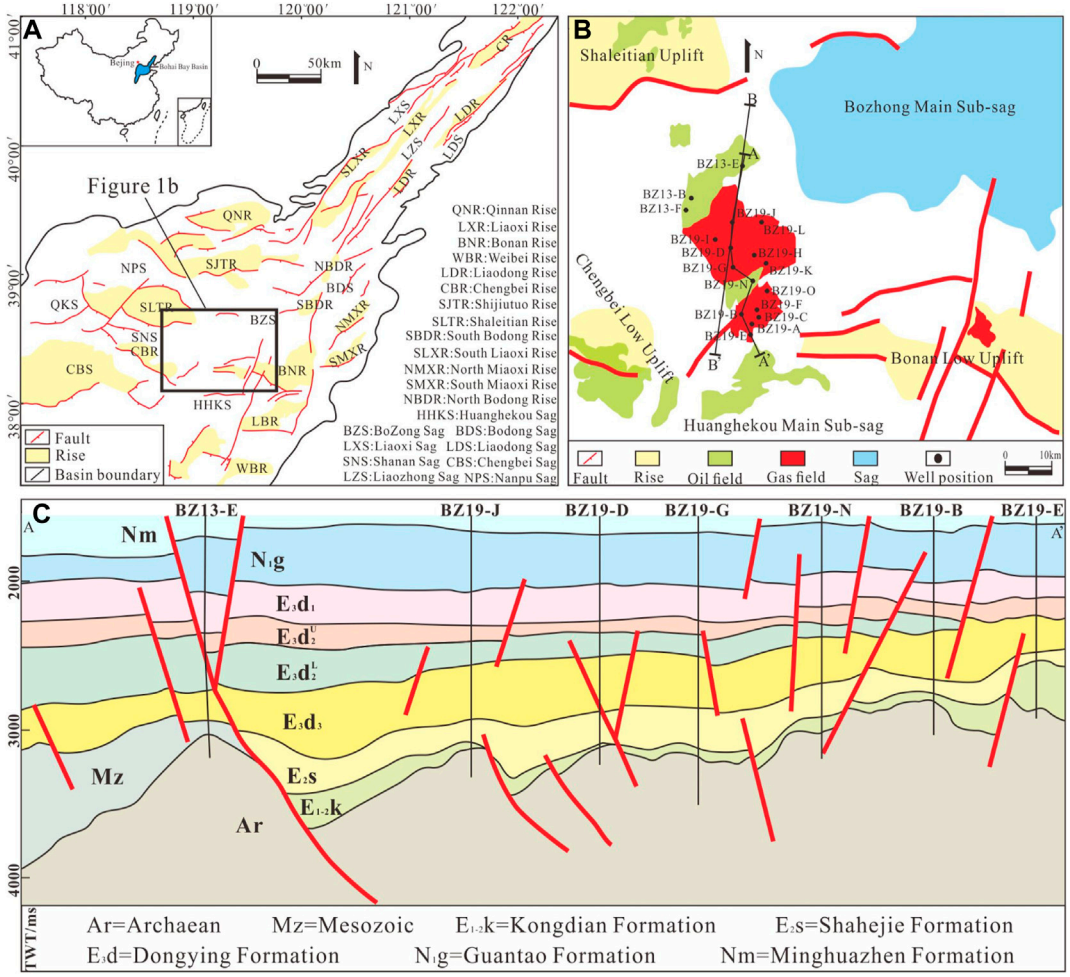

FIGURE 1
Geological features of the Bohai Bay Basin. **(A)** Location of the study area in the Bohai Bay Basin (modified after Ye et al., 2020); **(B)** Simplified structural map of the Bozhong Sag (modified after Xue & Li, 2018); **(C)** Typical geological section through BZ19-6 and adjacent areas (location of the section see Figure 1B)).

2 Geological setting

The Bohai Bay Basin with an area of 20×10^4 km^2, in eastern China, is a Mesozoic and Cenozoic superimposed basin developed on the base of the Paleozoic craton in North China via strike-slip and pull-apart interactions (Allen et al., 1997; Hou et al., 2001; Li et al., 2010; Liang et al., 2016). The Bozhong Sag, a secondary tectonic unit, is the largest hydrocarbon-generating sag in the Bohai Bay Basin (Wan et al., 2009). It is surrounded by the Jiao-Liao uplift to the east, Chengning uplift to the west, Liaodong Bay Depression to the north and Jiyang Depression to the south and has an area of approximately 2×10^4 km^2 (Figure 1A) (Xu et al., 2019). Since the Mesozoic, the Bozhong Sag has experienced a series of intense tectonic movements, forming a complex fracture system mainly composed of normal faults and locally developed strike-slip faults (Li et al., 2010). These faults control not only the structural evolution of the basin but also the formation and distribution of the basement hydrocarbon reservoir (Tong et al., 2015).

The tectonic evolution of the basin created favourable geological conditions for the formation of buried hills in basement uplifts. During this evolution, the Luliang movement involved strong migmatization and granitization, and the Jining, Galidon and Haixi tectonic movements were the main orogenic movements during the Paleozoic era; these movements manifested as vertical uplift in the North China Platform, resulting in the absence of Upper Ordovician-lower Carboniferous sedimentation (Qi et al., 2013). During the Indosinian period, due to the collision between the South China and North China plates (Wang et al., 2018), the Bozhong Sag was subjected to a nearly S-N oriented

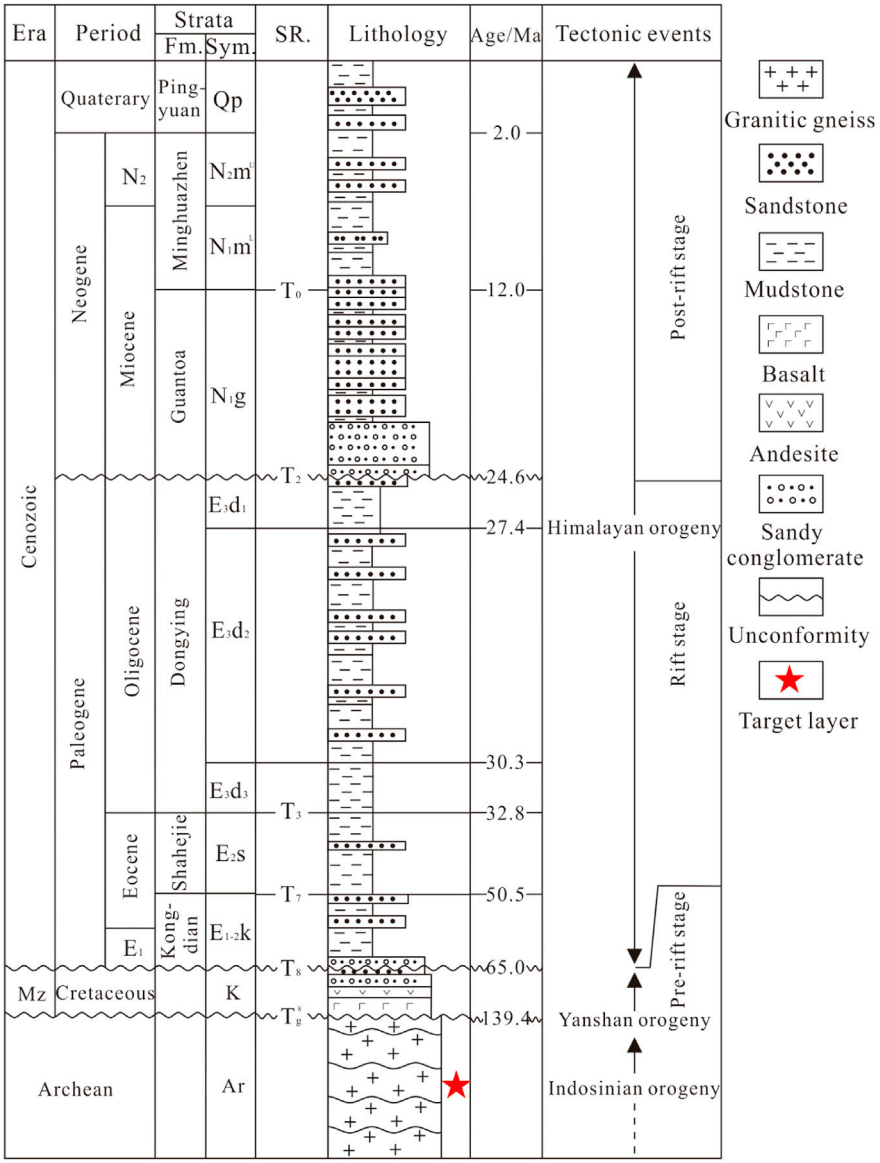

FIGURE 2
Stratigraphic column in the study area, showing the lithology and tectonic event (modified after Zhao et al., 2020). Fm.=Formation; Sym.=Submember; SR.=Seismic reference; Mz=Mesozoic; E_1=Paleocene; N_2=Pliocene.

compressional stress field, which produced a series of folds nappe from south to north and nearly W-E oriented thrust fault systems (Li et al., 2013; Wang et al., 2019b, 2019a), resulting in an E-W oriented uplift-sag pattern. At this time, tectonic movement played a crucial role in the formation of buried hills (Yu and Koyi, 2016). Under the influence of NE-oriented subduction and the retreat of the Paleo-Pacific plate during the Yanshanian period (Hou et al., 1998), the basin experienced three stages of tectonic evolution, namely, early Yanshanian compression-torsion, middle Yanshanian tension and late Yanshanian compression-torsion (Zhou et al., 2003), and developed a series of NE-oriented faults and associated fold structures (Wang et al., 2019b; 2019a); these tectonic activities caused widespread deformation in the North China Craton region and was the key period of buried hills deformation (Figure 1C) (Li et al., 2013; Zhu et al., 2017). The Himalayan period was mainly influenced by the India-Eurasia plate collision and the subduction of the Pacific plate; the pre-existing NE-oriented and nearly W-E oriented large-scale faults were reactivated (Qi et al., 2013; Peng et al., 2018; Wang et al., 2018), and a series of alternating topographic depressions and uplifts formed between the fault zones.

The study area is located on the deep structural ridge in the southwestern part of the Bozhong Sag in the Bohai Bay Basin. It is adjacent to the Bonan low uplift in the southeast and is connected to the Chengbei low uplift in the southwest, Huanghekou Sag in the south and Bozhong Sag in the north. This area shows the characteristics of an uplifted anticline structural belt (Hou et al., 2019) (Figure 1B). Drilling wells in the study area encountered, from top to bottom, the Quaternary Pingyuan Formation (Qp), Neogene Minghuazhen Formation ($N_{2\text{-}1}M$) and Guantao Formation (N_2g); Paleogene Dongying Formation (E_3d), Shahejie Formation ($E_{3\text{-}2}S$), and Kongdian Formation ($E_{2\text{-}1}K$); and Mesozoic (Mz) and Archean (Ar) strata. Mesozoic, Paleozoic and Proterozoic strata are completely absent in the BZ19-6 block. The Archean buried hill in the BZ13-2 block is partially covered by Mesozoic rocks. Archean metamorphic rocks compose the oldest crystalline basement in the Bozhong Sag and are the main object of this study. The burial depth is approximately 4000–5500 m (Figure 2), and it is the deepest buried hill reservoir of metamorphic rock in the Bohai Bay Basin.

3 Data and methods

We identified the lithologies and fracture types by observing eight wells (BZ19-B, BZ19-G, BZ19-J, BZ19-K, BZ19-L, BZ19-N, BZ19-O, BZ13-E) with a total core length of 51.7 m and 306 sidewall cores and determined the development of fractures and the degree of filling. A total of 277 ordinary and casting thin sections were collected and observed to identify the microscopic characteristics of features, filling and dissolution along microfractures. Casting thin sections (30 μm thick) with blue dye resin and cathodoluminescence were used to analyse the effective cracks and pores (Nabway and Kassab, 2013; Lai et al., 2019). The clay minerals and microstructure were observed by scanning electron microscopy (SEM). A total of 136 analyses of reservoir physical property, including porosity and permeability, and 13 analyses of whole-rock diffraction were collected to obtain the mineral composition of different rock types.

Logging data, including conventional and imaging logging data from 18 wells, were obtained to interpret the fracture characteristics, including orientation, dip angle, scale, and fracture density (Cui et al., 2013). In this study, we calculated the fracture linear density as the total number of fractures per unit core length or the total number of fractures divided by the total length in the imaging log data (Ortega et al., 2006). In particular, the linear density discussed in this paper is the uncorrected original density. The principle of fracture occurrence identification by imaging logging is as follows: For any plane that is not parallel or perpendicular to the well axis and intersects with the drilling hole, its intersection surface is an elliptical surface, which is displayed as a sine wave curve on the expanded diagram (Li et al., 2020). The core observation is a statistical calculation of all fractures visible to eyes, including short fractures with small openings that cannot be detected by imaging logs and fractures parallel to the well axis. Therefore, the fracture linear density calculated by imaging logging is much lower than that observed in cores due to the different observation scales and methods of core and imaging logging. In addition, a 3D seismic dataset of approximately 1824 km^2 covering the study area was obtained from the Tianjin Branch of the China National Offshore Oil Corporation. The size of each data bin was 25 m × 25 m, and the overall vertical sampling rate of the seismic volume was 2 ms with a primary frequency of 35 Hz. All the above information was provided by the Tianjin Branch of China National Offshore Oil Corporation.

4 Results

4.1 Lithological characteristics

The lithologies of the Archean buried hills in the study area are mainly regional metamorphic rocks formed from Archean (tonalite-trondhjemite-granodiorite; TTG) protoliths under different degrees of migmatization (Zhang et al., 2019; Ye et al., 2021a), which can be further divided into migmatitic granite (Figures 3A,B), migmatitic gneiss (Figures 3C,D) and gneiss (Figures 3E,F) according to migmatization degree. The migmatitic granite is light in overall colour with granitic metamorphic structure, and the few melanosomes are usually distributed with veins as sparse streaks and spots (Figure 3A). These rocks are mainly composed of quartz, plagioclase and alkali feldspar (Figure 3B), of which felsic light-coloured minerals account for a large proportion, with contents of 80–90%, and only a small amount of biotite is present (<5%) (Table 1). The melanosome content is higher in the migmatitic gneiss, which is usually distributed in massive and strips in the groundmass (Figure 3C). In thin sections under crossed-polarized light, the feldspar surfaces appear strongly altered, and a small amount of biotite is weakly curved (Figure 3D). X-ray diffraction (XRD) data show that the felsic content is reduced to 60–80%, and the contents of biotite and hornblende are increased compared with those of migmatitic granite, accounting for 10–20% of the total (Table 1). After partial melting of the original rock occurs during migmatization, the felsic component is separated, and the remainder is rich in dark minerals, which together form gneiss (Vanderhaeghe et al., 1999). The degree of migmatization is lowest in the gneiss, and the columnar minerals are oriented, with an obvious gneissic structure (Figures 3E,F). The gneiss is mainly composed of plagioclase, quartz and biotite. The XRD data show that the biotite content of these rocks reaches 30% (Table 1). Most of the biotite is lamellar and elongated with bending deformation characteristics and strong chloritization, and it shows weak banding and schistosity (Figure 3F). In addition to the regional metamorphic rocks, some intrusive rocks (mainly diabase) are

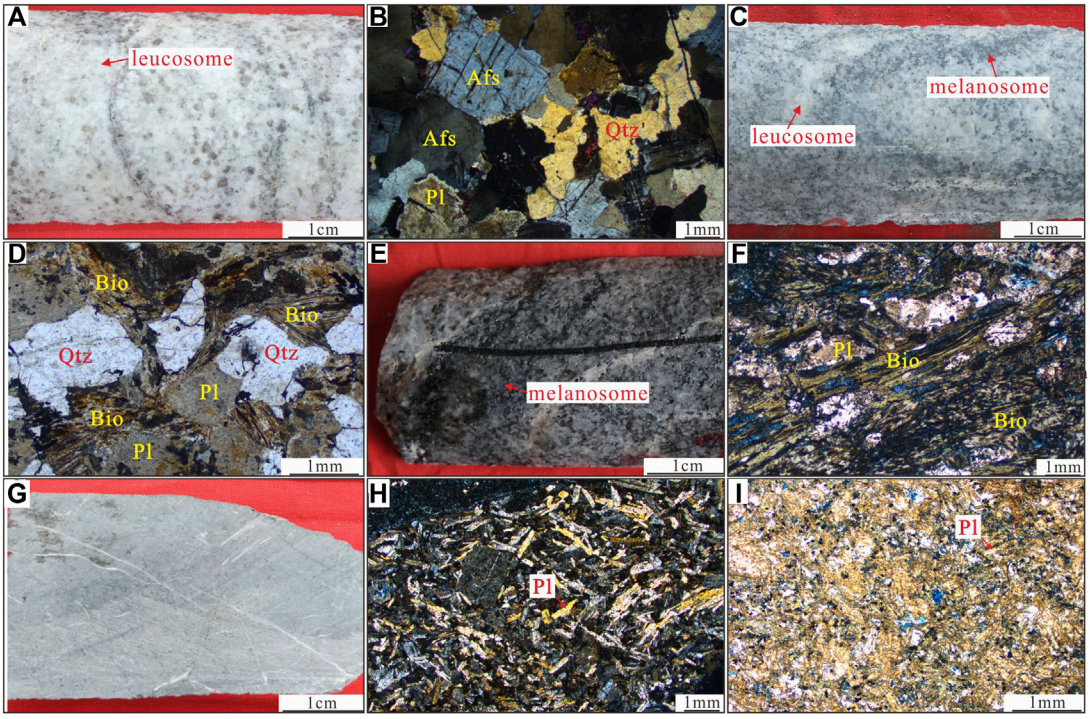

FIGURE 3
Petrological characteristics of the Archean metamorphic rocks in the study area. **(A)** Migmatitic granite, core, with a typical granitic metamorphic structure and many leucosomes, BZ13-E, 4718m; **(B)** Migmatitic granite, thin section, with plagioclase, K-feldspar and quartz, BZ19-G,4597m; **(C)** Migmatitic gneiss, core, the melanosome are usually distributed in massive and strips in the matrix, BZ13-E, 4717m; **(D)** Migmatitic gneiss, thin section, the feldspar surface is strongly altered, BZ19-N, 4490m; **(E)** gneiss, core, with obvious gneissic structure, BZ19-K, 5127m; **(F)** gneiss, thin section, most biotite is lamellar and shows strong chloritization, BZ19-G, 4613m; **(G)** diabase, core, BZ19-O, 4867m; **(H)** diabase, thin section, with a typical gabbroic structure, BZ19-B, 4076m; **(I)** diabase, thin section, with intense alteration, BZ19-G, 4830m; Qtz=quartz, Pl = plagioclase, Afs = alkaline feldspar, Bio=biotite.)

TABLE 1 X-ray diffraction (XRD) analyses showing the whole-rock mineralogy of intrusions and metamorphic rocks from the Bozhong sag (weight Percent, %).

Well	Depth/m	Qtz	Kfs	Pl	Cal	Dol	Py	Ank	Hbl	Cl	Bi	Lithology
BZ19-6-I	4955	24.0	31.0	33.0	3.0	-	-	-	-	4.0	5.0	Migmatitic Granite
BZ19-6-I	5305	22.0	22.0	39.0	6.0	1.0	-	-	-	4.0	6.0	
BZ19-6-K	5126	26.0	9.0	56.0	-	-	-	2.0	-	3.0	4.0	
BZ19-6-K	5127	27.0	17.0	47.0	-	-	-	3.0	-	2.0	4.0	
BZ19-6-K	4800	18.2	8.0	36.1	4.8	-	0.3	-	9.0	12.6	11.0	Migmatitic Gneiss
BZ19-6-M	4682	12.5	6.6	50.1	4.6	1.0	0.4	-	3.0	6.1	15.7	
BZ19-6-M	4602	17.3	6.9	46.5	8.1	-	-	-	-	7.0	14.2	
BZ19-6-M	4882	18.0	11.7	36.4	2.6	1.7	2.7	-	5.0	8.0	13.9	
BZ19-6-K	5127	23.0	10.0	31.0	1.0	-	-	1.0	-	3.0	31.0	Gneiss
BZ19-6-M	4560	18.5	7.7	32.3	6.1	-	2.2	-	3.2	4.0	26.0	
BZ19-6-O	5310	12.0	16.7	30.2	3.5	-	-	-	-	7.8	29.8	
BZ19-6-O	4868	17.6	12.0	36.2	0.8	-	1.6	0.3	-	30.2	1.3	Diabase
BZ19-6-I	5250	23.1	8.4	27.1	13.8	-	-	-	1.5	22.3	3.8	

Qtz=quartz, Kfs=K-feldspar, Pl=plagioclase, Cal=calcite, Dol=dolomite, Py=pyrite, Ank=ankerite, Hbl= hornblende, Cl= clay, Bi=biotite.

TABLE 2 Main fracture types of Archaean metamorphic rocks in the study area.

Types	Subtypes	Charateristics	Formation mechanism
Tectonic fractures	Tension fracture	They have unstable occurrence, short lengths, and rough surfaces and are surrounded by mineral grains. Unfilled or half-filled fractures are usually predominant	When the local extensional tectonic stress exceeds the ultimate tensile strength of the rock itself, the rock fracture produces tension fractures
	Shear fracture	They occur consistently, are straight and smooth, and cut mineral grains; they often appear as conjugate X shapes. Shear fractures are commonly filled with ankerite and calcite	When the three principal stresses are compressive stresses and the derived shear stress exceeds the limit of the shear strength of the rock itself, a shear fracture is generated
	Micro fracture	In feldspar, they usually form along the cleavage planes and appear as regular and straight cracks; in quartz, they usually appear as disordered cracks	Microfractures are fractures less than 100 mm with width and less than 10 mm in length, and their genesis is the same as that of macro fractures. Microfractures are often developed at the defects or weak points of rocks, such as the cleavage planes of minerals and the boundaries of mineral grains
Dissolution fractures	Weathering dissolution fracture	They usually have a rough surface, network distribution, irregular shape and high density. They are interlaced and connected with dissolution pores and fractures and are often found on the tops of buried hill	On the basis of the original fractures, weathering and dissolution reconstruction in the later period are superimposed
	Inner dissolution fracture	The core is "dendritic" and the fracture wall is irregular and not smooth; they are mostly developed near faults	Under the influence of deep fluid or organic acid, the original rock minerals or cement in the buried hills are dissolved into fractures, which make the original fractures expand and extend

scattered in the buried hills within the study area. The diabase has a typical gabbroic structure (Figure 3G). The main phenocrysts are plagioclase (Figure 3H). The mafic intrusions tend to show intense alteration (Figure 3I), with clay mineral contents reaching 20% (Table 1). The Archean buried hills have undergone multistage fluid alteration and multistage filling in pores and fractures. The XRD and thin sections show that the filling materials mainly include ankerite, calcite and clay minerals.

4.2 Fracture development characteristics

After the formation of the Archean metamorphic basement in the Bohai Bay Basin, a large number of fractures developed through long-term complex tectonic movements. We call these fractures related to tectonic activity tectonic fractures (Aydin, 2000), those related to mineral dissolution are called dissolution fractures (Liu et al., 2020). According to their formation mechanisms, scale and formation positions, tectonic fractures can be subdivided into tension fractures, shear fractures and microfractures (Zhao et al., 2020), and dissolution fractures can be subdivided into weathering and inner dissolution fractures. Through detailed observations and descriptions, and consideration of with the regional geological setting, the main fracture types and characteristics are identified and summarized (Table 2; Figure 4).

4.2.1 Tectonic fractures

The tectonic fractures are unevenly distributed through the cores (Figure 4). Tension fractures are generally caused by ruptures in the direction perpendicular to the inferred stress when the extensional tectonic stress exceeds the tensile strength of the rock itself (Wang et al., 2017). These fractures appear to be unstable in occurrence, short, and quite wide, with rough surfaces in the core, as shown by the surrounding minerals (Figure 4A). Tension fractures are usually poorly filled (Figure 4A). Shear fractures are formed when the rock is ruptured by applying shear force that exceeds the rock shear strength (Lyu et al., 2017; Zhang et al., 2020). Core observations reveal that the planar morphology is generally conjugate X-shaped; shear fractures commonly develop in groups and are characterized by stable occurrence, a straight and smooth appearance, and small crack openings (Figure 4A). This morphology is also seen in the penetration of cut mineral grains (Wang et al., 2017). Shear fractures are commonly filled with ankerite and calcite (Figure 4A).

Microfractures are very common in these metamorphic rocks according to thin section observations and SEM (Figure 4E-O), with widths less than 0.5 mm. According to the relationship between fractures and mineral particles, three types of microfractures have been identified: 1) intra-particle fractures, 2) inter-particle fractures and 3) trans-particle fractures. Inter-particle fractures mainly occur between mineral grains, and their length is limited by the grain edges. They are commonly widely developed within alkaline feldspar (mainly micro plagioclase) and quartz. In feldspars, the intra-particle fractures are usually ruptured along with cleavage fractures. They have regular and straight features (Figure 4E), with a width of 6 μm (Figure 4N). However, in quartz, the intra-particle fractures usually appear as disordered cracks (Figure 4F). Microcracks with a width of 4 μm are visible under scanning electron microscope (Figure 4O). Inter-particle fractures are developed on the edges of mineral grains, which shows the phenomenon of surrounding mineral grains (Figure 4G). Trans-particle fractures cut through the mineral grains, and the cut mineral grains are often relatively displaced, with regular and straight shapes and long extents (Figures 4H–J). The trans-particle fractures directly displace

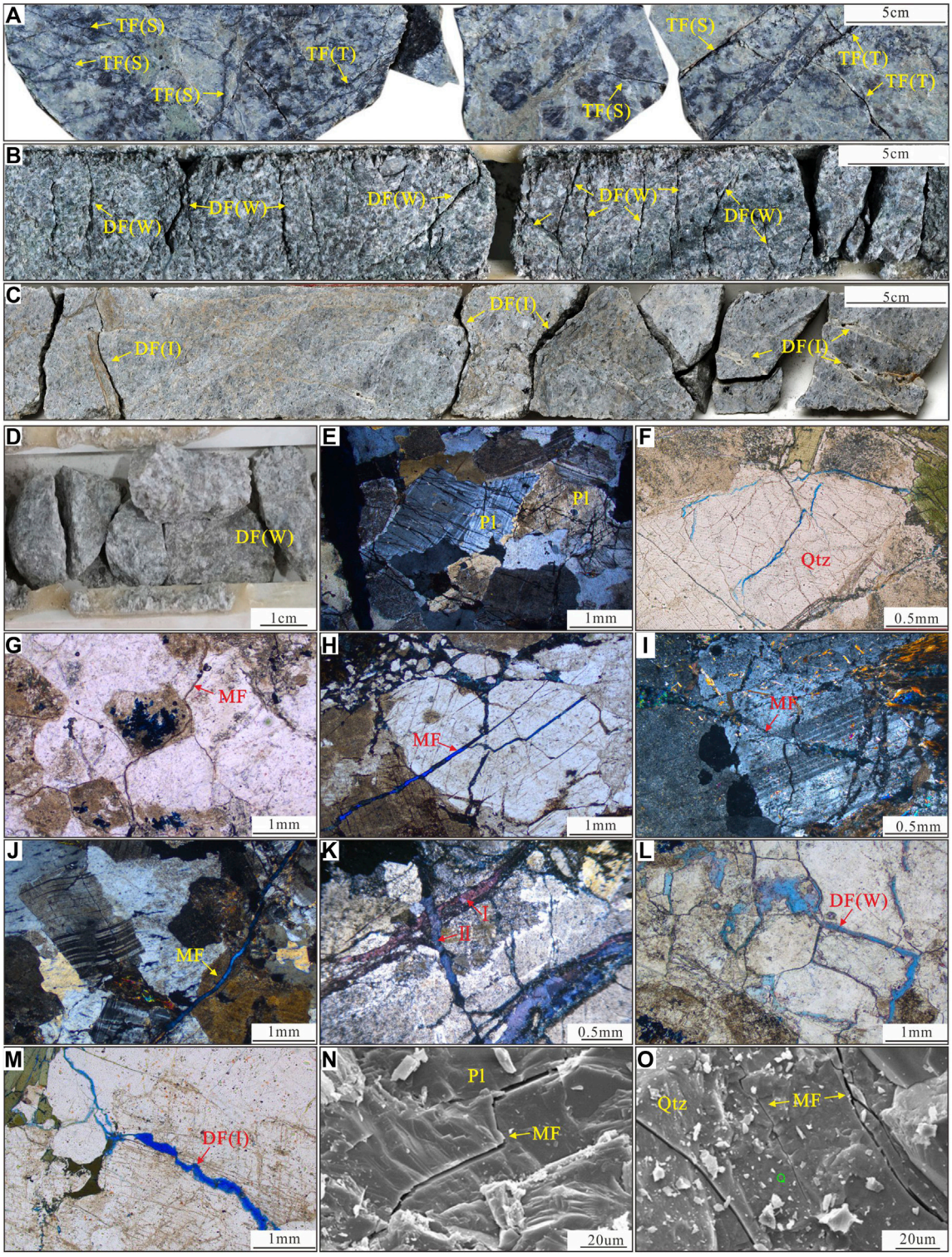

FIGURE 4
Fractures in cores and thin sections. **(A)** Tension fractures and shear fractures in a core, well BZ19-G, 4597.6-4598.1 m; **(B)** Weathering dissolution fractures in a core, well BZ19-G, 4538.3-4538.7 m; **(C)** Inner dissolution fractures in a core, well BZ19-L, 5525.25-5525.70 m; **(D)** Weathering dissolution fractures with strong fragmentation in a core, well BZ19-G, 4538 m; **(E)** Intra-particle fractures in feldspars with regular and straight features, thin section, well BZ19-G, 4599 m; **(F)** Intra-particle fractures in quartz with disorderly cracks, thin section, well BZ19-J, 4614 m; **(G)** Inter-particle fractures, thin section, well BZ19-F, 4487 m; **(H)** Trans-particle fractures, thin section, well BZ19-N, 4497 m; **(I)** Trans-particle fractures directly dissevered the plagioclase bicrystal; thin section, well BZ19-G, 4559 m; **(J)** Trans-particle fractures caused nearby plagioclase twin-crystal bending deformation; thin section, BZ19-G, 4598m; **(K)** Multistage fracture development, thin section, well BZ19-B, 4265 m;
(*Continued*)

FIGURE 4
(L) Weathering dissolution fractures are often distributed in a network, thin section, well BZ19-H, 4584 m; **(M)** Inner dissolution fractures in thin sections, well BZ19-O, 5156 m; **(N)** Intra-particle fractures in feldspars, SEM image, well BZ19-O, 4856 m; **(O)** Intra-particle fractures in quartz, SEM image, well BZ19-M, 4898m; Qtz=quartz, Pl=plagioclase, TF(T)=tension fractures, TF(S)=shear fractures, DF(W) = weathering dissolution fractures, DF(I)=inner dissolution fractures, MF= microfractures).

plagioclase bicrystals (Figure 4I), and nearby plagioclase twin-crystal bending deformation is present (Figure 4J), indicating that the trans-particle fractures formed under shear force. The early fractures are cut by late fractures, indicating that fractures of multiple stages have developed in the study area (Figure 4K).

4.2.2 Dissolution Fractures

The Archean metamorphic rock buried hills have been strongly modified by dissolution associated with geological fluids, and many dissolution fractures developd. According to the source and distribution of the fluids, we subdivide the dissolution fractures into weathering dissolution fractures and inner dissolution fractures.

The top interface of the Archean buried hill in the study area has been strongly modified by weathering and eluviation (Xu et al., 2020), and a large number of low-angle and high-density fractures without obvious directivity are observed in the cores (Figure 4B). These fractures mainly developed at the top of the buried hill near unconformity surfaces in the 50–100 m range, and strong fragmentation is observed (Figure 4D). The weathering dissolution fractures observed in thin sections are often distributed in networks and interlaced with dissolution pores and tectonic fractures (Figure 4L). We define the pre-existing fractures on the tops of buried hill in the study area that formed after dissolution by atmospheric freshwater as weathering dissolution fractures.

Some dissolution fractures are usually found far from the Archean top surface, in this paper, we call these fractures inner dissolution fractures to distinguish them from the weathering dissolution fractures mentioned above. The inner dissolution fractures are mainly fractures formed in the deep part of the buried hill that were modified by dissolution and transformed by organic acid fluids. Fractures are filled by early carbonate minerals that are then dissolved. In the study area, the inner dissolution fractures in the cores have widths of up to 2 mm (Figure 4C). The aperture of the initial fracture is enlarged after dissolution modification (Zhao et al., 2018). The core is "dendritic", and the shape of the fracture wall becomes irregular, unsmooth and serrated (Figure 4C). Although the newly formed fractures have evident corrosion characteristics, the original shapes and distributions of the initial fractures remain distinguishable (Figure 4M).

4.3 Characteristic parameters of fractures

A basic method to study the development degree and distribution of fractures in metamorphic rocks is to measure fracture parameters and statistical fracture filling in cores. According to the observation and analysis of existing core fractures, the results show that tectonic fractures are dominant in the study area, accounting for 71.7% of all fractures, with tension fractures accounting for 16.56% of all fractures and shear fractures accounting for 55.14%. There are relatively few dissolution fractures, which account for 28.3% of all fractures; weathering dissolution fractures account for 24.2%, and inner dissolution fractures account for only 4.1% (Figure 5A). Fractures are developed at low angles (dips of 0°–30°), accounting for 47.75%; moderate angles (dips of 30°–60°) account for 32.35%, and high-angle fractures (dips of 60°–90°) account for 19.9% (Figure 5B). Microscopic, observation reveals that trans-particle fractures account for 53.6% of microfractures, and intra-particle and inter-particle fractures account for 29.7 and 16.7%, respectively (Figure 5E).

The early fractures experienced strong filling, which produced three types of fractures: fully filled (45%), partially filled (23%) and open (32%) (Figure 5C), among which both open fractures and half-filled fractures are effective fractures. The filling materials are mainly composed of ankerite (52.7%), calcite (38.1%) and clay minerals (11.2%) (Figure 5D). The fractures show strong inhomogeneity in the cores, with the average linear densities of fractures ranging from 24 m^{-1} to 56 m^{-1} and with linear density reaching 68 m^{-1} (Figure 5F).

The analysis of the fracture characteristics of the comprehensive columnar section from well BZ19-D (Figure 6) shows that fractures from this single well show obvious changes in the vertical direction. The average linear densities of fractures are calculated by using sine or cosine curves displayed in dynamic images from FMI imaging logs. According to the change in the logging curve from top to bottom, the well is divided into upper and lower parts: the part above 4475 m and the part below 4475 m (Figure 6). The results show that the upper fractures are generally well developed, the dip angles are smaller than those of the lower fractures, and the average linear density of fractures reaches 1.57 m^{-1}. The lower fractures are not as continuously developed as the upper ones, and have an average linear density of 0.98 m^{-1}. However, there are also a few sections with dense fractures. The reasons for the differential development are discussed in the following Section 5.1.

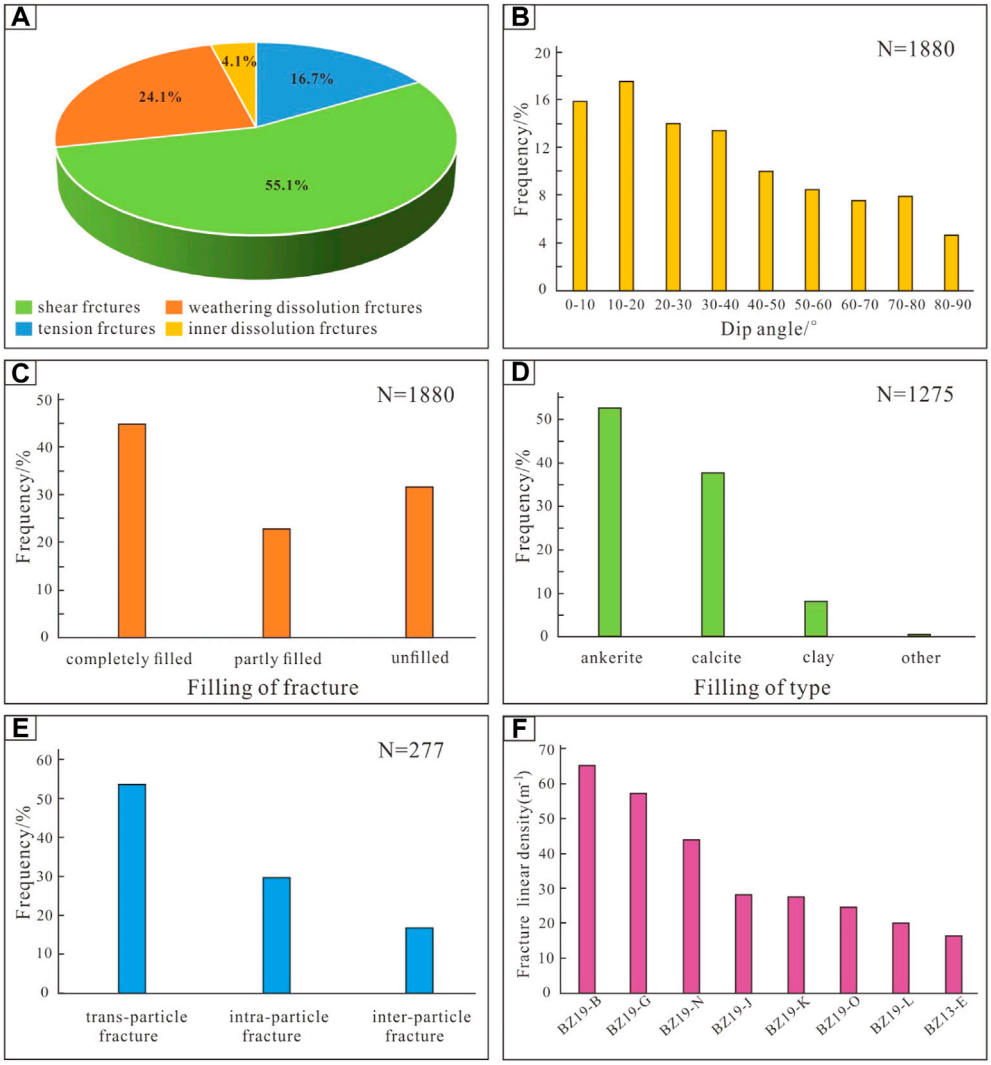

FIGURE 5
Statistical plot of the characteristic parameters of the fractures. **(A)** Statistical results of fracture types in cores; **(B)** Frequency distribution of fracture dip angle in cores; **(C)** Frequency distribution of fracture fillings types in cores; **(D)** Frequency distribution of fracture filling materials in cores; **(E)**. Frequency distribution of microfractures types in thin sections; **(F)** Fracture density of cores in coring wells).

5 Discussion

5.1 Controlling factors of fractures in metamorphic hills

Fracture formation and development in rocks are controlled by both internal and external factors (Ding et al., 2013; Ju and Sun, 2016; Ye et al., 2021b). The internal factors include the lithology, mineral composition and structure of metamorphic rocks. External factors are factors associated with tectonic movement, weathering, and hydrothermal activity (Ding et al., 2012; Zeng et al., 2013).

5.1.1 Lithology

Lithology is the most important internal factor controlling the development of fractures (Ju and Sun, 2016; Wang et al., 2016; Dai et al., 2019; Zheng et al., 2020). Due to the various mineral compositions of different lithologies, the mechanical properties and fracture degrees of rocks significantly vary, which results in great differences in fracture development degree among different rocks under the same stress (Wang et al., 2017).

Migmatization controls the lithological distribution and influences the degree of fractures development in buried hills of metamorphic rocks. Extensive regional metamorphism

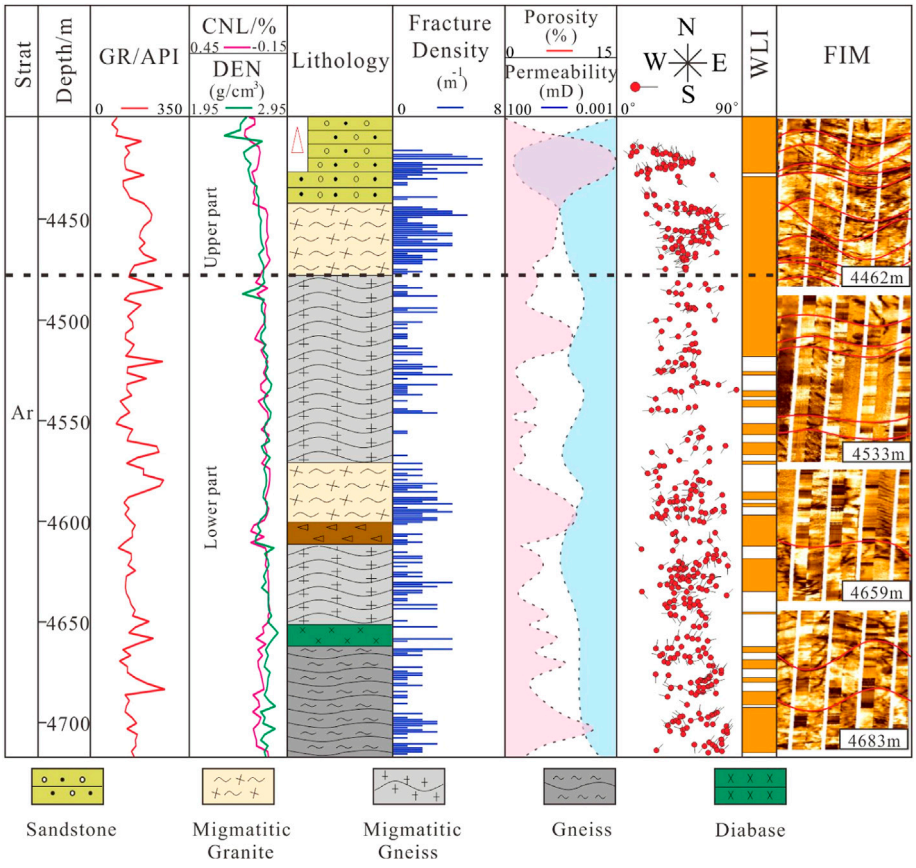

FIGURE 6
Fracture characteristics of the comprehensive columnar section from well BZ19-D.

occurred in the North China Block during 2.55–2.50 Ga (Ye et al., 2021b), and the rocks dominated by TTG underwent strong migmatization under a mantle plume-tectonothermal regime (Geng et al., 2016); as a result, the rocks of Archean buried hill are heterogeneous (Wang and Li, 2014). The degree of migmatization is strongly controlled by the heat source (Vanderhaeghe et al., 1999). Near the heat source, granitic magma is formed by the preferential melting of felsic minerals, and migmatitic granite is formed by ascent, convergence and crystallization. Near the heat source, there are residual melanosomes in the rock, which are mainly migmatitic gneiss. The rock far from the heat source shows the lowest degree of migmatization, and the rock is dominated by melanosomes, which are rich in iron and magnesium minerals such as biotite, and gneissic structure has developed.

The statistical analysis of core fracture density indicates significant differences in the degree of fracture development among various lithologies (Figure 7E). The average linear densities of fractures are highest in migmatitic granite at 60 m^{-1} (Figure 7A), followed by migmatitic gneiss and gneiss at 45 m^{-1} and 27 m^{-1}, respectively (Figures 7B,C), whereas the average linear densities of fractures are least developed in diabase at only 10 m^{-1} (Figure 7D). In addition, fracture density statistics based on imaging logging data confirm that fractures are most densely developed in migmatitic granite, and significantly less developed in gneiss and diabase than in migmatitic gneiss (Figure 6, Figure 8).

As feldspar has two cleavage directions, it is a brittle mineral and easily fractures under stress. Quartz is also subject to rupture under strong stress (Guo and Zhang, 2014; Li et al., 2016); however, biotite and amphibole have good ductility, strong plasticity and poor brittleness, and are more susceptible to bending deformation than feldspar and quartz and difficult to fracture under stress (Jarvie et al., 2007). Previous triaxial stress experiments on Archean metamorphic rocks from the Bohai Bay Basin have shown that rocks rich in felsic minerals have higher Poisson's ratios (mostly above 0.25) and lower elastic moduli (20–30 GPa) and thus have lower compressive strengths and are more prone to fractures than mafic rocks (Ye et al., 2022). Compared with the other metamorphic rocks in the buried hills of the Bohai Bay Basin, the migmatitic granites are more

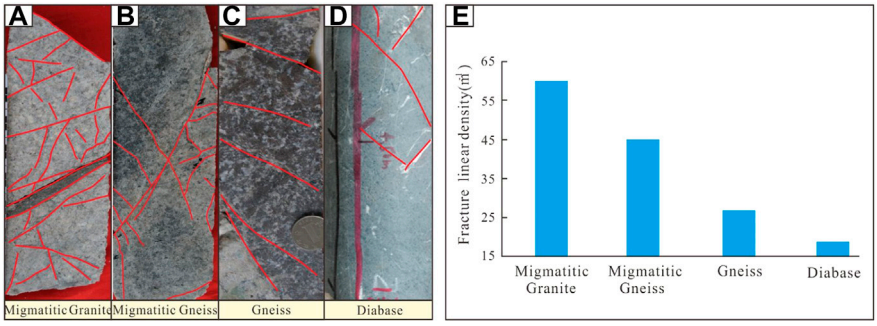

FIGURE 7
(A) Fracture linear densities of migmatitic granite core; **(B)** Fracture linear densities of migmatitic gneiss core; **(C)** Fracture linear densities of gneiss core; **(D)** Fracture linear densities of diabase core; **(E)** Schematic diagram comparing linear densities of fractures in different lithologies.

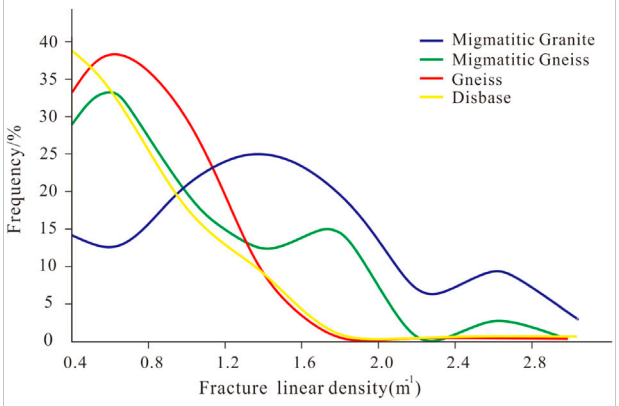

FIGURE 8
The fracture linear densities of different lithologies of Archaean buried hill in the study area obtained from imaging logging data.

likely to be broken and to develop more fractures under the same stress because they have the highest degree of migmatization and high brittleness (Maréchal et al., 2004; Ding et al., 2012; Lander and Laubach, 2015; Li et al., 2017; Li, 2022). Furthermore, the uneven distribution of lithologies and mineral contents results from migmatization; hence, the heterogeneity of the rock mass in the study area is enhanced and leads to the uneven distribution of the stress field inside the rock. These phenomena have contributed to the complexity of fracture development in the study area.

5.1.2 Tectonic movement

Strong tectonic activity and stress conditions control the nature, occurrence and scale of fracture development in buried hills, and thus are important external factors that affect fractures in rocks (Yin et al., 2019).

5.1.2.1 Tectonic Stress Field

The Archean basement in the study area has been controlled by many strong tectonic stress fields, including the Indosinian, Yanshanian and Himalayan tectonic movements, which formed a structural system with mainly normal faults and partially developed strike-slip faults (Li et al., 2010). Influenced by the collision between the South China plate and the North China Plate during the Indosinian period, a series of NWW-oriented thrusting folds and NW-oriented to nearly E-W oriented faults formed in the Bozhong area under NE-SW oriented compression (Cheng et al., 2018) (Figure 9, Figure 10). These faults dip to the south and have a gentle bottom in seismic profiles (Figure 10). The Yanshanian period was influenced by oblique subduction of the Paleo-Pacific plate beneath the Eurasian plate and deep mantle upwelling (Cui et al., 2020). The study area was controlled by a NW-oriented left-spinning torsional stress field (Hou et al., 1998; Cao et al., 2015), under which many nearly NE-oriented compressional-torsional faults and strike-slip faults developed (Figure 9). Meanwhile, the existing reverse faults were negatively reversed under back-arc extensional stress, controlling the Mesozoic stratigraphic deposition. In the late Yanshanian period, differential uplift occurred in the study area due to NW-oriented re-extrusion, which caused the BZ19-6 block to be significantly uplifted and the Mesozoic strata to be completely eroded (Figure 10). Because of the decrease in rock strength after rupture, the pre-existing nearly E-W oriented faults of the Indosinian period and the NNE-oriented faults of the Yanshanian period had different degrees of extensional activation under the strong S-N oriented extensional action during the Himalayan period, improving the effectiveness of the faults (Wang et al., 2018).

5.1.2.2 Control of faults on fractures

Many scholars have examined the relationship between faults and fractures and found that faults control the development of

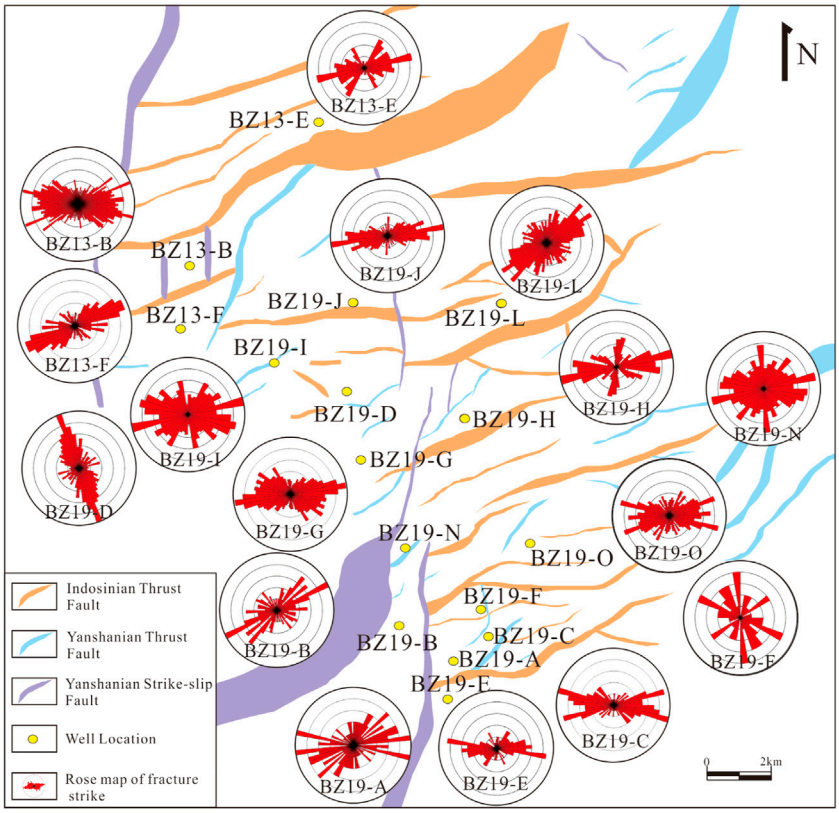

FIGURE 9
Directions of faults and fractures in the metamorphic rocks of the study area. The faults shown in this figure are the larger major faults in the study area. Fault data are modified from Xue et al., 2021 and fracture orientations are derived from the imaging logs of 16 wells.

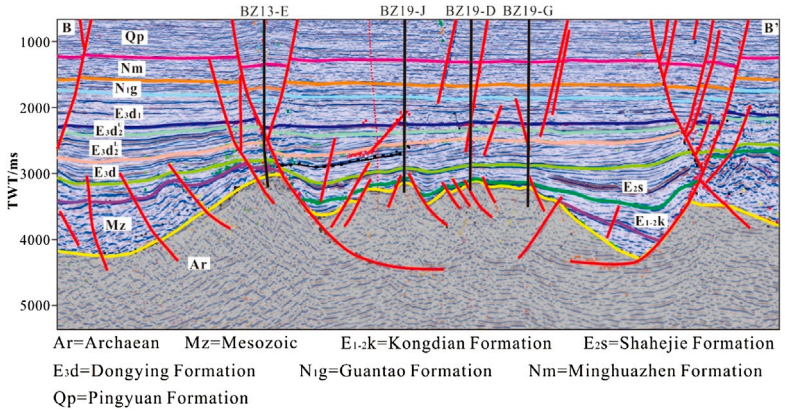

FIGURE 10
Characteristics of the seismic profile along the B-B′ line in the study area (Profile position is shown in Figure 1B). A–A′ represents the profile position of Figure1C and B–B′ represents the profile position of Figure10.

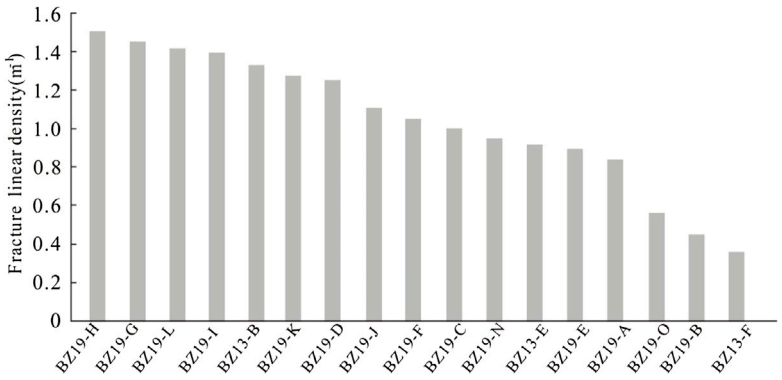

FIGURE 11
Histogram of fracture linear density for different wells in the study area (Fracture linear density is derived from the imaging logs of 17 wells).

fractures by influencing the surrounding tectonic stress strength (Kim et al., 2000; Yin and Wu, 2020; Lan et al., 2021). Ding et al. (2012) and Lyu et al. (2019) concluded that the development of fractures is mainly related to the distance to the fault, with the degree of fracture development decreasing with increasing distance from the fault. In the study area, due to the complex tectonic movement and the simultaneous production of a large number of fractures, the fracture development in each well is controlled by multiple nearby faults, so the relationship between fracture density and fault distance cannot be well shown. However, according to a rose diagram of fracture trends in 16 exploration wells, the orientation of tectonic fractures is mainly parallel or almost parallel to the orientation of adjacent faults, which shows that faults play an important role in fracture development. During the Indosinian period, the local stress caused by NE to nearly E-W oriented faults caused fractures to develop parallel to the fault direction. The development of a large number of nearly E-W oriented fractures in the study area indicates that the local stress of the faults generated under the strong compression and thrust was strong in the Indosinian period, which was the key period for the large-scale development of fractures. Moreover, as shown by wells BZ19-A, BZ19-B, BZ13-F, BZ19-H and BZ19-N, many NE-oriented fractures are developed and parallel to the adjacent NE-oriented faults, which proves that the local stress caused by NE-oriented faults in the Yanshanian period also produce some fractures (Figure 9). In addition, fracture density is partially controlled by the fracture effect (Souque et al., 2019). Wells BZ19-C, BZ19-F, and BZ19-H are located at the intersections of multiple fault zones (Figure 9), resulting in stress release centrally and a fracture density as high as 1.5 m^{-1}. (Figure 11). It should be noted that although the lithology of wells BZ19-C and BZ19-F is gneiss, they have high fracture densities, which shows that the controlling effect of tectonics on fractures is greater than that of lithology in the study area.

5.1.3 Fluid modification

The effect of dissolution on fracture improvement is obvious (Ye et al., 2020a). Fractures generated in the early stage provide effective migration pathways for fluids. The circulation of fluids promotes the evolution of the water–rock system, material migration and enrichment. These processes lead to a series of transformation reactions between minerals (Dou et al., 2010) and promotes fracture modification.

Metamorphic rock dissolution is mainly controlled by two types of fluids: atmospheric freshwater during the surface exposure period and organic acids and carbon dioxide generated by the thermal evolution of organic matter during the burial period (Ye et al., 2022). During this process, atmospheric freshwater dissolves and hydrates calcium carbonate minerals as well as silicate and aluminosilicate minerals in rocks to generate clay minerals such as illite, kaolinite and chlorite (Tan et al., 2014; Hong et al., 2020), and the original tectonic fractures expand and dissolve to form weathering dissolution fractures (Figure 12A). These fractures are interlaced with dissolution pores and tectonic fractures (Figure 4L). Furthermore, the study area was laterally docked with the hydrocarbon source rocks of the Shahejie Formation; therefore, the organic acids and carbon dioxide produced by the mature hydrocarbon source rocks of the Shahejie Formation migrated into the fractures of the inner buried hill. The unstable minerals (such as calcite and ankerite) filling the early fractures were again dissolved under the action of organic acids (Figure 12B). Thus, inner dissolution fractures were formed, which enhanced fracture effectiveness (Giammar et al., 2005; Aminul Islam, 2009; Liu et al., 2022). In this process, local tectonic fractures improved the

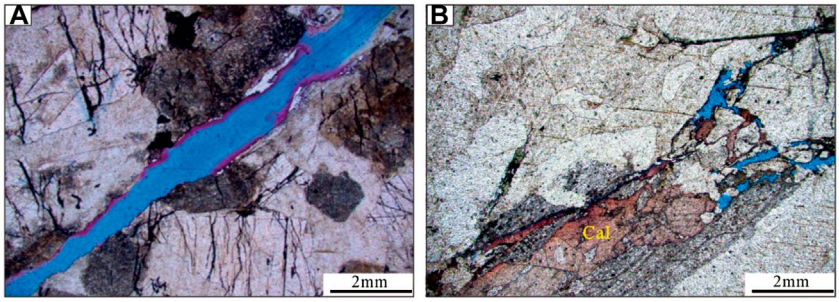

FIGURE 12
Dissolution fractures in thin sections of metamorphic rocks in the study area **(A)** Early tectonic fractures exhibiting corrosion and expansion, well BZ19-G, 4599 m; **(B)** The mineral of calcite in the filling fracture is partially dissolved, which makes the initial fracture effective, BZ13-G,4732 m).

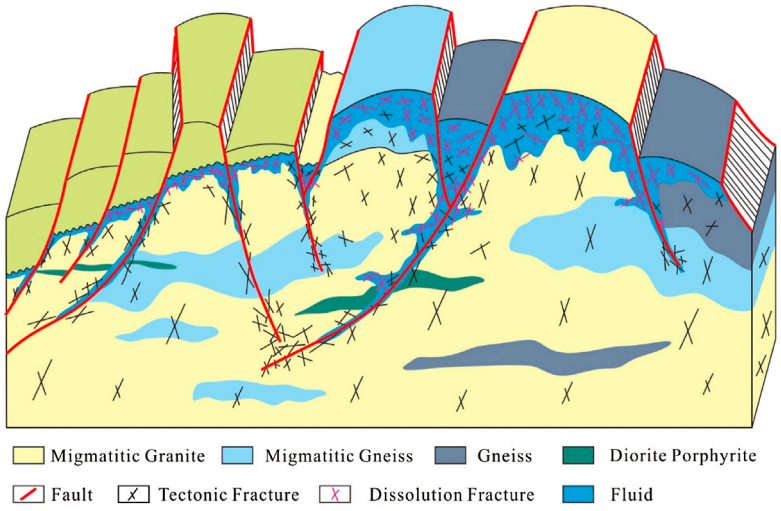

FIGURE 13
The distribution pattern of fractures in buried hill of metamorphic rocks.

permeability of the reservoir, enhanced the fluidity of the fluid, and facilitated dissolution. The existing dissolution pores and fractures made the reservoir more prone to producing fractures under the action of tectonic stress, and the two processes complemented each other.

In general, stronger dissolution occurred within the weathering crust near the tops of buried hill, and dissolution in the inner buried hill was mainly controlled by the development of fractures. All kinds of minerals near the fractures show obvious alteration characteristics (You et al., 2021), while with increasing distance far from the fractures, the degree of alteration obviously weakens until gradually transforming into normal rock without alteration. This phenomenon has been confirmed by thin section observation and mineral diffraction studies as part of the exploration of buried hill in the PL nine to one oilfield (Wang et al., 2015).

5.2 Fracture development pattern

The fracture development of buried hill in the study area varies significantly in the vertical direction due to the superposition of rock lithology, tectonic stress and later fluid modification. Here, the above controlling factors are used to establish a "native influence, multiphase superposition, fluid modification" model of fracture development in buried hill of metamorphic rocks (Figure 13).

The main rock type in the study area is migmatitic granite, which has more brittle minerals than gneiss, laying a good foundation for the development of fractures. The strong compressional collision during the Indosinian and the left-lateral strike-slip and thrust activities during the Yanshanian provided external conditions favourable for fracture formation. Under their combined effects, multiple phase fractures were

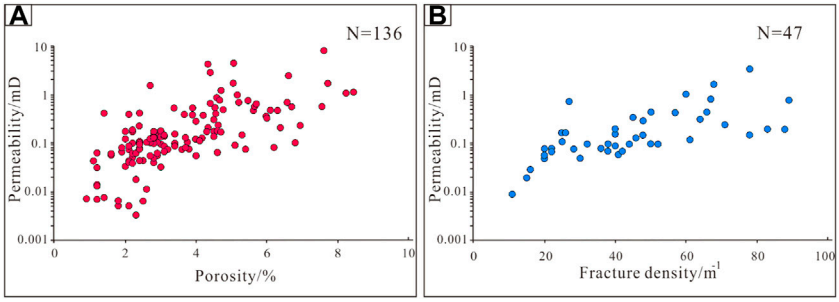

FIGURE 14
Physical property relationships of buried hill reservoir core samples in the study area. **(A)** The relationship between porosity and permeability; **(B)** The relationship between permeability and fracture linear density).

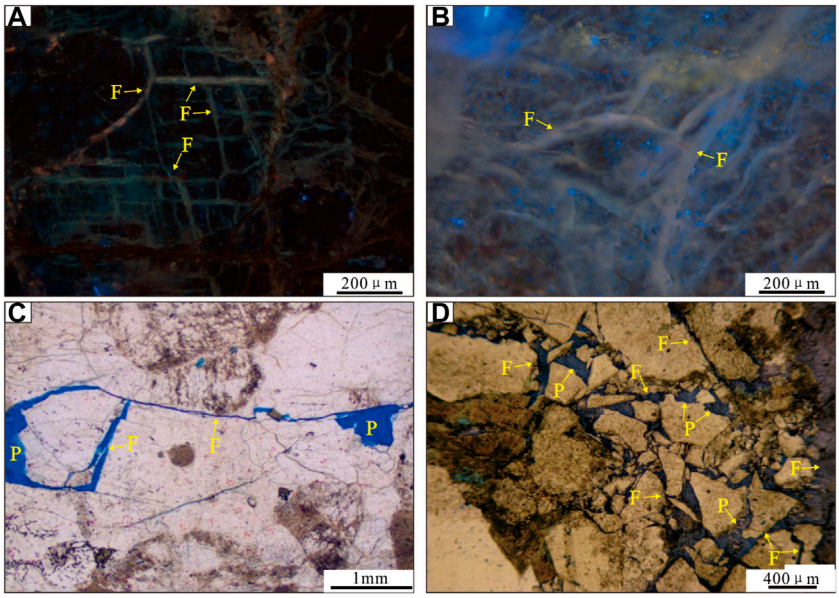

FIGURE 15
Thin-section photomicrographs and fluorescence scanning photos showing fractures and pores in the Archean metamorphic rocks in the study area. **(A)** Fractures in migmatitic granite under fluorescence scanning photos, show significant oil and gas displays, BZ19-G, 4544 m; **(B)** Fractures in migmatitic gneiss under fluorescence scanning photos, show significant oil and gas displays, BZ13-E, 4628 m; **(C)** Fractures act as channels to connect the secondary pores BZ19-J, 4903 m; **(D)** Secondary pores develop along the fractures, BZ19-B, 4432 m; P = secondary pore, F = fracture).

superimposed, resulting in the formation of many tectonic fractures in buried hills. In the stress concentration areas, such as the sides of faults and intersections, "mesh-like" fracture dense zones formd. Influenced by the differential uplift between the Indosinian and Yanshanian periods, the high part of the buried hill experienced strong weathering and erosion. The openings of the existing tectonic fractures near the top of the buried hill enlarged and formed a "layered" weathering fracture zone under the action of atmospheric freshwater dissolution. The reservoir space was dominated by weathering dissolution fractures, and a few dissolution pores were also developed. The absence of Mesozoic strata in the BZ19-6 block, in contrast to the BZ13-2 block, reflects the longer exposure time and thicker weathering fracture zone development in the former block. The Himalayan tectonic movement reactivated the fractures that were closed and filled earlier. The pre-existing faults and unconformities are the weak zones in buried hill and the dominant pathways for fluid

migration in the later stage. The organic acids and carbon dioxide produced by the mature hydrocarbon source rocks of the Shahejie Formation were transported to the inner buried hill, and the primary fractures around the faults were enlarged through dissolution to form dendritic inner dissolution fractures. This process is key to the development of effective fractures in buried hill; however, it is difficult for fractures to develop in areas far from faults or where gneiss is present.

5.3 Contributions of fractures to reservoir quality

The basement reservoirs of the Archean metamorphic rocks in the Bohai Bay Basin have experienced transformations and processes such as metamorphic recrystallization, weathering, dissolution, and tectonic disruption over a long geological period, developing storage space that is complex and heterogeneous (Luo et al., 2005). The basement petrophysical properties of 136 samples were statistically analysed according to the degree of fracture development (Figure 14A). The reservoir physical properties in the study area vary widely, with porosity mainly between 2 and 8% and permeability between 0.1×10^{-3} μm^2 and 1×10^{-3} μm^2. Further statistics on the relationship between fracture density and physical properties show that fracture density is positively correlated with permeability (Figure 14B), indicating that fractures contribute significantly to reservoir physical properties. Furthermore, we observe in thin sections that most dissolution pores do not exist in isolation but are connected by fractures (Figures 15C,D), which is conducive to the formation of effective reservoir space and enhancement of basement reservoir properties. However, except for some samples with strong fragmentation, the rocks with obvious fracture development observed in many thin sections do not have high porosity (Figure 4J). Migmatite has close to no primary porosity, and its porosity is mainly controlled by later dissolution. Fractures provide migration channels for later erosive fluids (such as organic acids and CO_2), and only rocks superimposed with dissolution can develop higher porosity. Therefore, the influence of fractures on rock porosity is indirectly controlled, and the formation of high porosity rocks is related to the configuration of the source and migration path of erosive fluids (such as unconformities, source rocks, and deep and large faults). In addition, in the core fluorescence scanning images, oil and gas are clearly present in these fractures (Figures 15A,B), which implies that fractures can provide effective space for oil and gas storage and/or migration pathways for later oil and gas seepage (Ding et al., 2013; Guo et al., 2016). These results imply that the development degree of fractures determines the distribution of favourable reservoirs (Zeng and Li, 2009).

6 Conclusion

1) Fractures in the study area can be divided into two genetic types: tectonic fractures and dissolution fractures. Tectonic fractures can be divided into tension fractures, shear fractures and microfractures, while dissolution fractures include weathering dissolution fractures and inner dissolution fractures. Tectonic fractures are widely developed in the study area. There is obvious variation in the degree of fracture development in the vertical direction within single wells.
2) Fracture development is controlled by lithology, tectonics and fluid activity. The migmatitic granite is the most favourable lithology for fracture development, having a higher content of brittle minerals than other lithologies. The Indosinian and Yanshanian were key periods for the development of fractures due to tectonic movements in the study area, and the pre-existing fractures are reactivated during the Himalayan period. Organic acids and CO_2 generated by the thermal evolution of atmospheric freshwater and organic matter are dissolved along the fractures.
3) Fracture-intensive zones are the main development sites for hydrocarbon reservoirs, which enhance the porosity and permeability of buried hill of Archean metamorphic rocks and provide effective space for oil and gas storage and migration. They play an important role in the formation of large-scale reservoirs.

Data availability statement

The original contributions presented in the study are included in the article/supplementary material, further inquiries can be directed to the corresponding author.

Author contributions

WW is responsible for the idea, writing and revision of this paper. WW, XZ, XL, PL and XR are responsible for the data analysis and drawing. XS and JY is responsible for reviewing and editing.

Funding

National Natural Science Foundation of China (No. 41790453, No. 41972313); Science and Technology Department Project of Jilin Province (Grant No.20200403068SF, 20210101108JC).

Conflict of interest

Authors XZ and XL were employed by the Tianjin Branch of China National Offshore Oil Corporation.

The authors declare that the research was conducted in the absence of any commercial or financial relationships that could be construed as a potential conflict of interest.

Publisher's note

References

Achtziger-Zupančič, P., Loew, S., and Hiller, A. (2017). Factors controlling the permeability distribution in fault vein zones surrounding granitic intrusions (Ore Mountains/Germany). *J. Geophys. Res. Solid Earth* 122 (3), 1876–1899. doi:10.1002/2016JB013619

Allen, M. B., Macdonald, D. I. M., Xun, Z., Vincent, S. J., and Brouet-Menzies, C. (1997). Early Cenozoic two-phase extension and late Cenozoic thermal subsidence and inversion of the Bohai Basin, northern China. *Mar. Petroleum Geol.* 14 (7-8), 951–972. doi:10.1016/S0264-8172(97)00027-5

Ameen, M. S., Buhidma, I. M., and Rahim, Z. (2010). The function of fractures and *in-situ* stresses in the Khuff reservoir performance, onshore fields, Saudi Arabia. *Bulletin* 94 (1), 27–60. doi:10.1306/06160909012

Aminul Islam, M. (2009). Diagenesis and reservoir quality of bhuban sandstones (Neogene), titas gas field, bengal basin, Bangladesh. *J. Asian Earth Sci.* 35 (1), 89–100. doi:10.1016/j.jseaes.2009.01.006

Aydin, A. (2000). Fractures, faults, and hydrocarbon entrapment, migration and flow. *Mar. Petroleum Geol.* 17 (7), 797–814. doi:10.1016/S0264-8172(00)00020-9

Bazalgette, L., Petit, J.-P., Amrhar, M., and Ouanaïmi, H. (2010). Aspects and origins of fractured dip-domain boundaries in folded carbonate rocks. *J. Struct. Geol.* 32 (4), 523–536. doi:10.1016/j.jsg.2010.03.002

Cao, X. Z., Li, S. Z., Xu, L. Q., Guo, L. L., Liu, L. P., Zhao, S., et al. (2015). Mesozoic–Cenozoic evolution and mechanism of tectonic geomorphology in the central North China Block: Constraint from apatite fission track thermochronologyfission track thermochronology. *J. Asian Earth Sci.* 114 (1), 41–53. doi:10.1016/j.jseaes.2015.03.041

Carvalho, I. de S., Mendes, J. C., and Costa, T. (2013). The role of fracturing and mineralogical alteration of basement gneiss in the oil exhsudation in the Sousa Basin (Lower Cretaceous), Northeastern Brazil. *J. S. Am. Earth Sci.* 47, 47–54. doi:10.1016/j.jsames.2013.06.001

Chen, G. B., Li, T., Yang, L., Zhang, G. H., Li, J. W., and Dong, H. J. (2021). Mechanical properties and failure mechanism of combined bodies with different coal-rock ratios and combinations. *J. Min. Strata Control Eng.* 3 (2), 023522. doi:10.13532/j.jmsce.cn10-1638/td.20210108.001

Cheng, Y. J., Wu, Z. P., Lu, S. N., Li, X., Lin, C. Y., Huang, Z., et al. (2018). Mesozoic to cenozoic tectonic transition process in zhanhua sag, Bohai Bay Basin, east China. *Tectonophysics* 730 (1), 11–28. doi:10.1016/j.tecto.2018.02.010

Cui, F. H., Xu, X. U., Zheng, C. Q., Yao, W. G., and Shi, L. (2020). The paleo-Pacific plate subduction and slab roll-back beneath eastern North China Craton: Insights from the Late Mesozoic granitoids in Xingcheng area, Western Liaoning Province. *Acta Petrol. Sin.* 36 (8), 2463–2492. doi:10.18654/1000-0569/2020.08.12

Cui, J. D., Zhang, J. Z., and Zhang, H. Y. (2013). Features of the carboniferous volcanic rocks fracture reservoirs in Hongshanzui oilfield, Junggar Basin. *J. Earth Sci.* 24 (6), 997–1007. doi:10.1007/s12583-013-0397-z

Cuong, T. X., and Warren, J. K. (2009). Bach ho field, a fractured granitic basement reservoir, cuu long basin, offshore se vietnam: a "buried-hill" play. *J. Petroleum Geol.* 32 (2), 129–156. doi:10.1111/j.1747-5457.2009.00440.x

Dai, X. J., Tang, H. F., Zhang, T., Zhao, P. J., Xu, C. M., Kong, T., et al. (2019). Facies architecture model of the shimentan formation pyroclastic rocks in the block-T units, xihu sag, east China sea basin, and its exploration significance. *Acta Geol. sinica-. Engl. Ed.* 93 (4), 1076–1087. doi:10.1111/1755-6724.13807

Ding, W. L., Li, C., Li, C. Y., Xu, C. C., Jiu, K., Zeng, W. T., et al. (2012). Fracture development in shale and its relationship to gas accumulation. *Geosci. Front.* 3 (1), 97–105. doi:10.1016/j.gsf.2011.10.001

Ding, W. L., Zhu, D. W., Cai, J. J., Gong, M. L., and Chen, F. Y. (2013). Analysis of the developmental characteristics and major regulating factors of fractures in marine-continental transitional shale-gas reservoirs: A case study of the carboniferous-permian strata in the southeastern ordos basin, central China. *Mar. Petroleum Geol.* 45, 121–133. doi:10.1016/j.marpetgeo.2013.04.022

Dou, L. R., Wei, X. D., Wang, J. C., Li, J. L., and Zhang, S. H. (2015). Characteristics of granitic basement rock buried-hill reservoir in Bongor Basin, Chad. *Acta Pet. Sin.* 36 (8), 897–904,925. doi:10.7623/syxb201508001

Dou, S. M., Chen, F. R., Yang, Y. Q., W, S. J., Kang, M. L., and Zhang, R. (2010). Estimation of saturation index for the precipitation of secondary minerals during water-rock interaction in granite terrains. *Geochimica* 39 (4), 326–336. doi:10.19700/j.0379-1726.2010.04.004

Eig, K., and Bergh, S. G. (2011). Late Cretaceous-Cenozoic fracturing in Lofoten, North Norway: Tectonic significance, fracture mechanisms and controlling factors. *Tectonophysics* 499 (1-4), 190–205. doi:10.1016/j.tecto.2010.12.002

Fu, Q., You, Y. C., and Wu, Z. (2003). Tectonic episodes and reservoir fissure systems in Caotai metamorphic. *buried hill Reserv.* 30 (5), 18–20. doi:10.3321/j.issn:1000-0747.2003.05.005

Geng, Y. S., Shen, Q. H., Du, L. L., and Song, H. X. (2016). Regional metamorphism and continental growth and assembly in China. *Acta Petrol. Sin.* 32 (9), 2579–2608. CNKI:SUN:YSXB.0.2016-09-001.

Giammar, D. E., Jr, R. G. B., and Peters, C. A. (2005). Forsterite dissolution and magnesite precipitation at conditions relevant for deep saline aquifer storage and sequestration of carbon dioxide. *Chem. Geol.* 217 (3), 257–276. doi:10.1016/j.chemgeo.2004.12.013

Guo, P., Yao, L. H., and Ren, D. S. (2016). Simulation of three-dimensional tectonic stress fields and quantitative prediction of tectonic fracture within the Damintun Depression, Liaohe Basin, northeast China. *J. Struct. Geol.* 86, 211–223. doi:10.1016/j.jsg.2016.03.007

Guo, T. L., and Zhang, H. R. (2014). Formation and enrichment mode of Jiaoshiba shale gas field, Sichuan Basin. *Petroleum Explor. Dev.* 41 (1), 31–40. doi:10.1016/s1876-3804(14)60003-3

Guo, Y., Wang, Y. C., Wei, A. J., Wu, H. M., Ye, T., Gao, K. S., et al. (2017). Characteristics and controlling factors of volcanic reservoir in buried hill -- a case study of Cretaceous in Qinhuangdao 30A area in Bohai Sea Area. *Acta Sedimentol. Sin.* 35 (2), 343–357. doi:10.14027/j.cnki.cjxb.2017.02.012

Han, C. C., Tian, J. J., Hu, C. L., Liu, H. L., Wang, W. F., Huan, Z., et al. (2020). Lithofacies characteristics and their controlling effects on reservoirs in buried hills of metamorphic rocks: A case study of late paleozoic units in the Aryskum depression, South Turgay basin, Kazakhstan. *J. Petroleum Sci. Eng.* 191 (0), 107137. doi:10.1016/j.petrol.2020.107137

Hong, D., Cao, J., Wu, T., Dang, S., Hu, W., and Yao, S. (2020). Authigenic clay minerals and calcite dissolution influence reservoir quality in tight sandstones: Insights from the central Junggar Basin, NW China. *Energy Geosci.* 1 (1–2), 8–19. doi:10.1016/j.engeos.2020.03.001

Hou, G. T., Qian, X. L., and Cai, D. S. (2001). The tectonic evolution of Bohai basin in mesozoic and cenozoic time. *Acta Sci. Nat. Univ. Pekin.* 37 (6), 845–851. doi:10.3321/j.issn:0479-8023.2001.06.016

Hou, G. T., Qian, X. L., and Song, X. M. (1998). Study on formation mechanism of Bohai Bay Basin. *Acta Sci. Nat. Univ. Pekin.* 34 (4). doi:10.13209/j.0479-8023.1998.033

Hou, M. C., Cao, H. Y., Li, H. Y., Chen, A. Q., and Wei, A. J. (2019). Characteristics and controlling factors of deep buried-hill reservoirs in the BZ19-6 structural belt, Bohai sea area. *Nat. Gas. Ind.* 39 (1), 33–44. doi:10.3787/j.issn.1000-0976.2019.01.004

Jarvie, D. M., Hill, R. J., Ruble, T. E., and Pollastro, R. M. (2007). Unconventional shale-gas systems: The Mississippian Barnett Shale of north-central Texas as one model for thermogenic shale-gas assessment. *Am. Assoc. Pet. Geol. Bull.* 91 (4), 475–499. doi:10.1306/12190606068

Ju, W., and Sun, W. F. (2016). Tectonic fractures in the lower cretaceous xiagou formation of qingxi oilfield, jiuxi basin, NW China part one: Characteristics and controlling factors. *J. Petroleum Sci. Eng.* 146, 617–625. doi:10.1016/j.petrol.2016.07.042

Kim, Y.-S., Andrews, J. R., and Sanderson, D. J. (2000). Damage zones around strike-slip fault systems and strike-slip fault evolution, Crackington Haven, southwest England. *Geosci. J.* 4 (2), 53–72. doi:10.1007/BF02910127

Lai, J., Li, D., Wang, G. W., Xiao, C. W., Hao, X. L., Luo, Q., et al. (2019). Earth stress and reservoir quality evaluation in high and steep structure: The Lower Cretaceous in the Kuqa Depression, Tarim Basin, China. *Mar. Petroleum Geol.* 101, 43–54. doi:10.1016/j.marpetgeo.2018.11.036

Lan, S. R., Song, D. Z., Li, Z. L., and Liu, Y. (2021). Experimental study on acoustic emission characteristics of fault slip process based on damage factor. *J. Min. Strata Control Eng.* 3 (3), 033024. doi:10.13532/j.jmsce.cn10-1638/td.20210510.002

Lander, R. H., and Laubach, S. E. (2015). Insights into rates of fracture growth and sealing from a model for quartz cementation in fractured sandstones. *Geol. Soc. Am. Bull.* 127 (3-4), 516–538. doi:10.1130/B31092.1

Li, A., Ding, W. L., He, J. H., Dai, P., Yin, S., and Xie, F. (2016). Investigation of pore structure and fractal characteristics of organic-rich shale reservoirs: A case study of lower cambrian qiongzhusi formation in malong block of eastern yunnan province, south China. *Mar. Petroleum Geol.* 70, 46–57. doi:10.1016/j.marpetgeo.2015.11.004

Li, A., Ding, W. L., Wang, R. Y., He, J. H., Wang, X. H., Sun, Y., et al. (2017). Petrophysical characterization of shale reservoir based on nuclear magnetic resonance (nmr) experiment: A case study of lower cambrian qiongzhusi formation in eastern yunnan province, south China. *J. Nat. Gas Sci. Eng.* 37, 29–38. doi:10.1016/j.jngse.2016.11.034

Li, H., Qin, Q., Zhang, B. J., Ge, X. Y., Hu, X., Fan, C. H., et al. (2020). Tectonic fracture formation and distribution in ultradeep marine carbonate gas reservoirs: A case study of the maokou formation in the jiulongshan gas field, sichuan basin, southwest China. *Energy fuels.* 34 (11), 14132–14146. doi:10.1021/acs.energyfuels.0c03327

Li, H. (2022). Research progress on evaluation methods and factors influencing shale brittleness: A review. *Energy Rep.* 8, 4344–4358. doi:10.1016/j.egyr.2022.03.120

Li, S. Z., Suo, Y. H., Dai, L. M., Liu, L. P., Jin, C., and Liu, X. (2010). formation of Bohai Bay Basin and destruction of north China craton. *Earth Sci. Front.* 17 (4), 064–089. CNKI:SUN:DXQY.0.2010-04-009.

Li, S. Z., Suo, Y. H., Santosh, M., Dai, L. M., Liu, X., Yu, S., et al. (2013). Mesozoic to cenozoic intracontinental deformation and dynamics of the north China craton. *Geol. J.* 48 (5), 543–560. doi:10.1002/gj.2500

Li, W., Dou, L. R., Wen, Z. G., Zhang, G. Y., and Hu, Y. (2017). Buried-hill hydrocarbon Genesis and accumulation process in Bongor Basin, Chad. *Acta Pet. Sin.* 38 (11), 1253–1262. doi:10.7623/syxb201711004

Li, X., Yan, W. P., Cui, Z. Q., Guo, B. C., Liang, K., and Tao, Z. (2012). Prospecting potential and targets of buried-hill oil and gas reservoirs in Bohai Bay Basin. *Petroleum Geol. Exp.* 34 (2), 140–139. doi:10.11781/sysydz201202140

Li, Y., Hou, G. T., Hari, K. R., Neng, Y., Lei, G. L., Tang, Y., et al. (2018). The model of fracture development in the faulted folds: The role of folding and faulting. *Mar. Petroleum Geol.* 89, 243–251. doi:10.1016/j.marpetgeo.2017.05.025

Li, Y., Zhou, D., Wang, W., Jiang, T., and Xue, Z. (2020). Development of unconventional gas and technologies adopted in China. *Energy Geosci.* 1 (1–2), 55–68. doi:10.1016/j.engeos.2020.04.004

Liang, J. T., Wang, H. L., Bai, Y., Ji, X. Y., and Duo, X. M. (2016). Cenozoic tectonic evolution of the Bohai Bay Basin and its coupling relationship with Pacific plate subduction. *J. Asian Earth Sci.* 127, 257–266. doi:10.1016/j.jseaes.2016.06.012

Liu, C., Xie, Q. B., Wang, G. W., Zhang, C. J., Wang, L. L., and Qi, K. N. (2016). Reservoir properties and controlling factors of contact metamorphic zones of the diabase in the northern slope of the Gaoyou Sag, Subei Basin, eastern China. *J. Nat. Gas Sci. Eng.* 35, 392–411. doi:10.1016/j.jngse.2016.08.070

Liu, G. P., Zeng, L. B., Li, H. G., Ostadhassan, M., and Rabiei, M. (2020). Natural fractures in metamorphic basement reservoirs in the Liaohe Basin, China. *Mar. Petroleum Geol.* 119, 104479. doi:10.1016/j.marpetgeo.2020.104479

Liu, Y., Chen, L., Tang, Y., Zhang, X., and Qiu, Z. (2022). Synthesis and characterization of nano-SiO2@octadecylbisimidazoline quaternary ammonium salt used as acidizing corrosion inhibitor. *Rev. Adv. Mater. Sci.* 61 (1), 186–194. doi:10.1515/rams-2022-0006

Luo, J. L., Morad, S., Liang, Z. G., and Zhu, Y. S. (2005). Controls on the quality of Archean metamorphic and Jurassic volcanic reservoir rocks from the Xinglongtai buried hill, Western depression of Liaohe basin, China. *Bulletin* 89 (10), 1319–1346. doi:10.1306/05230503113

Lyu, W. Y., Zeng, L. B., Zhang, B. J., Miao, F. B., Lyu, P., and Dong, S. Q. (2017). Influence of natural fractures on gas accumulation in the Upper Triassic tight gas sandstones in the northwestern Sichuan Basin, China. *Mar. Petroleum Geol.* 83, 60–72. doi:10.1016/j.marpetgeo.2017.03.004

Lyu, W. Y., Zeng, L. B., Zhou, S. B., Du, X. S., Xia, D. L., Liu, G., et al. (2019). Natural fractures in tight-oil sandstones: A case study of the upper triassic yanchang formation in the southwestern ordos basin, China. *Am. Assoc. Pet. Geol. Bull.* 103 (10), 2343–2367. doi:10.1306/0130191608617115

Maerten, L., Maerten, F., and Lejri, M. (2018). Along fault friction and fluid pressure effects on the spatial distribution of fault-related fractures. *J. Struct. Geol.* 108, 198–212. doi:10.1016/j.jsg.2017.10.008

Maréchal, J. C., Dewandel, B., and Subrahmanyam, K. (2004). Use of hydraulic tests at different scales to characterize fracture network properties in the weathered-fractured layer of a hard rock aquifer. *Water Resour. Res.* 40 (11). doi:10.1029/2004WR003137

Nabway, B. S., and Kassab, M. A. (2013). Porosity-reducing and porosity-enhancing diagenetic factors for some carbonate microfacies: A guide for petrophysical facies discrimination. *Arab. J. Geosci.* 17 (11), 4523–4539. doi:10.1007/s12517-013-1083-2

Nelson, R. A., Moldovanyi, E. P., Matcek, C. C., Azpiritxaga, I., and Bueno, E. (2000). Production characteristics of the fractured reservoirs of the La Paz field, Maracaibo basin, Venezuelafield, Maracaibo basin, Venezuela. *Am. Assoc. Pet. Geol. Bull.* 84 (11), 1791–1809. doi:10.1306/8626c393-173b-11d7-8645000102c1865d

Ni, J. L., Guo, Y., Wang, Z. M., Liu, J. L., Lin, Y. X., and Li, Y. (2011). Tectonics and mechanisms of uplift in the central uplift belt of the Huimin depression. *J. Earth Sci.* 22 (3), 299–315. doi:10.1007/s12583-011-0183-8

Ni, J. L., Liu, J. L., Tang, X. L., Yang, H. B., Xia, Z. M., and Guo, Q. J. (2013). The wulian metamorphic core complex: A newly discovered metamorphic core complex along the sulu orogenic belt, eastern China. *J. Earth Sci.* 24 (3), 297–313. doi:10.1007/s12583-013-0330-5

Ortega, O. J., Marrett, R. A., and Laubach, S. E. (2006). A scale-independent approach to fracture intensity and average spacing measurement. *Am. Assoc. Pet. Geol. Bull.* 90 (2), 193–208. doi:10.1306/08250505059

Parnell, J. (2010). Potential of palaeofluid analysis for understanding oil charge history. *Geofluids* 10 (1-2). doi:10.1111/j.1468-8123.2009.00268.x

Peng, J. S., Wei, A. J., Sun, Z., Chen, X. L., and Zhao, D. J. (2018). Sinistral strike slip of the zhangjiakou-penglai fault and its control on hydrocarbon accumulation in the northeast of shaleitian bulge, Bohai Bay Basin, east China. *Petroleum Explor. Dev.* 45 (2), 215–226. doi:10.1016/S1876-3804(18)30025-9

Qi, J. F., Li, X. G., Yu, F. S., and Yu, T. C. (2013). Cenozoic structural deformation and expression of the "tan-Lu fault zone" in the west sag of Liaohe depression, bohaiwan basin province, China. *Sci. China Earth Sci.* 56 (10), 1707–1721. doi:10.1007/s11430-013-4617-2

Salah, M. G., and Alsharhan, A. S. (1998). The precambrian basement: A major reservoir in the rifted basin, gulf of suez. *J. Petroleum Sci. Eng.* 19 (3), 201–222. doi:10.1016/S0920-4105(97)00024-7

Shen, B. T., Topias, S., and Mikael, R. (2015). Modelling fracture propagation in anisotropic rock mass. *Rock Mech. Rock Eng.* 48 (3), 1067–1081. doi:10.1007/s00603-014-0621-x

Song, B., Hu, Y. J., Bian, S. Z., Han, H. D., Cui, X. D., and Zhang, J. (2011). Reservoir characteristics of the crystal basement in the Xinglongtai buried-hill, Liaohe Depression. *Acta Pet. Sin.* 32 (1), 77–82. doi:10.1631/jzus.A1000135

Souque, C., Knipe, R. J., Davies, R. K., Jones, P., Welch, M. J., and Lorenz, J. (2019). Fracture corridors and fault reactivation: Example from the chalk, isle of thanet, kent, england. *J. Struct. Geol.* 122, 11–26. doi:10.1016/j.jsg.2018.12.004

Tan, G., Qiu, H., Yu, T., Liu, S., and Hao, J. (2014). Characteristics and main controlling factors of hydrocarbon accumulation in ordovician yingshan formation in yubei area, tarim basin. *Oil Gas Geol.* 35 (1), 26–32. doi:10.11743/ogg20140104

Tong, K. J., Qi, C., Nie, L. L., and Na, F. (2015). Evaluation of effectiveness of metamorphosed basement buried hill reservoirs. *Oil Gas Geol.* 36 (5). doi:10.11743/ogg20150509

Tong, K. J., Zhao, C. M., Lü, Z., Zhang, Y. C., Zheng, H., Xu, S., et al. (2012). Reservoir evaluation and fracture chracterization of the metamorphic buried hill reservoir in Bohai Bay Basin. *Petroleum Explor. Dev.* 39 (1), 62–69. doi:10.1016/S1876-3804(12)60015-9

Vanderhaeghe, O., Burg, J.-P., and Teyssier, C. (1999). Exhumation of migmatites in two collapsed orogens: Canadian cordillera and French variscides. *Geol. Soc. Lond. Spec. Publ.* 154 (1), 181–204. doi:10.1144/GSL.SP.1999.154.01.08

Wan, G., Tang, L., Zhou, X., Yu, Y., and Chen, X. (2009). Tectonic characteristics of the tanlu fault zone in bodong area of Bohai Sea. *Acta Pet. Sin.* 30 (3), 342–346. doi:10.7623/syxb2009004

Wang, G. Z., Li, S. Z., Li, X. Y., Zhao, W. Z., Zhao, S. J., Suo, Y. H., et al. (2019a). Destruction effect on Meso-Neoproterozoic oil-gas traps derived from Meso-Cenozoic deformation in the North China Craton. *Precambrian Res.* 333, 105427. doi:10.1016/j.precamres.2019.105427

Wang, G. Z., Li, S. Z., Wu, Z. P., Suo, Y. H., Guo, L. L., and Wang, P. C. (2019b). Early Paleogene strike-slip transition of the tan-Lu fault zone across the southeast Bohai Bay Basin: Constraints from fault characteristics in its adjacent basins. *Geol. J.* 54 (2), 835–849. doi:10.1002/gj.3344

Wang, R. Y., Ding, W. L., Zhang, Y. Q., Wang, Z., Wang, X. H., He, J. H., et al. (2016). Analysis of developmental characteristics and dominant factors of fractures in lower cambrian marine shale reservoirs: A case study of niutitang formation in cen'gong block, southern China. *J. Petroleum Sci. Eng.* 138, 31–49. doi:10.1016/j.petrol.2015.12.004

Wang, S., and Li, S. (2014). Migmatite and its geodynamic implications. *Earth Sci. Front.* 21 (01), 21–31. CNKI:SUN:DXQY.0.2014-01-003.

Wang, X. H., Wang, R. Y., Ding, W. L., Yin, S., Sun, Y. X., Zhou, X. H., et al. (2017). Development characteristics and dominant factors of fractures and their significance for shale reservoirs: A case study from ϵ1b2 in the cen'gong block, southern China. *J. Petroleum Sci. Eng.* 159, 988–999. doi:10.1016/j.petrol.2017.08.007

Wang, X., Zhou, X. H., Xu, G. S., Liu, P. B., and Guan, D. Y. (2015). Characteristics and controlling factors of reservoirs in Penglai 9-1 large-scale oilfield in buried granite hills, Bohai Sea. *Oil Gas Geol.* 36 (2), 262–270. doi:10.11743/ogg20150211

Wang, Y., Zhou, L. Y., Liu, S. F., Li, J. Y., and Yang, T. N. (2018). Post-cratonization deformation processes and tectonic evolution of the North China Craton. *Earth-Science Rev.* 177 (1), 320–365. doi:10.1016/j.earscirev.2017.11.017

Xie, Y. H., Zhang, G. C., Shen, P., Liu, L. F., and Yang, S. B. (2018). Formation conditions and exploration direction of large gas field in Bozhong sag of Bohai Bay Basin. *Acta Pet. Sin.* 39 (11), 1199–1210. doi:10.7623/syxb201811001

Xu, C. G., Du, X. F., Liu, X. J., Xu, W., and Hao, Z. W. (2020). Formation mechanism of high-quality deep buried-hill reservoir of Archaean metamorphic rocks and its significance in petroleum exploration in Bohai Sea area. *Acta Geol. Sin.* 41 (2), 235–247,294. doi:10.19762/j.cnki.dizhixuebao.2021132

Xu, S., Hao, F., Xu, C. G., Zou, H. Y., Zhang, X. T., Zong, Y., et al. (2019). Hydrocarbon migration and accumulation in the northwestern Bozhong subbasin, Bohai Bay Basin, China. *J. Petroleum Sci. Eng.* 172, 477–488. doi:10.1016/j.petrol.2018.09.084

Xue, Y. A., and Li, H. Y. (2018). Large condensate gas field in deep archean metamorphic buried hill in Bohai Sea: Discovery and geological significance. *China Offshore Oil Gas* 30 (3), 1–9. doi:10.11935/j.issn.1673-1506.2018.03.001

Xue, Y. A., Li, H. Y., Xu, P., Liu, Q. C., and Cui, H. Z. (2021). Recognition of oil and gas accumulation of Mesozoic covered buried hills in Bohai sea area and the discovery of BZ 13-2 oilfield 33(1), 13–22. doi:10.11935/j.issn.1673-1506.2021.01.002

Yang, K. J., Qi, J. F., Yu, Y. X., Ping, Y. Q., Gao, Q., and Lv, J. (2016). Differential evolution and reservoir forming conditions of buried hills in Liaodong Bay Area. *Nat. Gas. Geosci.* 27 (6), 1014–1024. doi:10.11764/j.issn.1672-1926.2016.06.1014

Ye, T., Chen, A. Q., Hou, M. C., Niu, C. M., and Wang, Q. B. (2021a). Characteristic of the Bodong segment of the Tanlu Fault Zone, Bohai sea area, eastern China: Implications for hydrocarbon exploration and regional tectonic evolution. *J. Petroleum Sci. Eng.* 201, 108478. doi:10.1016/j.petrol.2021.108478

Ye, T., Chen, A. Q., Niu, C. M., Wang, Q. B., and Guo, L. L. (2020a). Characteristics and vertical zonation of large-scale granitic reservoirs, a case study from Penglai oil field in the Bohai Bay Basin, North China. *Geol. J.* 55 (12), 8109–8121. doi:10.1002/gj.3932

Ye, T., Chen, A. Q., Niu, C. M., Wang, Q. B., and Hou, M. C. (2022). Characteristics, controlling factors and petroleum geologic significance of fractures in the archean crystalline basement rocks: A case study of the south jinzhou oilfield in Liaodong Bay depression, north China. *J. Petroleum Sci. Eng.* 208, 109504. doi:10.1016/j.petrol.2021.109504

Ye, T., Chen, A. Q., Niu, C. M., and Wang, Q. B. (2021b). Structural, petrophysical and lithological characterization of crystalline bedrock buried-hill reservoirs: A case study of the southern jinzhou oilfield in offshore Bohai Bay Basin, north China. *J. Petroleum Sci. Eng.* 196, 107950. doi:10.1016/j.petrol.2020.107950

Ye, T., Niu, C. M., Wang, Q. B., Gao, K. S., Sun, Z., and Chen, A. Q. (2020). Identification of metamorphite lithology in paleo buried hill by composition_structure classification: A case from archean in Bohai Sea. *Lithol. Reserv.* 33, 154–164.

Ye, T., Niu, C. M., and Wei, A. J. (2020b). Characteristics and genetic mechanism of large granitic buried-hill reservoir, a case study from PengLai oil field of Bohai Bay Basin, north China. *J. Petroleum Sci. Eng.* 189, 106988. doi:10.1016/j.petrol.2020.106988

Yin, S., Han, C., Wu, Z. H., and Li, Q. M. (2019). Developmental characteristics, influencing factors and prediction of fractures for a tight gas sandstone in a gentle structural area of the Ordos Basin, China. *J. Nat. Gas Sci. Eng.* 72, 103032. doi:10.1016/j.jngse.2019.103032

Yin, S., and Wu, Z. H. (2020). Geomechanical simulation of low-order fracture of tight sandstone. *Mar. Petroleum Geol.* 117, 104359. doi:10.1016/j.marpetgeo.2020.104359

You, L., Xu, S. L., Mao, X. L., Zhong, J., Jiao, Y. Q., and Xiong, X. F. (2021). Reservoir characteristics and genetic mechanisms of the mesozoic granite buried hills in the deep-water of the qiongdongnan basin, northern south China sea. *Acta Geol. sinica-. Engl. Ed.* 95 (1), 259–267. doi:10.1111/1755-6724.14635

Yu, F. S., and Koyi, H. (2016). Cenozoic tectonic model of the Bohai Bay Basin in China. *Geol. Mag.* 153 (5-6), 866–886. doi:10.1017/S0016756816000492

Yue, X. W., Dai, J. S., and Wang, K. (2014). Influence of rock mechanics parameters on fracture development. *J. Geomechanics* 20 (4), 372–378. doi:10.3969/j.issn.1006-6616.2014.04.005

Zeng, L. B., and Li, X. Y. (2009). Fractures in sandstone reservoirs with ultra-low permeability: A case study of the upper triassic yanchang formation in the ordos basin, China. *Am. Assoc. Pet. Geol. Bull.* 93 (4), 461–477. doi:10.1306/09240808047

Zeng, W. T., Zhang, J. C., Ding, W. L., Zhao, S., Zhang, Y. Q., Liu, Z. J., et al. (2013). Fracture development in Paleozoic shale of Chongqing area (South China). Part one: Fracture characteristics and comparative analysis of main controlling factors. *J. Asian Earth Sci.* 75 (5), 251–266. doi:10.1016/j.jseaes.2013.07.014

Zhang, C., Yang, H. X., Feng, J., and Liu, J. L. (2019). Granitic gneiss domes from the Paleoproterozoic orogen in eastern Liaoning: The typical structural styles in hot orogem. *Acta Petrol. Sin.* 35, 2926–2942. doi:10.18654/000-0569/2019.09.20

Zhang, X. M., Shi, W. Z., Hu, Q. H., Zhai, G. Y., Wang, R., Xu, X., et al. (2020). Developmental characteristics and controlling factors of natural fractures in the lower paleozoic marine shales of the upper Yangtze Platform, southern China. *J. Nat. Gas Sci. Eng.* 76, 103191. doi:10.1016/j.jngse.2020.103191

Zhao, G., Ding, W. L., Sun, Y. X., Wang, X. H., Tina, L., Shi, S. Y., et al. (2020). Fracture development characteristics and controlling factors for reservoirs in the Lower Silurian Longmaxi Formation marine shale of the Sangzhi block, Hunan Province, China. *J. Petroleum Sci. Eng.* 184 (0), 106470. doi:10.1016/j.petrol.2019.106470

Zhao, K. K., Jiang, P. F., Feng, Y. J., Sun, X. D., Cheng, L. X., and Zheng, J. W. (2021). Investigation of the characteristics of hydraulic fracture initiation by using maximum tangential stress criterion. *J. Min. Strata Control Eng.* 3 (2), 023520. doi:10.13532/j.jmsce.cn10-1638/td.20201217.001

Zhao, X., Hu, X., Xiao, K., Jia, Y., and Amp, P. E. (2018). Characteristics and major control factors of natural fractures in carbonate reservoirs of Leikoupo Formation in Pengzhou area, Western Sichuan Basin. *Oil Gas Geol.* 39 (1), 30–39,152. SINOPEC. doi:10.11743/ogg20180104

Zhao, X. Z., Jin, F. M., Wang, Q., and Bai, G. P. (2015). Buried-hill play, jizhong subbasin, Bohai Bay Basin: A review and future propespectivity. *Am. Assoc. Pet. Geol. Bull.* 99 (1), 1–26. doi:10.1306/07171413176

Zheng, H., Zhang, J., and Qi, Y. (2020). Geology and geomechanics of hydraulic fracturing in the Marcellus shale gas play and their potential applications to the Fuling shale gas development. *Energy Geosci.* 1 (1–2), 36–46. doi:10.1016/j.engeos.2020.05.002

Zhou, L. H., Li, S. Z., Liu, J. Z., and Gao, Z. P. (2003). The yanshanian structural style and basin prototypes of the mesozoic Bohai Bay Basin. *Prog. Geophys.* 2003 (4), 692–699. doi:10.1016/S0955-2219(02)00073-0

Zhou, X. H., Xiang, H., Yu, S., Wang, G., and Yao, C. H. (2005). Reservoir characteristics and development controlling factors of JZS Neo-Archean metamorphic buried hill reservoir in Bohai Sea. *Petroleum Explor. Dev.* 32 (6), 17–20. doi:10.3321/j.issn:1000-0747.2005.06.004

Zhu, R. X., Zhang, H. F., Zhu, G., Meng, Q. R., Fan, H. R., Yang, J., et al. (2017). Craton destruction and related resources. *Int. J. Earth Sci.* 106 (7), 2233–2257. doi:10.1007/s00531-016-1441-x

Zou, H. Y., Zhao, C. M., Yin, Z. J., Cai, Y. J., and Teng, C. Y. (2013). Outcrop model of fracture development in neoarchean crystalline buried hill in Bohai Bay Basin. *Nat. Gas. Geosci.* 24 (5), 879–885. CNKI:SUN:TDKX.0.2013-05-002.

Frontiers in Earth Science

Investigates the processes operating within the major spheres of our planet

Advances our understanding across the earth sciences, providing a theoretical background for better use of our planet's resources and equipping us to face major environmental challenges.

Discover the latest Research Topics

See more →

Frontiers

Avenue du Tribunal-Fédéral 34
1005 Lausanne, Switzerland
frontiersin.org

Contact us

+41 (0)21 510 17 00
frontiersin.org/about/contact